



UNITED NATIONS
UNIVERSITY



ORKUSTOFNUN

Geothermal Training in Iceland *2014*



Reports of the 6-month UNU Fellows
at the United Nations University
Geothermal Training Programme, 2014



UNITED NATIONS
UNIVERSITY

UNU-GTP

Geothermal Training Programme

Orkustofnun, Grensásvegur 9
IS-108 Reykjavík, Iceland

Geothermal Training in Iceland 2014

**Reports of the 6-month UNU Fellows at the
United Nations University
Geothermal Training Programme in 2014**

*Edited by
Málfríður Ómarsdóttir,
Lúdvík S. Georgsson and
Ingimar G. Haraldsson*

**ISBN 978-9979-68-370-4
ISSN 1670-7400**

The photo on the front page shows the Fellows of the 36th annual UNU Geothermal Training Programme in 2014 in Nordurárdalur, W-Iceland, with Mt. Baula rhyolitic dome in the background.

Back row from left: Ali Hosseinzadeh (Iran), Jaime Hernandez (El Salvador), Hilary Mwawasi (Kenya), George M. Dayan (Kenya), Leon Ntihabose (Rwanda), Abdelrahman Ali Osman (Sudan), Abraham Khaemba (Kenya), Daniel Gorfie (Ethiopia), Valdemar de Viveiros Pereira (Portugal), Luo Chao (China), Miguel Calderon Torres (Ecuador).

Mid row: Yid-Lai Zelada (El Salvador), Maria da Graça Rangel (Portugal), Melissa Nkapieni (Kenya), Miyir Mohamed (Djibouti), Moira Bawasu (Papua New Guinea), Fatumati Mnzava (Tanzania), Alice Uwase (Rwanda), Melissa A. de Freitas (St. Vincent & the Grenadines), Maureen Ambunya (Kenya).

Front row: Billy Awili Oketch (Kenya), Emily Kahiga (Kenya), Samuel N'gan'ga (Kenya), Djama Robleh Djama (Djibouti), Leakey Auko (Kenya), Melese Mekonnen (Ethiopia), Felix Nzioka (Kenya), Daniel Villarroel Camacho (Bolivia), Edwin Wanyonyi (Kenya).

INTRODUCTION

The 36th annual session of UNU-GTP was held from April to October 2014. A total of twenty nine UNU Fellows from fourteen countries in six continents completed the traditional six-month courses. They came from Bolivia (1), China (1), Djibouti (2), Ecuador (1), El Salvador (2), Ethiopia (2), Iran (1), Kenya (11), Papua New Guinea (1), Portugal (2), Rwanda (2), St. Vincent and the Grenadines (1), Sudan (1), and Tanzania (1). The UNU Fellows were trained in six lines of specialization in 2014, in: Chemistry of Thermal Fluids (7 Fellows), Reservoir Engineering (6), Drilling Technology (5), Geothermal Utilization (5), Borehole Geology (4) and Environmental Science (2). They were all on fellowships from the Icelandic Government and the UNU. Nine UNU Fellowships were co-funded by the Kenya Electricity Generating Company (KenGen) and Geothermal Development Company (GDC) in Kenya, two Portuguese from the Azores were co-funded by the EES-Grants system, and one from Ethiopia was co-funded by ICEIDA. Five new countries were added in the 6-month training in 2014, UNU Fellows from Bolivia and Ecuador were the first to come from S-America, while other new countries include St. Vincent and the Grenadines, Sudan and Portugal. Thus, during 1979-2014, 583 scientists and engineers from 58 countries have completed the annual six-month courses, or equivalent. Of these, 37% have come from countries in Asia, 36% from Africa, 15% from Latin America and the Caribbean, 11% from Central and Eastern Europe, and 1% from Oceania. Among them have been 118 women (20%). Over 90 professionals have received shorter training in Iceland (2 weeks to 4 months).

Seventeen former UNU Fellows (from El Salvador 1, Ethiopia 1, Kenya 9, Malawi 2, Nicaragua 1, Rwanda 1 and Tanzania 2) undertook MSc studies in 2014 under cooperation agreements with the University of Iceland, and Reykjavík University. The traditional six month courses at the UNU-GTP constitute 25% of the MSc studies. Five (1 from El Salvador and 4 from Kenya) defended their MSc thesis, and seven started their MSc studies in 2014. Forty fellows had completed an MSc degree from the University of Iceland at the end of 2014, under a Fellowship from UNU-GTP. Two Fellows continued their PhD studies in 2014. Both are from Kenya.

Our annual UNU Visiting Lecturer this year was Dr. Malcolm Grant, a reservoir engineer and one of New Zealand's foremost geothermal experts. He gave a series of lectures on reservoir engineering and geothermal development.

The seventh event in the UN Millennium series of Short Courses / Workshops for the Americas was the "*Short Course VI on Utilization of Low- and Medium-Enthalpy Geothermal Resources and Financial Aspects of Utilization*" which was organized and conducted by the UNU-GTP and LaGeo S.A. in Santa Tecla, El Salvador in March 23-29, 2014. The lecturers came from El Salvador (12), Iceland (4), Costa Rica (2), Mexico (2), Nevis (1), Kenya (1), and World Bank (1). The number of registered participants (apart from lecturers) was 55 in all, from Chile (4), Colombia (2), Costa Rica (3), Dominica (1), Ecuador (2), Guatemala (2), Honduras (1), Mexico (3), Montserrat (1), Nevis (2), Nicaragua (5), Peru (1), others (2) and the host country El Salvador (26). This was the first official UNU-GTP event for Montserrat to participate in.

The tenth annual Millennium event in Africa, "*Short Course IX on Exploration for Geothermal Resources*", was held in Kenya, November 2-23, 2014. This was a well-attended event with 58 participants from 18 African countries (including Yemen) plus 56 lecturers and field instructors (mostly from Kenya, but four from Iceland (ISOR and UNU-GTP), and six from the neighbouring countries (Ethiopia (2), Eritrea, Tanzania, Rwanda and Uganda). Zimbabwe was a new country participating for the first time in a UNU-GTP events. The Short Course was co-hosted by the UNU-GTP, KenGen and GDC. The course was very well received by the participants, who were also impressed by the great development of geothermal taking place in Kenya.

UNU-GTP's activities in customer-designed courses continued in 2014. The beginning of the year saw the final stage of the *On-Site Training in Borehole Geology, Environmental Sciences and Drilling*

Supervision in Rwanda, during the geothermal drilling project in Karisimbi in Rwanda, which ended in March. The first new event was the *Workshop for Geothermal Development Donors* held in Iceland on May 27-28. The workshop was financed by the Icelandic International Development Agency (ICEIDA) and was organized as a follow-up to a Donors Collaboration Meeting jointly hosted by the African Union and ICEIDA. Two short courses, the first of an extensive series through 2014-2016, funded by the EEA-Grant system were held in the Azores of Portugal. The first one was the double event *Workshop on Geothermal for Decision-Makers* and *Short Course I on Geological Exploration of Geothermal Fields*, held in September 8-20, the second one the *Short Course II on Geothermal Utilization and Geothermal Power Plants*, held in November 17-29. Finally, UNU-GTP held a *Short Course on Geothermal Exploration* in Mexico during November 24-29 in cooperation with the Mexican Centre of Innovation in Geothermal Energy (CeMIEGeo), which also financed the course.

The teaching and research supervision of the UNU-GTP in 2014 was carried out as follows: by geothermal specialists from ISOR (Iceland GeoSurvey) 55%, the University of Iceland and Reykjavik University, 15%, and specialists at other institutions, energy utilities and consulting engineering offices, about 30%. Many thanks are due to the teachers and supervisors and their institutions. The availability of top quality supervisors for the various lines of studies offered is of vital importance to the UNU-GTP operations. Warm thanks are also due to the permanent staff, Thórhildur Ísberg, Ingimar G. Haraldsson, Málfríður Ómarsdóttir, María S. Gudjónsdóttir and Markús A.G. Wilde.

Finally, we want to remind the readers that the reports presented here are written as a part of an academic exercise, and in most cases under a considerable time pressure. The reports have been written under close guidance of the supervisors. We are grateful for the dedication of the UNU Fellows and the teachers in their work at the UNU Geothermal Training Programme. Furthermore, we would like to point out that all the reports of the UNU-GTP from the start in 1979 are available through our website: www.unugtp.is, where they are published in colour.

With warmest regards from Iceland,
Lúdvík S. Georgsson, director

Information about the UNU Geothermal Training Programme

The Geothermal Training Programme of the United Nations University has operated at Orkustofnun (the National Energy Authority) in Iceland since 1979 with six months annual courses for professionals who mostly come from the developing countries. Candidates must have a minimum of one year practical experience in geothermal work in their home countries prior to the training, and, preferably, they should be within 40 years of age. Specialized training has been given in geological exploration, borehole geology, geophysical exploration, borehole geophysics, reservoir engineering, environmental studies, chemistry of thermal fluids, geothermal utilization, and drilling technology. Each trainee attends only one specialized course. The training is conducted in English.

The hallmark of the training is to give university graduates engaged in geothermal work very intensive on-the-job training in their chosen fields of specialization. The trainees work side by side with geothermal professionals in Iceland, mostly staff members of ISOR – Iceland GeoSurvey, an agency actively working on most aspects of geothermal exploration and development. The training is tailor-made for the individual and the needs of his/her institution/country. The aim is to assist developing countries with significant geothermal potential to build up groups of specialists that cover most aspects of geothermal exploration and development. Priority is given to candidates from institutions where geothermal work is already under way. All candidates are selected by private interviews and receive scholarships (covering tuition, per diem and international travel) financed by the Government of Iceland and the UNU, or others. Upon completion of their training the participants receive a UNU Certificate. Further description can be found at our internet home page: www.unugtp.is.

TABLE OF CONTENTS

7.	Ambunya, M.N.: Natural-state model update of Olkaria Domes geothermal field.....	1
8.	Auko, L.O.: Evaluation of fluid - mineral interaction in the Menengai geothermal system, Central Rift, Kenya	39
9.	Bawasu, M.L.: Borehole stratigraphy and alteration mineralogy of well HE-6, Hellisheidi, SW-Iceland	65
10.	Calderón Torres, M.A.: Study of Chachimbiro and Chacana geothermal projects, Ecuador, and volumetric assessment.....	91
11.	Dayan, G.M.: Drilling fluid design for geothermal wells.....	123
12.	De Freitas, M.A.: Geothermal resource assessment of the Wotten Waven geothermal field – Dominica, West Indies	157
13.	Gorfie Beyene, D.: Electrical control and protection system of geothermal power plants	187
14.	Hernández Ayala, J.A.: Gas - mineral equilibrium in the Berlín geothermal field, El Salvador	209
15.	Hosseinzadeh, A.: Air quality impact assessment: H ₂ S dispersion modelling for the Sabalan geothermal power plant, NW-Iran	237
16.	Kahiga, E.W.: Borehole geology and hydrothermal alteration mineralogy of well MW-13, Menengai geothermal field, Kenya	261
17.	Khaemba, A.W.: Well design, cementing techniques and well work-over to land deep production casings in the Menengai field.....	295
18.	Luo Chao: Thermodynamic and thermoeconomic optimization of a geothermal power plant in Sichuan, China	325
19.	Mekonnen Berehannu, M.: Geochemical interpretation of discharge from Reykjanes wells RN-29 and RN-32, SW-Iceland.....	351
20.	Mnzava, F.J.: Subsurface geology and hydrothermal alteration of well HE-4, Hellisheidi geothermal field, SW- Iceland	369
21.	Mohamed Abdillahi, M.: Predicting output curves for deep wells in the Asal Rift, Djibouti.	399
22.	Mwawasi, H.M.: Feasibility study of using a downhole pumping system in Menengai well MW-17 for geothermal utilization	421
23.	Ng'ang'a, S.I.: Cementing processes in geothermal well drilling: application and techniques.....	445
24.	Nkapiiani, M.N.: Application of stable isotope geochemistry to tracing recharge and flow systems of fluids in the Olkaria geothermal field, Kenya	483

25.	Ntihabose, L.: Well test analysis and temperature and pressure monitoring of Krafla and Nesjavellir high-temperature geothermal fields, Iceland	505
26.	Nzioka, F.K.: Preliminary design of a hot water distribution system for greenhouse heating, Olkaria, Kenya	535
27.	Awili Oketch, B.: Analysis of stuck pipe incidents in Menengai	567
28.	Ali Osman, A.: Increased exergetic efficiency by using a back pressure turbine for high wellhead pressures at Hellisheidi geothermal power plant	595
29.	Rangel, M.G.V.M.: Temperature model and tracer test analysis for the Ribeira Grande geothermal system, São Miguel Island, Azores	615
30.	Robleh Djama, D.: Borehole geology and alteration mineralogy of well RN-12, Reykjanes geothermal field, SW-Iceland.....	643
31.	Uwase, A.: Preliminary Terms of Reference (TOR) and Environmental Impact Assessment (EIA) of geothermal exploration drilling in Bugarama, Rwanda.....	675
32.	Villarroel Camacho, D.G.: Geochemical studies of geothermal fluid and evaluation of well test results from wells SM-01, SM-02 and SM-03, Sol de Mañana field, geothermal project, Laguna Colorada, Bolivia	697
33.	Viveiros Pereira, V.: Calcium carbonate scaling control in geothermal well PV8 in Sao Miguel, Azores, combining chemical inhibition and mechanical reaming.....	721
34.	Wanyonyi, E.W.: Fluid-rock interaction and initial aquifer geochemistry in the Olkaria geothermal system	745
35.	Zelada Quán, Y.L.: Analysis of variations in the characteristics of the geothermal fluid produced from the Sudureyri low-temperature geothermal system in NW-Iceland.....	765



UNITED NATIONS
UNIVERSITY

UNU-GTP

Geothermal Training Programme

Orkustofnun, Grensasvegur 9,
IS-108 Reykjavik, Iceland

Reports 2014
Number 7

NATURAL-STATE MODEL UPDATE OF OLKARIA DOMES GEOTHERMAL FIELD

Maureen Nechesa Ambunya

Kenya Electricity Generating Company – KenGen

P.O. Box 785 – 20117

Naivasha

KENYA

mambunya@kengen.co.ke

ABSTRACT

The Olkaria Domes geothermal field is located at the southeast edge of the Greater Olkaria geothermal area (GOGA). The area is bound approximately by the Ol’Njorowa gorge to the west and a ring of domes to the east and south of the field. The Olkaria Domes field is a high-temperature field with most of the wells producing two-phase fluid. This report aims at discussing and updating the natural-state model of the Olkaria Domes field reservoir, incorporating data from recently drilled wells. Several 3-D natural-state numerical models of the entire GOGA geothermal system have been developed, the first in 1987 by G.S. Bödvarsson and K. Pruess. Downhole profiles of temperature and pressure in the wells were interpreted to obtain the natural state of the reservoir in the wells’ locale. Previous work was incorporated and an inclusive model developed that forms the basis of a simple numerical model for the natural state that could provide the standard, pre-exploitation natural state of the Olkaria Domes field reservoir. In this report, the main focus will be on updating the natural-state model of the Olkaria Domes field, equivalent to the undisturbed formation before exploitation of the resource began. Previous models have been developed, the latest completed in 2012 by the Mannvit/ÍSOR/Vatnaskil/Verkís consortium.

1. INTRODUCTION

The Greater Olkaria geothermal area (GOGA) is one of the most exploited geothermal systems in the world. It is located in the East African Rift system that extends from the afar triple junction at the Gulf of Aden in the north to the south in Beira, Mozambique (Abbate et al., 1995). The rift is part of a continental divergent zone where spreading results in the thinning of the crust and the eruption of lavas and associated volcanic activities (Lagat, 2004). There are two divisions in the East African Rift valley: the Eastern and the Western rift valleys. Geothermal activity is rampant in many areas of the Kenyan rift, which is a segment of the East African Rift that runs from Lake Turkana to Lake Natron in northern Tanzania. There are about fourteen geothermal prospects (Figure 1) that are associated with Quaternary volcanic centres occurring in the axial region of the Kenyan rift (Omenda, 1998). Currently, two geothermal prospect areas are under exploitation for electricity production: the GOGA area and the Eburru geothermal field. In the Menengai geothermal field, drilling activities are currently ongoing in

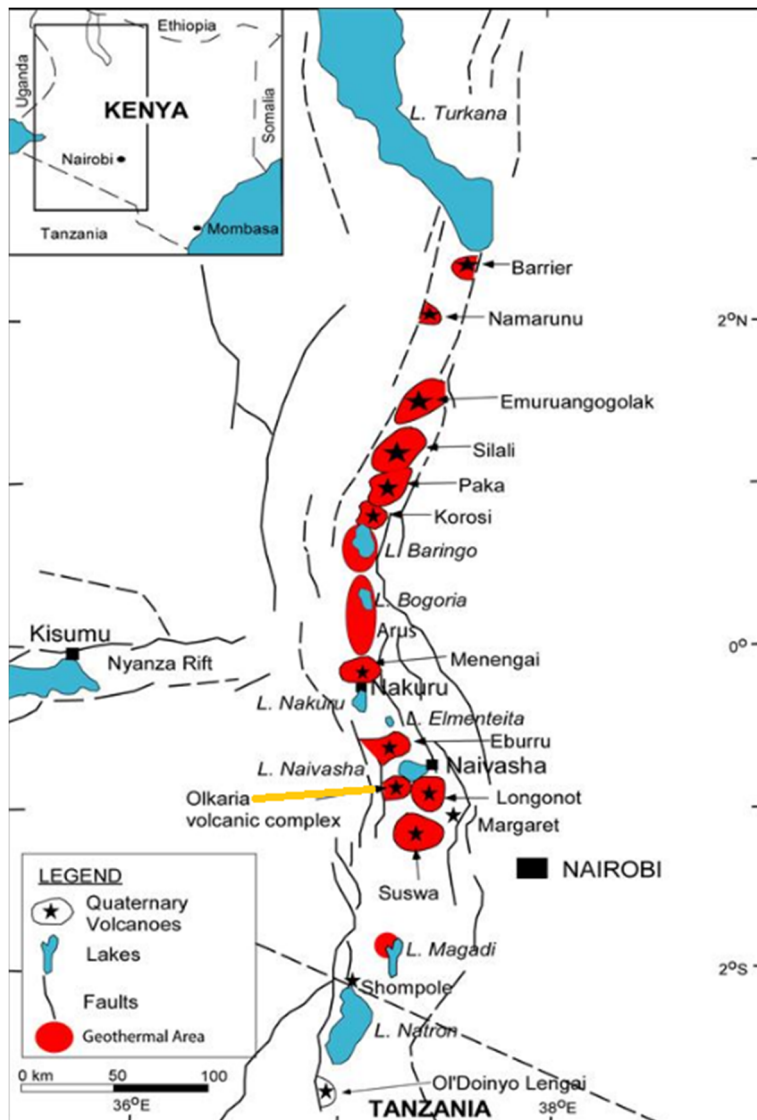


FIGURE 1: Location of Greater Olkaria geothermal area and other volcanic centres in Kenya (Ofwona et al., 2006)

preparation for future exploitation. GOGA is in the southern part of the Kenyan rift, located to the south of Lake Naivasha and roughly 120 km northwest of Nairobi city.

In the 1950s, exploration of geothermal resources in Kenya started with geological surveys in the region between Olkaria and Lake Bogoria in the northern part of the rift. The result was the drilling of two exploration wells, X-1 and X-2, in Olkaria field in which high temperatures were encountered at depth (Kenya Power Company, 1984). The success of these wells lead to further studies including surface exploration and resource capacity assessments. By 1976, six deep wells had been drilled and the field was eventually subdivided into various prospect sectors for easier development. The sectors were named with respect to Olkaria hill as shown in Figure 2.

In 1981 the first 15 MWe generating unit harnessing steam from the Olkaria East field was commissioned. Later, in 1982 and 1985, two additional units (units 2 and 3), each 15 MWe, were commissioned, respectively. Olkaria II, located in the Olkaria Northeast sector, was commissioned in 2003, producing 70 MWe. An additional 35 MWe turbine was commissioned

in May 2010, increasing the generating capacity to 105 MWe. Olkaria III, located in the Olkaria West field, currently generates a total capacity of 110 MWe. The first 12 MWe unit at Olkaria III was commissioned in 2000, a second 36 MWe unit was later commissioned in 2009 and the third 52 MWe unit was completed in February 2014. Currently, construction of a fourth 140MWe unit plant in the Olkaria East field is near completion as well as a 140 MWe plant in the Olkaria Domes geothermal field.

2. FIELD REVIEW

2.1 Olkaria Domes field development

KenGen, the state-run power generating company in Kenya, carried out a detailed geo-scientific survey in the Domes sector. The survey undertaken between 1992 and 1997 involved geology, geophysics, and geochemistry as well as heat flow measurements. Analysis of data from this study lead to the siting of three exploration wells, OW-901, OW-902 and OW-903 which were drilled between 1998 and 1999

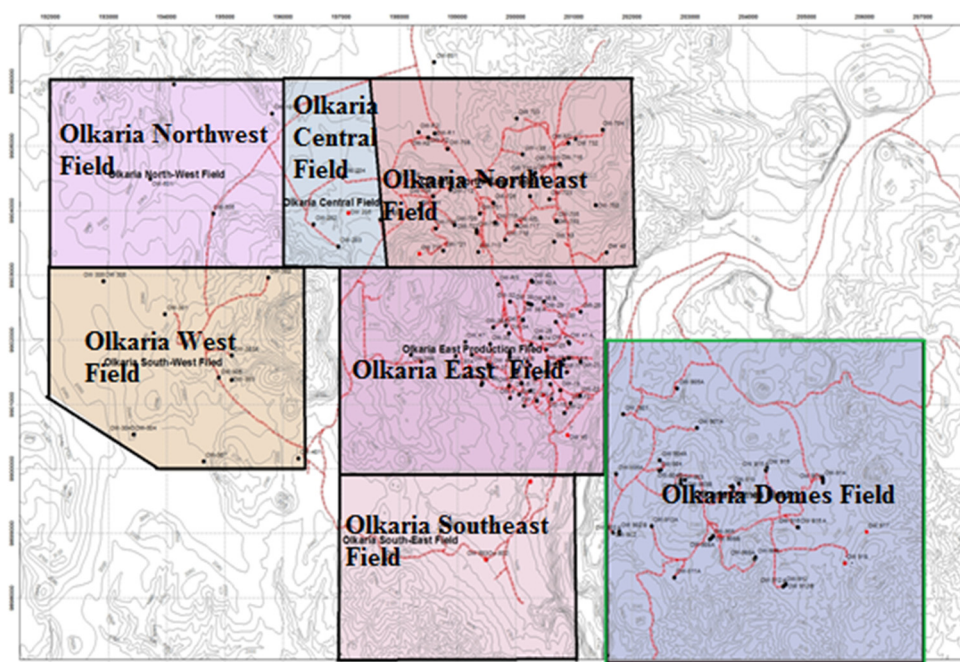


FIGURE 2: Olkaria field subsections

(Lagat, 2004). All three wells were successful and able to discharge steam. Down-hole data from the drilled wells was analysed and additional geophysical surveys were carried out with MT and TEM techniques. The success of the three exploration wells lead to appraisal drilling where six wells were drilled within the field. Since then there have been numerous drilling activities in the field and increased development.

2.2 Geological overview of Olkaria Domes field

Geo-scientific studies conducted over time in the Olkaria field indicate that the field is a remnant of an old caldera complex cut by N-S normal rift faults that became the centre for later eruptions, forming rhyolitic and pumice domes (Ofwona, 2002). The surface and subsurface rocks are dominated by pyroclastics, tuffs, rhyolites and some basalts which may vary considerably from one place to another. Figure 3 shows the structure within the Greater Olkaria volcanic complex. They include the ring

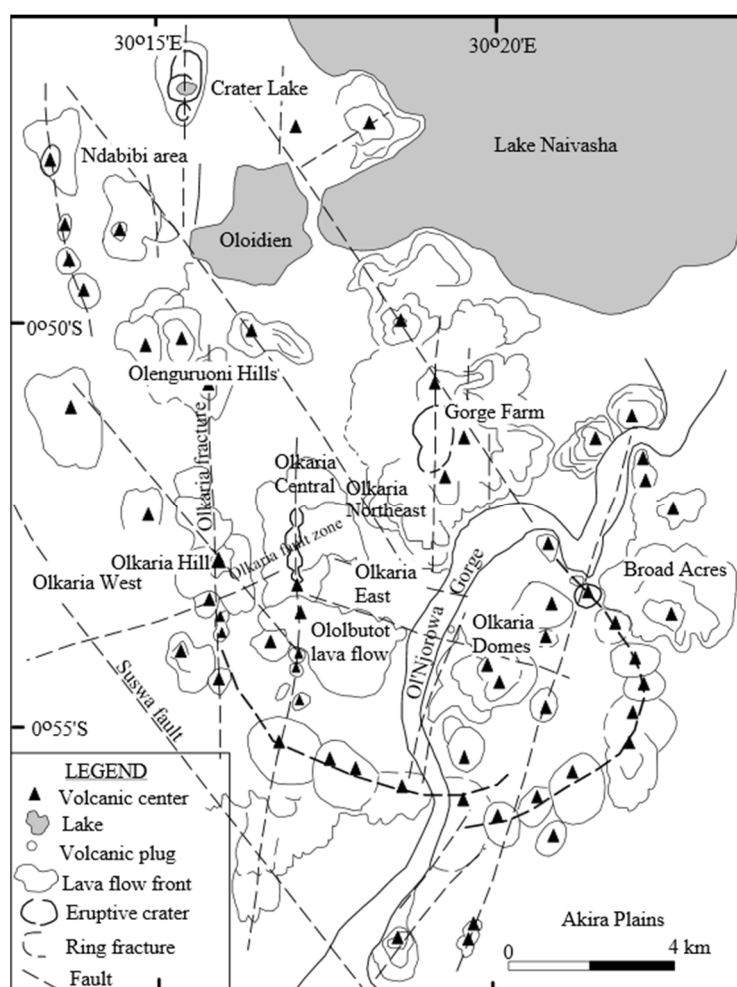


FIGURE 3: Structural map of Olkaria (Lagat, 2004)

structure, the Ol'Njorowa gorge, the ENE-WSW Olkaria fault and N-S, NNE-SSW, NW-SE and WNW-ESE trending faults (Lagat, 2004). In general, faults are very scarce in the Olkaria Domes field but dominate in other parts of the complex. In the Olkaria Domes area there are hydroclastic craters located on the northern part of the field that mark a magmatic explosion edge (Mungania, 1999). The craters form a row over which the extrapolated caldera rim trace (ring structure) passes. The field is also bound by Ol'Njorowa gorge that demarcates the field from the Olkaria East field.

OW-916 is a well drilled in the Olkaria Domes field and exhibits the typical lithology of most of the wells in the field. From Figure 4 we can deduce that the lithology of the Olkaria Domes field is dominated by pyroclastics, tuffs, rhyolites, trachytes and basalts with minor syenite intrusives.

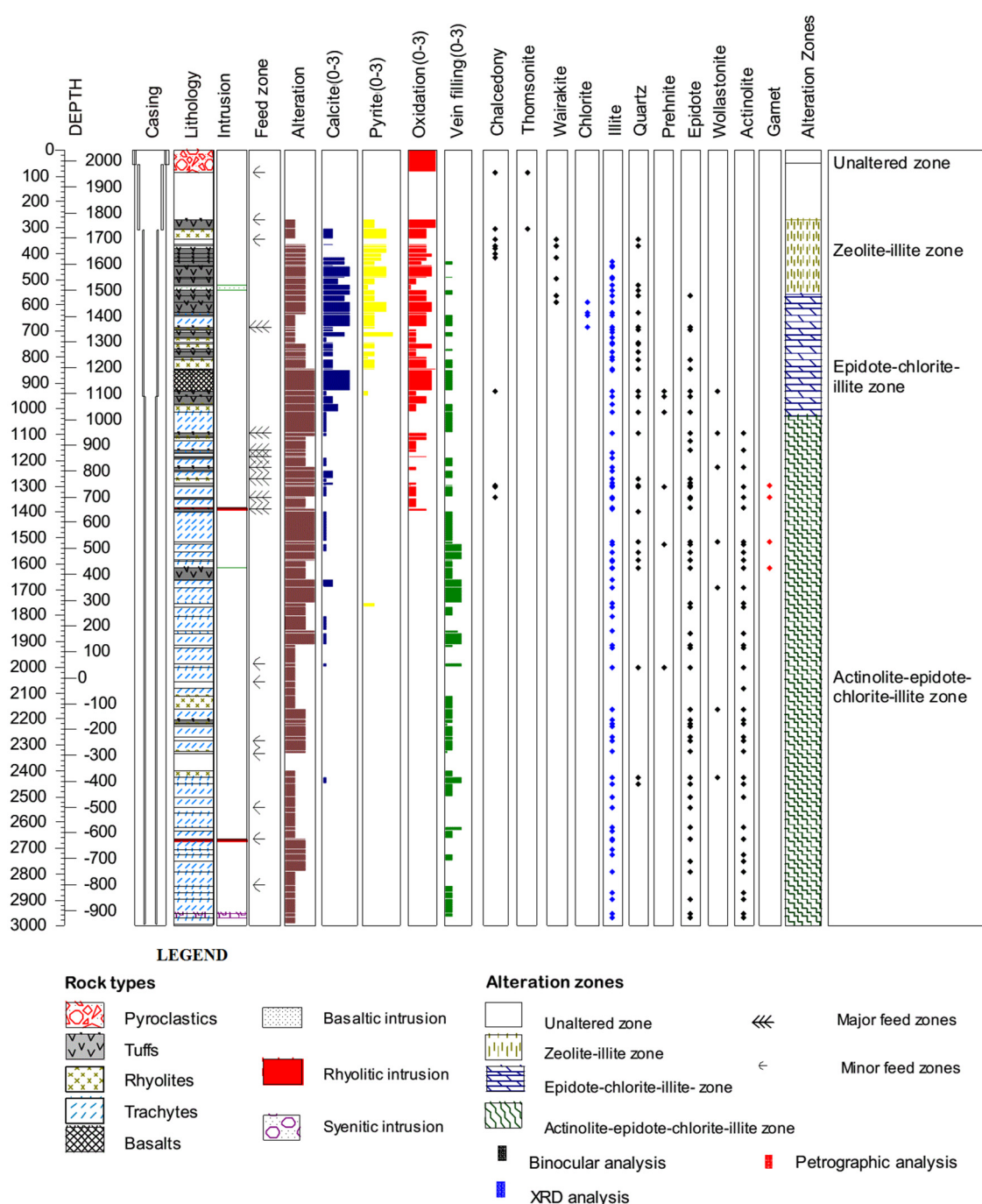


FIGURE 4: Hydrothermal alteration minerals in Well OW-916 (Mwangi, 2012)

2.3 Geophysical overview of Olkaria Domes field

In the analysis based on transient electromagnetic (TEM) and magneto-telluric (MT) soundings, at 0 m a.s.l., the high-temperature alteration (resistive core) dominates in the centre of the Olkaria Domes field (Wanjohi, 2011). In Figure 5 the high-resistivity anomaly of 50–120 Ωm extends over most of the area except in the northern and southern parts. This high-resistivity anomaly can be associated with the dominance of high-temperature alteration minerals (Kandie, 2010) and may indicate an area containing geothermal fluids of relatively high temperatures. Overlying the high-resistivity core is a lower resistivity ($<20 \Omega\text{m}$) layer in the northern and southern parts of the field. This could be a zone of high permeability where hydrothermal alteration is not advanced, suggesting a possible up-flow zone beneath (Wanjohi, 2011).

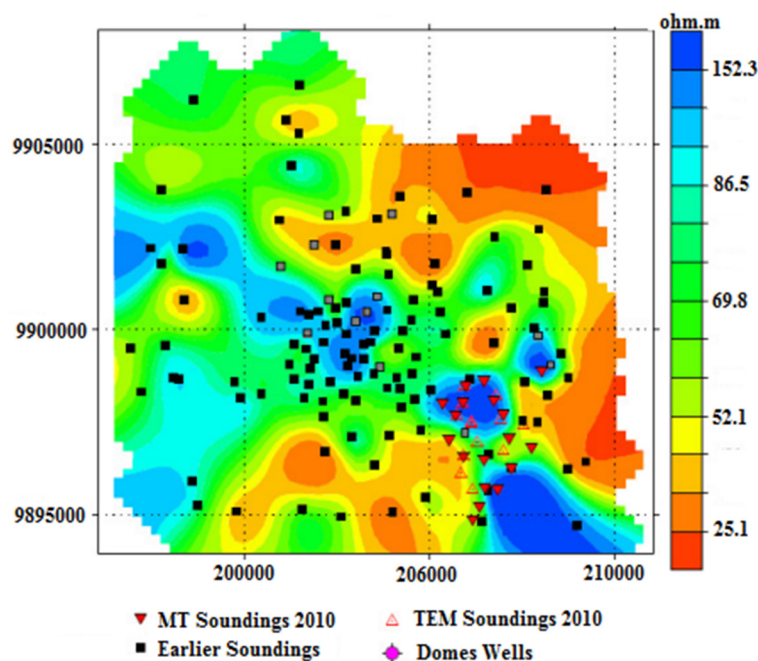


FIGURE 5: Iso-resistivity map of Domes area at sea level (Wanjohi, 2011)

2.4 Geochemical overview of Olkaria Domes

Geothermal fluids in the Olkaria Domes reservoir are bicarbonate in nature and correspond to peripheral waters (Malimo, 2009). The Olkaria Domes fluids seem to plot similarly to those of the Olkaria West and Olkaria Central fields, unlike the wells in the Olkaria East field and in Olkaria Northeast which discharge sodium-chloride type water of a mature nature. Solute and gas geothermometry indicate high temperatures in the range of 250–350°C (Malimo, 2009). Fluid extracted from the Olkaria Domes wells contain low calcium concentrations and high pH. Calcite scaling can be expected to be minimal in these wells but the fluid has to be separated at temperatures above 100°C to prevent silica scaling (Karingithi, 2000). Studies, done by Kamunya et al. (2014), show that wells in the Olkaria Domes field discharge a mixture of chloride and bicarbonate end-member water, as shown in Figure 6. Bicarbonate waters are found in areas to the

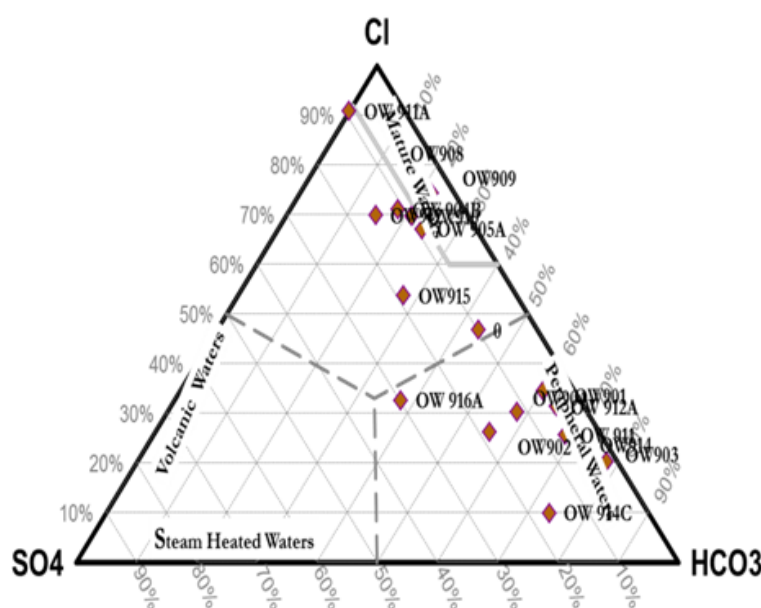


FIGURE 6: Water types of the Domes geothermal area (Kamunya et al., 2014)

northeast and southwest of the Olkaria Domes field. This could be due to the contribution of recharge fluids through the NE-SW faulting and the interpreted buried caldera that forms a concentric series of rhyolitic ash domes in the east, frequently referred to as the ring structure (Kamunya et al., 2014).

2.5 Temperature and pressure in Olkaria Domes geothermal field

Temperature and pressure models have become important tools in the calibration of natural-state models of geothermal systems before exploitation. The temperature plots of a few selected wells in the Olkaria Domes field (Appendix I) illustrate conductive heat flow down to 1000 m depth; below this depth convective flow is dominant. The calculated formation temperature and initial pressure, assumed to be the natural temperature and pressure conditions at the well location, are extrapolated from temperature and pressure measurements for a given well, taking into account the effect of boiling and internal flows. The data obtained is used as a basis for calibration of the numerical model. The location of the wells in the Olkaria Domes field is shown in Figure 7.

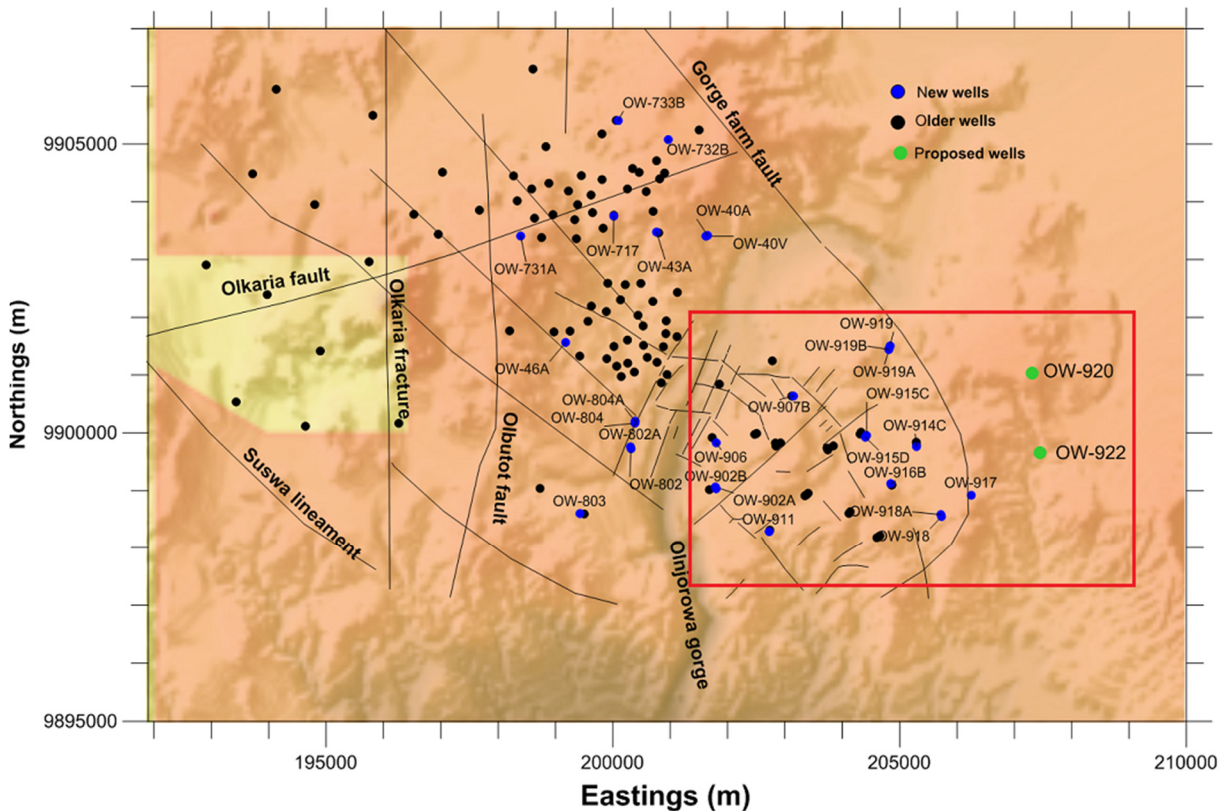


FIGURE 7: Wells in the Greater Olkaria geothermal field; the red box marks the Olkaria Domes field

Figure 8 shows the estimated formation temperature for Olkaria Domes vertical wells. The plot shows that a majority of the wells have the same characteristic nature of conductive heat transfer from the surface to around 1000 m depth, with convective heat flow below that depth.

A vertical cross-section in the NW-SE direction across the Olkaria Domes field is shown in Figure 9a. From the cross-section, an isotherm map was generated, showing the existence of hot plumes around Wells OW-916A, OW-916B, OW-912A, OW-915A, OW-909A, OW-910A, OW-901, OW-921A and OW-904B. These hot plumes of 260°C isotherm reach up to around 1000 m a.s.l. This is also seen in isotherm maps at different depths in Figure 10.

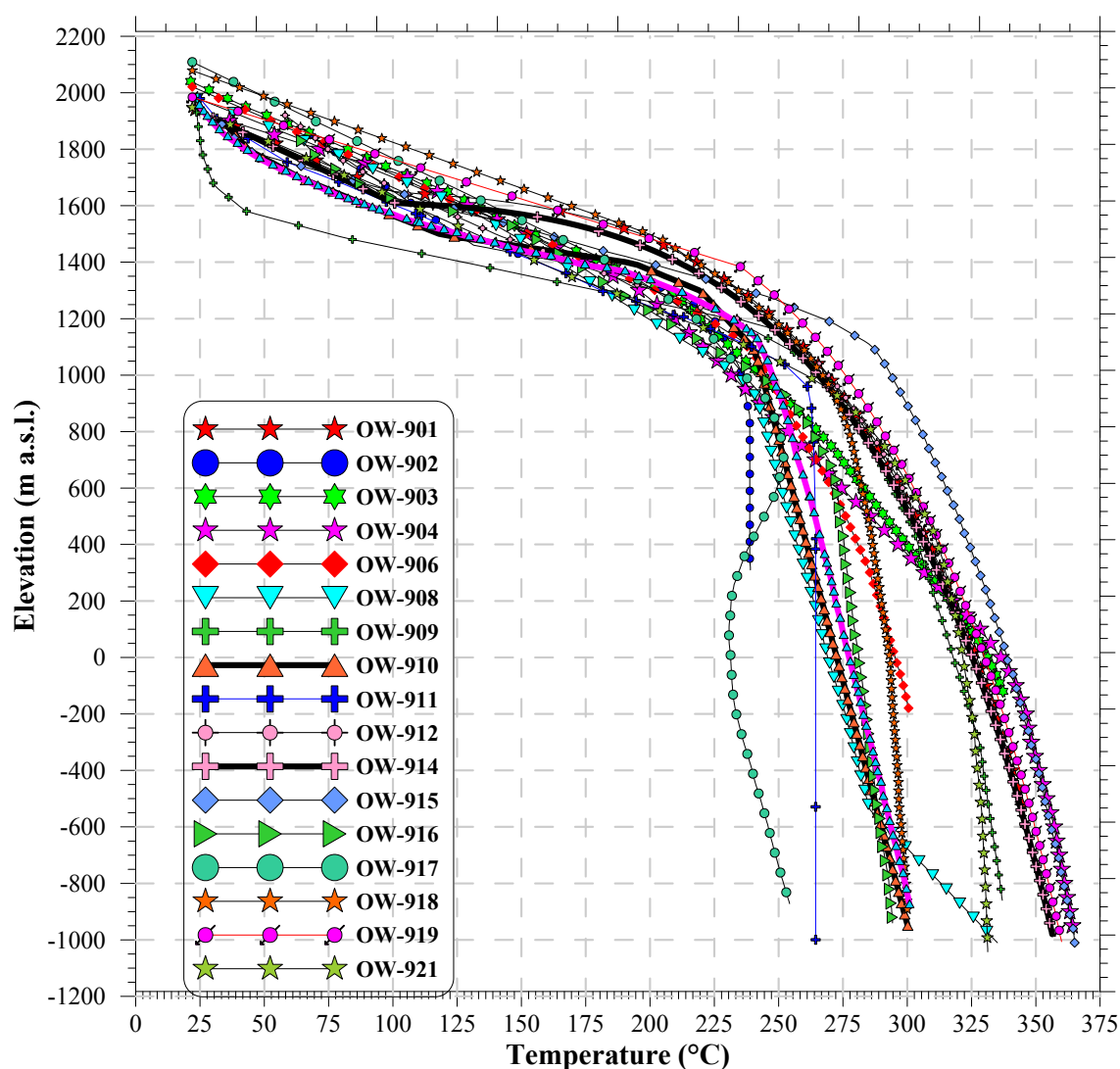


FIGURE 8: Estimated formation temperature plot for Olkaria Domes vertical wells

The isotherms in the southern part of the well field show low temperature around Well OW-911A, and in the southeast and northwest parts of the field they indicate cooling around Wells OW-918A, OW-905A and OW-907B. The isotherms indicate that the main up-flow zone for the Olkaria Domes field is located in the area around Wells OW-914 and OW-915 and eastward. Other minor up-flow zones are observed around Wells OW-901 and OW-904. Slight cooling is observed around Wells OW-910 and OW-916.

Pressure drives the flow of fluids in a reservoir and during production there is usually pressure drawdown in the field. Hence, pressure logging is performed in order to acquire information on the regional geothermal system and determine the initial reservoir pressure before production began (Stefánsson and Steingrímsson, 1980). The pressure logs in the Olkaria Domes wells have been studied and the pressure contours plotted at different depths (Figure 11). High-pressure regions are associated with the upflow zones in the field.

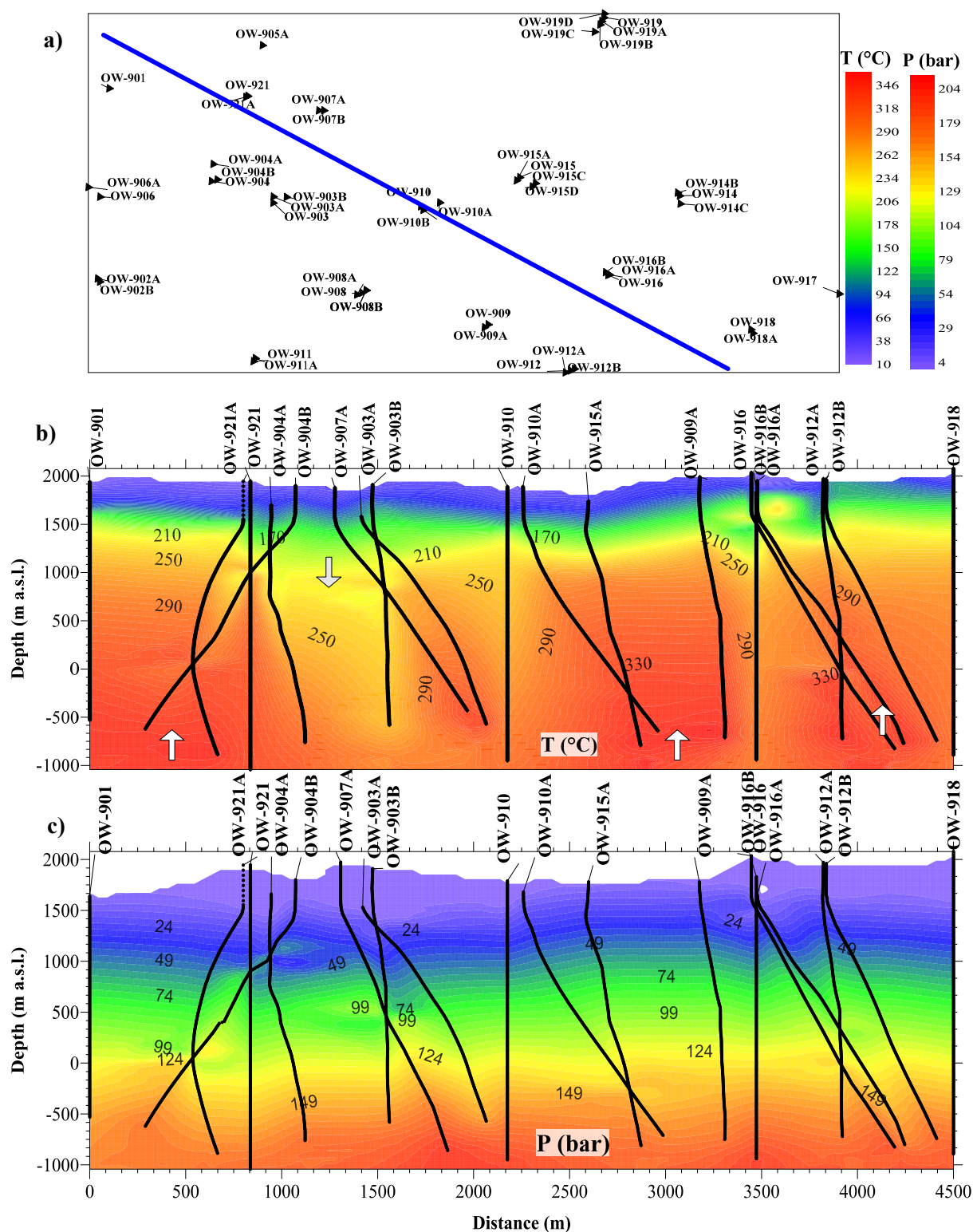


FIGURE 9: NW-SE cross-section; a) location; and vertical contours plotted for b) temperature and c) pressure; arrows indicate estimated direction of flow within the reservoir

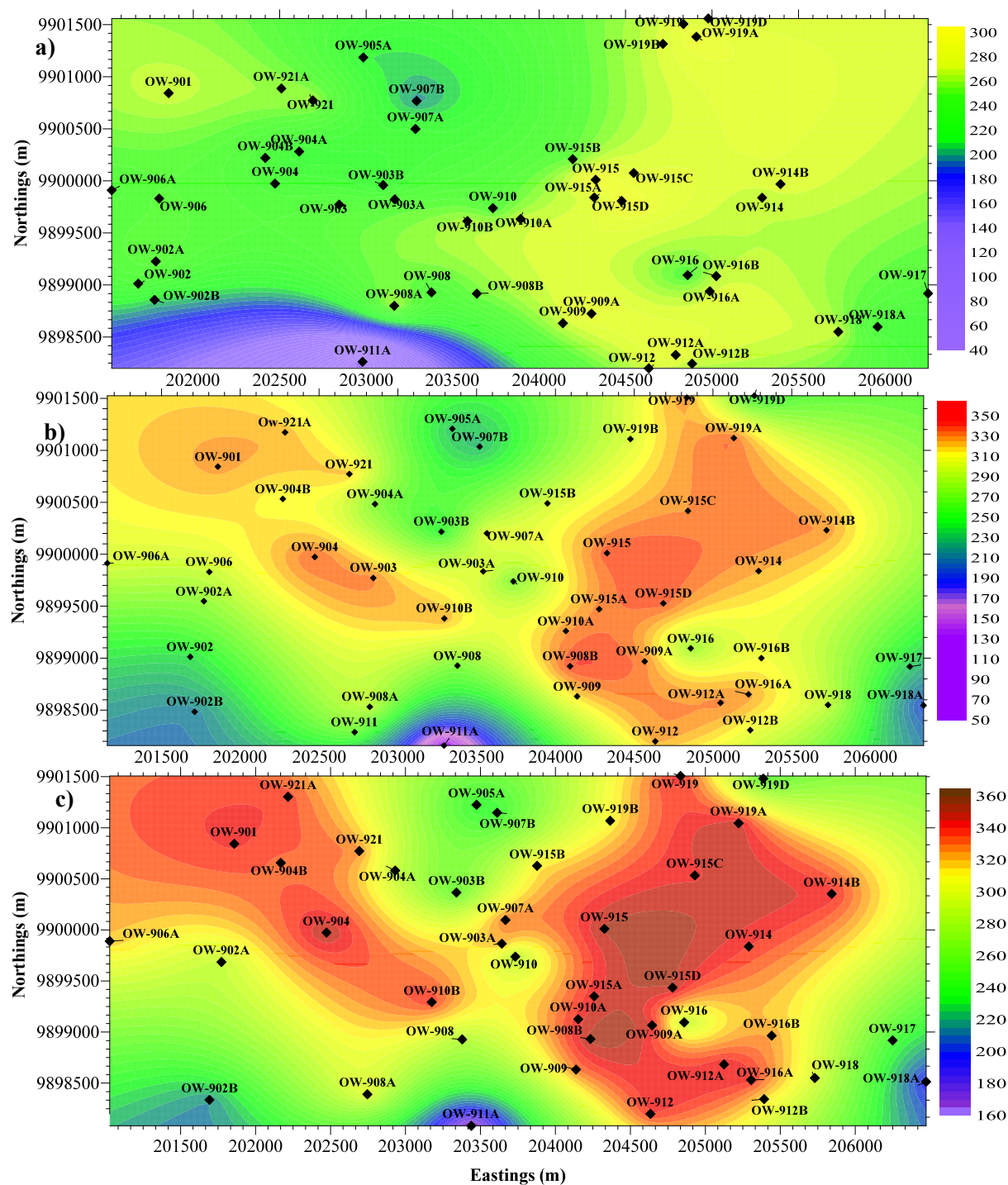


FIGURE 10: Temperature contours at a) 1000 m a.s.l.; b) 0 m a.s.l.; and c) 400 m b.s.l.

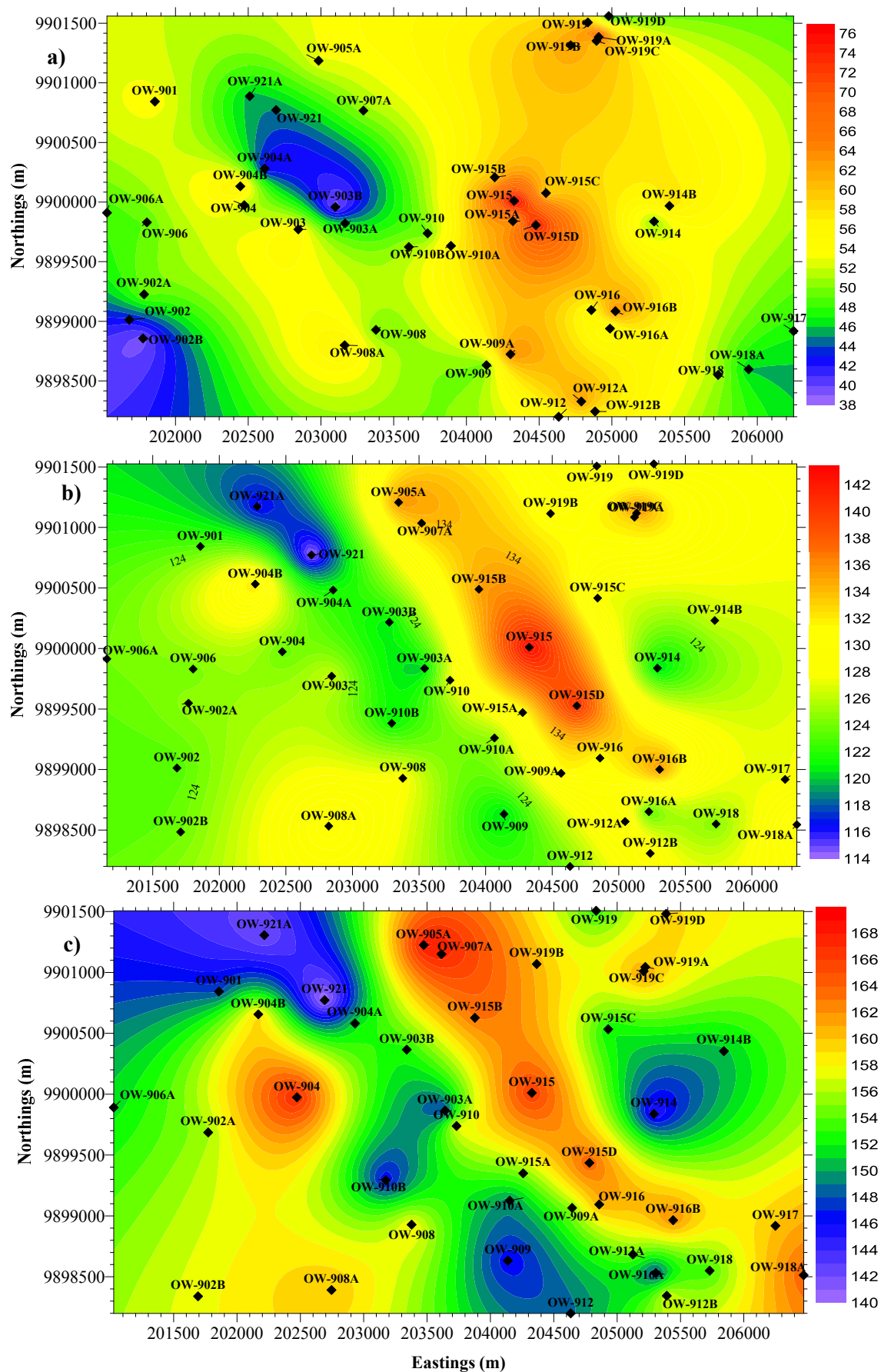


FIGURE 11: Pressure contours at a) 1000 m a.s.l.; b) 0 m a.s.l.; and c) 400 m b.s.l.

3. CONCEPTUAL MODELS

3.1 Fluid and heat flow in hydrothermal systems

Hydrothermal systems are comprised of fluid, heat, and permeability in a naturally occurring geological formation. Geothermal energy is the heat energy kept within the earth's crust and therefore forms the roots of a hydrothermal system. This energy can be accessed through drilling and harnessed using various technologies. The geothermal fluid transports energy from the crust to the surface. Hence, there is transfer of both mass (fluid) and thermal heat that plays a very important role in geothermal energy exploitation. The flow of fluid through porous and fractured media is described by two main equations; the pressure diffusion equation and Darcy's law. Darcy's law describing fluid flow in groundwater systems is given in Equation 1 (Bear, 1979):

$$Q = KA \frac{dh}{dl} \quad (1)$$

Values of K and h can be written in simple form as shown in Equation 2:

$$K = k \left(\frac{\rho g}{\mu} \right), h = \left(\frac{p}{\rho g} + z \right) \quad (2)$$

$$q = \frac{Q}{A} = -k \left(\frac{\rho g}{\mu} \right) * \frac{d}{dl} \left(\frac{p}{\rho g} + z \right) \quad (3)$$

where q is the fluid mass flux vector (kg/s m²), ρ is the fluid density, μ is the dynamic viscosity of the fluid, g is the gravitational constant, Q is the mass flow rate (kg/s), k is the rock permeability (m²), p is the fluid pressure (Pa), A is the cross-sectional area through which fluid flows, z is the force in z direction and l is the distance over which flow occurs.

In Equation 3 there are two forces acting in the direction of flow: the net pressure force and gravitational force in the direction of flow. For mass transfer evaluations as well as reservoir pressure changes in geothermal reservoirs, the pressure differential equation is used. It is a combination of mass conservation and Darcy's law for the mass flow. Equation 4 describes storativity, the property of mass extraction that controls how initial pressure changes occur in geothermal reservoirs. This property varies from one rock type to another.

$$\nabla m = \nabla P V \rho_w \{ \phi c_w + (1 - \phi) c_r \} \quad (4)$$

In the above equation, Δm is the change in mass (kg) stored, Δp is the change in pressure (Pa), ρ_w is the density of water, φ is the porosity, and c_w and c_r are the compressibility of water and rock, respectively.

In heat flow (thermal flow), a general heat conduction equation is given by:

$$Q = -K \nabla T \quad (5)$$

where Q is the heat flux density (J /s m²), K is the thermal conductivity of the material (J /s °C.m) and ∇T is the temperature gradient. Using Fourier's law combined with the principle of conservation of energy, Equation 6 can be derived:

$$\rho \beta \frac{dT}{dt} = \nabla (K \nabla T) + M_p \quad (6)$$

where ρ is the density, β is the heat capacity (J /kg °C) of the material, M is an immersed heat source/sink density (J /s kg), ∇T is the temperature gradient, t is the time and K is the thermal conductivity of the material.

Since the process of heat transport through permeable media in geothermal systems involves heat conduction through the rock matrix, fluid percolation through pores and fracture and heat transfer between the fluid and the rock matrix, an equation of heat transport can be deduced (Axelsson, 2012):

$$\langle \rho\beta \rangle \frac{dT}{dt} = -\beta_w \rho_w \mu \nabla T + \nabla \cdot (K \nabla T) \quad (7)$$

where ρ_w is the density of water, β_w is the heat capacity (J /kg °C) of the water, ∇T is the temperature gradient, t is the time, K is the thermal conductivity of the material, $\langle \rho\beta \rangle$ is the heat capacity of the rock matrix and μ is the dynamic viscosity of the fluid.

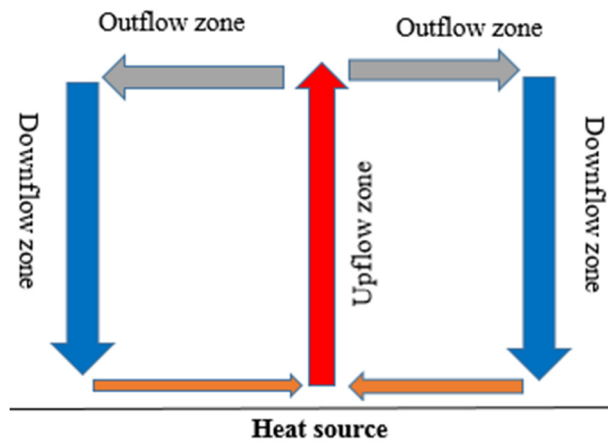


FIGURE 12: Flow characteristics within a cell

In natural-state geothermal systems, free convection is the most common heat transfer process. Due to variations in temperature in geothermal systems, buoyancy forces are produced as a result of variation in density. As meteoric water percolates beneath the earth, it is heated at great depths and rises back up to the surface, causing flow against the decreasing pressure gradient direction. This can be compared to a flow through a single cell (Figure 12).

The flow characteristics within a cell can be summarized by combining Equations 1, 4 and 7 and simplifying them into one function called the Rayleigh number:

$$R_a = \frac{\beta_w \rho_w g c_w \nabla T k h}{\nu K} \quad (8)$$

where R_a is the Rayleigh number, g is gravitational acceleration, c_w is the thermal expansion coefficient for water, k is rock permeability, β_w is the heat capacity of the fluid, ∇T is the temperature difference over a given distance, h is the thickness of the reservoir, ρ_w is the density of water, K is the thermal conductivity of the material and ν is the kinematic viscosity.

This number is used to estimate conditions for the development of a natural-state hydrothermal system. It gives the ratio of buoyancy forces to viscous resistance. For convective flow in a saturated aquifer, $R_a > 4\pi^2$ known as the critical Rayleigh number and the value normally ranges from 100 to 1000 in geothermal systems (Ofwona, 2002). Before exploitation, the initial fluid circulation in the hydrothermal reservoir is controlled by the dynamic balance of mass and heat but, during exploitation, fluid flow is controlled by the pressure gradient created by the discharging well.

3.2 Characteristics of Olkaria Domes wells

Unlike most of the wells in other Olkaria fields, wells in the Olkaria Domes field consist of 20" diameter surface casing down to a depth of 60 m, followed by 13 3/8" diameter anchor casing down to 300 m depth, followed by 9 5/8" diameter production casing down to 800-1200 m depth and finally 7" diameter slotted liners in the production hole (Figure 13). Temperature and pressure logs in the wells indicate that most

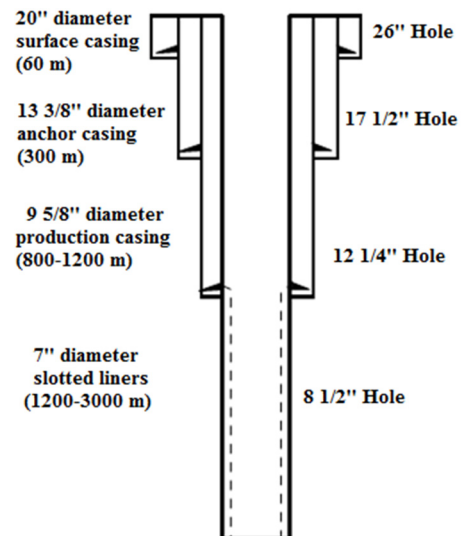


FIGURE 13: Casing design for most Olkaria Domes wells

wells have traversed multiple permeable zones (Figure 14). Due to an overall good permeability of the formation, most of the wells are very good producers. The formation permeability influences the ability of fluid to flow through the feed zones to the well, hence determining the inflow performance.

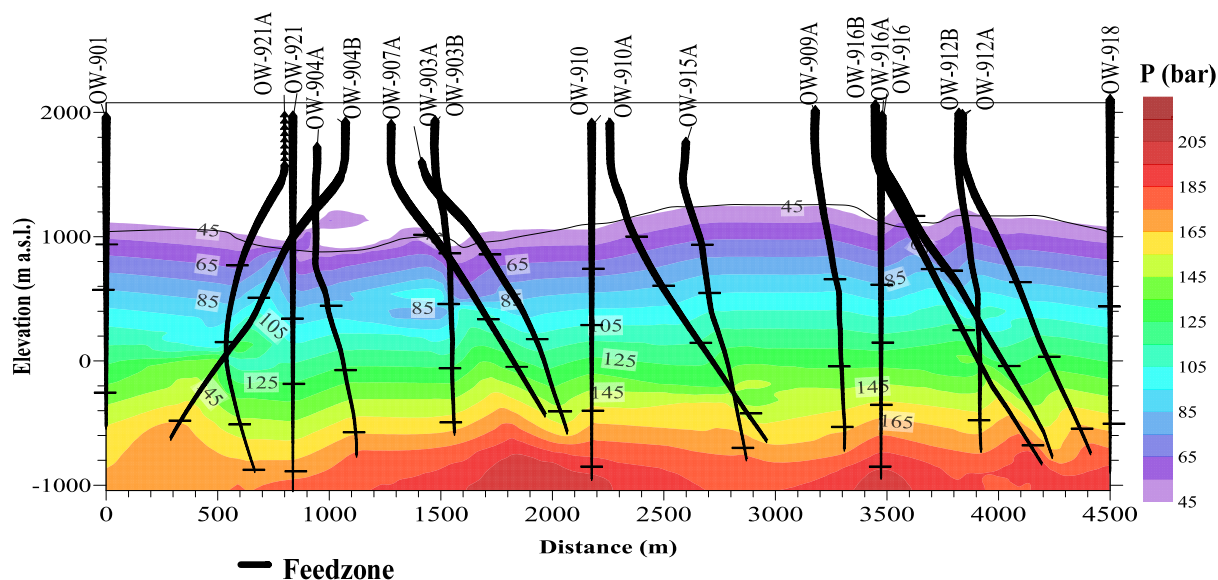


FIGURE 14: Pressure isobars with 50 bar isoline from 1000 m

The discharge test results obtained from discharging Olkaria Domes wells indicate that the fluid from the reservoir is two-phase fluid with high enthalpy. An enthalpy iso-map is shown in Figure 15; the eastern part of the field registers high enthalpy values compared to the western part of the field. This is in agreement with temperature contours and indicates that this eastern region is an up-flow zone within the field.

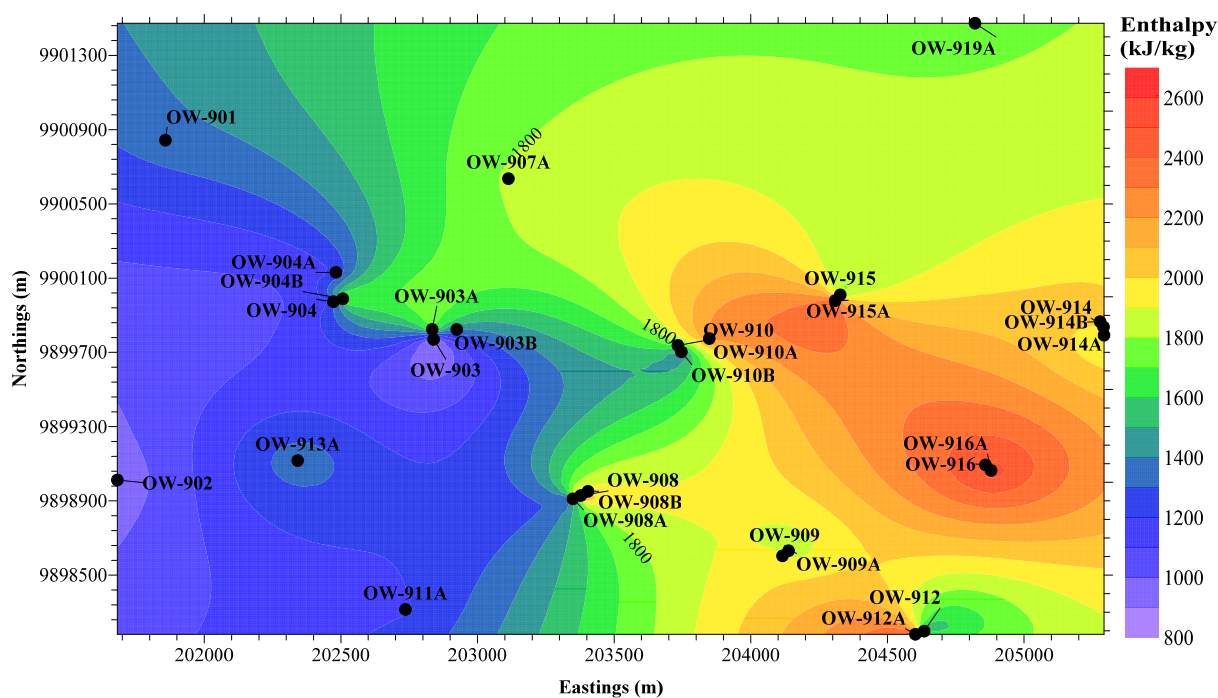


FIGURE 15: Enthalpy distribution in the Olkaria Domes field

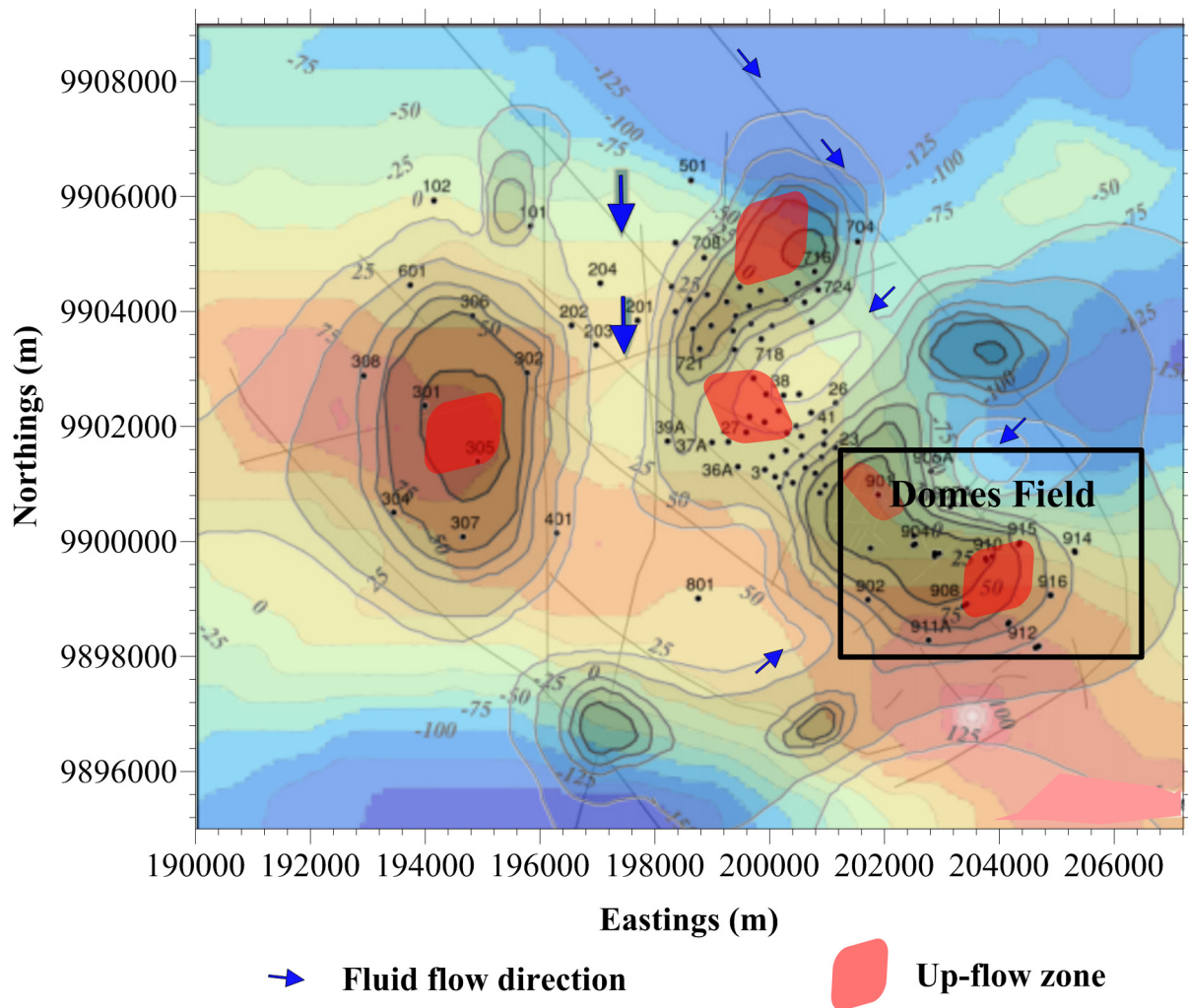


FIGURE 16: Conceptual model with up-flow zones in the Greater Olkaria geothermal area

3.3 Conceptual models of the Domes field

Conceptual models are important in field developmental plans, including selecting the locations and targets of future wells. They are descriptive or qualitative models incorporating and unifying the essential physical features of the systems (Grant et al., 1982). They are created using the analysis of geological and geophysical information, temperature and pressure data, as well as information on the chemical content of reservoir fluids. Through the use of conceptual models, resource assessment can be made including volumetric assessments and numerical modelling. The conceptual model of the GOGA area has been constantly updated and developed in past years (Mannvit/ÍSOR/Vatnaskil/Verkís Consortium, 2011). A simple conceptual model that describes the location of the heat source and features of the hydrological system within the entire Olkaria field is represented in Figure 16. One up-flow zone exists beneath the ring structure in the southeast corner of the Olkaria Domes field, related to the magmatic body evident beneath the area. This magmatic body is located in the centre of the Olkaria Domes area, while the up-flow zone is located in the southeast part of the area. Fracture-controlled permeability related to the ring structure could explain why the up-flow to the Olkaria Domes system is offset southeast of the heat source. The up-flow to the Eastern field and northwest part of the Olkaria Domes field could also be related to the magmatic body beneath the Olkaria Domes area, as well as the body beneath the Eastern field (Mannvit/ÍSOR/Vatnaskil/Verkís Consortium, 2012).). For the purpose

of this study, a simple conceptual model based on temperature information for Olkaria Domes is presented schematically in Figure 17.

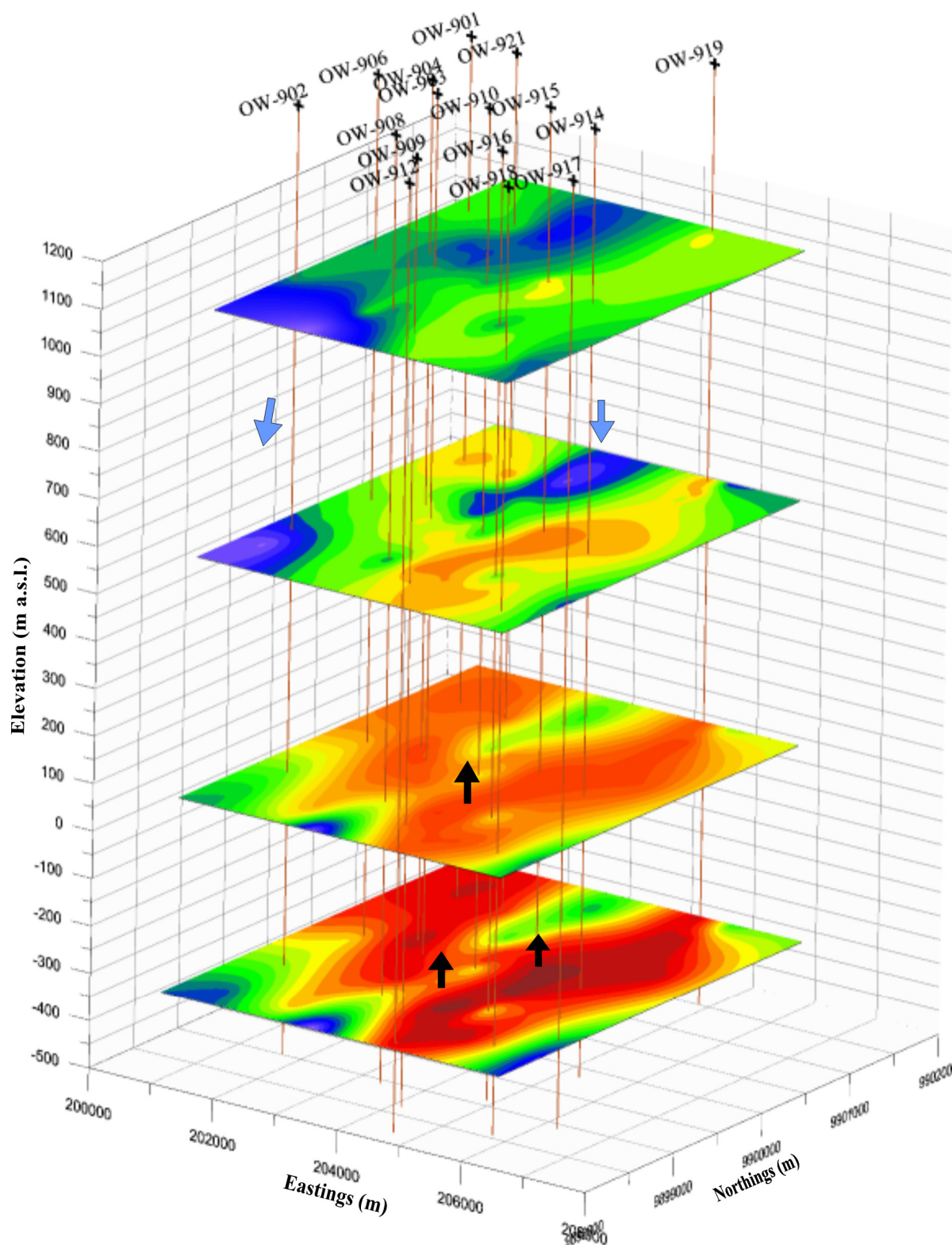


FIGURE 17: Simple conceptual model showing the location of up-flow zones (black arrows) in the Olkaria Domes area

4. NUMERICAL MODELLING

4.1 Theoretical review

TOUGH2 (Transport of Unsaturated Groundwater and Heat) is a general purpose numerical simulator used for modelling non-isothermal flow of multi-component, multi-phase fluids in one, two and three-dimensional porous and fractured media. It is mainly applied in geothermal reservoir studies, nuclear waste isolation studies, environmental assessment and remediation, and flow and transport in variably saturated media and aquifers (Pruess et al., 1999). The simple mass and energy balance equations solved by TOUGH2 can be written in general form as shown in Equation 9.

$$\frac{d}{dt} \int_{V_n} M^K dV_n = \int_{\Gamma_n} F^k \cdot n \, d\Gamma_n + \int_{V_n} q^k dV_n \quad (9)$$

where F = Mmass flux;
 q = Sinks and sources;
 n = Normal vector on the surface element, pointing inwards into Γ_n ;
 M = Mass per volume.

In Equation 9, the rate of change of fluid mass in V_n is equal to the net inflow across the surface Γ_n plus the net gain from the fluid sources.

Generally, TOUGH2 solves governing equations for the conservation of energy and mass using an integral finite volume structure on both regular and irregular grids. In the preceding sections, fluid flow was described with a multi-phase extension of Darcy's law and heat flux carried by both conduction (Fourier's law) and fluid convection. In a fluid mixture, there are several equations of state that can provide thermo-physical properties of the fluid depending on the characteristics of the system. TOUGH2 can handle sample problems for different equations of state as well as phase transition in the system and diffusion between different phases (Pruess et al., 1999).

When developing a model, the entire volume of the geothermal system is divided into numerous grid elements. The elements are designed in such a manner that each element or group of elements is assigned different hydrological and thermal properties using the conceptual model as a guide. To solve relevant equations for conservation and flow of heat and mass, both finite difference and finite element methods can be used in simulation for natural inflow and outflow in the system (Axelsson, 2013).

4.2 Previous numerical models

Several 3-D natural-state numerical models of the entire Olkaria geothermal system have been developed over the years; the first one in 1987 by G.S. Bødvarsson and K. Pruess. The model focussed on the natural state of the Olkaria geothermal system, deducing that the natural recharge to the system amounted to about 600 kg/s, mainly from the Olkaria East field and partially from the Olkaria Northeast and West fields (Bødvarsson and Pruess, 1987). After several updates from different studies, Ofwona (2002) updated the 1987 model on the basis of both new well data and an additional decade of monitoring data. The same grid was used with an area of about 110 km² and a thickness of 1550 m. From his model, it was concluded that the natural state of the system could be simulated by 565 kg/s hot recharge distributed between the western and eastern parts of the Olkaria system, with two up-flow zones in the Northeast sector and one in the East sector. He also concluded that the Olkaria geothermal system is an open system with pressure draw-down confined to production zones (Ofwona, 2002). More recent work was done 2011 and 2012 by a Consortium composed of the Icelandic companies: Mannvit, ISOR, Vatnaskil and Verkis. Their updated model consisted of a grid that covered an area of 720 km² and a thickness of 3600 m. The model depth ranges between 1900 m a.s.l. and 1700 m b.s.l. and has 15 layers, each containing 2463 elements. The model was designed using the TOUGH2/iTOUGH2 code

which is extensively used in modelling liquid-dominated reservoirs all over the world. From the model it was concluded that the natural state of the system could be simulated by providing sources with just over 200 kg/s of fluids with an average enthalpy of 1600 kJ/kg.

4.3 An update to the existing 3D natural-state model of the Olkaria Domes field

4.3.1 General approach

For the purpose of this study, the most recent numerical model of the entire Olkaria geothermal field, created from the ongoing cooperation between the Mannvit/ÍSOR/Vatnaskil/Verkís consortium and KenGen team, was used. The new wells in the Olkaria Domes field were incorporated into the model in order to update the natural-state model of the field. The horizontal mesh grid for the entire Olkaria system (Figure 18) covers an area of 720 km² and covers a depth range from about 2000 m a.s.l. to 1700 m b.s.l. The mesh consists of 36,945 elements and 144,597 connections. The mesh grid has scarce elements near the boundary but becomes dense at the centre of the geothermal system. This is because at the centre of the geothermal system, thermodynamic variable gradients are likely to be greater (in space and time). The top and bottom layers are inactive with 4940 elements. They are set inactive so as to restrain the temperature and pressure gradients in the model, hence conserving a constant temperature and pressure in the top and bottom layers while limiting fluid flow into or out of the adjacent layers.

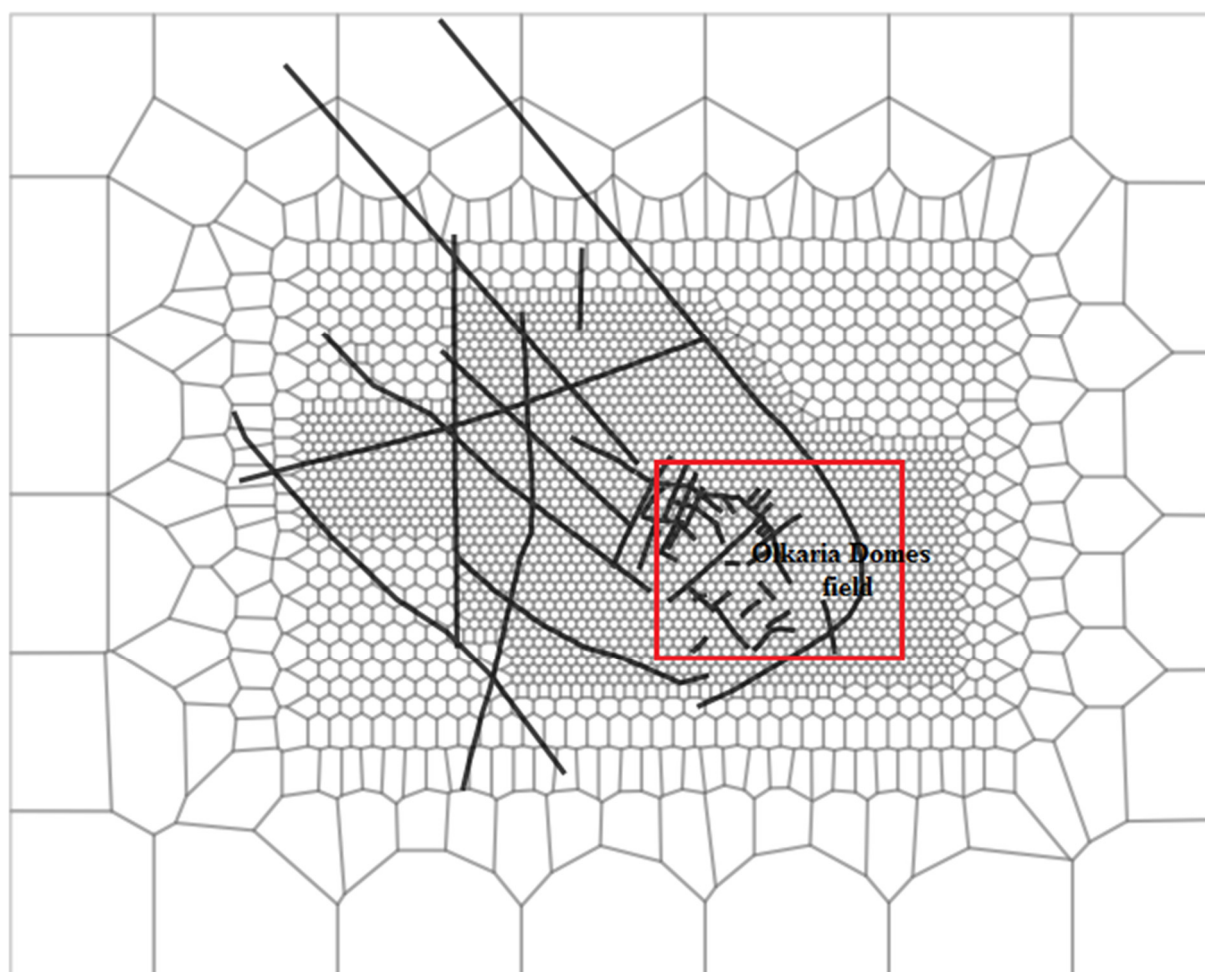


FIGURE 18: The numerical model mesh grid of GOGA (Mannvit/ÍSOR/Vatnaskil/Verkís Consortium, 2012); the red box marks the Olkaria Domes field

The vertical view of the model consists of a total of 15 layers. The top 13 layers are 200 m thick and the bottom two layers are 400 m thick (Figure 19). Layers B and P represent the top and bottom layers, respectively, and both layers are inactive.

There are several different rock types assigned to the elements in the model. Distribution of the rock types was determined by the hydrological flow patterns in the field (as observed in the temperature and pressure logs). Figure 20 shows the distribution of rock types in the numerical model. There are 31 rock types in the entire model. An assumption is that all the rock types have the same physical properties such as density, thermal conductivity and specific heat capacity but with different permeability and porosity (Table 1). Different permeability in horizontal and vertical directions is assigned for different rock types but is the same in the y direction. Porosity and permeability values ranged between the lowest permeable to highest permeable rock types, as shown in Table 1.

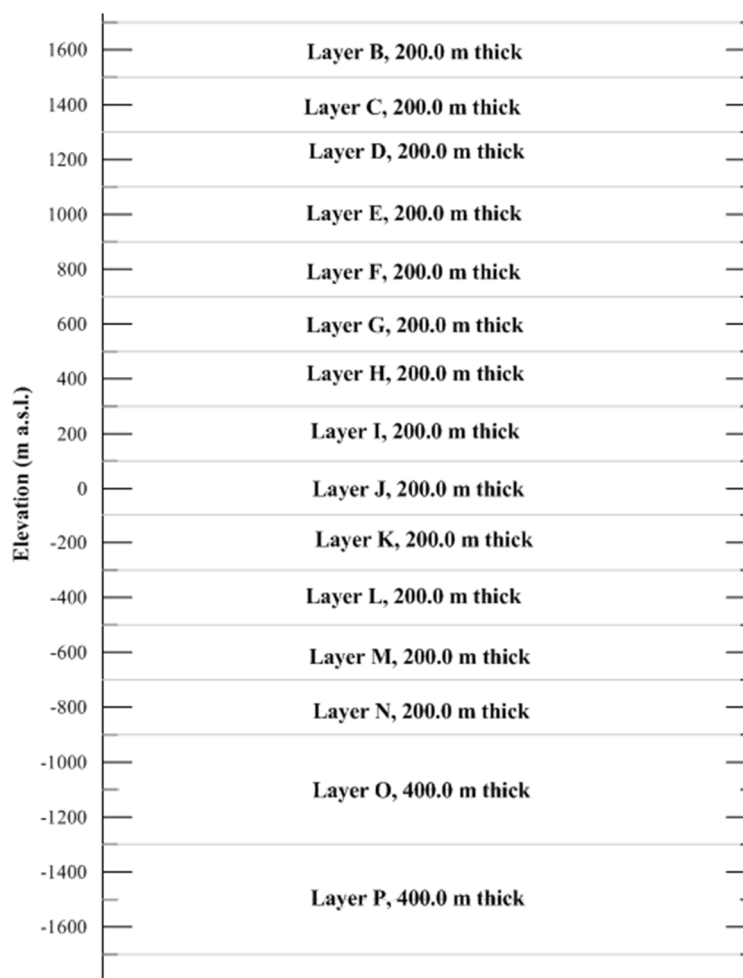


FIGURE 19: Vertical view of the numerical model mesh for the Olkaria geothermal system, showing layer names and thicknesses

TABLE 1: Physical properties for rocks in the numerical model of the Olkaria Geothermal system

Rock physical properties		Permeable rock	Low permeability rock
Density (kg/m^3)		2650	2650
Specific heat capacity ($\text{kJ}/(\text{kg.K})$)		860	860
Thermal conductivity ($\text{W}/(\text{m}^\circ\text{C})$)		2.0	2.0
Permeability (mD):	Horizontal	0.204	0.0479
	Vertical	2.472	0.0026
Porosity (%)		15	8

4.3.2 Changes made using the current model and discussion

Injection rates and enthalpy values of the sources were adjusted gradually until there was no more change in the model results. A heat source was introduced in element (OB459) to account for the high temperature in the wells around this region. From the temperature isotherm map (Figure 10), a conspicuously low temperature is noted in the field around Wells OW-905A, OW-907B and OW-903B.

To improve the fit in the model, new rock types and a cold source were added to the model (Figure 20). A rock type called BARIA with low permeability was introduced as a barrier that hinders flow of fluid

between the up-flow zone and the cold region. The barrier reduces the flow of heat and mass to the cold region and also reduces the low-enthalpy fluid flow across to the up-flow zone. Some wells indicated a temperature inversion at the bottom of the reservoir, hence, the permeability of rock type EBCL in layers M and N was progressively adjusted until an improved match between simulated and observed data was achieved. In general, the permeability distribution and the strength of the mass and heat up-flow into the system were adjusted and the model was then re-run until a reasonable match between the calculated and measured data was reached. Table 2 shows the final calibrated properties of the sources defined in the model.

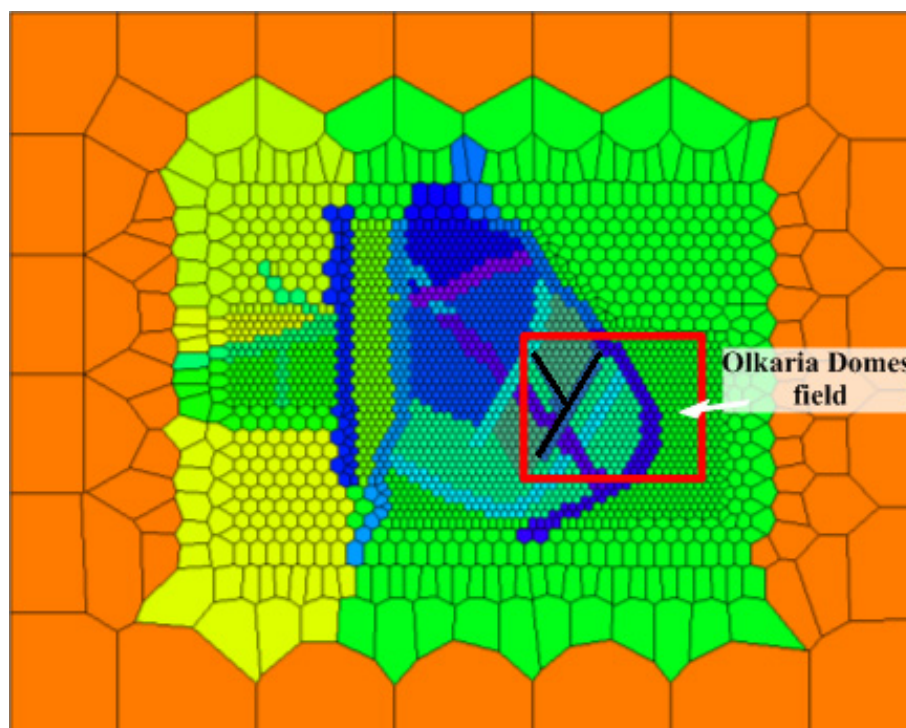


FIGURE 20: Distribution of rock types within the reservoir; black line is the BARIA rock type (modified from Mannvit/ÍSOR/Vatnaskil/Verkís, 2012)

TABLE 2: Properties of sources

Properties	Hot source	Cold source
Flow rate (kg/s)	70.80	5.78
Average enthalpy (kJ/kg)	1640	950

4.3.3 Results and discussion

Appendix II shows graphs of pressure and temperature calculated by the calibrated model compared with estimated formation temperatures. The model calculations fit the measured data well for most of the wells. An exception, however, is observed in areas within low-temperature zones. Some changes were made in the model so as to obtain a reasonable fit around these areas. This included introducing a barrier rock type and a cold source. Other modifications included changing the rate of mass and heat flow into the system as well as permeability changes. Calculated temperature and pressure contours are presented in Figures 21 and 22. The temperature contours closely match with temperature contours obtained from measured data but for pressure there is a bit of mismatch between the two.

Figure 23 shows the downhole temperature and pressure calculated by the model as a function of the estimated formation temperature and pressure. For a perfect match, the points should fall into some trend of a straight line. The spread of the points gives an idea of the quality of the fit of the model.

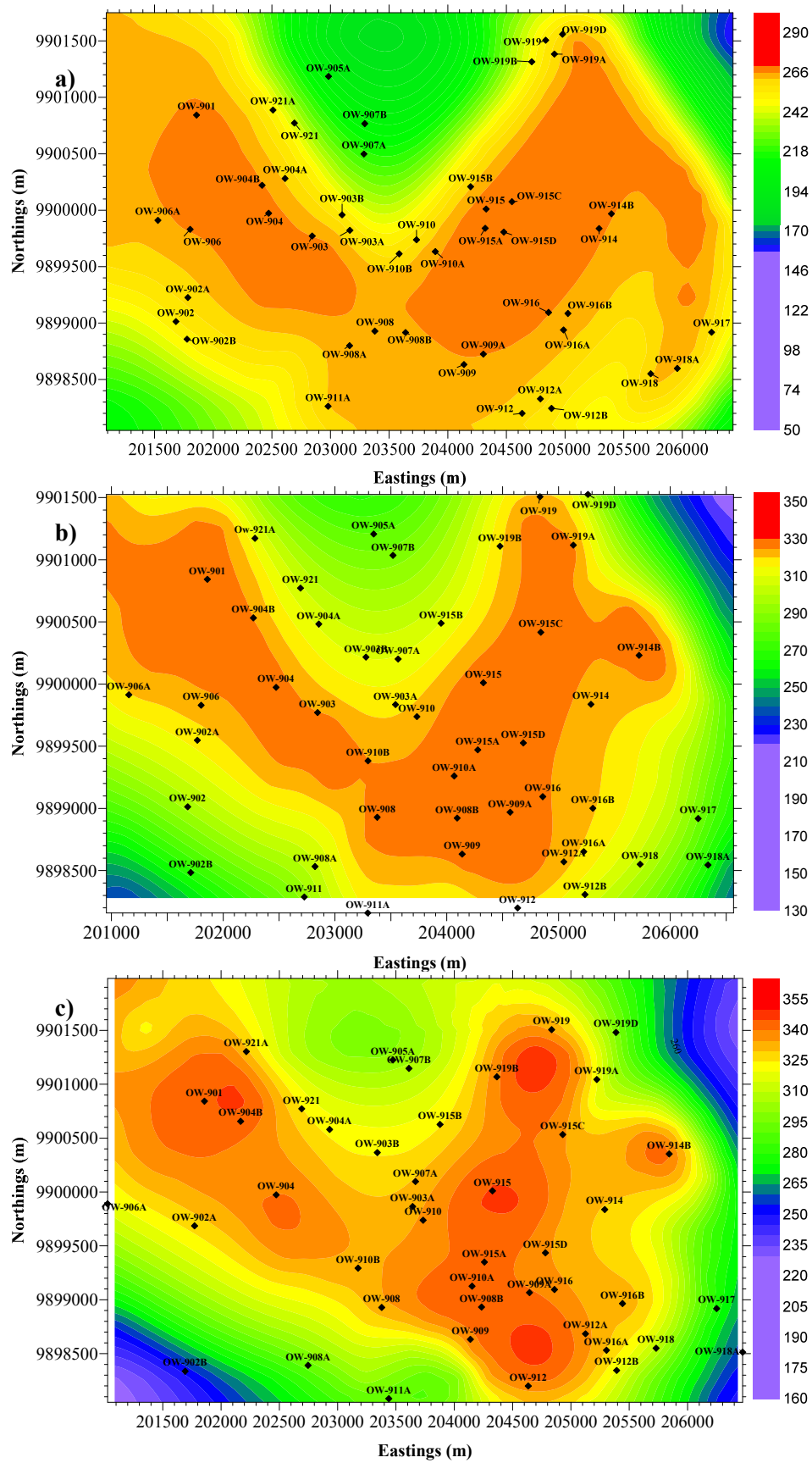


FIGURE 21: Calculated temperature contours:
a) Layer E; b) Layer J; c) Layer L

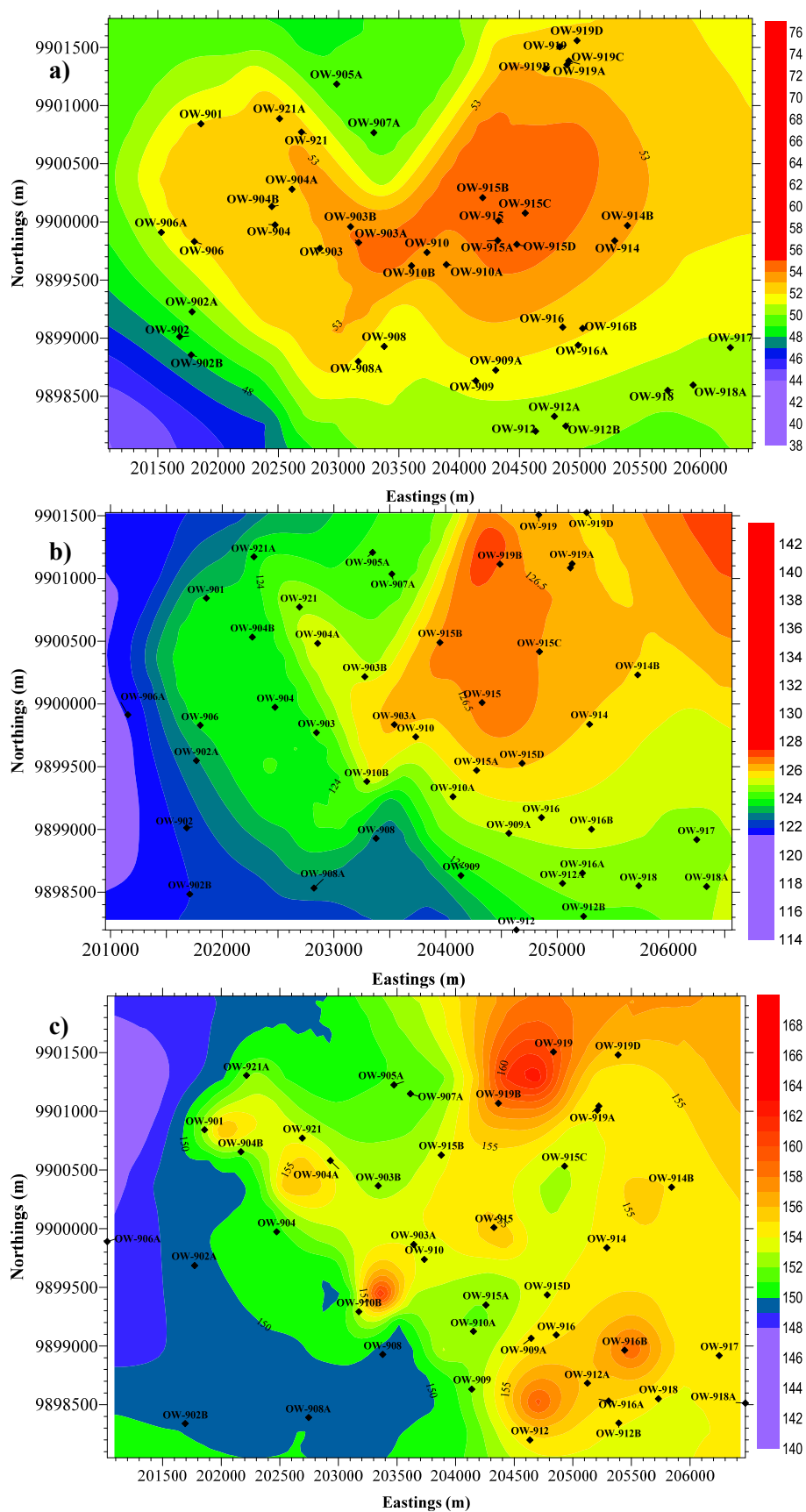


FIGURE 22: Calculated pressure contours:
a) Layer E; b) Layer J; c) Layer L

5. CONCLUSIONS AND RECOMMENDATIONS

The Olkaria Domes reservoir can be classified as a convective cell with a magmatic intrusion in the central part of the field. Associated with the magma intrusion is the major up-flow zone in the southeast part of the field and a minor up-flow zone in the northwest part of the field. From the temperature and pressure models, these up-flow zones are manifested as hot plumes and surrounded by cold down-flow zones. This type of convection flow within the reservoir indicates good recharge to the system.

The major up-flow zone in the field extends all the way to the eastern part of the field. An initial study concluded that the up-flow zone was in the southeast part of the field. But from the research presented here, the zone extends to the eastern part of the field.

To obtain the best match, Olkaria Domes field can be simulated for natural state by an injection of a total mass of about 71 kg/s and enthalpy of 1650 kJ/kg of water. To acquire a better match between the measured values and the calculated model in the region of local cooling around Wells OW-907A and OW-905A, a cold source of 5.78 kg/s and enthalpy of 950 kJ/kg is introduced.

From the cross-sectional temperature plot, one can see that hot plumes are surrounded by cold down flow zones. This is an indication of good recharge to the system.

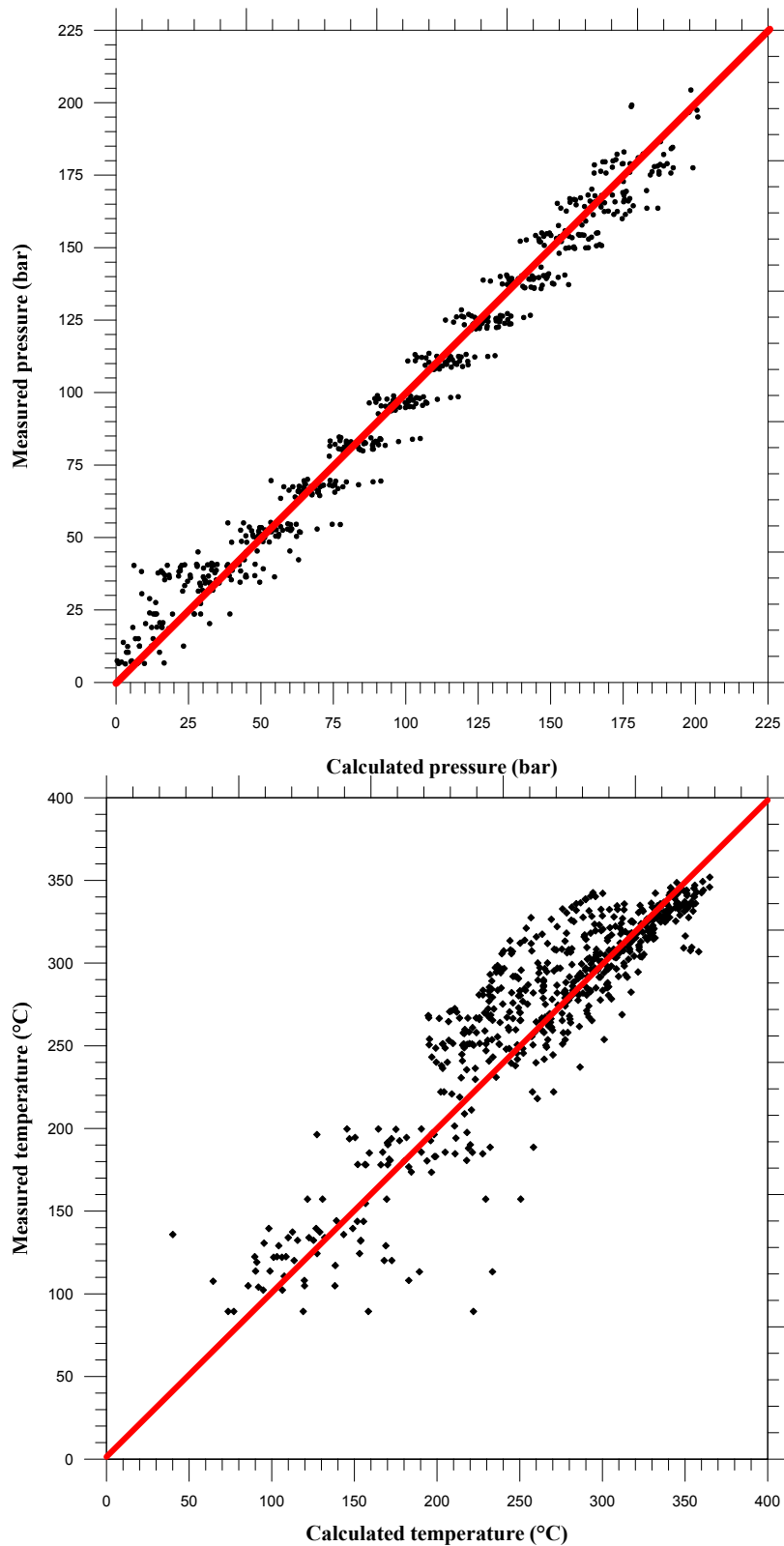


FIGURE 23: a) Downhole pressure calculated by the model as a function of estimated formation pressure; b) Downhole temperature calculated by the model as a function of estimated formation temperature

The model should be updated to include Well OW-922 which was recently drilled outside the ring structure. This would help to delineate the possible extent of the resource outside the ring structure.

And perhaps one or two wells should be drilled north of Well OW-907B to measure the extent of the local cooling in the area.

ACKNOWLEDGEMENTS

My sincere gratitude goes to Mr. Lúdvík S. Georgsson, the Director of the UNU Geothermal Training Programme for the opportunity to take part in the Programme, the Deputy Director, Mr. Ingimar Gudni Haraldsson, for his help and support, Ms. Thórhildur Ísberg, Mr. Markús A.G. Wilde and Ms. Málfríður Ómarsdóttir for their great support during my study and stay in Iceland, to the staff of UNU, Orkustofnun and ÍSOR, to my supervisors, Dr. Andri Arnaldsson from Vatnaskil Consulting Engineers and Ms. Saeunn Halldórsdóttir from ISOR, for their diligent assistance and advice during my research project, to my employer, the Kenya Electricity Generating Company Ltd. for the chance to attend the training, and to the UNU fellows: thank you for the magnificent time and discussions we shared.

Thanks to my wonderful mother for her love and encouragement, and my sister Phanice for the great support. Finally, I thank God for His sufficient grace that made the programme possible.

REFERENCES

- Abbate, E., Passerini, D., and Zan, L., 1995: Strike-slip faults in a rift area: A transect in the Afar Triangle, East Africa. *Tectonophysics*, 241, 67-97.
- Axelsson G., 2012: The physics of geothermal energy. In: Sayigh, A. (ed.), *Compreh. Renew. Energy*, 7, 3-50.
- Axelsson, G., 2013: Dynamic modelling of geothermal systems. *Paper presented at "Short Course V on Conceptual Modelling of Geothermal Systems" organised by UNU-GTP and LaGeo, Santa Tecla, El Salvador*. UNU-GTP, CD-16, 21 pp.
- Bear, J., 1979: *Hydraulics of groundwater*. McGraw-Hill, Inc., NY, 569 pp.
- Bödvarsson, G.S., and Pruess, K., 1987: *Numerical simulation studies of the Olkaria geothermal field*. Kenya Power Company, Ltd., internal report.
- Grant, M.A., Donaldson, I.G., and Bixley, P.F., 1982: *Geothermal reservoir engineering*. Academic Press, New York, 369 pp.
- Karingithi, C.W., 2000: Geochemical characteristics of the Greater Olkaria geothermal field, Kenya. Report 9 in: *Geothermal training in Iceland 2000*. UNU-GTP, Iceland, 165-188.
- Kamunya, M.K., Wafula, E., and Wamalwa, R., 2014: *Update of the Olkaria geochemical conceptual model*. KenGen, Kenya, internal report.
- Kandie, J.R., 2011: *Geology report of East of Olkaria Domes*. KenGen, Kenya, internal report.
- Kenya Power Company, 1984: *Background report for scientific and technical review meeting*. Kenya Power Co., Ltd., internal report prepared by KRTA, 254 pp.
- Lagat, J.K., 2004: *Geology, hydrothermal alteration and fluid inclusion studies of the Olkaria Domes geothermal field, Kenya*. University of Iceland, MSc thesis, UNU-GTP, Iceland, report 2, 79 pp.

Malimo, S.J., 2009: Interpretation of geochemical well test data for wells OW-903b, OW-904b and OW-909, Olkaria Domes, Kenya. Report 17 in: *Geothermal training in Iceland 2009*. UNU-GTP, Reykjavík, 319-344.

Mannvit/ÍSOR/Vatnaskil/Verkís Consortium, 2011: *Revision of the conceptual model of the Greater Olkaria geothermal system- Phase I*. Mannvit/ÍSOR/Vatnaskil/Verkís, Reykjavík, 100 pp.

Mannvit/ÍSOR/Vatnaskil/Verkís Consortium, 2012: *Development of the numerical model of the Greater Olkaria geothermal system - Phase I*. Mannvit/ÍSOR/Vatnaskil/Verkís, Reykjavík, 95 pp.

Mungania, J., 1999: *Summary of updates of the geology of the Olkaria Domes geothermal field*. KenGen - Kenya Electricity Generating Company, Ltd., unpubl. report.

Mwangi, D.W., 2012: Borehole geology and hydrothermal mineralisation of well OW-916, Olkaria Domes geothermal field, Naivasha, Kenya. Report 24 in: *Geothermal training in Iceland 2012*. UNU-GTP, Iceland, 541-571.

Ofwona, C.O., 2002: *A reservoir study of Olkaria East geothermal system, Kenya*. University of Iceland, MSc thesis, UNU-GTP, Iceland, report 1, 74 pp.

Omenda, P.A., 1998: The geology and structural controls of the Olkaria geothermal system, Kenya. *Geothermics*, 27-1, 55-74.

Pruess, K., Oldenburg, C., and Moridis, G., 1999: *TOUGH2, user's guide version 2.0*. Lawrence Berkeley National Laboratory, 197 pp.

Stefánsson, V., and Steingrímsson, B.S., 1980: *Geothermal logging I, an introduction to techniques and interpretation*. Orkustofnun, Reykjavík, report OS-80017/JHD-09, 117 pp.

Wanjohi, A., 2011: *Geophysics report east of Olkaria Domes (Akira) geothermal field*. KenGen, Kenya, internal report.

APPENDIX I: Temperature and pressure profiles with formation temperatures in selected Olkaria Domes wells

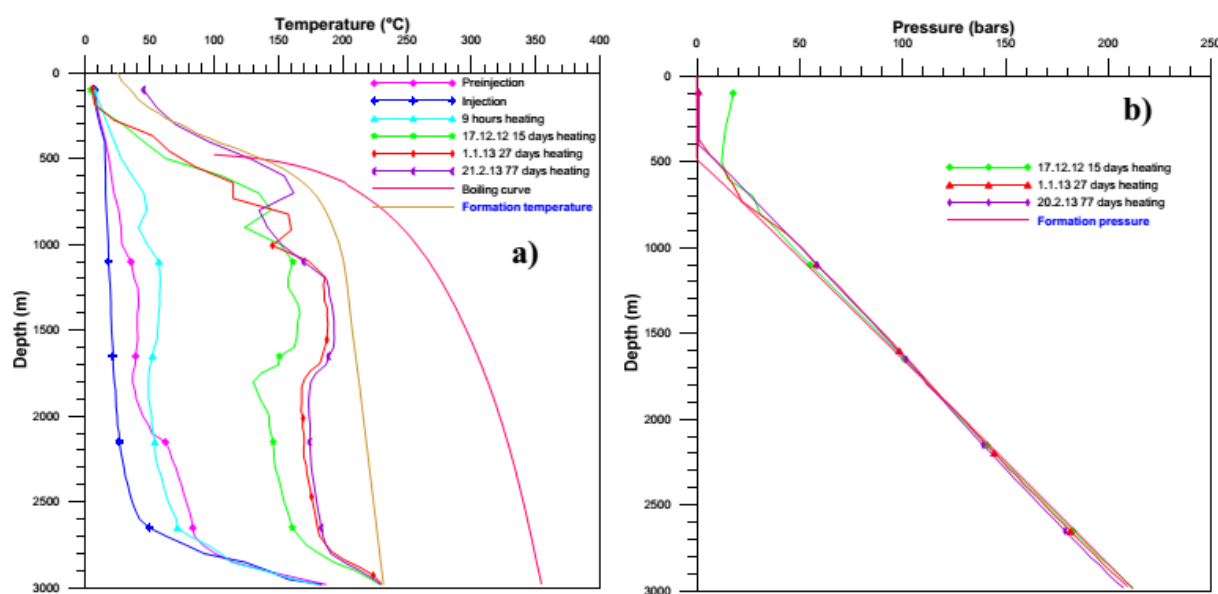


FIGURE 1: Well OW-907B: a) Temperature profiles; b) Pressure profiles

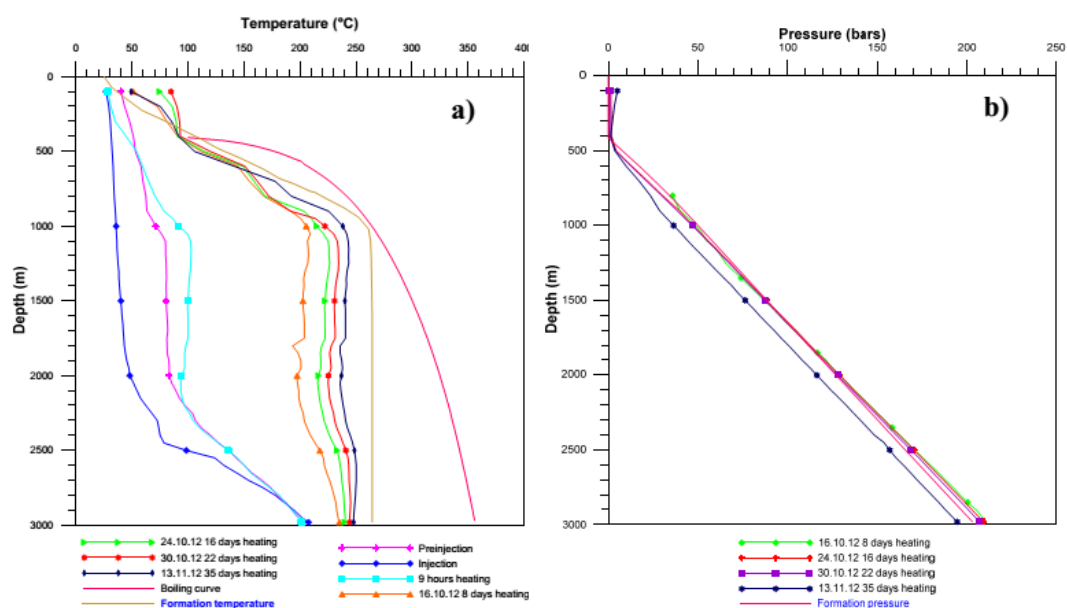


FIGURE 2: Well OW-911: a) Temperature profiles; b) Pressure profiles

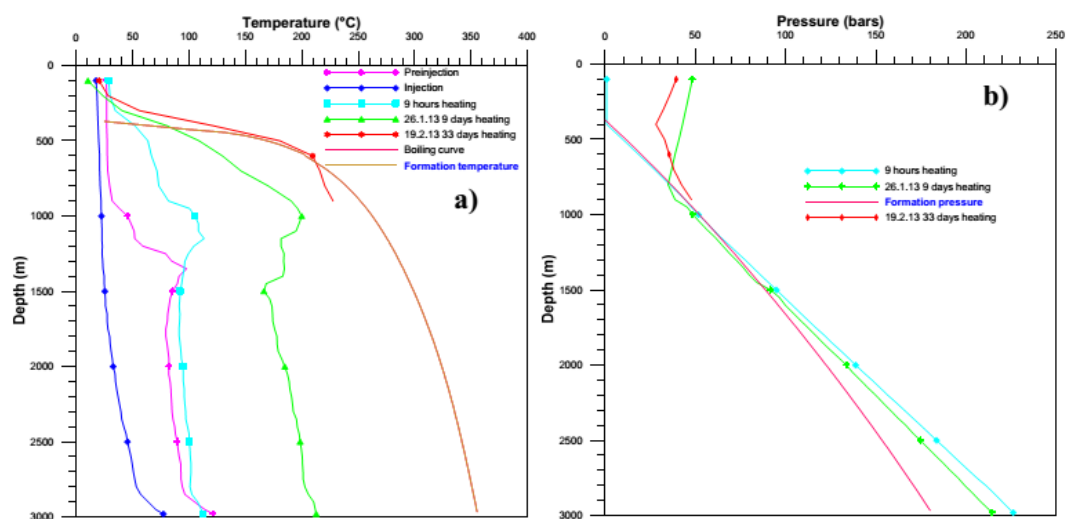


FIGURE 3: Well OW-914C: a) Temperature profiles; b) Pressure profiles

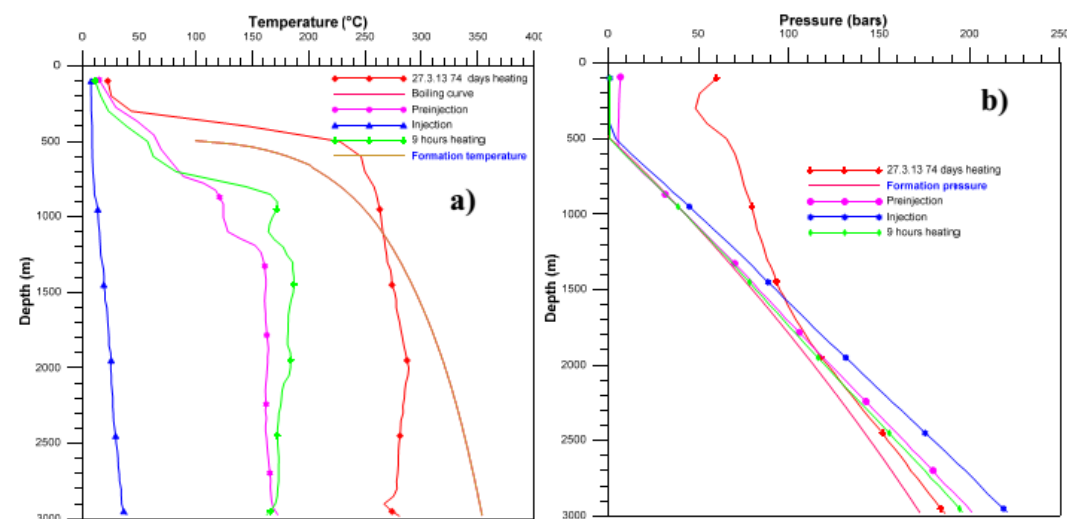


FIGURE 4: Well OW-915C: a) Temperature profiles; b) Pressure profiles

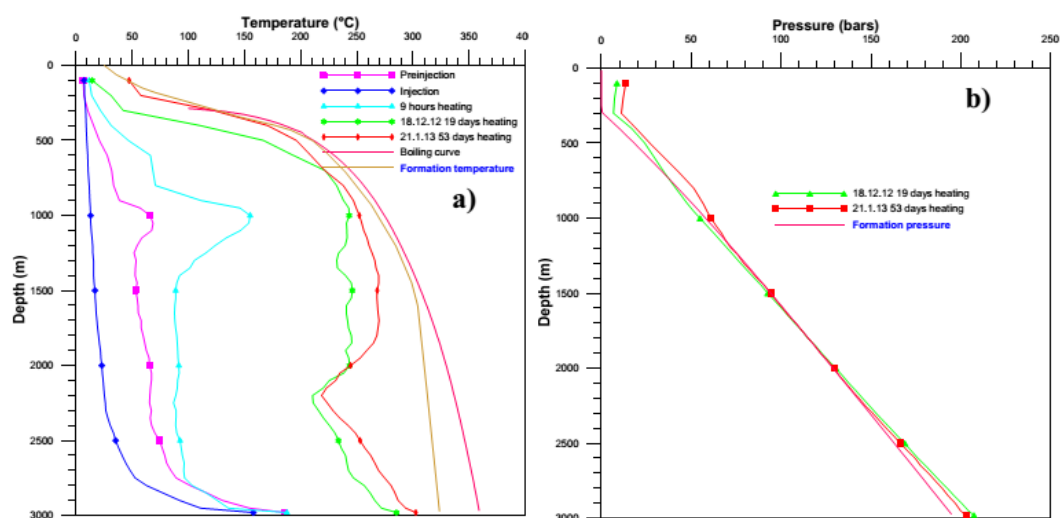


FIGURE 5: Well OW-916B: a) Temperature profiles; b) Pressure profiles

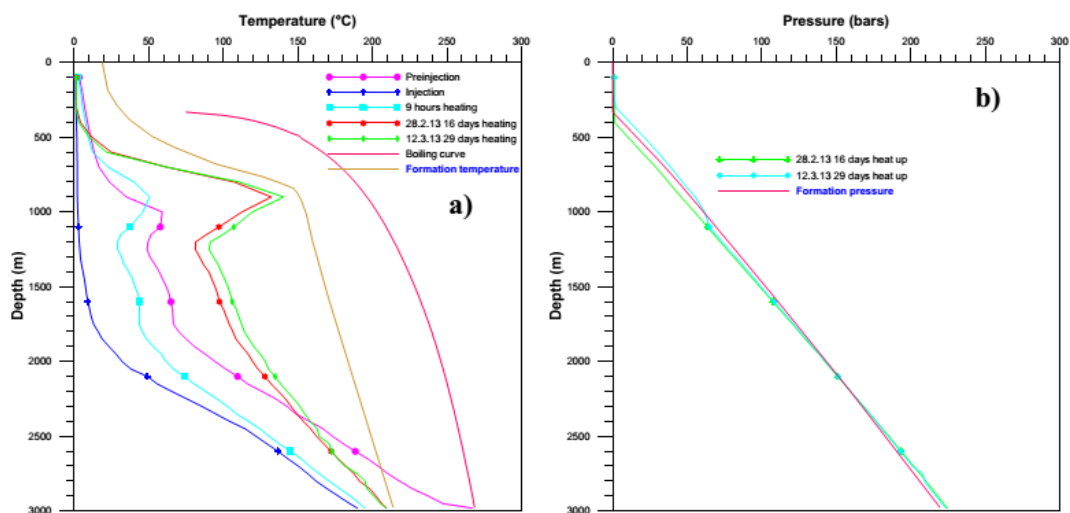
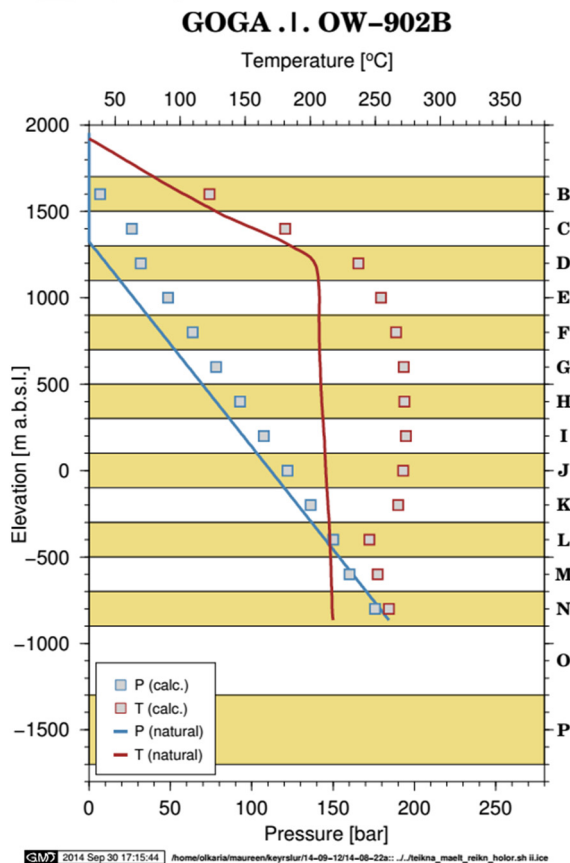
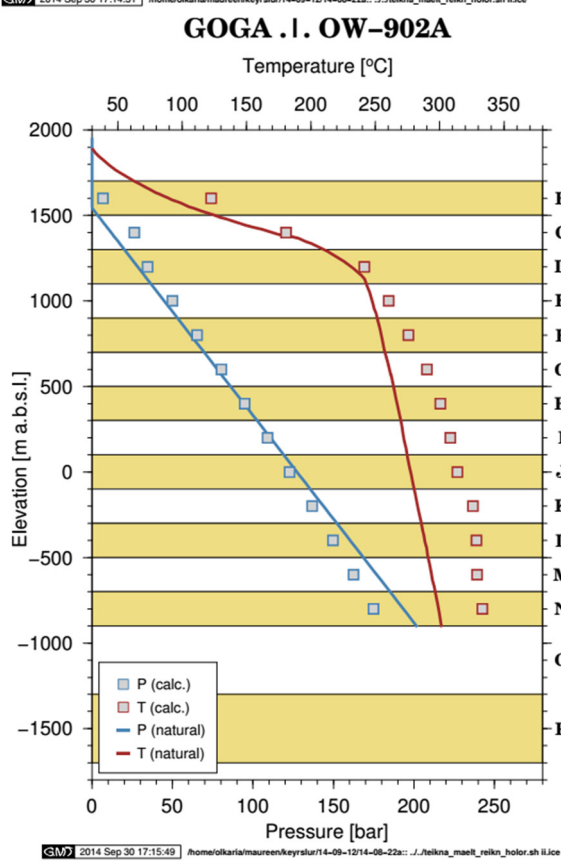
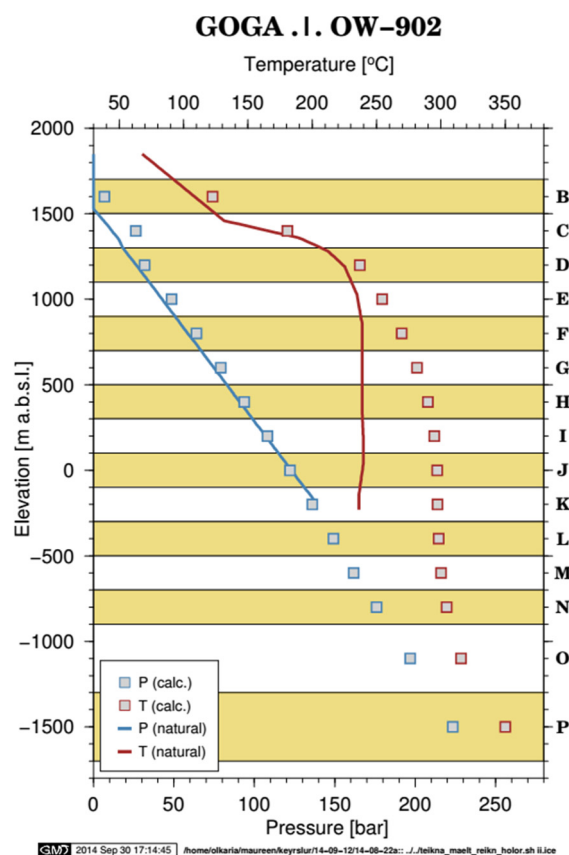
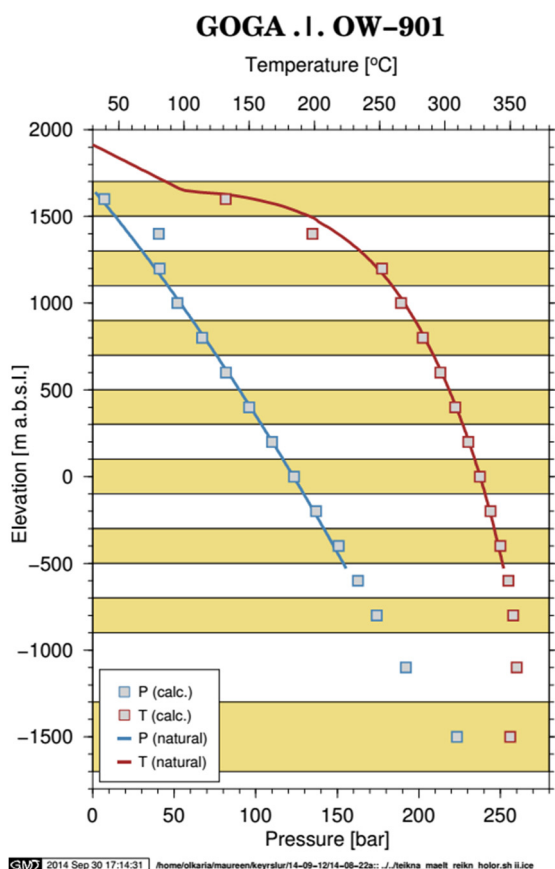
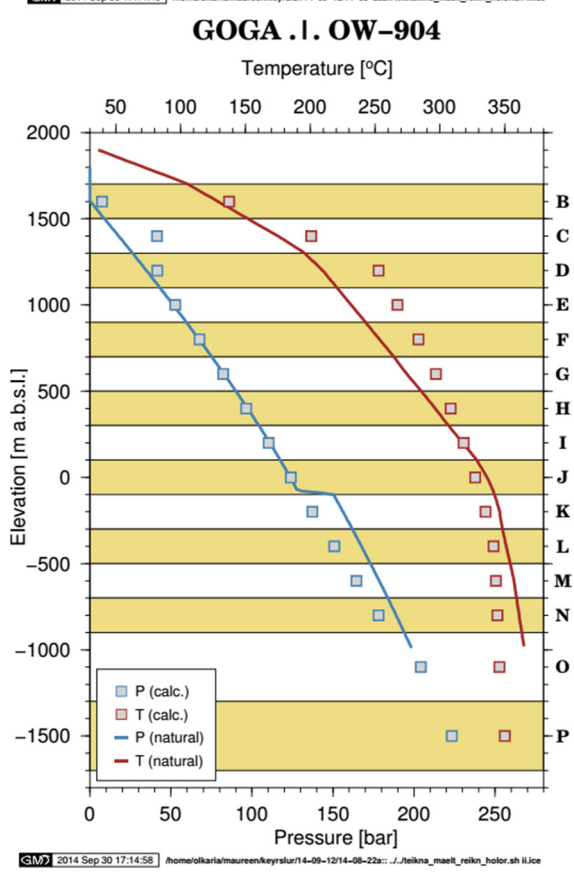
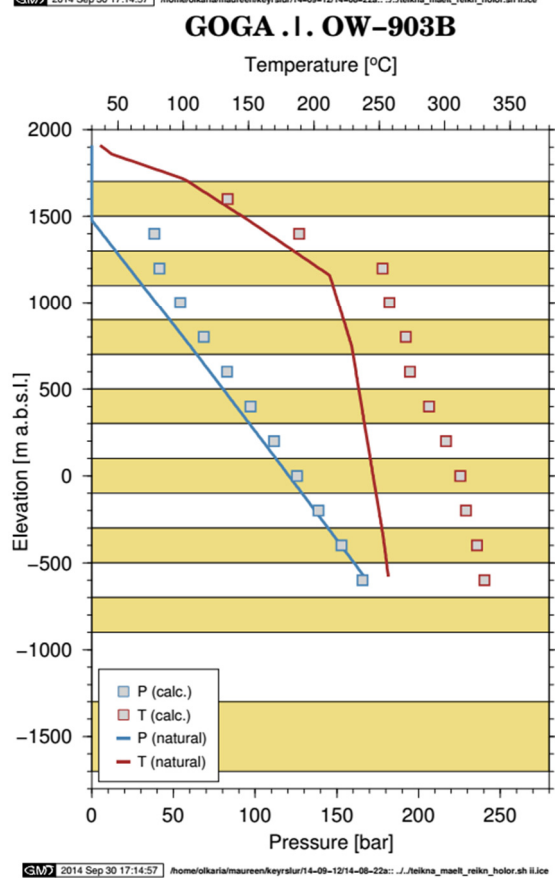
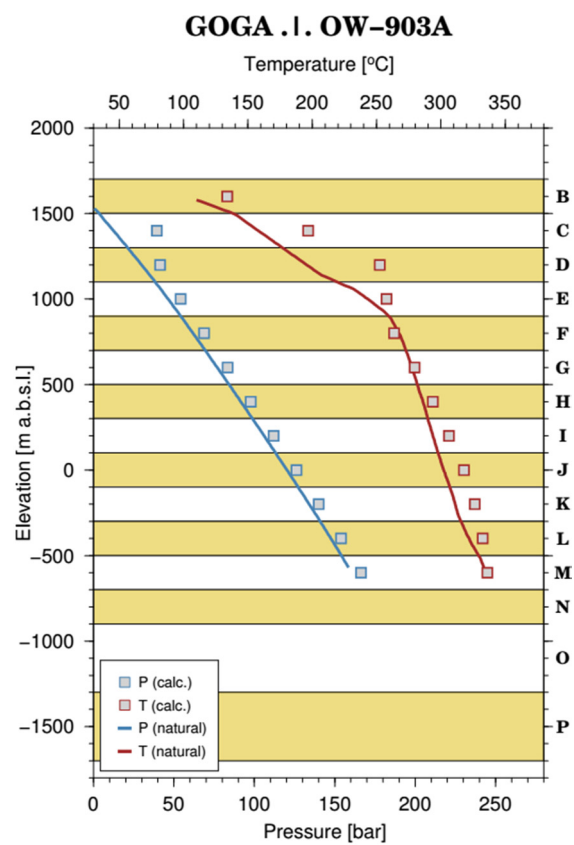
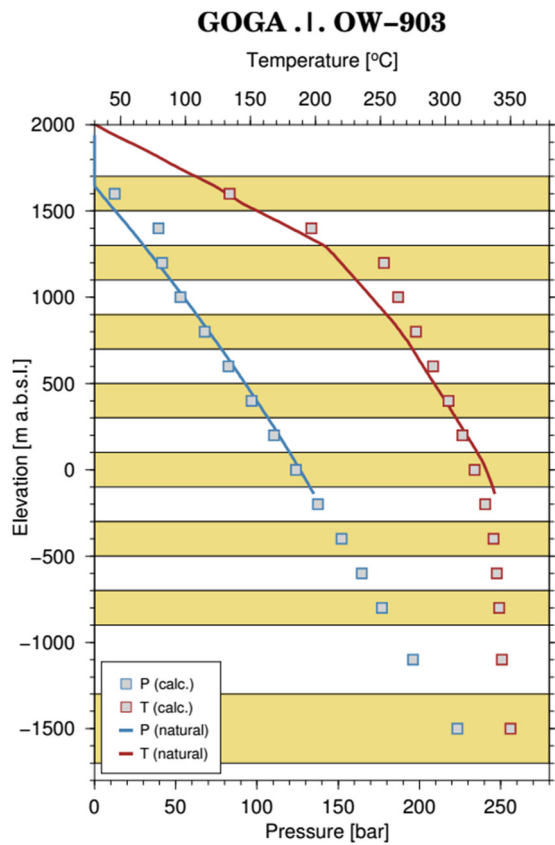
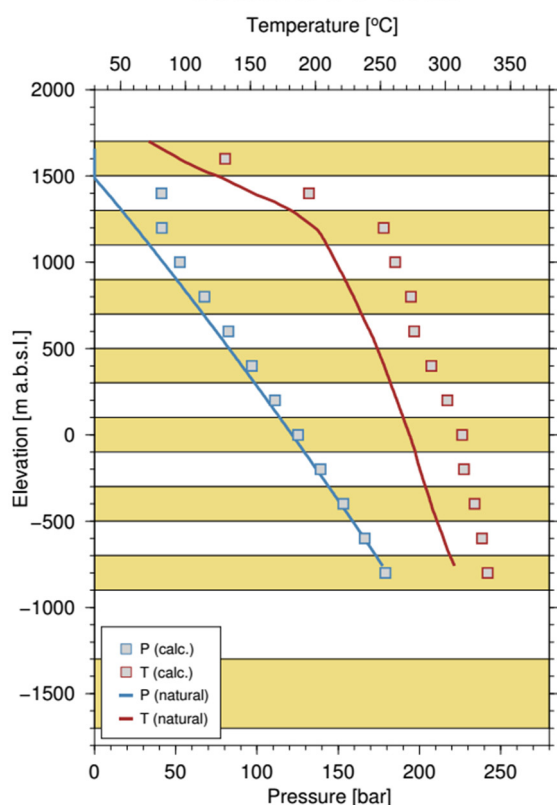
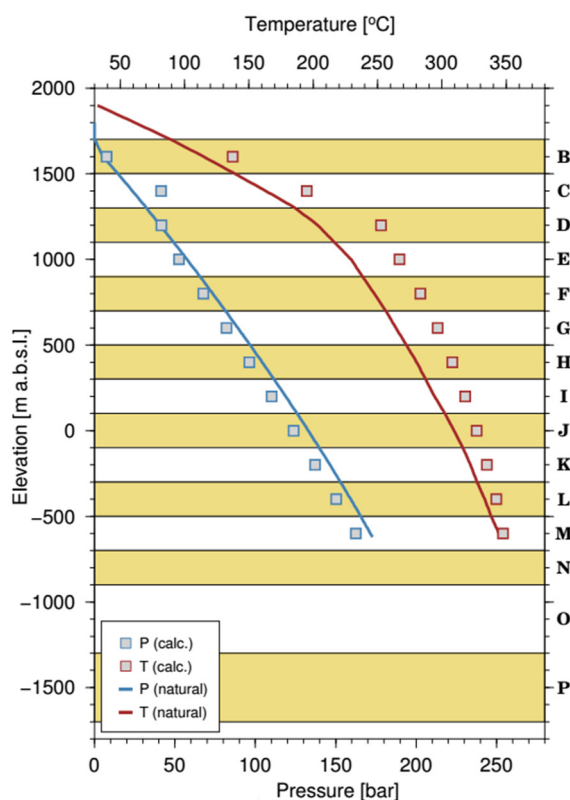
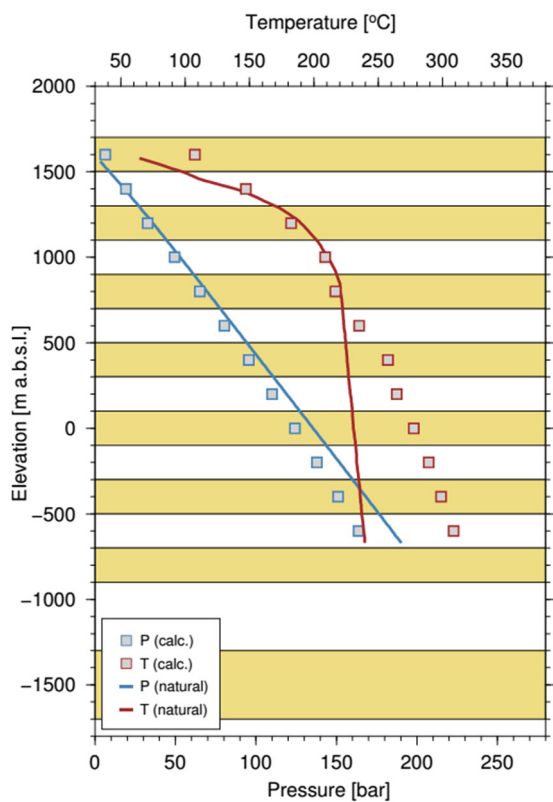
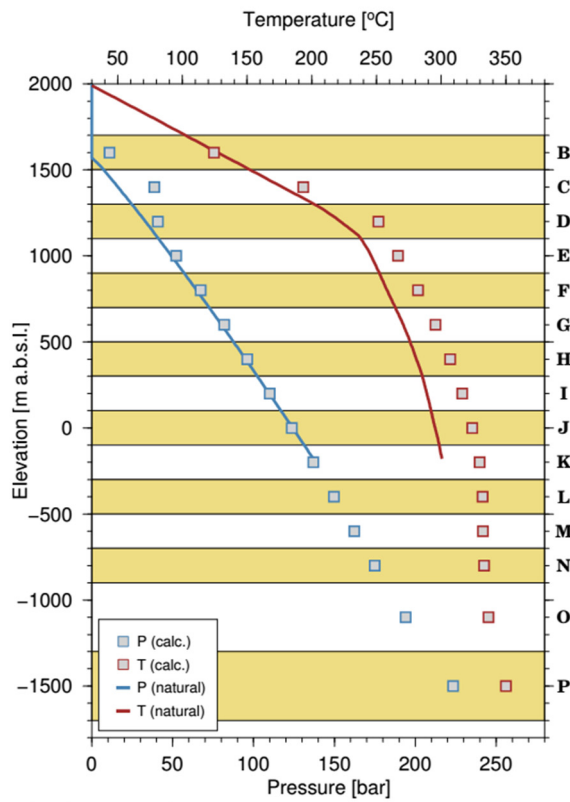


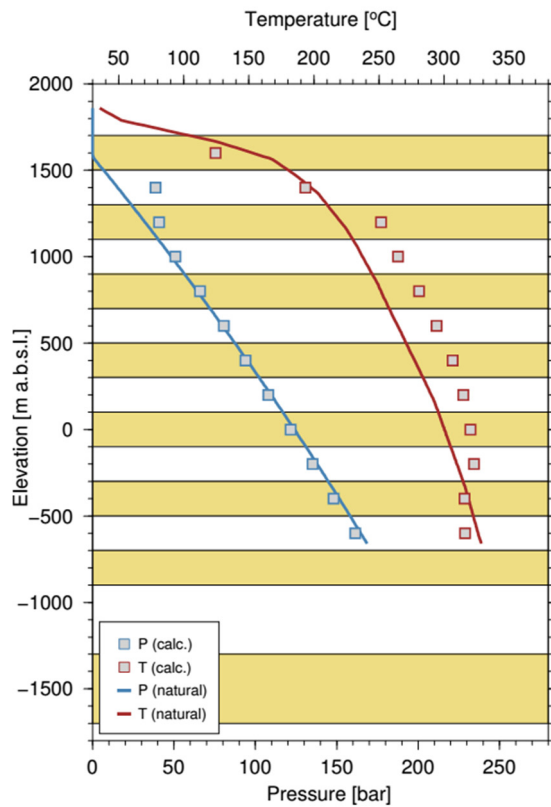
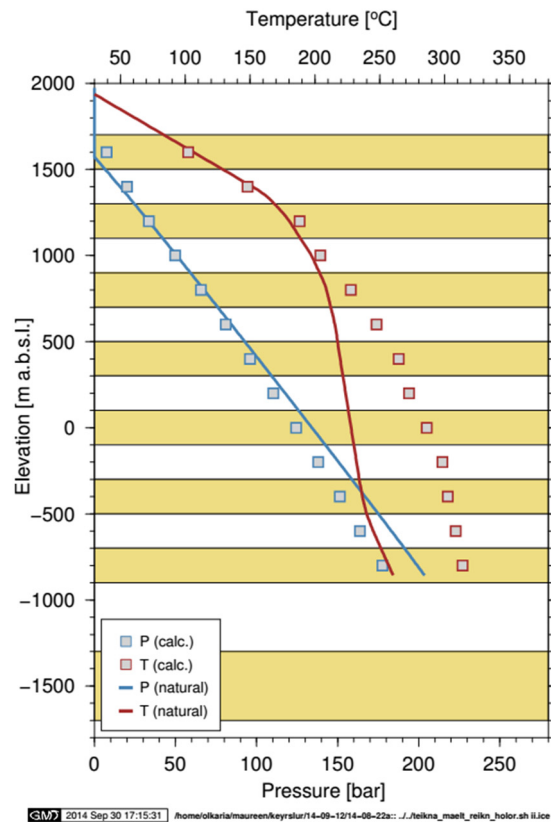
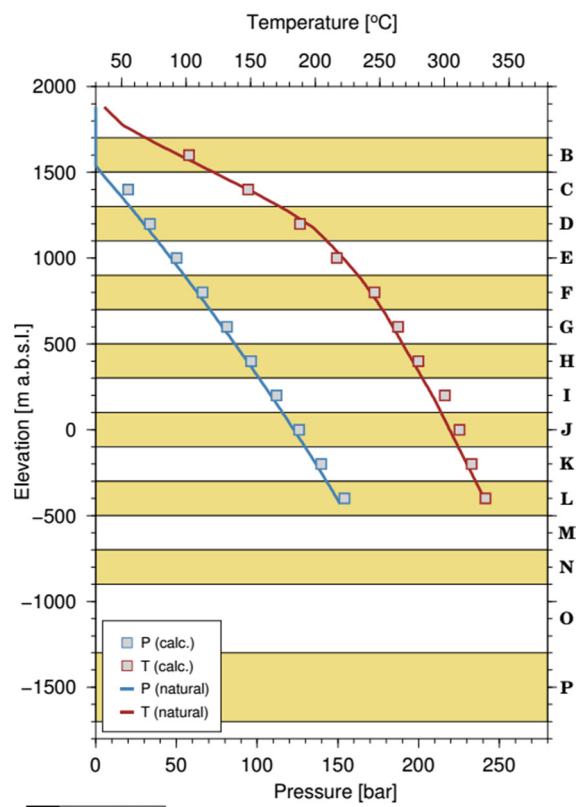
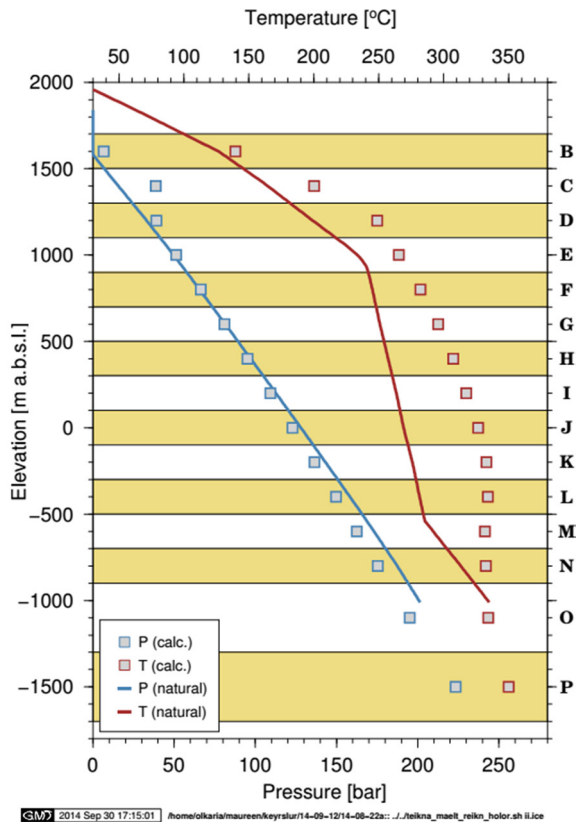
FIGURE 6: Well OW-919: a) Temperature profiles; b) Pressure profiles

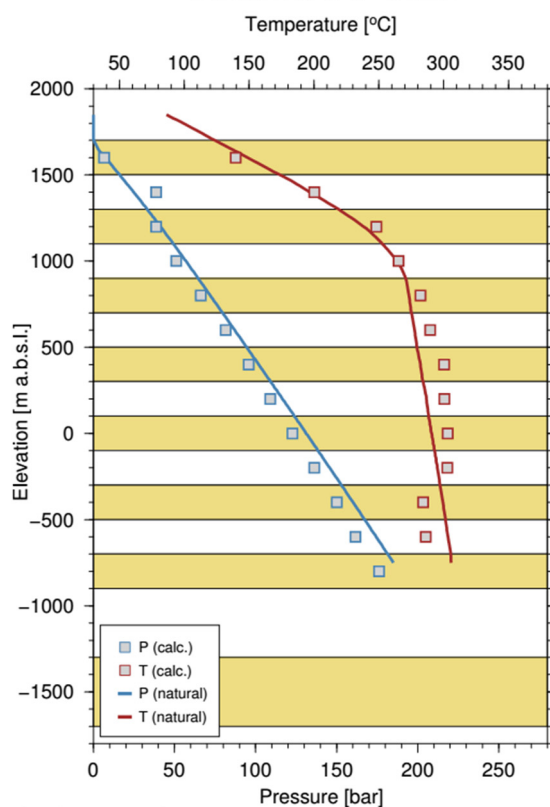
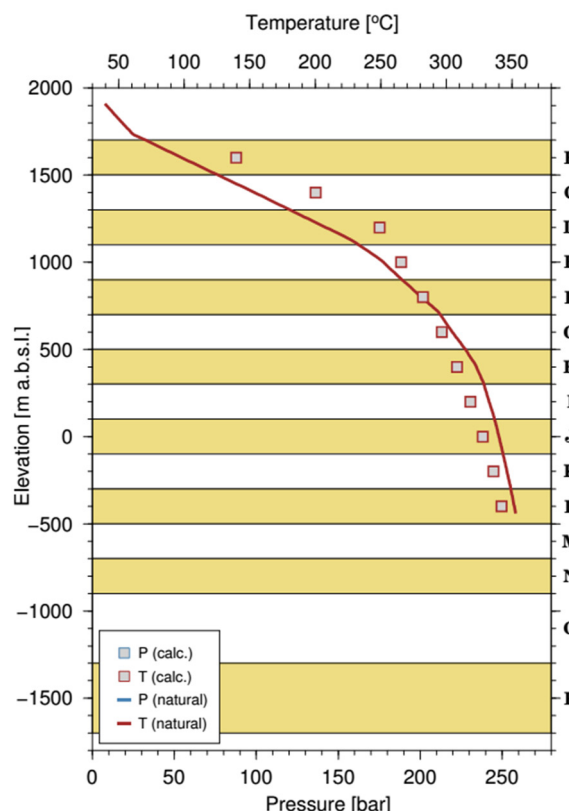
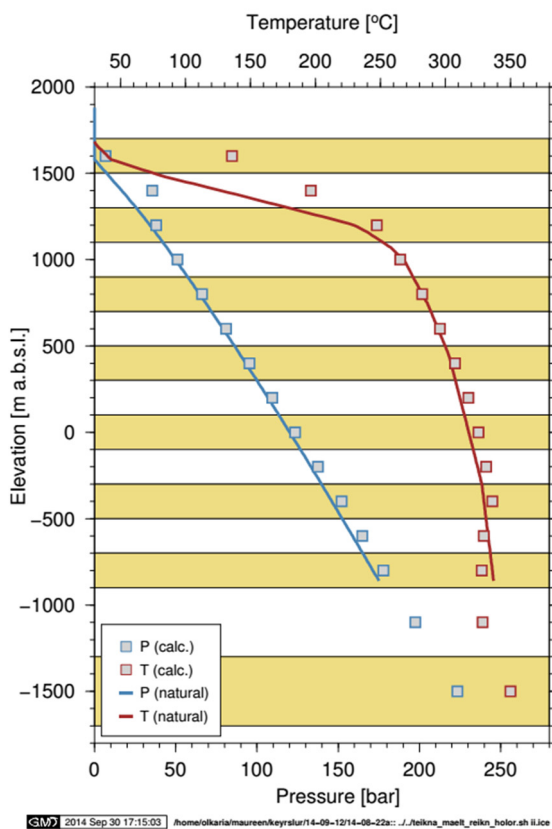
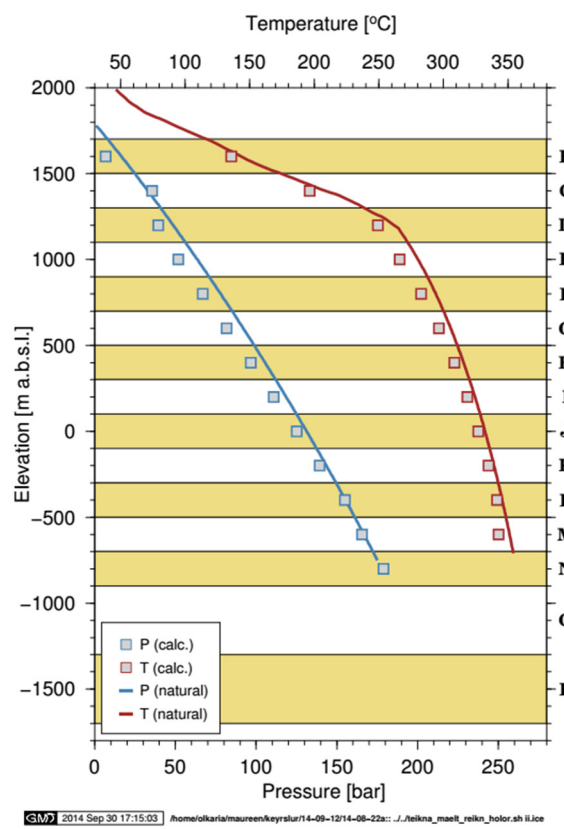
APPENDIX II: Calibration results from the updated 3-D natural-state model

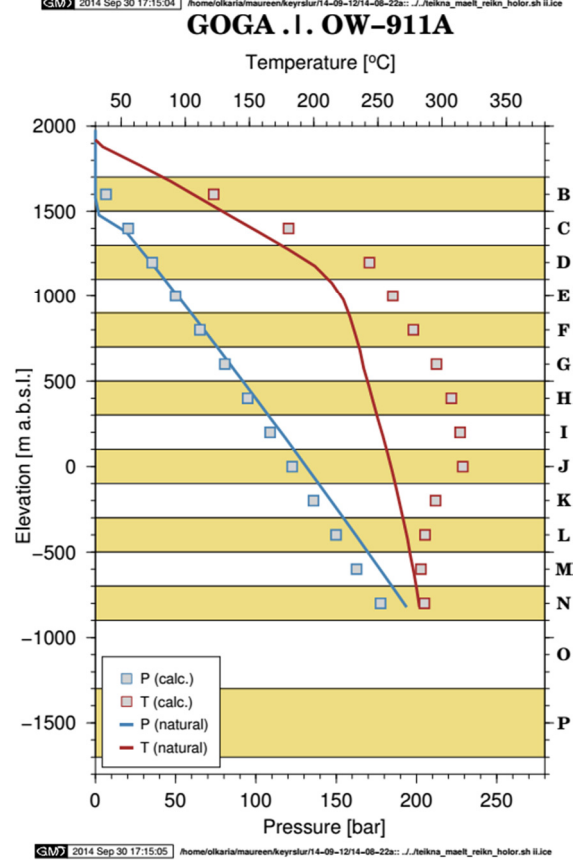
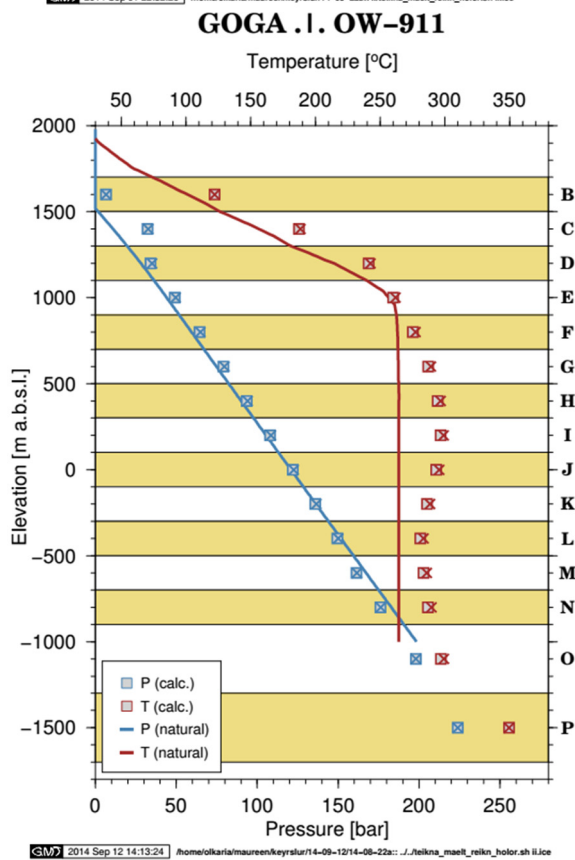
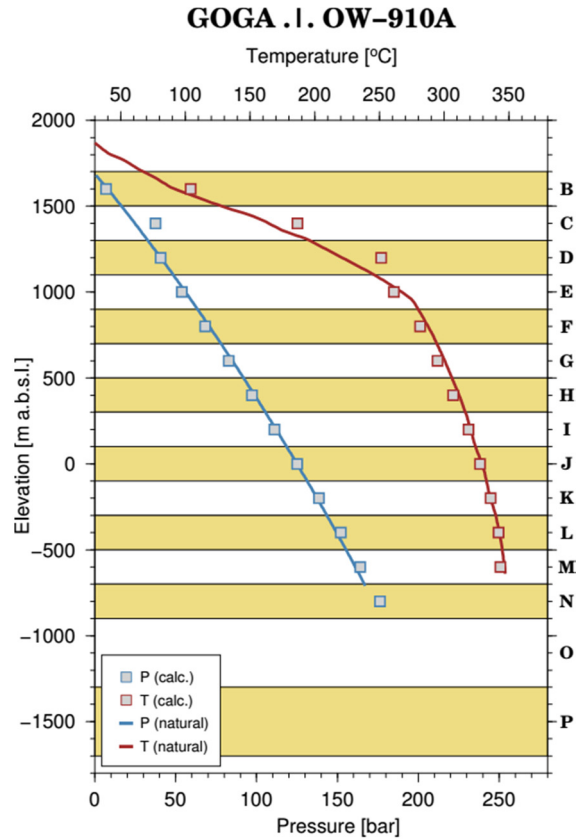
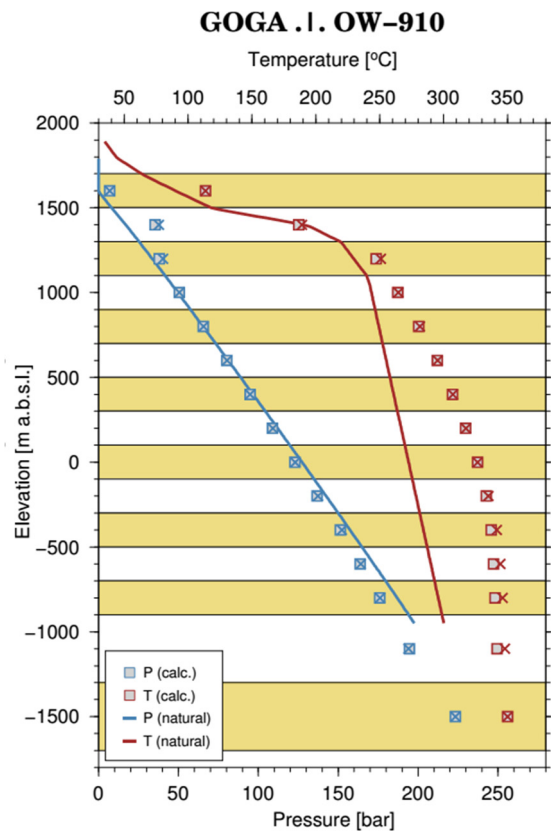


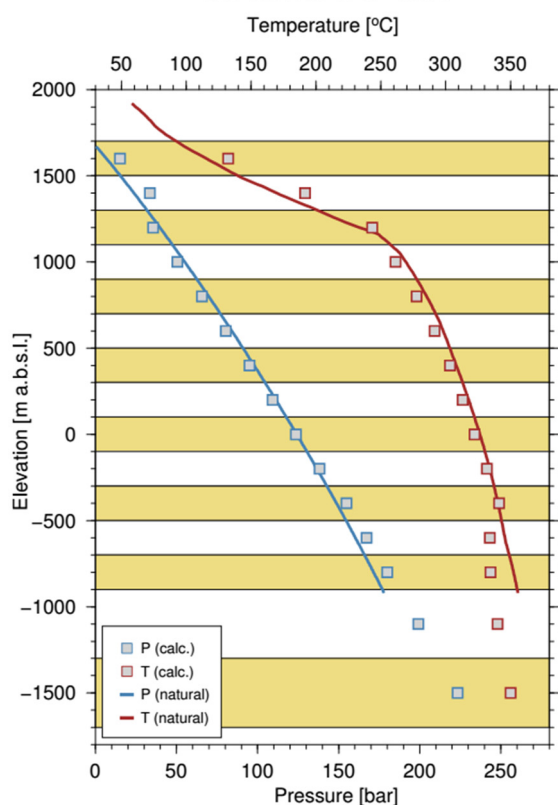
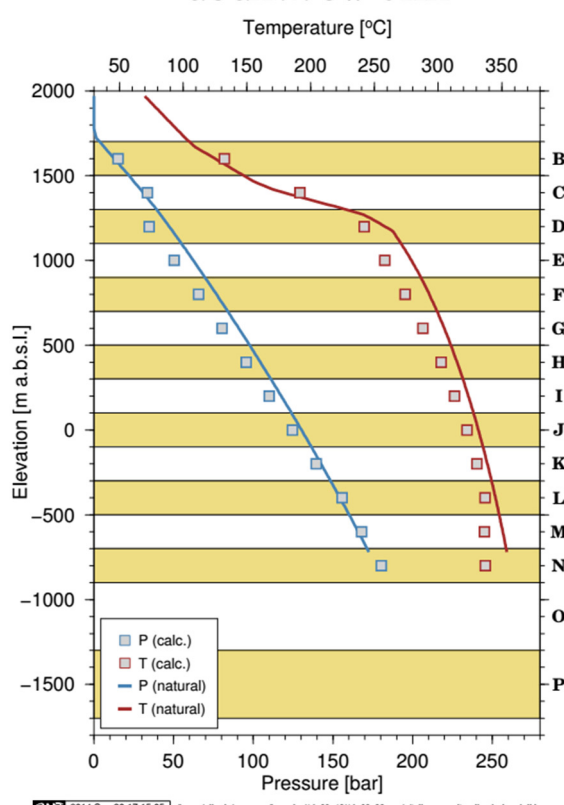
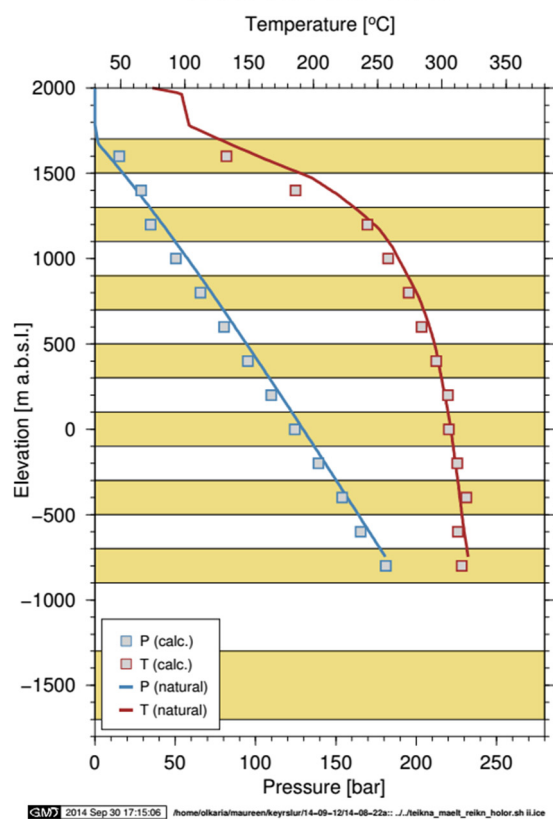
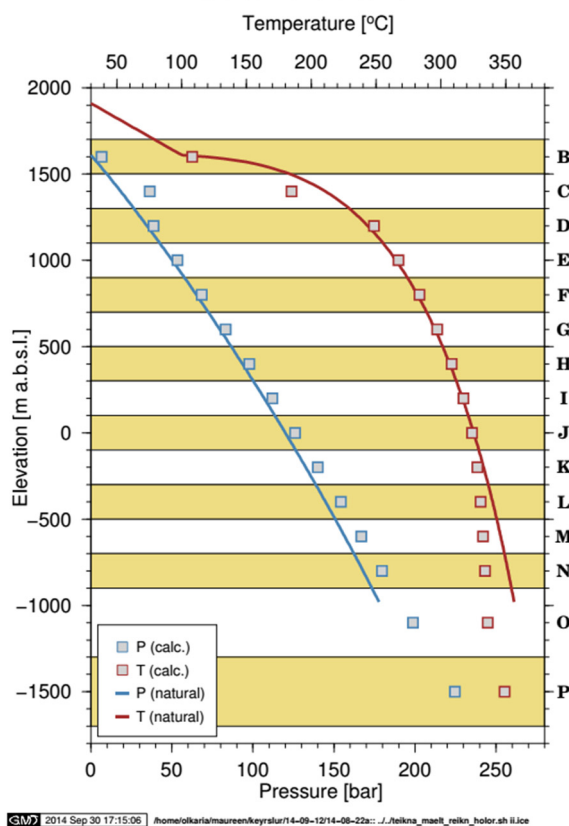


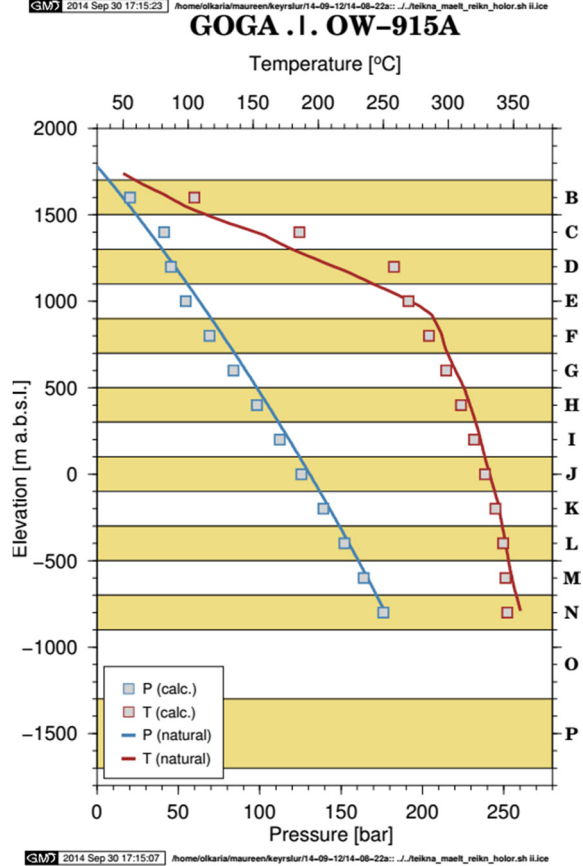
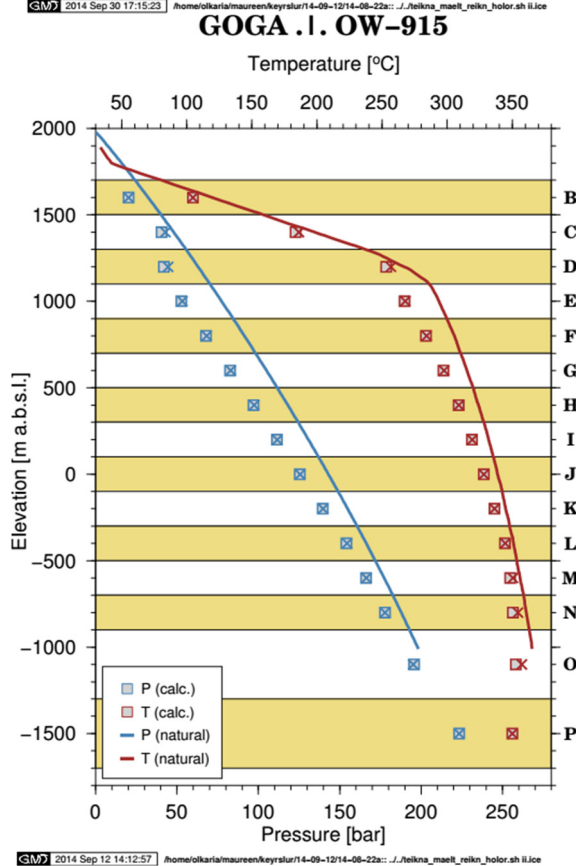
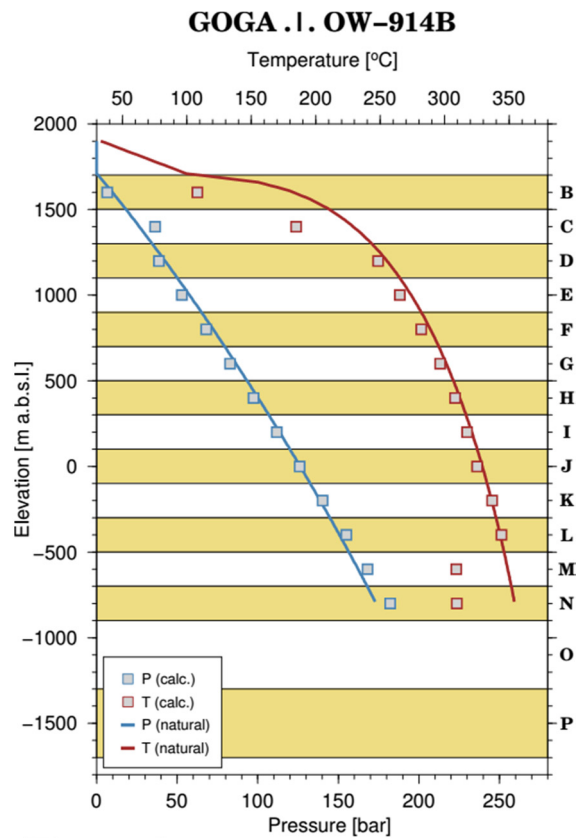
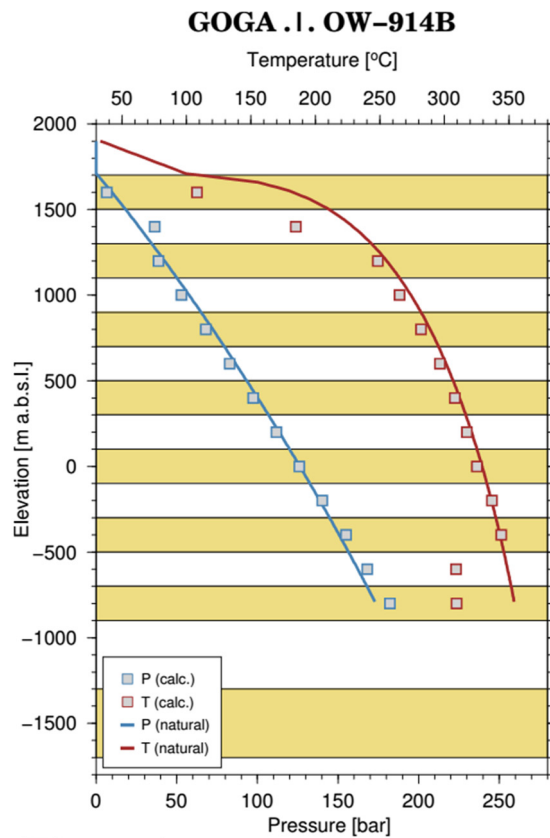
GOGA .I. OW-904A**GOGA .I. OW-904B****GOGA .I. OW-905A****GOGA .I. OW-906**

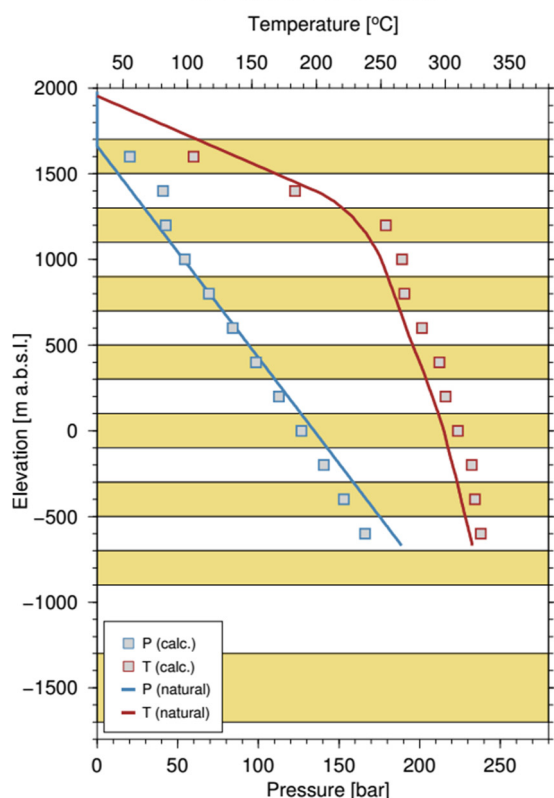
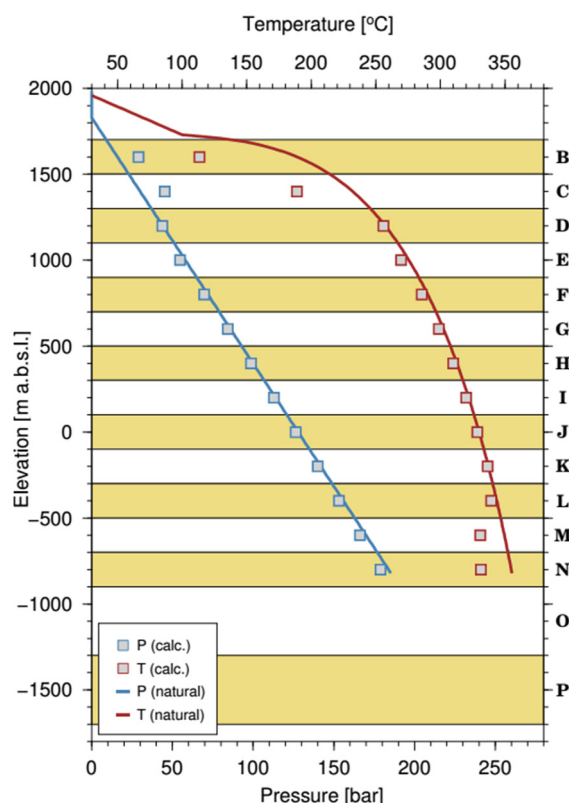
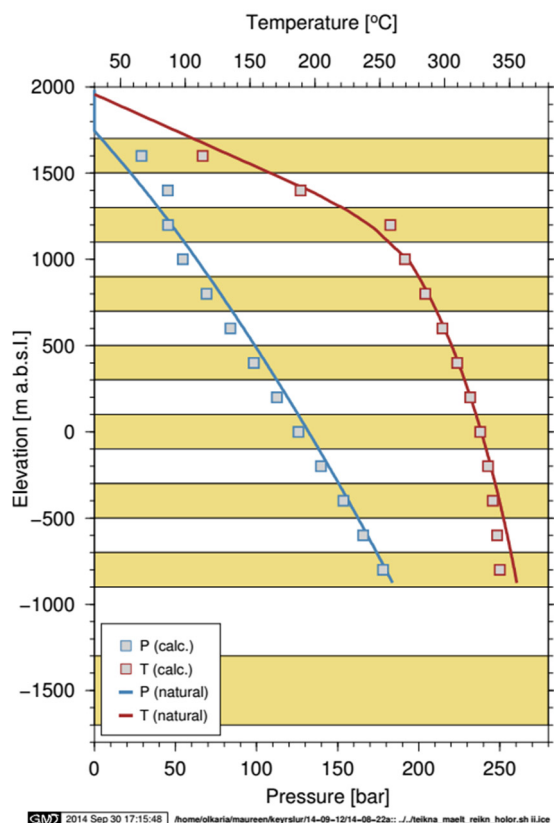
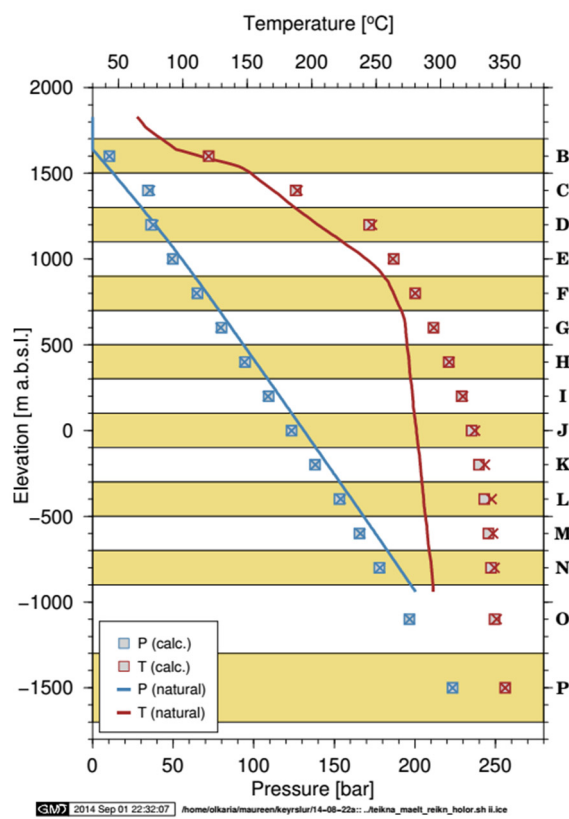
GOGA .I. OW-906A**GOGA .I. OW-907B****GOGA .I. OW-907A****GOGA .I. OW-908**

GOGA .I. OW-908A**GOGA .I. OW-908B****GOGA .I. OW-909****GOGA .I. OW-909A**

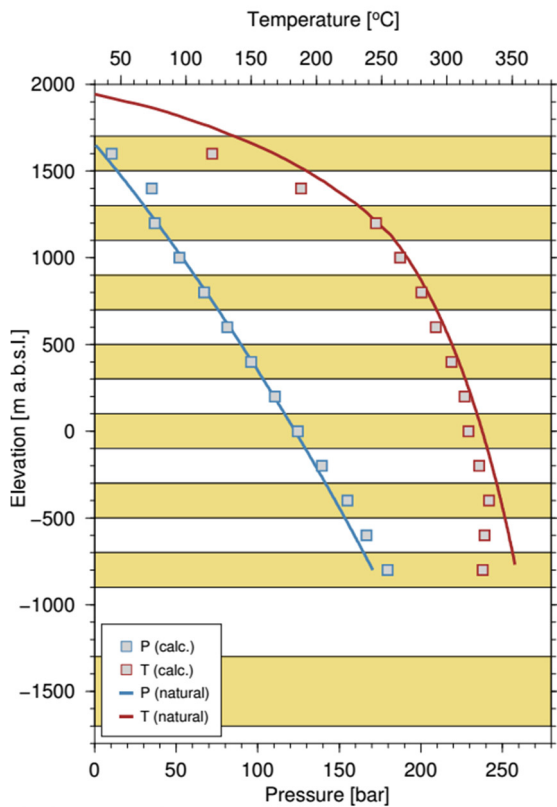


GOGA .I. OW-912**GOGA .I. OW-912A****GOGA .I. OW-912B****GOGA .I. OW-914**

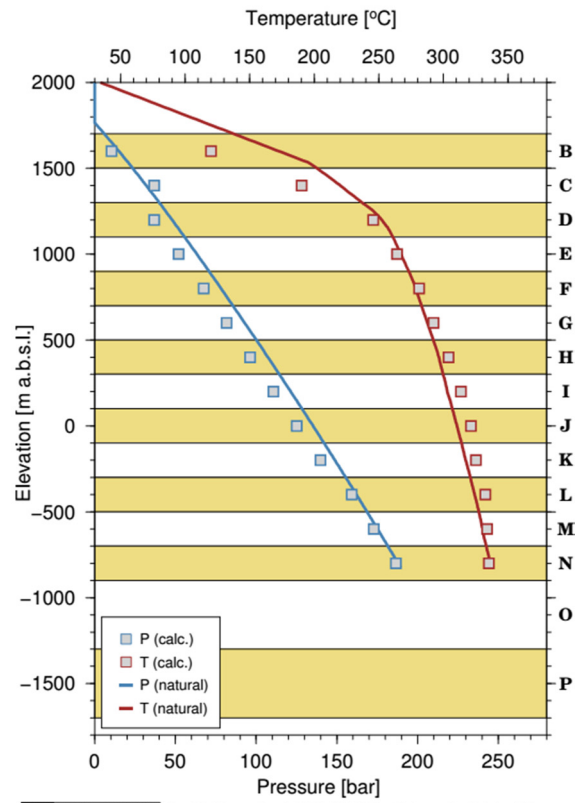


GOGA .I. OW-915B**GOGA .I. OW-915C****GOGA .I. OW-915D****GOGA .I. OW-916**

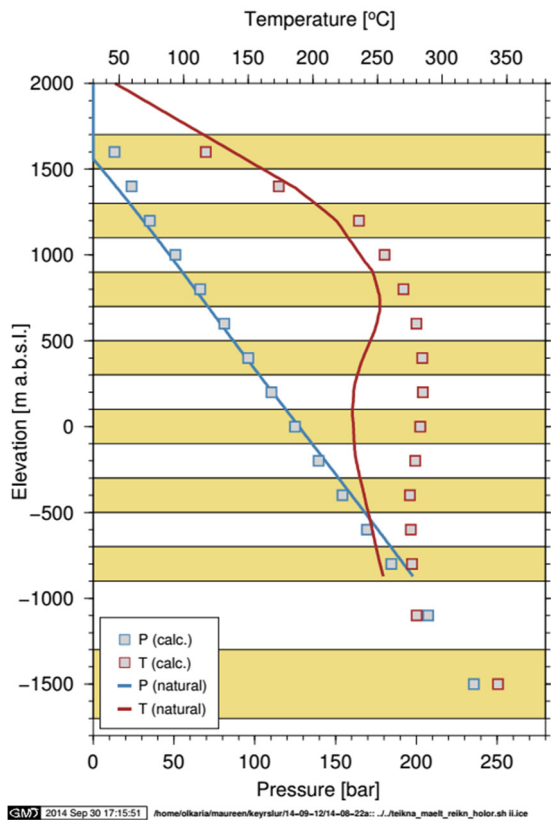
GOGA .I. OW-916A



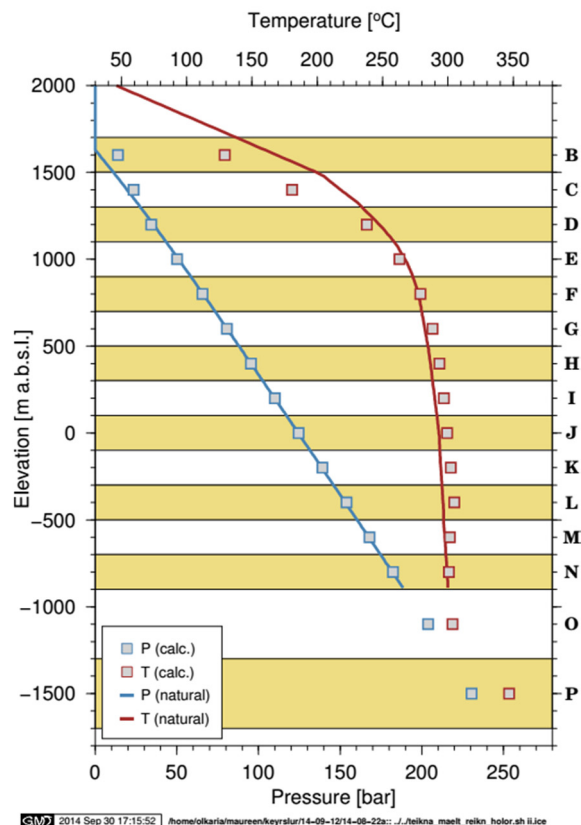
GOGA .I. OW-916B

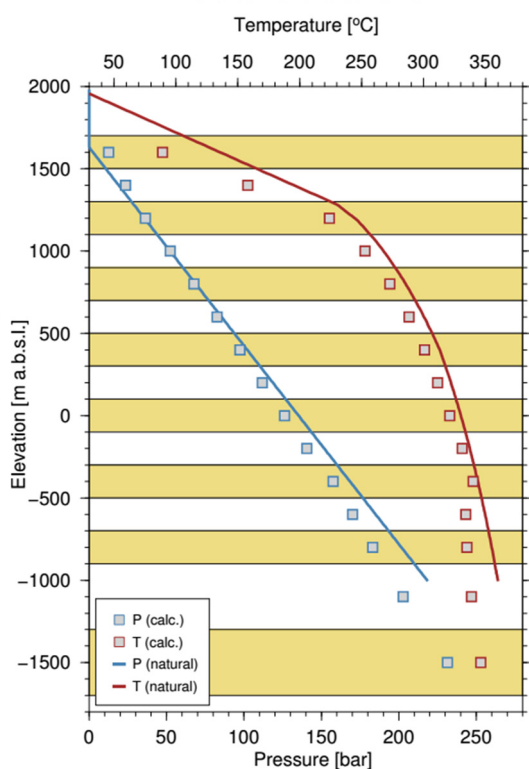
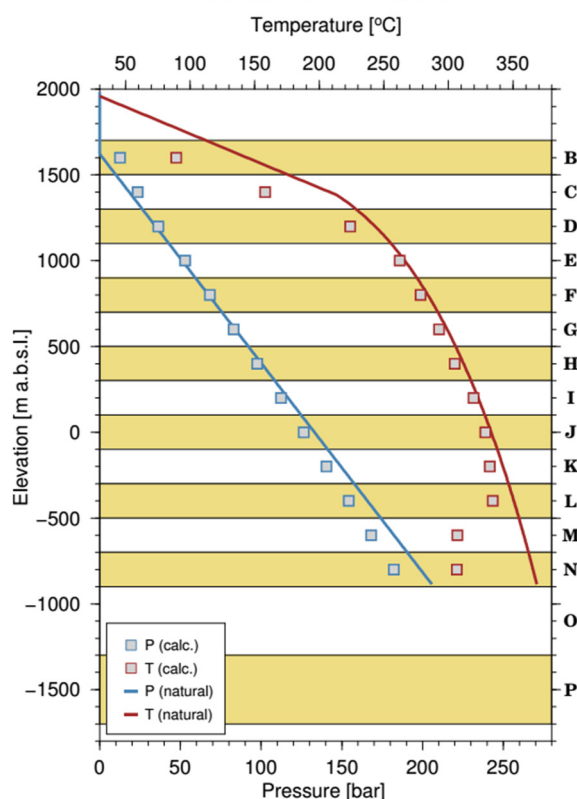
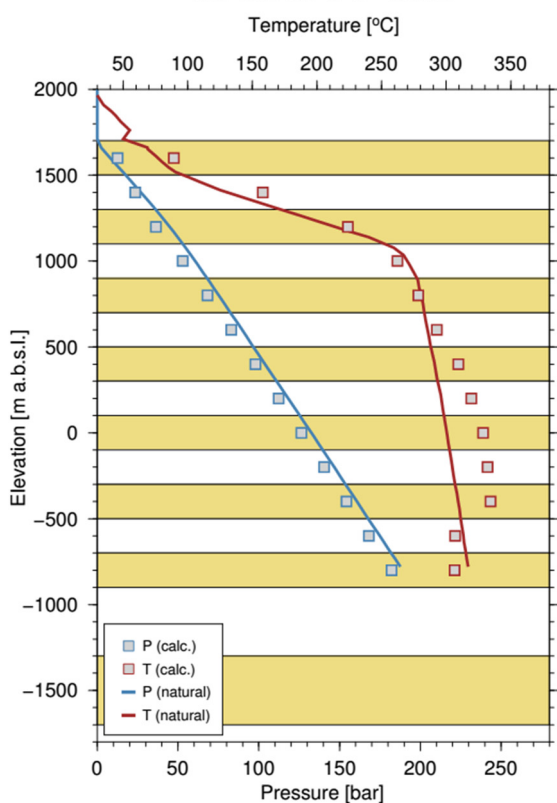
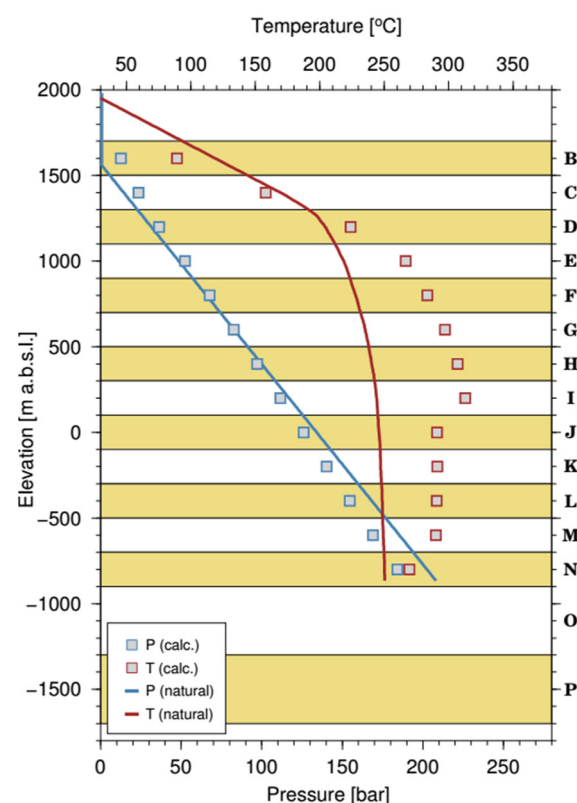


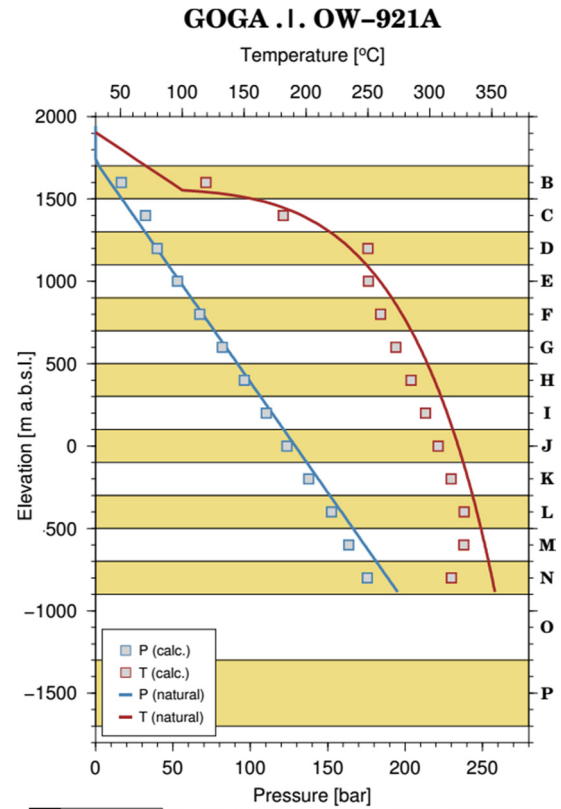
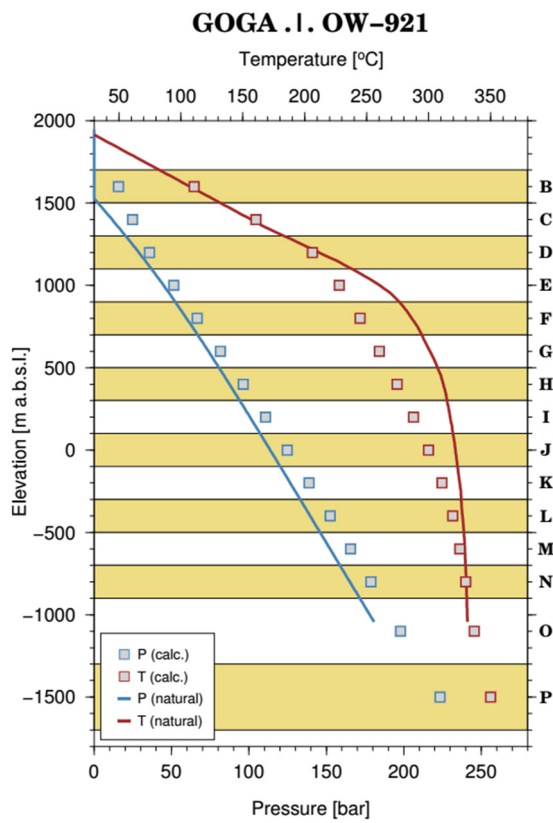
GOGA .I. OW-917



GOGA .I. OW-918



GOGA .I. OW-919**GOGA .I. OW-919A****GOGA .I. OW-919B****GOGA .I. OW-919D**



GM 2014 Sep 30 17:15:13 /home/olkar/maureen/keys/rst/14-09-12/14-08-22a: /J./Reikna_maeli_holor.sh ilice



UNITED NATIONS
UNIVERSITY

UNU-GTP

Geothermal Training Programme

Orkustofnun, Grensasvegur 9,
IS-108 Reykjavik, Iceland

Reports 2014
Number 8

EVALUATION OF FLUID - MINERAL INTERACTION IN THE MENENGAI GEOTHERMAL SYSTEM, CENTRAL RIFT, KENYA

Leakey Ochieng Auko

Geothermal Development Company - GDC

P.O. Box 17700-20100

Nakuru

KENYA

lochieng@gdc.co.ke, leakeyochieng@gmail.com

ABSTRACT

The geothermal reservoir fluid composition, water-rock interaction and possible causes of excess enthalpy were studied in the Menengai geothermal system, Kenya. The reservoir fluid composition and aqueous speciation distribution were assessed based on two models: first assuming that the excess enthalpy was caused by two-phase reservoir fluids (water and vapour) and, secondly, assuming single liquid phase reservoir fluids. The calculated chemical composition of major non-volatile components is relatively similar in both models except when the well discharges approach dry steam. The concentration of the volatiles in reservoir water is significantly lower when assuming a liquid and vapour reservoir and higher when assuming a liquid only reservoir. For these reasons, H₂S geothermometers give significantly lower values when assuming a two-phase reservoir. Moreover, the geothermometer temperatures show a remarkable discrepancy as a result of mixing of fluids from different feed zones that may affect the fluid equilibrium at a given temperature. The exception to this is for wells where the discharges approach dry steam. While there is some uncertainty due to the model calculations, virtually all the common Ca-bearing minerals observed in Menengai are under-saturated. However, andradite and epidote, which also contain Fe (III), show mixed saturation states, whereas Fe (II) bearing minerals are oversaturated; this might be affected by the calculated Fe activity that is sensitive to precipitation and dissolution. Menengai aquifer waters are saturated with respect to albites and K-feldspars. The calculated activity of volatiles in the aquifer water in relation to mineral buffers is model-type dependent. Therefore, activities of the volatiles are close to equilibrium with volatile mineral buffers when assuming two-phase reservoir fluids, while a departure is observed when assuming a liquid reservoir. The trends displayed by the non-volatile Cl concentration in the total well discharge and in the liquid phase as a function of discharge enthalpy suggests that Menengai has a heterogeneous reservoir, with excess enthalpy predominantly caused by phase separation and conductive heat transfer from hot rock or magma to the circulating fluids, also compounding to form superheated steam.

1. INTRODUCTION

Geochemistry in the context of geothermal systems is a multifaceted geoscience that takes into account various physical and chemical processes under different geological conditions. The physical processes include heat and mass transfer, temperature-pressure gradients, permeability and porosity and hydrological fluid flow, just to name a few. The chemical processes include fluid composition, the source of the fluid and fluid-rock interaction. This study focuses on the geochemistry of the Menengai geothermal system, located in the central segment of the Kenya Rift Valley (Figure 1). Development of the field is underway with the primary goal of generating electricity. So far wells have been drilled into the liquid-dominated high temperature geothermal reservoir, most of which have discharged two-phase fluids. However, some wells have discharge enthalpy corresponding to vapour-dominated conditions in the reservoir and have discharged single-phase vapour only.

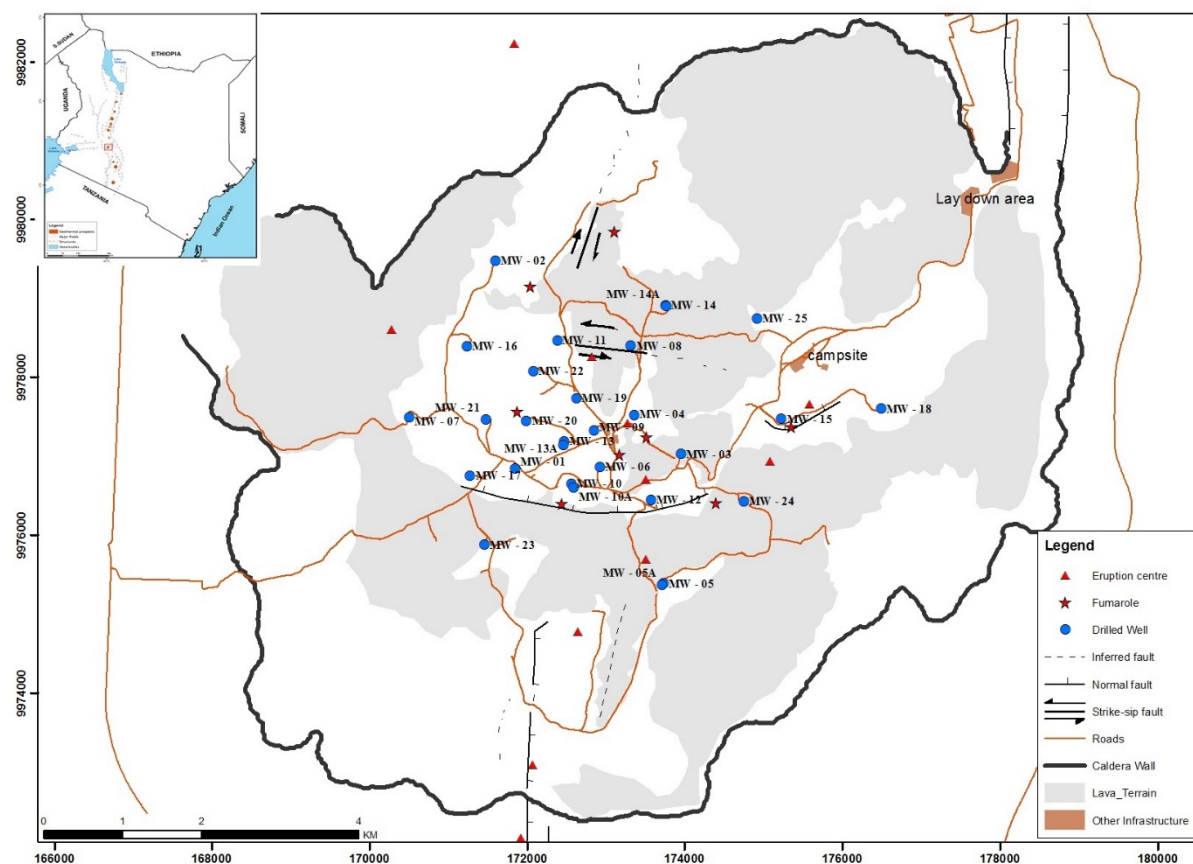


FIGURE 1: Location map of Menengai geothermal field

Previously it was established that the chemistry of the fluids discharged from the Menengai wells was of Na-HCO₃ type (Kipng'ok, 2011; Sekento, 2012; ELC, 2013; Malimo, 2013). The fluid composition of well discharges at the surface is variable, particularly with respect to volatile concentrations. The causes of such variability may be many, including heterogenic reservoir composition and phase predominance (liquid dominated or two phase reservoir fluids) but also boiling induced by heat addition or phase segregation, both of which would lead to increased measured discharge enthalpy at the surface (Arnórsson et al., 2007).

In this study the geothermal reservoir fluid composition, water-rock interaction, and possible causes of discharge excess enthalpy were studied in the Menengai geothermal system, Kenya. The study report was carried out in partial fulfilment of the requirements of the six month diploma course at the United Nations University Geothermal Training Programme (UNU-GTP) with a specialisation in the field of chemistry of thermal fluids.

2. GEOLOGY AND GEOTHERMAL ACTIVITY

2.1 Geology

Menengai is an elliptical piecemeal caldera of the Krakatau-style, formed through different episodes of collapse that are associated with two major eruptions, thus leading to the partly superposed lava flows of different ages. The lava flow covers virtually the entire caldera floor (Figure 1). The rocks conform to the pre-, syn- and post caldera volcanic activities that started about 0.18 Ma (UP and GDC, 2013; Leat, 1984). The surface and subsurface geology of Menengai geothermal field is predominantly trachytic with intercalations of tuff and pyroclastics. Pulses of trachyphonolite are reported to be present in Menengai. Studies of drill cuttings from various wells have also revealed lenses of syenitic intrusions. The varying texture of the trachytes and the intermittent tuff intercepted reflect different eruption episodes. In addition, the highly altered basalt penetrated by some wells at greater depths is presumed to be older than the caldera and could correspond to pre-caldera volcanics that date about mid to late Pleistocene. Geothermal activity manifests on the surface in the form of weak fumaroles, steaming grounds and steam vents, most of which are structurally controlled (Mbia, 2014; Kipchumba, 2013; Lopeyok, 2013; UP and GDC, 2013; Mibei and Lagat, 2012; Omondi, 2011).

Mibei and Lagat (2011) grouped the structural systems in the Menengai field into caldera ring structures, a Molo tectono-volcanic axis, a solai graben and dominant NNW-SSE, NNE-SSW trending faults and fractures. On a regional scale, Menengai caldera is exclusively affected by NNE-SSW striking normal fault kinematics cutting the caldera rim to the north of the Ol' rongai and Solai and Makalia fault system which forms the fissure zone, and the aligned craters north of Ronda Hill to the south, while the western sectors appear to be unaffected. In addition, at the northern rim, the NNE oriented Solai graben cuts the caldera rim, but this fault system is subdued and, therefore, cannot be traced further into the caldera (UP and GDC, 2013; Mibei and Lagat, 2012; Leat, 1984).

UP and GDC (2013) suggested that it appears likely that the local structures with different fault kinematics in the caldera could have formed as a direct consequence of magmatic injection into the uppermost crust and are independent of the regional tectonic stress field. These local structures are perceived to be responsible for the resurgence in an extensional regime and control fumarolic activity.

The majority of the subsidiary structures inside the caldera floor have different orientations and could demonstrate the possible result of an interference pattern between the regional stress field and a local stress-field perturbation. It is, therefore, postulated that central-caldera structures are incompatible with the remainder of the structural inventory and, thus, are interpreted to reflect a local, magmatically driven stress-field perturbation (UP and GDC, 2013). Simiyu (2009) pointed out that the formation of the resurgent dome at the centre of the caldera could be indicative of on-going magmatic activity at depth; therefore, it is reasonable to assume that magma is at a shallower depth around the summit. This is affirmed by the immense shallow seismic events within the caldera centre, north eastern caldera rim and the Olbanita area which, together, embody the areas overlying the heat sources for the geothermal system. These areas have the lowest average v_p/v_s ratios, corresponding to depths of around 4.3 – 5 km. The geometry of the heat source is also underpinned by past (Simiyu and Keller, 2001) and recent (GDC, 2014) gravity measurements which indicate an intrusive body at about 4 km depth with high gravity anomalies concentrated at the summit of the caldera. The joint MT and TEM data reflect a low resistivity anomaly, indicating a magma chamber or a heat source at depths greater than 4 km beneath the Menengai geothermal system (Wamalwa, 2013, 2011; Gichira, 2012).

2.2 Hydrology

The surface drainage is mainly focused on the eastern and western parts of the area and the hydrological flow is mainly directed to the north (Mungania, 2014). Permanent rivers within the precincts of Menengai are the Molo and Rongai in the northwest while the ephemeral rivers are

Wanyororo, Crater and Olbanita in the eastern part. The conduits of the closely spaced network of faults, fractures and fissures essentially control the hydrogeological regime of Menengai system, as demonstrated by N-S trending fault/fractures which channel the disappearing stream in the paleo crater-lake region and other areas (Lagat et al., 2010; Sekento, 2012; Mbia, 2014).

In light of the stable deuterium isotopes, the origin of geothermal fluids in Menengai is typically considered to be comprised of meteoric component. The thermal fluids discharged from Menengai reservoir contain H₂O with a δD value in the range of -10 ‰ to -20 ‰ from fumarolic discharge (Geotermica Italiana Srl, 1987) which correlates with a δD value of about -15.7 ‰ for well MW-04 condensate, while its computed deep δD value is about -4.52‰ due to the susceptibility of steam to isotopic fractionation (Sekento, 2012). In addition, Sekento (2012) further established that thermal fluids from Menengai wells MW-01, MW-04 and MW-06 show a mixture of local groundwater and Lake Nakuru waters.

2.3 Hydrothermal alteration mineralogy

The primary mineralogy of the Menengai rocks consists of olivines, pyroxenes, amphiboles, feldspars, volcanic glass and Fe-Ti oxides including ilmenite and magnetite. The main hydrothermal alteration minerals that have been observed in subsurface rock cuttings include: zeolites, chalcedony, quartz, pyrite, calcite, smectite, hematite, illite, albite, actinolite, chalcopryrite, fluorite, pyrrhotite, epidote, wollastonite, titanite (sphene), chlorite, and actinolite (Kahiga, 2014; Kipchumba, 2013; Lopeyok, 2013; Mibei, 2012; Omondi, 2011). The alteration mineralogy shows a depth zonal distribution with progressive depth: (1) zone of no alteration, (2) smectite-zeolite zone, (3) illite-quartz zone; (4) illite-quartz-wollastonite zone and (5) epidote-wollastonite-actinolite-illite zone (Kipchumba, 2013; Lopeyok, 2013; Mibei, 2012).

The occurrence of these minerals could be a function of varying rock composition within the lithostratigraphy of the geothermal system, changes in temperature with time, pulses of magmatic input and a varying degree of water-rock interaction. Multiple studies have demonstrated that various mineral assemblages, presented in Tables 2 and 3, could potentially buffer the concentration of gases CO₂, H₂S and H₂ in the aquifer fluids of the six discharged two-phase wells used in this study. A considerable number of these mineral buffers have been observed in Menengai except for grossular-andradite garnets and prehnite. Nevertheless, prehnite crystals in drill-cuttings are known to be too small for even electron microprobe analysis (<20µm) (Freedman et al., 2010). Therefore, the possibility of prehnite occurrence cannot be discounted. Albeit not discernible in the presently intercepted Menengai rock cuttings, grossular-garnet and prehnite were still considered in order to evaluate the mineral-solution equilibrium, with respect to H₂S and H₂, since they control the concentration of these gases in most volcanic geothermal systems.

3. CHEMICAL DATA BASE AND DATA HANDLING

3.1 Sampling and analysis

Sampling and analysis of water and steam samples were carried out, as previously described in detail by Arnórsson et al. (2006). Collection of steam and water samples was done using a chromium steel Webre separator attached fairly close to the wellhead of each well during a horizontal discharge testing. The liquid samples were collected into polyethylene bottles while the gas samples were collected in pre-weighed 325-340 ml evacuated gas sampling flasks containing 50 ml of 40% w/v NaOH solution to react with the major non-condensable gases (CO₂ and H₂S), while residual gases (CH₄, H₂, N₂ and O₂) occupy the head space. Water samples were treated upon collection, depending on the analysis required. Samples to be used for the determination of pH, TDS, conductivity, total

carbonates carbon (TCC), Cl, F and B were collected and untreated. Samples for SiO₂ analysis were diluted ten times using deionized water to avoid polymerization of monomeric silica. Samples to be analyzed for cations and SO₄ were filtered through a 0.45 µm millipore membrane. Cation samples were preserved with 1 ml nitric acid, while 1 ml of 0.2 M Zn-acetate solution was added to the samples for SO₄ analysis to precipitate the sulphides in the form of ZnS.

An analysis of the water samples for determination of pH, TDS, conductivity, and TCC was done at the Geothermal Development Company (GDC) laboratory a few hours after sampling. Analysis of CO₂ as TCC and H₂S in the water samples was carried out titrimetrically using 0.1M HCl and 0.001M Hg-acetate, respectively, with the H₂S analysis being done on site. Analysis of the major aqueous cation components (Na, K, Ca, Mg, Fe, Al and Li) was done using the AAS. Chloride analysis was done titrimetrically using the argentometric Mohr's method using AgNO₃ while fluoride was analysed using ISE. The analysis of B, SiO₂ and SO₄ was done spectrophotometrically using UV/Vis, using major reagents such as curcumin, ammonium molybdate, and barium chloride, respectively. Steam samples were analysed for CO₂, H₂S, CH₄, H₂, N₂ and O₂. Non-condensable gases (CH₄, H₂, N₂ and O₂) in the head space of the sampling bulb were analysed by using a Shimadzu model gas chromatograph while analysis for CO₂ and H₂S from the NaOH condensate was done titrimetrically in the same way as the water samples. The chemical results are presented in Table 1.

TABLE 1: Chemical composition of well discharges collected at Menengai geothermal field

Well No.	Sample No.	Sampling date	h ^{dt} (kJ/kg)	p ^{wh} , bar-g	p ^s , bar-g	pH/T°C	Liquid phase components (mg/kg)															Vapour phase (mmole/kg)					
							CO ₂	H ₂ S	B	SiO ₂	Na	K	Mg	Ca	F	Cl	SO ₄	Al	Fe	TDS	CBE ^{ic} (%)	CO ₂	H ₂ S	H ₂	CH ₄	N ₂	O ₂
MW-12	414	27-Feb-13	1600	8.618	8.27	8.5/23.8	3454	74.8	0.319	302	2327	92	0.27	0.23	64	581.3	291	0.35	0.01	4830	-0.5	4758	50.1	243.7	19.2	29.4	0.00
MW-12	438	25-Mar-13	1492	2.965	2.76	9.0/23.9	4554	91.8	0.214	440	3479	68	3.50	0.03	75	705.5	358	0.27	0.68	5980	4.6	2840	27.9	147.2	14.3	7.8	0.00
MW-12	474	6-May-13	1580	5.861	4.14	8.7/22.9	4579	159.8	0.326	528	3567	116	0.35	0.47	64	908.0	227	0.49	0.28	5820	6.2	2862	33.0	115.8	11.7	4.3	0.0
MW-03	323	12-Nov-12	1267	0.483	0.34	7.6/23.4	4796	18.36	0.396	247	2950	99	3.13	0.27	97	984.9	355	0.85	0.78	6210	-4.7	906	2.4	5.8	13.5	24.4	3.2
MW-03	422	8-Mar-13	1303	0.517	0.19	8.6/24.1	4169	10.88	0.089	241	3310	105	4.11	0.03	106	999.4	421	1.2	1.53	6040	2.9	834	2.6	5.6	16.2	12.0	0.4
MW-03	524	3-Jun-13	1249	0.793	0.38	9.3/23.4	4280	12.92	0.127	239	3305	39	3.85	0.12	93	921.0	299	1.4	0.93	5850	0.3	910	1.6	5.0	14.0	7.8	0.9
MW-01	339	28-Nov-11	1191	4.482	2.41	8.9/24.5	7700	15.98	1.400	398	4195	274	0.61	2.878	110	745.5	184	N/A	3.08	7650	-5.5	2924	1.6	3.4	11.4	13.0	0.0
MW-01	353	9-Dec-11	966	4.826	2.76	8.8/21.8	7722	10.54	1.300	367	4358	264	0.93	1.412	114	568.0	178	N/A	3.07	7800	-2.2	6327	6.0	4.0	8.6	16.4	0.0
MW-01	310	10-Oct-12	1358	9.997	7.24	8.5/23.2	6038	70.72	1.175	443	4122	186	N/A	1.08	111	636.3	214	N/A	N/A	7860	5.3	4340	13.1	85.8	25.0	13.2	1.7
MW-01	767	7-Sep-13	1008	3.792	1.03	8.9/20.6	5228	0	0.002	521	3534	135	N/A	0.16	133	600.3	217	N/A	N/A	6170	3.2	2489	0.1	0.0	20.1	60.8	0.0
MW-04	325	18-Nov-11	1378	5.654	3.45	9.1/29.4	5698	241.4	1.874	411	3906	120	0.60	3.029	151	929.5	358	N/A	0.58	7040	-1.8	1900	34.4	78.1	4.4	16.6	0.0
MW-19	241	29-Apr-14	1594	4.413	2.9	7.3/21.5	479	11.9	0.485	286	425	49	N/A	0.1	37	74.6	259	N/A	N/A	1132	-1.4	306	3.4	9.6	0.2	86.3	5.5
MW-19	299	12-May-14	2093	9.308	8.62	9.6/23	407	20.4	1.141	589	683	23	N/A	0.1	71	314.7	226	N/A	N/A	1312	-4.1	240	5.2	29.3	0.7	66.8	1.6
MW-20	95	23-Mar-14	2132	8.963	8.28	8.9/20.9	2232	36.72	0.680	618	2030	246	N/A	0.01	201	579.1	280	N/A	N/A	2840	6.2	1684	10.5	105.7	26.9	0.0	0.0
MW-20	125	3-Apr-14	2376	12.07	12.1	8.8/19.9	2836	73.1	0.657	740	2139	334	N/A	0.01	272	613.6	128	N/A	N/A	3240	1.4	2212	15.3	154.8	34.7	3.5	0
h ^{dt} : Total discharge enthalpy (kJ/kg)																											
p ^{wh} : Well head pressure; p ^s : Sampling pressure																											
CBE ^{ic} (%) difference : (Σ ^z cations ^{.m} .anions ^{.m} - Σ ^z anions ^{.m} .cations ^{.m} + Σ ^z anions ^{.m} .anions ^{.m})*100																											
N/A: Analysis of the chemical component not available																											

h^{dt}: Total discharge enthalpy (kJ/kg)p^{wh}: Well head pressure: p^s: Sampling pressureCBE^{ic} (%) difference : (Σ^zcations - Σ^zanions . ^manions) / (Σ^zcations . ^mcations + Σ^zanions . ^manions) *100

N/A: Analysis of the chemical component not available

3.2 Data quality

Prior to interpretation of the available data of the well discharge chemical analysis, the ubiquitous initial check of the quality based on the Charge Balance Error (CBE) was done by means of the following equation, which is based on electro-neutrality conditions:

$$CBE(\%) = \frac{\sum z_{cat}.m_{cat} - \sum z_{an}.m_{an}}{\sum z_{cat}.m_{cat} + \sum z_{an}.m_{an}} .100\% \quad (1)$$

where z_i is the charge of an ion, i , and m_i is the molal concentration of i (mol/kg). A CBE of the order of magnitude of 10% is invariably regarded as satisfactory (Arnórsson, 2000). Therefore, for the potentially complete data set of the aqueous component from the selected wells, a CBE within the permissible threshold was selected. For the water samples with a pH above 8.5, speciation of total inorganic carbon as HCO_3^- and silica as H_3SiO_4^- was taken into account in the CBE calculations. The gaseous components' atmospheric contamination was used as a criterion for selecting suitable data for interpretation.

3.3 Concentration of the liquid and vapour components

Several studies on the subject of the chemistry of fluids collected from Menengai wells indicate that the fluids are generally of Na- HCO_3 type with a varying composition of the non-condensable gases (Malimo, 2013; ELC, 2013; GAB, 2013; Sekento, 2012; Kipng'ok, 2011). As already pointed out, this study will focus on evaluating the mineral-fluid interaction determined from modelled aquifer water from the chemical compositions of the liquid and vapour collected from 6 selected wells (MW-12, MW-03, MW-01, MW-04, MW-19, MW-20) in Menengai field (Table 1). The fluids are predominantly of Na- HCO_3 type with varying appreciable amounts of chloride content in excess of 500 mg/kg in all the aforementioned wells, except well MW-19 eventually discharged single phase steam only. In addition, SiO_2 also forms part of the major components dissolved in the liquid phase, which is strikingly high in wells MW-19 and MW-20 with concentrations above 500 mg/kg.

The measured discharge enthalpy of the wells spanned between 966 to 2376 kJ/kg. The wells display a variable magnitude of excess enthalpy from intermediate to the high with MW-19 discharge showing dry steam characteristics. CO_2 , H_2 and H_2S constitute the main volatile gas components that preferentially partitioned into the vapour phase sampled at sampling pressures of about 0.19 to 12.1 bar-g. The concentrations of these gases at the mentioned sampling pressures range from 240 to 6327, 0 to 243, 0.1 to 50.1 mmole/kg in the order of the highest to the lowest, respectively. The other major gases are N_2 and CH_4 . Although the selected well MW-04 sample, identified herein as 325, displays a different trend from most of the other wells used in this study, other discharge samples from this well display a similar pattern as that of the other wells. The unavailability of certain components, indicated by (N/A), limited the evaluation fluid equilibrium with minerals that contain Fe and Al (in section 4.2).

3.4 Reservoir fluid composition

After taking into account the analytical quality of the data collected at varying pressures, the selected data set was modelled for aqueous speciation for the purposes of evaluating the reservoir fluid composition and mineral saturation state. The WATCH 2.4 program (Arnórsson et al., 1982; Bjarnason, 2010) was used for this exercise. Menengai wells intercepted a high temperature liquid dominated reservoir with the well discharges having a varying degree in the measured excess enthalpies (i.e. the enthalpy of the discharged fluids is higher than that of the enthalpy of steam saturated liquid at the aquifer temperature: $h^{dl} > h^{fl}$). A twofold approach was used to reconstruct the aquifer fluid composition and the data was used in assessing the mineral fluid equilibria. Firstly, in Model 1, the reservoir was assumed to be liquid only, no heat transfer ($Q^e = 0$) from the rock to the

liquid, no immobilisation of liquid on the formation ($M^{e,l} = 0$) and no additional vapour inflow or loss of vapour ($M^{e,v} = 0$); therefore, no discharge enthalpy was taken into account in the WATCH program since boiling is adiabatic (Arnórsson et al., 2007). In addition, the well discharge enthalpy is the same as that of the parent aquifer fluid.

In Model 2, the system was considered to be closed and that the excess well discharge enthalpy was accounted for by two-phase liquid and vapour reservoir fluid, the cause of the excess enthalpy being heat transfer ($Q^e \neq 0$) to fluids. It is for this reason that the processes leading to the excess discharge enthalpy will also be evaluated, based on the presented data.

The reservoir fluid composition was calculated with the aid of the WATCH 2.4 program (Arnórsson et al., 1982; Bjarnason, 2010). For conservation of mass we have:

$$m_i^{f,t} = m_i^{d,t} = m_i^{d,v} X^{d,v} + m_i^{d,l} (1 - X^{d,v}) \quad (2)$$

where $m_i^{f,t}$, $m_i^{d,t}$, $m_i^{d,v}$, and $m_i^{d,l}$ stand for molal concentration of the dissolved component i for the parent liquid, total discharge, in vapour and in liquid, respectively. $X^{d,v}$ is the vapour mass fraction of the well discharge, hence, the liquid mass fraction becomes $(1 - X^{d,v})$. For conservation of enthalpy we have:

$$h^{f,t} = h^{d,t} = h^{d,v} X^{d,v} + h^{d,l} (1 - X^{d,v}) \quad (3)$$

and

$$X^{d,v} = \frac{h^{d,t} - h^{d,l}}{h^{d,v} - h^{d,l}} \quad (4)$$

where $h^{d,t}$, $h^{d,v}$, and $h^{d,l}$ designate the total discharge enthalpy, enthalpy of saturated steam and enthalpy of saturated liquid, respectively.

For Model 1, the vapour fraction in the reservoir is considered to be zero, and the reservoir enthalpy is calculated based on the reservoir temperature, assuming liquid only. For Model 2, the reservoir is considered to include a vapour fraction, i.e. the mass and enthalpy equations are solved using the measured discharge enthalpy as the total enthalpy of the system along with the reservoir temperature. The quartz geothermometer temperature was adopted, assuming that the aquifer fluids are in equilibrium with quartz.

3.5 Aqueous speciation and mineral saturation

The aqueous speciation distribution was calculated using the WATCH 2.4 program (Arnórsson et al., 1982; Bjarnason, 2010). From those, the mineral saturation state was calculated from:

$$SI = \log(Q/K) \quad (5)$$

where K is the equilibrium solubility constant and Q is the activity product (Q) given by:

$$Q = \prod_i a_i^{v_i} \quad (6)$$

and a_i represents the respective aqueous species activities raised to the power of its stoichiometric coefficient v_i , which is negative for reactants and positive for products.

This study focused on assessing the saturation state of selected hydrothermal minerals including end-members of solid solutions. The minerals include: anhydrite, andradite-grossular, calcite, clinozoisite-epidote, fluorite, hematite, magnetite, Al-prehnite, pyrite, pyrrhotite, wollastonite, albite, K-feldspar, anorthite, paragonite and muscovite. A summary of the alteration mineralogy in Menengai geothermal system is presented in Section 2.3 of this report.

The equilibrium constants for dissolution reactions involving various individual minerals used in this study are presented in Table 2, adopted from the work of Karingithi et al. (2010) and Arnórsson, and Stefánsson (1999). The aforementioned authors took into account the standard thermodynamic properties (ΔG_f^0 , S^0 , V^0 , C_p^0) of the various mineral dissolution reactions and derived them from a wide range of sources. Feldspar solubility constants used in this study are those given by Arnórsson, and Stefánsson (1999) and are valid from 0 to 350 at saturated water and vapour pressure. Equations describing the temperature dependence of the solubility constants of reactions for end member feldspars are also given in Table 2, taking into account the acid calorimetry results for the microcline and sanidine (K- feldspars) solubility constants. The saturation state of other minerals, such as anhydrite and micas, were also evaluated. Thermodynamic data of anhydrite solubility constants were retrieved from Gudmundsson and Arnórsson (2005), based on an experiment which took into consideration the Na-SO₄ iron pairing, whereas the mica functions were based on the Na-K geothermometry equation of Fournier (1991).

The mineral-gas reactions that could potentially control the concentrations of CO₂, H₂S, and H₂ in the aquifer liquid and temperature equations for their equilibrium constants are listed in Table 3, adopted from the work of Karingithi et al. (2010) and Arnórsson et al. (2010) who retrieved thermodynamic data of various minerals from a wide range of sources, as already pointed out. The equations in Table 3 assume a unit activity of all minerals and liquid water (H₂O_(l)). However, as for the equilibrium curves shown and discussed in chapter 5.5, their respective equations were slightly modified to take into account the activities of end-members of minerals that form solid solutions (epidote, garnet and prehnite).

Then, considering reaction 3 in Table 3 we have:

$$\log K = \frac{2}{3} \log (a_{epi}) + \log(a_{H_2S}) - \frac{1}{3} \log (a_{pyr}) - \frac{1}{3} \log (a_{pyrr}) - \frac{2}{3} \log (a_{pre}) - \log(a_{H_2O}) \quad (7)$$

Taking the activities of pyrite (pyr), pyrrhotite (pyrr) and water to be equal to unity, but those of epidote and prehnite in the epidote and prehnite solid solutions to be both 0.8, and in order to determine the equilibrium concentration of aqueous (H₂S) in the initial aquifer, Equation 12 is reduced to:

$$\log(a_{H_2S}) = \log K + \frac{2}{3} \log (a_{pre}) - \frac{2}{3} \log (a_{epi}) \quad (8)$$

At the time of this present study, there was no data available on the mineral activity from Menengai geothermal system, therefore, the mineral compositions were assumed to be the same as those of the Olkaria system, taken from Karingithi et al. (2010) and Arnórsson et al. (2010). For end-member epidote [(Ca₂Al₂FeSi₃O₁₂(OH)], the activity was taken to be 0.8, for end-member prehnite [(Ca₂Al₂Si₃O₁₀(OH)₂] the activity was taken to be 0.8, assuming Al-prehnite, and activity on the order of 0.3 and 0.2 was chosen for grossular and clinozoisite, respectively.

TABLE 2: Temperature equations for equilibrium constants for individual mineral dissolution reactions; the logK is valid in the range 0 to 350°C and at saturated water vapour pressure; unit activity was selected for all minerals and liquid water (Karingithi et al., 2010; Arnórsson, 2009; Stefánsson and Arnórsson, 2005)

Mineral	Abbreviation	Reaction	Log (K) function
1 Andradite	and	$and + 4H^+ + 8H_2O_{(l)} = 3Ca^{+2} + 2Fe(OH)_4^- + 3H_4SiO_4^0$	$+940.225 - 15419.3/T + 0.58092.T - 0.0002971.T^2 - 421.727.logT$
2 Calcite	cal	$cal + 2H^+ = Ca^{+2} + H_2O_{(l)} + CO_{2(aq)}$	$-68.271 + 4385.24/T - 0.007525.T + 28.856.logT$
3 Clinozoisite	czo	$czo + 12H_2O_{(l)} = 2Ca^{+2} + 3Al(OH)_4^- + 3H_4SiO_4^0 + OH^-$	$+36.052 - 6854.78/T + 0.13236.T - 0.00013749.T^2 - 33.508.logT$
4 Epidote	epi	$epi + 12H_2O_{(l)} = 2Ca^{+2} + Fe(OH)_4^- + 2Al(OH)_4^- + 3H_4SiO_4^0 + OH^-$	$+893.547 - 27077.4/T + 0.54124.T - 0.0003022.T^2 - 398.380.logT$
5 Fluorite	flu	$flu = Ca^{+2} + 2F^-$	$+64.54 - 4318/T - 25.74.logT$
6 Grossular	gro	$gro + 4H^+ + 8H_2O_{(l)} = 3Ca^{+2} + 2Al(OH)_4^- + 3H_4SiO_4^0$	$-517.662 + 17623.7/T - 0.14343.T + 203.808.logT$
7 Magnetite	mag	$mag + 4H_2O_{(l)} = 3Ca^{+2} + 2Fe(OH)_4^- + Fe^{+2}$	$+949.951 - 24258.2/T + 0.51474.T - 0.0002402.T^2 - 417.136.logT$
8 Prehnite	pre	$pre + 10H_2O_{(l)} = 2Ca^{+2} + 2Al(OH)_4^- + 3H_4SiO_4^0 + OH^-$	$+833.950 - 25642.8/T + 0.5035.T - 0.0002941.T^2 - 369.297.logT$
9 Pyrite	pyr	$pyr + 2H^+ + H_2O_{(aq)} = 2H_2S_{(aq)} + Fe^{+2}$	$-1.397 - 461.30/T - 0.0009128.T + 1.626.logT$
10 Pyrrhotite	pyrr	$pyrr + 2H^+ = 2H_2S_{(aq)} + Fe^{+2}$	$-3.043 + 1579.06/T + 0.0001987.T + 0.120.logT$
11 Quartz	qtz	$qtz + 2H_2O_{(l)} = H_4SiO_4^0$	$-34.188 + 197.47/T - 5.851 \times 10^{-6}.T^2 + 12.245.logT$
12 Wollastonite	wol	$wol + 2H^+ + H_2O_{(l)} = Ca^{+2} + H_4SiO_4^0$	$-127.096 + 8151.38/T - 0.2981.T + 49.282.logT$
13 Anhydrite	anh	$anh + 2H^+ = Ca^{+2} + SO_4^{2-}$	$+78.414 - 3247.2/T - 9.03 \times 10^{-7}.T^2 - 28.723.logT$
Felspars			
14 Low Albite	alb ^l	$NaAlSi_3O_8 + 8H_2O_{(l)} = Na^+ + Al(OH)_4^- + 3H_4SiO_4^0$	$-96.267 + 305542/T^2 - 3985.50/T - 28.588 \times 10^{-6}.T^2 - 35.7790.logT$
15 High Albite	alb ^h	$NaAlSi_3O_8 + 8H_2O_{(l)} = Na^+ + Al(OH)_4^- + 3H_4SiO_4^0$	$-97.275 + 306065/T^2 - 3313.51/T - 28.622 \times 10^{-6}.T^2 - 35.851.logT$
16 Microline	mic	$KAlSi_3O_8 + 8H_2O_{(l)} = K^+ + Al(OH)_4^- + 3H_4SiO_4^0$	$-78.594 + 311970/T^2 - 6094.13/T - 27.766 \times 10^{-6}.T^2 - 30.308.logT$
17 Sanidine	san	$KAlSi_3O_8 + 8H_2O_{(l)} = K^+ + Al(OH)_4^- + 3H_4SiO_4^0$	$-77.837 + 316431/T^2 - 5744.85/T - 27.712 \times 10^{-6}.T^2 - 29.738.logT$
18 Anorthite	ano	$CaAl_2Si_2O_8 + 8H_2O_{(l)} = Ca^{+2} + 2Al(OH)_4^- + 3H_4SiO_4^0$	$-88.591 + 326546/T^2 - 2720.61/T - 40.100 \times 10^{-6}.T^2 - 31.168.logT$
Thermodynamic data used in Equations 1-12 was retrieved from a wide range of sources as elucidated by Karingithi et al. (2010) while that of anhydrite (Equation 13) from Gudmundsson and Arnórsson (2005). The solubility of end-member feldspars (Equations 14-18) were adopted from Arnórsson and Stefánsson (1999, 2000).			

TABLE 3: LogK-temperature equations for mineral pair and mineral assemblage reactions that may control the gas concentrations in solution; the equations are valid in the range 0–350°C at vapour saturation pressures; unit activity was selected for all minerals and liquid water

		Reaction	Log (K) function
1	CO ₂	$czo + cal + \frac{3}{2}qtz + \frac{1}{2}H_2O_{(l)} = \frac{3}{2}pre + CO_{2(aq)}$	$-0.890 + 7251.5/T^2 - 1710.6/T + 0.0041887 + 0.0000002683T^2 - 0.0624\log T$
2	CO ₂	$\frac{2}{5}czo + cal + \frac{3}{5}qtz + \frac{1}{5}H_2O_{(l)} = \frac{3}{5}gro + \frac{1}{5}H_2O_{(l)} + CO_{2(aq)}$	$-1.449 - 40536/T^2 - 2135.9/T + 0.00656397 + 0.000002725T^2 - 0.193\log T$
3	H ₂ S	$\frac{1}{3}pyr + \frac{1}{3}pyrr + \frac{2}{3}pre + \frac{2}{3}H_2O_{(l)} = \frac{2}{3}epi + H_2S_{(aq)}$	$+13.608 + 592324/T^2 - 9346.7/T - 0.043552T + 0.000029164T^2 + 5.139\log T$
4	H ₂ S	$\frac{2}{3}gro + \frac{1}{3}pyr + \frac{1}{3}pyrr + \frac{2}{3}qtz + \frac{4}{3}H_2O_{(l)} = \frac{2}{3}epi + \frac{2}{3}wol + H_2S_{(aq)}$	$+13.659 + 555082/T^2 - 9256.6/T - 0.043608T + 0.000028613T^2 + 5.148\log T$
5	H ₂ S	$2gro + \frac{1}{4}pyr + \frac{1}{2}mag + 2qtz + 2H_2O_{(l)} = 2epi + 2wol + H_2S_{(aq)}$	$-0.836 - 216659/T^2 - 2847.3/T + 0.008524T - 0.000002366T^2 + 0.152\log T$
6	H ₂ S	$\frac{1}{4}pyr + \frac{1}{2}pyrr + H_2O_{(l)} = \frac{1}{4}mag + H_2S_{(aq)}$	$+13.589 + 590215/T^2 - 9024.5/T - 0.044882T + 0.000029780T^2 + 5.068\log T$
7	H ₂	$\frac{4}{3}pyrr + \frac{2}{3}pre + \frac{2}{3}H_2O_{(l)} = \frac{2}{3}epi + \frac{2}{3}pyr + H_{2(aq)}$	$-1.640 - 124524/T^2 - 777.19/T - 0.0005501T + 0.000007756T^2 - 0.565\log T$
8	H ₂	$\frac{2}{3}gro + \frac{4}{3}pyrr + \frac{2}{3}qtz + \frac{2}{3}H_2O_{(l)} = \frac{2}{3}epi + \frac{2}{3}wol + \frac{2}{3}pyr + H_{2(aq)}$	$-1.544 - 151109/T^2 - 752.389/T - 0.0005868T + 0.000007080T^2 - 0.532\log T$
9	H ₂	$6gro + 2mag + 6qtz + 4H_2O_{(l)} = 6epi + 6wol + H_{2(aq)}$	$+1.444 - 273812/T^2 - 3962.1/T + 0.002401T + 0.000001304T^2 + 0.979\log T$
10	H ₂	$\frac{2}{3}pyrr + H_2O_{(l)} = \frac{3}{4}pyr + \frac{1}{4}mag + H_{2(aq)}$	$-1.654 - 95456.8/T^2 - 621.84/T - 0.001257T + 0.000007569T^2 - 0.600\log T$
The wide range of sources of thermodynamic data used to obtain the temperature equations is outlined by Karingithi et al. (2010) and Arnórsson et al. (2010)			

4. RESERVOIR FLUID COMPOSITION AND TEMPERATURES

4.1 Reservoir fluid chemical composition

The reservoir fluid compositions calculated, assuming liquid only reservoirs (Model 1) and two-phase reservoirs (Model 2), are given in Tables 4 and 5, respectively.

TABLE 4: Chemical composition of initial aquifer fluid assuming liquid only reservoir (Model 1)

Well No.		MW12	MW12	MW12	MW03	MW03	MW03	MW01	MW01	MW01	MW01	MW04	MW19	MW19	MW20	MW20
Sample No.		414	438	474	323	422	524	339	353	310	767	325	241	299	95	125
$h^{d,l}$ (kJ/kg)		876	969	1040	777	768	767	932	912	992	1011	946	840	1099	1121	1219
$T^{f,qtz}$		205.3	225.5	240.4	183.1	181.1	180.8	217.5	213.2	230.4	234.4	220.5	197.3	252.7	257.3	276.5
pH		6.5	6.6	6.7	6.7	6.7	6.8	6.7	6.3	6.7	6.6	6.9	6.5	7.2	6.8	7.0
Dissolved solids (mg/kg)	B	0.3	0.2	0.3	0.3	0.1	0.1	1.2	1.1	1.0	0.0	1.6	0.4	0.9	0.6	0.5
	SiO ₂	283	363	429	211	206	206	333	313	385	402	348	254	488	504	589
	Na	2181	2874	2896	2524	2825	2848	3510	3713	3586	2725	3306	377	567	1656	1702
	K	86	56	94	85	90	34	229	225	162	104	102	44	19	201	266
	Mg	0.25	2.9	0.28	2.68	3.5	3.3	0.510	0.79	0	0	0.508	0	0	0	0
	Ca	0.22	0.02	0.38	0.23	0.03	0.1	2.41	1.2	0.94	0.12	2.56	0.09	0.08	0.01	0.01
	F	60	62	52	83	90	80	92	97	96	102	128	33	59	164	217
	Cl	545	582	737	843	853	794	624	484	553	463	787	67	261	472	489
	SO ₄	291	358	227	355	421	299	184	178	214	217	358	259	226	280	128
	Al	0.33	0.22	0.4	0.73	1.02	1.21	N/A	N/A	N/A	N/A	N/A	N/A	N/A	N/A	N/A
	Fe	0.01	0.56	0.23	0.67	1.31	0.80	2.58	2.62	N/A	N/A	0.49	N/A	N/A	N/A	N/A
	TDS	4527	4940	4725	5313	5156	5040	6400	6645	6839	4758	5958	2007	1088	2317	2578
Dissolved gases (mg/kg)	CO ₂	16386	25508	27407	9862	8932	9230	27467	47806	30068	29102	17673	1933	2137	15467	22137
	H ₂ S	178	241	341	28	22	19	22	39	120	0.8	384	24	47	66	165
	H ₂	31.0	51.7	44.1	1.8	1.8	1.4	1.0	1.2	22.5	0.0	24.2	2.3	10.0	39.4	63.9
	CH ₄	19.3	39.9	35.3	31.3	38.0	31.1	29.9	20.4	52.1	73.8	10.9	0.4	1.9	79.5	113.7
	N ₂	51.0	39.0	21.1	97.1	49.2	31.0	59.5	66.4	48.0	391.0	73.2	269.7	319.7	0	22.9
	O ₂	0	0	0	13.9	0	4.4	0	0	7.1	0	0	19.7	8.7	0	0
$h^{d,l}$: Liquid enthalpy (kJ/kg) at aquifer quartz temperature																
$T^{f,qtz}$: Aquifer temperature based on quartz geothermometer temperature																

$h^{d,l}$: Liquid enthalpy (kJ/kg) at aquifer quartz temperature

$T^{f,qtz}$: Aquifer temperature based on quartz geothermometer temperature

The chemical composition, with respect to major non-volatile elements, is relatively unaffected by the selection of the model when calculating the reservoir fluid composition from the data on water and vapour collected from the well discharges at the surface. The exception to this is when the well discharges approach dry steam (Figure 2). The concentrations of non-volatiles, including SiO₂, Na, K, Mg, Ca, F, Cl, SO₄, Al and Fe, were, however, systematically lower when assuming a liquid-only reservoir compared to two-phase reservoirs.

When assuming reservoir vapour to be present, the concentration of the volatiles in the reservoir water phase is significantly lower than when assuming a single liquid reservoir. The reason for the former is that the volatiles, including CO₂, H₂S, H₂, CH₄, N₂ and O₂, tend to partition into the vapour phase where CH₄ and H₂ somewhat completely enter a steam phase, with little amounts in the liquid phase, whereas CO₂ and H₂S are distributed between the two phases. Also, there is some variability in the elemental concentrations between wells. The depletion of H₂ in the reservoir fluids of some samples from wells MW-03 and MW-01 could be due to boiling processes. It is worth noting that the reconstructed reservoir fluid chemistry of well MW-19 sample 241 seemingly does not agree with that of the other wells and could have been subdued by a possible discharge that was dominated by residual drilling fluid prior to its eventual single-phase steam-only discharge.

TABLE 5: Chemical composition of initial aquifer fluid assuming liquid and vapour reservoir (Model 2)

Well No.		MW12	MW12	MW12	MW03	MW03	MW03	MW01	MW01	MW01	MW01	MW04	MW19	MW19	MW20	MW20
Sample No.		414	438	474	323	422	524	339	353	310	767	325	241	299	95	125
$h^{d,t}$ (kJ/kg)		1600	1492	1580	1267	1303	1249	1191	966	1358	1011	1378	1594	1293	2132	2376
$T^{f,qtz}$		194	204	221	130	125	121	183	207	210	234	176	184	240	240	260
pH		7.7	8.0	7.9	8.6	8.7	8.8	8.2	7.4	7.9	6.6	8.3	8.0	8.1	8.0	8.0
Dissolved solids (mg/kg)	B	0.31	0.18	0.28	0.38	0.08	0.12	1.26	1.12	1.08	0.00	1.77	0.45	0.94	0.57	0.54
	SiO ₂	290	378	445	235	230	233	359	317	404	402	384	258	504	515	608
	Na	2232	2991	3009	2810	3159	3220	3788	3764	3755	2725	3648	383	585	1693	1758
	K	88	58	98	94	100	38	247	228	169	104	112	44	20	205	274
	Mg	0.26	3.01	0.30	2.98	3.92	3.75	0.55	0.80	0.00	0.00	0.56	0.00	0.00	0.00	0.00
	Ca	0.22	0.03	0.4	0.26	0.03	0.12	2.6	1.22	0.98	0.12	2.83	0.09	0.09	0.01	0.01
	F	61	64	54	92	101	90	99	98	101	102	141	33	61	168	224
	Cl	557	606	766	938	953	897	674	491	579	463	869	68	270	483	505
	SO ₄	279	308	191	338	402	291	166	154	195	167	334	234	194	234	105
	Al	0.34	0.23	0.41	0.81	1.15	1.36	0	0	0	0	0	0	0	0	0
	Fe	0.01	0.58	0.24	0.74	1.46	0.91	2.78	2.65	0	0	0.54	0	0	0	0
TDS	4633	5142	4909	5916	5765	5700	6907	6738	7160	4758	6575	2038	1124	2369	2662	
Dissolved gases (mg/kg)	CO ₂	3710	4536	4489	3961	3697	4415	7619	10383	6316	29102	5754	348	559	2356	3365
	H ₂ S	189	206	265	25	24	17	18	27	95	1	385	18	43	79	128
	H ₂	0.18	0.17	0.23	0	0	0	0	0.02	0.12	0	0.04	0.01	0.14	0.3	0.76
	CH ₄	0.11	0.14	0.19	0.01	0.01	0.01	0.06	0.29	0.29	73.79	0.02	0	0.03	0.63	1.39
	N ₂	0.18	0.08	0.07	0.02	0.01	0	0.07	0.58	0.17	391.04	0.06	0.42	3.23	0	0.21
	O ₂	0	0	0	0	0	0	0	0	0.04	0	0	0.05	0.12	0	0
Vapour phase (mg/kg)	CO ₂	221860	160304	162727	44897	40255	41595	174121	1045559	241781	0	94849	15524	18309	81343	102886
	H ₂ S	1635	964	1213	74	71	48	61	419	474	0	990	122	177	346	530
	H ₂	523	384	305	13	13	11	8	32	221	0	180	23	108	236	332
	CH ₄	327	296	244	237	281	236	251	553	512	0	81	4	21	475	590
	N ₂	863	290	146	736	364	235	500	1804	472	0	545	2754	3456	0	119
	O ₂	0	0	0	105	0	34	0	0	69	0	0	201	94	0	0
$h^{d,t}$: Total measured discharge enthalpy (kJ/kg)																
$T^{f,qtz}$: Aquifer temperature based on quartz geothermometer temperature																

$h^{d,t}$: Total measured discharge enthalpy (kJ/kg)

$T^{f,qtz}$: Aquifer temperature based on quartz geothermometer temperature

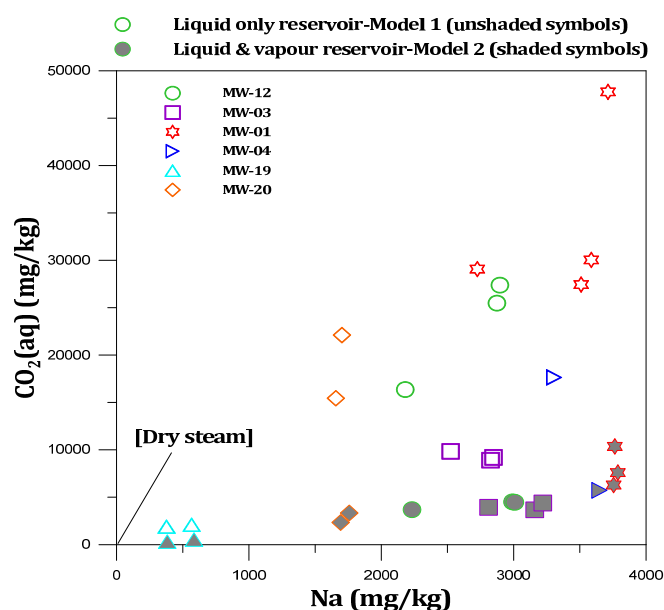


FIGURE 2: Correlation of the concentration of major non-volatile and major volatile components in Menengai aquifer waters

In addition, in both models the boron concentration in reservoir liquids from wells MW-01, MW-04 and MW-19 is generally higher than in the other wells. This could be due to the occurrence of boiling at different depths, determining the enrichment in boric acid in the steam-heated overlying aquifer waters (ELC, 2013). On the other hand, fluoride concentration is distinctly high in Menengai reservoir fluids and ranges from 32 to 217 mg/kg, with well MW-20 having an excess of 150 mg/kg. The fluoride content in the fluids was compared with that of Olkaria 15 and 310, presented in Arnórsson et al. (2010); this high concentration could be reminiscent of the deep fluids of the Kenya's Rift.

4.2 Aquifer temperature

Quartz, Na/K and H₂S were used to estimate the reservoir temperature, using both Models 1 and 2 (Figure 3). The Na/K gives the lowest value of the estimated temperature, although the result is the same for both models as it is based on a ratio (Table 1 in Appendix I). H₂S gives the highest temperature when assuming a liquid-only reservoir, and with a lower temperature when assuming a reservoir with vapour present; this is due to the low dissolved volatile concentrations in the latter case, as the H₂S tends to partition into the vapour phase.

Generally, the results for both models indicate an outright discrepancy in the geothermometer temperatures in most of the wells except for a near conformity seen in well MW-20 and sample 241 of well MW-19 for Na/K against quartz. The conformity in wells MW-19 and MW-20 could substantiate that the samples might have been diluted by condensed steam since their high discharge enthalpy approaches that of dry steam. Samples from well MW-20 and sample 339 from well MW-01 show good conformity between the H₂S and quartz geothermometer temperatures, assuming a liquid only reservoir due to high dissolved H₂S in the aquifer water. The discrepancy in other well samples could be due to the mixing of fluids from different aquifers of significantly varying temperatures, as discussed by Arnórsson (2000). Relatively high sulphate content in the wells showing the non-conformity may confirm the lower temperatures (<200°C), whereas relatively low sulphate content, i.e. in well MW-20, gives high temperatures.

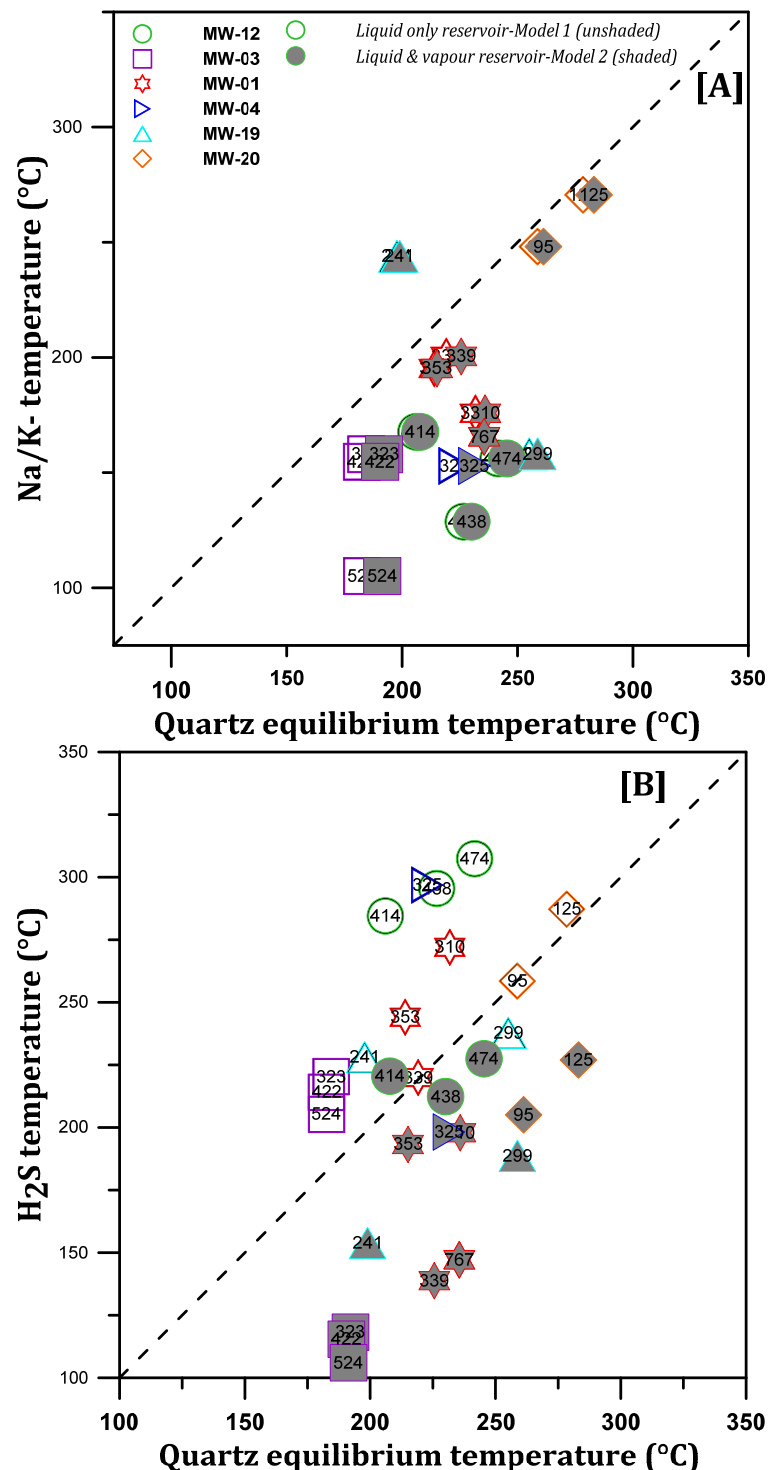


FIGURE 3: Relationship between geothermometer temperatures in Menengai wells, based on Models 1 and 2; A) Quartz function of Fournier and Potter (1982), Na/K (Giggenbach, 1988), B) H₂S (equilibrium with the assemblage of magnetite + pyrite + pyrrhotite was assumed (Equation 6 - Table 3))

GAB (2013) pointed out that, at depths below 2000 m, the wells penetrated a soft layer (magma) and encountered super-heated steam with measured temperatures of almost 400°C and pressure that was

well below critical pressure (P_c), 160 bars as compared $P_c = 221$ bars. In this typical scenario, most wells encountered one or two aquifers above the zone of super-heated steam, one at ~1000-1300 m depth and the other at 1500-1800 m. The upper aquifer seems to be sub-boiling, at ~200°C. The deeper liquid water aquifer is hotter, likely around 250°C. Therefore, the geothermometer temperatures may represent mixed reservoir fluid composition and may not represent a given fluid equilibrated at a given temperature.

5. FLUID MINERAL INTERACTION

Water-rock interaction is conventionally viewed as an irreversible acid-base titration where the water with its dissolved gases acts as the acid while the aggregate of the rock forming minerals act as the base to form stable or metastable secondary minerals. Equilibrium between the hydrothermal solutions and individual minerals was evaluated in this study. This included common hydrothermal minerals observed in the Menengai field and other volatile mineral buffers that potentially control the concentration of CO_2 , H_2S and H_2 in most volcanic geothermal systems.

5.1 Calcite, wollastonite, fluorite and anhydrite

The saturation states of calcite, wollastonite, fluorite and anhydrite in the initial aquifer waters, calculated for selected wells in the Menengai geothermal system, are presented in Figure 4. Generally, the log Q values of calcite (Figure 4A) display a remarkable departure from the equilibrium constant curve for virtually all the samples computed by Model 1, except for sample 325 from well MW-04 which is slightly over saturated (0.2 SI units), possibly due to its high measured pH value (Table 1). The departure is in the range of 0.2 to -2.56 SI units with a mean of -1.44 SI units, reflecting under-saturation of the initial aquifer fluids with respect to calcite.

Alternatively, Model 2 yields a considerable scatter with a mean deviation of -0.3 SI units, for instance five under saturated, two near equilibrium and ten samples under-saturated. It is also worth noting that the computed pH value for Model 2 is 8.8 on average, which is higher than that of Model 1 (on average 6.7 pH units), affecting the calculated activities of aqueous $\text{CO}_{2(\text{aq})}$. Therefore, the pH value obtained for the parent liquid water affects the saturation state of calcite and other minerals whose solubility is pH dependent. Calcite appears in almost the entire stratigraphic column of most Menengai wells.

Calcite under-saturation could be attributed to the high content of dissolved CO_2 which buffers the aquifer pH and consequently affects the kinetics of the solubility of wollastonite; other silicate minerals will be discussed below. Karingithi et al. (2010) also pointed out that the saturation state of wollastonite, fluorite and calcite are intimately dependent on analytical errors and thermodynamics. Therefore, analytical uncertainties resulting from a possible error during the measurement of the pH may be another possible cause for under-saturation. Wollastonite (Figure 4B), fluorite (4C) and anhydrite (4D) are strongly under-saturated in the aquifer waters based on both Models 1 and 2. The removal of Ca from the solution, in order to precipitate calcite from the flashed water and ultimately lead to low Ca in the discharged water, could also substantiate the under-saturation of wollastonite, fluorite and anhydrite. Therefore, the under-saturation of these minerals could also be a function of the kinetics of their dissolution in relation to that of calcite precipitation. Anhydrite is a common hydrothermal mineral found in the lower portions of the chlorite-epidote zone (Freeman et al., 2010). Its stability is considered to be linked with that of epidote (Gudmundsson and Arnórsson, 2005). The observed under-saturation of epidote could also lead to the under-saturation of anhydrite.

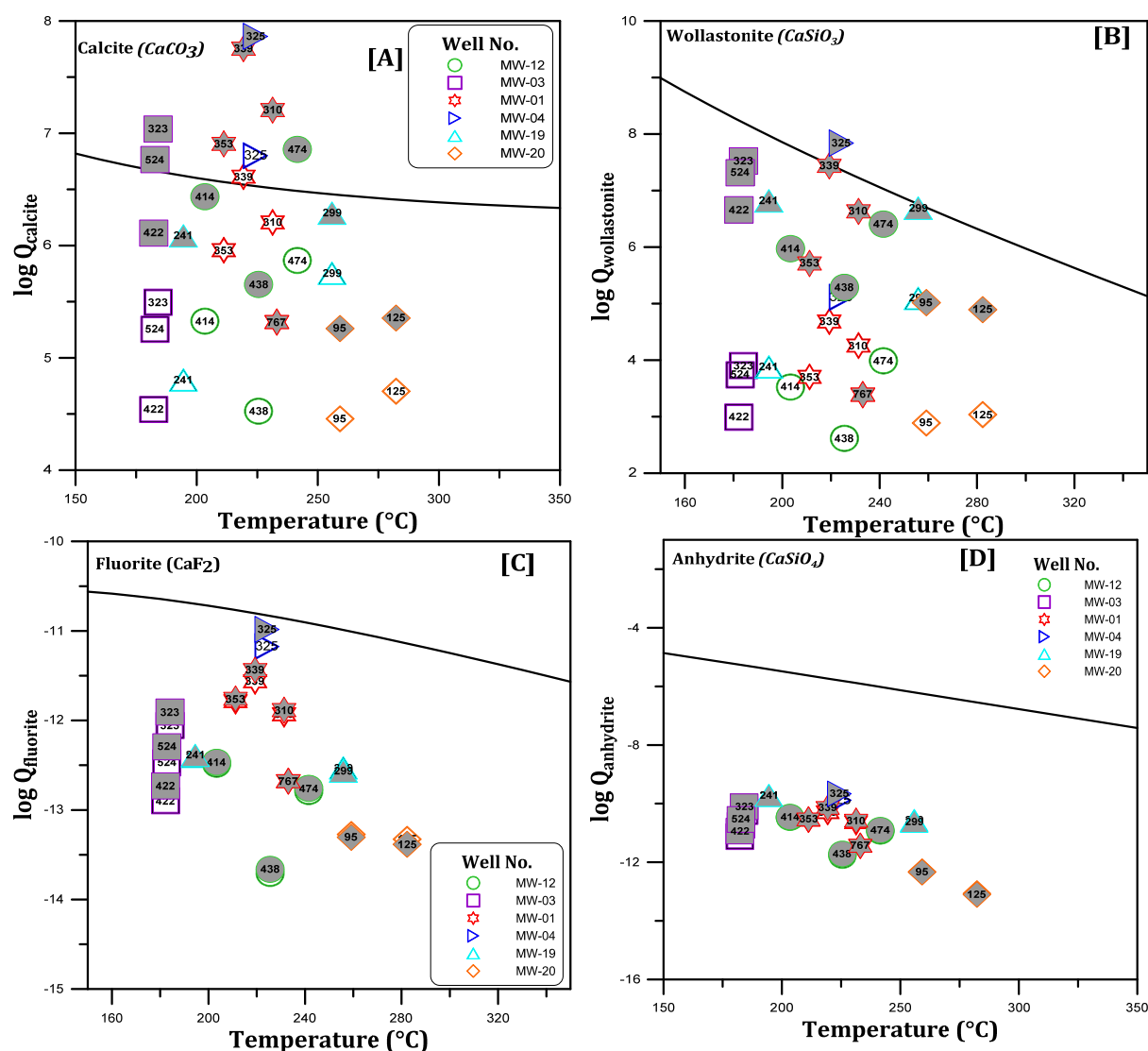


FIGURE 4: Saturation state of Menengai aquifer waters with respect to calcite (A), wollastonite (B), fluorite (C) and anhydrite (D); Model 1: unshaded symbols, Model 2: shaded

5.2 Andradite–grossular, clinozoisite–epidote, and prehnite

Menengai aquifer waters show under-saturation with respect to grossular (Figure 5A), clinozoisite (Figure 5B), and prehnite (Figure 6A) in both models. The $\log Q$ values of andradite, based on Model 1, have remarkably deviated from the equilibrium curve (under-saturated) with a mean SI of -5.3, although sample 353 from well MW-01 is close to equilibrium. Alternatively, when assuming a liquid and vapour reservoir, the andradite SI values seem to reflect oversaturation with an average of 3.6 SI units; but two samples, 414 and 438, from well MW-12, are under-saturated and are somewhat close to the equilibrium curve.

The state of epidote saturation in Menengai waters, based on Model 1, indicates a deviation corresponding to indistinct SI values in the range of -1.37 to 0.97 with some being oversaturated (samples 474 and 323 from wells MW-12 and MW-03, respectively) whereas the rest of the samples are under-saturated. On the other hand, upon assuming a liquid and vapour reservoir (Model 2), epidote is oversaturated (1.56 SI units on average) in virtually all the samples.

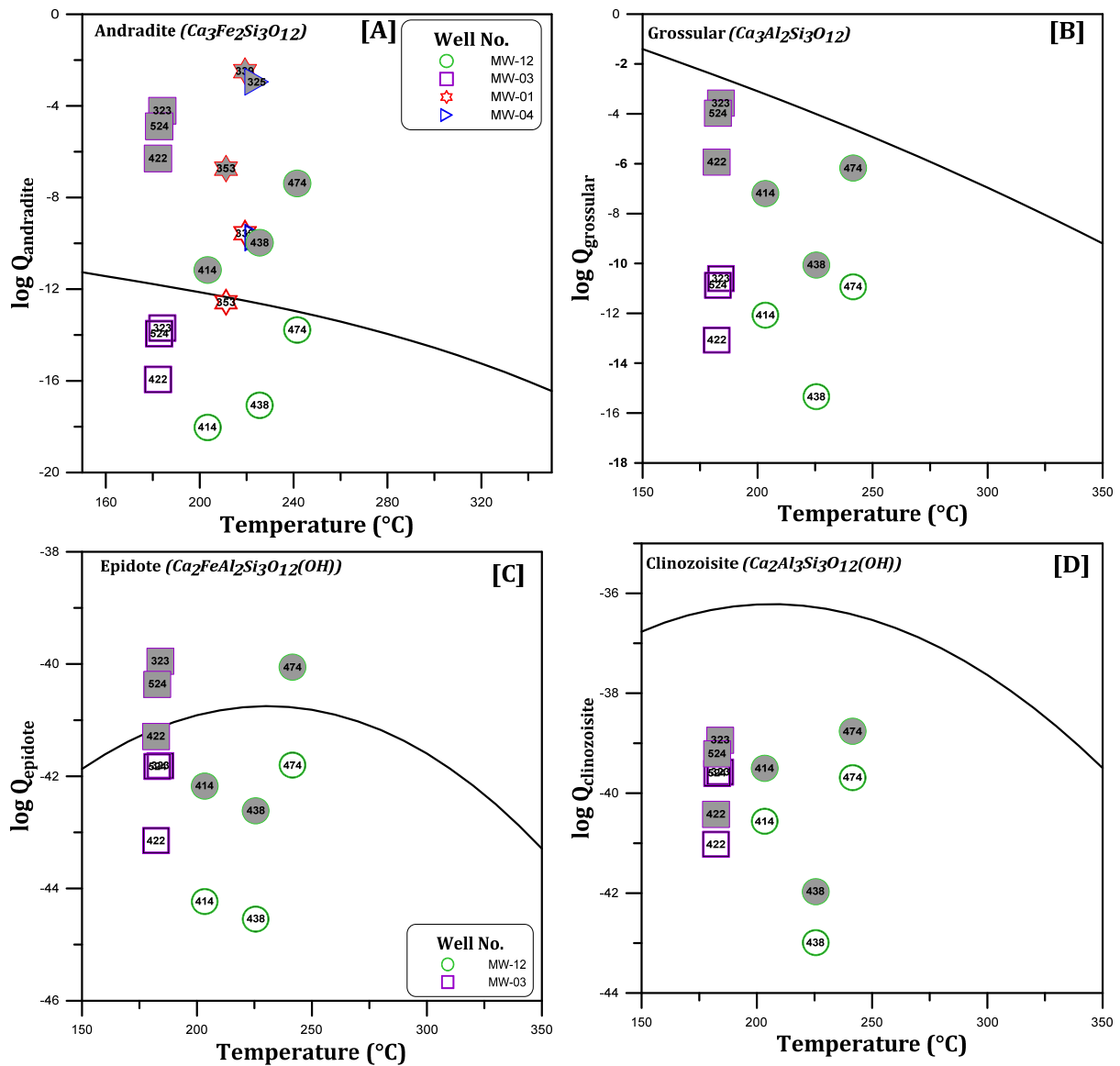


FIGURE 5: Saturation state of Menengai aquifer waters with respect to andradite (A), grossular (B), epidote (C) and clinozoisite (D); Model 1: unshaded symbols; Model 2: shaded

The saturation state of these minerals can be attributed to the following: The solubility of the Ca-alumino-silicate minerals, particularly the garnet minerals (grossular and andradite), is strongly dependent on the pH as per their stoichiometric reactions. Gudmundsson and Arnórsson (2005) concluded that since garnet invariably forms under contact metamorphism, its oversaturation in the Krafla aquifer fluids owes its existence to a temporary development due to magmatic intrusions in the reservoir. Albeit not observed in the rock cuttings, this reason could also explain oversaturation of andradite-garnet in the Menengai aquifer waters when computed with Model 2, while taking into account the intercepted intermittent magmatic intrusions.

The scatter from equilibrium displayed by the OH bearing silicates could also be due to the stoichiometry of the respective minerals, the OH-bearing silicates (epidote, clinozoisite and prehnite) having the largest number of cations per OH. For minerals (andradite and epidote) which contain Fe (III), over-estimation of the $Fe(OH)_4^-$ activity is considered to be the possible cause for the positive SI values recorded, as per the study of ferrous and ferric hydrolysis constants above 200°C by Arnórsson et al. (2002) and underpinned by Karingithi et al. (2010).

5.3 Magnetite, pyrite, and pyrrhotite

Menengai initial aquifer waters are systematically oversaturated with respect to magnetite (9 SI units on average in both models), pyrite and partly with pyrrhotite which has a few samples that are undersaturated when computed with respect to the two models (Figure 6).

The generally observed oversaturation of these minerals in Menengai aquifer waters compares with that of the initial aquifer waters of Námafjall (Gudmundsson and Arnórsson, 2005) and that of Olkaria (Karingithi et al, 2010). It, therefore, follows that the deviation of logQ values of these Fe (II) bearing minerals is largely due to the variations in the calculated activities (Gudmundsson and Arnórsson, 2005; Karingithi et al., 2010). The activity of Fe^{2+} is mostly affected by dissolution or precipitation of Fe, which varies considerably. Another possible reason for the deviation from equilibrium in most of the Fe-sulphides, as well as the previously discussed Fe-bearing silicates, could be due to the high Fe content in some of the well discharge that is, in some cases, recorded in high content in condensate samples that might be a result of analytical uncertainties. Moreover, a possible cathodic corrosion of the casing material cannot be discounted as a likely cause of the elevated Fe contents in the discharged fluids and, hence, the scatter in the selected samples.

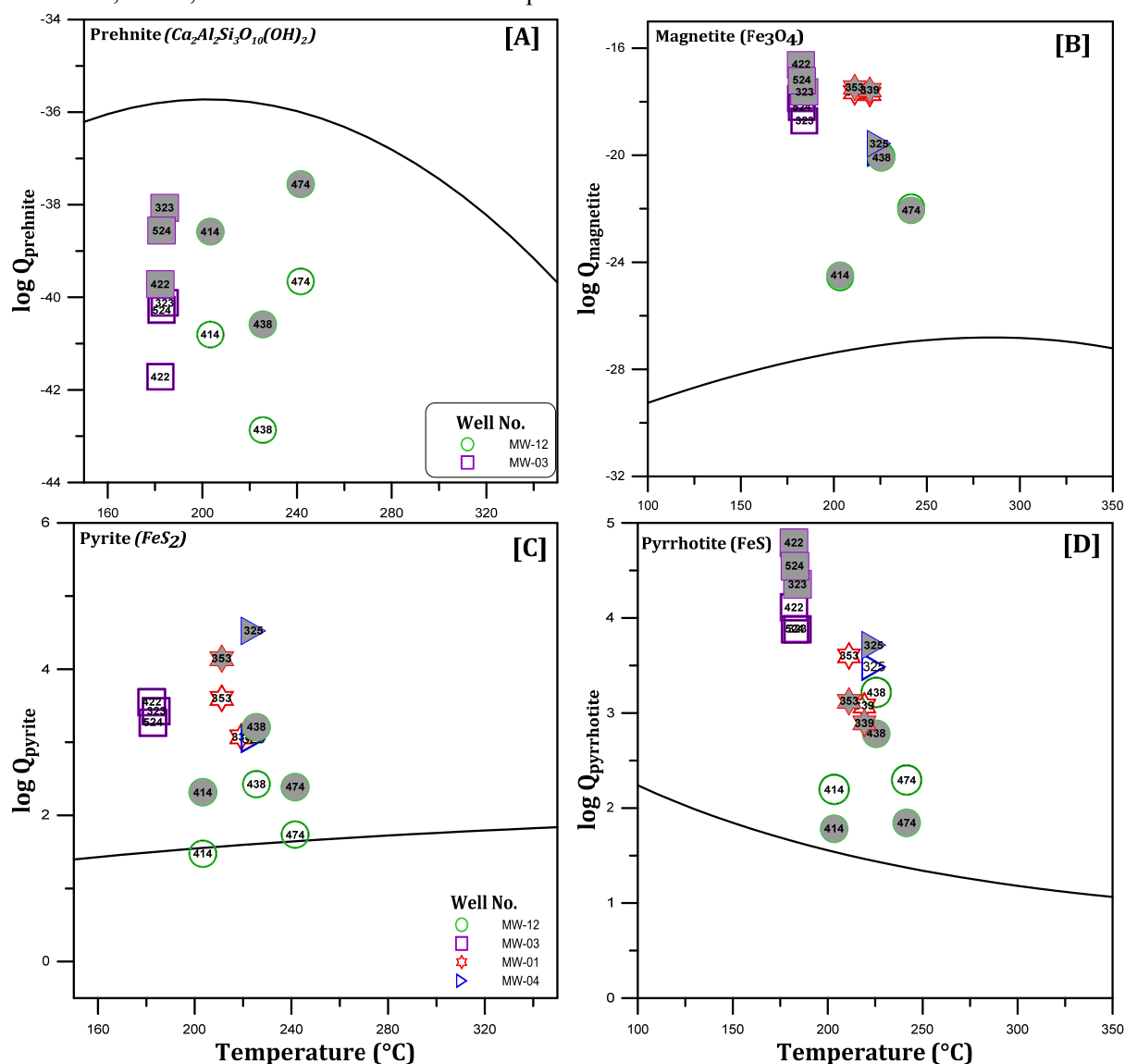


FIGURE 6: Saturation state of Menengai aquifer waters with respect to prehnite (A), magnetite (B), pyrite (C) and pyrrhotite (D); Model 1: unshaded symbols; Model 2: shaded

5.4 Feldspar saturation state

In Menengai, both sanidines and plagioclases occur as the major groundmass component as well as phenocrysts, while albite is the secondary mineral from the feldspars (Kipchumba, 2013; Mibei, 2012). The saturation state of pure Na, K feldspars solubilities in aquifer waters was reconstructed, based on the two models, and is presented in Figure 7. The results show that the water from wells MW-12 and MW-03 are close to super-saturation with respect to low and high albite and microcline and sanidine with a few data points showing a very slight deviation. The high dissolved CO_2 in the aquifer waters may enhance feldspar dissolution since its solubility is pH dependent, thus might lead to super-saturation. The saturation state of the feldspars generally might have been affected by Al analysis and the calculation of the $\text{Al}(\text{OH})_4^-$ activity.

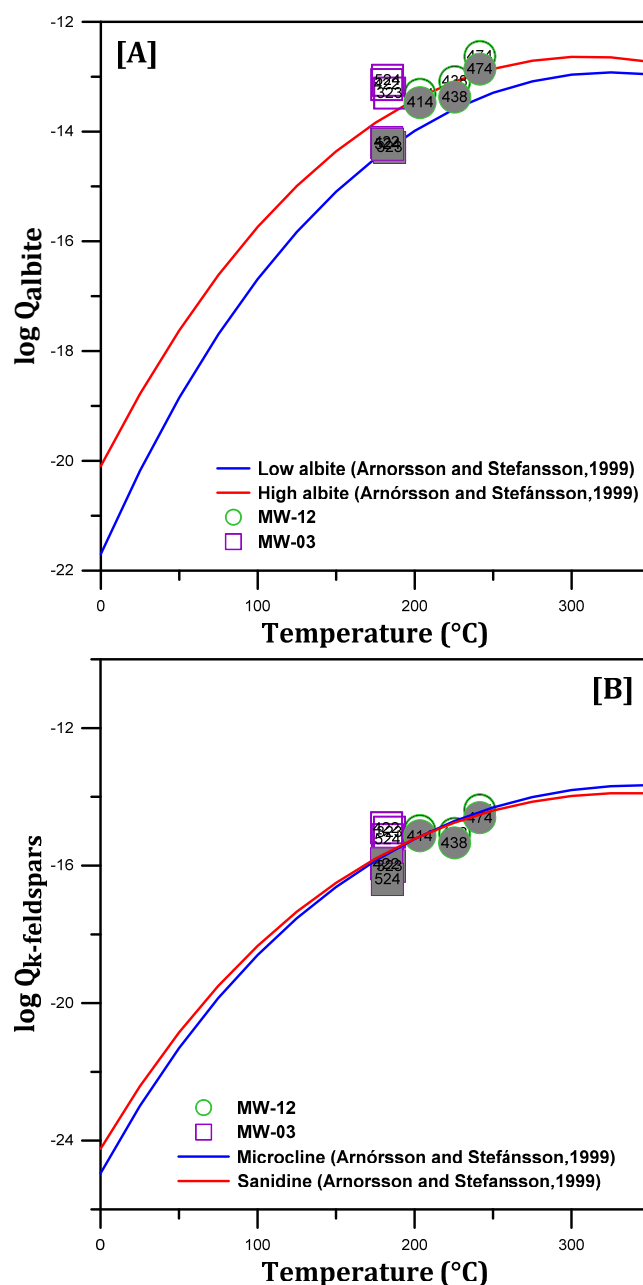


FIGURE 7: The saturation state of end-member feldspars as a function of temperature for pure albite (A) and K-feldspars in Menengai aquifer waters (B)

On the other hand, anorthite is under-saturated in Menengai aquifer waters, as marked by the departure from equilibrium (Figure 1 in Appendix II). Stefánsson and Arnórsson (2000) observed that the saturation state of anorthite in natural waters is somewhat different from that of albite and K-feldspars. The activity ratio of $\text{Ca}^{2+}/\sqrt{H^+}$, which is a function of temperature in geothermal waters, controls the aqueous concentration of calcium which is dependent on mineral (epidote, prehnite, and quartz) equilibrium. In addition, the under-saturation of anorthite could also be attributed to the earlier explained highly dissolved CO_2 , pH discrepancy and low Ca^{2+} content which have an effect on the activity ratio of $\text{Ca}^{2+}/\sqrt{H^+}$. Analytical uncertainties of Al, Ca, and SiO_2 as well as calculation of the $\text{Al}(\text{OH})_4^-$ activity might affect the saturation state of feldspars. To eliminate the effect of the analytical uncertainties of Al and aqueous SiO_2 , the Na^+/K^+ activity was computed while considering the simultaneous equilibrium of the feldspars.

Na^+/K^+ activity ratio versus temperature (Figure 2 in Appendix II) corresponds well with the simultaneous equilibrium of low albite/microcline for temperatures above 200°C , typical of well discharges that are approaching dry steam, and high albite/sanidine for temperatures below 200°C . It has been suggested that the Na^+/K^+ activity ratio in geothermal waters is controlled by equilibrium between solution and low albite and microcline when temperatures exceed 200°C (Stefánsson and Arnórsson, 2000).

5.5 Volatile mineral buffers CO₂, H₂S and H₂

The equilibrium curves of mineral assemblages that could potentially control the activities of the main reactive gases CO₂, H₂S, H₂ were compared with that of the calculated dissolved gas concentrations. The results for both models are shown in Figure 8.

For CO₂, the activities of CO₂(aq) in the reservoir water are calculated to be much higher, assuming a liquid only reservoir (i.e. Model 1), whereas the CO₂(aq) concentrations are lower when assuming reservoir vapour to be present together with the liquid water. The reason for this has to do with two things: first, the calculated reservoir pH values are lower in the case of liquid only reservoirs, resulting in higher calculated activities of CO₂(aq); second, assuming reservoir vapour to be present, a considerable fraction of the CO₂ enters the vapour phase, decreasing the total dissolved CO₂ concentration in the liquid phase, as well as the activities of aqueous CO₂(aq). Similar trends were observed with respect to H₂S.

With respect to CO₂(aq), the reservoir fluids, assuming no reservoir vapour to be present (Model 1), results in excess CO₂ compared to possible mineral buffer equilibrium values. However, assuming a reservoir vapour fraction to be present, conditions close to equilibrium were observed. The same is true for H₂S except the difference between the two models was insignificant, i.e. calculated H₂S(aq) concentrations were close to those predicted by mineral buffer reactions.

With respect to H₂, the results are different. Assuming a liquid only reservoir, calculated reservoir H₂ concentrations were orders of magnitude higher compared to when assuming two-phase reservoirs, i.e. liquid and vapour phases. The reason for this is that H₂ is very insoluble. Upon initial boiling (vapour formation), H₂ will quantitatively enter the vapour phase, resulting in very low concentrations of H₂ in the boiled water; in turn, in two phase reservoirs all the H₂ is within the vapour phase. The measured H₂(aq) concentrations for both models were somewhat out of equilibrium with respect to common mineral buffers. This may, in fact, be an artefact

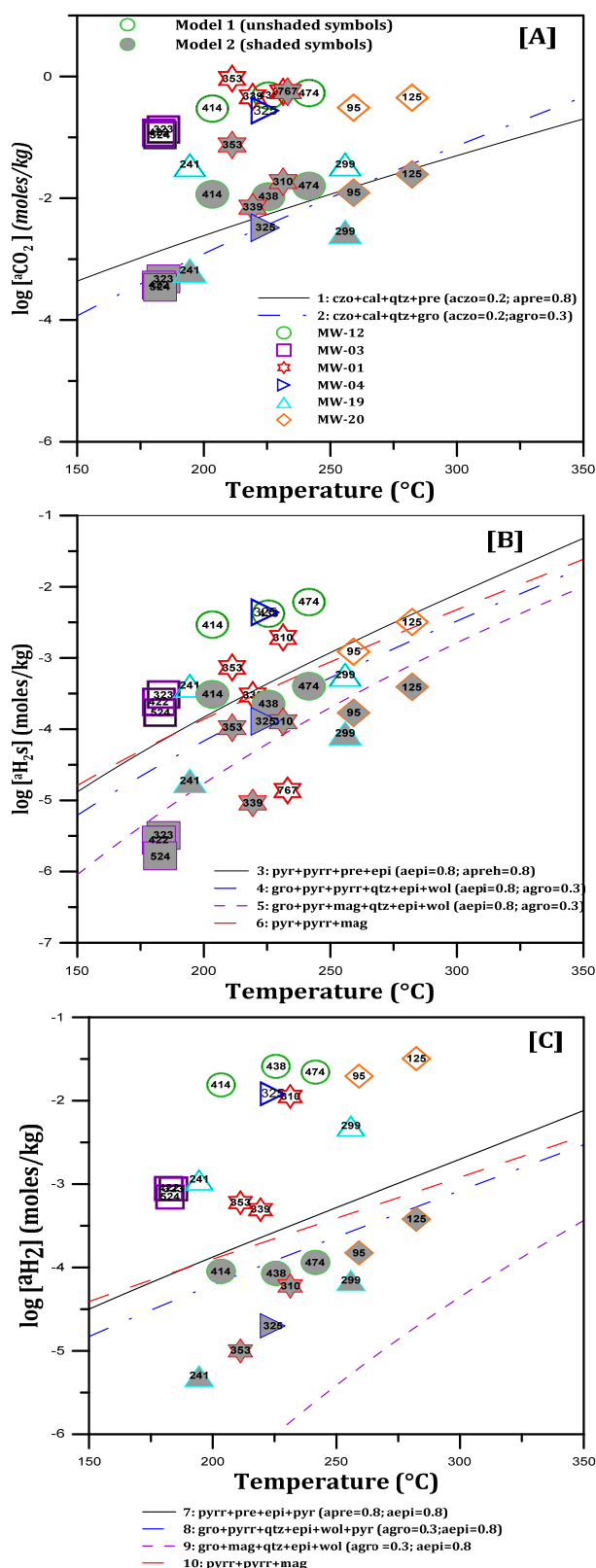


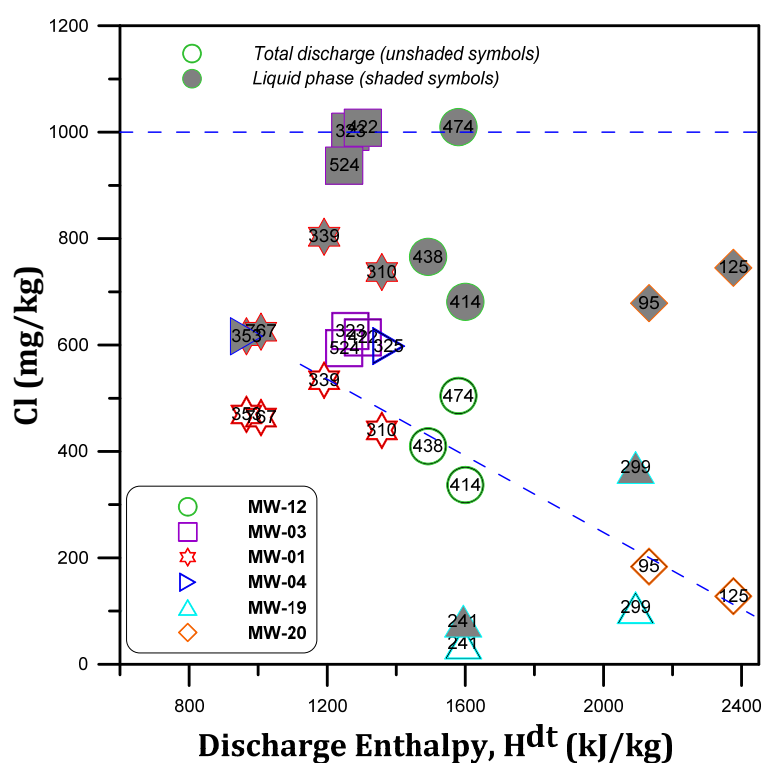
FIGURE 8: State of equilibrium between dissolved CO₂ (A), H₂S (B) and H₂ (C) in the aquifer waters of Menengai wells with several mineral assemblages

related to the assumptions made when calculating the reservoir fluid composition from samples collected at the well-head.

These factors need to be considered when assessing the source of volatile gases in the geothermal reservoir. In fact, calculated excess reservoir gas concentrations relative to mineral buffer reactions, like that observed for CO_2 and H_2 , may be the consequence of the model being applied while calculating the reservoir fluid composition rather than true observation. Formation of vapour, either in the reservoir upon heat addition or because of phase separation of liquid water and vapour, may be of importance when making reservoir fluid calculations.

6. THE CAUSE OF EXCESS ENTHALPY

The cause of calculated excess reservoir gas concentration and excess discharge enthalpy may be the result of the same process. For the calculations of reservoir composition, it was assumed that the system was isolated, i.e. no exchange of either matter or energy could take place from the reservoir to the sampling condition. Boiling in natural geothermal systems may, however, not be isolated as heat from hot rock or magma may induce boiling (closed system). Also, the density of the vapour is much less than liquid water; therefore, depending on the hydrological nature of the system, phase separation (open system), either full or partial, may take place (Arnórsson et al., 2007; Scott et al., 2014). As pointed out by Scott et al. (2014), the latter process may be studied by looking at the concentration of a non-volatile like Cl in the liquid phase discharge and the total discharge as a function of the discharge enthalpy. A plot of this for the geothermal well discharges in Menengai geothermal system is shown in Figure 8. As observed, the Cl concentration in the total discharge decreases with increasing enthalpy. On the other hand, the Cl concentration in the liquid phase is relatively constant between 600-1000 ppm and does not increase significantly with increasing enthalpy.



increase in Cl concentration in the liquid phase with an increase in enthalpy (wells MW-04, MW-01, and MW-03 and partly MW-12). On the other hand, a constant Cl concentration in the total discharge with increasing enthalpy (wells MW-03 and MW-04) was also observed. Therefore, this fits the model of conductive heat transfer from intrusions or magma to the circulating fluids to induce boiling, thus contributing to the excess enthalpy and even forming superheated steam. The remarkably high bottom-hole temperatures and conductive profiles in most wells may substantiate these chemical observations. On a similar note, GAB (2013) postulated the presence of a conductive layer that separates the magma from the zone of superheated steam.

7. CONCLUSIONS

- Two models were adopted in calculating aquifer fluid composition and aqueous species distribution for selected water and steam samples from Menengai wells. The first model assumes a liquid-only reservoir where calculated enthalpy corresponding to equilibrium aquifer temperature was used. The second model considers a liquid and vapour reservoir, where measured enthalpy was used. The calculated chemical composition of major non-volatile components is relatively unaffected by the model used to calculate the reservoir fluid composition; the exception to this is when the well discharges approach dry steam. On one hand, the concentration of the volatiles in reservoir water is significantly lower, assuming a liquid and vapour reservoir, but higher assuming a single-phase liquid reservoir. In principle, the former is attributed to the preferential partitioning of the volatile components into the vapour phase, consequently leading to low H₂S geothermometer temperatures.
- There is a remarkable discrepancy in the calculated geothermometer temperatures, except for well discharges that approach dry steam, typically due to mixing of fluids from different feed zones; nonetheless, the estimated temperature is in excess of 200°C which could correspond to a sub-boiling zone. However the mixing of fluids may affect the fluid equilibrium at a given temperature.
- The saturation state of individual minerals depends on the model-type adopted, thermodynamics, pH and elemental concentration and the stoichiometry of the reaction. The SI values calculated in both models yield under-saturation of all the Ca-bearing as well as pH dependent minerals. This could be caused by removal of Ca from the solution by calcite precipitation in the depressurization zone around wells that might be exacerbated by the high dissolved CO₂ that buffers the pH. The exception to this is with andradite and epidote, both of which show under-saturated and oversaturated conditions in both models. The minerals contain Fe (III) and could be due to overestimation of Fe(OH)₄⁻ activity. On the other hand, Fe (II) bearing minerals are oversaturated, although this might be affected by the calculated Fe²⁺ activity that is sensitive to precipitation and dissolution. The aquifer waters at temperatures above 200°C have closely approached equilibrium with respect to low-albite and microcline, while at temperatures below 200°C the waters have closely approached equilibrium with high-albite and sanidine.
- The activity of volatiles in the aquifer water in relation to mineral buffers is also model-type dependent. Therefore, activities of volatiles are close to equilibrium with volatile mineral buffers when assuming two-phase reservoir fluids while a departure is observed when assuming a liquid reservoir. Therefore, an unambiguous conclusion on the mineral assemblages that control the concentration of volatile components cannot be ascertained due to the uncertainty attributed to the model calculations as well as to the sensitivity of the reactive gases to the phase separation process.

- The wells drilled in the boiling aquifers of the Menengai geothermal system yield excess enthalpy. Therefore, the trend displayed by the non-volatile Cl concentration in the total well discharge and in the liquid phase as a function of discharge enthalpy suggests that Menengai has a heterogeneous reservoir, with excess enthalpy predominantly caused by partial or full phase separation, with significant contributions from heat transfer from hot rock or magma compounding to form superheated steam in certain wells. It is inherently critical to take into account phase segregation, conductive heat addition and other processes leading to excess enthalpy while calculating reservoir composition since the concentration of volatile components is sensitive to such processes.

ACKNOWLEDGEMENTS

I would like to thank all who, in one way or another, contributed to the success of this course. I would like to express my gratitude to the Government of Iceland and the United Nations University Geothermal Training Programme's (UNU-GTP) current director, Mr. Lúdvík S. Georgsson, for giving me the opportunity to take part in the six months course. I would also like to thank Geothermal Development Company (GDC) for granting me the precious chance and time to undertake this noble training.

I am so grateful to the entire UNU-GTP staff: Dr. Ingvar Birgir Fridleifsson, former UNU-GTP director, Mr. Ingimar G. Haraldsson, Ms. Málfríður Ómarsdóttir, Ms. Thórhildur Ísberg, Ms. María Gudjónsdóttir and Mr. Markús A.G. Wilde, for their guidance, time and help in various capacities that made the whole training successful. Special thanks also go to Ms. Rósa S. Jónsdóttir, for availing reference material at a time when I needed them.

I am greatly indebted to my supervisor, Prof. Andri Stefánsson of the University of Iceland, for his patience and time in guiding me throughout the project period. The impacted knowledge is greatly appreciated. I would also wish to thank Thráinn Fridriksson for his productive contribution on the chemistry of thermal fluids.

I would finally like to thank the 2014 UNU-GTP fellows, most specifically those who specialised in field of chemistry of thermal fluids, for the memorable moments, the candid friendship and productive critics.

Finally, I give thanks to God for the sufficient grace, divine favour and blessings upon my life.

REFERENCES

Arnórsson, S. (ed.), 2000: *Isotopic and chemical techniques in geothermal exploration, development and use. Sampling methods, data handling, and interpretation*. International Atomic Energy Agency, Vienna, 351 pp.

Arnórsson, S. and Stefánsson, A., 2005: Wet-steam well discharges. II. Assessment of aquifer fluid compositions. *Proceedings of the World Geothermal Congress, Antalya, Turkey*, 11 pp.

Arnórsson, S., and Stefánsson, A., 1999: Assessment of feldspar solubility constants in water in the range 0-350°C at P_{sat} . *Am. J. Sci.*, 299, 173-209.

Arnórsson, S., Sigurdsson, S. and Svavarsson, H., 1982: The chemistry of geothermal waters in Iceland I. Calculation of aqueous speciation from 0°C to 370°C. *Geochim. Cosmochim. Acta*, 46, 1513-1532.

Arnórsson, S., Stefánsson, A., and Bjarnason, J.Ö., 2007: Fluid-fluid interaction in geothermal systems. *Reviews in Mineralogy & Geochemistry*, 65, 229-312.

Arnórsson, S., Bjarnason, J.Ö., Giroud, N., Gunnarsson, I., and Stefánsson, A., 2006: Sampling and analysis of geothermal fluids, *Geofluids*, 6, 203-216.

Arnórsson, S., Gunnarsson, I., Stefánsson, A., Andréðóttir, A., and Sveinbjörnsdóttir, Á.E., 2002: Major element chemistry of surface- and ground waters in basaltic terrain, N Iceland I. Primary mineral saturation. *Geochim. Cosmochim. Acta* 66, 4015–4046.

Arnórsson, S., Angcoy, Jr., E.C., Bjarnason, J.Ö., Giroud, N., Gunnarsson, I., Kaasalainen, H., Karingithi, C., and Stefánsson, A., 2010: Gas chemistry of volcanic geothermal systems. *Proceedings World Geothermal Congress 2010, Bali, Indonesia*.

Bjarnason, J.Ö., 2010: *The chemical speciation program WATCH, version 2.4*. ISOR - Iceland GeoSurvey, Reykjavik, Iceland. Accessible at webpage: www.geothermal.is/software.

ELC, 2013: *Provision of consultancy services for the feasibility study for 90 MW Menengai Geothermal Power Project*. Preliminary reservoir capacity report, GDC unpublished report.

Fournier, R.O., 1991: Water geothermometers applied to geothermal energy. In: D'Amore, F. (coordinator), *Application of Geochemistry in Geothermal Reservoir Development*. UNITAR/UNDP publication, Rome, 37-69.

Fournier, R.O., and Potter, R.W. II, 1982: A revised and expanded silica (quartz) geothermometer. *Geoth. Res. Council Bull.*, 11-10, 3-12.

Freedman, A. J.E., Bird, D.K., Arnórsson S., Fridriksson, T., Elders, W.A., and Fridleifsson, G. Ó., 2010: Hydrothermal mineral record CO₂ partial pressures in Reykjanes Geothermal System, Iceland. *Proceedings of the World Geothermal Congress 2010, Bali, Indonesia*.

GAB, 2013: *Report of the geothermal advisory board*. Complete draft report, GDC, Kenya, unpublished internal report.

GDC, 2014: *Interpretation of gravity and magnetics data from the Menengai geothermal field*. GRA gravity and magnetic preliminary study project report, GDC, Kenya, unpublished internal report.

Geotermica Italiana Srl., 1987: *Geothermal reconnaissance survey in the Menengai-Bogoria area of the Kenya Rift Valley*. UN (DTCD)/ GOK.

Gichira, J.M., 2012: Joint 1D inversion of MT and TEM data from Menengai geothermal field, Kenya. Report 11 in: *Geothermal Training in Iceland 2012*. UNU-GTP, Iceland, 137-167.

Giggenbach, W.F., 1988: Geothermal solute equilibria. Derivation of Na-K-Mg-Ca geothermometers. *Geochim. Cosmochim. Acta*, 52, 2749-2765.

Gudmundsson, B.T., and Arnórsson, S., 2005: Secondary mineral-fluid equilibria in the Krafla and Námafjall geothermal systems, Iceland. *Applied Geochemistry*, 20, 1607-1625.

Gunnarsson, I. and Arnórsson S., 2000: Amorphous silica solubility and the thermodynamic properties of $\text{H}_4\text{SiO}_4^\circ$ in the range of 0° to 350°C at P_{sat} . *Geochim. Cosmochim. Acta*, 64, 2295-2307.

Kahiga, E.W., 2014: Borehole geology and hydrothermal alteration mineralogy of well MW-13, Menengai geothermal field, Kenya. Report 16 in: *Geothermal Training in Iceland* 2014. UNU-GTP, Iceland, 261-294.

Karingithi, C.W., Arnórsson, S., and Grönvold, K., 2010: Processes controlling aquifer fluid compositions in the Olkaria geothermal system, Kenya. *J. Volc. Geothermal Res.* 196, 57-76.

Kipchumba, L. J., 2013: Borehole geology and hydrothermal alteration of wells MW-08 AND MW 11, Menengai geothermal field, Kenya. Report 10 in: *Geothermal Training in Iceland* 2013. UNU-GTP, Iceland, 143-176.

Kipng'ok, J., 2011: Fluid chemistry, feed zones and boiling in the first geothermal exploration well at Menengai, Kenya. Report 15 in: *Geothermal Training in Iceland* 2011. UNU-GTP, Iceland, 281-302.

Lagat, J., Mbia, P., and Mutoria, C., 2010: *Menengai prospect: Investigations for its geothermal potential*. GDC, Kenya, internal report, 64 pp.

Leat, P.T., 1984: Geological evolution of the trachytic caldera volcano Menengai, Kenya Rift Valley. *J. Geological Society*, 141, 1057-1069.

Lopeyok, T.P., 2013: Borehole geology and hydrothermal mineralization of wells MW-09 AND MW - 12, Menengai geothermal field, Kenya. Report 15 in: *Geothermal Training in Iceland* 2013. UNU-GTP, Iceland, 289-324.

Malimo, S.J., 2013: Fluid chemistry of Menengai geothermal wells, Kenya. *Geothermal Resources Council Transactions*, 37, 425-430.

Mbia, P.K., 2014: *Sub-surface geology, petrology and hydrothermal alteration of Menengai geothermal field, Kenya*. University of Iceland, MSc thesis, UNU-GTP, report 1, 87 pp.

Mibei, G.K., 2012: Geology and hydrothermal alteration of Menengai geothermal field – Case study: wells MW-04 and MW-05. Report 21 in: *Geothermal Training in Iceland* 2012. UNU-GTP, Iceland, 437-465.

Mibei, G.K. and Lagat, J., 2011: Structural controls in Menengai geothermal field. *Proceedings of Kenya Geothermal Congress, Nairobi*.

Mungania, J., and Lagat, J., (ed.), Mariita, N.O., Wambugu, J.M., Ofwona, C.O., Kubo, B.M., Kilele, D.K., Mudachi, V.S., Wanjie, C.K., and Korio, R.K., 2004: *Menengai volcano: Investigations for its geothermal potential*. KenGen, Kenya, internal report, 93 pp.

Omondi, C., 2011: Borehole geology and hydrothermal mineralisation of wells MW-01 and MW-02, Menengai geothermal field, Central Kenya Rift Valley. Report 30 in: *Geothermal Training in Iceland* 2011. UNU-GTP, Iceland, 737-773.

Scott, W. S., Gunnarsson, I., Arnórsson, S., and Stefánsson, A., 2014: Gas chemistry, boiling and phase segregation in geothermal systems, Hellið, Iceland. *Geochim. Cosmochim. Acta*, 124, 170-189.

Sekento, L.R., 2012: Geochemical and isotopic study of the Menengai geothermal field, Kenya. Report 31 in: *Geothermal Training in Iceland* 2012. UNU-GTP, Iceland, 769-792.

APPENDIX II: Saturation state of aquifer waters of Menengai with respect to minerals

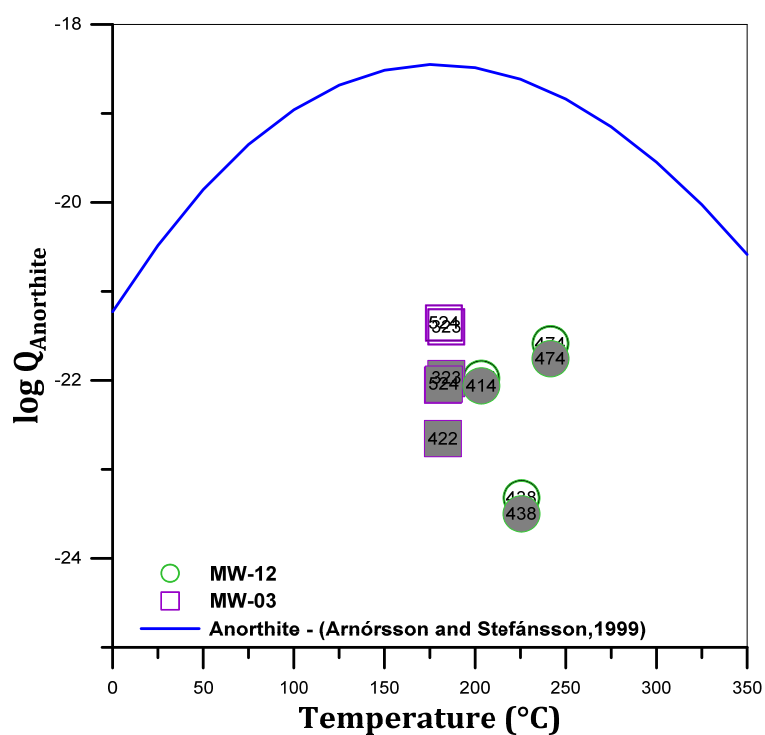


FIGURE 1: The saturation state of end-member feldspars as a function of temperature for anorthite in Menengai aquifer waters

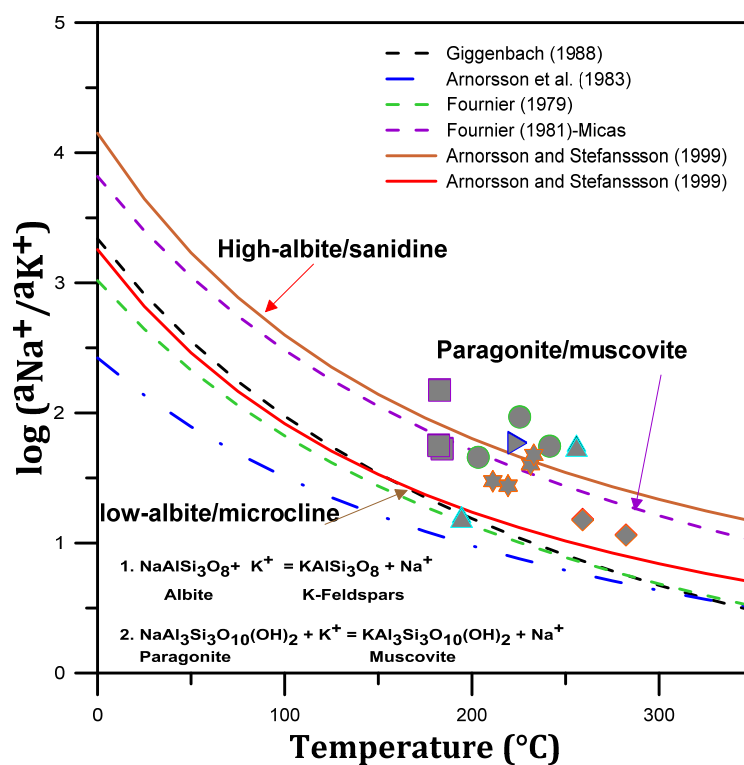


FIGURE 2: Aqueous Na^+/K^+ activity ratios versus temperature



UNITED NATIONS
UNIVERSITY

UNU-GTP

Geothermal Training Programme

Orkustofnun, Grensasvegur 9,
IS-108 Reykjavik, Iceland

Reports 2014
Number 9

BOREHOLE STRATIGRAPHY AND ALTERATION MINERALOGY OF WELL HE-6, HELLISHEIDI, SW-ICELAND

Moira Lunge Bawasu

Geological Survey Division, Mineral Resources Authority
Mining Haus, Poreporena Freeway
P.O. Box 1906
Port Moresby, 121
PAPUA NEW GUINEA
mbawasu@mra.gov.pg

ABSTRACT

Well HE-6 is located in the Hellisheidi high temperature geothermal field in southwest Iceland. Drilled in 2002 to explore the conditions of the geothermal system, well HE-6 is now discharging at a rate of 29.4 kg/s with an enthalpy of 1950 kJ/kg. The stratigraphic units in well HE-6 are comprised of 4 distinct hyaloclastite formations, 3 lava units and 2 possible intrusions, one being of intermediate composition. There are four alteration zones: smectite-zeolite (376-730 m), smectite-mixed layer clay-chlorite (730-800 m), chlorite (800-1000 m) and chlorite-epidote (1000-1018 m). Fourteen aquifers were located along lithological contacts, intrusive boundaries, fractures and faults, indicating good, permeability zones. The distribution of hydrothermal alteration minerals, such as pyrite and calcite, also depict valuable permeable zones. Calcite forms a platy structure at boiling temperatures and the homogenization temperatures range from 240 to 275°C. This homogenization temperature of the platy calcite represents the highest alteration temperature range and conforms to the present formation temperatures in the well. However, the alteration temperatures are actually lower than the present formation temperatures in the well, indicating that the well may be heating up.

1. INTRODUCTION

Borehole geological logging is an important part of subsurface geothermal exploration which contributes to the understanding of the natural conditions in the geothermal system and its production characteristics prior to utilization (Steingrímsson and Gudmundsson, 2006). Before drilling exploration wells, the geothermal reservoir is broadly outlined from the initial geological, geophysical and geochemical exploration studies on the surface. Geothermal drilling has been carried out in Iceland for decades which makes it an ideal place to study borehole geological logging. Well HE-6, a production well in the Hellisheidi high temperature geothermal field, has been assigned to the writer for this purpose. The main resolution of the geological logging in boreholes is twofold: firstly to locate and characterize the permeability in the geothermal reservoir, and secondly to assess the condition of the system regarding alteration (Franzson, 2014).

1.1 Well HE-6

The Hellisheidi high temperature geothermal field is situated 45 km east of Reykjavik, Iceland (Figure 1). This geothermal field has been exploited and utilized by Reykjavik Energy for electricity and district heating and has a power plant presently producing 303 MW_e and 133 MW_{th} (Gunnlaugsson, 2012). Well HE-6 is situated at 384632E, 395257N (ISN 93 coordinate system) and 420 meters above sea level. It is a directional well striking N25°E with an inclination of 35° (Jónsson et al., 2002ab; Richter et al., 2002). The well was drilled to 2001 m in 2002 to explore the temperature and permeability conditions of the geothermal system. Well HE-6 is now discharging at a rate of 29.4 kg/s with an enthalpy of 1950 kJ/kg (Gunnlaugsson, 2014).

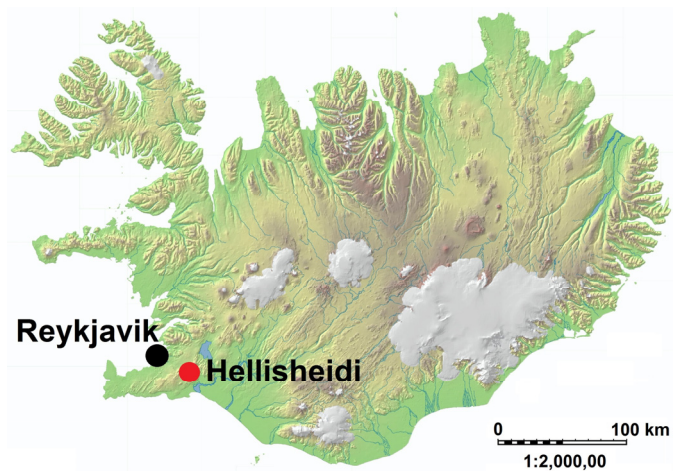


FIGURE 1: Location of Hellisheidi high temperature geothermal field in Iceland

2. GEOLOGICAL SETTING

2.1 Geology of Iceland

Iceland is located between 63°23'N to 66°30'N and 13°30'W to 24°30'W in the North Atlantic Ocean and south of the Great Arctic Circle. Formed entirely by volcanic activity and centred directly on the active diverging plates of North America in the west and Eurasia in the east, Iceland is spreading apart at a rate of 1 cm per year in both directions. This divergence occurs at the Mid Atlantic Ridge which runs northeast-southwest through the centre of Iceland, marked locally by the Reykjanes Ridge in the south and the Kolbeinsey Ridge in the north (Wolfe et al., 1997). The spreading is associated with a deep seated mantle plume directly under the Vatnajökull glacier, evident from the recent eruption of the Grímsvötn volcanic system on 4 September 2014. The geological map of Iceland (Saemundsson, 1979), first published over three decades ago, has been refined over the years and is shown in Figure 2.

Iceland has experienced intermittent glacial periods through time due to its northerly location. Today, glaciers and ice caps cover about 11% of the land area which is 11,400 km² out of the 103,125 km² area of Iceland. The surface rocks are made up of post glacial and interglacial lavas and sub-glacial hyaloclastites. The youngest rocks are located in the centre of Iceland, in the active rift zones, Quaternary formations are found in and along the margins of these rift zones and older Tertiary formations occur away from the rift zones to the east and west (Figure 2). Fissure swarms and central volcanoes mark these zones (Saemundsson, 1979).

The Northern Rift Zone (NRZ), Eastern Rift Zone (ERZ), Western Rift Zone (WRZ) and Reykjanes Rift Zone (RRZ) in Figure 2 are large, 40 to 50 km wide rift zones made up of smaller, 5 to 15 km wide (up to 200 km in length) volcanic fissure swarms. High temperature geothermal fields are confined to the active rift zones characterized by reservoir temperatures of more than 200°C at 1 km depth, whereas low-temperature areas are located outside the volcanic rift zone, having lower than 150°C reservoir temperatures at 1 km depth.

The Hengill volcanic system, which hosts the Hellisheidi high temperature geothermal field, is one of these volcanic systems and lies directly on a triple junction between the RRZ, WRZ and the South

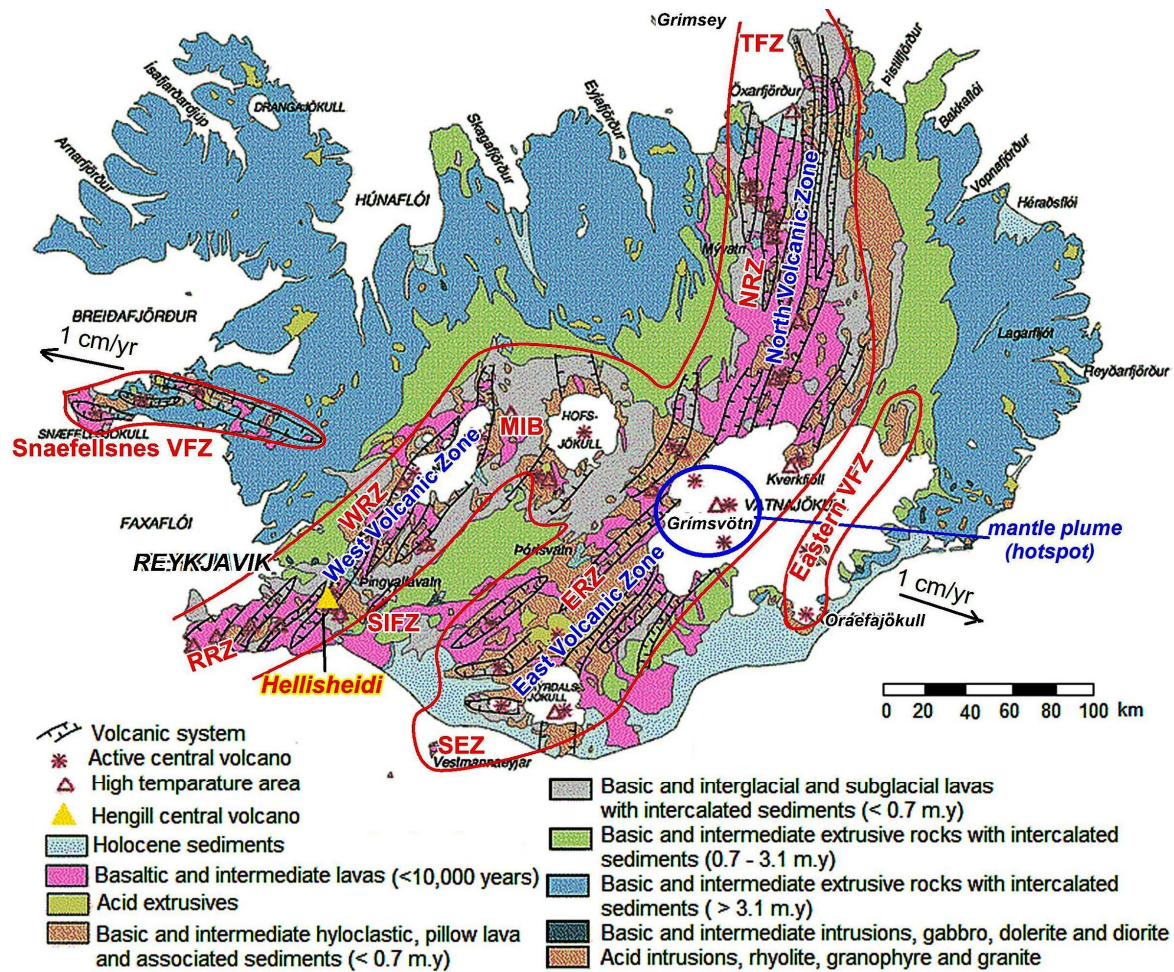


FIGURE 2: The regional geological map of Iceland (modified from Saemundsson, 1979) showing the volcanic systems and fissure swarms, location of the mantle plume, rift systems, direction of the spreading and the location of the Hellisheidi high temperature geothermal field in the Hengill central volcano

Iceland Fracture Zone (SIFZ). The WRZ continues north-eastward from Hengill and connects to the NRZ through the Mid-Icelandic Belt (MIB), a transform zone (Einarsson, 1991). The NRZ continues north from the Vatnajökull glacier. The SIFZ in the south and the Tjörnes Fracture Zone (TFZ) in the north are transform zones which connect the volcanic rift zones to the segments of the Mid-Atlantic-Ridge. Due to rift relocations, the WRZ is apparently a failing rift zone while the ERZ will eventually become the main spreading zone in South Iceland (Saemundsson, 1979; Hardarson et al., 1997).

2.2 Hellisheidi high temperature geothermal field

The Hellisheidi high temperature geothermal field, centred by the Hengill central volcano is situated in the WRZ on a triple junction where two active rift zones meet a seismically active transform zone (Helgadóttir et al., 2010) (Figure 2). The geology of Hellisheidi has been mapped in detail by Saemundsson (1995) (Figure 3). The dominant rock formations in the Hellisheidi field are hyaloclastites which formed subglacially when magma cooled during an eruption into the base of the glacier, forming pillow basalts, breccias and tuffs. Occasionally these hyaloclastites are disturbed by lava successions which flowed to the lowlands during interglacial and interstadial periods. Hellisheidi is within the northeast-southwest fault zone and graben of the Hengill central volcano (Franzson et al., 2005).

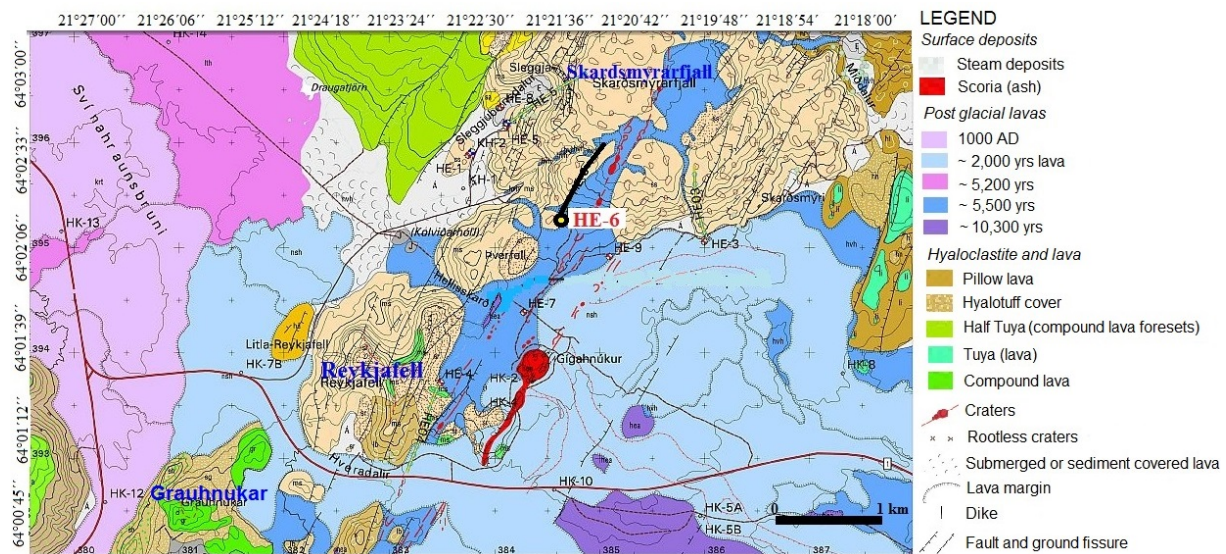


FIGURE 3: Geological map of the Hellisheidi high temperature field (modified from Saemundsson, 1995) showing the location of well HE-6 drilled north-eastward towards Mt Skarðsmýrarfjall

The northeast-southwest faults and fractures which form part of the 5 to 15 km wide and 40 to 50 km long fissure swarm bisects the Hengill central volcano. Major up- and outflow zones in the field are largely related to volcanic fissures of 2000 and 5000 years of age (Saemundsson 1995; Björnsson 2004; Franzson et al., 2005). The fissure swarm has been the drilling target in the Hellisheidi field (Helgadóttir et al., 2010). Well HE-6 is located directly southwest of Mt Skarðsmýrarfjall (Figure 3) and 1 km west of the 5000 year old row of fissures and was drilled directly northeast towards the core of the Hengill geothermal system (Jónsson et al., 2002a).

3. ANALYTICAL METHODS

3.1 Binocular and petrographic microscope analysis

An Olympus binocular microscope was used to analyse 509 cutting samples collected at 2 m intervals during drilling, representing a total of 1018 m of the subsurface rocks from well HE-6. Thirty thin sections were analysed using a Leica petrographic microscope. Logging procedures for binocular and petrographic analyses, from the Iceland GeoSurvey (ISOR), were used to establish the subsurface stratigraphy and alteration mineralogy. This was done based on the visual abundances of the primary and secondary minerals and their characteristics in each sample.

A preliminary binocular microscope analysis was carried out at the drill-site as the rock cuttings were collected during drilling. This is critical to assess the alteration temperatures of the geothermal reservoir because the drilling progress is heavily dependent on this preliminary assessment. Further detailed analyses were carried out at the ISOR labs in Reykjavik.

Petrographic microscope analysis is more precise in establishing the mineral assemblage of each stratigraphic unit and alteration mineralogy. Samples were selected based on the binocular microscope analysis and prepared for thin-section at an external laboratory. The thin-section preparation takes a fair amount of time and is, therefore, undertaken at a later stage as detailed understanding of the reservoir characteristics becomes important for future predictions of the geothermal system. The time relationships of the alteration mineral depositions are established during the petrographic study.

3.2 Use of the geophysical measurements and drilling data

During the drilling process a number of measurements are taken to estimate different reservoir parameters which are important to assess several different parameters and conditions of the well. Steingrímsson and Gudmundsson (2006) and Steingrímsson (2011) describe in detail the techniques involved in the acquisition of different types of well logging measurements in Iceland. These well logs make it possible to study the well, its geometry, the rock formation and fractures, the reservoir temperature and fluid pressures and feed points connecting the well to the geothermal reservoir. The geophysical measurements used during this study are: neutron logs, resistivity logs, gamma logs, caliper logs and the temperature logs which were acquired from the ISOR database and from the drill reports (Jónsson et al., 2002ab; Richter et al., 2002). Below is the description of what each of these logs was used for in this study:

- i. *Temperature logs* were used to locate aquifers or feed points. The effects, of a hot or cold flow into or out of the well from the formation, cause a sudden increase or decrease in the temperature, providing important clues to the location of aquifers in the borehole.
- ii. *Natural gamma logs* were used to refine lithological boundaries including alteration zones. As different rock types contain different amounts of radioactive isotopes (K, Th, and U), gamma logs can reveal if lithological units are of evolved chemical compositions. Gamma rays also generally show low values in the fresh rocks and a general increase in the altered zones. They can also be used to locate aquifers since alterations zones are often connected to aquifers.
- iii. *Neutron logs* were also used to locate aquifers. Similar to the natural gamma log, the rise and fall of the measurements assist in locating a porous formation which generally gives a high spike. Water saturated basalts (aquifer hosted basalts) show moderate to high spikes, indicative of porous zones.
- iv. *Resistivity logs* were used to refine the lithological boundaries (or thickness) and the alteration zones. Fresh rocks have higher resistivity compared to altered rocks due to the infiltration of water, lowering the resistivity.
- v. *Caliper logs* were also used alongside the other geophysical measurements to locate and confirm aquifers in the well. The diameter of the well expands, indicated by a spike in the caliper reading when a possible permeable zone is encountered. Caliper logs thus reveal wash-out and caves in the well. These logs are also used to estimate the volume of cement needed for casing operations.

Some important information in the drilling reports (Jónsson et al., 2002ab; Richter et al., 2002) was used to assist in this study. This information included the circulation losses and the depths of the casings. The circulation losses reliably assisted with the identification of large, medium and small feed zones.

3.3 Fluid inclusion analysis

Fluid inclusion temperatures of platy calcite crystals sampled at 814 m, 840 m and 906 m were analysed using a microthermometric heating and cooling stage under a Laborlux 12 Leitz microscope. These crystals represent the altered and permeable zones of the geothermal reservoir and were picked under the binocular microscope and prepared using the standard procedure for microthermometry of fluid inclusion at ISOR (Gudfinnsson, 2011).

The fluid inclusion analysis is a reliable measure of the thermal history of the geothermal reservoir and is usually undertaken after the binocular microscope analysis. Fluid inclusion temperature measurements deduce the original temperatures of the fluids trapped within the crystal during its growth and recrystallization. The platy calcite crystals contain inclusions of liquid aqueous solutions and gas bubbles; the gas bubble forming process in each crystal is reversed by heating to determine the temperatures when they were trapped. The crystals are heated until the fluid homogenizes in a single phase (i.e. bubble disappears) and the temperature is measured. On cooling, the vapour bubble will reappear as it is trapped within the crystal.

3.4 X-ray diffractometer analysis

The X-ray diffractometer (XRD) analysis of the clay compositions was conducted on 40 selected rock cutting samples in a XRD machine; the model type being Bruker AXS D8 Focus. Each sample was selected based on binocular microscope analysis to aid the interpretation of the alteration zones within the geothermal reservoir. The clay minerals contain large percentages of water trapped between their crystal lattices. The clays are silicate sheets, part of a general but important group within the phyllosilicates. Most clay minerals are chemically and structurally analogous to other phyllosilicates but contain different amounts of water. The clays are important temperature dependent minerals and give information on the alteration temperatures of the formation in the geothermal reservoir. However, it is difficult to identify specific types of clay under both the binocular and petrographic microscopes. Therefore, the XRD analysis is very important because it permits a detailed determination of the clays.

A standard XRD procedure practised by ISOR was used for the preparation of the samples. It is important to note that two types of sample were prepared from each depth; one sample was treated with glycol ($C_2H_6O_2$) solution while the other was untreated but placed in a desiccator. Both these samples were stored for 24 hours prior to the analyses, however, thicker samples took over 48 hours in the desiccator. The analyses of these samples were made on the XRD machine. However, a third measurement was taken, after heating the glycolated sample on an asbestos plate to completely dehydrate the sample. A measurement is recorded for each sample as untreated, glycolated and heated.

4. RESULTS

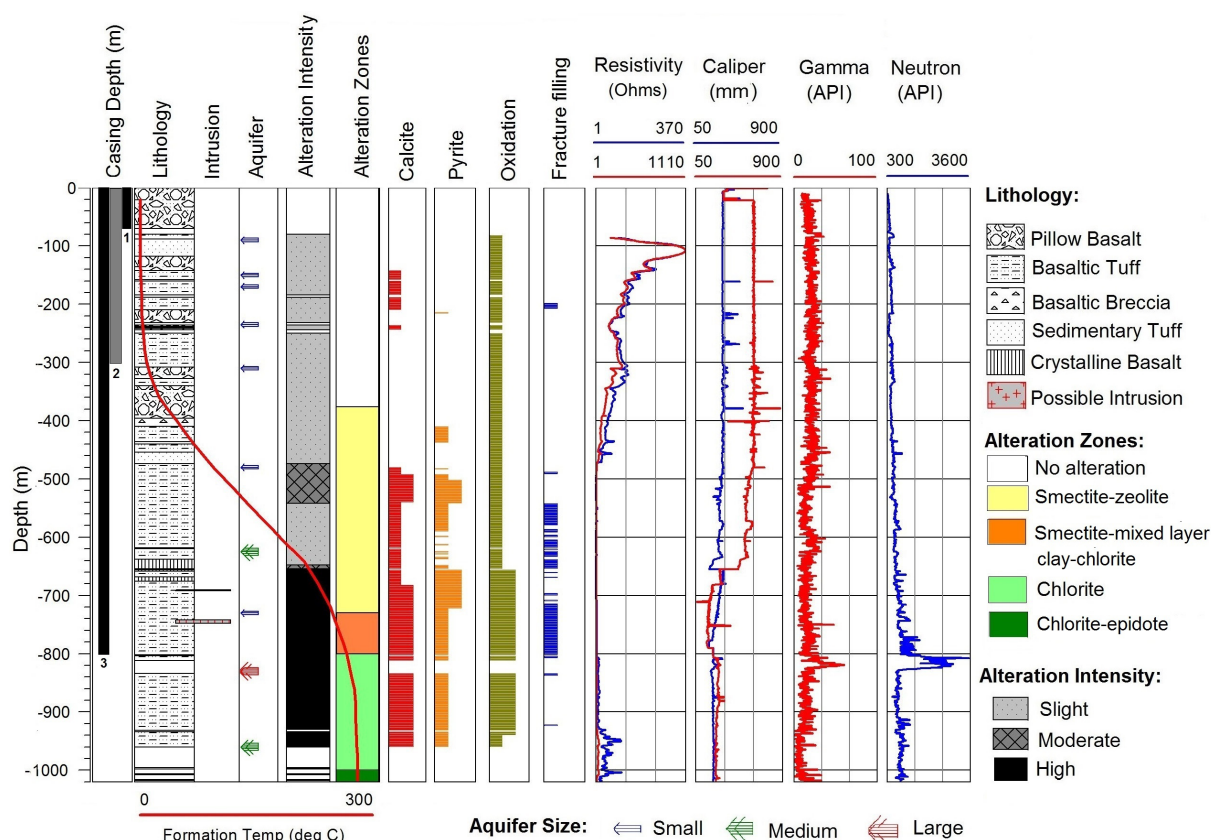
4.1 Stratigraphy of well HE-6

The stratigraphy of well HE-6 correlates well with the preliminary stratigraphic observations (Jónsson et al., 2002ab; Richter et al., 2002), although a few minor differences were observed. The rocks are predominantly of basaltic hyaloclastite formations, some basaltic lavas and two intrusions, one being basaltic, the other chemically more evolved. The classification of each rock unit is based on the rock compositions and their crystallinity. The primary minerals of the basaltic rocks are glass, olivine, plagioclase, pyroxene and opaque minerals, mostly magnetite and ilmenite. Palagonite is the first stable alteration product of volcanic glass and has replaced some glass during the formation of the hyaloclastites sub-glacially. The classification of the different units (pillow lava, breccia, and tuff) within the hyaloclastite formation is based on the visual abundance of glass in the primary mineral assemblages. The hyaloclastite formation is distinguished from both the lavas and intrusions based on the abundance of glass. The intrusions are aphyric and often less altered than the host rock. The lavas can be either crystallized or aphyric.

Four hyaloclastite formations were intersected in well HE-6, three lava units and two minor possible intrusions (Figure 4). The hyaloclastite formations were encountered at: 0-88 m (Hyaloclastite I), 118-436 m (Hyaloclastite II), 440-454 m (Hyaloclastite III) and 474-1018 m (Hyaloclastite IV). Lava units, or crystallized basalts, were encountered at: 88-118 m (Lava I), 436-440 m (Lava II), and 454-474 m (Lava III). The two possible basalt intrusions were encountered at 690-692 and 742-748 m. Figure 4 shows a stratigraphic profile of well HE-6 including the alteration intensity and zones, aquifers, formation temperature and the geophysical measurements taken during the drilling.

Hyaloclastite I (0-88 m): This formation consists of two units, pillow basalts from 0-80 m and basaltic tuff from 80-88 m.

0-80 m - pillow basalt: This unit consist of approximately 10% glass, partially crystalline basalt with phenocrysts of olivine, pyroxene and plagioclase. The glass and basaltic fragments have many vesicles. Pillow basalts occur at the surface and down to 70 m. From the surface to 70 m, the pillow basalt unit is



Stratigraphy:

Hyloclastite I (0-88 m): this formation consists of two units, *pillow basalts* from 0-70 m and *basaltic tuff* from 80-88 m; olivine and glass are the first to show signs of oxidation as they are coated with limonite along fractures and as fillings in the vesicles.

Lava I (88-118 m): Crystalline Basalt; this crystalline basalt unit is the largest lava sequence in well HE-6 with a width of approximately 30 m. Limonite and siderite coats some of the crystal surfaces with their orange-brown dirty radiating crystals. Opaline silica deposited on some crystal surfaces.

Hyloclastite II (118-436 m): alternating *pillow basalts* and *basaltic tuff* units and a single unit of *basalt breccia*. The intensity of oxidation in the pillow basalt increases at 118 m. Calcite first appeared at 142 m filling vesicles; Pyrite occurs at 410 m and zeolites (scolecite, analzyme, thomsonite) occur at 412 m onward.

Lava II (436-440 m): Crystalline Basalt

Hyloclastite III (440-454 m): Mostly of basaltic tuff

Lava III (454-474 m): Crystalline Basalt

Hyloclastite IV (474-1018 m): The intensity of pyrite increases from 656 m in the sedimentary tuff and oxidation is intense giving the yellowish-red dirty appearance. Quartz, wairakite and phrenite start to occur within the basaltic tuffs at 804 m depth. The clays are reddish-yellowish-whitish-green coloured, mostly mixed layered clays from 676 m to approximately 800 m. Chlorite green colour is noticeable in the samples after 812 m. Two possible *intrusions* were encountered in the basaltic tuffs from 690-692 m and 742-748 m respectively.

Alteration Zones:

No alteration (0-376 m)
Smectite-zeolite (376-730 m)
Smectite-mixed layer clay-chlorite (730-800 m)
Chlorite (800-1000 m)
Chlorite-epidote (1000-1018 m)

FIGURE 4: Stratigraphy, alteration, aquifers and geophysical logging data

relatively fresh with no fillings in the vesicles. However, the olivine and glass are the first to show signs of oxidation as they are coated with limonite along fractures and as fillings in the vesicles.

80-88 m - basaltic tuff: The unit consists of approximately 90% glass with the rest composed of basaltic rock with phenocrysts of olivine, pyroxene and plagioclase. Similar to the pillow basalt unit, vesicles are common. This unit is relatively fresh from 80 m for approximately 8 meters down to a section with few of the vesicles filled with opaline silica, limonite and siderite.

Lava I (88-118 m): This crystalline basalt unit is the largest lava unit in well HE-6 with a thickness of approximately 30 m.

88-118 m – Crystalline basalt: This unit is greyish to dark in colour, fine grained with consolidated microcrystalline phenocrysts of olivine, plagioclase, pyroxene and magnetite. The rock and crystals are relatively fresh with traces of creamy white opaline silica deposited on some crystal surfaces. Limonite and siderite coat some of the crystal surfaces with their orange-brown radiating crystals.

Hyaloclastite II (118-436 m): This formation is the single largest hyaloclastite formation in well HE-6 with a thickness of approximately 318 m, comprising several alternating pillow basalts and basaltic tuff units and a single unit of basalt breccia. There was a circulation loss at 158-160 m, 184-188 m, 232-236 m and at 244-250 m.

118-142 m - pillow basalt: This unit consists of approximately 10% glass, partially crystalline basalt and basaltic rock compositions with phenocrysts of olivine, pyroxene and plagioclase. The glass and basaltic phenocrysts have many vesicles. The intensity of oxidation in the pillow basalt increases at 118 m as more crystals are coated with both siderite and limonite. Opaline silica and chalcedony occur on the crystal surfaces or as fillings in some vesicles.

142-210 m - basaltic tuff: This unit is grey to black in colour and consists of approximately 90% glass with the rest composed of basaltic rock with phenocrysts of pyroxene and plagioclase. The glass alters to brown coarse grain palagonite. Calcite first appears at 142 m, filling vesicles of the basaltic tuffs, and the glass has been partially palagonized. Chalcedony and opaline silica are deposited on the crystals and in some of the vesicles.

210-244 m - pillow basalt: greyish-black coarse grained and highly porous crystals (vesicular) of partially crystallized basaltic glass, olivine, plagioclase and pyroxene. From 212-214, no glass was seen in the cuttings. Amorphous silica is deposited on the surfaces of the cuttings. Siderite and limonite fill fractures in the cuttings as well. Siderite occurs as small spherules with a radiating pattern and is yellowish to reddish brown in colour. There was a circulation loss from 244-250 m.

250-308 m - basaltic tuff: Brown to greyish-black, partially recrystallized glass with pyroxene and plagioclase phenocrysts. Amorphous silica occurs on the crystal surfaces with siderite and limonite filling fractures. Some glass altered to palagonite.

308-328 m - pillow basalt: Greyish-black coarse grained and highly porous crystals (vesicular) of partially crystallized basaltic glass, with olivine, plagioclase and pyroxene. Amorphous silica is deposited on the surfaces of the cuttings. Siderite and limonite fill fractures of the cuttings as well.

328-340 m - basaltic tuff: Brown to greyish-black, partially recrystallized glass with pyroxene and plagioclase phenocrysts. Some of the glass has been altered to palagonite and is porous with a significant amount of vesicles. Amorphous silica is deposited on the surfaces of the cuttings. Siderite and limonite fill fractures.

340-396 m - pillow basalt: Massive and consolidated, partially crystalline basalt with glass, olivine, plagioclase and pyroxene. Very porous but no vesicle fillings; glass is altered to palagonite. Amorphous silica and chalcedony are deposited on the crystal surfaces. Siderite and limonite fill fractures and occur on some crystal surfaces. Scolecite and analcime were identified in the thin-section analysis at 392 m. Zeolites occur together with calcite filling vesicles of mostly glass.

396-410 m - basaltic breccia: The basaltic breccia was intersected at 396 m, with a total thickness of 14 m. This unit consists of approximately 50% glass, with some crystalline to partially crystallized glass, and approximately 50% crystalline basaltic rock comprising phenocrysts of olivine, pyroxene and plagioclase. Some of the glass has been altered to palagonite. There are a number of vesicles, however, most of them have no fillings, while the few that have are filled predominantly with amorphous silica. While scolecite was noted in the overlying pillow basalt unit, the basaltic breccia appeared relatively

fresh and no zeolites were seen. Siderite and limonite occur on the crystal surfaces, giving a yellowish-red colour, while fine clays have formed along some of the vesicles in the glass and palagonite.

410-436 m - basaltic tuff: This unit is brown to black and consists of approximately 90% glass and occasional olivine, pyroxene and plagioclase phenocrysts. This unit is also highly vesicular and some of the pores are filled with amorphous silica. Clay, siderite and limonite occur along fractures. Most of the glass is palagonized and chalcedony appears, together with opaline silica, filling the vesicles. Pyrite occurs at 410 m along fractures and on some crystal surfaces while the zeolites occur at 412 m. Thomsonite, a low temperature zeolite, was identified in the binocular analysis. Fine grained clays and calcite occur along the fractured surfaces of the glass.

Lava II (436-440 m)

436-440 m - crystalline basalt: This unit is similar to the previous unit (Lava I) and is approximately 4 m thick. It is grey to dark in colour, fine grained with consolidated microcrystalline phenocrysts of olivine, plagioclase, pyroxene and magnetite. The rock and crystals are relatively fresh, and a little creamy white opaline silica is deposited on some crystal surfaces. Limonite and siderite coat some of the crystal surfaces.

Hyaloclastite III (440-454 m)

440-454 m - basaltic tuff: This unit consists mostly of glass (90%) and some phenocrysts of olivine, pyroxene and plagioclase. Most of the glass is partially palagonized and is highly vesicular. Some of the pores are filled with opaline silica and chalcedony. Clays, siderite and limonite occur along fractures and as fillings in the vesicles. Pyrite is also seen along the crystal fractures. Zeolite crystals are present in the cuttings but were impossible to distinguish through the binocular microscope.

Lava III (454-474 m)

454-474 m - crystalline basalt: This unit is similar to the previous two crystalline basalt units and is approximately 20 m thick. It is grey to dark in colour, fine grained with consolidated microcrystalline phenocrysts of olivine, plagioclase, pyroxene and magnetite. There was some recrystallized glass mixed within the cuttings. The rock is relatively fresh, with a little creamy white opaline silica deposited on crystal surfaces. Limonite and siderite coat some of the crystal surfaces.

Hyaloclastite IV (474-1018 m): There are no cuttings from the following intervals: 618-620, 654-656, 802-804, 812-834, 932-934, 960-996, 998-1006 and 1008-1016.

474-638 m - basaltic tuff: This unit consists predominantly of altered glass and partially crystallized glass, mixed with a few plagioclase phenocrysts. The vesicles have been filled by opaline silica, clays and zeolites. The zeolites were difficult to distinguish under the binocular microscope. Calcite and zeolites fill vesicle spaces and calcite also occurs as vein infills. Yellow and white clays occur along fractures and vesicle fillings. Limonite and siderite coat some of the crystal surfaces and are quite intense in this section.

638-658 m - sedimentary tuff: This unit is comprised of cuttings grey to black in colour, fine grained, laminated mudstones and sandstones mixed with altered glass, palagonites and phenocrysts of plagioclase. The unit has a significant amount of calcite and zeolites filling the vesicles, and clays, together with the calcite, fill veins and fractures. The intensity of clay alteration is high in this unit. Olivine and glass have been completely altered to smectite and mixed layer clays. Pyrite crystals occur in the sedimentary tuff units at 648 m. The intensity of pyrite increases from 656 m and oxidation is intense, resulting in a yellowish-red dirty appearance.

658-668 m - basaltic tuff: This unit also consists predominantly of clay altered glass with partially crystallized glass mixed in with a few plagioclase phenocrysts. Olivine and glass have been completely altered to smectite and mixed layered clays. The vesicles have been filled by opaline silica, clays and zeolites. The zeolites are difficult to distinguish under the binocular microscope. Calcite and zeolites fill

vesicle spaces and calcite also occurs as vein fillings. Yellow and white clays occur along fractures and as vesicle fillings. Limonite and siderite coat some of the crystal surfaces and are quite intense in this section. Sulphide (mostly pyrite) is disseminated throughout.

668-676 m - sedimentary tuff: This unit is similar to the unit encountered at 638 m, grey to black in colour, fine grained, laminated mudstones and sandstones mixed with clay altered glass, palagonites and phenocrysts of plagioclase. Calcite and zeolites fill the vesicles, and the clays, together with calcite, fill veins and fractures. The intensity of the clay alteration is also high in this unit. Olivine and glass have been completely altered to smectite and mixed layered clay. Pyrite crystals occur in the sedimentary tuff units at 648 m. Sulphide (mostly pyrite) is disseminated throughout.

676-1018 m - basaltic tuff: This is the thickest single unit intersected in the hyaloclastite formation; it occurs for approximately 442 m, assuming all the units that were lost due to circulation losses were part of this same formation. Basaltic tuff consists of approximately 90% glass with the rest being composed of basaltic rock with phenocrysts of olivine, pyroxene and plagioclase. Similar to the other units, there are numerous vesicles in both the glass and basalt units which were encountered at 676-802, 804-812, 834-932, 934-960, 996-998, 1006-1008 and 1016-1018 m. The intensity of clay alteration is much higher at 658 m in the basaltic tuffs with some glass and olivine completely altered to clay minerals. Quartz, wairakite and prehnite start to occur within the basaltic tuffs at 804 m. The clays are reddish-yellowish-whitish-green coloured, mostly mixed layer clay from 676 to approximately 800 m. Chlorite texture and green colour is noticeable in the samples after 800 m.

4.1.1 Intrusions


Two possible intrusions were encountered in the basaltic tuff unit (Hyaloclastite IV) at 690-692 m and 742-748 m. Both intrusions are composed of microcrystalline olivine, plagioclase, pyroxenes and magnetite phenocrysts. The intensity of clay alteration in the basaltic tuff is quite intense as most of the glass and olivine have been partially to completely altered. Pyrite and calcite occur as fracture fillings, while some calcite and zeolites occur as fillings in the vesicles. A spike occurs in the gamma log at 742 m (Figure 4) which may indicate that the intrusion is of intermediate chemical composition. There is no spike at 690 m indicating that this intrusion is of basaltic composition.

4.2 Alteration mineralogy

4.2.1 Alteration of the primary mineral assemblages

The primary minerals of the basaltic hyaloclastite formations, basaltic lavas (crystalline unit) and intrusions in well HE-6 are predominantly glass, olivine, plagioclase, pyroxene and opaque minerals, mostly magnetite and ilmenite. Table 1 shows the primary minerals in well HE-6 and some of their most common alteration products.

TABLE 1: Primary minerals of the rocks studied in well HE-6 and the common alteration products

Sensitivity to alteration	Primary rock minerals	Alteration mineral products; <i>*Not identified in this study</i>
Most  Least	Glass Olivine Plagioclase Pyroxene Opaque (mostly magnetite and ilmenite)	clay, calcite clay, calcite, smectite, chlorite clay, calcite, albite, wairakite clay, calcite, chlorite, smectite, epidote (including actinolite*) limonite, siderite, clay, pyrite, (including sphene*)

The primary minerals are relatively fresh from the surface to approximately 114 m. Figure 5A shows fresh basaltic phenocrysts of olivine, plagioclase, pyroxenes and glass in the basaltic tuff unit at 34 m. As depth in the well increases, temperature and fluid chemistry changes and the primary minerals become unstable under the new physiochemical conditions. The primary minerals alter to secondary mineral products by their interaction with hot water (and steam which helps the dissolution of the primary minerals, replacement and the precipitation of new minerals).

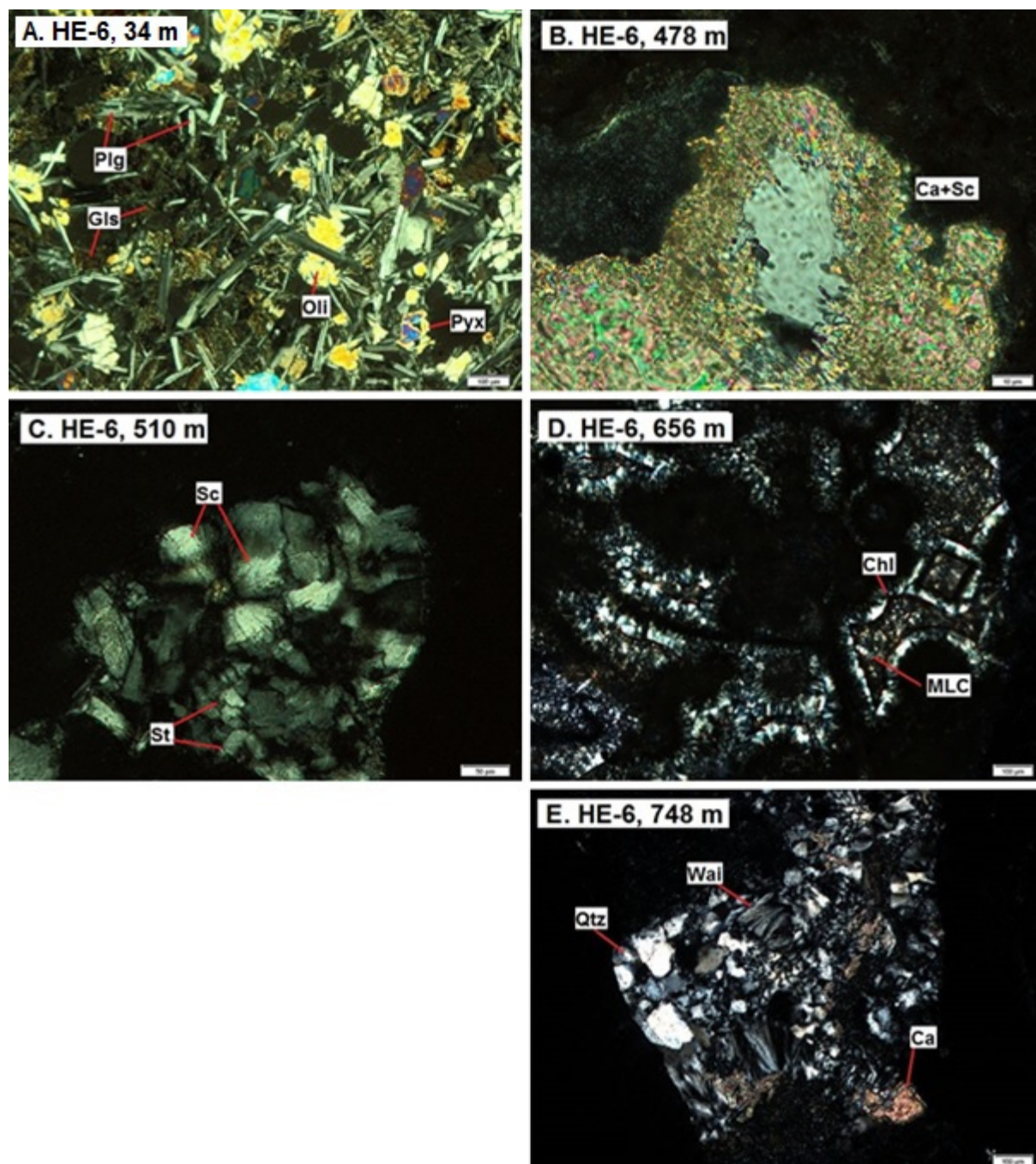


FIGURE 5: Photomicrographs of some of the samples studied, taken under transmitted light (crossed polars): A) Glass (Gls), olivine (Oli) and plagioclase (Plg) crystals in the basaltic tuff unit; B) Calcite (Ca) and scolecite (Sc) filling vesicle in the sedimentary tuff unit; C) Sc and stilbite (St) occur as fillings in the vesicles of the glass; D) Chlorite (Chl) replacing mixed layer clay (MLC); E) Quartz (Qtz) and wairakite (Wai) are formed and calcite (Ca) replaces the plagioclase

Glass is the first to alter and is replaced by calcite at 142 m, mostly along the fractures. *Olivine* is also early to alter to clays and calcite along fractures; this was seen at 158 m in the petrographic study. *Plagioclase* alters to clays and calcite at 394 m, noticeable from the increase in clay alteration intensity. At deeper levels (greater than 750 m depth), the plagioclase alters to albite which was seen in the petrographic study. Albite alteration of plagioclase starts at temperatures above 220°C and is known as albitization. *Pyroxene* alters to clays and calcite along fractures at relatively shallow levels in the geothermal system (Franzson, 2014). At deeper levels, chlorite replaces the pyroxenes more easily; this was seen at 808 m and, at greater depths, the pyroxene alters to epidote and actinolite. Epidote and actinolite are high temperature minerals which occur in high temperature geothermal systems in Iceland at temperatures ranging between 250 to greater than 300°C (Franzson, 2014). Opaque minerals usually alter within oxidation zones, characterized by the presence of limonite, pyrite and sometimes sphene.

4.2.2 Hydrothermal alteration

The hydrothermal minerals identified in well HE-6 are shown in Table 2 and are presented in their mineral groups and order of occurrence. Figure 6 shows the depth range at which the alteration minerals were formed and the alteration zones based on clay analyses.

TABLE 2: Alteration minerals identified in well HE-6, structural formula, formation temperature range and depth of first occurrence

Mineral groups/ minerals	Chemical formula (Gribble and Hall, 1992) <i>*not specified</i>	Formation temperatures (Saemundsson and Gunnlaugsson, 2014) <i>*estimate numbers</i>	Depth of first occurrence
<i>Oxide:</i> Limonite	FeOOH.nH ₂ O	from low temp < 40°C *	2 m
<i>Carbonates:</i> Siderite Calcite	FeCO ₃ CaCO ₃	from low temp < 40°C * < 40°C - 280°C *	80 m 142 m
<i>Sulphides:</i> Pyrite	FeS ₂	< 40°C - > 200°C *	216 m
<i>Zeolites:</i> Scolecite Thomsonite Analcime Stilbite Laumontite Wairakite	Ca[Al ₂ Si ₃ O ₁₀].3H ₂ O NaCa ₂ (Al,Si) ₅ NaAlSi ₂ O ₆ .H ₂ O Na ₂ CaK ₂ [Al ₂ Si ₇ O ₁₂].4H ₂ O Ca[Al ₂ Si ₄ O ₁₂].4H ₂ O CaAlSi ₂ O ₆ .H ₂ O	80 - 120°C 50 - 120°C 50 - 170°C 80 - < 150°C 120 - 180°C > 200°C *	392 m 410 m 392 m 510 m 656 m 748 m
<i>Clays:</i> Smectite Mixed layer clay Chlorite	(1/2Ca,Na)(Al,Mg,Fe) ₄ (Si,Al) ₈ O ₂₀ (OH) ₄ .nH ₂ O (smectite and chlorite complex)* (Mg,Al,Fe) ₁₂ (Si,Al) ₈ O ₂₀ (OH) ₁₆	50 - 170°C 200 - 230°C 230 - 290°C	378 m 748 m 808 m
<i>Others minerals:</i> Opaline silica Chalcedony Quartz Prehnite Epidote	SiO ₂ SiO ₂ SiO ₂ CaAl[AlSi ₃ O ₁₀](OH) ₂ Ca ₂ Fe ³⁺ Al ₂ [Si ₃ O ₁₂](OH)	< 100°C 70 - 200°C 180 - > 300°C 240 - 250°C 250 - > 300°C	80 m 118 m 748 m 912 m 1000 m

Oxides and carbonate:

Limonite forms by the oxidation of ferrous minerals, such as magnetite, which is found in all the basalts and occurs immediately at shallow levels to depths of more than 600 m in the well. It is dark or yellowish brown, sometimes reddish and opaque with a slight metallic lustre and forms thin layers with a globular surface coating.

Siderite was identified at 80 m and occurs together with limonite down to more than 600 m. Similar to limonite, the crystals are tabular, however, have spherules and show a radiating pattern. Siderite usually pseudomorphs after limonite and is yellowish brown or reddish brown in appearance.

Calcite is the most common carbonate precipitate in well HE-6 and forms at all temperature ranges, however, it is not stable at temperatures above 300°C (Table 2). Calcite is generally white but may be coloured by impurities and was first identified at 142 m. It has a vitreous lustre, conchoidal fractures and occurs in various forms from granular to orthorhombic. Platy calcite was recognized at depths greater than 800 m in the well.

Sulphides:

Pyrite is the most common sulphide mineral in well HE-6 and was first identified at 216 m. It forms yellowish cubic crystals which have a strong metallic lustre. Pyrite is abundant at 510 m to 540 m and from 656 m to the bottom of the stratigraphic profile (i.e. 1018 m) which may indicate good permeable zones.

Zeolites:

Scolecite was identified at 392 m together with calcite, analcime and clay, filling vesicles of the pillow basalts. Scolecite is a colourless or white, fibrous zeolite with a vitreous, or slightly silky lustre, and forms between 80°C and 120°C (Table 2). It is four-sided, densely packed, and forms aggregates where the crystal fibres radiate from a single point, growing thicker, and may separate towards an obtuse point at the end. The fractures are uneven and thick, having faint longitudinal marks. Figure 5B shows the typical fibrous structure of scolecite surrounded by calcite, filling the vesicles in the pillow basalt unit at 478 m.

Thomsonite is a radiating zeolite, identified at 410 m, and forms at temperatures ranging between 70°C and 110°C. The crystals are prismatic, acicular, elongated, bladed, slightly flattened, with a slanted end. They form dense masses of radiating clusters, with mammillary structures whose surface are finely bristled. Its colour is mainly white and is translucent with a vitreous or pearly lustre and has uneven fractures.

Analcime is another low temperature zeolite identified at 392 m and forms between 50 and 170°C. It is also known as analcite and forms colourless or white, many sided (trapezohedral) crystals with vitreous lustres and conchoidal fractures.

Stilbite is a low temperature zeolite mineral identified at 510 m. It forms between 80°C to less than 150°C. It is commonly observed as thick tabular crystals with pointed terminations. The crystals often grow wider towards the end, forming shelf-like aggregates which develop ends like a “bow-tie”.

Stilbite is generally milky white, clear and translucent. In the petrographic study, stilbite occurred mostly with scolecite. Figure 5C shows scolecite and stilbite filling vesicles in the sedimentary tuff formation at 510 m.

Laumontite was identified at 656 m and forms at temperatures ranging from 120 to 230°C. It is a radiating or tabular zeolite and creates thin elongated fibres, or prisms, with longitudinal marks and a square end. A cross-section of the crystal is square and it is normally white, but may be pale pink or reddish brown.

Wairakite is a zeolite mineral with an analcime structure but contains a calcium ion (Gribble and Hall, 1992). It is the calcium rich variant related to analcime that forms between 200 and 300°C, i.e. at higher temperatures than the other zeolites. It was first identified at 748 m together with quartz.

Clays:

Smectite is the most common clay mineral group in well HE-6 and occurs at 378 m to depths of more than 900 m. Smectite is a low temperature clay formed from the alteration of glass and the ferromagnesian primary minerals and occurs at temperatures ranging from 50 to 170°C. Smectite precipitates in pores and occurs as linings in vesicles at shallower depths but occurs with mixed layer clay at deeper levels.

Mixed layer clay was identified at 748 m in well HE-6 and forms at temperature ranges between 200 and 230°C. The mixed layer clay is a product of reactions involving clay minerals end member in which the different kinds of clay layers alternate with each other. In well HE-6, the mixed layer clay is a complex of smectite and chlorite clay minerals. It appears coarse grained around the fine grained smectite clay and is identified by the brightly coloured radiating crystals under transmitted light (crossed polars) in the petrographic study.

Chlorite is generally green, radiating, flaky or fibrous aggregates and was first identified at 808 m. It is a common secondary mineral formed from the alteration of mafic primary minerals or smectite, filling the vesicles and occurs at temperatures between 230 and 290°C. It replaces the mixed layer clay completely at higher temperatures. Chlorite is sometimes colourless in thin-section with no pleochroism and has a low order maximum interference colours (rarely above grey). Figure 5D shows chlorite replacing mixed layer clay at 656 m in the well.

Silica and other minerals:

Opaline silica forms at temperatures of less than 100°C and was first identified in the well at 80 m. It is almost amorphous, and is softer and less dense than all other silica minerals. The most common variety is pale or milky white, opaque (sometimes translucent) with a vitreous or greasy lustre.

Chalcedony is another silica mineral that occurs at much higher temperatures than opaline silica, at 70°C to 200°C. It is often regarded as amorphous and forms tiny thread-like crystals identified by their greyish blue colour and slight vitreous or greasy lustre. Chalcedony was first identified at 118 m by the binocular analysis.

Quartz appears at temperatures above 180°C and was first identified at 748 m together with wairakite. It is white-milky white or grey and is translucent or opaque and has a vitreous lustre and uneven or conchoidal fractures. Quartz forms hexagonal prismatic crystals which end in slanted crystal faces meeting at a point, i.e. a six sided pyramid. Figure 5E shows the occurrence of quartz, wairakite and calcite in thin-section analysis. The quartz and wairakite crystals have low order interference colours and are distinguished by their various optical properties.

Prehnite was first identified at 912 m and forms at temperatures ranging between 240 and 250°C. It forms small spherical clusters of crystals with vitreous lustre, sometimes pale green, white or grey in colour. The crystal clusters are radiating, and this is visible when broken up. The fracture is irregular and the streak is white.

Epidote was not seen in this study but was identified at 1000 m in the preliminary stratigraphic study (Jónsson et al., 2002b). It is a product of hydrothermal alteration of the feldspars and pyroxenes and forms at 250°C to temperatures greater than 300°C. Epidote is prismatic and fibrous with striations and is usually yellow-green or greenish black in colour.

4.2.3 Alteration zones

The first and last appearance of the hydrothermal minerals studied under both the binocular and petrographic microscopes were combined with the clay analyses from the XRD to create a time relationship of the minerals relating to the formation temperatures in well HE-6. Figure 6 shows the

sequence of mineral deposition in the well. Five alteration mineral zones have been identified in well HE-6:

i. Unaltered zone (0-376 m): This zone, although relatively unaltered, consists of oxides (limonite), carbonates (siderite and calcite) and silica minerals (opaline silica and chalcedony). The presence of these minerals suggests a carbonaceous cold groundwater system warming up.

ii. Smectite and zeolite zone (376 – 730 m): This zone is well defined and is quite extensive in comparison to the other zones. It comprises, all the low temperature zeolites (scolecite, analcime, thomsonite, stilbite) and smectite clays. Calcite, chalcedony and opaline silica occur, and are only accessory minerals that do not define the alteration mineral zonation boundaries. The temperature range for the occurrence of this mineral assemblage is a little under 40 to just over 170°C.

iii. Smectite, mixed layer clay and chlorite zone (730 – 800 m): This zone is a transitional zone, predominantly consisting of smectite with some occurrence of mixed layer clay and chlorite. The temperature range for the occurrence of these minerals ranges from a little under 180 to 290°C.

iv. Chlorite zone (800 – 1000 m): This zone is also well defined, and is the second largest zone studied. The temperatures defining the zone range from a little under 230 to 290°C.

iv. Chlorite and epidote (1000 – 1018 m): This zone is predominantly of chlorite and epidote with temperatures ranging from 250 to over 300°C. Although epidote was not identified in this study, it was referred to in an ISOR report (Jónsson et al., 2002b). This zone is quite common in the high temperature geothermal systems in Iceland (Franzson, 2014). Epidote has been found in nearby wells, in well HE-3 at 792 m (Getaneh, 2001) and in well HE-9 at 660 m (Eshaghpour, 2003).

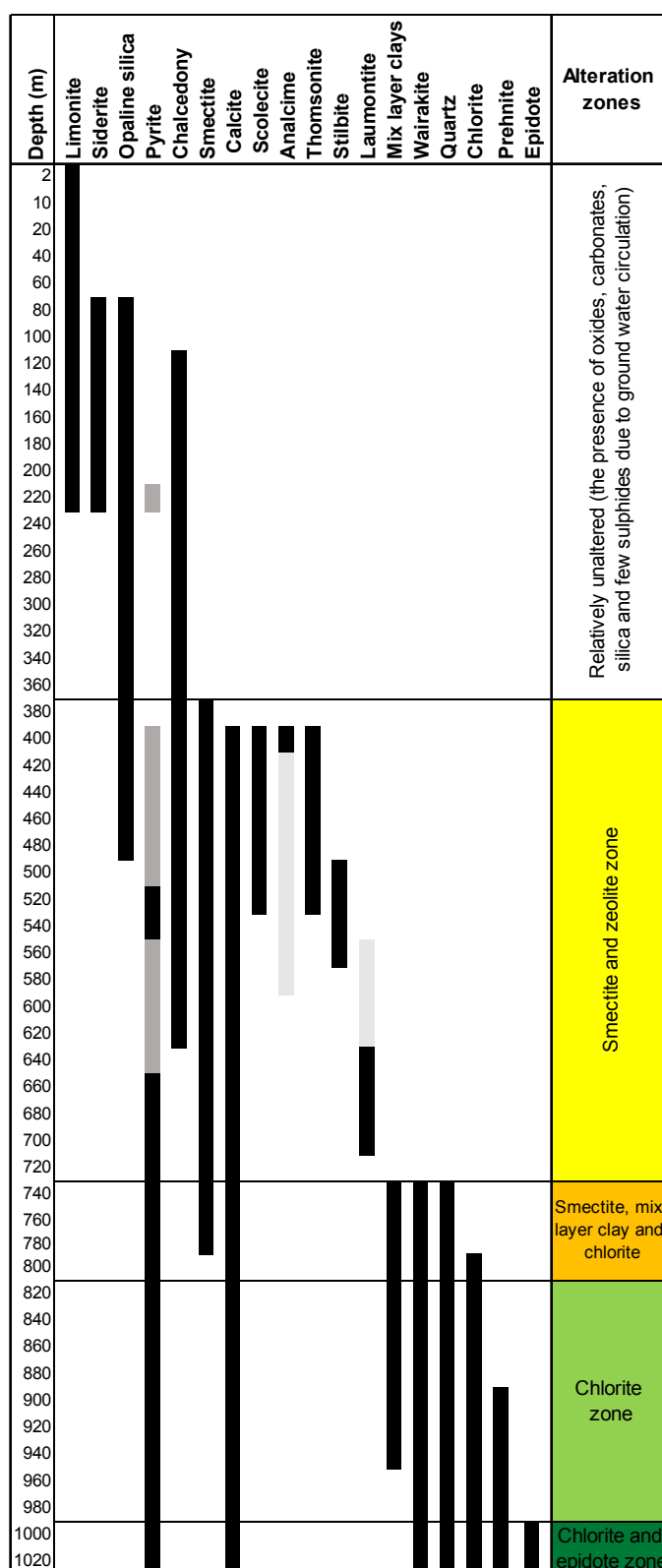


FIGURE 6: Sequence of mineral deposition in well HE-6: The black shades indicate strong occurrence, the dark grey shade indicate weak occurrence, while the light grey shade indicates a probable occurrence

4.3 Clay mineralogy from the XRD analysis

The clay minerals are the predominant hydrothermal alteration products in this borehole. Table 3 shows the summary of the results from the XRD analyses. Figure 7 shows examples of some of the interpretations from the XRD clay measurements. The following clay minerals were detected.

TABLE 3: XRD results for the clay analyses

No.	Depth (m)	Untreated (Å)	Glycolated (Å)	Heated (Å)	Clay type
1	162	nd	Nd	nd	nd
2	262	nd	Nd	nd	nd
3	318	nd	Nd	nd	nd
4	336	nd	Nd	nd	nd
5	376	13	17	nd	Smectite
6	404	16.9	17	10.01	Smectite
7	450	15	17	10	Smectite
8	472	15	17	nd	Smectite
9	480	14	17	10	Smectite
10	500	nd	Nd	nd	nd
11	516	13	17	13	Smectite
12	552	14	17	16-Oct	Smectite
13	590	13	17	16-Oct	Smectite
14	600	14.16	14.31	10.01	Smectite
15	630	12.9	16.9	9.8	Smectite
16	650	13.59	13.9	10.01	Smectite
17	660	12.9	16.9	12/9.8	Smectite
18	690	12.9	16.9	12/9.8	Smectite
19	700	13.59	13.9	10.01	Smectite
20	720	14	17	13	Smectite
21	730	13.9	10.01	7.21	Chlorite+Smectite
22	740	14.47/13.07	10.01	7.21	Chlorite+Smectite
23	752	30/14	31/17	14	Smectite+MLC
24	782	31/14	31/17	14	Smectite+MLC
25	788	17.67/15.05	10.01	7.27	Chlorite+Smectite
26	794	14.29/12.97	10.01	7.18	Chlorite+Smectite
27	800	14.59/13.04	10.01	7.18	Chlorite+Smectite
28	808	31/14	31/17	14	Chlorite+MLC
29	810	14.59/13.04	10.01	7.18	Chlorite+MLC
30	846	14.5	14.5	14.5	Chlorite
31	850	15.12	15.12	7.33	Chlorite
32	866	14.5	14.5	14.5	Chlorite
33	880	14.97	14.97	7.28	Chlorite
34	892	31/14	32/15.5	12	Chlorite+MLC
35	900	14.97	14.97	7.28	Chlorite
36	910	14.47	14.47	7.23	Chlorite
37	934	31/14	32/15.5	12	Chlorite+MLC
38	940	14.47	14.47	7.23	Chlorite
39	954	14.3	14.3	14.5	Chlorite unstable
40	960	14.47	10.2	7.23	Chlorite

Smectite, the most common low temperature clay mineral in Iceland geothermal systems (Kristmannsdóttir, 1985) occurs from 376 to 800 m in well HE-6. However, smectite exists as a single clay from only 376 to 730 m, detected from 15 samples. Smectite occurred predominantly from 730 to 800 m with mixed layer clay and chlorite. Smectite and chlorite coexisted in two samples representing

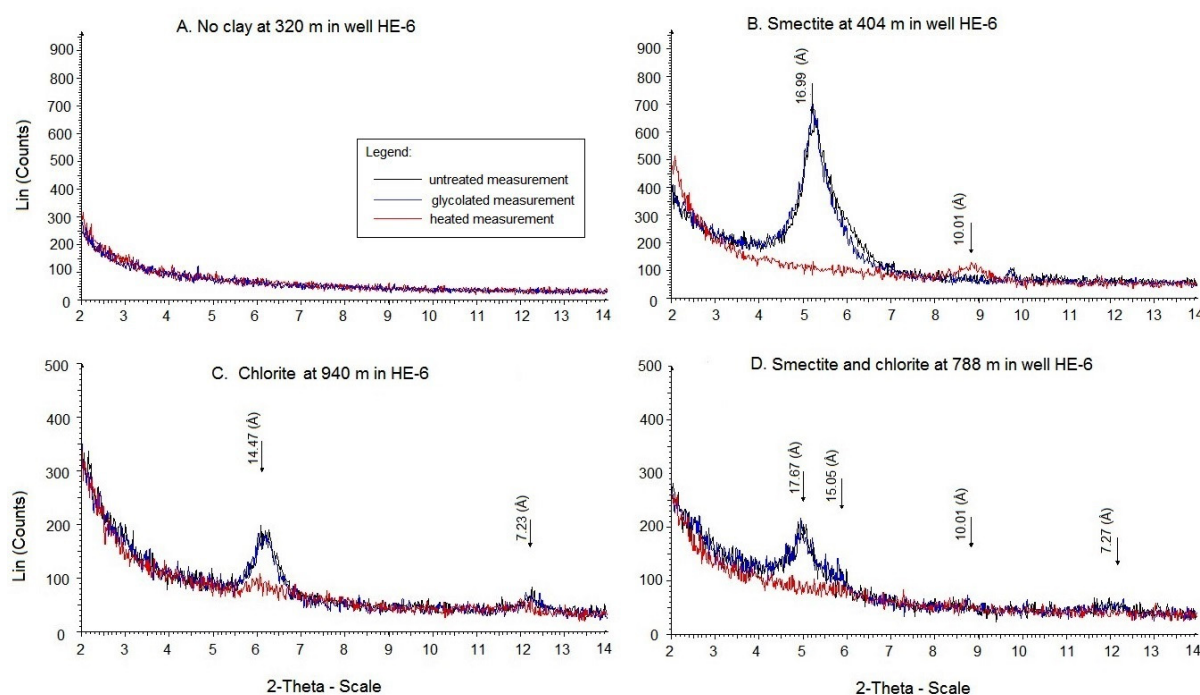


FIGURE 7: The XRD measurements for the clay analyses in well HE-6: A) No clay was detected at 320 m; B) Smectite clay was detected at 404 m; C) Smectite and chlorite were detected at 788 m; D) Chlorite was detected at 940 m

730 to 752 m. This was followed by the coexistence of, again, smectite and mixed layer clay in two samples representing 752 to 788 m. From 788 to 800 m, the smectite and chlorite coexist again, identified in 3 samples. Chlorite occurred predominantly from 800 to 960 m in 13 samples, although a few samples between these depths contained chlorite and mixed layer clay.

The X-ray diffraction patterns of the clays may vary depending on the humidity, exposure to certain organic molecules, heat treatment and exchangeable cations (Wilson, 1987). The X-ray diffraction patterns which show no peaks in all the measurements are typical for samples lacking clays (Figure 7A). The smectite clay usually has an untreated basal reflection between 13 and 15 Ångstroms (Å). When saturated with ethylene glycol, the reflection of smectite will swell to about 17 Å and, when heated to 400°C, the reflection will collapse to about 10 Å. Figure 7B shows the typical X-ray diffraction pattern for smectite. Chlorites have their peak at approximately 14 to 14.5 Å, depending on the individual species (Figure 7C). Peak positions are unchanged by ion saturation, treatment with ethylene glycol, or heating.

Clay minerals are composed of only two types of structural units (octahedral and tetrahedral sheets) and, therefore, different types of clay minerals can coexist, giving rise to mixed layer clays. The mixed layer clays sometimes result in much higher Ångstrom values (see examples in Table 3; mixed layer clay and smectite or mixed layer clay and chlorite). The peaks appear quite distinct in samples containing two or more clays and are identifiable by their individual diffraction patterns as shown in Figure 7D, a sample containing smectite and chlorite clays.

4.4 Calcite microthermometry from fluid inclusion

Platy calcite, representing the hydrothermal alteration at 814 m, 840 and 906 m, was analysed to deduce the homogenization temperatures in the well at the time of formation. Figure 8 is a photomicrograph of the fluid inclusion containing gas bubbles analysed at 840 m. The summary of the depth, number of



FIGURE 8: Secondary fluid inclusion from fracture fillings of platy calcite in the mixed layer clay-chlorite zone at 840 m

crystals and analyses of each crystal are shown in Table 4 and the statistical analyses presented in Figure 9.

The homogenization temperature range for platy calcite at 814 m (Platy calcite 1 in Figure 9) is from 240°C to 270°C. The homogenization temperature range for platy calcite at 840 m (Platy calcite 2) gave a narrow range from 265°C to 270°C. Because these two samples occur not far apart in the well, the statistical analyses are shown together in Figure 9A. The platy calcite from 906 m has a homogenization temperature ranging from 260°C to 275°C, shown in Figure 9B.

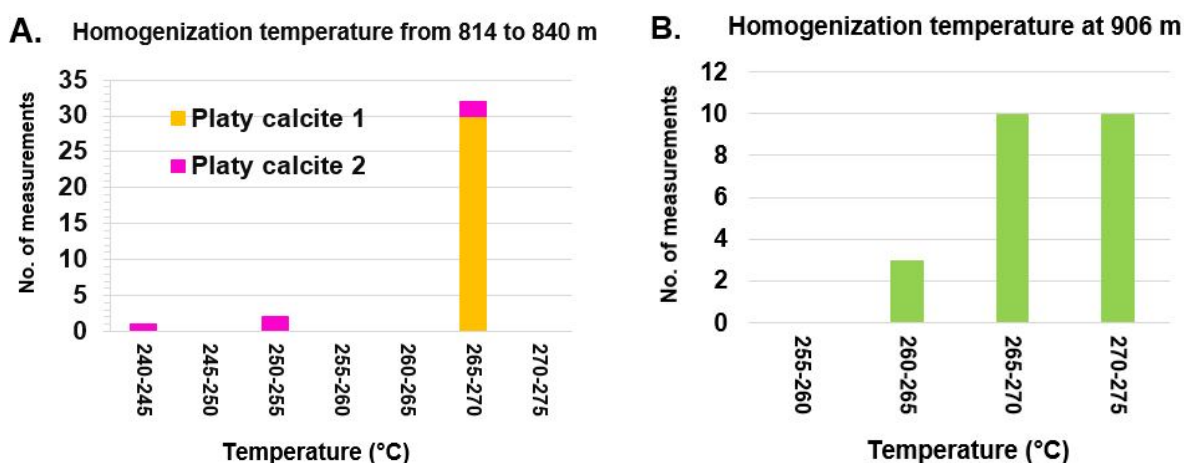


FIGURE 9: The homogenization temperatures in the geothermal system

TABLE 4: Fluid inclusion measurements from well HE-6

Depth (m)	Crystals (No.)	No. Measurements
814	1	5
840	1	30
906	1	23
Total:	3	58

The homogenization temperature in an alteration mineral represents a restricted past temperature in the geothermal system (Franzson et al., 2014). The platy calcite formations are secondary inclusions which occurred mostly in fracture fills within the chlorite zone of this geothermal system.

A comparison can be made between the alteration mineral temperatures, the formation temperatures and the homogenization temperature of the platy calcite to deduce the past and present temperature conditions of the geothermal system. Figure 10 shows temperature versus depth with the interpreted temperatures of the alteration minerals, homogenization temperature of platy calcite and the formation temperature taken from the drilling data. The boiling point curve is added for comparison as that depicts the maximum temperature attainable in a water dominated system (Franzson et al., 2014).

An approximate equilibrium exists between the alteration temperatures and the formation temperatures at shallow levels of the well, less than 500 m depth (Figure 10). This is seen by the appearance of analcime, scolecite and thomsonite, the low temperature zeolites. As the depth in the well increases, the alteration temperature curve shifts slightly lower beneath the formation temperature curve which indicates that the geothermal system in the upper 1000 m of well HE-6 has heated up. This is possibly related to the heat emitted from the 2000 and 5000 year old fissure eruptions to the east of well HE-6 (Figure 3). Lack of cuttings below 1018 m, due to circulation losses, makes it impossible to compare

deeper depths. However, it can be seen from Figure 10 that the formation temperature has decreased below about 1500 m depth, indicating cooling in the geothermal system in that area.

Fluid inclusion temperatures fill in the gap of the alteration temperatures and gives the history of the temperature variation during the lifetime of the geothermal system (Franzson et al., 2014). In this study, the homogenization temperatures of the platy calcite conform relatively well with the present formation temperature of the geothermal system.

4.5 Aquifers (feeder zones)

The locations of the aquifers, identified from temperature profiles logged during drilling, is shown in Figure 11. The geophysical logs and the circulation losses helped with the determination of these aquifers. The size of the aquifers is based on the change in the temperature gradient of each curve. The aquifers are grouped as large, medium and small. The aquifers and their locations are shown in Figure 11, together with the alteration mineral curve, the formation temperature curve (this was taken after the drilling process was completed) and the boiling point curve for comparison. The identified aquifers are listed below:

i. Small aquifers: Nine small aquifers were observed at 90, 150, 170, 310, 480, 730, 1280, 1500 and 1625 m depths. Only 3 of these small aquifers are in the production zone of the geothermal reservoir, the rest occur above the production zone and have been cased off.

ii. Medium aquifers: Four medium aquifers were identified at 235, 625, 960 and 1025 m. Only 2 of these aquifers are in the production zone of the geothermal reservoir, the two higher up have been cased off.

iii. Large aquifer: Only one large aquifer, located at 830 m, is in the production zone of the geothermal reservoir.

The aquifers at 830 and 960 m are further indicated by loss zones. Apart from high intensity alteration, sheared or fractured rocks, the abundance of some minerals such as calcite, quartz and sulphide (mostly pyrite) occur commonly adjacent to these aquifers as vein fillings or well-formed crystals.

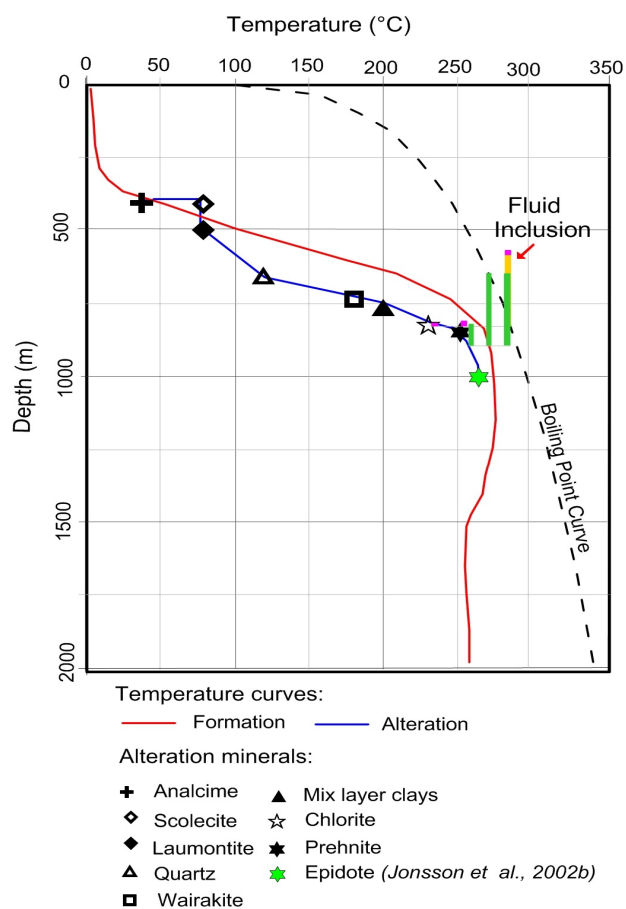


FIGURE 10: Temperature versus depth showing the formation and alteration temperature curves in well HE-6

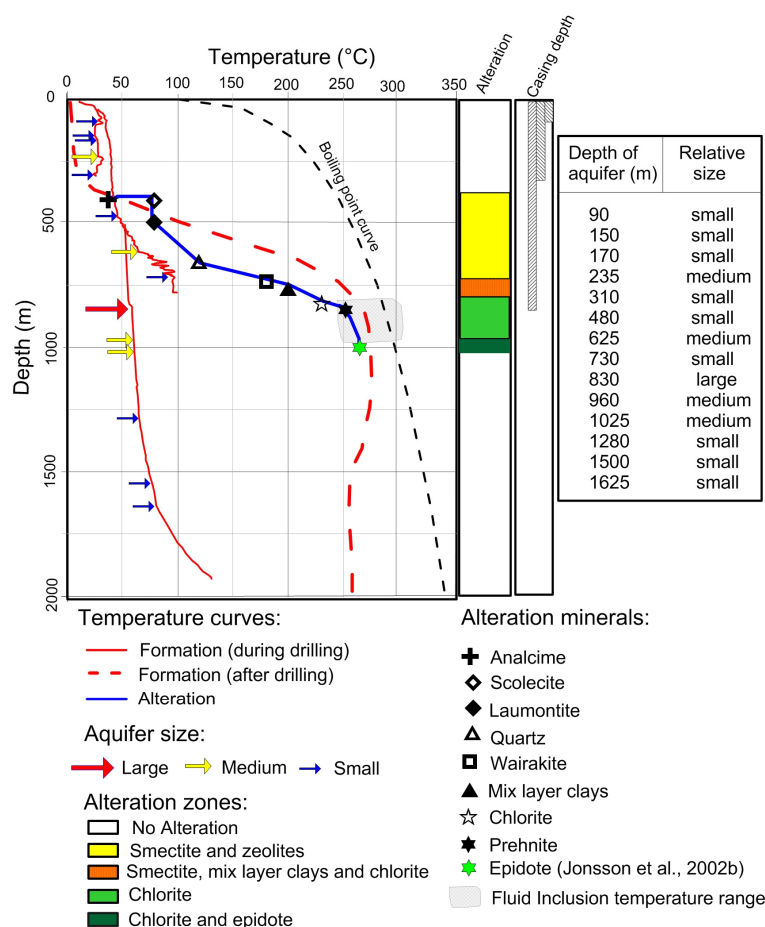


FIGURE 11: Temperature versus depth showing the formation temperature curve, alteration temperature curves and the location of the aquifers

5. DISCUSSION

Identifying and understanding the controls on permeability is the key to a productive geothermal reservoir in high temperature systems. The study of permeability can be achieved by studying the structures, mineralogy and rock types (Reyes, 1990). Assessment of the geothermal system and the potential for productivity is also largely dependent on the study of the hydrothermal alteration minerals. The formation of these hydrothermal alteration minerals depends mainly on the permeability, temperature, fluid composition, host rock composition and the age span of the hydrothermal activity in the geothermal system. These issues were addressed by using the various analytical studies undertaken and presented in this report.

5.1 Permeability

The permeability in well HE-6 is related to lithological contacts, intrusive contacts, fractures and major faults. The aquifers gave good indications of permeability of the reservoir rocks. There were 14 aquifers identified in the well. The temperature logs measured during the three drilling phases were used to locate these aquifers in addition to circulation losses and geophysical loggings (Jónsson et al., 2002ab; Richter et al., 2002). However, not all the aquifers may have been identified because there is the possibility that some smaller aquifers may have been overlooked, for example, due to very small gradient changes in the temperature logs or they might have been clogged by mud during drilling. One main factor that can

affect the interpretation of the temperature logs is the location of the pivot point in wells and the use of mud while drilling (Helgadóttir et al., 2010).

In a high temperature geothermal system, heat is transported from the depths to the surface mainly by two processes, heat conduction and convection (Hjartarson, 2014; Figure 12). Aquifers are very important in promoting conductivity and heat transfer in a high temperature geothermal system. Therefore, permeability is crucial for good conductivity and convection in the system.

In Iceland, the permeability of the reservoir rocks is controlled predominantly by stratigraphic boundaries in the upper part of the wells, while faults and fractures, along intrusive boundaries control permeability in the deeper parts of the well (Franzson et al., 2001). The Hellisheidi field is dominated by northeast-southwest striking major faults and fractures intersected by easterly striking features which may affect the permeability (Hardarson et al., 2007). The alteration mineralogy of the reservoir rocks can also be affected by the permeability in the geothermal reservoir. Therefore, by studying the alteration minerals, we can deduce and confirm this speculation locally in well HE-6.

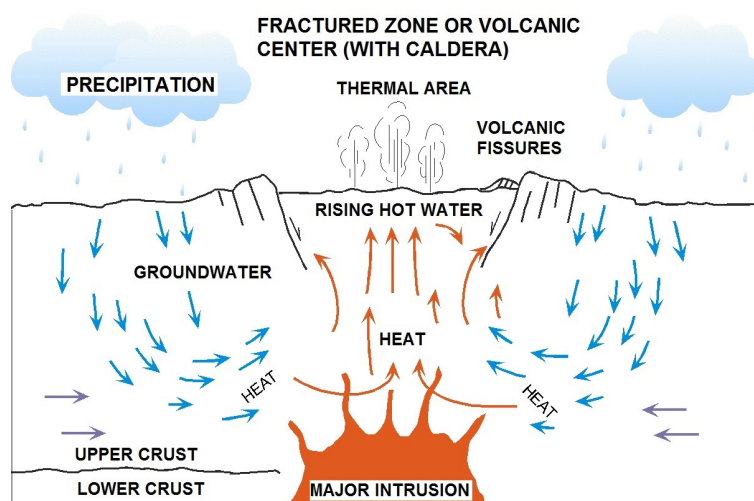


FIGURE 12: Conceptual model of a high temperature geothermal system (Hjartarson, 2014)

5.2 Alteration minerals

In geothermal environments, primary minerals alter and secondary minerals are formed. The mineral alteration temperature diagram in Figure 13 shows the stages of alteration in high temperature geothermal systems in Iceland. The factors that cause this hydrothermal process are the permeability, temperature, pressure, fluid chemistry, initial composition of the rock and the duration of the hydrothermal activity. These factors are independent, but the effects of one or more of the factors can exert a dominant influence on the location and extent of the hydrothermal alteration (Lagat, 2007). Some of these factors affecting the hydrothermal minerals encountered in well HE-6 are examined.

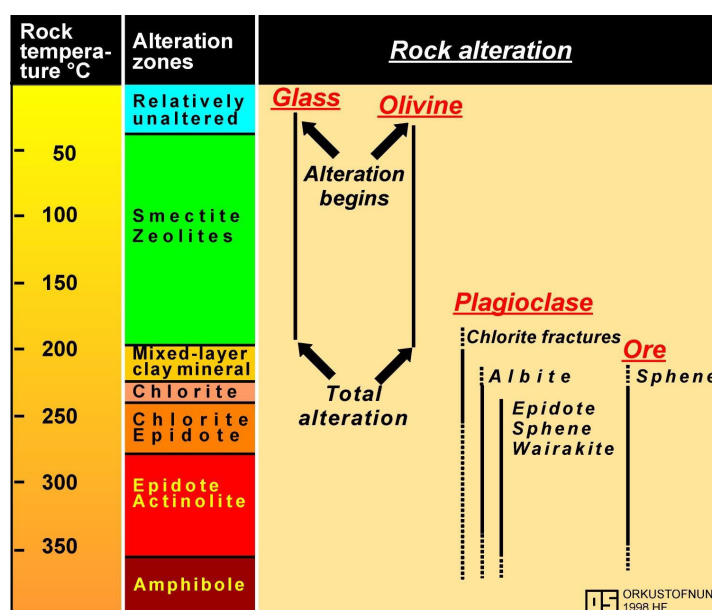


FIGURE 13: Mineral alteration temperature diagram (from Franzson, 2014)

High rock permeability and porosity should result in extensive alteration and low permeability and porosity should result in limited alteration (Franzson, 2014). However, in this study, the porosity of the rock was not a good measure of

permeability. Even though most volcanic rocks are porous they may not be permeable as often seen in altered hyaloclastite formations. Tuff and breccia are highly porous or permeable to begin with. However, they alter easily and the alteration products tend to plug the permeability. Therefore, these formations often form cap rocks. Of the hyaloclastites, the pillow lavas frequently remain quite permeable (Franzson et al., 2001).

A rise in temperature causes the primary minerals in the host rocks to alter to secondary minerals, resulting in the precipitation of new minerals. Some of the minerals identified are zeolites, clays, quartz, and prehnite. These minerals are temperature dependant and, therefore, act as geothermometers in identifying temperature changes in the geothermal system. In this study, 4 alteration zones were identified in well HE-6. These are the smectite-zeolite zone, the smectite-mixed layer clay-chlorite zone, the chlorite zone and the chlorite-epidote zone.

A comparison between alteration minerals, the fluid inclusion temperature range and the formation temperatures in Figure 10 gives a clue about the history of the geothermal system in this particular area. Three geothermal phases may exist within this geothermal system; the first one is related to the present conditions, the second one relates to a cooling episode caused by an inflow of the surrounding groundwater system, and a third one may be related to the geothermal up-flow reheating the system to its present conditions. This heating up probably relates to the renewed geothermal outflow along the 2000 and 5000 years old volcanic fissures (Franzson et al., 2005).

A comparison of the formation temperatures and hydrothermal alteration from several wells, including well HE-6, in a conceptual model of the Hellisheidi and Hverahlíð reservoirs, proposed three up-flow zones beneath Gráuhnúkar, Reykjafell and Hverahlíð (Helgadóttir et al., 2010). Well HE-6 is north of Reykjafell and south of Skardsmýrarfjall (Figure 3). Cross-sections suggest minor cooling west of Skardsmýrarfjall (Figure 14) while towards the southeast of Skardsmýrarfjall, it could be in equilibrium but there is heating up taking place beneath Gráuhnúkar in the southwest sector and in Hverahlíð (not shown in Figure 3). Figure 14 shows an example of the conceptual model and cross-section view taken from Franzson et al. (2005).

Since the Hellisheidi high temperature field is surrounded by cold ground water systems (Franzson, 2014), any change in the permeability may affect the conditions in the geothermal reservoir. For

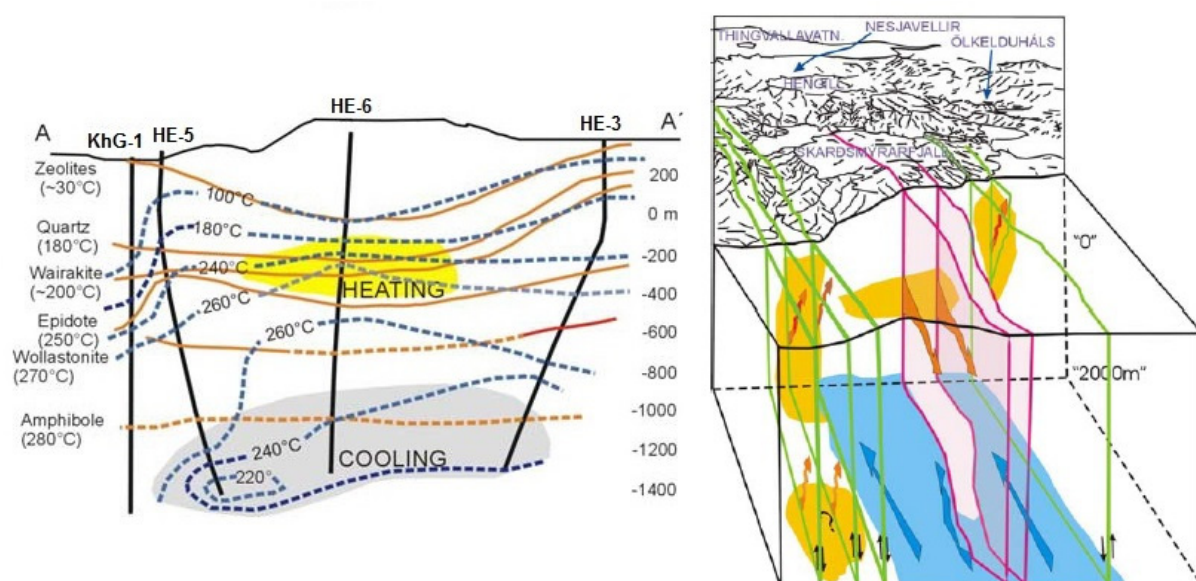


FIGURE 14: The conceptual model of the Hellisheidi high temperature geothermal field showing the cold water inflow into the geothermal reservoir beneath Skardsmýrarfjall and the cross-section of four wells including well HE-6 (Franzson et al., 2005)

example, if the pressure of the geothermal system is higher than the surrounding cold groundwater system, any permeability change will result in an outflow and heating up will occur. High pressure in the surrounding groundwater system will cause an intrusion of cold water into the geothermal system resulting in cooling in that area. This heating and cooling applies to high permeability zones and was observed in well HE-6.

6. CONCLUSIONS

Borehole geological logging is an integral part of subsurface geothermal exploration which adds to the understanding of the natural conditions in the geothermal reservoir. It involves a combination of studies to produce a conceptual model and history of the geothermal system. These studies include:

- i. Lithological logging, to identify the host rocks, alteration minerals and structures.
- ii. Petrographic studies to define host rock minerals, alteration minerals, structures and sequence of mineral deposition.
- iii. XRD analyses to define the clay zones and confirm the alteration mineralogical zones.
- iv. Fluid inclusion measurements to deduce the homogenization temperatures of the alteration minerals and salinity in the geothermal reservoir.

This study of well HE-6 is an exploratory or introductory experience for the author, being new to the study of geothermal systems. All the results presented in this report are the findings from this study, except where otherwise quoted. Several conclusions can be made from the findings of this work:

The stratigraphy of well HE-6 is comprised predominantly of four distinct hyaloclastite formations, three lava sequences and two possible intrusions, one being of intermediate composition. The hyaloclastite formations, made up of pillow basalts, breccias and tuffs, are porous in comparison to the basaltic lavas and intrusions. The rocks were not a good measure of permeability in this study because the cuttings were too small for a detailed analyses on the porosity. However, in studies undertaken for Icelandic rocks, the hyaloclastite units are not always permeable because hydrothermal alteration can plug permeability in easily altered rocks such as breccias and tuffs. Pillow basalt is the most permeable unit of the hyaloclastites because it consists of a smaller amount of glass, which is most sensitive to alteration.

The 14 aquifers identified in this study were along lithological contacts, intrusive boundaries, and along faults and fractures which are indicative of high permeability zones. The mineral structures of some hydrothermal alteration minerals such as quartz, calcite and pyrite can depict good permeable zones. These minerals occurred mostly as vein fillings or well-formed crystals adjacent to the aquifers.

The mineralogical studies recognized four distinct alteration zones: smectite-zeolite zone, smectite-mixed layer clay-chlorite zone, chlorite zone and chlorite-epidote zone. The chlorite-epidote alteration zone is the highest mineral alteration temperature zone encountered for the upper 1018 m of the borehole. The temperatures of the alteration minerals formed a hypothesis regarding the history of the geothermal system suggesting three geothermal phases: the first one is related to present conditions, the second one relates to a cooling episode caused by an inflow of the surrounding groundwater system, and a third one may be related to volcanic activity causing geothermal up-flow and reheating the system to its present condition.

ACKNOWLEDGEMENTS

I would like to express my sincere appreciation to my supervisor Dr. Björn S. Hardarson for his support during the initiation, development and completion of this project. His advice and wealth of knowledge on the Icelandic geothermal systems has enabled me to successfully present this work. I thank him for his patience, time and commitment to my learning. Dr. Hjalti Franzson, whose tremendous support, co-ordination and facilitation of the various lectures and analytical studies is acknowledged and sincerely appreciated. Ms. Helga Helgadóttir's immense patience, time, effort and knowledge gave me motivation and enthusiasm that drove this project forward. She is thanked for her assistance with the binocular, petrographic and fluid inclusion studies. Mr. Sigurdur Jónsson is acknowledged and thanked for his time, effort and guidance on the preparation of the XRD measurements and analyses. Ms. Sveinborg Gunnarsdóttir is thanked for her time and assistance during the binocular microscope analyses and the introduction to petrel and petrographic analysis. Ms. Júlíana Gunnarsdóttir is not forgotten for her kind assistance during the binocular microscope analyses. Ms. Rósa Jónsdóttir's help to locate the maps and reports at the National Energy Library was invaluable.

I am grateful to the United Nations University and the Icelandic Government for funding this Geothermal Training Programme. I thank Mr. Lúdvík S. Georgsson, the Director of the United Nations University Geothermal Training Programme, for my acceptance to this training programme. Mr. Ingimar Gudni Haraldsson (Deputy Director), Mr. Markus Wilde (Service Manager), Ms. Maria Guðjónsdóttir (Project Manager), Ms. Málfríður Ómarsdóttir (Environmental Scientist) and Thórhildur Ísberg (School Manager) are sincerely thanked for their tremendous support. This awesome team at the UNU-GTP made my whole experience of Iceland a memorable one. All the presenters for the UNU-GTP introductory lecture courses for 2014 are whole-heartedly thanked for their time to share their geothermal knowledge.

I thank the Mineral Resources Authority (MRA) for my participation specifically, Mr. Philip Samar (Managing Director), Mr. Nathan Mosusu (Geological Survey Division Head) and Ms. Dulcie Saroa (Geological Mapping and Mineral Exploration Branch Manager) for releasing me from my responsibilities at the MRA to undertake this training. I am very grateful to Reykjavik Energy for allowing access to data from well HE-6 and specifically thank Dr. Einar Gunnlaugsson (Chief Geologist) for his assistance in relation to my project.

Finally, I would like to thank the UNU-GTP 2014 fellows for their friendship. Special acknowledgement to my course mates, Djama Robleh Djama, Fatumati Jumanne Mnzava, Emily Wangari Kahiga and my flatmate Melissa de Freitas for their invaluable friendship, care and support. I would not have been able to persevere, had it not been for the support of my loving husband, William Bawasu, my immediate family and extended relatives and friends in Papua New Guinea. I thank the almighty God for this knowledge and the support that each one of those mentioned gave to me.

REFERENCES

- Björnsson, G., 2004: Reservoir conditions at 3-6 km depth in the Hellisheidi geothermal field, SW-Iceland, estimated by deep drilling, cold water injection and seismic monitoring. *Proceedings of the 29th Workshop on Geothermal Reservoir Engineering, Stanford, CA*, 8 pp.
- Einarsson, P., 1991: Earthquakes and present-day tectonism in Iceland. In: Björnsson, S., Gregersen, S., Husebye, E.S., Korhonen, H., and Lund, C.E. (editors), *Imaging and understanding the lithosphere of Scandinavia and Iceland. Tectonophysics*, 189, 261-279.

Eshaghpour, M., 2003: Borehole geology and alteration mineralogy of well HE-9, Hellisheidi geothermal field, SW-Iceland. Report 8 in: *Geothermal training in Iceland 2000*. UNU-GTP, Iceland, 165-187.

Franzson, H., 2014: *Introductory lecture to borehole geology*. UNU-GTP, Iceland, unpublished lecture notes.

Franzson, H., Gudlaugsson, S.P. and Fridleifsson, G.Ó., 2001: Petrophysical properties of Icelandic rocks. *Proceedings of the 6th Nordic Symposium on Petrophysics, Trondheim, Norway*, 14 pp.

Franzson, H., Helgadóttir H.M., and Gudfinnsson G.H., 2014: *Fluid inclusion study in alteration minerals from well RN-29 at Reykjanes high-temperature field*. ÍSOR - Iceland GeoSurvey, Reykjavík, report ISOR-2014/002, 16 pp.

Franzson, H., Kristjánsson, B.E., Gunnarsson, G., Björnsson, G., Hjartarson, A., Steingrímsson, B., Gunnlaugsson, E., and Gislason, G., 2005: The Hengill-Hellisheidi geothermal field development of a conceptual geothermal model. *Proceedings of the World Geothermal Congress 2005, Antalya, Turkey*, 7 pp.

Getaneh, E., 2001: Borehole geology and alteration mineralogy in the upper half of well HE-3, Hellisheidi, SW-Iceland. Report 4 in: *Geothermal training in Iceland 2001*. UNU-GTP, Iceland, 59-82.

Gribble, C.D., and Hall, A.J., 1992: *Optical mineralogy principles and practice*. UCL Press, London, 302 pp.

Gudfinnsson, G.H., 2011: *Preparation of secondary minerals in drill cuttings for microthermometry of fluid inclusions*. ÍSOR – Iceland GeoSurvey, Reykjavík, unpublished internal memo.

Gunnlaugsson, E., 2012: The Hellisheidi geothermal project – financial aspects of geothermal development. Presented at “Short Course on Geothermal Development and Geothermal Wells”. UNU-GTP and LaGeo, Santa Tecla, El Salvador, 9 pp.

Gunnlaugsson, E., 2014: *Hengill field excursion, presentation on the Hellisheidi high-temperature geothermal field*. UNU-GTP, Iceland, unpublished lecture notes.

Hardarson, B.S., Fitton, J.G., and Pringle, M.S., 1997: Rift relocation - a geochemical and geochronological investigation of a paleo-rift in northwest Iceland. *Earth Planet Sci. Lett.*, 153, 181-196.

Hardarson, B.S., Helgadóttir, H.M., and Franzson, H., 2007: *The Hellisheidi power plant. The injection area by Gráuhnúkar*. ÍSOR – Iceland GeoSurvey, Reykjavík, report ISOR-2007/001 (in Icelandic), 29 pp.

Helgadóttir, H.M., Snæbjörnsdóttir, S.O., Nielsson, S., Gunnarsdóttir, S.H., Matthíasdóttir, T., Hardarson, B.S., Einarsson, G.M., and Franzson, H., 2010: Geology and hydrothermal alteration in the reservoir of the Hellisheidi high temperature system, SW-Iceland. *Proceedings of the World Geothermal Congress 2010, Bali, Indonesia*, 9 pp.

Hjartarson, A., 2014: *Introductory course to hydrology and hydrogeology*. UNU-GTP, Iceland, unpublished lecture notes.

Jónsson, S.S., Steingrímsson, B., Hermannsson, Franzson, H., Birgisson, K., Daniélson, E.P., Gudnason, Ó., 2002a: *Hellisheidi – well HE-6. 1st part: drilling of 13 3/8" production part from surface to 310 m depth*. Orkustofnun, Reykjavík, report OS-2002/030 (in Icelandic), 42 pp.

Jónsson, S.S., Richter, B., Sigurdsson, Ó., Steingrímsson, B., Hermannsson, G., Einarsson, E.M., and Skarphedinsson, K., 2002b: *Hellisheidi – well HE-6. 3rd part: drilling of 8 ½" production part from 813 to 2013 m depth*. Orkustofnun, Reykjavík, report OS-2002/047 (in Icelandic), 59 pp.

Kristmannsdóttir, H., 1985: The role of minerals in geothermal energy research. *Proceedings of the Uppsala Symposium on Clay Minerals, Modern Society*, 8 pp.

Lagat, J., 2007: Hydrothermal alteration mineralogy in geothermal fields with case examples from Olkaria Dome Geothermal Field, Kenya. *Presented at "Short Course II on Surface Exploration for Geothermal Resources"*, UNU-GTP and KenGen, Lake Naivasha, Kenya, 26 pp.

Reyes, A.G., 1990: Petrology of Philippine geothermal systems and the application of alteration mineralogy to their assessment. *J. Volc. Geoth. Res.*, 43, 279-309.

Richter, B., Franzson, H., Sigurdsson, Ó., Magnússon, E.M., Gudnason, Ó., 2002: *Hellisheidi – well HE-6. 2nd part: drilling of 9 ⅝" production part from 310 to 813 m depth*. Orkustofnun, Reykjavík, report OS-2002/047 (in Icelandic), 45 pp.

Saemundsson, K., 1979: Outline of the geology of Iceland. *Jökull*, 29, 7-28.

Saemundsson, K., 1995: *Geological map of the Hengill area 1:50,000*. Orkustofnun, Reykjavík.

Saemundsson, K., and Gunnlaugsson, E., 2014: *Icelandic rocks and minerals* (2nd ed.). Forlagid, ehf., Reykjavík, 232 pp.

Steingrímsson, B., 2011: Geothermal well logging: Geological wireline logs and fracture imaging. *Presented at "Short Course on on Geothermal Drilling, Resource Development and Power Plants"*, organized by UNU-GTP and LaGeo, Santa Tecla, El Salvador, 11 pp.

Steingrímsson, B., and Gudmundsson, Á., 2006: Geothermal borehole investigations during and after drilling. *Presented at "Workshop for Decision Makers on Geothermal Projects in Central America"*, organized by UNU-GTP and LaGeo in San Salvador, El Salvador, 10 pp.

Wilson, M. J., 1987: X-ray powder diffraction: In: Wilson, M.J. (ed.), *A handbook of determinative methods in clay mineralogy*. Blackie, Glasgow and London, 26-98.

Wolfe, C.J., Bjarnason, I.T., Van Decar, J.C., Solomon, S.C., 1997: Seismic structure of the Iceland plum. *Nature*, 385, 245-247.



UNITED NATIONS
UNIVERSITY

UNU-GTP

Geothermal Training Programme

Orkustofnun, Grensasvegur 9,
IS-108 Reykjavik, Iceland

Reports 2014
Number 10

STUDY OF CHACHIMBIRO AND CHACANA GEOTHERMAL PROJECTS, ECUADOR, AND VOLUMETRIC ASSESSMENT

Miguel Angel Calderón Torres

Electricity Corporation of Ecuador - CELEC EP
Ministry of Electricity and Renewable Energies
December 6th Avenue N26-235, Transelectric Building
Quito
ECUADOR
miguel.calderon@celec.gob.ec

ABSTRACT

Chachimbiro and Chacana geothermal fields are located in the Andes ridge in the north of Ecuador. Previous prefeasibility studies of geology, geochemistry and geophysics were reviewed and the acquired information was used to generate different scenarios for volumetric assessment of the geothermal fields depending on the results from resistivity models and geothermometers.

Chachimbiro was treated as a high-temperature field in the volumetric assessment, supported by the presence of a high-temperature resistivity structure. Chacana was treated in a similar way, but as an intermediate- to low-temperature system. Using similar processes with different scenarios may help to advance them to the next stages of exploration. The true conditions of the fields must be discovered by drilling. With an exploratory drilling campaign, the estimation of the models would partly be fixed to more accurate parameters.

1. INTRODUCTION

The main objectives of this study were to review available data from Chachimbiro and Chacana, geothermal fields in northern Ecuador, and using part of the information to make volumetric assessments. To reach these goals an overview was made of the geology, geochemistry and geophysics already published in the consultancy reports of prefeasibility studies in order to develop a conceptual model for the Chachimbiro and Chacana geothermal projects (SYR, 2012a; SYR, 2012b). Estimations of the potential and power capacities of the geothermal fields were deduced from volumetric assessments of both projects. Different scenarios were selected for the fields depending on the resistivity pattern and the temperatures deduced from geothermometers. Chachimbiro was treated as a high-temperature system; two areas in Chacana were treated in a similar way but as medium- to low-temperature systems, partly due to recent volcanism (in the 17th century). These are only examples, but further analysing of the data and using similar processes with different scenarios may be useful for comparison and for advancing to the next stages with respect to the exploration and development of the fields.

Additionally, it may be useful to compare some examples of volumetric assessment for Chachimbiro to an older model already done for that field (Torres and Urquiza, 2013). Extensive information was gained

in the review of previous work from the two geothermal fields. The results show different possibilities of the characteristic features of each geothermal field, suggesting the establishment of various modelling alternatives, including volumetric assessment based on their main parameters.

Ecuador is located in the northern part of South America, between 01°30' N and 05°00' S, and between 75°12' and 81°00' W (Figure 1). The surface area of Ecuador is 283,561 km², and there are diversities in climate caused by the presence of the Andes ridge, the influence of the sea and jungles.

Ecuador is a country which, due to its geological and geographical conditions, has the capability to develop renewable energy, especially hydropower, from river flows. Geothermal energy is a very promising field for the national goals of changing the energy matrix through developing renewable energies. Currently, geothermal fields in Ecuador are being studied, which includes making conceptual models.

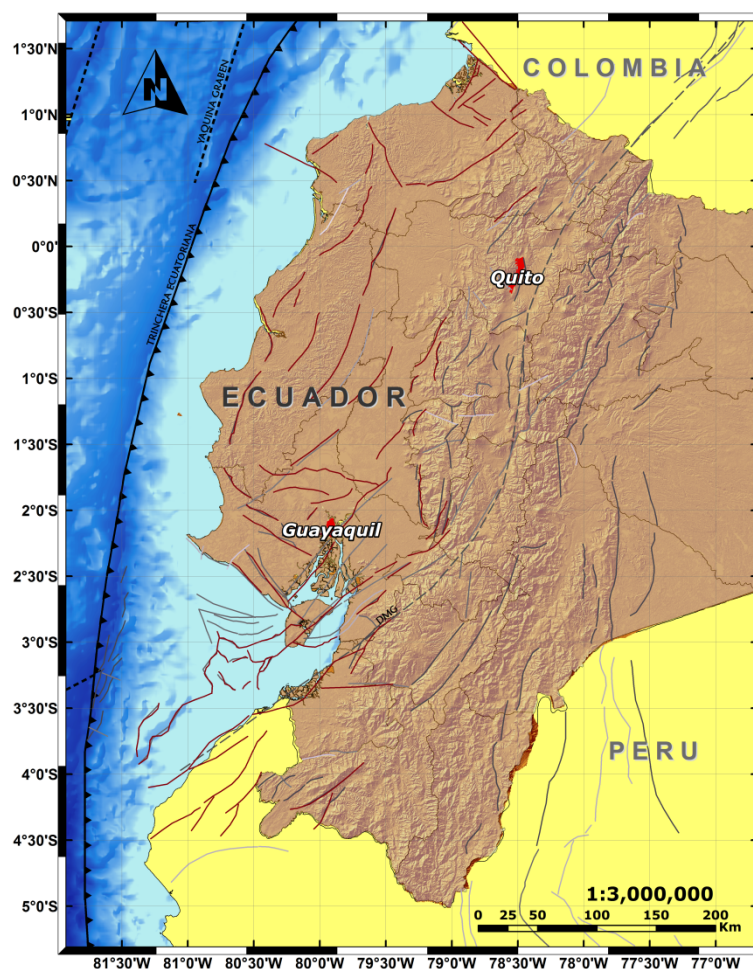


FIGURE 1: Geographical map of Ecuador, showing the capital city Quito, located in the Andes ridge

Chachimbiro geothermal field is located in the eastern part of the Andes occidental ridge, in the northern province of Imbabura (Figure 2), located 75 km north of Quito, the capital city. This complex is characterized by a set of mixed chloride-bicarbonate warm springs, with temperatures between 25 and 61°C, located up to 5.5 km apart from each other. In addition, this area of interest has cold gas manifestations with hydrothermal alteration in its higher topographical zones.

Chacana geothermal project is at the crest of Real Andes ridge, in the north-central mountainous region of Ecuador, located 40 km east of Quito (Figure 3). The topography of the area is rugged, and its elevation is between 3200 and 4600 m a.s.l. The isotopic composition of samples taken from the surface of warm springs shows that the water has a meteorological origin with a neutral alkaline-chloride chemistry, and temperatures between 58 and 72°C.

2. GEOLOGICAL SETTINGS OF THE GEOTHERMAL PROSPECTS

Chachimbiro and Chacana are parts of the Ecuadorian Quaternary volcanic arc, along with 60 volcanoes, formed by subduction of the Nazca Plate under the northern Andean block of the South American Plate.

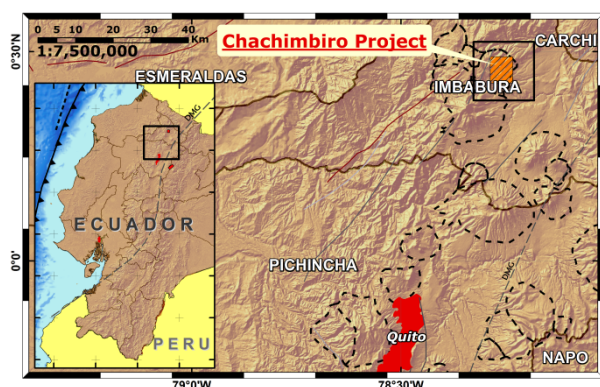


FIGURE 2: Chachimbiro geothermal project, located 75 km north of Quito

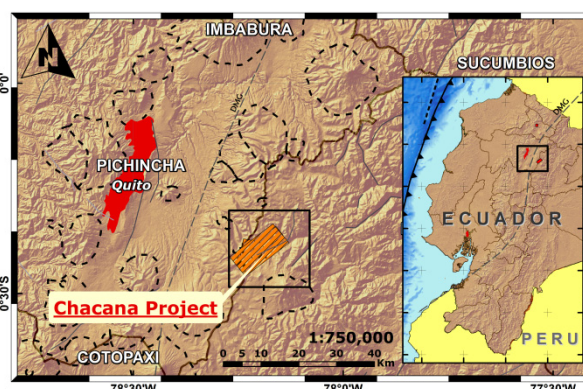


FIGURE 3: Chacana geothermal project is located 40 km east of Quito

The convergence between the Nazca and South American plates is estimated to be 60-80 mm/yr with the direction of convergence between N81°E and N120°E (SYR, 2012a; SYR, 2012b).

Several Quaternary volcanic centres occur near the Chachimbiro and Chacana projects, shown by black dashed lines in Figures 2 and 3.

2.1 Chachimbiro

2.1.1 Volcanic evolution of Chachimbiro

The Chachimbiro project area is located in the Chachimbiro volcanic complex (Figures 4 and 5), composed of andesitic lava flows and pyroclastic deposits associated with dacitic domes. The thickness of the Chachimbiro volcanic materials is approximately 1000 m (SYR, 2012a). The Chachimbiro volcanic complex was formed in three stages (Figure 4).

In the first stage an Andesitic stratovolcano was formed with big effusive flows of lava streaming radially from the eruptive centre. After the formation, the volcano suffered a collapse and generated a debris avalanche flowing towards the east. These events occurred in medium Pleistocene between 500,000 and 300,000 years ago. This stage is known as Chachimbiro 1.

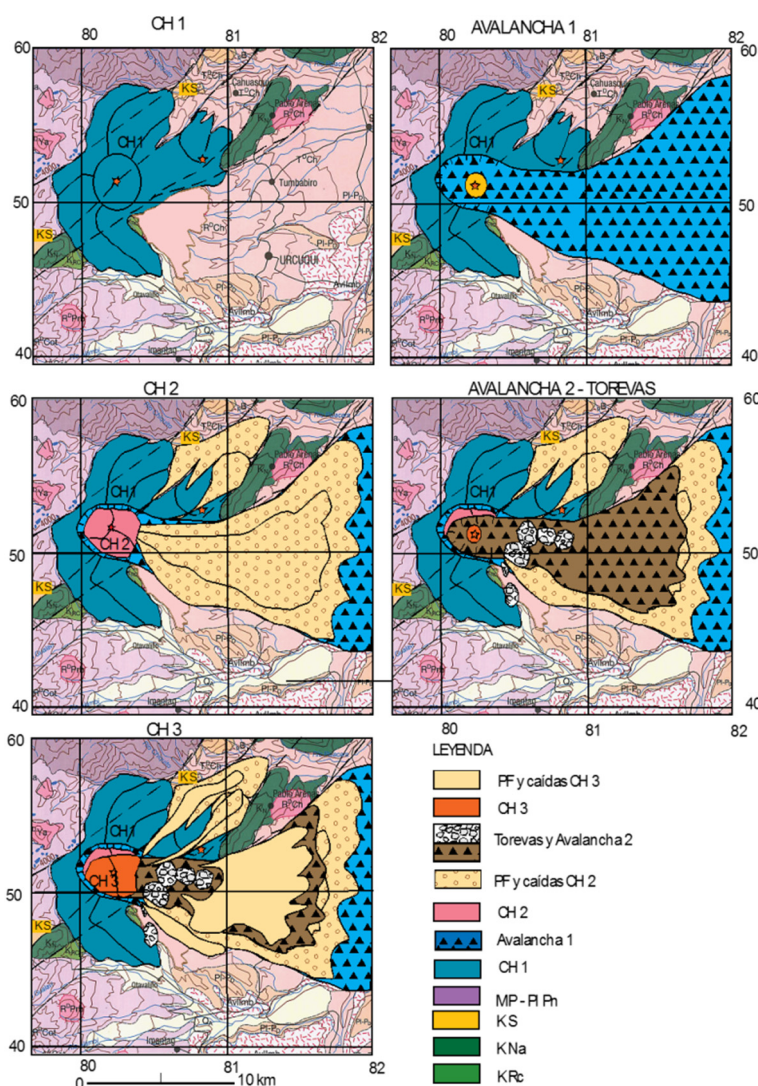


FIGURE 4: Evolution of Chachimbiro volcanic complex (Ruiz, 2011)

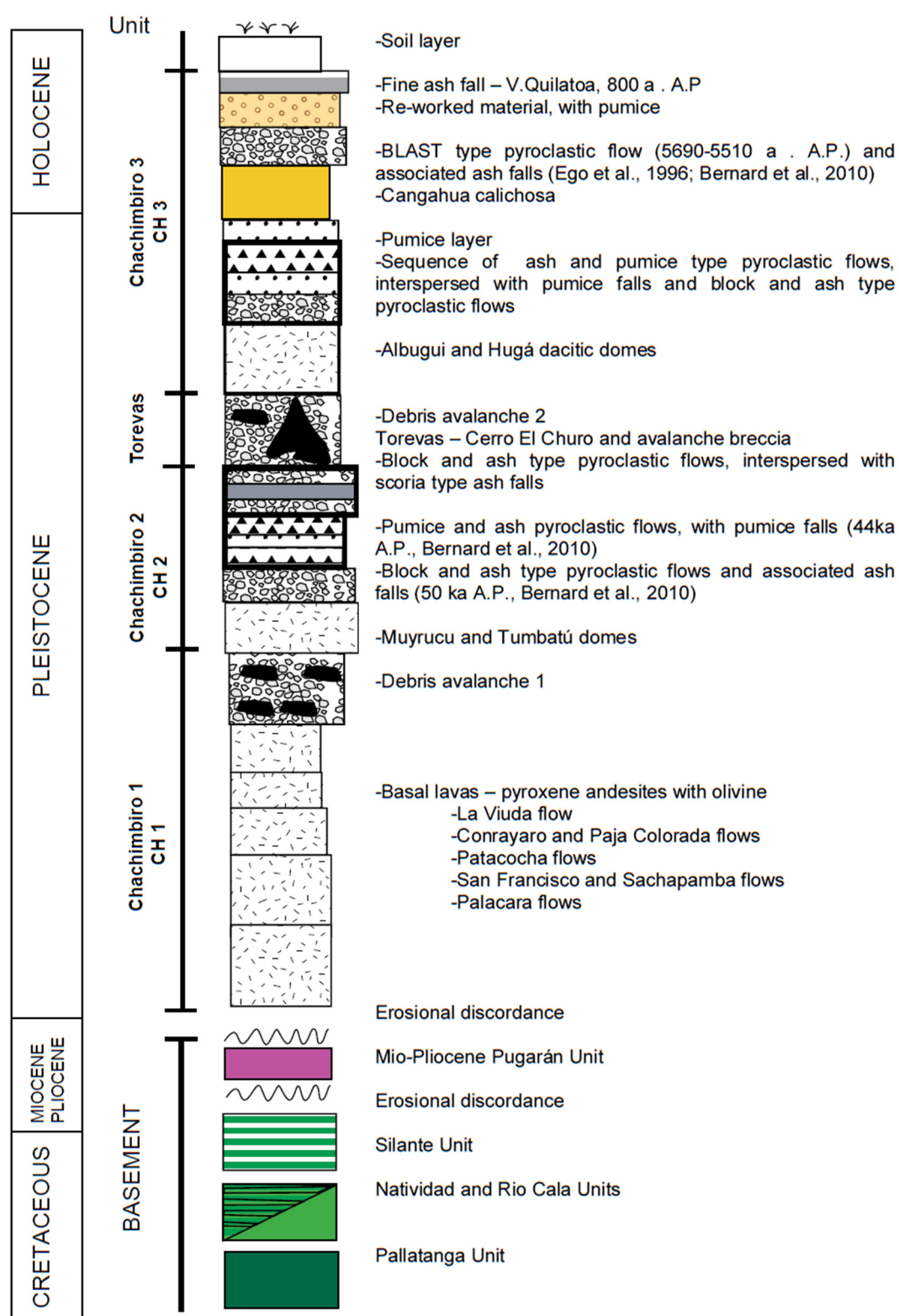


FIGURE 5: Lithological column of the volcanic and Cretaceous rocks at Chachimbiro (Ruiz, 2011)

In the second stage, andesitic and dacitic domes were formed by eruptions in the collapsed caldera. A second landslide occurred flowing to the east with an escarpment associated with the first collapse. Some of these domes were displaced from their original locations. This stage is called Chachimbiro 2 and the events occurred between 120,000 and 50,000 years ago.

In the last stage, new domes of dacitic-andesitic composition were formed extending into the Holocene, located at the same place as the second landslide. These events occurred 30,000 years ago, and are known as Chachimbiro 3. The stages of formation of the Chachimbiro caldera are shown in Figures 4 and 6 and the geological succession is shown in Figure 5.

2.1.2 Stratigraphy associated with the Chachimbiro caldera

The basement in the Chachimbiro caldera consists of Cretaceous rocks which piled up in the subduction zone, composed of five geological formations (Figure 5). The oldest geological formation in the basement is the Pallatanga unit which is formed by basaltic lavas and sediments associated with oceanic shelf basalts. The Río Cala unit consists mainly of massive lavas of basaltic-andesitic composition, and volcanic rocks with local sandstone lenses (SYR, 2012a). Above, the Natividad unit is a sedimentary sequence of turbiditic sandstones, mudstones, cherts, and interbedded lavas and tuffs that are basaltic to basaltic andesite in composition. The Natividad unit has a dominant Cretaceous lithology. The next geological formation is the Pilaton unit which is composed of sedimentary rocks with massive volcanic conglomerates, breccias, sandstones and cherts. Finally, the Silante unit consists of micro breccias and massive volcanic tuffs interbedded with layers of volcanic shale and sandstone. The Silante unit is of Upper Cretaceous age and depicts the continental volcanic products (Figure 5).

The tertiary volcanics in the Chachimbiro area are represented by the Pugaran volcanic unit of Upper Tertiary age, especially Miocene-Pliocene. This volcanic unit is composed of andesitic lava flows and hornblende dacite tuffs and breccias (SYR, 2012a).

In the study area, Quaternary volcanic products from other volcanic centres occur on the margins of the Chachimbiro complex. These include andesitic lava flows from the Cotacachi stratovolcano south of the map in Figure 6, and pyroclastic deposits associated with the Piribuela dacitic dome, also to the south.

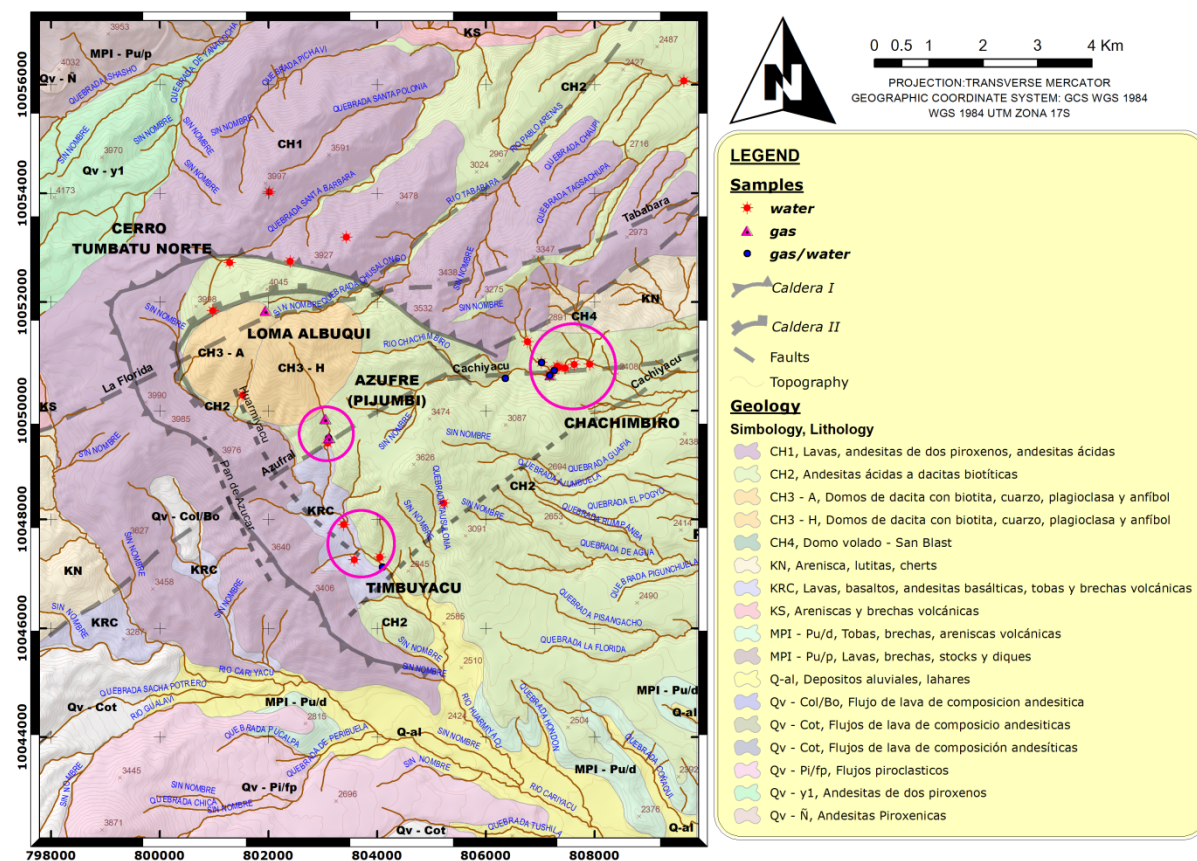


FIGURE 6: Chachimbiro geothermal project area: geological and structural map (modified from Torres and Urquiza, 2013)

Andesites and rhyodacites associated with the Yanaurco volcano overlap the Chachimbiro volcanic on the northwest slope (Figure 6). An unconformity is at the contact between the Cretaceous and overlying Tertiary and Quaternary volcanics (Figure 5). The thickness of the Chachimbiro volcanics varies, with a maximum of about 1000 m in the area of the Hugá dome, located in the centre of the caldera.

2.1.3 Structural geology

The fault system in the study area has played an important role in the origin of the caldera and the potential location and circulation of the geothermal fluids.

The NE-SW striking Florida fault system forms the contact between the Cretaceous Natividad and Silante units (Figure 6). This fault complex underlies the eruptive centres for the Huanguarillo volcano and the Hugá-Albuji domes, indicating that its deep fractures contribute to the rise of lavas from the Chachimbiro volcanic complex.

The Azufral fault system, in the central portion of the project area, also trends NE-SW (Figure 6), which indicates that it is a right lateral strike slip fault system (SYR, 2012a) which may represent the contact between the Natividad and Rio Cala formations. The Azufral fault system is marked by the occurrence of gas seeps and hydrothermal alteration, which could be evidence of the circulation of geothermal fluids.

2.1.4 Thermal manifestations

In the Chachimbiro geothermal project, four areas of thermal manifestation were studied. Two of them are warm springs called Chachimbiro and Timbuyacu, the others are gas manifestations in places called Pijumbí and Minas de Azufre (Figure 6).

The Timbuyacu field is located where the surrounding topography lies between 2750 and 2860 m a.s.l. The gas consists mostly of CO₂, with low concentrations of H₂S. The temperature of the water in the two hot spring areas is below 45°C. The Chachimbiro field is located where the surrounding topography lies between 2520 and 2620 m a.s.l. The water temperatures in the hot springs are up to 61°C. Pijumbí and Minas de Azufre gas manifestations are located in higher topographic places, along the Azufral fault in a northeasterly direction. The distance between the two places is approximately 2 km.

2.2 Chacana

2.2.1 Chacana volcanic caldera complex

Early studies of Hall and Mothes (1997) and Hall et al. (2000), showed that Chacana is a big caldera structure of rhyolitic composition with all its characteristic features, formed in large siliceous eruptions. The Chacana caldera complex is 40 km long in a N-S direction and 10-15 km long in an E-W direction. The diameter, including outer flanks, is approximately 50 km, making Chacana the largest caldera in the northern part of the Andes ridge. The evolution of the caldera dates back more than 2.5 My, according to its radiometric date (Hall et al., 2000).

The flanks of the Chacana caldera are composed of deposits of ignimbrites, ash flows, glassy lavas, breccias and tuffs (Figure 7). This volcanic succession is called “tablones”, and has a thickness of over 1200 m and an estimated volume of 670 km³, based on surface area and thickness.

The depression of the Chacana caldera was formed by subsidence and a collapse of the volcanic structure, due to emissions of large volumes of eruptive material and the eviction of magma from its magma chamber. The central depression is composed of pyroclastic material and younger lavas from Late Pleistocene. Subsequently, breccias and tuffs filled the depression.

Faults, dikes and breccias usually define the boundaries of calderas. In the Chacana caldera these boundaries do not have continuity due to regional tectonic faulting and deep erosion during the last glacial periods, especially in the central and eastern parts which are also affected by surface runoff. The western part of the Chacana caldera is well preserved.

2.2.2 Stratigraphy associated with the Chacana caldera

The basement of the caldera consists of metamorphic rocks from the Mesozoic era, defined as green pelitic schists, quartz-feldspar gneisses, and partly meta-granites. Above an unconformity, a sequence of lavas is deposited, breccias and tuffs of andesitic-basaltic composition approximately 200 m thick (Figure 8). This volcanic sequence is from late Miocene to Pliocene and is called the Pisayambo formation. Above, the geological formation Ninarumi was formed by lava flows and breccias of a sandy matrix with angular blocks of andesitic lava and lahar deposits. The estimated thickness is 200-260 m. None of these formations outcrop in the project area, but are seen at the surface to the southwest at the border of the caldera (SYR, 2012b).

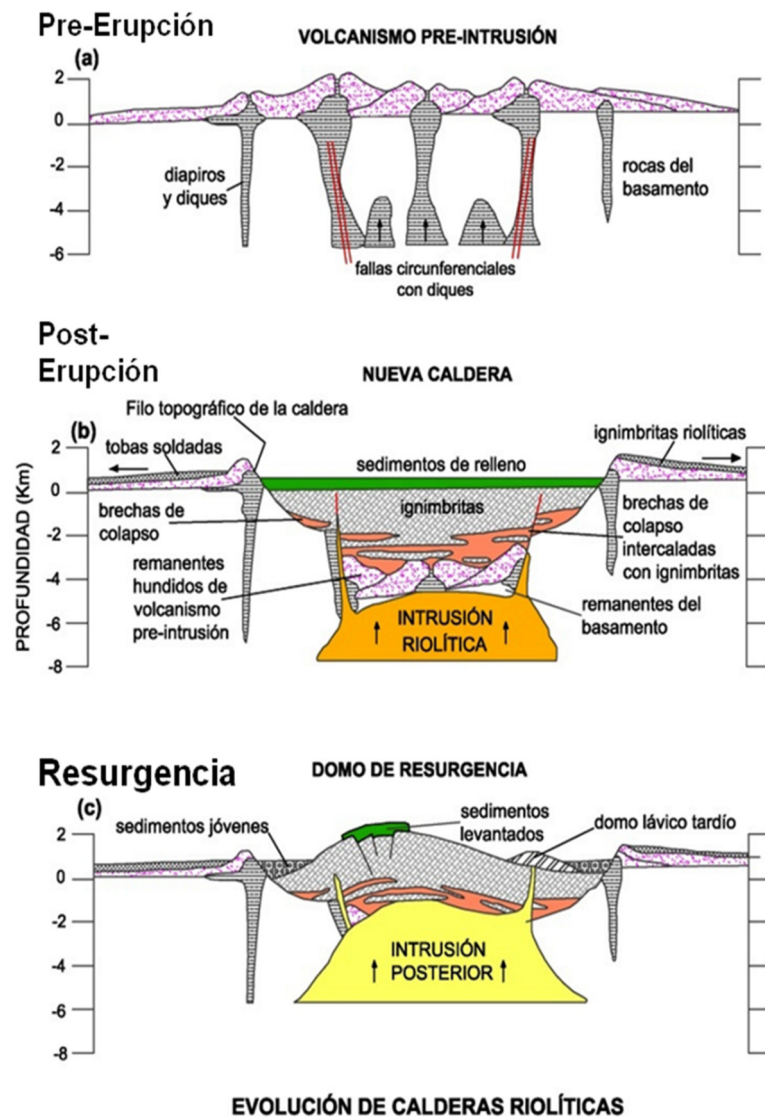


FIGURE 7: Evolution of the Chacana caldera complex (SYR, 2012b)

Intrusions or dikes of fine-grained and andesitic-dacitic composition are associated with the collapse of the caldera through circumferential faulting (SYR, 2012b).

The intra-caldera fill in Figure 8 began with eruptive products during eruptions that filled the depression. These products are composed of fine- to medium-grained volcanic breccias and tuffs, as well as massive ignimbrites and lavas. The thickness is approximately 700 m. In addition, many volcanic centres of andesitic-rhyolitic composition inside the caldera erupted and were affected by propylitic alteration. This sequence of events is known as the Baños rhyolite series, and it is shown in Figure 8 as SRB (SYR, 2012b).

Black lava flows were deposited on top of the Baños rhyolite series, composed of lavas of Si-rich andesitic-dacitic composition, interbedded with layers of auto-breccias (SYR, 2012b). Its total thickness is between 200 and 400 m; this sequence is known as black dacitic and andesitic lavas (LDA in Figure 8).

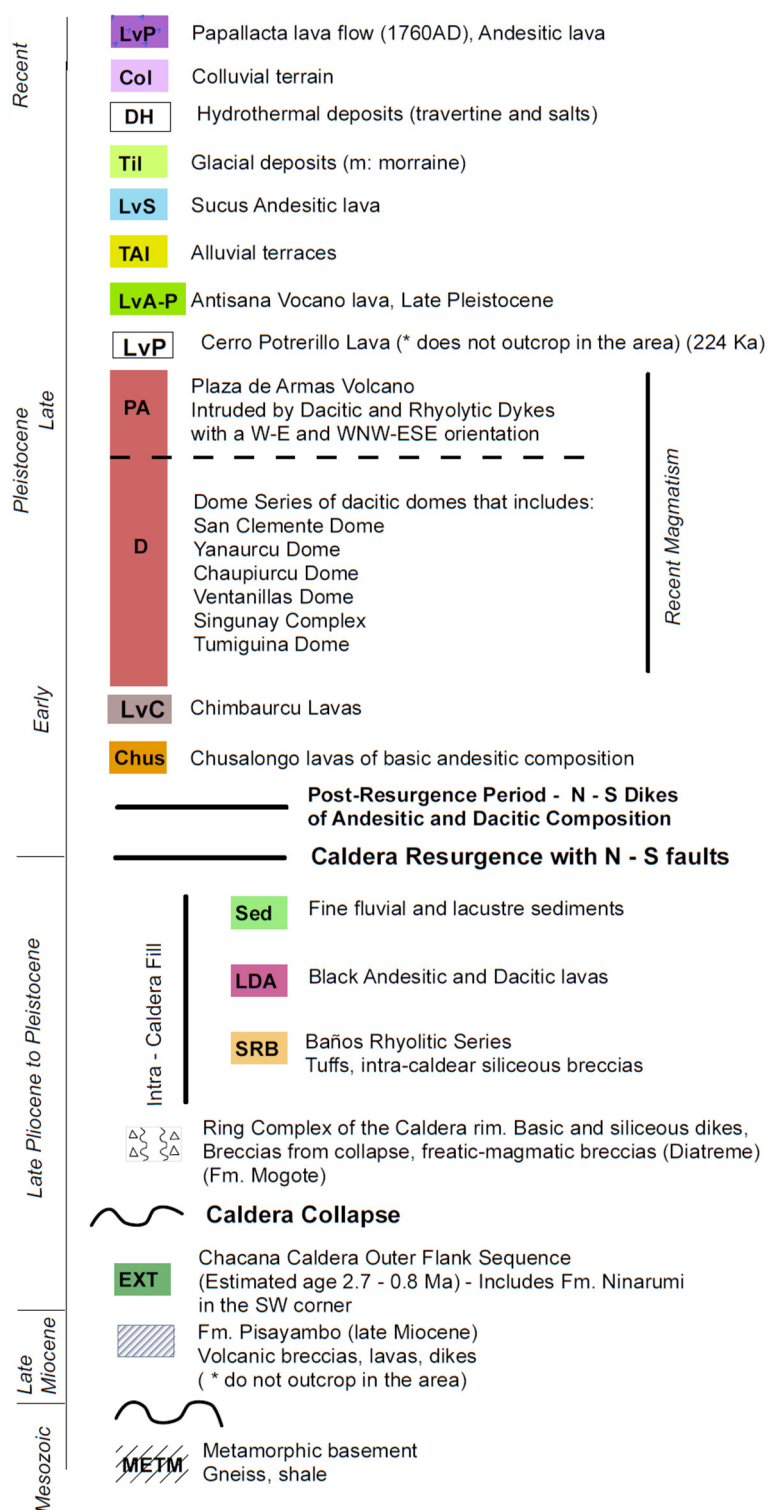


FIGURE 8: Lithological column associated with the Chacana caldera (SYR, 2012b)

The thick dashed yellow line corresponds to the western caldera rim, intersected by mapped faults. A fault in a NNE-SSW direction is at the contact between the metamorphic basement of Mesozoic age to the east and the Chacana caldera to the west, as shown with the thin dashed yellow line in Figure 9.

Finally, over the black lava flows, a sedimentary sequence composed of layers of sandstones, breccias, or cobbles was deposited. The bottom of this sedimentary sequence was formed by fine-grained sandstones of lacustrine origin and detrital micro-breccias. The thickness is approximately 150 m, seen at the centre of the caldera.

The resurgence stage of the Chacana caldera (Figure 7) occurred after deposition of LDA and during the sedimentary sequence, between 1.5-0.9 My, through Si-rich dikes, intrusions of dacitic composition in the axial zone of the caldera.

2.2.3 Structural geology

The main structural feature of the Chacana caldera is related to the resurgence stage. It has N-S direction and has been the main source of magma and eruptive activity during the late Pleistocene, and for the rhyolitic province of Ecuador, i.e. during the last 200,000 years, and especially during the last 50,000 years (Mothes and Hall, 2008). It is known as the Chacana rift and is located in the central axis of the caldera depression. Its youngest volcanic activity is expressed in lava flows that are believed to be about 31,000 years old.

In the project area and its surroundings, several regional faults of tectonic origin were mapped (Soulas et al., 1991; Yepes et al., 1990; Yepes and Ramón, 2000), as shown in Figure 9. Five of them are considered important for the past volcanism and important for the circulation of geothermal fluids due to their permeability (SYR, 2012b).

The Rio Blanco fault is shown as number 6 in Figure 9. It has a NE-SW direction and is more than 40 km long. Tumiguina fault is represented by number 2 in Figure 9 and this lineament has a NE-SW direction. Tambo fault runs in a NE-SW direction, parallel to the Tumiguina fault, and is associated with Jamanco, Cachiyacu and Papallacta geothermal springs in the Chacana field, represented by no. 3 in Figure 9. The Sucus fault has a NE-SW direction and can be identified as no. 4 in Figure 9. Towards the north in the caldera is the Ramos Sacha fault, in a NE-SW direction, shown as no. 5 in Figure 9; it intersects the Chacana rift. No. 1 in Figure 9 corresponds to the Rio Antisana fault with a NW-SE direction, i.e. almost perpendicular to most of the other faults, caused by displacement and faulting as a result of the NE-SW trending movements of Tumiguina, Sucus, and Ramos Sacha faults (SYR, 2012b).

Finally, red dots represent dacitic domes along the Chacana rift, and yellow stars represent the thermal manifestations at the surface (Figure 9).

2.2.4 Thermal manifestations

Three main geothermal springs are known in the Chacana project area (Figure 10). The hottest spring (73°C) is near Jamanco (3450 m a.s.l.) and lies on a small E-W fault near its intersection with the Tambo fault. The second hottest spring (64°C) is at Cachiyacu (3880 m a.s.l.), located at the intersection of the Tambo and San Clemente faults. The third hottest spring (59°C) is at Termas (3300 m a.s.l.), a commercially developed recreational site, located near the intersection of the Tumiguina fault and the metamorphic basement boundary. The first and second springs lie near the intersection with the Chacana Rift (Figure 9).

3. GEOCHEMISTRY

3.1 Chachimbiro – liquid and gas geothermometers

The Chachimbiro geothermal field is composed of a set of hot springs of chlorine-sodium and chlorine-bicarbonate waters, the temperature is around 61°C, and they are used as a tourist attraction with swimming pools. Timbuyacu field is located 5.5 km southwest of Chachimbiro, and has the same

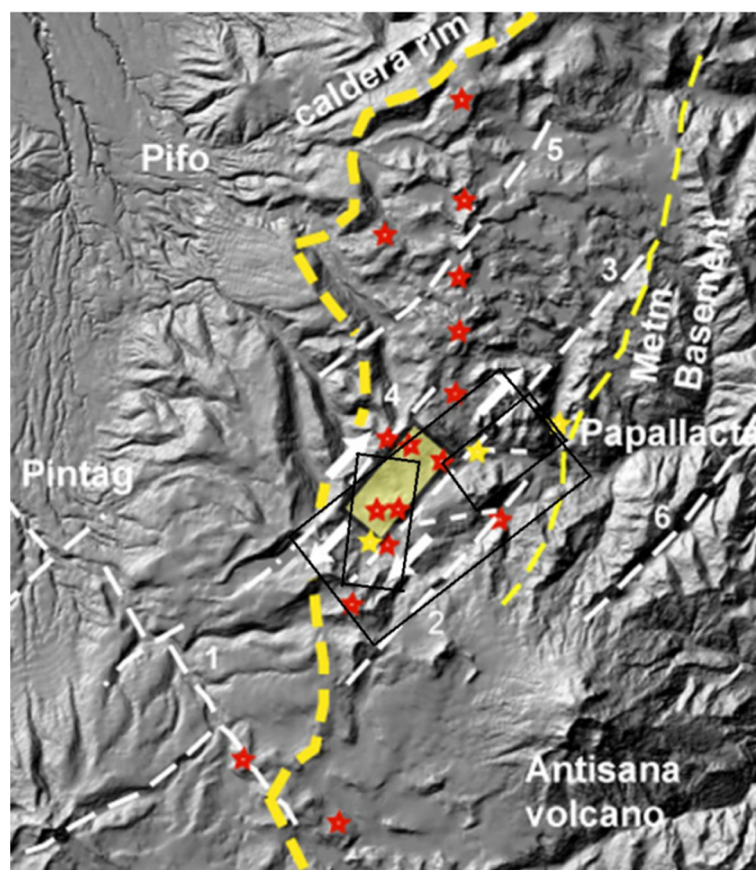


FIGURE 9: Chacana project: Diagram of the principal lineaments and faults in the project area: Symbols for faults and lineaments: 1= Rio Antisana; 2= Tumiguina; 3= Tambo; 4= Sucus; 5= Ramos Sacha; 6= Rio Blanco; thin dashed yellow line = border of caldera structure and metamorphic basement; red stars denote late Pleistocene volcanic centres of Chacana Rift; yellow stars = main hot springs (SYR, 2012b)

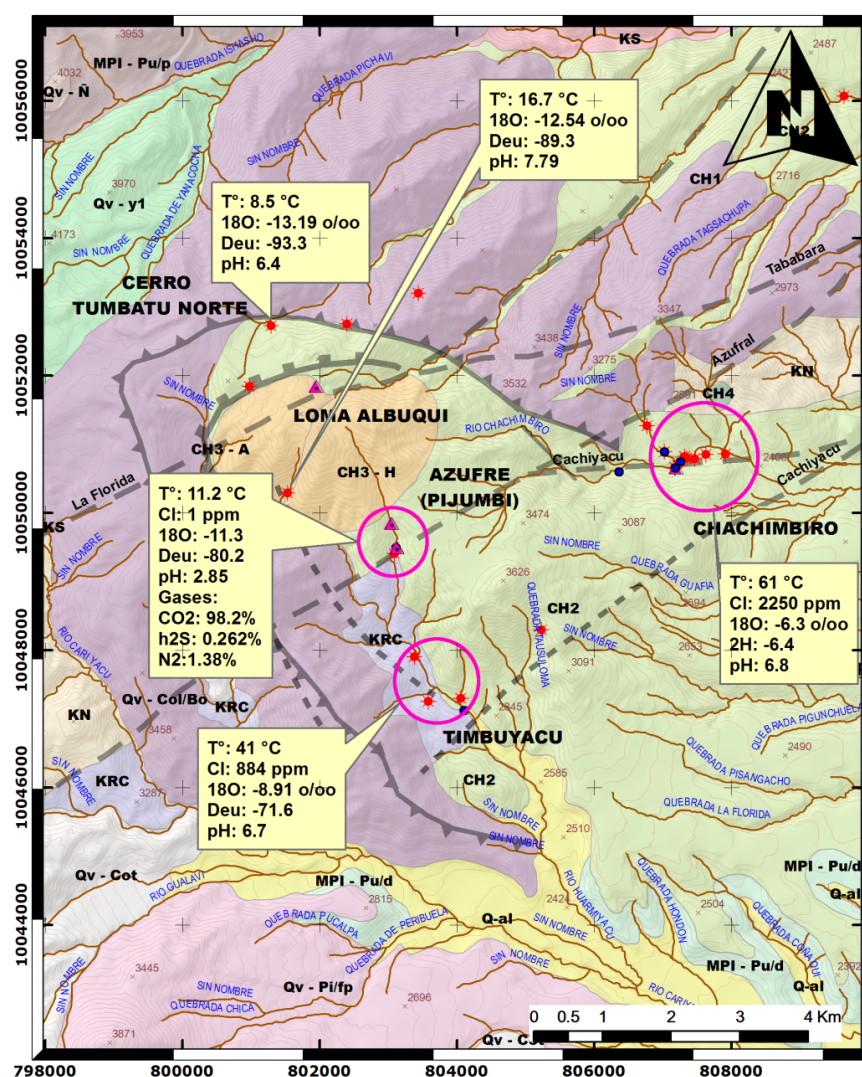


FIGURE 10: Geochemical map of Chachimbiro (modified from SYR, 2012a)

inferred by cation geothermometers and Giggenbach's geothermometers applied to samples of water which have characteristics of geothermal water with high concentrations of HCO₃. Also, the temperature of the reservoir was inferred by gas geothermometers. In addition, the recharge and recharge zone were defined. Finally, a geochemical conceptual model was developed (SYR, 2012a).

In the previous study (SYR, 2012a), the composition and chemical properties of samples from warm springs and gas manifestations did not conclude in a satisfactory geochemical model of Chachimbiro, after comparison with known results of other geothermal systems. With respect to thermal characteristics, the geochemistry of Chachimbiro suggests three scenarios of a hydrological model (Figure 11).

The first scenario suggests an intermediate-temperature geothermal system, characteristic of a magmatic-hydrothermal and alkaline-chloride reservoir, based on the chloride composition of warm springs, isotopic evidence of a magmatic source of water, carbon, sulphur and helium, and through geothermometers of Na/K and CO/CO₂-CH₄/CO₂, with temperatures at 225-235°C and 280-315°C for liquid and gas, respectively (Figure 12) (SYR, 2012a).

chemical properties as the Chachimbiro field. The temperature at Timbuyacu is approximately 41°C (Figure 10). Timbuyacu provides hot water for tourist sites. In addition, this area of interest has cold gas manifestations with hydrothermal alteration in its higher topographical zones, at over 3300 m a.s.l., at the surface of the Azufre, Pijumbi and Minas de Azufre streams (Figure 10) (Torres and Urquiza, 2013).

From the chemical and isotopic analyses of the water samples, the origin of the water is defined as well as its interactions with rocks, and the fluid temperature (Figure 11). In this study, the water samples were classified through Giggenbach diagrams Cl-SO₄-HCO₃ (Figure 12), the relationship between δD vs. δ¹⁸O (Figure 13), and by defining the origin of the waters. The temperature of a possible reservoir was

Samples from Chachimbiro and Timbuyacu have characteristics of geothermal water with high concentration of HCO_3 (Figure 12) and, therefore, support the hypothesis of the first scenario. The samples from Azufre are composed of sulphides of volcanic origin. On the other hand, in the water classification in the Giggenbach diagram (Figure 12), the samples called Cerro Tumbatú, Azufre met, Timbuyacu met and Loma Albuji represent meteorological water (Torres and Urquiza, 2013).

From the percentage of Deuterium (D or ^2H) and ^{18}O (δD vs $\delta^{18}\text{O}$, Oxygen-18) isotopic analyses, it was also possible to define the origin of the water samples (Figure 13). The water samples from Cerro Tumbatú, Azufre met and Azufre show a good alignment with the worldwide meteorological line (Torres and Urquiza, 2013).

The second scenario suggests that the geothermal fluids correspond to immature water, and the temperature is $110\text{--}125^\circ\text{C}$. This model suggests that the water is of deep metamorphic origin and could be warmed by igneous intrusions. This model is supported by decreasing temperatures in the streams located at higher elevations (Figure 10) (SYR, 2012a). The temperature range was obtained through K-Mg geothermometers and oxygen and sulphur isotopes.

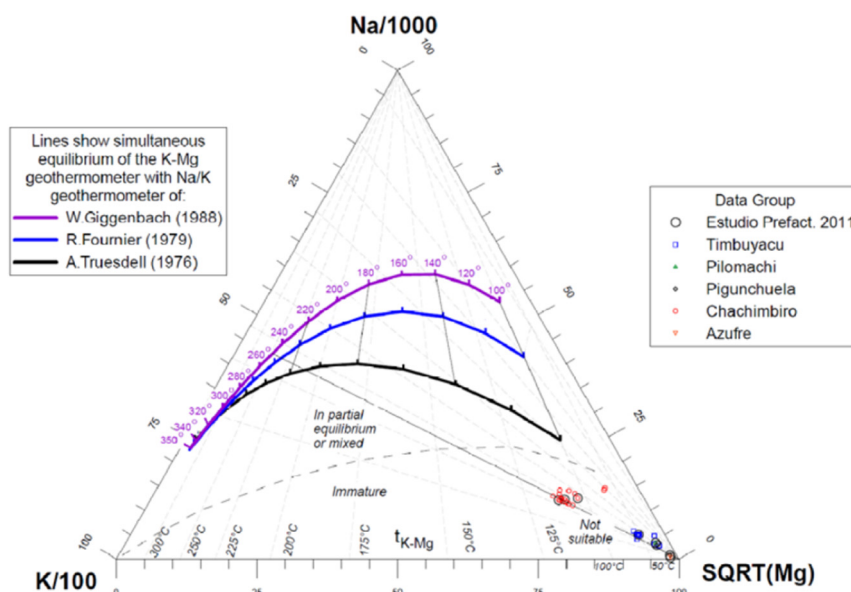


FIGURE 11: Ternary diagram showing relative concentrations of Na, K and $\sqrt{\text{Mg}}$ in relation to three Na/K geothermometers and the K-Mg geothermometer; the Chachimbiro waters plot in the field of “immature” waters due to their relatively high Mg; the maximum K-Mg temperature is approximately 110°C ; the Na/K ratios reach temperatures of $210\text{--}250^\circ\text{C}$, depending on the geothermometer equation used (GeothermEx, 2011)

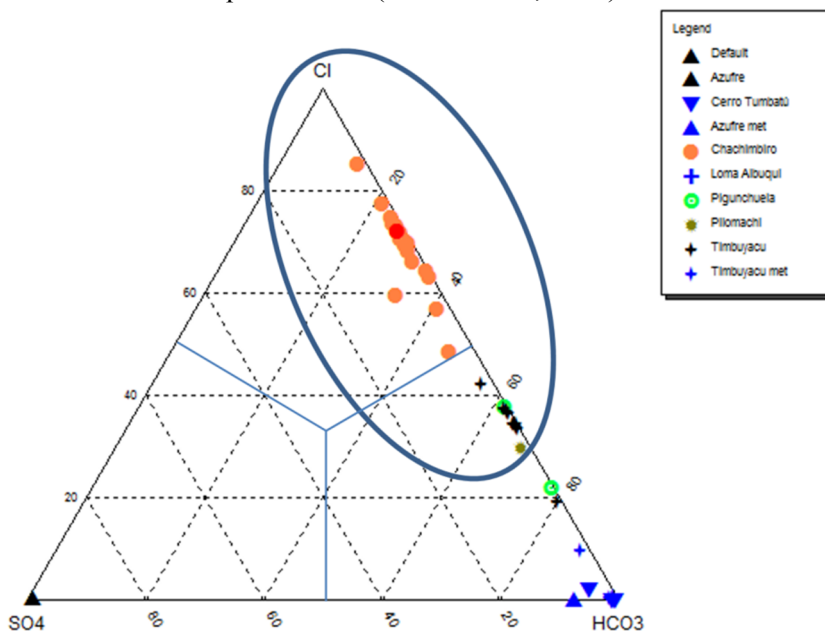


FIGURE 12: Giggenbach diagram $\text{Cl}\text{--}\text{SO}_4\text{--}\text{HCO}_3$; the samples inside the oval represent the waters of the Chachimbiro project and have chemical properties of a geothermal reservoir (Torres and Urquiza, 2013)

The third scenario suggests a cooling geothermal system with temperatures between 110 and 125°C as in the second scenario, supported by the same reasons as for the second scenario (SYR, 2012a), i.e. that the water is of deep metamorphic origin and could be warmed by igneous intrusions, supported by decreasing temperatures in the streams located at higher elevations (Figure 10).

3.2 Chacana – liquid, gas and mixed method geothermometers

The Chacana caldera complex is characterized by young volcanism, as late as in the 17th century, which represents the heat source of this system. Inside the Chacana complex, water samples from the Cachiyaçu, Jamanco and Papallacta thermal springs were collected and analysed (SYR, 2012b). The focus is on the results from Cachiyaçu and Jamanco; Papallacta was not included.

These groups of thermal springs show a clear SW-NE alignment called the Tambo fault (Cachiyaçu-Jamanco-Papallacta), indicating the presence of lineament-controlled permeability (Figure 14) (SYR, 2012b).

The chemical composition of the water samples shows partial equilibrium with high concentrations of $\text{HCO}_3\text{-CO}_2$. To establish whether chemical equilibrium between water, gas and rocks has been reached, the saturation index (SI) was calculated for each sample. The equilibrium temperatures are shown in the SI vs. T diagram and are approximately 180 and 230°C for Jamanco and Cachiyaçu, respectively (Figures 15 and 16) (SYR, 2012b).

Quartz and Na/K geothermometers were utilized and mostly confirmed these deep temperatures. The quartz geothermometer gave temperatures of around 150°C for Jamanco and 170°C for Cachiyaçu. The Na/K geothermometer gave higher

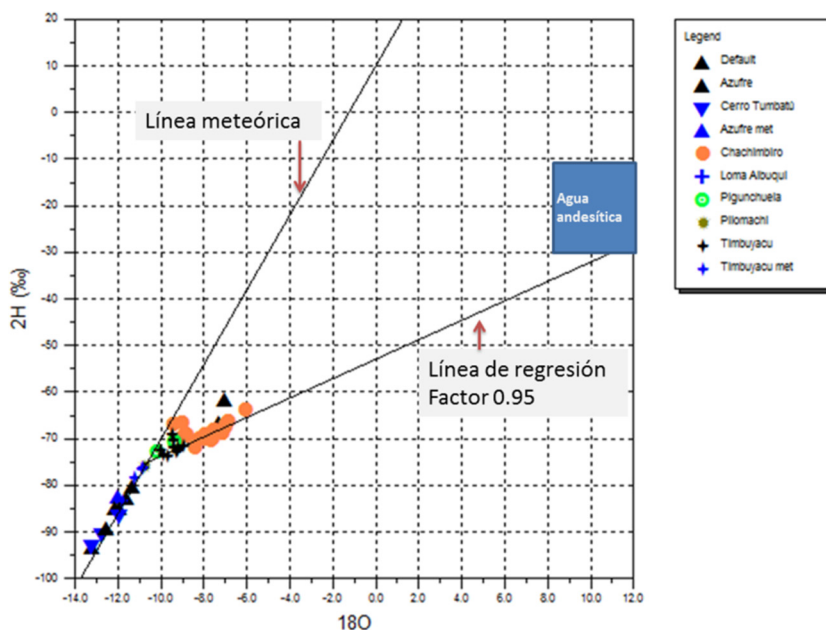


FIGURE 13: δD vs. $\delta^{18}\text{O}$ isotopic analyses suggest meteorological origin of the water (Torres and Urquiza, 2013)

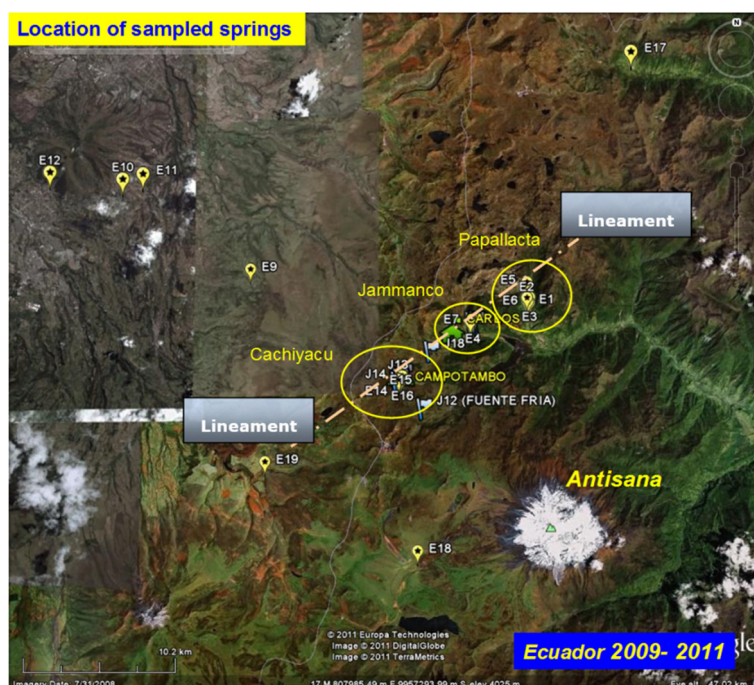


FIGURE 14: Location of the sampled thermal springs; the alignment of the Cachiyaçu, Jamanco and Papallacta hot springs has been highlighted, suggesting the presence of a high-permeability zone (or lineament) (SYR, 2012b)

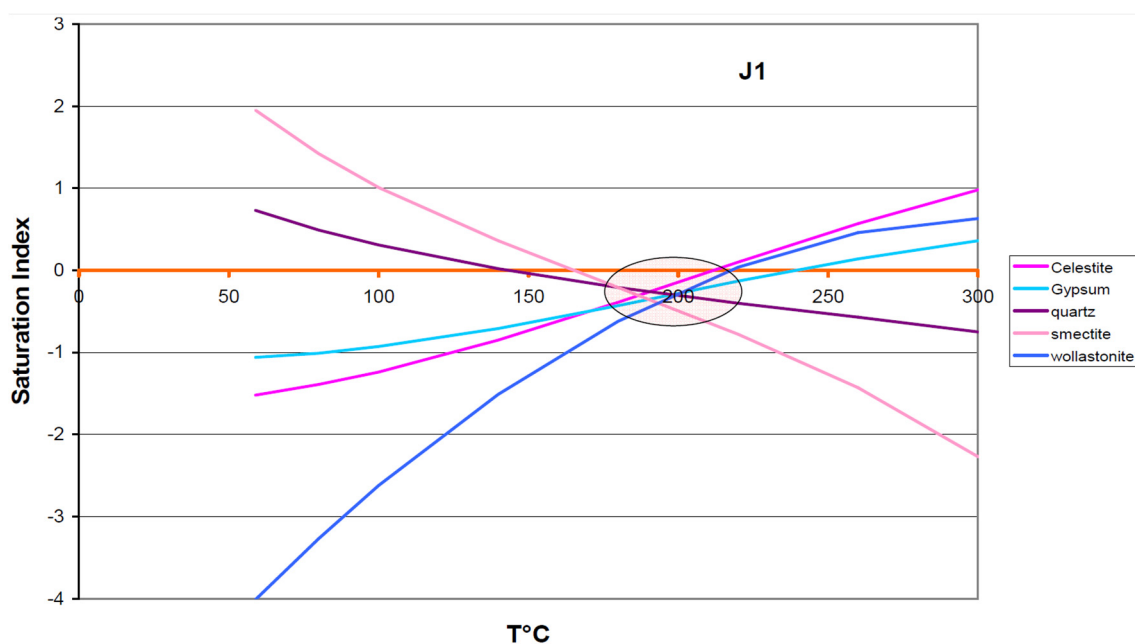


FIGURE 15: Temperature vs. Saturation Index for Jamanco hot spring J1 (SYR, 2012b)

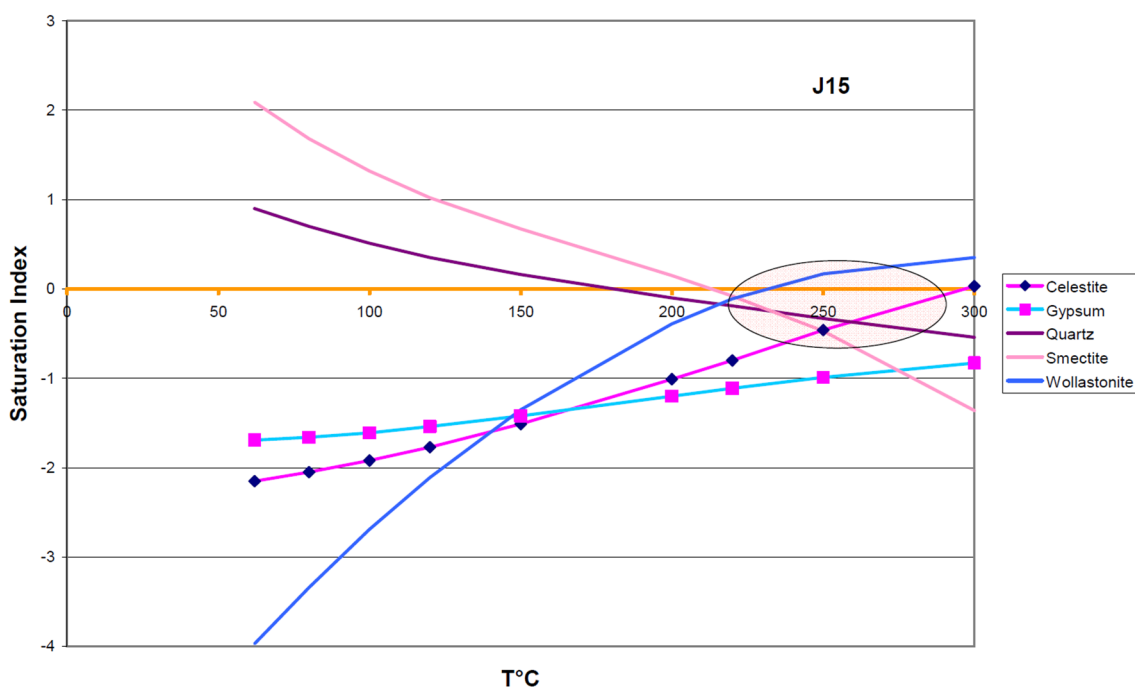


FIGURE 16: Temperature vs. Saturation Index for Cachiyacu hot spring J15 (SYR, 2012b)

temperatures, 180 and 230°C for Jamanco and Cachiyacu, respectively, confirming the estimation made based on the saturation index of minerals (SYR, 2012b).

Samples from Cachiyacu and Jamanco have high concentrations of helium due to bubbling gases with CO₂ content. The isotopic composition of helium, up to 7.6 R/Ra, shows clearly that the heat source is magmatic, and is rich in volatiles. Using gas geothermometers, the estimation of temperatures is approximately 240 and 360°C for Jamanco and Cachiyacu, respectively (SYR, 2012b).

Differences in the salinity from water samples from Cachiyacu and Jamanco confirm a mixing process and/or dilution process between deep saline fluids and shallow fluids of meteorological origin.

From the acquired data, three geochemical fluid models for the Chacana project were defined (SYR, 2012b):

- The first model suggests an intermediate-high-temperature source, 180 and 240°C for Jamanco and Cachiyacu, respectively, supported by the Na/K geothermometer and gas geothermometers.
- The second model suggests a temperature of approximately 130-150°C at Jamanco and 170-200°C at Cachiyacu, based on the quartz geothermometer, anhydrite saturation (at Jamanco) and mixed method geothermometry.
- The third model suggests a geothermal system with immature waters due to recent magmatic intrusions that did not reach water-reservoir rock chemical equilibrium. This is supported by high concentrations of magnesium and calcite.

Geothermal fluids of the Cachiyacu and Jamanco fields show similar chemical and isotopic compositions but have different water-rock interaction processes and mixing processes with shallow fluids, which is explained by the fact that there is not a uniform isotopic composition of deuterium, which would be evidence of one deep reservoir (SYR, 2012b).

4. GEOPHYSICS

The geophysical methods applied for the exploration of Chachimbiro and Chacana projects are as follows: a resistivity survey including MT (magnetotellurics) and TEM (transient electromagnetics); magnetic survey; gravimetric survey and micro seismicity survey (SYR, 2012a and SYR, 2012b).

The parameters controlling the resistivity of rocks are: water content, the salinity of the fluid, temperature and the alteration of the rock. In geothermal research the resistivity methods are the main methods applied to determine the size of high-temperature geothermal reservoirs as the resistivity structure of a geothermal system reflects the geothermal alteration of the rocks. At temperatures of 150-230°C, smectite and zeolites are the dominant alteration minerals. Smectite is a layered clay silicate with high cation exchange capacity and, hence, has low resistivity. At temperatures exceeding 240°C, the smectite is transformed into chlorite, a more resistive mineral and, at temperatures exceeding 250°C, chlorite and epidote are the dominant minerals. The resistivity structure of a high-temperature system with reservoir temperature exceeding 250°C reflects the alteration of the system and is characterized by a low-resistivity cap underlain by a high-resistivity core. This characteristic reflects the temperature in the geothermal system, which caused alteration by the heating of the rocks and reflects the peak temperature experienced by the system, be it at present or in the past. Thus, resistivity measurements reveal the alteration but do not indicate whether cooling has occurred after the alteration was formed because the resistivity profile only captures the alteration in the formation, irrespective of any later cooling of the system. If the reservoir undergoes cooling, the resistivity will prevail and, in that case, the resistivity structure will not reflect the present temperature in the geothermal system (Arnason et al., 2000).

It is well known that geothermal fields, at least in volcanic environments, are commonly overlain by a caprock with low-resistivity smectite clay alteration. The permeability of the formation is significantly reduced by quite low smectite concentrations; in particular, secondary permeability is inhibited in smectite-bearing rocks even when they are fractured (Hickman and Davatzes, 2010; Lutz et al., 2010). Smectite-bearing rocks, therefore, act as a cap dividing the geothermal field hydrology into a shallower field's cooler meteoric zone and a deeper higher temperature zone. This deeper zone, or "geothermal reservoir", will be more resistive than the smectite cap as the temperature-dependent smectite is

converted to the more resistive chlorite and illite clays (Ussher et al., 2000; Flóvenz et al., 2005) which are altered at higher temperatures.

By the inversion of magnetotelluric (MT) data, the clay caprock can be defined; its extension and its shape as the high-resistivity core defines the reservoir. This method is used to determine the size of the reservoir. MT soundings may endure a static shift due to irregularities at the surface, as is often the case in high-temperature areas where low resistivity reaches the surface. Prior to the inversion, this shift in the soundings is corrected for by the use of TDEM soundings at the same location as the MT sounding.

A magnetic survey (Lopez, 2012a and b) was carried out inside the Chacana caldera to get information on hydrothermal alteration. A gravimetric survey (Lopez, 2012a and b) was also carried out to confirm the main faults and geological structures that dominate the flow of geothermal fluids. Finally, a microseismic survey (Ruiz, 2012a and b) was carried out to find the relationship of permeability with the main active faults.

In high-temperature geothermal systems, usually the caprock overlies the geothermal system and the base of the caprock may exhibit the temperature where smectite alters to more resistive minerals, around 230°C. By joint comparison of geology, geochemistry and other scientific information, the natural state of a geothermal reservoir and its flow pattern will be inferred (Cumming, 2009).

It is necessary to know whether the reservoir of a geothermal system is defined by a resistive anomaly of depth such as a dome, a positive gravimetric anomaly, or a negative magnetic anomaly (Torres and Urquiza, 2013).

With recent developments in MT inversion code and computer capacity, 3D MT inversion now generally has sufficient resolution to resolve most of the static shift related to topography and lateral resistivity variations, so TDEM serves mainly as a check on quality and data consistency (Cumming and Mackie, 2010). There is, however, a dispute on this and the 3D codes may or may not correct for static shift. Using TDEM at every MT station to correct for the static shift is, therefore, recommended for use (Árnason, personal information).

4.1 Chachimbiro

Interpretation of MT, TDEM, gravimetric and magnetometric data was used to define the boundaries of the geothermal reservoir, to identify the possible production zone, geothermal aquifer and caprock (Torres and Urquiza, 2013).

4.1.1 MT/TDEM Survey

MT soundings were made at 70 locations and a 3D resistivity model was generated by inversion of the MT data. A grid of 150 m × 150 m × 15-100 m for the final inversion model, including topographical information, (x, y and z, the depth) was used.

A TDEM survey was made at 36 stations to mitigate static shift of the MT stations as a static shift was observed in resistivity curves at high frequencies. The joint inversion of MT and TDEM data was used to find and correct for the static shift. After the corrections, the data was verified as being of good quality. Consequently, the data was processed and the results are shown in the cross-sections, whose locations are shown in Figure 17, while Figures 18 to 21 show the cross-sections.

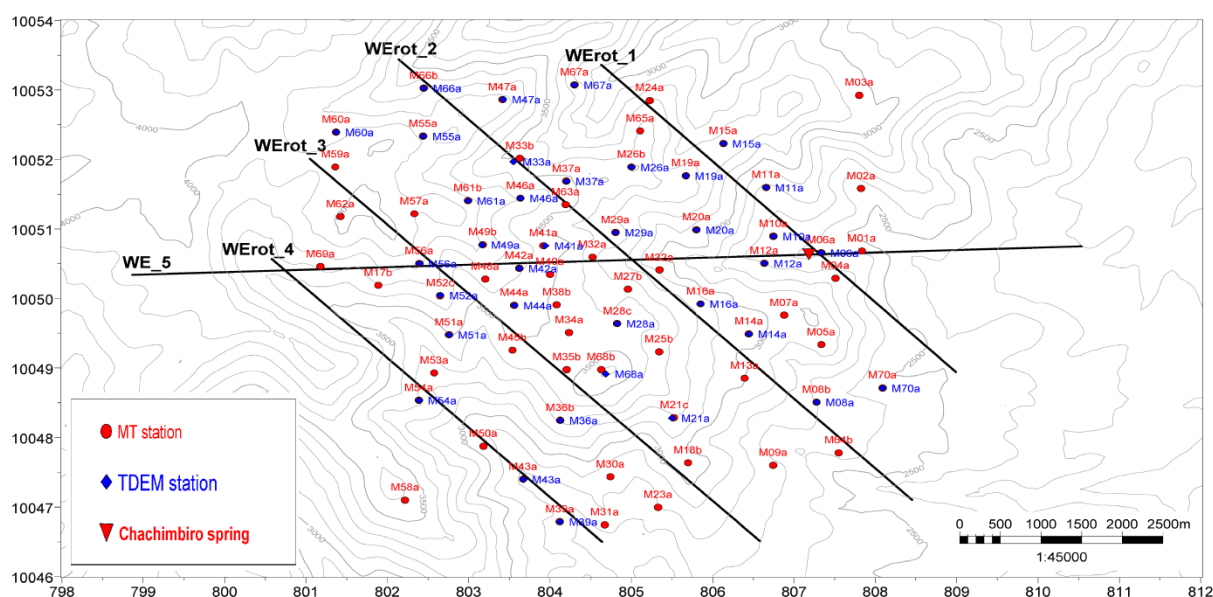


FIGURE 17: Chachimbiro project: Location of MT stations (red dots), and MT-TDEM stations (blue dots) (modified from WesternGeco, 2012)

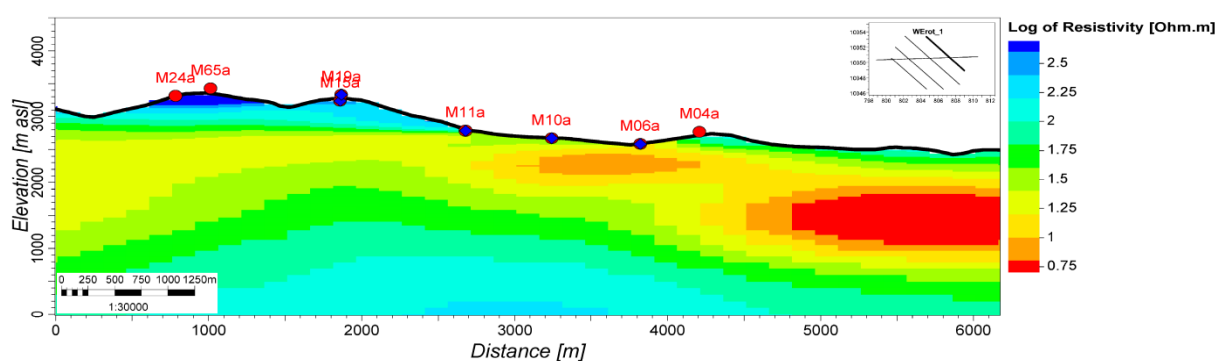


FIGURE 18: Chachimbiro, section WE_rot1, NW-SE resistivity cross-section (modified from WesternGeco, 2012)

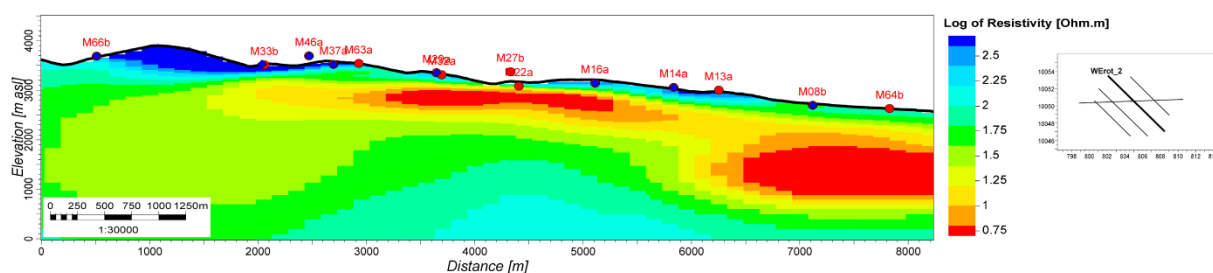


FIGURE 19: Chachimbiro, section WE_rot2, NW-SE resistivity cross-section (modified from WesternGeco, 2012)

The results from the MT inversion displayed on the resistivity cross-sections show a characteristic high-temperature system with a low-resistivity cap underlain by a high-resistivity core. This is clearly seen in Figure 22 where the isotherms have been sketched based on the resistivity images and geochemical data, following the conceptual guidelines detailed by Cumming (2009) (SYR, 2012a).

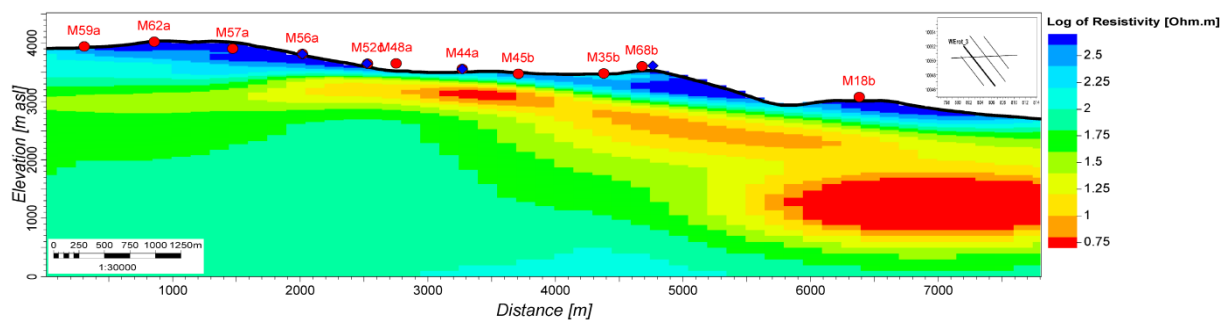


FIGURE 20: Chachimbiro, section WE_rot3, NW-SE resistivity cross-section (modified from WesternGeco, 2012)

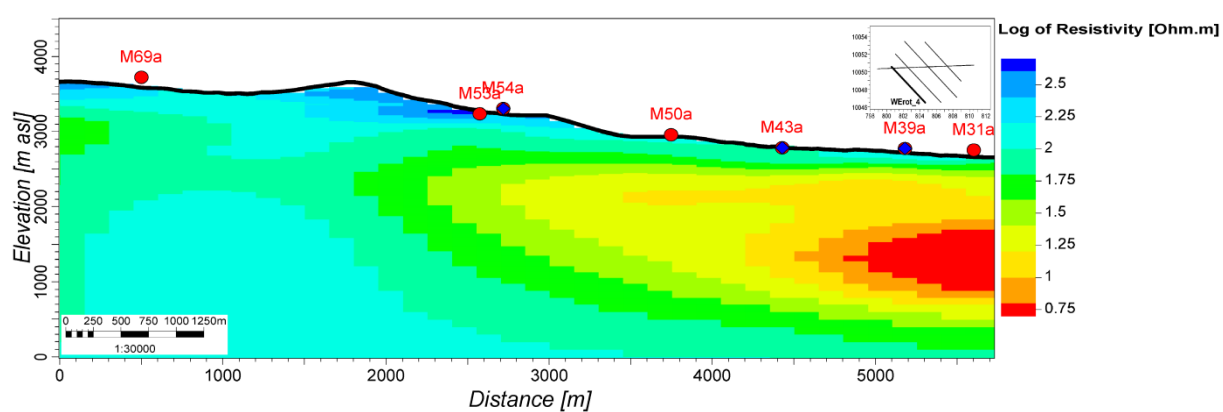


FIGURE 21: Chachimbiro, section WE_rot4, NW-SE resistivity cross-section (modified from WesternGeco, 2012)

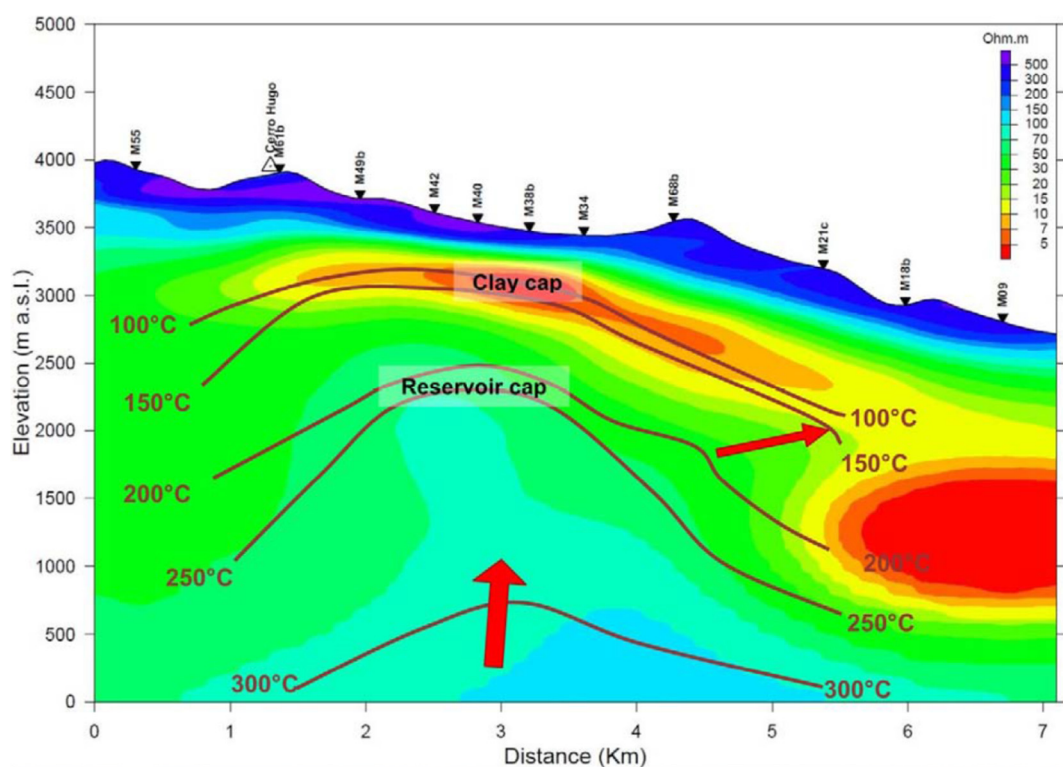


FIGURE 22: Section WE_rot2Profile, NW-SE resistivity cross-section (WesternGeco, 2012)

4.1.2 Other geophysical methods

In Chachimbiro project area, a gravity survey was carried out, with 700 points with 500 m spacing in the project area and surroundings. Most points were taken in areas accessible by roads, but a few were measured in areas where accessibility was limited. The results show that Chachimbiro has a big contrast in density values between ash and tuff, with values of 1.2-2.2 g/cm³, and lava flows at the surface with values of 2.3-2.8 g/cm³. The tuff density values increase, on the other hand, as do lavas when the reservoir temperature is above 200°C (SYR, 2012a).

A magnetic survey was performed on 14 geo-referenced profiles in a NW-SE direction and 2-4 km in length. The main target of this study was to detect hydrothermal alteration associated with the destruction of magnetite by sulphate water commonly found at the surface in high-temperature geothermal fields. The results are generally consistent with the pattern of deeper alteration detected by the MT (SYR, 2012a).

In the Chachimbiro project area, a set of 6 seismic stations were installed to gather information and interpret the seismic behaviour of the field. During the seismic study, 862 seismic events were registered; 40 of them were located in the project area. These seismic events were below magnitude 3 on the Richter scale. In addition, most of the low-frequency events were detected around the seismic stations.

4.2 Chacana

4.2.1 MT survey

In the Chacana geothermal project, the geological settings of the area are complex, chaotic, and therefore probably have a corresponding complex resistivity structure. Inversion of MT data is commonly used to obtain resistivity values below 500 m of depth (SYR, 2012b). The MT soundings included 100 points on a regular grid at 1000 m spacing, covering the entire Chacana project area. In addition, 30 additional stations with 700 m spacing were added to the survey for most promising areas based on initial results (for location see Figure 23). According to acquisition and quality assurance, the

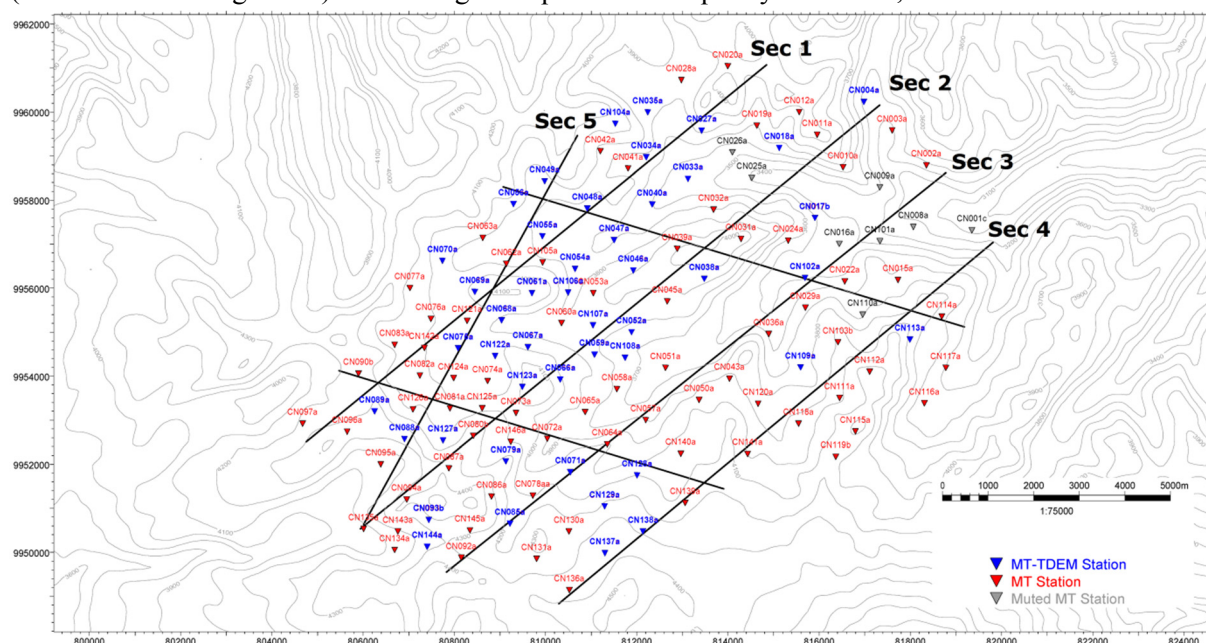


FIGURE 23: Chacana project, location of MT stations (red triangles) and MT-TDEM stations (blue triangles) (modified from WesternGeco, 2012)

signals close to 1 Hz define the base of the caprock. Also, the absence of noise sources for MT sites helps in obtaining good quality data. In addition, 50 TDEM soundings were carried out at MT sites that experienced the greatest static shift (Figure 23). Given the limited number of TDEM soundings, and their wide spacing, a map of the shallow resistivity structure is not considered meaningful.

The interpretation of the Chacana resistivity structure is based on the 3D resistivity inversion described by WesternGeco (2012) (SYR, 2012b). 1D inversion models were used to compare the 3D inversion performance, and were consequently corrected by TDEM soundings at 50 sites which showed static shift. The areas of interest are the low-resistivity anomalies. Conductive low resistivity anomalies were found in the Jamanco, Cachiycu, Chimbaucru and Plaza de Armas locations (Figure 24).

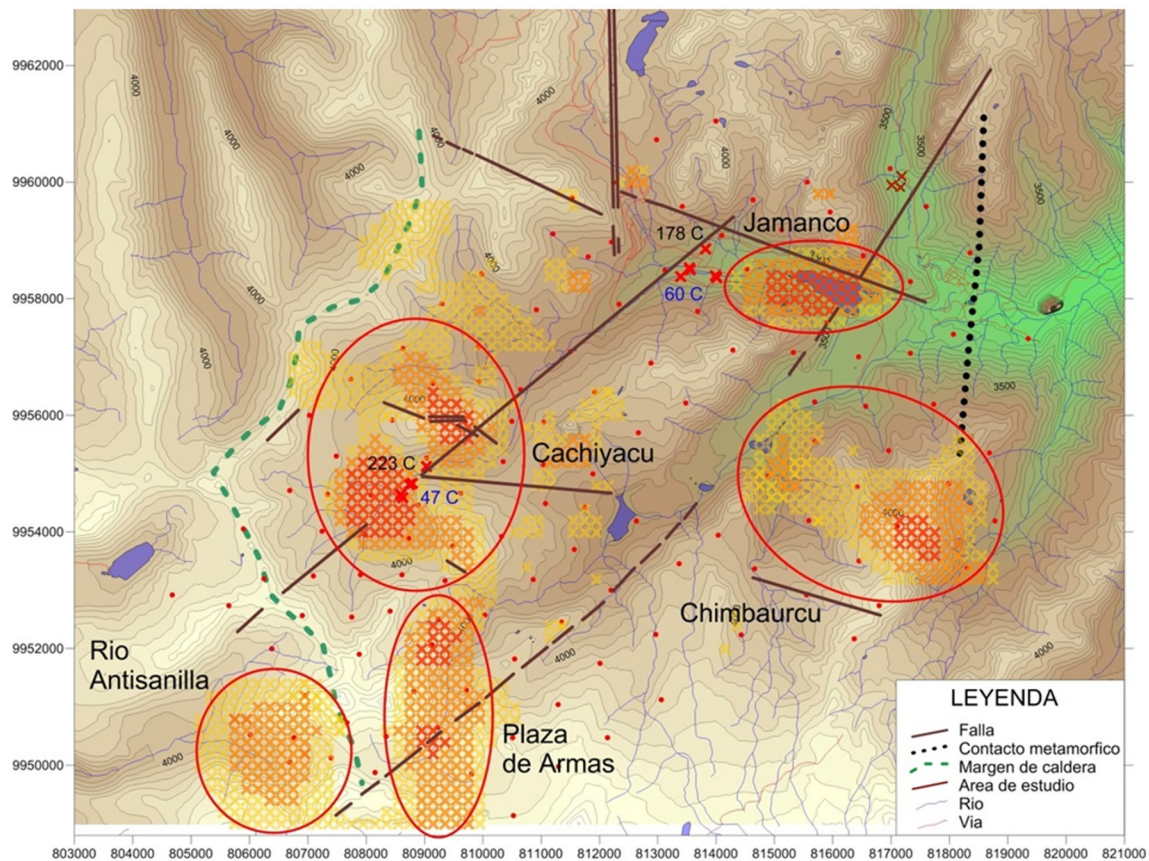


FIGURE 24: Low-resistivity anomalies in Chacana, also showing temperatures of hot springs with average temperature (blue nos.); and Na/K (Giggenbach, 1988) geothermometer temperatures (black nos.); high-resistivity areas are superimposed in red on topography (modified from SYR, 2012b)

After analysing the cross-sections in Figures 25-28, the results of the resistivity measurements can be summarized in the presence of three resistive layers. The first layer corresponds to resistivity values between 3 and 50 ohmm and can be associated with the caprock of the geothermal system. The second layer has resistivity values between 50 and 300 ohmm, and is believed to relate to geothermally altered rocks (high-resistivity core) with the possible existence of a geothermal reservoir. The last layer has resistivity values above 300 ohmm and could be related to the metamorphic basement according to the geological settings of the Chacana geothermal project.

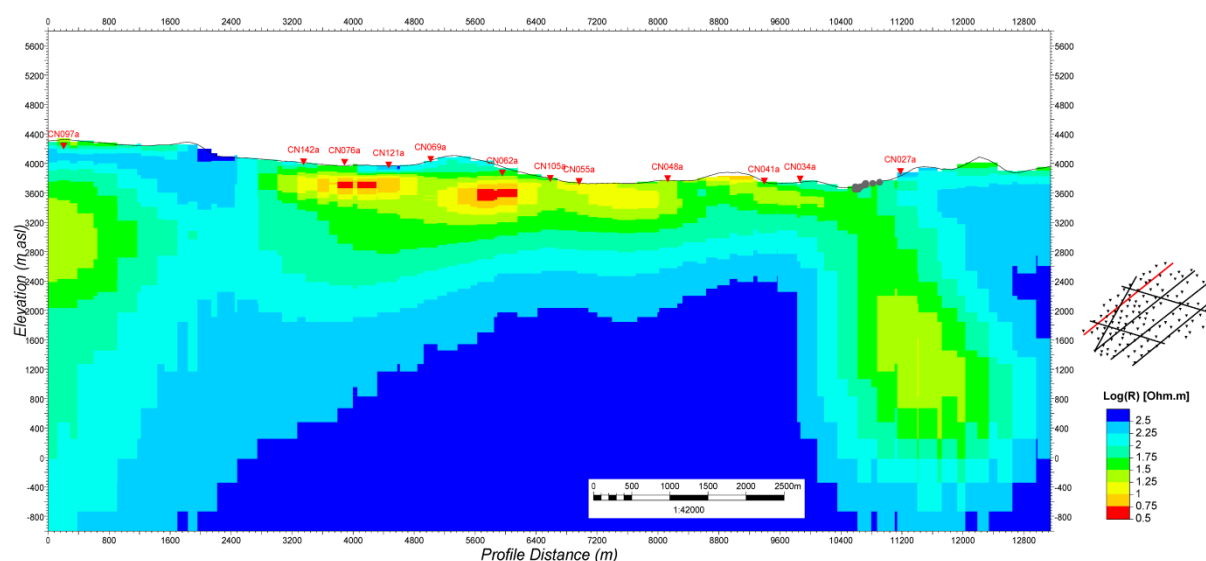


FIGURE 25: Chacana; Section 1, SW-NE resistivity cross-section with two conductive anomalies between 3.2 and 6.4 km, located in Cachiyacu zone (modified from WesternGeco, 2012)

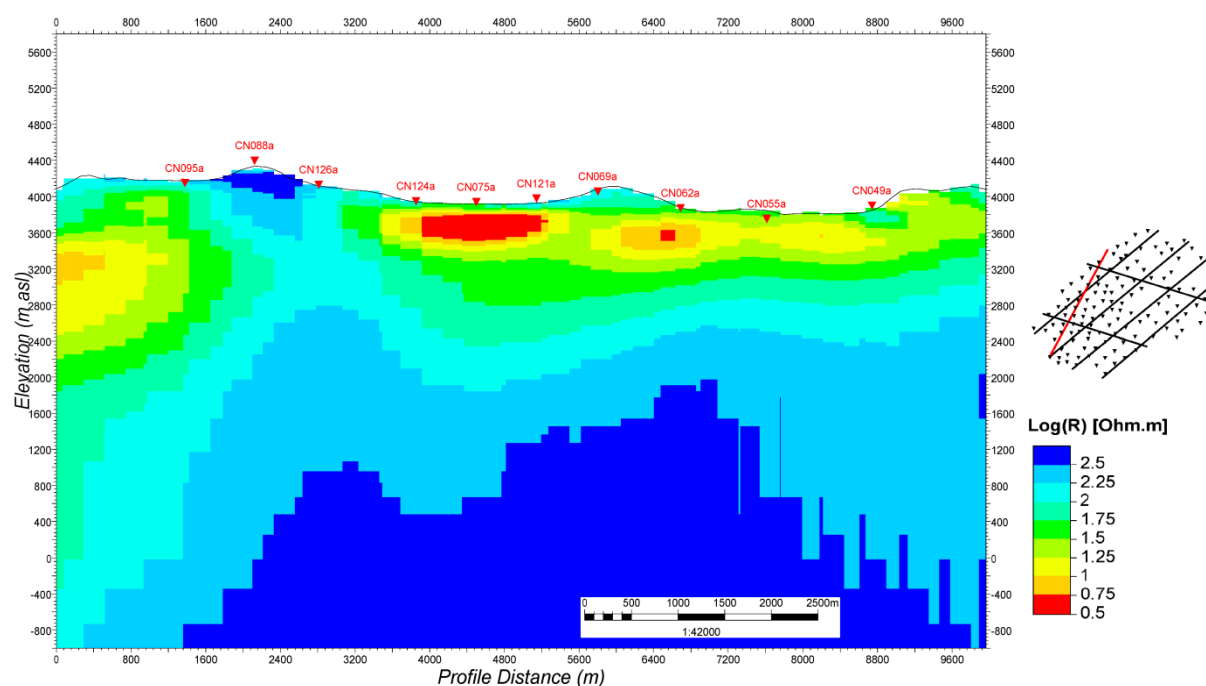


FIGURE 26: Chacana; Section 5 SW-NE cross-section with Cachiyacu conductive anomaly between 4 and 6 km (modified from WesternGeco, 2012)

Some of the low-resistivity anomalies coincide with geothermal manifestations on the surface in all sections, evidence of the ascent of geothermal fluids with its interaction with the rocks (clay alteration) through faults. The conductive anomaly in Section 2 (Figure 27) coincides with Jamanco hot spring. Another conductive anomaly can be seen in Figure 28, and its location coincides with the south of Plaza de Armas, where a convex structure like a dome of low resistivity appears. This anomaly is intersected by the main fault in a SW-NE direction that cuts the caldera rim.

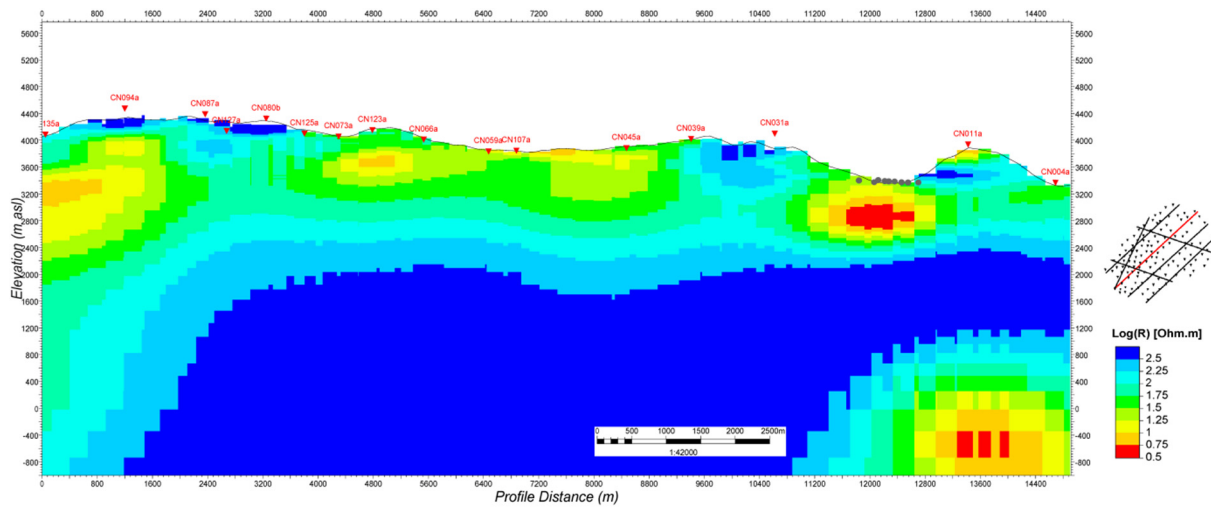


FIGURE 27: Chacana; Section 2 SW-NE cross-section with conductive anomaly in Jamanco zone at 12 km (modified from WesternGeco, 2012)

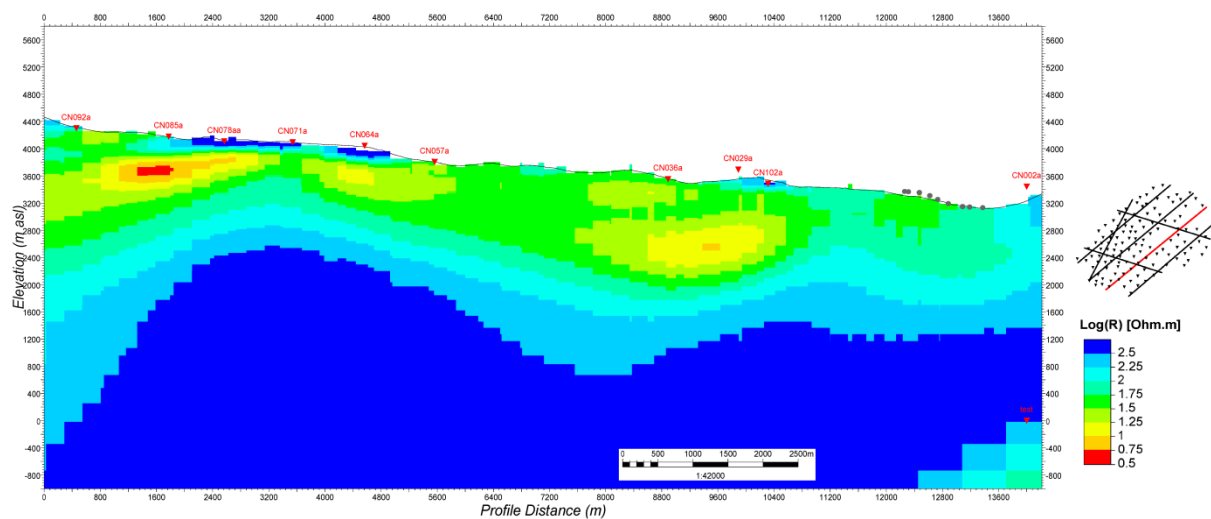


FIGURE 28: Chacana; Section 3 SW-NE cross-section showing a conductive anomaly between 1.5 and 3 km in Plaza de Armas zone (from WesternGeco, 2012)

As is shown in the cross-sections in Figures 27-30, the conductive anomalies present different shapes and a non-uniform pattern. Depending on the zone, the caprock will be absent. The thickness, depth and resistivity of the layer at the springs are encouraging and, if there is geothermal up-flow, it is likely to be at this location, probably associated with the fault system. At depths below 1000 m, the metamorphic basement may be delineated, with high-resistivity values to the east of the inferred contact and lower resistivity within the caldera to the east. Below 1000 m of depth, the resistivity values change from 30 to 50 ohmm. Such low contrast in resistivity values, suggests that the depth of the caldera floor in this region is between 1000 and 1500 m (SYR, 2012b). Low-resistivity values (< 50 ohmm) are found inside the caldera down to 750 m depth, and even further down 1500 m depth on the southeast border of the caldera. This may suggest alteration from a fossil geothermal system (SYR, 2012b).

To determine if the Chacana area is a high-temperature system cannot be inferred by the resistivity structure alone. The resistivity characteristic could be that of a high-temperature system, or the remnant of one. The low-resistivity cap is not continuous. However, the resistivity characteristic could be that of a high-temperature system that has, at some point, reached or exceeded temperatures of 250°C.

Geothermometers do not indicate such a high temperature at present, so we can assume that the geothermal system has cooled down but with the resistivity characteristic still prevailing.

If the temperature in the system has never exceeded 230°C the resistivity character could be interpreted in a different way. In that case, the low-resistivity anomaly would be indicative of a geothermal reservoir caused by the hot geothermal fluid in the rock matrix.

4.2.2 Other geophysical methods

Other geophysical methods were applied in the Chacana project as explained at the beginning of this section, but that data is not necessary for the goals of this report. The main method used was MT measurements. Below, a brief description is though given of the rest of the geophysical methods which were used in the Chacana project (SYR, 2012b).

A gravity survey with a total of 700 gravity points was done in the Chacana field and north of it. The survey was focused on a finding of long scale structures as contrasts between ash and tuff formations. The density values of the ash and tuff formations would be between 1.8 and 2.2 g/cm³, and lava flows at the surface have a density value of between 2.3-2.8 g/cm³, as was described for Chachimbiro. When ash and tuff formations are heated to over 200°C, buried and located at the subsurface, their density values are closer to the lava flow density values. In these cases, it is preferable to make a more careful mapping of the surface geology. It is also necessary to consider the density values of the rocks in the Chacana area which has such a rugged and scarped topography. The gravity anomalies are related to topographic elevation, and by working with different density values, it was possible to define the boundaries and structures in the Chacana caldera. Inside the Chacana caldera, the density values are below and up to 2.0 g/cm³; these would include the anomalies close to Cachiyacu hot springs. This material corresponds to a tuff formation with sedimentary layers. In the southwest part of the caldera, filling material was identified.

A magnetic survey was also made, with the objective of detecting hydrothermal alteration associated with the destruction of magnetite by sulphate water commonly found in high-temperature geothermal fields. The magnetic field pattern shows a good correlation with the gravity survey results in the studies made by SYR (2012b), especially in the Cachiyacu area.

Finally, a total of 10 portable seismometers were located inside and outside the Chacana caldera. The epicentres of seismic events were correlated with the NE-SW direction of the faults through the Chacana caldera, and the NW-SE lineaments to the north and west of the caldera. Most of these seismic events are tectonic or volcano-tectonic, caused by fractures in the rocks. Long period events, associated with a flow of fluids, are located on the flanks of Antisana volcano; these suggest the existence of an active hydrothermal system.

As a result of this study, it could be assumed that the basement has active fractures associated with permeability, but this permeability would be limited in the absence of seismic events north of the caldera.

5. VOLUMETRIC ASSESSMENT

To calculate the potential or power capacity of a geothermal field, one of the methods most applied is the volumetric method. The volumetric method is considered one of the main static modelling methods, and is used in the first stage of development when the data is limited (Muffler and Cataldi, 1978). The volumetric method is often applied with the Monte Carlo method (Sarmiento and Steingrímsson, 2007). Due to non-uniform factors such as changes in permeability, and changes in recharge and transmissivity, the production capacities of reservoirs with the same heat content can be different. Furthermore, the dynamic response of a reservoir to production is also not considered in the volumetric method. However,

the volumetric method has a basis that allows for comparison between different geothermal systems (Axelsson et al., 2013).

The volumetric method is based on estimating the total thermal energy stored in a volume of rock. The fraction of the thermal energy recovered from this volume of rock compared to the total thermal energy is defined as the recovery factor and is difficult to estimate. The recovery factor depends on the nature of the system and, if reinjection is applied, the permeability, porosity, recharge etc. (Axelsson et al., 2013).

The new results presented in this study are volumetric assessments of Chachimbiro geothermal field, and Cachiyaçu and Jamanco areas from Chacana geothermal field. Due to a lack of boreholes and exploratory drillings, some values of the different parameters for volumetric assessment were assumed, making approximations and comparisons with other geothermal fields. The accuracy of this must be confirmed through drilling in the future.

Based on the resistivity studies, the Chachimbiro field is treated as a high-temperature field and the assessment assumes a flash power plant utilization when calculating the power production capacity. The Cachiyaçu and Jamanco areas are treated as low- or intermediate-temperature fields and the assessment assumes a binary power plant utilization when calculating the power production capacities of the areas. To determine if the Chacana area is a high-temperature system cannot be inferred by the resistivity structure alone. The resistivity characteristics could be that of a high-temperature system, but it may also show remnant alteration.

Surface area

The size of a geothermal resource defines the economic aspects for its exploration and development. If the geothermal resource is large, the economic profit can be expected to be large as well. The geoscientific data for the Chachimbiro project area is estimated between two geological structures, the Azufral fault in SE-NW direction and the border of the caldera. Inside this area, the Hugá dome is located as a possible boundary limiting the promising area; the Cachiyaçu fault intersects the Azufral fault. Then, with regard to the geological information, the boundaries of the possible reservoir are between two NE-SW trending faults, intersected by the borders of the caldera (Torres and Urquiza, 2013). Thus, according to the geology, the surface area for Chachimbiro is of the size 3-12 km² (Figure 29). According to the MT 3D model, the horizontal area that delineates the high-

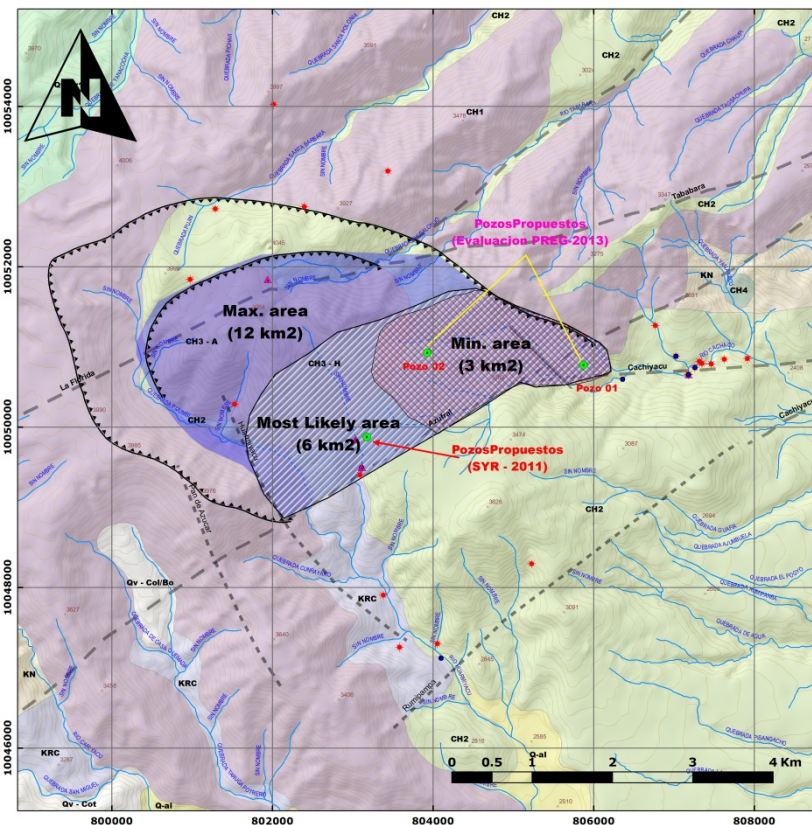


FIGURE 29: Map of the probable size of geothermal areas in Chachimbiro project (modified from Torres and Urquiza, 2013)

temperature system, i.e. the area delineated by contact between the low-resistivity cap and the high-resistivity core (250°C), is approximately 16 km². The surface area for Chachimbiro used in the volumetric assessment is 3-12 km² and a most likely value of 6 km² is assumed (Table 1). In the calculations here we will use the cautious approach of 12 km² as the maximum.

For Chacana, the surface area of the reservoir is defined by a probabilistic assessment related to geological and geophysical information. Due to the considerable uncertainty associated with this, an appropriate range was defined according to the resource potential. It must be emphasized that the Chacana project has five areas of interest defined by resistive anomalies, but in two of them thermal manifestations are at the surface, i.e. Cachiyacu and Jamanco, and the analysis involved these two areas. Thus, the resulting resource areas for the alternative boundaries for Cachiyacu are between 0.56 and 5.5 km², and most likely an area of 1.75 km² (Figure 30 and Table 2). For Jamanco the surface area is estimated between 0.25 and 1.72 km², with a most likely area of 0.65 km² (Figure 30 and Table 3) (SYR 2012b). According to the MT results, the low-resistivity anomaly under Cachiyacu has a horizontal extension of 6 km². The low resistivity anomaly under Jamanco has a corresponding size of 2 km². This was found by comparing the resistivity cross-sections published here to resistivity maps in the report from SYR (2012b). Under Jamanco, a deep seated low-resistivity anomaly may be an indication of the heat source.

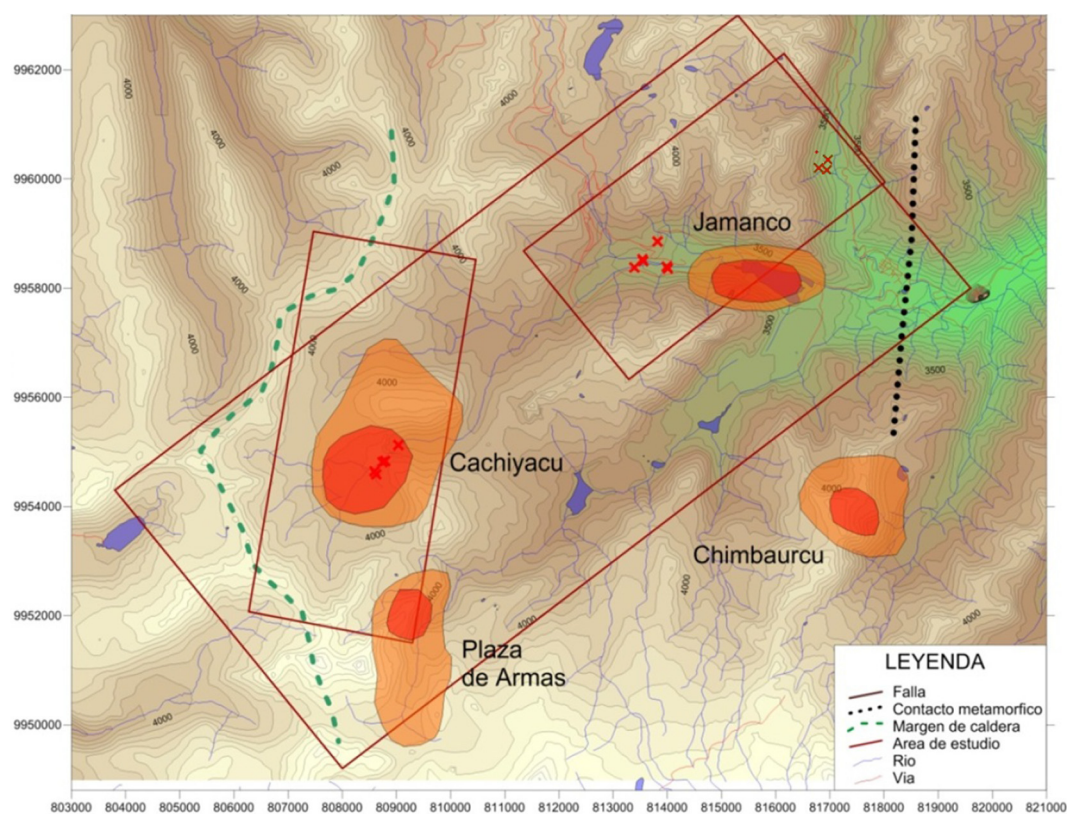


FIGURE 30: Map of resource boundaries for the Chacana project resistivity anomalies; boundaries are also shown for Plaza de Armas and Chimbaucru anomalies (SYR, 2012b)

Thickness

For Chachimbiro project area, the base of the reservoir is defined as between 2000 and 2100 m depth, and the top is approximately at 500 m depth, derived from the MT models. Therefore, the most likely value for the thickness is assumed as being 1500 m in the volumetric assessment. A minimum and a maximum values are set to 1000 and 2000 m, respectively, due to uncertainties of the depth of the reservoir. The reservoir depth cannot be derived directly from MT models in the case of high-temperature systems. For Chacana, the same thickness is used as in the Chachimbiro model with

Chacana considered to be a high-temperature system that is cooling down, i.e. 1500 m. On the other hand, if Chacana is considered to consist of separate low-temperature fields, the thickness of the reservoir would be the thickness of the low-resistivity anomaly at each area. For the two areas in question, Cachiyacu and Jamanco, the thickness would be the same, 500 m. Because of this uncertainty, the thickness in the volumetric assessment is assumed to be in the range of 500-1500 m with a most likely value of 1000 m.

Rock density

The reservoir rock for Chachimbiro project corresponds to andesitic composition rocks from the Natividad geological unit of Tertiary volcanism and, therefore, is assumed to have a rock density of 2700 kg/m^3 , based on an average from comparison with similar geothermal fields.

In the Chacana project, the reservoir rock is composed of lavas and breccias interbedded by andesitic and basaltic compositions from the Pisayambo geological formation from Upper Miocene-Pliocene. The density of this kind of rock is assumed to be 2700 kg/m^3 .

Porosity

The porosity is the ratio between the volume of the pores and the total volume of the rock matrix, including the pores. These rock properties change depending on the system. For the Chachimbiro project, the porosity is assumed to have an average value of 10%. For the Chacana project, the porosity is assumed to be in the range of 5-15%, given that the Chacana field is dominated by fractures and its volcanism is younger than in the Chachimbiro project.

Rock specific heat

The andesitic rocks in the Chachimbiro project have an average rock specific heat of $990 \text{ J/kg}^\circ\text{C}$. For the Chacana project, the possible value assumed is $900 \text{ J/kg}^\circ\text{C}$; these will be confirmed or modified after drilling begins.

Temperature

The temperature of a reservoir can be estimated using isotopes and liquid and gas geothermometers. Geothermometers are based on temperature-dependent, water-rock reactions which control the chemical and isotopic composition of thermal water. These methods are applicable only to hot-water systems with the common chemical constituents of thermal water (SiO_2 , Na, K, Ca, Mg, Cl, HCO_3 , and CO_3) (Brooke et al., 1978).

For the Chachimbiro project the maximum temperature selected is 320°C , based on the results from the geothermometers. Geophysics, through MT cross-sections, clearly shows the presence of a resistivity anomaly, like a dome, supporting the suggestion that a conductive core below the caprock is a reservoir with similar properties to other high-temperature geothermal systems. Therefore, the minimum and most likely temperatures selected are 200 and 240°C , respectively.

In the Chacana project, in addition to geothermometers, the mixed method was applied. Remember that the two areas of interest, Cachiyacu and Jamanco fields, have different temperature manifestations at the surface. Using geochemical information for each area, the maximum temperature for Jamanco is 180°C , and the minimum temperature ranges between 140 and 170°C . Finally, for the Cachiyacu area, the maximum temperature is approximately 240°C , and the minimum temperature ranges between 170 and 180°C . These ranges of values are supported by the MT cross-sections and suggest a cooling down geothermal system of intermediate-low temperature, where the resistivity anomalies would be considered as the reservoirs.

Fluid density and specific heat

The fluid density and specific heat were calculated from steam tables, based on temperature and considering a constant liquid pressure.

Recovery factor

To estimate the potential of a geothermal system involves defining a recovery factor that is a fraction of the heat content inside the reservoir which could be extracted to the surface (Brooke et al., 1978; Cumming, W., 2009). Due to the different behaviour of geothermal systems, usually this is estimated to be between 10% and 25%, according to studies presented by Brooke et al. (1978), and Sarmiento and Steingrímsson (2007). This range of values is assumed for Chachimbiro and Chacana projects in all the areas.

Conversion efficiency and rejection temperature

The heat of a reservoir cannot be transformed to electricity with 100% efficiency, because thermal energy needs to be converted into mechanical energy, and must use part of the generated work to generate electrical energy (Brooke et al., 1978). Old studies show that temperatures over 150-200°C have a conversion efficiency of 10-20% (Grant et al., 1982).

The conversion efficiency is dependent both on the reservoir and the rejection temperature. In the volumetric assessment, the Chachimbiro geothermal field is treated as a high-temperature field. Therefore, a flash power plant utilization scheme is considered with a final/rejection temperature of 40°C. The conversion efficiency was chosen in the range of 8-12% accordingly.

The Chacana geothermal field is treated as a low- or intermediate-temperature field. Therefore, a binary power plant utilization scheme is considered, with a final/rejection temperature of 80°C and the conversion efficiency is in the range of 13-16% and 10-14% for Cachiyacu and Jamanco areas, respectively. The conversion efficiency is lower for the case of Jamanco since the reservoir temperatures are assumed to be lower.

Plant life

The minimum lifetime estimated is 25 years, necessary to recover the investment, considering an internal rate of return (IRR). For Chachimbiro and Chacana project, 25 years are used.

The volumetric assessment was carried out using the Monte Carlo method. The input data for the calculations is presented in Tables 1-3 for the three cases: Chachimbiro geothermal field, and Cachiyacu and Jamanco areas from Chacana geothermal field. Results for the Chachimbiro geothermal field are presented as a discrete probability distribution in Figure 31, and as a cumulative probability distribution in Figure 32. The main results for all three cases are presented in Table 4 below.

TABLE 1: Input parameters for the volumetric estimate of Chachimbiro

Input variables	Units	Minimum	Most likely	Maximum	Distribution
Surface area	[km ²]	3	6	12	Triangle
Thickness	[m]	1000	1500	2000	Triangle
Rock density	[kg/m ³]		2700		Fixed
Porosity	[%]		10.0		Fixed
Rock specific heat	[J/kg°C]		990		Fixed
Temperature	[°C]	200	240	320	Triangle
Fluid density	[kg/m ³]	667	813	865	Triangle
Fluid specific heat	[J/kg°C]		4770		Fixed
Recovery factor	[%]	10.0	15.0	25.0	Triangle
Conversion efficiency	[%]	8.0	10.0	12.0	Triangle
Plant life	[years]		25		Fixed
Rejection temperature	[°C]		40		Fixed

According to the statistics of the probability distribution in Figure 31, it is seen that the volumetric model predicts with 90% confidence that the electrical power production capacity of the Chachimbiro field lies between 75–185 MWe for 25 years. From the statistics of the cumulative probability in Figure 32, it can be seen that the volumetric model predicts with 90% probability that at least 74 MWe can be produced from the field for the same production period.

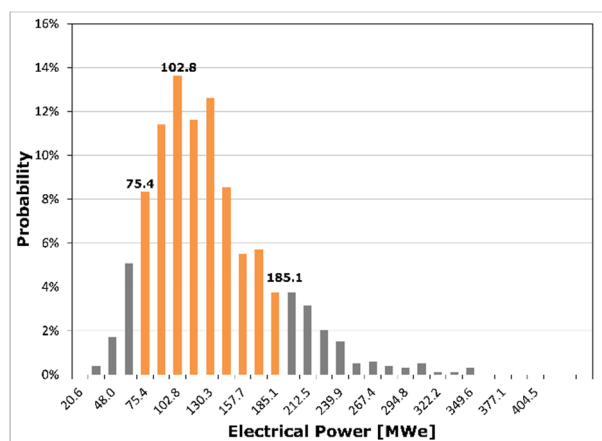


FIGURE 31: Monte Carlo volumetric discrete probability distribution for electrical power distribution in Chachimbiro

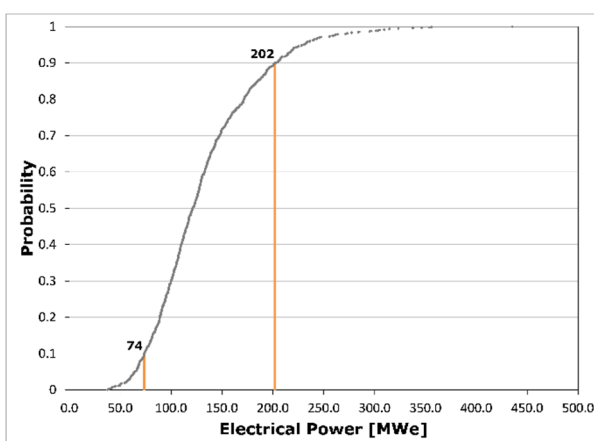


FIGURE 32: Monte Carlo volumetric cumulative probability distribution for electrical power production in Chachimbiro

TABLE 2: Input parameters for the volumetric estimate of Cachiyacu

Input variables	Units	Minimum	Most likely	Maximum	Distribution
Surface area	[km ²]	0.56	1.75	5.5	Triangle
Thickness	[m]	500	1000	1500	Triangle
Rock density	[kg/m ³]		2700		Fixed
Porosity	[%]	5.0	10.0	15.0	Fixed
Rock specific heat	[J/kg°C]		900		Fixed
Temperature	[°C]	170	190	240	Triangle
Fluid density	[kg/m ³]	813	876	898	Triangle
Fluid specific heat	[J/kg°C]		4450		Fixed
Recovery factor	[%]	10.0	15.0	25.0	Triangle
Conversion efficiency	[%]	13.0	15.0	16.0	Triangle
Plant life	[years]		25		Fixed
Rejection temperature	[°C]		80		Fixed

TABLE 3: Input parameters for the volumetric estimate of Jamanco

Input variables	Units	Minimum	Most likely	Maximum	Distribution
Surface area	[km ²]	0.25	0.65	1.72	Triangle
Thickness	[m]	500	1000	1500	Triangle
Rock density	[kg/m ³]		2700		Fixed
Porosity	[%]	5.0	15.0	15.0	Fixed
Rock specific heat	[J/kg°C]		900		Fixed
Temperature	[°C]	140	170	180	Triangle
Fluid density	[kg/m ³]	886	898	926	Triangle
Fluid specific heat	[J/kg°C]		4400		Fixed
Recovery factor	[%]	10.0	15.0	25.0	Triangle
Conversion efficiency	[%]	10.0	13.0	14.0	Triangle
Plant life	[years]		25		Fixed
Rejection Temperature	[°C]		80		Fixed

For the Cachiyacu and Jamanco areas from Chacana geothermal field, the results of the volumetric model are presented in Table 4. The model predicts with 90% confidence that the electrical power production capacity of the two areas lies between 10-40 MWe and 1-5 MWe for 25 years, respectively. The model predicts with 90% probability that at least 11 MWe can be produced from the Cachiyacu field and at least 1 MWe can be produced from the Jamanco area for 25 years. This is shown in Figures 33 to 36.

TABLE 4: Monte Carlo volumetric generation capacity estimates for Chachimbiro geothermal field, and Cachiyacu and Jamanco areas from Chacana geothermal field

Statistical sizes	Power [MWe] Chachimbiro	Power [MWe] Cachiyacu	Power [MWe] Jamanco
Most probable value	103	18	2
90% confidence interval	75 - 185	10 - 40	1 - 5
90% limit	74	11	1

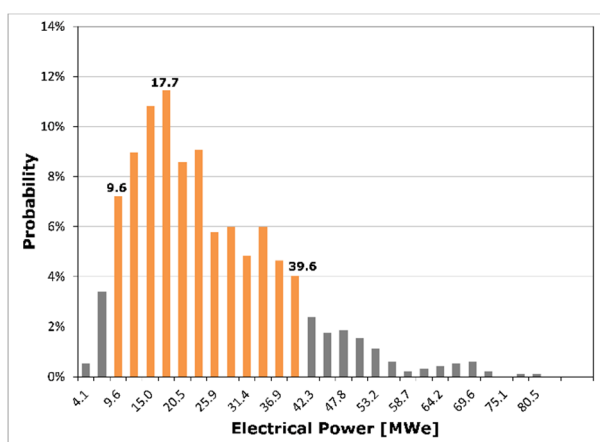


FIGURE 33: Monte Carlo volumetric discrete probability distribution for electrical power distribution in Cachiyacu

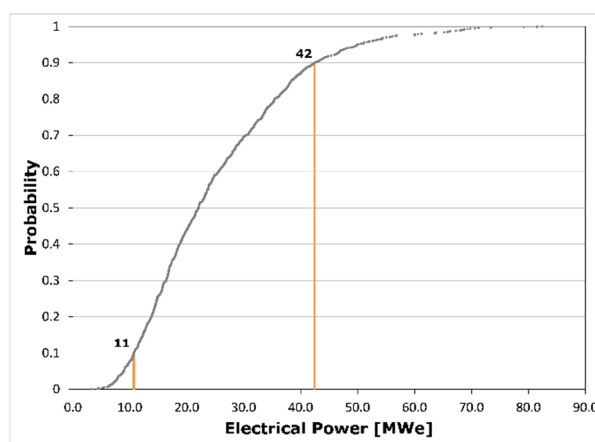


FIGURE 34: Monte Carlo volumetric cumulative probability distribution for electrical power production in Cachiyacu

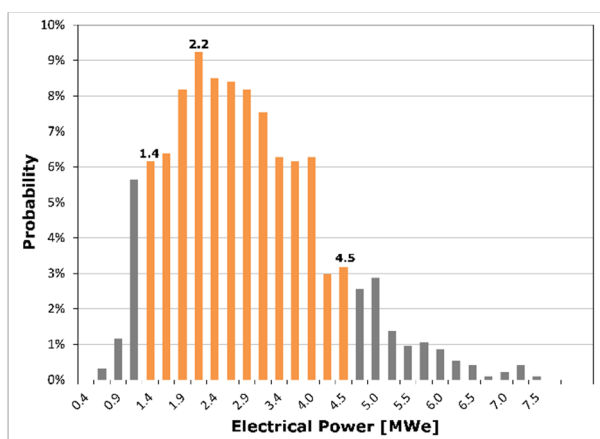


FIGURE 35: Monte Carlo volumetric discrete probability distribution for electrical power distribution in Jamanco

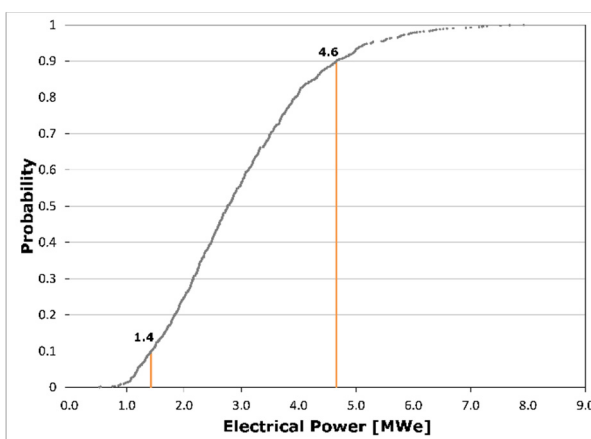


FIGURE 36: Monte Carlo volumetric cumulative probability distribution for electrical power production in Jamanco

6. CONCLUSION AND RECOMMENDATIONS

A review of prefeasibility studies (SYR, 2012a; SYR, 2012b) of two geothermal fields in Ecuador was shown to be a good preparation for selecting the most important information to use in a volumetric assessment of the geothermal systems. The main outputs from this study can be presented as follows:

- Volumetric assessments of the Chachimbiro and Chacana geothermal fields are presented in this study. Due to a lack of boreholes and exploratory drillings, some values of different parameters for the volumetric assessment were assumed through approximations and comparisons with other geothermal fields. The accuracy must be confirmed by the drilling campaign in the future.
- **Chachimbiro** geothermal field was treated as a high-temperature field in the volumetric assessments. This was based on the resistivity structure and confirmed by the geothermometers that indicated a reservoir temperature range of 200-320°C. The minimum size of the geothermal area was assumed from surface manifestations as 3 km² and the maximum size derived from the resistivity model was assumed to be 16 km². The thickness of the reservoir was defined as 1500 m. The assessment assumed a flash power plant utilization when calculating the electrical power production capacity.
- **Chacana** geothermal field was treated as a low- or intermediate-temperature field based on the geothermometers. The resistivity character could be that of a high-temperature system, or a remnant of one. Determining if the Chacana field is a high-temperature system could not be derived from the resistivity structure alone. The Chacana field was divided into two sub-areas, Cachiyaçu and Jamanco areas, based on surface geology, geochemistry and the results of the MT resistivity model. The temperature range indicated by geothermometers was 170-240°C for Cachiyaçu, and 140-180°C for Jamanco. The minimum size of the Cachiyaçu, derived from the surface manifestations, was assumed to be 0.56 km² and the maximum size derived from the resistivity model was assumed to be 6 km². The minimum size for Jamanco was 0.25 km² and the maximum size 2 km². In the case of a high-temperature system that has cooled down, the thickness was defined as 1500 m whereas for the case of a low-temperature reservoir, the thickness was defined as that of the low-resistivity anomaly, i.e. 500 m. These values were used as maximum and minimum thicknesses in the volumetric calculations. The assessment assumed a binary power plant utilization when calculating the electrical power production capacities.
- The volumetric model predicted with 90% confidence that the electrical power production capacity of the Chachimbiro field lies between 75–185 MWe for a production period of 25 years. For Chacana geothermal field, the volumetric model predicted with 90% confidence that the electrical power production capacity lies between 10-40 MWe and 1-5 MWe for 25 years for Cachiyaçu and Jamanco areas, respectively.
- The next stage in the development of these geothermal projects should be the drilling of exploration wells. Chachimbiro and Chacana projects could have many scenarios leading to different estimations of the potential capacity generation of the fields.
- The true conditions of the fields must be discovered through drilling. Through drilling of exploration wells, the estimation of models could partly be fixed with more accurate parameters. That would help to make better decisions regarding the development of the geothermal fields.

ACKNOWLEDGEMENTS

I would like to express my gratitude to the UNU-GTP, especially to Mr. Lúdvík S. Georgsson, the Director of the Geothermal Training Programme, for giving me the opportunity to participate in this Training Programme. I am sure that it will contribute to the development of geothermal energy in Ecuador. I also would like to extend my sincere gratitude to the UNU-GTP staff: Mr. Ingimar G. Haraldsson, Ms. María S. Gudjónsdóttir, Ms. Thórhildur Ísberg, Mr. Markús A.G. Wilde and especially Ms. Málfríður Ómarsdóttir for her priceless friendship.

I am greatly indebted to my supervisors: Svanbjörg Helga Haraldsdóttir, Saeunn Halldórsdóttir and Ragna Karlsdóttir, and also to Magnús Ólafsson and Benedikt Steingrímsson, who shared partly their experience and knowledge in a short time. Thanks Svana; your guidance will be my way henceforth.

I am grateful to my employer, the Electricity Corporation of Ecuador – CELEC EP, and specifically Mr. Carlos Eduardo Barredo, Director, for granting me the opportunity to attend the training and for providing the information used in this work. Thanks go to my colleagues and all the team.

Thanks to the 2014 UNU fellows for friendships formed, especially to Daniel Villarroel and Jaime Hernández. Last, but not least, fondly, all my appreciation goes to Maureen Ambunya (mrembo).

And my special gratitude goes to my family for all their support and for accompanying me through their prayers.

REFERENCES

Axelsson, G., Arnaldsson, A., Ármannsson, H., Árnason, K., Einarsson, G., Franzson, H., Fridriksson, T., Gudmundsson, G., Gylfadóttir, S., Halldórsdóttir, S., Hersir, G., Mortensen, A., Thordarson, S., Jóhannesson, S., Bore, C., Karingithi, C., Koech, V., Mbithi, U., Muchemi, G., Mwarania, F., Opondo, K., Ouma, P., 2013: Updated conceptual model and capacity estimates for the Greater Olkaria geothermal system, Kenya. *Proceedings of the 38th Workshop on Geothermal Reservoir Engineering, Stanford University, Stanford, CA*, 16 pp.

Árnason, K., Karlsdóttir, R., Eysteinnsson, H., Flóvenz, Ó.G., and Gudlaugsson, S.Th., 2000: The resistivity structure of high-temperature geothermal systems in Iceland, *Proceedings of the World Geothermal Congress 2000, Kyushu-Tohoku, Japan*, 923-928.

Brooke, C.A., Mariner, R.H., Mabey D.R., 1978: Hydrothermal convection systems with reservoir temperatures $\geq 90^{\circ}\text{C}$, In: Muffler, L.J.P. (editor), *Assessment of geothermal resources of the United States*. Geological Survey Circular, 1978, prepared in coop. with the Department of Energy, 18-85 pp.

Cumming, W., 2009: Geothermal resource conceptual models using surface exploration data. *Proceedings of the 34th Workshop on Geothermal Reservoir Engineering, Stanford University, Stanford, CA*, 6 pp.

Cumming, W., and Mackie, R., 2010: Resistivity imaging of geothermal resources using 1D, 2D and 3D MT inversion and TDEM static shift correction illustrated by a Glass Mountain case history. *Proceedings of the World Geothermal Congress 2012, Bali, Indonesia*, 10 pp.

Flóvenz, Ó.G., Spangenberg, E., Kulenkampff, J., Árnason, K., Karlsdóttir, R., and Huenges, E., 2005: The role of electrical interface conduction in geothermal exploration. *Proceedings of the World Geothermal Congress 2005, Antalya, Turkey*, 9 pp.

GeothermEx, 2011: *Chemistry of fluids in Chachimbiro geothermal project, Ecuador*. GeothermEx, report (in Spanish) prepared for SYR, Ecuador, October, 18 pp.

Giggenbach, W.F., 1988: Geothermal solute equilibria. Derivation of Na-K-Mg-Ca geothermometers. *Geochim. Cosmochim. Acta*, 52, 2749-2765.

Grant, M.A., Donaldson, I.G., and Bixley, P.F., 1982: *Geothermal reservoir engineering*. Academic Press, New York, 369 pp.

Hall, M. and Mothes, P., 1997: Chacana caldera - the largest rhyolitic eruptive centre in the northern Andes. *Abs. Memorias LAVCEI Mtg, México*, 14 pp.

Hall, M., Mothes, P., and Cotton, J., 2000: *The Chacana caldera complex, Ecuador*. Poster (in Spanish).

Hickman, S., and Davatzes, N., 2010: In-situ stress and fracture characterization for planning of an EGS stimulation in the Desert Peak geothermal field, Nevada. *Proceedings of the 35th Workshop on Geothermal Reservoir Engineering, Stanford University, Stanford, CA*, 13 pp.

Lopez, E., 2012a: Geophysical model. In: SYR, *Initial prefeasibility study to develop a conceptual model for the Chachimbiro geothermal project*. SYR, prepared for CELEC EP, Ecuador, March, Appendix.

Lopez, E., 2012b: Geophysical model. In: SYR, *Initial prefeasibility study to develop a conceptual model for the Chachimbiro geothermal project*. SYR, prepared for CELEC EP, Ecuador, June, Appendix.

Lutz, S.L., Hickman, S., Davatzes, N., Zemach, E., Drakos, P., and Robertson-Tait, A., 2010: Rock mechanical testing and petrologic analysis in support of well stimulation activities at the Desert Peak geothermal field, Nevada. *Proceedings of the 35th Workshop on Geothermal Reservoir Engineering, Stanford Univ., Stanford, CA*, 9 pp.

Mothes, P. and Hall, M., 2008: Rhyolitic calderas and centres clustered within the active andesitic belt of Ecuador's Eastern Cordillera. *IOP Conf. Series*.

Muffler, L.P.J., and Cataldi, R. 1978: Methods for regional assessment of geothermal resources. *Geothermics*, 7, 53-89.

Ruiz, G., 2011: Geologic model. In: SYR, *Initial prefeasibility study to develop a conceptual model for the Chachimbiro geothermal project*. SYR, report.

Ruiz, M., 2012a: Geophysical model. In: SYR, *Initial prefeasibility study to develop a conceptual model for the Chachimbiro geothermal project*. SYR, prepared for CELEC EP, Ecuador, March, 54-68.

Ruiz, M., 2012b: Geophysical model. In: SYR, *Initial prefeasibility study to develop a conceptual model for the Chachimbiro geothermal project*. SYR, prepared for CELEC EP, Ecuador, June, 72-92.

Sarmiento, Z. F. and Steingrímsson, B., 2007: Computer programs for resource assessment and risk evaluation using Monte Carlo simulation. *Presented at "Short Course on Geothermal Development in Central America – Resource Assessment and Environmental Management, organized by UNU-GTP and LaGeo, San Salvador, El Salvador*, 11 pp.

Soulas, J.-P., Egüez, A., Yepes, H., Pérez, V.H., 1991: Active tectonics and seismic risk in the Ecuadorian Andes and the southern tip of Colombia (in Spanish). *Boletín Geológico Ecuatoriano*, 2, 3-11.

SYR, 2012a: *Initial prefeasibility study to develop a conceptual model for the Chachimbiro geothermal project*. SYR, prepared for CELEC EP, Ecuador, March, 123 pp.

SYR, 2012b: *Initial prefeasibility study to develop a conceptual model for the Chachimbiro geothermal project*. SYR, prepared for CELEC EP, Ecuador, June, 173 pp.

Torres, L., and Urquizo, M., 2013: *Assessment of initial prefeasibility study of Chachimbiro geothermal project*. University of El Salvador, San Salvador, Geothermal diploma course, report (in Span.), 74 pp.

Ussher, G., Harvey, C., Johnstone, R., and Anderson, E., 2000: Understanding the resistivities observed in geothermal systems. *Proceedings of the World Geothermal Congress 2000, Kyushu-Tohoku, Japan*, 6 pp.

WesternGeco, 2012: *MT/TDEM survey Chachimbiro, Ecuador. Modelling with 3D inversion*. WesternGeco, prepared for SYR, Ecuador, report (in Spanish), 38 pp.

Yepes, H. and Ramón, P., 2000: *Ríos Orientales project – preliminary study of seismic hazards*. EMAAP-Q, report (in Spanish).

Yepes, H., Ramón, P., Fernández, L., and Egüez, A., 1990: *Papallacta project - study of seismic hazards*. EMAAP-Q, report (in Spanish), 47 pp.



UNITED NATIONS
UNIVERSITY

UNU-GTP

Geothermal Training Programme

Orkustofnun, Grensasvegur 9,
IS-108 Reykjavik, Iceland

Reports 2014
Number 11

DRILLING FLUID DESIGN FOR GEOTHERMAL WELLS

George Moshe Dayan

Kenya Electricity Generating Company Ltd. – KenGen

P.O. Box 785-20117

Naivasha

KENYA

georgemoshed@gmail.com, gmoshe@kengen.co.ke

ABSTRACT

Drilling is a key process in the development of geothermal resources, whether at the exploration stage or in a fully developed field. It constitutes up to 35-50% of project costs. Successful completion of a well at minimal cost is, therefore, imperative. One area that highly affects both successful completion of a well and its cost is the drilling fluid program. Drilling fluids have advanced over the years, more so in petroleum drilling; however, some of the technologies in the oil sector may not be relevant in geothermal drilling and could just escalate the well costs. It is imperative to design a simple drilling fluid program that will not only ensure a quality well but also minimise the cost of the well. This paper seeks to address the selection of a drilling fluid best fit for geothermal wells.

1. INTRODUCTION

Drilling is a key process in the development of geothermal resources, whether at the exploration stage or in a fully developed field. It also constitutes one of the highest costs in geothermal projects, i.e. up to 35-50% (Kipsang, 2013). It is therefore imperative not only to successfully complete a well but also to ensure it is done at the minimum cost that is possible. One area that highly affects both the successful completion of a well and its costs is the drilling fluid program. A drilling fluid program entails details on the drilling fluid to be used in the various well sections and possible actions to be undertaken in case of special hole conditions. The drilling program is one of the critical components in successfully completing a drilling project. Selection of drilling fluids also involves appreciating the costs involved with each system. These can be either direct or indirect costs. Direct costs are those incurred in the purchase, handling and utilization of the drilling fluid. They include personnel costs and technology costs, for instance hiring an air drilling package, among others. These normally constitute up to 15% of the well costs (Kipsang, 2013). Indirect costs, on the other hand, are costs which can be traced to the effects of the drilling fluid technology used. This is because different fluid systems have varying effects on the well which could either enhance or impede the drilling process; these costs could be in terms of several extra drilling days or fishing operations among others. The reservoir quality is also affected by the drilling fluid as some fluids lead to more formation damage. Drilling fluids have advanced over the years, more so in petroleum drilling; however, some of the technologies in the oil sector may not be relevant in geothermal drilling and could escalate well costs. It is imperative to design a simple drilling fluid program that will not only ensure a quality well but also minimise the cost of the well.

2. DESCRIPTION OF DRILLING FLUIDS

The drilling process mainly involves cutting the rock and bringing the cuttings to the surface. A drilling rig is equipped with several tools and equipment to aid in the cutting and transportation of these cuttings. One of the key systems needed is the circulation system which includes pumps, compressors, tanks, a water pond and, most important, the drilling fluid.

In its simplest form, a drilling fluid is any fluid circulated in a well in order to bring out the cuttings from the wellbore. This can be as simple as plain water or as complex as a fluid mixture with several chemical additives. For a long time drilling fluids were mainly designed to bring cuttings to the surface; however, with advancement in the drilling sector, research has proven that drilling fluids affect drilling performance and, eventually, well performance (Baker Hughes, 1995). Today drilling fluids are designed to take care of more than just cuttings. There are basically three types of drilling fluid systems: mud, air and aerated systems (Ava, 2004).

For drilling fluid to function, a circulation system is needed; this can be either direct circulation or reversed circulation; in this study, we shall focus on direct circulation. Figure 1 shows the key equipment in a drilling fluid direct circulation system, for air/gas or aerated drilling systems; compressors and boosters are incorporated into the system.

The drilling fluid is pumped from the mud tanks up the Kelly hose through the drill pipe to the drill bit. At the drill bit, the fluid jets out at high pressure, lifting with it the freshly cut rock beneath the bit up the annulus, while cooling the bit and the formation at the same time. The fluid containing the rock must possess enough kinetic energy to move all the way to the surface with the cuttings. Once the fluid reaches the surface at the diverter, it flows to the shale shaker through the flow line where the cuttings are separated and the fluid is re-circulated. The quality of the fluid in the tank is continuously monitored for correct PH, viscosity and other parameters (Skalle, 2011).

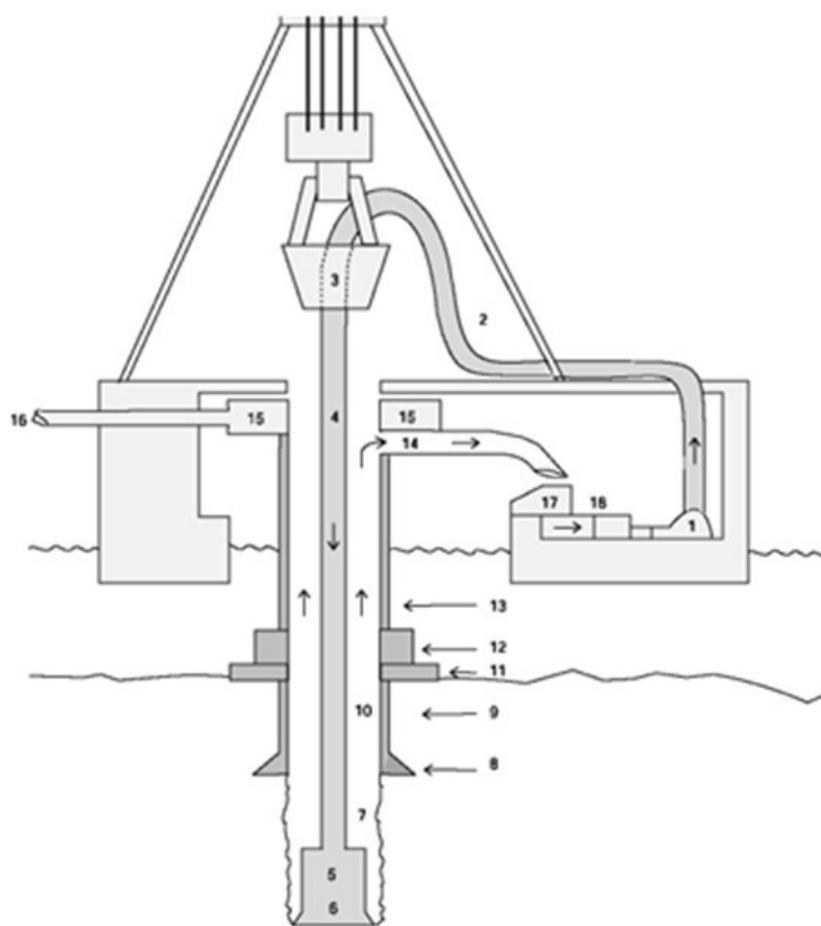


FIGURE 1: Circulation system (Ava, 2004)

2.1 Functions of drilling fluid

The initial key functions of drilling fluids were transporting cuttings to the surface, cooling the bit and drill string and controlling the sub-surface pressures. Today, however, with the advancement in

drilling technologies, the drilling fluid has evolved to embrace several new functions. Nevertheless, the preceding still remain the key functions that any drilling fluid program must meet. Moreover, it is important that the drilling fluid is designed with the right properties for each function.

2.1.1 Hole cleaning

This involves carrying the cuttings from beneath the bit, transporting them to the surface and releasing them. The aim is to transport all the cut material as fast as possible to avoid any accumulation failure which could lead to several drilling challenges such as:

1. High torque which could lead to the drill stem snapping;
2. Stuck pipe, probably leading to the loss of the drill stem;
3. Hole pack off;
4. Damage to formation;
5. Excessive over pull during trips, hence reducing the life of the drill string; and
6. Slow rate of penetration.

Hole cleaning is the main action for which drilling fluid design is done. A fluid must have adequate viscosity, density and flow, at the right rate to carry the cuttings to the surface.

2.1.2 Well control

When preparing a drilling fluid, one must always remember that it is actually the key well control system. The pressures in a well increase with depth. When the formation fluid has higher pressures than those of the fluid in the well, a kick or blow out may occur. On the other hand, an overbalanced drilling fluid may cause formation damage by exerting excessive pressure on the formation wall. The key property of the fluid to be monitored in this case is the density.

2.1.3 Maintain borehole stability

A single well profile has formations with varying properties: some fractured, erodible or swelling. These could result in very problematic formations during the drilling process. The drilling fluid is the main option in addressing these and ensuring the borehole is kept stable to ensure the drill bit and stem runs through successfully to the total depth.

2.1.4 Protecting formation from damage

This has become an increasingly important function of drilling fluids. In geothermal drilling, aerated fluids are used in the production zone with the aim of minimizing formation damage. Formation damage may occur mainly due to plugging of the formation's natural porosity, either by solids or plugging associated with fluid filtration.

Other functions of drilling fluid include:

1. Cooling and lubricating the bit and drill stem;
2. Improving the rate of penetration by cleaning the surface to be drilled;
3. Contributing to drill string buoyancy; and
4. Retrieval of formation data.

2.2 Types of drilling fluids

A drilling fluid in its simplest form can be plain water; however, many times the properties of water must be improved to achieve the various tasks required of a drilling fluid. The basic composition of a drilling fluid is a base fluid, with a continuous fluid phase and can be water, oil or air. Various

additives are introduced to these base fluids to achieve a given property, for instance viscosifiers are added to improve the viscosity of the fluid (Darley and Gray, 1988). The drilling fluids are, therefore, classified depending on the base fluid used: water, oil or air. Nevertheless, all drilling fluids have essentially the same properties; only the magnitude varies. These properties include density, viscosity, gel strength, filter cake, water loss, and electrical resistance (Baker Hughes, 1995). It is important to note that drilling fluids in geothermal drilling are rather simple since the formation that is drilled through many times is under-pressurised.

2.2.1 Water based drilling fluids

These have water as the continuous base and can be either fresh or saline water. This is the main type of fluid used in geothermal drilling, more so for the upper cased well sections. Active and inert solids are normally added to change the mud properties. Common active additives include bentonite and polymers, mainly used for improving on viscosity, which is important for the cuttings transport capacity of the mud. Inert solids include particles added to the mud, such as formation particles; a common substance normally added to increase mud density is barite (Darley and Gray, 1988). This, however, is rarely used in geothermal drilling.

Bentonite mud made by mixing bentonite into water has the advantage of gelling and also forming a filter cake around the wall of the well. The gel assists in suspending the cuttings in case the circulation is stopped, reducing the chance of the cuttings dropping down on the string. The filter cake is important in reducing loss of circulation since it forms an impermeable layer around the wall, and it also helps in increasing well stability. The filter cake, however, can be problematic if it is too thick and can also hinder good cementing jobs if not cleaned off. Polymers like bentonite are added with the aim of improving the viscosity of the mud; however, they have poor gelling properties and do not form a filter cake (Baker Hughes, 1995).

Other special water-based muds can be made to address specific well situations. These, however, are rare in geothermal drilling, but are common in oil drilling, and include:

1. Emulsion muds-oil in water;
2. Inhibited muds-large amounts of dissolved salts added to the mud; and
3. Lime treated muds.

Caustic soda is normally added to improve the pH of the fluid.

Also used in the oil sector is oil-based mud where oil is used as the continuous fluid phase and additives are put in to achieve various properties. This is rarely utilised in geothermal drilling, both because of costs and environmental concerns.

2.2.2 Air and aerated drilling fluids

Air drilling involves the utilisation of compressed air as the drilling fluid. Normally, this air is delivered through the string just like typical drilling mud, but with higher velocities and carries up with it the cuttings. It is a very efficient method for drilling in dry or frozen formations. Once water is encountered, then the cuttings transportation capacity is greatly hampered (Skalle, 2011). In geothermal drilling, this is mainly applied for drilling the surface section of the well where many times the rock is competent and very hard. Air hammer drilling is applied in Iceland and in the Kenya-Menengai geothermal project for drilling the surface hole (Thórhallson, 2014).

There are various types of air drilling, all depending on the liquid volume fraction, LVP, which indicates how much liquid is in the system and is a measure of the density of the fluid mixture: zero LVP implies no liquid, while one implies 100% liquid (Hole, 2006). All air drilling systems have LVP of less than one. Also of significance is the method of injection of the air stream into the system;

this can be either through the drill pipe or through the annulus (Lyons et al., 2009). In geothermal projects, the most common method used is the drill pipe injection method.

1. *Dust drilling*: Compressed air is used as the sole drilling fluid; this is ideal in dry areas where we do not expect to encounter liquids. It is used with air hammers. Normally, there is zero LVP, implying the system is 100% air.
2. *Mist drilling*: Air drilling with the addition of liquids, normally water and soap. This is introduced when a wellbore gets liquid influx during dust drilling.
3. *Foam drilling*: Foam is created by combining water, surfactants and air. Has better cuttings carrying capacity.
4. *Aerated drilling*: In this type of drilling, air or nitrogen is added to the drilling mud. The mud can be water-bentonite, water-polymer or water-foam. The water-foam drilling is also called stable foam drilling and involves the use of water mixed with surfactants or air. This is the most common form of aerated drilling used in the geothermal industry.

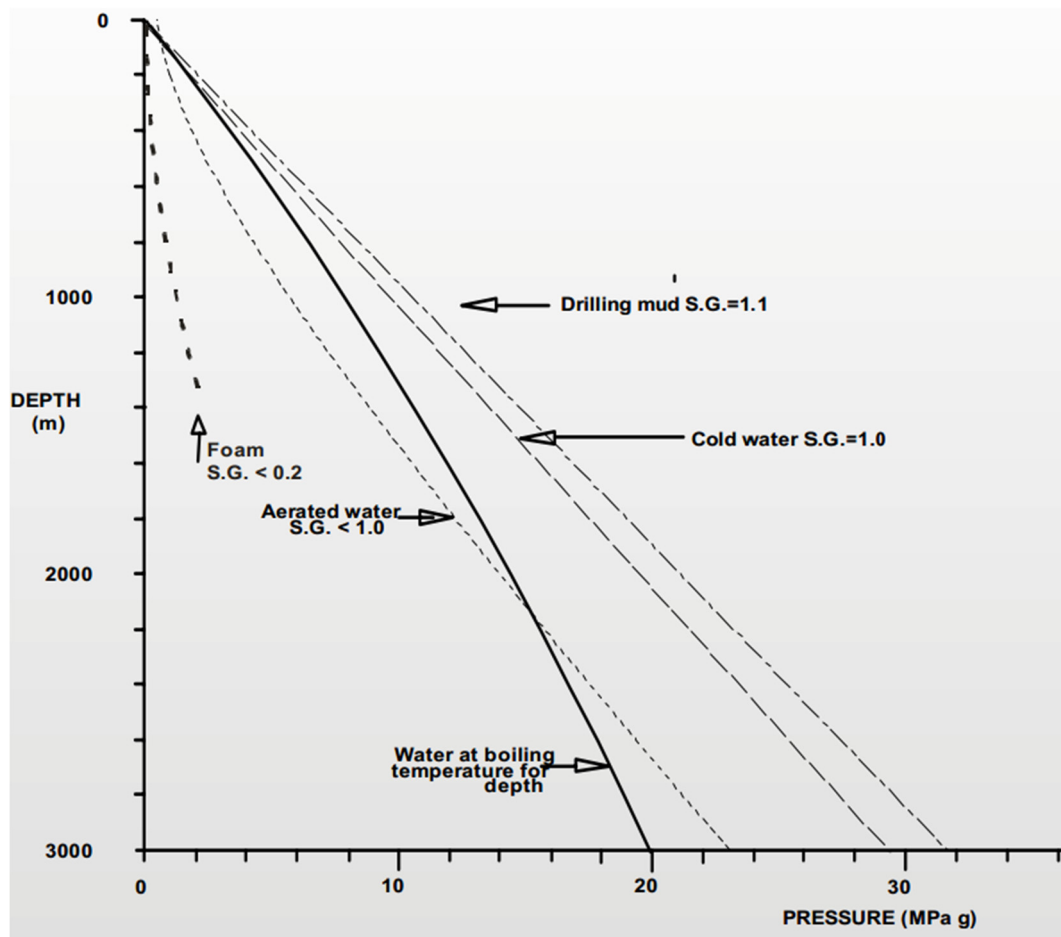


FIGURE 2: Down hole pressures (Hole, 2006)

The introduction of air drilling in geothermal systems is mainly due to the fact that most geothermal formation pressures are significantly lower than the hydrostatic column of water at any depth within the system, as illustrated in Figure 2 (Hole, 2006).

Figure 2 indicates the specific gravities of the various drilling fluid, indicating the importance of aerated systems in keeping the drilling fluid under-pressurised in comparison with the formation pressure.

2.3 Operating principle of drilling fluids

The working principle of any drilling fluid depends upon the function for which it is designed. Most drilling fluids are, from the onset, designed to lift the cuttings to the surface and control the well. As the drilling progresses and special conditions are encountered, the drilling fluid may be redesigned to perform other functions. However, in all cases the drilling fluid parameters considered are viscosity, velocity and density; other properties such as gel strength, filter cake, water loss, are dependent on the former (Darley and Gray, 1988).

To discuss the operation of drilling fluids, we shall consider the main functions of drilling fluids as identified earlier: hole cleaning, well control, protection of the formation and borehole stability.

2.3.1 Hole cleaning

Hole cleaning results from the continuous transportation of cuttings from beneath the bit to the surface where they are released. This is the key function of any drilling fluid and, hence, is the main controlling factor in fluid design. The key factors affecting cutting transportation are drilling fluid and cuttings velocity. The drilling fluid velocity depends on the rheological parameters of the fluid, density, the pump rate and the annular geometry of the well, whereas the key cuttings parameters are density, diameter and shape (Mitchell and Miska, 2011).

Cuttings generated in a well experience a downward movement due to gravity, resulting in negative velocity relative to the fluid's velocity. This negative velocity is termed cutting slip velocity, V_{sl} , and is key in determining cuttings transport. The movement of the cuttings up the annulus is the result of a net upward velocity, called cutting transport velocity, V_t ; this is the difference between the fluid annular velocity V_a and the cuttings slip velocity V_{sl} . This implies that in designing a fluid for efficient hole cleaning, we must appreciate how the cuttings behave and calculate the expected slip velocity (Rehm et al., 2012).

The slip velocity can be determined depending on the type of fluid and flow regime; for laminar flows, there are different relationships for Newtonian and non-Newtonian fluids due to the effect of the fluid's rheological properties. In turbulent flow, the rheological properties have no effect (Darley and Gray, 1988).

Hole cleaning, however, is not just about carrying the cuttings out but also ensuring minimal cuttings concentration in the well during the drilling operation. For trouble free drilling, the cuttings concentrations in the well, C_a , should be below 5%, and the fluid parameters must be controlled to achieve this (Azar and Samwel, 2007). An additional way of designing a fluid is to consider its cuttings capacity index (CCI); this is a relationship based on various fluid parameters that are key for ensuring hole cleaning. This was arrived at from various field studies which concluded that for efficient hole cleaning in vertical and near vertical wells, $CCI \geq 1$. The drill bit also plays a key role in effective hole cleaning; therefore, bit hydraulics must be considered when designing the drilling fluid (Rehm et al., 2012).

The following equations relate the various key hole cleaning parameters and how to arrive at them:

Critical annular velocity

This is a key parameter and is the minimal annulus velocity at which the cuttings concentration in the annulus reaches its threshold value and can be obtained by (Rahimov, 2009):

$$V_{ac} = \frac{1667ROPD_b^2}{60C_a(D_b^2 - D_p^2)} + V_{sl} \quad (1)$$

where V_{ac} = Critical annular velocity (ft/s);

- V_{sl} = Slip velocity of cuttings (ft/s);
 ROP = Rate of penetration (ft/hr);
 C_a = Cuttings concentration in the annulus (%);
 D_b = Drill bit diameter (in); and
 D_p = Drill pipe outside diameter (in).

To maintain a specific cuttings concentration (C_a) in the annulus, the annular velocity must not go below this.

Cuttings slip velocity

Several correlations have been developed for slip velocity, all of them based on Stokes law with the exception of those developed by Walker and Mayes (Mitchell and Miska, 2011).

Cuttings slip velocity for Newtonian fluid, Stokes law.

From Stokes law, the slip velocity (V_{sl}) of an object falling through a viscous fluid is given by:

$$V_{sl} = \frac{d_s^2 g (\rho_s - \rho_f)}{18\mu} \quad (2)$$

$$V_{sl} = \frac{2}{3} \sqrt{\frac{3gd_s(\rho_s - \rho_f)}{f\rho_s}} \quad (3)$$

$$C_D = \frac{4}{3} g \frac{d_s}{V_{sl}^2} \left(\frac{\rho_s - \rho_f}{\rho_f} \right) \quad (4)$$

- where d_s = Particle diameter (m);
 ρ_s = Cuttings density (kg/m³);
 ρ_f = Fluid density (kg/m³);
 μ = Dynamic viscosity (kg/ms);
 g = Acceleration due to gravity (m/s²);
 C_D = Drag Coefficient; and
 f = Particle friction factor – obtained from graph in Appendix I.

Equations 2 and 3 apply for Newtonian fluids (e.g. water) in laminar and turbulent flow, respectively. Equation 4 gives the drag coefficient corresponding to the slip velocity calculated (Mitchell and Miska, 2011).

To determine the flow regime, we calculate the Reynolds number of the particles (Re_p):

$$Re_p = 928.2 \frac{\rho_f d_s V_s}{\mu} \quad (5)$$

- where ρ_f = Fluid density (kg/m³);
 d_s = Particle diameter (m);
 V_s = Slip velocity (m/s); and
 μ = Newtonian viscosity of the fluid (Pa s).

When $Re_p \leq 1.0$, this defines a laminar flow regime; $1.0 \leq Re_p \leq 2000$ defines a transition flow regime, and $Re_p > 2000$ defines turbulent flow.

Calculation of slip velocity for Non-Newtonian drilling fluid

Stokes law does not give an accurate approach for determining the slip velocity in non-Newtonian fluids, due to the effect of rheological parameters on the fluid (Guo and Liu, 2011). Several correlations have been developed to determine slip velocity in non-Newtonian fluids, described below:

Moore correlation

Moore suggested the use of an apparent viscosity (μ_a) instead of the Newtonian viscosity of the fluid as used in Stokes law (Rahimov, 2009). Apparent viscosity is based on a pseudo plastic fluid model and is given by:

$$\mu_a = \frac{K}{144} \left(\frac{D_h - D_p}{V_a} \right)^{(n-1)} \left(\frac{2 + \frac{1}{n}}{0.0208} \right)^n \quad (6)$$

And the slip velocity for laminar flow, where $Re_p \leq 1.0$, is given by:

$$V_{sl} = 82.86 \frac{d_p^2 (\rho_p - \rho_f)}{\mu_a} \quad (7)$$

Slip velocity for transitional flow, $1.0 \leq Re_p \leq 2000$:

$$V_{sl} = 2.90 \frac{d_p (\rho_p - \rho_f)^{0.667}}{\rho_f^{0.333} \mu_a^{0.333}} \quad (8)$$

Slip velocity for turbulent flow, $Re_p > 2000$:

$$V_{sl} = 1.54 \sqrt{\frac{d_p (\rho_p - \rho_f)}{\rho_f}} \quad (9)$$

where K = Consistency index (lbf secn/100 ft²);
 n = Flow behaviour index (dimensionless);
 ρ_f = Weight of drilling fluid (ppg);
 ρ_p = Weight of rock particles (ppg);
 V_a = Fluid velocity in annulus (ft/s);
 μ_a = Apparent viscosity (cP);
 D_h = Hydraulic diameter for annulus (in);
 D_p = Pipe diameter (in); and
 d_p = Diameter of cuttings (in).

Chien correlation

This is similar to Moore's correlation in that it also uses the apparent viscosity in calculating Reynolds number. Chien's analysis is based on a Bingham fluid model. The following equations apply:

$$\mu_a = \mu_p + 5 \frac{\tau_y d_s}{V_a} \quad (10)$$

where μ_a = Apparent viscosity (cP);
 μ_p = Plastic viscosity (cP);
 τ_y = Yield stress (lbf/100 ft²); and
 V_a = Fluid velocity in annulus (ft/s).

$$V_{sl} = 0.0075 \left(\frac{\mu_a}{\rho_f d_p} \right) \left[\left(\sqrt{\frac{36800 d_p \left(\frac{\rho_p - \rho_f}{\rho_f} \right) + 1}{\frac{\mu_a}{\rho_f d_p}}} \right) - 1 \right] \quad (11)$$

Equation 10 gives the apparent viscosity to be used in polymer type drilling fluids. For bentonite, Chien proposed the use of plastic viscosity (Rahimov, 2009). Equation 11 gives accurate slip velocity

when the viscous properties of drilling fluids are abnormally high, i.e. when $\mu_a/\rho_f d_p > 10$; otherwise, Chien proposed a simpler equation for normal fluids:

$$V_s = 1.44 \sqrt{\frac{d_p(\rho_p - \rho_f)}{\rho_f}} \quad (12)$$

Walker and Mayes correlation

In this correlation, the drill cuttings are assumed to be shaped like a circular disc, unlike the above two cases where the particles are assumed to be spherical. Hence, the particles will fall through the fluid with the flat face lying horizontal. The shear rate, called the boundary shear rate (γ_b), at which a particle's movement switches from laminar to turbulent, is calculated by:

$$\gamma_b = \frac{186}{d_p \sqrt{\rho_f}} \quad (13)$$

The shear stress developed by the particles as they fall through the drilling fluid is given by:

$$\tau_p = 7.9 \sqrt{T_p(\rho_p - \rho_f)} \quad (14)$$

Once the stress is determined, the corresponding shear rate is determined by using annular power law constants:

$$\gamma_p = \frac{\tau_p^{1/n_a}}{K_a} \quad (15)$$

If $\gamma_p < \gamma_b$ or $Re_p < 100$, then the slip velocity of a particle is in the laminar zone and is determined by:

$$V_s = 0.02 \tau_p \left(\frac{\gamma_p d_p}{\sqrt{\rho_f}} \right)^{0.5} \quad (16)$$

If $\gamma_p > \gamma_b$ or $Re_p > 100$, then the slip velocity of a particle is in the turbulent zone and is determined by:

$$V_s = 0.28 \frac{\tau_p}{\sqrt{\rho_f}} \quad (17)$$

where T_p = Particle thickness (in);
 γ_b = Boundary shear rate (1/s);
 γ_p = Shear rate corresponding to τ_p (1/s);
 τ_p = Shear stress developed by particles (lbf/100 ft²);
 K_a = Consistency index in annulus (lbf secn/100 ft²); and
 n_a = Flow behaviour index in annulus (dimensionless).

Calculating minimum annular velocity for hole cleaning:

$$V_a = V_{st} + V_t \quad (18)$$

$$V_t = \frac{\pi d_b^2}{4AC_a} \left(\frac{ROP}{3600} \right) \quad (19)$$

where ROP = Rate of penetration (ft/hr)- R_d ;
 C_a = Cutting concentration factor in the wellbore = 0.04;
 d_b = Bit diameter in inches; and

A = Cross-sectional area of flow path (in²).

But for best hole cleaning, the value of the rise velocity, V_r , should approach the annular velocity, (Rahimov, 2009).

From this, the minimum flow rate Q_{min} required for this velocity, V_a , is gotten by (Guo and Liu, 2011):

$$Q_{min} = 60 V_a A V_{a-w} = \frac{\left[\frac{P_g}{P}\right] \left[\frac{T_{av}}{T_g}\right] (Q_g + Q_m)}{\frac{\pi}{4} (D_b^2 - D_p^2)} \quad (20)$$

where Q_m = Volumetric flow of drilling mud/water (m³/s); and
 V_a = Fluid velocity in annulus (m/s).

Another method based on a power law fluid, which closely represents the behaviour of drilling fluids, involves the determination of the minimum velocity required to transport the fluid and cuttings mixture V_{mix} ; this is based on a cuttings concentration already defined earlier as C_a (Mitchell and Miska, 2011). The below equations are used:

$$V_{mix} = \frac{0.0475 V_{sl}}{0.05 - C_a} \quad (21)$$

$$V_{mix} = \frac{Q_c + Q_m}{A} \quad (22)$$

$$Q_c = V_t C_a \frac{\pi}{4} (D_h^2 - D_p^2) \quad (23)$$

where V_{mix} = Velocity of the cuttings and fluid mixture (m/s); and
 Q_c = The volumetric flow rate of the cuttings generated at the bit (m³/s).

By substituting Equation 23 into Equation 22, we solve for the value of Q_m , which is the volumetric flow of mud required to attain V_{mix} .

The efficiency of hole cleaning is checked by either monitoring the CCI, the annular volumetric cuttings concentration, C_a or the ratio of the cuttings transport velocity (CTR) R_t to the cuttings annular velocity V_a , R_t . In vertical drilling, it is recommended that R_t should be a minimum of 0.5-0.55 (Azar and Samuel, 2007).

$$CCI = \frac{\rho K V_a}{400,000} \quad (24)$$

$$C_a = \frac{R_d D_b^2}{1.27 R_t Q_m} \quad (25)$$

$$(CTR) R_t = 1 - \frac{V_{sl}}{V_a} \quad (26)$$

where CCI = Cuttings carrying index;
 CTR = Cuttings transport rise; and
 ROP = Rate of penetration (m/hr)- R_d .

The K factor power law fluids is shown in Appendix II.

Hole cleaning in aerated drilling

When designing hole cleaning for aerated drilling, the practise is to design the incompressible drilling fluid to have a minimum lifting capability for the planned open hole interval. This implies the fluid

should be capable on its own in maintaining a minimum concentration of rock cuttings in the largest annulus section of the well (Lyons et al., 2009). The assumption in this approach is that the incompressible fluid can carry the cuttings on its own, and that the injection of air into the fluid will enhance this capacity.

To fulfil this, the average velocity of the incompressible fluid V_f in the largest annulus section must be equal or greater than the sum of the critical velocity V_c and the terminal velocity V_t of the average size rock cutting particle in the drilling fluid (Lyons et al., 2009). This is the same as in normal drilling while using mud, hence the equations described in the preceding section for minimum annular velocity and flow rates will apply in determining V_f .

However, the annular velocity of the air and the incompressible fluid mixture can be gotten by:

$$V_{a-w} = \frac{\left[\frac{P_g}{P}\right] \left[\frac{T_{av}}{T_g}\right] (Q_g + Q_m)}{\frac{\pi}{4} (D_b^2 - D_p^2)} \quad (27)$$

And the volumetric flow of air Q_{air} at any depth in the well is given by:

$$Q_{air} = \left(\frac{P_g}{P}\right) \left(\frac{T_{av}}{T_g}\right) Q_g \quad (28)$$

where P_g = Atmospheric pressure at the compressor inlet (N/cm² abs);
 P = Pressure entering the pipeline (N/cm² abs);
 T_g = Temperature of the air entering the compressor (°C);
 T_{av} = Average temperature of the air over a depth interval;
 Q_g = Volumetric flow rate of the compressible gas (ft³/s); and
 Q_m = Volumetric flow rate of the incompressible fluid (ft³/sec).

Q_m is the minimum mud flow rate required to attain the minimum annular flow velocity, V_f for efficient hole cleaning. Equation 27 shows that it is possible to increase the annular velocity without increasing the flow of mud by adjusting the flow rate of the air Q_g ; this means better hole cleaning with minimal increase in fluid density, important for under-pressurised formations.

Aerated drilling using stable foam

Aerated drilling with stable foam introduces a new phase that must be monitored. Normally the surfactants, water and air, flow down the drill pipe as a normal aerated fluid. However, as it goes through the bit nozzles, the high shearing action leads to the generation of foam. This foam flows up the annulus as stable foam. To maintain the stability of this foam and avoid disintegration into a new phase, it is important to monitor a parameter known as the foam quality (Lyons et al., 2009). The foam quality at the entrance is defined by:

$$\Gamma = \frac{Q_g}{Q_g + Q_m} \quad (29)$$

where Γ = Foam quality.

Usually, the foam quality should be maintained at 0.98 at the exit point and at least 0.6 at the bottom hole. This is done by monitoring the pressure at which the mixture exits in the horizontal flow line at the surface. A gauge is normally installed at the surface at the back pressure valve in the horizontal flow line to check the exit pressure. The back pressure valve reading is calibrated to correspond to various foam quality values and can then be adjusted to achieve the required foam quality (Rehm et al., 2012). At the exit flow line, the volumetric flow rate, Q_{bp} for the compressed air exiting is used to calculate the foam quality and is gotten by:

$$Q_{bp} = \frac{P_g T_{av} Q_g}{P_{bp} T_g} \quad (30)$$

where P_{bp} = Back pressure.

The back pressure valve is adjusted to get the pressure necessary for the desired foam quality of 0.98.

Air drilling

The use of air, alone, as the drilling fluid is sometimes considered; this is especially beneficial if the water table is low or in areas with a scarce water resource. In geothermal drilling, an air hammer has been used in drilling the upper well sections which have hard rock and may take longer to drill using conventional rotary drilling. This has been practised with success in geothermal fields in Menengai, Kenya and in Iceland.

In designing the air system, the main issue is the minimum gas volume requirement for good hole cleaning. This can be determined by using the minimum velocity criterion or the minimum kinetic energy criterion. We shall consider the minimum velocity criterion. This criterion uses the same hole cleaning concept as in normal drilling, where the aim is to exceed the cutting terminal velocity; hence, we first determine this velocity in the air. Once this velocity is determined, then the fluid flow rate is designed to exceed it (Guo and Liu, 2011).

The minimum required gas velocity is given by (Guo and Liu, 2011):

$$V_g = V_{sl} + V_{tr} \quad (31)$$

$$V_{sl} = \sqrt{\frac{4gD_s(\rho_s - \rho_g)}{3\rho_g C_D}} \left(\frac{\varphi}{1 + D_s/D_H} \right) \quad (32)$$

The volumetric flow rate can then be obtained from:

$$Q_g = 60 \left(\frac{A}{144} \right) V_g \quad (33)$$

$$Q_{go} = \frac{PT_o}{TP_o} Q_g \quad (34)$$

where Q_g = Volumetric flow rate of gas (cfm);
 Q_{go} = Volumetric flow rate of gas in the standard condition (scfm);
 V_g = Minimum required gas velocity (ft/s);
 D_s = Solid particle (ft);
 ρ_s = Cuttings density (lbm/ft³);
 V_{sl} = Cutting slip velocity in air (ft/s);
 C_D = Drag coefficient accounting for the effect of particle shape;
 φ = Particle sphericity factor, obtained from graph in Appendix I (-); and
 D_H = Hydraulic diameter of flow path (ft).

2.3.2 Well control

Well control is all about controlling kicks and eliminating kicks, hence limiting the chance of a blowout. Kicks and blowouts occur when the fluid pressure in the formation exceeds the pressure of the drilling fluid in the well. When a kick is not contained and stopped, it leads to a blowout which is a more difficult situation. In geothermal drilling, the fluid acts both to cool the hot fluid and also keep the formation fluid pressure under check. The key parameter checked is the mud weight. The hydrostatic pressure due to the drilling fluid is obtained from the formula:

$$P = MW * TVD * 0.052 \quad (35)$$

Another key parameter is the equivalent circulating density (ECD); this is the density of the mud due to the effect of pump pressure applied on it for circulation. This is normally higher than the fluid's specific density, and is given by:

$$ECD = \frac{MW + P_a}{0.052 * D} \quad (36)$$

The ECD results in a new pressure called the bottom hole circulating pressure (BHCP) which is the actual pressure the drilling fluid has during circulation (Azar and Samuel, 2007). It is important to consider this pressure during the design process in order to ensure that it is kept low; it is given by:

$$BHCP = ECD * 0.052 * D \quad (37)$$

where P =The hydrostatic pressure (bars);
 MW =Mud density (kg/m³);
 P_a =Annulus frictional pressure drop at a given circulation rate (Pa); and
 D =Depth (m).

In geothermal drilling the production zone is often drilled using aerated water and foam which, many times, is a form of underbalanced drilling; the aim is to allow formation fluid to flow into the well, hence reducing damage to the formation. This, however, exposes the operation to higher chances of a kick and/or a blowout.

2.3.3 Protection of formation

There are two main parts of borehole drilling, the upper section which is normally totally cased and cemented, and the pay zone, which in geothermal wells is usually cased using slotted liners. The pay zone, or the main hole, in many geothermal hot temperature wells ranges from 700 m up to 3000 m or beyond. Prevention of formation damage is especially important when drilling the pay zone. Permeability is one of the most important properties of a geothermal reservoir. During drilling, the cuttings generated can clog the rocks, leading to loss of permeability. The inert components of drilling fluids can also flow into the formation, blocking aquifers or other permeable zones.

In geothermal drilling, aerated drilling is often introduced in the production zones. This is because it is possible to achieve better hole cleaning with compressed air, hence reducing the tendency of cuttings to clog the formation. The aerated drilling fluid has a lesser density than normal mud, hence causing less formation damage. In some cases water is used to drill with high viscous polymer sweeps, used when making connections. The aim in both cases is to reduce the formation damage by having as few cuttings and other solids getting into the formation as possible (Hole, 2006).

Designing a drilling fluid to help reduce formation damage involves appreciation of the well's drilling window, which is the margin between the fracture and pore pressure, shown in Figure 3. As a drilling practise, wellbore pressure should always be greater than pore pressure, both in static and dynamic conditions. However, it should not surpass the fracture pressure gradient; otherwise, costly drilling challenges

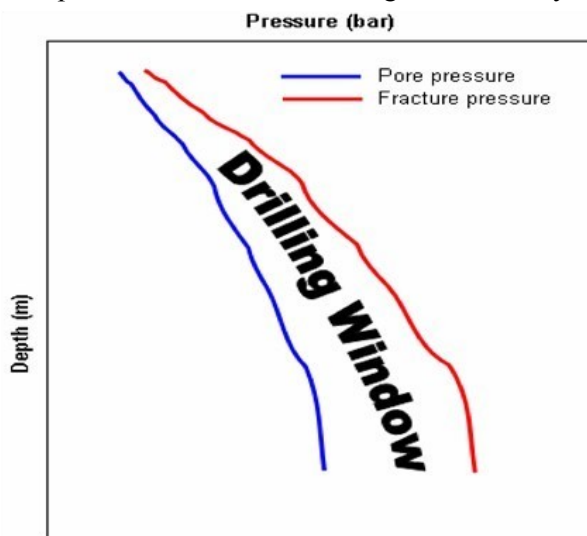


FIGURE 3: Drilling window
(Rahimove, 2009)

such as loss of circulation and formation damage occur. Geothermal reservoirs are characterised with subnormal pore pressures. Hence, the drilling window is wider. The tighter the drilling window, the tougher the drilling will be (Vollmar et al., 2013). However, when drilling the main hole, pressures below the pore pressure are desired in order to reduce formation damage. Hence, aerated drilling is used to achieve this.

2.3.4 Maintain borehole stability

The aim of drilling is to create a pathway in the ground to access a given resource; in a geothermal system, the resource is hot fluid from the ground. This may require drilling to depths ranging from 500 m to 3000 m or beyond. It is important to keep this path, borehole, intact as we drill on. This is done by casing the various well sections and cementing them. However, prior to casing and cementing, there is still need for well stability. The drilling fluid provides this stability.

In an undisturbed formation, the rock matrix and the pore pressure are able to withstand the overburden pressure. When a borehole is made in this system, an imbalance of forces is created. There will be a net tangential force which tends to cause the formation to move to fill the new cavity formed. This increases with depth due to the increase in overburden pressure. The diagrams in Figure 4 illustrate the scenarios before, during, and after drilling (Ava, 2004).

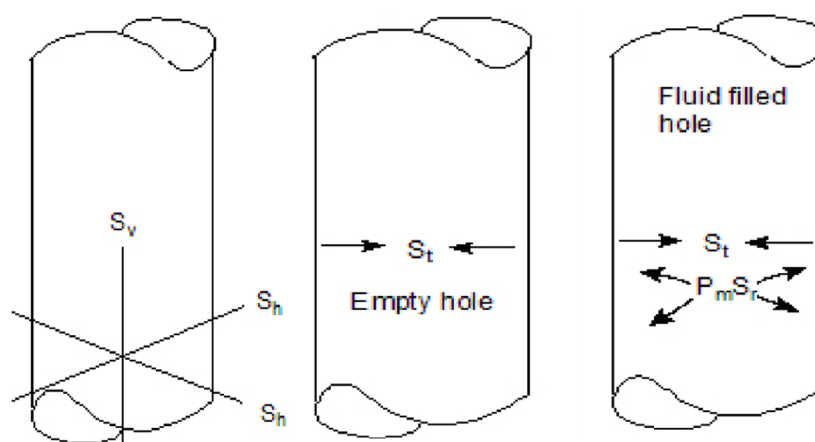


FIGURE 4: Stress conditions in a borehole (Ava, 2004)

The drilling fluid provides a radial pressure which balances against the instability created in the formation due to the borehole. The density of the drilling fluid is a key factor of this radial pressure. In some cases, barite or other inert solids are added to the drilling fluid in case of an over pressurised formation (Ava, 2004).

An unstable formation is also caused by fluid seepage from the borehole into the formation. Drilling fluids, such as bentonite, form an impermeable layer on the wall of the borehole which reduces the seepage. This is of great significance in clay formations (Chemwotei, 2011).

2.4 Drilling fluid equipment

The drilling fluid equipment forms the circulation system of the rig and is mainly used for applying pressure on the fluid and providing a channel for fluid to flow. The basic setup is made up of mud pits, mud pumps, mud mixing equipment and contaminant removal equipment. The mud pumps provide the pressure needed for the drilling fluid to flow through this system into the well and up with the cuttings. The selection of the pumps will depend upon the hydrostatic pressures expected to be handled during the drilling process.

In aerated drilling, an additional system is included, depending on the type of gas to be used. Most geothermal drilling uses aerated water and foam with two primary compressors and one booster.

2.4.1 Criteria for selection of drilling fluid equipment

The key equipment in the drilling fluid system is the mud pump. This is responsible for supplying the hydraulic pressure needed to move the drilling fluid from the pump through the entire drill string, and back to the mud tanks. Figure 5 illustrates the sum of the pressures that constitute the pressure to be supplied by the pump (Baker Hughes, 1995). Pumps are rated for hydraulic power, maximum pressure and maximum flow rate. Any of these can be used for our design criteria in selecting our pump. Once the drilling program is known, it is possible to determine the required flow rates and pressure in drilling the various well sections. Of significance is that the pump must supply adequate flow to achieve the required annular velocity for effective hole cleaning.

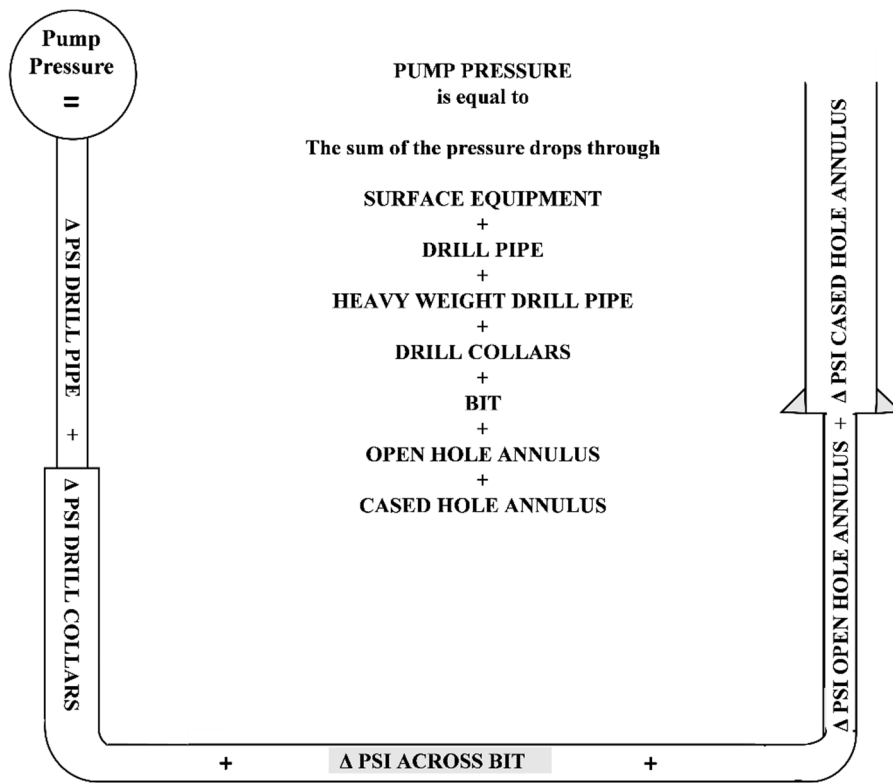


FIGURE 5: Pressure loss in a pump (Baker Hughes, 1995)

The required pump flow rate is calculated based on annular volumes and required up flow velocity (Lapeyrouse, 2002).

$$Q = \frac{(D_h^2 - D_p^2)}{24.5} * v \quad (38)$$

where D_h = Well or casing diameter (m);
 D_p = Outside diameter of drill pipe (m); and
 v = Desired annular velocity (m/s).

The ideal minimum velocity when using mud is 0.3 m/s and while using water is 0.7 m/s (Chemwotei, 2011).

The flow rate required is calculated for the various well sections and the maximum flow rate required is then used to select the pump. Another significant parameter is the pump pressure rating; this should normally be at least 1.5 times the total pressure losses, which are illustrated in Figure 5. The pressure losses are comprised of:

$$p_{total} = p1 + p2 + p3 + p4 + p5 \quad (39)$$

where $p1$ = Losses through surface equipment;
 $p2$ = Losses through drill pipe/drill collars;
 $p3$ = Losses through the rock bit;
 $p4$ = Losses between the outer diameter of the drill pipe and drill collar, and wall of the hole; and
 $p5$ = Losses in the mud motor (when used, e.g. directional drilling).

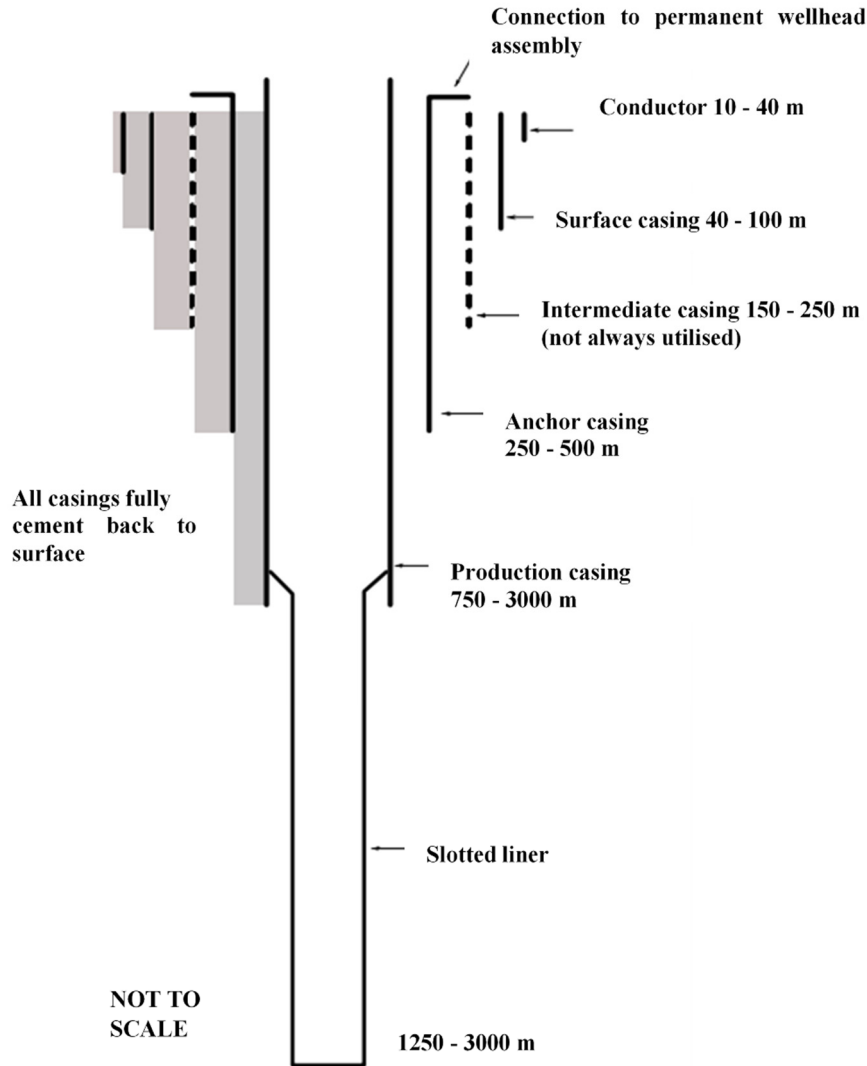


FIGURE 6: Well profile (Hole, 2007)

The pressure losses have the form (Gabolde and Nguyen, 2014):

$$p = NB \quad (40)$$

Calculation for N in the drill string is given by:

$$N = \frac{LQ^{1.8}}{901.63D^{4.3}} \quad (41)$$

Calculation for N in the annulus is given by:

$$N = \frac{LQ^{1.8}}{709.96(D_o + D_i)^{1.8}(D_o - D_i)^3} \quad (42)$$

where p = Pressure loss (kPa);
 N = Pressure losses for pure water;
 B = Coefficient corresponding to circulating mud;
 D_o = Annulus outside diameter (in);
 D_i = Annulus inside diameter (in);
 Q = Drilling fluid flow rate (l/min); and
 L = Length of drill string (for N in drill pipe is the length of the drill pipe for the drill collar and surface equipment) (m).

The coefficient B corresponds to circulating mud and is given by:

$$B = d^{0.8}\mu_p^{0.2} \quad (43)$$

Pressure loss in bit nozzles P_d is given by:

$$P_d = \frac{dQ^2}{(2959.41)(0.95^2 A^2)} \quad (44)$$

Hence, we get:

$$P_{total} = (N_1 + N_2 + N_3 + N_4 + N_5)B + P_d d \quad (45)$$

where d = Specific gravity (kg/l);
 μ_p = Plastic viscosity (cP);
 A = Area of nozzles (in²);
 N_1 = Pressure loss coefficient in the surface equipment;
 N_2 = Pressure loss coefficient in the drill pipe;
 N_3 = Pressure loss coefficient in the drill collar;
 N_4 = Pressure loss coefficient in the hole/drill collar annulus; and
 N_5 = Pressure loss coefficient in the hole/drill pipe annulus.

Once these are calculated, the pump power required is calculated from:

$$P_{power} = \frac{pQ}{600\eta_m\eta_t} \quad (46)$$

where P_{power} = Pumping power (kW);
 p = Pump discharge pressure (bar) = 1.5* P_{total} ;
 Q = Fluid flow rate (l/min);
 η_m = Pump mechanical efficiency, assumed to be 0.85; and
 η_t = Transmission efficiency, assumed to be 0.9 (for motor).

It is important to note that these losses depend upon fluid viscosity, density and the flow rate, so we must consider this effect as we design the fluid. Higher flow rates, viscosities and density imply higher pressure losses, hence a more expensive drilling fluid system. The system losses are normally higher for turbulent flow than for laminar flow; turbulent flow occurs at high velocity and smaller annular space, while laminar flow tends to occur at lower velocities. From the above calculations, we can select the right pump for the drilling activities.

2.5 Drilling fluids and challenges in geothermal drilling

Drilling challenges vary in type and severity depending upon the well. However, the main challenges encountered in most situations are stuck pipe, loss of circulation and well control. Most of these challenges are due to the geology of the formation.

Drilling challenges can either be due to formation challenges or equipment failure. The most difficult challenges are normally those associated with the formation since many times we are not able to see what is in the formation and have to rely on the data to try and visualise the actual situation in the borehole. One of the worst challenges is a stuck pipe situation. Many times this leads to loss of drilling time, expensive fishing operations, formation damage and possibly a loss of the drill string. Apart from depleting the moral of the crew, a stuck pipe leading to fishing operations normally escalates the price of the well. As such, any well advised drilling team will do all in its power to avoid a stuck pipe situation. Appreciation of drilling fluids and their interaction with various formations can help save a stuck pipe situation from escalating.

2.5.1 Loss of circulation

This is the total or partial loss of drilling fluids due to highly permeable zones, cavernous formations and natural or induced fractures during drilling. Often this affects well control, borehole stability and may lead to formation damage. Loss of circulation is often dependent on how the drilling fluid interacts with the formation during the drilling process. The main causes are:

1. Formation pore spaces are too large, or the particles in the fluid are too small to allow filter cake formation;
2. Hydrostatic pressure is sufficient enough to force wellbore fluids into the pore spaces;
3. Hydrostatic pressure causes a natural fracture to open up and take wellbore fluid; and
4. Hydrostatic pressure induces fractures in weak formations.

From the above causes, we notice that most of them are related to the hydrostatic pressure, which is a property of the drilling fluid, highlighting the significance of drilling fluids in managing loss of circulation challenges. There are other causes related to how fast the drill pipes or casings are run in hole, among other things (Baker Hughes, 1995).

The severity of the loss is classified by the volume of fluid loss per unit time: seepage losses with losses of up to 1.6 m³/hr; partial losses with losses ranging from 1.6 m³/hr to 79 m³/hr; complete losses when no returns are got on surface. In order to determine the right treatment for the drilling fluid to heal the loss, we must identify the type of loss zone. The table below describes the common loss zones and the possible type of losses (Ava, 2004).

TABLE 1: Loss zones

Loss zones	Type of loss
Porous and permeable sands and gravel	Losses start as a gradual reduction in pit volume. If drilling proceeds, the losses could become complete. These zones usually occur near the surface.
Natural fractures	May occur in any type of rock. Usually these losses are partial but may progress to complete loss as drilling proceeds or if the fluid density increases.
Induced fractures	Sudden and complete losses.
Vugular formations	Usually located in limestone. Losses here can be sudden (located at the bit) and complete. On occasion, the bit may drop a few inches before the loss.

Losses in geothermal drilling are mostly due to encountering permeable zones or fractures, either natural or induced. There are several ways of handling loss of circulation, and many loss-of-circulation materials have been developed to suit various situations. However, in general the action taken depends upon the location of the loss zone within the well.

There are various loss-of-circulation policies applied in various situations, but the general tendency is to switch to water and drill blind whenever a complete loss is encountered. Minor or seepage losses can be controlled by adding 10-60 kg/m³ of LCM to the drilling fluid. Increasing the quantity of LCM can be done to tackle higher losses. However, if the loss persists, then three main options can be explored:

1. Drill on blind with water;
2. Switch to aerated drilling; and
3. Stop and plug the well.

Table 2 gives a summary of some actions that can be taken to handle losses:

TABLE 2: Loss of circulation policy

Severity of loss	Loss section	Action
Seepage losses with losses of up to 1.6 m ³ /hr	Upper well section	Add LCM to the drilling fluid, ranging from 10 to 60 kg/m ³ .
	Main hole	Usually this section is drilled with water or aerated fluids. Continue drilling but spot polymer pills at every connection.
Partial losses from 1.6 m ³ /hr to 79 m ³ /hr	Upper well section	115-230 kg/m ³ of LCM is spotted in pill form.
	Main hole	Switch to aerated drilling or drilling on with water but spot polymer pills at every connection.
Complete loss	Upper well section	230-430 kg/m ³ of LCM is spotted in pill form. If loss persists, consideration of stopping the drilling to plug the loss zone should be looked into, to avoid hole cleaning challenges which could lead to stuck pipe.
	Main hole	Switch to aerated drilling or continue drilling with water and polymer pills at each connection. Proper hole cleaning and wiper trips should be done before any new connection.

The treatment given to loss of circulation in the main hole is applied in a manner such as to avoid any clogging of the cavities, since they are key to the well's production. Often the tendency is to drill blind. Hole cleaning challenges are handled by high viscosity polymer sweeps.

2.5.2 Stuck pipe

Stuck pipe can be described as a situation where both axial motion and sometimes rotary motion of a drill string in a borehole is lost. This, at times, may be accompanied with blocking of the bit such that circulation through the drill pipe is not possible. There are several causes of stuck pipe, however, most are due to geological challenges which are dependent on the nature of the formation. The most common formation challenge is instability. An unstable formation for whatever reason is more likely to cave in on the drill string and possibly lead to a stuck pipe. The other common cause of stuck pipe is poor hole cleaning situations, either due to loss of circulation or poor drilling fluid design and differential sticking.

Differential sticking is a result of the drill pipe getting stuck on the wall of the well. This is due to the formation of a sticky layer called a filter cake. The filter cake is a good property of any drilling fluid

because it prevents losses of the drilling fluid. However, there is a limit to the thickness that is considered beneficial (Bourgoyne et al., 1991).

The best solution to handling stuck pipe is to avoid any stuck pipe situations. This can be done by keenly monitoring well lithology to appreciate the formation. Drilling parameters such as ROP, formation pressures, drilling fluid properties and losses are some of the key things to be checked. The common indication of an abnormality is an increase in torque during drilling, or an over pull encountered when tripping out of the hole. Proper data collection and interpretation is a sure way to minimize stuck pipe situations or to quickly solve such situations.

The role of drilling fluids in handling stuck pipe is more important in the prevention of stuck pipe than in freeing the stuck string or retrieving the fish. Since most stuck strings are due to formation challenges, it is important to appreciate the type of formation being drilled through, before redesigning the drilling fluid to combat it. The main types of problem formations are:

1. Erodible formations: These include soft tertiary sequence evaporates, permafrost and some highly fractured formations; these could also include unconsolidated formations of sand and gravel. Erosion of these formations may lead to an over-gauge borehole which leads to poor hole cleaning, one of the causes of stuck pipe. In some cases, if the formation is fractured, this could lead to slippage and, hence, stuck pipe.
2. Geo-pressured formations: These are formations with pore pressures higher than the hydrostatic pressure of the drilling fluid. These, if not permeable, tend to cave into the borehole once drilled through.
3. Dipping formations: These are formations that lie at an angle to the horizontal plane being drilled through. The challenge with this is if they are plastic (more common in slates and shales), they end up being mobile and flow into the borehole when drilled through.
4. Reactive formations: These are naturally occurring bentonitic shales which contain clays that react with the mud filtrate and hydrate. The hydrated shells then fall and swell into the borehole.

Other formation-related challenges could include collapsing cement blocks from an upper cased section and green cement (Ava, 2004).

2.5.3 Well control

Abnormal formation pressures are rarely encountered in geothermal systems. However, this still remains an area that must be watched in order to ensure proper well control. Most times, the drilling fluid pressure exceeds that of the formation in geothermal drilling. However, when drilling using aerated fluids, the density of the drilling fluid is reduced, and then the formation fluid pressure exceeds the drilling fluid pressure.

One of the challenges encountered in well control in geothermal drilling is poor cooling of the well, leading to high temperatures and, hence, high pressures. This may occur when there is continuous loss or a sudden total loss of circulation (Moore, 1974).

A key issue in well control is monitoring the drilling fluid to keep losses minimal and keep the drilling fluid pressure as near to the formation pressure as possible. This requires knowledge of the formation pressure. One way of estimating the formation pressure is using the d exponent, a dimensionless number. The d exponent is related to the differential pressure between the drilling fluid and the pore fluid. This value is used to adjust the drilling fluid density. The d exponent usually increases with depth but, as the formation becomes over pressured, it will decrease (Moore, 1974). The d component is given by:

$$d_{exp} = \frac{\log\left(\frac{R}{60N}\right)}{\left(\frac{12W}{1000d_b}\right)} \quad (47)$$

where R = ROP;
 N = Rotary RPM;
 W = Force on bit;
 d_b = Bit diameter; and
 d_{exp} = Drilling exponent.

The d_{exp} is corrected for the effect of mud density changes, as well as changes in WOB, bit diameter and rotary, as follows (Moore, 1974):

$$d_{mod} = d_{exp} \frac{\rho_n}{\rho_e} \quad (48)$$

where ρ_n , the mud density, is equivalent to a normal pore pressure gradient and ρ_e is the equivalent mud density at the bit while circulating. The new d_{mod} is then used to calculate the equivalent mud density at that differential pressure and, finally, the formation pressure from the following equations:

$$\rho_e = 7.65 \log[(d_{mod})_n - (d_{mod})_{abn}] + 16.5 \quad (49)$$

$$P_f = 0.052 * \rho_e \quad (50)$$

where ρ_e = Is the equivalent mud density at the bit while circulating;
 $(d_{mod})_n$ = Equivalent mud density at the normal pressure;
 $(d_{mod})_{abn}$ = Equivalent mud density at abnormal pressure.

Once the formation pressure is determined, we compare it with the fluid density and adjust accordingly.

3. DRILLING FLUID DESIGN FOR DRILLING A 2500 M GEOTHERMAL WELL

The main interest in drilling a geothermal well is to access the steam resource located several hundred meters down, or more. To do this, we must drill through sections that are of less significance and may even block the producing reservoir with colder fluids. The most important part of the well is the steam zone, normally called the main hole. This is the area believed to be producing the required steam in the well. Wells normally have four main sections: surface hole, anchor hole, production hole and main hole. The first three sections are normally cased using steel casings and cemented off to seal off unwanted aquifers and also to stabilize the area as we drill on. The main hole, which can run from 800 m to 1500-3000 m depending on the well prognosis, is normally set with slotted liners. Figure 6 illustrates a 3000 m well casing design for a regular size well (Hole, 2006). There are many methods for determining the casing depths. However, as a general rule, the depths are set such that at least 1/3 of the entire well drilled is cased.

A typical well design would include:

Conductor casing: 30" set at a depth of 24 m, either driven or drilled.

Surface casing: 20" casing setting 26" diameter hole, drilled to 100 m depth.

Anchor casing: 13 3/8" casing set in a 17 1/2" hole drilled to 300 m depth.

Production casing: 9 5/8" casing set in a 12 1/4" hole drilled to 850 m depth.

Open hole: 7" slotted liner set in an 8 1/2" hole drilled to 2500 m – total depth.

Once the well design is done, the next stage is to identify the drilling fluid to be used and prepare an appropriate drilling fluid program.

3.1 Drilling fluid materials and properties

The final desired property of any drilling fluid will determine the materials it constitutes. As earlier discussed, the constitution of a drilling fluid is guided by optimising costs and performance; these are considered optimal when we have good hole cleaning and lowest circulation system pressure losses. Other issues, such as loss of circulation, are best handled when they arise. But, at the design stage, a guide is made on how to handle them. To optimise a fluid for hole cleaning and least pressure drop, we must appreciate the fluid's rheology, which describes the behaviour of a fluid when a force is applied to it. Once we characterise this behaviour, we can select what materials to add to our drilling fluid to improve upon its performance in hole cleaning and minimizing pressure drop.

The behaviour of fluids under force/stress can be characterised as: Newtonian - where the shear rate increases linearly with shear stress; these fluids include water and oil; non-Newtonian, which exhibit a non-linear relationship between shear stress and the shear rate. The behaviour of Newtonian fluids is undesirable in drilling as it leads to higher pressure loss in the system, due to increased viscosity, and also poor gel strength, which is key in hole cleaning. To correct these problems, various materials can be added, depending on which property is being corrected. The main properties checked are viscosity, yield point and gel strength (Darley and Gray, 1988).

Non-Newtonian fluids can be classified into four different types, depending on the additives. For geothermal drilling, the main additives are either bentonite or polymer, which are viscosifiers, leading to either a Bingham plastic fluid or pseudo-plastic / power law fluid. These fluids display a zero shear rate at the initial change in shear stress, after which the relationship is either linear or non-linear (Darley and Gray, 1988). Figure 7 illustrates the behaviour of various drilling fluids (Darley and Gray, 1988):

As can be seen, Newtonian fluids do not exhibit the gelling property required. Bentonite-based mud normally exhibits a Bingham-plastic fluid model, which has a higher viscosity and high yield strength; the yield strength is a measure of its gelling strength. This is important for suspending cuttings when circulation stops. The water-polymer drilling fluid exhibits a power law of behaviour which has poorer gel strength but lower viscosities. However, increasing the concentration of polymers, such as starch in bentonite, results in a Dialant behaviour, in which there is an adverse rise in fluid viscosity (Darley and Gray, 1988).

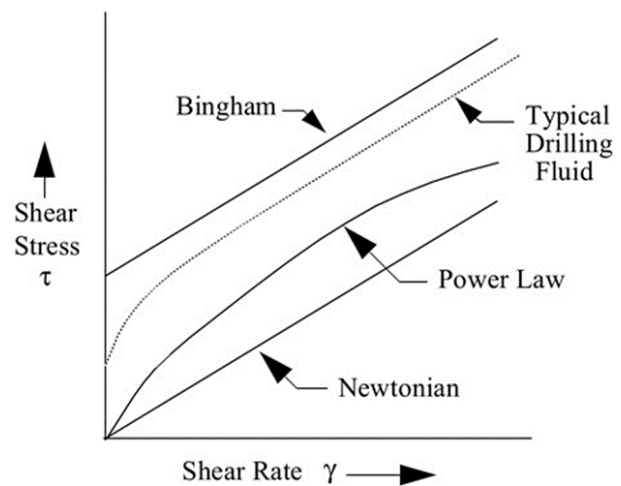


FIGURE 7: Fluid rheological behaviour
(Baker Hughes, 1995)

Another key area in designing a fluid system is its flow regime. A fluid flow can be categorised as: plug flow, laminar flow, transitional flow or turbulent flow. The fluid's flow regime affects both the cutting carrying capacity and pressure losses in the system. In general, laminar flow leads to lower pressure loss but poorer hole cleaning. Turbulent flow leads to better hole cleaning but higher pressure losses.

From this we see that any drilling fluid design must consider viscosity, yield and gel strengths, and the density of the fluid.

3.1.1 Viscosity

Viscosity is a description of the thickness of a drilling fluid and, hence, its resistance to motion. It is normally measured in centipoises. In the field, it is a common practise to measure viscosity in terms of funnel viscosity, (secs/qt), which is how long it takes one quart of fluid to pass through the funnel. This gives a view of how thick a fluid is, but is not used in calculations regarding viscosity. For Bingham fluids (water-bentonite), we use plastic viscosity, which is the viscosity at which the fluid is past its yield point. This is measured using a viscometer. Figure 8 shows a Bingham plastic Rheogram.

Plastic viscosity is calculated once the viscometer readings at RPM of 300 and 600 are taken.

$$PV = \theta_{600} - \theta_{300} \quad (51)$$

$$YP = \theta_{300} - PV \quad (52)$$

where PV = Plastic viscosity, (cP);
 YP = Yield point (dynes/cm²); and
 $\theta_{600}, \theta_{300}$ = Dial readings at 600 and 300RPM.

This relationship is true whenever bentonite is used as the viscosifier. However, the introduction of other additives, such as starch polymers, leads to a more complex drilling fluid which is best analysed by the power law model (Baker Hughes, 1995).

Viscosity decreases with an increase in temperature, but increases with cuttings content. For geothermal drilling from various field results, a plastic viscosity of 10-20 centipoises is found appropriate for hole cleaning (Finger and Blankenship, 2010). This can be varied to optimise between hole cleaning and pressure drop.

Efficient removal of solids at the surface is important in reducing the solid contents of a fluid. There are graphs that illustrate the effect of total solid content on viscosity; these should be used when designing for viscosity.

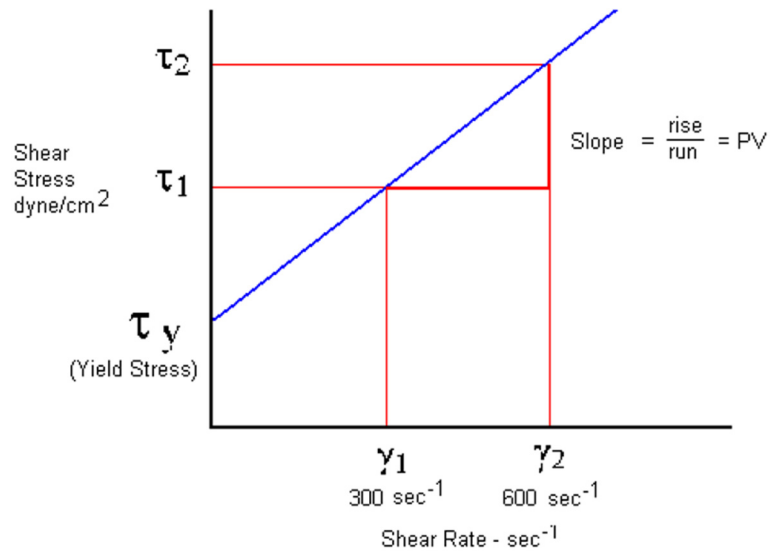


FIGURE 8: Bingham plastic rheogram (Ava, 2004)

3.1.2 Yield point and gel strength

This behaviour indicates a resistance to flow until a certain minimum shear stress, the yield stress of the fluid, is reached. Every fluid exhibits this behaviour, at least some minimal value. This property determines the yield and gelling strengths of a fluid, properties which are of great significance in cutting carrying and suspension. The suspension is more important when circulation stops, so that the fluid can suspend the cuttings till circulation resumes; this property is not exhibited by water and is one key area where bentonite plays a major role. Bentonite and other clays, when mixed with water, result in a Bingham fluid with a higher gelling and yield point, as illustrated in Figure 7. Polymers, on the other hand, have poorer gelling properties. There is, however, a limit to the useful value of gelling; very high gel strength implies higher pressures needed to break the fluid to start flowing.

Hence, bentonite is often mixed with starch to reduce its gelling property to acceptable limits. Increased solid content leads to higher gel and yield strengths; efficient surface removal should be maintained to reduce this (Skalle, 2011). Yield strengths of 35-125 kPa are common in geothermal drilling (Finger and Blankenship, 2010).

3.1.3 Density

When designing for fluid density in geothermal drilling, we must appreciate that most geothermal systems have pore pressures lower than hydrostatic pressure, implying that we need to keep our density as low as possible. However, low density has two main disadvantages: lower cutting carrying capacity, and poorer filter cake formation. Filter cake is of high importance in geothermal drilling since we need to form a slight impermeable layer to reduce fluid loss into the formation during drilling; loss of drilling fluid is quite costly and can also lead to formation damage (Darley and Gray, 1988).

It is common to use a density ranging from 1.00 to 1.15 g/m³ in geothermal drilling (Finger and Blankenship, 2010). However, if higher densities are needed, then barite is the most common material used as a densifier. A good understanding of the formation pressures expected is paramount in designing for density. The formation pressures can be estimated. Aerated drilling is one significant way of reducing the density of the fluid. This is employed in drilling the main hole. However, generally the lower the solids content of the drilling fluid, the lower the viscosity. Therefore, the surface removal system is key. Table 3 is a summary of the key drilling fluid properties and their values for geothermal drilling (Finger and Blankenship, 2010).

To achieve the parameters shown in Table 3 and keep within the desired range, a good mixing must be undertaken and keen monitoring of the fluid maintained. The graph in Appendix III shows the relationship of water-based bentonite, density, yield point viscosity and solid contents. Wyoming bentonite is normally used in geothermal drilling; this is because it has the highest yield, hence does not result in a high increase in fluid density, compared to other clays. This is illustrated in the graph in Appendix III.

TABLE 3: Fluid properties

Property	Range
Density	1.03-1.15 g/m ³
Funnel viscosity	35-55 Sec
Plastic viscosity	0.01-0.02 Pa-s
Yield	35-125 kPa
pH	9-10

3.1.4 Drilling fluid materials

These are added to the base fluid, water, to achieve specific properties for a given purpose. The main additives to water are weighting agents, viscosifiers, filtration control, LCMs, and conditioners for pH control materials. Geothermal fluids are normally simply, constituted of the base fluid-water, viscosifiers, either bentonite or polymer, and conditioners, usually caustic soda (Ava, 2004) (Table 4).

3.2 Calculation of key drilling fluid parameters

A drilling fluid program forms part of a well's drilling program and is simply a guide on the preparation and utilisation of the proposed drilling fluids for the various well sections. It is normally prepared by the drilling engineer with knowledge of the well's prognosis. The key part of the drilling program is determination of the drilling fluid parameters to be used when drilling the various well sections. This is important for good hole cleaning, minimising pressure drop in the system and optimising bit hydraulics. Here, we shall assume a regular well with a profile as described at the beginning of Section 3. The aim is to determine the drilling fluid parameters to be utilised for good

whole cleaning, minimal pressure drop and optimised bit hydraulics. The equations described in the preceding sections will be applied. The following will be determined:

1. Minimum annulus velocity effective hole cleaning for the various well sections;
2. Minimum flow rate for the required annulus velocity for the various well sections for when using either mud or water;
3. System pressure drop;
4. Equivalent circulating density for the various well sections;
5. CCI and C_a ; and
6. Summary.

TABLE 4: Drilling fluid additives

Type	Description/function	Material
Densifier	These are compounds dissolved or suspended in the drilling fluid to increase its density; can be any substance denser than water.	Commonly used is barite.
Viscosifiers	Improve on the drilling fluid viscosity, hence enhancing drilling fluid's ability to remove cuttings from the wellbore and to suspend cuttings and weight materials during periods of no circulation.	Mainly used in geothermal is bentonite; polymers are also used, however they lack gel strength, so do not suspend cuttings.
Filtration control material	These reduce the amount of filtrate lost from the drilling fluid into a subsurface formation.	Bentonite, polymers, starches, and thinners or defloculates; all function as filtration-control agents.
Conditioners	These are alkalinity and pH-control additives which are used to optimize pH and alkalinity in water-base drilling fluids.	NaOH, KOH, $\text{Ca}(\text{OH})_2$ and $\text{Mg}(\text{OH})_2$.
LCM	These can be broadly defined to include any material that seals or bridges against permeable or fractured formations to inhibit the loss of whole drilling fluid.	In geothermal drilling, the most common is mica flakes.

Assumptions:

1. Mud density of 1150 kg/m^3 is used for mud drilling and water density of 1000 kg/m^3 ;
2. Turbulent flow is assumed;
3. Drill pipe size of OD 5" is used in the calculations;
4. Aerated drilling commences in the main hole; and
5. The upper well section is drilled using either water or mud; no aerated drilling.

Steps of calculation:

1. Calculation of minimum annular velocity: Section 2.3.1 will be used to calculate the minimum annular velocity required for effective hole cleaning for the various well sections.
2. The minimum flow rate for the drilling fluid to achieve the minimum velocity is then calculated.
3. Calculate cuttings carrying index, and cuttings concentration ratio.
4. Calculate the ECD (equivalent circulating density) and BHCP (bottom hole circulation pressure).
5. The results of these are shown in Tables 5 and 6.

Results and analysis:

TABLE 5: Fluid parameters

Hole diameter (inches)	Hole depth (m)	Water: MW=1, Viscosity = 1.17 cP		Mud: MW=1, Viscosity = 15 cP		CCI	R_t	C_a
		Annular velocity (m/s)	Flow rate (l/m)	Annular velocity (m/s)	Flow rate (l/m)			
26"	100	0.7	13000	0.48	9500	1.5	0.65-0.78	0.021
17-1/2"	300	0.7	7980	0.5	5700	1.7	0.63-0.7	0.015-0.023
12-1/4"	850	0.7	4650	0.5	3618	1.6	0.67-0.78	0.011-0.017
8-1/2"	2500	0.78	2044	-	-	1.6	0.73	0.013

TABLE 6: Fluid parameters

Hole diameter (inches)	Hole depth (m)	Water: MW = 1, Viscosity 1.17 cP		Mud: MW = 1.15, Viscosity = 20 cP		CCI	R_t	C_a	ECD	BHCP
		Annular velocity (m/s)	Flow rate (l/m)	Annular velocity (m/s)	Flow rate (l/m)					
26"	100	0.7	13000	0.4	6620	-	0.55-0.78	0.021-0.053	-	-
17-1/2"	300	0.7	7980	0.3	2898	1.4	0.52-0.7	0.015-0.055	9.6	33
12-1/4"	850	0.7	4650	0.26	1560	1.3	0.45-0.78	0.011-0.058	8.36	83
8-1/2"	2500	0.78	2044	-	-	1.3	0.73	0.013	8.59	252

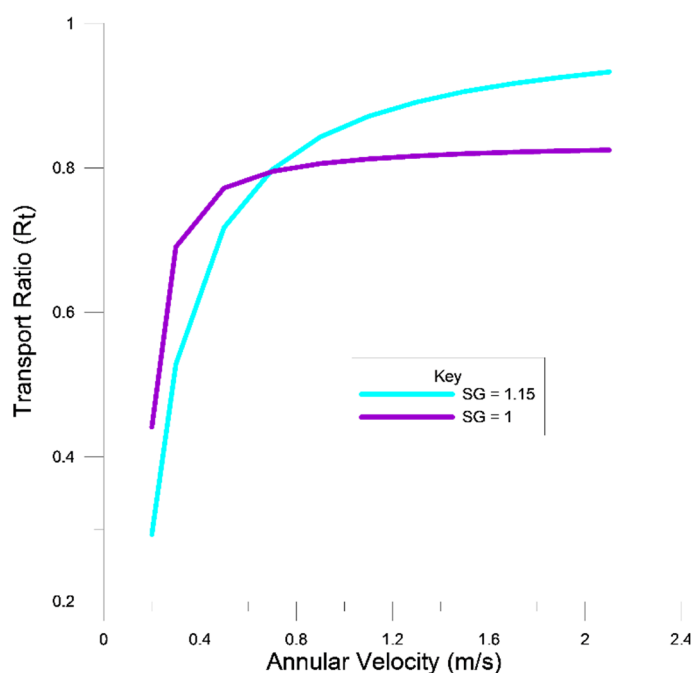


FIGURE 9: Graph of annular velocity vs. transport ratio

Discussion of tables

From Tables 5 and 6 we see the effects of changes in viscosity and density of mud on the various drilling parameters. Assuming a fixed size of the cuttings generated, we can compare the annular velocity, density and viscosity to the R_t , CCI, C_a , ECD and BHCP.

Transport ratio, R_t vs. annular velocity and density

This is an indication of hole cleaning efficiency and helps to indicate whether the annular velocity selected is sufficient to move the cuttings out of the hole for trouble-free drilling. As discussed earlier, this ratio should not be less than 0.5 for trouble-free drilling. From the two tables, we notice that an increase in annular velocity results in an increase in the transport ratio, well above the minimum of 0.5, and an increase in fluid density and viscosity equally results in an increase in the transport ratio. A plot of annular velocity against transport ratio is

shown in Figure 9. The plots show the effects of density on R_t . It is, however, important to note that this increase in density must not be due to an increase of solid particles (cuttings) in the fluid, but as a fluid property in itself. This effect of density is important, more in the upper well sections. Where achieving the high flow rates for the required annular flow rates is difficult we can, instead, design a fluid with higher viscosity and density to increase the transport ratio.

Transport ratio vs. cuttings concentration

These two have an inverse relationship such that the increase in one leads to a reduction in the other. This creates a dilemma in selecting the fluid parameters and properties. From the results, it is clear that the increase in density and viscosity results in a reduction in C_a , yet the same results in an increase in R_t , due to a reduction in flow rates. Figure 10 shows plots illustrating this.

Flow rate vs. ECD and BHCP

The flow rate used is dependent upon the annular velocity and the well cross-section. If the cross-section is kept constant, the only variable we have is annular velocity. The higher the annular velocity required, the higher the flow rates needed. The annular velocity, as shown earlier, depends on the cuttings' slip velocity. If we have higher annular velocity and flow rates, we end up with higher ECD and eventually BHCP. This is because the pressure losses in the system are dependent on flow rate, density and viscosity of the fluid. The higher these parameters are, the higher the losses and pumping costs will be. In addition, higher BHCP implies higher chances of loss of circulation and formation damage.

3.3 Air and aerated drilling fluid

Aerated drilling is used in geothermal drilling with the aim of reducing the formation damage resulting from increased drilling fluid pressure on the formation wall. As drilling progresses, the density of the fluid increases because of cuttings and other solid content in the fluid; this increase results in higher BHCP with depth. Figure 11 shows a typical well, indicating the drilling window and the effect of increased mud density (Vollmar et al., 2013). Introduction of air in the fluid helps lower the density and

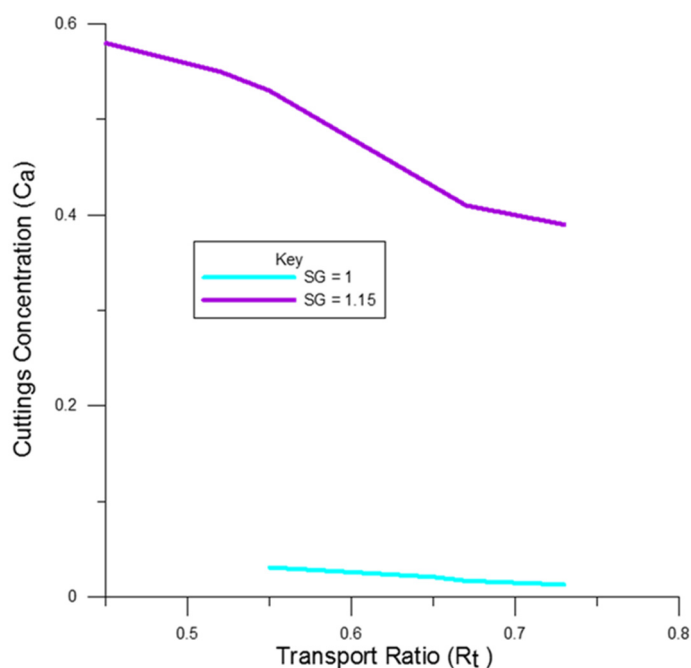


FIGURE 10: Graph of transport ratio vs. cuttings concentration

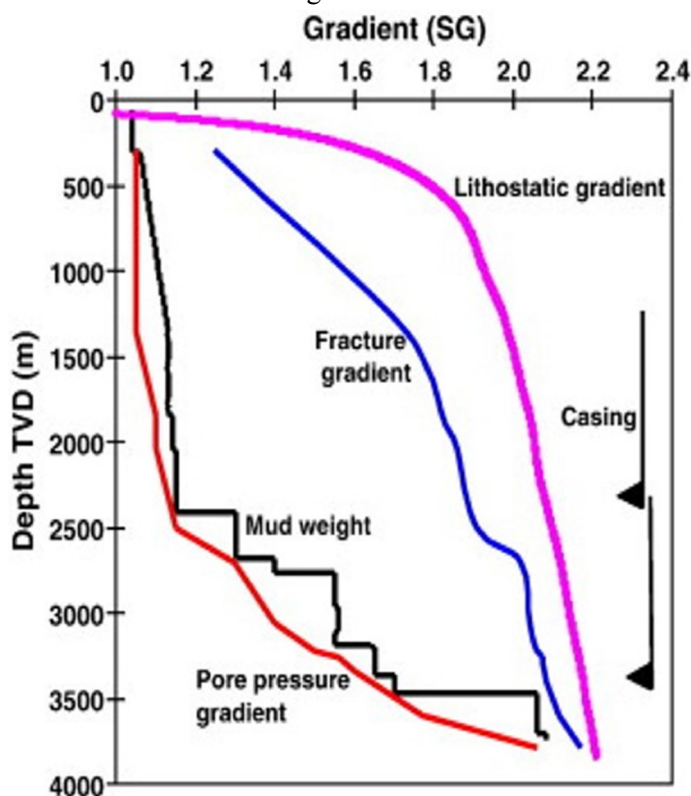


FIGURE 11: Drilling window (Vollmar et al., 2013)

subsequently reduces the damage on the formation.

As can be seen in Figure 11, the higher the fluid density, the greater the formation damage. When drilling the main hole, the tendency is to try and keep the fluid pressure below the pore pressure, which results in an underbalanced system. The ratio of air to water pumped into the hole, and the back pressure applied to the 'exhaust' or flow line from the well, allow the down-hole pressures in the hole to be 'balanced' with the formation pressure in the permeable zones, thus allowing for the return of the drilling fluids to the surface and, therefore, maintaining drilling fluid circulation. In fact, the term 'under-balanced' drilling, as applied to this form of geothermal drilling, is a misnomer (Hole, 2006).

Several graphs have been developed (Lyons et al., 2009), based on the criteria described earlier in the hole cleaning section, for selecting the minimum volumetric flow rates for various well profiles. One such graph is shown in Appendix IV. These can be used in selecting the adequate velocity for the well profile.

For aerated drilling, we must have knowledge of the formation pressures so that we intentionally design the drilling fluid to have lower pressure at the desired points. We first design for the minimum flow rate for optimum hole cleaning, as earlier described. Then we select the appropriate air flow rates for the system's mud flow rate at the desired depth. As to whether we achieve the desired underbalanced drilling can only be assessed by comparing the formation pressures at depth to the drilling fluid pressure.

4. CASE STUDIES

4.1 Drilling fluid design – Olkaria-Kenya scenario

Olkaria geothermal field is one of the largest geothermal production fields in Kenya, with over 300 MWe installed capacity. Several deep geothermal wells have been drilled in this field. A study of one of the wells, OW 717, was considered to appreciate the application of drilling fluid design in geothermal drilling. Well OW 717 is a vertical geothermal well drilled to 3000 m TVD. The well has a regular profile and was drilled in a total of 45 days. The parameters used for the various well sections are shown in Table 7 (KenGen, 2012):

TABLE 7: Fluid parameters

Hole diameter (inches)	Hole depth (m)	Water		Mud		Pressure loss (bar)	CCI	C _a	ECD (bar)	BHCP (bar)
		Annular velocity (m/s)	Flow rate (l/m)	Annular velocity (m/s)	Flow rate (l/m)					
26"	100	-	-	0.3	4792	59				
17-1/2"	303.5	-	-	0.3	3600	76	1.3	0.002	9.6	29
12-1/4"	749.5	0.9	3900	-	-	105	3.2	0.003	8.5	84
8-1/2"	3000	2.1	3300	-	-	137	7.3	0.018	8.59	252

Drilling upper well section hole

Drilling the 26" hole in Olkaria was done using water-based bentonite. Because of the larger annular cross-section, this section of the well required higher flow rates in order to achieve the minimum hole cleaning requirements. It is impractical to achieve high pumping rates of up to 10,000 lpm. The solution here was to adjust the drilling fluid to higher density and viscosity, hence lowering the flow rates. This, however, increased the bottom hole pressures encountered. It is common practise to spud with mud of viscosity of up to 15 cP. This is achieved by mixing high yield bentonite, like Wyoming bentonite, with water, commonly used in geothermal drilling.

A look at the CCI and C_a achieved with these parameters indicated excellent hole cleaning. The C_a was well below the maximum allowed for trouble-free drilling, implying an even higher rate of penetration could be achieved before the limit was reached.

The actual drilling parameters for drilling the 12-1/4" and 8-1/2" sections showed higher flow rates and velocities than recommended by previous calculations. The effect was a higher BHCP which could lead to formation damage. The higher pressure losses resulting from the higher flow rates also implied more fuel being utilised and poor bit hydraulics.

Aerated drilling

Aerated drilling in Olkaria is introduced whenever a large loss in circulation is encountered. However, the main well section that is designed for aerated drilling is the main hole section, drilled from the production casing depth to total depth, normally 3000 m. The parameters used are 3300 lpm as the flow rate of water and 1800 scfm.

Loss of circulation policy

Minor losses encountered when drilling the surface and anchor casing are treated by drilling blind and spotting mud pills when making connections. Losses encountered in the production hole are handled by drilling blind if the loss is partial, or switching to aerated drilling in cases of full loss. Plugging is rarely done to heal losses unless the well is suspected to have collapsing formations. The main hole is drilled with aerated water and foam.

4.2 Drilling fluid design – Iceland scenario

Table 8 lists the parameters used when drilling part of well RN-19 in Reykjanes.

TABLE 8: Fluid parameters, well RN-19

Hole diameter (inches)	Hole depth (m)	Water		Mud	
		Annular velocity (m/s)	Flow rate (l/m)	Annular velocity (m/s)	Flow rate (l/m)
26"	84	-	-	-	-
21"	349	-	-	0.8	3600
17-1/2"	746	0.5	4800	-	-
12-1/4"	2500	1.0	3900	-	-

Drilling the upper well section

The surface hole was drilled to a 26" diameter using an air hammer to a depth of 84 m. The rest of the upper well section was drilled using mud with flow rates ranging from between 50 to 60 lps in the 21" hole to 80 lps in the 17-1/2" hole. The flow rates used in drilling the 17-1/2" section were high, indicating the challenge of drilling using water in large well sections. This can be seen in both the theoretical example and the Olkaria drilling scenario. The high flow rate implies higher frictional losses, hence higher BHCP, which leads to formation damage and possible drilling challenges.

Drilling the main hole

In Iceland, unlike Kenya, water is used in drilling the main hole. This was applied in drilling this well with a flow rate of 3900 lpm, giving an annular velocity of up to 1 m/s. Polymer pills were used in each connection to reduce challenges with the cuttings.

Loss of circulation policy

In Iceland, minor losses encountered during drilling are handled by drilling ahead with water and spotting with polymer or bentonite pills in every connection, when drilling the upper well section.

They can also be handled by using LCMs, such as mica flakes, introduced into the drilling fluid. Major losses encountered while drilling the upper well sections are healed by plugging, using cement.

4.3 Comparison and remarks

The key areas to be noted in drilling fluid design are hole cleaning, pressure losses and bit hydraulics. These, when optimised, will highly increase chances of successful drilling at lower drilling fluid costs. From the scenarios studied, the parameters calculated using the minimum annular velocity for hole cleaning resulted in the least pressure losses. This is because minimal flow rates were considered. The low pressure implies less BHCP which reduces formation damage in cases where drilling through a low pressure formation. The low pressure losses also imply less pumping power, hence saving on costs for drilling fluid.

In geothermal drilling, it is important to design a fluid utilising minimum flow rates. As shown above, the increase in pressure loss is highly dependent on the flow rates used, but it is advisable to begin with the minimum required rates for good hole cleaning, and advance to higher rates in case challenges are noted.

The two scenarios studied in Kenya and Iceland drilling used the actual field parameters used in drilling at the different sites. They both indicate parameters close to the theoretical minimum required, apart from in the main hole sections where much higher velocities were used. Whereas these all ensure excellent hole cleaning, as illustrated by the CCI and the C_a , the higher flow rates result in higher pumping pressures, which implies more fuel consumption. The higher pressure losses in the annulus also result in higher BHCP, which may lead to formation damage.

5. CONCLUSIONS

Fluid design is a wide and complex field of study. However, the key issues pertain to good hole cleaning and protection of a well's formation. Application of the hole cleaning principles gives good criteria for optimising the fluid system. It is important to keep the flow rates as near to the theoretical ones as possible to ensure optimal performance. Prior to any fluid design, the engineers must appreciate the formation profile, as well as the anticipated pore pressures and fracture pressures of the well. This will help in understanding the drilling window and in designing the mud. In general, in geothermal drilling, the tendency is to utilise fluid with densities as close to that of water as possible. Using annular velocities of 0.3 – 0.4 m/s for mud and 0.6 – 0.7 m/s for water is appropriate for good hole cleaning. A further study analysing the fluid parameters used in various wells and the formation pressure would be useful to further appreciate the application of the hole cleaning principles described herein.

ACKNOWLEDGEMENTS

I would like to express my deepest gratitude to the Government of Iceland and the United Nations University Geothermal Training Programme for according me the opportunity to undergo this training. My sincere gratitude to the UNU Geothermal Training Programme director, Mr. Lúdvík S. Georgsson, the deputy director, Mr. Ingimar G. Haraldsson, and the entire UNU-GTP staff and lecturers for their great support and assistance throughout the training.

I would also like to extend my gratitude to my employer, KenGen, under the directorship of Mr. Albert Mugo, for granting me the opportunity to come and study. My deepest gratitude to Mr. Sverrir

Thórhallsson of ÍSOR for good guidance and sharing of valuable knowledge and experience throughout my training. I would like to sincerely thank my supervisor from Mannvit Engineering, Mr. Thóroddur Sigurdsson, for his good guidance and technical support throughout my project work.

Special thanks go to all my family members, especially my wife, son and daughter for their moral support.

Above all, I would like to sincerely thank the Almighty God for good care, protection and guidance during the six months training in Iceland.

REFERENCES

Ava, 2004: *Drilling fluids manual*. AVA S.p.A, Rome, Italy, 483 pp.

Azar, J.J., and Samuel, R.G., 2007: *Drilling engineering* (1st ed.). Pennwell Corp., Tulsa, OK, United States, 486 pp.

Baker Hughes., 1995: *Drilling engineering workbook: A distributed learning course* (1st ed.). Baker Hughes INTEQ, Houston, TX, United States, 395 pp.

Bourgoyne, A.T., Millheim, K.K., Chenevert, M.E., and Young, F.S., 1991: *Applied drilling engineering* (2nd ed.). Society of Petroleum Engineers, Richardson, TX, United States, 502 pp.

Chemwotei, S.C., 2011: Geothermal drilling fluids. Report 10 in: *Geothermal training in Iceland 2011*. UNU-GTP, Iceland, 365-390.

Darley, H.C.H., and Gray, R.G., 1988: *Composition and properties of drilling and completion fluids* (5th ed.). Gulf Publishing Company, Houston, TX, United States, 643 pp.

Finger, J., and Blankenship, D., 2010: *Handbook of best practices for geothermal drilling*. Sandia National Laboratories, Albuquerque, NM, United States, report SAND2010-6048, 84 pp.

Gabolde, G., and Nguyen, J.P., 2014: *Drilling data handbook* (9th ed.). Editions Technip, Paris, 576 pp.

Guo, B., and Liu, G., 2011: *Applied drilling circulation systems. Hydraulics, calculations and models* (1st ed.). Gulf Publishing Company, Burlington, VT, United States, 262 pp.

Hole, H., 2006: *Lectures on geothermal drilling and direct uses*. UNU-GTP, Iceland, report 3, 32 pp.

Hole, H., 2006: Aerated fluids for drilling of geothermal wells. Lecture 1 in: *Lectures on geothermal drilling and direct use*. UNU-GTP, Iceland, report 2006-3, 1-12.

KenGen, 2012: *Well OW-717 completion report*. KenGen – Kenya Electricity Generating Co., Ltd., Kenya, unpublished report, 22 pp.

Kipsang, C., 2013: Cost model for geothermal development. Report 11 in: *Geothermal training in Iceland 2013*. UNU-GTP, Iceland, 365-390.

Lapeyrouse, N.J., 2002: *Formulas and calculations for drilling production and work over* (2nd ed.). Gulf Publishing Company, Burlington, VT, United States, 224 pp.

Lyons, C.W., Guo, B., Graham, L.R., and Hawley, D.G., 2009: *Air and gas drilling manual* (3rd ed.). Gulf Publishing Company, Burlington, VT, United States, 308 pp.

Mitchel, R.F., and Miska, S.Z., 2011: *Fundamentals of drilling engineering* (1st ed.). Society of Petroleum Engineers, Richardson, TX, United States, 696 pp.

Moore, P.E., 1974: *Drilling practices manual*. The Petroleum Publishing Company, Tulsa, OK, 228 pp.

Rahimov, E., 2009: *Through tubing rotary managed pressure drilling*. University of Stavanger, Norway, MSc thesis, 84 pp.

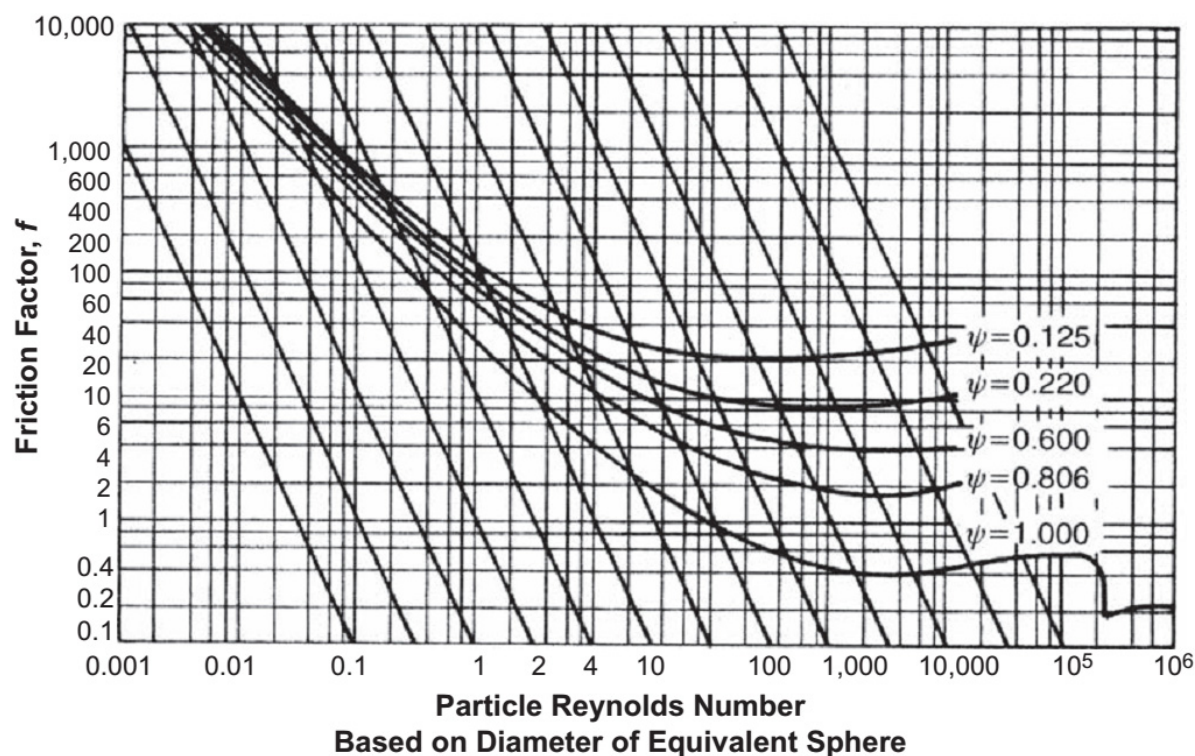
Rehm, B., Haghshenas, A., Paknejad, A., Hughes, J., and Schubert, J., 2012: *Underbalanced drilling limits and extremes* (1st ed.). Gulf Publishing Company, Houston, TX, United States, 629 pp.

Skalle, P., 2011: *Drilling fluids engineering* (1st ed.). Pal Skalle & Vervus Publishers, APS, 132 pp.

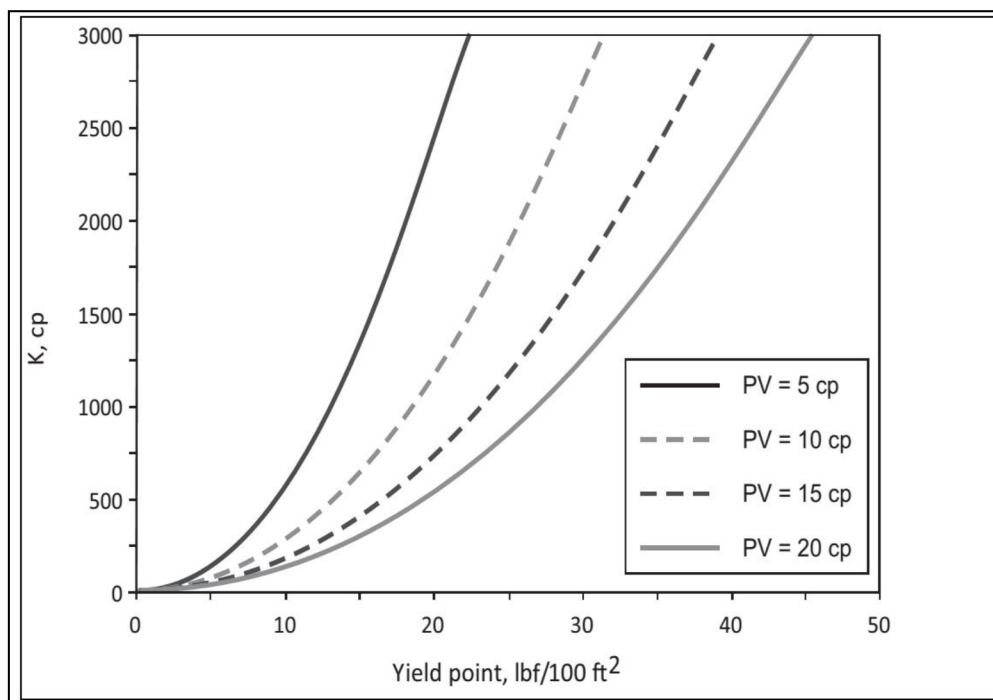
Thórhallson, S., 2014: *Geothermal drilling technology*. UNU-GTP, Iceland, unpublished lecture notes.

Vollmar, D., Witting, V., and Bracke, R., 2013: Distributed parameters models. Geothermal drilling best practices: the geothermal translation of conventional drilling recommendations - main potential challenges. In: Bracke, R., Harvey, C., and Rueter, H. (editors), *Geothermal exploration best practices*. IGA-Academy, report 0104-2013, 12 pp.

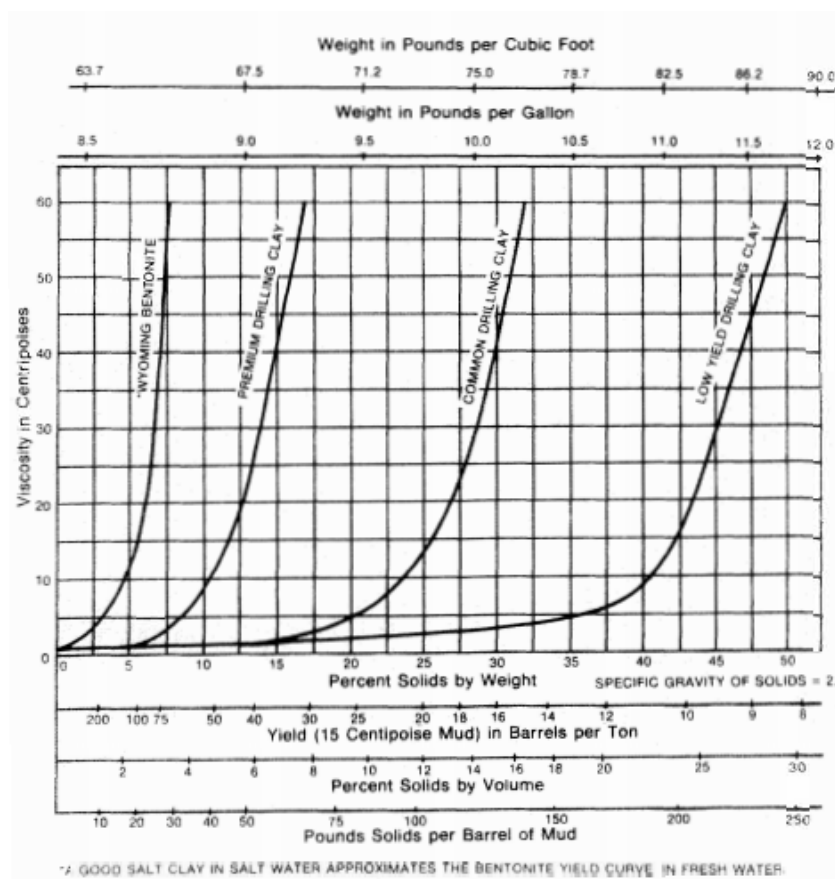
APPENDIX I: Friction factor for calculating Particle slip velocity (Mitchel and Miska, 2011)



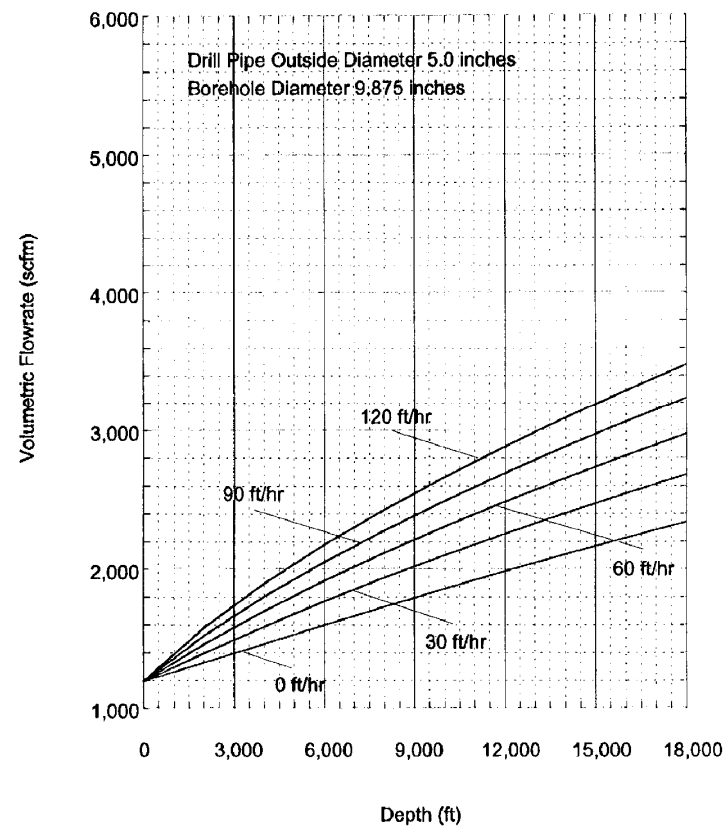
APPENDIX II: K factor for power law fluid (Mitchel and Miska, 2011)



APPENDIX III: Effects of clay concentration on viscosity of fresh water (Darley and Gray, 1988)



**APPENDIX IV: Direct circulation minimum volumetric flow rates
(Mitchel and Miska, 2011)**





UNITED NATIONS
UNIVERSITY

UNU-GTP

Geothermal Training Programme

Orkustofnun, Grensasvegur 9,
IS-108 Reykjavik, Iceland

Reports 2014
Number 12

GEOHERMAL RESOURCE ASSESSMENT OF THE WOTTEN WAVEN GEOHERMAL FIELD – DOMINICA, WEST INDIES

Melissa Anne De Freitas

Energy Unit

Ministry of National Security, Air and Sea Port Development
Kingstown

SAINT VINCENT AND THE GRENADINES

m.defreitas89@gmail.com

ABSTRACT

Geothermal resource assessment involves the estimation of the geothermal energy that can be extracted from a reservoir and utilized economically for a specified time period. It is based on the evaluation of surface discharge, well logs and other geoscientific information obtained via geological, geophysical and geochemical measurements. This report is aimed at conducting a geothermal resource assessment of the Wotten Waven geothermal field in Dominica, based on available surface exploration data and data obtained from three exploratory wells: WW-01, WW-02 and WW-03, by establishing a simple natural-state numerical model of the Wotten Waven field and through the determination of the field's resource potential. The success of recent exploratory work resulted in the proposed installation of a 10-15 MW_e plant for domestic consumption with plans to extend the capacity to 120 MW_e by 2020. Available downhole temperatures indicate the presence of a 234-250°C high-temperature reservoir of 600-2000 m thickness at depths greater than 100 m b.s.l. A conservative volumetric analysis confirms with a 90% probability that the current Wotten Waven field should be able to sustain a capacity of 10-15 MW_e for up to 100 years. A natural-state numerical model modelled over an area of 5 km² requires 80 kg/s of fluid with an enthalpy of approximately 3300 kJ/kg to be injected into three pre-determined heat sources giving a thermal input of approximately 260 MW_t. A more detailed numerical model is needed to cater for a greater reservoir surface area to accurately model the reservoir conditions of the Wotten Waven field, including data from the newly drilled production and injection wells. Once the wells are put into production, a production model should be set up to simulate the response of the reservoir (pressure, enthalpy, etc.) to utilization and to assist in optimizing the power production during future utilization.

1. INTRODUCTION

The Caribbean islands face extraordinary challenges associated with the generation and utilization of energy for their various needs. Most island nations depend almost entirely on a constant influx of petroleum for their energy needs which leaves these countries vulnerable to the instability of international oil prices, resulting in much of a country's Gross Domestic Product (GDP) being allocated to fuel import.

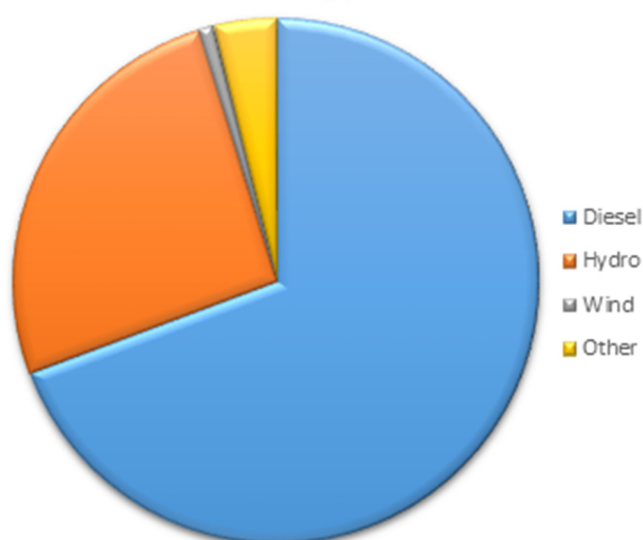


FIGURE 1: Energy matrix of Dominica (based on 2008 estimates in NREL, 2012)

The Commonwealth of Dominica occupies an area of approximately 750 km² and has a relatively small population of just about 72,800 inhabitants. The island's small population has resulted in a low demand for energy, with a peak demand of 14.7 MW_e. Economic projections show an expected annual growth of 2.7% to 25 MW_e by 2028. Regardless of this, in 2008 Dominica had the highest electricity rates in the Caribbean (NREL, 2012) at USD \$0.4567 per kilowatt-hour (kWh). Figure 1 shows the energy matrix of the island of Dominica, based on 2008 statistics.

Renewable energy may, therefore, be the most cost efficient energy source for Dominica, given current costs and available technology. The Caribbean region facilitates an abundant supply of

renewable energy resources. Many volcanic islands of the Eastern Caribbean have large geothermal prospects and are currently exploring this possibility. The possibility for geothermal energy was being explored in Dominica as early as 1977. Although there has been some extremely optimistic studies that suggest that the island's geothermal potential is as high as 1390 MW_e, more realistic exploratory work suggests that it may range from 100-300 MW_e (NREL, 2012). The Wotten Waven site is the current priority of Dominica's aim for geothermal development and, with the recent success of exploratory drilling, the Government aims to construct a small 10-15 MW_e plant for the local market to meet the current peak demand, with plans to do further exploration and to upgrade to a 60 MW_e plant by the end of 2018 and an additional 60 MW_e by the end of 2020 (Maynard-Date and George, 2013).

This report seeks to conduct a geothermal resource assessment of the Wotten Waven geothermal field, based on data obtained from three exploratory wells: WW-01, WW-02 and WW-03. Basically, a geothermal resource assessment involves the estimation of geothermal energy that may be extracted from a reservoir and utilized economically for a specified time period of usually less than 100 years (Sarmiento and Steingrímsson, 2011). It consists of evaluating surface discharge and downhole data through the integration of data obtained by geological, geochemical and geophysical measurements. A volumetric assessment of the Wotten Waven field was conducted to determine its resource potential while an initial numerical model was set up to model the natural conditions of the Wotten Waven field. A volumetric assessment is usually done during the early stages of development when data are often quite limited. Although proven to be fairly accurate, the volumetric model does not account for the amount of vertical or lateral recharge to a geothermal system, and reserves may be underestimated. These reservoir conditions, though not considered in volumetric calculations, are sensitized through numerical modelling. Sarmiento and Björnsson (2007) describe numerical modelling as the best approach in conducting reserve evaluation.

2. BACKGROUND

The Caribbean is home to thousands of islands extending from The Bahamas in the north to Trinidad and Tobago in the south. Dominica, the Nature Island of the Caribbean, lies at the centre of the Lesser Antilles island arc (Figure 2). The islands of the Lesser Antilles are located between the Anegada

Passage and the South American continental plate margin. It was formed by a subduction zone as a result of the collision between the North and South American plate margins with the minor Caribbean plate. This has led to the formation of several volcanically active islands on the oceanic crust of the Caribbean Plate (Smith et al., 2013). Dominica is the most rugged of the Lesser Antilles and occupies a total land area of 750 km². It has one of the highest concentrations of live volcanoes in the world (Lindsay et al., 2005). Unlike its Caribbean neighbours, Dominica has nine potentially active volcanoes. Frequent earthquakes and confirmed geothermal activity throughout the island indicate that it may be underlain by an active magma reservoir.

2.1 Geology of Dominica

Dominica is primarily composed of volcanic rocks and their weathered by-products (see geological map in Appendix I). The volcanic stratigraphy of the island is subdivided according to Miocene, Pliocene, Older Pleistocene and Younger Pleistocene units. The Wotten Waven geothermal field is located in the south-central part of the island, 8 km east-northeast of the capital, Roseau, in and around the communities of Laudat, Wotten Waven and Trafalgar (Figure 3). South-central Dominica is dominated by the central graben - a 12 km long, 7 km wide depression that is marked by a chain of low hills (Smith et al., 2013). The graben's eastern and southern borders are buried under pyroclastic deposits that erupted from two calderas located within the graben's structure. The Wotten Waven caldera was first described as a large "volcano-tectonic depression (Lindsay et al., 2005). It is approximately 7 km in length and 4.5 km in width and is parallel to the Pelean volcanic chain that borders the margin of the Central Graben, thought to be partly fault controlled (Lindsay et al., 2005).

Historically referred to as "Grande Soufrière", this region that includes the Valley of Desolation, the Boiling Lake, Plat Pays Volcanic Complex, Wotten Waven/Micotrin and Mourne aux Diaboles, is the most thermally active in Dominica, characterized by numerous hot springs and fumaroles with temperatures in the range 40-96 and 91-99°C, respectively (Lindsay et al., 2005).

2.2 Geochemistry of the Wotten Waven geothermal field

The European Union, along with the Governments of Dominica and France initiated a programme called Géothermie Caraïbes in 2008. This programme consisted of a geological and geochemical survey of the

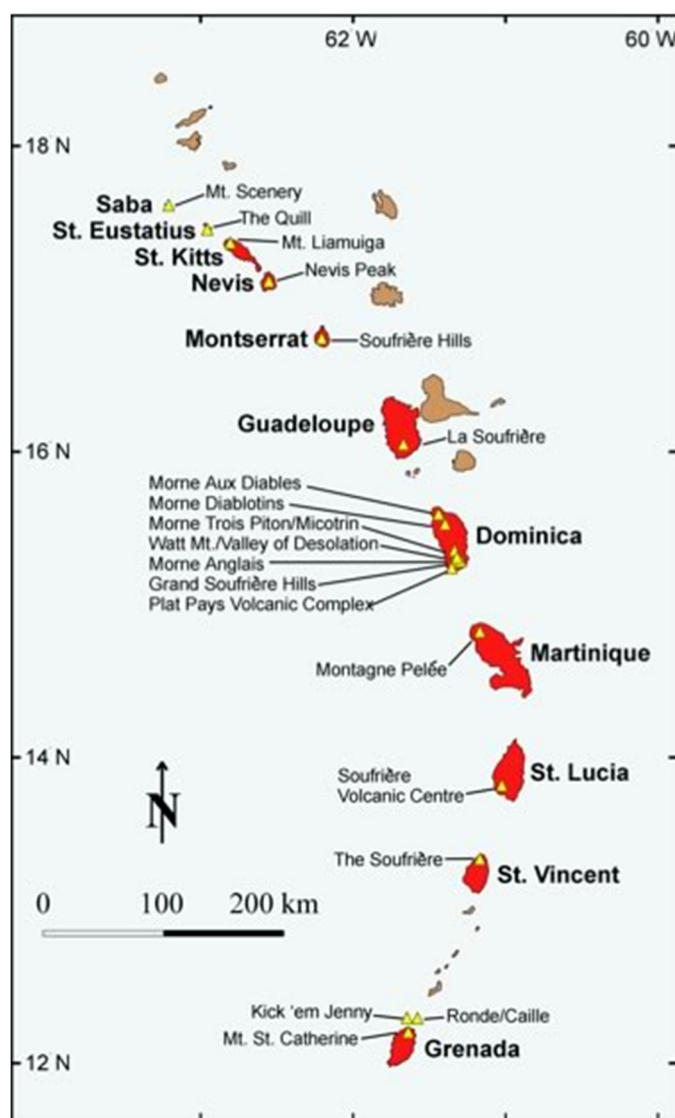


FIGURE 2: Lesser Antilles volcanic island arc (Lindsay et al., 2005)

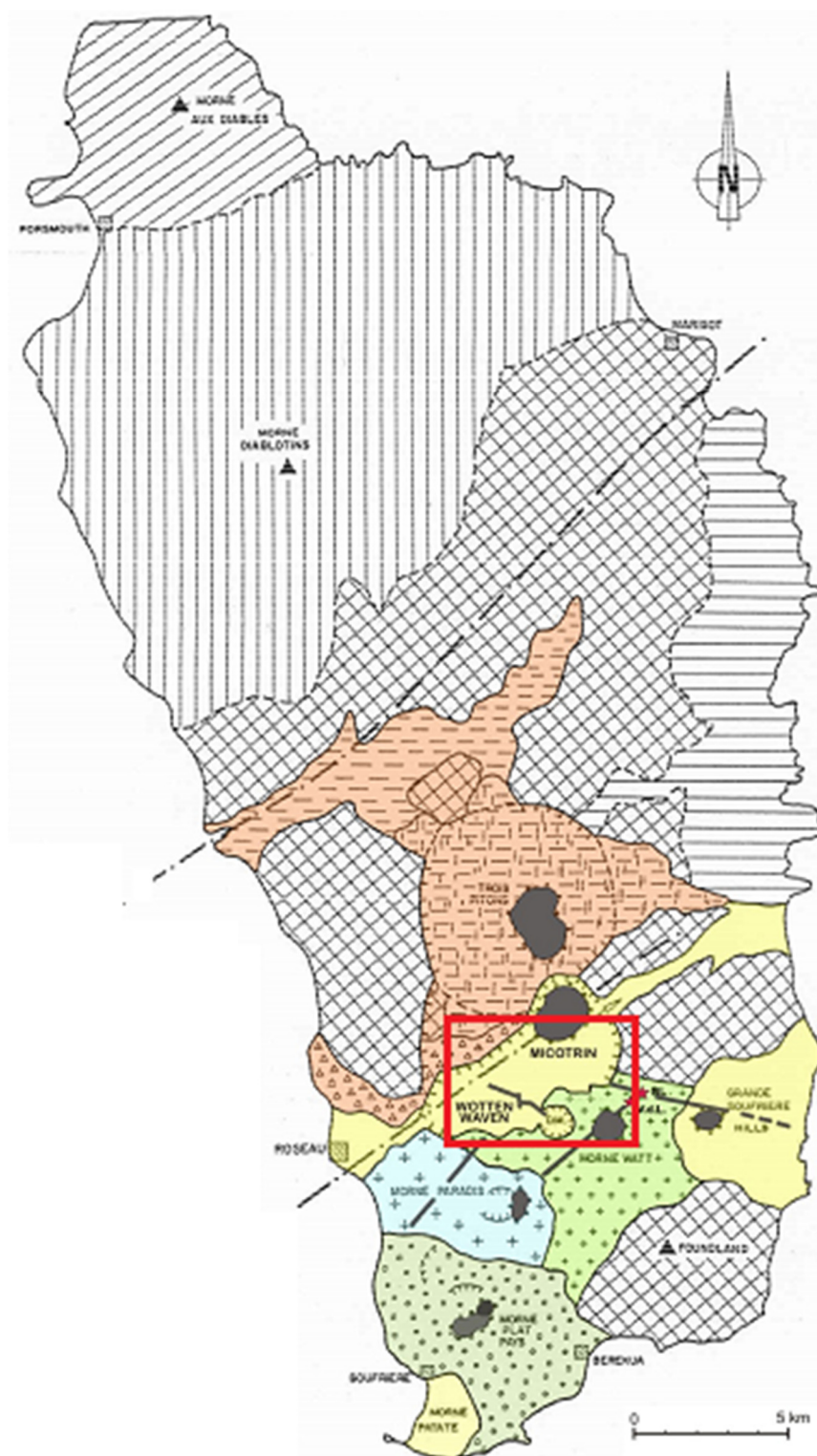


FIGURE 3: Location of the Wotten Waven Field in Dominica deep Na-Cl reservoir, extending deep below the Micotrin dome. Geothermometry data suggests that reservoir temperatures may be in the range of 250-300°C.

Wotten Waven geothermal field. Geochemical results revealed that the fluid chemistry of the field is consistent with waters that classically occur in hydrothermal areas. Primary waters consisting of Na-Cl and secondary waters (acid sulphate type, Ca-Na-HCO₃ type and Na-HCO₃-SO₄ type) have been identified in the Wotten Waven area and near the Boiling Lake / Valley of Desolation. Ca-Na-Cl mineralised water discharged from the Valley of Desolation containing no sea water was interpreted as one piece of evidence that the fluid had a distinct origin. Further analysis confirms a relationship between the fluids of Wotten Waven and The Valley of Desolation, suggesting that they might be derived from a common source (Traineau and Lasne, 2008).

Chemical and isotopic data were obtained for springs located in the River Blanc and Roseau River valley. Surface manifestations present in the vicinity of the River Blanc were thought to be a part of a lateral fluid outflow from a deep high-temperature Na-Cl reservoir (Traineau and Lasne, 2008). An updated conceptual model of the area (Figure 4) provides the likely location of the

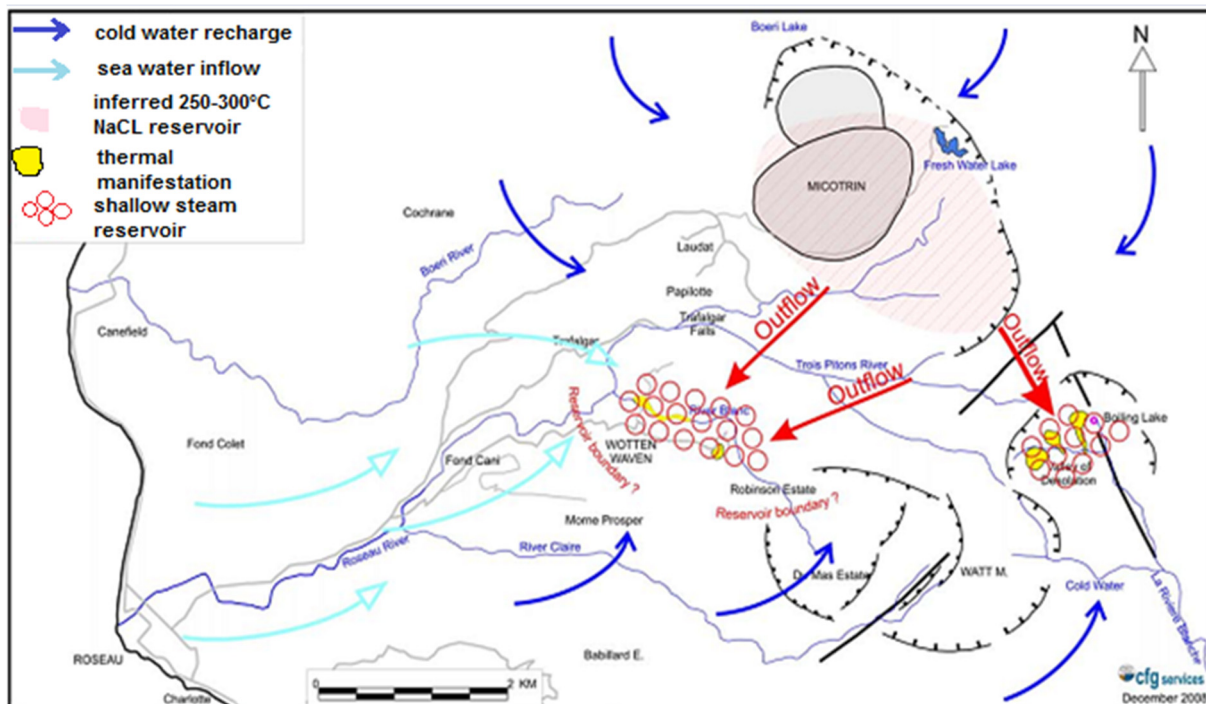


FIGURE 4: Conceptual model of the Wotten Waven geothermal field
(Traineau and Lasne, 2008)

2.3 Geophysics of the Wotten Waven geothermal field

2.3.1 Magnetotelluric (MT) / Transient Electromagnetic (TEM) survey

A joint MT/TEM survey was undertaken in 2008 to obtain a better understanding of the potential geothermal system in the Wotten Waven / Laudat / Trafalgar region. Thirty-two MT soundings were measured across a region of 25 km². A low natural MT signal activity resulted in a low signal to noise ratio in the low frequency range. As a result, most soundings revealed unusable data below 1 Hz, and the penetration depth was thus limited to 100-400 m depth (Baltassat et al., 2008).

MT data, shown in Figure 5, revealed the presence of a highly conductive layer ($>2 \Omega\text{m}$), with the top of this layer located 200-500 m above sea level, with a thickness ranging from 250-300 m (Baltassat et al., 2008). This conductive layer was identified as the cap rock of the potential geothermal system. It over-lays a more resistive layer which was interpreted as the possible reservoir. Baltassat et al. (2008) assumed that a possible reservoir, therefore, exists below the conductive layer, extending from Wotten Waven eastwards to the Boiling Lake-Valley of Desolation area.

2.3.2 Gravimetric investigation

A total of 106 gravity stations were measured, covering a total area of 30 km². The results of gravity surveys have been virtually unchanged throughout the years (Baltassat et al., 2008). Gravity modelling revealed an anomaly – the possible heat source of the geothermal system - a low density intrusion related to recent volcanic activity, seen in Figure 6. The geophysical information presented in Figure 6 has led to estimations of the reservoir thickness which is later presented in sections on Volumetric and Numerical Models in later chapters. With an estimated thickness of 250-300 m, the caprock extends to elevations ranging from 200 m – 500 m a.s.l. It is, therefore, possible that the base of the caprock may extend to 100-200 m b.s.l. According to Figure 6, the dense magmatic intrusion of non-uniformed Thickness may be located at 1000 m b.s.l. It is, therefore, safe to approximate the reservoir thickness as ranging between 600 and 2000 m.

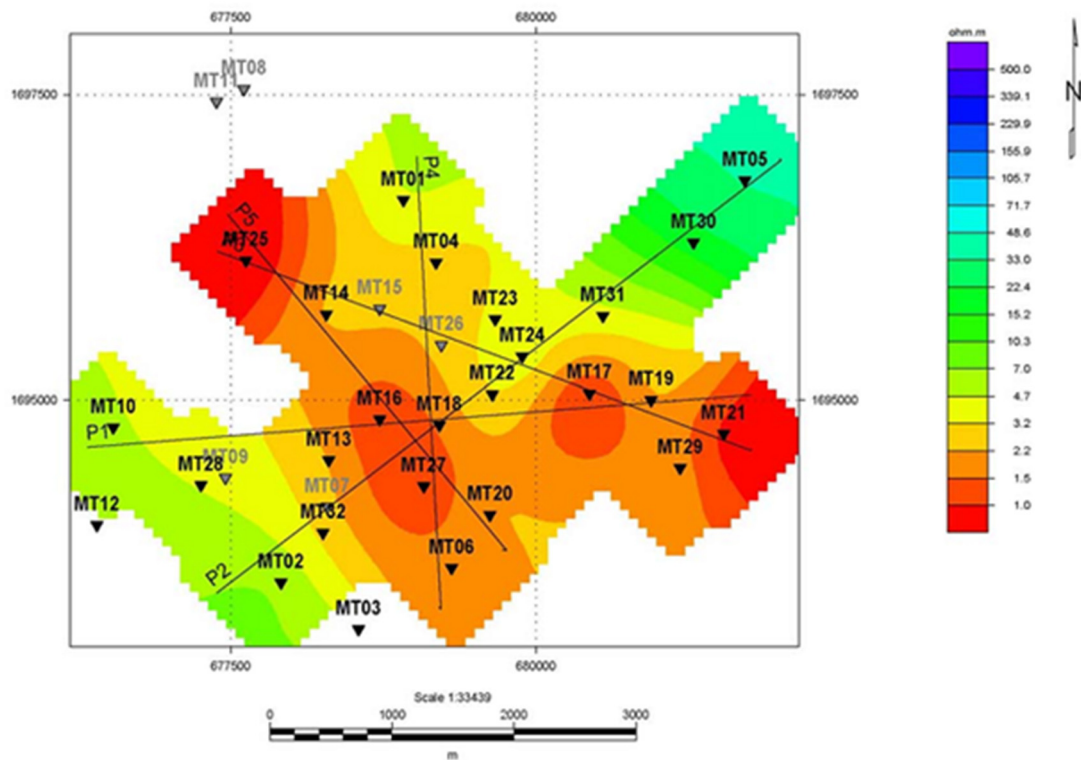


FIGURE 5: Resistivity map at a depth of 300 m extending from Wotten Waven to the Boiling Lake (Baltassat et al., 2008)

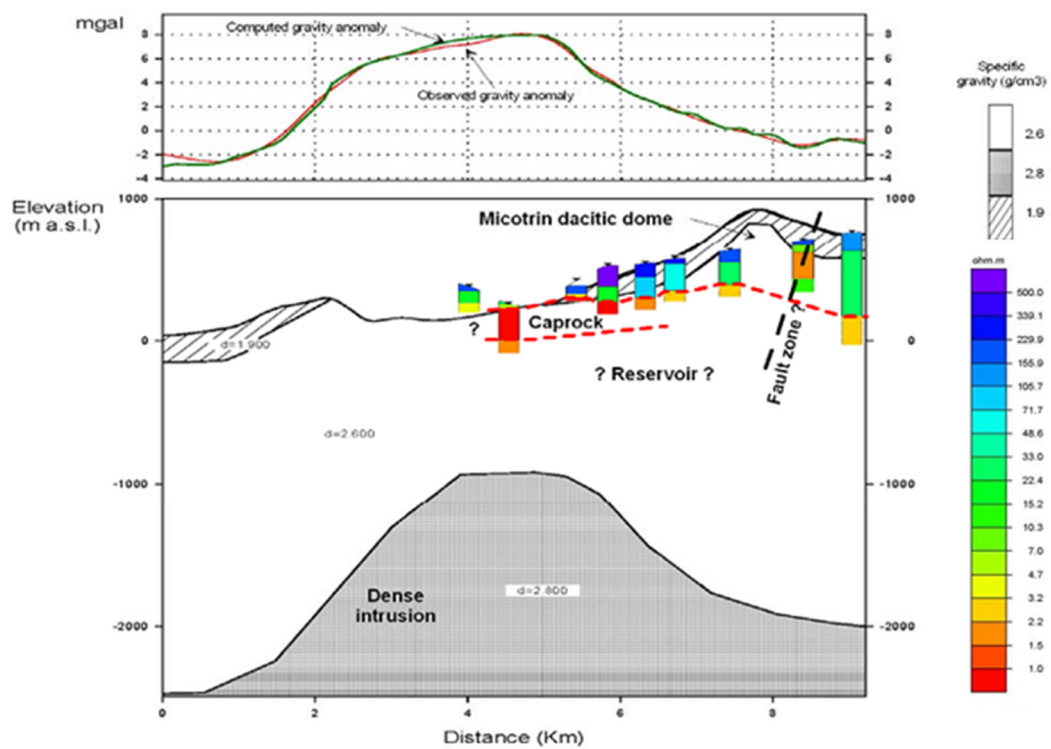


FIGURE 6: Proposed E-W cross-section showing the potential geothermal reservoir based on observed and modelled gravity data (Baltassat et al., 2008)

3. TEMPERATURE AND PRESSURE LOGS FROM EXPLORATORY WELLS

Temperature and pressure profiles are the most important tools in geothermal exploration and development. Although aimed primarily at determining formation temperatures and reservoir pressures, temperature and pressure logs can provide information on feed-zones and aquifers, fluid and heat flow and the overall physical state of the geothermal system. It is also, therefore, a very useful tool in field management. They can be measured at different periods during a well's lifetime, whether it be during drilling, immediately after drilling, during the well's warm up period, during injection and production testing, and anytime thereafter for general maintenance and monitoring. Circulation and fluid flow in wells during drilling and flow testing will cool the well and thus screen the conditions in the formation. The determination of the formation temperature would, therefore, be difficult or even impossible (Steingrímsson, 2014; Grant and Bixley, 2011). After drilling, the well is usually shut off; then well temperatures will eventually recover and gain equilibrium with the formation.

Dominica's three exploratory wells, WW-01, WW-02 and WW-03 were drilled between December 16, 2011 and April 27, 2012, obtaining depths of 1200, 1468 and 1613 m, respectively. Figure 7 shows the location of the three wells. WW-01 is located along the Trafalgar-Wotten Waven link road, while both WW-02 and WW-03 are located in the Laudat area. The target location of these wells was determined from the 2008 geochemical and geophysical surveys.

The temperature and pressure profiles available for WW-01, WW-02 and WW-03 were plotted against measured depths. They are measured during injections and production tests and for each well there exists 1-2 static profiles which represent warm up data.

3.1 Well WW-01

Well WW-01 was drilled from March 29, 2012 till April 27, 2012, with the well pad located at 270 m a.s.l., shown in Figure 7. Drilling reports (Thorbjörnsson, 2012), as well as injection test logs, revealed the presence of three major feed zones located at 31, 720 and 895 m depths. Production testing was done on June 27, 2012 with static temperature and pressure profiles, measured the previous day. A maximum temperature of approximately 239°C was recorded at a measured depth of 700 m. This corresponded with the geothermometry of fluids collected during the flow test, yielding temperatures of 236-237°C (Thorbjörnsson, 2012). Production testing also confirmed the presence of feed zones, revealed during the injection test, seen as minor temperature changes at these zones in Figure 8.

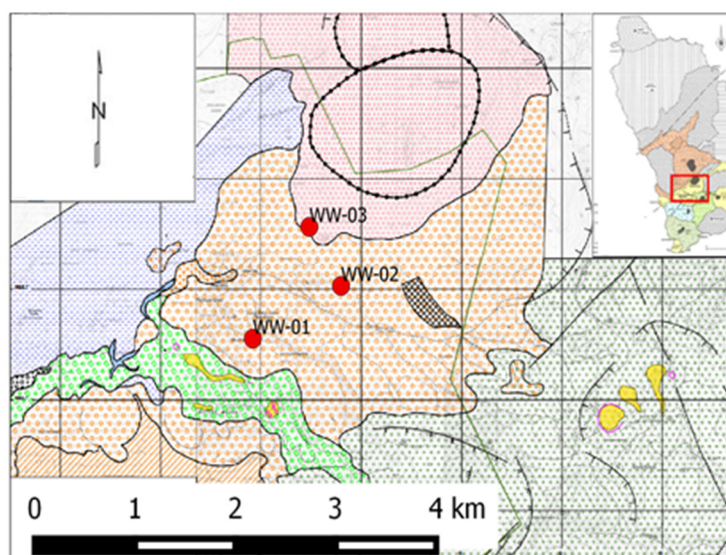


FIGURE 7: Location of exploratory wells in Wotten Waven field

The static logs provide information on the natural, undisturbed state of the well. Figure 9 shows that the well has a wellhead pressure of approximately 11 bar. A wellhead pressure develops when there is an internal flow in the well, so that the fluid boils, steam accumulates in the upper part of the well and, as

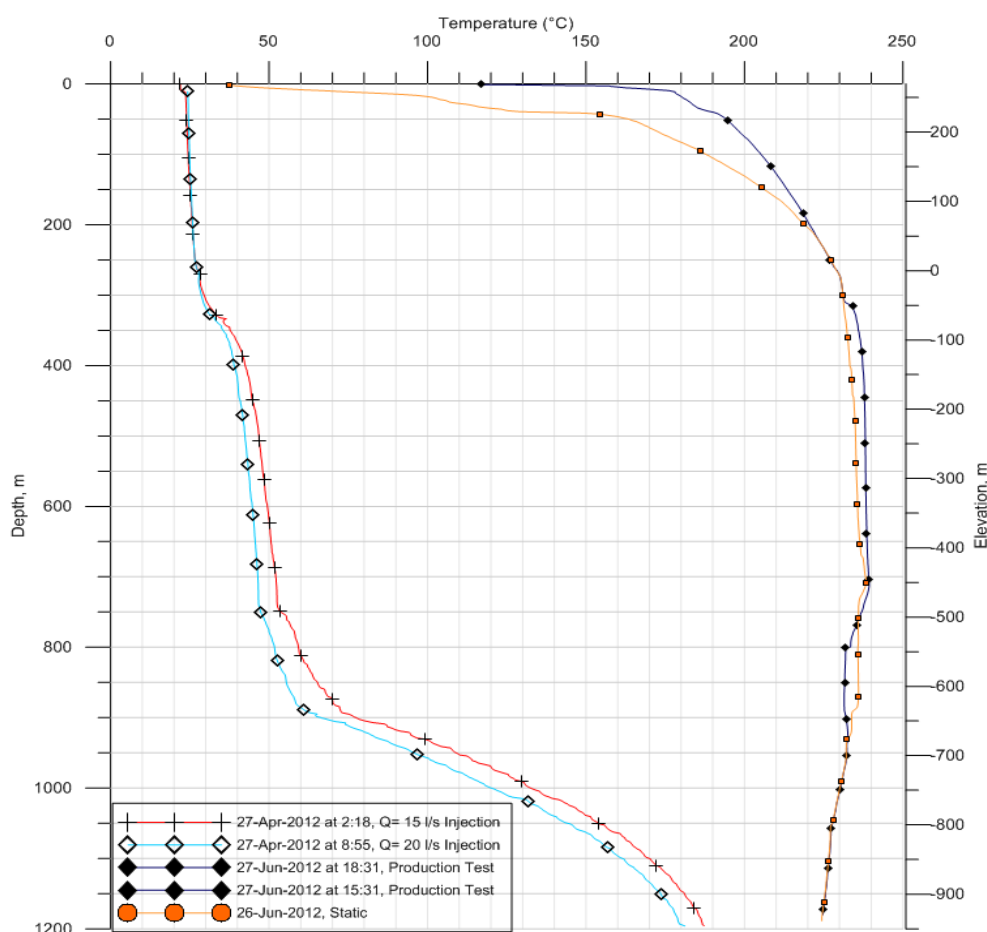


FIGURE 8: Temperature log for well WW-01 in Wotten Waven field, Dominica

a result, pressure is built up at the wellhead (Grant and Bixley, 2011). This may also be due to a build-up of gas released from the geothermal fluid. Due to this pressure, the water table is located at a measured depth of 37.5 m. Static temperature profiles reveal much about the type of heat present in the well. In impermeable rock, heat is transported via conduction. This produces a characteristic linear profile with changes in thermal conductivity altering the temperature gradient (Steingrímsson, 2014; Grant and Bixley, 2011). Figure 8 reveals a linear profile at a measured depth of approximately 0-300 m with varying temperature gradients, suggesting that perhaps the upper 300 m is an impermeable layer of rock heated via conduction. This corresponds to the magnetotelluric data which suggested that the impermeable caprock is approximately 250-300 m thick. In Figure 8, below 300 m depth, the temperature profile is relatively isothermal. Isothermal profiles may either reflect a circulation of fluid or convective heating. In temperature logs, convective profiles may be represented by isothermal sections, inversions, and boiling sections (Grant and Bixley, 2011).

3.2 Well WW-02

Well WW-02 is located in Laudat at approximately 590 m a.s.l., as shown in Figure 7. The well was drilled between December 17, 2011 and January 28, 2012. Temperature and pressure profiles from injection testing, production testing and logging during warm up were plotted against measured depth (Figures 10 and 11).

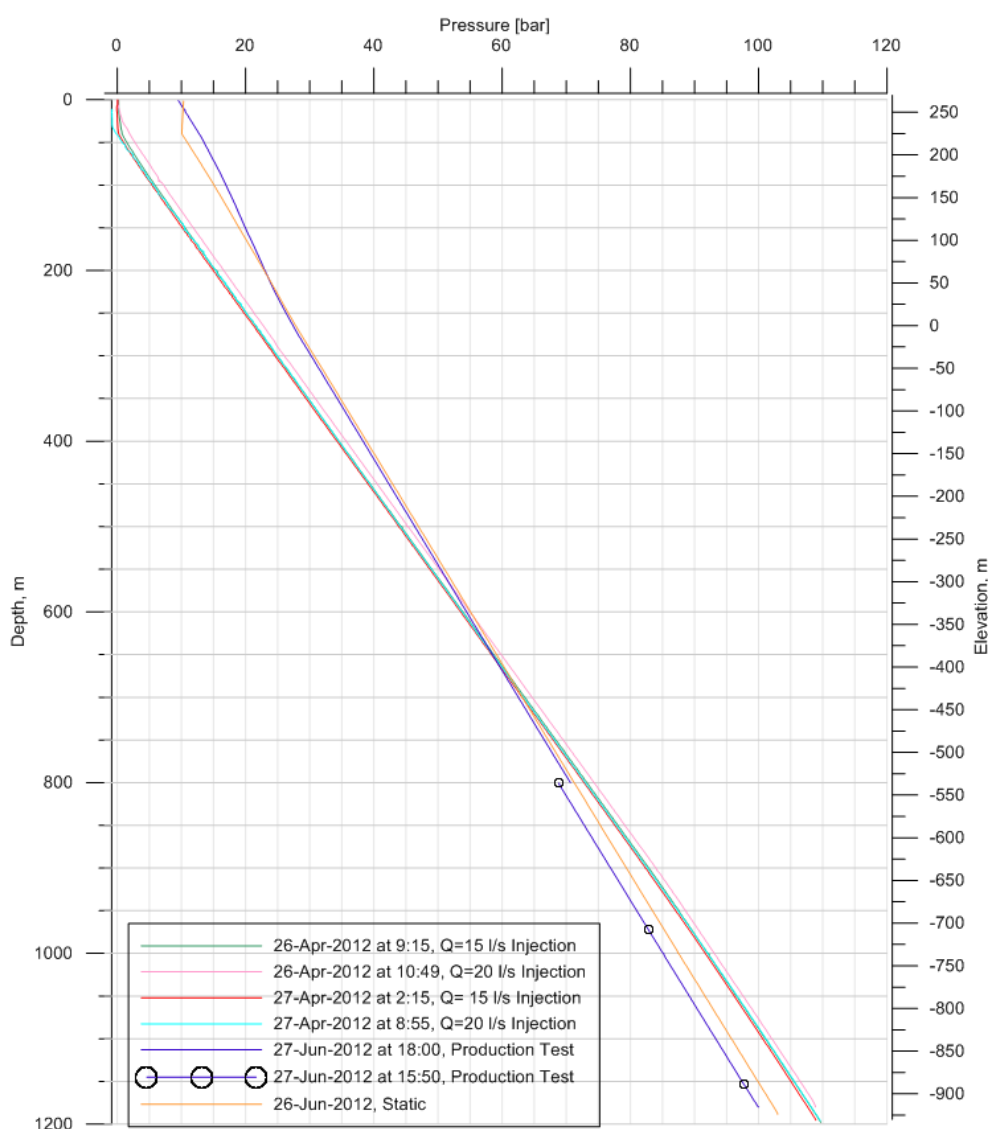


FIGURE 9: Pressure log for well WW-01 in Wotten Waven field, Dominica

WW-02 was closed immediately after drilling, thereby allowing it to heat up for 38 days before the temperature and pressure profiling was run on March 6. A maximum temperature of 236°C was observed at a measured depth of approximately 1140 m. Figure 11 reveals a wellhead pressure (WHP) of approximately 32 bar; the static pressure profile reveals that the boiling level is at a measured depth of 740 m. However, upon extrapolation, the March 6 profile shows that the static water table is at 300 m depth.

Permeable zones were located by identifying circulation losses as well as fluid inflows encountered during drilling and by injectivity and production tests. Temperature profiles suggest a very permeable formation, since many minor inflows and losses can be seen in Figure 10. At a measured depth of 430 m, circulation losses were observed. However, as this was the depth of the casing, Egilson and Thorbjörnsson (2012) concluded that the casing was not deep enough to reach into the geothermal reservoir and, therefore, future production casings in the area should be set at greater depths. Other major permeable zones could be identified in Figure 10 at 860 m and 900 m depths.

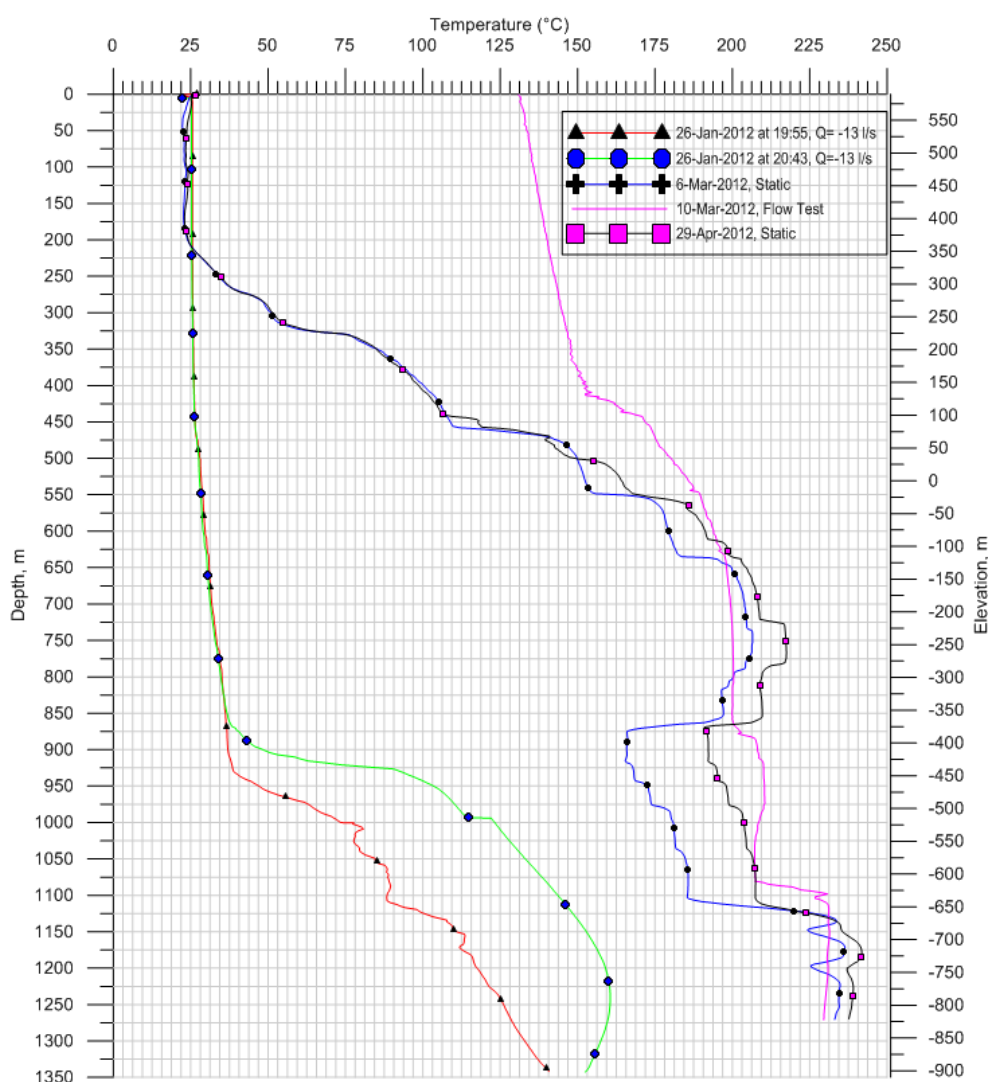


FIGURE 10: Temperature log for well WW-02 in Wotten Waven field, Dominica

The static profile run on March 6 indicated that at the measured depth interval 860-1110 m, cooling was still occurring after drilling, therefore suggesting that this particular region is the best connected part of the well (Egilson and Thorbjörnsson, 2012). A static profile, repeated on April 29, 2012, yielded temperatures greater than 240°C.

3.3 Well WW-03

Well WW-03 is located in Laudat at approximately 560 m a.s.l. The well was drilled between February 15 and March 14, 2012. Three temperature and pressure profiles measured during injection and static conditions were plotted against measured depths (Figures 12 and 13).

Three feed zones were identified at measured depths of approximately 965, 1095 and 1181 m, seen in Figure 12. From the static temperature profile in Figure 12, a maximum temperature of 245°C was recorded at a depth of approximately 950 m. This is in agreement with the geothermometry of sampled fluids which suggest an estimated temperature of 247°C (Egilson and Óskarsson, 2012).

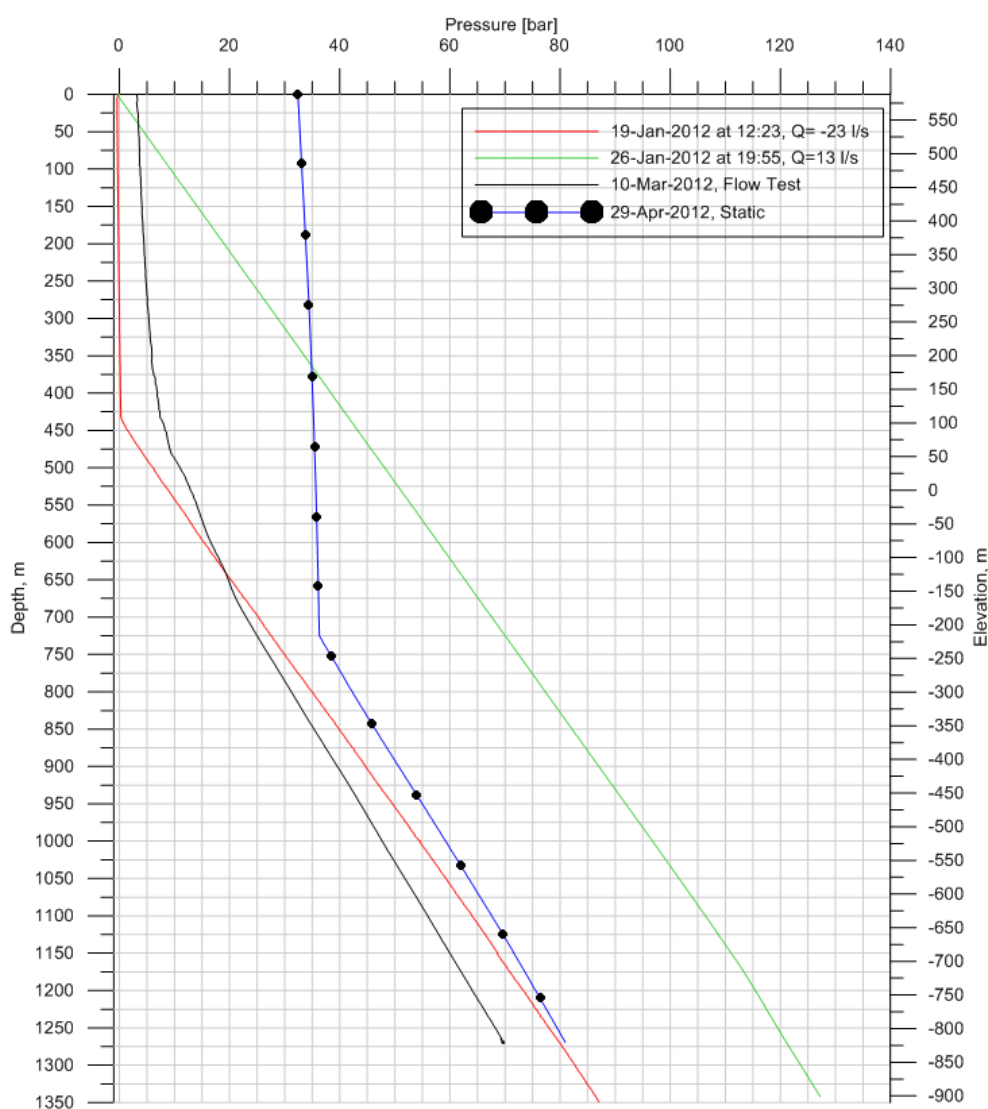


FIGURE 11: Pressure log for well WW-02 in Wotten Waven field, Dominica

In the static pressure profile, a WHP of 39 bar can be observed, resulting in the boiling level being located at a measured depth of 730 m. Extrapolation of this profile reveals a static water table at 55 m.

At the top of the water column, the temperature is just over 210°C, therefore suggesting that the well would flow easily once the gas cap was removed. On April 17, the well was opened for flow testing, however no flowing logs could be recorded because of a casing collapse (Egilson and Óskarsson, 2012).

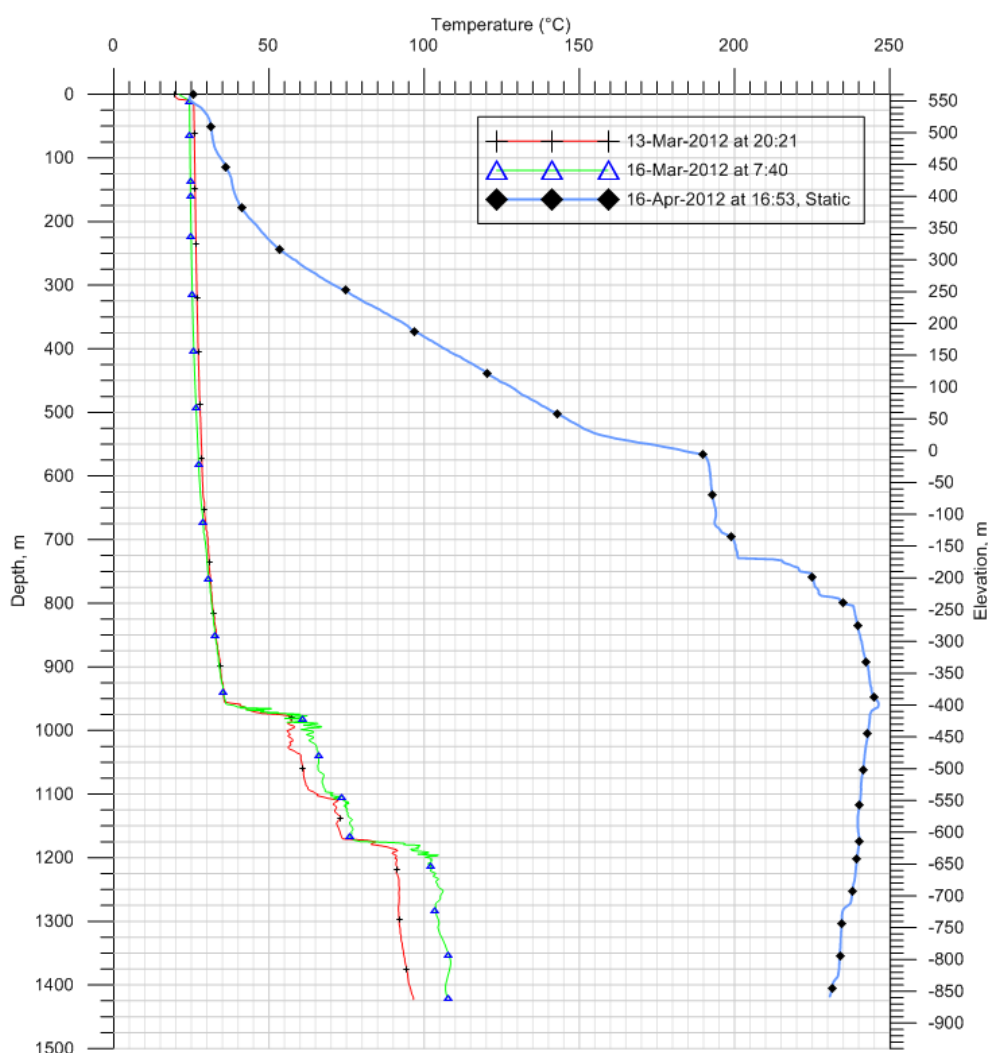


FIGURE 12: Temperature log for Well WW-03 in Wotten Waven field, Dominica

4. CONCEPTUAL MODEL

A conceptual model is the basis for all other types of geothermal models. It is a qualitative model of a geothermal system incorporating the essential physical features of the system discovered by the analysis of available exploratory, drilling and well data (Axelsson, 2014).

The 2008 conceptual model proposed by Traineau and Lasne (2008), shown in Figure 14, is based on geochemical sampling done in the vicinity of Wotten Waven, Trafalgar, Micotrin and the Valley of Desolation. It outlines the proposed fluid flow pattern at depth. The geochemical analysis of fluids in the Wotten Waven and the Boiling Lake areas has confirmed a relationship between these areas and the potential Na-Cl reservoir located beneath the Micotrin lava dome. This may be explained by a lateral outflow from Micotrin towards both Wotten Waven and the Boiling Lake/Valley of Desolation. A marked absence of mineralised salt water in fluids sampled at the Boiling Lake, in comparison to those sampled at Wotten Waven, has suggested that there is an inflow of sea water (light blue arrows) from the west towards Wotten Waven, with no effects at the Valley of Desolation. Cold water inflows represented in the conceptual model (dark blue arrows) may be interpreted as sites of natural recharge.

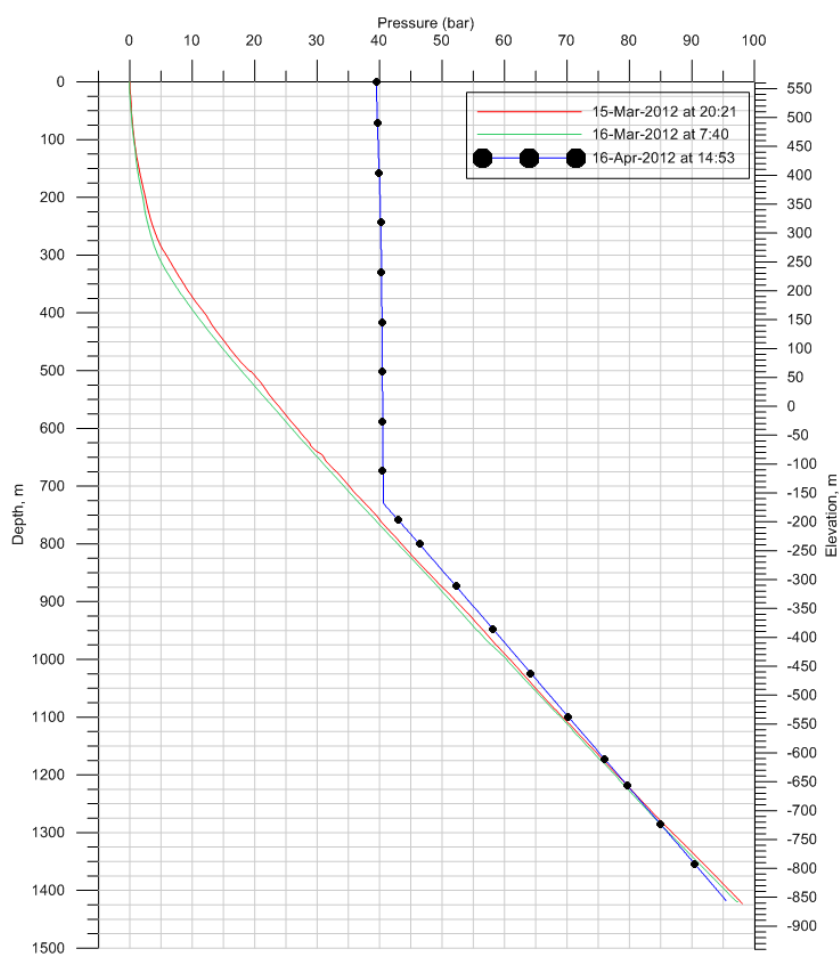


FIGURE 13: Pressure log for Well WW-03 in Wotten Waven field, Dominica

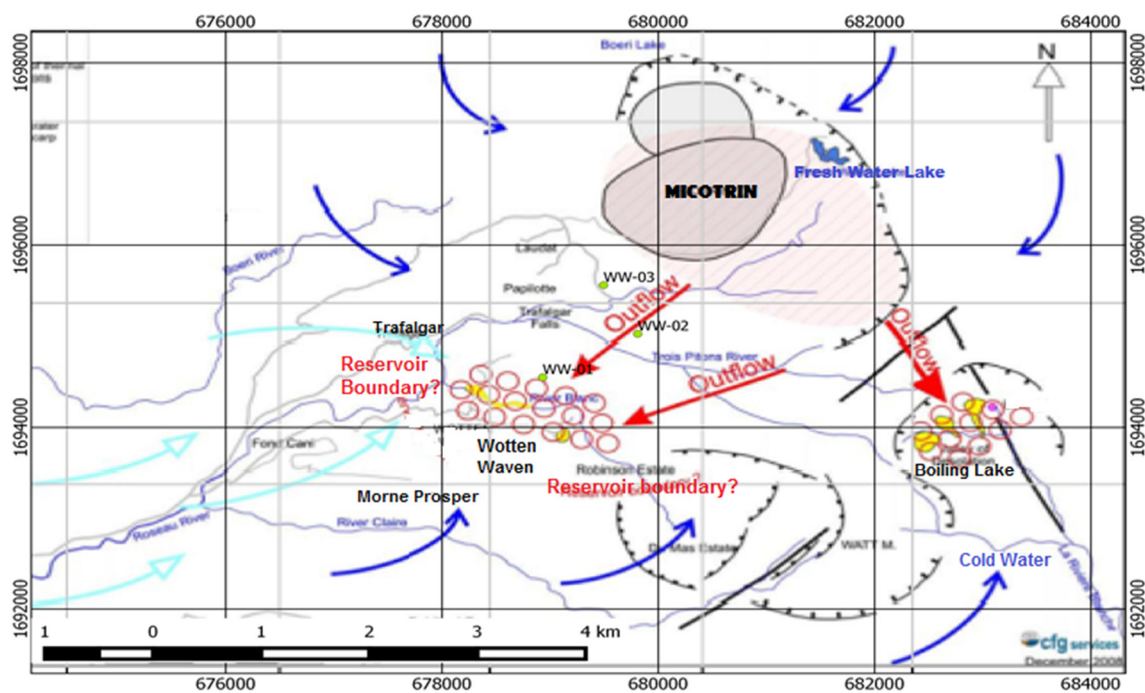


FIGURE 14: Conceptual model of the Wotten Waven field, with locations of the exploratory wells (modified from Traineau and Lasne, 2008)

This conceptual model was used to locate sites for drilling. The three exploratory wells are, therefore, ideally located laterally between Micotrin and the sites of natural thermal discharge in Wotten Waven, away from the effects of salt and cold water inflows. The temperature logs of wells WW-01, WW-02 and WW-03 further confirm this early conceptual model since they indicate that they were drilled in the proposed outflow from Microtrin which is feeding the Wotten Waven field. The logs do not confirm a reservoir boundary, which indicates that the reservoir boundary is set far from the exploratory wells.

5. MODELLING METHODS - LITERATURE REVIEW

5.1 Volumetric modelling

The volumetric method is the main static modelling method used in geothermal resource assessment. During the early stages of geothermal development, in initial-stage assessment, it is considered the most practical approach. Simple volumetric calculations done to determine the generating capacity of potential power plants in the Philippines have proven that this method can reliably predict the minimum commitment for geothermal fields, with as little as two or three exploratory wells (Sarmiento and Björnsson, 2007).

The volumetric method is based on approximate estimates of the total heat energy stored in a volume of rock, including both the thermal energy contained in the rock matrix and water (or steam) in its pores. The total heat in a liquid-dominated geothermal system may be estimated as follows (Halldórsdóttir, 2014):

$$Q = Q_R + Q_W \quad (1)$$

$$\text{And} \quad Q_R = A \cdot h \cdot [\rho_r c_r (1 - \emptyset) \cdot (T_r - T_c)] \quad (2)$$

$$Q_W = A \cdot h \cdot \rho_w c_w \emptyset \cdot (T_r - T_c) \quad (3)$$

where Q_R = Thermal energy of rock (J);
 Q_W = Heat of the water (J);
 A = Surface area of the reservoir (m^2);
 h = Thickness of the reservoir (m);
 ρ_r = Rock density ($\text{kg} \cdot \text{m}^{-3}$);
 c_r = Specific heat capacity of rock ($\text{J} \cdot \text{kg}^{-1} \cdot \text{K}^{-1}$);
 \emptyset = Rock Porosity (-);
 T_r = Temperature of reservoir ($^{\circ}\text{C}$);
 T_c = Cut-off/base temperature ($^{\circ}\text{C}$);
 ρ_w = Density of water ($\text{kg} \cdot \text{m}^{-3}$);
 c_w = Specific heat capacity of water ($\text{J} \cdot \text{kg}^{-1} \cdot \text{K}^{-1}$).

The recoverable heat, Q_R , defined as the energy that is technically recovered by the system, is controlled by the recovery factor, R .

$$Q_R = R \cdot Q \quad (4)$$

The recovery factor is dependent on the nature of the geothermal system, incorporating factors such as permeability, porosity, significance of fractures and recharge as well as to what extent reinjection is applied. It is often approximated to be in the range of 0.05-0.25.

For electrical generation, only a small portion of the recoverable heat can be utilized. This is dependent on a factor known as the conversion efficiency, η . The correlation between the thermal conversion efficiency and reservoir temperatures can be seen in Figure 15.

$$Q_E = \eta \cdot Q_R \quad (5)$$

The electrical power potential, P , relative to a time period, t , is given as:

$$P = \frac{Q_E}{t} \quad (6)$$

One of the main drawbacks of volumetric modelling is that it does not account for natural recharge to the reservoir, or increased recharge due to drawdown, or for the important role of permeability. In such cases, volumetric modelling may lead to overestimates, although there have been some reported cases of underestimation (Grant and Bixley, 2011). In order to address these uncertainties, the Monte Carlo approach is often applied. This statistical method assigns a probability distribution to each parameter in the volumetric calculation. The Monte Carlo simulation calculates and produces a probability distribution for the final estimate of electrical (or heat) energy. This approach determines the 10% value, which is often referred to as proven, i.e. the 90% probability that the stored heat estimate would exceed this value.

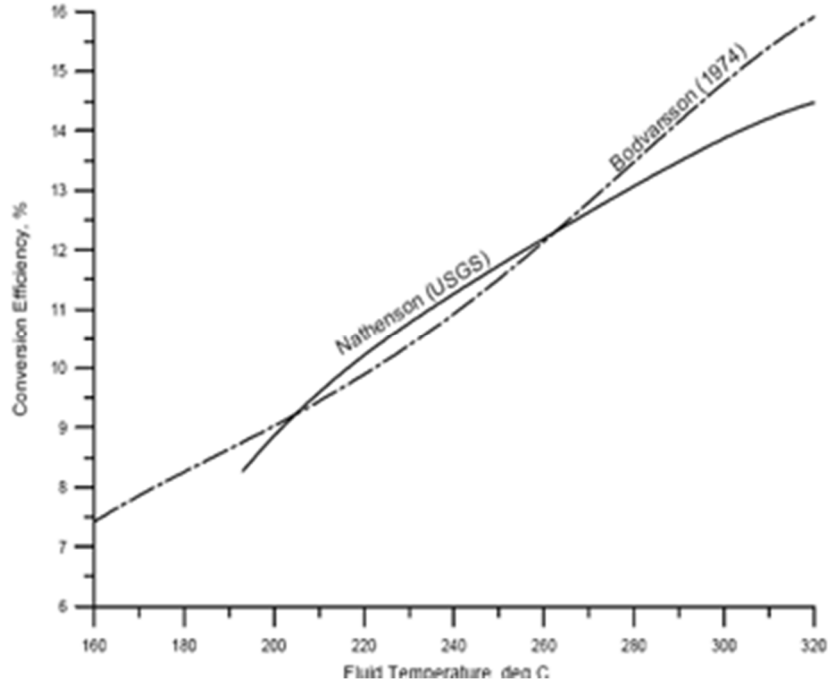


FIGURE 15: Relationship between conversion efficiency and reservoir temperature (Sarmiento and Steingrímsson, 2011)

5.2 Numerical modelling

TOUGH2 is a numerical simulator for multi-dimensional, non-isothermal heat flows of fluid in porous and fractured media. Through the application of Darcy's Law, TOUGH2 solves mass and energy balance equations that describe fluid and heat flow in such systems (Pruess et al., 1999). The TOUGH2 model consists of a number of interconnected elements. For each element, equations defining the accumulated heat and mass as well as the heat and mass flux and points of generation (i.e. heat sources and sinks) are set up (Gylfadóttir, 2014). The basic mass and energy equation describing this kind of flow is expressed as:

$$\frac{d}{dt} \int_{V_n} M^k dV_n = \int_{\Gamma_n} F^{k \cdot n} d\Gamma_n + \int_{V_n} q^k dV_n \quad (7)$$

Equation 7 expresses the equivalence of the rate of change of fluid mass in sub-volume V_n to the sum of the net inflow across the surface and the net gain from fluid sources and sinks. The $\frac{d}{dt} \int_{V_n} M^k dV_n$ term represents the total mass and heat accumulation in sub-volume V_n . The $\int_{\Gamma_n} F^{k \cdot n} d\Gamma_n$ term represents the mass and heat fluxes through the subsurface Γ_n while the $\int_{V_n} q^k dV_n$ term represents the sources and sinks of mass and heat.

For numerical simulation, the continuous space and time must be discretized by introducing volume and area averages (Pruess et al., 1999; Gylfadóttir, 2014).

The mass/heat accumulation term in Equation 7 becomes:

$$\frac{d}{dt} \int_{V_n} M^k dV_n = \frac{d}{dt} V_n M_n \quad (8)$$

The source and sink term becomes:

$$\int_{V_n} q^k dV_n = V_n q_n \quad (9)$$

The mass/heat flow term becomes:

$$\int_{\Gamma_n} F^k \cdot n d\Gamma_n = \sum_m A_{nm} F_{nm} \quad (10)$$

where M_n is the average value of mass/heat in V_n
 A_{nm} is the area between V_n and V_m
 q_n is the average flow rate of source/sink in V_n
 F_{nm} is the average value of normal flow over A_{nm}

Substituting Equations 8, 9, 10 into 7 gives:

$$\frac{dM_n}{dt} = \frac{1}{V_n} \sum_m A_{nm} F_{nm} + q_n \quad (11)$$

The governing TOUGH2 equations are discretized as first order finite difference equations and solved between consecutive time-steps by the Newton-Raphson iteration scheme.

6. ANALYSIS

6.1 Volumetric model

The accuracy of the volumetric method is dependent on both the development and maturity of a given geothermal field. While stated that this method can be done with as little as two to three exploratory wells, accuracy increases as more well data become available. The Monte Carlo method is a probabilistic method that accounts for the great uncertainties in the selected parameters.

In order to obtain a model with a higher chance of accuracy, the following parameters must be approximated using geological, geochemical, geophysical and logging data:

- Surface area of the geothermal reservoir;
- Reservoir thickness;
- Rock porosity;
- Specific heat and densities of rock and water;
- Reservoir and base temperature;
- Recovery factor;
- Plant conversion efficiency.

The surface area of the Wotten Waven geothermal field was estimated by finding the area of the confirmed geothermal resource, i.e. the area surrounding the three exploratory wells, as well as

extending just beyond the areas of natural thermal discharge in Wotten Waven, as shown in Figure 14. A triangular distribution was assigned and the confirmed area of 5 km² was set as the minimum, while the maximum area was extended to 20 km² to include areas of thermal manifestations in Boiling Lake. The most likely area was estimated to be 10 km².

Reservoir thickness was also assigned a triangular distribution. It was estimated from the results of the gravity survey, discussed in Section 2, which proposed a total reservoir thickness ranging from 600 to 2000 m. The minimum thickness, however, was selected as 500 m, the maximum 2000 m and the most likely thickness was selected as 1000 m. These values also correspond with values suggested by Muffler and Cataldi (1978), in the event that geophysical data failed to reveal the reservoir thickness.

Geological data as well as lithological logs have revealed that andesite is the primary rock type of the Wotten Waven geothermal field. This corresponds to a porosity of 10% and rock density of 2600 kg/m³. Porosity and rock density are given a fixed value.

Muffler (1979) suggested that in estimating the total accessible resource, one must assume that the geothermal reservoir has a single characteristic temperature. Geothermometry suggests a value for reservoir temperatures ranging between 250 and 300°C. Reservoir temperature is normally assigned a triangular distribution. The value for the minimum temperature was selected to be 150°C. This temperature is close to the minimum required useable temperature for a conventional binary plant. The maximum temperature was, consequently, assigned the value of 300°C, corresponding to the geothermometry results. There is an almost zero probability that the reservoir temperature is greater than this value. The most likely temperature was selected to be 230°C since the highest downhole temperatures for the three exploratory wells ranged from 234 to 245°C. This value, according to Muffler (1979), may therefore be considered as the characteristic reservoir temperature. The values for the specific heat and densities of the rocks and water were determined based on the reservoir temperature values.

The recovery factor is defined as the ratio of extracted thermal energy (measured at the well-head) to the total geothermal energy contained in given volumes of rock and water (Muffler, 1979). In typical cases of permeability and porosity, the recovery factor may be as high as 25% in convective systems, however, it may approach zero in unfractured, impermeable rock. The recovery factor can though be estimated based on the type of geothermal system, i.e. whether it is convective or conductive, the porosity of the rock, the type of fluid present in rock pores, reservoir temperature, permeability, effects of natural recharge, and the type of technology used to extract this thermal energy. Most Recover Factor estimations are based on approximations for idealised permeable, convective systems, with little attention paid to less permeable, non-ideal cases. This has resulted in exaggerated geothermal assessments. Muffler (1979) approximated a linear relationship between porosity and Recovery Factor which gives a value of 25% corresponding to the 10% value for the porosity of Andesitic rock. This value is considered to be unrealistically and the recovery factor variable is assigned a triangular distribution ranging from 10 to 25% to account for non-ideal reservoirs.

The plant utilization factor / conversion efficiency is dependent on the efficiency of the geothermal plant. It incorporates both the conversion of thermal energy into mechanical energy and consequently mechanical energy into electrical energy. An estimate for conversion efficiency assumed a uniform distribution ranging from 5-11%, partially based on the correlation between reservoir temperature and conversion efficiency presented in Figure 15.

The volumetric assessment was carried out using the Monte Carlo method. The input data presented in Table 1 was used in the calculations for generation periods of 30, 50 and 100 years. Results for a typical generation period of 30 years are presented as a discrete probability distribution in Figure 16, and as a cumulative probability distribution in Figure 17, while results for 50 years are presented in Appendix II and those for 100 years in Appendix III.

TABLE 1: Input parameters for the volumetric assessment

Input variables	Units	Minimum	Most likely	Maximum	Distribution
Surface area	km ²	5	10	20	Triangle
Thickness	m	500	1000	2000	Triangle
Rock density	kg/m ³		2600		Fixed
Porosity	%		10		Fixed
Rock specific heat	J/kg°C		900		Fixed
Temperature	°C	150	230	300	Triangle
Fluid density	kg/m ³	712	827	917	Triangle
Fluid specific heat	J/kg°C		4700		Fixed
Recovery factor	%	10.0	15.0	25.0	Triangle
Conversion efficiency	%	5.0		11.0	Uniform
Plant life	years		30, 50, 100		Fixed
Rejection temperature	°C		35		Fixed

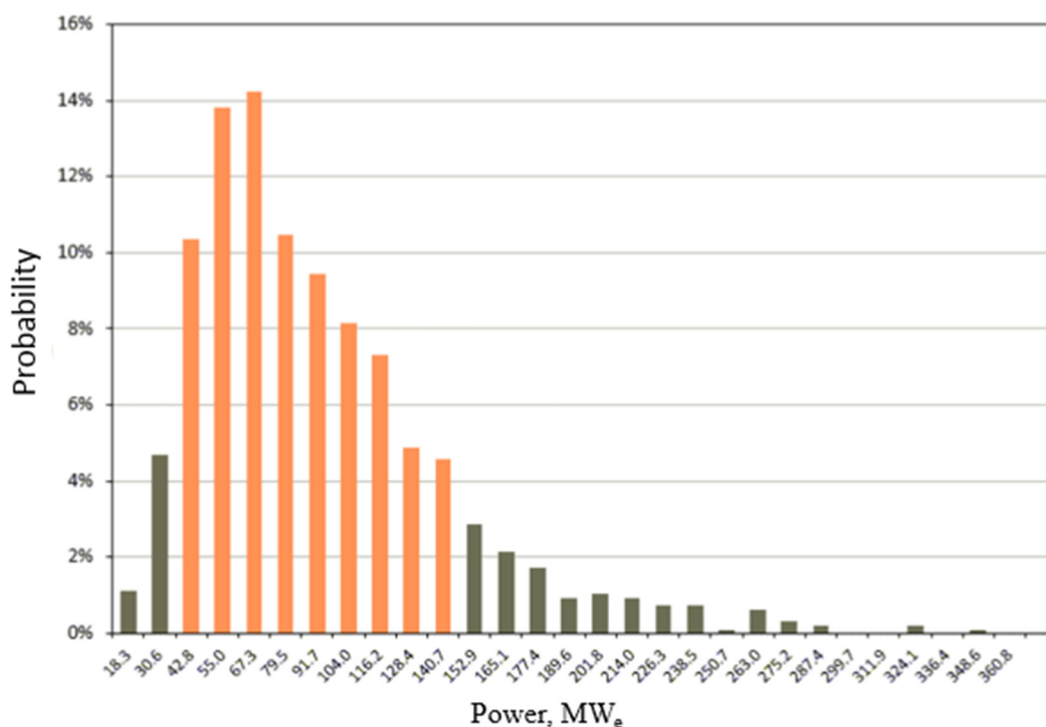


FIGURE 16: Monte Carlo volumetric discrete probability distribution for electrical power production for a period of 30 years

A discrete probability distribution deals with the probabilistic properties of observable pre-defined values. It is characterised by a limited number of possible observations. In Figure 16, the most probable value for electrical power production is 67 MWe with a probability of approximately 14%. This corresponds to a total heat content of over 4860 TJ and, according to Equation 4, a total recoverable energy of 730 TJ. The histogram illustrates with 90% confidence that power production capacity is between 42 and 140 MWe for a production period of 30 years, which is the normal economic lifetime for geothermal power plants.

The cumulative frequency distribution in Figure 17 is comparable to a probability distribution function, plotted by the frequency of each number. The vertical axis represents the cumulative frequency distribution, while the horizontal axis is equal to the corresponding random values for electrical power production. The cumulative frequency equivalent to the maximum value for production is always 1,

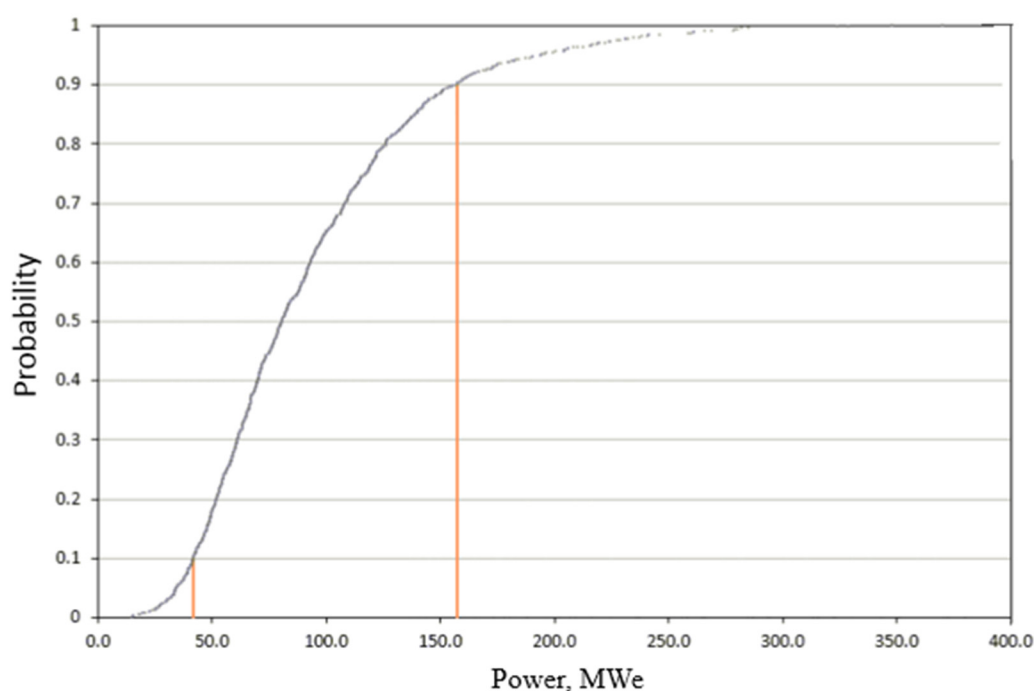


FIGURE 17: Monte Carlo volumetric cumulative probability distribution for electrical power production for a period of 30 years

while that corresponding to the minimum possible value is 0. In Figure 17, the probability that power production capacity is greater than 42 MWe is 90% for a production period of 30 years. This value, supported by the outcome of the exploration wells, may be considered to represent an estimate of the proven reserves for the Wotten Waven geothermal field, i.e. the capacity that can be estimated with increased certainty based on geoscientific data (Sarmiento and Steingrímsson, 2011).

A similar approach was taken for the generation periods of 50 and 100 years (see Appendices II and III). The results of all the estimates are summarized in Table 2.

TABLE 2: Monte Carlo volumetric generation capacity estimates for generation periods of 30, 50 and 100 years

Statistical sizes	Power (MWe)		
	30 years	50 years	100 years
Most probable value	67	48	19
90% confidence interval	42-140	26-92	15-45
Mean	93	60	30
Median	81	54	28
Standard deviation	51	28	12
90% limit	42	28	14

After the successful completion of exploratory wells WW-01, WW-02 and WW-03, the Government of the Commonwealth of Dominica has proposed the development of a small 10-15 MWe power plant in Wotten Waven (Maynard-Date and George, 2013). Based on the assessment results for the 30 year generation time period, the reservoir should be able to sustain a minimum of 42 MWe. If the generating period were extended to 50 years, the 90% limit indicates that the reservoir should be able to sustain a minimum of 28 MWe. If the time period were extended to 100 years, the 90% limit shows that the reservoir should be able to sustain a minimum of 14 MWe. The current Wotten Waven geothermal field should be able to sustain a power plant with a maximum capacity of 10-15 MWe for 100 years. These

values, however, may not reflect the true potential of the Wotten Waven field, since the Volumetric Method does not account for either natural recharge of the system or the effects of reinjection.

6.2 Numerical modelling

A simple natural-state numerical model for the Wotten Waven geothermal field was developed for this project. A TOUGH2 grid file was created using the RockEditor software package which uses the Amesh program (Haukwa, 1999) that generates discrete grids for numerical modelling of flow and transport problems, formulated on the integral finite difference method (Mwarania, 2014). The model covers an area of 5 km², with a thickness of 2 km and is subdivided into 1428 grid elements. It was specifically designed to focus on the finer model blocks centred on the location of the three exploratory wells, as seen in Figure 18. The larger, coarser blocks were placed around the edges of the model where less accuracy was required.

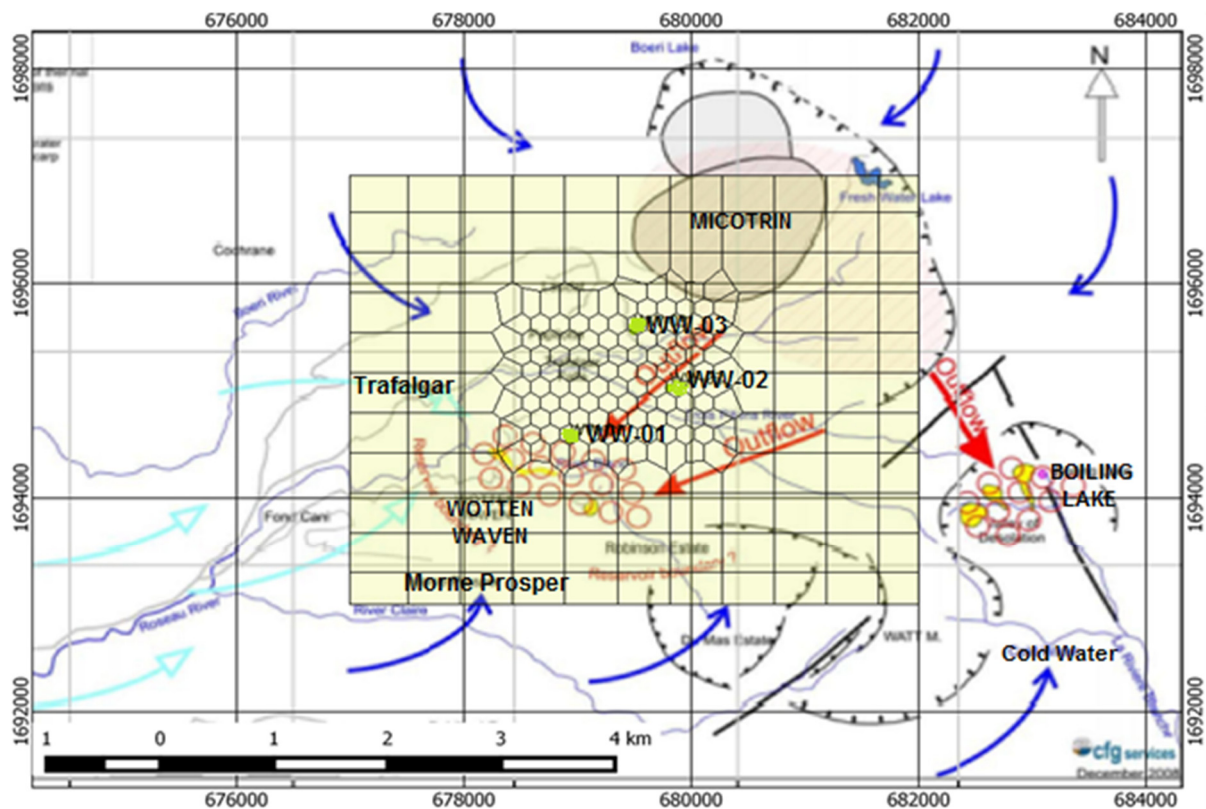


FIGURE 18: Horizontal mesh of the numerical model with an underlying conceptual model from Traineau and Lasne (2008)

The mesh boundary is set far from the exploratory wells, delimited by the Boiling Lake in the east, Trafalgar in the west and Micotrin and Morne Prosper in the north and south, respectively, as shown in Figure 18. The model is composed of six layers (Figure 19) and has a vertical depth of 2000 m, ranging between 100 m a.s.l and 1800 m b.s.l. The top and bottom layers, representing the caprock and bedrock, respectively, are set as inactive and relatively impermeable as compared with the inner layers. A constant temperature and pressure of 32.5°C and 14.67 bars is maintained in the caprock, with the outer mesh of the bedrock set at a lower temperature than the finer mesh elements, thereby limiting fluid flow to layers B-E. The average surface temperature, obtained from well logs, was assumed to be 25°C and a geothermal gradient of 50°C/km was set up at the boundaries. For simplicity, the geological conditions

were assumed to be constant. For each layer of the model, the horizontal mesh remains the same as shown in Figure 18.

Four different rock types were assigned to different regions within the model. It was assumed that all elements had the same porosity, thermal conductivity and specific heat, however, permeability and, to some extent, density varied in each rock type. In real cases, permeability differs in the x, y and z dimensions, however for the purpose of this project, permeability was assumed to be equal in all directions (Table 3).

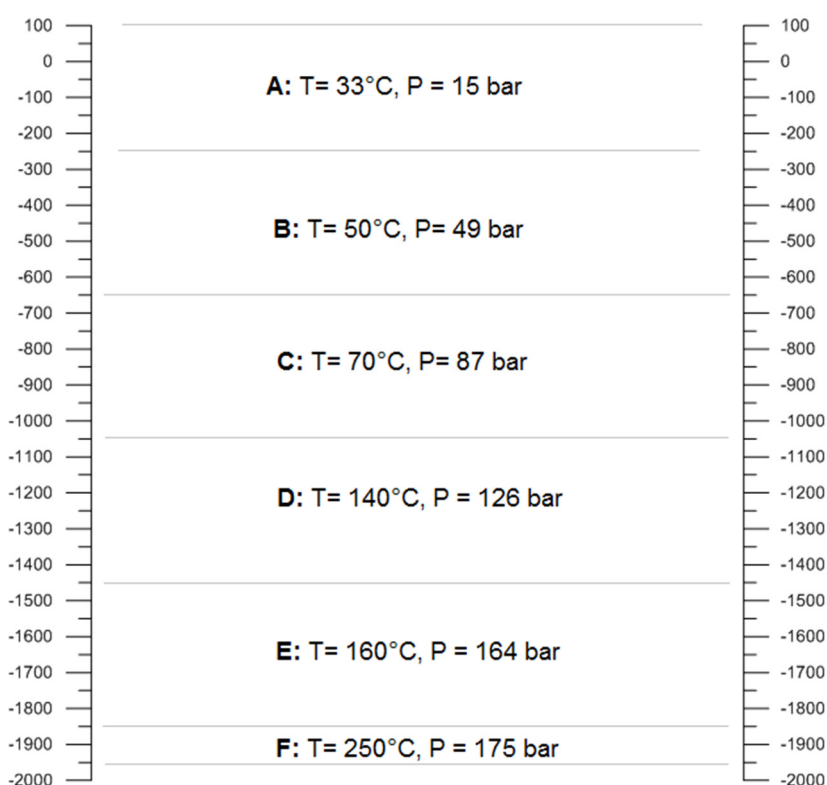


FIGURE 19: The vertical grid of the numerical model

TABLE 3: Table showing varying rock properties of rock types used in model

Rock	Density (kg/m ³)	Porosity	Thermal conductivity (W/m°C)	Specific heat (kJ/kg·K)
CPRCK	2650	10%	2.1	850
BDRCK	2650	10%	2.1	850
PERMR	2640	10%	2.1	850
PERMM	2650	10%	2.1	850

The formation temperatures of wells WW-01, WW-02 and WW-03 were estimated using the static temperature profiles. Heat sources were implemented in layer E of the model, to simulate upflows, while a sink was implemented in layer A to simulate natural discharge from the system. An important assumption made in the TOUGH2 model was that the geothermal fluid is that of pure water. Inflow to the Watten Waven field, or outflow from Microtin, as speculated in the conceptual model, was modelled as upflow by implementing sources. The location, flow rate and enthalpy of the pre-defined sources and sinks can be seen in Table 4.

TABLE 4: Flow rates and enthalpy of various pre-determined sources/sinks in the numerical model

Source/ Sink	Flow rate (kg/s)	Enthalpy (kJ/kg)
EA413SOU01	25.0	1117
EA332SOU02	35.0	1095
EA349SOU03	20.0	1055
AA147SIN01	2.e-09	2.e+02

A natural-state model simulates the geothermal field's physical state prior to production. It is designed to verify the validity of previous conceptual and volumetric models. As described by Mwarania (2014), a natural-state model is simulated for a long period of time until steady state is achieved. Natural state was achieved by manually adjusting the permeability distribution as well as the enthalpy and flow rates of pre-determined heat sources and sinks, seen in Figure 20. In achieving steady state, as seen in Table 4, a total of 80 kg/s of fluid with an enthalpy of approximately 3300 kJ/kg was injected into three elements giving a thermal input of approximately 260 MW_t, which corresponds to 7 MW_e. Although small in comparison to the volumetric assessment, this value corresponds well with the combined estimated capacity of the three exploratory wells, 7.3 MW_e (GDU, 2013). This value reflects the small production area in the model. Further modelling for the Wotten Waven field includes extending the production area, while placing more heat sources in the model that will result in a higher flow rate and enthalpy.

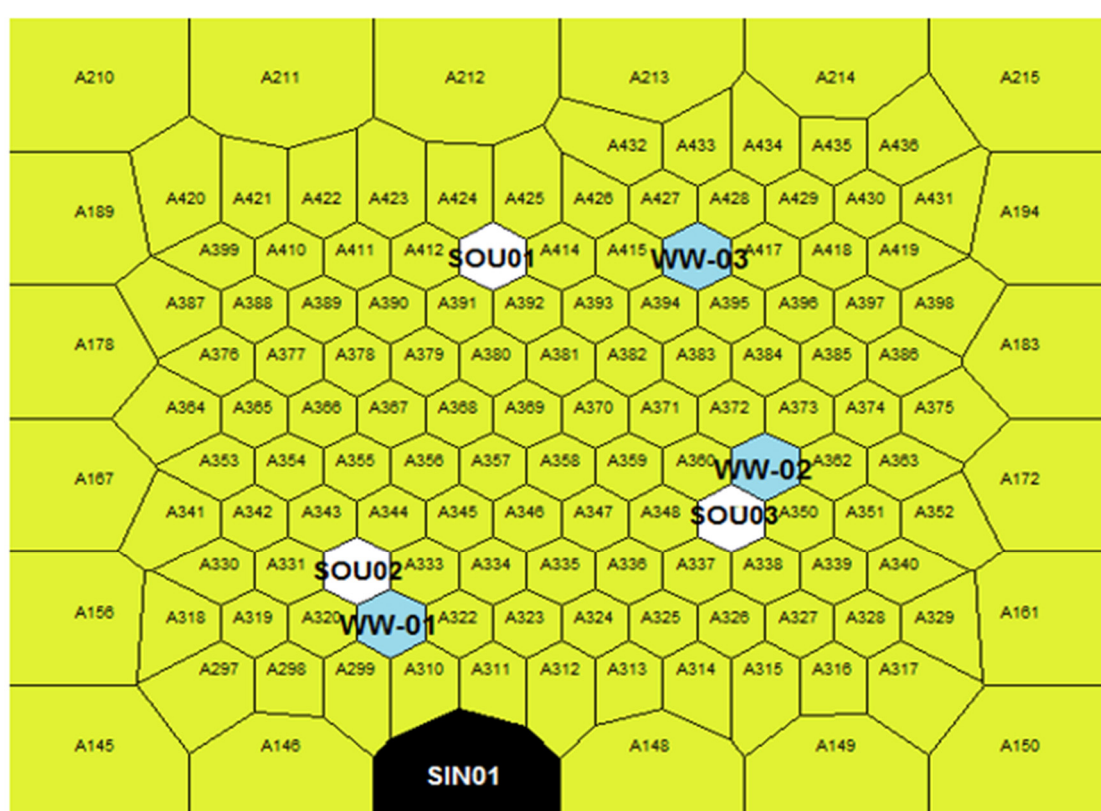


FIGURE 20: Location of exploratory wells, sources and sinks in the numerical model

The modelled results are presented in Figures 21-23, where the results of the natural-state model are compared to the estimated formation temperatures for the three exploratory wells. The modelled and measured data presented show fairly good correlations. The modelled plot illustrates the characteristic linear plot as seen in the temperature logs of wells WW-01, WW-02 and WW-03 from 100 m a.s.l to -200 m b.s.l – the cap rock of the geothermal system. The isothermal profile was modelled by increasing the permeability of rocks in Layers B-E. This model suggests that the geothermal reservoir may in fact be located at depths as shallow as 100 m b.s.l. This is in agreement with the geophysical model in Figure 6 and is further confirmed by the temperature logs of the three exploratory wells. Inversion was modelled at elevations greater than 1200 m b.s.l. This was achieved by increasing the permeability of the rocks around wells WW-02 and WW-03. The numerous feed zones present in WW-02 (Figure 9) support this hypothesis, that a more permeable formation may in fact be present in the vicinity.

A major discrepancy in Figures 21-23 is the downwards shift of the modelled data. Figure 19 shows the vertical numerical grid generated, with its associated temperatures and pressures. In the numerical model, a vertical depth of approximately 2 km was considered and subdivided into six layers, with the thickness of each layer ranging from 100 to 400 m. In order to correct the shift observed in Figures 21-23, a more sensitive model would have to be developed, with thinner layers to account for more detailed changes in temperature and rock permeability.

Many assumptions made while developing the model should be revised when the model is developed further. Theoretically, a uniform geological section was considered, ignoring the effects of fractures, faults and folds. A single rock type with varying permeability was assumed, thereby disregarding many practical considerations.

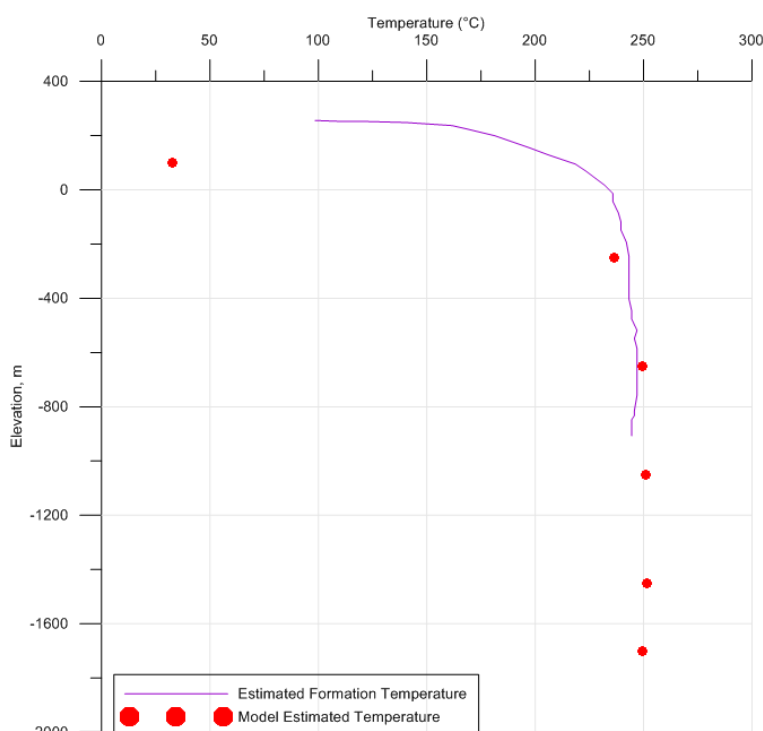


FIGURE 21: Modelled versus measured temperature profiles for Well WW-01

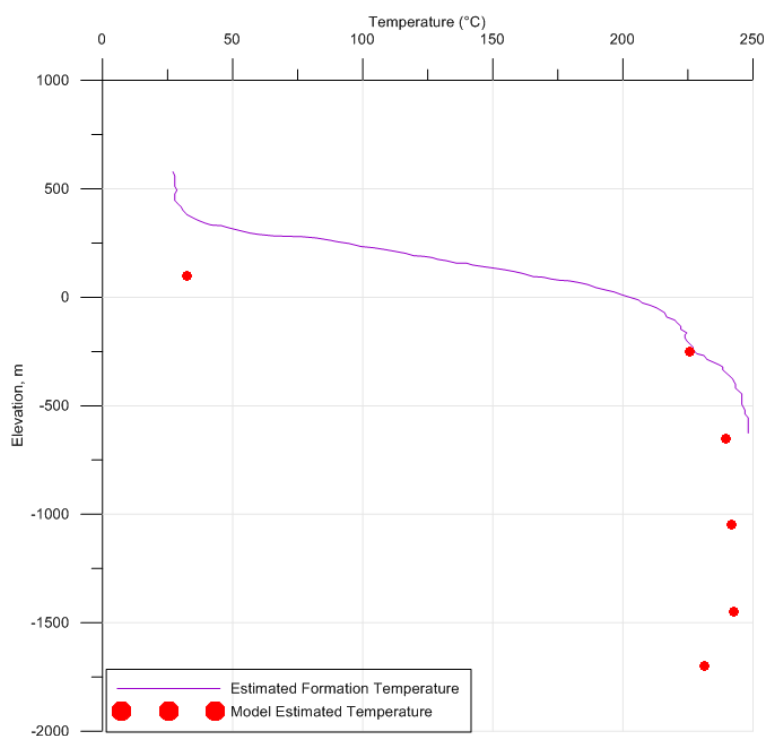


FIGURE 22: Modelled versus measured temperature profiles for Well WW-02

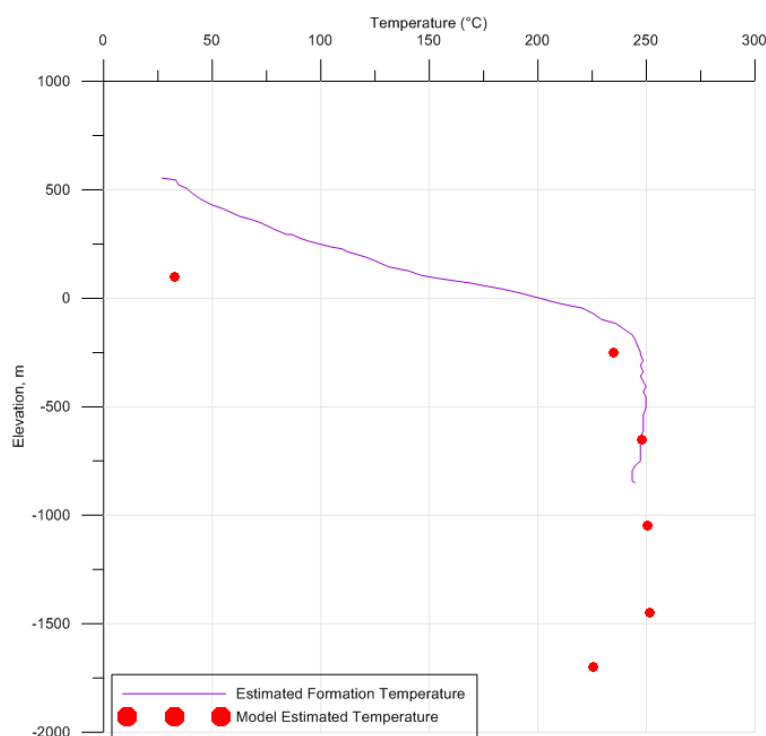


FIGURE 23: Modelled versus measured temperature profiles for Well WW-03

7. CONCLUSIONS

This project was conducted to jointly estimate the resource potential and set up a natural-state numerical model of the Wotten Waven geothermal field. A volumetric model set up for a reservoir area of 5-20 km², and a resource temperature of 150-300°C, revealed that the current Wotten Waven geothermal field should be able to sustain a power plant of the capacity 10-15 MW_e for a maximum time period of 100 years. More exploratory drilling needs to be done, however, if the government plans on expanding the capacity to 120 MW_e by 2020.

Temperature logs from exploratory wells WW-01, WW-02 and WW-03, drilled between 2011 and 2012, confirm the earlier conceptual model from 2008. The logs indicate that the wells were drilled in the proposed outflow from Microtrin volcano feeding the Wotten Waven field. The logs show no indications of boundaries, suggesting that the reservoir boundary is far from the exploratory wells.

The numerical natural-state model of the Wotten Waven field was set up for a total area of 5 km². Natural state was simulated by manually adjusting the permeability distribution as well as the enthalpy and flow rates of pre-determined heat sources and sinks. In achieving steady state, a total of 80 kg/s of fluid, with an enthalpy of approximately 3300 kJ/kg, was injected into three elements, giving a thermal input of approximately 260 MW_t. The numerical model confirmed the presence of a very permeable geothermal reservoir at depths greater than 100 m b.s.l., with an even more permeable formation located around wells WW-01 and WW-02.

A more detailed numerical model should be developed for a greater reservoir surface area to accurately model the reservoir conditions of the Wotten Waven field, including data from the newly drilled production and injection wells. Once the wells are put into production, a production model should be set up to simulate the response of the reservoir (pressure, enthalpy, etc.) to utilization and to assist in optimizing the power production during future utilization.

ACKNOWLEDGEMENTS

I am extremely grateful to the UNU-GTP for granting me the opportunity to participate in the six month UNU Geothermal Training Programme. I would like to acknowledge and extend my heartfelt gratitude to the director, Mr. Lúdvík S. Georgsson, and his deputy, Mr. Ingimar G. Haraldsson. I am thankful to the staff of the UNU-GTP, Ms. Thórhildur Ísberg, Mr. Markús Wilde, Ms. María Guðjónsdóttir and Ms. Málfríður Ómarsdóttir for their support during this time. To all the lecturers and staff members of ÍSOR, Orkustofnun and Reykjavík Geothermal Ltd, thank you for your willingness to share your knowledge and experience.

I would like to express my gratitude to my supervisors, Dr. Gudni Axelsson and Ms. Saeunn Halldórsdóttir, for their excellent guidance and constant supervision, as well as to Ms. Sigríður Sif Gylfadóttir, Ms. Svanbjörg Helga Haraldsdóttir and Mr. Grímur Björnsson for their invaluable assistance during the preparation of this report.

I would like to thank the Director of the Energy Unit of St. Vincent and the Grenadines, Mr. Ellsworth Dacon, as well as the Minister of National Security, Sea Ports etc. - Prime Minister Dr. Hon. Ralph E. Gonsalves, for recommending me and granting me permission to attend this programme. I would also like to extend special thanks to Mr. Alexis George from the Geothermal Project Management Unit in the Ministry of Public Works, Energy and Ports, Commonwealth of Dominica, for allowing access to and granting permission to utilize and publish this data.

Heartfelt thanks to my family and friends back home for their encouragement, motivation and prayers. May God bless you all.

Thanks to the 2014 UNU Fellows for all the good times shared during the past 6 months. Special acknowledgements go to the Reservoir Engineering Fellows - Miyir, Miguel, Maria, Maureen and Leon, and to my roommate Moira, for sharing their knowledge, skills and experiences during this course.

Finally, thanks to God Almighty, through whom nothing is impossible.

REFERENCES

Axelsson, G., 2014: *Simple modelling*. UNU-GTP, Iceland, unpublished lecture notes.

Baltassat, J.M., Coppo, N., Pajot, G., and Dupont, F., 2008: *Magnetotelluric and gravimetric investigations of the geothermal potential in the Roseau valley (Dominica, WI)*. Final report. BRGM, France, 71 pp.

Egilson, Th., and Óskarsson, F., 2012: *Laudat – Dominica flow test of well WW-03*. ÍSOR – Iceland GeoSurvey, Reykjavík, short report ÍSOR-12042 for the Government of the Commonwealth of Dominica, Ministry of Public Works, Energy and Ports, 17 pp.

Egilson, Th., and Thorbjörnsson D., 2012: *Flow test of well WW-02 Laudat, Dominica*. ÍSOR – Iceland GeoSurvey, Reykjavík, short report ÍSOR-12030 for the Government of Dominica, 13 pp.

GDU, 2013: *Dominica geothermal energy development project*. Geothermal Development Unit, Commonwealth of Dominica, project brief for the Ministry of Public Works, Energy and Ports, 15 pp.

Grant, M.A., and Bixley, P.F., 2011: *Geothermal reservoir engineering* (2nd Ed.). Academic Press, New York, 359 pp

Gylfadóttir, S.S., 2014: *Numerical modelling of geothermal systems*. UNU-GTP, Iceland, unpublished lecture notes.

Halldórsdóttir, S., 2014: *Volumetric assessment of geothermal fields*. UNU-GTP, Iceland, unpublished lecture notes.

Haukwa, C.B., 1999: *AMESH, A mesh creating program for the integral finite difference method, user's guide version 1.0*. Lawrence Berkeley National Laboratory, 54 pp.

Lindsay, J.M., Smith, A.L., Roobol, M.J., and Stasiuk, M.V., 2005: Dominica. In: *Volcanic hazard atlas of the Lesser Antilles*. University of the West Indies, Seismic Research Unit, 48 pp.

Maynard-Date, A., and George, A., 2013: A Caribbean geothermal success story. Presented at "Short Course VI on Utilization of Low- and Medium- Enthalpy Geothermal Resources and Financial Aspects of Utilization", organised by UNU-GTP, La Geo, Santa Tecla, El Salvador, 7 pp.

Muffler, L.P.J. (editor), 1979: *Assessment of geothermal resources of the United States - 1978*. USGS Circular 790, Arlington, VA.

Muffler, L.P.J., and Cataldi, R., 1978: Methods for regional assessment of geothermal resources. *Geothermics*, 7, 53-89.

Mwarania, F.M., 2014: *Reservoir evaluation and modelling of the Eburru geothermal system, Kenya*. University of Iceland, MSc thesis, UNU-GTP, Iceland, report 2, 66 pp.

NREL, 2012: *Energy policy sector analysis in the Caribbean 2010-2011, Assessing Antigua and Barbuda; the Bahamas, Dominica, Grenada, St. Lucia, St. Kitts and Nevis; and St. Vincent and the Grenadines*. OAS, 123 pp.

Pruess, K., Oldenburg, C., and Moridis, G., 1999: *TOUGH2, user's guide version 2.0*. Lawrence Berkeley National Laboratory, 197 pp.

Sarmiento, Z.F., and Björnsson, G., 2007: Geothermal resource assessment – volumetric reserves estimation and numerical modelling. Presented at "Short Course on Geothermal Development in Central America – Resource Assessment and Environmental Management", organised by UNU-GTP and La Geo, Santa Tecla, El Salvador, 11 pp.

Sarmiento, Z.F., and Steingrímsson, B., 2011: Resource assessment 1: Introduction and volumetric assessment. Presented at "Short Course on Geothermal Drilling, Resource Development and Power Plants", organised by UNU-GTP and La Geo, Santa Tecla, El Salvador, 15 pp.

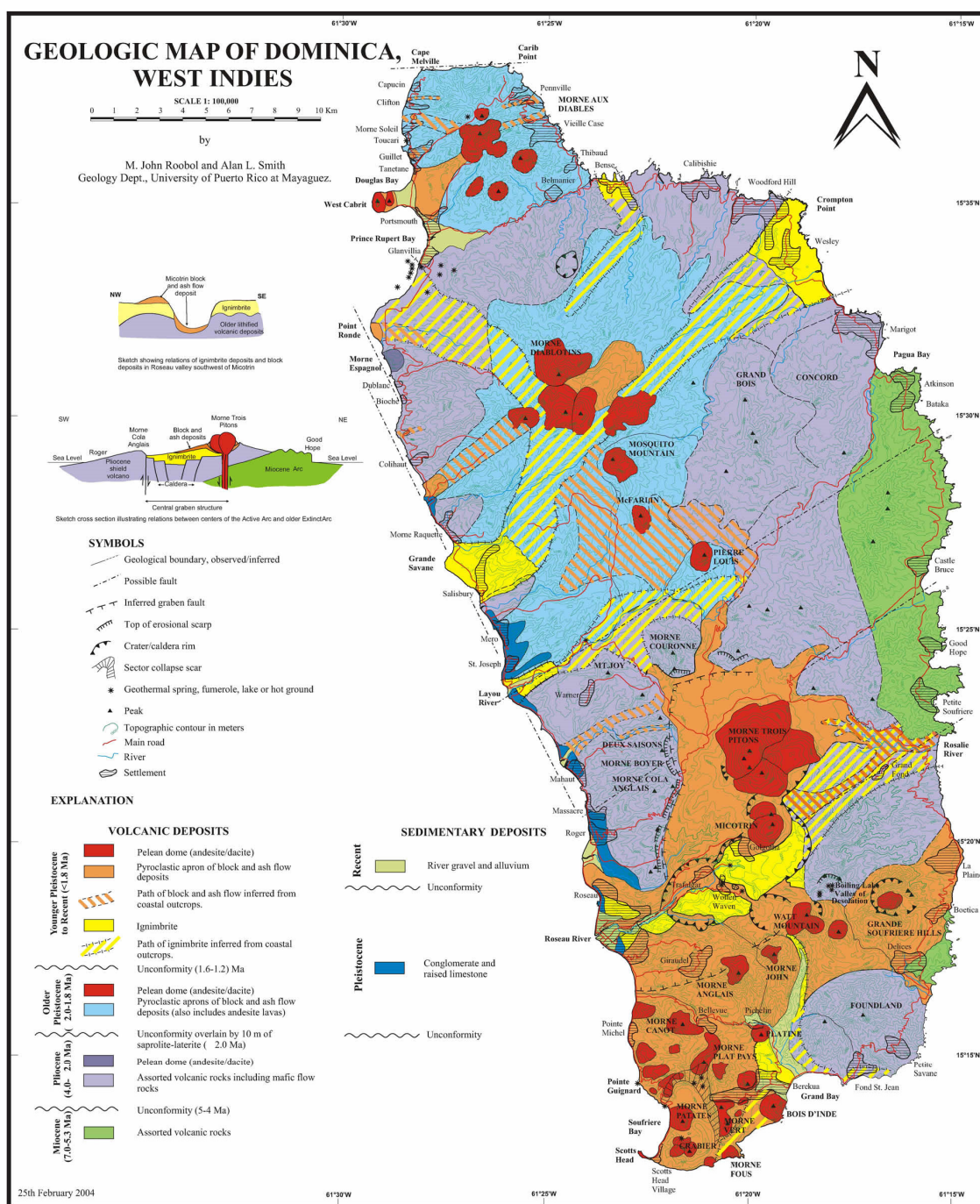
Smith, A.L., Roobol, M.J., Mattioli, G.S., Fryxell, J.E., Daly, G.E., and Fernandez, L.A., 2013: *The volcanic geology of the mid-arc Island of Dominica, Lesser Antilles. The surface expression of an island-arc batholith*. The Geological Society of America, USA, 249 pp.

Steingrímsson, B., 2014: *Borehole geophysics- well logging*. UNU-GTP, Iceland, unpublished lecture notes.

Thorbjörnsson, D., 2012: *Flow test of well WW-01 Wotten Waven, Dominica*. ÍSOR – Iceland GeoSurvey, Reykjavík, short report ÍSOR-12067 for the Government of Dominica, 9 pp.

Traineau, H., and Lasne, E., 2008: *Geological and geochemical survey of the Wotten Waven geothermal field, Dominica, West Indies*. CFG Services, report for Programme Européen INTERREG III-B-Espace Caraïbes, 65 pp.

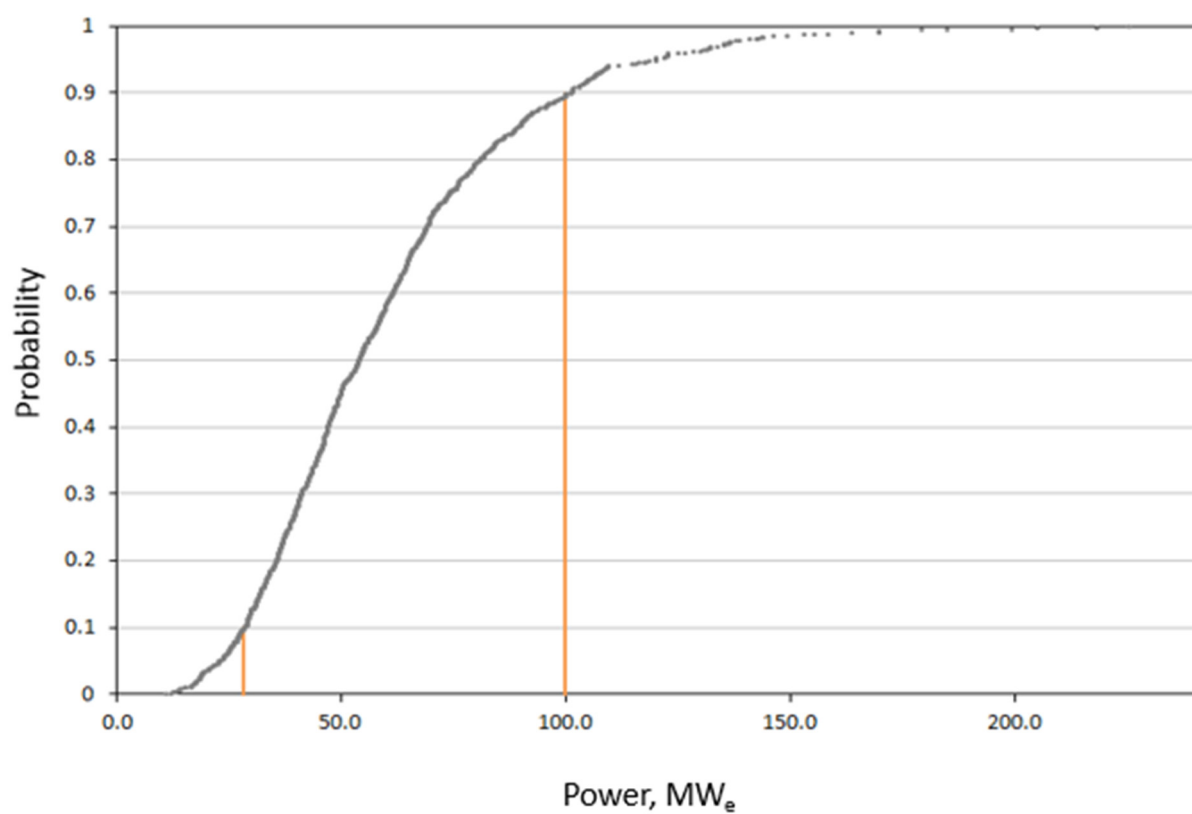
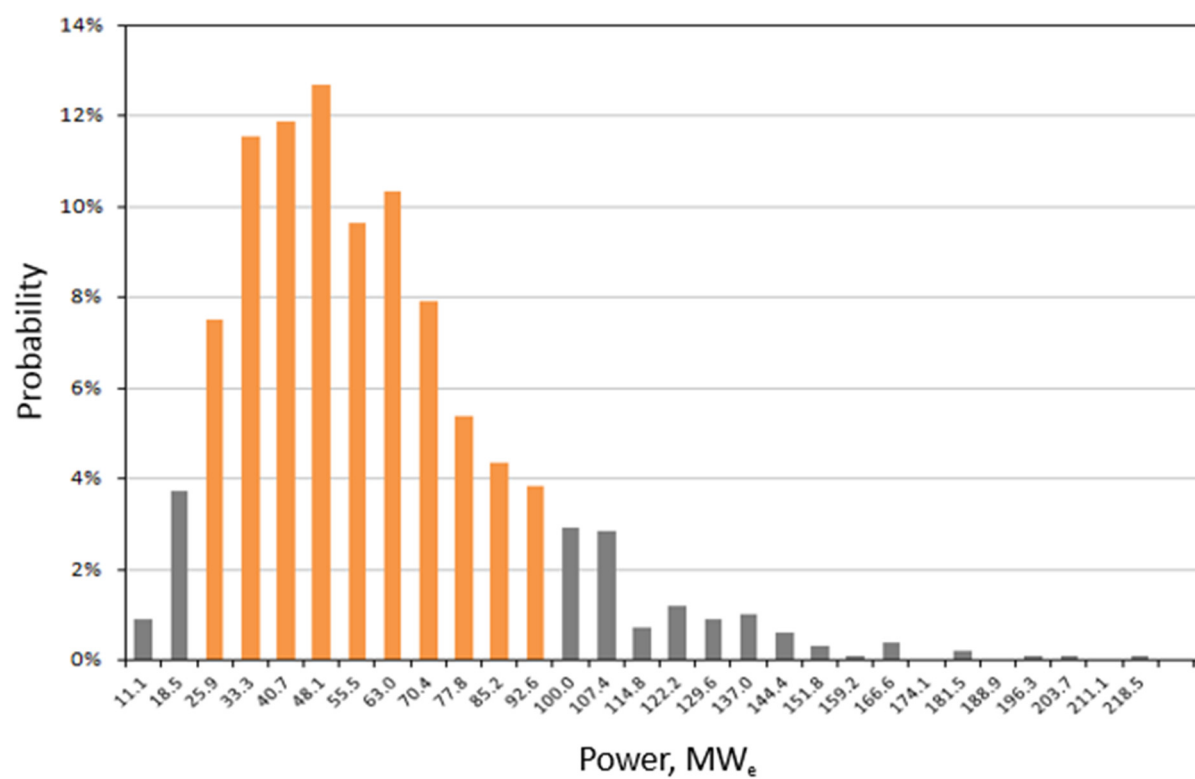
APPENDIX I: Geological map of the island of Dominica



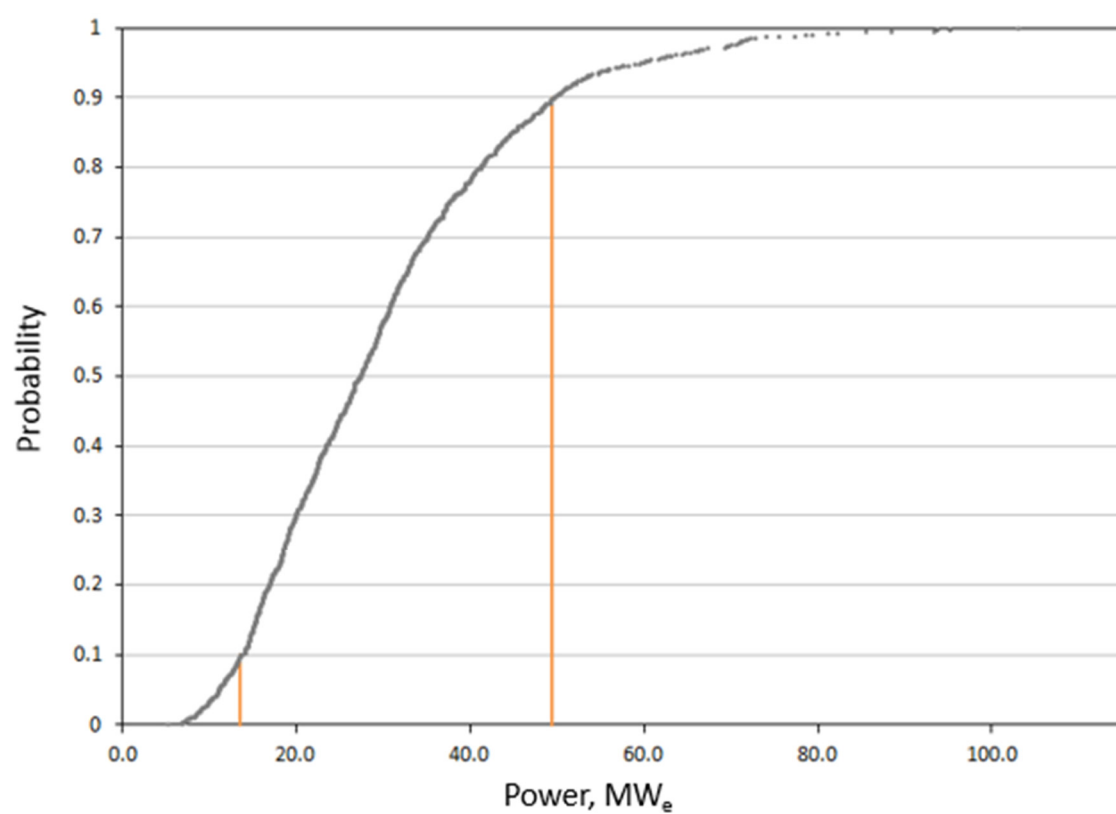
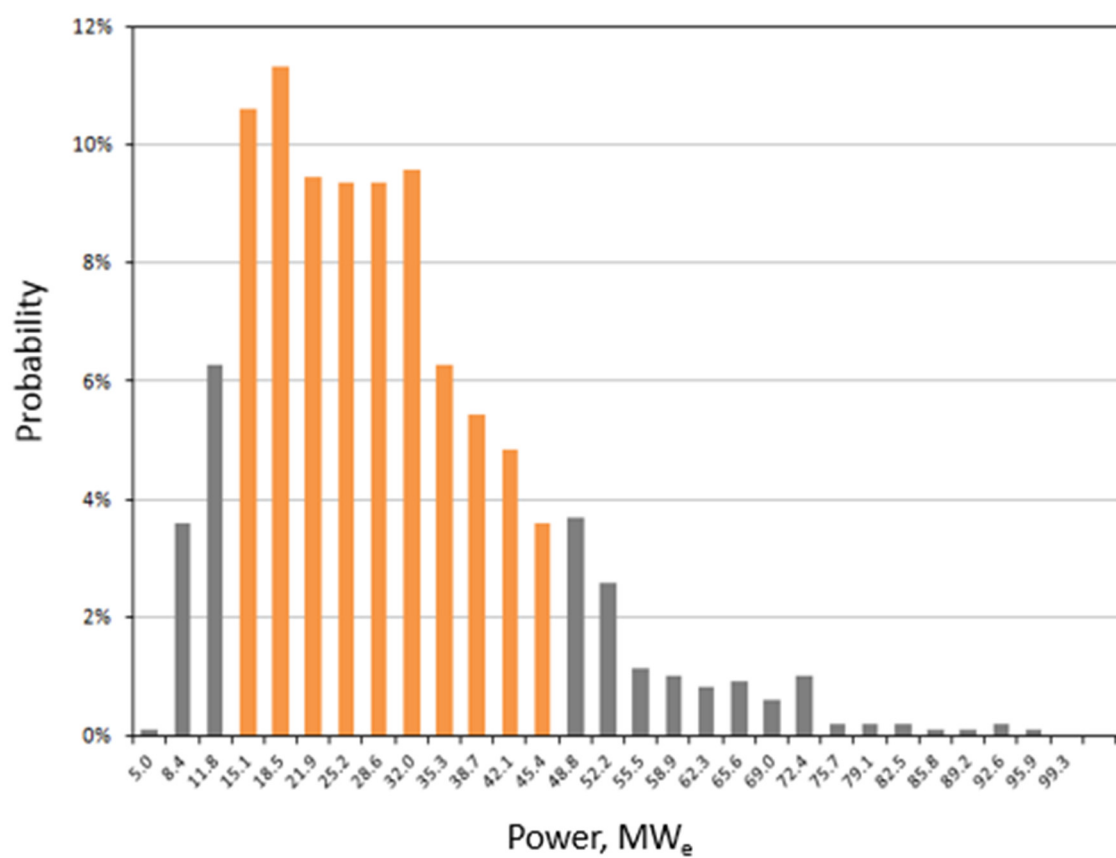
Present Affiliations: MJR, Saudi Geological Survey, P.O.Box 54141, Jeddah 21514, Saudi Arabia; ALS, Dept. of Geological Sciences, California State University, 5500 University Parkway, San Bernardino, California 92407, USA. Fieldwork supported by NSF grants EAR 7717064, EAR 9527273, OEDG 01119934 and NASANCC W-0088.

Note: To print this map at the correct scale of 1:100,000, the 10 kilometer bar scale has to be 10 cm long.

APPENDIX II: Distributive (above) and cumulative (below) probability distribution for a generating period of 50 years



APPENDIX III: Distributive (above) and cumulative (below) probability distribution for a generating period of 100 years





UNITED NATIONS
UNIVERSITY

UNU-GTP

Geothermal Training Programme

Orkustofnun, Grensasvegur 9,
IS-108 Reykjavik, Iceland

Reports 2014
Number 13

ELECTRICAL CONTROL AND PROTECTION SYSTEM OF GEOTHERMAL POWER PLANTS

Daniel Gorfie Beyene

Ethiopian Electric Power Company

P.O. Box 1233

Addis Ababa

ETHIOPIA

dantech72@yahoo.com

ABSTRACT

This study explores the use of electrical controls and a protection system in a geothermal power plant for smooth and reliable operation of the plant. Geothermal power is a renewable energy and is also used as a baseload for the supply of electricity in the grid. To fulfil this goal, great measures must be taken in the selection of electrical protection equipment for the different electrical components, such as the transformer and the generator, as described in the report. A geothermal power plant must also be furnished with a proper control system for controlling different components of the plant such as the turbine, the generator, the transformer, the excitation system and other related accessories so that when some abnormal condition occurs in the system, proper action can be taken.

1. INTRODUCTION

Energy is one of the most fundamental elements of our universe. The significance of energy is especially vital for developing countries like Ethiopia. On-demand energy in the form of electricity and modern fuels is the lifeblood of modern civilization and is a critical factor for economic development and employment. In 2013, the total installed capacity of electrical power in Ethiopia was more than 2,200 MW, mainly from hydro power plants, with some help from wind and a small pilot geothermal power plant.

Ethiopia launched a long-term geothermal exploration undertaking in 1969. Over the years, a good inventory of the potential target areas has been built up and a number of the more important sites have been explored. About 16 geothermal prospects are judged as having potential for electricity generation. A much larger number could be developed for applications in agriculture, agro-industry, etc.

Ethiopia could generate a huge amount of energy from geothermal resources, both for local consumption and export. However, an important constraint for this is the lack of finances. On this point, the government is considering various options that could help develop the resource while reviewing the overall energy policy of the country. One option is to invite private investors to participate in the geothermal resource utilization sector, like the Corbetti geothermal power plant project which is planned to be totally built by the private sector.

In the above perspective, the government is planning to increase the country's power generation capacity by developing the identified geothermal resources in the prospect areas. The Aluto-Langano geothermal power plant is located 200 km south of Addis Ababa and started operation in 1998. Two generation units can supply 7.28 MW in total, about 3.5 MW each. There are two types of turbines: one is a high-temperature vapour type that revolves the generator directly (6,000 rounds/min); the other is a media (isopentane/isobutane) turbine with heated by middle-temperature vapour heating the media to revolve the generator (1,500 rounds/min).

This report mainly focusses on the electrical controls and protection system for a geothermal power plant, with emphasis on how the control system and various electrical protective relay schemes could be integrated to provide reliable operation of the Aluto-Langano geothermal power plant.

2. OVERVIEW OF GEOTHERMAL POWER PLANTS

The basic types of geothermal power plants in use today are steam condensing turbines and binary cycle units. Steam condensing turbines can be used either in flash or dry-steam plants operating at sites with intermediate- and high-temperature resources ($\geq 150^\circ\text{C}$). The power plant generally consists of pipelines, water-steam separators, vaporizers, de-misters, heat exchangers, turbine generators, cooling systems, and a step-up transformer for transmission into the electrical grid.

Binary-cycle plants, typically organic Rankine cycle (ORC) units, are commonly installed to extract heat from low-temperature geothermal fluids (generally from 70 to 170°C) derived from hydrothermal and enhanced geothermal system type reservoirs. Binary plants are more complex than condensing ones since the geothermal fluid (water, steam or both) passes through a heat exchanger for heating another working fluid. This working fluid, such as isopentane or isobutene with a low boiling point, vaporizes, drives a turbine, and is then air cooled or condensed with water, as shown in Figure 1. Binary plants are often constructed as linked modular units of a few MW in capacity.

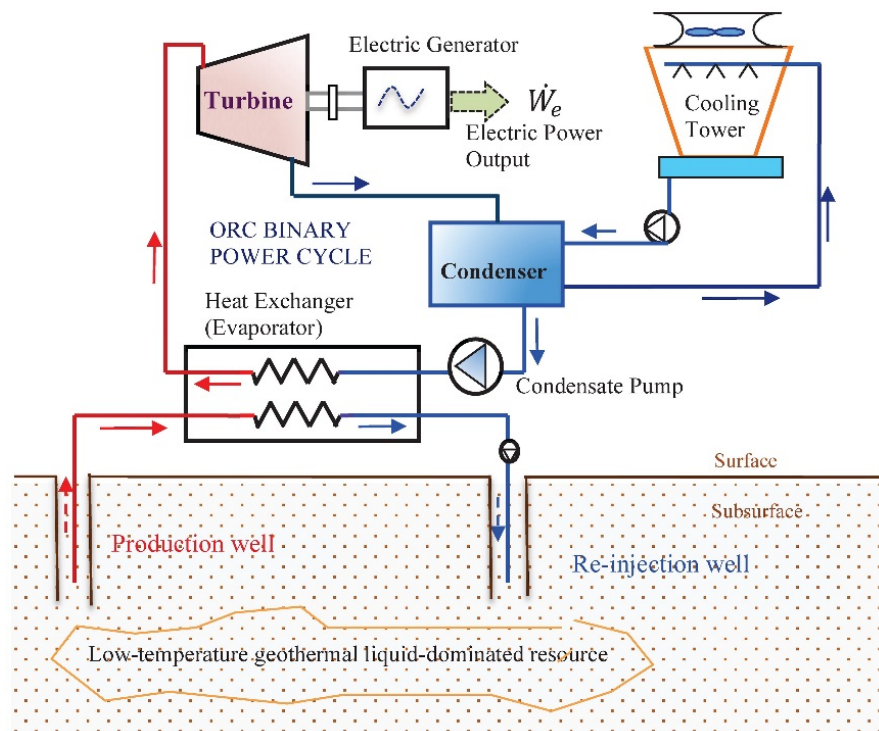


FIGURE 1: A schematic diagram showing the basic concept of a low-temperature geothermal binary ORC system for electrical power generation (Ismail, 2013)

There are also combined or hybrid plants, which comprise two or more of the above basic types, such as using a binary plant as a bottoming cycle with a flash steam plant, to improve versatility, increase overall thermal efficiency, improve the load-following capability, and efficiently cover a wide resource temperature range.

2.1 Binary cycle power plants

The binary cycle power plant uses an organic working fluid instead of steam (geothermal fluids). In this system the primary fluid (brine) is extracted from the low-temperature (intermediate-temperature) geothermal resource from the production well. Figure 1 shows the principal elements of this type of plant. The primary (reservoir) fluid carries the heat and efficiently transfers this heat to the low-boiling-point working fluid, using an effective heat exchanger.

The organic fluid is then condensed in a similar manner to the steam in the flash power plant, except that a shell and tube type condenser rather than direct contact is used. The fluid in a binary plant is recycled back to the heat exchanger and forms a closed loop. The cooled reservoir fluid is again re-injected back into the reservoir. A binary cycle plant typically varies in size from 500 kW to 25 MW.

3. MAIN ELECTRICAL COMPONENTS OF A GEOTHERMAL POWER PLANT

In geothermal power plants the steam rotates a turbine that activates a generator, which produces electricity. In order to make the electricity production feasible, many electrical and mechanical components are needed, as shown in Figure 2.

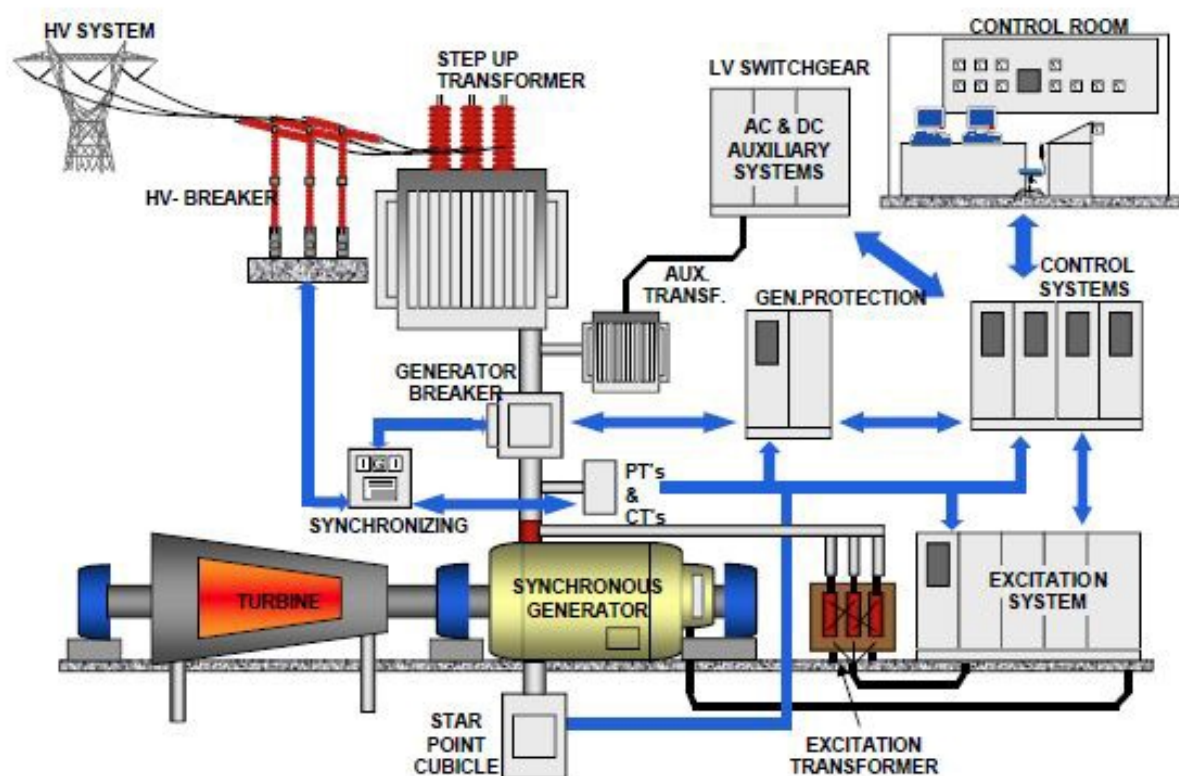


FIGURE 2: Main electrical, control and instrumentation parts of a geothermal power plant (ABB, 2014)

3.1 Generator

The generator is an electro-mechanical device that converts mechanical energy to alternating current electrical energy. The generator is composed of four basic components: the shaft, the exciter, the rotor and the stator. The turning of the turbines powers the exciter to send an electrical current to the rotor.

Generators appear in a number of sizes, ranging from less than 1 MW (typically in a cogeneration plant) to 600 MW. Generated voltages are generally constrained in the range of 6.6 kV to 33 kV due to design limitations in the generator insulation systems. This means that step-up transformers are generally needed to connect the generator to the transmission system or grid.

3.2 Generator excitation system

The main functions of the excitation system are to provide a variable DC current to the field winding for controlling terminal voltage with suitable accuracy, ensure stable operation with the network and/or other machines, contribute to transient stability subsequent to a fault, communicate with the power plant control system and keep the machinery within permissible operating ranges.

3.3 Governor system

The governor system is a vital control system in a geothermal power plant as it regulates the steam turbine speed, power and regulation of the grid frequency in response to control signals such as speed error and power error compared to the desired values. This action takes place in a closed loop control system in which control action goes on till the power mismatch is reduced to zero. The governor system, as shown in Figure 3, receives speed and power signals that are then compared with the reference values and adjusts them to the desired values.

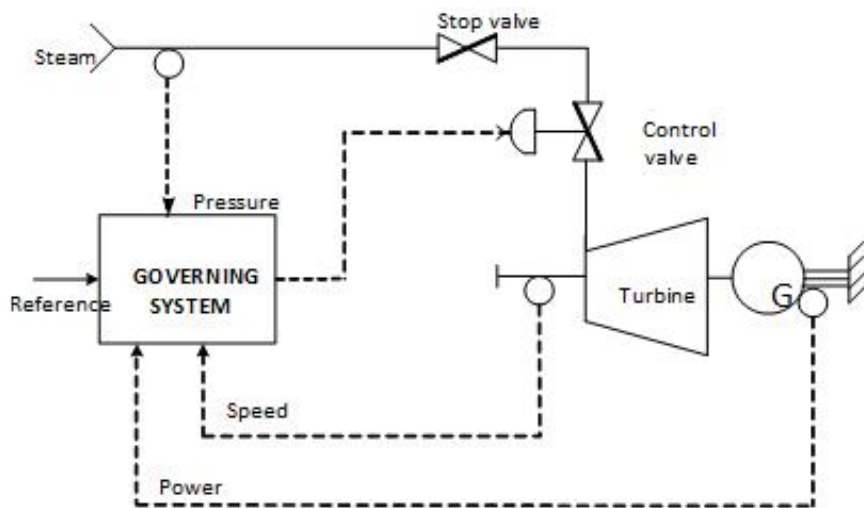


FIGURE 3: Steam turbine governing scheme

Control valve (CV) is a hydraulic valve used for automatic control of fluid flow in response to a command from the governing system. If the steam pressure is below the predefined level, the governor system sends a command signal to close the control valve.

The four main functions of the governing system are as follows:

a) **Emergency:** To limit or control the speed rise to an acceptable limit upon a load rejection (when the unit is suddenly disconnected from the load).

- b) **Turbine:** To control the power that is generated by controlling the position of the steam governing valve.
- c) **Start-up and stop:** To control the speed of the turbo generator during initial run-up and synchronization.
- d) **Normal operation:** To match the power and participate in the control of system frequency. It is mainly divided into:
 - i. Pressure control for constant steam pressure (maximum power)
 - ii. Power control for constant output power

3.4 Power transformer

The power transformer transforms the voltage from the generator to a high voltage necessary for transmission over the utility's electricity grid (transmission network). Depending on the size of the system, transmission voltages will range from 33 kV to 500 kV.

Limitations on the insulation design which can be achieved on rotating machinery prohibit the generator from producing high voltage without the use of a step-up transformer (Fassbinder 1997).

The power transformer (Figure 4) must fit the generator so that the transformer can totally utilize the generator's active and reactive power capacity. The standard *C57.116-1989 IEEE Guide for Transformers Directly Connected to Generator* describes how this characteristic must be matched to the situation (ABB, 2004):

- Transformer MVA rating;
- Short circuit impedance of the transformer;
- The secondary (high-voltage) rating;
- The primary (low-voltage) rating.



FIGURE 4: A power transformer

3.5 Station start-up transformer

The station start-up transformer is a power transformer (usually 400V AC secondary voltage) used to connect the power station to the transmission system so that power is available for the plant equipment when the plant is being started. Power plants are routinely brought down for servicing of major pieces of equipment. Generally, this transformer is used whenever the station auxiliary transformer is unavailable such as during planned maintenance or repairs.

3.6 Station or unit auxiliary transformer

The station or unit auxiliary transformer is connected to the generator output by a tap off of the isolated Phase Bus Duct. The high-voltage winding of the transformer is designed to match the generator output voltage and the low voltage is supplied for different pumps and other auxiliary systems in a power plant, shown in Figure 5. This transformer and the station start up transformer have to be specified and connected in a configuration so that the output voltage will be in phase.

The unit auxiliary transformer is the normal power source for the station equipment when the plant is operating. Once the generator is

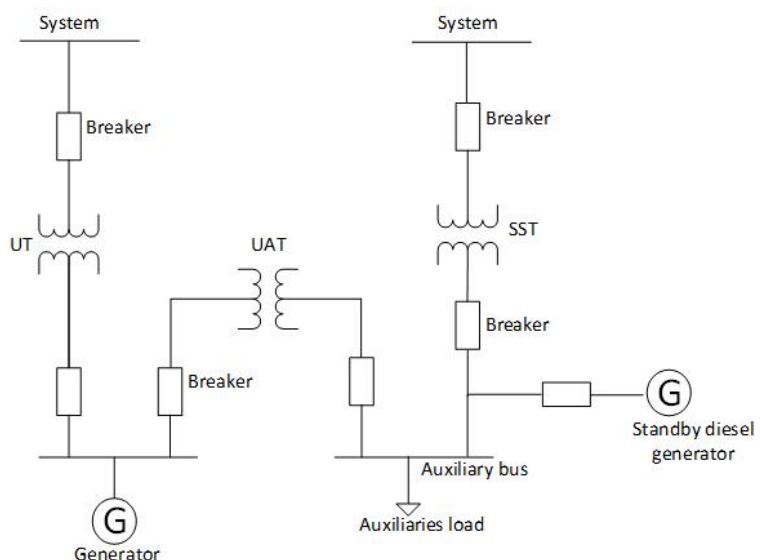


FIGURE 5: Single line diagram for a supply of a generation station's auxiliary power

brought on line and is connected to the transmission grid, the station load can be transferred from the start-up transformer.

3.7 Standby diesel generator

The standby diesel generator is a vital electrical component in any power plant for delivering power to main components of the unit during start-up in the case of a total black-out in the system. The sequence of operations for delivering power to the auxiliary load is as follows:

- a) Using the unit auxiliary transformer directly tapped from the unit;
- b) Using station service transformer tapped from the system or grid;
- c) Using standby diesel generator.

The rating of the standby diesel generator must supply most of the power consumed by auxiliary load for a short time when a black start of the plant is required.

3.8 Ventilation system

The ventilation system of a geothermal power plant is a mandatory process for the circulation of clean air in the power plant. It is used for the following:

- Filtering of H_2S ;
- Circulating and cooling air in the control room;
- Cooling different electrical components such as excitation equipment and protection equipment;
- Discarding heat from the cooling unit to the atmosphere.

3.9 Auxiliary power consumption

The auxiliary power consumption is the electrical power needed to drive the pumps and fans that support the operation of a power plant. The power consumption of a geothermal power plant is high compared with other power plants, since the plant is comprised of different high rating motors for:

- Cooling tower fans;
- Cooling pumps;
- Feed pumps;
- Air compressors
- Lube oil pump (hydraulic system);
- Fire water pump;
- Brine pump;
- Ventilation system.

As an example, the generated capacity of the Berlin binary geothermal power plant is 12.5 MVA and the total power consumed by pumps and fans is approximately 1.3 MVA, hence 10.4 % of the total power generated is consumed by the auxiliary load (ENEX, 2014).

3.10 DC auxiliary power system

The direct current system in thermal generating stations is provided for the following functions:

- Supply to trip coils and closing coils of switchgear for switching operations;
- Indication: Indicating lamps, alarm and annunciation, etc.;
- Energizing the holding and operating coils in control and interlock schemes, and in protection schemes;
- Power supply to communication equipment and supervisory control;
- Supervisory control and data acquisition system (SCADA);
- Emergency lighting including inverter;
- Generator exciter field flashing;
- Lubricant oil pump;
- Different sensors (temperature, pressure, gas and other);
- Control system of PLC.

The system consists of a storage battery with its associated eliminator type chargers, providing the stored energy system required to ensure adequate and uninterruptible power for critical power plant equipment. The battery and battery circuits should be properly designed, safeguards maintained, and the emergency requirements should be carefully estimated to ensure adequate battery performance during emergencies.

3.11 Motors

The power station auxiliary motors used for the control of valves to several hundred kilowatts for driving the air compressor, cooling tower fan, cooling water pumps, the feed pump to drive isopentane/butane from the condenser and feed it into the vaporizer inlet etc. The motors are generally of squirrel cage type with a soft starter for quick starting and reduced starting current. The motor should meet, without difficulty, a voltage variation of +5 percent and a frequency variation of +4 percent. A reduction of wider voltage fluctuation and transient voltage dips of greater magnitude during system faults must not affect the operation of the motors. Condensate pumps are customarily frequency inverter controlled.

4. ELECTRICAL CONTROL SYSTEM

The main electrical control system in a geothermal power plant is associated with the start and stop sequence for the unit and with optimum running control of power (real and reactive), voltage and frequency. The type of control equipment and the levels of control to be applied to a geothermal plant are affected by such factors as number, size and type of turbine and generator. The control equipment for a geothermal power plant include control circuits/logic, control devices, indication, instrumentation and protection at the main control board and at the unit control board for generation, conversion and transmission operation, including grid interconnected operation of the geothermal station to other stations. These features are necessary in order to provide operators with the facilities required for the control and supervision of the station's major and auxiliary equipment.

4.1 Sensors, transducers and actuators

Sensors: Sensors are important mechatronic devices for the measurement of physical variables such as pressure, temperature, level etc. and change them to an electrical signal.

Transducer: It is a device that converts a primary form of energy into a corresponding signal required by the control system (PLC input signal). Normally transducers are installed in or on the machine to make appropriate measurements of vibration, position, speed, and pressure.

Actuators: These are used in the conversion of electrical energy to mechanical energy to do the final desired work. Some actuators usually found in a geothermal power plant are the steam guide inlet guide,

Servo valve position controllers, Solenoid valves, and relays to open or close the circuit breaker.

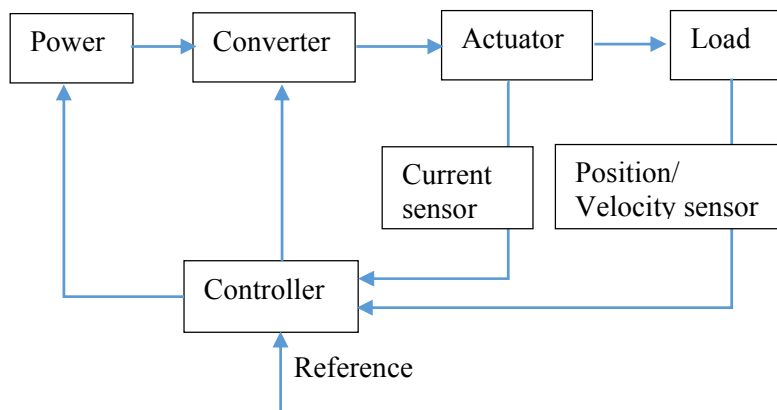


FIGURE 6: The composition of a controlled drive system

The complete control drive of the system is shown in Figure 6; the sensor measure signals and sends a command to the controller to give the desired level of voltage and current to the actuator for the desired movement of the mechanical load.

Different types of sensors (flammable gas detectors, pressure detectors, temperature detectors and level sensors) have to be placed on the main mechanical components of the

geothermal power plant such as the turbine, condenser, evaporator, valves and pipelines in order to take proper action before components suffer severe damage.

4.2 Conventional control system with relay logic (mechanical/analogue electronic governor)

Control systems of the power plant are broadly classified under four main categories:

1. **Manual control:** Whereby each item in the prestart chain checks: starting, synchronizing, loading and stopping, and a sequence is selected and performed in turn by hand, whether mechanically or by push buttons.
2. **Semi-automatic control:** Whereby, from a single manual starting impulse, a unit may be brought to the ready to synchronise conditions by automatic selection, performance, and provision of a sequence of controls. Likewise, a similar stopping impulse completely shuts down the unit. Synchronizing and loading and running controls remain manual functions from the local and remote control points.
3. **Fully automatic control:** Whereby means are provided for running up, automatically synchronizing and loading up to a predetermined quantity on receipt of a single starting impulse. Subsequent manual variations of loading and excitation may be provided as a remote control function. The corresponding stopping impulse will cause the load to be reduced, the unit to be disconnected from the busbars and the turbine to be shut down completely.
4. **Offsite supervisory control:** Starting, stopping, switch closing or opening and other functions are initiated from a remote point, together with indications of successful operations of voltage and load control and of the repetition of alarm conditions at the remote control point.

4.3 Computer-based control of a geothermal power station

Recent practice for controlling geothermal power plants is based on a combination of computer-based and non-computer-based equipment utilized for unit, plant and system control. Control of a power plant from local, centralized and offsite modes of operation and supervision are listed in Table 1.

The control system receives input signals (status signals) from main equipment such as the turbine or the generator, and from various other accessory equipment, such as (temperature, pressure, and level), governor, exciter, and automatic synchronizer. Status inputs are obtained from control switches and level and function switches indicative of pressure, position, etc., throughout the plant. The proper combination of these inputs to the control system logic will provide outputs to the valves, motors, breakers, governor, the exciter, and other equipment to start or shut down the unit. Any abnormalities

TABLE 1: Summary of control hierarchy for electrical power plants

Control category	Subcategory	Remarks
Location	Local	Control is local at the controlled equipment or within sight of the equipment
	Centralized	Control is remote from controlled equipment, but within plant
	Offsite	Control location is remote from the project
Mode	Manual	Each operation needs a separate and discrete initiation; could be applicable to any of the three locations
	Automatic	Several operations are precipitated by a single initiation; could be applicable to any of the three locations
Operation (supervision)	Attended	Operator is available at all times to initiate control action
	Unattended	Operation staff is not normally available at the project site

in the inputs must prevent the unit's start-up or, if already on-line, provide an alarm or initiate its shutdown. Supervisory control from an offsite station or group of power stations is also provided sometimes. A schematic overview of power plant automation with a supervisory control and data acquisition (SCADA) system is shown in Figure 7.

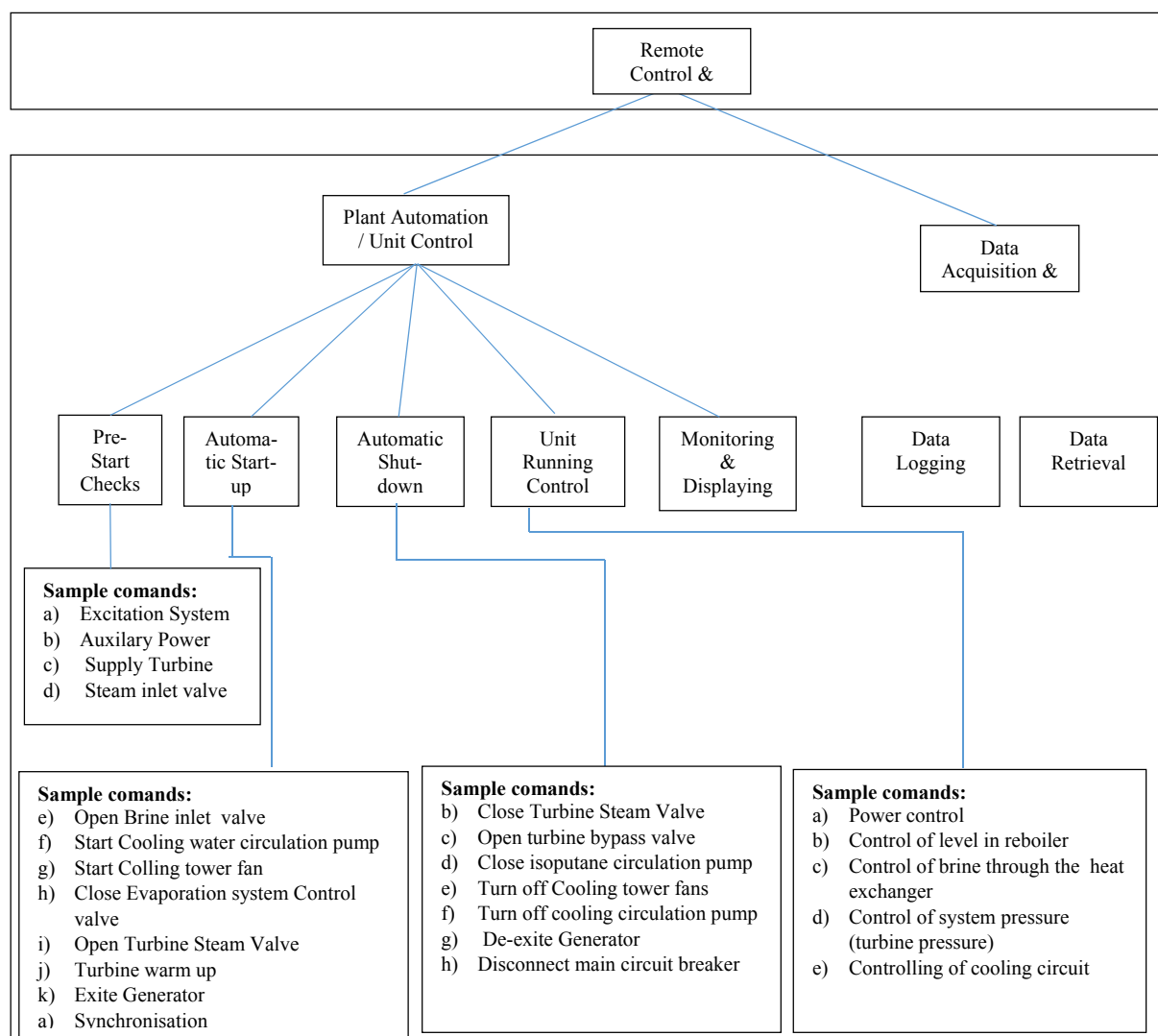


FIGURE 7: Schematic overview of power plant automation with a supervisory control and data acquisition (SCADA) system

4.4 PLC and SCADA system

SCADA is a technology that enables a user to collect data from one or more distant facilities and/or send control instructions to the facilities. Modern control rooms utilize the far more cost-effective supervisory control and data acquisition (SCADA) systems, including programmable logic controllers (PLCs), and distributed computer control systems with graphic display screens, to implement a vast array of control schemes. The SCADA control scheme also provides flexibility in control, alarming, sequence of events recording, and remote communication that was not possible with the hardwired control systems (Figure 8).

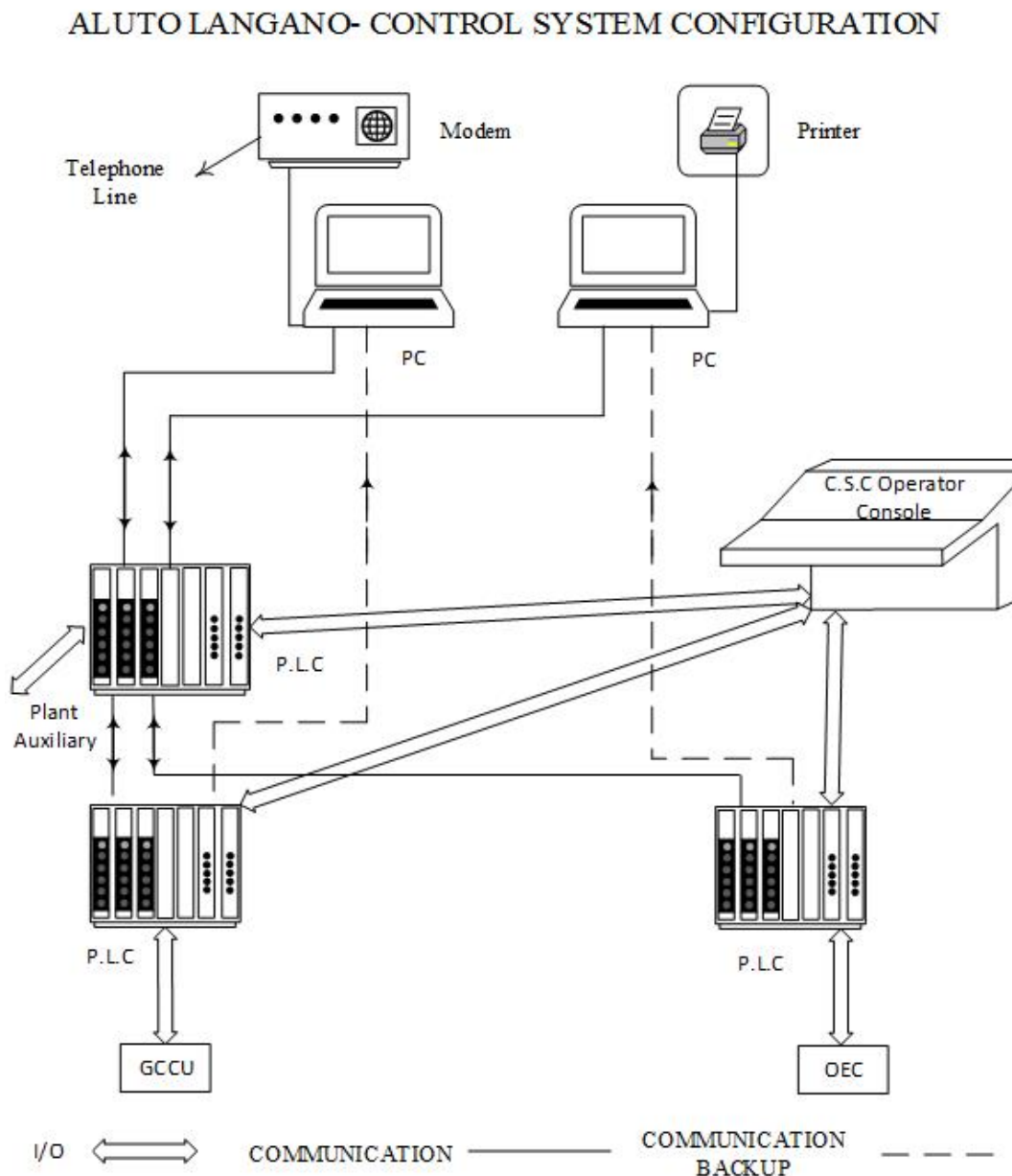


FIGURE 8: SCADA system hardware with PLC controller
(Ormat, 1997)

The SCADA interface system allows operators to:

- Start-stop the machinery and change the set point of the plant baseload;
- Obtain written reports of all parameters about the power plant;
- Monitor the plant status and control the alarm summery, events and analyse them.

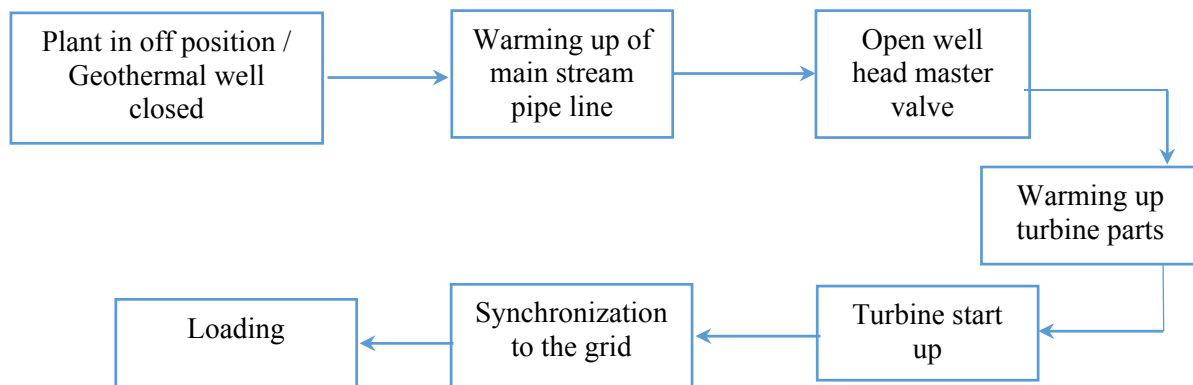


FIGURE 9: Start-up sequence of a geothermal power plant

The control system of a geothermal power plant has a big role in the smooth operation of unit start-up and shut down, summarized in Figure 9.

5. SYNCHRONIZING

Before connecting a generator in parallel with other machines, it is necessary to prove that the incoming machine and the running system have the same frequencies and voltages, and are in phase. The methods employed in electric power stations are described below.

Manual synchronizing: In this method, incandescent lamps are connected across the respective phases of the incoming and running voltage buses. Voltage of the incoming machine is matched with the system voltage by manually adjusting the excitation of the machine. The frequency and phase angle differences are indicated by lamps. Lamps will flicker with a frequency equal to the difference between the frequencies of incoming machinery and the running system. When the phase and frequencies are matched, the lamps will extinguish. This is the indication of synchronism of the machine with the system. The breaker is then closed manually.

Manual synchronizing is simple and cheap. This requires personal supervision and the judgment of the operator. This type of synchronization is not suited for automatic or remote control of the unit. However, this has normally been provided as a standby in power stations for use in case of failure of the automatic/synchronizing equipment.

Automatic synchronizing: Synchronizing equipment (Figure 10) performs the following functions automatically:

- It continuously controls the terminal voltage of the incoming machinery until it is almost equal to the voltage of the system to which it is to be connected;
- It controls the speed of the prime mover so that the frequency difference is within the predetermined value;
- It energizes the closing coil of the circuit breaker associated with the incoming machinery at an instant when the phase difference between the two sources is sufficiently small and only when conditions (i) and (ii) have been simultaneously satisfied.



FIGURE 10: Automatic synchronoscope

6. ELECTRICAL PROTECTION SYSTEM

Power system protection is the process of making the production, transmission, and consumption of electrical energy as safe as possible from the effects of failures and events that place the power system at risk. It is cost prohibitive to make power systems 100% safe or 100% reliable. Power system protection must determine from the measurements of currents and/or voltages whether the power system is operating correctly. Three elements are critical for protective relays to be effective: measurements, data processing, and control.

The high costs associated with large generating and transforming plants accentuate the need for reliable, high speed schemes of protection to:

- a) Minimise fault damage and so reduce the possible need to replace the plant (capital outlay);
- b) Reduce repair outage time and so minimise the need to run a lower merit (less cost-efficient) plant in order to meet the demand (revenue expenditure);
- c) Assist in maintaining system stability.

6.1 Main components of protection systems

The main components of protection systems are discussed briefly below.

- **Current & voltage transformers**, also called instrument transformers. Their purpose is to step down the current or voltage of a device to measurable values, within the instrumentation measurement range 5 A or 1 A in the case of current transformers (CTs), and 110 V or 100 V in the case of voltage (or potential) transformers (VTs/ PTs). Hence, protective equipment inputs are standardized within the ranges above.
- **Protective relays** are intelligent electronic devices (IEDs) which receive measured signals from the secondary side of CTs and VTs and detect whether the protected unit is in a stressed condition (based on their type and configuration) or not. A trip signal is sent by protective relays to the circuit breakers to disconnect the faulty components from the power system if necessary (Reimert, 2006).
- **Circuit breakers** act upon open commands sent by protective relays when faults are detected and upon close commands when faults are cleared. They can also be manually opened, for example, to isolate a component for maintenance.

6.2 Generator protection

Power station generators should be protected against mechanical, electrical, and thermal damage that may occur as a result of abnormal conditions in the plant or in the utility system to which the plant is electrically connected. The protection of a generator presents a very challenging problem because of its system connections on three different sides, as shown Figure 11. On one side, it is connected to the prime mover; on the other side, it has to run in synchronism with the grid. On yet another (third) side, it is connected to the source of DC excitation. Thus, it is obvious that generator protection is very complex compared to protection for other elements of the power system.

If there is a fault on a steam generator, it is not enough to open the main circuit breaker connecting it to the power grid; the following must be done as well:

- Steam supply to the turbine is stopped or bypassed;
- Field circuit of the generator is interrupted;
- Field coils are connected across a resistor to dissipate the stored energy;
- Generator is kept running at a slow speed with the help of a barring gear till it cools down uniformly, so as to avoid uneven expansions.

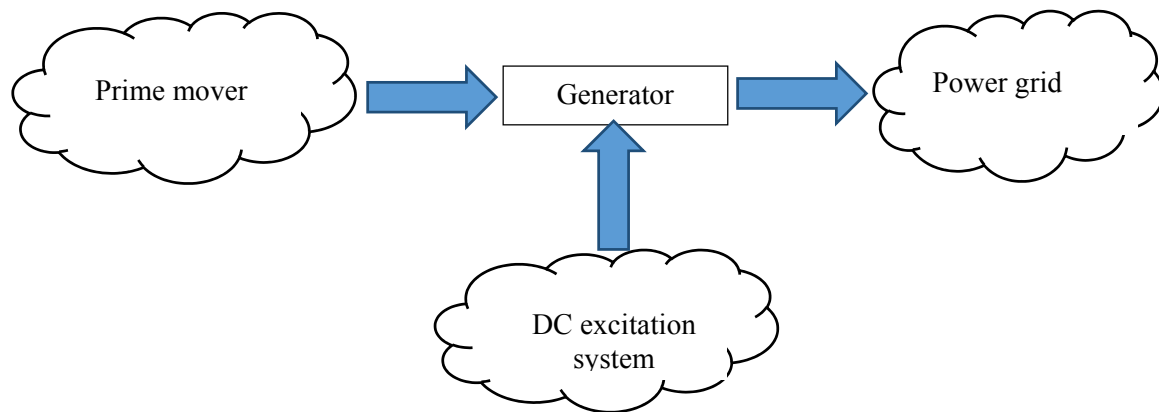


FIGURE 11: Principles of generator protection

Putting the generator back online is a rather slow process because all the parameters (temperature and pressure) have to be progressively built up to avoid thermal shock which would result in uneven expansion which, in turn, might cause unacceptable vibration. Therefore, an unscheduled outage of a geothermal power station is avoided as far as possible.

6.2.1 Generator faults

Stator faults: Stator faults involve the current carrying conductors and must be cleared quickly from the power system by a complete shutdown of the generator. There may be faults to earth, between phases or between turns of a phase, singly or in combination. The great danger from all faults is the possibility of damage to the insulation of the stator core and stator winding due to the heat generated at the point of the fault. Figure 12 shows the hierarchy of various electrical faults on a generator.

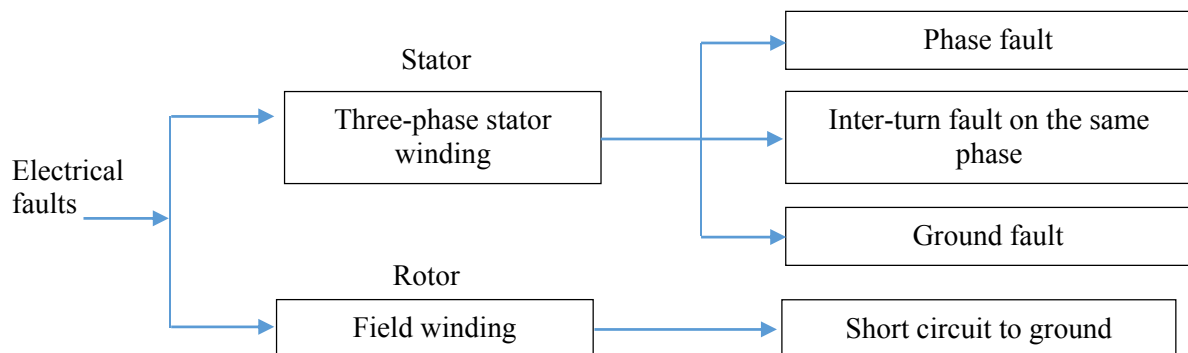


FIGURE 12: Various electrical faults on a generator

Phase-to-phase faults and inter-turn faults are both less common than earth faults. It is relatively easy to provide protection for phase-to-phase faults, but inter-turn faults are, on the other hand, more difficult to detect and protection is not usually provided. Generally, inter-turn faults quickly involve contact with earth via the stator core and are tripped by stator earth-fault protection.

Rotor faults: The rotor carries the field winding which is kept isolated from the ground. Neither the positive nor the negative terminal of the dc supply is grounded. Thus, any ground fault on the rotor field winding does not affect the workings of the alternator. However, a subsequent fault would cause a section of the rotor winding to be short circuited, giving rise to a secondary flux which opposes the main flux in the proximity of the shorted turns, causing distortion in the distribution of the main flux. The flux will become concentrated on one pole but dispersed over the other and intervening surfaces. The

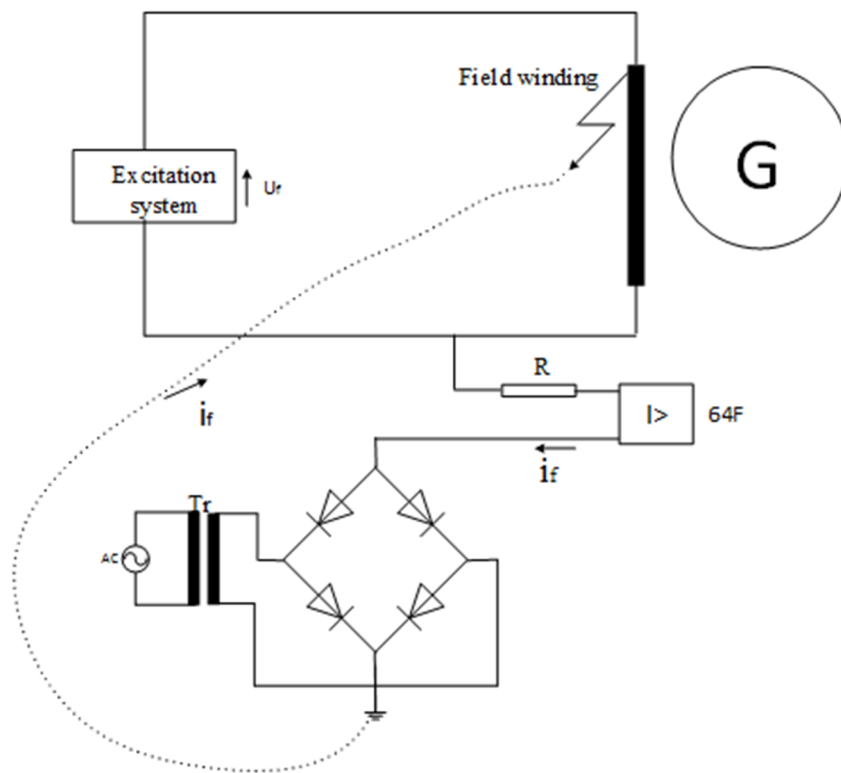


FIGURE 13: Rotor ground fault protection of generator by DC injection method

resulting asymmetry in the electromagnetic forces will cause severe vibrations of the rotor. In a modern generator, the inertia of rotation is very large and the rotor-to-stator clearances are very small, therefore, there is a likelihood of permanent damage to the turbo-alternator. In light of the above, the very first fault on the field winding must be detected and the set tripped in a controlled manner. An arrangement for rotor earth fault detection and protection is shown in Figure 13, wherein an external voltage source is superimposed on the rotor circuit. This external voltage source is grounded so that the very first rotor earth fault causes a dc fault current to flow, which is easily detected by an over current relay (Paithankar, and Bhide, 2003).

6.2.2 Abnormal operating conditions

A generator cannot be considered in isolation because of the large number of other equipment connected to it. Even though there is no electrical fault in the generator, if one of its associated pieces of equipment develops a fault, then it has serious implications for the generator. Every auxiliary piece of equipment connected to the generator is a likely source of trouble. There are a large number of possible faults, as well as combinations of faults, on these pieces of equipment, that threaten the operation of the generator (Paithankar, and Bhide, 2003).

Instances where there is no direct electrical fault in the generator but one or more of its associated pieces of equipment develops a fault or an abnormality may lead to an abnormal operating condition, which may or may not be serious. However, all abnormal operating conditions need to be detected as quickly and as sensitively as possible so that corrective action can be taken and a possible shutdown averted or anticipated. Some prominent abnormal operating conditions, shown in Figure 14, need to be carefully considered while providing protection to the generator:

Over-speeding

Assume that a power station generator is supplying its rated real electrical power P_e , to the grid. Its mechanical input P_m is nearly equal to P_e , (except for the losses) and the machine runs at constant synchronous speed N_s . If the generator is tripped due to some fault and disconnected from the grid, P_e becomes zero. However, the mechanical power input P_m cannot be suddenly reduced to zero. Therefore, it leads to a situation where the generator has full input mechanical power but no output electrical power (no load). This would cause the machine to accelerate to dangerously high speeds if the mechanical input is not quickly reduced by the speed-governing mechanism.

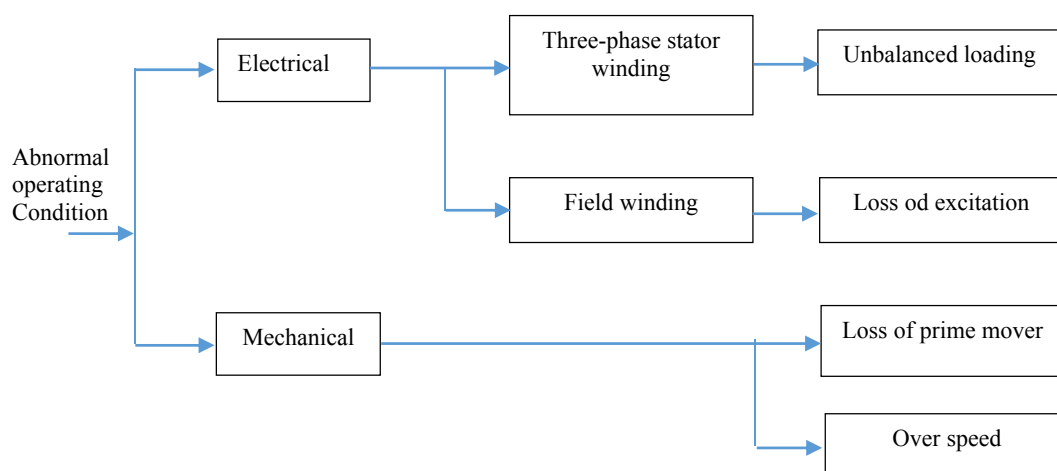


FIGURE 14: Various abnormal operating conditions of a generator

The protection against such an eventuality can be provided by sensing the over-speeding and taking steps such as operating the steam valve so as to stop steam input to the turbine. The speed-governing mechanism or the speed governor of the turbine is basically responsible for detecting this condition. The over-speeding can also be detected either by an over-frequency relay or by monitoring the output of the tacho generator mounted on the generator shaft. The logic of protection against over-speeding is shown in Figure 15.

Mechanical protection of genset

A computerized vibration monitoring system supplies the information necessary to assess the mechanical condition of the rotary components of the genset (turbine/generator). A variety of supervisory parameters in x and y directions is continuously measured using the sensor attached the genset, as shown in Figure 16, and provides critical information on machinery problems such as imbalance, shaft misalignment, bent or cracked rotors, and bearing failure. The data is then fed to the control system, which can shut down the machinery in case of abnormal operations.

Unbalanced loading

If there is an unbalanced loading of the generator, then the stator currents have a negative sequence component. The stator field, due to these negative sequence currents, rotates at synchronous speed but in a direction opposite to the direction of the field structure on the rotor. Thus, the negative sequence stator armature magneto motive force (mmf) rotates at a speed $-N_s$ while the rotor field speed is $+N_s$. Therefore, there is relative velocity between the two. This causes double frequency currents,

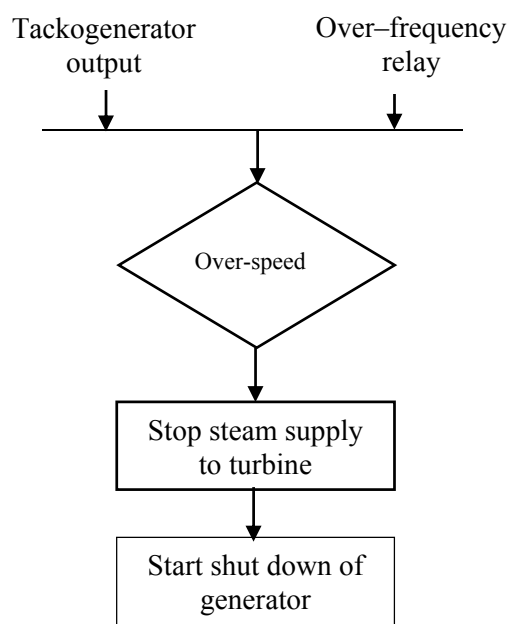


FIGURE 15: Protection against over-speeding

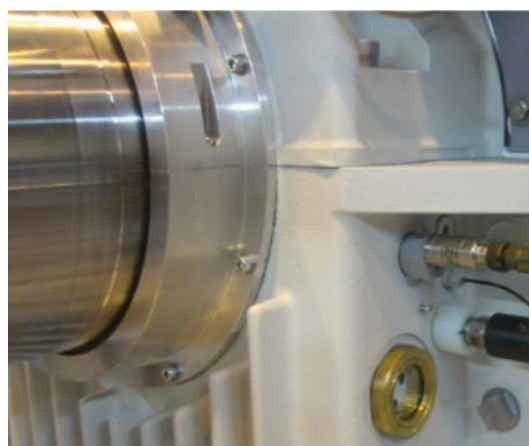


FIGURE 16: Genset vibration detector

of large amplitude, to be induced in the rotor conductors and iron. Thus, if the stator carries unbalanced currents, then it is the rotor which is overheated. How long the generator can be allowed to run under unbalanced loading depends upon the thermal withstanding capacity of the machine.

Loss of excitation

There are several possible causes due to which field excitation may be lost, namely:

- Loss of field to main exciter;
- Accidental tripping of the field breaker;
- Short circuit in the field winding;
- Poor brush contact in the exciter;
- Field circuit breaker latch failure;
- Loss of ac supply to excitation system.

Loss of prime mover

With a loss of mechanical input, the generator continues to remain synchronized with the grid, running as a synchronous motor. The machine, now, draws a small amount of active power (compared to its rating) from the grid in order to drive the turbine and meet the losses taking place in the machine. At the same time, the machine supplies reactive power to the grid since its excitation is intact. Running in this mode is harmful to a prime mover like a steam turbine.

When the machine runs as a motor, there is a churning of trapped steam in the turbine causing objectionable temperature rise and damage to the blades. Therefore, the loss of the prime mover needs quick detection followed by tripping of the generator, i.e. open generator switch.

6.3 Transformer protection

Transformers are critical and expensive components of power systems like generators. Due to the long lead time for repair of and replacement of transformers, a major goal of transformer protection is limiting the damage to a faulted transformer. When a fault occurs in a transformer, the damage is proportional to the fault time. The transformer should, therefore, be disconnected as fast as possible from the network. Fast reliable protective relays are, therefore, used for detection of faults.

The sizes of the transformer and the voltage level have influence on the extent and choice of protective equipment. Monitors prevent faults and protective relays limit the damage in case of a fault. The cost for the protective equipment is marginal compared to the total cost and the cost involved in case of a transformer fault.

6.3.1 Electrical protection

Overcurrent protection: Overcurrent relays generally provide the same level of protection as power fuses. Higher sensitivity and fault clearing times can be achieved in some instances by using an overcurrent relay connected to measure the residual current. This application allows pick up settings to be lower than the expected maximum load current. It is also possible to apply an instantaneous overcurrent relay set to respond only to faults within the first 75% of the transformer.

Overcurrent relays do not have the same maintenance and cost advantages found with power fuses. Protection and control devices, circuit breakers and station batteries are required. The overcurrent relays are a small part of the total cost and, when this alternative is chosen, differential relays are generally added to enhance transformer protection. In this instance, the overcurrent relays will provide backup protection for the differentials.

Differential protection: The most widely accepted device for transformer protection is called a restrained differential relay. This relay compares the current values flowing into and out of the transformer windings. To assure protection under varying conditions, the main protection element has a multislope restrained characteristic. The initial slope ensures sensitivity to internal faults while allowing for up to 15% mismatch when the power transformer is at the limit of its tap range (if supplied with a load tap changer). At currents above rated transformer capacity, extra errors may be gradually introduced as a result of CT saturation.

Over-excitation: The flux level within a transformer is proportional to the voltage applied to the transformer and inversely proportional to the frequency of the applied voltage. When over-excitation conditions that are above transformer design limits occur, the transformer core becomes saturated, resulting in a build-up of heat with eventual damage to the transformer.

Generator transformers are especially subject to over-excitation as such transformers are connected directly to the generator terminals. Voltage and frequency conditions at the generator terminals are subject to voltage and frequency variations, especially during start-up of the generator.

Over-excitation protection should be considered for all large transformers utilized as generator unit transformers, or those that are connected to portions of the power system conducive to causing transformers to become overexcited. Such protection should consist of relaying that is capable of directly responding to the level of excitation that exists such as volts/hertz relaying.

Backup protection: Backup protection, typically overcurrent or impedance relays applied to one or both sides of the transformer, perform two functions. One function is to back up the primary protection, most likely a differential relay, and operate in the event of its failure to trip.

The second function is protection for thermal or mechanical damage to the transformer. Protection that can detect these external faults and operate in time to prevent transformer damage should be considered. The protection must be set to operate before the through-fault withstanding capability of the transformer is reached. If, because of its large size or importance, only differential protection is applied to a transformer, clearing of external faults before transformer damage can occur by other protective devices must be ensured.

6.3.2 Mechanical protection

There are several mechanical protection relays installed on the power transformer. The operation of these relays (listed below) is almost instantaneous (no time delay):

- Buchholz relay;
- Winding temperature indicator;
- Oil temperature indicator and pressure relief.

All the above relays are operated mechanically and electrical circuit is needed for alarm and tripping circuits.

A *Buchholz relay* is a protection device for monitoring the gas and oil movements in oil immersed transformers. It is used on practically all power transformers with the exception of small distribution sizes. In practice, it has proved to be the only protective device that can clear certain types of faults. The Buchholz relay relies on the principle that during fault conditions, gas is generated inside the transformer tank from the insulating oil. An example of a Buchholz relay device is shown in Figure 17 (Ahmed, 2005).



FIGURE 17: Buchholz relay



FIGURE 18: Winding temperature indicator

Winding temperature indicator. A temperature indicator simulates the winding temperature. The temperature of the winding depends on the transformer load (i.e. the current through the winding) and the temperature of the cooling medium (oil). These two parameters are measured and made to interact in the instrument. The oil temperature is measured as usual with a bulb in a pocket. The measuring system also has a specially designed heating element to measure the transformer load. This heating element is a thermal model of the winding. The heating element is connected to the current transformer (CT) via a *matching resistance* or a *matching unit* to allow setting the correct winding temperature gradient. A sample of a winding temperature indicator is shown in Figure 18.

An oil temperature indicator is similar to a winding temperature indicator except that it depends only on the temperature transferred by the bulb (no current transformer is used).

A pressure relief valve is a device designed to protect a power transformer during an over-pressure event. An over-pressure event refers to any condition which could cause pressure in the transformer to increase beyond the specified design pressure. During internal faults of a

power transformer, there will be an increase in temperature associated with impurities in oil and some increase in pressure. This pressure is sufficient to damage the transformer. The pressure relief device is applied to prevent the transformer from this dangerous event.

The pressure relief device consists of a spring which normally is uncompressed. When the pressure is increased in the transformer, the spring is compressed and provides a path for gases to exit the transformer. Compressing the spring may close an electrical contact, and this contact will trip circuit breakers associated with an alarm. Figure 19a shows the pressure relief device in normal condition (before a fault occurs), while Figure 19b shows the fault condition at which the compressed gases are released from the transformer.

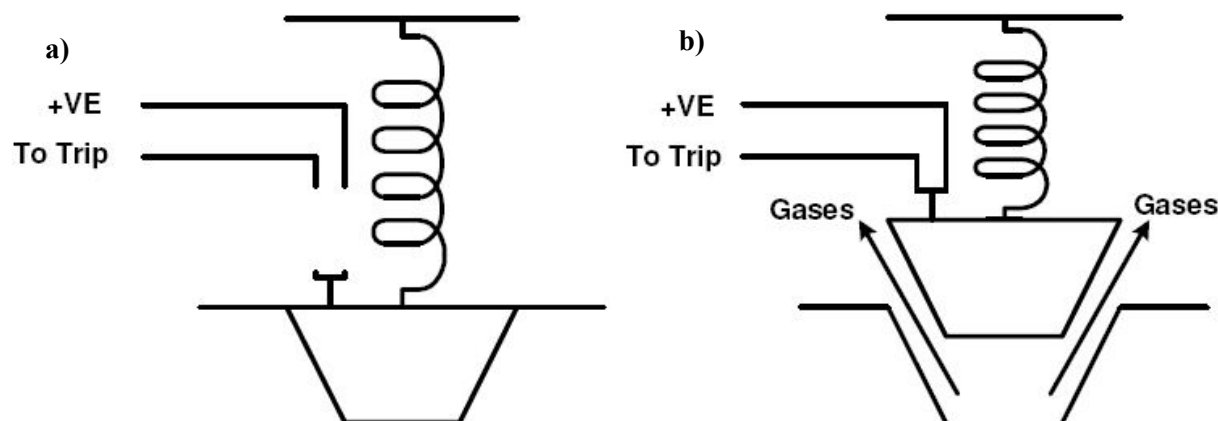


FIGURE 19: Pressure relief, a) before fault occurrence; b) during fault

7. THE ALUTO-LANGANO GEOTHERMAL POWER PLANT ELECTRICAL SYSTEM

7.1 General

The Aluto-Langano geothermal power plant is a pilot power plant in Ethiopia constructed by Ormat and started operation in 1998. The power plant is comprised of two power generation systems, the combined cycle steam (GCCU) and binary system (OEC). These units generate power of 11 KV which is supplied to the 11 KV main bus.

7.2 Generators

The plant is composed of two power generating units. The GCCU consists of one 5.9 MVA generator driven by on steam turbine and one organic turbine. The OEC also consists of one 5.9 MVA generator driven by two organic turbines.

A 375 KVA diesel generator was installed in the plant as a standby emergency power source to supply power to the main components of the power plant.

7.3 Transformers

The transformers installed in the power plant are:

- a) One step-up power transformer to convert the 11 KV power to the main bus to the 15 KV level of the grid.
- b) Two auxiliary transformers which supply power to the loads of the OEC and GCCU units. Each one of the power generating units has a dedicated pad-mounted transformer of 11/0.4 KV (750 KVA and 1250 KVA).
- c) One transformer having a capacity 400 KVA (11/0.4KV) which supplies power to the station's auxiliary load distribution panel.

7.4 Protection systems

The main power transformer and generators are protected by the protection relays installed in the panel which, when activated, isolates the transformer and generator from the main bus and the grid by the circuit breaker, as shown in Figure 20 with explanations in Table 2.

7.5 Bus to grid synchronization

The following procedure (sequence of operation) is taken directly from the operating manual of Aluto geothermal power plant, prepared by the Ormat Company (Ormat, 1997):

- a) Set the “ Bus Selector” switch at “BUS to GRID” position;
- b) By using selector “Speed”, the speed adjustment should be regulated (Raise/Slow) at a rate of 10 rpm/s;
- c) By using selector “Voltage”, bus voltage can be changed to much the grid voltage.
- d) Monitor generator parameters – frequency, voltage and synchroscope. Adjust as per paragraphs (c) and (d) to get the best matching.
- e) While synchroscope is on zero and voltage and frequency of bus are matched to grid, push “Synch Push Button” for two seconds.
- f) When synchronization is completed, turn bus selector to “OFF” position.



TABLE 2: Generator protection and labelling description

Code	Description/Type of protection	Code	Description/Type of protection
38	Bearing temperature protection	CPT	Control power transformer
26	Thermal protection	VAR	Volt ampere reactive meter
12	Over-speed	CT	Current transformer
27	Under voltage protection	SC	Surge capacitor
59	Over voltage protection	VR	Voltage regulator
25	Synchronizing check sync.	VC	Voltage controller
15	Speed matching	VT	Voltage transducer
32	Reverse power	CT	Current transducer
60	Phase balance voltage	SA	Surge arrester
59N	Ground over voltage	VS	Voltmeter switch
50/5186	Time over current with voltage restraint	V	Voltmeter
94	Lockout relay, avoiding re-connection after fault	A	Ammeter
87G	Tripping relay	W	Wattmeter
40	Generator differential		
46	Loss of field excitation		
49	Phase balance		
	Generator over voltage protection		

8. CONCLUSIONS

The role of this project was to define an effective control and protection system for effective and reliable operation of a geothermal power plant. In order to deliver the power generated from the plant to the consumer, as well as operating the plant smoothly, special care is a must in the selection of a proper control and protection system.

If a protection scheme does not operate correctly, the result can be extensive damage to the power equipment with consequent high repair cost and perhaps long average times. Hence, proper training should be conducted for power plant technicians and engineers who are responsible for installing, testing and calibrating the protection equipment.

In order to make the geothermal power plant unattended or controlled at a distance, a modern control system must be installed. In addition to the working procedure of the SCADA system, a plant operator should also be equipped with basic software skills in case some problem happens in the software itself.

ACKNOWLEDGEMENTS

I wish to express my sincere thanks to Mr. Lúdvík S. Georgsson, Director of UNU Geothermal Training Programme, for offering me the chance to participate in this training. I would also like to thank Mr. Ingimar G. Haraldsson, Ms. Málfríður Ómarsdóttir, Ms. Thórhildur Ísberg and Mr. Markús A.G. Wilde for their kindness and efficient help during the training and for helpful guidance and support.

I would like to respect and thank my supervisor, Mr. Bjarni Bjarnason, for his valuable guidance and kind supervision which made me complete the project on time and shaped the present work as presented.

Finally, I wish also to thank all the other UNU Fellows during my time in the training period.

REFERENCES

- ABB, 2004: *Transformer handbook*. ABB group, Zurich, website: www.abb.com/transformer, 213 pp.
- ABB, 2014: *Control system for steam and gas turbines*. ABB group, Zurich, 70 pp.
- Ahmed, S.E., 2005: *Practical introduction to power system protection and control*. PIPSPC, 94 pp.
- ENEX, 2014: *Binary geothermal power plant operation and instruction manual for 7.8 MW*. ENEX, San Salvador.
- Fassbinder, S., 1997: *Power generation. Energy efficient design of auxiliary systems in fossil-fuel power plants*. ABB group, Zurich, 362 pp, webpage: [www05.abb.com/global/scot/scot221.nsf/veritydisplay/5e627b842a63d389c1257b2f002c7e77/\\$file/Energy%20Efficiency%20for%20Power%20Plant%20Auxiliaries-V2_0.pdf](http://www05.abb.com/global/scot/scot221.nsf/veritydisplay/5e627b842a63d389c1257b2f002c7e77/$file/Energy%20Efficiency%20for%20Power%20Plant%20Auxiliaries-V2_0.pdf).
- Ismail, B.I., 2013: *ORC-based geothermal power generation and CO₂-based EGS for combined green power generation and CO₂ sequestration*. In: Tech Open Publishing, website: www.intechopen.com.
- Ormat, 1997: *Aluto geothermal power plant operation manual for 7.28 MW*. Ormat Technologies, Ethiopia.

Paithankar, Y.G., and Bhide, S.R., 2003: *Fundamentals of power system protection*. Prentice-Hall of India Private, Ltd., New Delhi, 301 pp.

Reimert, D., 2006: *Protective relaying for power generation systems*. CRC Press, Taylor & Francis Group, 592 pp.



UNITED NATIONS
UNIVERSITY

UNU-GTP

Geothermal Training Programme

Orkustofnun, Grensasvegur 9,
IS-108 Reykjavik, Iceland

Reports 2014
Number 14

GAS - MINERAL EQUILIBRIUM IN THE BERLÍN GEOTHERMAL FIELD, EL SALVADOR

Jaime Alberto Hernández Ayala

LaGeo S.A. de C.V.

15 Av. Sur, Col. Utila

Santa Tecla, La Libertad

EL SALVADOR, C.A.

jhernandez@lageo.com.sv

ABSTRACT

The aquifer fluid composition at the depth of the volcanic geothermal system of Berlín, El Salvador, was reconstructed based on samples of steam and liquid from discharge fluids of 14 two-phase producer wells sampled during the period from July to October 2013 using the chemical speciation program WATCH 2.4. Berlín geothermal field is a liquid-dominated field with discharge enthalpies close to that of the reservoir liquid, except for well TR18B which has higher enthalpy because of phase segregation between the liquid and fluid phase in the depressuration zone around the well. The objectives of this study were to interpret deep fluid gas composition with the purpose of understanding gas behaviour in the geothermal system. The state of equilibrium between CO₂, H₂S and H₂ in the aquifer water and selected mineral assemblages that could potentially fix the concentrations of these reactive gases, in the temperature range from 200 to 300 °C, were studied. Field scale distribution of these gases, along with N₂, indicates that the H₂S and H₂ are temperature controlled; CO₂ follows a similar pattern in field scale distribution as N₂ which is a conservative gas in geothermal systems. Aquifer liquid H₂S concentration at the Berlin geothermal field is controlled by a close approach to equilibrium with the mineral assemblages. Hydrogen concentration for most of the wells lies close to equilibrium with the epidote-wollastonite-grossular-magnetite-quartz hydrothermal mineral assemblage. The aquifer concentration of CO₂ species was observed to fall below equilibrium with respect to the mineral buffers, suggesting that the concentration of the gas is source controlled.

1. INTRODUCTION

Two high-temperature geothermal fields are managed by LaGeo S.A. de C.V. in El Salvador, Ahuachapán geothermal field in the west part of the country and Berlín geothermal field in the east. Combined, these geothermal fields, with a total nominal installed capacity of 204.4 MWe, produce around 23% of the total electricity generation in El Salvador.

Electricity generation from the Berlín geothermal field began in 1992, when two 5 MWe back pressure power units went online. From 1997 to 1999, 8 producers and 10 injector wells were drilled in the field, a new 56 MWe (2 x 28 MWe) condensation unit was built and the previous two back pressure

units were disconnected. A new exploration project was carried out under the shareholder agreement Enel–GESAL (now LaGeo) to explore the southern part of the field and additional production wells were drilled during 2003 to 2005. Operation of Unit 3 (44 MWe condensation unit) started in 2007 and, in 2008, Unit 4, a 9.4 MWe combined cycle power plant was commissioned. The total installed capacity of this field is currently 109.4 MWe, which is equivalent to around 7% of the total install capacity of El Salvador, with a 13% contribution to national electricity production.

Since production at Berlín geothermal field was started in 1992, the reservoir response and management of field operations has been well documented and several studies related to geochemical interpretation of gases and aquifer fluid compositions have been made (D'Amore and Tenorio, 1999; Montalvo and Axelsson, 2000; Renderos, 2002; Jacobo, 2003; Ruggieri et al., 2006; Hernández, 2012). The role of gas geochemistry in assessing the reservoir becomes more relevant, especially in geothermal fields, with a long utilization history. A common consequence of long-term utilization is an increase in the vapour to liquid ratio in the discharges of producing wells due to reservoir pressure drawdown. Many geochemical processes affect the concentrations and ratios of reactive and unreactive gases in the fluids of volcanic geothermal systems. These processes may include a supply of gases from the magma heat source, from the atmosphere and from the water-rock interactions in the geothermal system. In gas geochemistry studies, the premise is the assumption of a close approach to equilibrium in the aquifer, either among specific reactive gases commonly present in geothermal well discharges or between some reactive gases and potential mineral buffers in the geothermal field. Due to the relatively high abundance and reactivity of the main geothermal gases (CO_2 , H_2S and H_2), these components were viewed with particular interest in their ability to elucidate the physical nature of hydrothermal systems. Early studies provided compelling evidence that fluid compositions were controlled by equilibrium with select hydrothermal alteration minerals commonly identified in well cuttings, and many studies have shown that the aquifer fluid concentrations reactive geothermal gases closely approach equilibrium with specific hydrothermal mineral assemblages (Angcoy, 2010; Arnórsson et al., 2007, 2010; Karingithi et al., 2010; Scott, 2011).

In this study, an attempt is made to model the aquifer fluid composition in the Berlín geothermal field, using chemical data from water and steam discharge samples obtained from 14 production wells. Solute geothermometers were calculated and used to model aquifer fluid compositions and evaluate specific mineral-gas equilibria that may potentially control the concentrations of the reactive gases (CO_2 , H_2S and H_2) in aquifer fluid in the geothermal reservoir. Such geochemical assessments provide insights on current reservoir conditions.

2. BERLÍN GEOTHERMAL FIELD

The Berlin geothermal field is located about 110 km east of San Salvador, the capital city of El Salvador, in the district of Usulután, between the cities of Alegria and Berlín (Figure 1). It is located on the northern flank of the Berlín-Tecapa volcanic complex, inside a system of faults in the southern part of the east-west oriented Central American graben. The Berlín geothermal field is a volcanic liquid-dominated high temperature system (Saemundsson, 2009) with temperatures in the range of 280°C to 300°C in the central zone, and 240°C to 270°C in the southwest zone according to measured temperatures in the production wells.

A summary with information related to the geothermal production wells in operation at the Berlín geothermal field is presented in Table 1.

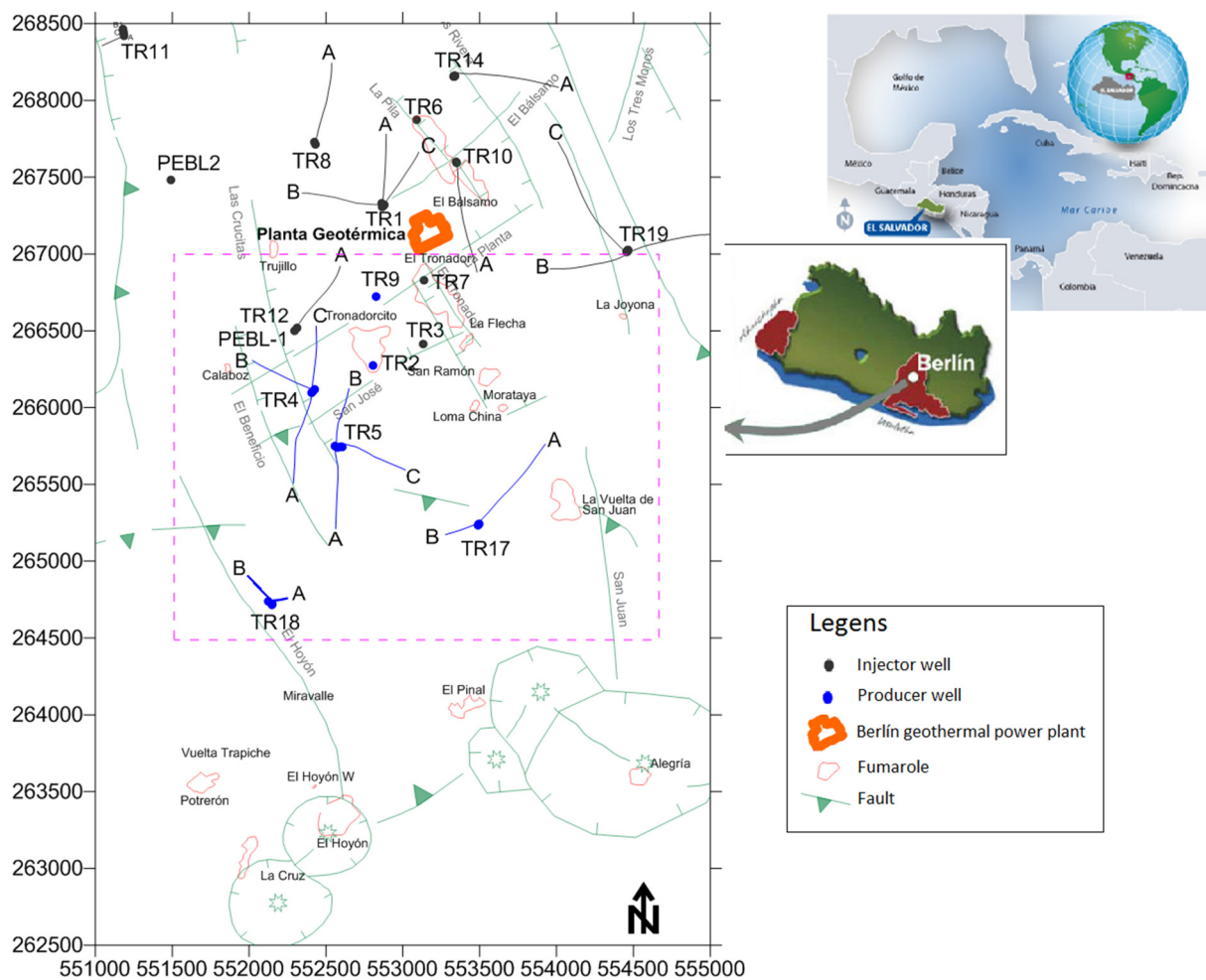


FIGURE 1: Berlín geothermal field: pink rectangle shows the spatial reference for field-scale distribution maps

2.1 Geological overview

High temperature geothermal activity in Central America is focused around plate subduction zones. El Salvador borders the Middle America Trench, an active subduction boundary and seismic zone between the Cocos and Caribbean plates. As a consequence, El Salvador is bisected by the volcanic front, a linear belt of active volcanoes and an accompanying seismic zone. The geologic and tectonic processes of both plate margins contribute directly to generating the main parameters for geothermal resources: heat and rock permeability. The volcanoes along the Central American volcanic arc supply the heat and the tectonic interactions between the plates generate the faults and seismicity that induces secondary permeability. Intense tropical precipitation contributes to the third parameter needed in a geothermal resource: geothermal fluids (Barrios et al., 2011).

Berlín geothermal field is categorized as a volcanic geothermal systems (Saemundsson, 2009). Associated with volcanic activity, Berlín geothermal power plants are located on the northern flanks of Holocene volcanoes with no history of eruptive activity in the past 500 years (Barrios et al., 2011). The heat sources for such systems are associated with magma chambers of the Berlín-Tecapa volcanic complex which was formed by the caldera of the Berlín strata volcano, and composed of a series of peripheral volcanic cones that expelled andesitic lava and scoria which emerge around the craters in the southeast part of the caldera of the old Berlín volcano (Correia et al., 1996). This volcanic complex is a stratovolcano composed of alternating lava flows, pyroclastics and andesitic epiclastites of

andesitic-basaltic nature. It is located inside the system of faults in the southern part of the E-W oriented Central American graben, in the zone of crustal weakness produced by the intersection of the NW-SE and NE-SW faults of the Central American graben.

TABLE 1: Summary of information on production wells in Berlin geothermal field

Well	Lambert projection ^a		Elevation a.s.l. (m)	Condition deviation	Depth b.g.l. (m)	Circulation losses (m)	Temperature logging ^b (°C)	Finished	Started
	Northing	Easting						Drilling	Production
	Y	X						(dd/mm/yyyy)	
TR2	266276	552802	752	VERT	1903	PL: ..805-1800 TL: 1799-1903	281	06/02/1978	02/20/2002
TR4	266098	552405	767	VERT	2379	PL: 1865-1948 TL: 1948-2379	280	07/08/1980	05/06/2011
TR4B	266270	552090	767	N-56-W	2292	PL: 1869-1892 TL: 1944-2292	294	03/30/1998	07/02/1999
TR4C	266450	552436	767	N-05-W	2179	PL: 1761-2179 TL: 1752	283	08/24/1998	01/02/1999
TR5	265744	552606	853	VERT	2086	PL: 1650-1830 TL: 1830-2086	301	07/04/1981	04/11/1999
TR5A	265250	552583	840	S-03-W	2325	PL: 1900-2000 TL: 2000-2194	296	08/29/1998	29/09/1999
TR5B	266073	552636	840	N-17-E	2097	PL: 1671-2000 TL: 2000-2097	297	12/31/1998	16/02/2000
TR5C	265590	552999	840	S-70-E	2343	PL: 1864-1996 TL: 1996-2343	301	03/23/1999	29/09/1999
TR9	266723	552826	649	VERT	2298	PL: 1448-1663 TL: 1663-2298	275	12/28/1980	01/01/1995
TR17	265243	553497	1073	VERT	2600	PL: -- TL: 1400-2000	253	12/01/2003	02/04/2007
TR17A	265709	553888	1073	N-36-E	2690	PL: 1750-1820 TL: 2000-2690	285	06/22/2004	05/13/2007
TR17B	265183	553300	1073	S-74W	1845	PL: -- TL: 1263-1845	269	01/03/2005	02/04/2007
TR18	264716	552149	995	VERT	2660	PL: -- TL: 1875-2660	266	02/25/2004	02/04/2007
TR18A	264760	552230	995	N-77-E	1085	PL: -- TL: ..929-1085	266	06/30/2004	02/04/2007
TR18B	264843	552055	1013	N-40-O	1194	PL: -- TL: .. 866-1194	240	09/24/2012	08/08/2013

^a: coordinates for total lost-circulation zone in the well (WGS84/Zone 16N).

^b: maximum temperature record on well logging

Two main active fault segments are recognized in the eastern part of El Salvador. A strike-slip system consists of mainly E-W faults, synthetic (WNW-ESE) and antithetic (NNW-SSE) Riedel shears, and NW-SE tensional structures. This last fault system, running NW-SE, is considered the most recent, active and important because it permits the ascent of the fluids from depth to the surface. The NNW-SSE fault system is the most important regionally as it is responsible for the formation of the Central American graben and also the active Quaternary volcanic chain of the country. Some of the most recent volcanic edifices such as Cerro Pelón, Laguna de Alegría and Cerro de Alegría, are aligned along the same course, indicating that this tectonic system is active and does not only exist in the Berlín zone, but in the whole country. This system has generated a graben that cuts through the northern part of this caldera. The majority of the hydrothermal manifestations and the geothermal field itself are found inside this structure (Correia et al., 1996).

This alkaline volcanic complex alternates basaltic to andesitic lava flows and scoria, and andesitic to dacitic ignimbrites which were produced during major eruptions (Raymond et al., 2005). Permeable fractures and fault zones, but also permeable strata such as ignimbrites and lavas, control the flow of water in this volcanic geothermal system.

2.2 Alteration mineralogy

Hydrothermal alteration of rocks and minerals is the result of chemical exchange that occurs during water-rock interactions between hydrothermal fluids (hot water) and the primary minerals and glass in the rock hosting the hydrothermal fluids. Primary minerals are replaced by secondary (alteration) minerals because the primary minerals are unstable in the fluid and secondary minerals are stable. Which types of alteration minerals are formed depends upon the geological setting, temperature and fluid properties in the system. Formation of alteration minerals may include the following processes: (1) transformation of mineral phases, (2) growth of new minerals, (3) dissolution and/or precipitation of minerals, (4) ion exchange reactions between rock minerals and fluid, etc.

The rocks intersected by geothermal wells in the Berlin geothermal field mainly consist of volcanic rocks and volcanic breccias. These rocks are always affected to a variable degree by hydrothermal alteration. Alteration of primary minerals occurs similarly in most geothermal fields, but some are specific to some fields. According to Ruggieri et al., (2010), four hydrothermal alteration zones, summarized in Table 2, have been recognized in the Berlin geothermal field, formed at increasing temperature and different depths: (1) from the surface to 670-700 m b.g.l., a relatively low temperature assemblage, consisting of clay minerals, heulandite, quartz and calcite occurs; (2) from 670-700 to 1100-1630 m b.g.l., the main hydrothermal phases are calcite, chlorite, quartz and a lesser amount of wairakite, laumontite, anhydrite, illite and illite-montmorillonite mixed-layers; (3) from 1100-1630 to 1460-1840 m b.g.l., epidote and albite occur together with most of the minerals of the previous hydrothermal assemblage; (4) below 1460-1840 m b.g.l., epidote, quartz and albite are the main hydrothermal phases while chlorite, actinolite, wairakite, adularia, prehnite, anhydrite and hydro-garnet occur in variable amounts.

TABLE 2: Hydrothermal minerals and depth ranges of the four alteration zones recognized in the Berlín geothermal field (Ruggieri et al., 2006)

Depth b.g.l. (m)		Hydrothermal minerals	
min	max	Abundant	Moderately abundant to trace
0	670-800	Nontronite, montmorillonite, corrensite, quartz, calcite, heulandite	Saponite
670-800	1100-1630	Calcite, chlorite, quartz	Wairakite, laumontite, anhydrite, illite, illite-montmorillonite, corrensite
1100-1630	1460-1840	Albite, quartz, chlorite, calcite	Illite, wairakite, adularia, prehnite, epidote
1460-1840	?	Epidote, albite, quartz	Adularia, prehnite, anhydrite, chlorite, actinolite, wairakite, hydro-garnet, calcite (Widespread titanite and pyrite without depth distribution)

Hydrothermal alteration minerals at Berlín geothermal field appear both as replacements of the primary minerals, as well as fillings in cavities or fractures crosscutting the rock. Figure 2 shows the distribution of the hydrothermal alteration zones at depth and the first appearances of minerals in the Berlín geothermal field. The abundance of the hydrothermal minerals and the alteration style are partially controlled by the bulk chemistry of the rock (Table 3). The shallowest alteration zone is characterized by the presence of relatively low-temperature minerals. At greater depth, hydrothermal phases, such as epidote, wairakite, prehnite, and hydro-garnets, typical of higher temperature conditions, occur. Quartz, calcite and chlorite are widespread in most of these zones (Ruggieri et al., 2006).

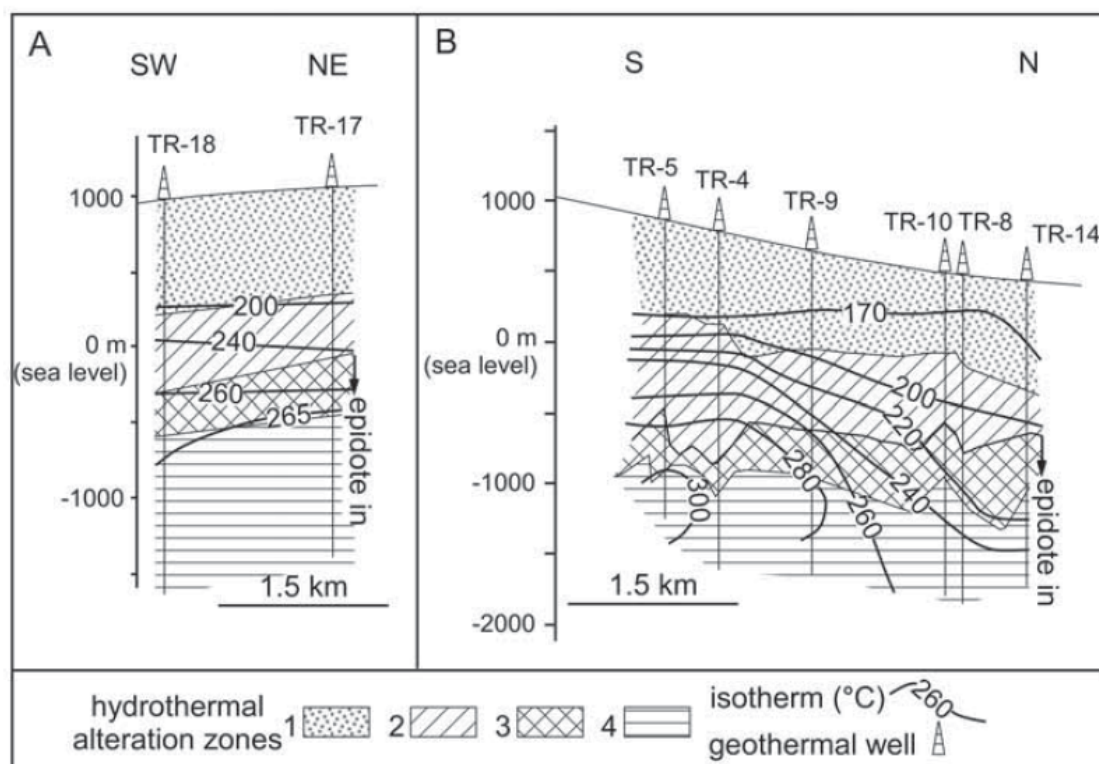


FIGURE 2: Distribution of the hydrothermal alteration zones with depth and the first appearances of minerals and corresponding subsurface temperatures indicated (reprinted from Ruggieriet al., 2006); Alteration zones are those reported in Table 2: particular characteristic minerals of each zone are: 1) calcite + clay minerals, 2) chlorite + calcite + quartz, 3) chlorite + calcite + quartz + albite \pm epidote \pm prehnite, 4) epidote + quartz + albite \pm prehnite

TABLE 3: Primary minerals, order of replacements and alteration products of Berlín geothermal field

Order of replacement	Primary minerals	Alteration products
<div style="display: flex; align-items: center;"> <div style="writing-mode: vertical-rl; transform: rotate(180deg); margin-right: 5px;">Increasing order</div> <div style="font-size: 2em; margin-right: 5px;">↑</div> </div>	Volcanic glass Olivine Pyroxene, amphiboles Ca-plagioclase Sanidine, orthoclase, microcline Magnetite Quartz	Clays, zeolites, quartz, calcite Clays, chlorite, Fe-oxides Chlorite, illite, calcite, pyrite, actinolite, clays Calcite, epidote, quartz, sphene, illite/sericite, anhydrite, prehnite, wairakite Adularia, illite/sericite Hematite, pyrite, sphene No alteration

2.3 Fluid chemistry

Berlin Geothermal reservoir is liquid-dominated, sub-boiling at depth with temperatures ranging up to 300°C. Three different types of aquifers have been identified: (1) a shallow low-salinity aquifer at a depth between 200 and 300 m a.s.l.; (2) an intermediate saline aquifer with temperature around 200°C and located around sea level; and (3) a deeper saline aquifer at a depth ranging from -800 to -1,800 m a.s.l with temperature around 300°C (Hernández, 2012). The bulk of the production from the field is from the depth of neutral and mature NaCl aquifers. The initial aquifer fluid has moderate Cl content

(from 2500 to 6500 mg/kg), low Fe and Mg (<1.0 mg/kg), low sulphates (<25.0 mg/kg) and slightly-acid to neutral pH (from 5.0 to 6.0); CO₂ levels varies from 200 to 1100 mg/kg (TR17A and TR4). The non-condensable gas content at these values corresponds to around 0.15 to 0.51%w/w.

2.4 Well discharge enthalpies

The samples in this study were obtained from 14 producing wells with total discharge enthalpies of about 1100 to 1700 kJ/kg (Table 4). Most of the well discharges have liquid enthalpy (i.e. the enthalpy of the discharged fluid is equal, or very close, to the enthalpy of steam-saturated liquid at the aquifer temperature). The productive zones in the well are mostly below 1700 m depth (b.g.l). According to Magaña (2012), the overburden pressure prevents extensive boiling of the fluid throughout the field typically induced by reservoir pressure drawdown; a thermodynamic equilibrium can be inferred in the initial aquifer fluid nourished geothermal wells in Berlín, based on values of total discharge enthalpy and initial aquifer enthalpy calculated using quartz, Na/K and Na/K/Ca geothermometers.

The discharge enthalpy in well TR18B is higher than the liquid enthalpy of the steam-saturated geothermal fluid. Well TR18B is the shallowest steam-saturated liquid well in Berlín geothermal field and, in later sections, it will be demonstrated that phase segregation primarily accounts for the discharge enthalpy of this well.

2.5 Conceptual model

Conceptual models are descriptive or qualitative models, not used for calculations. They are mainly based on geological information, both from surface mapping and the analysis of subsurface data, remote sensing data, results of geophysical surveying, information on the chemical and isotopic content of the fluid in surface manifestations and reservoir fluid samples collected from wells, information on temperature and pressure conditions based on analysis of available well logging data, as well as other reservoir engineering information (Axelsson, 2013).

The actual conceptual model of the Berlín geothermal field is based on the integration and interpretation of multi-disciplinary inputs from LaGeo's geoscientists (Figure 3).

The producing reservoir is related to the presence of a resistive deep aquifer with resistivity above 40 ohm-m in correspondence with the occurrence of prophylic facie, whose formation temperature is in the range of 240 to 300°C (Monterrosa and Santos, 2013). It is estimated that the reservoir aquifer has a temperature range of between 250 to 310°C, according to measured temperatures in the production wells. Overlying the geothermal reservoir are two shallower aquifers. A groundwater aquifer close to the surface is recharged by local rain in the area, and a deeper aquifer of an intermediate temperature (150 to 200°C) is found around sea-level and is about 300 m thick (Montalvo and Axelsson, 2000).

The heat source is associated with an active magmatic chamber of the Berlín-Tecapa volcanic complex, which is mainly of andesitic nature, recently formed (<0.1 My) and, according to geophysical studies, housed at a depth of about 6 km. Fumaroles and hydrothermal activity south of the Berlín geothermal field are evidence of the magma chamber and its activity. Based on the distribution of well logging temperatures, quartz geothermometers, hydrogen gas anomalies and geo-volcanological studies, it is believed that there are 2 upflowing regions. The major natural outflow of the reservoir is towards the central and northwest area, located close to the production well pads of wells TR4 and TR5. The second upflow zone is to the south in the vicinity of wells TR17 and TR18. It is postulated that during upflow in this second region, the hot fluid is mixed with surface water from the inflow zone on the top of the volcanic complex and, as a result, the temperature of the geothermal fluid is lower compared to the fluid in the central upflow zone (LaGeo, 2012).

TABLE 4: Chemical analysis of water and steam samples from production wells at the Berlín geothermal field

Sample	Well	Date of sampling month/year	Discharge enthalpy kJ/kg	SP ^a bar-g	Aquifer temp.		Liquid phase (ppm)										Ionic balance (CBE%) ^c	Vapor phase (mmol/kg)								
					°C ^b	plf ^c	SiO ₂	B	Na	K	Mg	Ca	Al	Fe	F	Cl		SO ₄	CO ₂ ^d	NH ₃	CO ₂	H ₂ S	H ₂	CH ₄	N ₂	O ₂
2013-1388	TR-2	10/2013	1171	9.4	284	5.90	746	118	3874	683	0.086	117	0.63	0.12	0.52	7048	14.7	2.55	0.45	1.9	0.696	0.213	0.014	0.0030	0.012	0.0002
2013-1373	TR-4	10/2013	1291	8.0	288	6.84	786	95	3222	594	0.019	58	0.47	0.01	1.02	5428	15.2	4.74	0.13	-1.5	1.329	0.259	0.018	0.0036	0.047	0.0002
2013-1374	TR-4B	10/2013	1316	11.1	281	7.05	718	82	2403	484	0.011	32	0.74	0.01	0.75	4257	12.4	12.4	0.19	0.9	1.940	0.153	0.019	0.0034	0.043	0.0002
2013-1375	TR-4C	10/2013	1290	11.0	275	6.86	678	121	3886	675	0.022	142	0.73	0.03	0.67	7164	19.6	7.2	0.29	2.3	1.49	0.24	0.017	0.0035	0.035	0.0002
2013-1164	TR-5	07/2013	1278	10.1	282	6.12	733	115	3536	712	0.059	57	0.43	0.03	0.48	6018	11.5	2.7	0.23	-1.4	1.08	0.29	0.016	0.0031	0.024	0.0002
2013-1378	TR-5A	10/2013	1216	10.2	272	6.75	663	97	2950	534	0.038	60	0.30	0.65	0.74	5380	18.5	4.2	0.16	2.4	0.91	0.22	0.012	0.0027	0.027	0.0003
2013-1379	TR-5B	10/2013	1182	10.2	295	6.31	816	140	4230	765	0.121	139	0.32	0.68	0.61	7947	13.2	2.6	0.42	3.2	0.86	0.19	0.012	0.0026	0.010	0.0001
2013-1163	TR-5C	07/2013	1193	11.0	275	6.08	681	132	3744	715	0.11	132	0.63	0.06	0.63	6840	12.4	2.6	0.21	1.4	0.99	0.24	0.013	0.0030	0.019	0.0005
2013-1380	TR-9	10/2013	1189	10.4	247	7.09	519	95	3110	487	0.011	156	0.64	0.03	0.82	5887	22.4	4.2	0.37	3.4	0.73	0.20	0.015	0.0030	0.014	0.0003
2013-1389	TR-17	10/2013	1141	6.9	277	6.04	719	129	4283	736	0.158	189	0.22	0.23	0.79	7650	10.2	2.6	0.21	0.3	0.85	0.15	0.004	0.0002	0.015	0.0002
2013-1390	TR-17A	10/2013	1156	7.3	244	7.10	517	123	4167	620	0.15	273	0.33	0.10	1.15	7636	25.5	3.1	0.22	1.2	0.49	0.11	0.001	0.0002	0.012	0.0001
2013-1391	TR-17B	10/2013	1101	7.5	281	6.70	742	131	4090	675	0.152	215	0.20	0.73	0.93	7564	17.8	2.6	0.18	1.9	0.60	0.10	0.001	0.0001	0.009	0.0001
2013-1407	TR-18	10/2013	1168	9.6	268	7.49	645	84	1875	308	0.011	34	0.99	0.04	0.76	3248	24.8	20.3	0.35	0.8	1.96	0.37	0.003	0.0005	0.056	0.0002
2013-1408	TR-18B	10/2013	1693	8.6	238	6.01	502	82	1911	332	0.011	71	0.92	0.09	3.48	3384	17.7	9.0	1.68	0.6	6.33	0.46	0.036	0.0006	0.089	0.0012
2013-1182	TR-18B	07/2013	1822	5.0	249	6.90	597	95	2348	383	0.279	148	2.92	1.06	4.81	4198	25.3	9.3	15.5	-0.1	2.56	0.44	0.016	0.0007	0.035	0.0011
2013-1208	TR-18B	07/2013	1748	5.0	244	6.65	566	107	2210	397	0.172	126	1.85	0.54	-	4209	26.5	12.8	6.83	2.9	4.79	0.71	0.016	0.0005	0.074	0.0006
2013-1236	TR-18B	08/2013	1680	11.9	235	5.94	470	88	2077	332	0.011	88	1.14	0.02	3.95	3516	24.2	13.0	3.25	-1.5	8.75	0.59	0.061	0.0008	0.131	0.0003
2013-1244	TR-18B	08/2013	1472	11.8	238	5.98	488	89	2118	353	<0.01	89	0.94	0.13	4.42	3724	24.0	13.3	2.82	0.2	6.90	0.55	0.048	0.0006	0.101	0.0004
2013-1250	TR-18B	08/2013	1489	11.6	241	5.97	504	80	2094	347	<0.01	84	0.92	0.09	3.99	3652	23.3	14.1	1.99	-0.1	7.18	0.49	0.054	0.0005	0.097	0.0006
2013-1409	TR-18B	10/2013	1693	8.7	237	6.04	495	90	1885	332	0.014	71	-	-	3.04	3438	18.3	9.4	1.25	1.9	6.64	0.46	0.031	0.0005	0.069	0.0002
2013-1549	TR-18B	12/2013	1150	9.0	234	6.21	476	89	2043	345	0.046	74	-	-	2.98	3653	22.6	14.0	-	1.3	7.25	0.46	0.048	0.0006	0.102	0.0004
2014-0066	TR-18B	01/2014	1653	9.5	241	6.06	516	85	2079	358	<0.01	75	-	-	3.22	3629	24.1	14.0	0.83	0.0	7.86	0.45	0.049	0.0006	0.111	0.0019
2014-0217	TR-18B	02/2014	1652	9.2	241	6.39	516	97	2099	367	<0.01	76	-	-	3.01	3595	26.5	16.9	1.07	-1.0	7.34	0.43	0.036	0.0004	0.084	0.0007
2014-0360	TR-18B	04/2014	1652	9.2	240	6.59	511	82	1958	313	<0.01	70	-	-	3.45	3511	21.9	11.8	0.72	1.7	9.84	0.45	0.063	0.0008	0.146	0.0001
2014-0891	TR-18B	07/2014	1676	9.0	235	6.39	484	89	1989	316	<0.01	68	-	-	2.61	3415	24.9	11.6	0.74	-0.4	8.33	0.43	0.054	0.0006	0.120	0.0002

a: SP: sampling pressure

b: temperature was based on the quartz geothermometer (Gudmundsson and Arnórsson, 2002)

c: pH was measured at laboratory using automatic temperature compensation (ATC) at 25°C

d: total carbonate carbon as CO₂

e: calculated according Equation 1

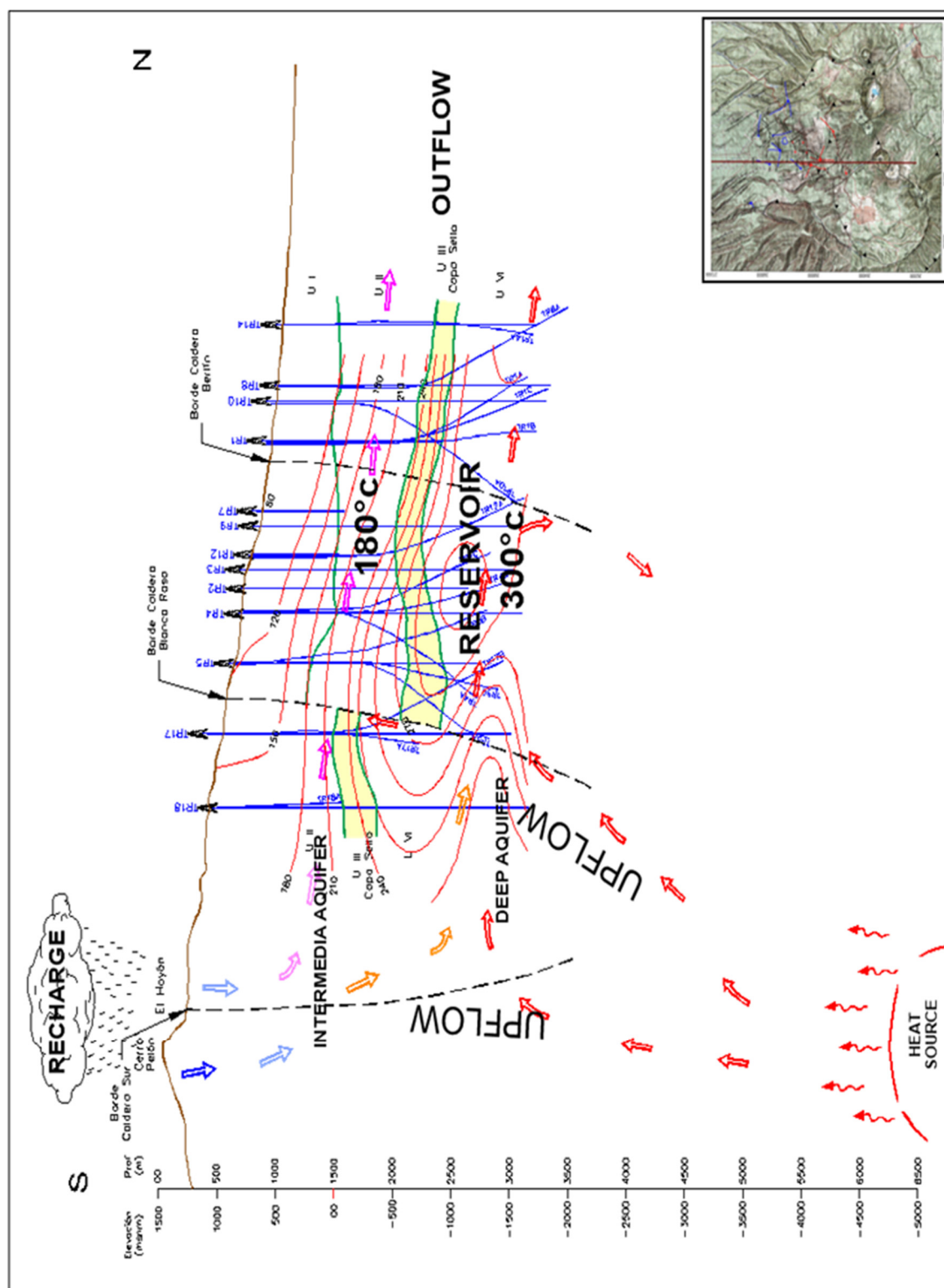


FIGURE 3: Vertical cross-section of the conceptual model of Berlin geothermal field (Monterrosa and Santos, 2013)

The geothermal fluid, consequently, flows through the main reservoir, moving from south to north or northwest along the NNW-SSE graben to reach the zone of well TR5. The upflow from the south moves to the northwest along the NW-SE system of faults El Hoyón, El Beneficio, Las Crucitas, San Juan y el Tronador to reach the central part where it changes course to the ENE-WSW, through the San José and La Planta faults. A tracer test carried out at Berlin geothermal field showed no flow between the reinjection zone (located in the north) and the production zone (Montalvo and Axelsson, 2000). The outflow of the systems is not known with any certainty but has been correlated with some of the hot springs located to the north (Monterrosa and Santos, 2013).

3. METHODOLOGY

Determination of the chemical composition of high temperature aquifer fluids involves sampling, treatment and chemical analysis of surface well discharge fluids and, secondly, the calculation of initial aquifer fluid chemical compositions.

This section describes the sampling and analysing methods used for the samples in this study. Aquifer chemical compositions were calculated from analysis of discharged water and steam phase using the chemical speciation program WATCH (Arnórsson et al., 1982; Bjarnason, 2010), version 2.4. A phase segregation model (Angcoy, 2010; Arnórsson et al., 2007, 2010; Karingithi et al., 2010; and Scott, 2011) was applied to calculate initial aquifer fluid composition in well TR18B after identification of the process which produced discharge enthalpies in excess of that of vapour-saturated liquid at the aquifer temperature for that well.

3.1 Sampling and physico-chemical analysis

The chemical composition of the deep water of a geothermal reservoir is a product of the source of water, water rock interactions and, in the case of volcanic environments, of magma degassing into the geothermal system. Chemical composition of geothermal fluid therefore provides important information about the characteristics of deep geothermal systems, which could be related with thermodynamic, geological and hydrological data. The accuracy and precision of the results obtained during integration of geochemical data are directly related to the quality of the chemical database which is dependent on using specific sampling techniques to achieve representative samples of the system under study, as well as qualified personnel, appropriate facilities and the use of appropriate analytical methods and instruments. Considering these needs, LaGeo geochemical laboratory has been accredited under ISO/IEC 17025 since 2003.

The primary data for this study were obtained from the water and gas discharges sampled during routine monitoring of 14 production wells in Berlín geothermal field. All fluids were sampled during the period from July to October 2013 except for samples collected from well TR18B which was sampled during the period from July 2013 to July 2014. Table 4 shows the chemical compositions of the water and steam samples used in this study.

Samples of water and steam for individual wells were collected at constant pressure; all the samples were collected and analysed by the geochemical laboratory of LaGeo. A chromium-nickel stainless (N316) steel Webre separator was connected in the two-phase pipeline by the wellhead to collect samples of water and steam. In some cases, samples were collected at separator stations. Water samples were cooled and steam was condensed using a stainless steel cooling coil prior to sampling. Condenser cooling was achieved using a 5-Gallon drum ice/water bath surrounding the coils. Calibrated Bourdon-tube type gauges were used for the measuring the sampling pressure.

Steam samples for non-condensable gas analysis were collected in duplicate into evacuated single stopcock valve gas bottles containing 50 ml of 4M NaOH solution. The strong base solution is used to capture the major non-condensable gases (CO_2 and H_2S) while residual gases (H_2 , He, CH_4 , Ar, N_2 and O_2) occupy the head space of the gas bottle. Water samples for analysis of all components except for pH, total carbonate carbon, NH_4 and SiO_2 , were filtered on site to prevent interaction with any suspended matter. The samples were treated in different ways, depending on the component to be analysed and the analytical methods; a general sampling procedure table specifying the treatment and sub samples for two-phase geothermal wells is shown in Table 5.

The non-condensable gases in the headspace of the gas sampling bulb (H_2 , He, CH_4 , Ar, N_2 and O_2) were analysed by gas chromatography, while CO_2 and H_2S in the base solution were analysed by potentiometric titration. Total carbonate carbon concentration and pH in the liquid phase were

determined in the laboratory immediately upon return from the field (within 3–5 days) by potentiometric titration and a calibrated pH electrode, respectively. The major aqueous components were analysed by various methods: atomic absorption spectrometry (SiO₂, B, Na, K, Mg, Ca, Li, Al and Fe); spectrophotometry (SO₄); and ion selective electrode for F, Cl and NH₃.

TABLE 5: Sample treatment for determination of major chemical components in geothermal fluids according to sampling procedures in the geochemical laboratory of LaGeo

Phase	Treatment	Container	Specification	Analysis
Liquid	Filtered/filter membrane pore size 0.45 µm; 1.0 ml conc. HNO ₃ (Suprapur)	250 ml HDPE bottles	FA ^a	B, Na, K, Mg, Ca, Li, Al and Fe
	Unfiltered, completely filled bottle, air-free	250 ml amber glass bottles	pH and total carbonate carbon	pH, T-CO ₂ /HCO ₃
	Filtered/filter membrane pore size 0.45 µm	250 ml HDPE bottles	FU ^b	Cl, SO ₄ , F and EC ^c
	0.5 ml conc H ₂ SO ₄	250 ml amber glass bottles	Ammonia	NH ₃
	Dilution; 10 ml of sample added to 90 ml of distilled, deionized water	100 ml HDPE bottles	Silica	Total and monomeric silica (SiO ₂)
	Unfiltered	80 ml HDPE bottles	Isotopes	δ ² H, δ ¹⁸ O
Steam	None	80 ml HDPE bottles	Isotopes	δ ² H, δ ¹⁸ O
	Evacuated double port gas bottle containing 50 ml of 2N H ₃ BO ₃	Sampling: approx. 300 ml double port bottle; Storage: 250 ml amber glass bottles	Ammonia	NH ₃
	Evacuated single stopcock valve gas bottles containing 50 ml of 4M NaOH	Approx. 300 ml single stopcock valve gas bottles	Gas sample	CO ₂ and H ₂ S in NaOH, residual gases in gas phase (H ₂ , He, CH ₄ , Ar, N ₂ and O ₂)

^a: FA: filtered and acidified ^b: FU: filtered and unacidified

^c: EC: electric conductivity

3.2 Data handling

The chemical characteristic of the discharges fluid in production wells in the Berlín geothermal system was carried out by the geochemical laboratory of LaGeo. The total fluid from the wells was assumed to be representative of the deep brine in a liquid-dominated geothermal reservoir.

The pressure at which samples are taken is an important variable as it, together with the enthalpy of the discharging fluid determines the ratio between water and steam in the discharge. Samples were collected at pressures generally between 6.5 and 11.5 bar-g. As sampling conditions are different between wells, analytical results are not directly comparable because the distribution of component concentrations, both in water and steam, depend on the sampling pressure. For this reason, normalization of the chemical data is necessary before comparing individual wells or two samples from the same well. The chemical composition in water and steam for all the wells, except for well TR18B, was calculated at 10 bar-a vapour pressure (180°C) with the aid of the WATCH program using the data of total discharge enthalpy and sampling pressure. Quartz, Na/K and Na/K/Ca geothermometers were calculated. A single initial aquifer fluid temperature was chosen as a good approximation of the “real” temperature of the reservoir. Initial aquifer fluid compositions were computed using a reference temperature calculated in a previous step for reconstruction of the aquifer’s initial composition.

In general, three different models are used in the evaluation of initial aquifer fluid composition or initial reservoir fluid (Arnórsson and Stefánsson, 2005a). The first model corresponds to an isolated system so boiling is adiabatic, where the enthalpy of the well discharge is that of the initial aquifer fluid. The second and third models correspond to closed and open systems, respectively; for both systems, the enthalpy of the well discharge is considered to be higher than that of the initial aquifer fluid and the reason for the excess enthalpy is either conductive heating of the aquifer fluid after depressuration boiling, or phase segregation of the two phases. In the case of conductive heating, the composition of the total discharge does not change as the net result is removal of water molecules along with some gas from the liquid phase to the steam phase. In the case of phase segregation the steam, after boiling starts some distance from the well, is preferably discharged from the well. Capillary forces between the liquid and surfaces of the minerals and rocks in the reservoir hinder the liquid phase from discharging from the well; the liquid phase stays behind in the reservoir. In this model, discharge enthalpies from such systems can be greatly in excess of the initial fluid enthalpy, and the composition of the total well discharge is different from that of the initial aquifer fluid, i.e. the total concentrations of dissolved solid components, such as silica, boron or chloride, calculated in the total discharge, strongly decrease with increasing discharge enthalpy.

For all the geothermal wells, except for well TR18B, the evaluation of the initial aquifer fluid compositions were calculated using Model 1 (Arnórsson and Stefánsson, 2005b). According to this model, the depth level of first boiling is within the well and the thermodynamic system is considered to be an isolated system, in which case boiling is adiabatic. In this model, it is a reasonable assumption to take the total well discharge composition to represent the initial aquifer fluid. No mineral precipitation or dissolution is assumed as the fluid is modelled from the aquifer to the surface. The calculation of initial aquifer fluid compositions for well TR18B which displays “excess” enthalpy, was calculated using the concepts applicable to the open system phase segregation model or Model 3 (Arnórsson et al., 2007, 2010).

3.3 Data quality analysis

Data quality verification is essential to ensure that the data is suitable for implementation of geochemical tools and the interpretation of data that helps answer questions about the geothermal system. Evidence about discrepancies or exceeded control limits should be investigated.

Two main criteria were used to set up data quality control. For quality analysis of chemical data of the steam phase, the O₂ content in samples was used; it was assumed that no O₂ was present in the geothermal gas. Samples with data values lower than one percent (<1.0%) of O₂ with respect to total Non-Condensable Gases (NCG) were accepted as normal; higher values providing evidence of the presence of oxygen indicated air contamination. In this case, the analyses could be corrected by subtracting the atmospheric component, as described by Zhen-Wu (2010).

For quality analysis of chemical data of the liquid phase, ionic balances or the percent of the charge balance error (CBE%) were used (Equation 1). When ionic compounds dissolve in water, they are dissociated into ions. The CBE% is the percentage difference between positive charges (cations) and negative charges (anions) in a water sample.

$$CBE \% = \left(\frac{\sum z_{cation} * m_{cation} - \sum z_{anion} * m_{anion}}{\sum z_{cation} * m_{cation} + \sum z_{anion} * m_{anion}} \right) \cdot 100\% \quad (1)$$

where z_i = Charge of an ion i ;
 m_i = Molal concentration of i (mol/kg).

The calculus of CBE% helps to determine water analysis accuracy, and is based on the principle of electro-neutrality which proposes that the sum in mmol/kg or meq/l of the cations must be equal to the sum of anions in a solution.

The purpose in checking the cation-anion balance in a water analysis is to validate the water analysis results. More than 5.0% difference in the cation-anion balance might imply that the analysis is not accurate or a major cation or anion was not considered in the CBE% calculation. It is important to note that WATCH's equation for CBE% calculus considers the average of the sum of the cations and anions; therefore, the CBE% limit using the WATCH program must be <10.0% approximately.

3.4 Selection of aquifer fluid reference temperature

For the liquid phase, four solute geothermometers were calculated: (1) sodium-potassium (Na/K) (Truesdell, 1976), (2) Na-K (Arnórsson et al., 1998), (3) sodium-potassium-calcium (Na/K/Ca) (Fournier and Truesdell, 1973), and (4) quartz geothermometer (Gudmundsson and Arnórsson, 2002). Geothermometer equations used in this study are presented in Table 6.

The Quartz geothermometer was selected for the reference temperature and was calculated using data from Table 4. The WATCH program was run using total discharge enthalpy and sampling pressure data. Quartz geothermometer temperature was calculated using total silica (as SiO₂) concentration in water initially in equilibrium with quartz after adiabatic boiling to 10 bar abs. vapour pressure. Data of aquifer temperatures and fluid enthalpy calculated from geothermometry are shown in Table 7.

TABLE 6: Geothermometer equations; valid in the range 0-350°C at P_{sat}

Geothermometer	Equation (T in °C)	Source
Na/K ^a	$\frac{856}{0.857 + \log\left(\frac{Na}{K}\right)} - 273.15$	(1)
Na/K ^b	$733.6 - 770.551 \cdot Y + 378.189 \cdot Y^2 - 95.753 \cdot Y^3 + 9.544 \cdot Y^4$	(1)
Na-K-Ca ^c	$\frac{1647}{\log\left(\frac{Na}{K}\right) + \beta \cdot \log\left(\frac{Ca^{0.5}}{Na}\right) + 2.24} - 273.15$	(1)
SiO ₂ ^d	$-132.2 + 0.036206 \cdot X + (55.865 \cdot 10^{-6}) \cdot X^2 - (2.699 \cdot 10^{-8}) \cdot X^3 + 128.277 \cdot \log(X)$	(2)

(1) Arnórsson (2000); (2) Gudmundsson and Arnórsson (2002).

^a: Valid in the range from 100 to 275°C.

^b: Y represents the logarithm of the molar Na⁺/K⁺ activity ratio at equilibrium with pure low-albite and pure microcline.

^c: Concentrations are in mol/kg and $\beta = 1/3$ was used.

^d: X represents total silica (as SiO₂) concentration in water initially in equilibrium with quartz after adiabatic boiling to 10 bar abs. vapour pressure (180°C).

The Na/K geothermometer, according to Arnórsson et al. (1998), is based on feldspar solubility constants. The Na/K geothermometer of Truesdell (1976) was used for comparison of results between both Na/K geothermometers. The results were generally very close, in most cases within +/- 3.0°C.

The Na/K geothermometer shows a systematic discrepancy, with significantly lower temperatures than those given by the quartz geothermometer. According to Gudmundsson and Arnórsson (2002), this discrepancy is due to faulty calibration of the former geothermometer or partial re-equilibration in the depressurization zone around the discharging well. A new water-rock chemical equilibrium is attained in reservoirs where water resides for short periods of time, and the process of chemical re-equilibrium is faster for quartz than Na/K. The differences in temperature between Na/K, and Na/K/Ca, compared with the quartz geothermometer, was between 2 and 33°C, and are very close in wells TR4B, TR5, TR5A, TR5C, TR9 and TR17A; in most cases, the differences were minor, 10.0°C between Na/K and quartz; and 5.0°C between Na/K/Ca and quartz. Initial aquifer temperatures derived from geothermometry were compared with temperatures measured downhole in wells TR2, TR4, TR4C, TR5B, TR18 and TR18B.

TABLE 7: Aquifer temperatures and fluid enthalpy calculated from geothermometry

Sample	well	$h^{d,t}$	$h^{f,tlog}$	$h^{f,tqtz}$	Aquifer temperature (°C)					Aquifer temperature differences (°C)	
		(kJ/kg)			T_{log}^a	T_{qtz}^b	$T_{Na/K}^c$	$T_{Na/K}^d$	$T_{Na/KCa}^e$	$T_{qtz} - T_{log}$	$T_{qtz} - T_{Na/KCa}$
2013-1388	TR2	1171	1241	1255	281	284	259	258	265	2.6	18.4
2013-1373	TR4	1291	1236	1277	280	288	264	265	273	7.9	15.2
2013-1374	TR4B	1316	1310	1242	294	281	275	278	280	-12.8	0.7
2013-1375	TR4C	1290	1251	1209	283	275	257	256	262	-8.2	12.9
2013-1164	TR5	1278	1349	1248	301	282	275	278	283	-18.6	-0.3
2013-1378	TR5A	1216	1321	1193	296	272	262	262	269	-24.4	2.8
2013-1379	TR5B	1182	1327	1314	297	295	262	262	267	-2.3	27.4
2013-1163	TR5C	1193	1349	1211	301	275	269	270	269	-25.7	6.2
2013-1380	TR9	1189	1210	1074	275	247	246	242	248	-27.6	-0.2
2013-1389	TR17	1141	1101	1218	253	277	256	255	259	23.6	17.2
2013-1390	TR17A	1156	1262	1058	285	244	240	235	244	-40.9	0.2
2013-1391	TR17B	1101	1180	1240	269	281	252	249	254	11.9	27.1
2013-1407	TR18	1168	1165	1175	266	268	251	248	257	2.1	10.9
2013-1408	TR18B	1693	1039	1029	240	238	257	256	252	-2.0	-14.0

$h^{d,t}$: Total discharge enthalpy;

$h^{f,tlog}$: Fluid enthalpy calculated using maximum temperature recorded on well logging;

$h^{f,tqtz}$: Fluid enthalpy calculated using quartz geothermometer temperature;

^a: Maximum temperature recorded on well logging;

^b: Temperature was based on quartz geothermometer (Gudmundsson and Arnórsson, 2002);

^c: Temperature based on Na/K geothermometer (Arnórsson et al., 1998);

^d: Temperature based on Na/K geothermometer (Truesdell, 1976);

^e: Temperature based on Na/K/Ca geothermometer (Fournier and Truesdell, 1973).

3.5 Aquifer fluid composition modelling

The calculation of chemical composition of fluid in isolated boiling system (adiabatic boiling) is based on the conservation of mass and energy; under conditions where water and steam samples are collected at the same pressure (P^s), Equation 2 gives the concentration of chemical component i in the initial aquifer fluid of a wet-steam well (Arnórsson, 2008):

$$m_i^{d,t} = m_i^{f,l} = m_i^{d,l}(1 - X^{d,v}) + m_i^{d,v} \cdot X^{d,v} \quad (2)$$

where $m_i^{d,t}$ = Concentration of component i in total discharge;
 $m_i^{f,l}$ = Concentration of component i in the initial aquifer fluid;
 $m_i^{d,v}$ = Concentration of component i in vapour discharge;
 $m_i^{d,l}$ = Concentration of component i in liquid discharge;
 $X^{d,v}$ = Vapour fraction in the discharge at vapour pressure P^s (by mass).

For components that partition almost exclusively in the liquid phase, at P^s , $m_i^{d,v}$ is taken to be zero by the WATCH program, and for gaseous components that are present in insignificant concentrations in liquid samples, therefore not analysed, $m_i^{d,l}$ is taken to be zero. The steam fraction of a well discharge is given by Equation 3:

$$X^{d,v} = \frac{h^{d,t} - h^{d,l}}{h^{d,v} - h^{d,l}} \quad (3)$$

where $h^{d,t}$ = Total discharge enthalpy (kJ/kg);
 $h^{d,l}$ = Liquid discharge enthalpy (kJ/kg);
 $h^{d,v}$ = Vapour discharge enthalpy (kJ/kg).

It is important to note that to determine the steam to water ratio in a wet steam well discharge at a specific pressure, it is necessary to know the total discharge enthalpy from measurements.

3.5.1 Phase segregation model

According to the phase segregation model (Model 3), the thermodynamic system is considered an open system. This model assumes that the steam phase moves preferentially into the well while water is retained in the aquifer due to capillary forces between the liquid and surfaces of the rock and minerals in the feed zones of the well. This process causes changes in the discharge enthalpy and the chemical composition of the well discharge to differ from those of the initial aquifer fluid. The use of the phase segregation model in this study involves several assumptions: (1) an excess of enthalpy is due to phase segregation only; (2) phase segregation occurs at a specific vapour pressure (P^g); and (3) that the vapour fraction in the initial aquifer fluid is zero.

The pressure at which phase segregation occurs affects the calculated composition of the initial aquifer fluid. It is considered likely that phase segregation occurs over a pressure interval between the aquifer pressure and the vapor pressure of the fluid entering the well rather than at a single pressure.

In general, the initial aquifer fluid composition calculations, using the phase segregation model, involve two steps after constituting the aquifer temperature and the aquifer vapour pressure. The first consists of calculating the liquid and steam composition from discharge data (chemical composition of water and steam and discharge enthalpy) at the phase segregation pressure (P^g) at which phase segregation is assumed to occur. The second step involves calculating the initial aquifer composition from the fluid compositions at P^g , assuming that the enthalpy before phase segregation occurred is the same as that of the vapour-saturated liquid at the aquifer temperature (Giroud, 2008).

For well TR18B, P^g was calculated as follows:

- chemical data was calculated at 10 bar-a vapour pressure (180°C); the WATCH program was run using total discharge enthalpy and sampling pressure data;
- quartz geothermometer (t_{qtz}) temperature from Gudmundsson and Arnórsson (2002) was calculated using calculated silica concentration at 180°C;
- reservoir pressure (P^R) was calculated using t_{qtz} and steam tables;
- P^g was calculated as a midway pressure between wellhead pressure (WHP) and P^R .

Phase segregation temperature (T^e) was calculated using P^g and steam tables. Intermediate aquifer fluid compositions were calculated using T^e as the reference temperature; the WATCH program was run using total discharge enthalpy and sampling pressure data.

The initial aquifer fluid compositions were calculated using chemical data from Table 4: P^g was the sampling pressure, t_{qtz} was the reference temperature and the pH of the fluid was calculated at T^e .

Equation 2 can be rewritten and the concentration of chemical component i in the initial aquifer fluid calculated as follows:

$$m_i^{f,t} = m_i^{g,l}(1 - X^{e,v}) + m_i^{g,v} \cdot X^{e,v} \quad (4)$$

where $m_i^{f,t}$ = Concentration of component i in initial aquifer fluid;
 $m_i^{g,v}$ = Concentration of component i in vapour discharge;

$m_i^{g,l}$ = Concentration of component i in liquid discharge;
 $X^{e,v}$ = Vapour fraction after depressurization boiling to P^g before retention of liquid in the aquifer.

As before for non-volatile species, $m_i^{g,v}$ is taken to be zero. Equation 5, given the vapour fraction $X^{e,v}$ at phase segregation pressure (P^g), is as follows.

$$X^{e,v} = \frac{h^{f,l} - h^{e,l}}{h^{e,v} - h^{e,l}} \quad (5)$$

where $h^{f,l}$ = Initial aquifer fluid liquid enthalpy (based on reference temperature) (kJ/kg);
 $h^{e,l}$ = Intermediate zone liquid enthalpy at phase segregation pressure P^g (kJ/kg);
 $h^{e,v}$ = Intermediate zone vapour enthalpy at phase segregation pressure P^g (kJ/kg).

Chemical component concentrations in the initial aquifer fluid of well TR18B, were calculated by the method just described.

3.5.2 Evaluation of processes leading to excess discharge enthalpy in well TR18B

When the discharge enthalpy of a well exceeds that of steam-saturated water at the aquifer temperature (which is the case in well TR18B), it is referred to as displaying “excess” enthalpy. As previously mentioned, a different model needs to be selected to explain the cause of elevated well enthalpy. There are two most common processes that can lead to excess discharge enthalpy. The first one is conductive heat transfer from the aquifer rock to the fluid flowing through the depressurization zone around discharging wells; the second one is due to phase segregation or relative permeability of liquid water and vapour leading to their partial or total separation (Karingithi et al., 2010). Additionally, excess enthalpy may be due to the presence of steam in the initial aquifer fluid. However, the effects of conductive heat transfer or phase segregation, or both, generally seem to be more important (Arnórsson et al., 2007).

Measurements of the total discharge enthalpy of well TR18B are in the range of 1500 to 1800 kJ/kg. Liquid discharge enthalpy calculated by using quartz geothermometer temperature and logging temperature provide values of around 1050 kJ/kg.

To identify the processes leading to the excess of discharge enthalpy in well TR18B, the two processes mentioned above were taken into account. Cl concentration in the total discharge, and evaluation of the relationship between Na/K and quartz geothermometers, using the concentration of chemical species in the total discharge, were used. According to Arnórsson et al. (2007), if the concentration of a non-volatile, conservative component like Cl in the total discharge of a well stays about constant, despite variations in excess discharge enthalpy, the cause of the excess enthalpy is due to conductive heat transfer from the aquifer rock to the flowing fluid. As already indicated, it is reasonable to assume that the system is isolated since conductive heat transfer from the aquifer rock to the fluid increases the relative proportion of steam without affecting the total two phase fluid composition, i.e. the enthalpy and total well discharge composition remains the same as that of the initial aquifer fluid. On the other hand, if the excess enthalpy is due to phase segregation, Cl concentration in the total discharge approaches zero as the discharge enthalpy approaches that of saturated steam.

Calculated Cl concentration in the total discharge (Figure 4) shows that the concentration of Cl decreases with increasing enthalpy, and approaches zero at the enthalpy of pure steam. Quartz geothermometer temperatures together with the Na/K temperature were calculated according to both conductive heat transfer and phase segregation models for well TR18B (Figure 5).

The calculated temperature according to the Na/K geothermometer is not affected by either model, but the calculated quartz geothermometer temperature is affected by which model is used. When using the conductive heat transfer model, the calculated quartz temperature is systematically lower than the Na/K temperature and the difference increases with increasing discharge enthalpy. This result indicates that phase segregation is the dominant cause of excess discharge enthalpy in well TR18B. Model 3 (Arnórsson et al., 2007, 2010) was, therefore, used to calculate the initial aquifer fluid composition for the well.

3.6 Mineral equilibria and thermodynamic data

Thermodynamics gives a qualitative means of calculating the stable relationships between various phases of various compounds or combinations of compounds (mineral assemblages). The fact that a mineral assemblage changes into a different assemblage means that the new association has a lower free energy than the old at a given pressure and temperature and mineral association of all the alternative phases. Although a geothermal system, as a whole, is an open system with continual inflow and outflow of mass and heat, thermodynamics consider the geothermal reservoir as a bulk of small systems in equilibrium behaving locally as closed system. According to this model, the chemical composition of fluids in the geothermal reservoir approaches equilibrium with respect to several alteration minerals.

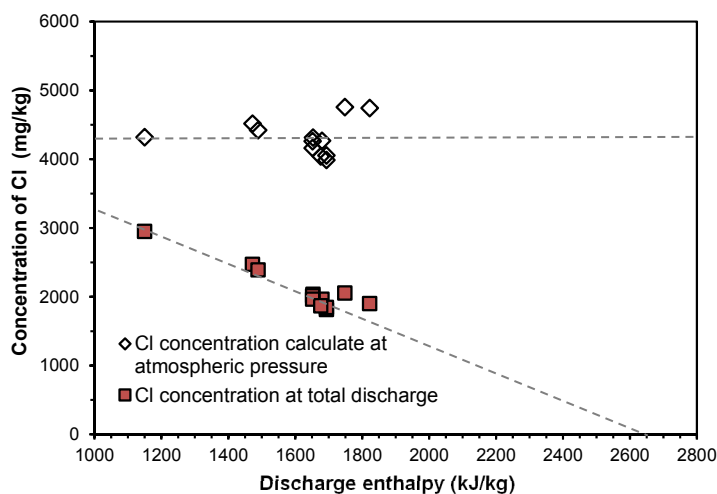


FIGURE 4: Relationship between Cl and discharge enthalpy in Well TR18B; Cl concentration in the total discharge approaches zero as the well discharge enthalpy approaches that of dry steam; this relationship further supports the theory that phase segregation is the cause of excess well discharge enthalpy in Well TR18B

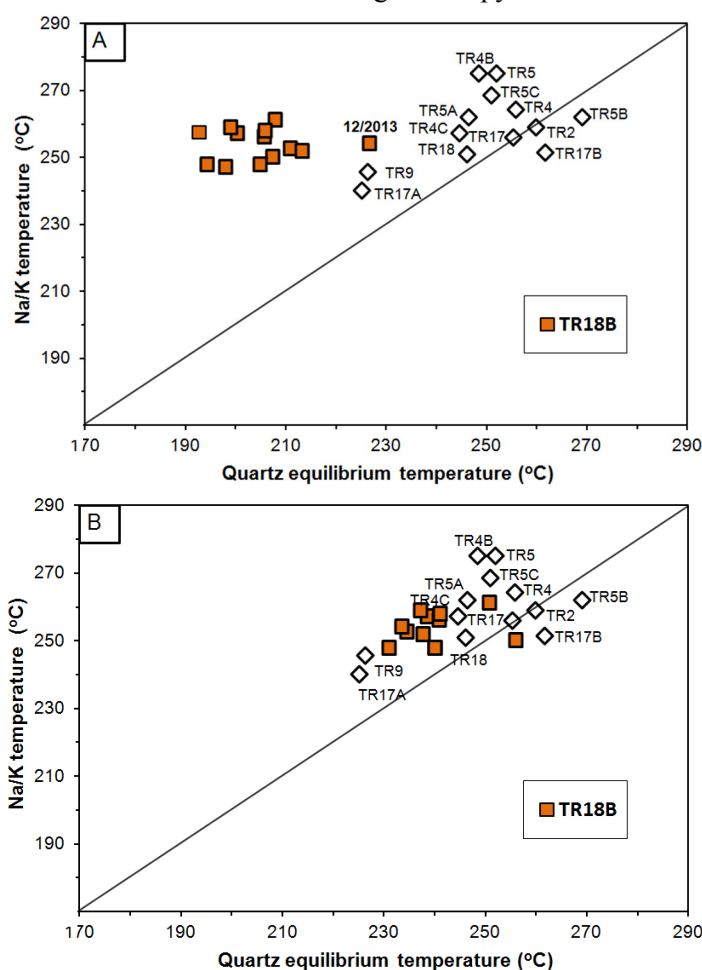
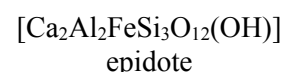
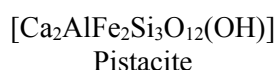
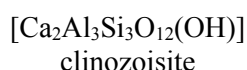


FIGURE 5: Relationship between Na/K and quartz geothermometers: Quartz equilibria temperature was calculated using the concentration of chemical species in total discharge according to conductive heat transfer (Model A) and phase segregation (Model B) for Well TR18B

The application of thermodynamics is an attempt to model local mineral equilibria that could potentially control the gas partial pressures in the reservoir. The calculus of equilibria between minerals, gases and liquid involve knowing the concentration of gases in equilibrium with the mineral assemblage and the activity of the species involved in the geothermal fluid. In this study, the concentration and activities of aqueous species were obtained with the aid of the WATCH program and several assumptions were made: (1) ideal behaviour in the mineral solid solution, (2) no vapour present in the initial liquid aquifer, and (3) unit activity for all minerals (anhydrite, calcite, hematite, magnetite, pyrite, pyrrhotite, quartz and wollastonite), except for epidote and prehnite solid solutions.

Data from selected microprobe analysis and structural formulae of epidote and prehnite from well core samples of the Berlin geothermal field reported by Ruggieri et al. (2006) was used to calculate the activities of end-members in epidote $[\text{Ca}_2\text{Al}_2\text{FeSi}_3\text{O}_{12}(\text{OH})]$ and prehnite $[\text{Ca}_2\text{Al}_2\text{FeSi}_3\text{O}_{10}(\text{OH})_2]$. Primary data, given in weight percent oxide and the calculated chemical formula and end-member activity for each individual mineral analysis, as well as the average, are provided in Table 8. The average activities of end-member epidote and prehnite were calculated to be 0.72 and 0.66, respectively, resulting in a clinozoisite activity of 0.28. These values are similar to the average compositions in other geothermal systems (Arnórsson et al., 2010; Karingiti et al., 2010; Scott, 2011).

Most epidote solid solutions in geologic systems fall within the compositional range between clinozoisite and epidote, 2 common end-member components of epidote solid solution.



Ferric iron can occupy the M1 and M3 sites. The activity composition relationships for epidote and clinozoisite were calculated according to Freedman et al. (2010), using data from Table 8. Mineral buffer reaction equilibrium between dissolved H_2S , CO_2 and H_2 is plotted against the mineral assemblages that could potentially fix the concentrations of these reactive gases (see later in Figure 7). The equilibrium curves for the gas-mineral assemblages are based on the respective equations for the end-member minerals according to thermodynamic data for H_2S , CO_2 and H_2 as given by Arnórsson et al. (2010). The log k -temperature equations and the reactions for which equilibrium constant curves have been drawn are listed in Table 9. The activities in the solid solution minerals were taken into account for the elaboration of each equilibrium curve. To explain this further, consider reaction 6 in Table 9.

TABLE 8: Results of microprobe analysis and structural formulae of epidote and prehnite from well core samples of the Berlin geothermal field (modified from Ruggieri et al., 2006)

Well	Weigh percent oxide					n_{Fe}	n_{Al}	$X_{\text{Fe,M3}}$	Chemical formula	a_{epi}
	SiO_2	Al_2O_3	CaO	FeO	SUM				Unit formula epidote	
TR-5B	38.57	26.10	23.66	9.68	98.01	0.63	2.38	0.21	$\text{Ca}_{1.96}\text{Al}_{1.04}\text{Fe}_{0.63}\text{Si}_{2.99}\text{O}_{12.5}(\text{OH})$	0.63
TR-8A	38.04	22.00	23.38	15.03	98.45	0.99	2.03	0.33	$\text{Ca}_{1.97}\text{Al}_{1.13}\text{Fe}_{0.99}\text{Si}_{2.99}\text{O}_{12.5}(\text{OH})$	0.77
TR17A	38.67	26.58	23.40	10.48	99.13	0.67	2.40	0.22	$\text{Ca}_{1.92}\text{Al}_{1.56}\text{Fe}_{0.67}\text{Si}_{2.95}\text{O}_{12.5}(\text{OH})$	0.66
TR-18	37.89	22.50	22.61	16.19	99.19	1.05	2.06	0.34	$\text{Ca}_{1.88}\text{Al}_{1.93}\text{Fe}_{1.05}\text{Si}_{2.94}\text{O}_{12.5}(\text{OH})$	0.81
								Average:	$\text{Ca}_{1.94}\text{Al}_{2.29}\text{Fe}_{0.76}\text{Si}_{2.97}\text{O}_{12.5}(\text{OH})$	0.72
Well	SiO_2	Al_2O_3	CaO	FeO	SUM	n_{Fe}		$X_{\text{Fe,Prehnite}}$	Unit formula prehnite	a_{pre}
TR-17	43.6	20.9	26.07	3.84	94.41	0.43		0.43	$\text{Ca}_{3.92}\text{Al}_{1.57}\text{Si}_{6.12}\text{O}_{20}(\text{OH})_2$	0.57
TR-17	38.8	25.4	23.04	9.21	96.45	0.26		0.26	$\text{Ca}_{3.50}\text{Al}_{1.74}\text{Si}_{5.50}\text{O}_{20}(\text{OH})_2$	0.74
								Average:	$\text{Ca}_{3.71}\text{Al}_{1.66}\text{Si}_{5.81}\text{O}_{20}(\text{OH})_2$	0.66

TABLE 9: Log K-temperature equations for the equilibrium constants for pure mineral and reactions for mineral assemblage reactions that may control the gas concentrations in a reservoir; data valid in the range from 0 to 350°C, at Psat; Source of thermodynamic data used to obtain the temperature equations is outlined by Karingithi et al. (2010)

#	Species	Equilibrium reaction for the gas mineral assemblages
1	CO ₂	$czo + cal + \frac{3}{2}qtz + H_2O = \frac{3}{2}pre + CO_{2,aq}$
2	CO ₂	$\frac{2}{5}czo + cal + \frac{3}{5}qtz = \frac{3}{5}gro + \frac{1}{5}H_2O_l + CO_{2,aq}$
3	H ₂ S	$\frac{1}{3}pyr + \frac{1}{3}pyrr + \frac{2}{3}pre + \frac{2}{3}H_2O_l = \frac{2}{3}epi + H_2S_{aq}$
4	H ₂ S	$\frac{1}{4}pyr + \frac{1}{2}pyrr + H_2O_l = \frac{1}{4}mag + H_2S_{aq}$
5	H ₂ S	$\frac{2}{3}gro + \frac{1}{3}pyr + \frac{1}{3}pyrr + \frac{2}{3}qtz + \frac{4}{3}H_2O_l = \frac{2}{3}epi + \frac{2}{3}wol + H_2S_{aq}$
6	H ₂ S	$2gro + \frac{1}{4}pyr + \frac{1}{2}mag + 2qtz + 2H_2O_l = 2epi + 2wol + H_2S_{aq}$
7	H ₂	$\frac{4}{3}pyrr + \frac{2}{3}pre + \frac{2}{3}H_2O_l = \frac{2}{3}epi + \frac{2}{3}pyrr + H_{2,aq}$
8	H ₂	$\frac{2}{3}pyr + H_2O_l = \frac{3}{4}pyr + \frac{1}{4}mag + H_{2,aq}$
9	H ₂	$\frac{2}{3}gro + \frac{4}{3}pyrr + \frac{2}{3}qtz + \frac{4}{3}H_2O_l = \frac{2}{3}epi + \frac{2}{3}wol + \frac{2}{3}pyr + H_{2,aq}$
10	H ₂	$6gro + 2mag + 6qtz + 4H_2O_l = 6epi + 6wol + H_{2,aq}$
#	Species	log K-temperature equations (°K)
1	CO ₂	$-0.890 + 7251.5/T^2 - 1710.6/T + 0.004188T + 0.000002683T^2 - 0.064\log T$
2	CO ₂	$-1.449 - 40536/T^2 - 2135.9/T + 0.0065639T + 0.000002725T^2 - 0.193\log T$
3	H ₂ S	$13.608 + 592324/T^2 - 9346.7/T - 0.043552T + 0.000029164T^2 + 5.139\log T$
4	H ₂ S	$13.659 + 555082/T^2 - 9256.6/T - 0.043608T + 0.000028613T^2 + 5.148\log T$
5	H ₂ S	$-0.836 - 216659/T^2 - 2847.3/T + 0.008524T - 0.000002366T^2 + 0.152\log T$
6	H ₂ S	$13.589 + 590215/T^2 - 9024.5/T - 0.044882T + 0.000029780T^2 + 5.068\log T$
7	H ₂	$-1.640 - 124524/T^2 - 777.19/T - 0.0005501T + 0.000007756T^2 - 0.565\log T$
8	H ₂	$-1.544 - 151109/T^2 - 752.389/T - 0.0005868T + 0.000007080T^2 - 0.532\log T$
9	H ₂	$1.444 - 273812/T^2 - 3962.1/T + 0.002401T + 0.000001304T^2 - 0.979\log T$
10	H ₂	$-1.654 - 95456.8/T^2 - 621.84/T - 0.001257T + 0.000007569T^2 - 0.600\log T$

$$2gro + \frac{1}{4}pyr + \frac{1}{2}mag + 2qtz + 2H_2O_l = 2epi + 2wol + H_2S_{aq} \quad (6)$$

Taking the activities of grossular (gro) and epidote (epi) to be equal to 0.3 and 0.72, respectively, and taking the activities of pyrite (pyr), magnetite (mag), quartz (qtz), wollastonite (wol) and water (H₂O_l) to be equal to unity we have:

$$\log K = 2epi + H_2S_{aq} - 2gro \quad (7)$$

$$\log [H_2S] = \log K - 2 \log(0.72_{epi}) + 2 \log(0.3_{gro}) \quad (8)$$

The equilibrium curves for the gas-mineral assemblages were done using the log K-temperature value for each reaction and calculating the concentration of dissolved reactive gas (each 5°C) in the range from 200 to 300°C (473 to 513°K).

4. RESULTS AND DISCUSSION

4.1 Aquifer fluid composition

Information on the initial aquifer fluid chemical composition from Table 10 was used to study the distributions of reactive and conservative elements, both volatile and non-volatile, in the Berlin geothermal field. Field-scale distributions using “natural neighbour” together with “radial funct” gridding methods are shown in Figure 6.

Figure 6a shows the field-scale distribution of quartz equilibrium temperature in the Berlín geothermal field. The quartz geothermometer distribution suggests the flow moves along the NW-SE graben with the maximum temperatures in well pads TR4 and TR5 in the central and northwest part of the field. Quartz geothermometer temperatures were compared with temperatures measured downhole in wells TR2, TR4, TR4C, TR5B, TR18 and TR18B. Temperatures inferred from geothermometry were generally very close to the measured maximum temperature in the well in most cases, within $\pm 5.0^{\circ}\text{C}$. The discrepancy in some of the wells may be due to the aquifer in the wells producing at different horizons than what corresponds to where maximum temperature in the well is measured during well logging. Discharged fluid is usually a mixture of water from different feed zones in the well and the analysis of the discharge yields a weighted average composition of the feed zones

Figure 6b shows the field-scale distribution of Cl. The distribution shows an increase in the Cl concentration in the aquifer fluids from the west to the east with the higher concentrations in the zone of the production well pad TR17. Quartz geo temperatures are higher ($>10.0^{\circ}\text{C}$) than the maximum temperatures measured downhole in wells TR17 and TR17B. According to Magaña (2012), wells TR17 and TR17B are in equilibrium with wairakite and suggest the possibility of evaporation for adiabatic expansion of the fluids in this zone. Higher Cl concentration in the east part of the field could be caused by boiling and steam loss of the fluids. This is in agreement with the N_2 and H_2 depletion in the fluids in that part of the field (Figures 6d and 6e). Moreover, the main source of Cl in the aquifer fluids is progressive dissolution of the host rock; the high concentration of Cl in well TR17 could indicate the deepest fluid feed zone. In contrast, well TR18B shows the lowest Cl concentration, lowest temperature, high N_2 content and strongly suggests a possible interaction (mixing and boiling process) among the geothermal fluid and recharging meteoric waters coming from the south. According to Scott (2011), a large depletion in H_2 , relative high N_2 content and low Cl concentration, which is the case of well TR18B, could be evidence of cold recharge.

The distributions of CO_2 and N_2 on the scale of the geothermal field are shown in Figures 6c and 6d, respectively. As can be seen in both figures, they appear to follow similar patterns. N_2 is generally known to be conservative in geothermal fluids and its concentration in the fluid is, therefore, source controlled. The similar pattern in the field scale distribution in the geothermal field, therefore, indicates that CO_2 might also be source controlled. In the case of the former, its source is dissolution of basaltic rock, magma degassing or the dissolution of hydrothermal calcite precipitated in an earlier stage of the geothermal system; for the latter, the source is recharging air-saturated meteoric water or the CO_2 is degassed into the system from melting oceanic crust. Concentrations in aquifer fluids can also be affected by degassing prior to entering the producing zone of a well.

The field scale distributions of H_2 and H_2S are shown in Figures 6e and 6f, respectively. Especially for H_2S , the highest concentrations of these gases are calculated in the proximity of the proposed upflow zones, where the highest temperatures are found. The concentrations of H_2S and H_2 appear to follow similar patterns as the quartz geothermometer indicated: the concentrations of these gases are temperature controlled. Accordingly, the highest concentrations of these gases should indicate the hottest parts of the system.

It is evident that the lowest H_2 concentrations are calculated in the south area. The cause could be related with the boiling process or steam loss from the fluid into wells TR17 and TR17B. Both gases

H₂ and H₂S partition into the vapour phase; however, due to the lower solubility of H₂ in liquid water, H₂ is more sensitive to the presence of a vapour phase than H₂S and is considered a more reliable indicator of the equilibrium vapour fraction. H₂S and H₂ are generated by reactions with the rock that can bring their concentrations back into equilibrium after degassing has occurred.

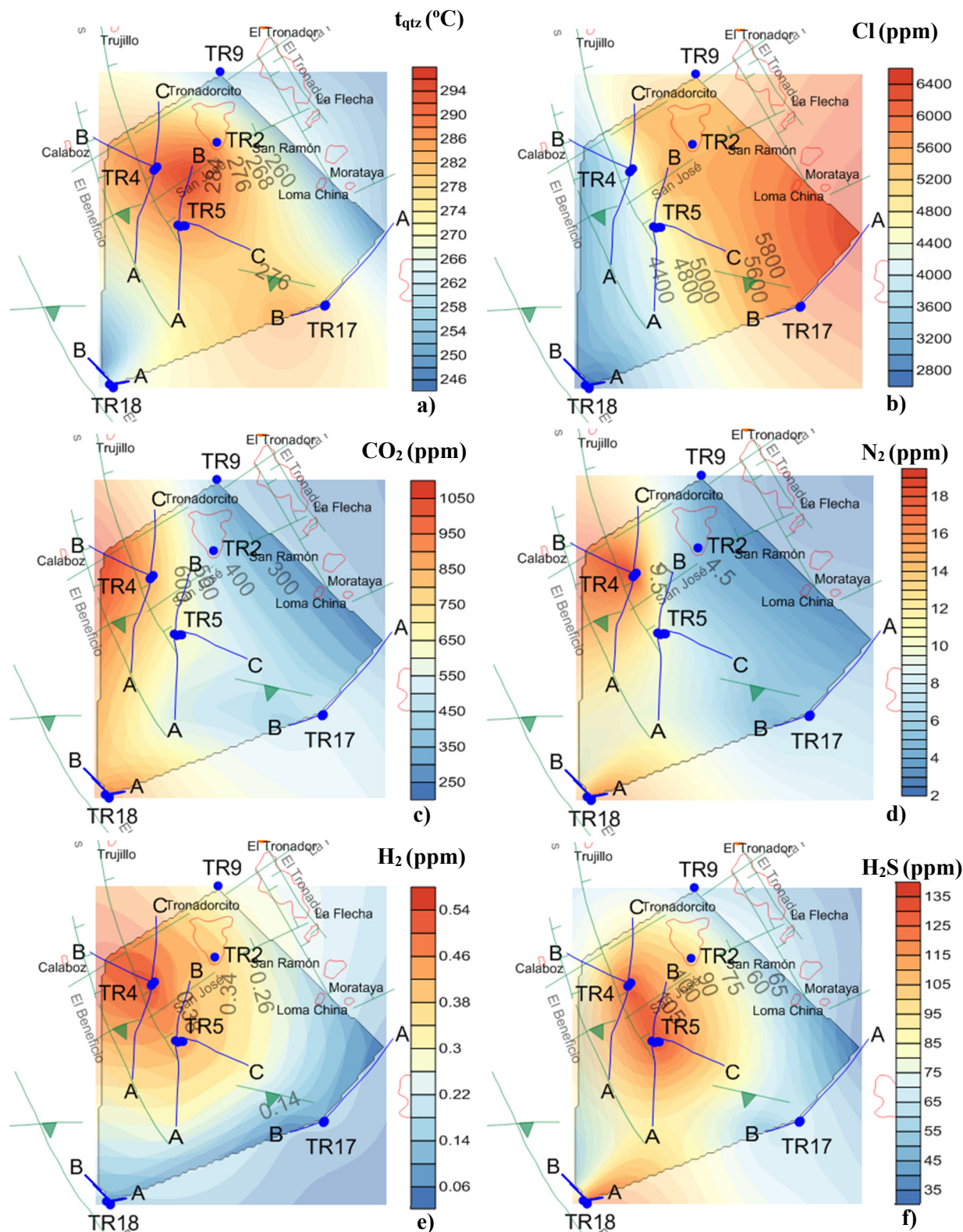


FIGURE 6: Field-scale distribution of temperature based on: (a) quartz geothermometer; (b) concentration of Cl; (c) CO₂; (d) N₂; (e) H₂; and (f) H₂S throughout the Berlin geothermal field

TABLE 10: Calculated chemical composition of the initial liquid phase in the aquifer feeding production wells at the Berlin geothermal field

Sample	Well	Discharg enthalpy kJ/kg	Aquifer temp. °C ^a	Liquid phase (mg/kg)														Chemical species (log mol)					
				pH ^b	SiO ₂	B	Na	K	Mg	Ca	Al	Fe	F	Cl	SO ₄	CO ₂ ^c	H ₂ S	H ₂	CH ₄	N ₂	H ₂ CO ₃ ^d	H ₂ S	H ₂
2013-1388	TR-2	1171	284	4.98	565	89	2933	517	0.07	89	0.48	0.09	0.39	5336	11.1	415	98	0.39	0.64	4.5	-2.03	-2.54	-3.71
2013-1373	TR-4	1291	288	5.54	578	70	2370	437	0.01	43	0.35	0.01	0.75	3993	11.2	862	130	0.53	0.86	19.4	-1.71	-2.43	-3.58
2013-1374	TR-4B	1316	281	5.80	558	63	1868	376	0.01	25	0.58	0.01	0.58	3308	9.6	1066	64	0.48	0.67	15.0	-1.62	-2.74	-3.62
2013-1375	TR-4C	1290	275	5.46	537	96	3079	535	0.02	112	0.58	0.02	0.53	5676	15.5	762	93	0.40	0.65	11.3	-1.77	-2.57	-3.70
2013-1164	TR-5	1278	282	5.07	563	88	2714	546	0.05	44	0.33	0.02	0.37	4619	8.8	615	127	0.41	0.64	8.8	-1.86	-2.43	-3.69
2013-1378	TR-5A	1216	272	5.50	527	77	2343	424	0.03	48	0.24	0.52	0.59	4273	14.7	461	86	0.28	0.50	8.5	-1.98	-2.60	-3.86
2013-1379	TR-5B	1182	295	5.27	598	103	3101	561	0.09	102	0.23	0.50	0.45	5825	9.7	563	98	0.35	0.61	4.2	-1.89	-2.54	-3.76
2013-1163	TR-5C	1193	275	4.95	540	105	2966	566	0.09	105	0.50	0.05	0.50	5419	9.8	507	93	0.31	0.55	6.1	-1.94	-2.57	-3.81
2013-1380	TR-9	1189	247	5.52	445	82	2669	418	0.01	134	0.55	0.03	0.70	5051	19.2	257	53	0.24	0.39	3.1	-2.24	-2.82	-3.92
2013-1389	TR-17	1141	277	5.07	543	97	3233	556	0.12	143	0.17	0.17	0.60	5774	7.7	510	70	0.10	0.05	5.8	-1.94	-2.69	-4.30
2013-1390	TR-17A	1156	244	5.58	434	103	3496	520	0.13	229	0.28	0.08	0.97	6406	21.4	197	32	0.02	0.02	2.9	-2.36	-3.05	-5.00
2013-1391	TR-17B	1101	281	5.50	557	98	3068	506	0.11	161	0.15	0.55	0.70	5674	13.4	369	48	0.02	0.01	3.6	-2.08	-2.86	-5.00
2013-1407	TR-18	1168	268	5.90	516	68	1500	246	0.01	27	0.79	0.03	0.61	2598	19.8	974	138	0.07	0.08	17.5	-1.66	-2.41	-4.46
2013-1408	TR-18B	1693	238	5.03	477	78	1816	315	0.01	67	0.00	0.00	3.31	3216	16.8	777	43	0.20	0.03	6.9	-1.76	-2.90	-4.00
2013-1182	TR-18B	1822	249	5.19	575	91	2260	369	0.27	142	2.81	1.02	4.63	4040	24.4	244	32	0.07	0.02	2.1	-2.26	-3.04	-4.46
2013-1208	TR-18B	1748	244	5.16	545	103	2126	382	0.17	121	1.78	0.52	0.00	4050	25.5	254	50	0.07	0.02	4.4	-1.99	-2.84	-4.46
2013-1236	TR-18B	1680	235	4.89	437	82	1933	309	0.01	82	1.06	0.02	3.68	3272	22.5	1493	78	0.47	0.05	14.2	-1.47	-2.65	-3.63
2013-1244	TR-18B	1472	238	4.92	456	83	1979	330	0.00	83	0.88	0.12	4.13	3480	22.4	1118	68	0.35	0.04	10.3	-1.60	-2.71	-3.76
2013-1250	TR-18B	1489	241	4.95	472	75	1962	325	0.00	79	0.86	0.08	3.74	3423	21.8	1116	59	0.38	0.03	9.5	-1.60	-2.77	-3.72
2013-1409	TR-18B	1693	237	5.00	470	86	1790	315	0.01	67	0.00	0.00	2.89	3264	17.4	829	44	0.17	0.02	5.4	-1.73	-2.89	-4.07
2013-1549	TR-18B	1150	234	5.00	451	85	1935	327	0.04	70	0.00	0.00	2.82	3460	21.4	950	46	0.29	0.03	8.4	-1.67	-2.88	-3.84
2014-0066	TR-18B	1653	241	5.03	490	80	1973	340	0.00	71	0.00	0.00	3.06	3444	22.9	991	43	0.28	0.03	8.9	-1.65	-2.91	-3.86
2014-0217	TR-18B	1652	241	5.13	491	92	1995	349	0.00	72	0.00	0.00	2.86	3417	25.2	902	40	0.20	0.02	6.5	-1.69	-2.94	-4.00
2014-0360	TR-18B	1652	240	5.02	485	78	1860	297	0.00	66	0.00	0.00	3.28	3335	20.8	1219	43	0.36	0.04	11.4	-1.56	-2.90	-3.75
2014-0891	TR-18B	1676	235	5.02	485	78	1860	297	0.00	66	0.00	0.00	3.28	3335	20.8	1219	43	0.36	0.04	11.4	-1.62	-2.91	-3.75

^a: temperature based on quartz geothermometer (Gudmundsson and Arnórsson, 2002)^b: pH at aquifer temperature reported in the column to the left^c: total carbonate carbon as CO₂^d: used as aquifer water CO₂ concentrations in mineral assemblage-gas equilibria

4.2 Mineral assemblages

Secondary minerals such as epidote and albite, which coexist with quartz, illite, chlorite, calcite, wairakite, adularia and prehnite, are found in drill cuttings from Berlin geothermal field. In several samples, minor amounts of titanite and pyrite are also observed without clear depth distribution (Rugierri et al., 2006).

One difficulty in making the determination of which mineral assemblage is involved in controlling the gas concentrations in the geothermal fluid is that the equilibrium concentrations of gases predicted by different possible mineral buffers fall within a narrow range, even within the range of uncertainty inherent in the process of fluid sampling and analysis. Additionally, different mineral assemblages have been identified to control reactive gas concentrations in geothermal fields of different geological settings (Scott, 2011). However, Arnórsson et al. (2007) pointed out that some of the different mineral assemblages give very similar aqueous H_2S , H_2 and CO_2 equilibrium concentrations when the end member activities of the solid solution minerals are properly chosen.

The equilibrium curves of the mineral assemblages that could potentially fix the concentrations of the reactive gases H_2S , H_2 and CO_2 in the Berlin geothermal field (reactions 1-10, Table 10) are plotted in Figure 7, in the temperature range 200 to 300°C and at the selected mineral compositions ($a_{\text{epi}}=0.72$, $a_{\text{czo}}=0.28$, $a_{\text{pre}}=0.66$, $a_{\text{gro}}=0.3$).

The activity of the H_2S species for the fluids in Berlin geothermal field are shown in Figure 7a. At the selected mineral compositions, it is difficult to distinguish between which of the 3 mineral

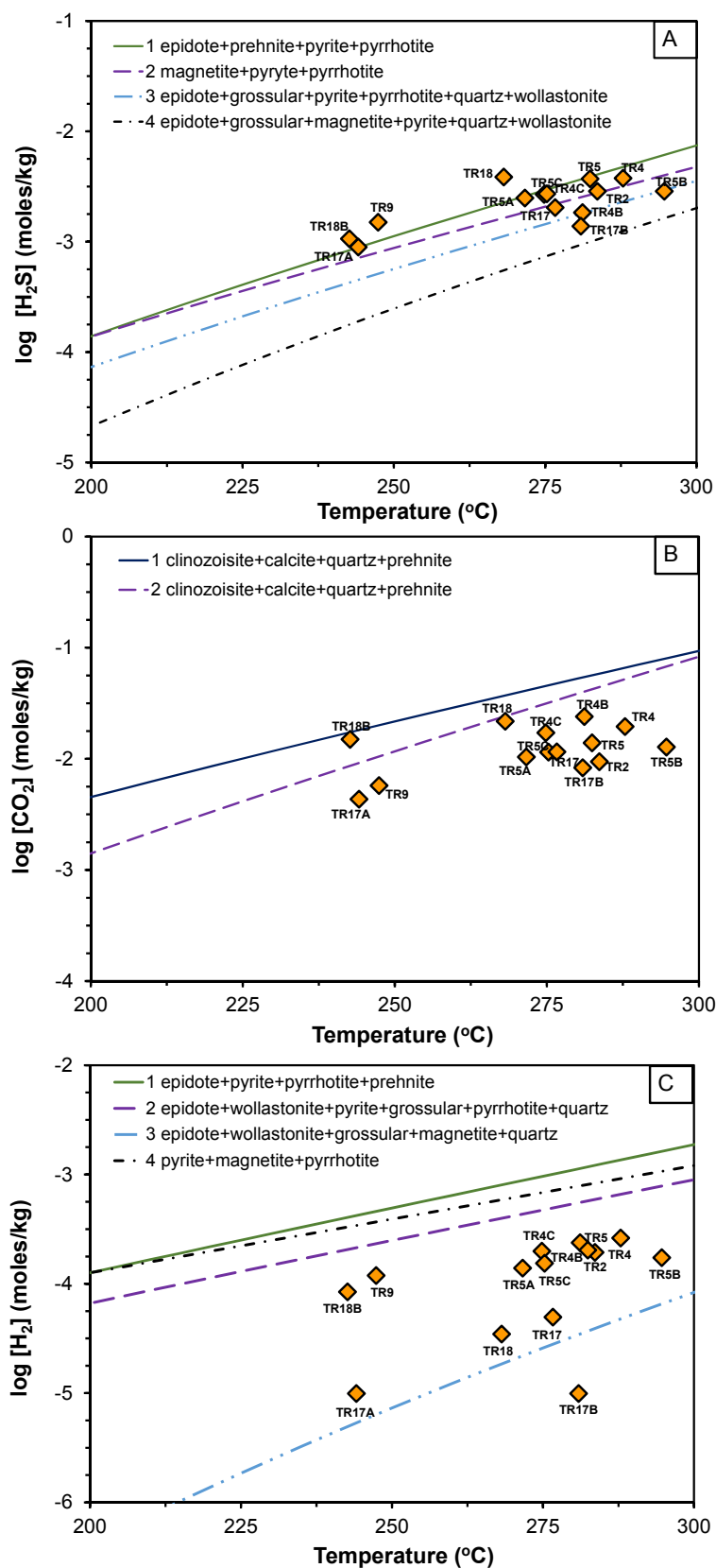


FIGURE 7: Mineral buffer reaction equilibrium between dissolved (a) H_2S , (b) CO_2 and (c) H_2 in the aquifer liquid of production wells of Berlin geothermal field

assemblages control the gas concentrations, because the equilibrium gas concentrations given by the different mineral assemblages are quite similar throughout the temperature range of interest; the concentrations given by mineral buffer 1 (epi-pre-pyr-pyrr) and buffer 2 (mag-pyr-pyrr) mineral assemblages differ by only 0.13 to 0.29 log units. However, if considering that the H_2S data randomly moved around the equilibrium curves, mineral buffers 1 (epi-pre-pyr-pyrr) and 3 (epi-gro-pyr-pyrr-qtz-wol) seem to be more probable. The concentration of H_2S in Berlin geothermal field does, however, clearly indicate a temperature control.

Concentration of the CO_2 species in Berlin geothermal field is shown in Figure 7b. The CO_2 species concentration for some wells lies close to the equilibrium line for the mineral assemblage used in this study, but there seems to be no clear temperature trend. The concentrations seem to be constant for the temperature range of the Berlin field. One explanation for this is that the CO_2 concentration is not, in fact, controlled by equilibrium with a mineral assemblage but is rather source-controlled. CO_2 concentration in the field-scale distribution appears to follow a similar pattern as that of N_2 , which is generally known to be source controlled.

Concentration of H_2 (Figure 7c) in the Berlin field seems to be in two categories. All data points, except for wells TR17, TR17A, TR17B and TR18, seem to align in a temperature controlled relationship although they are not very close to the equilibrium lines shown in Figure 7c; wells TR17, TR17A, TR17B and TR18 seem to be depleted of H_2 when compared to the rest of the wells. These depleted wells are all wells on the south side of the production field.

If considering mineral assemblage 3 (epi-wol-gro-mag-qtz), the relatively large stoichiometric coefficients in reaction (10) of Table 9 show that the equilibrium aqueous concentrations of H_2 are strongly affected by the compositions of grossular garnet. Figure 8 illustrates how variable compositions of grossular garnet affect the equilibrium curves of this reaction. Equilibrium gas concentrations given by the other mineral assemblages in Figure 7c assume unit activity, for all the minerals are not significantly affected by adjusting the curve for activities of the solid-solution minerals prehnite and epidote.

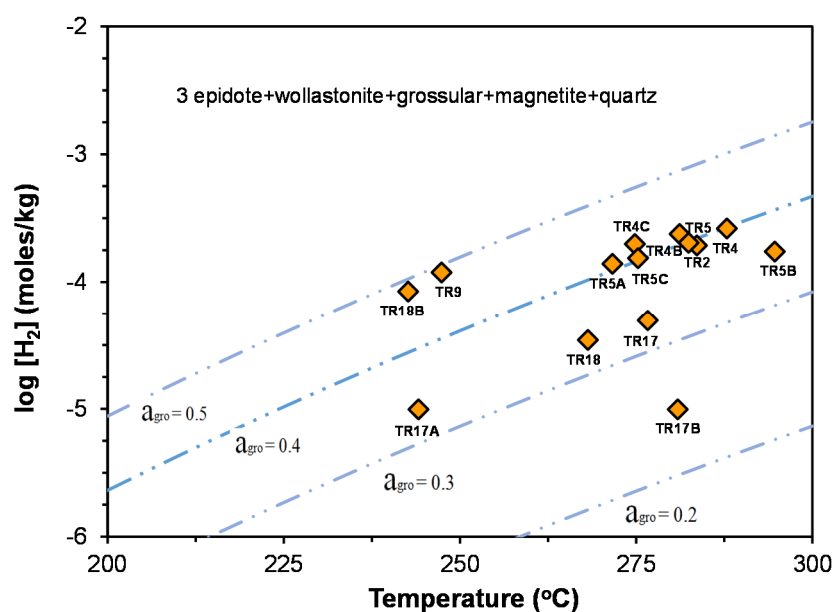


FIGURE 8: Mineral buffer reaction equilibrium between dissolved H_2 and mineral assemblages considered by reaction 10 in Table 9, at variable compositions of grossular

Hydrogen concentration for most of the wells (TR5, TR5A, TR5C, TR2, TR4, TR4B and TR4C) lies close to the equilibrium line, using compositions of a grossular value of 0.4 ($a_{\text{gro}}=0.4$), while wells TR18B and TR9 closely approach equilibrium with the mineral assemblages using $a_{\text{gro}}=0.5$. Angcoy (2010) concluded that the H_2 concentrations in the silicic volcanic of the Mahanagdong geothermal field in the Philippines best corresponded to the epi-wol-gro-mag-qtz mineral assemblage.

As mentioned before, wells of the north zone (TR17, TR17A, TR17B and TR18) are depleted in H_2 . A possible explanation for this is that they represent waters that have not equilibrated yet due to short reaction times in the geothermal reservoir. Scott (2011) concluded that apparent H_2 depletion in well fluids on the edges of Hellisheidi geothermal field, Iceland, was a result of insufficient equilibrium time.

5. SUMMARY AND CONCLUSIONS

This study is based on the results of the calculation of aquifer fluid composition at depth of the volcanic geothermal system of Berlín, El Salvador, using chemical speciation program WATCH 2.4 and chemical data from water and steam discharge samples collected and analysed by geochemical laboratory of LaGeo from 14 currently producing wet-steam wells. All fluids were sampled during the period from July to October 2013, except for samples collected from well TR18B which was sampled during the period from July 2013 to July 2014.

All the well discharges have liquid enthalpy (i.e. the enthalpy of the discharged fluid is equal, or very close, to the enthalpy of steam-saturated liquid at the aquifer temperature) except for well TR18B. The evaluation of initial aquifer fluid compositions for wells with liquid enthalpy were calculated according to a model where the depth level of first boiling is within the well and the thermodynamic system is considered an isolated system.

It was shown that the process of phase segregation, caused by the retention of liquid onto mineral grain surfaces, best accounts for the observed decreasing concentrations of Cl in the total well discharge with an increase in discharge enthalpy; similarly, evaluation of the relationship between Na/K and quartz geothermometers suggests that the main cause of elevated discharge enthalpy is caused by phase segregation in the depressurization zone around the well. Modelling of aquifer fluid compositions using the phase segregation model was applied to well TR18B.

The chemical composition of the deep water reservoir in the Berlín geothermal field indicated that the reservoir is liquid-dominated and sub-boiling at depth with an aquifer fluid temperature based on a quartz geothermometer in the range of 240-285°C in the south, and from 275 to 300°C in the central and northeast zones. Field-scale distribution of the concentration of selected gases, in the initial aquifer fluid in the production zone of the Berlín geothermal field, shows that H_2S and H_2 appear to follow similar patterns as indicated by the quartz geothermometer. This indicates that the concentrations of gases are temperature controlled, whereas CO_2 appears to follow a similar pattern as N_2 , which is generally known to be source controlled in geothermal systems.

The concentration of the H_2S species is clearly controlled by close approach to equilibrium with mineral assemblages known to actively control H_2S species concentration in geothermal systems (Angcoy, 2010; Arnórsson et al., 2007, 2010; Karingithi et al., 2010; Scott, 2011). However, considering that the H_2S species concentration randomly scatters around the equilibrium curves of at least three mineral assemblages, it is difficult to ascertain which of the 3 mineral assemblages controls the gas concentration. Equilibrium gas concentrations given by the different mineral assemblages are quite similar throughout the temperature range of interest.

The concentration of H_2 seems to be in two categories: most of the wells seem to be controlled by a close approach to equilibrium with respect to a mineral assemblage consisting of epidote-wollastonite-grossular-magnetite-quartz, except for wells TR17, TR17A, TR17B and TR18. These wells seem to be depleted in H_2 in comparison with the rest of wells. The depletion in H_2 in wells TR17, TR17A, TR17B and TR18, when compared to others, could indicate insufficient equilibrium time for the recharging geothermal fluids.

ACKNOWLEDGEMENTS

This is a great chance to express my sincere thanks to the United Nations University Geothermal Training Program and the Government of Iceland for granting me the opportunity to be a fellow in this excellent program. Special thanks go to the director of the UNU-GTP, Mr. Lúdvík S. Georgsson, and to Ms. Thórhildur Ísberg, Mr. Ingimar G. Haraldsson, Mr. Markús A. G. Wilde and Ms. Málfríður Ómarsdóttir for their assistance throughout these six months and for making every fellow feel welcome in Iceland.

I would like to express my appreciation to my employer, LaGeo S.A. de C.V. for allowing me to participate in UNU-GTP, to my boss, Roberto Renderos, for his trust and support, and to all my colleagues at the Geochemical Laboratory and Studies Department for their valuable assistance and help during my project.

Special thanks to Thráinn Fridriksson for his excellent work and guidance throughout the chemistry specialization course. Thanks to all other ÍSOR staff and lecturers. Sincere thanks to my supervisor, Ingvi Gunnarsson, for being an outstanding guide and for his extra effort and time spent trying to understand my “fancy” English. Certainly this report could not have been completed without his guidance and input.

I say thank you to all 2014 UNU Fellows, especially to the Chemistry or Landspítali group: Melissa, Yid, Melese, Edwin, Leakey, and Daniel “teschemacherite” Villarroel for their company, fruitful discussions and fun times during these six months in Iceland.

I would also like to take this opportunity to thank my family and my wife for giving me moral support, love, prayers and encouragement. Finally, I want to thank God for good health, strength and his blessings during my stay in Iceland.

REFERENCES

Angcoy Jr., E.C., 2010: *Geochemical modelling of the high-temperature Mahanagdong geothermal field, Leyte, Philippines*. University of Iceland, MSc thesis, UNU-GTP, report 1, 79 pp.

Arnórsson, S. (ed.), 2000: *Isotopic and chemical techniques in geothermal exploration, development and use. Sampling methods, data handling, interpretation*. International Atomic Energy Agency, Vienna, 351 pp.

Arnórsson, S., 2008: Chemical thermodynamics of two-phase geothermal systems. International Conference on the Properties of Water and Steam, Berlin, Germany.

Arnórsson, S., and Stefánsson, A., 2005a: Wet-steam well discharges. I. Sampling and calculation of total discharge compositions. *Proceedings of the World Geothermal Congress 2005, Antalya, Turkey*, 8 pp.

Arnórsson, S., and Stefánsson, A., 2005b: Well-steam well discharges II. Assessment of aquifer fluid compositions. *Proceedings of the World Geothermal Congress 2005, Antalya, Turkey*, 11 pp.

Arnórsson, S., Stefánsson, A., and Bjarnason, J.Ö., 2007: Fluid-fluid interaction in geothermal systems. *Rev. Mineralogy & Geochemistry*, 65, 229-312.

Arnórsson, S., Sigurdsson, S. and Svavarsson, H., 1982: The chemistry of geothermal waters in Iceland I. Calculation of aqueous speciation from 0°C to 370°C. *Geochim. Cosmochim. Acta*, 46, 1513-1532.

Arnórsson, S., Andrésdóttir, A., Gunnarsson, I., and Stefánsson, A., 1998: New calibration for the quartz and Na/K geothermometers – valid in the range 0-350°C (in Icelandic). *Proceedings of the Geoscience Society of Iceland Annual Meeting, April*, 42-43.

Arnórsson, S., Angeoy Jr., E.C., Bjarnason, J.Ö., Giroud, N., Gunnarsson, I., Kaasalainen, H., Karingithi, C., and Stefánsson, A., 2010: Gas chemistry of volcanic geothermal systems. *Proceedings of the World Geothermal Congress 2010, Bali, Indonesia*, 12 pp.

Axelsson, G., 2013: Conceptual models of geothermal systems – Introduction. *Presented at “Short Course V on Conceptual Modelling of Geothermal Systems”, UNU-GTP and LaGeo, Santa Tecla, El Salvador*, 12 pp.

Barrios, L., Hernández, B., Quezada, A., and Pullinger, C. 2011: Geological hazards and geotechnical aspects in geothermal areas, the El Salvador experience. *Presented at “Short Course on Geothermal Drilling in Central America – Resource Development and Power Plants”, UNU-GTP and LaGeo, Santa Tecla, El Salvador*, 14 pp

Bjarnason, J.Ö., 2010: *The speciation program WATCH* (vers. 2.4). ISOR – Iceland GeoSurvey, Reykjavík.

Correia, H., Jacobo, H., Castellanos, F., Tenorio, J., Handal, S., and Santos, P., 1996: *Synthesis of geoscientific information of a conceptual model of Berlín geothermal field*. Internal report, CEL, El Salvador, 30 pp.

D’Amore, F., and Tenorio, J., 1999: Chemical and physical reservoir parameters at initial conditions in Berlín geothermal field, El Salvador: A first assessment. *Geothermics*, 28, 45-73.

Fournier, R.O., and Truesdell, A.H., 1973: An empirical Na-K-Ca geothermometer for natural waters. *Geochim. Cosmochim. Acta*, 37, 1255-1275.

Freedman, A. J.E., Bird, D.K., Arnórsson, S., Fridriksson, Th., Elders, W.A., Fridleifsson, G.Ó., 2010: Hydrothermal mineral record CO₂ partial pressures in Reykjanes geothermal system, Iceland. *Proceedings of the World Geothermal Congress 2010, Bali, Indonesia*, 11 pp.

Giroud, N., 2008: *A chemical study of arsenic, boron and gases in high-temperature geothermal fluids in Iceland*. University of Iceland, Faculty of Science, PhD thesis, 110 pp.

Gudmundsson, B.T. and Arnórsson, S., 2002: Geochemical monitoring of the Krafla and Námafjall geothermal areas, N-Iceland. *Geothermics*, 31, 195-243.

Hernández M., C.B., 2012: Aquifer fluid compositions at the Berlín geothermal field, El Salvador in 2012. Report 12 in: *Geothermal training in Iceland 2012*. UNU-GTP, Iceland, 169-202.

Jacobo, P., 2003: Gas chemistry of the Ahuachapán and Berlín geothermal fields, El Salvador, Report 12 in: *Geothermal Training in Iceland 2003*. UNU-GTP, Iceland, 275-304.

Karingithi, C.W., Arnórsson, S., and Grönvold, K., 2010: Processes controlling aquifer fluid compositions in the Olkaria geothermal system, Kenya. *J. Volc. & Geotherm. Res.*, 196, 57-76

LaGeo, 2012: *Conceptual model of the Berlín geothermal system*. LaGeo S.A. de C.V., Studies and Production Departments, internal report (in Spanish), 143 pp.

Magaña, M.I., 2012: *Geochemical model. Berlín geothermal system*. LaGeo S.A de C.V., Geochemical Department, internal report (in Spanish), 21 pp.

Montalvo, F., and Axelsson, G., 2000: Assessment of chemical and physical reservoir parameters during six years of production-reinjection at Berlín geothermal field (El Salvador). *Proceedings of the World Geothermal Congress 2000, Kyushu-Tohoku, Japan*, 2153-2158.

Monterrosa, M., and Santos, P., 2013: Conceptual models for the Berlín geothermal field, Case history. *Presented at "Short Course V on Conceptual Modelling of Geothermal Systems", UNU-GTP and LaGeo, Santa Tecla, El Salvador*, 9 pp.

Raymond, J., Williams-Jones, A.E., and Clark, J.R., 2005: Mineralization associated with scale and altered rock and pipe fragments from the Berlín geothermal field, El Salvador; implications for metal transport in natural systems, *J. Volcanology & Geothermal Research*, 145, 81-96.

Renderos, R., 2002: Chemical characterization of the thermal fluid discharge from well production tests in the Berlín geothermal field, El Salvador. Report 12 in: *Geothermal Training in Iceland 2002*. UNU-GTP, Iceland, 205-232.

Ruggieri, G., Dallai, L., Nardini, I., Henriquez, E.T., and Arias, A., 2010: Thermo-chemical variations of the hydrothermal fluids in the Berlin geothermal field (El Salvador). *Proceedings of the World Geothermal Congress 2010, Bali, Indonesia*, 7 pp.

Ruggieri, G., Petrone, C.M., Gianelli, G., Arias, A., and Henriquez, E.T., 2006: Hydrothermal alteration in the Berlin geothermal field (El Salvador): new data and discussion on the natural state of the system. *Periodico di Mineralogia*, 75, 347-353.

Saemundsson, K., 2009: Geothermal systems in global perspective. *Presented at "Short Course IV on Exploration for Geothermal Resources", UNU-GTP, KenGen and GDC, Lake Naivasha, Kenya*, 11 pp.

Scott, S., 2011: *Gas chemistry of the Hellisheidi geothermal field*. University of Iceland, MSc thesis, 63 pp.

Truesdell, A.H., 1976: Summary of section III - geochemical techniques in exploration. *Proceedings of the 2nd U.N. Symposium on the Development and Use of Geothermal Resources, San Francisco, 1*, liii-lxxix.

Zhen-Wu, B.Y., 2010: Gas geochemistry of the Miravalles, Pailas and Borinquen geothermal areas of Costa Rica, and a comparison with Reykjanes and Theistareykir geothermal fields, Iceland. Report 33 in: *Geothermal Training in Iceland 2010*. UNU-GTP, Iceland, 731-766.



UNITED NATIONS
UNIVERSITY

UNU-GTP

Geothermal Training Programme

Orkustofnun, Grensasvegur 9,
IS-108 Reykjavik, Iceland

Reports 2014
Number 15

AIR QUALITY IMPACT ASSESSMENT: H₂S DISPERSION MODELLING FOR THE SABALAN GEOTHERMAL POWER PLANT, NW-IRAN

Ali Hosseinzadeh

SUNA – Renewable Energy Organization of Iran
Yadegare Emam Highway, Poonake Bakhtari Ave., Shahrake Ghods
P.O. Box 14155-6398, Tehran
IRAN
Ali_hz61@yahoo.com

ABSTRACT

In this study, the AERMOD dispersion modelling was applied to estimate the spatial distribution of H₂S concentrations in northwest Sabalan geothermal area. These estimates were made to assess the potential environmental impact of H₂S due to the exploitation of the proposed 55 MW_e Sabalan geothermal power plant. The study was done to provide recommendations concerning the local air quality and health effects in the populated areas close to the geothermal field, and for the workers in the vicinity of the proposed geothermal power plant. Two scenarios based on different locations of the power plant (emission source) were modelled, for 1, 8, and 24 hours, and 8 months averaging time, using available meteorological data from January to August, 2009. The modelling results are compared to the international ambient air quality and occupational standards. The results show that no significant health and environmental impacts are expected in northwest Sabalan geothermal area due to the proposed geothermal power plant.

1. INTRODUCTION

Compared to fossil fuels, geothermal energy is an environmentally friendly energy source for electricity generation because no combustion of fuel takes place during its production. The use of geothermal energy instead of fossil fuel effectively contributes to a reduction in CO₂ emissions. According to the EPA, the average rate of carbon dioxide emissions for coal-fired power plants and natural gas power plants is 1020 kg CO₂/MWh and 515 kg CO₂/MWh, respectively. Whereas for a geothermal power plant it is about 82 kg CO₂/MWh (Holm et al., 2012). In addition, compared to natural gas-fuelled electrical power plants, geothermal power plants produce no nitrous oxide. Nevertheless, as with any other source of energy, production of electricity derived from geothermal energy also causes environmental pollution, although on a much smaller scale (Gupta and Roy, 2007). One of the highlighted environmental issues in utilising geothermal systems is the discharge of non-condensable gases (NCG) to the atmosphere. The NCG present in geothermal fluid are a mixture of CO₂, H₂S, H₂, Hg, NH₃ and CH₄. Among all the NCG emitted, H₂S is of the greatest environmental concern, not only because of its noxious smell in low concentrations, but also due to its toxicity and health impacts at high concentrations (Kristmannsdóttir et al., 2000).

The commissioning of a 55 MW_e power plant in the Sabalan geothermal field certainly means a big step for geothermal development in Iran. However, the impacts associated with a geothermal development project may include negative effects on local air quality. Therefore, an assessment of the impacts of the proposed power plant on air quality is an integral part of the environmental assessment of this project. One way to study the air pollution is to use models that can predict the spatial distribution, and concentration of the pollutant with time (Nyagah, 2006).

Modelling air pollution is an important tool in devising strategies to manage the air pollution (Ólafsdóttir et al., 2014). Air quality models attempt to simulate the physical and chemical processes in the atmosphere; those may involve transport, dispersion, deposition and chemical reactions, to estimate pollutant concentrations at a downwind receptor location (Hung, 2010).

There are five general types of air dispersion models: Box model, Gaussian model, Lagrangian model, Eulerian model, and Computational Fluid Dynamics (CFD) model. The Gaussian model is the most commonly used model type. It assumes that the air pollutant dispersion has a Gaussian distribution and is normally used for predicting the dispersion of continuous, buoyant air pollution plumes originating from ground-level or elevated sources. Gaussian models may also be used for predicting the dispersion of non-continuous air pollution plumes. Examples of Gaussian models are: OSPM, UBM, CALINE4, UK-ADMS, and AERMOD (Holmes and Morawska, 2006).

AERMOD, the recommended model by the US EPA, has been used to model the distribution of various air pollutants including Hg, SO₂, NO_x, PM₁₀ and H₂S. AERMOD uses a Gaussian and a bi-Gaussian approach in its dispersion models. It can calculate from hourly to the annual concentrations average of pollutants in ambient air. The model handles a variety of pollutant sources in a wide variety of settings such as rural and urban as well as flat or complex terrain (Kumar et al., 2004).

The aim of this report is to use dispersion modelling for assessment of the temporal and spatial distribution of H₂S in the generation site and populated areas close to the planned 55MW_e Sabalan geothermal power plant. The predicted H₂S ground level concentrations will be compared to the international ambient air quality guidelines and occupational safety standards.

2. HYDROGEN SULPHIDE

Sources of H₂S are both natural and anthropogenic. It is released from volcanoes, sulphur springs, undersea vents, swamps, salt marshes, and stagnant bodies of water, and is found in association with crude petroleum and natural gas. Hydrogen sulphide is also associated with municipal sewers and sewage treatment plants, landfill gases, manure handling operations, pulp and paper operations, and geothermal power plants (EOHP, 2006).

2.1 Physical and chemical properties

Hydrogen sulphide (H₂S) is a flammable, colourless gas at ambient temperature and pressure with a characteristic odour of rotten eggs (Table 1). The levels of hydrogen sulphide in the air are typically low. The amount of hydrogen sulphide naturally found in the air has been estimated at 0.11-0.33 ppb (0.15-0.46 µg/m³). Lower levels (0.02-0.07 ppb; 0.03-0.1 µg/m³) have been observed in some remote areas (EOHP, 2006).

Hydrogen sulphide does not absorb the solar radiation reaching the troposphere and, thus, is photochemically stable. The atmospheric lifetime of H₂S is affected by ambient temperature and other ambient conditions including humidity, sunlight, and the presence of other pollutants. Decreased temperatures

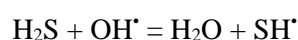
and sunlight, as well as lower levels of hydroxide radicals in northern regions during winter, increase the atmospheric residence time of H₂S (Idriss et al., 2004).

TABLE 1: The physicochemical properties of H₂S (SCOEL, 2007)

Properties	Description
Empirical formula	H ₂ S
Molecular weight	34.08 g/mol
Freezing point at 101.3 kPa	-85.5°C
Boiling point at 101.3 kPa	-60.7°C
State at room temperature	Gas
Vapour pressure at 25.5°C	2026 kPa
Vapour density (air=1)	1.19
Flammability	Extremely flammable
Explosive limits in air (vol/vol)	Lower limit:4.3% , Upper limit: 45.5%
Solubility(w/w) in water at 20 °C	0.4%
Odour	Strong odour of rotten eggs

After emission into the air, H₂S is dispersed and eventually removed. Resident time in the atmosphere ranges from about one day to more than 40 days, depending upon season, latitude, and atmospheric conditions.

H₂S released to the atmosphere is oxidized in reactions with OH[•] radicals. The probable mechanism of this hydrogen absorption reaction is as follows:



With the reaction rate constant $k_{298} = (4.5 \pm 1.0) 10^{-12} \text{ cm}^3 \text{ molecule/sec}$.

Dependency of the rate constant (K) on temperature (T) follows the Arrhenius equation:

$$K = A e^{-E/RT}$$

where A , E and R are the Arrhenius constant (frequency factor), activation energy and universal gas constants, respectively.

The SH[•] radical is oxidized to a transient molecule HSO₃, and then to sulphuric acid (H₂SO₄) as a final product. Other parallel reactions of H₂S with other oxidants such as NO₂, O₂ and O₃ are not important, being much slower than the oxidation with OH[•] radicals (Idriss et al., 2004).

2.2 Health and environmental impacts

Human health effects of exposure to hydrogen sulphide, an irritant and asphyxiate, depend on the concentration of the gas, the length of exposure, the state of health, and age and level of activity of the person exposed. Observations of effects on people exposed to different concentrations of H₂S in the air indicate that there is a progression in the severity of adverse health effects. Because of the sensitivity of the olfactory nerves, it is possible for the human to detect the presence of H₂S in the air at a concentration of < 0.14 mg /m³. The odour is very offensive at 4.2 - 7 mg/m³ and, at a concentration of 210 mg /m³, the olfactory nerves are unable to detect the odour, presumably because of olfactory nerve damage or sensory overload. A dose dependent progression of adverse effects starts with eye irritation at 14 - 28 mg/m³ and ending with collapse and death at 1400 - 2800 mg/m³ (MESB, 2000).

Because hydrogen sulphide is a gas, inhalation is the major route of exposure to hydrogen sulphide. Inhalation exposure to hydrogen sulphide causes health effects in many systems. Health effects that have been observed in humans due to exposure to hydrogen sulphide include ocular, neurological, cardiovascular, metabolic, respiratory, reproductive effects and death. Respiratory, neurological, and ocular effects are the most sensitive end-points in humans. There are no adequate data on carcinogenicity (WHO, 2003).

Most human data are derived from acute poisoning case reports, occupational exposures, and limited community studies (WHO, 2003). According to the U.S. Occupational Safety and Health Administration records, there were 80 fatalities in 57 H₂S incidents from 1984 to 1994 (Fuller and Suruda, 2000).

Hydrogen sulphide is found in nearly all high-temperature ($T > 150^{\circ}\text{C}$) geothermal fluids. It is probably formed by one or more of the following mechanisms: reaction of sulphur that is present in reservoir rocks with hot water, magmatic exhalation, or thermal metamorphism of marine sedimentary rocks (Wahl, 1977). Some studies in geothermal active areas have indicated that chronic exposure to H₂S increases nervous system diseases and cardiovascular diseases, as well as respiratory diseases (Bates et al., 2002; Durand and Wilson, 2006).

Several studies have shown that exposure to H₂S at low levels can increase plant growth and/or the rate of physiological processes in a variety of species. Positive growth and physiological responses to pollutant exposure has sometimes been termed as a “fertilizer” effect. However, the increment of plant photosynthetic rates in the absence of corresponding enhanced dry weight accumulations can be a stress response to a toxic compound. Plants may increase their rate of photosynthesis in order to keep up with the required rate of injury compensation and repair. Once plants are unable to keep up with the required rate of repair, detectable reductions in plant dry weight accumulation may occur (Khalil et al., 1996; De Kok et al., 1997).

2.3 Ambient air quality standards for hydrogen sulphide

There are no ambient air quality standards for H₂S environmental concentrations in Iran. Criteria pollutants (NO₂, SO₂, CO, HC(NMHC) and SPM (Suspended Particulate Matter) are the pollutants involved in air quality assessment in Iran. Therefore, WHO guidelines and standards (WHO, 2000) have been adopted in Iran. The standards for H₂S vary between countries, although many use the WHO recommendations (Table 2).

TABLE 2: Various ambient air quality standards for H₂S

Country/Agency	Relevant Law	Value ($\mu\text{g}/\text{m}^3$) ^a	Averaging period
WHO	Air Quality Guidelines 2nd Edition, 2000	150 7	24 hours 30 minutes
Iceland	Regulation 514/2010, Annex 1	50	24 hours
New Zealand	Ambient Air Quality Guidelines, 2002	7	1 hour
State of California, USA	State Ambient Air Quality Standards, Cal EPA 2005	42	1 hour
State of New York, USA	State Ambient air quality standard, DEC 2005	14	1 hour
State of New Mexico, USA	State Ambient air quality standard	14	1 hour
State of Arizona, USA	State Ambient air quality standard, (AAAQGs) 1999	180	1 hour
Europe	Air Quality Guidelines for Europe, 2000	150 7	24 hours 30 minutes
Germany	Odour Threshold Values for Ambient Air Quality Protection, FEA, 2004	3	-
Korea	Atmospheric and Environmental Protection Laws (Chap. 3 Sec.30)	84 ^b 28 ^c	- -

^aThe conversion factors for hydrogen sulphide in air (25°C, 101.3 kPa) are $1 \text{ mg}/\text{m}^3 = 0.717 \text{ ppm}$, $1 \text{ ppm} = 1.394 \text{ mg}/\text{m}^3$. ^bIn industrial areas. ^cIn residential areas

2.4 Occupational health guidelines for hydrogen sulphide

People who work in certain industries can be exposed to high levels of hydrogen sulphide. These industries include rayon textiles manufacturing, pulp and paper mills, petroleum and natural gas drilling operations, wastewater treatment plants, geothermal power plants, smelting and mining. The occupational exposure standards provide threshold limits for chemical substances in the working environment based on the health effects safety guidelines (Aráuz, 2014). At present, there is no regulation for the occupational exposure limits for hydrogen sulphide in Iran. Hence, ACGIH, OSHA and NIOSH guidelines have been adopted in Iran. The occupational exposure limits for H₂S vary between different institutes and countries (Table 3).

TABLE 3: International occupational exposure limits for H₂S

Country	Level (ppm)	Level $\mu\text{g}/\text{m}^3$	Averaging Period	Guideline Type	Date of Implementation	Relevant Law	Ref.
UK	10	14000	15 min	¹ MEL		New	a
	5	7000	8 hours ² TWA	MEL		New	a
USA	20		8 hours TWA	³ PEL-C		OSHA Regulations (Standards 29 CFR)	b
	10	14000	10 min ceiling	⁴ REL-C	2003	NIOSH	c
	0.1		1 hour	⁵ ERPG-1	2003	Emergency Response Planning Guideline	d
	30		1 hour	⁶ ERPG-2	2003	Emergency Response Planning Guideline	d
	100		1 hour	⁷ ERPG-3	2003	Emergency Response Planning Guideline	d
	10	14000	8 hours	⁸ TLV-TWA	2009		
	15	21000	15 min	TLV- ⁹ STEL		ACGIH	e

a.HSE, 2002. Occupational Exposure Limits 2002. HSE Books, Sudbury.

¹Maximum Exposure Limits

b. OSHA 2006 29CFR1910.1000, Table Z-2

²Time-Weighted Average (TWA): time-weighted average concentration for a conventional 8-hour workday and a 40-hour workweek, to which it is believed that nearly all workers may be repeatedly exposed, day after day, without adverse effect.

³Permissible Exposure Limit (PEL-C): regulatory limit (ceiling) on the amount or concentration of a substance in the air, and they are enforceable.

c.NIOSH Pocket Guide to Chemical Hazards (NPG).<http://www.cdc.gov/niosh/npg/npg.html>

⁴Recommended Exposure Levels (REL-C): refers to the concentration that should not be exceeded during any part of the working exposure (ceiling).

d.AIHA Emergency Response Planning Guidelines Committee, 2004. 2004 Emergency Response Planning Guidelines (ERPG) Update Set, American Industrial Hygiene Association, Fairfax.

⁵ERPG-1: The maximum airborne concentration below which it is believed nearly all individuals could be exposed for up to 1 hour without experiencing more than mild, transient adverse health effects or without perceiving a clearly defined objectionable odour.

⁶ERPG-2: The maximum airborne concentration below which it is believed nearly all individuals could be exposed for up to 1 hour without experiencing or developing irreversible or other serious health effects or symptoms that could impair an individual's ability to take protective action.

⁷ERPG-3: The maximum airborne concentration below which it is believed individuals could be exposed for up to 1 hour without experiencing or developing life-threatening health effects.

e. https://www.acgih.org/about/committees/c_tlvpa.htm

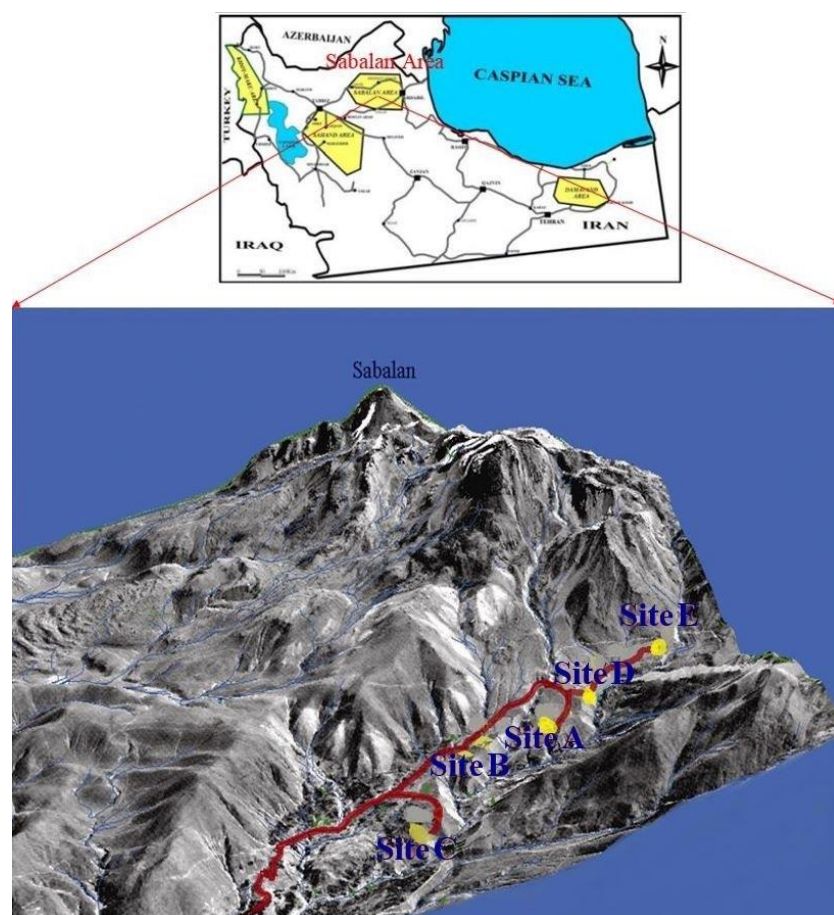
⁸Threshold Limit Value (TLV): exposure limits "to which it is believed nearly all workers can be exposed day after day for a working lifetime without ill effect".

⁹Short Term Exposure Limit (STEL): the concentration to which it is believed that workers can be exposed continuously for a short period of time without suffering from irritation, chronic or irreversible tissue damage, or narcosis.

3. NORTHWEST SABALAN GEOTHERMAL FIELD

3.1 History of geothermal development in NW-Sabalan

Interest in geothermal energy originated in Iran when James R. McNitt, a United Nations geothermal expert, visited the country in December 1974. In 1975, a contract among the Ministry of Energy, ENEL (Ente Nazionale per l'Energia Elettrica) of Italy and TB (Tehran Berkeley) of Iran was signed for geothermal exploration in the northwest part of Iran (Renewable Energy Organization of Iran, 2014).



In 1983, the result of investigations defined Sabalan, Damavand, Khoy-Maku and Sahand regions as four prospective geothermal sites in northwest Iran. As a result of further investigation in the 1990s, following a long gap, the northwest Sabalan geothermal area was proposed as a first priority of the geothermal potential regions for detailed exploration (Renewable Energy Organization of Iran, 2014). This field lies on the northwest flank of a large strato-volcano named Mt. Sabalan, within the province of Ardabil in northwest Iran (Figure 1).

From 1998 to 2005, detailed exploration studies were conducted by SUNA of Iran and Sinclair Knight Merz Ltd (SKM) of New Zealand in two stages. The first one included geological, geochemical and geophysical surveys, and the second one the drilling of three deep exploration wells and two shallow injection wells.

FIGURE 1: Location of northwest Sabalan geothermal field

According to the results of geo-based surveys and well testing, NW-Sabalan geothermal field was identified as a potential reservoir for power generation purposes. Numerical modelling of the reservoir was also performed from 2004 to 2005 and the capacity of the field was estimated at being able to sustain 55 MW of power production (SKM, 2005a).

The next stage of the NW-Sabalan geothermal field development began in 2007. At that time, the EDC (Energy Development Corporation) technical team of the Philippines reviewed all the available data from NW-Sabalan. A new MT survey, re-sampling and re-evaluation of all thermal springs in the area, detailed geological mapping and remote sensing and a new discharge test of Wells NWS-1 and NWS-4 were the activities proposed and conducted prior to any future drilling in order to determine the centre of the geothermal system (EDC, 2007).

According to the results of detailed geophysical and geological investigations, the drilling and testing program for the delineation phase was carried out between May 2008 and December 2012. During this phase, six new exploratory wells (NWS-6D, NWS-7D, NWS-8D, NWS-9D, NWS-10D and NWS-11RD) were drilled and one existing well (NWS-5D) was deepened. In addition, well logging and discharge testing were accomplished

for five production wells (NWS-5D, NWS-6D, NWS-7D, NWS-9D and NWS-10D). The results of discharge well testing revealed that the total capacity of these five wells and the previous two wells is 31 MW of electricity and 72 MW of thermal power. Furthermore, the characteristics of the Sabalan reservoir were being precisely assessed using well logging and discharge tests on the production wells (Kosari, 2011). At present, the tender for a 5 MW portable power plant is in progress. Hence, the construction of the first geothermal power plant in Iran is to be completed in 2016-17; if the contractor is selected in 2014.

3.2 Characteristics of the northwest Sabalan geothermal field

3.2.1 Project area

The northwest Sabalan geothermal field is located in zone 38 of the UTM coordinate system, between 733500E - 745000E and 4232500N - 4243500N in the Moil valley on the western slopes of Mt. Sabalan Mountain. The geothermal project site is approximately 2 km southeast of Moil village, with 1,600 inhabitants, and about 16 km south of Meshkinshahr city, with 160 thousand residents. Two other villages are found to the northwest of the area, Valezir, with a population of approximately 250 inhabitants, and Dizo, with 90 inhabitants.

Sparse subsistence farming and small-scale livestock activity predominates in the area. Agricultural activities and cattle farming modify a large part of the vegetation near the project area. A substantial part of the area is pastureland. The region is considered an ecologically sensitive area with a large number of springs and touristic resorts. The cold and hot springs, beautiful and unique landscapes, hiking trails, vast plains, national monuments and favourable weather conditions are all part of the natural characteristics of the project area (Porkhial, 2010). Access to the area is provided by an asphalt road from Meshkinshahr city to the village of Moil and then by gravel road to the project site. Moreover, Khiyavchai River is the major drinking water resource for Meshkinshahr residents and agricultural activities run along the site.

3.2.2 Geological settings

Tectonically, Sabalan volcano lies on the south Caspian plate, which underlies the Eurasian plate to the north and overlies the Iranian plate, producing northwestwardly compression (McKenzie, 1972). Mt. Sabalan is located in a Quaternary (Pleistocene-Pliocene) andesitic volcanic complex that covers an area of approximately 2500 km² and NW Sabalan geothermal field is part of this area. Volcanic deposits of Sabalan volcano are characterized by altered andesitic, dacitic and trachydacitic lavas, pyroclastics, lahars, tuffs and domes that date from 0.2 – 1.3 Ma, using the K-Ar dating method (TBCE, 1979).

The project area is located within the Moil Valley, which, on satellite and aerial photographic imagery, can be seen to be a major structural zone. The stratigraphy of the Moil valley, where the deep exploration wells are located, can be divided into four major rock formations (SKM, 2005a) (Figure 2):

1. Dizu Formation - Quaternary alluvium, fan and terrace deposits.
2. Kasra Formation - Pleistocene post-caldera trachyandesitic flows, domes and lahars.
3. Taos Formation - Pleistocene syn-caldera trachydacitic to trachyandesitic domes, flows and lahars.
4. Valhazir Formation - Pliocene pre-caldera trachyandesitic lavas, tuffs and pyroclastics.

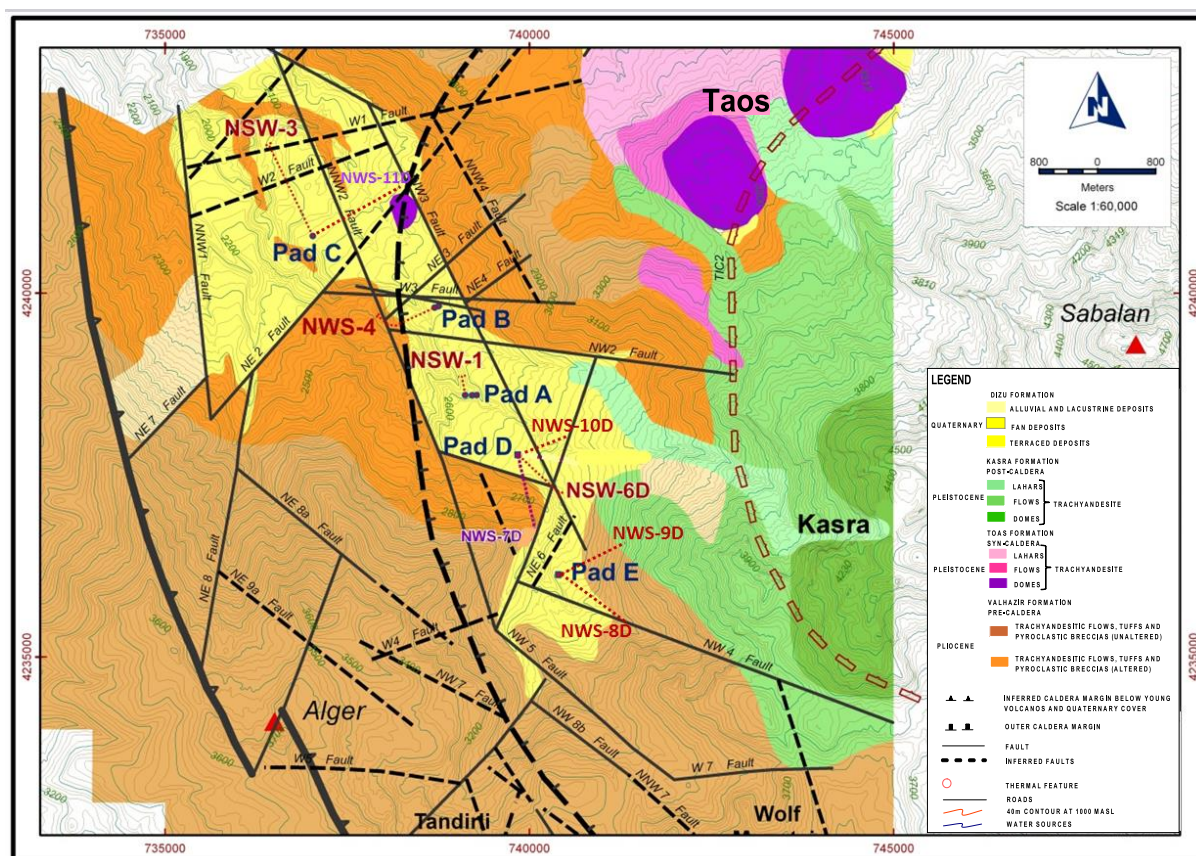


FIGURE 2: Geology of the NW Sabalan geothermal field (modified from Bogie et al., 2000)

Faridi (2010) mapped the structure of the Sabalan volcano and concluded that it is deformed in an active tectonic regime. This deformation has led to the elongation of the Sabalan caldera parallel to the regional σ_3 axis. It was concluded that the Sabalan caldera is associated with an extensive hydrothermal system and fracturing in the inner and outer calderas causing the thermal source fluids to readily ascend to the surface (Kosari, 2011).

3.2.3 Geochemistry

The occurrence of chloride springs in NW Sabalan is significant since these springs indicate the presence of deep, mineralized fluids, at depth. As a rule, geothermometric calculations are done only for chloride springs; hence, temperature estimates given by other thermal waters are insignificant and should be disregarded. Low silica and cation geothermometer temperatures (~ 150 - 200°C), estimated from Gheynarde and Khosrowsu chloride springs, are expected to be mainly due to the dilute and mixed nature of these surface features. On the other hand, the presence of acid-sulphate warm springs in NW Sabalan suggests near-surface boiling in the area. Since there are no gas manifestations such as sulfatases, steaming grounds, gas vents or extensive acid-altered grounds, the extent of near-surface boiling may be localized (EDC, 2007).

The results of exploration drilling in the Moil Valley in NW Sabalan confirmed the presence of a liquid-dominated reservoir with outflows of steam and water to surface thermal areas with temperatures ranging from 225 to 240°C .

Geochemical analysis of fluid samples collected during discharge testing of 7 production wells (NWS-1, NWS-4, NWS-6D, NWS-7D, NWS-5D, NWS-9D and NWS-10D) indicates that the liquids discharged from the wells can be classified as a slightly alkaline, medium salinity, sodium-chloride waters. Quartz geothermometer yields estimates of a reservoir temperature between (230 - 245°C); on the

other hand, the cation geothermometer yielded estimates of a reservoir temperature higher than 260°C. This may be an indication that the deep geothermal fluid in NW Sabalan is fully equilibrated, and the highest reservoir temperature that can be expected is that given by the cation thermometer (~260°C) (EDC, 2007). The scaling potential assessment of the fluid in the wells indicates that all the wells have a high potential to form calcite scales; silica scaling is not expected to occur in the wells.

The composition of the gas dissolved in the deep liquid is represented by 98-99% in weight of CO₂ and 1-2% of H₂S and N₂. He, Ar, H₂ and CH₄ are all at very low proportions (Amistoso et al., 2013; SKM, 2004 and 2005b).

4. H₂S EMISSIONS FROM SABALAN GEOTHERMAL POWER PLANT

4.1 Concentration of H₂S in steam

According to discharge testing of the NW-Sabalan geothermal wells, the weight percent of non-condensable gases (NCG) in the steam phase is calculated to be about 2-3%, based on a steam mass percentage of about 20%.

The concentration of H₂S in steam in each well is different and varies from 83 ppm to 256 ppm (Amistoso et al., 2013; SKM, 2004, 2005b). Given that the production capacity of each geothermal well is approximately 5 MWe, the average concentration of H₂S is about 170 ppm.

4.2 Sabalan geothermal power plant

The long-term target capacity of electrical power generation in the NW-Sabalan geothermal project is expected to be 55 MWe. The proposed Sabalan geothermal power plant, in accordance with the initial design, consists of a 5 MWe pilot unit and two 25 MWe single flash units. At present, the renewable energy organization of Iran (SUNA) is in the process of constructing five MWe pilot units in the field that is expected to be commissioned in 2016-2017 as the first Iranian geothermal power plant.

The term 'single flash power plant' refers to an energy conversion process in which a pressurized geothermal fluid is flashed to produce a mixture of steam and liquid. After that, phases are isolated using a steam separator and the steam is sent to a turbine to drive an electric generator and produce energy. The steam exhaust from the turbine is passed through a condenser, which produces a condensate stream and non-condensable gases (Millachine, 2011). The non-condensable gases (including H₂S) are vented out of the condensers to the atmosphere in the cooling towers to enhance dispersion (Aráuz, 2014). In this way, approximately 97% of H₂S, along with other non-condensable gases (NCG), is discharged to the atmosphere and the rest of the NCG is released from a silencer, steam traps and the collection area (Franco, 2010). A simplified representation of the condensing cycle of a single flash geothermal power plant is shown in Figure 3 (Kagel, 2008).

Based on the Sabalan reservoir steam specifications and the engineering equation solver (EES) program, the steam consumption is calculated to be 2.3 kg/s per MWe, assuming that the steam enters the turbine at approximately 151°C and at 5 bar and exits the turbine at 0.1 bar pressure and 46°C saturation temperature (Radmehr, 2005). Hence, the flow rate of steam that is required for the 55 MWe Sabalan geothermal power plant is about 127 kg/s, or approximately 450 ton/h. As aforementioned, the concentration of H₂S in the steam is estimated at about 170 ppm. According to the total flow rate of the steam, the emission of H₂S from Sabalan geothermal power plant is appraised at about 21.6 g/s or 77.7 kg/h.

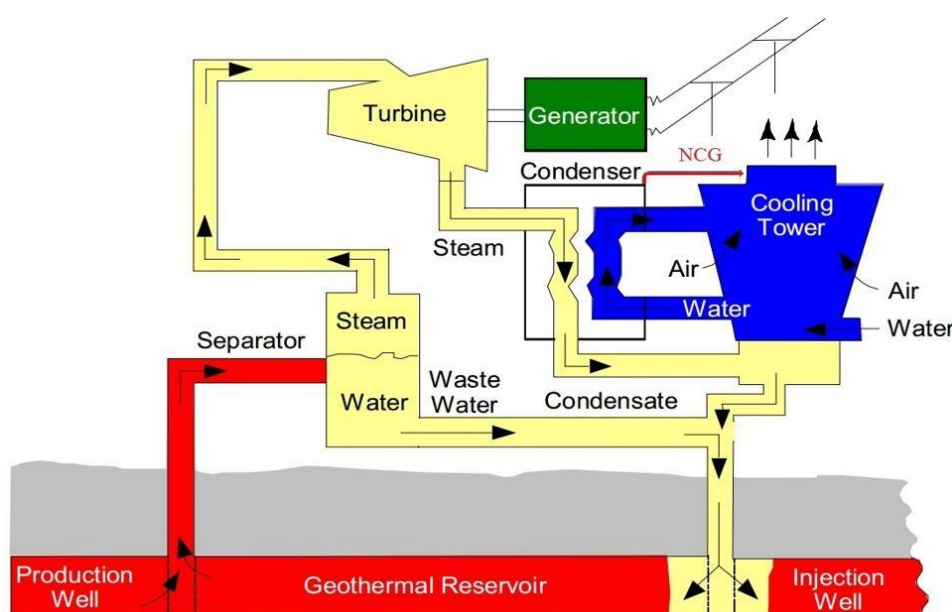


FIGURE 3: Simplified schematic of the condensing cycle at the proposed Sabalan geothermal power plant

5. DISPERSION MODELLING

Dispersion modelling uses mathematical equations to describe the atmosphere, dispersion, chemical and physical processes influencing a pollutant released from sources of a given geometry to calculate concentrations at various receptors (Holmes and Morawska, 2006). Dispersion models can provide concentration, or deposition, estimates over an almost unlimited grid of user-specified locations, and can be used to evaluate different emission scenarios. In this capacity, air dispersion modelling is a useful tool in assessing the air quality impacts associated with existing or proposed emission sources. The results of the dispersion modelling analysis can be used to develop control strategies that should ensure compliance with assessment criteria (DEC, 2005).

The models require information on the source, or sources, including pollutant emission rates, and meteorological data. In addition, they also need information on the topography of the study area (Figure 4). The models then use this information to simulate mathematically the pollutant's transport and dispersion. The output is air pollutant concentrations, for a particular time period, usually at specific receptor locations (Vallero, 2008).

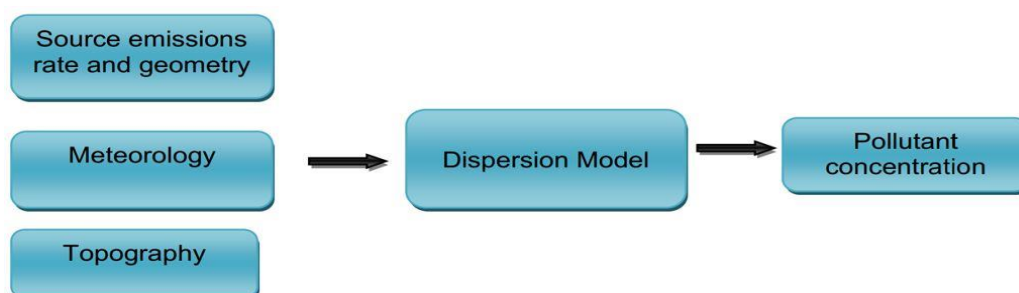


FIGURE 4: A schematic representation of the input-output of an air dispersion model (Neshuku, 2012)

5.1 Gaussian plume dispersion model

This type of model assumes that the pollutant disperses according to the normal statistical distribution (Holmes and Morawska, 2006). At the point of release, the pollutant concentration is at maximum and decreases in both lateral and vertical directions following normal distribution. The most general form of the Gaussian dispersion equation that is used for point source emissions is (Macdonald, 2003):

$$C(x, y, z; H) = \frac{Q}{2\pi U_s \sigma_y \sigma_z} \exp \left[-\frac{y^2}{2\sigma_y^2} \right] \left[\exp \left\{ -\frac{(z-H)^2}{2\sigma_z^2} \right\} + \exp \left\{ -\frac{(z+H)^2}{2\sigma_z^2} \right\} \right], \quad (1)$$

where C = steady-state concentration at a point (x, y, z) , $\mu\text{g}/\text{m}^3$;
 Q = pollutant emission rate, $\mu\text{g}/\text{s}$;
 U_s = mean wind speed at release height;
 σ_y, σ_z = standard deviation of lateral and vertical spread parameters, m;
 y = horizontal distance from plume centreline, m;
 x = downwind distance from plume source, m;
 H = effective stack height ($H = h + \Delta h$) where h = physical stack height and Δh = plume rise;
 z = vertical distance from ground level, m.

The first and second exponential terms represent the lateral and vertical dispersions, respectively. The Gaussian distribution determines the size of the plume downwind from the source (Figure 5). The plume size is dependent on the stability of the atmosphere and the dispersion of the plume in the horizontal and vertical directions. These horizontal and vertical dispersion coefficients (σ_y and σ_z respectively) are merely the standard deviation from normal on the Gaussian distribution curve in the y and z directions. The dispersion coefficients are functions of wind speed, cloud cover, and surface heating by the sun. The Gaussian distribution requires that the material in the plume be maintained. In other words, the plume edge must be allowed to reflect from the ground without losing any pollution. In addition, the Gaussian distribution and plume rise depend on the ground being relatively flat along the path of the plume. The topography affects atmospheric wind flow and stability; therefore, uneven terrain caused by hills, valleys, and mountains will affect the dispersion of the plume so that the Gaussian distribution must be modified (EPA, 2006).

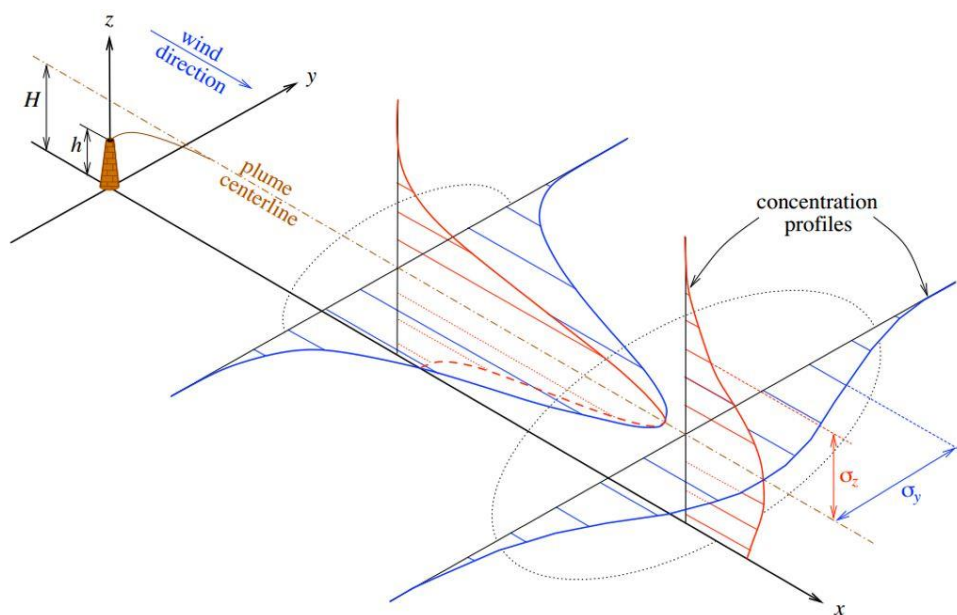


FIGURE 5: Graphical representation of double Gaussian distribution in the plume (Stockie, 2011)

5.2 AERMOD dispersion model

There is a large body of literature addressing the application of different atmospheric dispersion models and the use of these models for different situations, the evaluation of the sensitivity and uncertainty of modelling pollutant dispersion, human exposure risk assessment, as well as the usefulness of these models for epidemiological applications (Zouet al., 2010).

Dispersion software programs based on the Gaussian plume equation are widely applied to estimate the dispersions of various pollutants. AERMOD (AMS/US EPA) is a near field (less than 50 km) steady state Gaussian plume model based on planetary boundary layer (PBL) turbulence structure and scaling concepts, including treatment of both surface and elevated sources over both simple and complex terrain. It is applicable to rural and urban areas, and multiple sources including point, area, and volume sources (Vora, 2010). The model has the capacity to employ hourly sequential pre-processed meteorological data to estimate concentrations of pollutants at receptor locations at different time scales ranging from 1 h to 12 months. AERMOD can incorporate various complex algorithms and concepts. It is applied to evaluate the dispersion of a number of pollutants, including PM₁₀, hydrogen cyanide (HCN), SO₂, sulphur hexafluoride (SF₆), VOCs, NO₂ and H₂S (Seangkiatiyuth, 2011).

The AERMOD modelling system comprises a meteorological pre-processor (AERMET), a terrain pre-processor (AERMAP) and the dispersion model (AERMOD) (Figure 6).

The major purpose of AERMET is to calculate boundary layer parameters to be used by AERMOD. The AERMET requires standard meteorological observations such as wind speed, wind direction, temperature and cloud cover. It also needs the surface characteristic parameters of albedo, surface roughness and the Bowen ratio (Neshuku, 2012). It then makes use of this data for the calculations of the planetary boundary layer (PBL) parameters such as: Mixing height (z), Monin – Obukhov length (L), temperature scale, convective velocity scale (w) and surface heat flux (H) (Cimorelli et al., 2004).

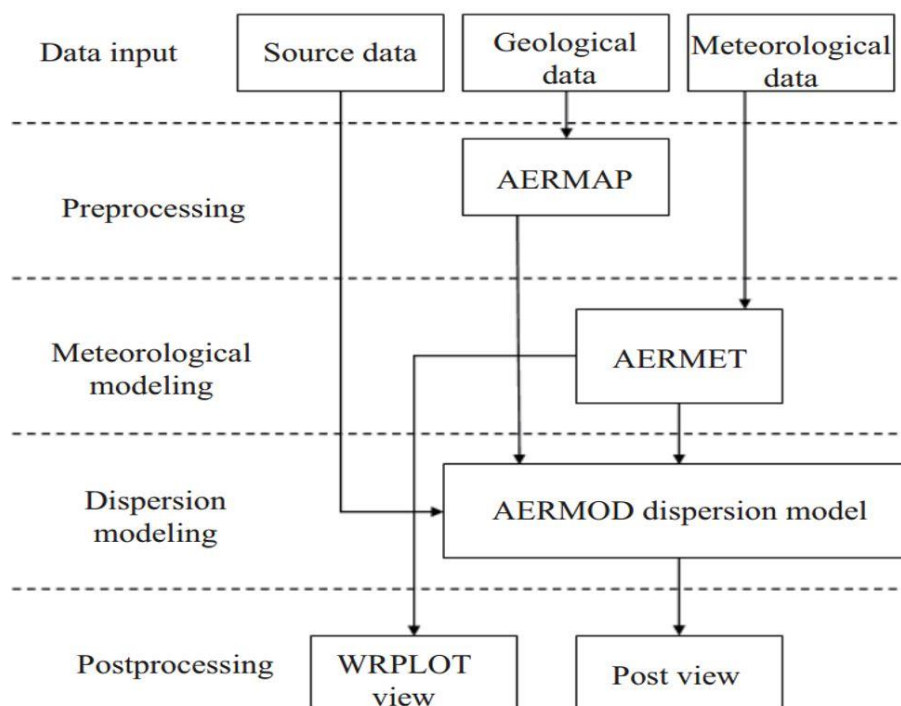


FIGURE 6: Data flow in the AERMOD modelling (Seangkiatiyuth, 2011)

The meteorological interface, internal to AERMOD, uses these parameters to generate profiles of the needed meteorological variables, such as lateral and vertical turbulent fluctuations (v , w), vertical profiles of wind speed (u) and potential temperature gradient ($d\theta/dz$).

The second module, AERMAP is used to calculate the terrain height scale (h_c) for each receptor location, which is used to calculate the dividing streamline height. AERMAP also generates receptor grids for AERMOD. The input to AERMAP is the topographical data in a format of Digital Elevation Mapping (DEM) files. The information generated from AERMAP is then passed on to AERMOD as the location of receptors, the receptor's height above mean sea level and the receptor specific terrain height scale (h_c) (Cimorelli et al., 2004). AERMOD then uses this information from the two pre-processors to compute concentrations of pollutants, taking into account the changes in the dispersion rate with height and making use of non-Gaussian plumes in convective conditions (Perry et al., 2005).

5.2.1 Input data

Source data

According to the primary design of Sabalan geothermal power plant, it is assumed that H_2S and other NCG are vented to the atmosphere through cooling towers. Given that there is no geothermal power plant in NW Sabalan field yet, the source input model is based on the accessible data from a part of Nesjavellir geothermal power plant with similar power capacity (60 MW) (Ólafsdóttir et al., 2014) and Sabalan reservoir steam specifications. In addition, according to the proposed locations for the geothermal power plant (GPP) in northwest Sabalan geothermal project, the following scenarios are identified for H_2S dispersion modelling in the study area:

- Scenario1: it is assumed that the emission source of the Sabalan geothermal power plant (GPP) station is located at site D at 739793 mE and 4237851 mN in zone 38 of the UTM coordinate system.
- Scenario2: it is assumed that the emission source of the Sabalan geothermal power plant (GPP) station is located at site B at 738715 mE and 4239776 mN in zone 38 of UTM coordinate system.

The source input model (Table 4) assumes full load operation capacity for a whole year without considering yearly maintenance or overhaul.

TABLE 4: Source input data.

Source	Capacity (MW)	Coordinate (UTM)		Base elevation (m.a.s.l.)	Stack height (m)	Stack inside diameter (m)	Gas exit temperature (°C)	Gas exit velocity (m/s)	Emission rate (g/s)
		x	y						
GPP-Site_D (Scenario1)	55	739793	4237851	2747	13	17.8	46	9.6	21.6
GPP-Site_B (Scenario 2)	55	738715	4239776	2489	13	17.8	46	9.6	21.6

Meteorological data

The required surface meteorological data for the model, temperature, humidity, precipitation, wind speed and direction and solar radiation were collected by a meteorological station in the Sabalan geothermal field; cloud cover was provided by the Meshkinshahr metrological station, 12 km north of the study area for the period January to August 2009. The upper-air meteorological data were not recorded in the area. Therefore, they were computed by the upper air estimator within AERMET, based on hourly surface meteorological data. Land surface characteristics (albedo, surface roughness, Bowen ratio) for AERMET meteorological pre-processor were set based on the topography and land use in the Sabalan geothermal field.

The predominant winds during the measured time in the NW Sabalan geothermal area blow from the southeast to northwest (Figure 7a) and the main wind speed is 2 ± 1.5 m/s (60%) (Figure 7b).

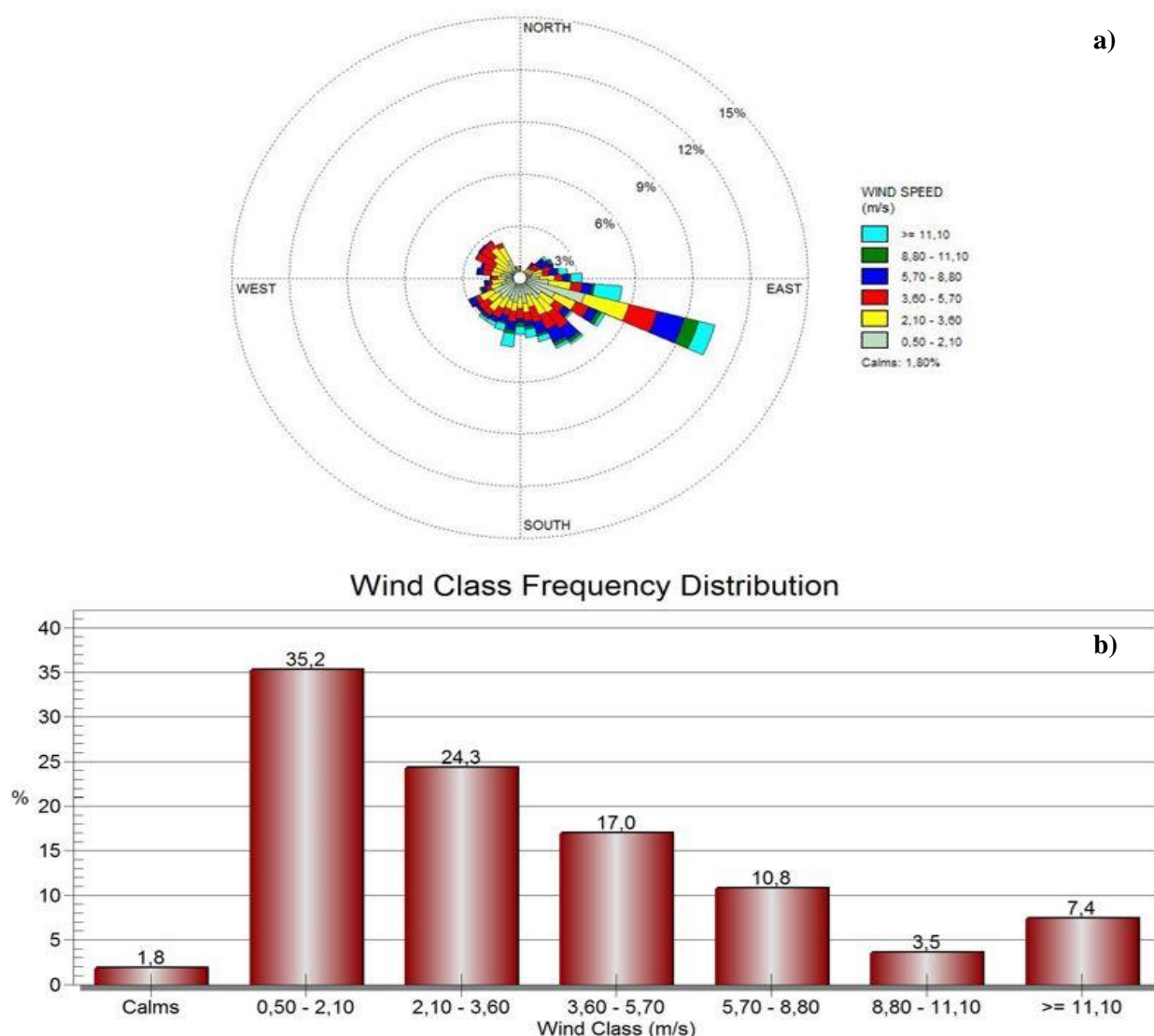


FIGURE 7: Wind rose (a) and wind class frequency distribution (b) in the NW Sabalan weather station January to August in 2009

Terrain data and receptors

There are two basic types of input data that are needed to run the terrain pre-processor (AERMAP). First, AERMAP requires an input file that directs the actions of AERMAP through a set of options, and defines the receptor and source locations. Secondly, AERMAP needs standardized computer files of terrain data and is programmed to read only the USGS format (EPA, 2004).

In this study, the required digital elevation model (DEM) of the study area was downloaded from a USGS website. The DEM file was imported to the terrain pre-processor to calculate the critical dividing streamline height and to determine the hill height scale for each receptor (Figure 8). According to the geographical features of the study area, the flat and elevated option was selected in the model.

For the receptors, considering the populated areas (Moil, Dizo and Valezir villages) near the proposed Sabalan geothermal power plant, discrete Cartesian receptors and uniform Cartesian grids were used in the modelling to determine the area with maximum predicted H_2S concentrations. On the terrain map, the location of the receptor zone was identified using satellite imagery from Google Earth.

With the aim of providing a higher resolution of predicted H_2S concentrations for the area in the vicinity

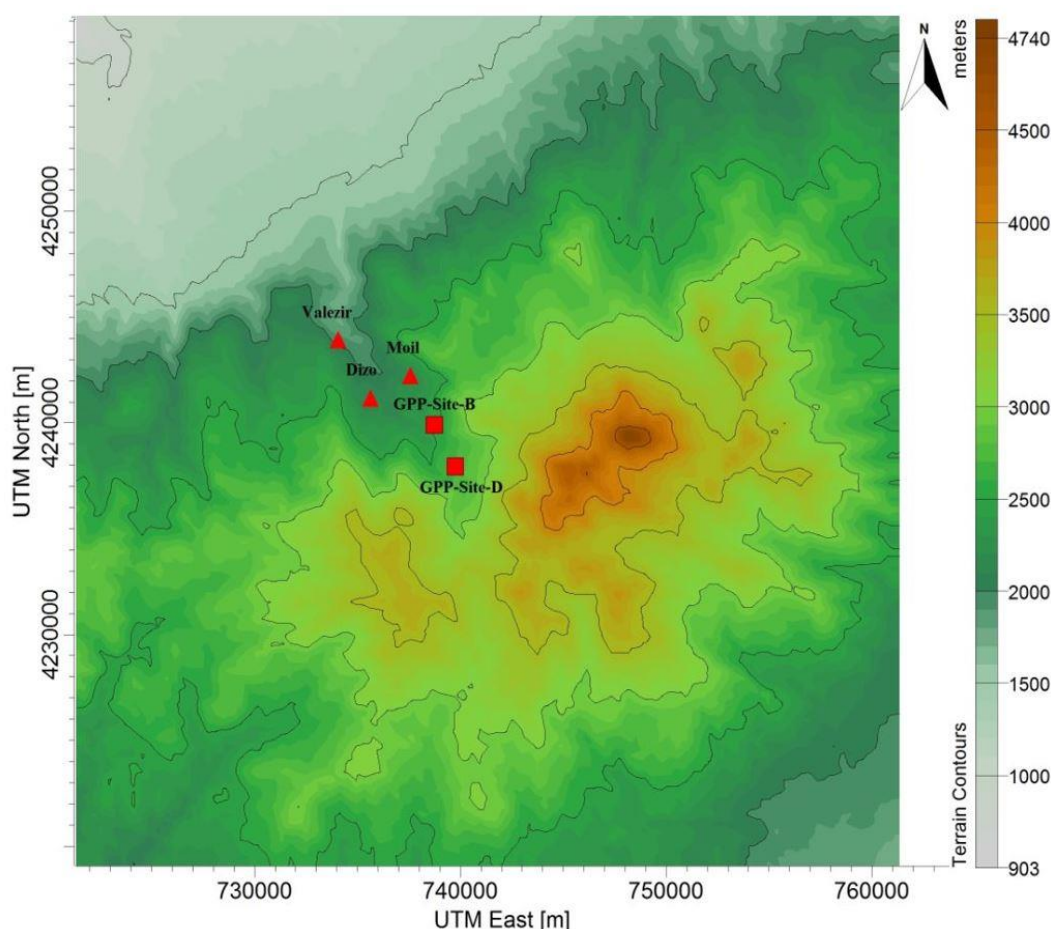


FIGURE 8: The terrain contour map of the study area. Red triangle show locations of populated areas, red squares GPS sites

of the power plant, as well as extending to a broader area from the source, the following grid sizes and resolutions were used together:

- Grid 1 – 39 km × 39 km at 1000 m resolution
- Grid 2 – 15 km × 15 km at 300 m resolution
- Grid 3 – 1.4 km × 1.4 km at 20 m resolution

6. MODELLING RESULTS

After importing all the required data and parameters for running the AREMOD dispersion modelling, the model was finalized to compute the spatial distribution of the plume and H₂S ground level concentrations in the study area.

According to the ambient air quality standards and occupational health guidelines for H₂S for the period average from January to August in 2009, and due to the lack of accurate annual meteorological data, 24, 8 and 1-hour averaging options were chosen to analyse the concentration of H₂S.

The ambient air quality standard for H₂S concentration over 24 hours is 150 µg/m³, according to the World Health Organization (WHO), and 50 µg/m³, according to the Icelandic air quality guideline. The threshold limit value for H₂S concentration over 8 hours is 14000 µg/m³, set by the American Conference of Governmental Industrial Hygienists (ACGIH). H₂S air quality standards for 1-hour exposure vary

widely, even in the same country. For instance, in California, it is $42 \mu\text{g}/\text{m}^3$, in New York $14 \mu\text{g}/\text{m}^3$, in Arizona $180 \mu\text{g}/\text{m}^3$ and, in New Zealand the standard is $7 \mu\text{g}/\text{m}^3$ (Peralta et al., 2013).

6.1 Results for scenario1

The results of the AERMOD modelling for H_2S concentration for the period January to August in 2009 is shown in Figure 9, when the emission source is located at site D. It indicates that the predicted H_2S concentration is very low at the study area. The highest predicted 8 month average H_2S concentration is $2,68 \mu\text{g}/\text{m}^3$, which occurs near the power plant at E739693 m and N4237871 m. Moreover, the Moil, Valezir and Dizo villages, the nearest inhabited areas to the proposed geothermal power plant (GPP), are almost located outside of the plume pathway and the predicted H_2S concentration is about $0.1 \mu\text{g}/\text{m}^3$.

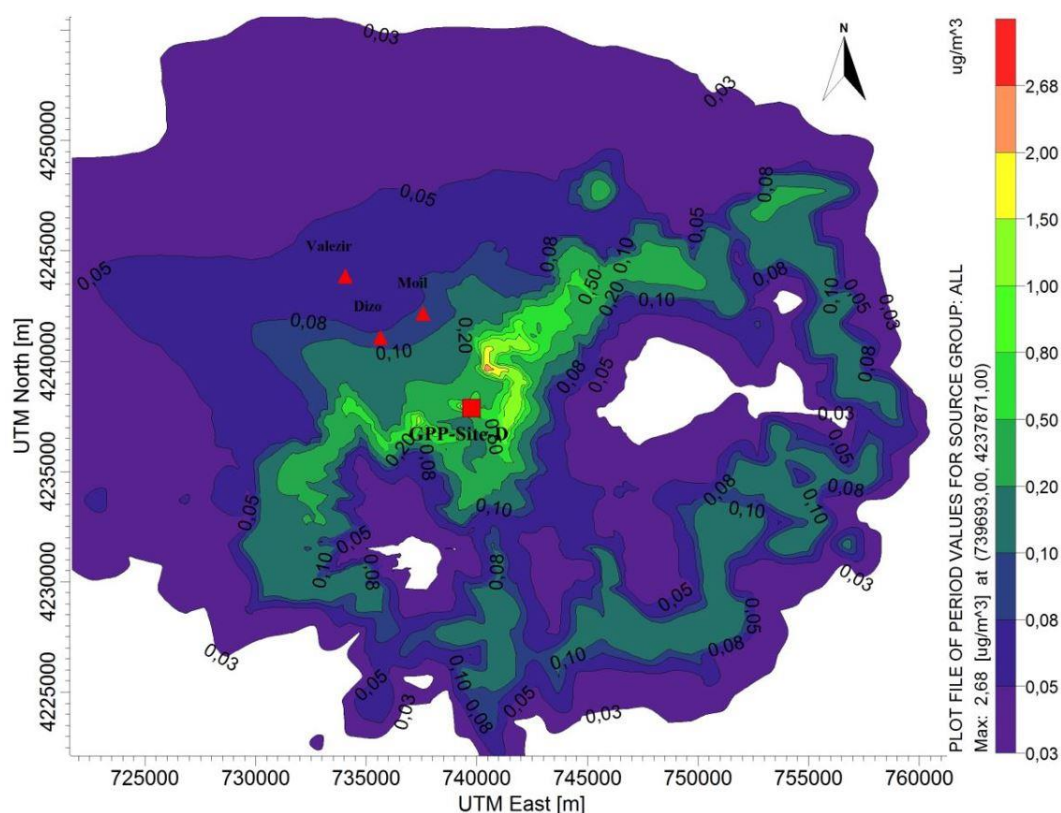
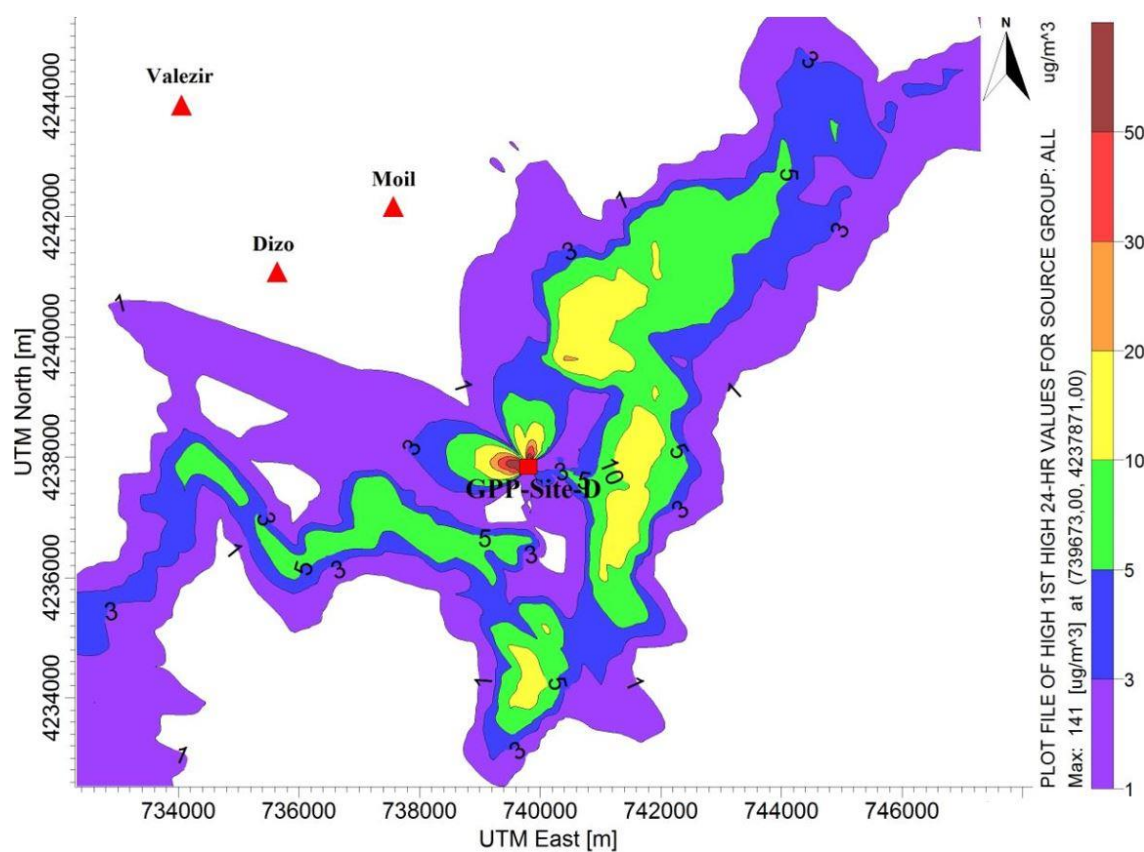
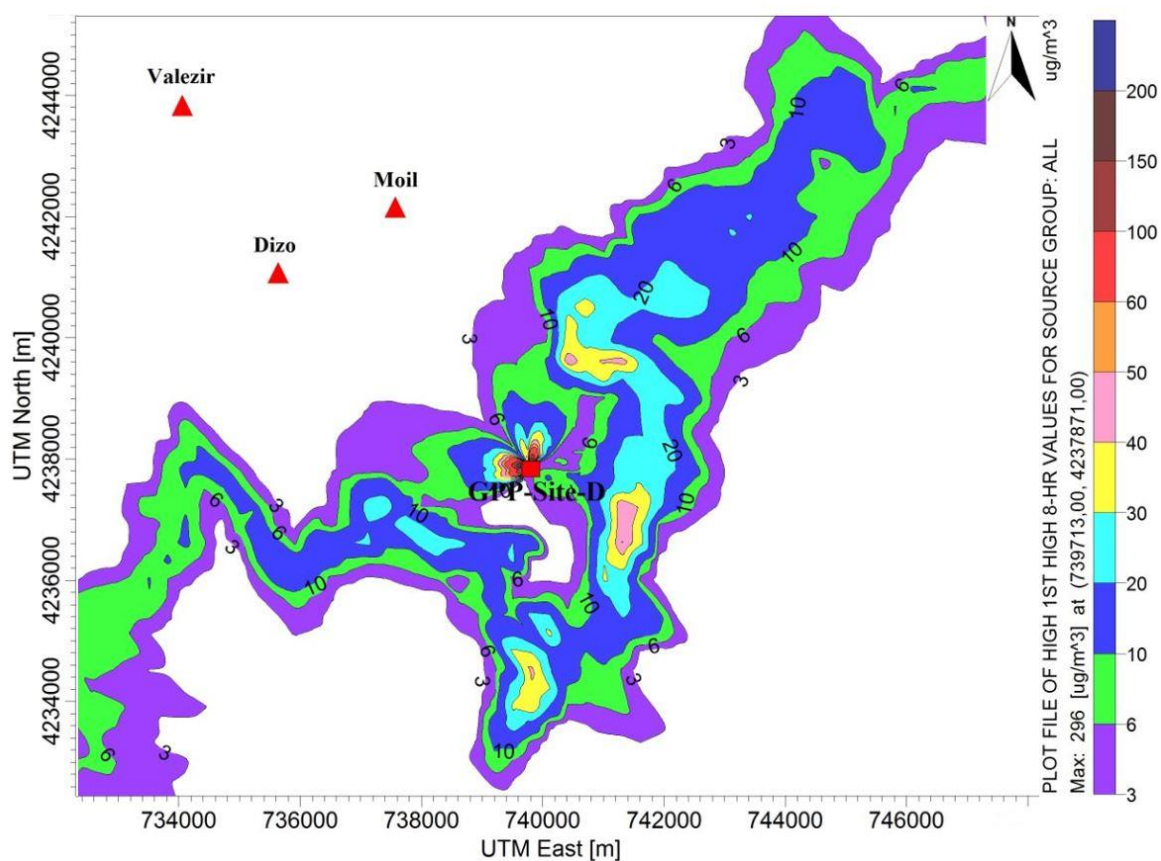


FIGURE 9: Predicted H_2S average concentration for the period January to August in 2009 for scenario 1

The spatial distribution of predicted H_2S concentration for a 24-hour averaging time shows that the most common H_2S concentrations in the area are less than $10 \mu\text{g}/\text{m}^3$ (Figure 10). The maximum levels of H_2S occur north and northwest of the power station, up to $100 \mu\text{g}/\text{m}^3$, which is in agreement with the predominant winds that blow from the southeast to the northwest. The highest predicted H_2S concentration is $141 \mu\text{g}/\text{m}^3$, 100 m northwest of the power plant.

The dispersion model reveals that for a 24-hour averaging period, H_2S concentrations are below the WHO ambient air guideline ($150 \mu\text{g}/\text{m}^3$ averaged over 24 hours), but exceed the Iceland H_2S air ambient standard value ($50 \mu\text{g}/\text{m}^3$ averaged over 24 hours) in the small area northwest of the source. This area is not considered to have significant impact on public health due to the absence of major human activities.

The AERMOD modelling for an 8-hour averaging time of H_2S concentration (Figure 11) shows that the highest predicted H_2S concentration is $296 \mu\text{g}/\text{m}^3$, northwest of the power plant (Figure 12). The H_2S concentration is, for the most part, in the range of $5\text{--}20 \mu\text{g}/\text{m}^3$, which is well below the threshold limit value for an 8-hour average concentration, $14000 \mu\text{g}/\text{m}^3$ (ACGIH).

FIGURE 10: Predicted 24-hour average H_2S concentrations for scenario 1FIGURE 11: Predicted 8-hour average H_2S concentrations for scenario 1

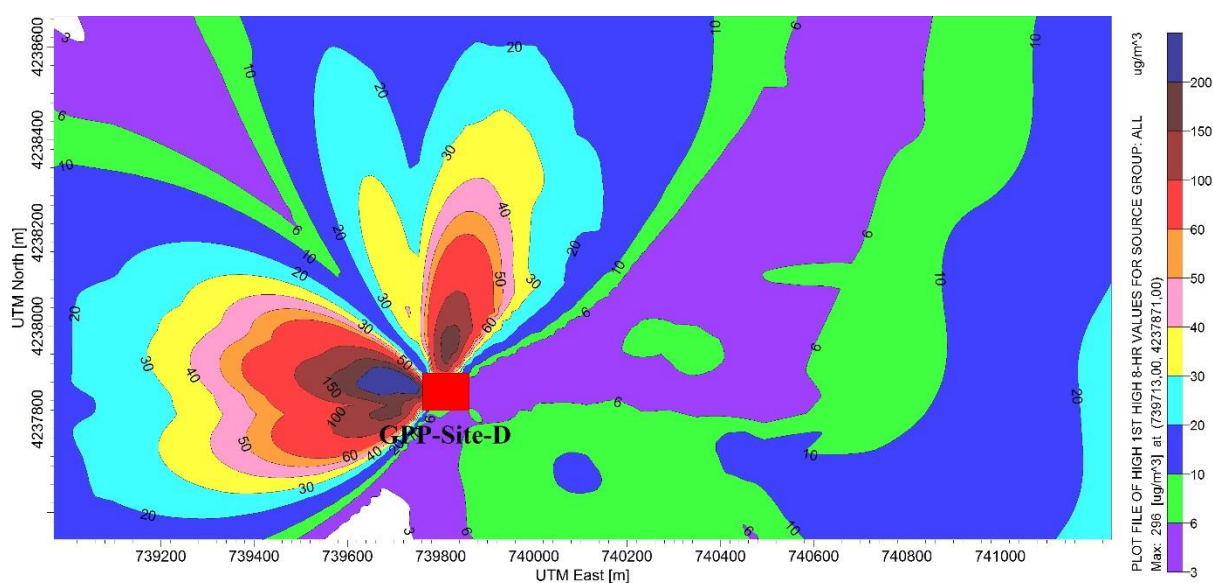


FIGURE 12: Predicted 8 hour average H₂S concentrations emitted close to source for scenario 1

The forecasted maximum H₂S concentrations in an 1-hour averaging time indicates that the highest H₂S concentration is 1020 µg/m³ northwest of the power plant (Figure 13). The maximum level of H₂S for all the computed averaging periods takes place at the same location, on the northwest side of the power plant, in agreement with predominant winds that blow from the southeast to the northwest. This part constitutes a small portion of the study area while for a large part of the area the predicted concentrations range between 10 and 100 µg/m³. According to the H₂S dispersion pattern in Figure 13, the high levels of the H₂S concentration plume are located east, northeast and southeast of the proposed power plant.

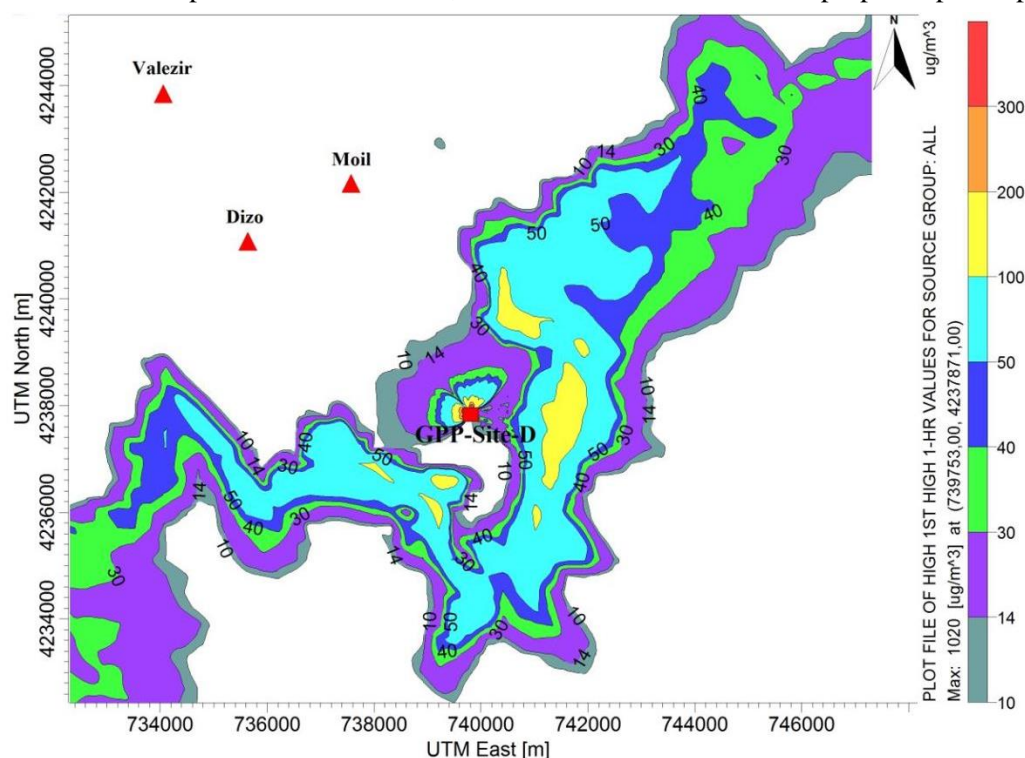


FIGURE 13: Predicted 1-hour average H₂S concentration for scenario 1

In this area, the predicted H₂S concentrations in a 1-hour averaging time are higher than for New Zealand (7 µg/m³), California (42 µg/m³) and New York (14 µg/m³), but less than for Arizona (180 µg/m³) ambient air quality standards.

6.2 Results for scenario2

The spatial distribution of predicted H₂S concentrations for 1, 8, 24 hours and the averaging time for 8 months from January to August in 2009, were also modelled for scenario 2. The results reveal that there are not many differences between the results of the two scenarios. Therefore, in this part of the report, only the results of the AERMOD modelling for H₂S concentrations for a 24-hour averaging period that are important for a health and environmental assessment are shown in Figure 14.

The results indicate that the highest predicted H₂S concentration is equal to 141 µg/m³, 125 m northwest of the power plant. The most common levels of concentration in the area are less than 10 µg/m³ for a 24-hour averaging time. The simulation shows that the H₂S concentration goes up to 3 µg/m³ in Dizo village, but Moil and Valezir villages are still located outside of the plume pathway. The predicted H₂S concentrations are well below both WHO and Icelandic ambient air standards in the populated area. Therefore, the study suggests that there is no danger to public health and the environment in this area.

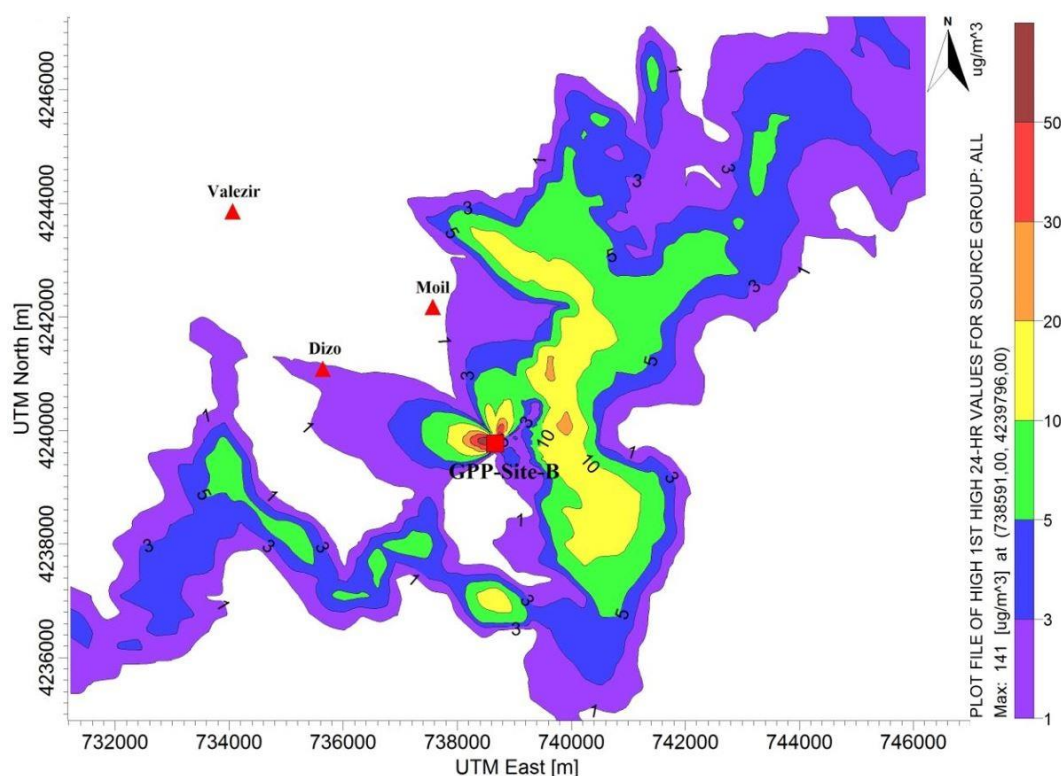


FIGURE 14: Predicted 24-hour average H₂S concentrations for scenario 2

7. CONCLUSIONS

The results of dispersion modelling for scenario 1 indicated that all the populated areas near the planned power plant are located outside the prevailing plume pathway during the modelled period. Furthermore, the dispersion pattern shows that the highest predicted H₂S concentrations for all averaging times occur in the immediate vicinity of the power plant (emission source), in agreement with predominant winds that blow from the southeast to the northwest. The highest predicted H₂S concentrations for the time period: 24hours, 8hours, 1hour, and 8 months are 2.68 µg/m³, 141 µg/m³, 296 µg/m³ and 1020 µg/m³, respectively.

The plume pathway can reach Dizo village for a 24-hour averaging time in scenario 2, since the emission source is nearby. Nevertheless, the modelled value is less than H₂S air quality standards for a 24-hour averaging time.

The results show that the predicted H₂S concentrations do not exceed the WHO ambient air guideline value for H₂S (150 µg/m³ averaged over 24 hours) in either scenario. Whereas, for both scenarios at the limit area close to the source, the predicted H₂S concentrations exceed the Icelandic H₂S air ambient standard value (50 µg/m³ averaged over 24 hours).

The occupational exposure limit for H₂S in a workplace, based on the ACGIH occupational safety guideline, is 14000 µg/m³ for an 8-hour average and that limit is never exceeded in the study area. However, the predicted H₂S concentration is above the guidelines for New Zealand (7 µg/m³), California (42 µg/m³) and New York (14 µg/m³) but less than for the Arizona (180 µg/m³) ambient air quality standards for a 1-hour average in the large area of northwest Sabalan geothermal field.

The results for both scenarios reveal that spatial distributions of predicted H₂S concentrations follow almost the same pattern, and the difference in location of the Sabalan geothermal power plant in northwest Sabalan geothermal site has no significant effect on the spread of the predicted H₂S plume.

In general, according to the simulation dispersion pattern and the levels of predicted concentrations, the exploitation of the proposed 55 MW Sabalan geothermal power plant does not have a significantly adverse effect on the air quality in the study area. Furthermore, no health impacts are expected for area residents.

Although no environmental and health impacts are anticipated in the study area, dispersion modelling revealed that the large area around the proposed Sabalan geothermal power plant is continuously exposed to H₂S. Therefore, it is recommended that H₂S background levels and during the operation of the geothermal power plant are monitored continuously in the northwest Sabalan geothermal area in order to assess environmental and health impacts and to suggest mitigating actions if required.

H₂S dispersion modelling is an essential component of environmental and health impact assessment in geothermal areas. It can be used to examine different scenarios, to ensure that the environmental implications of H₂S emission are considered before the decision for construction of a geothermal power plant is taken.

ACKNOWLEDGEMENTS

I would like to express my sincere gratitude to the UNU-GTP for awarding me this scholarship to participate in the six month training programme. I am grateful to my employer, Renewable Energy Organization of Iran and Moshanir Consulting Engineering Company, for giving me this opportunity to undergo geothermal training in Iceland. Best regards are expressed to Mr. Lúdvík S. Georgsson, director of the UNU Geothermal Training Programme, for his hospitality and selfless dedication to the UNU Fellows. Many thanks to Ms. Málfríður Ómarsdóttir, Ms. Thórhildur Ísberg, Ms. María S. Guðjónsdóttir, Mr. Ingimar Gudni Haraldsson, Mr. Markús A.G. Wilde, and all 2014 UNU fellows for their support, help and the wonderful time we had together during these six months.

I want to give special thanks to my supervisors, Dr. Thröstur Thorsteinsson, Dr. Snjólaug Ólafsdóttir, Dr. Brynhildur Davíðsdóttir and Dr. Matthew J. Roberts, for their dedication, availability, support and guidance while working on this report.

My deepest gratitude goes to my dear wife and my family for their moral and emotional support during these six months. This project is dedicated to my wife, Sepideh Montazer, for her support, and encouragement throughout these six months in Iceland.

REFERENCES

Amistoso, A.E., Buscato, N.M., and Aragon, G.M., 2013: *Discharge testing of NWS6D evaluation report*. Energy Development Corporation, report for SUNA – Renewable Energy Organization of Iran, 25 pp.

Aráuz T., M. A., 2014: *Modeling H₂S Dispersion from San Jacinto Tizate Geothermal Power Plant, Nicaragua*. University of Iceland, Reykjavík, UNU-GTP, MSc thesis, 88 pp.

Bates, M. N., Garrett, N. and Shoemack, P., 2002: Investigation of health effects of hydrogen sulfide from a geothermal source. *Archives of Environmental Health*, 57-5, 405-411.

Bogie, I., Cartwright, A.J., Khosrawi, K., Talebi, B., and Sahabi, F., 2000: The Meshkinshahr geothermal prospect, Iran. *Proceedings of the World Geothermal Congress 2000, Kyushu-Tohoku, Japan*, 997-1002.

Cimorelli, A.J., Perry, S.G., Venkatram, A., Weil, J.C., Paine, R. J., Wilson, R.B., Lee, R.F., Peters, W.D., Brode, R.W. and Paumier, J.O., 2004: *AERMOD: Description of model formulation*. EPA, report-454/R-03-004, 91 pp. Website: www.epa.gov/scram001/7thconf/aermod/aermod_mfd.pdf

DEC, 2005: *Approved methods for the modelling and assessment of air pollutants in New South Wales*. Department of Environment and Conservation, New South Wales, 63 pp. Website: www.environment.nsw.gov.au/resources/air/ammodelling05361.pdf

De Kok, L.J., Stuver, E., Rubinigg, M., Westerman, S., and Grill, D., 1997: Impact of atmospheric sulfur deposition on sulfur metabolism in plants: H₂S as sulfur source for sulfur deprived Brassica Oleracea L. *Botanica Acta*. 110-5, 411-419.

Durand, M. and Wilson, J.G., 2006: Spatial analysis of respiratory disease on an urbanized geothermal field. *Environmental Research*, 101-2, 238-245.

EDC, 2007: *A review of NW Sabalan geothermal area resource assessment and development*. Energy Development Corporation, report for SUNA – Renewable Energy Organization of Iran, 61 pp.

EOHP, 2006: *Ambient air guidelines for hydrogen sulphide*. EOHP - Environmental & Occupational Health Program Division of Environmental Health, Maine Center for Disease Control & Prevention, Maine Department of Health & Human Services, 15pp. Website: www.maine.gov/dep/waste/publications/documents/ambientairguidelines.pdf

EPA, 2006: *Lesson 6: Plume Dispersion and Air Quality Modelling*. EPA, 18 pp, Website: [yosemite.epa.gov/oaqps/EOGtrain.nsf/fabbfcfe2fc93dac85256afe00483cc4/c9862a32b0eb4f9885256b6d0064ce2b/\\$FILE/Lesson%206.pdf](http://yosemite.epa.gov/oaqps/EOGtrain.nsf/fabbfcfe2fc93dac85256afe00483cc4/c9862a32b0eb4f9885256b6d0064ce2b/$FILE/Lesson%206.pdf).

EPA, 2004: *Users guide For the AERMOD terrain pre-processor (AERMAP)*. EPA-454/B-03-003, 106 pp. Website: www.michigan.gov/documents/deq/deq-aqd-aqe_aermapug_257866_7.pdf

Faridi, M., 2010: *Structural geology of Mount Sabalan*. SUNA - Renewable Energy Organization of Iran, report, 62 pp.

Franco N., L.A., 2010: Hydrogen sulphide abatement during discharge of geothermal steam from well pads: A case study of well pad TR-18, El Salvador. Report 13 in: *Geothermal training in Iceland 2010*. UNU-GTP, Iceland, 183-212.

Fuller, D.C., and Suruda, A.J., 2000: Occupationally related hydrogen sulfide deaths in the United States from 1984 to 1994. *J. Occup. Med.* 42-9, 939-942.

Gupta, H., and Roy, S., 2007: *Geothermal energy: an alternative resource for the 21st century*. Elsevier B.V., Amsterdam, 279 pp.

Holm, A., Jennejohn, D. and Blodgett, L., 2012: *Geothermal energy and greenhouse gas emissions*. Website: geo-energy.org/reports/GeothermalGreenhouseEmissionsNov2012GEA_web.pdf, 14 pp.

Holmes, N.S., and Morawska, L., 2006: A review of dispersion modelling and its application to the dispersion of particles: An overview of different dispersion models available. *Atmospheric Environment*, 40-30, 5902-5928.

Hung, N.T., 2010: *Urban air quality modelling and management in Hanoi, Vietnam*. National Environmental Research Institute, Aarhus University, Denmark, PhD Thesis, 219 pp. Website: www2.dmu.dk/pub/phd_hung.pdf.

Idriss, A., Foster, K.R., Yee, D., Palczynski, R., Dixon, E., Jackson, W. and Kinneburgh, C., 2004: *Assessment report on reduced sulphur compounds for developing ambient air quality objectives*. Report prepared for Alberta Environment, 165 pp. Website: environment.gov.ab.ca/info/library/6664.pdf.

Kagel, A., 2008: *The state of geothermal technology, part II: surface technology*. Geothermal Energy Association, publication for the U.S. Department of Energy, 89 pp.

Khalil, M.S., Kord, M., and El-Daly, F.A., 1996: Some enzymatic activities of radish and tomato plants fumigated with a mixture of sulphur dioxide and hydrogen sulphide. *Egyptian J. Physiological Science*, 2-1/2, 81-90.

Kosari T., A., 2011: Interpretation of geochemical well test data for well NWS-6D, NW-Sabalan, Iran: An implication for scaling potential and recommended inhibition methods. Report 18 in: *Geothermal Training in Iceland 2011*. UNU-GTP, Iceland, 357-390.

Kristmannsdóttir, H., Sigurgeirsson, M., Ármannsson, H., Hjartarson, H. and Ólafsson, M., 2000: Sulfur gas emissions from geothermal power plants in Iceland. *Geothermics*, 29-4/5, 525-538.

Kumar, A., Jampana, S.S., Varadarajan, Ch., 2004: Application of the United States Environmental Protection Agency's AERMOD model to an industrial area. *Environmental Progress*, 23-1, 12-18.

Macdonald, R., 2003: *Theory and objectives of air dispersion modelling*. University of Waterloo, Waterloo, 27 pp. Website: www.engga.uwo.ca/people/esavory/MME474A_Part1.pdf.

McKenzie, D.P., 1972: Active tectonic of Mediterranean region. *Geophys. J. Internat.*, 30-2, 109-185.

MESB, 2000: *Health effects of low-level hydrogen sulfide in ambient air*. Michigan Environmental Science Board, a science report to Governor John Engler, 43 pp. Accessible at: www.michigan.gov/documents/h2srept_3700_7.pdf.

Millachine, M.A., 2011: *Guidelines for optimum gas extraction system selection*. University of Iceland, Reykjavík, MSc thesis, 54 pp.

Neshuku, M.N., 2012: *Comparison of the performance of two atmospheric dispersion models (AERMOD and ADMS) for open pit mining sources of air pollution*. University of Pretoria, MSc thesis, 102 pp.

Nyagah, E.M., 2006: Hydrogen sulphide dispersion and modelling for Nesjavellir power station using Gaussian and numerical models. Report 15 in: *Geothermal Training in Iceland 2006*. UNU-GTP, Iceland, 291-314.

Ólafsdóttir, S., Gardarsson, S.M., Andradóttir, H.O., 2014: Spatial distribution of hydrogen sulfide from two geothermal power plants in complex terrain. *Atmospheric Environment*, 82, 60-70.

Peralta, O., Castro, T., Durónb, M., Salcido, A., Celada-Murillo, A., Navarro-González, R., Márqueza, C., García, J., Rosa, J., Torres, R., Villegas-Martínez, R., Carreón-Sierra, S., Imaz, M., Martínez-Arroya, A., Saavedra, I., Espinosa, M. and Torres-Jaramillo, A., 2013: H₂S emissions from Cerro Prieto geothermal power plant, Mexico, and air pollutants measurements in the area. *Geothermics*, 46, 55–65.

Perry, S.G., Cimorelli, A.J., Paine, R.J., Brode, R.W., Weil, J.C., Venkatram, A., Wilson, R.B., Lee, R. F., and Peters, W.D., 2005: AERMOD: A dispersion model for industrial source applications. Part II: model performance against 17 field study databases. *J. Applied Meteorology*, 44-5, 694-708.

Porkhial, S., Shabihkhani, R., Oladnia, S. and Moridi, A., 2010: Environmental monitoring of air, soil and surface water resources; a case study on Meshkinshahr geothermal field development. *Proceedings of the World Geothermal Congress 2010, Bali, Indonesia*, 7 pp.

Radmehr, B., 2005: Preliminary design of a proposed geothermal power plant in NW-Sabalan area, Iran. Report 15 in: *Geothermal Training in Iceland 2005*. UNU-GTP, Iceland, 265-296.

Renewable Energy Organization of Iran, 2014: *Geothermal energy resources and development in Iran*, SUNA – Renewable Organization of Iran, Deputy for Executive and Technical, Geothermal Energy Office. Website: www.suna.org.ir/en/executive/geothermalenergy/geothermalen.

SCOEL, 2007, *Recommendation from the scientific committee on occupational exposure limits for hydrogen sulphide*. SCOEL, 17 pp. Website: ec.europa.eu/social/BlobServlet?docId=3864&langId=en

Seangkiatiyuth, K., Surapipith, V., Tantrakarnapa, K. and Lothongkum, A. W., 2011: Application of the AERMOD modelling system for environmental impact assessment of NO₂ emissions from a cement complex. *J. Environmental Sciences*, 23-6, 931–940.

SKM, 2004: *Well NWS-4 discharge evaluation report*. Sinclair Knight Merz, report for SUNA – Renewable Energy Organization of Iran, 27 pp.

SKM, 2005a: *NW-Sabalan geothermal feasibility study*. Sinclair Knight Merz, report for SUNA – Renewable Energy Organization of Iran, 150 pp.

SKM, 2005b: *Geochemical evaluation of well NWS-1 discharge test*. Sinclair Knight Merz, report for SUNA – Renewable Energy Organization of Iran, 24 pp.

Stockie, J.M., 2011: The mathematics of atmospheric dispersion modelling. *SIAM Review*, 53-2, 349-372. Website: people.math.sfu.ca/~stockie/atmos/paper.pdf.

TBCE, 1979: *Geothermal power development studies, Sabalan zone*. TBCE, Geophysical Survey, report to Ministry of Energy, Islamic Republic of Iran.

Vallero, D., 2008: *Fundamentals of air pollution*. Elsevier Inc., Amsterdam, 942 pp. Website: books.google.is/books?id=4AV2Wds_NZAC&pg=PA581&lpg=PA581&dq#v=onepage&q&f=false.

Vora, J., 2010: *Dust dispersion modelling for opencast mines*. National Institute of Technology Rourkela, India, BSc thesis, 55 pp. Website: ethesis.nitrkl.ac.in/1760/1/jinesh.pdf.

Wahl, E. F., 1977: *Geothermal energy utilization*. John Wiley & Sons, NY, 302 pp.

WHO, 2000: *Hydrogen sulphide*. World Health Organization, regional office for Europe, 7 pp. Website: www.euro.who.int/__data/assets/pdf_file/0019/123076/AQG2ndEd_6_6Hydrogensulfide.PDF

WHO, 2003: *Hydrogen sulphide: Human health aspects*. World Health Organization, concise chemical assessment document, 53, 35 pp.

Zou, B., Benjamin Zhan, F., Gaines Wilson, J. and Zeng, Y., 2010: Performance of AERMOD at different time scales. *Simulation Modelling Practice and Theory*, 18 612-623.



UNITED NATIONS
UNIVERSITY

UNU-GTP

Geothermal Training Programme

Orkustofnun, Grensasvegur 9,
IS-108 Reykjavik, Iceland

Reports 2014
Number 16

BOREHOLE GEOLOGY AND HYDROTHERMAL ALTERATION MINERALOGY OF WELL MW-13, MENENGAI GEOTHERMAL FIELD, KENYA

Emily W. Kahiga

Geothermal Development Company - GDC

P.O Box 17700-20100

Nakuru

KENYA

ewangari@gdc.co.ke, w.kahiga@gmail.com

ABSTRACT

Rock cuttings provide a realistic picture on down-hole stratification and alteration. Therefore, the study of cuttings is essential in order to evaluate the dynamics of the geothermal system, such as permeability, temperature, size and depth of the reservoir. In this study, four different analytical methods (binocular, petrographic, microthermometry and X-ray diffractometry) were applied to analyse cuttings from well MW-13, located in the Menengai geothermal field, Kenya. This is a vertical production well, drilled to a depth of 2001 m. Well MW-13 was aimed at tapping NNW-SSE structures associated with the Molo and Solai Tectono-Volcanic Axes (TVA) which cut the Menengai caldera. Four rock types are encountered which include: trachyte (most dominant), tuff, pyroclastics and syenite. From litho-stratigraphic correlation of well MW-13 with other Menengai wells, several inferred faults have been identified, while a complicated tectonic scenario exists between some of the wells. The shallow section of the well is characterized by low-temperature hydrothermal alteration minerals which evolve to form high-temperature ones at greater depths. Four alteration zones, based on mineralogical assemblages, were identified: smectite-zeolite, quartz-smectite, epidote-quartz, and illite-wollastonite-actinolite-quartz. The uppermost 30 m section is unaltered. A comparison on the inferred alteration temperature, homogenization temperature (T_h) and the boiling point curve shows that the system was in boiling conditions at some point in time. The measured temperatures do not reflect the current formation temperature. On correlating temperature logs to circulation losses, penetration rates (ROP), and lithological characteristics, eight permeable zones have been identified. The main sources of permeability are faults and lithological contacts. A brief comparison of clays in Menengai and Olkaria geothermal systems indicates that high-temperature clays appear at shallower depths in Olkaria wells than in Menengai wells. It is speculated that the different ages of the two systems are accountable for the dissimilarities noted.

1. INTRODUCTION

1.1 General information

Menengai geothermal field is one of the major high-temperature geothermal fields in Kenya, located within the Kenya Rift, in the East Africa Rift System (EARS). The EARS (roughly 6,000 km long) is an intracontinental ridge system (Chorowicz, 2005), and is mainly characterized by uplifting due to plumes beneath the rift system. At least two mantle plumes (Afar and Kenya) are recognized beneath the EARS (Rogers et al., 2000). The Kenya Rift encompasses the Turkana and Kenya rift zones (Bosworth et al., 1986) and is characterized by an active 500 km long continental extension which is 60-80 km wide (Strecker and Melnick, 2013). Leat (1984) describes Menengai as a Late Quaternary volcano, which is situated about 24 km south of the equator, 10 km north of Nakuru town, and defined by coordinates 35°04'S and 0°12'E (Figure 1). The field is characterized by a shield volcano with its highest peak at an elevation of 2278 m.a.s.l. and two fault systems: the Ol'rongai and the Solai (Figure 3). Geothermal resource exploration and development in Menengai field kicked off in 2009 and so far about 25 wells have been drilled. This project concentrates on the geological aspects of Menengai geothermal field; well MW-13 borehole geology is given the most attention. Well MW-13 is the thirteenth well, located within the caldera summit northeast of well MW-09 and directly north of well MW-10 (Figure 4). It is a vertical production well drilled to 2001 m depth, and was aimed at tapping NE-SW striking faults, as well as NNW-SSE structures associated with the Molo and Solai Tectono-volcanic axes (TVA). The well was also intended to supplement studies on the reservoir's physical characteristics such as rock permeability, storage capacity, boundary conditions, size and depth of the reservoir and chemical characteristics. It also provides data on hydrothermal mineralogy, subsurface structures, system capping and litho-stratigraphy, necessary for updating the Menengai geothermal conceptual model.

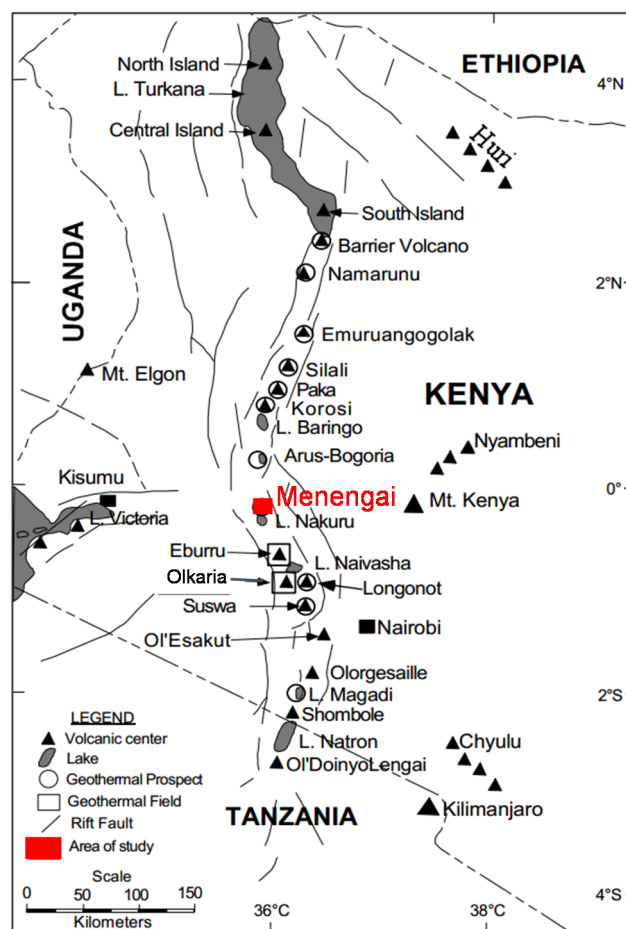


FIGURE 1: Map showing part of the EARS; Menengai caldera is located within the Central Kenya Rift (modified from Lagat, 2004)

1.2 Purpose of the project

This project study is aimed at critically evaluating the borehole geology and hydrothermal mineral alteration of Menengai well MW-13 via various lab analyses such as binocular and petrographic, among others. The project training is carried out as a partial fulfilment of a six months course in Borehole Geology at the United Nations University Geothermal Training Programme (UNU-GTP) in Iceland. The analyses are aimed at:

- Identifying and describing the different rocks encountered in well MW-13 and thereby updating knowledge on the litho-statigraphy and sub-surface structures in Menengai geothermal field;

- Studying the hydrothermal alteration minerals in the well with an aim of understanding better the water-rock interaction processes in the field, and thus providing clues on past and present conditions in the Menengai reservoir;
- Using the results to correlate well MW-13 with data from other Menengai wells with the aim of better characterizing the Menengai geothermal system with regard to its geophysical characteristics, including fault structures; and
- Attempting to compare the clays in Menengai wells with that of Olkaria wells.

1.3 Previous work in Menengai

Numerous studies have been carried out in Menengai, both in the past and present, with different aims, ranging from geological, scientific research, academic reasons, government interests, geothermal exploration, and so on. Dixey (1946) studied the erosion and tectonics in the East Africa System in which Menengai is located. McCall (1957) more specifically reviews the Menengai caldera and suggests a Krakatoan type of caldera collapse, while McCall (1967) describes the geology of the Nakuru-Thomson's Falls-Lake Hannington area and, hence, that of Menengai volcano. Jones (1975; 1985) further discusses the geological evolution of the Menengai trachytic caldera, whereas Jones and Lippard (1979) attempted to estimate the age of Menengai rocks. Leat (1984 and 1991) extensively discusses the geological and volcanological evolution of the Menengai volcano and concludes that it developed during three major phases.

Early Menengai geothermal exploration work was carried out by Geotermica Italiana Srl. (1987) when a reconnaissance survey for the geothermal resource took place in the area. Tole (1996), in his review on geothermal energy research in Kenya, lists the Menengai crater as one of the prospects and proposes more research to evaluate the field's potential. More geothermal exploration work at the Menengai-Ol'banita area was conducted by BGR (2009). In 2004, KenGen carried out detailed surface geothermal exploration, which confirmed that Menengai could host a viable geothermal resource for exploitation (KenGen, 2004). Other previous studies (Simiyu and Keller, 1997; 2001; Mariita and Keller, 2007) explain the presence of a high gravity anomaly along the rift volcanic centres and interpret them to be a result of a shallow magma chamber and dykes along the rift axis. GDC (2010) conducted intense integrated geothermal mapping in the Menengai prospect area which confirmed previous work. The study resulted in a clearer citation of the major geological structures and geothermal manifestations in the prospect area while the geophysical measurements confirmed the presence of a heat source beneath the Menengai caldera. Additionally, gas geothermometry estimated reservoir temperatures to be in excess of 250°C (Kipchumba, 2013). The intense studies were used to site exploration wells, and exploratory drilling started in 2011. Since then, numerous studies have been progressively carried out to re-evaluate the geothermal system. For instance, several studies on completed wells have been carried out (Kipng'ok, 2011; Gichira, 2012; Lopeyok, 2013). In addition, more recent studies (Wamalwa, 2011) confirm the presence of a heat source (at about 7 km depth), as well as high porosity and permeability. Further structural mapping has recently been carried out (Strecker and Melnick, 2013), aimed at re-evaluating the Nakuru area in light of the ongoing geothermal exploration.

2. GEOLOGY AND STRUCTURAL SETTING

2.1 Regional geology and tectonic setting

The Kenyan segment of the East African Rift System (EARS) is the eastern branch of the Africa Rift System; the other two branches include the western and southeastern. The Kenya rift system extends from Lake Turkana in the north of Kenya, to the north of Tanzania near Lake Natron (Figure 1). Hetzel and Strecker (1994) and Smith and Mosely (1993) concluded that rifting was initiated by rift faults within the Late Proterozoic basement of the Mozambique belt, adjacent to the eastern margin of the

Tanzania craton. Active faulting started during the Cretaceous period, around 119 to 120 Ma, resulting in rapid subsidence and thick deposition along the Sudan-Kenya NW-SE trending troughs (Guiraud et al., 2005). Folding, as explained by Ali Kassim et al. (2002), then followed due to dextral transpression, forming the ENE–WSW fold belt. Uplifting, rifting, folding and thrusting continued during the Paleocene times (Tole, 1996; Guiraud et al., 2005; Guiraud and Bosworth, 1999), shortly followed by regression in the Early and Middle Eocene. The last stage in the development of the Rift (from Late Eocene to Late Oligocene) was characterized by strong magmatic and tectonic changes (Guiraud et al., 2005; Chorowicz, 2005; MacDonald, 2003), as well as domal uplifting of about 300 m (Kipchumba, 2013). From Early Miocene to Pliocene, the collision between the African-Arabian and Eurasian plates intensified (Guiraud et al., 2005; Tole, 1996), leading to intense volcanic eruptions, uplifting and subsequent faulting episodes. Baker and Wohlenberg (1971) described the basaltic, phonolitic and trachytic volcanism that followed during the Late Pliocene, while uplift and graben faulting resulted in the present day rift structures. Baker et al. (1988) suggested that this faulting was triggered by a convecting mantle, opening up fractures which served as conduits for Quaternary volcanic activity and the development of many large shield volcanoes of silicic composition along the rift axis. Menengai is one of the shield volcanoes among others, such as Olkaria, Eburru, Suswa, Longonot, Korosi, Paka, Silali, Emurungogolak, and the Barrier Complex (Figure 1).

2.2 Geology of Menengai volcano

The Menengai caldera is located north of Lake Nakuru, and within the Kenyan rift (Figure 1). Leat (1991) describes that trachytic magma eruptions have continuously been recorded for the last 6.2 Ma. Figure 2 shows the surface geology and various geological structures of Menengai caldera. The oldest exposed rock unit is the Mau Tuffs (Leat, 1991), found to the west of Lake Nakuru, and the Subukia Trachyphonolite (Leat, 1983) located on the eastern flank (Figure 2). The subsequent volcanic unit is marked by the Pliocene Bahati Trachytes and Tuffs (5.1-2.0 Ma) which are highly faulted. The Early Pleistocene Limuru Trachytes (1.96 ± 0.04 Ma) followed and are exposed in the area in a scattered manner (Baker et al., 1988; Crossley, 1979). According to Leat (1991), the evolution of the Mbaruk Basalt and Trachyte (about 1 Ma) followed, and are mainly visible at the southern part of Menengai (Figure 2).

The youngest group of volcanic rocks is associated with the eruption of two ignimbrites and the collapse of the 77 km² Menengai caldera (Leat, 1984). According to Leat et al. (1984), Menengai caldera is part of a trachytic central volcano of late Quaternary age and its volcanic activity started just before 0.18 Ma. Macdonald et al. (2011) further explained the geological evolution of the Menengai caldera. Its onset was a shield-building phase, also termed Pre-caldera activity by Leat (1984). The eruption of two voluminous ash-flow tuffs (about 29 km³) followed, each preceded by major pumice falls. Two caldera-forming events (Syn-caldera activity) then followed (29 ka and 8 ka, respectively), accompanied by an eruption of a 20-30 km³ ash-flow. Post-caldera activity is largely marked by a series of lava flows (at least 70 flows) (Leat, 1984; Mibei and Lagat, 2011). Strecker and Melnick (2013) established that volcanic deposits related to Post-caldera activity are exposed in the immediate vicinity of the caldera.

2.3 Structural setting of Menengai volcano

Structures in the Menengai volcano are poorly exposed due to the intensive cover of recent lavas on the caldera floor. Nevertheless, numerous studies (GDC, 2010; KenGen, 2004; Simiyu and Keller, 1997; Strecker and Melnick, 2013; Leat, 1984) have assessed various structures of significance in this field and the surroundings. On a regional scale, Menengai caldera is affected to the north and south by NNE striking normal faults, while the western section appears unaffected. The major structures are as discussed below.

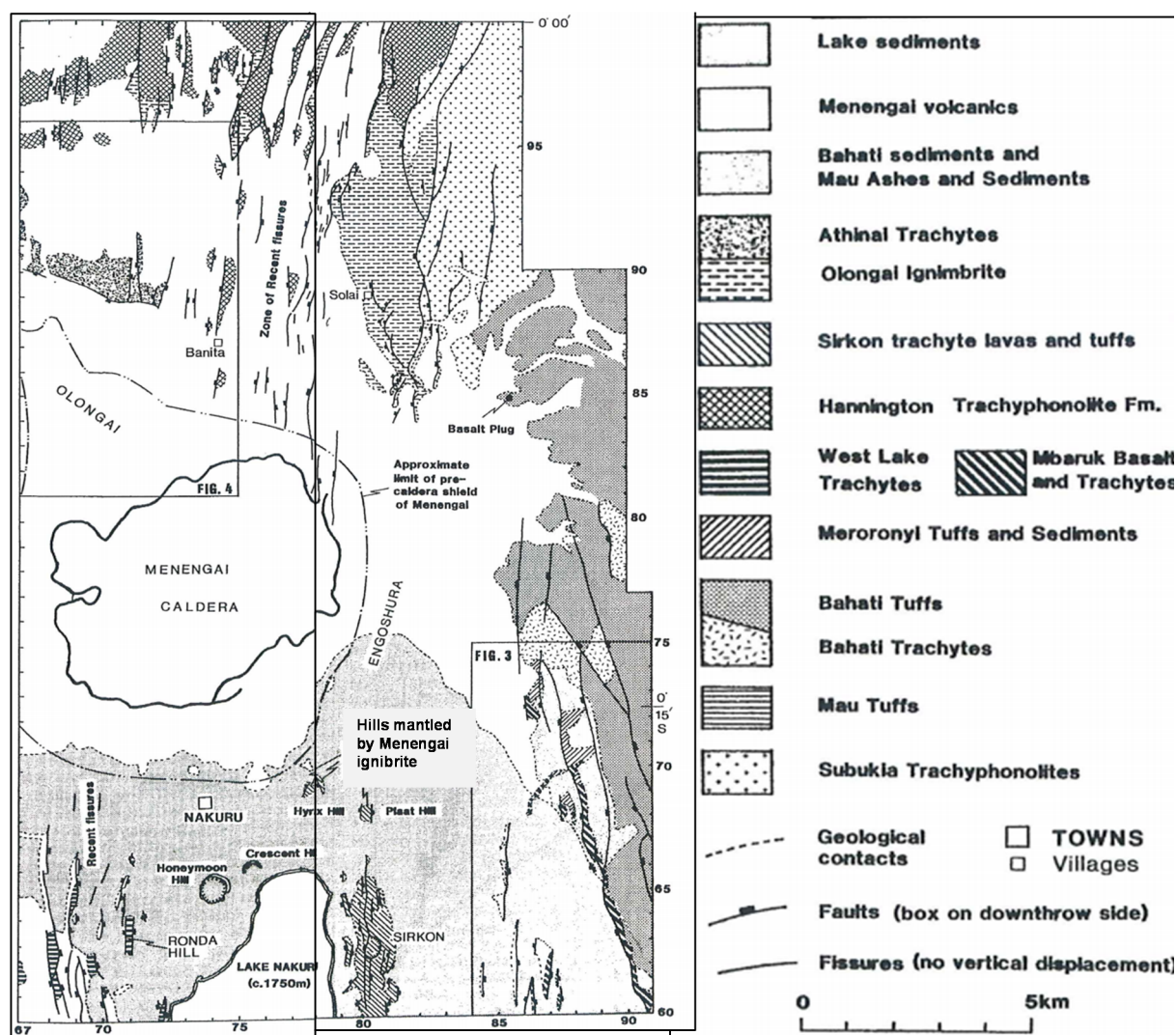


FIGURE 2: Geological map of Nakuru area, showing the surface geology of Menengai caldera, its outline, faults, fissure zones and other structures; the Menengai volcanics are undifferentiated to emphasize the geology of older formations (modified from Leat, 1991)

2.3.1 Ol'rongai structural system

The Ol'rongai structural system (Figure 3) forms part of the larger Molo tectono-volcanic axis (TVA) (Geotermica Italiana, 1987). Mibei and Lagat (2011) and Mibei (2012) deduced that the Ol'rongai system is associated with a system of young NNE-SSW striking normal faults and fractures along which volcanic eruptions have taken place. Most likely this explains the presence of aligned craters and fumaroles on the surface along this fault zone, as shown by Strecker and Melnick (2013) and Lynne et al. (2006). Leat (1984) associates the Ol'rongai system with a NW-SE trending ridge where Pre-caldera rock units are seen; therefore, the Ol'rongai fault system should be older than the Solai system which cuts into the caldera on the NNE side.

2.3.2 Solai Tectono-volcanic axis and Makalia fault system

The Solai TVA system (Figure 3) is a narrow (4 km wide on average) graben, defined by a NNE-SSW orientation through Lake Solai (Figure 2) (Mibei and Lagat, 2011). The Solai TVA is part of the Solai graben which Leat (1984) interpreted as being continuous with a swarm of very young faults. The Solai fault system is younger than the Menengai caldera as it cuts the caldera wall to the north, disappears below the pyroclastic cover, and reappears on the SW corner of the caldera. In the same context,

Strecker and Melnick (2013) confirmed that a similar NNE-SSW aligned lineament can be traced farther south along the caldera floor; the lineament is characterized by a 1 km wide NNE oriented volcano-tectonic zone which hosts NNE-SSW elongated eruptive centres. This suggests that the Makalia fault system (Figure 3) is an extension of the Molo system, and is further inferred by Strecker and Melnick (2013), proposing that the two systems, Solai and Makalia, may coincide, thus, forming an extensional fault system.

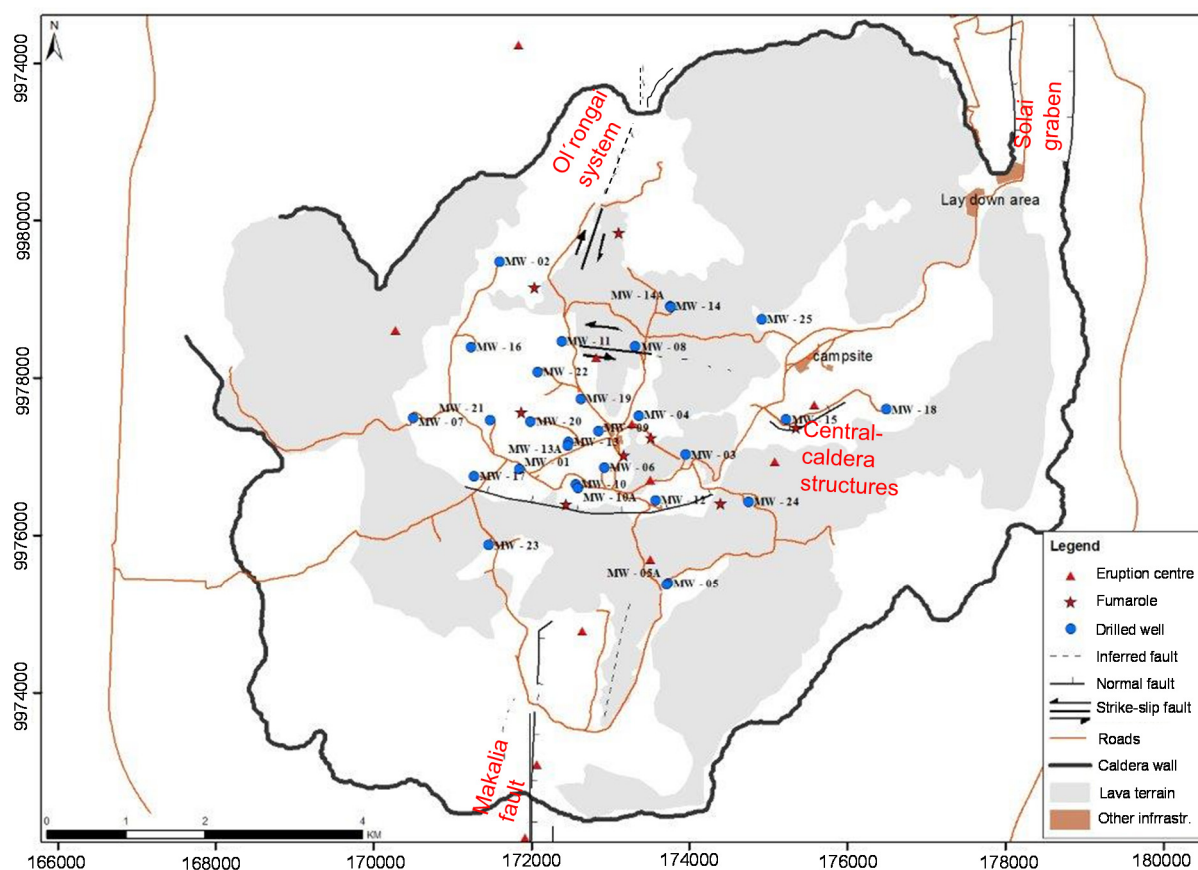


FIGURE 3: Structural map of Menengai geothermal field (modified from Strecker and Melnick, 2013)

2.3.3 The Menengai caldera and ring faults

The Krakatau-style Menengai caldera is elliptical in shape, with embayed walls up to 300 m high and measures approximately 12×8 km (Leat, 1984). Apart from the Post-caldera lavas that cover the caldera floor, the circular rim of the Menengai caldera is well-preserved. Nevertheless, the ring structure has been disturbed by the Solai system on the northeast side, implying that the ring fault is older than the Solai system. Additionally, recent Post-caldera lava flows from eruptive centres have spread over the caldera wall on the southern side (Strecker and Melnick, 2013). An embayed ring fracture is evidenced by the presence of surface expressions of faults and randomly spaced Post-caldera vents close to the caldera wall (Leat, 1984; Strecker and Melnick, 2013).

2.3.4 Central-caldera structures

According to Strecker and Melnick (2013), there are numerous linear features oriented either ESE-WNW or E-W, in the central area of the Menengai caldera. Leat (1984) suggests a region of weakness in the central part through which magma easily ascended onto the surface. The central-caldera structures display a different orientation from that of feeder-dykes. Strecker and Melnick (2013) attributed this to doming which is associated with magma intrusions. Resistivity studies by Wamalwa (2011) and Simiyu

and Keller (2001) confirm magma injection and a low-resistive zone along the central-caldera features. Additionally, these features are characterized by numerous fractures with aligned fumaroles (Figure 3), some of which are active and sulphurous.

3. SAMPLING AND ANALYTICAL METHODS

3.1 Sampling

Rock cuttings provide a realistic picture of down-hole stratification and alteration and thus, are useful for characterizing down-hole alteration temperatures and composition (Marks et al., 2009). During drilling, cuttings were collected at a 2 m interval depth for lithologic logging. A binocular microscope was used to analyze the cuttings at the rig site, aimed at developing an initial litho-stratigraphy and estimating down-hole temperatures by using alteration mineralogy. The resulting data were applied in defining the casing depth and directing drillers on geotechnical aspects, especially with regard to the type of formation, fracturing, temperature, etc. Sample portions were eventually taken to the ISOR (IcelandGeoSurvey) laboratory for detailed analysis. Binocular, petrographic, X-ray diffraction and fluid inclusion studies, under proper and ample guidance, were also carried out on the cuttings at ISOR.

3.2 Analytical Methods

3.2.1 Binocular microscope analysis

An Olympus SZX12 stereo microscope was used to critically investigate the physical characteristics of the rock cuttings such as the rock type, color, texture and grain size, rock fabric, primary and secondary alteration mineralogy. Other various geological and structural aspects were also studied using the cuttings such as intrusive activity, permeability and feeder zones, mineral sequences, porosity, vein fillings, litho-stratigraphic boundaries and the grade of alteration. Rock cuttings, placed in sample holder boxes, were sufficiently wetted to enhance reflectivity, and then mounted on the stage of the binocular microscope. Careful inspection of the cuttings was then carried out and the observations were noted down for interpretation. During the binocular analysis, representative samples, based on the noted observations, were carefully selected and prepared for advanced scrutiny by using other analytical techniques.

3.2.2 Petrographic microscope analysis

A LeitzWetzlar petrographic microscope was used to study thirty thin sections. The analysis was aimed at confirming the various observations made during the initial binocular studies such as the rock type, texture, porosity and alteration minerals. Additional observations made included recognizing alteration minerals which were not identifiable using a binocular microscope and defining mineral sequences, which are rarely distinguished in the cuttings by binocular analysis.

3.2.3 X-ray diffractometer analysis

This technique is mainly used for identification of clay minerals, which is important in assessing alteration temperatures in geothermal systems. Clay minerals are known to have diverse mineralogy and crystal structures, thus, are not easily distinguishable by microscopic analysis. Thirty six samples were chosen from representative depths, and prepared for XRD studies. A Bruker AXS, D8 Focus diffractometer (Bragg-Brentano goniometer) was used, with Ni-filtered Cu α radiation at 1.54 Å wavelength at 40 mA and 40 kV, with fixed 0.5° (1 mm) divergence and receiving slits and NaI scintillation counter with a 0.2 mm detector slit. The recorded peaks and patterns were processed and identified by using both the *JADE* software (Materials Data, Inc.) and the Powder Diffraction File (PDF) database of the International Centre for Diffraction Data (ICDD).

3.2.4 Fluid inclusion analysis

Any process that interferes with the growth of a perfect crystal may cause trapping of primary fluid inclusions. Secondary fluid inclusions are, however, trapped along healed cracks. Analysis of fluid inclusions, also known as microthermometry, is the observation of various phase changes in fluid inclusions under controlled conditions of heating and cooling (Harvey and Browne, 2000). At ambient temperatures, all types of inclusions contain a liquid aqueous solution and a gas bubble (Lagat, 2004). The inclusion is heated and the homogenization temperature (T_h) measured. Microthermometry studies help in deciphering the temperature of past geologic events such as tectonics and uplifting. Roedder (1984) compares fluid inclusions to a self-contained geothermometer preserving a specific temperature of a past event. Thus, fluid inclusion analysis objectively gives a simple specific history and prediction on the behaviour of a geothermal system. For this study, two grains of secondary quartz were carefully collected from a representative depth range. Each grain, one at a time, was then slowly heated on a Linkam THSMG 94 freezing and heating stage. The T_h was measured for further interpretation. A total of 71 inclusions were analysed.

The data acquired from all of the above analyses were assimilated and compiled using LogPlot 2007 (RockWare Inc., 2007), a software which is beneficial in correlating and interpreting geological and geotechnical data.

4. BOREHOLE GEOLOGY

As described earlier, well MW-13 is near the Menengai caldera summit, northeast of well MW-09 and directly north of well MW-10 (Figure 4).

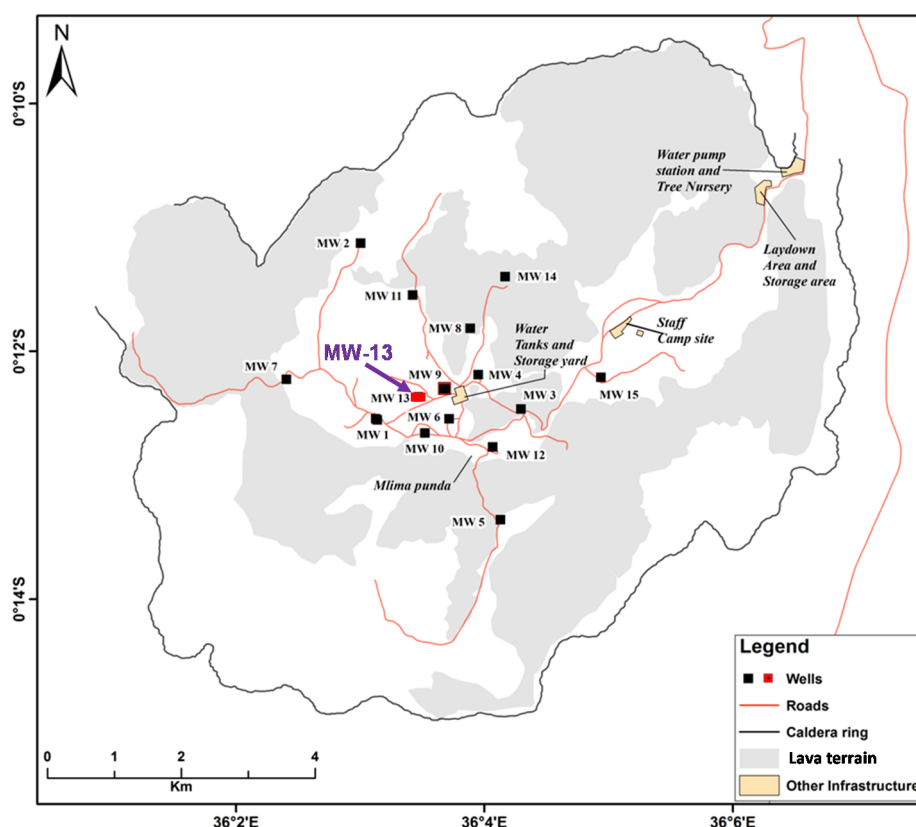


FIGURE 4: Location of well MW-13, highlighted in red colour

4.1 Drilling of well MW-13

MW-13 was spudded on 1st January 2013 and completed on 8th June, 2013; the well was drilled to a depth of 2001 m CT (Cellar Top). A total of 159 days were spent on this well operation: 81 days on drilling while 78 days on downtime, attributed mainly to repairs on a damaged crown block (Figure 5). Four different drilling phases (Figure 5), each with a different casing size, were employed as described below. Note that all referred depths are as measured from the cellar top (CT).

Phase one, 26" hole: The 26" hole was drilled to a depth of 50.30 m, with mud and water as drilling fluids. Total loss of circulation was encountered at a depth of 7.5 to 8.5 m where a 6 m³ cement plug of density 1.9 g/cm³ was completed. Cement returns were received on the surface after primary cementing, after which 2 backfills were performed. A total of 83.87 tons (cement plugs inclusive) of neat cement were used for cementing the 20" surface casing, which was set at 47.5 m.

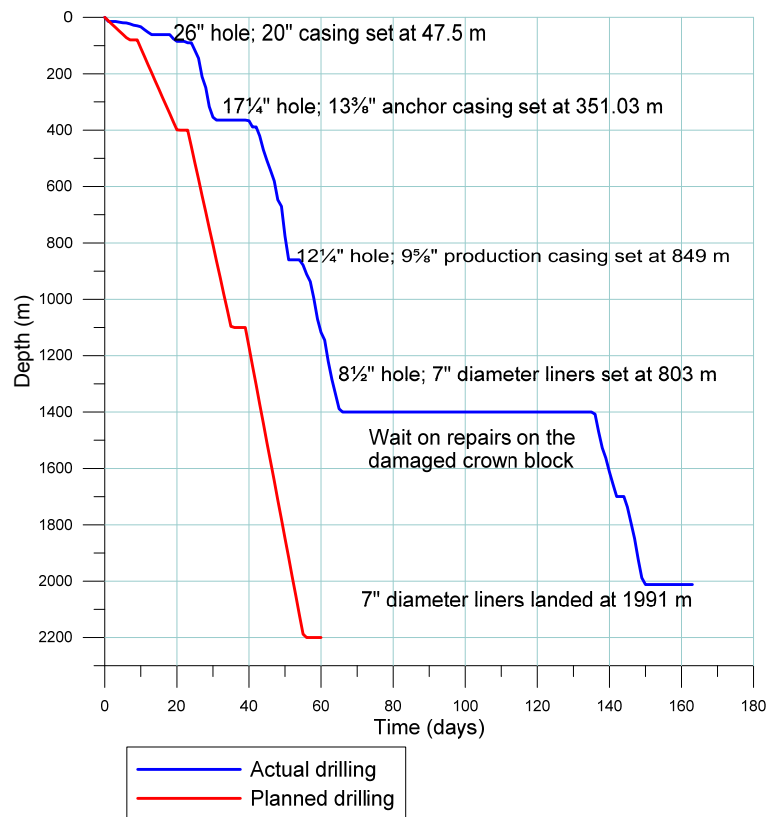


FIGURE 5: Graphical representation of well MW-13 drilling progress

Phase two, 17 1/4" hole: Drilling of this section was done to a depth of 353.1 m. This zone was characterized by a total loss of circulation and, hence, LCM (Loss Circulation Material) was used to cure the loss zones and regain circulation. At 120 m, curing of losses failed completely, leading to drilling blind to a casing depth of 353.1 m. Wiper trip was conducted and the 13 3/8" anchor casing was set at 351.03 m on 1st February, 2013. A total of 147.88 m³ cement slurry with a density of 1.72 to 1.85 g/cm³ was used before cement was received on the surface.

Phase three, 12 1/4" hole: Drilling of this section of the hole started on 4th February, 2013, to a total depth of 859 m. The well was logged at 355 m showing 1.0° inclination. Mud was used as the drilling fluid in this segment with full returns received through to 849 m depth, at which the 9 5/8" production casing was set on 21st February, 2013. Primary cementing was done with two backfills before returns were received on the surface. A total of 6.6 tons of cement at 1.72 g/cm³ density was used in this zone.

Phase four, 8 1/2" hole: This final part of the hole was drilled using aerated water and foam, to a depth of 2001 m. Drilling progressed successfully, after one bit change at 1106 m, until 7th March, 2013, at 1389 m depth, where a travelling block struck on the crown block during POOH (Pulling Out Of Hole) to change the 8 1/2" bit and stabilizer sleeve, damaging three sheaves. Repairs on site were not successful; therefore, the damaged sheaves were extracted and taken away for maintenance. Drilling resumed on 17th May, 2013, with alternating total loss to partial circulation. Successful drilling was conducted to 30th May, 2013, with wiper trip being performed up to the casing shoe prior to running liners. On 1st June 2013, 7" diameter liners were run in hole with 102 joints of slotted liners and 2 plain liners. The liner was landed at 1991 m with the top set at 803.15 m. Well logging commenced on 1st June 2013, whereby a dummy was run but encountered an obstruction at 1044 m. This led to the use of 3 1/2" diameter

drill pipes, enabling a successful tool run. The 3½" diameter drill pipes were POOH and logging was done again with a clear dummy run to 1979 m. A SFTT (Static Formation Temperature Test) and a pressure test were executed successfully. The well was capped with a class 900 master valve on 8th June, 2013.

4.2 Stratigraphy

Well MW-13 stratigraphy is dominated by trachyte lavas and some intermittent tuff intercalations. Other minor rock formations include pyroclastics and syenitic intrusions. The lithological sequence is described below and shown in Figure 6; rock descriptions are based on the analysis of cuttings, supported by petrographic and XRD analyses.

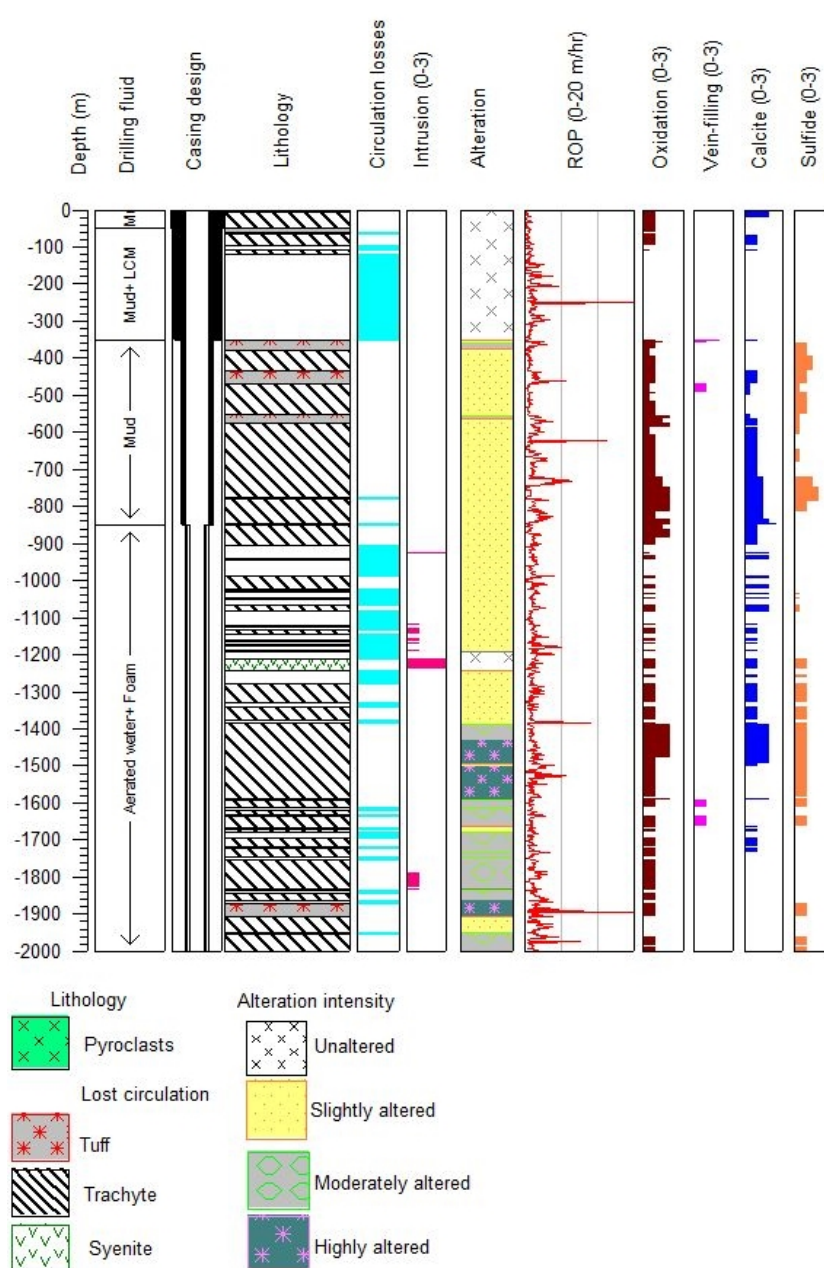


FIGURE 6: Well MW-13 lithology, the intensity of alteration, oxidation, vein-infilling and penetration rates

Pyroclastics are clastic rocks primarily composed of volcanic materials such as unconsolidated ash and bombs. Pyroclastics in well MW-13 are encountered at shallow depth (top 4 m); surface alteration, mainly oxidation, is noted at this depth range (Figure 6). In binocular microscopy, the volcanic unit appears as grey to brownish grey pumice lapilli particles, obsidian, glass and lithics of trachytic composition. Pyroclastics further appear as a thin sheet at 1590 to 1592 m. At shallower depths, the pyroclastic formation resembles Post-caldera lavas as described by Leat (1984), probably originating from eruptions within the caldera. The deeper sequence signifies an old land surface, appearing as a reddened oxidized soil horizon. In the deeper pyroclastic formation, sulphides, calcite and clay alteration and oxidation are notable in the cuttings.

Trachyte occurs alternating with tuff and syenite at 50 m and 1198 m, respectively, and appears till the bottom of the well (Figure 6). It is the dominant rock type in well MW-13, with minor tuff intercalations at greater

depths. The rock colour varies from light to dark grey and grey to greenish/brownish grey, fine to medium grained, and predominantly porphyritic. The variation in crystallinity (different rock textures such as fine to medium grained, porphyritic, phaneritic, aphanitic) is attributed to the age differences in the evolution of Menengai caldera, as demonstrated by Leat (1984 and 1991). Therefore, the age of the trachyte in well MW-13 ranges from Pre- to Syn- and Post-caldera. Additionally, the cuttings show well-elongated phenocrysts of sanidine, as well as prismatic phenocrysts of pyroxenes. The matrix is composed of flow oriented feldspar grains in a fine to medium grained groundmass. At greater depth, in thin sections, nepheline is notable as colourless to greenish, stubby mineral grains with no cleavage. The alteration of this formation is highest at contact boundaries, and its primary minerals are altered to both high and low temperature secondary minerals.

Tuff: The tuff layers in well MW-13 divide trachyte lavas, thus acting as marker horizons separating Pre- and Post-caldera volcanic activities. Therefore, tuff mainly relates to Syn-caldera activity in Menengai. The rock type was first observed at 50 m and later appears intermittently to the bottom of the well, intercalated with trachyte and syenitic intrusions. Tuff is recognized in well MW-13 by its frothy, vesicular and aphyric texture, as well as felsic colours such as brownish grey. The vesicles are mainly filled with calcite, clays, pyrite, quartz, and actinolite at high temperatures. A tuff layer observed at 1872 to 1906 m has high permeability, high ROP, contains sulphides and shows poor crystallinity, similar characteristics as observed in a deep tuff horizon in wells MW-04, MW-06 (Mibei, 2012) and MW-09 (Lopeyok, 2013) and, thus, believed to be related.

Syenite appears as a white coarse-grained, porphyritic and fresh formation with prismatic pyroxene grains. The formation in well MW-13 occurred as thin lenses irregularly intercalated with trachyte from 1118 m. The syenitic formation zone was characterized by frequent losses; the formation is hard and compact as deduced from the low penetration rates during drilling, and very low sulphide content. Syenite in well MW-13 is consistently associated with high temperature minerals like epidote, albite, actinolite and wollastonite. This signifies contact alteration resulting from the hot intrusion. The appearance of empty cavities in cuttings is also of key interest, probably confirming the aforementioned indication of localized geothermal activity. The syenitic intrusion probably correlates to the proposed existence of an axial intrusion beneath Menengai volcano (Leat, 1984).

4.2.1 Lithology of well MW-13

0-4 m: Pyroclastics. Fine to medium grained heterogeneous rock fragments that show varied colours such as green, black, brown, grey and reddish. A vesicular frothy texture was also noted. Oxidation, attributed to surface alteration due to rock interaction with air and water, and minor calcite were noted in the cuttings.

4-50 m: Medium-grained trachyte. Relatively fresh dark greyish black lava, equigranular, medium grained lava that is feldspar porphyritic, with easily notable pyroxene and sanidine phenocrysts. At 38 m, cuttings exhibit a peculiar greenish tinge. Alteration is noted by oxidation, calcite, amorphous silica, chalcedony and zeolites.

50-62 m: Tuff. A thin layer of brownish grey, vesicular and frothy cuttings. A few grains of sanidine porphyritic lava were also notable. Minor oxidation, amorphous silica, zeolites and pyrite define alteration in this zone.

64-352 m: Fine-grained trachyte. Black grey to felsic brownish grey, fine grained feldspar porphyritic lava which is fairly unaltered. Some vesicular cuttings were also noted. Alteration in this zone is defined by minor oxidation, clays, calcite and zeolites. The zone is permeable as deduced from frequent loss of cuttings at 68-74; 98-108; and 120-352 m.

352-380 m: Tuff. Brownish vesicular tuff fragments which exhibit moderate alteration. Greenish minerals and pyrite disseminations were notable on the surfaces and in the vesicles. Minor brownish

grey to green, fine-grained trachytic lava were also notable. Oxidation, calcite, clays and pyrite alterations dominate this well section to about 722 m depth.

380-434 m: Fine-grained trachyte. Greenish grey to white fine grained, feldspar porphyritic lava. Pyrite infillings and some minerals being slightly altered to brown and greenish clay minerals were noted.

434-472 m: Tuff. Brownish to greenish grey vesicular and frothy lava. Vesicles are mainly filled with clays and some oxidized minerals. Elongated sanidine phenocrysts were also notable.

472-552 m: Fine-grained trachyte. Greenish grey to black, relatively fresh, fine grained porphyritic lava, rich in elongated sanidine and pyroxene phenocrysts. Pyrite alteration decreased at 494 m.

552-576 m: Tuff. Greenish brown, vesicular and frothy rock fragments. An increase in clay alteration was noted at 552-556 and decreased at 556-564 m. At 564-576 m, the cuttings were reddish brown, quite compacted, aphanitic and exhibit assorted rock fragments with conspicuous sanidine phenocrysts. Minor trachytic cuttings were also notable.

576-982 m: Fine-grained trachyte. Greenish black to brown fine grained porphyritic lava which is fairly fractured, with well pronounced feldspar and pyroxene phenocrysts; fluid inclusions evident in some of the feldspar phenocrysts. At 778-786 and 848-850 m, some cuttings show a peculiar blue green tinge on the surfaces. Minor tuff fragments intermittently noted in the well segment, which is also characterized by frequent loss of circulation at 774-778; 846-850; 906-940; and 944-982 m. Chalcopyrite embedded in the groundmass was noted from 722 to 846 m.

982-1198 m: Fine-grained trachyte. Light grey porphyritic, relatively unaltered and fractured lava with well pronounced sanidine and pyroxene phenocrysts embedded in a fine grained groundmass. The common yellow green epidote colour was noted at 992 m and 1012 m. Albite, sphene and MLC started showing up in this depth range. Minor syenite cuttings were also noted. From 1124 m, pyroxene phenocrysts were more conspicuous and elongated. This zone is characterized by intermittent losses at 984-988; 996-998; 1012-1014; 1024-1028; 1030-1036; 1038-1042; 1044-1048; 1052-1066; 1070-1072; 1080-1082; 1084-1106; 1108-1118; 1120-1122; 1126-1132; 1146-1160; 1166-1172; 1176-1188; 1192-1198 and 1200-1208 m.

1208-1256 m: Syenite. White, coarse grained, quite fresh rock formation exhibiting prismatic grains of pyroxene, embedded in a feldspar-rich groundmass. Well distinguishable nepheline crystals were observed in thin section. Calcite-filled veins were also present. Epidote, pyrite and albite alteration was observed. This zone is described by intermittent losses occurring at 1208-1210; 1234-1236; 1240-1242; 1244-1250, and 1252-1256 m.

1256-1478 m: Fine-grained trachyte. Greyish black, fine grained feldspar porphyritic lava that is fairly unaltered. At 1384 m, a peculiar bluish mineral deposit in vesicular fragments was noted. Pyrite embedded with thin fibrous greenish grey and whitish crystals of actinolite and wollastonite, respectively, were noted. Intermittent losses occurring at 1258-1260; 1262-1280; 1310-1312; 1328-1340; 1376-1384; 1396-1398 and 1400-1402 m.

1496-1590 m: Medium-grained trachyte. Greenish grey to brown, medium grained pyroxene porphyritic lava that is fairly altered and shows prismatic and elongated pyroxene crystals. Some cavities that had not been filled were noted at 1562 m. At 1594 m, some cuttings were altered into bluish minerals. From 1496 to 1592 m, relatively high alteration was noted by the presence of minor calcite, clays, actinolite, wollastonite, pyrite and quartz.

1590-1592: Pyroclastics. Fine to medium grained assorted rock fragments that show a variety of colors such as green, black, brown, grey and reddish. A vesicular frothy texture was also noted. Circulation losses were encountered at 1518; 1524; 1544; 1572; 1578; 1584 and 1590 m.

1592-1832 m: Medium-grained trachyte. Greenish grey to brown medium grained pyroxene porphyritic lava, fairly altered, shows prismatic and elongated pyroxene crystals. Higher alteration at 1592 to 1734 m was marked by minor calcite, clays, actinolite, wollastonite, pyrite and quartz. However, alteration significantly diminished from 1734 to 1832 m. Circulation losses were observed at 1604; 1608; 1612-1620; 1630-1634; 1638; 1662; 1692; 1666-1670; 1678-1690; 1692-1696; 1712; 1718-1722; 1744-1754; 1758; 1772 and 1808 m.

1832-1842 m: Syenite. Whitish grey, coarse grained, relatively fresh formation, with pyroxene in a feldspathic groundmass. Circulation losses were noted at 1836-1842 m.

1842-1872 m: Fine-grained trachyte. Greenish grey, fine grained, fairly fractured lava with notable sanidine and pyroxene phenocrysts. Decreased effective permeability was indicated by reduced alteration and the absence of sulphides. Random reddish brown spotting was noted at increasing depth and a circulation loss zone was noted at 1864-1872 m.

1872-1906 m: Tuff. Greenish brown, aphanitic vesicular, reasonably altered lava, mixed with minor crystalline cuttings. Most of the vesicles are filled by clays and some tiny quartz crystals. The formation is medium soft and permeable as deduced from high penetration rates.

1906-2000 m: Medium-grained trachyte. Whitish brown to greyish green, fine to medium grained porphyritic lava that is relatively unaltered. Some cuttings of white fresh lava with mafic phenocrysts were also present. Some of the cuttings appear fresh and highly compacted, probably indicating diminishing effective permeability. However, at 1962-2000 m, the cuttings appeared reasonably altered to greenish clay minerals, with some minor alteration minerals also visible, such as wollastonite, actinolite and sulphides. Some cuttings demonstrated an unusual blue green tinge at 1958 m. Circulation losses were encountered at 1950-1954; 1984-1988 and 1990-1992 m.

4.3 Litho-stratigraphic correlation of well MW-13 and other wells

The stratigraphy of wells MW-13, MW-01 (GDC, 2013a), MW-04 and MW-06 (Mibei, 2012) and MW-09 and MW-12 (Lopeyok, 2013), has been interrelated to understand better the Menengai marker horizons, and infer sub-structures (Figure 7). From the lithological cross-section of these wells (Figure 7), trachyte is the dominant rock unit, with intercalations of pyroclastics, tuff and syenite. Post-caldera pyroclastics, tuff and trachytic lavas make up the upper lithological units; the cuttings exhibit a blocky nature; hence, they are the probable cause of losses in this upper zone. At 320 to 400 m, a tuff marker horizon was noted in all the wells, except for well MW-01 where the horizon appeared at 452 to 496 m. The tuff marker horizon was interpreted to be of Syn-caldera age. Another tuff marker horizon was encountered roughly between 450 and 750 m, where normal faults are interpreted between wells MW-01/ MW-06; MW-06/ MW-13; MW-13/ MW-09; MW-09/ MW-12 and MW-12/ MW-04.

Strecker and Melnick (2013) confirmed the presence of numerous linear structures in the central region of Menengai caldera (Figure 3), within which all the mentioned wells are located. Another tuff marker horizon was observed at about 1620 to 1700 m, though is evidently absent in wells MW-09 and MW-12. Finally, a syenitic marker horizon occurs at 1800 m to the bottom in nearly all the wells, with fresh glass being encountered in wells MW-04 and MW-06 at 2082 m and 2174 m, respectively. Perhaps the syenitic intrusion and the fresh glass occurrence are both related to a relatively shallow magma chamber below the Menengai volcano (Leat, 1984).

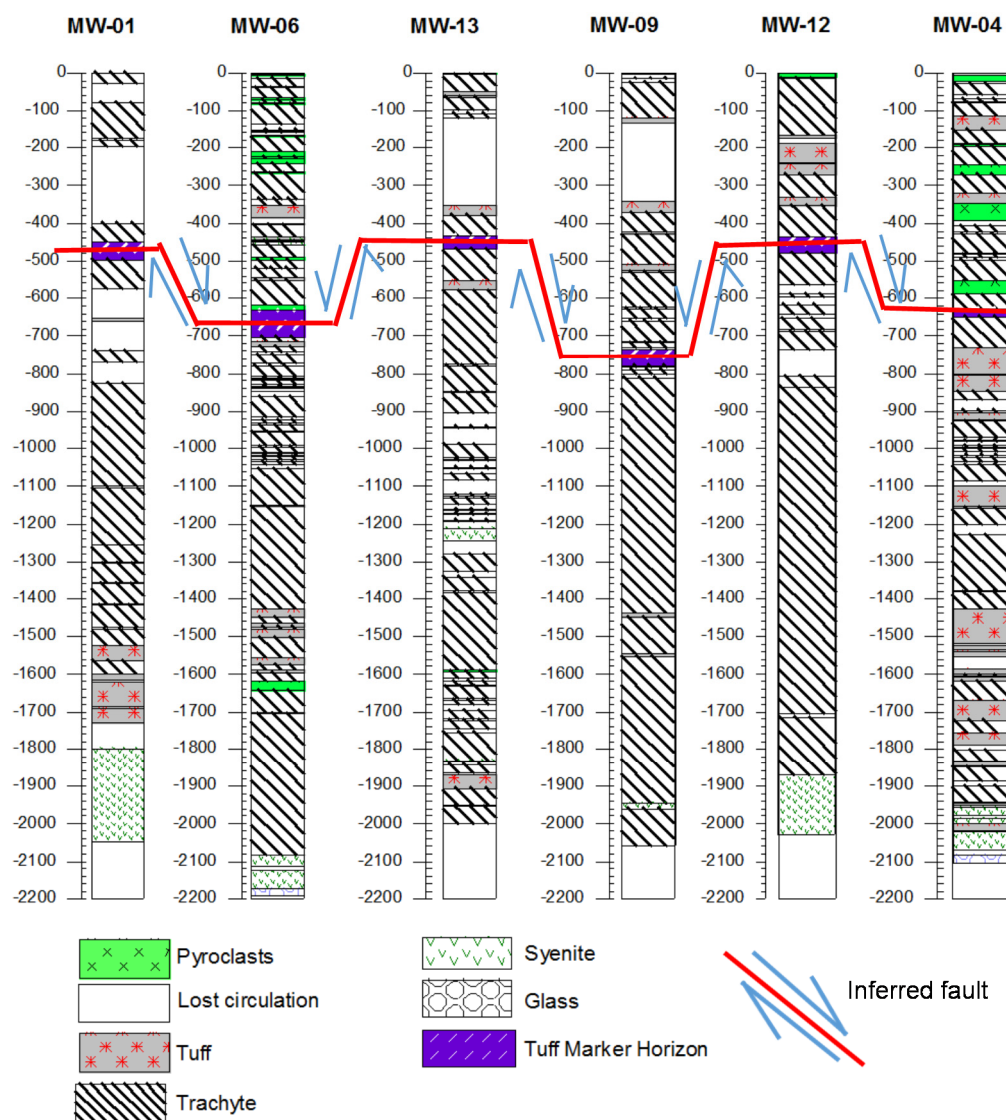


FIGURE 7: Stratigraphic correlation of wells MW-13, MW-01, MW-04, MW-06, MW-09 and MW-12 (GDC, 2013a, Mibei, 2012 and Lopeyek, 2013); inferred fault displacements are shown as half-arrows

An attempt to evaluate the throw, dip and strike of the inferred faults was made and the results are shown in Figure 8. This, of course, is very preliminary as limited data are available, particularly, structural geology. However, the regional NNE-SSW faults (Figure 3) may be cutting across the caldera floor. Furthermore, there are indications that some local faulting is present, for example, the ESE-WNW faulting seen in Figure 3. Figure 8 shows a possible scenario of faulting in the research area. From Figure 7, using the tuff marker horizon, it is inferred that there are faults between several of the Menengai wells. To some point, the throw can be

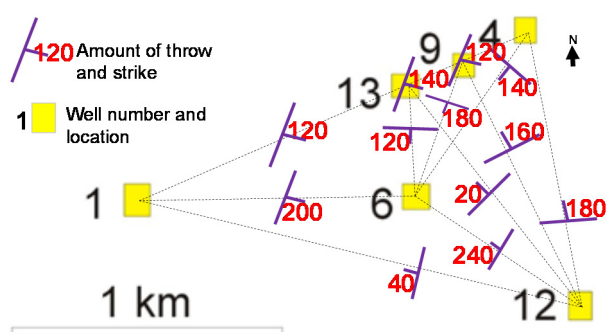


FIGURE 8: Inferred normal faults along wells MW-01, MW-04, MW-06, MW-09, MW-12 and MW-13, showing the inferred strike and throw of possible faults

deduced but it is difficult to define the strike. There seems to be a uniform strike across wells MW-01, MW13, MW-09 and MW-04, as indicated in Figure 8, with a throw averaging 130 m. Correlating the other faults, however, is highly complicated. It is known that the caldera was formed in at least two events, 29 ka and 8 ka ago (Macdonald et al., 2011), which complicates the tectonic scenario. One could also imagine that, in between these events, there might have been stepwise collapses, presently undetected, which could possibly explain the tectonic setting as deduced in Figure 8. It is, therefore, recommended that more detailed structural mapping should be executed to verify the existence of these deduced faults.

5. HYDROTHERMAL ALTERATION

Hydrothermal alteration is, in the simplest terms, a process by which rocks interact with hot fluids and, as such, primary minerals are transformed to secondary ones, with regard to their texture, structures and chemistry. It is fundamental to note that altering of parent rock institutes changes to various physical characteristics of rocks such as porosity and permeability. Reyes (2000) published a simplified and calibrated scale of hydrothermal alteration minerals (Figure 9) which shows the relative temperatures at which the various minerals are stable. Permeability and effective porosity, moreover, are vital to the flow of hot fluids; it is obvious that hydrothermal alteration increases with increased permeability and porosity. These two constraints allow for precipitation of alteration minerals in cavities.

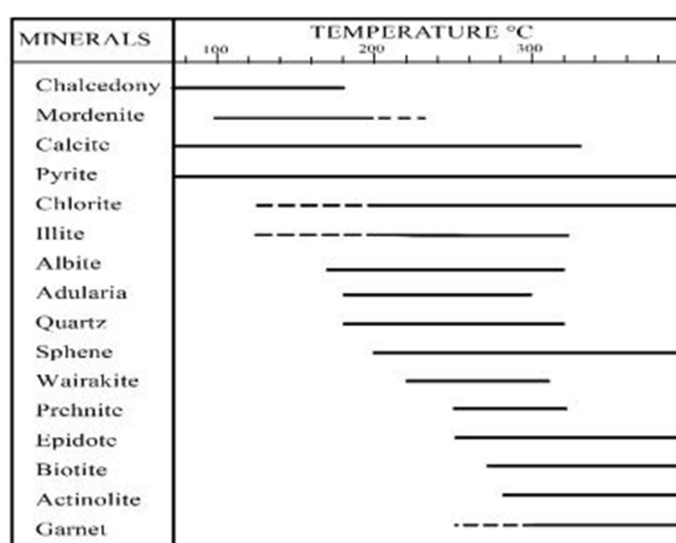


FIGURE 9: Common hydrothermal alteration minerals used as geothermometers and their temperature stability ranges (Reyes, 2000)

5.1 Alteration of primary minerals

As stated previously, trachyte is the dominant rock formation in well MW-13, followed by tuff, syenitic intrusions and minor pyroclastics. Volcanic glass, olivine, feldspar, pyroxenes and opaque minerals are the principal primary minerals observed in this well. When subjected to geothermal environments, the primary minerals are transformed to secondary ones via a number of processes such as replacement, deposition, and so on. The Bowens reaction series (Figure 10) illustrate a relative sequence on how the primary minerals are altered; the first minerals to form are also altered first, and vice versa. A discussion on how primary minerals alter in well MW-13 follows, in a decreasing order of susceptibility to alteration:

Volcanic glass: Even though not a mineral, glass is considered significant because it is very sensitive to alteration, and forms crucial hydrothermal minerals such as zeolites, clays, quartz and calcite, as observed in the study well. Volcanic glass forms from rapidly cooling magma. In well MW-13, volcanic glass, under a binocular microscope, is obsidian-like, black, aphanitic in texture and shows a good conchoidal fracture. In thin section analysis, altered glass is brown and anisotropic. Glass alteration starts right at the top (16 m), and increases to almost 100 % at about 100 m.

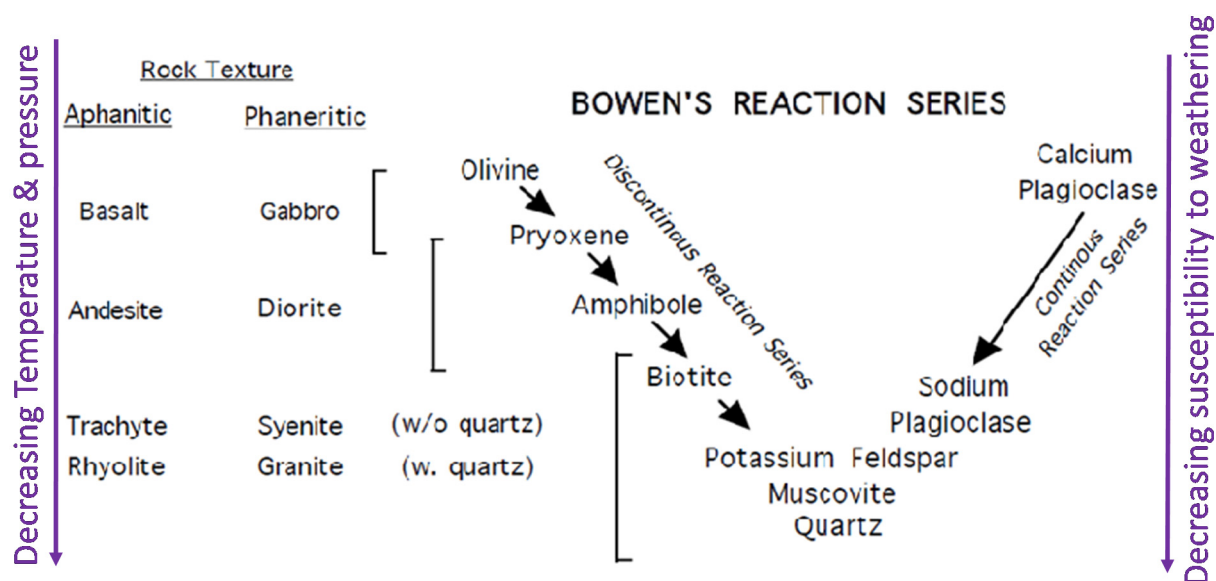


FIGURE 10: The Bowens reaction series (modified from Njue, 2010)

Olivine: In well MW-13, olivine is scarce and rarely fresh. It is distinguished by its unique irregular, sub-angular shape, as well as irregular fractures on the surfaces, often filled with altered minerals. In petrographic analysis, olivine is seen to not have clear cleavage, has parallel extinction and is easily distinguishable from pyroxenes, especially by its low relief and high birefringence. Olivine in well MW-13 is altered to clays and/or replaced by calcite. Its alteration is observed to set in at a depth of 88 m and, at 600 m, olivine is fully altered.

Feldspars: Feldspars form the most dominant mineral in well MW-13, especially in trachyte and in syenitic intrusions, noted by the felsic nature in these rock units. The principal feldspars encountered in this well are sanidine and plagioclase, both appearing in the groundmass and as phenocrysts. In cuttings, feldspars are observed as elongated, transparent to white/grey translucent crystals, occasionally showing twinning. They are distinguished from pyroxenes, quartz and zeolites by their simple twinning, low relief and non-pleochroism. Albite-alteration, noted by its dirty-like appearance and absence of twinning, first appears at 606 m in well MW-13. At the same depth, feldspars are noted to alter into clays and are also replaced by calcite, all the way to the bottom of the well. At 1220-1500 m, feldspar alteration increases to nearly 70%; epidote and quartz are observed to form from feldspars at this depth range.

Pyroxene: Pyroxenes are one of the earliest rock forming minerals and are resistant to alteration. In thin sections, they are easily identifiable by their good cleavage, moderate relief and interference colours, and straight extinction (orthopyroxene) or inclined extinction (clinopyroxene). In well MW-13, pyroxenes are observed as pale green to pale brown, with a metallic lustre and stubbier crystals, either embedded in a feldspar-rich groundmass or as phenocrysts. Alteration of pyroxene to clays and calcite was first noted at 830 m and 1174 m depth, respectively. The alteration increases to about 50%, starting from 1500 m to the bottom, the minerals being altered to calcite, actinolite and high-temperature clays.

Opaque minerals: These minerals are mainly marked by Fe-Ti oxides, and are quite resistant to alteration. In petrographic studies, fresh opaque minerals do not transmit light, and when altered, they allow light through and have an extremely high refractive index. Opaque minerals in well MW-13 alter into sphene and pyrite. Sphene was first noted at 606 m, and continues to the bottom of the well.

5.2 Description and distribution of hydrothermal alteration minerals in well MW-13

Several alteration minerals are observed in well MW-13 and their distribution is shown in Figure 11. Below is a description of the hydrothermal alteration minerals encountered in the studied well (in the order of increasing temperature).

Amorphous silica and chalcedony are the first alteration minerals observed in well MW-13. In the cuttings, the two almost similar minerals appear as vesicle and cavity in-fills (as coating along the walls) from 20 to 62 m depth. Chalcedony is pale blue, purplish to milky white in colour and appears as a lining of roundish crystals, while amorphous silica exhibits more or less the same colours but without a clear crystal form. At greater depths, chalcedony is replaced by secondary quartz.

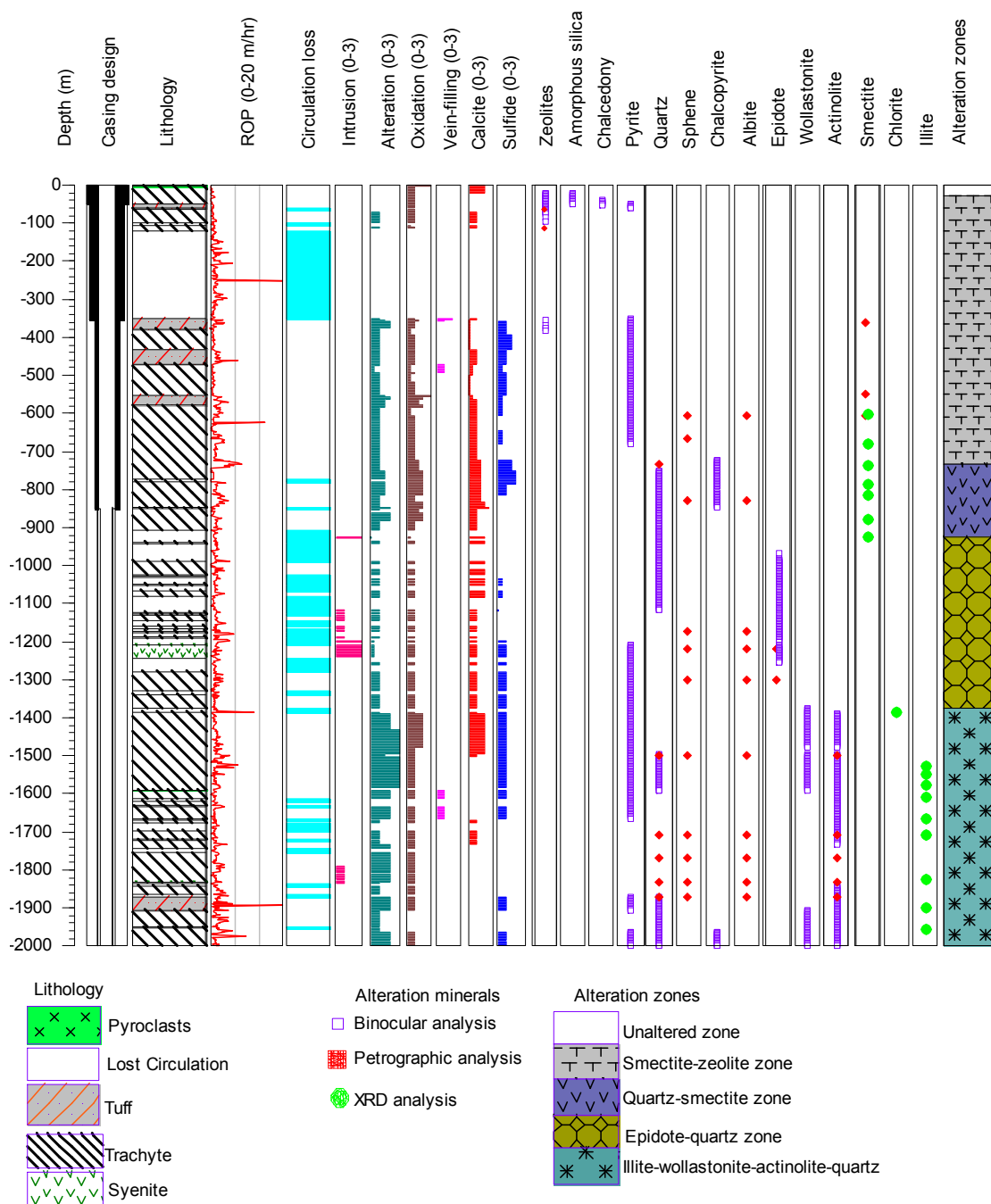


FIGURE 11: Distribution of hydrothermal alteration minerals in well MW-13

Zeolites mainly occur in fractures and vesicles and are milky white to transparent. In thin sections, zeolites are distinguished from quartz by their lower refractive index and obvious radiating and fibrous nature. According to Saemundsson and Gunnlaugsson (2014), zeolites are formed at relatively low temperatures (of up to 130°C) and are rarely associated with very intense alteration. They are found as minor constituents in altered rocks, and are sometimes formed from re-crystallization of volcanic glass (Kristmannsdóttir and Tómasson, 1978). Thomsonite and scolecite were first noted for sure at 26 m and 112 m, respectively. The zeolites then occur intermittently, in a minor amount, down to 382 m depth.

Secondary quartz appears as colourless to white hexagonal, euhedral to subhedral crystals, filling the cavities. In the cuttings, quartz is differentiated from zeolites by its higher refractive index. Secondary quartz is first seen at 750-1188, 1496-1592 and 1872-2000 m.

Calcite is easily distinguishable from feldspars by its high interference colours, fairly high relief and its obvious cleavage. In binocular analysis, calcite is best identified using dilute hydrochloric acid. This mineral is related to boiling, dilution and condensation of carbon dioxide in a geothermal system (Njue, 2010). It is worth noting that calcite may be formed by heating up fresh groundwater and, hence, is not related to geothermal activity all the time. This explains the reason for the appearance of calcite in nearly the entire well column. Abundant calcite was noted at 834-850, 926-1118 and 1390-1496 m.

Sulphides are ore minerals, primarily composed of metal and sulphur, and are commonly associated with intrusive activity in Iceland (Saemundsson and Gunnlaugsson, 2014; Holwell et al., 2012). Studies on sulphide ores led to the discovery of hydrothermal systems in the deep oceans (Vaughan, 2006) which further confirms that the presence of these minerals designates high permeability. In well MW-13, sulphides occur as disseminations, blebs and massive aggregates on the surfaces of cuttings, or are deposited in the cavities. *Pyrite* and *chalcopyrite* were positively identified in well MW-13. When unaltered, the two minerals exhibit a brassy yellow metallic lustre, with chalcopyrite having a distinct iridescent tarnish. Pyrite was first seen at 50 to 62 m in a tuff formation, deposited in the vesicles. It reappeared at 358 m, and continued irregularly to the bottom. Chalcopyrite first appeared at 722 to 750 m. The mineral only appeared again at the bottom-most section of the well.

Albite occurs as an alteration product of plagioclase feldspar. The mineral is distinguishable by its lower refractive index, lack of clear twinning, as well as its somewhat dirty appearance. Fractures on primary plagioclase minerals mark the first indication of alteration. Albite in well MW-13 was first observed at 606 m and extends to the bottom of the well.

Sphene forms at nearly all temperatures. It is opaque but transmits light when broken down to form titanite, and exhibits an extremely high refractive index. Sphene, in thin section, appears brown in colour with a very high relief and occurs as uneven sub-angular grains replacing opaque minerals. The mineral was first sited at a shallow depth of 606 m and remained sporadically to the bottom.

Epidote is distinguishable by its characteristic yellow green colour, both in binocular and petrographic analysis. Its appearance indicates a representative alteration temperature of about 240°C. Epidote was first observed in well MW-13 at 982 m as a yellow green transparent non crystalline mineral disseminated on the surfaces of cuttings. At 1508 m, epidote was evidently observed as prismatic crystals in a vesicle. Epidote at this depth occurs in association with quartz, pyrite and wollastonite.

Wollastonite gives a representative temperature of 270°C and remains stable even at temperatures beyond 300°C. It is easily identifiable in cuttings by its woollen-white-hair-like crystals that are commonly very fragile and fibrous. In petrographic analysis, this mineral is transparent and non-pleochroic. Wollastonite is known to occur in association with garnet and epidote in high-temperature systems (Saemundsson and Gunnlaugsson, 2014); it occurred with epidote, quartz, pyrite and actinolite in well MW-13. Wollastonite's first appearance was at 1376 m, and continued sporadically to the bottom of the well.

Actinolite may be confused for wollastonite because it is also fibrous but exhibits a slightly greenish colour, and is rarely deposited in vesicles. Actinolite occurs in very dense slender thread-like crystals embedded in the groundmass, and occurs mainly adjacent to intrusive bodies or deep in high-temperature geothermal systems. The mineral forms at a higher temperature of more than 280°C. In well MW-13, actinolite was first sited at 1388 m, and conspicuously continued, at alternating lithology sections, to the well bottom. At 1502 to 1590 m depth, the occurrence of actinolite was noted to be more abundant; this zone is relatively more altered and is interpreted to be a feeder zone, as will be discussed later.

Clays are common alteration products of nearly all rock-forming minerals and thus they appear from top to bottom of the well column. Clay minerals are phyllosilicates that bear water, trapped between their silicate sheets in large quantities. The minerals have different capacities of holding and/or releasing water, which contributes to variations in the clays; crystallinity changes with temperature. Typically, clay minerals form microscopic to sub-microscopic crystals (in some cases, crystallinity is totally limited); hence, it becomes a bit complicated to study these minerals under a microscope. As a result, and in order to compliment petrographic and binocular analysis, X-ray diffraction analysis for 36 samples in well MW-13 was carried out. Three types of clays were positively identified, as discussed below:

Smectite is a low-temperature (> 200°C) clay, easily distinguishable by its fine-grained brown texture and low birefringence in thin sections. The clay shows a swelling characteristic feature; therefore, smectite exhibits a variety of peaks in the XRD analysis. In well MW-13, smectite was first positively identified at 362 m in thin sections, and at 604 m in the XRD analysis. The recorded peaks were from 12.8 to 15 Å when untreated, 12.9 to 15.8 Å when treated with glycol and collapsing to 10.3 Å when heated (Figure 1 in Appendix I).

Chlorite is well distinguishable in the cuttings by its green radiating and fibrous crystals, mainly occurring in the vesicles. In the thin sections, chlorite is green in open polars and turns grey in crossed view. It is also weakly to non-pleochroic, and shows low birefringence. In the study well, chlorite first appears at 1384 m and was not present in subsequent samples. It exhibits characteristic unchanged peaks of 14.50 and 7.28 Å when untreated and glycolated, and completely collapses after being heated to 550°C. It signifies a minimum temperature of 200°C (Reyes, 2000).

Illite occurrence indicates temperatures greater than 200°C. The clay forms when K-feldspars are replaced and was first observed in the XRD analysis at 1526 m. In well MW-13, illite was not identifiable in either binocular or petrographic analysis; but in the XRD analysis, its characteristic 10.3 Å peak did not change in the untreated, glycolated and heated conditions (Figure 3 in Appendix 1).

5.3 Vesicles and vein fillings in well MW-13

Vesicles are open cavities in rocks that form when dissolved gases in molten magma escape during crystallization, when magma is erupted; the empty pores may later be filled by secondary minerals to form an amygdaloidal texture. On the other hand, veins are irregular discontinuous dike-like fissures/fractures in rocks that may be filled with secondary minerals and/or fluids. Veins and vesicles are important geothermal structures because they are good sources of permeability and porosity. Additionally, they allow the deposition of secondary hydrothermal alteration minerals which helps in estimating reservoir temperatures. Furthermore, the time sequence in which alteration minerals deposit in voids and fractures informs on the evolution of a geothermal system (Franzson, 2014), and reports on changes in the geothermal system with time. Proper studies on the deposited minerals give a very useful picture on the present conditions in a geothermal system, i.e. whether it is cooling, heating or in equilibrium.

Exclusive use of rotary bits may unfortunately cause loss of the important aforementioned textural relationships (Lagat, 2004). This seems to have affected cuttings from well MW-13. Nevertheless, a few amygdalae were noted; their sequence will be discussed later. In the 20 topmost sections, the vesicles were notably void. Low-temperature minerals such as zeolites, chalcedony, pyrite, calcite, quartz and clays were observed in voids from 20 to about 400 m. Zeolites and chalcedony evidently disappeared earlier while the rest carried on to greater depths. At 1200 m to the bottom, high-temperature mineralisation characterizes the vesicles and veins, for instance, wollastonite, epidote, actinolite and clays.

5.4 Mineralogical evolution in well MW-13

The time sequence, during which secondary minerals form in voids, gives a clear picture on the evolution of a geothermal system. The mineral deposition sequence informs on the history of a geothermal system, as well as predicting its future (Njue, 2010). Moreover, different minerals are stable at different physical and chemical conditions such as temperature, as previously discussed. Study of the order at which the minerals form can, therefore, act as a guide on the reservoir status of a system at the present time and, preferably, on the past and future as well. Only two paragenetic sequences (in vesicles) were clearly observed in well MW-13, demonstrated in Table 1, based on petrographic analysis.

TABLE 1: Mineral depositional sequence in well MW-13

Depth (m)	Alteration Sequence
	Early.....Late
1220	Calcite-albite-epidote
1500	Calcite-actinolite-chlorite

5.5 Mineral alteration zones

Based on the formerly mentioned different analyses, four different mineral alteration zones were recognized in well MW-13 (Figure 11). The zones are comprised of:

Unaltered zone (0-30 m): Lithologically, the zone is characterized by fresh pyroclastic and trachytic formations. Only surface alteration (oxidation) is notable in the cuttings.

Smectite-zeolite zone (30-750 m): This zone is marked by the intermittent presence of zeolites (thomsonite and scolecite) as well as smectite clays. Other alteration minerals in this zone include chalcedony, calcite, and pyrite. This mineralogical assemblage indicates temperatures below 200°C, inferred from the low-temperature minerals. The zone is also characterized by tuff and trachytic rock units, with sporadic circulation losses.

Quartz-smectite zone (750-982 m): The zone is marked by the first appearance of secondary quartz at 750 m. An increase in oxidation is notable in this zone (Figure 11). Trachyte and minor circulation losses characterize the zone, too.

Epidote-quartz- zone (982-1376 m): This zone is marked by the first appearance of epidote at 982 m. Additional alteration is noted by the occurrence of calcite, sulphides (e.g. pyrite), albite and oxidation. The mineralogical assemblage of this zone indicates temperatures above 200°C. The zone is mainly composed of blocky trachyte.

Illite-wollastonite-actinolite-quartz zone (1376-2000 m): This is the last mineralogical assemblage marked by high-temperature wollastonite and actinolite minerals, observed first at 1376 m and 1388 m, respectively. Temperatures in this zone exceed 270-290°C. Quartz remained persistent in this zone, as well as sporadic appearance of calcite, pyrite, albite and oxidation.

5.6 Fluid inclusion geothermometry

Alteration temperatures and temperatures logged soon after drilling is completed may not be reliable in defining the formation temperature of a geothermal system. Consequently, there is a definite need to compliment the various analyses, as discussed earlier. Fluid inclusion geothermometry, also termed microthermometry, involves investigating various phase variations in fluid inclusions under controlled conditions of heating and cooling (Harvey and Browne, 2000). Primary inclusions are trapped during the growth of crystal while secondary ones are formed during the healing process of a crystal.

In well MW-13, a total of 71 fluid inclusions, trapped in two grains of secondary quartz at 1550 m depth, were analysed. The comparative results are presented on a histogram (Figure 12). Based on measured and hydrothermal alteration temperatures, this zone has estimated temperatures ranging as high as 240 to above 300°C. GDC (2013b) reports a feed zone at 1500-1650 m depth range. The homogenization temperatures were measured in regular intervals, ranging between 275 and 320°C. Though not very clear, there seem to be two populations of the recorded temperatures. The lower temperature range is from 275 to 295°C, and the higher temperature range roughly records 300 to 315°C.

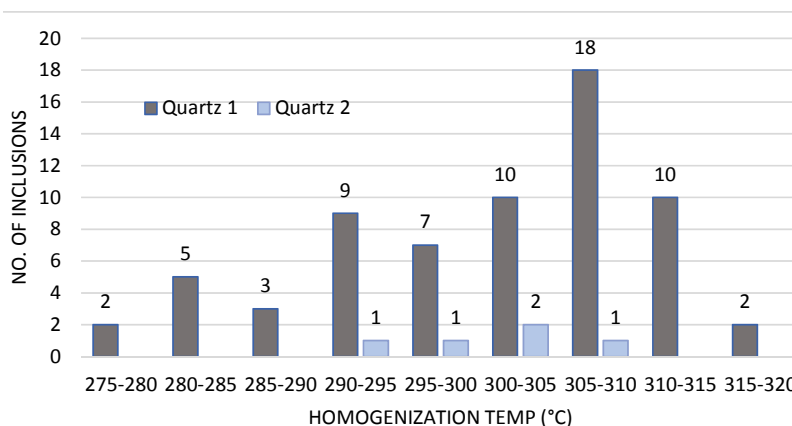


FIGURE 12: Histogram showing the results of fluid inclusion analysis in well MW-13

6. AQUIFERS

A geothermal aquifer is an underground permeable layer of rock or unconsolidated materials (gravel, sand, or silt) bearing hot fluids, including gases, which are extracted for geothermal exploitation. Aquifers, or feed zones, are located using various data such as temperature logs, circulation losses, well completion tests, hydrothermal alteration, and so on. Drilling parameters such as penetration rates (ROP) are also very useful; for instance, a high ROP may indicate the presence of an aquifer. Temperature logs indicate the location of both inflow and outflow in a well, whether cold or hot. Similarly, high hydrothermal mineral alteration is deduced to indicate permeability. Permeability enhances the flow of fluids, consequently leading to increased rock interaction with the geothermal fluids which may lead to a sudden increase in alteration minerals. Circulation losses may also indicate permeability, though care must be taken when using this parameter; other technical measures may cause the losses, for example, cuttings may get stuck in other fractures deep down the wellbore. It is worth noting that aerated drilling may cause slight disturbances in air/water equilibrium, thus causing circulation losses that are not necessarily related to feed zones.

In well MW-13, the first measured temperature log (3 hours heating in Figure 13) evidently showed an obstruction at approximately 1050 m. Therefore, pumping was conducted as an intervention measure. The second temperature log (15 minutes heating) showed higher temperatures at the inferred permeable 1400 to 1600 m section of the well, while the subsequent two logs indicated lower temperatures, attributed to the inflow of colder circulation fluids. The flowing profile confirms a progressive recovery of well temperature, but the profile also indicates stagnant conditions in the well from 1500 m to the bottom.

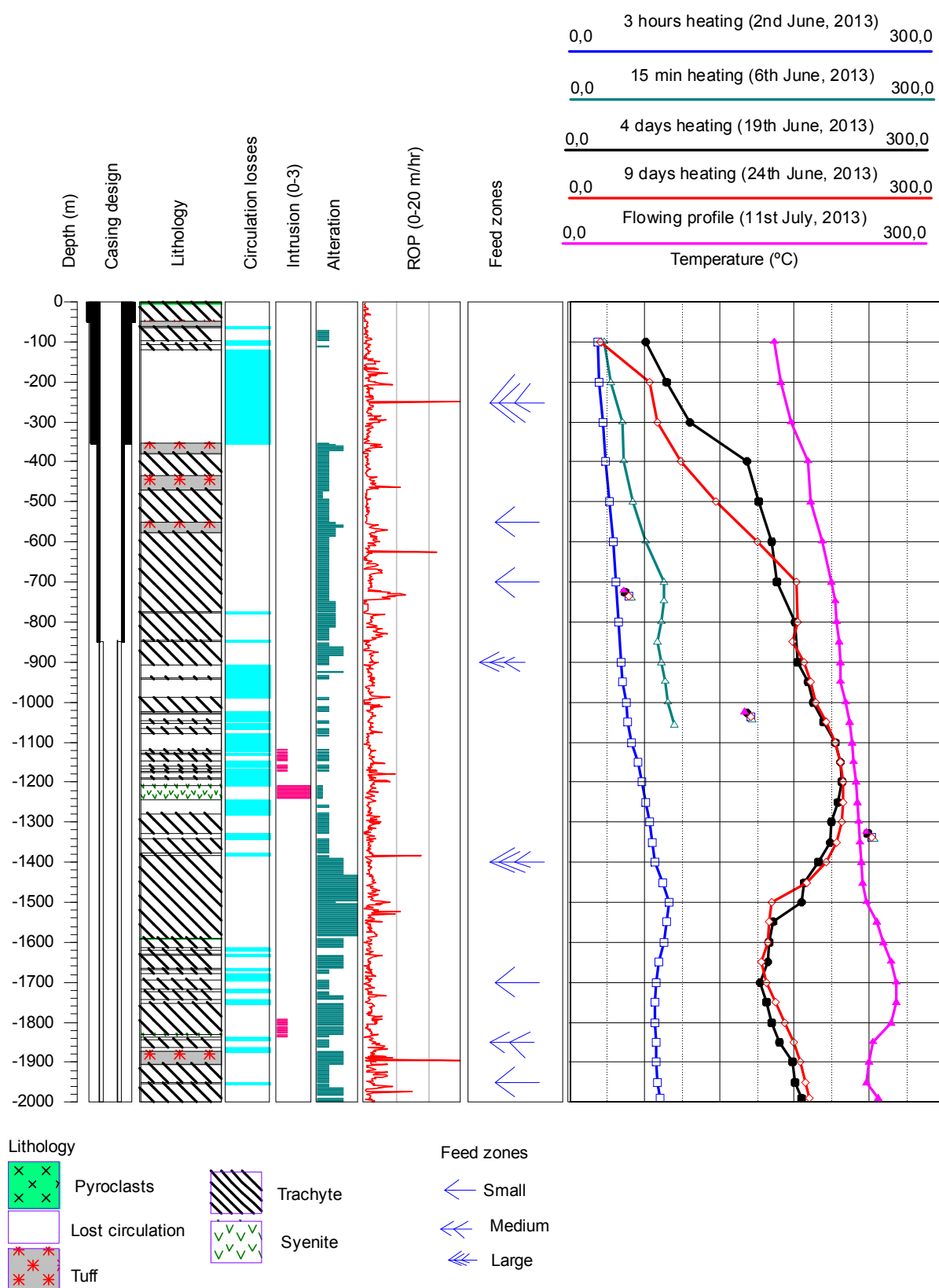


FIGURE 13: Well MW-13 aquifers deduced from the correlation of temperature logs, rates of penetration and lithology characteristics

6.1 High permeability zones

Having studied the stratigraphy, hydrothermal alteration and different temperature profiles, it becomes easier to deduce the location of feed zones in well MW-13. Temperature logs, circulation losses, increased alteration, penetration rates and lithological characteristics have been correlatively used to infer eight permeable zones in the study well. The feed zones are classified as either small, medium or large (Figure 13).

120-352 m is a large permeable zone, probably with several feed points, and was identified above the production portion of the well. The zone is inferred to be cold, hence it was cased off. The permeable zone was deduced from circulation losses and an increased rate of penetration during drilling.

550 m is a small feed zone associated with a tuff formation. It also appeared above the production section and was cased off. It was deduced from increased penetration rates, alteration and temperature.

700 m is associated with a fractured trachyte formation, as indicated by the increased ROP and circulation losses. A temperature gain was also notable at this zone which is above the production area.

900 m is the first large aquifer encountered within the production portion of the well. The aquifer is associated with a rise in temperature, as indicated by the 4 day duration heating log, circulation losses, and increased ROP. A slight increase of hydrothermal alteration was also notable.

1500 m is believed to be the depth of the main feed zone in well MW-13, where temperatures indicated a rise to more than 240°C during the flowing profile (Figure 13). The zone is characterized by high-temperature hydrothermal minerals, as previously shown in Figure 11, as well as circulation losses and increased penetration rates. At this zone, the earlier temperature logs (conducted shortly after pumping due to an obstruction) indicated a sharp decrease in temperature while a later profile (flowing) showed a rise at the same section. This indicates a colder inflow during pumping into the permeable zone, with a later remarkable recovery.

1700 m is a small hot feed zone marked by circulation losses, increased alteration and a temperature rise. For instance, the 4 day heating log showed a rise in temperature at 1700 m.

1850 m is linked to a permeable tuff formation, as indicated by increased penetration rates as well as circulation losses. The medium size aquifer was also deduced from increased alteration and temperatures (at 1850 m, a temperature increase was noted from the 4 day heating up profile).

1950 m is inferred to be responsible for the temperature rise at the well's bottom. The small feed zone is also associated with increased penetration rates and circulation losses.

6.2 Correlation of measured, formation, alteration and fluid inclusion homogenization temperatures

Formation and measured temperatures in a well may differ for a number of reasons. For instance, circulation during drilling cools the well. Given ample time, the well temperatures will recover and eventually equilibrate with the formation. It may also remain uncertain whether the observed alteration minerals reflect the current conditions in the geothermal system, or if they are related to different past thermal events (Lagat, 2004). Fluid inclusion homogenization temperatures are most reliable in interpreting temperatures of past geologic events (Sorby, 1858 in Roedder, 1984). However, microthermometry is time consuming and it is not logical to conduct the analysis for the entire well column. Besides, inclusions may not be always present. However, despite all such reservations, it is important to correlate all the temperatures with the aim of understanding the geothermal system in a deeper perspective.

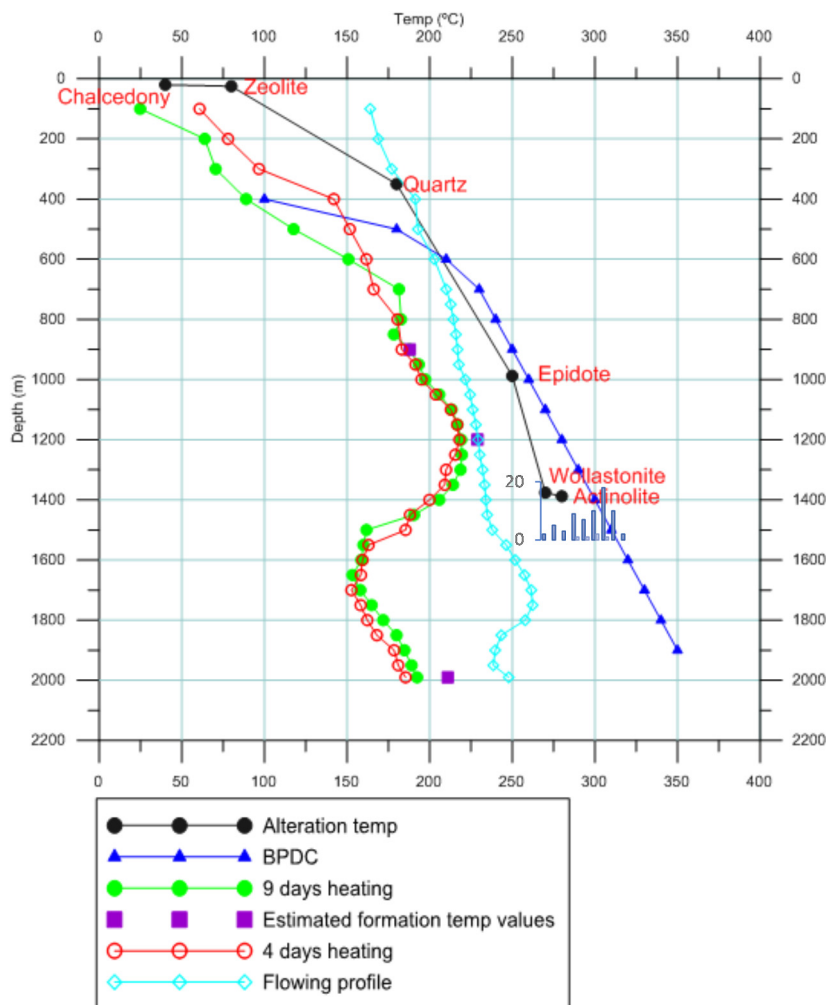


FIGURE 14: Correlation of measured, formation, interpreted hydrothermal alteration and fluid inclusion temperatures in well MW-13

Figure 14 demonstrates the correlation of measured, -formation, -alteration and fluid inclusion temperatures in well MW-13. The formation temperature was inferred from the measured temperatures, using Horner's method. However, it should be noted that the inference is not sufficiently reliable, as the 9 day heating time period (Figure 13) may not have been long enough for the well to have heated up sufficiently. The interpretations made are based on the assumption that the inferred formation temperature represents current conditions in the system.

On correlating fluid inclusions geothermometry with formation temperature, a progressive heating is notable; the recorded quartz homogenization temperature (298°C on average) is higher than the current formation temperature. The interpreted hydrothermal alteration temperature is in equilibrium with the fluid inclusion measurements and plot along or close to the boiling point

curve. This indicates that at some point, the system experienced boiling conditions. On the other hand, when the measured temperature is compared with homogenization, formation and interpreted alteration temperatures, a significant difference is seen. This, as explained earlier, is deduced to be attributed to pumping, due to a previous obstruction.

7. CLAY ALTERATION IN OLKARIA VOLCANIC COMPLEX

7.1 General information

The Olkaria volcanic complex is a Quaternary volcanic system located within the Kenyan rift system, south of Lake Naivasha (Figure 1). Macdonald et al. (2008) described the complex as a relatively young (20 ka), small-volume system dominated by frequent formations of peralkaline rhyolitic domes. Geothermal exploration and development have been ongoing in this high-temperature geothermal field since the early 1970s. Omenda (1998) reported the age of the rocks in the Olkaria complex to range from Pliocene to Holocene (4.5 to 0.4 Ma). The geology consists of four major formations, namely: the Upper Olkaria volcanics, Olkaria basalts, Plateau trachytes and Mau tuffs, as classified by Omenda (1998). Simiyu (1999) proposed the existence of a heat source beneath the complex, at about 6 km depth.

The fluid chemistry of this system is controlled by sodium bicarbonate and sodium chloride waters (Malimo, 2009) with calcite occurring as the most abundant carbonate (Omenda, 1998). The main structures that control permeability in the Olkaria volcanic complex are the N-S, NW-SE, NNW-SSE, and ENE-WSW faults, characterized by high fumarolic activity along the fault lines. The main hydrothermal minerals in the volcanic complex include zeolites, pyrite, calcite, albite, chlorite, epidote, prehnite, quartz, and sphene (Lagat, 2004; Ronoh, 2012).

7.2 Classification and occurrence of clays in Olkaria field

The distribution of clay minerals within a geothermal system gives important insights on the hydrology of the system. Additionally, clays are temperature dependent minerals and are, therefore, useful in predicting temperatures in the geothermal reservoir. The occurrence of low to high- temperature clays in Olkaria geothermal field (Figure 15) was confirmed during the exploratory drilling phase by Leach and Muchemi (1987). Additionally, numerous studies have been published on hydrothermal alteration in the Olkaria geothermal wells (Omenda, 1998; Lagat, 2004; Ronoh, 2012, Okoo, 2013). More specifically, the geothermal field is characterized by four types of clays which are noted mostly as vein and vesicle fillings. The clays include *smectite*, *kaolinite*, *illite* and *chlorite*, as seen in wells OW-902, OW-903, OW-39A and OW-912B, based on petrographic and XRD analyses.

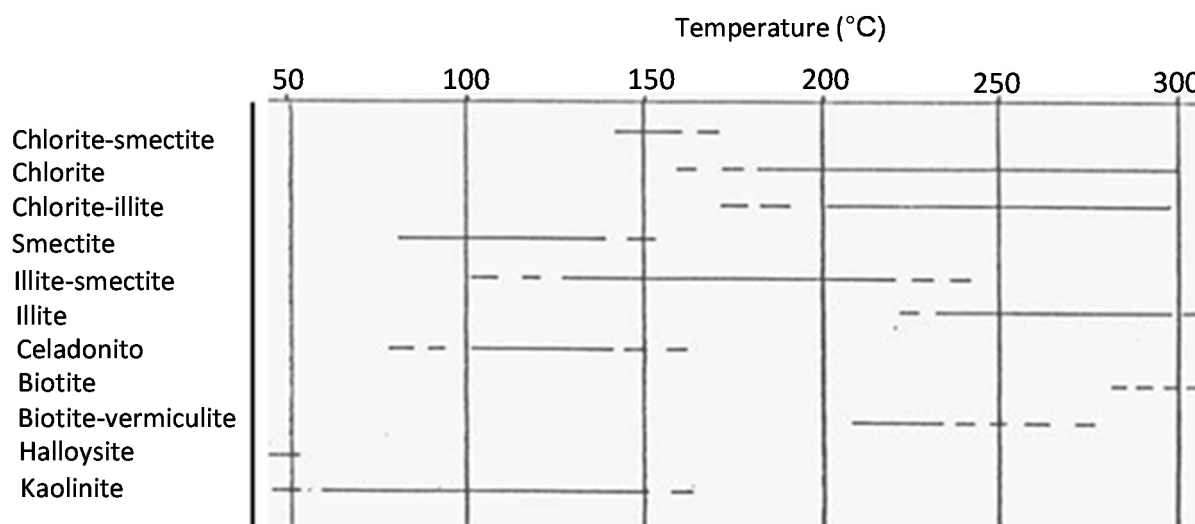


FIGURE 15: Clay minerals and their temperature ranges in Olkaria exploration wells (adapted from Leach and Muchemi, 1987)

7.3 Clays in Menengai field versus Olkaria field

Based on clay analysis results for Menengai wells, e.g. MW-13, MW-11, MW-06 and MW-08 (Mibei, 2012; Kipchumba, 2013), smectite clays are present at shallow depths (Figure 16) whereas, at present, smectite has not been detected, except in small amounts by XRD in Olkaria (Lagat, 2004; Musonye, 2012; Njathi, 2012; Ronoh, 2012; Mwangi, 2012; Otieno and Kubai, 2013; Okoo, 2013). However, in Olkaria wells, for example in wells OW-902, OW-903, OW-39A and OW-912B, illite and chlorite, high-temperature clays, first appear at shallower depths than observed in Menengai (Figure 16). It is striking, therefore, that high-temperature clays appear earlier in Olkaria than in Menengai. It has been speculated that the dissimilarities in the occurrence of clays in Menengai and Olkaria fields is due to age differences between the two systems. The Olkaria system is probably older and, therefore, the geothermal system may have had a longer time to evolve, as opposed to the Menengai system. Of course, other factors such as differences in the permeability of the two fields cannot be ruled out without sufficient evaluation.

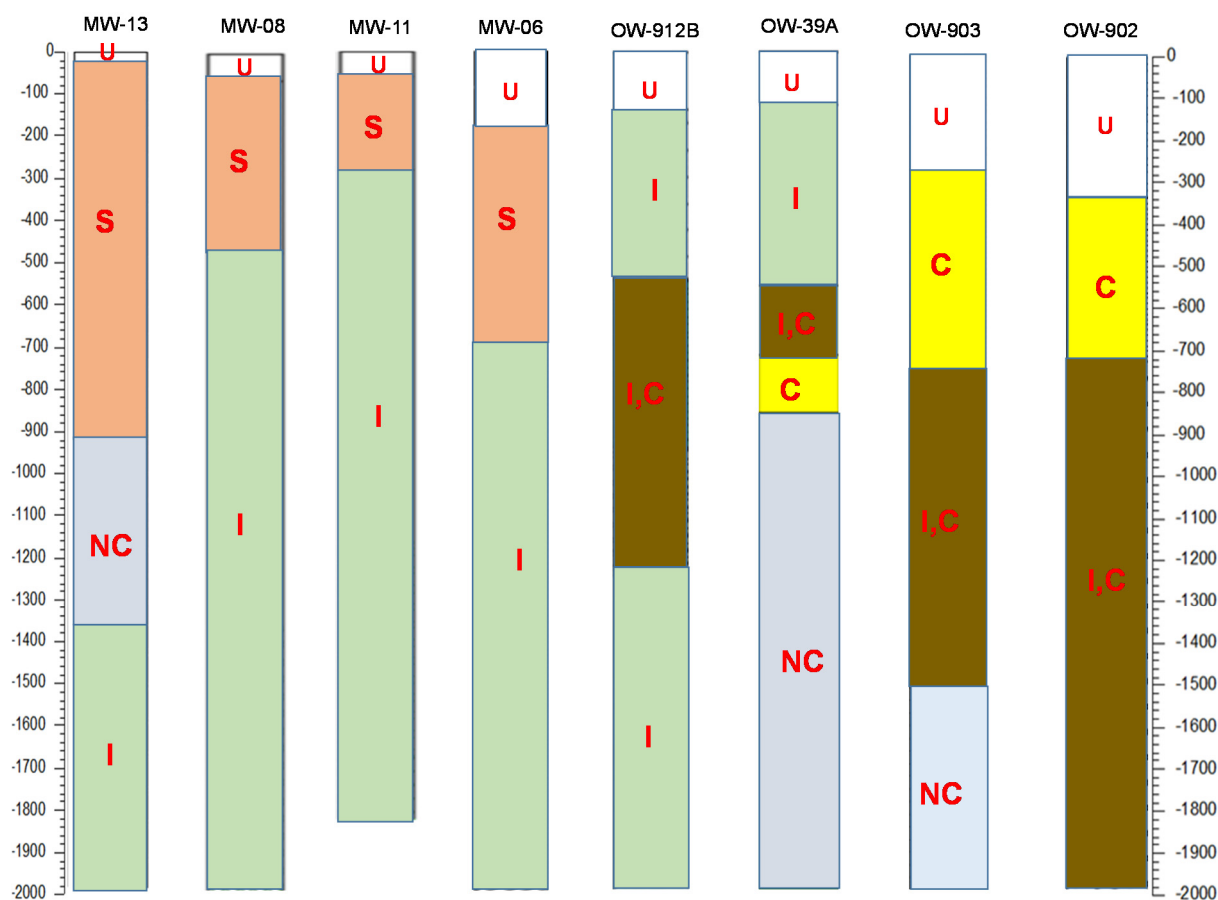


FIGURE 16: Clay occurrence in Menengai versus Olkaria wells; NC = no identifiable clays, U = unaltered, S = smectite, C = chlorite, I = illite (modified from Mibei 2012; Kipchumba, 2013, Lagat, 2004; Okoo, 2013; Ronoh, 2012)

8. DISCUSSION

The litho-stratigraphy of well MW-13 closely correlates to that of most other wells previously drilled in Menengai geothermal field, i.e. MW-01, MW-04, MW-06, MW-09 and MW-12, as demonstrated in Figure 8. Trachyte, tuff, pyroclastics and syenite are the four rock units encountered in well MW-13, with trachyte being the most dominant. The upper 300 m is characterized by pyroclastic and trachytic lavas of Post-caldera age, inferred from their heterogeneous and blocky nature (Leat, 1984), well-demonstrated in the cuttings. In well MW-13, a brownish to greenish tuff formation encountered from 434 to 472 m is deduced to correlate to a Syn-caldera marker horizon, separating the Post and Pre-caldera lavas in Menengai caldera. From 472 m to the well bottom, the lithology is characterized by Pre-caldera lavas, mainly trachytic, intercalated by thin lenses of tuff and syenitic intrusion.

Stratigraphic correlation of well MW-13 and other studied wells within the caldera reveals several normal faults (Figure 7), inferred from the Syn-caldera tuff marker horizon. Only a few of the faults seem to display a consistent throw and strike (Figure 8). The tectonic scenario may be significantly complicated as a result of the two caldera-forming events, 29 ka and 8 ka, respectively (Macdonald et al., 2011). Additionally, the two collapse events might have taken place in a stepwise manner, presently undetected, which could possibly explain the tectonic setting as deduced in Figure 8. It is, therefore, recommended that more detailed structural mapping should be executed to verify the existence of these deduced faults.

Litho-stratigraphic correlation displays a fairly similar sequence in the evolution of the Menengai volcano. For instance, the youngest lavas appear on the uppermost part of the litho-stratigraphy. The different textures in the cuttings further confirm the different eruption episodes of the volcano. A pyroclastic formation at approximately 1600 m is noted in wells MW-06 and MW-13; the deeper sequence signifies an old land surface, appearing as a reddened oxidized soil horizon. Additionally, a syenitic intrusion characteristically appears at the bottommost part. It probably relates to the proposed existence of an axial intrusion beneath Menengai volcano (Leat, 1984).

Hydrothermal alteration minerals in well MW-13 were observed deposited in vesicles, cavities and veins and/or as replacements of primary minerals. Different alteration minerals are stable at different physico-chemical conditions, e.g. temperature (Reyes, 2000). The minerals can, therefore, be used to accurately predict the alteration temperatures in a system. In well MW-13, low-temperature minerals, such as zeolites, characterized the upper sections. The system gradually evolved to form high-temperature minerals such as epidote, wollastonite and actinolite, occurring at 982 m, 1376 m and 1388 m, respectively. Additionally, some alteration minerals, such as sulphides, are directly related to permeability. In the study well, pyrite and chalcopyrite appear in significant amounts where the formation is believed to be permeable. The occurrence evidently decreases towards the well bottom (Figure 11), probably indicating reduced effective permeability. Besides, the time sequence in which alteration minerals deposit, informs on the evolution of the geothermal system. From the study, four mineral alteration zones have been identified. In order of increasing depth, the mineralogical assemblages include (1) the smectite-zeolite zone, (2) the quartz-smectite zone, (3) the epidote-quartz-zone, and (3) the illite -wollastonite-actinolite-quartz zone.

The homogenization temperatures (T_h), recorded in 71 fluid inclusions from two quartz crystals at 1550 m, range from 275 to 320°C. The average 298°C homogenization temperature is higher than the current formation temperature, thus, progressive heating is notable. The inferred hydrothermal alteration temperature is in equilibrium with T_h , and both plot along or close to the boiling point curve. This indicates that the system experienced boiling conditions at some point in its life. Since then, slight cooling might have occurred. The comparison of the measured temperature with the other types of temperatures shows a significant difference. This is attributed to the vast volume of cold water that was pumped into the well during drilling operations. When drilling is completed, this water flows back into the well. It is clear that the well had not yet recovered to formation temperatures when the heating-up temperature logs were executed. It is worth noting that the flow profile shows a positive temperature recovery at shallower depths but, from 1500 m, the profile shows stagnancy in the flow which probably indicates reduced permeability.

Eight permeable zones were inferred from a correlative analysis of temperature logs, circulation losses, increased alteration, formation penetration rates and lithological characteristics. However, critical caution should be emphasized when using circulation losses to infer permeability; other technical measures may cause the losses, for example, cuttings may get stuck in other fractures deep down the wellbore, and later on flushed out suddenly. During aerated drilling, slight disturbances in the air/water equilibrium may appear as a circulation loss even though it is not. The temperature measurements for well MW-13 appear insufficient to aid in finding the exact location of the feed points. Nevertheless, ample correlation of the aforementioned parameters has aided in the location of permeable zones at around 120-352, 550, 700, 900, 1400-1600, 1700, 1850 and 1950 m depth. The main feed zones in the well are believed to be at 1400 to 1600 m. From the flow profile measurements, a rise in temperature to more than 240°C is notable at 1500 to 1850 m (Figure 13). More temperature measurements would be very useful in studying the permeability in well MW-13, which, in turn, would aid in updating the geothermal conceptual model for Menengai field.

An attempt to compare Menengai and Olkaria volcanic systems showed that the two systems closely correlate in terms of geology and geophysics. However, the Olkaria system is 20 ka (Macdonald et al., 2008) and is rhyolite-dominated. On the other hand, the Menengai volcano is trachytic, and is marked by two caldera-forming events, occurring 29 ka and 8 ka ago, respectively (Leat et al., 1984; Leat, 1991;

Macdonald et al., 2011). Thus, it becomes critical to evaluate which system is younger/older. Heat sources are present at about 6 km in both systems (Simiyu, 1999; Simiyu and Keller, 1997; Wamalwa, 2011). Interestingly, high-temperature clays (illite and chlorite) appear in Olkaria wells, for example in wells OW-902, OW-903, OW-39A and OW-912B, at significantly shallower depths than that observed in Menengai in wells MW-13, MW-06, MW-08 and MW-11, as illustrated in Figure 16. Therefore, the other critical question is whether the different ages of the two geothermal systems is responsible for the variations noted in the clay alteration mineralogy. Other probable reasons may be differences in the permeability of the two fields.

9. CONCLUSIONS

The following conclusions can be drawn from the comprehensive study of well MW-13 samples:

- 1) The lithology is composed of four different rock units, namely trachyte, tuff, pyroclastics and syenite; trachyte is the most dominant. The lithology closely relates to that of previously studied wells. A tuff marker horizon was encountered at around 450 m;
- 2) The shallow section of the well is characterized by low-temperature hydrothermal alteration minerals which evolved to form high-temperature ones at greater depths. The occurrence of sulphides in the well signifies permeability;
- 3) Four alteration zones, based on mineralogical assemblages, were identified. They include (1) the smectite-zeolite zone, (2) the quartz-smectite zone, (3) the epidote-quartz-zone, and (3) the illite -wollastonite-actinolite-quartz zone. The uppermost 30 m section is unaltered;
- 4) The inferred alteration temperature and homogenization temperature plot along the boiling point curve. The system was in boiling conditions at some point in time, and slight cooling may have occurred. The measured temperatures do not reflect the current formation temperature;
- 5) Eight permeable zones have been identified; the main feed zone is at 1400 m. The feed zones include 120-352, 550, 700, 900, 1400-1600, 1700, 1850 and 1950 m. The main sources of permeability are faults and lithological contacts; and
- 6) High-temperature clays first appear at shallower depths in Olkaria wells than in Menengai wells. It is highly suspected that the different ages of the two systems are accountable for the differences noted.

ACKNOWLEDGEMENTS

I am genuinely grateful to UNU-GTP and the Government of Iceland for giving me a chance to attend this noble course and for financing it. My very heart-felt appreciation goes to the UNU Geothermal Training Programme staff, Mr. Lúdvík S. Georgsson, Mr. Ingimar Gudni Haraldsson, Ms. Málfríður Ómarsdóttir, Ms. Maria S. Guðjónsdóttir, Mr. Markús A.G. Wilde, Ms. Thórhildur Ísberg and Rósa for their commitment and unquestionable support till the end of this project work; I have learned so much from your high-level spirit of teamwork and excellence.

To my advisors, Dr. Björn S. Hardarson, Dr. Hjalti Franzson, Ms. Helga Margrét Helgadóttir, Ms. Sveinborg Hlíf Gunnarsdóttir, and Saeunn, Sigurdur, Signý, Magnus, and the entire Iceland GeoSurvey (ÍSOR) staff: truly, thank you very much for your indisputable guidance throughout, amidst your busy schedules; your level of professionalism and patience with me during the training is totally incredible.

I must frankly acknowledge my employer, Geothermal Development Company (GDC) and, in particular, the Chief Executive Officer, Dr. Silas Simiyu, for nominating and granting me permission to attend this dynamic and informative course; this can never be a waste, I am a more equipped geothermist.

My most profound gratefulness goes to my caring family and friends back home in Kenya for their reassurance and prayers, and for being tolerant of my absence. To my charming husband, Daniel, I am forever indebted to you for believing in me and encouraging me to go for this course; you are so resilient, kind and influential, you have a big room in my heart.

2014 UNU Fellows, you are an awesome company that has kept me going strong. For the light moments and ideas we shared, I say a big thank you. To the Borehole Geology Class 2014, yours is a more exceptional case; together we endured and the special harmony we had is outstanding. Words can never be enough to thank you all.

To my working colleagues back in Kenya, I am also grateful for according me great support, encouragement and advice in various aspects. Just to mention a few, Lucy, Loice, Jeremy and Gerald, you are wonderful guys in my life.

Lastly, I would not have made it were it not for God's divine mercies and sufficient grace, He has been, and forever will be, my supreme source of strength, to Him be all the glory.

REFERENCES

- Ali Kassim, M., Carmignani, L., Conti, P., and Fantozzi, P.L., 2002: Geology of the Mesozoic-Tertiary sedimentary basins in southwestern Somalia. *J. African Earth Sciences* 34, 3-20.
- Baker, B.H., and Wohlenberg, J., 1971: Structural evolution of the Kenya Rift Valley. *Nature*, 229, 538-542.
- Baker, B.H., Mitchell, J.G., and Williams, L.A.J., 1988: Stratigraphy, geochronology and volcano-tectonic evolution of the Kedong-Naivasha-Kinangop region, Gregory Rift Valley, Kenya. *J. Geol. Soc. London*, 145, 107-116.
- BGR, 2009: Geothermal exploration at Menengai-Ol'banita prospect. BGR, Germany, website: www.bgr.bund.de.
- Bosworth, W., Lambiase, J., and Keisler, R., 1986: A new look at Gregory's Rift: The structural style of continental rifting. *Eos*, 67, 577-583.
- Chorowicz, J., 2005: The East African Rift System. *J. African Earth Sciences*, 43, 379-410.
- Crossley, R., 1979: The Cenozoic stratigraphy and structure of the western part of the rift valley in southern Kenya. *J. Geol. Soc. London*, 136, 393-405.
- Dixey, F., 1946: Erosion and tectonics in the east African system. *Quart. J. Geol. Soc. London*, 102, 339-388.
- Franzson, H., 2014: *Petrographic analysis of hydrothermal minerals in thermal reservoirs*. UNU-GTP, Iceland, unpubl. lecture notes.
- GDC, 2010: *Menengai geothermal prospect, an investigation for its geothermal potential*. GDC, Nakuru, Kenya, Geothermal Resource Assessment Project, internal report.
- GDC, 2013a: *Borehole geological report of well MW-01*. GDC, Nakuru, Kenya, internal report, 16 pp.
- GDC, 2013b: *MW-13, preliminary discharge test report*. GDC, Nakuru, Kenya, internal report, 1 pp.

Geotermica Italiana Srl., 1987: *Geothermal reconnaissance survey in the Menengai-Bogoria area of the Kenya Rift Valley*. UN(DTCD)/Government of Kenya, report.

Gichira, J.M., 2012: Joint 1D inversion of MT and TEM data from Menengai geothermal field, Kenya. Report 11 in: *Geothermal training in Iceland 2011*. UNU-GTP, Iceland, 137-167.

Guiraud, R., and Bosworth, W., 1999: Phanerozoic geodynamic evolution of north-eastern Africa and the north-western Arabian platform. *Tectonophysics*, 315, 73–108.

Guiraud, R., Bosworth, W., Thierry, J., and Delplanque, A., 2005: Phanerozoic geological evolution of northern and central Africa: an overview. *J. African Sciences*, 43, 83-143.

Harvey, C., and Browne, P., 2000: Mixed-layer clays in geothermal systems and their effectiveness as mineral geothermometers. *Proceedings of the World Geothermal Congress 2000, Kyushu-Tohoku, Japan*, 1201-1205.

Hetzel, R., and Strecker, M.R., 1994: Late Mozambique belt structures in western Kenya and their influence on the evolution of the Cenozoic Kenya Rift. *J. Structural Geology*, 16-2, 189-201.

Holwell, D.A., Abraham-James, T., Keays, R.R., and Boyce, A.J., 2012: The nature and genesis of marginal Cu–PGE–Au sulfide mineralisation in Paleogene Macrodykes of the Kangerlussuaq region, East Greenland. *Miner. Deposita*, 47, 3-21.

Jones, W.B., 1975: *The geology of the Londiani area of the Kenya Rift Valley*. Univ. of London, UK, PhD thesis, ?? pp.

Jones, W.B., 1985: Discussion on geological evolution of trachytic caldera and volcanology of Menengai volcano, Rift Valley, Kenya. *J. Geol. Soc. London*, 142, 711-712.

Jones, W.B., and Lippard, S.J., 1979: New age determination and geology of Kenya rift – Kavirondo rift junction, west Kenya. *J. Geol. Soc. London*, 136, 63 pp.

KenGen, 2004: *Menengai volcano: Investigations for its geothermal potential*. KenGen, Kenya, Geothermal Resource Assessment Project, unpubl. report.

Kipchumba, J. L., 2013: Borehole geology and hydrothermal alteration of wells MW-08 and MW-11, Menengai geothermal field, Kenya. Report 10 in: *Geothermal training in Iceland 2013*. UNU-GTP, Iceland, 143-176.

Kipng'ok, J., 2011: Fluid chemistry, feed zones and boiling in the first geothermal exploration well at Menengai, Kenya. Report 15 in: *Geothermal training in Iceland 2011*. UNU-GTP, Iceland, 281-302.

Kristmannsdóttir, H., and Tómasson, J., 1978: Zeolite zones in geothermal areas in Iceland. In: Sand, L.B., and Mumpton (editors), *Natural zeolites, occurrence, properties, use*. Pergamon Press Ltd., Oxford, 277-284.

Lagat, J.K., 2004: *Geology, hydrothermal alteration and fluid inclusion studies of the Olkaria Domes geothermal field, Kenya*. University of Iceland, MSc thesis, UNU-GTP, Iceland, report 1, 79 pp.

Leach, T.M., and Muchemi G.G., 1987: Geology and hydrothermal alteration of the North and West exploration wells in the Olkaria geothermal field, Kenya. *Proceedings of the 9th New Zealand Geothermal Workshop*, Geothermal Institute, Auckland, 187-192.

Leat, P.T., 1983: *The structural and geochemical evolution of Menengai caldera volcano, Kenya Rift*

Valley. University of Lancaster, UK, PhD thesis, 482 pp.

Leat, P.T., 1984: Geological evolution of the trachytic caldera volcano Menengai, Kenya Rift Valley. *J. Geol. Soc. London*, 141, 1057-1069.

Leat, P.T., 1991: Volcanological development of Nakuru area of the Kenyan Rift Valley. *J. Afric. Earth Sci.*, 13, 483-498.

Leat, P.T., MacDonald, R., and Smith, R.L., 1984: Geochemical evolution of the Menengai caldera volcano, Kenya. *J. Geophys. Res.*, 89, 8571-8592.

Lopeyok, T.P., 2013: Borehole geology and hydrothermal mineralization of wells MW-09 and MW-11, Menengai geothermal field, Kenya. Report 15 in: *Geothermal training in Iceland 2013*. UNU-GTP, Iceland, 289-324.

Lynne, B.Y., Campbell, K.A., Perry, R.S., Browne, P.R.L., and Moore, J.N., 2006. Acceleration of sinter diagenesis in an active fumarole, Taupo volcanic zone, New Zealand. *Geology*, 34, 749-752.

MacDonald, R., 2003: Magmatism of the Kenya Rift Valley: a review. *Earth sciences*, 93, 239-253.

MacDonald, R., Bagiński, B., Leat, P.T., White, J.C., and Dzierżanowski, P., 2011: Mineral stability in peralkaline silicic rocks: information from trachytes of the Menengai volcano, Kenya. *Lithos*, 125, 553–568.

MacDonald, R., Belkin, H.E., Fitton, J.G., Rogers, N.W., Nejbert, K., Tindle, A.G., and Marshall, A.S., 2008: The roles of fractional crystallization, magma mixing, crystal mush remobilization and volatile melt interactions in the genesis of a young basalt - peralkaline rhyolite suite, the Greater Olkaria volcanic complex, Kenya Rift Valley. *J. Petrology*, 49, 1520-1530.

Malimo, S.J., 2009: Interpretation of geochemical well test data for wells OW-903B, OW-904B and OW-909, Olkaria Domes field, Kenya. Report 17 in: *Geothermal training in Iceland 2009*. UNU-GTP, Iceland, 336-337.

Mariita, O., and Keller, G., 2007: An integrated geophysical study of the northern Kenya Rift, Kenya. *J. African Earth Sciences*, 48, 80-94.

Marks, N., Schiffman, P., Zierenberg, R.A., Franzson, H., and Fridleifsson, G.Ó., 2009: Hydrothermal alteration in the Reykjanes geothermal system: Insights from Iceland deep drilling program well RN-17. *J. Volcanol. & Geoth. Res.*, 189-2010, 172-190.

McCall, G.J.H., 1957: The Menengai caldera, Kenya colony. *Proceedings of the 20th International Geol. Congress, Section 1*, 55-69.

McCall, G.J.H., 1967: *Geology of the Nakuru-Thomson's Falls-Lake Hannington area*. Geological Survey of Kenya, report 78, 122 pp.

Mibei, G., 2012: Geology and hydrothermal alteration of Menengai geothermal field. Case study: Wells MW-04 and MW-05. Report 21 in: *Geothermal training in Iceland 2012*. UNU-GTP, Iceland, 442-448.

Mibei, G.K., and Lagat, J., 2011: Structural controls in Menengai geothermal field. *Proceedings of the Kenya Geothermal Congress 2011, Nairobi, Kenya*, 28-37.

Musonye, X.S., 2012: Borehole geology and alteration mineralogy of well OW-914A, Domes area, Olkaria geothermal field, Central Kenya Rift. Report 23 in: *Geothermal training in Iceland 2012*. UNU-GTP, Iceland, 501-540.

Mwangi, D.W., 2012: Borehole geology and hydrothermal mineralisation of well OW-916, Olkaria Domes geothermal field, Naivasha, Kenya. Report 24: *Geothermal training in Iceland 2012*. UNU-GTP, Iceland, 541-571.

Njathi, D.W., 2012: Borehole geology and hydrothermal mineralisation of well OW-911A, Olkaria Domes geothermal field, Central Kenya Rift Valley. Report 25: *Geothermal training in Iceland 2012*. UNU-GTP, Iceland, 573-600.

Njue, L.M., 2010: Borehole geology and hydrothermal mineralisation of well HE-27, Hellisheidi geothermal field, SW-Iceland. Report 24 in: *Geothermal training in Iceland 2010*. UNU-GTP, Iceland, 493-524.

Okoo, J.A., 2013: Borehole geology and hydrothermal alteration mineralogy of well OW-39A, Olkaria geothermal project, Naivasha, Kenya. Report 24 in: *Geothermal training in Iceland 2013*. UNU-GTP, Iceland, 547-576.

Omenda, P.A., 1998: The geology and structural controls of the Olkaria geothermal system, Kenya. *Geothermics*, 27-1, 125-130.

Otieno, V. and Kubai, R., 2013: Borehole Geology and Hydrothermal Mineralisation of Well OW-37A, Olkaria East Geothermal Field, Kenya. Report 2 in: *Geothermal Training in Kenya 2012 – 2013*, 105 pp.

Reyes, A.G., 2000: *Petrology and mineral alteration in hydrothermal systems. From diagenesis to volcanic catastrophes*. UNU-GTP, Iceland, report 18, 1998, 77 pp.

RockWare, 2007: *LogPlot Program*. RockWare, Inc., USA.

Roedder, E., 1984: *Fluid inclusions*. Mineral. Soc. Am., Rev. Mineral., 12, Washington, DC, 7 pp.

Rogers, N., Macdonald, R., Fitton, G.J., Smith, M., and Barreino, B., 2000: Two mantle plumes beneath the East African rift system: Sr, Nd and Pb isotope evidence from Kenya Rift basalts. *Earth & Planetary Sci. Letters*, 176-3/4, 387-400.

Ronoh, I.J., 2012: Borehole geology and hydrothermal alteration of well OW-912B, Olkaria Geothermal field, Central Kenya Rift Valley. Report 29 in: *Geothermal training in Iceland 2012*. UNU-GTP, Iceland, 695-732.

Saemundsson, K., and Gunnlaugsson, E., 2014: *Icelandic rocks and minerals* (2nd ed.). Forlagið ehf and Reykjavík.

Simiyu, S.M., 1999: Seismic velocity analysis in the Olkaria geothermal field. *Proceedings of the 24th Workshop on Geothermal Reservoir Engineering, Stanford University, Stanford*, 6 pp.

Simiyu, S.M., and Keller, G.R., 1997: Integrated geophysical analysis of the East African plateau from gravity anomalies and recent seismic studies. *Tectonophysics*, 278, 291-314.

Simiyu, S.M., and Keller, G.R., 2001: An integrated geophysical analysis of the upper crust of the southern Kenya Rift. *Geophys. J. Int.* 147, 543-561.

Smith, M., and Mosley, P., 1993: Crustal heterogeneity and basement influence on the development of the Kenya Rift, East Africa. *Tectonics*, 12, 591-606.

Strecker, M.R., and Melnick, D., 2013: *Structural characteristics of Menengai caldera, central Kenya Rift, Republic of Kenya: preliminary assessment of the structural characteristics of Menengai caldera and regions farther north, Nakuru, Kenya*. GDC, Kenya, unpublished report.

Tole, M.P., 1996: Geothermal energy research in Kenya: a review. *J. African Earth Sci.*, 23, 565-575.

Wamalwa, A.M., 2011: *Joint geophysical data analysis for geothermal energy exploration*. University of Texas, El Paso, Tx, PhD thesis, 101 pp.

Vaughan, D.J., 2006: Sulphide mineralogy and geochemistry, vol. 61, description. Mineralogical Society of America., website: www.minsocam.org/msa/rim/Rim61.html.

APPENDIX I: Typical XRD patterns for smectite and illite clay minerals in well MW-13

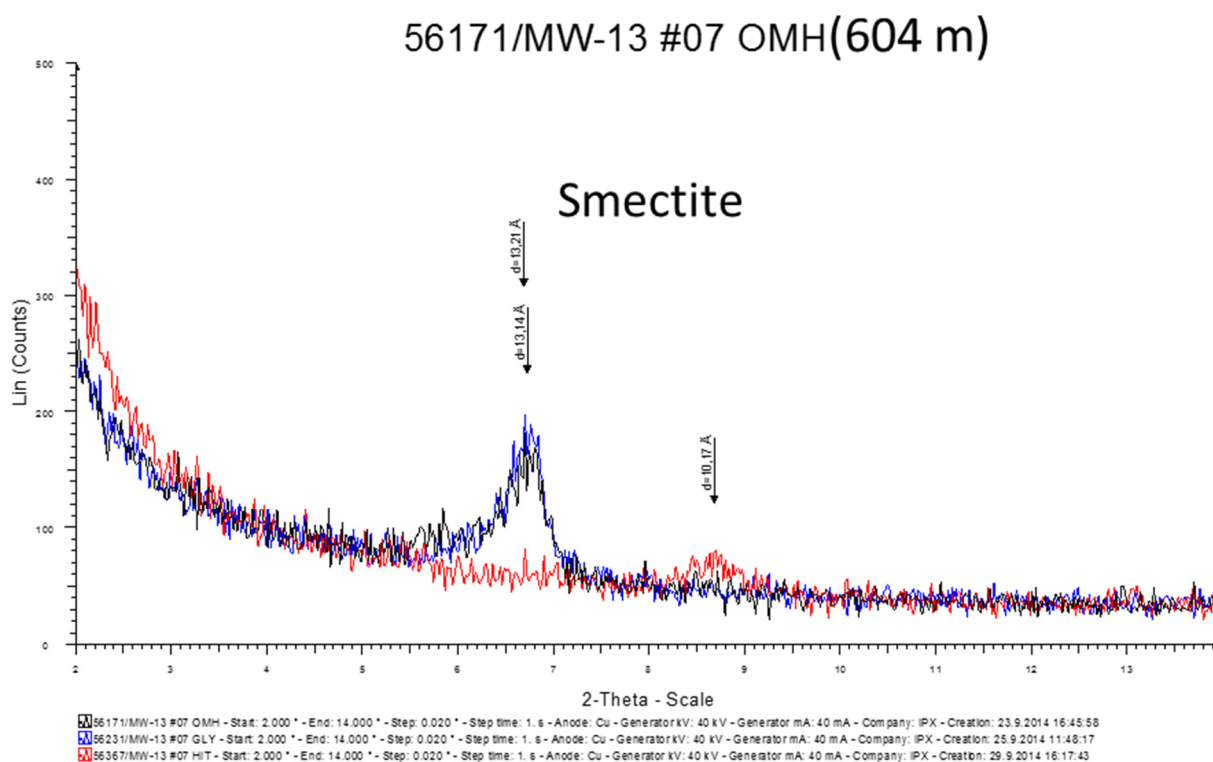


FIGURE 1: Smectite clay at 604 m, well MW-13

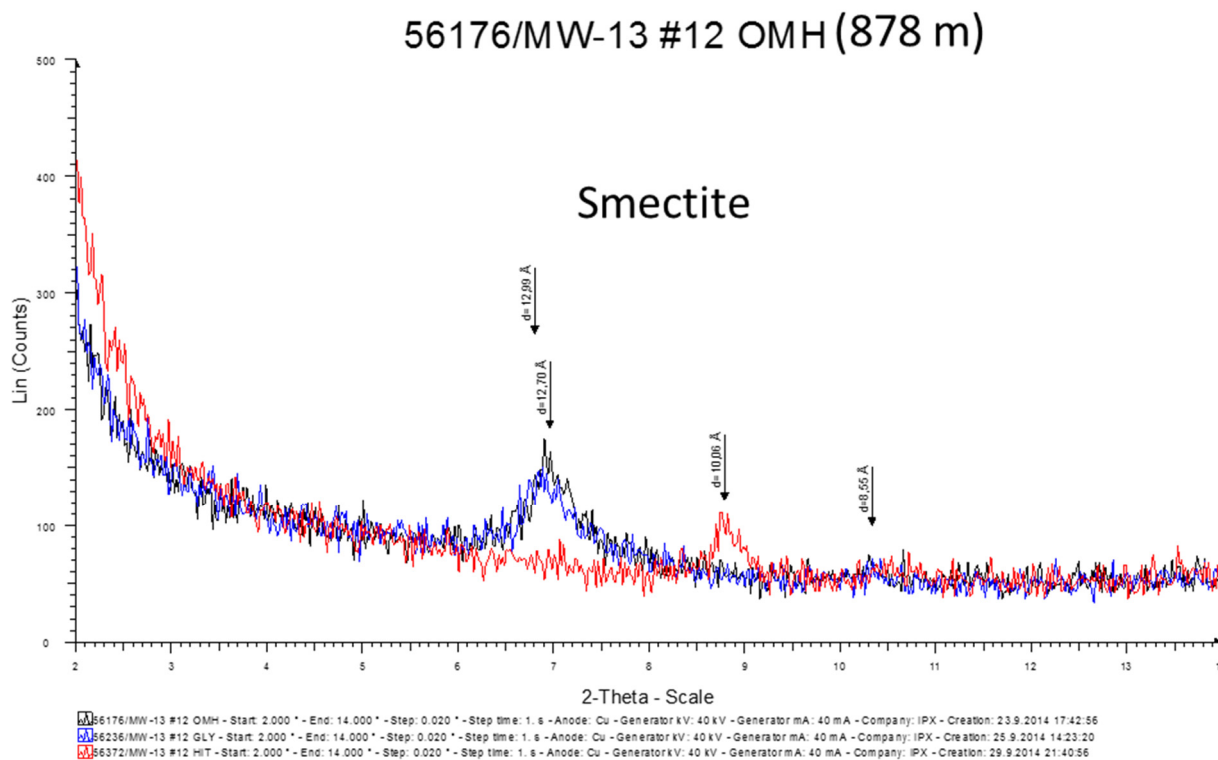


FIGURE 2: Smectite clay at 878 m, well MW-13

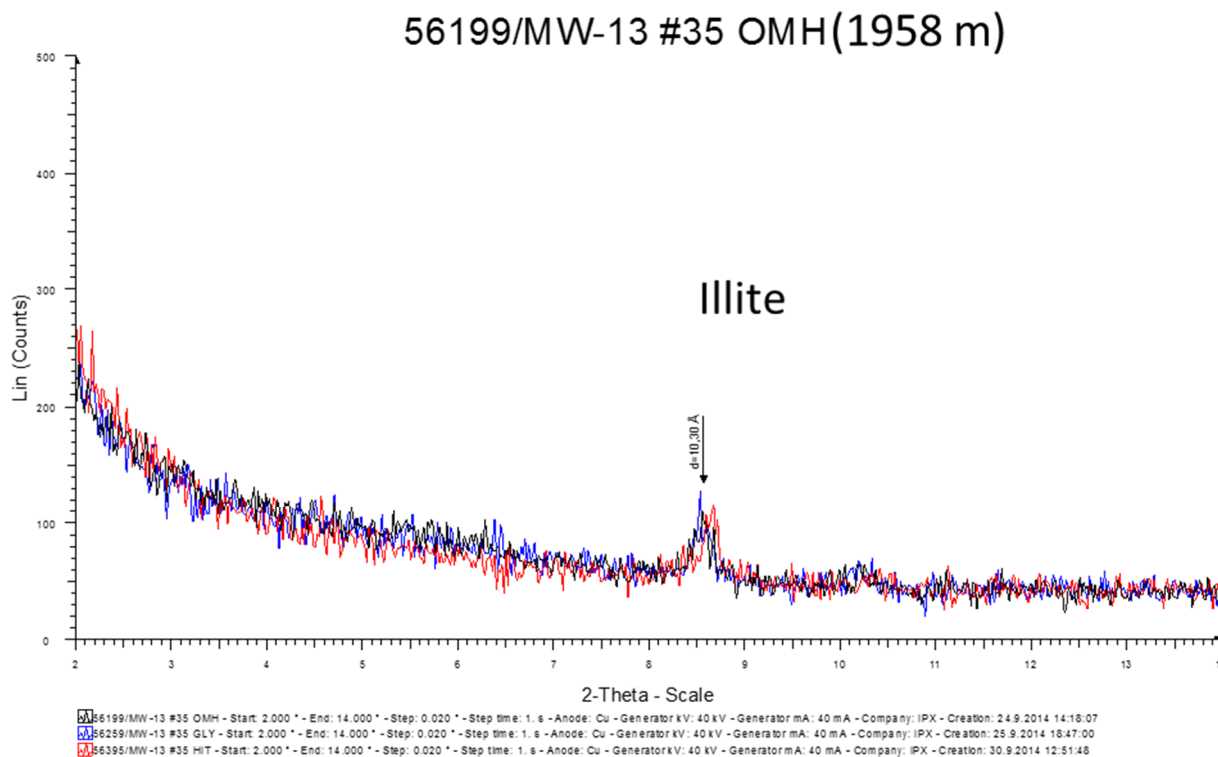


FIGURE 3: Illite clay at 1958 m, well MW-13



UNITED NATIONS
UNIVERSITY

UNU-GTP

Geothermal Training Programme

Orkustofnun, Grensasvegur 9,
IS-108 Reykjavik, Iceland

Reports 2014
Number 17

WELL DESIGN, CEMENTING TECHNIQUES AND WELL WORK-OVER TO LAND DEEP PRODUCTION CASINGS IN THE MENENGAI FIELD

Abraham Wamala Khaemba

Geothermal Development Company, Ltd.

P.O. Box 17700-20100

Nakuru

KENYA

akhaemba@gdc.co.ke

ABSTRACT

Drilling has been ongoing at Menengai high temperature field since 2011. The wells are of regular well design with a 20" surface casing set at 60-70 m, 13 $\frac{3}{8}$ " anchor casing set at about 400 m depth and 9 $\frac{5}{8}$ " production casing set at between 800-1400 m. The intent is to drill the wells to a total depth of 2500-3000 m, with slotted 7" liners run to the bottom. All the casings used are grade K55, with threaded couplings.

Data from offset wells drilled earlier have helped design the depth of the production casing in order to avoid cold inflows into the wells. Wells located at the centre of the field, which is at a higher elevation, have production casings set at about 850 m, while the production casings for other wells have been designed to be set deeper, down to 1400 m.

With a good number of wells at the Menengai field having the production casing being set at 1400 m, this paper looks at: designing wells with a 9 $\frac{5}{8}$ " K55 production casing, slurry design and the most effective method for cementing the casings. Cementing methods that will be discussed include cementing with a cement head and plugs, two stage cementing, cementing with C-Flex RPL from the peak using the inner string method, reverse circulation cementing with an inner string and flap gate valve collar, and foam cementing.

The paper looks at a number of wells which have already been completed. Pressure and temperature logs are analysed as well as the borehole geology to identify the cold inflow zones in wells already drilled. The remedial mechanisms available for sealing off the cold zones in completed wells are then researched and the most effective method to be applied at the Menengai field identified. The methods include use of External casing packer (ECP) and tie back design.

1. INTRODUCTION

This paper will use data from the first twenty wells drilled at Menengai. All the wells are vertical and of standard size.

The design of Menengai wells, the drilling fluid program and the geology are shown in Figure 1. The wells are designed as follows:

- The conductor casing of diameter 30" is driven to ground at about 3 m.
- A 26" diameter hole is drilled to 80 m, then cased with 20" surface casing and cemented back to the surface.
- A 17½" diameter hole is drilled to a depth of 400 m. The 13⅜" anchor casing is run and cemented back to the surface.
- A 12¼" diameter hole is drilled to between 800-1400 m; the 9-5/8" production casing is run and cemented back to surface.
- An 8½" production section is drilled to TD (total depth) of 2500-3000 m. A slotted 7" liner is then placed at the bottom of the 9 5/8" casing with a liner hanger which stretches down to the bottom of the production section.

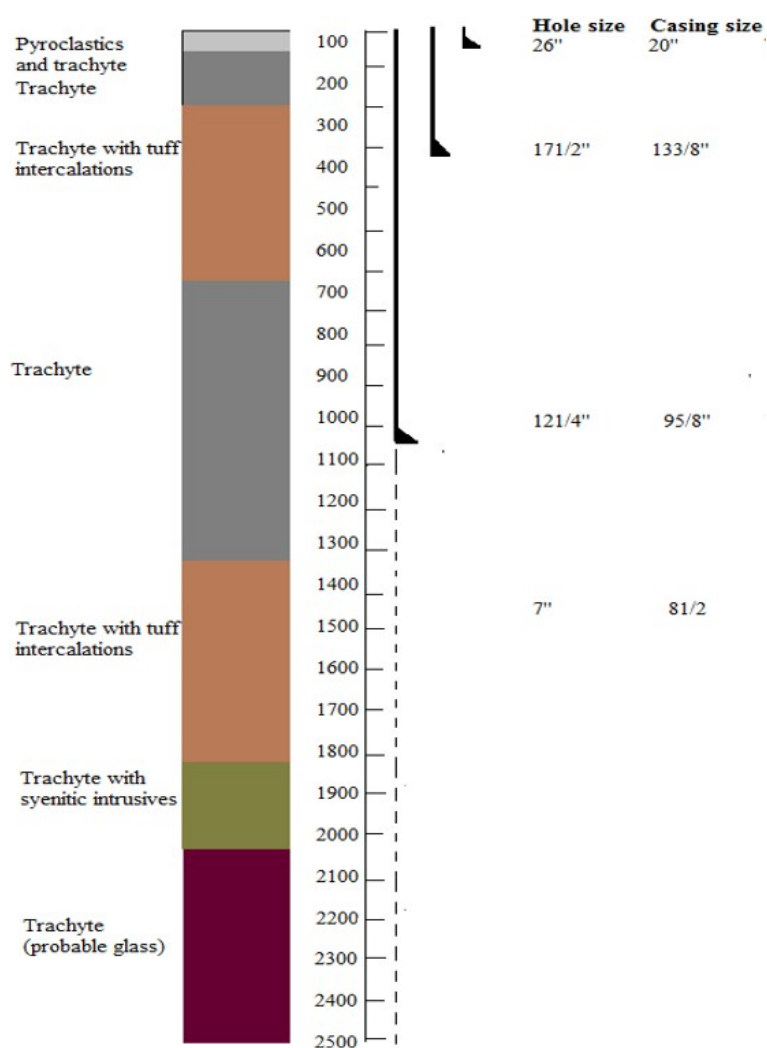


FIGURE 1: Menengai well cross-section with expected geology

The location of wells that have already been drilled in Menengai is shown on the geological map in Figure 2. The Menengai caldera is an elliptical depression with minor and major axes measuring about 11.5 km and 7.5 km, respectively. As per Mungania (2004), the circular rim of the caldera ring fault is well preserved with a vertical cliff at some places measuring up to about 400 m. The ring structure has only been disturbed by the Solai graben faults on the NE end and one fracture at the SSW end. The caldera floor is covered with post caldera lavas such that it is not possible to estimate the collapse depth or any structures that may mark the caldera floor. However, most of the caldera infill lavas are fissure eruptions that prefer fracture openings. The floor of the Menengai geothermal prospect area depicts extensional tectonics with the main trough trending N-S north of Menengai and NNW-SSE for the section south of Menengai. This sharp trend change is associated with the extent of Cambrian craton/orogenic belt contacts.

Wells located at the center of the field have their production casing depth between 800 m and 1100 m (Table 1). In most of these wells the casing has been sufficient to isolate cold zones. Wells drilled on the edge of the field have a deeper production casing set, from 1100 m to 1400 m, to isolate cold zones which could be as deep as around 1300 m.

The presence of cold zones below the production casing shoe indicates that the production casing has been set at a shallow depth.

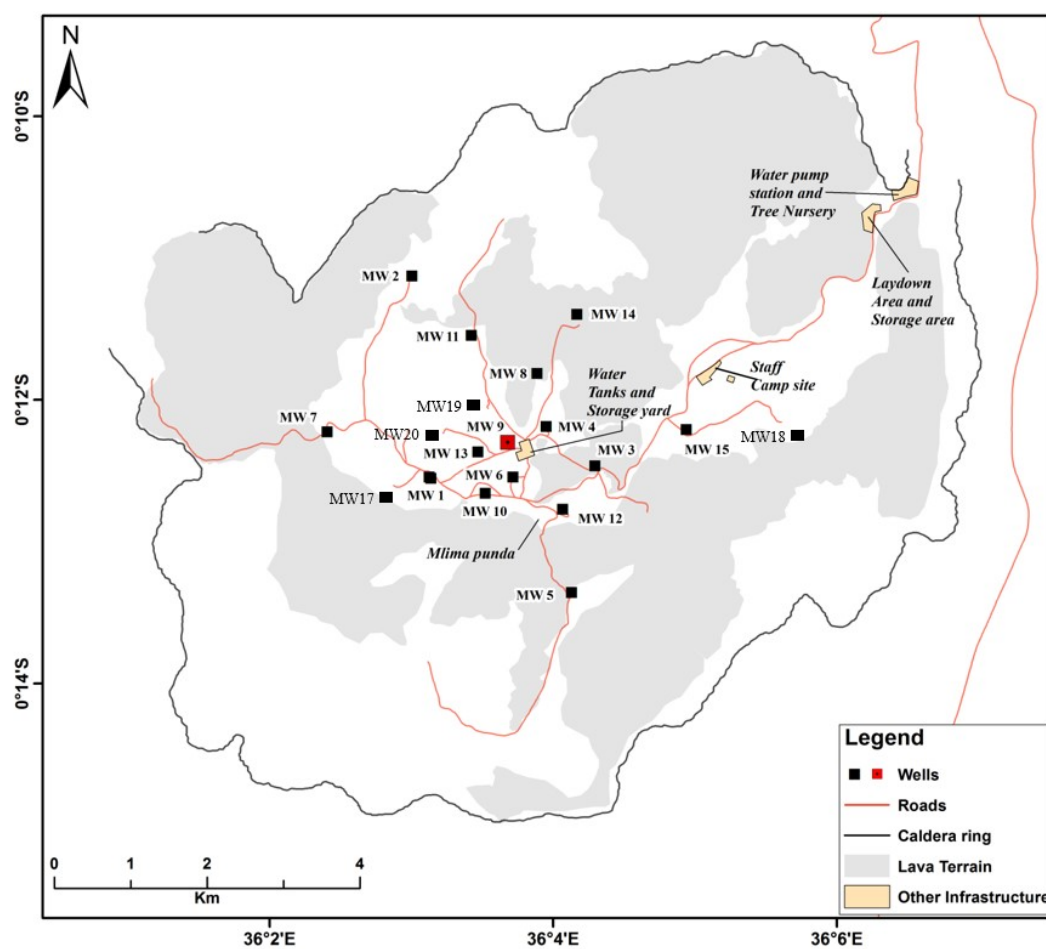


FIGURE 2: Map of Menengai showing drilled wells

TABLE 1: Wells data showing location, production casing depth and total drilled depth

Well	Location			Production casing depth (m)	Depth (m)
	Easting	Northing	Elevation (m)		
MW-01	171847	9977684.9	2064	842	2206
MW-02	171599.63	9979477.57	1898	802.04	3200
MW-03	177332	9977854.9	2032	1096.46	2117
MW-04	177331.4	997607	2085	1105.66	2096
MW-06	172853	997676.1	2095	1100.59	2202.96
MW-07	170488.1	9977450.9	1924	1179	2118
MW-08	173231.3	9978225.3	2015	928.05	2355
MW-09	172848	9977442.1	2105	867	2088
MW-12	172433.5	9976892.7	2106	854.5	2054.15
MW-11	172374	997536.1	1993	888.29	1842.37
MW-05A	173688	99777481	2052	862.64	2095.65
MW-15	175197.39	99777481.5	1959	946.27	1679.62
MW-13	172464	9977193	2081	856.34	2012.11
MW-16	171196	9978355	1965	1167.03	2414
MW-17	171275	9975756	2060	1004.57	2218.17
MW-19	172629	9977753	2085	847	2501.4
MW-20	172017	9977442	2105	1199.2	2461
MW-21	171473.52	9977800	2131.4	1302.85	2730
MW-22	172080	997780.79	2055	1329	2762
MW-10A	172016.79	9977442.1	2085	845	2161.45

2. LITERATURE REVIEW

2.1 Well design

Conditions to consider while designing wells include: sub surface conditions to be encountered, equipment to be used, material performance and the recognition of drilling practices needed to ensure performance. Design steps necessary to drill a deep well safely include:

- I. Taking geological and reservoir engineering advice on likely sub surface rock and fluid properties;
- II. Determining depths for casing and well completion;
- III. Selecting casing diameters, thicknesses, cementing materials and cementing programs;
- IV. Deciding on drilling fluids, drill string assemblies and well heads; and
- V. Nominating necessary equipment, tools, materials, support facilities and site requirements.

Particular geological information required for well design include:

- I. Rock type or formation, and the location of any specific stratigraphic marker beds;
- II. Compressive strengths and the degree of consolidation;
- III. Faulting, fracturing and gross permeability; and
- IV. Effects of drilling activities on formation like swelling of water sensitive clays.

The depth of all casings and liners are chosen to ensure safety and to safely contain well conditions from surface operations.

2.2 Casing design

The design of casings should include the effects of pressure and temperature changes that may occur at any time or depth during drilling or operation of the well. For each of the stress regimes, calculations should be done to establish that there is an adequate margin of strength in the casing string at all depths. Casing specifications should be selected or well conditions restricted to ensure that the minimum design factors are met. Information needed for the casing design include: mud weights, formation pressures, fracture gradients, casing seats, casing sizes, directional plans, cement program, temperature profiles and produced fluid chemical composition. Casing strings that are normally run include:

Conductor pipe: Run from the surface to shallow depths to protect near surface unconsolidated formations, seal off shallow water zones, provide protection against shallow gas flows and protect the foundation platform.

Surface casing: Run to prevent caving in of weak formations that are encountered at shallow depths. It should be set in competent rock. It provides protection against shallow blow outs and should be deep enough to support the BOP for drilling to the anchor casing shoe depth. This casing is used to case off poorly consolidated soil and loose material.

Anchor casing: Set in a transition zone, below or above an over pressurized zone to seal off a severe loss zone and protect against problematic formations. This casing protects surface aquifers against contamination during drilling and acts as a second pressure barrier during the life of the well. This casing supports the BOP and later the final production well head. Casing should be deep enough to allow for the well to be killed while drilling to the production casing depth.

Production casing: Run to isolate producing zones and provide reservoir fluid control. The casing is chosen on the basis of the expected depth and the temperatures of fluids to be included and isolated. It conveys steam and water to the surface.

Liner casing: string of casing that does not run to the surface but hangs inside the production casing. Can be slotted or perforated to allow reservoir fluid to flow into the well. Types of liners include: drilling liners, production liners, tie back liner, scab liner, scab tie back liner.

2.3 Casing diameter selection

The inside diameter of the casing should be selected to accommodate:

- Downhole equipment, liners and test gear required to complete the well;
- Drilling tools and fluids to drill the remainder of the well to completion;
- Sufficient annular clearances to run and cement concentric casing strings;
- Use of casing sizes which are standard and readily available on the market; and
- The geothermal fluid that flows to the surface during testing and production.

Note: While drilling the next whole section, it should be possible to achieve acceptable flow velocities inside the casings without high pressure losses. Drift diameters should be larger than the outside diameters of any tools and other equipment to be run through the casings. Casing pipe diameters are selected from API SPEC 5CT which specifies:

- Process of manufacture;
- Chemical composition;
- Mechanical properties;
- Testing procedures;
- Dimensions, weights and lengths;
- Threading and coupling;
- Inspection; and
- Markings.

2.4 Casing depth selection

The depth of production casing is determined by the depth at which fluids from the colder formations need to be isolated from entering the hole. One of the main determinants is the minimum depth for safety reasons. Government regulations at times specify minimum casing depth. From a technical point of view, the four main criteria used are:

- In the *New Zealand code of practice* the criteria is that the pressure from the overburden (soil) at the last casing shoe shall exceed the pressure from a steam filled well. Once the final depth of the well has been decided, hydrostatic pressure for the Boiling point-depth curve (BPDC) is drawn to that depth. Minimum depth of casing according to the (NZS, 1991) method is then found by extending the bottom hole pressure up the well until it intersects the overburden line. This will be the minimum production casing depth. By repeating the procedure, casing depths for the anchor and surface casings can be determined as shown in Figure 3.
- In Iceland, a BPD is assumed for new fields. From well simulation the pressure profile for a flowing well is determined assuming inflow at the bottom. Liquid will immediately be transformed into a

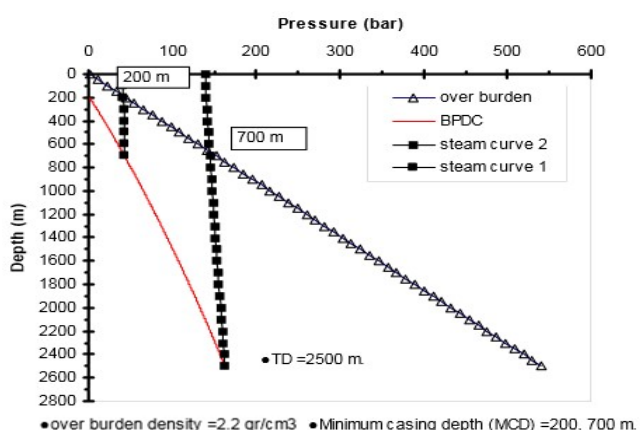


FIGURE 3: The New Zealand method to determine minimum casing depth (Hosseini-Pourazad, 2005)

two phase flow up the well. Minimum casing depth is determined by how long a column of heavy mud 1.4g/cm^3 is required to balance this pressure, shown in Figure 4.

- III. Another criterion is to use the actual downhole temperature and pressure measurements. Typically, fluid turns to two phase flow halfway up the hole. This pressure profile is balanced by pure water only. Pumping only water into the well ensures the drill string can be retrieved, even if there is an underground blow out in the well, as shown in Figure 5.

2.5 Casing materials

Steel casings are selected from API SPEC 5CT or 5L. Where gases are present, casing materials are selected to minimize possibilities of failure by hydrogen embrittlement or by sulphide stress corrosion cracking.

Where axial strength is important, casing joints shall be API buttresses with proven strength in both tension and compression. The casing design should allow for changes in casing properties at elevated temperatures including tensile yield and ultimate strengths. The effects of plastic yield and of stress relaxation with time should be considered when programming casing settings, well operation procedures and workovers.

2.6 Casing service conditions and failure modes

According to Hole (2008), the effects of elevated temperatures on well components such as casings include:

- Change in the length of unrestrained casing;
- Compressive stress due to restriction (cemented casing);
- Reduction in steel strength; and
- Destruction in material competence, particularly flexible seals.

Factors affecting casing loading during different operations are shown in Table 2.

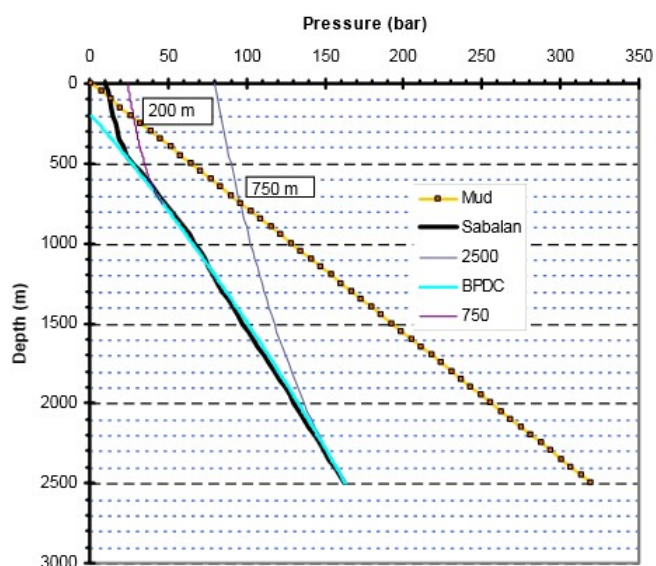


FIGURE 5: Icelandic method of determining casing depth using mud as a blowout preventer (Hossein-Pourazad, 2005)

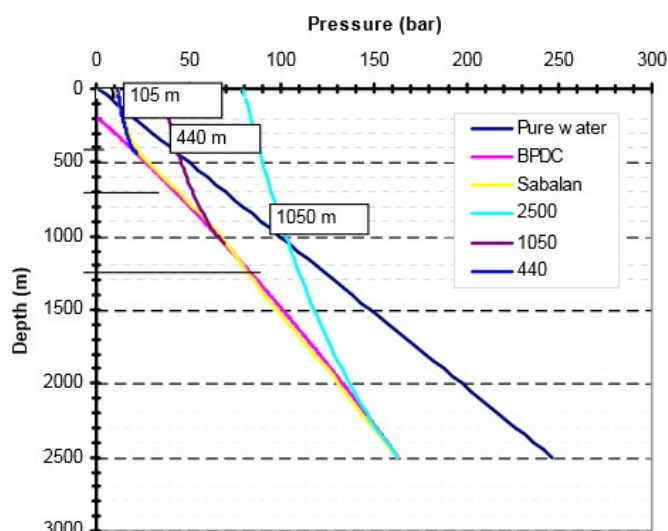


FIGURE 5: Icelandic method to determine the minimum depth of casing using pure water as a blowout preventer (Hossein-Pourazad, 2005)

TABLE 2: Factors affecting casing loading (Southon, 2005)

Stress	Installation	Injection	Production
Collapse	Cement column outside and water inside the casing; Biaxial tension	Biaxial load	Trapped water in uncemented sections in annulus
Burst	Surface pressure to lift cement; Gas accumulation	Injection pressure; Gas accumulation and depression of water table	Well head pressure
Tension/ compression	Cooling load; support of own weight	Axial load due to cooling	Thermal expansion

The different factors lead to primary modes of failure which are divided into axial and radial failures.

2.6.1 Axial stress conditions

Axial stress occurs due to:

- Casing self-weight;
- Temperature effects - Expansion and contraction; and
- Restraint from surrounding cement and connection of well head or hanger at the bottom.

Axial loading before and during cementing

Tensile force at any depth includes the weight of casing in air minus the buoyant effect of any fluid in the well until the annular cement sets:

$$F_p = \left[L_z W_z - (L_z - L_w) \frac{A_p}{n} \right] g \quad (1)$$

where F_p = Tensile force at surface from casing weight;
 L_z = Depth of casing;
 W_z = Unit weight of casing;
 L_w = Depth of water level in the well;
 A_p = Cross-sectional area of pipe;
 n = Mean specific volume of hot fluid; and
 g = Acceleration due to gravity.

The design factor applied is 1.8.

Axial loading after cementing

Thermal stresses can be calculated by imagining that casing expands outwards and then is forced back to its original length by axial compression (using the modulus of elasticity). The total axial stress in a cemented string varies continuously with depth and also with differences in temperature.

The compressive force due to temperature rise when the casing is constrained both longitudinally and laterally by cement is:

$$F_c = C_t [T_2 - T_1] A_p \quad (2)$$

where C_t = $Ea = 200 \times 12 \times 10^{-6} = 2.4 \text{ Mpa}/^\circ\text{C}$;
 F_c = Compressive force due to heating;
 C_t = Thermal stress constant for casing steel;
 T_1 = Neutral temperature (time cement sets);
 T_2 = Maximum expected temperature;
 A_p = Cross-sectional area of pipe;
 E = Modulus of elasticity; and
 a = Coefficient of linear thermal expansion.

The tensile loading, as calculated for the pre-cementing axial loading, remains in the casing after the cement sets up (ignoring stress relaxation with time); the resultant axial force (F_r) after cement set up and heating will be:

$$F_r = F_c - F_p \quad (3)$$

where F_r = Resultant axial force

The design factor utilised will be the minimum compressive strength/resultant compressive strength. The design factor should not be less than 1.2. The minimum strength refers to the lesser strength of the pipe body or connection.

Axial loading with buckling and bending

This section applies to the setting of liners. Liners are either hung in tension using a liner hanger or sit on the bottom of the well; in this case the liner is in compression. The liner is not cemented so it is not radially supported or constrained. The liners are subjected to axial self-weight compression and helical buckling, analysed for extreme fibre compressive stress:

$$F_c = L_z W_p g \left[\frac{1}{A_p} + \left(\frac{D e}{2 L_p} \right) \right] \quad (4)$$

where F_c = Total extreme fibre compressive stress due to axial and bending forces;
 L_z = Length of liner;
 W_p = Nominal unit weight of casing;
 g = Acceleration due to gravity;
 A_p = Cross-sectional area of pipe;
 D = Pipe outside diameter;
 e = Eccentricity (actual hole diameter minus D); and
 L_p = Net moment of inertia of pipe section, allowing for slotting or perforation.

The design factor should not be less than 1.

2.6.2 Radial stress conditions

Radial (Hoop or circumferential) loadings are applied primarily by internal and external fluid pressures. The ability of casings to resist the resultant differential pressures is listed in the API standards. Consideration must be given to:

- The differential pressures that occur before and during cementing operations
- Well fluid pressures in static conditions or when producing or reinjecting

Internal yield – Bursting

The design must ensure that adequate safety margins exist against internal yield or burst from high internal fluid pressure caused by a range of situations during and after cementing. Maximum differential burst pressures usually occur near the casing shoe or stage cementing collar ports and will apply when:

- The casing is filled with high density cement;
- The annulus is either completely filled with water back to the surface or partially filled with water as controlled by formation pressure;
- A restriction within the casing, such as a blocked float valve or a cementing plug which will hold differential pressure.

This is the worst case scenario; the hydrostatic pressure inside the casing at the shoe is caused by cement slurry and applied pressure minus the hydrostatic pressure in the annulus caused by the head of water in the annulus:

$$P_i = [(L_f G_f + P_p) - (L_z G_z)] g \quad (5)$$

where P_i = Maximum differential internal pressure;
 L_f = Height above casing shoe of the cement column;
 G_f = Cement slurry density;
 P_p = Applied pumping pressure;
 L_z = Height above casing shoe of water column in the annulus;
 G_z = Mean density of water in the annulus.

Design factor = Casing internal yield pressure/Differential burst pressure and should not be less than 1.5.

Collapse

The casing design should ensure a sufficient margin of safety against collapse due to external pressure from entrapped liquid expansion, applied pressure during pumping or static pressure from a dense liquid column such as cement slurry. Maximum differential external pressure occurs at the completion of displacement. The annulus is completely filled with high density slurry while the inside of the casing is filled with water.

$$P_z = [(L_z G_z + P_p) - (L_f G_f)]g \quad (6)$$

where P_z = Maximum differential external pressure;
 L_f = Height above casing shoe of water column inside the casing;
 G_f = Mean density of water inside the casing;
 P_p = Applied pumping pressure;
 L_z = Height above casing shoe of cement slurry column in annulus;
 G_z = Mean density of cement slurry in annulus;

The design factor = Casing collapse strength/net external pressure and shall not be less than 1.2.

2.7 Cement slurry design

Casings are cemented the full length to the surface to minimize casing expansion, especially during production. Slurry design depends on well information from logs and drilling operations such as:

- I. Temperature measurements. They provide valuable information for cementing such as in the determination of hole temperature, the location of aquifers and loss zones, the cross flow between aquifers, and locating the top of the cement. Both the bottom hole circulating temperature (BHCT) and bottom hole static temperature (BHST) should be determined. The temperature measured should be similar to conditions at the time of cementing.
- II. Caliper log. Measures well diameter; usually with 4 arms to investigate cavities, the amount of cement needed for cementing, and used in order to determine the location of packers.
- III. Cement bond logs. Done after cementing to determine the top of the cement, cement quality, and bonding of the cement to the casing and hole wall.

The design of cement slurry for a geothermal well considers a careful choice of cements, retarders, fluid loss additives, dispersants, silica flour, extenders, bentonite, mica flakes, friction reducer, calcium chloride, defoamers and mix water. Slurry should also be correctly placed in the annulus. Mainly Portland cement is used in the Menangai area. Slurry properties considered before cementing include:

- I. Slurry density (SG);
- II. Slurry yield (m^3/mT);
- III. Thickening time at bottom hole circulating temperature and bottom hole static temperature;
- IV. Fluid loss (mL);
- V. Free water composition (%);
- VI. Test pressure;
- VII. Compressive strength (MPa); and
- VIII. Filtration.

The slurry properties should be adequately tested in the laboratory to ensure the slurry meets stated conditions. The cement slurry should be monitored and measured during cementing to ensure that the concentrations of solids and additives are maintained as close as possible to design values. Use of high strength microspheres (HSM) is used to make low specific gravity slurries that can withstand high pressures. These slurries maintain low density at high pressures and still develop high compressive strength over a broad temperature range. There are new slurry techniques to improve the quality of slurry such as:

- Fibre reinforced cement slurry - Fibre improves cement toughness as a result of improved interfacial shear strength between the hydrated cement and fibre. Fibre reinforced cements are able to withstand higher tensile stresses than conventional cements and increases tensile strength and strain capacity, flexural and shear strength, ductility, toughness and resistance to cracking induced by thermal effects, shrinkage or other causes.
- Hollow microsphere slurry – Has a low specific gravity and can withstand high pressures. This allows for the use of cement designs that can maintain low density at high pressures and still develop relatively high compressive strength over a broad temperature range.
- Foamed cement slurry – Mixture of cement slurry with foaming agents and gas, usually nitrogen which is injected at high pressure into the base slurry and incorporates a foaming agent and foam stabilizer. The small, fine foam bubbles promote stronger cement walls around the bubbles and promote the setting of cement with increased integrity. The process creates stable lightweight slurry with low permeability and relatively high compressive strength.

2.8 Cement placement methods

2.8.1 Single stage cementing

Single stage cementing is the most common cementing operation used in geothermal drilling. The procedure, as shown in Figure 6, involves:

- Casing string with all the required cementing accessories such as float collar, guide/float shoe and centralizers are lowered in the well, with a few metres of rat hole left at the bottom.
- Cementing head is connected at the top of the casing. Cement plugs should be correctly placed in the cementing head.

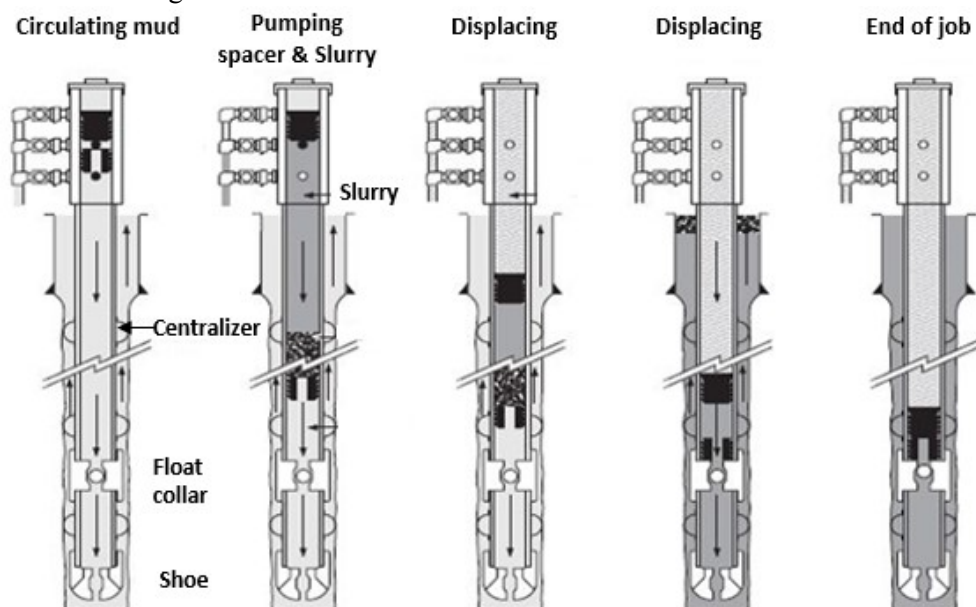


FIGURE 6: Single stage cementing procedure (Bett, 2010)

- The casing is circulated clean before cementing and thoroughly cooled.
- Bottom plug is released to wipe the casing clean and to form a barrier between the spacer and the drilling fluid in the casing, followed by a spacer and then cement slurry. When the bottom plug reaches the float collar, the diaphragm ruptures, allowing the spacer and slurry to flow through the plug, around the shoe, and then up the annulus.
- The top plug is released and displacing fluid is pumped. When the plug reaches the float collar, it lands on the bottom plug and stops the displacement process.

2.8.2 Inner string (Stinger) cementing

Inner string cementing allows large diameter casing to be cemented through the drill pipe or tubing that is inserted and sealed in floating equipment. Inner string cementing requires the installation of a stab in the casing string. A float collar with a sealing sleeve is usually installed two joints from the bottom of the casing string.

Casing is run into the well the normal way; then the inner string is run with a sealing adapter made up on the lower end and stabbed into the floating equipment to provide sealing/bore receptacle for the inner string sealing adapter. After stabbing in, water is circulated around the system to ensure that the stinger and annulus are clear of any debris and to cool down the well. This is followed by a spacer before slurry is pumped. The inner string cementing set up is shown in Figure 7.

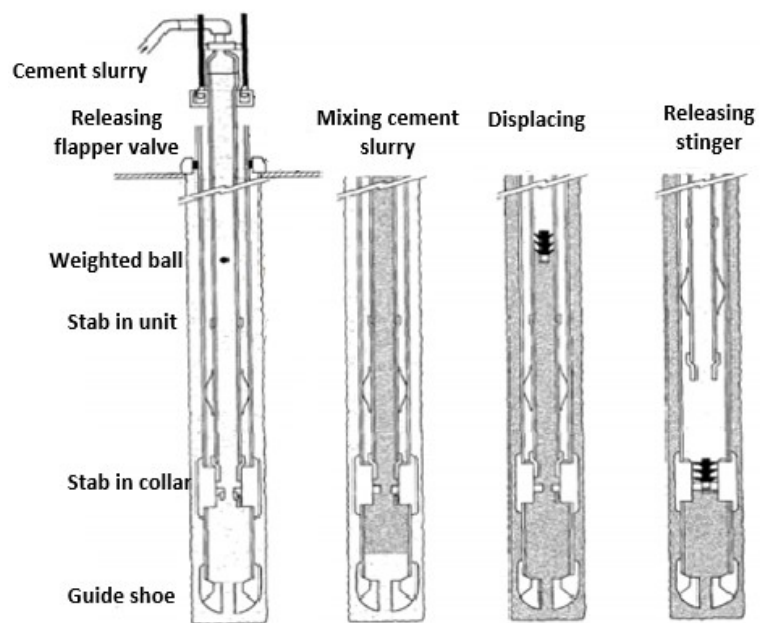


FIGURE 7: Inner string cementing and reverse cementing (Nelson, 1990)

Displacement of the slurry can be done with or without a plug. Inner string cementing has these advantages:

- I. Reduces the risk of cement slurry setting within the casing since cement reaches the annulus much faster than in conventional cementing methods;
- II. Does not require large diameter cementing plugs;
- III. Reduces cement contamination;
- IV. Reduces the amount of cement that has to be drilled out of large diameter casing;
- V. Decreases cementing displacement time; and
- VI. Allows cement slurry to be pumped until returns are obtained on the surface.

2.8.3 Reverse circulation cementing

Reverse circulation cementing is mainly used in well bores where loss of circulation is encountered. Slurry is pumped down the annulus, displacing the drilling fluid back up through the casing. The float equipment, differential fill up equipment and well head equipment must be modified. Reverse circulation can provide the following advantages:

- I. Reduces hydraulic horse power of cement slurry pumping equipment since gravitational flow works in favour of the slurry flow;
- II. Reduces the fluid pressure (Equivalent circulating density-ECD). ECD is calculated at the shoe by combining the effects of hydrostatic pressure and frictional fluid induced pressures in the casing. This is because the heavier and more viscous cement slurry is not circulated back to the surface through the casing;
- III. Enables shorter slurry thickening time since little or no retarders are used; and
- IV. Takes a shorter time to execute since no displacement is required.

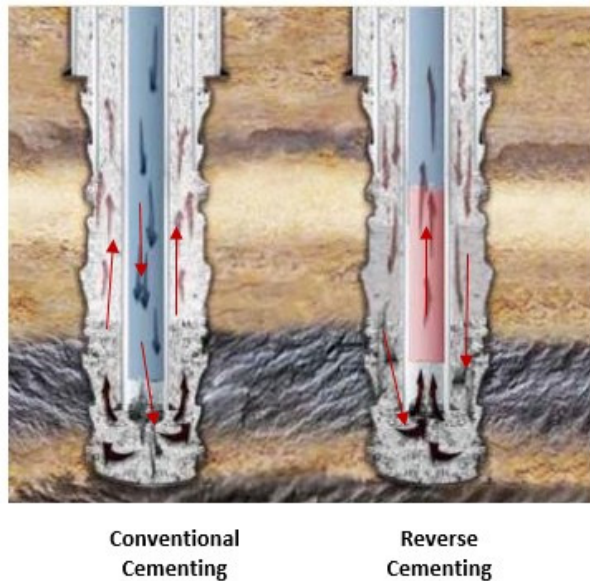


FIGURE 8: Reverse cementing (Nelson, 1990)

The main disadvantage of this method is that it is hard to ensure good cementing at the shoe. Reverse cementing is shown in Figure 8.

2.8.4 Two stage cementing

Two stage cementing makes use of a stage cementing collar in addition to the conventional cementing equipment (guide shoe and float). The procedure for conducting a two stage cementing operation is shown by Nelson (1990).

Cementing the First stage

Mixing and pumping of spacers and slurries during the first stage is similar to a single stage operation. After slurry mixing, the first stage plug is dropped and displaced until a positive indication of its landing in the float occurs. Some operators, when cementing production casings, displace the first stage using two fluids, leaving the casing below the stage collar filled with completion fluid and the upper casing filled with drilling mud. This mud is subsequently used to circulate the hole through the stage collar ports. Some types of stage collars allow the use of first stage wiper plugs.

Cementing Second stage

After the first stage is completed, the opening bomb is dropped and allowed to fall via gravity to the lower seat in the stage collar. Once the bomb is seated, pressure is applied until the retaining pins are sheared, forcing the lower sleeve to move downwards and uncover the ports. Usually a pressure of 1200 to 1500 psi will shear the retaining pins. A sudden drop in surface pressure indicates the opening of the ports. Once the ports of the stage collar have been opened, the well must be circulated until the mud is conditioned for the second stage. For cementing the second stage, spacers and slurries are mixed as in any single stage job. The closing plug is dropped after slurry mixing and is displaced to its seat in the stage collar. After the plug has seated, a minimum of 1500 psi above the second stage displacing pressure is required to close the stage-collar ports. Pressure is released from the casing after the ports are closed. Most second stages of two stage jobs are performed using low density filler slurries to allow circulation to the surface. Tail slurries are rarely used even if an open hole section is to be cemented. For the protection of the weakest part of the casing string, the stage collar is improved by increasing the density of the last portion of the cement slurry. Two stage cementing is shown in Figure 9.

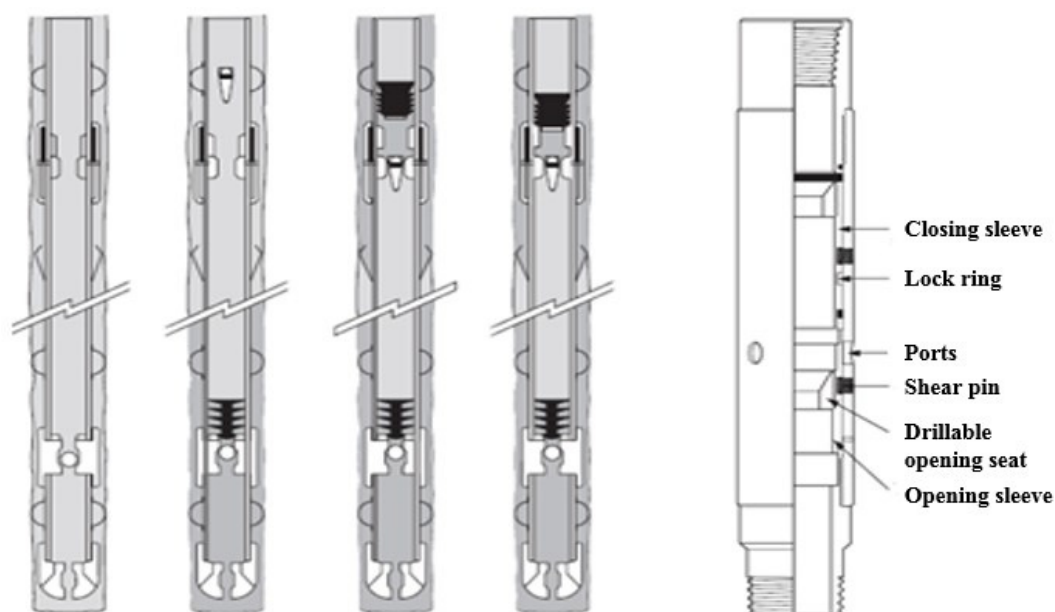


FIGURE 9: Two stage cementing procedure (Bett, 2010)

3. ANALYSIS OF MENENGAI WELLS

From temperature profiles of wells drilled at Menengai, from completion tests, during heat up and after discharge, the temperature along the wells can be noted and feed zones identified. This study takes a look at two wells: Menengai MW02, located on the edge of the field, with a production casing at 802.04 m, and Menengai MW19 at the centre of the field with a production casing at 847 m. The two wells have production casings set at a shallow depth than other wells in the field.

3.1 Menengai MW02

Menengai well MW02 was completed on 1st May 2011. Aquifers in MW02 were observed in zones shown by changes in the temperature logs. In addition, they were also characterised by an increase in circulation losses of drilling fluid, an increased proportion of high-temperature hydrothermal alteration minerals and changes in the penetration rates. Well MW02 encountered aquifers with relatively low temperature ($<80^{\circ}\text{C}$) at 400-600 m and 1100-1300 m. Four aquifers were notable at 500 m ($\sim 75^{\circ}\text{C}$), 1200 m ($\sim 80^{\circ}\text{C}$), 2300 m ($\sim 90^{\circ}\text{C}$) and 3200 m ($\sim 120^{\circ}\text{C}$). Figure 10 shows temperature and pressure plots for well MW02 during heating up after drilling.

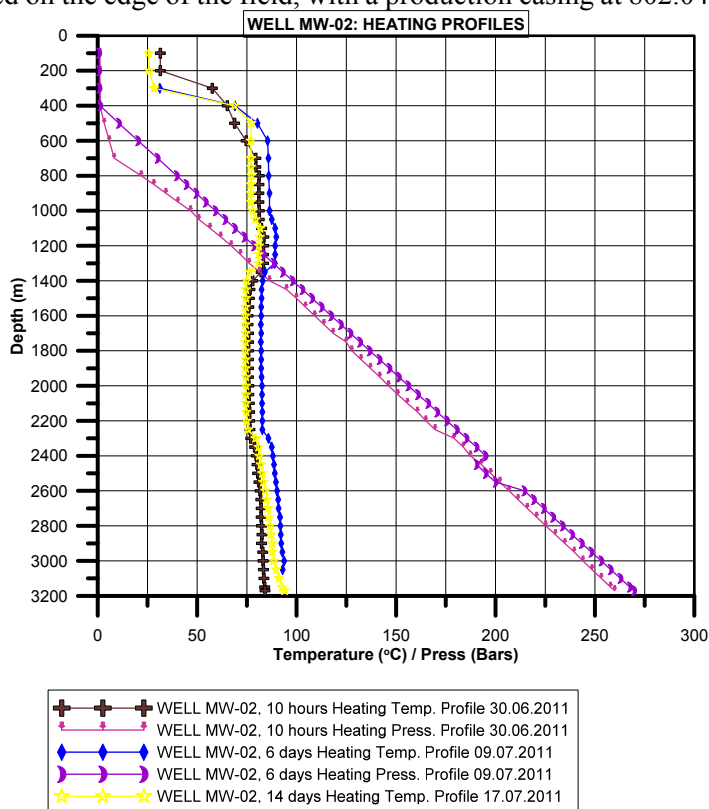


FIGURE 10: Menengai Well MW02 Temperature-pressure profiles

The well is located right at the western promontory fault, almost at the edge of the caldera floor, as shown in Figure 2. The rock formations in the well are heavily fractured and pyritized with partial circulation losses all through the well column. There is a sudden inflow of warm water into the well at 2300 m. There is an increase in temperature at 3100 m, implying a hot geothermal reservoir beneath the massive intrusion.

Temperature logs show an increase at about 1100 m of slightly hotter water flowing into the well. At about 1300 m, cold water flows into the well and, at about 2250 m, hot water (probably only just above 100°C) flows in and mixes with the cold water. At about 3000 m, the water flows out of the well. The rock formation between 1300 and 2250 m seems relatively cold but significantly hotter below 3000 m, according to Njue (2013).

3.2 Menengai well MW19

Menengai well 19 (MW19) was completed on the 12th December 2013. In well MW19, high temperature alteration minerals epidote, wollastonite and actinolite, indicating temperatures of 250°C, appear from a depth of 1464 m. Wollastonite is noted from depths of 1464 m to 1504 m. The well has several feed zones. The upper feed zones are at 500 m, 900 m and 1300 m. These feed zones have a cold zone up to 1300 m, thus the well needed to be cased off and the deeper feed zones in the well utilized. After 14

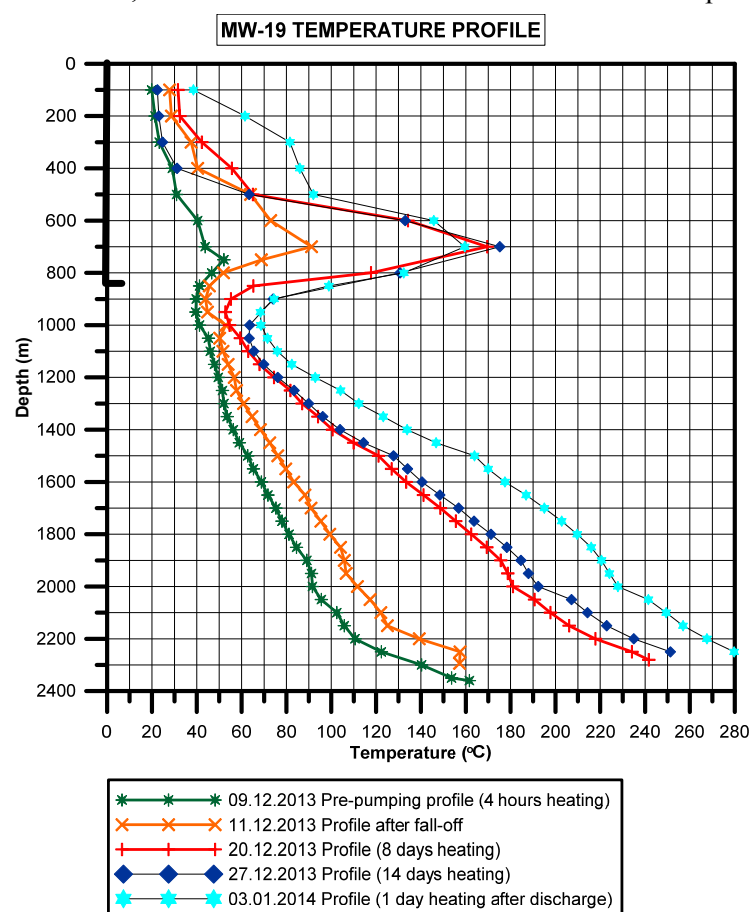


FIGURE 11: Menengai MW19 well profile after drilling

days of heating up, the upper reservoir between 800 m and 1000 m had temperatures up to and above 170°C while, after 1 day of discharge, the temperatures at the bottom of the well reached 280°C, as shown in plots in Figure 11.

Data from the two wells shows the presence of more than one aquifer in the wells. There is an upper aquifer and a lower aquifer with a cold zone between them from 1000-1300 m in both wells. The presence of a cold zone which has not been cased off has had an effect on the production of the wells, resulting in the need to land deep production casings up to a depth of 1400 m and to cement the casing for an effective and durable well (Lopeyok, 2014).

Because of the relatively low temperature in the upper zone, production has led to the precipitation of calcite in some wells, leading to a decrease in production and, hence, to costly workovers.

4. MENENGAI PRODUCTION CASING DESIGN AND CEMENTING

4.1 Casing design calculations

Grade K55 casings are used. K55 casing properties are shown in Table 3, while standard parameters for calculating casing loading are shown in Table 4.

TABLE 3: K55 Casing properties

Casing size (inches)	20	13 $\frac{3}{8}$	13 $\frac{3}{8}$	9 $\frac{5}{8}$	7
Grade	K55	K55	K55	K55	K55
Weight, PPF	94	54.5	68	47	26
Inside diameter, Inches	19.124	12.615	12.415	8.681	6.276
Drift diameter, Inches	18.936	12.459	12.259	8.525	6.151
Collapse, PSI	520	1130	1,950	3,880	4,320
Burst, PSI	2,110	2730	3,450	4,720	4,980
Burst with 1.1 DF PSI	1918	2482	3136	4291	
Tensile, KLBS	1,480	853	1,069	746	415
Thread type	BTC	BTC	BTC	BTC	BTC

TABLE 4: Parameters used to calculate production casing loading

Parameter		Parameter	
Size	9.625 inches	Casing capacity	38.18 l/m
Depth	1400 m	Gravity	9.810665 m/s ²
Casing wall thickness	0.472 inches	Density of water	1 SG (1000 kg/m ³)
Casing weight	47 pounds/foot	Density of cement	1.8 SG (1800 kg/m ³)
Casing grade	API-K55	Thermal stress constant for steel	2.4 Mpa/°C
Collapse resistance	26.8 MPa	Pipe body strength	332 daN * 10 ³
Internal yield	32.5 MPa	Casing cross sectional area	8756 mm ²

Axial loading before and during cementing will be calculated using Equation 1. The worst case theoretical axial load when cementing is when the casing is full of cement and the annulus is full of water.

TABLE 5: Conversion constants

Total axial load = Casing self-weight + Weight of casing
– Buoyancy

For calculations in standard units, the conversion factors are shown in Table 5.

Tensile

Tensile loading during primary cementing, while the casing is full of cement, is found using Equation 1:

$$\text{i.e. } F_p = \left[L_z W_z - (L_z - L_w) \frac{A_p}{n} \right] g \quad (\text{Tensile loading at the surface from casing weight})$$

$$\text{Casing self-weight} = \text{Depth} * \text{Weight} \left(\frac{3.28084}{2.2482014} \right) \text{ daN}$$

$$= 1400 * 47 * 1.4593 = 96,023.10 \text{ daN}$$

$$\text{Weight of cement} = \text{Depth} * \text{Capacity} * \text{Density} = 1400 * 38.19 * 1.8 = 96,238.8 \text{ daN}$$

Conversion factors	
m to feet	3.28084
daN to lbf	2.2482014
kgf to daN	0.9810665
inches to cm	2.54
inches to m	0.0254
N to daN	0.1

$$\text{Buoyancy Force} = \text{Density of Fluid} * \text{Volume displaced (Cross-sectional Area} * \text{Depth)} *$$

$$\text{Acceleration due to gravity} = 1400 * \left[\frac{(9.625 * 0.0254)^2 * 3.142}{4} \right] * 1000 * 0.981 = 64,478.087 \text{ daN}$$

$$\text{Total axial load} = \text{Casing self-weight} + \text{Weight of cement} - \text{Buoyancy}$$

$$= 96,023.10 + 96,238.8 - 64,478.087 = 127,783.813 \text{ daN}$$

K55 casing body yield strength = 332,000 daN (Gabolde and Nguyen, 2014)

$$\text{Safety Factor} = \frac{332,000}{127,783.183} = 2.598$$

With the safety factor at the recommended minimum of 1.8, it is safe to run 9⁵/₈", grade K55, 47 lb/ft. Casing to 1400 was recommended by Hole (2008).

Yield

Internal yield pressure while cementing to 1400 m (Burst) is calculated using Equation 5:

$$\text{The maximum differential pressure} = [(1400 * 1800) - (1400 * 1000)]9.81 = 10.987 \text{ MPa.}$$

Design limit for 9⁵/₈", grade K55, 47 lb/ft. casing is 32.5 MPa (Gabolde and Nguyen, 2014).

$$\text{Safety factor} = \frac{32.5}{10.987} = 2.96, \text{ above the design Factor of Safety as shown in Hole (2008).}$$

Collapse

Collapse during cementing using Equation 5:

The maximum differential pressure = [(1400 * 1000) - (1400 * 1800)]9.81 = -10.987. The pressure could be less depending on pumping pressure while displacing.

Design collapse resistance for 9⁵/₈", grade K55, 47 lb/ft. casing is 26.8 Mpa (Gabolde and Nguyen, 2014).

$$\text{Safety factor} = \frac{26.8}{10.987} = 2.43$$

It is safe to run 9⁵/₈", grade K55, 47 lb/ft. casings to 1400 m, since the factor of safety is above the design factor of safety of 1.2 from Hole (2008).

All the casings have Buttress thread connections. They have a longer thread and coupling run out and the threads are squarer resulting in a stronger connection than the strength of the casing body. The connection is stronger, 445 and 416 *10³ for buttress standard and buttress special clearance, respectively (Gabolde and Nguyen, 2014), thus the connection is safe to run K55, 9⁵/₈", 47 ppf casing to 1400 m. A thread compound should be used to provide a sealing mechanism.

Rig capacity

There are two types of rigs in use at Menengai, the 2,000HP rig with a hook load capacity of 450 tons (Bomco, 2011), and an Atlas Copco rig with a hook load capacity of 91 tons (Atlas Copco, 2011).

K55, 9⁵/₈", 47 lb/ft. casings have a nominal weight of 69.944 kg/m; running the casings to a depth of 1400 m, the total weight of the casings will be 97,921.6 kg. Since the total weight of the casings is beyond the limit of the predator rig, the casings can only be run using the 2,000 HP rigs.

4.2 Effective cementing method

In Menengai only single stage cementing has been used. Casings are run with shoe and float placed one joint off the bottom. The wells are circulated to clear the annulus and cool down the wells before the

cementing lines are pressure tested to 1500 psi (10 MPa). Pre-flush fluid is pumped at 1.00 SG, then the spacer at 1.5 SG. The lead slurry is mixed in the cementing equipment and pumped at about 1.72 SG with the tail slurry being pumped at 1.85 SG. The density is checked using a pressurized mud balance on the cementing unit.

The wiper plug is bumped then displaced with the casing capacity volume. Pressures are recorded while displacing and before bumping the plug. If returns are not received on the surface, the annulus is flushed with water and then the cement top fill is done after 8 hours. Top jobs are done until cement returns are received on the surface. The cementing procedure that has been in use at Menengai is illustrated in Appendix I. Cement bond logging has not been done, but the top of the cement is noted before commencement of drilling the next hole section. Instances have been recorded where the plug is tagged at a specific depth but there is no cement between the plug and the shoe. In Figure 12, the graph shows that in most cases the cementing was not effective since cement was tagged at a greater depth than the expected top of the cement depth. This could be an indication that the cement was not properly displaced.



FIGURE 12: Graph showing comparison of actual top of cement and expected top of cement depths inside the production casing

Using inner string cementing to the loss zone is a more appropriate cementing method. While using single stage cementing, displacing the cement has been a challenge. While displacing the cement in the large diameter casings, in most instances water separates from the cement and free water has been found below the top plug used while displacing the cement. An inner string cementing method is more appropriate since cement is displaced more effectively as the displacement capacity of the drill pipes is a lot less than in the casings, thus we can displace faster. Water should be pumped through the annulus at a constant rate to ensure the loss zone remains open; then cement should be pumped to the loss zone. The primary cementing job should be followed immediately with a backfill targeted to fill up the annulus to the surface while the annular rams on the BOP are closed. The inner string method is more advantageous as it is faster to circulate and cool the well since circulation is done through drill pipes (capacity of 9.05 l/m) (Gabolde and Nguyen, 2014), while in single stage cementing circulation is done through the 9 $\frac{5}{8}$ " casing (capacity of 38.18 l/m) (Gabolde and Nguyen, 2014), which takes more circulation time and has less annular pressure for lifting cuttings that may have dropped below the shoe. Due to the differences in the capacities, it takes shorter time to perform inner string cementing.

Cement test results, as shown in Appendices II and III, confirm that the cement slurry is suitably designed to for cementing deep production casings with high formation static temperatures of $\sim 150^{\circ}\text{C}$.

Cement should be tagged after 6 hours. If the cement level has dropped, the cement should be filled up to the surface by pumping via the kill line.

After the cement has set, a cement bond log should be carried out to evaluate the quality of the cementing job and to ascertain if any remedial work must be done before drilling the next hole section.

5. CASE STUDY OF DEEP PRODUCTION CASINGS

5.1 Krafla geothermal field and the IDDP-1 well

5.1.1 Krafla field

Krafla geothermal field is located within the northeast volcanic zone of Iceland. The Krafla fissure swarm, which is presently active, extends from Tjörnes Fracture Zone in the Öxarfjörður bay in the north and some 100 km to the south. Its width is approximately 5 km but varies considerably along the swarm. The high temperature geothermal field is located within the Krafla caldera, elongated in an EW-NS direction.

Drilling of exploratory wells in Krafla started in 1974. In some of the wells a temperature of 310° C was measured and it was assumed that the temperature of the system was close to the boiling point curve. Two distinct zones exist in Krafla: a lower zone, (1100 – 1300 m to at least 2200 m), is the up flowing zone which feeds the upper zone (extending down to 1100 m depth). The upper zone is water dominated and has a mean temperature of 205°C, whereas the lower zone is a two-phase system with temperatures ranging from 300°C to 350°C. Because of the relatively low temperature in the upper zone, production from this level caused calcite precipitation in the wells. As a result, production in Krafla has mostly been limited to the lower zone (Stefánsson and Steingrímsson, 1980). The first signs of boiling in the wells can be found during the warming up period. Boiling aquifers usually recover faster than other parts of a well and boiling begins in the aquifers in a well. This boiling initiates convection in the well and heats up the column above the boiling aquifer until the temperature aligns to the boiling point curve. Some of the wells, for instance well KJ-11, had two modes of flow. One mode was where only the liquid-dominated zone contributed to the flow, and the other mode was where both zones were active. This contributes to considerable cooling in the well. Well IDDP-1 was designed to tap steam from supercritical geothermal systems for wells with higher temperatures and more pressure for higher electric power output.

5.1.2 IDDP-1 well design

The drill plan for well IDDP-1 is shown in Figure 13 for a standard hole. Actual drilling of the well was done from 2008 to 2009. The surface and intermediate casings were set as per plan. However, a 13³/₈" anchor casing was set at 1957 m instead of the planned 2400 m due to drilling problems like a stuck string, twist offs, unsuccessful fishing attempts and side-tracking 3 times. The well was completed with a cemented 9⁵/₈" sacrificial casing and a 9⁵/₈" slotted liner set a few meters above quenched magma. The well was drilled to 2104 m. It was deemed not feasible to continue drilling well IDDP-1 (Elders and Fridleifsson, 2010).

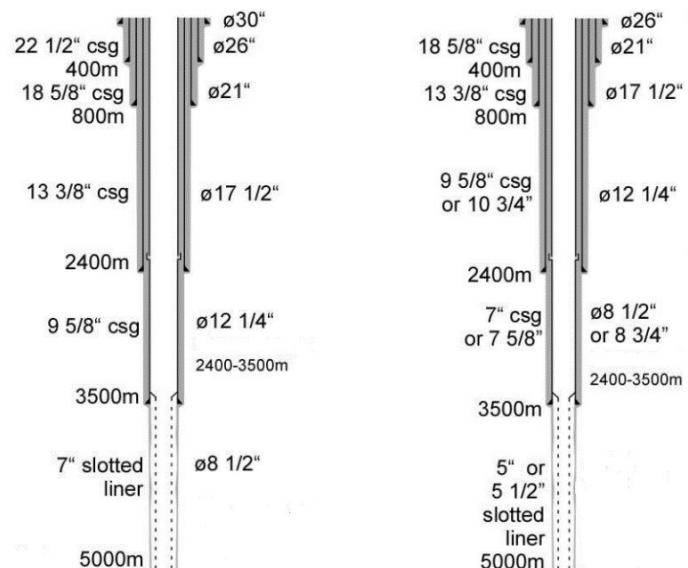


FIGURE13: IDDP-1 initial well design
(Thórhallsson et al., 2010)

5.1.3 IDDP-1 casing design

Casing strings

Two casing programmes of different diameters were evaluated, as shown in Figure 13. The design used casings available in the industry for both the standard hole and slim hole wells.

Design loads

Casings were designed to contain extreme conditions of a flowing well as well as a closed well. Design loads for these casings were calculated. Design factors considered were selected casing depths, highest temperature range and the saturation pressure at the highest temperature.

Internal yield pressure

Internal yield pressure was calculated in accordance with Section 4.1.1 of the API (1994); the findings are shown in Table 6.

TABLE 6: Internal yield pressure and well head shut in pressure

	Units	Well profile A		Well profile B	
Anchor casing	In/lb/ft.	13 ³ / ₈ "/68		10-3/4"	
Production casing	In/lb/ft.		9 ⁵ / ₈ "/47		7 ⁵ / ₈ "/33.7
Internal yield pressure	bar	238	326	278	352
Shut in pressure	bar	221	250/267	221	250/278
Ratio		1.08	1.3/1.22	1.26	1.41/1.27

Collapse pressure

Collapse pressure was calculated in accordance to the collapse pressure of API (1994), depicted in Figure 14. Collapse resistance was plotted as a function of temperature for casing sizes considered for the project. The temperature range for the design was 20-500°C.

Heating or cooling strain

Temperature changes of the casing cause strain (tension or compression) due to hindered thermal expansion. The effects of plastic yield and of stress relaxation with time were considered when setting the casings and for well operation procedures and down hole workovers to ensure thermal cycling was kept to the minimum.

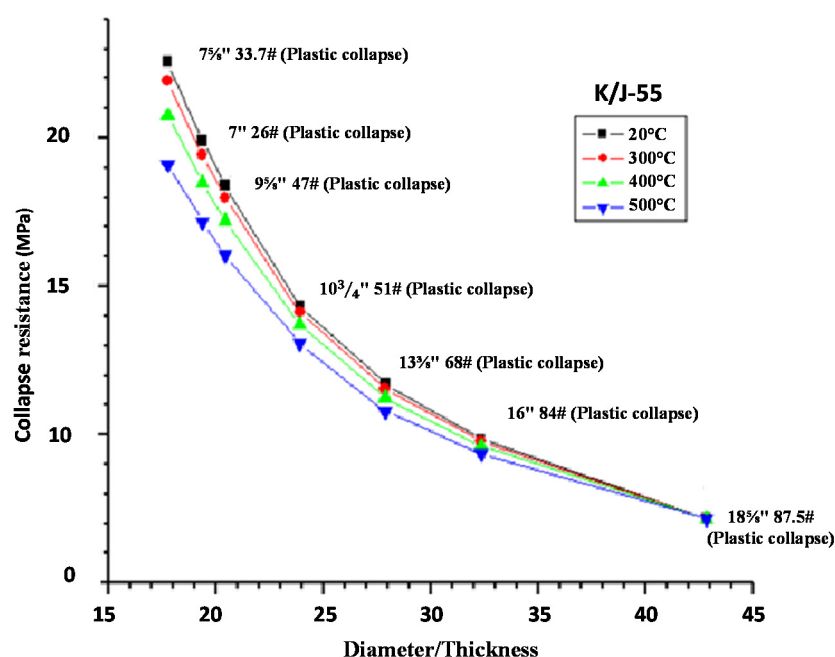


FIGURE 14: Collapse resistance of casing vs Diameter/Thickness ratio and effect of Temperature (Thórhallsson, et al., 2010)

5.1.4 IDDP well cementing

A Peak C-Flex RPL valve was used to carry out cementing but the seals melted due to high temperatures. A C-flex RPL is a sleeve-based cementing valve that allows access to the casing to casing annulus without reducing integrity of the casing string. By installing the C-Flex RPL, casing OD and ID are maintained. When the operation is completed, the C-Flex can be permanently locked in position. Cementing and displacing using a C-flex RPL is shown in Figure 15. The Peak C-Flex RPL is a mechanically operated valve which is operated by using a cementing tool attached to the drill pipe. The cementing tool is equipped with two latching dogs that match the latching profile inside the C-Flex RPL.

When the C-Flex RPL is operated, the cementing tool is latched into the C-Flex RPL and a force of 12-14 tons is set down to the valve, which opens leaving access to the annulus for cementing. Once the operation is done, 6 tons over-pull is applied to the cementing tool and the C-Flex RPL will close. When the valve closes it can be set in a permanent position by adding a force of 45 tons over-pull. The process is illustrated in Figure 14. The temperature rating for the C-Flex RPL is 130°C, but the seal can be changed to a more temperature resistant seal (Thórhallsson, et al., 2010). During cementing of the IDDP wells, the seals melted due to the very high temperatures.

Well IDDP-1 was drilled down into molten magma; it was possible to set a steel casing in the bottom; superheated, high pressure steam blew for months at temperatures exceeding 450°C.

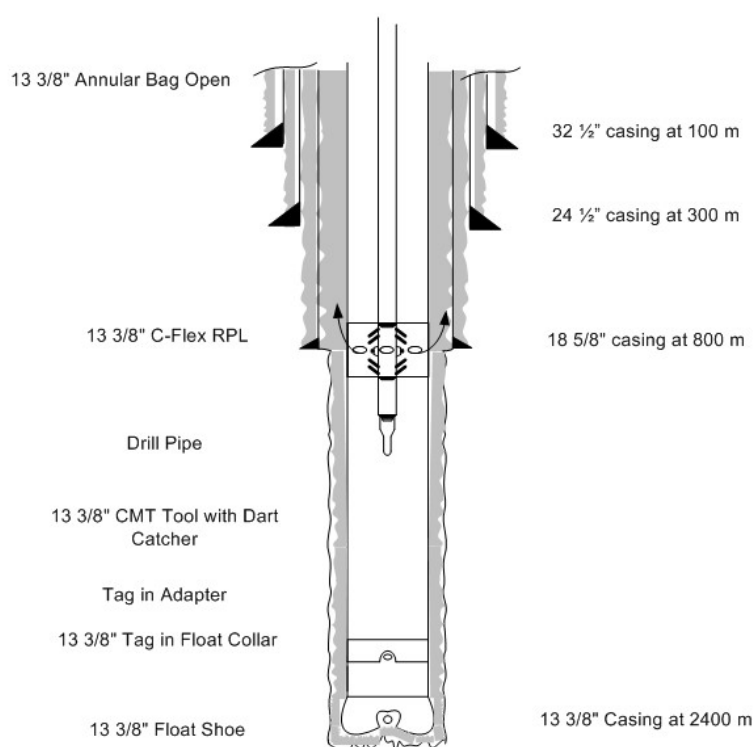


FIGURE 15: Inner string cementing with C-Flex RPL procedure (Thórhallsson, et al., 2010)

6. WELL WORK-OVER

The production casing string in a geothermal well can be subject to internal and external corrosion from the production or reinjection fluid on the inside of the casing and from the reservoir fluid on the outside of the casing. The casing can also be damaged by mechanical wear, particularly if the production casing is deviated from the vertical. Casing implosion can have a marked effect on the productivity of a well, immediately after the first discharge; severe cases can choke the well. Failures have the potential of allowing fluid to escape from the well into the surrounding formation or breaching to the surface. Causes of casing failure are:

- I. Casing can part while running in hole or part due to excessive pull when stuck;
- II. Excess pressure while bumping the plug too hard while cementing can cause burst failure;
- III. Wear caused by drilling below the casing or casing damage while fishing inside the casing;
- IV. Movement of plastic formations during completion operations;
- V. Internal or external corrosion or rod wear during producing life of a well; and
- VI. Subtle failure, undetected failure.

General classes of casing failures are divided into:

Casing leaks: these commonly occur with most failures. Major causes are improper make up during running, drill pipe wear, corrosion failure, and mechanical wear during the producing life of a well.

Split or burst casing: Caused by applying excess internal pressure, directly caused by operations or indirectly caused by inadequate design. Casing can also burst because of structural defects including

slag inclusions in the casing wall and uneven wall thickness. Split or burst casing due to mechanical action during operations may be due to faults in the program design. Casing may be split by jarring a packer loose with a malfunctioning slip segment. Casing may split when long heavy liners are set.

Parted casing: Always occurs at a connection, especially for special connections where the strength of the connection is less than the strength of the pipe body. Casing failures due to parting can be caused by design, operation or mechanical failure due to improper construction. Other causes of parted casings are pulling casing apart while working a stuck casing, bumping the plug too hard and during cementing.

Collapsed casing occurs while squeezing or treating below a packer set in the casing. This can occur when there is a poor cement job outside the casing (cement channelling), and the tubing casing's annulus is insufficiently pressurized. The pressure below the packer communicates outside the casing and up to the section above the packer.

Once the casing has failed due to one of the above reasons, reconstruction has to be done in order to continue using the well. Different repair methods exist for reconstruction of casings and the method to be selected depends on:

- I. How does the casing failure affect current and future operation;
- II. Is the internal diameter of the casing restricted;
- III. Is the casing worthy of recovering;
- IV. Can the failure be repaired in the normal course of future operations;
- V. Can an extra string of casing be run;
- VI. Can the string be patched or packed off;
- VII. Can casing be plugged or repaired later; and
- VIII. Is the point of failure inside another casing string?

Possible mechanisms for production casing failures are shown in Table 7.

TABLE 7: Production casing failure mechanism (Southon, 2005)

Casing failure mechanism	Conditions	Likely depth
Casing implosion	ΔT and casing to casing entrapment of fluids	Anywhere above shoe of the outer casing (s)
Compression failure in casing or couplings	ΔT and rapid heat up. Also an added condition is severe doglegs	High temperature fields and shallow where ΔT is greatest
Sulfide stress cracking	Temperatures below 80°C and high stress areas	Shallow with cold shut in conditions
Early (< 2 years) corrosion or casing holing (internal)	Sections with worn (thinned) casing or wells with very aggressive (low pH) production fluids	For aggressive fluids the first sign of problems is corrosion at the well head
Delayed corrosion (3-5 years)- Internal	Condensate level in shut in wells	At the water gas interface of shut in wells
Corrosion evidence after 5 years (external)	Corrosive fluid penetrating along micro fractures in casing cement	Any depth on the production casing

6.1 Ways of determining casing failures

6.1.1 Video record

Using downhole video cameras, casing failures can be readily identified by the deformation being segmented to one side of the casing circumference. Figure 16 shows a casing break, at a depth of 310.9 m, inside the buttress thread coupling. Video cameras can also show a non-symmetric collapse, probably a reflection that fluid is trapped in liner streaks rather than as a full annular slug of fluid during cementing. Collapse is normally located in the body of the casing and not near the couplings. At the couplings of the production casings, the trapped fluid occupies less annular space. Video cameras also show heavy scale build up on the casings and sections which have thinned out. Some videos of casing collapse have revealed relatively minor inward bulging of the casing wall, indicating a relatively small pocket size of trapped fluid

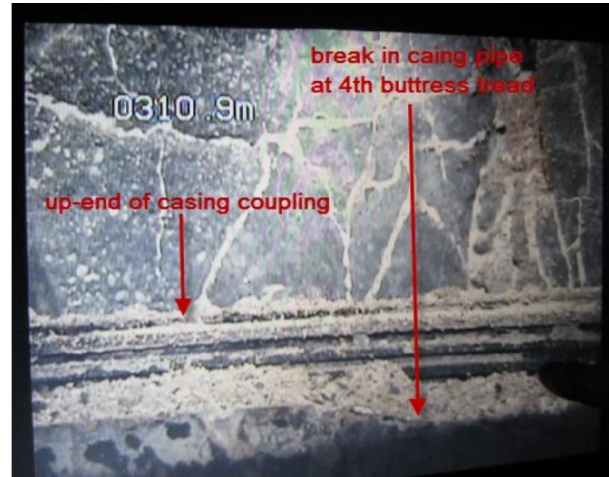


FIGURE 16: Casing break at 310.9 m
(Thórhallsson S., 2003)

6.1.2 Cement bond logs

A cement bond log (CBL) uses an acoustic amplitude curve to indicate cement bond integrity. CBL uses conventional sonic log principals of refraction to make its measurements. Sound travels from the transmitter, through mud and refracts along the casing mud interface and back to the receivers. The amplitude is recorded on the log in millivolts or as attenuation in decibels/foot or as a bond index. A travel curve is also presented. The actual value measured is the signal amplitude in millivolts. Attenuation is calculated by the service company based on its tool design, casing diameter and transmitter. Good cement is indicated by low amplitude, high attenuation and a high bond index. In a casing that is still unbonded (high amplitude railroad tracks on early arrivals on the VDL), amplitude curve reads high, BUT: late arrivals on VDL have shape and track porosity log shape. Figure 17 shows high amplitude variation at depths with casing problems and inadequate cementing.

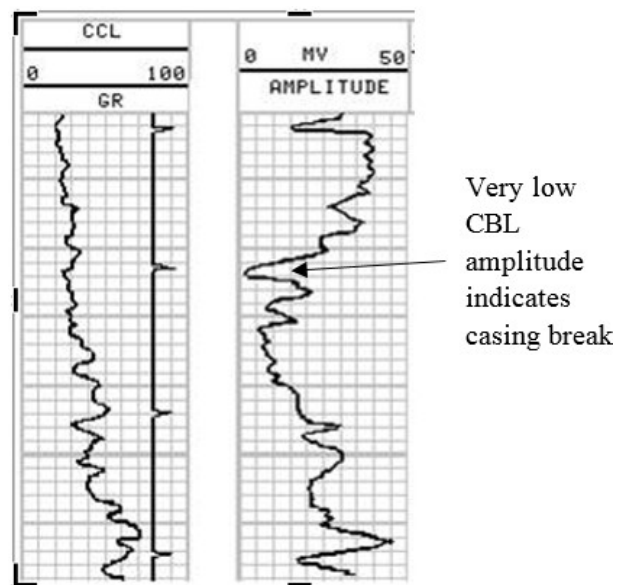


FIGURE 17: Cement bond output
(Steingrímsson, 2014)

6.1.3 Caliper logs

Calipers are electronic tools equipped with several arms to measure the diameter of casing. Arms centralize the tool in the hole. An electrical motor inside opens and closes the tool, controlled at the surface through the cable. The positions of the arms are detected through a variable resistor. Figure 18 shows a calliper log with a casing break at 175 m and the calliper tool, respectively.

Caliper logs are used to (Steingrímsson, 2014):

- Evaluate depositions in casings: calcite or silica
- Evaluate casing corrosion
- Evaluate casing damages

The practical solution for casing implosion is to take all necessary measures to avoid fluids, including unset cement getting into the well bore (Southon, 2005).

6.2 Casing reconstruction techniques

Tie back casing design

Run at the bottom of the tie back stub liner or casing, the tie back sealing nipple has multiple packing elements which provide a seal against the polished surface of the tie back sleeve. Tie back casings are usually cemented by conventionally circulating the slurries. The job is performed before landing the seal nipple into the tie back sleeve. However, the cementing may also be conducted with the tie back casing in place, using a stage collar located above the sealing nipple. Tie back liners must be cemented after their liner hangers have been set with the seal nipple landed into the sleeve. A stage collar can be run on top of the seal nipple, in the open position. The liner wiper plug must be able to land on the upper seal and close the collar ports. Apart from the special procedures given above, the considerations applicable to all cement jobs equally apply to tie back liner cementing. In most cases, hydrostatic pressures are not significant because cementing is done between casings and usually with extended slurries. The use of washes ahead of cement slurries will prevent mud or cement contamination and help to remove the mud from the annular space. This is especially important in tie back liner cementing, where no bottom plug is used to separate the mud from the cement inside the liner. If a completion fluid is in the hole, compatibility with the cement must be checked or large volumes of fresh water pumped ahead of the slurry. Salts used in completion brines may drastically affect a cement slurry's thickening time, causing a premature set or, conversely, resulting in excessively long times for the development of early compressive strength. Figure 19 shows tie back liner cementing. Tie back casing design has these advantages when applied to geothermal wells:

- I. Casing worn thin due to drilling can be covered over with new casing (tie back) at the end of drilling a well.

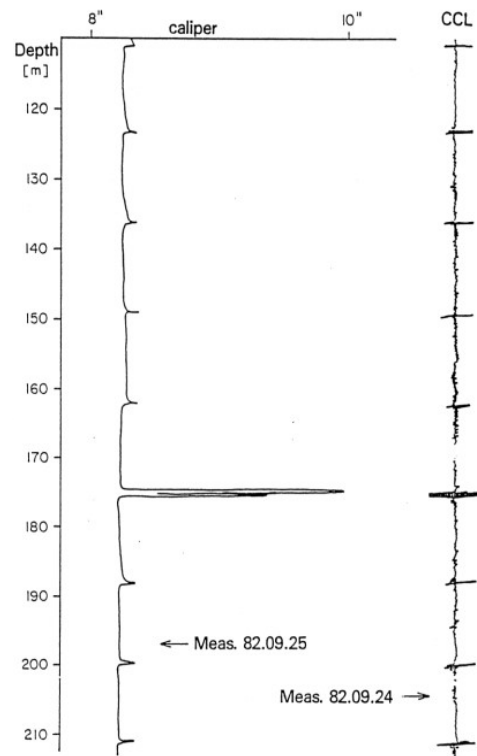


FIGURE 18: Caliper log (Steingrímsson, 2014)

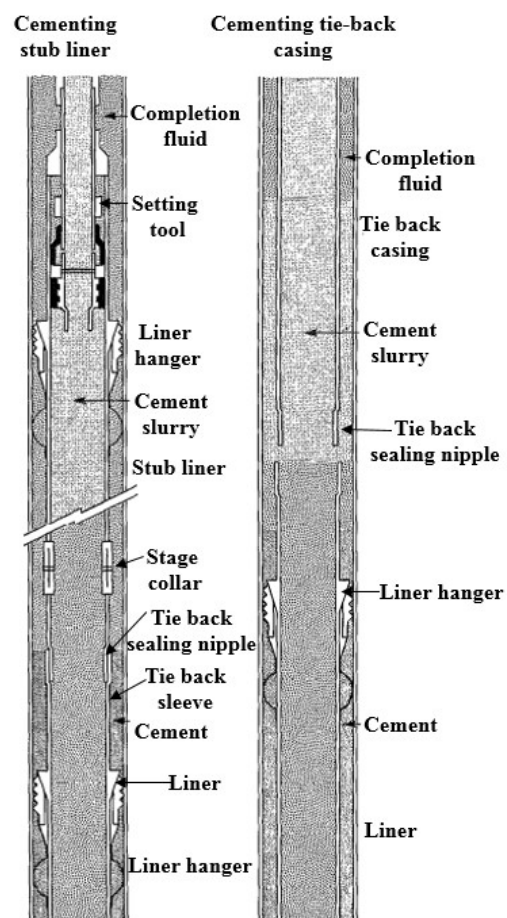


FIGURE 19: Tie back casing design (Nelson, 1990)

- II. It provides the opportunity for a perfect cement job in the critical casing to casing section of the well.

The tie back design has some drawbacks which are:

- I. The connection between the tie back and the liner will invariably leak down the lap during the productive life of the well.
- II. The tie back string is short and invariably lighter than a single production casing. If pre-tensioning is not imparted to the tie back, the tie back will yield in compression if the change in temperature (ΔT) is sufficiently large. For tie backs with buttress threads, this yielding will result in a loss of pressure containment. This yielding can be prevented if the maximum heat-up temperatures are known beforehand and the tie back is pre tensioned before cement sets. This will necessitate the use of latch down slip assemblies in the tie back receptacle or above the receptacle (Nelson, 1990).

For cementing the tie backs, a drillable bridge plug is required to be set in the liner to isolate the newly drilled production hole. The plug should be located immediately below or close to the tie back receptacle to avoid any fluid contamination of the slurry. A thick gel with a relatively high density should be used to prevent the heavy tie back cement slurry from falling through the liquid column.

Casing wear is more concentrated on built up sections of a deviated well. A tie back casing can be run in wells that have already been completed by first using the casing cutter to cut the liners up to just below the cold zone in the well. A drillable bridge plug should be located immediately below or close to the tie back receptacle to avoid any fluid contamination of the slurry.

6.2.2 Cement squeeze

If a casing has parted or there is casing damage and the casing is out of position, the casing can be milled before a cement squeeze job is done to secure the casing. If there is an obstruction while going in the hole, the string should be pulled out of the hole. An impression block is run in the hole to locate the casing damage. The impression block is pulled out, then a milling tool, either a taper mill or a water melon mill, is then run in the hole to mill the hole section clear. The hole is cleaned prior to running a bridge plug to a section below the casing damage depth. The bridge plug (drillable isolation tool) should be able to hold firmly inside the casing and should not allow cement below. Sand is put on top of the bridge plug to avoid its direct contact with the cement slurry. Cement is pumped down and forced through the leaking casing, as shown in Figure 20, until the damage is sealed.

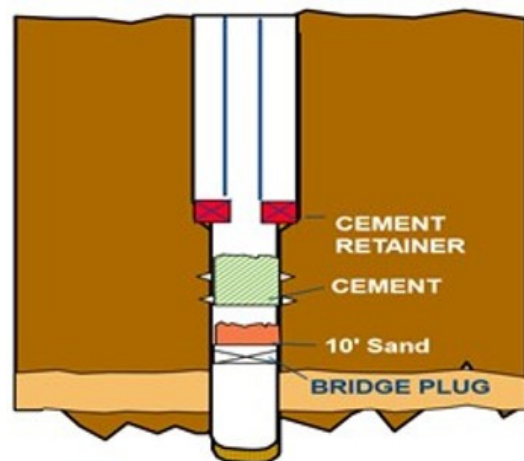


FIGURE 20: Cement squeeze job set up

Other methods that have been used for casing repair are:

- I. Running a blank sleeve inside the casing to seal off the damage. This option will have to be weighed with position reduction in well output due to a drop in mass flow inside the new casing. Liner breaks have been known to occur in some wells due to corrosion, material failure or inadequate liner design. This can be addressed by running a liner sleeve which would protect the well from collapse (Malate, 2003).
- II. Near surface damage can be repaired by excavating a pit around the well and replacing the bad casing with a new one. Excavations as deep as 12 m have been dug in Iceland to replace to replace a full length of casing down to the first threaded connection (Thórhallsson, 2003).
- III. Milling the damaged casing and squeezing cement behind the casing.

6.3 Reconstruction for Menengai wells

Tie back casing-Menengai well MW02

Menengai well MW02 has its production casing set at 790.8 m, as shown in Figure 21. The well has a cold inflow at 1300 m. A cemented casing needs to be run to a depth of 1400 m to seal off the cold inflow. The procedure will involve:

- I. Run in-hole a casing cutter and cut the liners at a depth below 1400 m.
- II. Run in-hole plain 7" casings with a bridge plug at the bottom.
- III. Run the casings with an expandable casing packer (ECP) as part of the casing string.
- IV. After running in-hole, inflate the ECP by pressurizing the casing.
- V. Once the ECP is inflated, cement the annulus through slots in the non-return valve above the ECP.
- VI. Wait for the cement to set.
- VII. Drill out the cement and the bridge plug to access the 7" slotted liners below. Figure 22 shows cementing of the tie back casing using ECP.

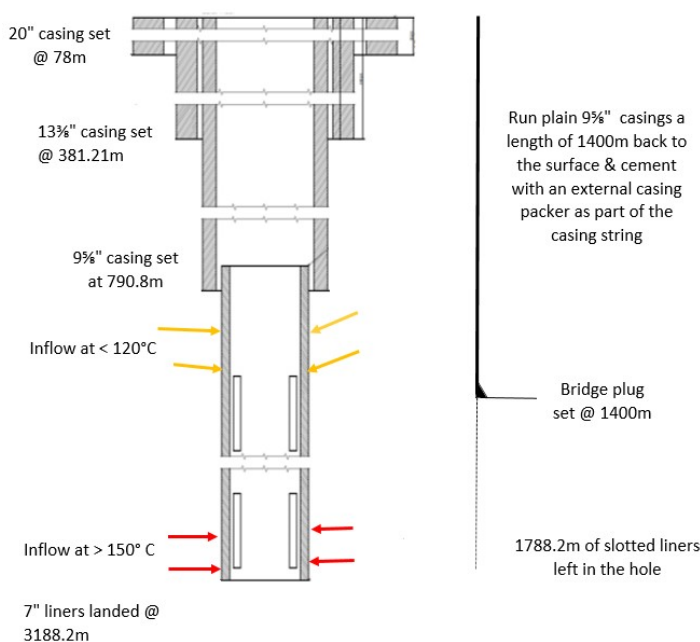


FIGURE 21: Tie back casing reconstruction for Well MW02

Scab liners

Another approach used for casing reconstruction is the use of scab liners or straddle packer assemblies. These approaches are more reliable and are longer-term solutions than cement squeezes, but they are somewhat limited in the length of damage that can be covered. In addition, they result in a greatly reduced hole size, which can severely affect both the productive capacity and access for subsequent remediation. This method is mostly applicable in the oil and gas industry.

7. CONCLUSIONS AND RECOMMENDATIONS

For the Menengai wells, it is feasible to run 9 5/8" K55 production casing to a setting depth of 1400 m to safely seal off shallow upper feed zones. Setting the production casing at deeper depths of up to 1400 m will help prevent scaling, which is a common problem in the Menengai field due to production from the shallow reservoirs. Caliper logs should be run before casings are run to accurately determine the amount of cement to be pumped.

To cement the production casings effectively, an inner string method of cementing should be used to fill up the cement during the primary cement job. For wells with major losses, temperature logs should be run to determine the location of the loss zone. Primary cementing should be done to the loss zone, then an immediate top job done. An inner string cementing method provides a more accurate way of determining the cement slurry volumes to be pumped and takes less time to displace the cement since less displacement capacity is used. Inner string cementing takes less time to execute and there is less chance of cement contamination by water. Cement bond logs should be done as part of the cementing process to evaluate the effectiveness of the cementing job; where it is noted that the cementing is not done properly, remedial cementing should be done before proceeding and drilling the next phase.

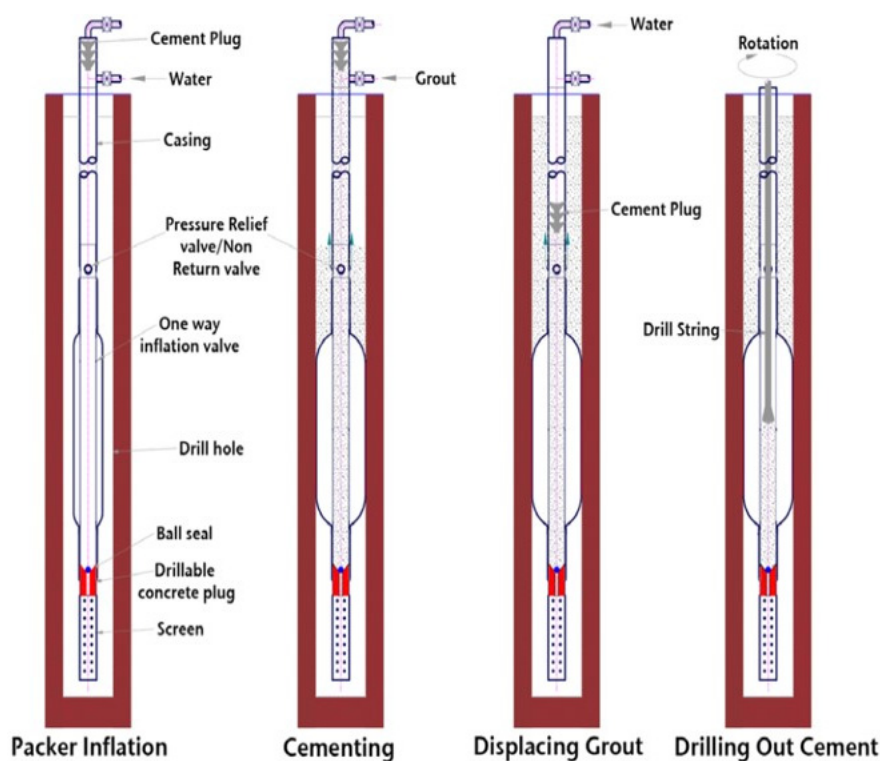


FIGURE 22: Cementing tie back with an External casing packer in the casing string (Nelson, 1990)

Completed wells that have a cold inflow below the production shoe can be worked-over by installing an extra casing string and cementing in order to seal the cold inflows. This can be done most effectively using the tie back casing design. The tie back casing design, with an external casing packer (ECP) as part of the string, provides better sealing to the formation once the packer has been inflated and cementing is done. For wells with high downhole temperatures that exceed the limit set for the ECP, a bridge plug with a cementing plug set on top is used to isolate the lower zone before running the new casing. The design can also withstand high temperatures and high pressures in geothermal conditions.

ACKNOWLEDGEMENTS

My sincere appreciation goes to UNU-GTP, the Government of Iceland and Geothermal Development Company Limited, Kenya for awarding me an opportunity to study in Iceland. I wish to specially thank Mr. Lúdvík S. Georgsson, Director, and Mr. Ingimar G. Haraldsson, Deputy Director. Many thanks to María S. Guðjónsdóttir, Thórhildur Ísberg, Málfríður Ómarsdóttir, Markús A.G. Wilde and Rósa S. Jonsdottir and all the staff of Orkustofnun and ISOR for facilitating my academic endeavours and stay in Iceland. To all, your commitment is humbling. Cheers for the 2014 UNU-GTP fellows for the amazing time we had together.

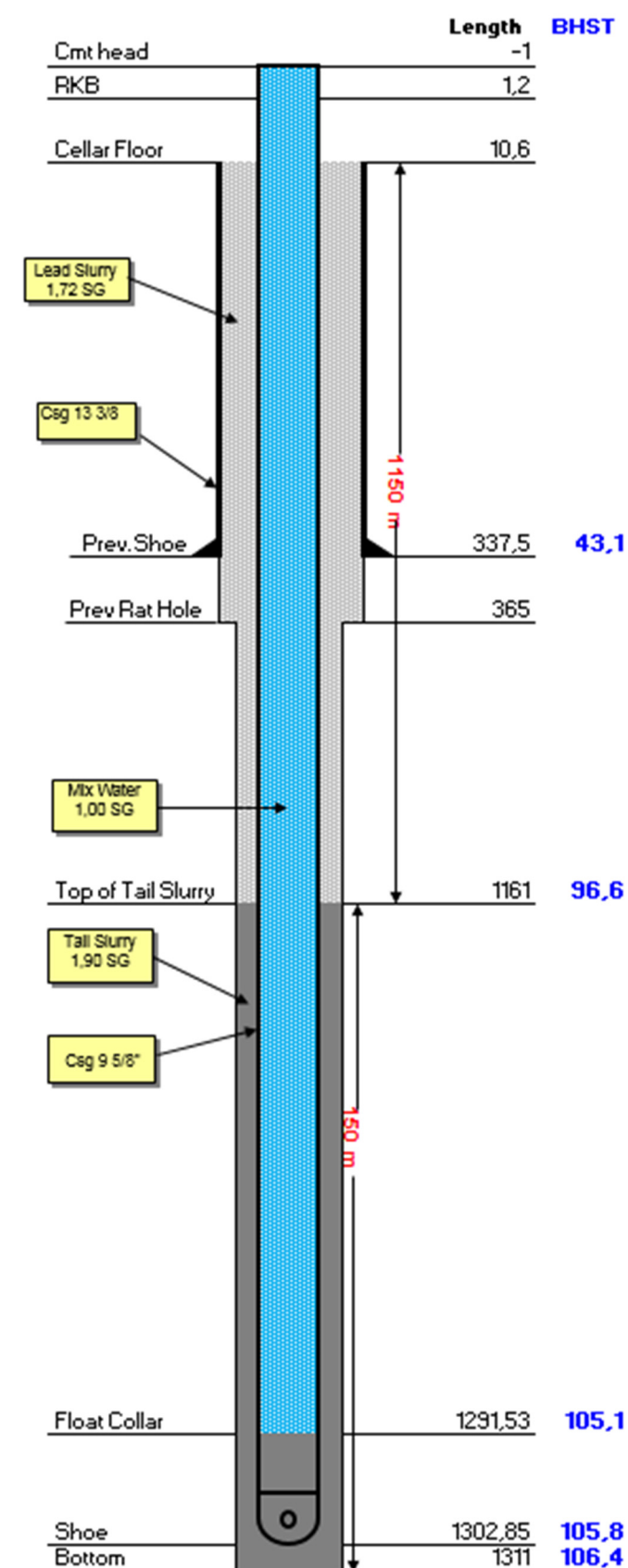
I am indebted to my supervisor, Mr. Arnar Bjarki Árnason, for his valuable input, fruitful ideas, critical comments and encouragement during my project work, to Mr. Sverrir Thórhallsson for advice during project work, and my colleague, Francis Wanjohi, for providing me with invaluable data.

My deepest gratitude to my family for the support I have received: my dear mom, Irene Naliaka Khaemba, and my two brothers for being my source of strength.

REFERENCES

- API, 1994: *Bulletin 5C3 on formulas and calculation for casing, tubing, drill pipe properties*. American Petroleum Institute, Exploration and Production Dept.
- Atlas Copco, 2011: The predator drilling system. Atlas Copco Oil and Gas Rigs, website: www.atlascopco.com/images/ac_predator_brochure_lores_tcm45-3526711.pdf.
- Bett, E.K., 2010: Geothermal well cementing, materials and placement techniques. Report 10 in: *Geothermal Training in Iceland 2010*. UNU-GTP, Iceland, 99-130.
- Bomco, 2011: Bomco VFD AC rig 2000HP. World Oil and Gas Central, website: www.worldoils.com/marketplace/equipdetails.php?id=668.
- Elders, A., and Fridleifsson, G.Ó., 2010: The science program of the Iceland Deep Drilling Project (IDDP): Study of supercritical geothermal resources. *Proceedings of the World Geothermal Congress 2010, Bali Indonesia*, 9 pp.
- Gabolde, G. and Nguyen, J.P., 2014: *Drilling data handbook* (9th edition). Editions Technip, Paris, 576 pp.
- Hole, H., 2008: *Geothermal well design - casing and wellhead*. Petroleum Engineering Summer School, Workshop 26, Dubrovnik, Croatia, June 2008.
- Hosseini-Pourazad, H., 2005: High temperature geothermal well design. Report 9 in: *Geothermal training in Iceland 2005*. UNU-GTP, Iceland, 111-123.
- Lopeyok, T., 2014: *Borehole geology of Menengai well MW-19*. GDC, Kenya, unpublished report.
- Malate, R.C.M., 2003: Well intervention techniques. In: Fridleifsson, I.B., and Gunnarsson, M.V. (eds.), *Lectures on the sustainable use and operating policy for geothermal resources*. Short course prior to the International Geothermal Conference, IGC 2003. UNU-GTP, Iceland, 219-244.
- Mungania, J., 2004: *Geological studies of Menengai geothermal prospect*. KenGen Ltd., Kenya internal report, 18 pp.
- Nelson, E.B., 1990: *Well cementing*. Schlumberger Educational Services, Texas, 487 pp.
- Njue, L., 2013: *Borehole geology of Menengai well MW-02*. GDC, Kenya, unpublished report.
- NZS, 1991: *Code of practice for deep geothermal wells*. Standards Association of New Zealand, Wellington, NZ, New Zealand Standard 2403, 93 pp.
- Southon, J.N.A., 2005: Geothermal well design, construction and failures. *Proceedings of the World Geothermal Congress 2005, Antalya, Turkey*, 6 pp.
- Stefánsson, V., and Steingrímsson, B., 1980: Production characteristics of wells tapping two-phase reservoirs at Krafla and Námafjall. *Proceedings of the 6th Workshop on Geothermal Reservoir Engineering, Stanford University, Stanford, CA*, 49-59.
- Steingrímsson, B., 2014: *Geothermal well logging, cement bond logs and caliper logs*, UNU-GTP Iceland, unpublished lecture notes.
- Thórhallsson, S., 2003: Geothermal well operation and maintenance. In: Fridleifsson, I.B., and Gunnarsson, M.V. (eds.), *Lectures on the sustainable use and operating policy for geothermal resources*. Short course prior to the International Geothermal Conference, IGC 2003. UNU-GTP, Iceland, 195-217.
- Thórhallsson, S., Pálsson, B., Hólmgeirsson, S., Ingason, K., Matthíasson, M., Bóason, H.A., Sverrisson, H., 2010: Well design and drilling plans of the Iceland deep drilling project (IDDP). *Proceedings of the World Geothermal Congress 2010, Bali, Indonesia*, 8 pp.

APPENDIX I: Menengai production casing cementing design



APPENDIX II: Laboratory report for 9%" cement slurry


GEOHERMAL DEVELOPMENT COMPANY
LABORATORY REPORT

This report is the property of GEOHERMAL DEVELOPMENT COMPANY and is intended for private information of the below named party. This report nor any party thereof may not be published or disclosed to a third party without the written approval of GDC.

Project #	GDC Menengai Kenya	Date	21-Aug-2014
Requestor	GDC-CMTNG	Report No.	GDC-CMT-0073
Well	MW-09A	Lab Tech.	Jowen Besaga
Rig	Kifaru-2 (Rig No.4)	Mud Type	N/A
Job Type	9-5/8 Casing Cement Slurry	Mud Wt. ppg	N/A
Test Reference	Confirm Test	Spacer Design	N/A
Sample Source	Laboratory/Field	Spacer Wt. ppg	N/A

Batch No.	Type	Conc.	Units	Remarks
Aug-14	Savannah Cement	94	#/sk	
	Silica Flour	0.00	%bwoc	
Old CPTDC	Mica	3.00	%bwoc	Dryblend
Old CPTDC	Bentonite Gel	2.00	%bwoc	Dryblend
Old CPTDC	Friction Reducer	0.35	%bwoc	Dryblend
Old CPTDC	Fluid Loss	1.00	%bwoc	Dryblend
New CPTDC	Retarder	0.15	%bwoc	Pre-Hydrate
Lab/Rig	Water	65.56	%	
	Calculated Density	14.34	ppg	1.72 g/cm ³
	Calculated Yield	1.51	cuft/sk	1.00 m ³ /ton
	Water Required	7.39	gal/sk	0.66 m ³ /ton
	Total Mix Fluid	7.39	gal/sk	0.66 m ³ /ton

Measured Density	Required	Tested	Thickening Time	Result
g/cm ³	1.72	1.72	Test Temp. BHCT (°C)	70
Free Fluid			Time to Temp. (min.)	15
Conditioning Time (hrs:min)	0:20	0:20	Initial Pressure (Mpa)	3.5
Conditioning Temp. (°C)	70	70	Final Pressure (Mpa)	10
Test Temp. (°C)	70	70	Initial Bc -	2.6
Test Angle (45°)	45°	45°	40 Bc (hrs:min)	4:23
Free Fluid (%)	<1	0.00	70 Bc (hrs:min)	6:11
Static Fluid Loss			100 Bc (hrs:min)	6:37
Conditioning Time (hrs:min)	0:20	0:20	40-100 Bc Time (hrs:min)	2:14
Conditioning Temp. (°C)	70	70	UCA Test	
Test Temp. (°C)	70	70	Test Temp. BHST (°C)	150
Collected fluid (mL)		69	Time to 3.45 MPa (hr:min)	3:24
Time (min.)		30.0	24 hr (MPa)	6.05
Measured (mL/30min)	<500	138		
Calculated API (mL/30min)	N/A	N/A		
Rheology	Atm	BHCT	Slurry Design:	
Test Temp. (°C)	27	70	Cement + 3% Mica (DB) + 2% Bentonite Gel	
Fann Reading @			(DB) + 1.0 % Fluid Loss (DB) + 0.35% Friction	
300 rpm	64	60	Reducer (DB) + 0.15% Retarder (PHY).	
200 rpm	52	42		
100 rpm	33	31		
6 rpm	11	4		
3 rpm	7	2		
600 rpm	94	98		
PV	46.5	43.5		
YP	17.5	16.5		
10 Sec Gel		3		
10 Min Gel		9		

NOTE : MIXING SEQUENCE :
 1. Pre-Hydrate Retarder into Mixing Water.
 2. Mix Dryblended Cement with Additives.

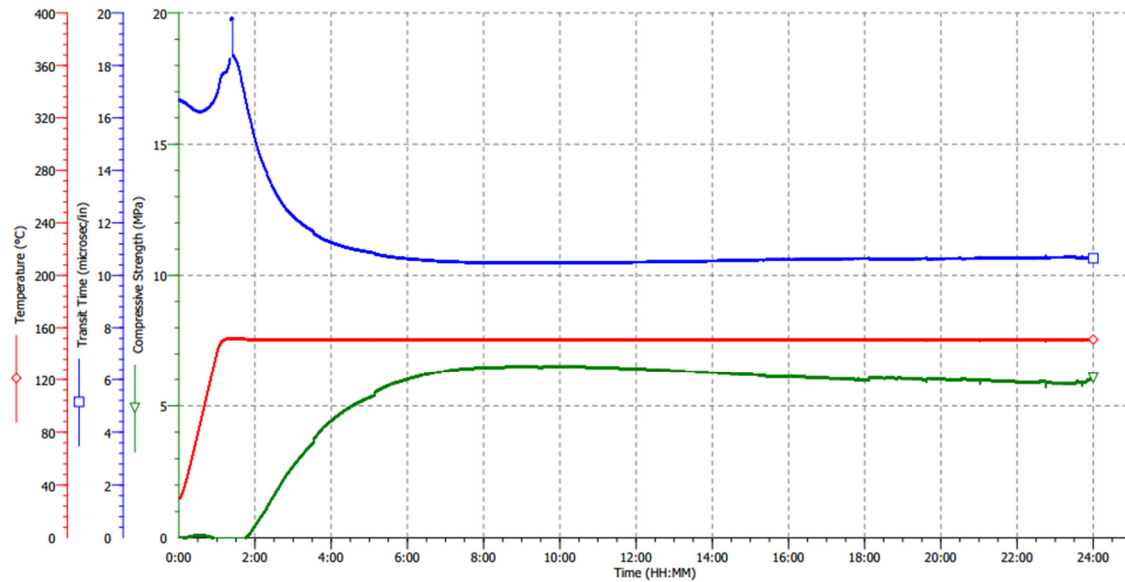
NOTICE : This report is the property of GEOHERMAL DEVELOPMENT COMPANY. Any user of the report agrees that GDC shall not be liable for any loss or damage which results from the use of the information in the report. GDC makes no warranties in respect to the information in the report, whether expressed or implied or for fitness for particular purpose.

APPENDIX III: 9% cement slurry compressive test plot

Well ID: MW-09A
Test Start: 8/20/2014 3:36:08 PM
Test Stop: 8/21/2014 3:36:08 PM

Operator: GDC
Final Compressive Strength: 6.05 MPa
Algorithm: Compressive strength type B (more than 14 lb/gal)

BHST: 150
0.345 MPa @ 1:56:21
3.45 MPa @ 3:24:58





UNITED NATIONS
UNIVERSITY

UNU-GTP

Geothermal Training Programme

Orkustofnun, Grensasvegur 9,
IS-108 Reykjavik, Iceland

Reports 2014
Number 18

THERMODYNAMIC AND THERMOECONOMIC OPTIMIZATION OF A GEOTHERMAL POWER PLANT IN SICHUAN, CHINA

Luo Chao

GuangZhou Institute of Energy Conversion,
Chinese Academy of Sciences,
No. 2 Nengyuan Rd. Wushan, Tianhe District,
Guangzhou
CHINA
luochao@ms.giec.ac.cn

ABSTRACT

This report presents intermediate- and high-temperature geothermal fields distributed in China. Sichuan geothermal area has been selected for a new power plant in the near future, based on governmental policy and energy company demand. Five types of geothermal power systems are designed and presented for it. Using the EES and Scilab software, comparison and optimization of these power systems are analysed, taking into account thermodynamic and thermoeconomic laws. The results show that, for this geothermal system, a binary system is better than other systems. The optimum capacity of the binary system is 3506 kW and 3773 kW for the Tuo-Bei and Yu-Lingong geothermal fields, respectively. The power production cost is 0.04 US\$/kWh for the binary system and the payback period is about 6 years. The thermodynamic and thermoeconomic optimization are determined by using basic data for the future power plant design in the Sichuan geothermal area.

1. INTRODUCTION

1.1 Objective and background

A geothermal power plant is different from a thermal power plant. The capacity of a geothermal power plant is not as easy to identify, compared with a thermal power plant as different capacity corresponds to different design criteria. In China, urban populations are provided with their electricity requirements, but rural areas need guaranteed electricity for socio-economic development. Fortunately, intermediate- to low-temperature geothermal resources are located in proximity to rural areas that are without access to grid electricity. Small-scale geothermal power plants can support electricity demand as well as create employment opportunities for the rural public. Existing geothermal power plants in China were built in the 1970s, their former designers and constructors have either retired or died. Recently, many big corporations have wanted to invest in geothermal power projects, during the “Twelfth Five-Year Plan”, because of energy shortages and the government inspired energy policy in China.

The object of this paper is to design different types of geothermal power plants and optimize them, based on the geothermal fields in Sichuan, China.

1.2 Comparison of power plants that utilize renewable energy

Electrical energy can be generated from various sources, through conventional sources such as nuclear, coal, diesel, etc., and via renewable sources, such as geothermal, wind, solar energy, etc. One of the greatest problems in using renewable energy sources is the great variability in the energy level, both in the short and long term. Geothermal energy is highly desirable because the source is not dependent on weather conditions, so it is among the most stable renewable energy sources. Geothermal energy has proven to be reliable, clean, and safe; therefore, it is increasingly explored for power production, heating and cooling. Geothermal energy produces electricity with minimal environmental impacts. Table 1 gives the energy and investment costs for electric energy production from renewables (Valdimarsson, 2014).

TABLE 1: Energy and investment costs for electric energy production from renewables

	Current energy cost (US¢/kWh)	Potential future energy cost (US¢/kWh)	Turnkey investment cost (US\$/kW)
Biomass	5 - 15	4 - 10	900 - 3000
Geothermal	2 - 10	1 - 8	800 - 3000
Wind	5 - 13	3 - 10	1100 - 1700
Solar (photovoltaic)	25 - 125	5 - 25	5000 - 10000
Solar (thermal electricity)	12 - 18	4 - 10	3000 - 4000
Tidal	8 - 15	8 - 15	1700 - 2500

1.3 Overview

The work in this study is primarily concerned with a geothermal energy utilization performance analysis and feasibility research. Section 2 presents intermediate- to high-temperature geothermal resources in China. Sections 3 and 4 concentrate on thermodynamic and thermoeconomic optimization, with Section 3 discussing the thermodynamic model of single-flash, double-flash, binary and flash-binary power systems, and the optimum value of turbine work and pressure, while Section 4 discusses the cost and thermoeconomic analysis of a binary system. Finally, a sensitivity analysis of geothermal temperature and flow rate are discussed. Finally, Section 5 presents the conclusions of this report.

2. GEOTHERMAL RESOURCE ASSESSMENT IN CHINA

2.1 Potential geothermal fields in China

In China, high-temperature geothermal resources are mainly distributed in South Tibet, West Sichuan, and West Yunnan; while intermediate-temperature geothermal resources are mainly distributed along the coastal areas of southeast China, including Guangdong, Hainan, Jiangxi, Hunan and Fujian. Figure 1 shows the main geothermal fields in China. The intermediate-temperature systems are, as expected, water-dominated. According to Wang and Ma (2005), the potential capacity of the geothermal resources for electrical production is about 8000 MW.

In Chaozhou, Guangdong province, the geothermal temperature is 104°C at 227 m; in Baoting, Hainan province, the geothermal temperature is 90°C at 168 m; in Sichuan, Jiangxi province, the geothermal temperature is 87.9°C at 520 m; in Ningxiang, Hunan province, the geothermal temperature is 102°C at 616 m; in Zhangzhou, Fujian province, the geothermal temperature is 121.5°C at 91 m. Table 2 gives the data on intermediate- to high-temperature (>120°C) geothermal fields in China (Lin and Liu, 2013; Wang and Ma, 2005).

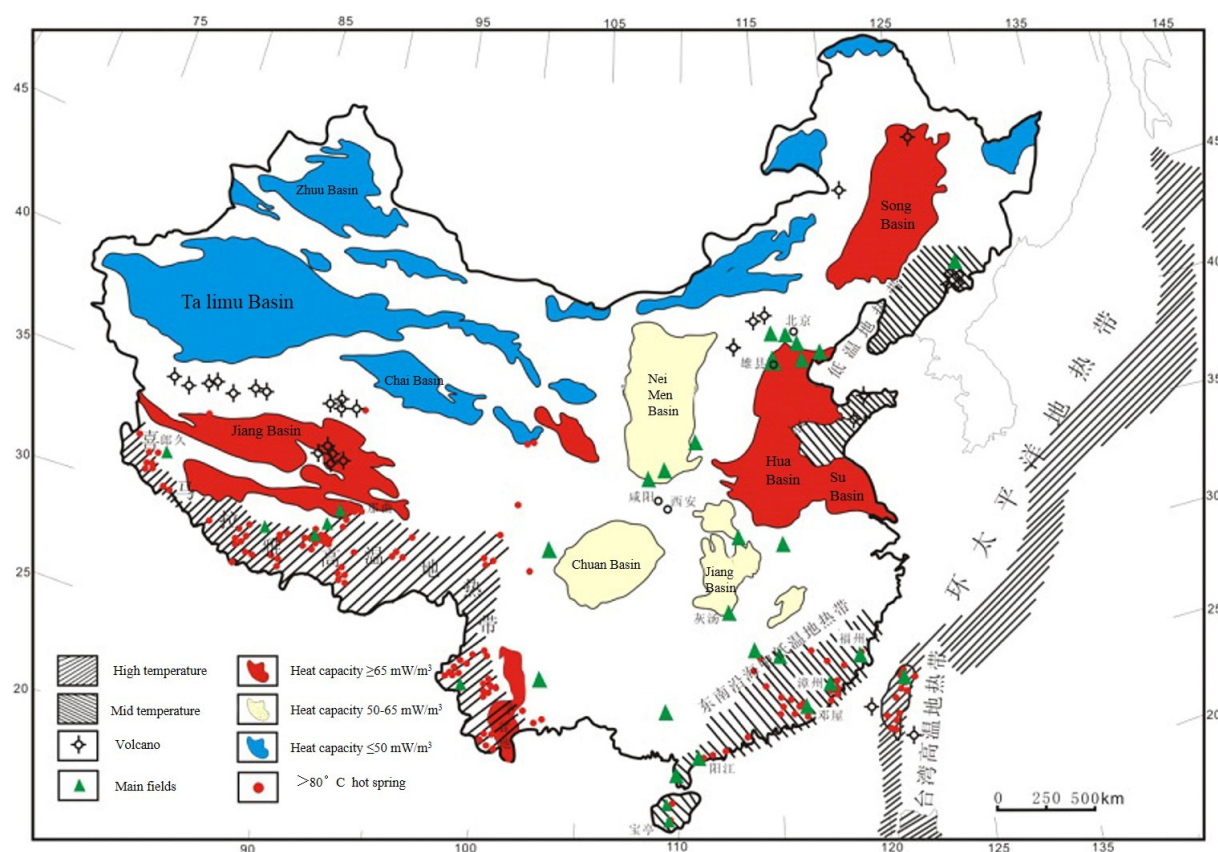


FIGURE 1: Geothermal fields in China

TABLE 2: Geothermal fields in China with intermediate to high temperatures

	Province		Name of field	Geothermal water (artesian flow)			Estimated reservoir data				Cooling water
				T (°C)	Flow rate (kg/s)	TDS (g/l)	T (°C)	Flow rate (kg/s)	Enthalpy (kJ/kg)	Gas mass fraction (%)	
1	Guang-dong	1	Yang-jiang	97	16.4	3	150-170	20-50	800	1	Y
		2	Deng-wu	87	4.5	0.33	135-160	100		0	Y
		3	Feng-liang	92	10.9	0.45	135-160	100		0	Y
		4	Chaozhou donghu	82	1	1.12	140			0	N
		5	Heping reshui	89	11.3	0.38	135			0	N
2	Tibet	6	Yang-bajing				141-172	70-100	1090	12-15	Y
		7	Yang-yi				188	70-80	1040	10-13	Y
		8	Na-qu					30-50			Y
		9	Lang-jiu				166	30-50	950	10-12	N
		10	Ta-ge-jia				189				N
		11	Cha-bu				228				N
		12	Bu-xiong-Lang-ji				245				N
3	Fujian	13	Fu-zhou	97	113	0.2-0.5	150-200	100-150	1050	8-10	N
		14	Zhang-zhou	105	87.8	9.1	130-170	80-100	950	5-6	Y
		15	Gui-an	90	23.3	0.37	143	50-80		0	Y
		16	Hua-an	93	115	0.25	120	80-150		0	Y
		17	Xia-men	91	50-70	14	130-170	50-100		0	Y
		18	San-ming				150			0	Y
		19	Quan-zhou				150			5	Y
4	Sichuan	20	Tuo-bei	96		2	170	20-50		0	Y
		21	Yu-lingong	92-100	5	1	180	20-50	800-1000	5-8	Y
		22	Ba-tang	80-100	3	0.7	250	20-50	900-1200	5-8	Y
		23	Li-tang	87			210	20-50	800-1000	5-8	Y

	Province		Name of field	Geothermal water (artesian flow)			Estimated reservoir data				Cooling water
				T (°C)	Flow rate (kg/s)	TDS (g/l)	T (°C)	Flow rate (kg/s)	Enthalpy (kJ/kg)	Gas mass fraction (%)	
5	Yunnan	24	Teng-chong	98	30-50	0.7-1.5	170-230	50-80		10-14	Y
		25	Rui-li	100	3-10	1	205	20-30		10-14	Y
		26	Yun-xian	100	30-50	0.5	180-210	50-80		10-14	Y
		27	Longlin bazhangla	100	9.01	0.71	210	20-40		10	Y
6	Hainan	28	Guan-tang	70-90			>150	30-60		0	Y
		29	Qi-xian-ting	93			>150	50-80		0	Y
		30	Lan-yang	93			>150	50-80		0	N
7	Hunan	31	Ning-xiang	90.5		<0.4	>120	80		0	Y
		32	Ru-cheng	92.5		0.658	>120	30		0	Y
8	Xinjiang	33	Hu zhu				100	10-20		0	N
		34	Tian shan				180	10-20		0	N

2.2 Weather conditions in Sichuan

Sichuan geothermal area is near Tibet; with intermediate- to high-temperature geothermal fields distributed in the west part of Sichuan. Because of governmental and energy corporation interests and policy, a new geothermal power plant may be built in the Sichuan province.

Weather data is taken from 2005. The data were recorded at 1 hour intervals. There are 7 hours missing from the dataset, so the data were extrapolated to 8760 hours. The data give the dry bulb temperature and relative humidity. The wet bulb temperature is then calculated for all valid data points. The dry and wet bulb temperatures from Jan 1st to Dec 31st are given in Figure 2.

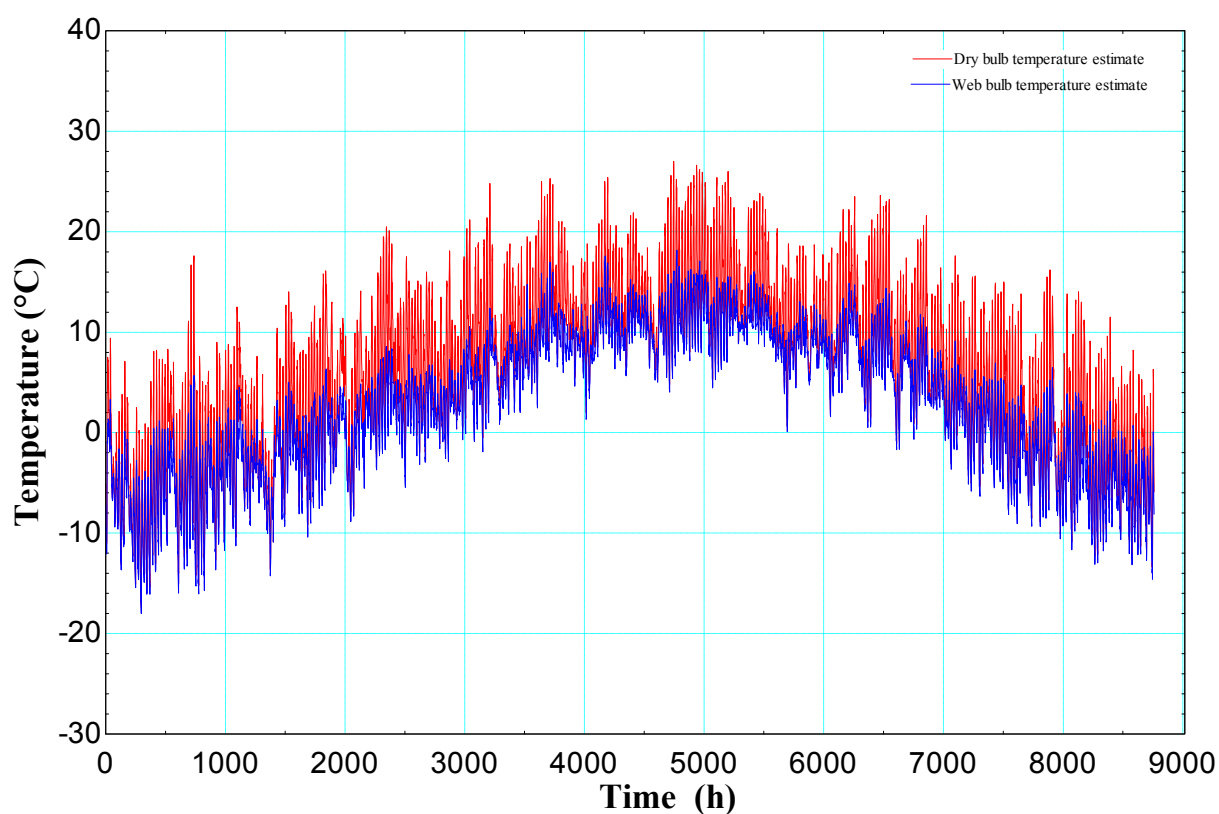


FIGURE 2: Dry bulb and wet bulb temperatures

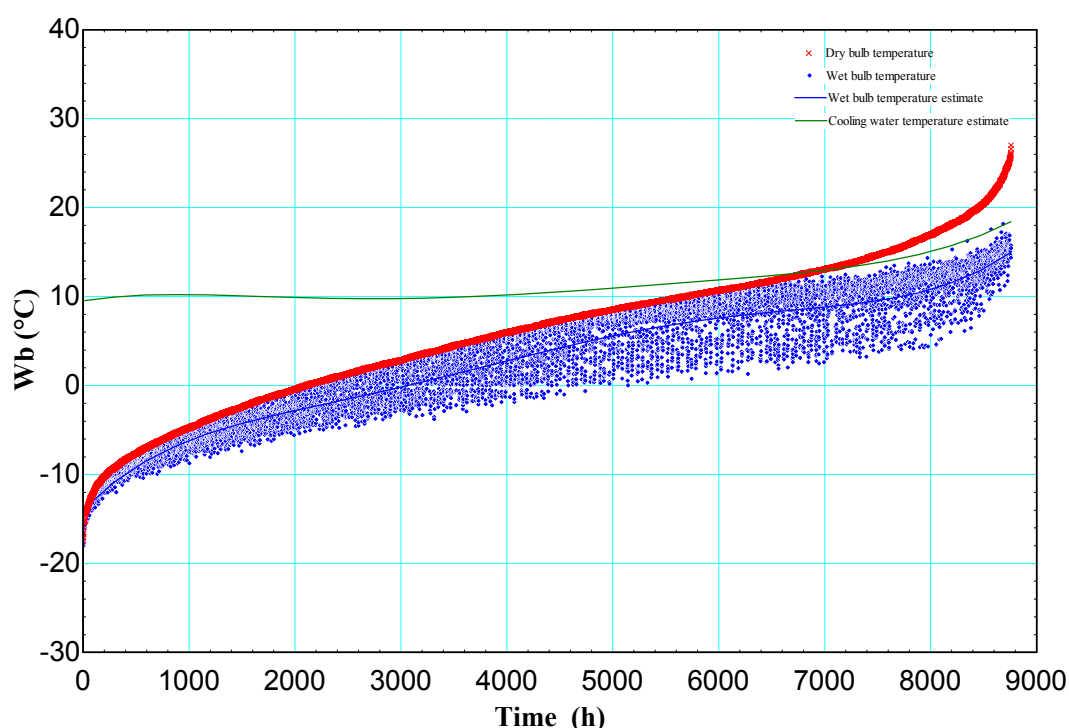


FIGURE 3: Cooling water temperature estimate

The duration curves for dry and wet bulb as well as estimated cooling water temperature are shown in Figure 3. The cooling water temperature is assumed to be 4°C higher than the wet bulb temperature at the hottest day. This temperature is assumed to be 10°C when the wet bulb temperature has fallen down to 0°C. The minimum cooling water temperature is assumed 10°C. A cooling water temperature of 15°C is selected in this paper for the design point (green line). The dry bulb temperatures are listed from the lowest to the highest.

Of the Sichuan geothermal fields, Tuo-bei and Yu-lingong were selected; non-condensed gas exists in the Yu-lingong geothermal field. In this report, single-flash, double-flash, binary and flash-binary power systems are designed for Tuo-bei field, and a gas-vapour-liquid binary system for Yu-lingong field. The assumptions for the geothermal system and technical characteristics of the plant systems are shown in Table 3.

TABLE 3: Parameters and boundary conditions of the power plant models for the Sichuan fields

	Parameter		Unit	Value
Geothermal reservoir	Tuo-bei	Temperature of reservoir	°C	170
		Mass flow rate	kg/s	50
		Gas mass fraction	%	0
	Yu-lingong	Temperature of reservoir	°C	180
		Mass flow rate	kg/s	50
Power plant system	Cooling water temperature		°C	15
	Temperature difference of cooling water		°C	10
	Turbine isentropic efficiency		%	80
	Pump isentropic efficiency		%	75
	Vaporizer heat transfer coefficient		kW/(m ² .°C)	1.1
	Preheater heat transfer coefficient		kW/(m ² .°C)	0.7
	Recuperator heat transfer coefficient		kW/(m ² .°C)	0.7
	Condenser heat transfer coefficient		kW/(m ² .°C)	1

2.3 Literature review

There are three main kinds of commercialized geothermal power technology: dry-steam power generation, which is applied to a dry-steam geothermal resource and accounts for about 27% of all installed geothermal plant capacity; flash power generation, which is applied to wet-steam or water-dominated geothermal resources and accounts for about 61% of all installed geothermal plant capacity; binary cycle power generation, which is applied to intermediate- to low-temperature water-dominated geothermal resources and accounts for about 11% of all installed geothermal plant capacity (Bertani, 2010).

Based on the temperature and properties of the water-dominated geothermal resource, different energy conversion systems can be utilized to maximize the extraction of energy from the geothermal fluid (Franco and Villani, 2009). Net power output, energy efficiency, exergy efficiency, thermal economics and sensitivity have also been theoretically studied (Jalilinasrabad et al., 2012; Rosyidet al., 2010). The flash-binary power system would increase production compared to a single-flash power system. Denizli power plant in Turkey gained 18% in power production by adding a binary cycle system (Dagdaz et al., 2005).

However, there are few studies about the match ability between a geothermal resource temperature and a power cycle. Also, most geofluids contain non-condensable gases, and the power output of the plant is affected by the gas mass fraction. There are few studies about a gas-vapour-liquid power plant. This report explores five different types of power system thermodynamic optimizations, including gas-vapour-liquid, and one case of thermoeconomic optimization.

3. THERMODYNAMIC OPTIMIZATION OF A GEOTHERMAL POWER PLANT

Thermodynamics can analyse the power generation from an energy view point; the fundamentals and mathematical model are found in DiPippo (2008). The main components of a flash and binary system are: a separator, a preheater, a vaporizer, a condenser and a turbine (Ahangar, 2012).

3.1 Single-flash system optimization

A single-flash system is the first scenario for Tuo-bei geothermal field; the conditions are shown in Table 3. A throttle valve, a separator, a turbine, a condenser and a cooling tower are the main equipment in the system. The separation pressure P_2 is the main variable used to optimize the turbine power output. Figure 4 shows the diagram of a single-flash system. Figure 5 shows the thermodynamic T-s diagram of the single-flash process.

Optimization focuses on obtaining optimum separation pressures which could maximize power output. Therefore, using the EES program, the separation pressure P_2 was varied in order to find the maximum net power output. The relationship between separation pressure and turbine work, using the second law of efficiency, is shown in Figure 6. The optimum pressure is $P_2=0.95$ bar; the maximum power, shown on the top of the red curve, is 2301 kW.

Table 4 shows the optimum thermodynamic properties of each process state in a single-flash system. The main results for a single-flash cycle are shown in Table 5. The injection temperature is about 98°C; the first and second laws of efficiency are 7.9% and 34.7%, respectively. The condenser area is about 1212 m².

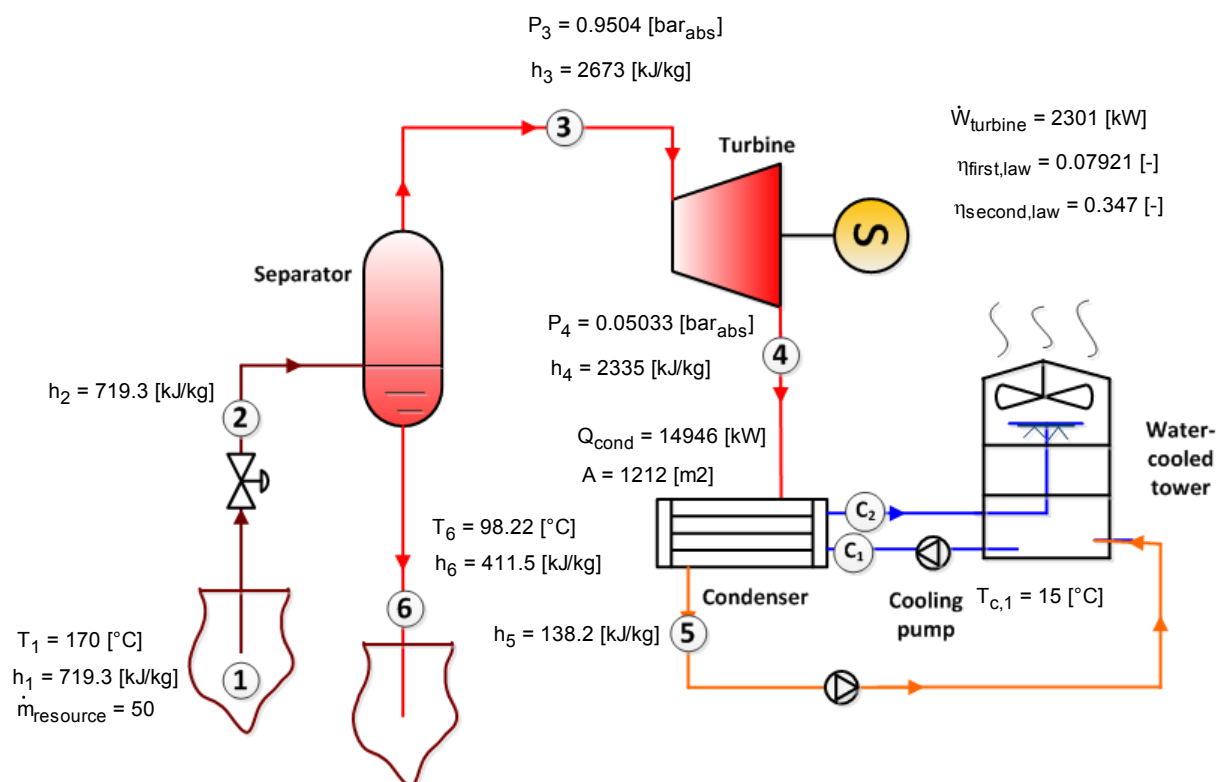


FIGURE 4: Single-flash system diagram

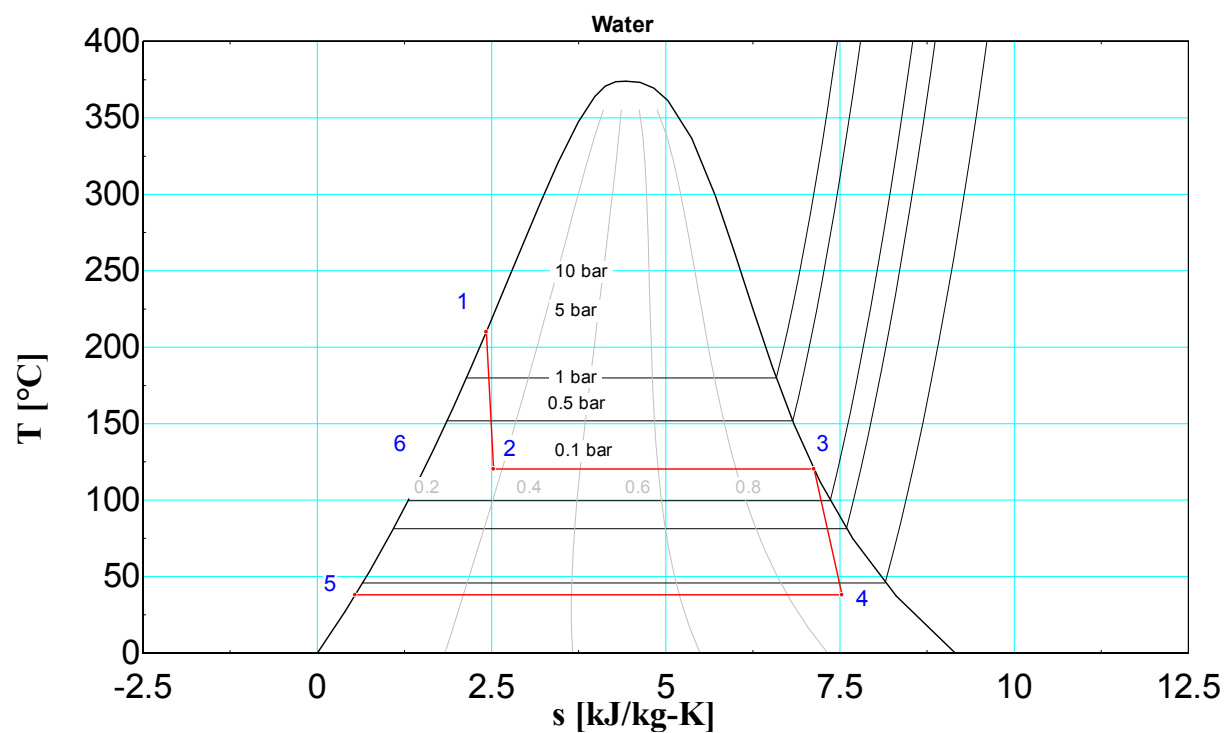


FIGURE 5: Single-flash T-s diagram

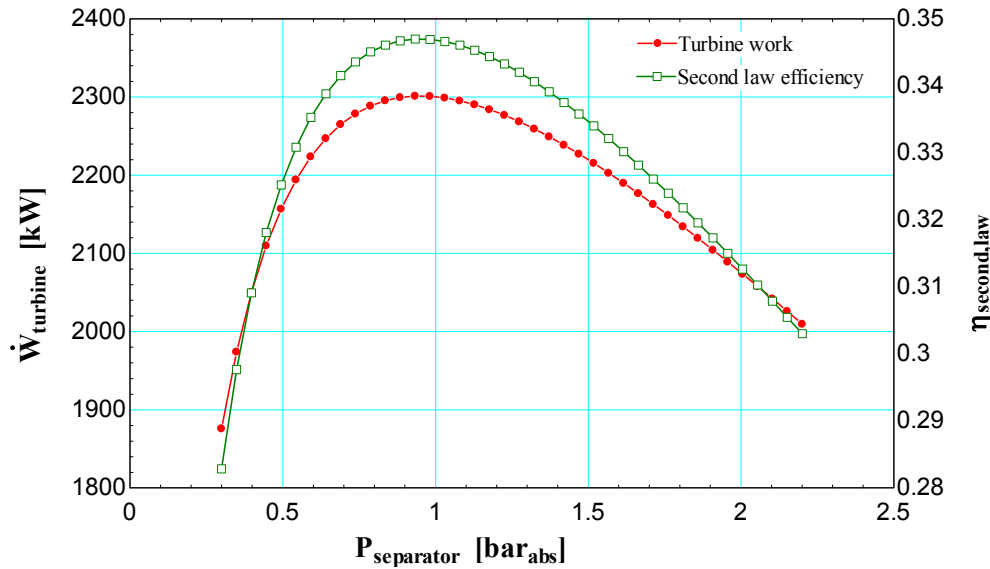


FIGURE 6: Separator pressure and turbine power relationship

TABLE 4: Thermodynamic optimization of single flash

State	Pressure P (bars)	Temperature T (°C)	Mass flow M (kg/s)	Steam quality x	Volume v (m ³ /kg)	Enthalpy h (kJ/kg)	Entropy s (kJ/kg°C)	Heat rate Q (kW)	Specific exergy e (kJ/kg)	Exergy rate Ex (kW)
1	7.92	170	50.0	0.000	0.001	719	2.04	35965	132.60	6632
2	0.95	98	50.0	0.136	0.243	719	2.12	35965	112.00	5576
3	0.95	98	6.8	1.000	1.777	2673	7.38	18176	550.00	3739
4	0.05	33	6.8	0.907	25.400	2335	7.65	15878	132.00	897
5	0.05	33	6.8	0.000	0.001	138	0.48	938	2.00	15
6	0.95	98	43.2	0.000	0.001	412	1.29	17798	42.00	1837
c1	-	15	357.3		0.001	63	0.22	22510	0.20	71
c2	-	25	357.3		0.001	105	0.37	37481	0.72	259

TABLE 5: Energy summary of single flash

No.	Item	Units	Optimum value
1	Separator pressure	bar	0.95
2	Turbine shaftwork	kW	2301
3	Cooling pump	kW	71.51
4	Turbine net output power	kW	2230
5	Condenser temperature	°C	33
6	Condenser capacity	kW	14946
7	Condenser area	m ²	1212
8	The first law efficiency	%	7.9
9	The second law efficiency	%	34.7

3.2 Binary system optimization

A binary power cycle is the second scenario for Tuo-bei geothermal field; the conditions are shown in Table 3. A vaporizer, aprehater, a working pump, a turbine, a condenser and a cooling tower are the

main components in the system. The vaporizer pressure, preheater pinch and preheater area are the main variables used to optimize the turbine power output. Figure 7 shows the diagram of a single-flash system. Figure 8 shows the thermodynamic T-s diagram of the single-flash process.

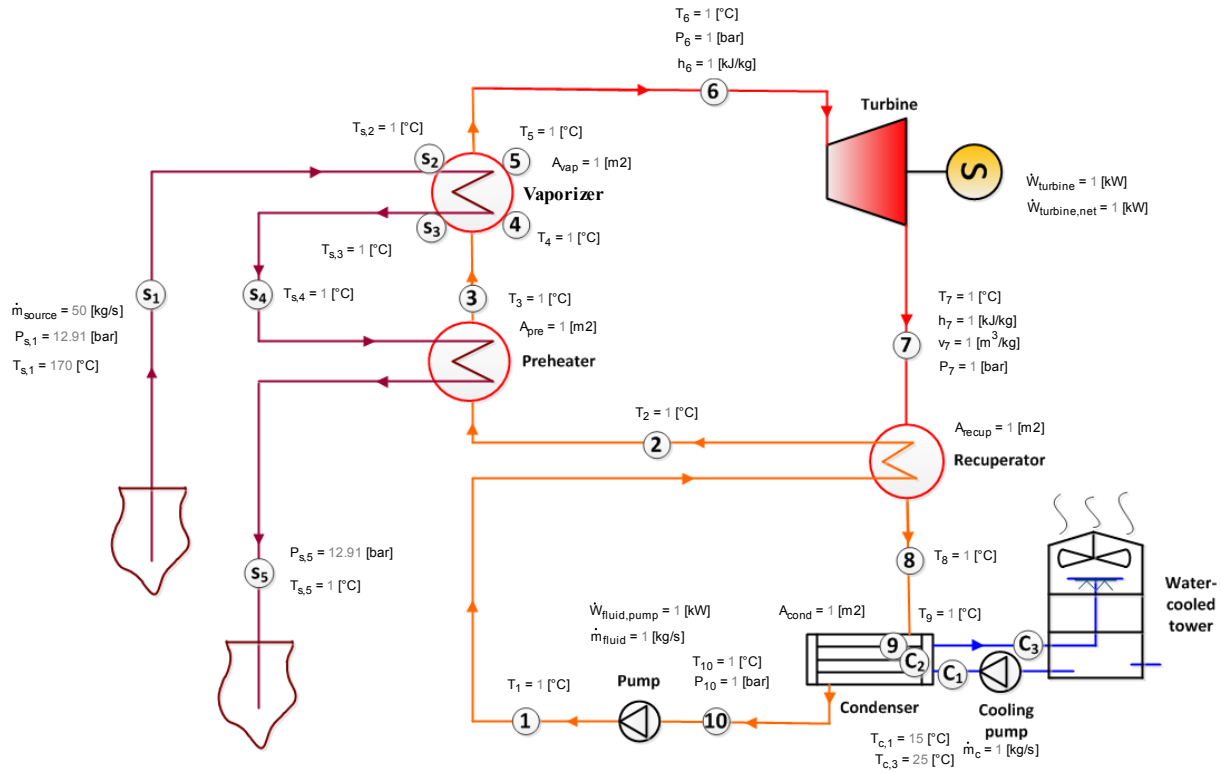


FIGURE 7: Binary system diagram

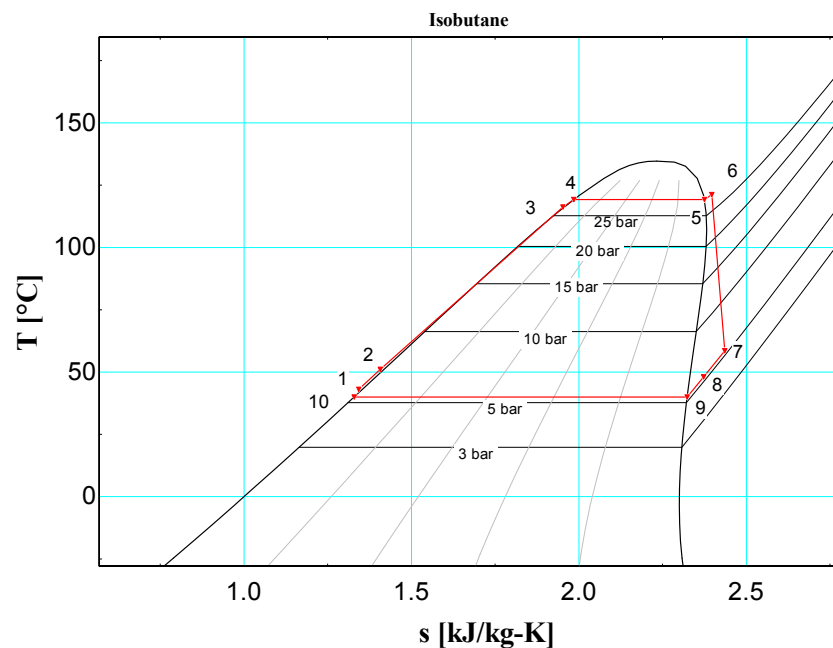
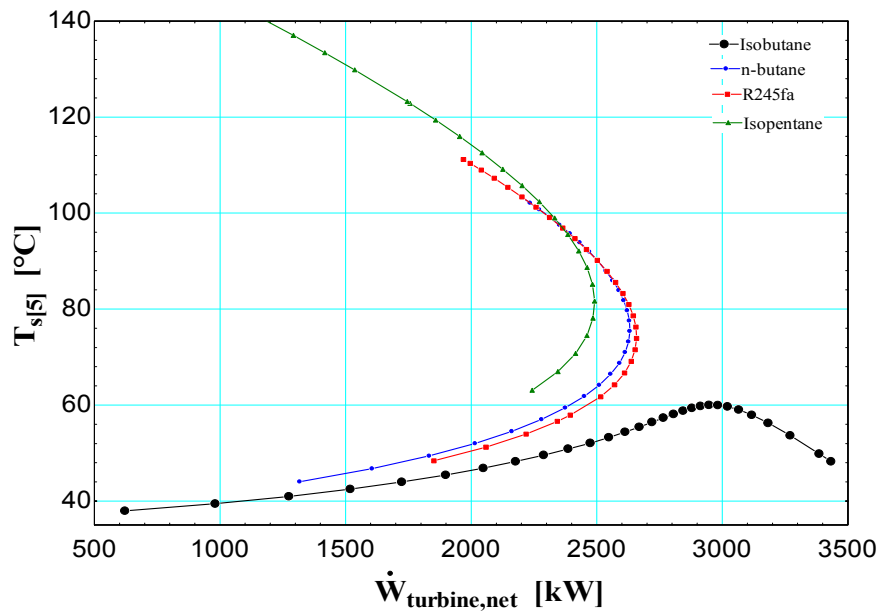


FIGURE 8: Binary T-s diagram



Optimization focuses on obtaining the optimum vaporizer pressure. Figure 9 gives the relationship of the turbine work and the injection temperature of four different working fluids. For isobutane, the maximum injection temperature is about 60°C. Therefore, the vaporizer pressure at 28 bar is the optimum vaporizer pressure for a binary cycle. The turbine shaft and net output power are 3506 kW and 3022 kW, respectively.

FIGURE 9: The relationship of turbine work and reinjection temperature

Figure 10 shows the relationship of efficiency, injection temperature and vaporizer pressure. The value of the first law of efficiency, second law of efficiency and the injection temperature are 12.9%, 45.4% and 59.7°C, respectively.

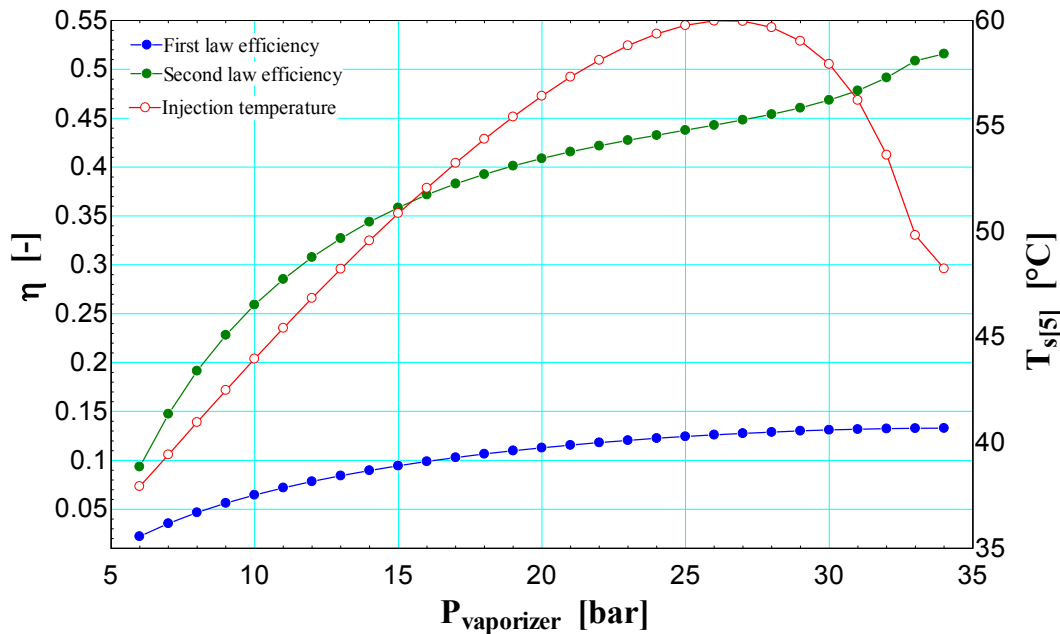


FIGURE 10: The relationship of efficiency, injection temperature and vaporizer pressure

Table 6 shows the optimum thermodynamic properties of each process state in a binary power system. The main results of the binary cycle are shown in Table 7.

TABLE 6: Thermodynamic optimization of a binary system

State	Pressure P (bars)	Temperature T (°C)	Mass flow m (kg/s)	Steam quality x	Volume v (m ³ /kg)	Enthalpy h (kJ/kg)	Entropy s (kJ/kg°C)	Heat rate Q (kW)	Specific exergy e (kJ/kg)	Exergy rate Ex (kW)
1	28.0	35	62.6	-100	0.002	284	1.274	17799	6.05	368
2	28.0	45	62.6	-100	0.002	311	1.358	19459	8.15	496
3	28.0	117	62.6	-100	0.002	525	1.963	32906	48.83	2971
4	28.0	119	62.6	-100	0.002	534	1.985	33451	51.12	3111
5	28.0	119	62.6	1	0.015	687	2.375	43039	91.78	5585
6	28.0	121	62.6	100	0.016	696	2.397	43578	94.09	5725
7	4.4	53	62.6	100	0.097	638	2.441	39964	23.61	1437
8	4.4	40	62.6	100	0.092	612	2.359	38311	21.00	1278
9	4.4	33	62.6	1	0.089	599	2.317	37497	20.11	1224
10	4.4	33	62.6	-100	0.002	278	1.269	17436	1.60	97
S1	12.9	170	50.0		0.001	720	2.041	35980	133.10	6655
S2	12.9	168	50.0		0.001	709	2.018	35455	129.50	6473
S3	12.9	124	50.0		0.001	523	1.573	26140	71.32	3566
S4	12.9	122	50.0		0.001	512	1.546	25610	68.44	3422
S5	12.9	60	50.0		0.001	251	0.826	12545	14.45	723
C1	-	15	485.0		0.001	63	0.224	30608	0.20	99
C2	-	25	485.0		0.001	103	0.362	50101	0.67	335
C3	-	25	485.0		0.001	105	0.368	50877	0.72	361

TABLE 7: Energy summary of binary system

No.	Item	Units	Optimum value
1	Vaporizer pressure	bar	28
2	Condenser pressure	bar	4
3	Turbine shaft work	kW	3506
4	Cooling pump	kW	129
5	Working pump	kW	355
6	Turbine net output power	kW	3022
7	Condenser temperature	°C	33
8	Condenser capacity	kW	20284
9	Vaporizer area	m ²	634
10	Preheater area	m ²	2157
11	Recuperator area	m ²	350
12	Condenser area	m ²	1742
13	The first law efficiency	%	13
14	The second law efficiency	%	45

3.3 Double-flash system optimization

The double-flash cycle is the third scenario for Tuo-bei geothermal field; the conditions are shown in Table 3. Two individual turbines are used in the system. The high separation pressure P_2 and low separation pressure P_8 are the main variables used to optimize the turbine power output. Figure 11 shows the diagram of a double-flash system. Figure 12 shows the thermodynamic T-s diagram of the process.

Optimization focuses on obtaining the optimum separation pressures for both separators to maximize power output. Therefore, the two separation pressures, P_2 and P_8 , were varied, using the EES program, in order to find the maximum net power output. The 3D relationship of high separation pressure, low

separation pressure and turbine work is shown in Figure 13, based on the Scilab programme. The optimum pressures were: $P_2=2.08$ bar; $P_8=0.39$ bar. The maximum power is shown, in the top left area, to be 2940 kW.

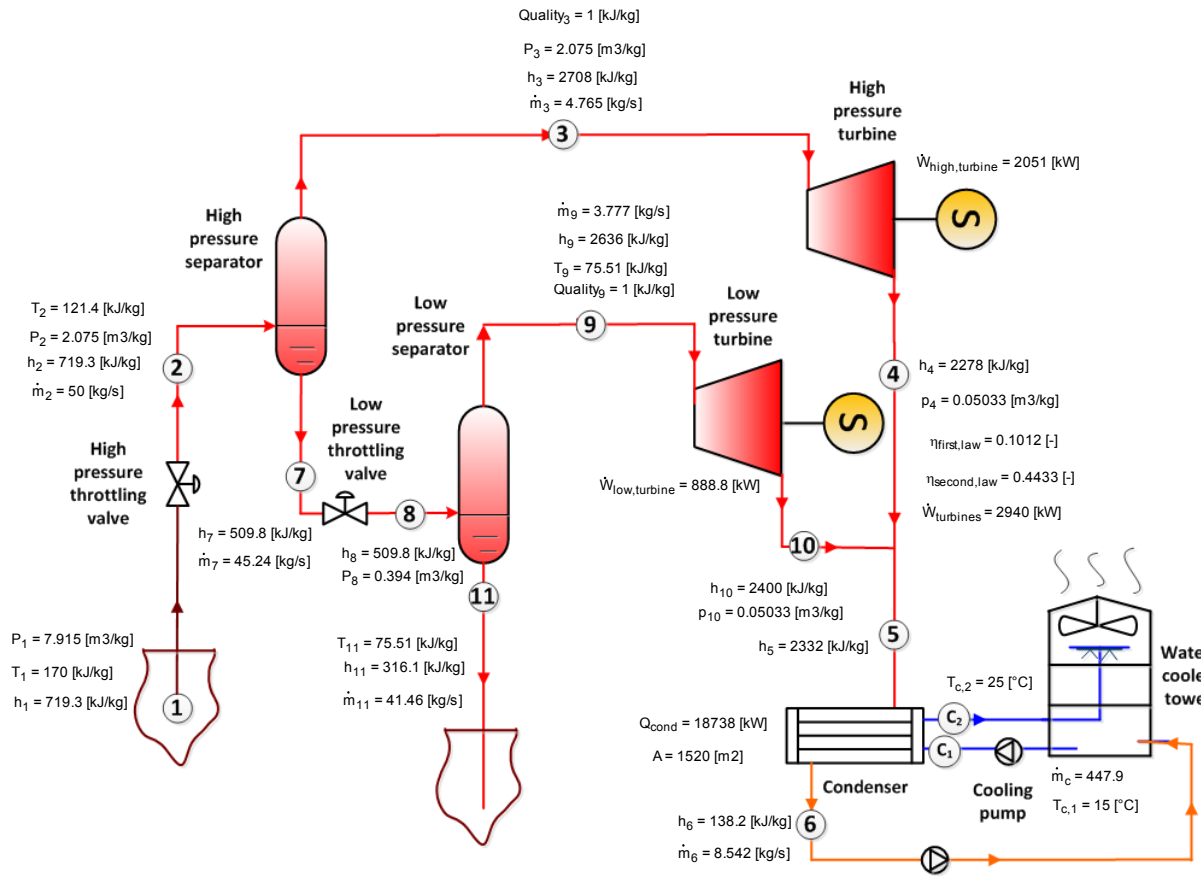


FIGURE 11: Double system diagram

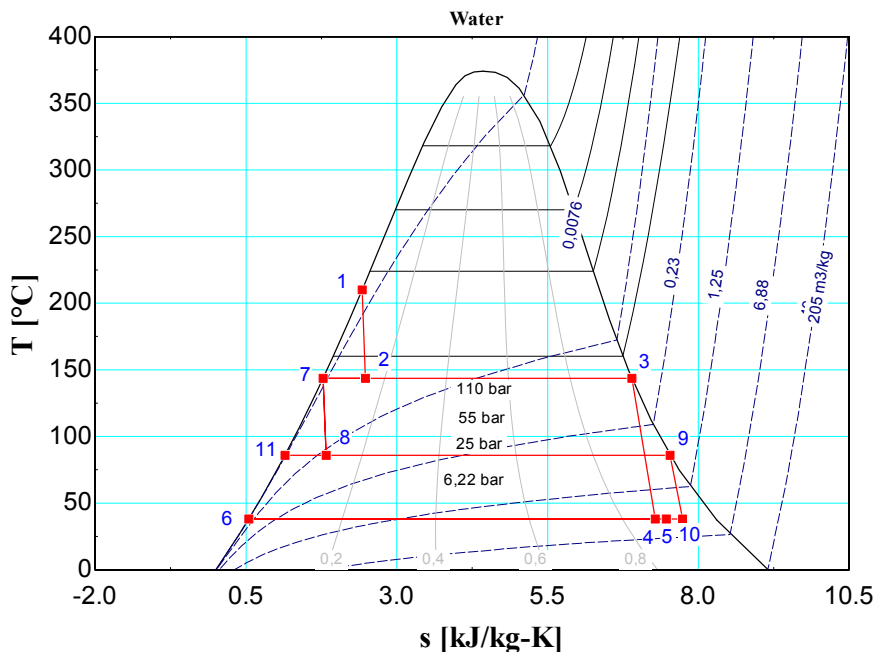


FIGURE 12: Double-flash T-s diagram

Table 8 shows the optimum thermodynamic properties of each process state in a double-flash system. The main results of the double-flash cycle are shown in Table 9. The injection temperature is about 76°C , the first and second laws of efficiency are 10% and 44%, respectively. The condenser area is about 1520 m^2 .

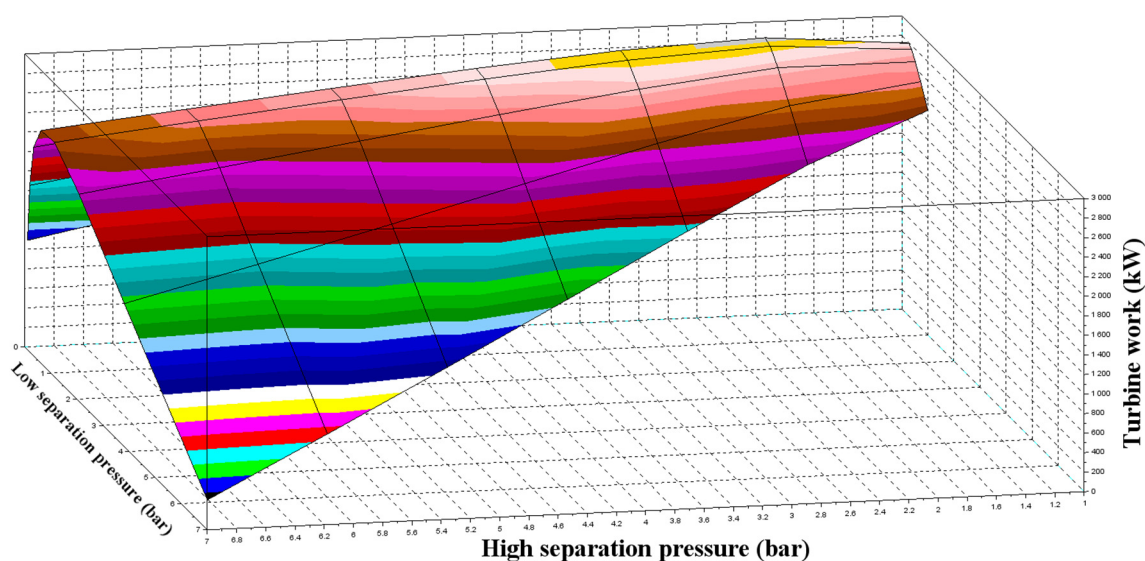


FIGURE 13: Low separator pressure, high separator pressure and turbine power relationship

TABLE 8: Thermodynamic optimization of a double-flash system

State	Pressure P (bars)	Temperature T(°C)	Mass flow m (kg/s)	Steam quality x	Volume v (m ³ /kg)	Enthalpy h (kJ/kg)	Entropy s (kJ/kg°C)	Heat rate Q (kW)	Specific exergy e (kJ/kg)	Exergy rate Ex (kW)
1	7.92	170	50.0	0.000	0.001	719	2.04	35965	133	6632
2	2.08	121	50.0	0.095	0.083	719	2.07	35965	124	6173
3	2.08	121	4.8	1.000	0.856	2708	7.12	12904	660	3145
4	0.05	33	4.8	0.883	24.740	2278	7.47	10855	128	612
5	0.05	33	8.5	0.906	25.370	2332	7.64	19920	132	1124
6	0.05	33	8.5	0.000	0.001	138	0.48	1181	2	19
7	2.08	121	45.2	0.000	0.001	510	1.54	23063	67	3028
8	0.39	76	45.2	0.083	0.339	510	1.58	23063	57	2582
9	0.39	76	3.8	1.000	4.051	2636	7.67	9956	426	1610
10	0.05	33	3.8	0.934	26.160	2400	7.87	9065	136	512
11	0.39	76	41.5	0.000	0.001	316	1.02	13106	23	972
c1		20	447.9		0.001	63	0.22	28267	0	88
c2		30	447.9		0.001	105	0.37	47030	1	325

TABLE 9: Energy summary of a double-flash system

No.	Item	Units	Optimum value
1	High-pressure separator pressure	bar	2.08
2	Low-pressure separator pressure	bar	0.39
3	High-pressure turbine output power	kW	2051
4	Low pressure turbine output power	kW	889
5	Total turbine shaft work	kW	2940
6	Cooling pump	kW	90
7	Total turbine net output power	kW	2850
8	Condenser temperature	°C	33
9	Condenser capacity	kW	70738
10	Condenser area	m ²	1520
11	The first law efficiency	%	10.12
12	The second law efficiency	%	44.33

3.4 Flash-binary system optimization

A flash-binary system is the fourth scenario for Tuo-bei geothermal field; the conditions are shown in Table 3. Flash and binary turbines are used in this system. The separation pressure P_{10} and vaporizer pressure P_5 are the main variables used to optimize the turbine power output. Figure 14 shows the diagram of a flash-binary system.

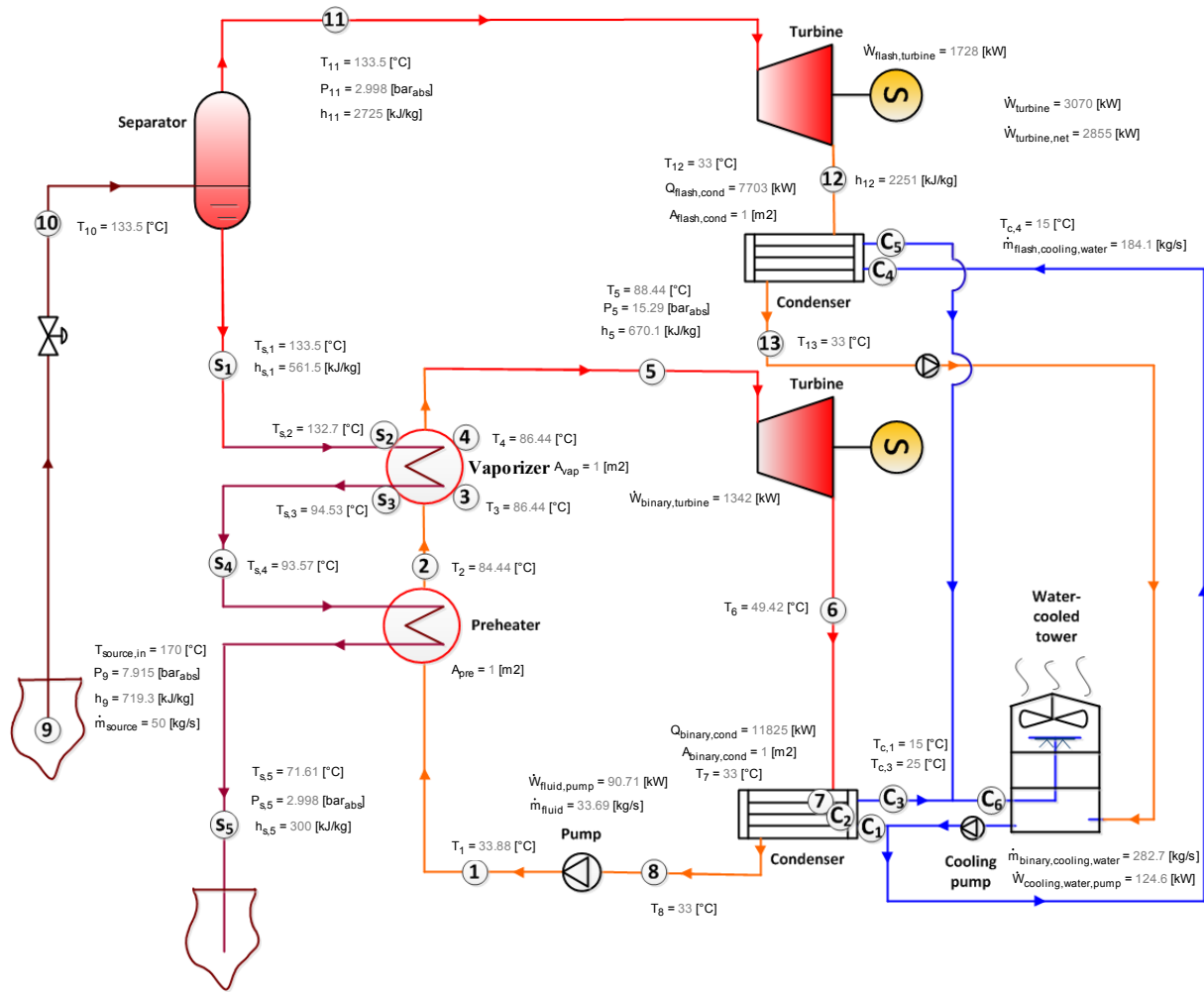


FIGURE 14: Flash-binary system diagram

Optimization focuses on obtaining the optimum separation pressures and vaporizer pressure which could maximize power output. Figure 15 shows the 3D relationship of separation pressure, vaporizer pressure and turbine work, based on the Scilab programme. The optimum pressures are: $P_{10}=2.998$ bar; $P_5=15.29$ bar. The maximum power, shown in the top left area, is 3070 kW.

Table 10 shows the optimum thermodynamic properties of each process state in a flash-binary system. The main results of the flash-binary cycle are shown in Table 11. The injection temperature is about 72°C. The area of the flash condenser, the binary condenser, the preheater and the vaporizer are about 625 m², 971 m², 382 m² and 327 m², respectively.

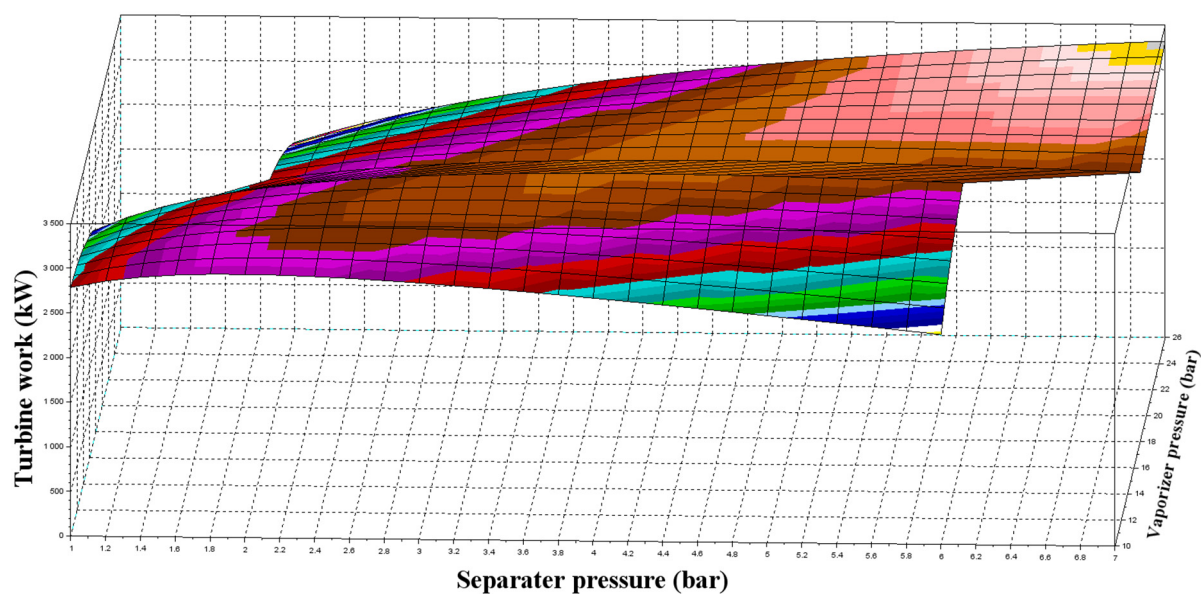


FIGURE 15: Separator pressure, vaporizer pressure and turbine power relationship

TABLE 10: Thermodynamic optimization of a flash-binary system

State	Pressure	Temperature	Mass flow	Steam quality	Volume	Enthalpy	Entropy	Heat rate	Specific exergy	Exergy rate
	P (bars)	T (°C)	m (kg/s)	x	v (m ³ /kg)	h (kJ/kg)	s (kJ/kg·°C)	Q (kW)	e (kJ/kg)	Ex (kW)
1	15.29	34	33.7	-100	0.002	282	1.27	9501	3.72	125
2	15.29	84	33.7	-100	0.002	419	1.69	14106	21.94	739
3	15.29	86	33.7	0.00	0.002	425	1.70	14312	23.13	779
4	15.29	86	33.7	1.00	0.024	665	2.37	22404	70.87	2388
5	15.29	88	33.7	100	0.025	670	2.39	22576	71.91	2423
6	4.40	49	33.7	100	0.095	630	2.42	21235	23.10	778
7	4.40	33	33.7	1.00	0.088	599	2.32	20187	20.51	691
8	4.40	33	33.7	0.00	0.002	279	1.27	9410	1.66	56
9	7.92	170	50.0	100	0.001	719	2.04	35965	132.60	6632
10	3.00	134	50.0	0.07	0.045	719	2.06	35965	127.50	6377
11	3.00	134	3.6	100	0.606	2725	6.99	9935	712.40	2597
12	0.05	33	3.6	100	24.430	2251	7.38	8207	126.90	463
13	0.05	33	3.6	100	0.001	138	0.48	504	2.27	8
S1	3.00	134	46.4		0.001	562	1.67	26026	81.53	3779
S2	3.00	133	46.4	-100	0.001	558	1.66	25868	80.53	3733
S3	3.00	95	46.4	-100	0.001	396	1.25	18364	39.31	1822
S4	3.00	94	46.4	-100	0.001	392	1.23	18174	38.44	1782
S5	3.00	72	46.4	-100	0.001	300	0.97	13905	20.94	971
C1	2	15	282.7		0.001	63	0.22	17841	0.20	93
C2	-	24	282.7			101	0.36	28609	0.60	171
C3	-	25	282.7			105	0.37	29655	0.72	205
C4	2	15	184.1		0.001	63	0.22	11619	0.20	37
C5	-	25	184.1		0.001	105	0.37	19312	0.72	133
C6	-	25	466.8		0.001	105	0.37	48967	0.72	338

TABLE 11: Energy summary of a flash-binary system

No.	Item	Units	Optimum value
1	Separator pressure	bar	2.998
2	Vaporizer pressure	bar	15.29
3	Flash turbine shaft work	kW	1728
4	Binary turbine shaft work	kW	1342
5	Total turbine shaft work	kW	3070
6	Working fluid pump	kW	91
7	Cooling pump	kW	125
8	Total turbine net output power	kW	2855
9	Injection temperature	°C	72
10	Flash condenser capacity	kW	7703
11	Flash condenser area	m ²	624.7
12	Binary condenser capacity	kW	11852
13	Binary condenser area	m ²	971
14	Vaporizer area	m ²	382.3
15	Preheater area	m ²	326.6

3.5 Gas-vapour-liquid binary system optimization

The gas-vapour-liquid binary system is just suitable for Yu-Lingong geothermal field, which includes 8% non-condensable gas; the conditions are shown in Table 3. Two separators and one gas-vapour vaporizer are used in the system. The first separation pressure P_{g1} and vaporizer pressure P_{12} are the main variables used to optimize the turbine power output. Figure 16 shows the diagram of a gas-vapour-liquid binary system.

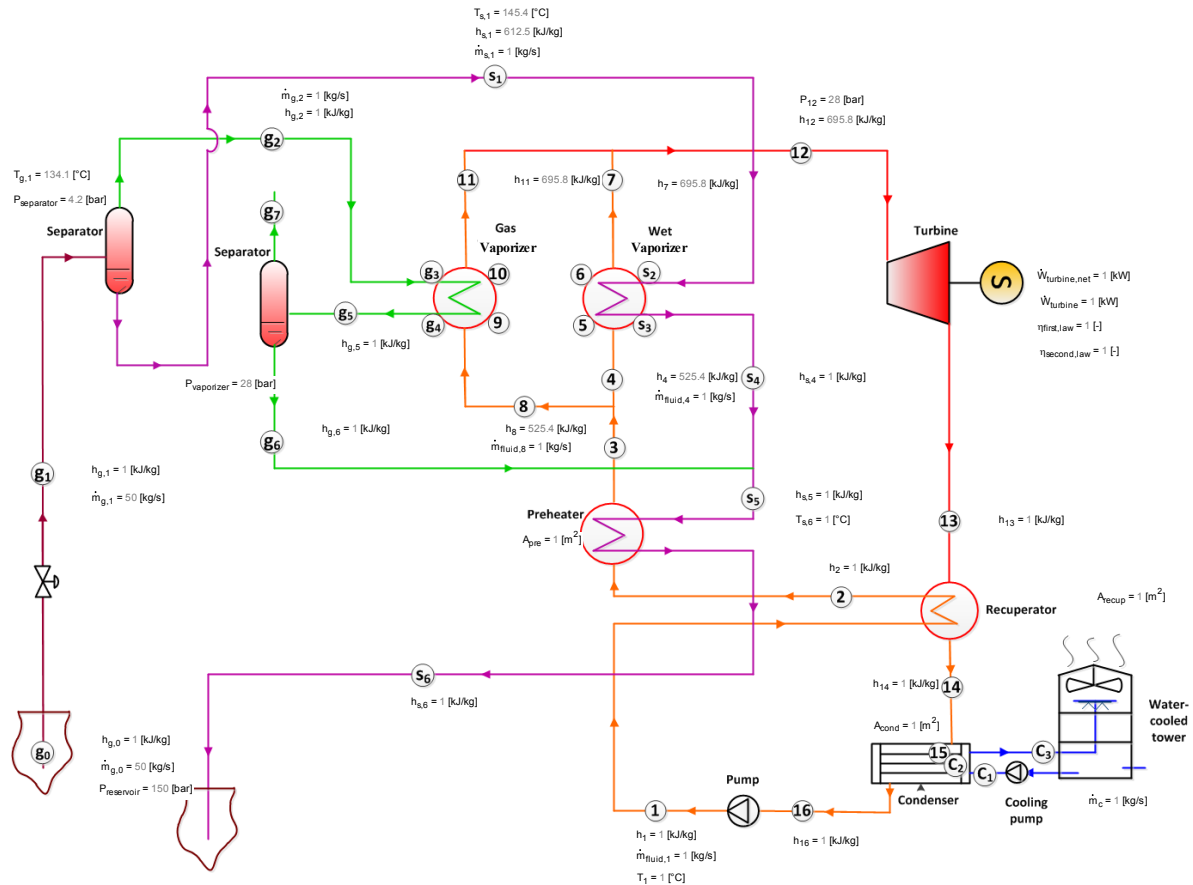


FIGURE 16: Gas-vapour-liquid binary system diagram

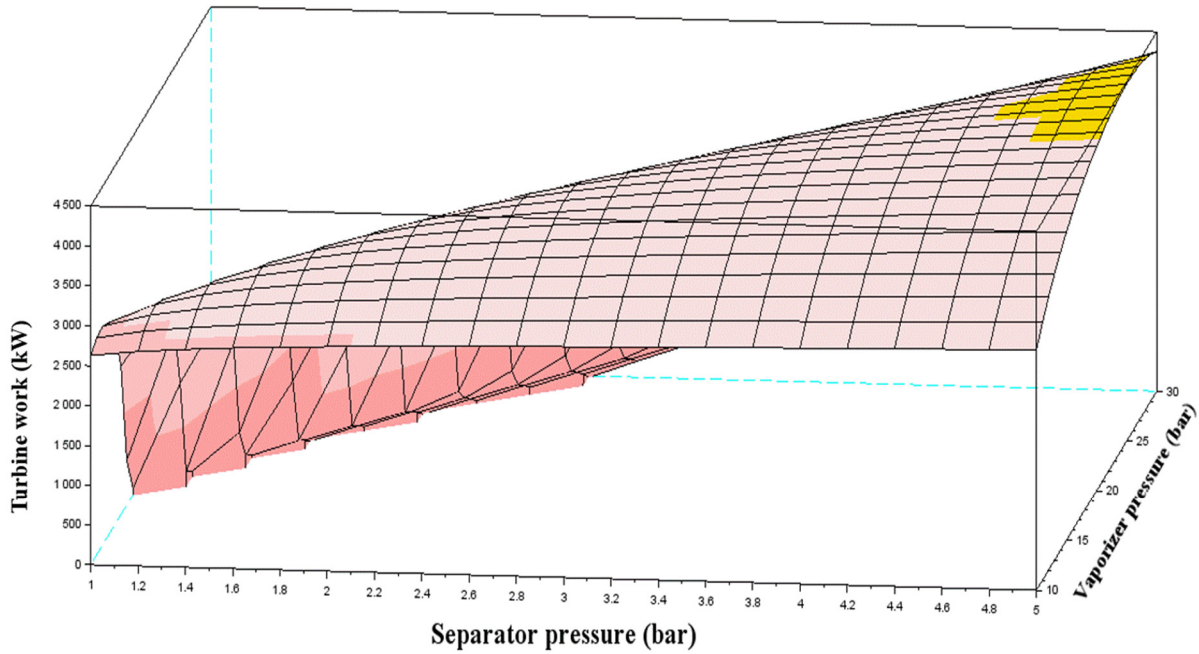


FIGURE 17: Separator pressure, vaporizer pressure and turbine power relationship of a gas-vapour-liquid binary system

Figure 17 gives the relationship of the separator pressure, vaporizer pressure and turbine power. The greater the separator and vaporizer pressure, the bigger the turbine work. However, the optimum thermodynamic parameters are affected by other factors. The constricting conditions are as follows: the maximum turbine work; the preheater pinch; the temperature pinch between T_{s6} and T_2 is more than 15°C ; and the injection temperature T_{s6} is between 50 and 60°C . Figure 18 gives the relationship of the vaporizer pressure and the injection temperature T_{s6} at a separator pressure of 4.2 bar. Therefore, the optimum separator and vaporizer pressure are 4.2 bar and 28 bar, respectively.

Table 12 shows the optimum thermodynamic properties of each process state in a gas-vapour-liquid binary system. The main results of the gas-vapour-liquid binary cycle are shown in Table 13. The injection temperature is about 51.85°C . The total turbine shaft work is 3773 kW, the areas of the gas-vapour vaporizer, wet vaporizer, preheater, recuperator and condenser are 662 m², 341 m², 1988 m², 360 m² and 5160 m², respectively.

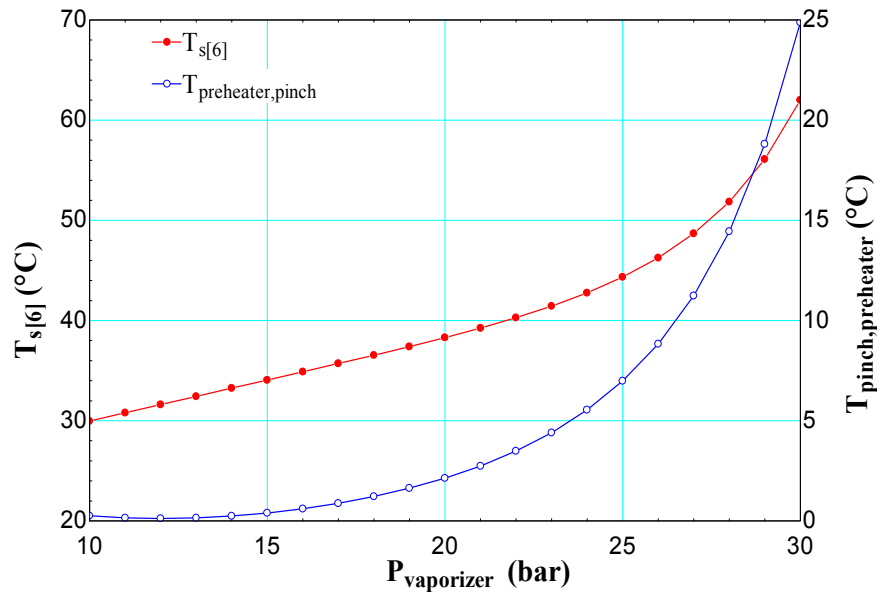


FIGURE 18: Vaporizer pressure, T_{s6} and preheater temperature pinch relationship

TABLE 12: Thermodynamic optimization of a gas-vapour-liquid binary system

State	Pressure	Temperature	Mass flow	Volume	Enthalpy	Entropy	Heat rate	Specific exergy	Exergy rate
	P (bars)	T (°C)	m (kg/s)	v (m ³ /kg)	h (kJ/kg)	s (kJ/kg.°C)	Q (kW)	e (kJ/kg)	Ex (kW)
1	28.0	25	56.6	0.002	261	1.20	14744	4.9	277
2	28.0	37	56.6	0.002	291	1.30	16493	6.5	370
3	28.0	117	56.6	0.003	525	1.96	29738	48.8	2764
4	28.0	117	23.4	0.003	525	1.96	12268	48.8	1140
5	28.0	119	23.4	0.003	534	1.99	12471	51.1	1194
6	28.0	119	23.4	0.011	687	2.38	16046	91.8	2144
7	28.0	121	23.4	0.011	696	2.40	16247	94.1	2197
8	28.0	117	33.3	0.003	525	1.96	17470	48.8	1623
9	28.0	119	33.3	0.003	534	1.99	17759	51.1	1699
10	28.0	119	33.3	0.011	687	2.38	22849	91.8	3051
11	28.0	121	33.3	0.011	696	2.40	23135	94.1	3128
12	28.0	121	56.6	0.011	696	2.40	39382	94.1	5325
13	3.3	47	56.6	0.129	629	2.45	35607	12.2	691
14	3.3	30	56.6	0.120	598	2.35	33864	9.9	560
15	3.3	23	56.6	0.116	586	2.31	33162	9.4	533
16	3.3	23	56.6	0.002	255	1.19	14410	0.4	22
S1	4.2	145.4	41.7		613	1.80	25523	97.0	4043
S2	4.2	144.3	41.7		608	1.78	25323	95.5	3980
S3	4.2	124.2	41.7		522	1.57	21748	70.4	2934
S4	4.2	123.1	41.7		517	1.56	21543	69.1	2878
S5	4.2	123.1	44.2		517	1.56	22861	69.1	3054
S6	4.2	51.85	44.2		217	0.73	9611	9.5	421
g0	150.0	180	50.0		714	1.93	35690	160.2	8011
g1	4.2	134.1	50.0		714	2.02	35690	132.6	6629
g2	4.2	134.2	8.3		1463	3.75	12182	383.8	3195
g3	4.2	133.8	8.3		1429	3.67	11899	373.9	3113
g4	4.2	124.2	8.3		818	2.15	6808	199.8	1664
g5	4.2	123.2	8.3		783	2.06	6520	190.3	1585
g6	4.2	123.2	2.5		518	1.56	1310	69.0	175
g7	4.2	123.2	5.8		899	2.28	5210	243.4	1410
C1	2.0	15	465.0	0.001	63	0.22	29346	0.2	92
C2	-	24.64	465.0	0.001	103	0.36	48081	0.7	314
C3	-	25	465.0	0.001	105	0.37	48779	0.7	337

TABLE 13: Energy summary of a gas-vapour-liquid binary system

No.	Item	Units	Optimum value
1	Vaporizer pressure	bar	28
2	Separator pressure	bar	4.2
3	Turbine shaft work	kW	3773
4	Cooling pump	kW	124.1
5	Working pump	kW	337.4
6	Turbine net output power	kW	3311
7	Condenser temperature	°C	24.6
8	Condenser capacity	kW	19453
9	Gas-vapour-liquid vaporizer area	m ²	661.7
10	Wet vaporizer area	m ²	341.8
11	Preheater area	m ²	1988
12	Recuperator area	m ²	360
13	Condenser area	m ²	5160
14	The first law efficiency	%	13.4
15	The second law efficiency	%	50

3.6 Comparison of different power systems

The calculations and optimization of four power plant scenarios were carried out for Tuo-bei geothermal field, as well as a gas-vapour-liquid binary system for Yu-lingong geothermal field. The main results for the Tuo-bei power systems are summarized in Table 14. Later in this report, the five scenarios for Tuo-bei geothermal field will be compared.

TABLE 14: Power system design comparison for Tuo-bei field

Item	Unit	Single flash	Binary cycle	Double flash	Flash-binary combined system	Gas-vapour-liquid binary system
W_{net}	kW	2230	3022	2850	2855	3311
$T_{\text{injection}}$	°C	98	60	76	72	52
A_{total}	m ²	1212	4583	1520	2305	8511
η_{first}	%	7.9	13	10	-	13.4
η_{second}	%	34.7	45	44	-	50

A binary system offers the maximum net power output and second law of efficiency. The total area of the binary system is the largest of the four scenarios, but an additional separator would be used in the other three scenarios. Therefore, a binary power system will be designed for Tuo-bei geothermal field. In Chapter 4, the economics of a binary system will be discussed.

4. THERMOECONOMIC OPTIMIZATION OF A GEOTHERMAL BINARY POWER PLANT

4.1 Methodology and process

The economic evaluation and analysis of a binary power plant were implemented by using the engineering economic methodology. There are three methods for economic evaluation (Bejan and Moran, 1996; Sun, 2008).

- The first is based on the average rate of return and payback period method. The payback period is defined as the length of time required for cash inflows received from the project to recover the original cash outlays required by the initial investment.
- The second is the Net Present Value (NPV) method. When the net present value method is used for project selection, the following rules apply: accept any project for which the present value is positive; reject any project with negative present value; the project with the highest present value is given the highest preference among various alternatives; if two projects are mutually exclusive, accept the one having the greater present value.
- The third is the internal rate of return method. The net present value method uses the interest rate, usually based on the company's cost of money. The internal rate of return method seeks to avoid the arbitrary choice of an interest rate; instead, it calculates an interest rate, initially unknown, that is internal to the project.

The economic conditions of the Tuo-bei geothermal binary power system are shown in Table 15. The exchange rate of Chinese Yuan for U.S. dollar is 6.5 Yuan per dollar in this report.

TABLE 15: Economic conditions of the Tuo-bei binary power plant

No.	Item	Unit	Value
1	Economic life span	year	25
2	Minimum attractive rate of return	%	10
3	Operation time for one year	h	8000
4	Income tax rate	%	17
5	Price of electricity for user	\$/kWh	0.09
6	Effective rate of return	%	10

4.2 Cost estimation and cash flow of power plant

The cost estimation of the binary system is shown in Table 16 (Bejan and Moran, 1996). The cooling tower cost is obtained from the Cooling Tower Depots. Total initial investment cost is the sum of the total capital cost and fuel cost: 9,767,000 US\$. Figure 19 shows the cash flow of the binary power system. The average annual profit is 1,308,000 \$/year, the average rate of return (ARR) is 13.4%, and the payback period is about 6 years. The main results are shown in Table 17.

TABLE 16: Binary power system cost

Item		Capacity	Unit	US\$/unit	Cost (\$)
PEC	Vaporizer	634	m ²	300	52,310
	Preheater	2157	m ²	300	139,360
	Recuperator	350	m ²	300	32,555
	Condenser	1742	m ²	280	109,654
	Organic fluid turbine	3506	kW	1000	302,977
	Working fluid Pump	355	kW	500	54,892
	Cooling water pump	129	kW	400	19,571
	Cooling tower				210,000
Purchased equipment costs (PEC):					921,319
Purchased equipment installation		33%	%PEC		304,035
Piping		35%	%PEC		322,462
Instrumentation and controls		12%	%PEC		110,558
Electrical equipment and materials		13%	%PEC		119,772
Land, Civil, structural		21%	%PEC		193,477
Direct cost					1,972,000
Indirect cost (engineering, construction)		15%	%DC		295,744
Total capital cost					2,267,000
Fuel cost		50	kg/s	150,000	7,500,000
O & M cost		3%	%TCC (per year)		68,021

TABLE 17: Results of cash flow analysis

No.	Item	Unit	Value
1	Average annual profit	\$/year	1,308,000
2	Average rate of return	%	13.39
3	Payback period	year	5.73

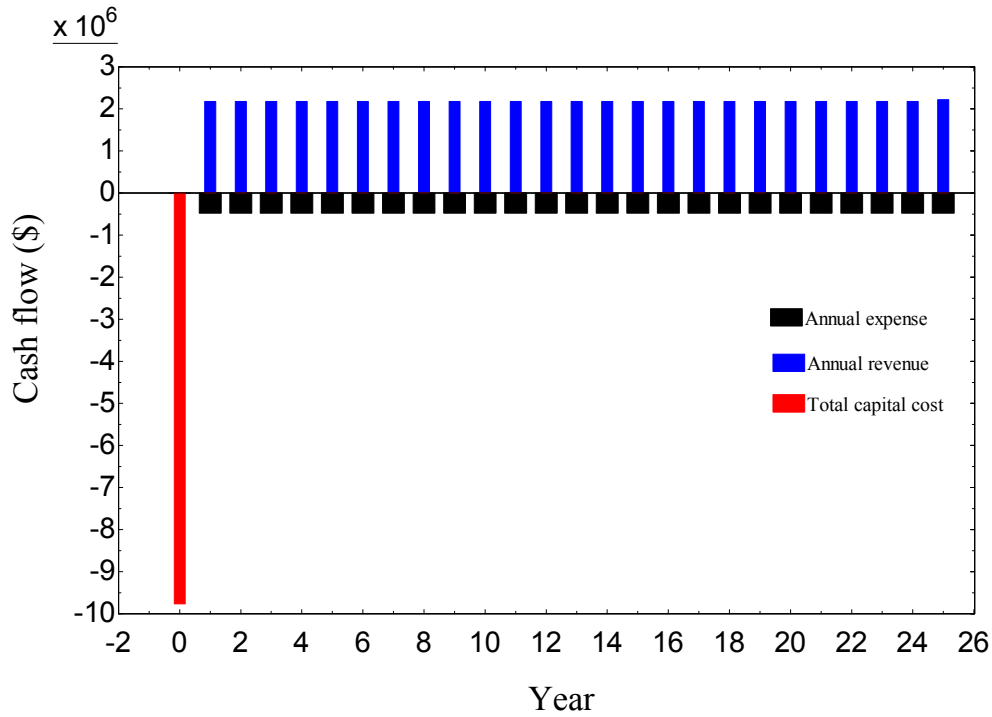


FIGURE 19: Cash flow of a binary power system

4.3 Exergy cost and thermoeconomic optimization

Thermoeconomics deal with the value of the energy within a plant. The analysis is based on exergy flows, and breaks the plant up into individual components, where each component can be analysed separately. The cost flow of products must be equal to the sum of all incoming cost flows for a power system and its components. In thermodynamics, the heat flow is usually considered as input, and work (power) as output. That is the reason for entering the heat cost flow as input and the work (power) cost flow as output. This balance is written as (Valdimarsson, 2011):

$$\sum_e C_{e,k} + C_{w,k} = C_{q,k} + \sum_i C_{i,k} + Z_k \quad (1)$$

where C = Cost rate (\$/s);
 Z = Investment cost rate (\$/s);
 e = Product or output (index);
 i = Feed or input (index);
 k = Number of components (index);
 q = Heat (index);
 w = Work or power (index).

4.3.1 Exergy costs

An exergy analysis model was built based on the binary system. Table 18 shows the investment cost rate and destructive exergy cost rate of the main components in the binary system. Each point of exergy cost and unit exergy cost is calculated from the exergy and exergy cost balance. Table 19 shows the results of each point in the binary system.

TABLE 18: Exergy cost rate of the main components in the binary system

Component	Capital cost rate (US\$/s)	O&M cost rate (US\$/s)	Destruction cost rate (US\$/s)
Vaporizer	0.0002164	0.00002403	0.005389
Preheater	0.0005766	0.00006402	0.002515
Recuperator	0.0001347	0.00001495	0.0003483
Working pump	0.0002271	0.00002522	0.0009479
Condenser	0.0004537	0.00005037	0.0104
Turbine	0.001254	0.0001392	0.008794

TABLE 19: Cost rate and unit exergy cost of the binary system

State	Exergy rate	Cost rate	Unit exergy cost	Unit exergy cost
	Ex (kW)	C (US\$/s)	c (US\$/kWh)	c (US\$/kJ)
1	368	0.02275	0.2223	0.00006176
2	496	0.0243	0.1764	0.000049
3	2971	0.03658	0.04432	0.00001231
4	3111	0.0372	0.04305	0.00001196
5	5585	0.04997	0.03221	0.000008947
6	5725	0.05076	0.03192	0.000008865
7	1437	0.01274	0.03192	0.000008865
8	1278	0.01133	0.03192	0.000008865
9	1224	0.01133	0.03332	0.000009257
10	97	0.01183	0.4378	0.0001216
S1	6655	0.02869	0.01552	0.000004311
S2	6473	0.0279	0.01552	0.000004311
S3	3566	0.01537	0.01552	0.000004311
S4	3422	0.01475	0.01552	0.000004311
S5	723	0.003115	0.01552	0.000004311
C1	99	0	0	0
C2	335	0	0	0
C3	361	0	0	0
Power prod.	3506	0.03942	0.04047	0.00001124

4.3.2 Thermoeconomic evaluation

A detailed thermoeconomic evaluation of the binary system should be based on the following variables: exergetic efficiency; exergetic destruction and loss ratio; relative cost difference; and the exergoeconomic factor (Dorj, 2005). The results of the designed power plant are calculated based on a binary system. The main results are shown in Table 20.

TABLE 20: Thermoeconomic evaluation of main components in the binary system

Component	Sum cost rate of destruction and capital investment	Exergetic efficiency	Relative cost difference	Exergetic destruction	Exergetic loss ratio
	(US\$/s)	(%)	-	(%)	(%)
Condenser	0.1133	21.6	12.71	13.91	3.832
Turbine	0.01019	81.76	0.1901	11.76	-
Working pump	0.00546	76.27	0.2346	1.267	-
Vaporizer	0.004491	85.17	0.05761	7.2	-
Preheater	0.003395	91.71	0.3685	3.362	10.86
Recuperator	0.001668	80.47	0.02698	0.47	-

4.3.3 Thermoeconomic optimization

The main purpose of thermoeconomic optimization is to achieve a balance between the expenditure on capital costs, and the exergy costs which will lead to a minimum cost of the plant product. The different components in the power system can be categorised as (Dorj, 2005):

- 1) “Ready-made” components selected from a manufacturer’s catalogue, such as pumps, turbines, etc.
- 2) Components specially designed, or “tailor-made” for the plant, e.g. heat exchangers, etc.

The first type of component is decided by a manufacturer. The second type of component is suitable for thermoeconomic optimization. The advantage of using the exergy method of thermoeconomic optimization is that the various elements of the plant can be optimized on their own; the effect of the given element on the whole plant can be taken into account by local unit costs of exergy fluxes or those of exergy losses.

Figure 20 shows the relationship between the vaporizer pressure and the total cost rate of destruction and capital investment for the condenser. The vaporizer pressure affects the sum of the cost rate of destruction and capital investment for the condenser; the minimum value of the cost rate for the condenser is 0.1132, and the vaporizer pressure is 27.4 bar. So the optimum vaporizer pressure is 27.4 bar for thermoeconomic optimization.

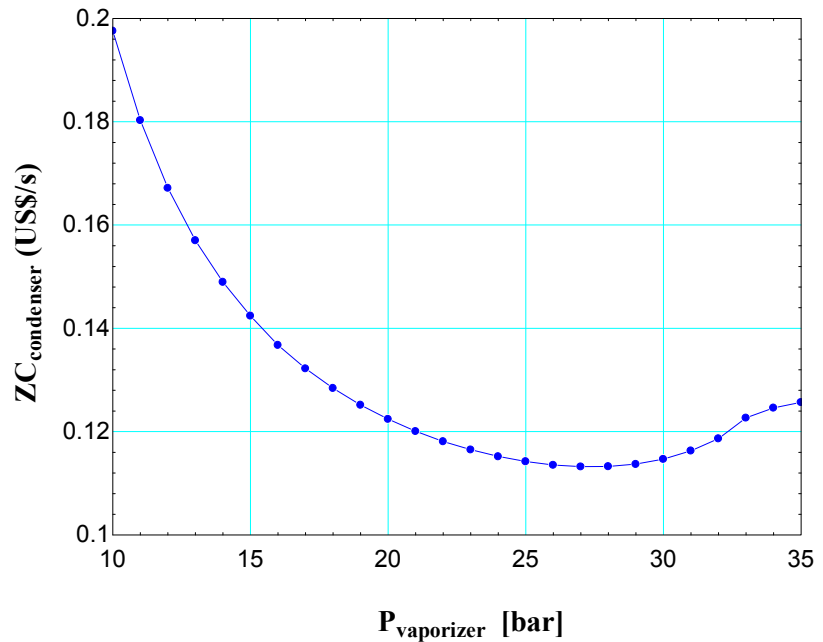


FIGURE 20: Vaporizer pressure and destruction and capital investment total cost rate of condenser

4.4 Sensitivity analysis

The geothermal water reservoir temperature and flow rate can affect the power production cost and specific net power output (Dorj, 2005; Estévez, 2012). When the mass flow rate is 50 kg/s, Figure 21 shows the reservoir temperature sensitivity to the power production cost and specific net power output for the binary system. For Tuo-bei geothermal field, the power production cost is about 0.04 US\$/kWh.

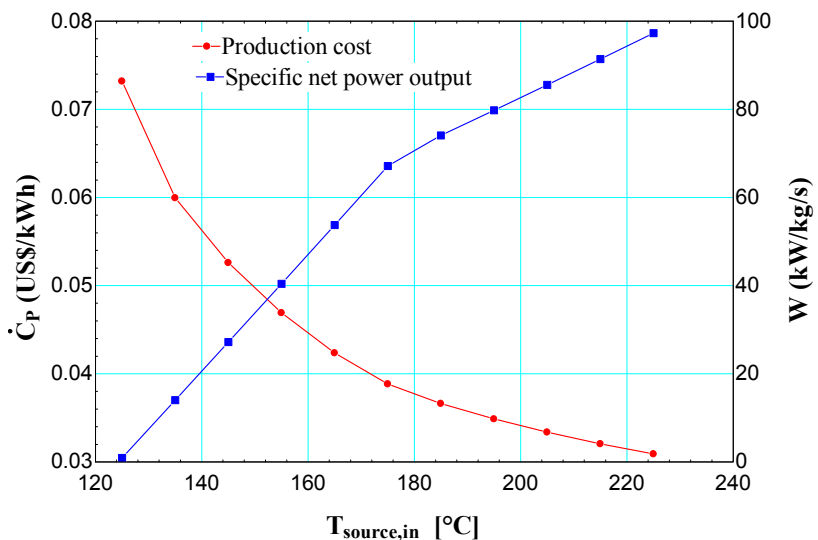
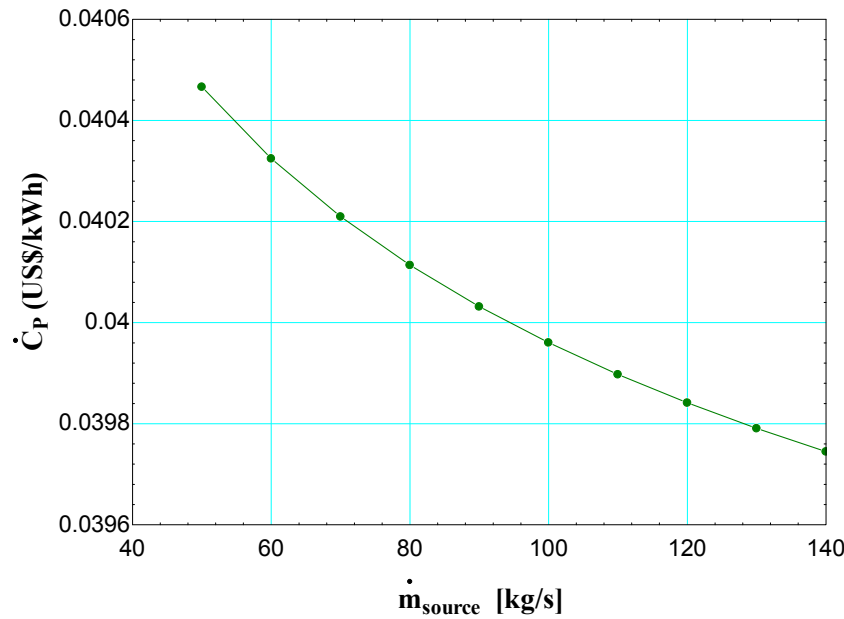


FIGURE 21: Source temperature sensitivity to power production cost and specific net power output



The specific net power output (blue line) increases with reservoir temperature. For Tuo-bei geothermal field, the specific net power output is about 59.76 kW/kg/s. Figure 22 shows the mass flow rate, which affects the power production cost, at a geothermal temperature of 170°C. The power production cost decreases by increasing the mass flow rate.

FIGURE 22: Mass flow rate sensitivity to power production cost

4.5 Economic feasibility based on PV value method

Based on the cash flow of the binary power system, the internal rate of return can be carried out (Sun, 2008). Figure 23 shows the curve of NPV as a function of the internal rate of return in the expected life span. When the NPV equals zero, the maximum internal rate of return is 17.02%. If the internal rate of return equals the average rate of return (13.39%), the NPV is 2,345,000\$, which is more than zero. Therefore, economically, a binary power system is feasible for Tuo-bei geothermal field.

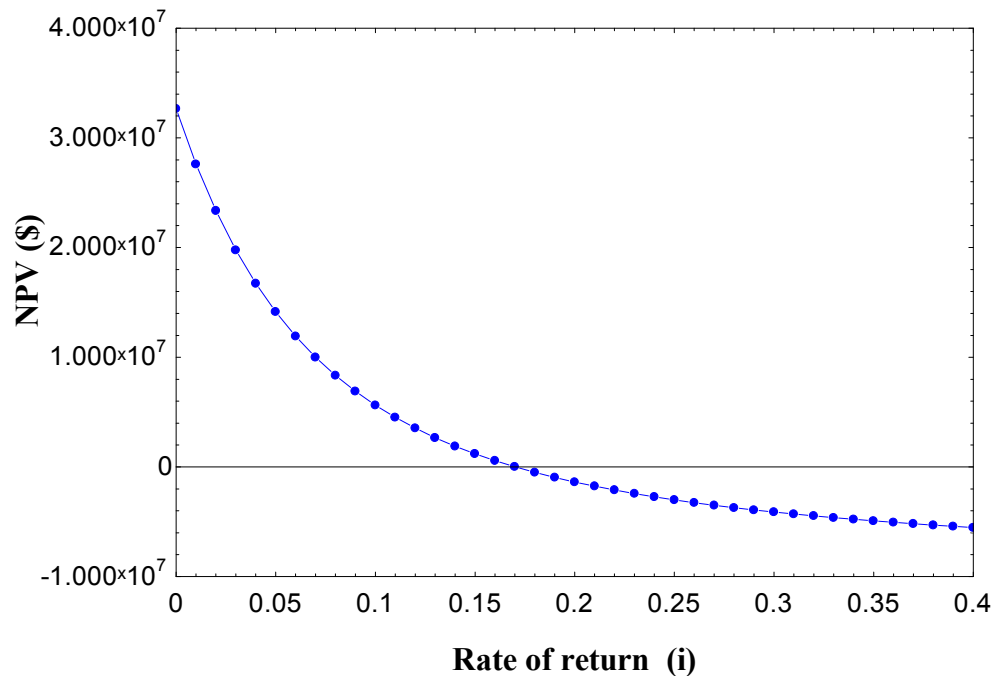


FIGURE 23: Relationship between NPV and internal rate of return

5. CONCLUSIONS

A new geothermal power plant is scheduled to be built in Sichuan Province in China. Five types of geothermal power systems were designed for the Sichuan geothermal area. Based on the thermodynamic and thermoeconomic analysis, the conclusions are as follows:

- 1) A new geothermal power plant was selected for the Sichuan geothermal area based on the demands of the energy company, and in accordance with government policies. The temperatures of Tuo-bei and Yu-lingong geothermal fields are more than 150°C. The fields are located far from cities. Because of lack of electricity, a geothermal power plant could improve the living standard of the local people.
- 2) Single-flash, binary cycle, double-flash and single-flash-binary combined power systems were designed for Tuo-bei field. A gas-vapour-liquid binary system was designed for Yu-lingong field. Based on a thermodynamic optimization analysis for these power systems, a binary cycle with a recuperator was selected for Tuo-bei field; the capacity of the power plant is 3506 kW. A gas-vapour-liquid binary system was designed for Yu-lingong field; the capacity of this power plant is 3773 kW.
- 3) The economic feasibility of a binary cycle with a recuperator was analysed, based on the payback period and NPV methods. The total capital investment is about 20,728,000 US\$, with a payback period of less than six years. When the internal rate of return is more than 17%, the net present value is less than zero.
- 4) Vaporizer pressure is the key variable parameter for a binary system. Thermoeconomic optimization of the main components in a binary power system shows that the condenser destruction and exergy loss is more than that of other components. The optimum pressure is 27.4 bar for Tuo-bei geothermal field.
- 5) The reservoir temperature and mass flow rate are sensitive for the power production cost. The higher the temperature and the larger the flow rate, the lower the power production cost. For the binary power system in Tuo-bei geothermal field, the power production cost is 0.04 US\$/kWh.

ACKNOWLEDGEMENTS

I would like to thank UNU-GTP for the support for this training. Thanks to Mr. Lúdvík S. Georgsson and Mr. Ingimar G. Haraldsson for giving me the precious study opportunity.

I would like to express the deepest and sincerest gratitude to my supervisor, Dr. Páll Valdimarsson. Thanks are extended for his selfless help during my project study.

Thanks to UNU-GTP staff for giving me a family feeling. Thanks for the friendship of our group.

Finally, I would like to express my deepest appreciation to my family. Thanks to my wife for her support and to my cute son, Jun.

REFERENCES

- Ahangar, F.A., 2012: Feasibility study of developing a binary power plant in the low-temperature geothermal field in Puga, Jammu and Kashmir, India. Report 6 in: *Geothermal training in Iceland 2012*. UNU-GTP, Iceland, 1-26.
- Bejan, A., and Moran, M., 1996: *Thermal design and optimization*. John Wiley & Sons, Inc., NY, 533 pp.
- Bertani, R., 2010: Geothermal power plants in the world 2005-2010 update report. *Proceedings of the World Geothermal Congress 2010, Bali, Indonesia*, 41 pp.
- Dagdas, A., Ozturk, R., and Bekdemir, S., 2005: *Thermodynamic evaluation of Denizli Kizildere geothermal power plant and its performance improvement*. *Energy Conversion and Management* 46, 245–256.
- Dipippo, R., 2008: *Geothermal power plants. Principles, applications, case studies and environmental impact*. Elsevier Ltd., Kidlington, UK, 493 pp.
- Dorj, P., 2005: *Thermoeconomic analysis of a new geothermal utilization CHP plant in Tsetserleg, Mongolia*. University of Iceland, MSc thesis, UNU-GTP, Iceland, report 2, 74 pp.
- Estévez S., J.R., 2012: *Geothermal power plant projects in Central America: technical and financial feasibility assessment model*. University of Iceland, MSc thesis, UNU-GTP, Iceland, report 4, 87 pp.
- Franco, A., and Villani, M., 2009: Optimal design of binary cycle power plants for water-dominated, medium-temperature geothermal fields. *Geothermics*, 38-4, 379-391.
- Jalilinasrabady, S., Itoi, R., Valdimarsson, P., Saevarsdóttir, G., Fujii, H., 2012: Flash cycle optimization of Sabalan geothermal power plant employing exergy concept. *Geothermics*, 43, 75-82.
- Lin W.J., and Liu Z.M., 2013: *Geothermal resource distribution and capacity estimation in China* (in Chinese). *China Geology*, 10 pp.
- Rosyid, H., Koestoer, R., Putra, N., Nasruddin Mohamad, A.A., and Yanuar, 2010: Sensitivity analysis of steam power plant-binary cycle. *Energy*, 35-9, 3578-3586.
- Sun C.X., 2008: *Feasibility study of geothermal utilization of Yangbajain field in Tibet autonomous region, P.R. China*. University of Iceland, MSc thesis, UNU-GTP, Iceland, report 3, 85 pp.
- Valdimarsson, P., 2011: Basic concepts of thermoeconomics. Presented at “Short Course on Geothermal Drilling, Resource Development and Power Plants”, UNU-GTP and LaGeo, San Salvador, El Salvador, 7 pp.
- Valdimarsson, P., 2014: *Thermodynamics of geothermal power production*. UNU-GTP, Iceland, unpubl. lecture notes.
- Wang J.Y., Ma W.B., 2005: *Geothermal utilization* (in Chinese). Chemical Industry Press, 147 pp.



UNITED NATIONS
UNIVERSITY

UNU-GTP

Geothermal Training Programme

Orkustofnun, Grensasvegur 9,
IS-108 Reykjavik, Iceland

Reports 2014
Number 19

GEOCHEMICAL INTERPRETATION OF DISCHARGE FROM REYKJANES WELLS RN-29 AND RN-32, SW-ICELAND

Melese Mekonnen Berehannu

Geological Survey of Ethiopia

Addis Ababa

P.O. Box 40069

ETHIOPIA

melese147@gmail.com

ABSTRACT

In this report, chemically analysed data from Reykjanes wells RN-29 and RN-32 are used to compare the aquifer temperatures of these wells using selected chemical geothermometers. Calcite and amorphous silica scaling potential is assessed for selected wells. The downhole temperature measurements, the intersection of anhydrite, wairakite, epidote, prehnite and quartz mineral saturation indices and quartz geothermometer results are used to predict the reservoir temperature. From these parameters, the reservoir temperature of Reykjanes well RN-29 is considered to be around 290°C. Similarly, for Reykjanes well RN-32 the reservoir temperature is considered to be around 250°C. The speciation program WATCH was used to calculate amorphous silica and calcite saturation for variably boiled well water. The chemical composition of the fluids was compared with that of a standard sea water composition and the results had the same composition in chloride and total dissolved solids. Reykjanes well RN-29 is assumed to be an excess enthalpy well. The deep liquid composition was computed by a phase segregation model and the results showed that the composition was quite different for volatile components, while the change was insignificant for non-volatile components. Reykjanes well RN-32 was assumed to have a liquid enthalpy in order to compute the deep fluid composition at 250°C reservoir temperature.

1. INTRODUCTION

The Reykjanes geothermal system is located on the southwest tip of the Reykjanes Peninsula in SW-Iceland (Figure 1). The geothermal surface manifestations at Reykjanes include altered rocks, steam vents, mud pits and warm ground (Fridriksson et al., 2006). The reservoir fluid in the Reykjanes system is hydrothermally modified seawater with some addition of magmatic gases (Arnórsson, 1978; Ólafsson and Riley, 1978; Freedman et al., 2010; Hardardóttir et al., 2009; Óskarsson et al., 2014). In Section 2 of this study, a general background of the Reykjanes field is provided: geological and structural setting, chemical studies of the area are described, and the drilling operations for wells RN-29 and RN-32 reviewed. In Section 3, the sampling and analysis of geothermal fluids is described, including fluid classification, geothermometers, and solution mineral equilibria. In this study, the chemically analysed data for Reykjanes wells RN-29 and RN-32 were used to evaluate deep fluid composition, solution mineral equilibria and to estimate subsurface temperatures in the geothermal systems. The subsurface

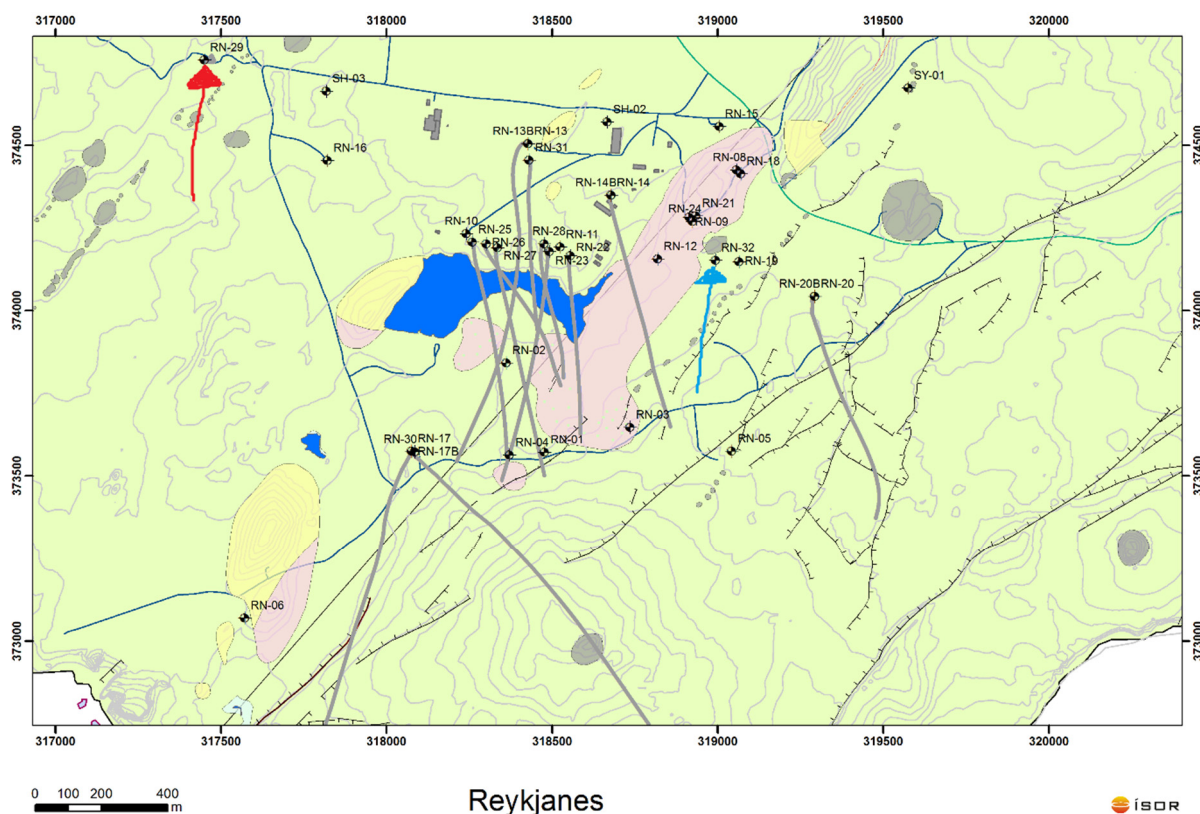


FIGURE 1: Location of wells RN-29 (in red) and RN-32 (in blue) at Reykjanes shown on a map showing surface topography, surface structural features and geothermal manifestations (from K. Saemundsson, pers. comm., revised maps)

temperatures predicted by various geothermometers are compared with measured (downhole) temperatures. Calculations of deep fluid composition were performed with the WATCH speciation program version 2.4 (Bjarnason, 2010). The enthalpy of the discharge from well RN-32 is similar to that of steam saturated water at the aquifer temperature. The enthalpy of the discharge from well RN-29 is higher than that of liquid water at the aquifer temperature. An attempt is made to apply and explore the sensitivity of calculated aquifer fluid composition to assumed phase segregation pressure for well RN-29. The state of chemical equilibria between the main hydrothermal alteration minerals and solutions of the gaseous components will be assessed. In Section 4, the deep fluid composition calculated with WATCH speciation program version 2.4 (Bjarnason, 2010), based on modelled liquid enthalpy and excess enthalpy, is provided. In Section 5, the results obtained from the modelling described in Section 4 are presented and discussed. In addition to assessing the state of equilibria with respect to mineral-solution and mineral-gas reactions, the change in chemical composition, fluid classification, geothermometers and production properties are described in this section. In Section 6, conclusions and directions for future work are presented and discussed.

2. REYKJANES GEOTHERMAL FIELD

2.1 Geological and structural setting

The Reykjanes geothermal system consists of young, highly permeable basaltic formations, transected by an intense NE-SW trending fault zone, and is tectonically active (Björnsson et al., 1970). The volcanic activity on the Reykjanes peninsula is concentrated along five distinct fissure swarms, but central volcanic complexes are notably absent at the four westernmost ones (Jakobsson et al., 1978).

The volcanic rocks are of basaltic composition ranging from picrite shield lavas through olivine tholeiite shield lavas and fissure products; no intermediate or rhyolitic rocks crop out west of the Hengill central volcano (Jakobsson et al., 1978). High temperature geothermal systems are found in all Reykjanes Peninsula fissure swarms. The Reykjanes geothermal area is located at the centre of swarms of active faults that facilitate hydrologic convection. High-level magma chambers have apparently not formed in the Reykjanes volcanic systems (Gudmundsson and Thórhallsson, 1986), and sheeted dike complexes are likely to serve as the magmatic heat source for the geothermal activity. Surface geothermal manifestations occur over an area of $\sim 1 \text{ km}^2$, but observations from more than 30 drillholes and several resistivity surveys indicate that the subsurface area of the active system is at least 2 km^2 , consistent with the findings of Björnsson et al. (1972) and Pálmason et al. (1985).

2.2 Geochemical studies

The Reykjanes geothermal water represents heated seawater with freshwater mixing (Ólafsson and Riley, 1978). However, fluid inclusion studies on borehole cuttings and stable isotope ratios of geothermal fluids and secondary minerals indicate that dilute fluids dominated the system at earlier times (Sveinbjörnsdóttir et al., 1986; Franzson et al., 2002; Pope et al., 2010). The difference in the composition of seawater and the geothermal water is due to interaction with the basaltic host rocks at elevated temperatures, with the geothermal water enriched in SiO_2 , K, Ca and depleted in SO_4 and Mg but with the same Cl concentration as the seawater (Björnsson et al., 1970, 1972; Arnórsson, 1978, 1983). The Reykjanes geothermal system has been identified as an active ore-forming system (Hardardóttir et al., 2001). Scales enriched in metals are common in pipelines at Reykjanes and they include the minerals sphalerite, bornite, digenite, galena, chalcopyrite, native silver, silver sulphides, gold (probably occurring in solid solutions or as submicroscopic inclusions) and pyrite among others, with abundances varying from well to well due to differences in the physical parameters of the wells (Hardardóttir et al., 2009). The Reykjanes geothermal system is surrounded by the ocean on three sides, only 1.5 km from the shoreline and extends southwest to the sea (Björnsson et al., 1971; Gudmundsson et al., 1981; Johnsson and Jakobsson, 1985).

2.3 Wells RN-29 and RN-32

The drilling operations at well RN-29 at Reykjanes were carried out by Iceland Drilling Co. for HS Orka, the operator of the field. Well RN-29 is a vertical well. The location of well RN-29 is shown in Figure 1. The drilling of the first stage was completed on April 7th 2010 at 306 m depth, and the second stage ended on April 29th at 902 m depth, and the third and the last stage of drilling was completed on June 8th at 2837 m. Samples of drill cuttings were collected at 2 m intervals and lithological and alteration analyses were carried out during the course of drilling. Well RN-29 intersects several hyaloclastite formations made from tuffs, tuffaceous sediments, breccias and pillow basalts. A few lava series were found in between hyaloclastite units. Holocene lavas and tephra units are at the surface. Around 40 basalt intrusions were identified, 17 of which are thicker than 10 m. The drilling of well RN-32 at Reykjanes was commissioned by HS Orka. Well RN-32 is designed as a production well and was drilled as a make-up well to provide steam to maintain 100 MWe generation in the Reykjanes power plant. The location of well RN-32 is shown in Figure 1. The well was drilled in 3 stages. The drilling of the first stage was completed on February 14th 2013 at 350 m depth, and the second stage ended on April 5th at 1080 m depth. The third and last stage of drilling was completed on April 16th at 1202 m. Well RN-32 goes through several hyaloclastite formations, made from Holocene lava, basaltic tuffs, basaltic breccias, fine- and medium-grained basalt and tuff rich sediments (Gunnarsdóttir et al., 2013).

3. CHEMISTRY OF GEOTHERMAL FLUIDS

3.1 Sampling and analysis of geothermal fluids

The collection of representative samples from discharging wells involves separate collection of the steam phase and the water phase. This is done with the aid of a Webre separator and a cooling device. Great care must be taken to separate steam completely from the liquid. The separator is connected to the steam line and kept open to rinse and warm it up for at least 10 min. Then it is closed and the sampling pressure (Ps) is recorded from the pressure gauge installed on the separator. The geothermal fluids are separated completely in order to discharge steam through the steam outlet, and liquid through the liquid outlet; each is rinsed for a few minutes before sampling. The condensed steam and the non-condensable gases are then collected into an evacuated double port bottle containing a concentrated solution of NaOH (40 wt%). The most abundant gases, CO₂ and H₂S, will dissolve in the caustic solution and the other gases will be collected in the head space. Figure 2 is a schematic diagram of the sampling procedure for geothermal wells.

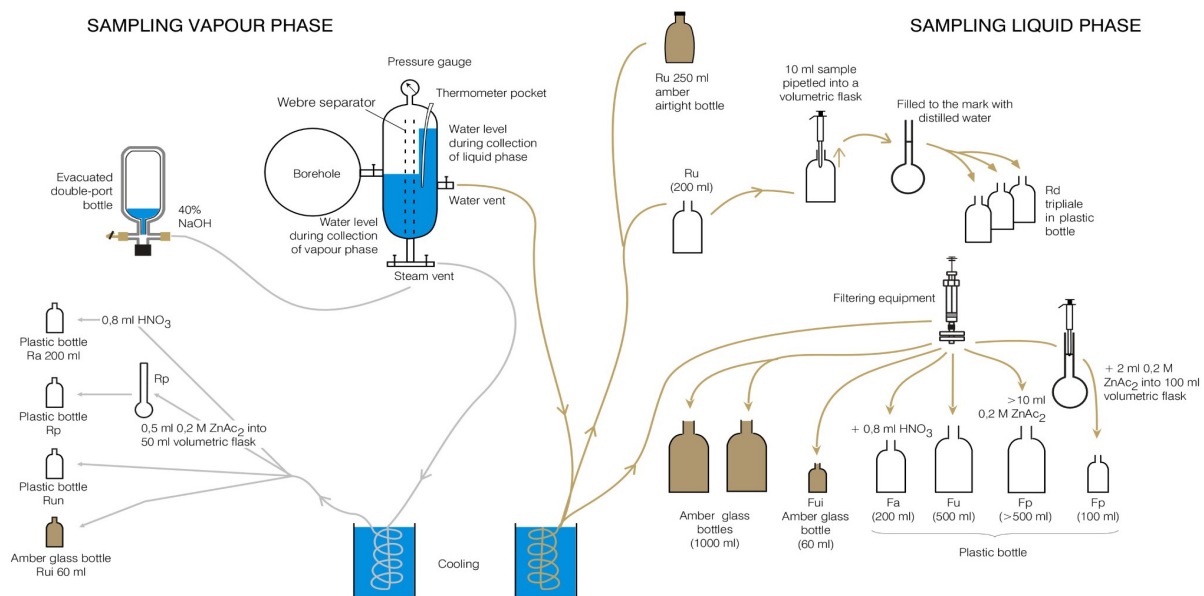


FIGURE 2: Collection of sample from a two-phase geothermal well for chemical analysis (from Ármannsson and Ólafsson, 2006)

Chemical analysis of geothermal water samples must meet certain levels of accuracy and reliability to be useful in identifying geochemical processes in hydrothermal systems. Quality control is largely a concern for the analytical laboratory, but the geochemist using the chemical data must also be concerned with analytical quality. Chemical analyses were examined for internal consistency by calculating the error in the ionic charge balance. To be considered internally consistent, chemical analyses must have less than 5% error in the charge balance. In this study, the geothermal water samples are from Reykjanes wells RN-29 and RN-32, and were collected in 2011 and 2014. All the sampling and analyses were carried out by ISOR (Iceland GeoSurvey). After collection, the samples were treated. A summary of the sample preparation methods is presented in Table 1. The analytical methods used are listed in Table 2. The results of the analyses are in Table 3. The charge balance error, which is reported in Table 3, is calculated by Equation 1:

$$CBE(\%) = \frac{\sum Z_{cat}M_{cat} - \sum Z_{an}M_{an}}{\sum Z_{cat}M_{cat} + \sum Z_{an}M_{an}} \times 100\% \quad (1)$$

where Z_i = Charge of an ion

M_i = Molar concentration of i (mol/Kg)

TABLE 1: Sample preparation methods

Treatment	Container	Specification	To determine
None; amber glass bottle with ground glass Stopper	250-300 ml glass	Ru (Rw, untreated)	pH, CO ₂ , NH ₄ , H ₂ S (if not in field), conductivity
Dilution; 5 ml of sample added to 45 ml of distilled, deionised water	3 x 100 ml plastic	Rd (raw, diluted) (1:10)	SiO ₂ if > 100 ppm
Filtration	200 ml plastic	Fu (filtered, untreated)	Anions
Filtration; 0.8 ml conc. HNO ₃ added to 200 ml sample	200 ml plastic	Fa (filtered, acidified)	Cations
Filtration; 2 ml 0.2 M ZnAc ₂ added to sample in 100 ml volumetric glass flask to precipitate sulphide	100 ml, plastic	Fa (Filtered, acidified)	SO ₄

TABLE 2: The analytical methods employed at Iceland GeoSurvey

Constituent	Fraction	Method
pH	Ru	pH-meter
CO ₂	Ru	Electrometric titration
H ₂ S	Ru	Titrimetric method
NH ₄	Ru	Spectrophotometry
SiO ₂	Rd	Spectrophotometry
F	Fu	Selective electrode
Cl	Fu	Ion chromatography
SO ₄	Fp	Ion chromatography
B	Fu	Spectrophotometry
Na	Fa	Atomic absorption spectroscopy – direct aspiration
K	Fa	Atomic absorption spectroscopy – direct aspiration
Mg	Fa	Atomic absorption spectroscopy – direct aspiration
Ca	Fa	Atomic absorption spectroscopy – direct aspiration
Al	Fa	Atomic absorption spectroscopy – graphite furnace
Fe	Fa	Atomic absorption spectroscopy – graphite furnace
TDS	Fu	Gravimetric
H ₂ , N ₂ , O ₂ , Ar, CH ₄	Gas bulb	Gas chromatography

TABLE 3: Measured discharge enthalpies, sampling pressures and analysis of major elements

LIQUID PHASE (mg/kg)																				
Well no.	Sample ID	SP (bar-g)	H (kJ/kg)	pH/°C	CO ₂	H ₂ S	NH ₃	B	SiO ₂	Na	K	Mg	Ca	F	Cl	SO ₄	Al	Fe	TDS	CBE (%)
RN-29	20140009	17.5	2250	5.15/22.5	45.5	1.44	2.06	13.1	1088	14630	2520	2.86	1950	0.27	28600	16.3	0.022	3.82	49880	-0.46
RN-29	20110005	16.5	1880	5.57/21.6	25.5	2.58	1.58	9.54	953	12320	2150	1.44	1580	0.24	24100	20.9	0.0277	0.901	41270	-0.71
RN-32	20140137	15.7	1029	6.37/22.1	10	0.27	1.3	7.99	649	10250	1490	1.14	1520	0.22	19950	27.1	0.128	0.485	34430	-0.27
VAPOUR PHASE (mg/Kg)																				
Well no.	Sample ID	CO ₂	H ₂ S	H ₂	O ₂	N ₂	CH ₄	NH ₃												
RN-29	20140009	11000	840	7.86	0.01	85.4	1.5	3.32												
RN-29	20110005	8530	300	0.73	91.8	935	0.53	2.35												
RN-32	20140137	660	32	0.25	0.01	34.3	0.03	3.97												

TDS - Total dissolved solids CBE - Charge balance error

SP - Sampling pressure

3.1 Fluid classification

The most common type of fluid found at depth in high-temperature geothermal systems is of near-neutral pH, with chloride as the dominant anion. Other waters encountered in geothermal areas are commonly derived from this deep fluid as a consequence of chemical or physical processes. These waters, the characteristics of which are described below, are classified according to the dominant anions:

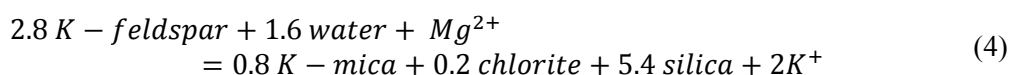
- 1) Chloride water type in which the chloride is the dominant anion and often attains concentrations in the thousands of mg/kg range.
- 2) Sulphate type water also known as acid-sulphate waters: these are invariably surface fluids formed by the condensation of geothermal gases into near surface, oxygenated groundwater.
- 3) Bicarbonate waters, which include those termed CO₂-rich fluids and neutral bicarbonate-sulphate waters, are the product of steam and gas condensation into poorly-oxygenated sub-surface ground waters.
- 4) Sulphate-chloride waters can form by several processes, and the following have been suggested: the mixing of chloride and sulphate waters at variable depths; near-surface condensation of volcanic gases into meteoric waters; and condensation of magmatic vapour at depth.

Most geochemical techniques may, with confidence, be applied only to specified types of fluids with limited ranges of composition. Any such interpretation of geothermal water samples, therefore, is best carried out on the basis of an initial classification. The Cl – SO₄ – HCO₃ ternary diagram is one of the diagrams for the classification of natural waters (Giggenbach, 1991). The position of a data point in such a triangular plot is obtained by first calculating the sum *S* of the concentrations *C_i* (mg/kg) of all three constituents involved:

$$S = C_{Cl} + C_{SO_4} + C_{HCO_3} \quad (2)$$

Once the sum percentages of Cl, SO₄ and HCO₃ are obtained, then $D = HCO_3 \% + 0.5Cl \%$ is computed. The Cl % and *D* are plotted as Y and X axes, respectively. In this diagram, composition ranges are indicated for several typical groups of water such as volcanic and steam-heated waters, mature waters and peripheral waters. The triangular Cl – SO₄ – HCO₃ diagram can be used to classify the geothermal waters, especially, and to filter out waters for geochemical techniques (Giggenbach, 1988).

Giggenbach (1988) pioneered techniques for the derivation of Na–K–Mg–Ca geoindicators. If only Na–K–Mg are considered, a triangular diagram can be used to distinguish between equilibrated, partially equilibrated and immature waters. Geothermometers can only be applied to equilibrated and partially equilibrated waters. The triangular diagram is based on the temperature dependence of the two reactions:



The position of a data point in the triangular plot is first used to obtain the sum *S* of the concentrations of *C* (in mg/kg) of all three constituents involved, as in the previous case; only individual constituents are manipulated differently.

$$S = C_{Na}/1000 + C_K/100 + \sqrt{C_{Mg}} \quad (5)$$

From the sum (*S*), $C_{Na}/1000\%$ and $\sqrt{C_{Mg}}\%$ are obtained, then $D = \sqrt{C_{Mg}}\% + 0.5 C_{Na}/1000 \%$ is computed. The Na% and *D* are plotted as Y and X axes, respectively. The area of partial equilibrium suggests either a mineral that has dissolved but has not attained equilibrium, or a water mixture that has reached equilibrium. A point close to the \sqrt{Mg} corner usually suggests a high proportion of relatively cold ground water, not necessarily “immature”.

3.2 Geothermometers

Geothermometers may be used to estimate the temperature of the reservoir fluid. They are valuable tools in the evaluation of new fields, and in monitoring the hydrology of systems in production.

Geothermometers are based on one or more constituents in geothermal fluids (either solutes or gases, and may include isotopes of elements) of which concentrations or proportions in a fluid are controlled, primarily by the temperature of the fluid and the surrounding rock. Many are based on particular chemical equilibrium reactions. Geothermometers can be applied to well or natural surface discharges to obtain approximate subsurface temperatures. The most important water geothermometers are silica (quartz and chalcedony), Na/K ratio and Na-K-Ca geothermometers. Others are based on cation ratios and any uncharged aqueous species, as long as equilibrium prevails (Arnórsson and Svavarsson, 1985). A temperature equation for a specific equilibrium constant refers to a specific mineral-solution reaction. Silica geothermometers are based on experimentally determined variations in the solubility of different silica species in water, as a function of temperature and pressure (e.g. Fournier, 1977). The basic reaction for silica dissolution is:



In most geothermal systems, deep fluids at temperatures $>180^\circ\text{C}$ are in equilibrium with quartz; it is stable up to 870°C and has the lowest solubility compared to other silica polymorphs. Quartz is common as a primary and secondary (hydrothermal) rock-forming mineral. Silica polymorphs with a less ordered crystal structure (i.e. chalcedony, opal, cristobalite) have higher solubilities than quartz and primarily form at temperatures lower than 180°C . The calibration used here to calculate quartz temperature is (Fournier, 1977):

$$T = 1309/(5.19 - \log S) - 273.15 \quad (\text{Quartz} - \text{no steam loss}) \quad (7)$$

Here S represents silica concentration as SiO_2 in mg/kg and T is temperature ($^\circ\text{C}$). The quartz geothermometer is best for reservoir conditions $>150^\circ\text{C}$. Below this temperature chalcedony, rather than quartz, probably controls the dissolved silica content. The Na/K geothermometer has steadily evolved over the past thirty years from the initial observation that low Na/K ratios were indicative of high temperature at depth, to increasingly more precise calibration of the temperature dependence of this ratio. In high-temperature systems, the temperature dependant variation of sodium and potassium in geothermal waters is due to ion exchange of these elements between co-existing alkali feldspars according to the reaction:



Chloride waters from high-temperature reservoirs ($\geq 180^\circ\text{C}$) are suitable for this geothermometer. For lower temperature reservoirs where fluids have long residence times, the Na-K geothermometer may, in some cases, be applicable. The calibrations used in this study are:

Fournier, 1979:

$$T = 1217/(1.483 + \log(\frac{\text{Na}}{\text{K}})) - 273.15$$

Giggenbach, 1988:

$$T = 1390/(1.75 + \log(\frac{\text{Na}}{\text{K}})) - 273.15$$

Arnórsson, 1983 ($250\text{--}350^\circ\text{C}$):

$$T = 1319/(1.699 + \log(\frac{\text{Na}}{\text{K}})) - 273.15$$

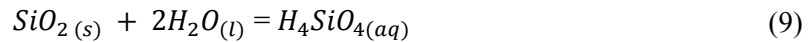
One of the advantages of this geothermometer is that it is less affected by dilution or steam loss as it is based on a ratio of concentrations. On the other hand, the Na-K geothermometer sometimes gives poor results below 100°C . It is also unsuitable if the waters contain high concentrations of calcium (Ca), as is the case for springs depositing travertine.

3.3 Solution mineral equilibria

The position of solution mineral equilibria may change as a result of the chemical and physical processes which take place in the geothermal fluid, both in the reservoir and as it ascends to the surface. The chemical processes centre around mineral-fluid reactions, both dissolution and deposition, while the dominant physical process is boiling, although conductive cooling and mixing are also important. Common dissolved constituents in the deep chloride reservoir fluids fall into two groups:

- 1) Conservative species (Cl, B, Br, As, Cs) which readily pass into solution, often before appreciable alteration of the host rock has occurred, and;
- 2) Common rock forming species (e.g. SiO₂, Na, K, Ca, Mg etc) whose solubilities are controlled by temperature dependant mineral-fluid equilibria and only enter the solution after alteration of the host minerals.

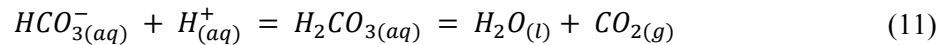
There are two types of mineral-fluid equilibria which need to be considered: solubility equilibria (e.g. quartz, calcite); and ion-exchange equilibria (e.g. Na and K between feldspars and micas). Solubility reactions determine how much of a particular species can enter or remain in solution before precipitation occurs. Temperature is the dominant control on mineral solubility in geothermal systems, but changes in pH, pressure or salinity can also have an effect. Silica and calcite equilibria are particularly important in geothermal systems, as they govern the amount of SiO₂ and Ca in solution, and are two of the main causes of scaling in wells. The solubility of any silica mineral can be written as:



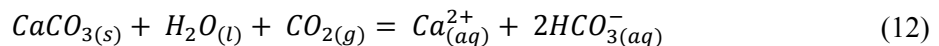
and the solubility constant is given by:

$$K_{\text{SiO}_2} = a_{\text{H}_4\text{SiO}_4} \quad (10)$$

Silicic acid is a weak acid and dissociates to yield hydrogen ions. If the pH of the solution is increased, that is it becomes more alkaline, then the solubility of silica will also increase as the hydrogen ions are consumed by the reactions:



Geothermal reservoir fluids are commonly close to saturation with respect to calcite (Arnórsson, 1989). The dissolution of calcite can be expressed by the equation:

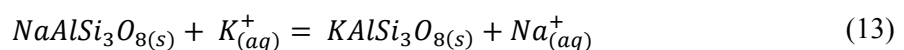


Calcite solubility, therefore, increases with increasing P_{CO_2} (up to $\text{mCO}_2 \sim 1$ mole/kg, Fournier, 1985).

The lowering of P_{CO_2} upon boiling, as carbon dioxide is lost to the steam phase, increases the pH of the solution and leads to supersaturation and precipitation of calcite. As carbon dioxide has minimum solubility at around 160-180°C, boiling near this temperature can lead to calcite supersaturation. As the temperature of the liquid phase decreases, the solubility of calcite increases. Cooling of a solution, either by boiling or conduction, can lead to greater undersaturation with respect to calcite and other carbonate minerals. Generally, calcite solubility is increased by decreasing temperature, increasing CO₂ partial pressure and increasing salinity.

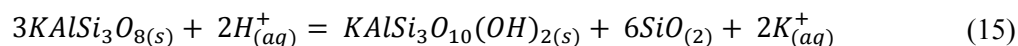
Ion exchange reactions involve the transfer of ions between two or more aluminosilicate minerals and control the ratios of cations in solution, including H⁺. This means that solution pH can be buffered by a silicate mineral assemblage. Observations on geothermal alteration assemblages show that the majority of secondary minerals are formed by reaction such as:

Albite – K-feldspar



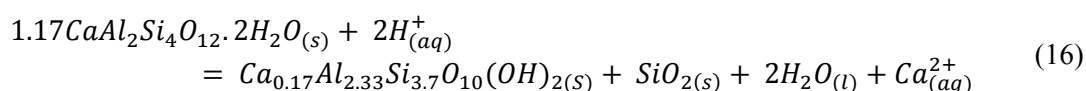
$$K = a_{Na}/a_K \quad (14)$$

K-feldspar – K-mica + quartz



$$\text{and } K = a_K/a_H$$

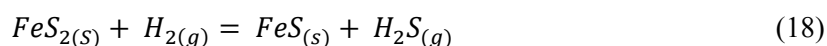
Wairakite – Ca-montmorillonite + quartz



$$K = a_{Ca}/a_{H^2} \quad (17)$$

Reactions also take place between minerals and gases, and the reaction of iron sulphide with hydrogen sulphide illustrates such a mineral-gas buffering reaction:

Pyrite – pyrrhotite



$$K = P_{H_2S}/P_{H_2} \quad (19)$$

4. CALCULATION OF DEEP FLUID COMPOSITION

4.1 The speciation program WATCH

Evaluation of chemical equilibria between minerals and solutions in natural water systems requires the determination of aqueous species activity and the knowledge of the solubility of the minerals found in the altered rocks. The large number of ions, ion pairs and complexes in the solution, particularly at elevated temperatures, requires the use of a computer program for the calculation of individual species activity from analytical data. In this study, the WATCH speciation program version 2.4 (Bjarnason, 2010) was used to calculate the component concentrations in the geothermal reservoir water, based on chemical analysis of water and steam samples collected from discharging wells. In the calculation of aquifer water composition, it is assumed that no transfer of heat or mass occurs on the way from the reservoir to the surface, i.e. the system was assumed to be isolated. The saturation index of secondary and primary minerals is defined by:

$$SI = \log (Q/K) \quad (20)$$

where K = The equilibrium solubility constant for a particular mineral dissolution reaction; and
 Q = The reaction quotient.

The equilibrium mineral-water reactions potentially controlling the geothermal water composition must involve the observed secondary minerals. In this study, the analytical data of samples collected at the wellheads (Table 3) were recalculated to the deep aquifer fluid conditions with the aid of the WATCH speciation program version 2.4 (Bjarnason, 2010). This procedure is relatively simple for wells discharging liquid enthalpy. In this case, the pressure drop induced by discharging the well is not enough to start boiling in the original aquifer fluid. The level of first boiling is within the well and it is reasonable to treat the aquifer and the well as an isolated system and to assume adiabatic boiling of the fluid. The WATCH speciation program calculates individual species activities in the aquifer fluid. This permits derivation of activity products for minerals and, from the solubility constants for these minerals, their state of saturation in the fluid can be obtained.

4.2 Excess enthalpy

If the pressure produced by a discharging well is sufficient to cause extensive boiling in the producing aquifer, it is common for the discharge enthalpy of the well to be significantly higher than the enthalpy of the aquifer fluid beyond the zone of depressurization around the well. The aquifer-well system is no longer isolated. The discharge enthalpy of the well can increase from its initial enthalpy in the aquifer fluid by conductive heat transfer between the aquifer rock and the flowing fluid, which is cooled by depressurization boiling. The aquifer-well is a closed system since there is an exchange of energy with the surrounding rock but the composition of the fluid does not change (model 2 in Arnórsson et al., 2010). Thus, in the isolated and closed systems, the total well discharge composition is equivalent to that of the initial aquifer fluid.

The measured discharge enthalpy for well RN-29 was 2250 kJ/kg in 2014 and 1880 kJ/kg in 2011, but the calculated aquifer fluid discharge enthalpy is 1290 kJ/kg at 290°C. The increase in the enthalpy as the fluid flows from the undisturbed aquifer to the wellhead is primarily due to segregation of the vapour and liquid water in the aquifer. The vapour phase flows to the well head while liquid water is partially or totally retained in the aquifer, adhering onto mineral grain surfaces by capillary forces. The mechanism of phase segregation is, therefore, an open system, causing both the enthalpy and composition of the flowing fluid to change from the initial aquifer conditions to the wellhead (model 3 in Arnórsson et al., 2010).

The deep fluid composition of wells with excess enthalpy may be calculated in two steps using the WATCH program, as explained by Arnórsson et al. (2010). The first step consists of calculating the vapour fraction and the liquid and vapour compositions at the pressure (P_g) at which phase segregation is assumed to occur. For this study, phase segregation pressure or temperature is considered to be 30°C lower than the aquifer temperature of 290°C, which was calculated by geothermometers, i.e. 260°C corresponding to a pressure of 46.9 bar-a. The second step involves calculating aquifer fluid composition from the liquid and vapour phase compositions at P_g , assuming that the flowing fluid enthalpy, before phase segregation occurred, is the same as that of vapour-saturated liquid at the aquifer temperature.

5. RESULTS AND DISCUSSION

5.1 Mineral saturation

The saturation index values are calculated to evaluate with which minerals the fluid is saturated, undersaturated and supersaturated. This was done using the WATCH program, which calculates $\log Q$ and $\log K$ values for 29 minerals, from which saturation index values are calculated. Figures 3, 4, and 5 show the saturation index values for the minerals anhydrite, wairakite, epidote, prehnite and quartz, all of which are found in drill cuttings from Reykjanes, calculated from deep liquid at different temperatures.

For well RN-29 in 2011, the graph shows that quartz approaches equilibrium at depth and becomes supersaturated through boiling; the solution is supersaturated with respect to prehnite and wairakite at all the temperatures; saturation with anhydrite and epidote appears to be

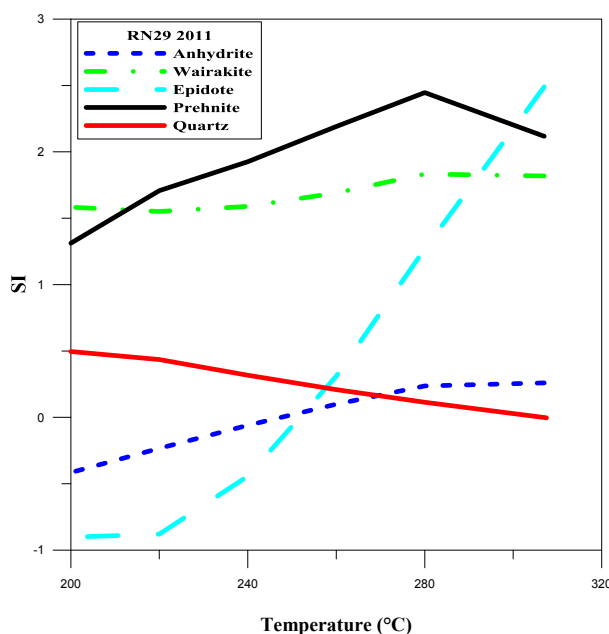


FIGURE 3: Saturation index of selected minerals against temperature for well RN-29 (2011)

temperature-dependent and the solution is supersaturated with respect to them at depth, becoming undersaturated at a lower temperature. The intersection of these mineral curve is assumed to be at the reservoir temperature. For well RN-29 in 2014: the solution similarly remained supersaturated with respect to prehnite and wairakite at all the temperatures; anhydrite and quartz reached equilibrium at a high temperature and the solution became supersaturated with respect to them at a low temperature; similarly, epidote is temperature-dependant and the solution becomes becomes supersaturated with respect to it at a high temperature but undersaturated at a low temperature. The slight difference in the samples was anticipated due to drilling fluid contamination because the RN-29 2011 sample was taken at the end of drilling.

For well RN-32 in 2014, the solution was supersaturated with respect to the minerals prehnite, wairakite and epidote were at all temperatures, however, quartz was in equilibrium at high temperatures and the solution became slightly supersaturated with respect to it at a low temperature; it was supersaturated with respect to anhydrite at high temperatures and became undersaturated at a low temperature. The intersection of the anhydrite and quartz curves helped to estimate the reservoir temperature.

5.2 Geothermometry

The temperature of the reservoir fluid was calculated using various geothermometers, as presented in Table 4. The quartz geothermometer of Fournier (1977) gives higher values in all cases, compared to the sodium/potassium geothermometers. On the other hand, the sodium potassium values calculated from Fournier (1979) and Giggenbach (1988) are very similar, but those calculated from Arnórsson et al.'s (1983) formula gave considerably lower results.

TABLE 4: Geothermometer results

Type of geothermometer	Authors	RN-29 (2014)	RN-29 (2011)	RN-32 (2014)
Quartz	(Fournier, 1977)	334°C	318°C	277°C
Sodium potassium	(Fournier, 1979)	279°C	280°C	261°C
Sodium potassium	(Giggenbach, 1988)	279°C	281°C	264°C
Sodium potassium	(Arnórsson et al., 1983)	266°C	267°C	236°C

The temperature logs show that the feed zone and maximum temperatures are at around 280 and 330°C, respectively, for well RN-29. For well RN-32, the feed zone and maximum temperatures are both at around 250°C.

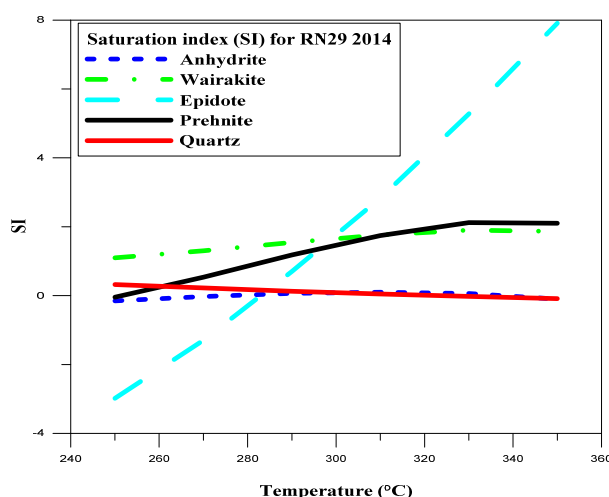


FIGURE 4: Saturation index of selected minerals against temperature for well RN-29 (2014)

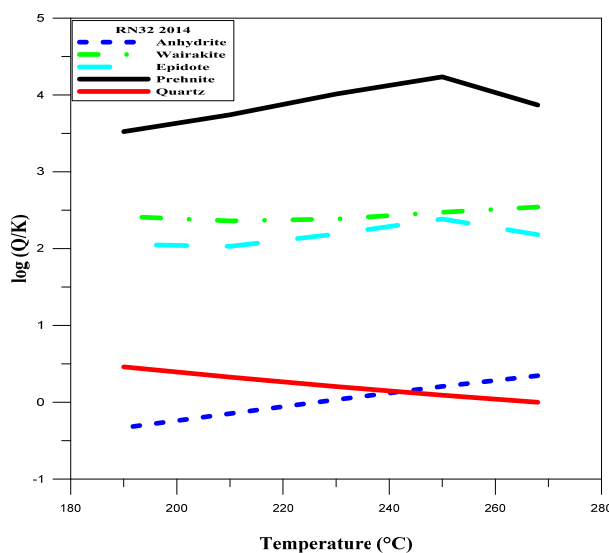


FIGURE 5: Saturation index of selected minerals against temperature for well RN-32

Based on mineral saturation curve intersections, geothermometers and temperature log values shown in Figure 6, the reservoir temperature is assumed to be 290°C for well RN-29 and 250°C for well RN-32.

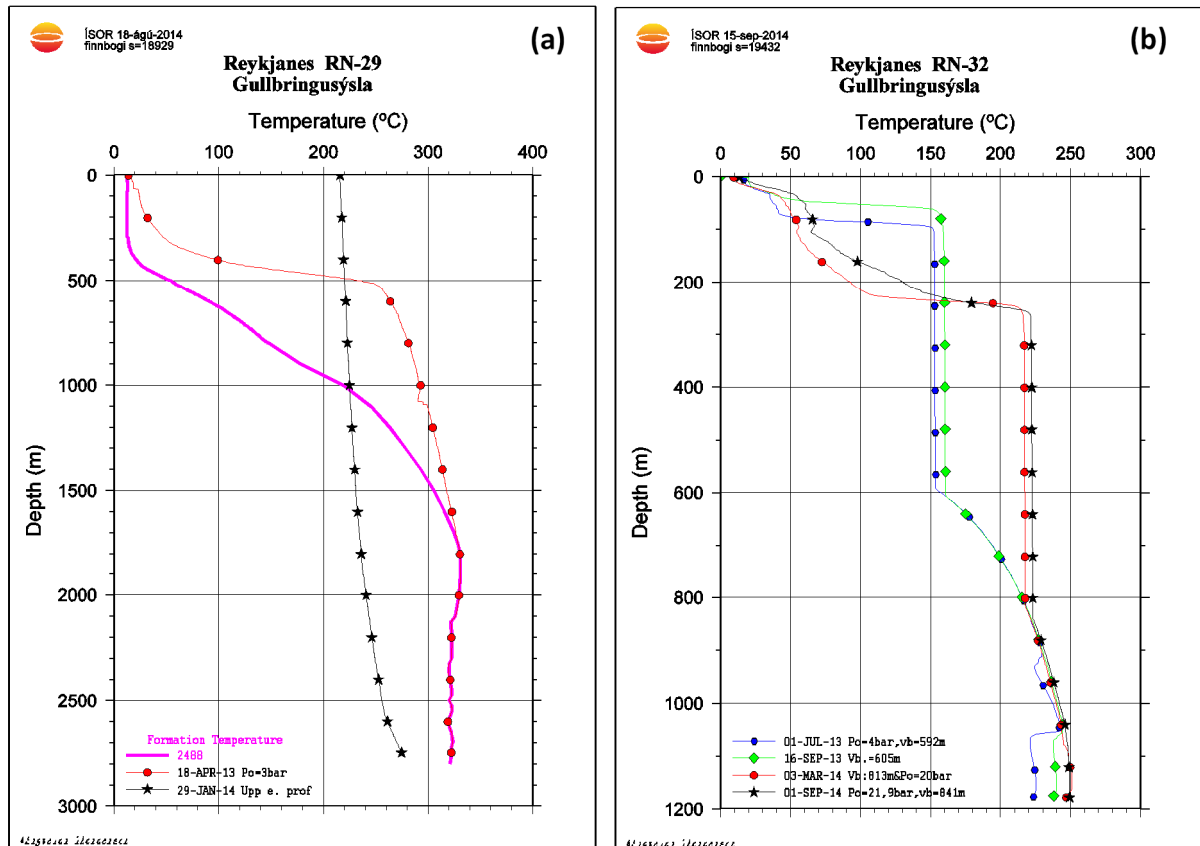


FIGURE 6: Temperature logs for wells RN-29 (a) and RN-32 (b)

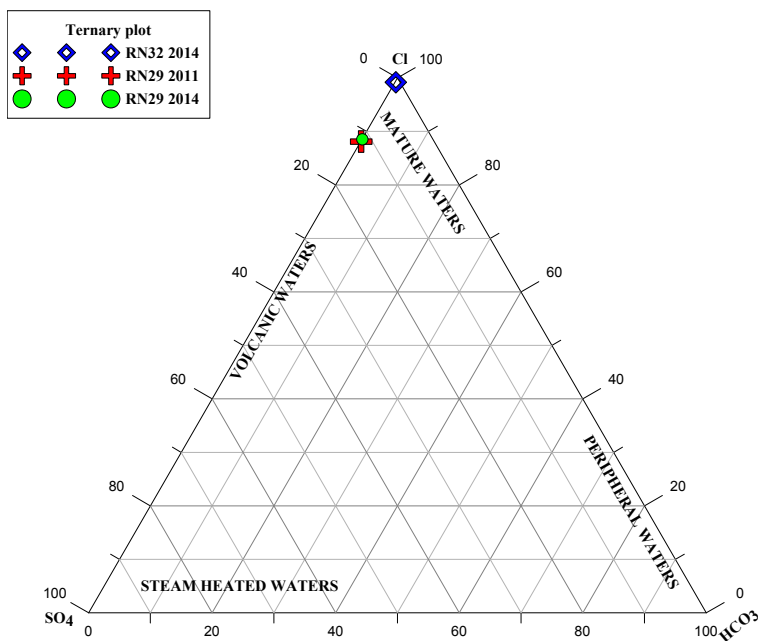


FIGURE 7: Cl-SO₄-HCO₃ ternary diagram

5.3 Ternary diagrams

The Cl-SO₄-HCO₃ ternary diagram is commonly used to classify geothermal waters based on the relative proportions of chloride, sulphate and bicarbonate ions. The diagram indicates several types of thermal fluids such as mature waters, peripheral waters, volcanic, and steam-heated waters. The degree of separation between data points for high chloride and bicarbonate waters gives an idea of the relative degrees of interaction of the CO₂ charged fluids at lower temperatures, and of the HCO₃ contents increasing with time and distance travelled underground. The ternary diagram in Figure 7 shows that the wells fluids from Reykjanes are classified as mature waters. Similarly, the Na-K-

Mg ternary diagram shown in Figure 8 indicates that the water is in equilibrium with rock and that the reservoir temperature in the range of 265-290°C.

5.4 Deep fluid composition

The chemical composition of the reservoir water has been calculated from a chemical analysis of water and steam samples collected separately at a known wellhead pressure. The results are presented in Table 5. From the results it may be seen that the concentrations of most of the constituents for well RN-29 are lower in 2011 than in 2014 with the exception of the components SO_4 , N_2 and O_2 which have higher concentrations than in 2014. The higher SO_4 concentration and lower H_2S concentration

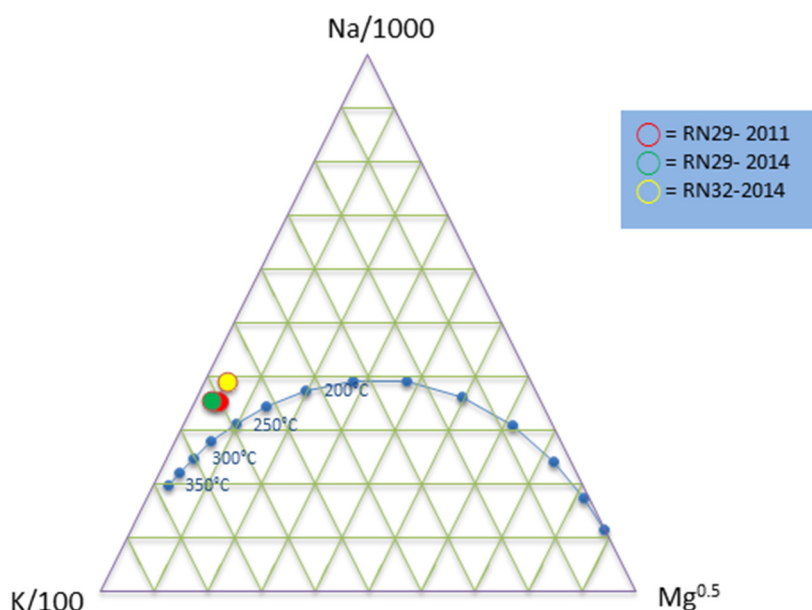


FIGURE 8: Na-K-Mg ternary diagram

are most likely due to remnants of the fresh water which was used during drilling, but N_2 and O_2 concentrations are due to air contamination of this particular steam sample. Well RN-32 has lower concentrations than well RN-29 in most of the constituents, with the exception of SO_4 . It is also apparent that the pH and the concentration of dissolved gases are much lower. This is almost certainly due to the effects of reinjection into the nearby well RN-20b.

TABLE 5: Aquifer water composition at reference temperatures of 290 and 250°C for wells RN-29 and RN-32, respectively; concentrations are in mg/kg

DISSOLVED SOLIDS													
Well no.	Sample ID	SiO_2	Na	K	Ca	Mg	Cl	F	B	SO_4	Fe	Al	TDS
RN29 2011 ^a	20110005	748	9673	1688	1241	1.13	18922	0.18	7.49	16.4	0.70	0.02	32402
RN29 2011 ^b	20110005	749	9674	1688	1241	0.79	1688	0.15	7.49	16.4	0.71	0.02	32405
RN29 2014 ^a	20140009	860	11564	1992	1541	2.26	22607	0.21	10.30	12.8	3.02	0.02	39427
RN29 2014 ^b	20140009	860	11564	1992	1541	2.26	22606	0.21	10.30	12.9	3.02	0.02	39426
RN32 2014 ^a	20140137	576	9091	1321	1348	1.01	17694	0.19	7.08	24.0	0.43	0.11	30536
Sea water	Standard	5.34	10800	390	450	1290	18800	1.30	4.50	2700	0.003	0.003	33960
DISSOLVED GASES													
Well no.	Sample ID	CO_2	H_2S	NH_3	N_2	O_2	CH_4	H_2	$\log(\text{Q/K})$ calcite	$\log(\text{Q/K})$ anhydrite	$\log(\text{Q/K})$ quartz	Deep liquid pH	
RN29 2011 ^a	20110005	1852	66.4	1.75	200	19.7	0.11	0.16	-0.555	0.109	0.129	4.7	
RN29 2011 ^b	20110005	1005	39.5	1.31	100	9.9	0.06	0.08	-0.193	0.201	0.093	4.9	
RN29 2014 ^a	20140009	2341	177.2	2.32	17.90	<0.01	0.31	1.65	-0.385	0.210	0.068	4.5	
RN29 2014 ^b	20140009	1190	102.0	1.97	8.39	<0.01	0.15	0.77	-0.375	0.243	0.068	4.7	
RN32 2014 ^a	20140137	84	3.9	1.60	3.89	<0.01	<0.01	0.03	-0.555	0.109	0.129	5.4	

a = For liquid enthalpy; b = For excess enthalpy

As regards the excess enthalpy of well RN-29, the computed deep liquid concentrations, based on liquid enthalpy and excess enthalpy, show the same results in most of the dissolved solids but it is different in pH and the concentration of dissolved gases. The lower CO_2 concentration also affects the pH of the computed deep liquid.

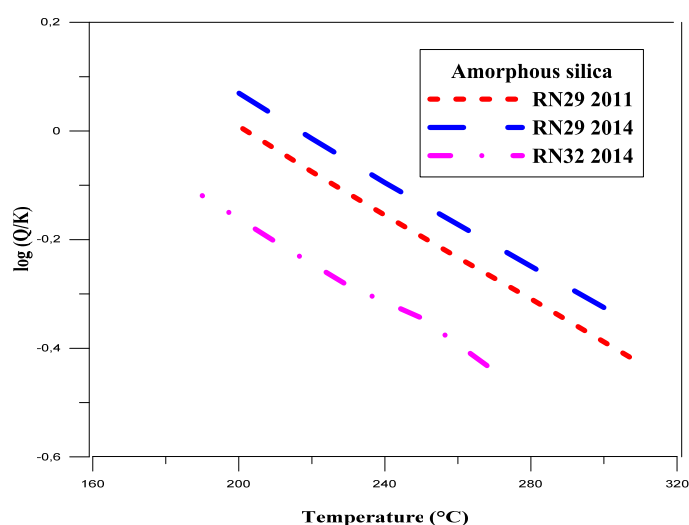


FIGURE 9: Changes in the saturation index of amorphous silica against temperature during boiling

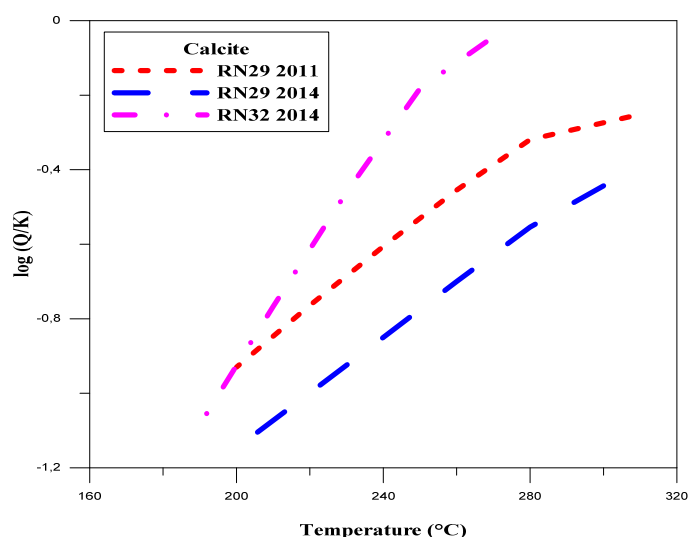


FIGURE 10: Changes in the saturation index of calcite against temperature during boiling

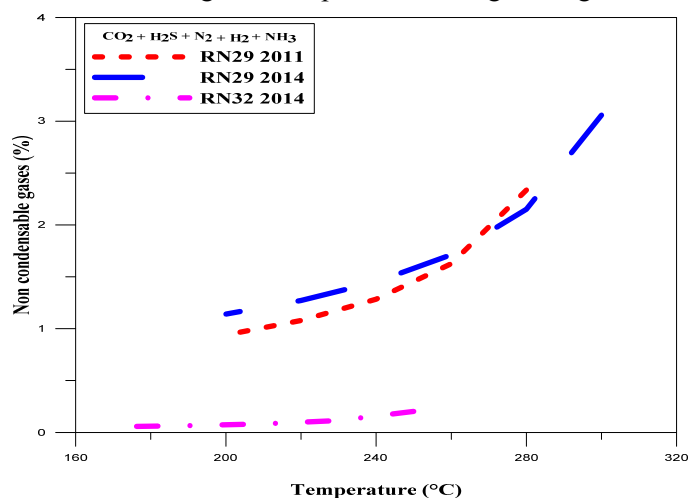


FIGURE 11: Non-condensable gas content against temperature during boiling

Also shown in Table 5 is the composition of standard seawater (Krauskopf, 1995) from which it may be seen that the deep liquid brines are very similar to seawater in terms of Na, Cl and total dissolved solids (TDS), but there are some differences in other components. These differences are mainly due to ion exchange equilibria between rock and water. When compared to seawater, the Reykjanes brine is deficient in magnesium (Mg), fluoride (F) and sulphate (SO_4) but enriched in potassium (K) and calcium (Ca). The amount of silica (SiO_2) in the geothermal brines is an order of magnitude higher than in seawater, as would be expected from its increased solubility with temperature.

5.5 Production properties

Scale deposition in production wells, pipelines and surface facilities is one of the most common problems encountered during the exploitation of geothermal systems as production of high-temperature liquid of near-seawater composition results in a pressure decrease and boiling in the wells during ascent. The boiling causes cooling and gas loss, which leads to the precipitation of base metal-rich sulphide scales (mainly sphalerite and minor chalcopryrite; Hardardóttir et al., 2009) and amorphous Fe-bearing silica, both in the well and in surface pipes. All the silicate minerals are likely to precipitate at lower temperatures. Figure 9 shows that at low temperatures ($< 200^\circ\text{C}$ for well RN-29, $< 160^\circ\text{C}$ for well RN-32) the amorphous silica starts to precipitate, and this might pose a problem in surface equipment and reinjection wells.

The deep liquid is slightly undersaturated with respect to calcite and becomes more undersaturated upon boiling, as seen in Figure 10. There should be no risk of calcite precipitation.

The non-condensable gas content (NGC) becomes lower when the temperature decreases with boiling, as the amount of vapour increases, as seen in Figure 11.

After boiling to 200°C, the NCG content in well RN-29 is about 1% (assuming liquid enthalpy), but about 0.2% in well RN-32.

5.6 Gas equilibria

The equilibrium curves of the mineral assemblages that could fix the concentrations of the reactive gases H_2 , H_2S , CO_2 are plotted in Figures 12-14. In this study the dissociation reactions of the hydrothermal minerals of H_2S , H_2 , and CO_2 are considered. The concentrations of H_2S , H_2 , CO_2 expressed in moles per kilogram are used to plot the graph.

As seen in Figure 12, the H_2 concentration of the sample from well RN-29 in 2014 may be controlled by the gro+pyrr+qtz+epi+wol+pyr mineral assemblage but, for well RN-29 in 2011, it is difficult to decipher which of the assemblages controls H_2 concentrations.

The H_2S concentration (Figure 13) for well RN-29 in 2014 appears to be controlled by the pyr+pyrr+pre+epi mineral assemblage but, for well RN-29 in 2011, it is nearer to gro+pyr+pyrr+qtz+epi+wol. CO_2 (Figure 14) appears to be controlled by the czo+cal+qtz+gro mineral assemblage in well RN-29, both in 2011 and 2014.

The sample from well RN-32 is far from any of these mineral assemblages, probably because of mixing with reinjection water.

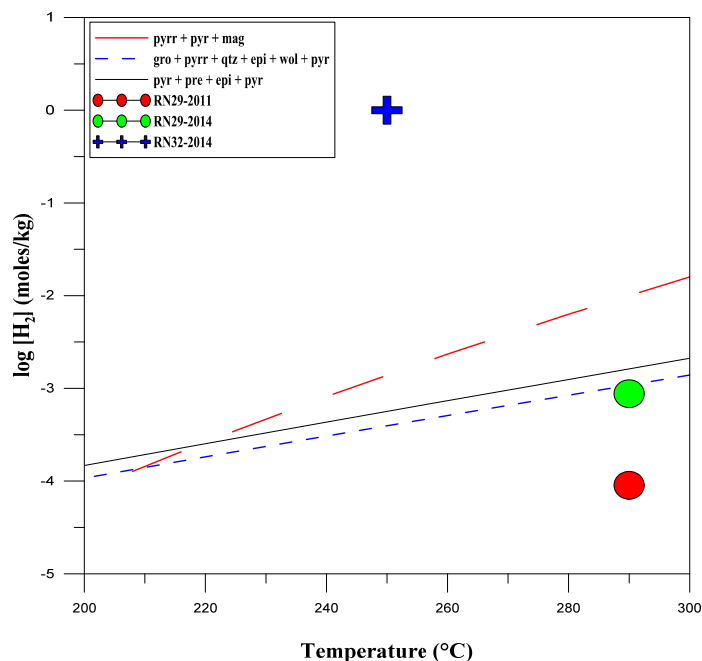


FIGURE 12: Measured concentrations of H_2 as a function of temperature, along with the mineral buffers which might control the H_2 concentration

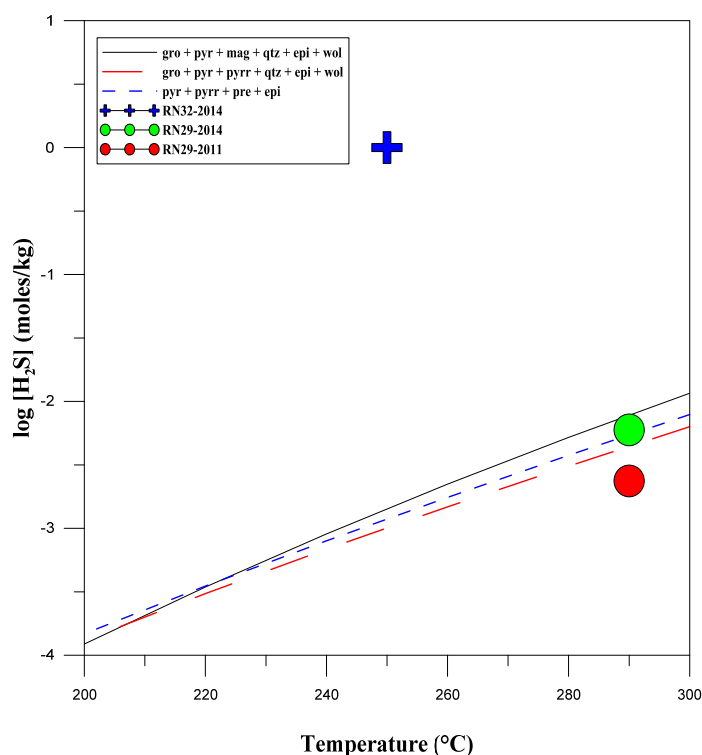


FIGURE 13: Measured concentrations of H_2S as a function of temperature, along with the mineral buffers which might control the H_2S concentration

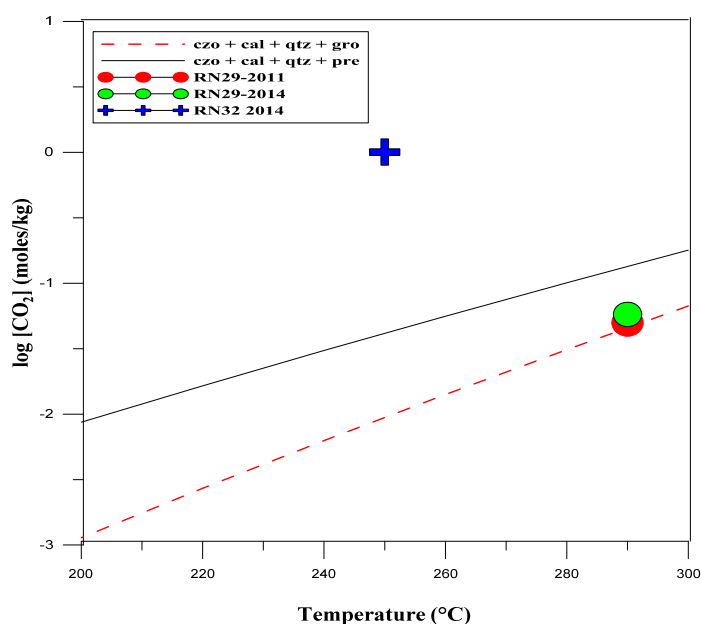


FIGURE 14: Measured concentrations of CO₂ as a function of temperature, along with the mineral buffers which might control the CO₂ concentration

6. CONCLUSIONS

Thermal waters of the Reykjanes field have Na and Cl concentrations similar to those of seawater. From geothermometers, mineral equilibria and temperature logs, it is suggested that the reservoir temperature of well RN-29 is around 290°C and that of well RN-32 about 250°C. Well RN-29 has a measured enthalpy of 2250 kJ/Kg, higher than what corresponds to liquid enthalpy at 290°C. Various processes can cause such enthalpy of the flowing fluid; it is assumed that the excess enthalpy is caused by phase segregation in the depressurization zone around the wells. Aquifer fluid component concentrations for well RN-29 were, thus, calculated on the basis of a phase segregation model, taking the phase segregation to take place at a temperature 30°C below the aquifer

temperature. The results thus obtained show significantly lower concentrations of volatile components, but there is an insignificant difference for non-volatile components. For well RN-32, liquid enthalpy was assumed when calculating the deep fluid composition. The deep liquid of well RN-32 is considerably less saline than that of well RN-29, and the concentration of dissolved gases, including CO₂ and H₂S is much lower. This is likely due to reinjection of separator fluid and condensate into nearby well RN-20b.

As the liquid boils, it becomes supersaturated with respect to amorphous silica at about 200 and 160°C for wells RN-29 and RN-32, respectively, so silica scaling is to be expected below those temperatures. Boiling should not, however, induce the precipitation of calcite. Hardardóttir et al. (2009) have, on the other hand, shown that sulphides will form upon boiling. The non-condensable gas content is rather low in well RN-29 (about 1% after boiling to 200°C), and very low in well RN-29.

ACKNOWLEDGEMENTS

I wish to thank the Government of Iceland and the United Nations University for supporting this training programme. Deepest thanks are expressed to Mr. Lúdvík S. Georgsson, director of the UNU Geothermal Training Programme and Mr. Ingimar Gudni Haraldsson, Deputy Director, for their excellent guidance and successful operation of the programme. My special thanks go to my supervisors, Mr. Finnbogi Óskarsson and Dr. Halldór Ármannsson, for their great help and critical advice during all stages of the data analysis and the preparation of this report. I wish to give my thanks to all lecturers and staff members at ÍSOR for their comprehensive presentations and willingness to share their knowledge and experience.

REFERENCES

- Ármannsson, H. and Ólafsson, M., 2006: *Collection of geothermal fluids for chemical analysis*. ÍSOR – Iceland GeoSurvey, Reykjavík, report ISOR-2006/016, 17 pp.
- Arnórsson, S., 1978: Major element geochemistry of the geothermal seawater at Reykjanes and Svartsengi. *Mineral Mag.*, 42, 209-220.
- Arnórsson, S., 1983: Chemical equilibria in Icelandic geothermal systems. Implications for chemical geothermometry investigations. *Geothermics*, 12, 119-128.
- Arnórsson, S., 1989: Deposition of calcium carbonate minerals from geothermal waters-theoretical considerations. *Geothermics*, 18, 33-39.
- Arnórsson, S., Angcoy, Jr., E.C., Bjarnason, J.Ö., Giroud, N., Gunnarsson, I., Kaasalainen, H., Karingithi, C., and Stefánsson, A., 2010: Gas chemistry of volcanic geothermal systems. *Proceedings of the World Geothermal Congress 2010*, Bali, Indonesia, 12 pp.
- Arnórsson, S., Gunnlaugsson, E., and Svavarsson, H., 1983: The chemistry of geothermal waters in Iceland II. Mineral equilibria and independent variables controlling water compositions. *Geochim. Cosmochim. Acta*, 47, 547-566.
- Arnórsson, S., and Svavarsson, H., 1985: Application of chemical geothermometry to geothermal exploration and development. *Geoth. Res. Council, Transactions*, 9-1, 293-298.
- Bjarnason, J.Ö., 2010. *The speciation program WATCH* (vers. 2.4). ISOR – Iceland GeoSurvey, Reykjavík.
- Björnsson, S., Arnórsson, S., and Tómasson, J., 1970: Exploration of the Reykjanes thermal brine area, *Geothermics*, Sp. issue, 2-2, 1640-1650.
- Björnsson, S., Arnórsson, S., and Tómasson, T., 1972: Economic evaluation of Reykjanes thermal brine area, Iceland. *Am. Assoc. Petr. Bull.*, 56-12, 2380-2391.
- Björnsson, S., Arnórsson, S., Tómasson, J., Ólafsdóttir, B., Jónsson, J., and Sigurmundsson, S.G., 1971: Reykjanes--Final Report on Exploration. Orkustofnun – National Energy Authority, report (in Icelandic), 122 pp.
- Fournier, R.O., 1977: Chemical geothermometers and mixing model for geothermal systems. *Geothermics*, 5, 41-50.
- Fournier, R.O., 1979: A revised equation for Na-K geothermometer. *Geoth. Res. Council, Trans.*, 3, 221-224.
- Fournier, R.O., 1985: The behaviour of silica in hydrothermal solutions. *Rev. Econ. Geology*, 2, 45-61.
- Franzson, H., Thórdarson, S., Björnsson, G., Gudlaugsson, S.Th., Richter, B., Fridleifsson, G.Ó., and Thórhallsson, S., 2002: Reykjanes high temperature field, SW-Iceland, geology and hydrothermal alteration of well RN-10, *Proceedings of the 27th Workshop on Geothermal Reservoir Engineering*, Stanford University, Stanford, CA, 233-240.
- Freedman, A.J.E., Bird, D.K., Arnórsson S., Fridriksson, Th., Elders, W.A., Fridleifsson, G.Ó., 2010: Hydrothermal mineral record CO₂ partial pressures in Reykjanes geothermal system, Iceland. *Proceedings of the World Geothermal Congress 2010*, Bali, Indonesia, 11 pp.

Fridriksson, T., Kristjánsson, B.R., Ármannsson, H., Margrétardóttir, E., Ólafsdóttir, S., and Chiodini, G., 2006: CO₂ emissions and heat flow through soil, fumaroles, and steam heated mud pools at the Reykjanes geothermal area, SW Iceland. *Applied Geochemistry*, 21, 1551–1569.

Giggenbach, W.F., 1988: Geothermal solute equilibria. Derivation of Na-K-Mg-Ca geothermometers. *Geochim. Cosmochim. Acta*, 52, 2749–2765.

Giggenbach, W.F., 1991: Chemical techniques in geothermal exploration. In: D'Amore, F. (coordinator), *Application of geochemistry in geothermal reservoir development*. UNITAR/UNDP publication, Rome, 119–144.

Gudmundsson, J.S., Hauksson, T., Tómasson, J., 1981: Subsurface exploration and well discharge characteristics, Reykjanes geothermal field in Iceland. *Proceedings of the 7th Workshop in Reservoir Engineering, Stanford University, Stanford, CA*, 61–69.

Gudmundsson, J.S. and Thórhallsson, S., 1986: The Svartsengi reservoir in Iceland. *Geothermics*, 15, 3–15.

Gunnarsdóttir, S., Stefánsson, H.Ö., Nielsson, S., Sigurgeirsson, M.A., 2013: *Well report RN-32: Drilling operations of well RN-32 from surface down to 1202 m*. ÍSOR – Iceland GeoSurvey, report ÍSOR 2013/041 (in Icelandic), 173 pp.

Hardardóttir, V., Brown, K.L., Fridriksson, Th., Hedenquist, J.W., Hannington, M.D., and Thórhallsson, S., 2009: Metals in deep liquid of the Reykjanes geothermal system, southwest Iceland: Implications for the composition of seafloor black smoker fluids. *Geology*, 37/12, 1103–1106.

Hardardóttir, V., Kristmannsdóttir, H., and Ármannsson, H., 2001: Scales formation in wells RN-9 and RN-8 in the Reykjanes geothermal field Iceland. *Proceedings of the 10th International Symposium on Water-Rock Interaction, Villasimius, Italy, Balkema, Rotterdam*, 851–854.

Jakobsson, S.P., Jónsson, J., and Shido, F., 1978: Petrology of the western Reykjanes Peninsula, Iceland. *J. Petrology*, 19-4, 669–705.

Johnsson, G.L., and Jakobsson, S.P., 1985: Structure and petrology of the Reykjanes Ridge between 62°55'N and 63°48'N. *J. Geophys. Res.*, 90-B12, 10073–10083.

Krauskopf, K.B., 1995: *Introduction to geochemistry* (2nd ed.). McGraw Hill publ., NY, 647 pp.

Ólafsson, J., and Riley, J.P., 1978: Geochemical studies on the thermal brine from Reykjanes (Iceland). *Chemical Geology*, 21, 219–237.

Óskarsson, F., Fridriksson, Th., and Thorbjörnsson, D., 2014: Geochemical monitoring of the Reykjanes geothermal reservoir 2003 to 2013. *Submitted for World Geothermal Congress 2015, Melbourne, Australia*, 8 pp.

Pálmason, G., Johnson, G.V., Torfason, H., Saemundsson, K., Ragnars, K., Haraldsson, G.I., Halldórsson, G.K., 1985: *Geothermal assessment of Iceland*. Orkustofnun, Reykjavík, report OS-85076 /JHS-10 (in Icelandic), 176 pp.

Pope, E.C., Bird, D.K., Arnórsson, S., Fridriksson, Th., Elders, W.A., 2010: Iceland Deep Drilling Project (IDDP): Stable isotope evidence of fluid evolution in Icelandic geothermal systems. *Proceedings of the World Geothermal Congress 2010, Bali, Indonesia*, 7 pp.

Sveinbjörnsdóttir, Á.E., Coleman, M.L., and Yardley, B.W.D., 1986: Origin and history of hydrothermal fluids of the Reykjanes and Krafla geothermal fields, Iceland. A stable isotope study. *Contrib. Mineral. Petrol.* 94, 99–109.



UNITED NATIONS
UNIVERSITY

UNU-GTP

Geothermal Training Programme

Orkustofnun, Grensasvegur 9,
IS-108 Reykjavik, Iceland

Reports 2014
Number 20

SUBSURFACE GEOLOGY AND HYDROTHERMAL ALTERATION OF WELL HE-4, HELLISHEIDI GEOTHERMAL FIELD, SW- ICELAND

Fatumati J. Mnzava

Ministry of Energy and Minerals, Geological Survey of Tanzania
P. O. Box 903 Dodoma
TANZANIA
Matterj4@yahoo.com

ABSTRACT

Intense geoscientific studies are needed before exploitation of geothermal resources commences. The studies involve multiple fields of geoscience including geology, geochemistry and geophysics during the exploration, production and monitoring stages. Well HE-4 is amongst the earliest deeper exploration wells in the Hellisheidi geothermal field with a total depth of 2008 m. The well was directionally drilled in 2001 towards SW from a drill pad east of Reykjafell mountain. This report covers the upper 1200 m of the well where binocular microscope, petrographic microscope, XRD-analysis, fluid inclusion analysis and geophysical logs were applied to gather and interpret data. The stratigraphy of well HE-4 is governed by two major formations which are hyaloclastite basalt and basaltic lava. Hyaloclastite basalt formations (including basaltic tuff, basaltic breccia and pillow basalt) alternate and dominate in the well, representing volcanic eruptions beneath a glacier. Basalt formations of fine- and fine- to medium-grained crystalline basalt appear occasionally, representing interglacial lava flows and intrusive rocks. Seven feed points were identified, two large ones located at 496 m and 1150 m and five smaller ones identified at 300 m, 580 m, 890 m, 900 m and 1100 m. Alteration zones are somewhat contradictory and are, therefore, based on two separate zones of clay minerals on the one hand and alteration mineral distribution on the other. Clay minerals show five zones within the well starting with an unaltered zone followed by a smectite zone at 82-642 m, which is interrupted by a thin layer of mixed layer clay at 450-458 m. A chlorite zone is then noted from 642-862 m, followed by a mixed layer clay zone from 862 to 1050 m and a chlorite amphibole zone from 1050-1200 m. The distribution of alteration minerals shows five zones starting with an unaltered zone, followed by a zeolite zone, then quartz and wairakite, epidote, and wollastonite zones. Correlation of alteration temperature and homogenization temperatures with the formation temperature of the system indicates that the upper part of the system is in equilibrium, the middle part from 414 to 784 m is heating up, while the lower part of the system is cooling.

1. INTRODUCTION

1.1 General information

Hellisheidi geothermal field is located in SW Iceland within the Hengill high temperature geothermal system. The other three geothermal fields within the system are Nesjavellir, Bitra, and Hverahlíð (Figure 1).

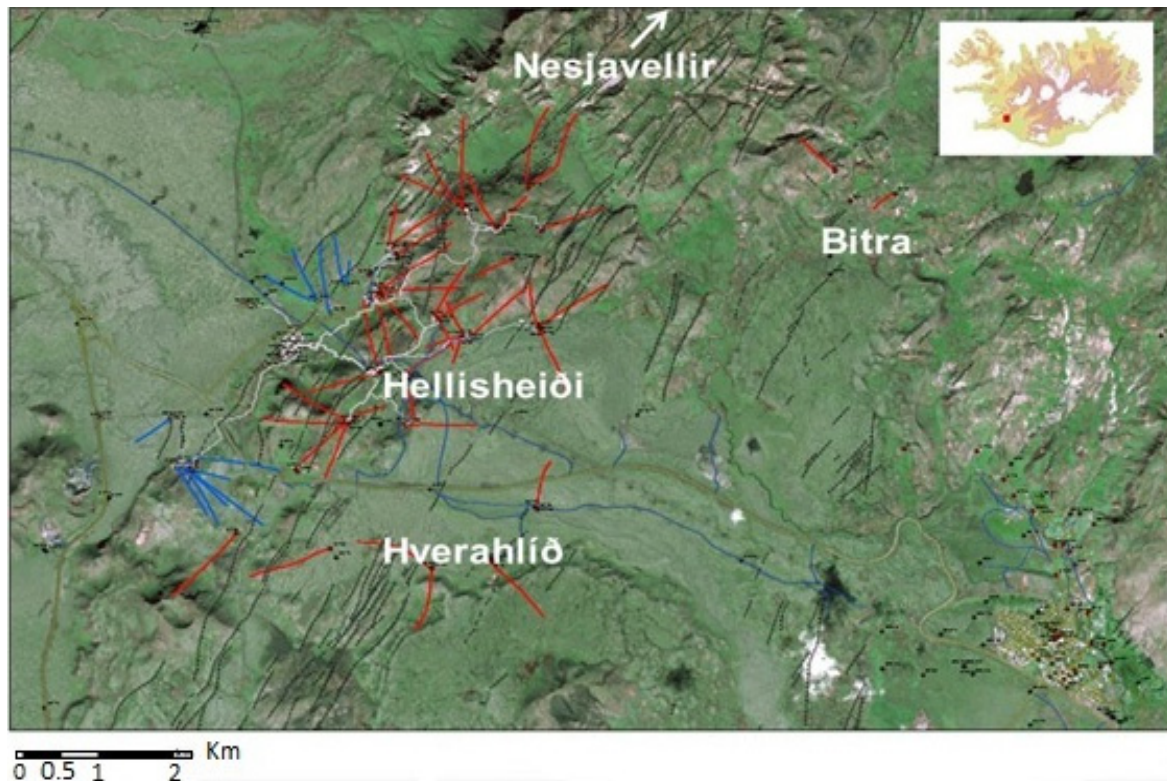


FIGURE 1: An aerial photograph of the Hengill area showing four high temperature geothermal fields

After assessing geothermal surface manifestations, surface geology, geochemistry and geophysics, exploration drilling remains a key factor for sub-surface studies in order to make physical contact with the geothermal system and its rock formations. During sub-surface geological studies, binocular, petrographic, fluid inclusion and X-ray diffractometer analyses provide information about the rock types, their physical properties and alteration. In combination with geophysical logging, including temperature, gamma, caliper, neutron-neutron and resistivity, it is possible to obtain a better understanding of major lithological changes and help to define aquifers that may be countable for geothermal production.

Well HE-4 is an exploration well, drilled directionally to a total depth of 2008 m. The well is situated in a small valley east of Reykjafell within the Hellisheidi high temperature geothermal system, as shown in Figure 2. The main objectives of the drilling were to obtain information about the stratigraphy and its geophysical properties, temperature and permeability, and to explore the capability of the geothermal fluid between Reykjafell mountain and Hveradalir valley south of Reykjafell (Gudmundsson et al., 2001a).

This study is the result of knowledge and experience acquired from the six months UNU Geothermal Training Program 2014 about geothermal exploration, production, monitoring and utilization of geothermal resources. The main focus was on borehole geology, assessing the lithological stratigraphy and alteration of the formations as well as the precipitation of hydrothermal minerals to gain a better understanding of the geothermal system and the surroundings in well HE-4.

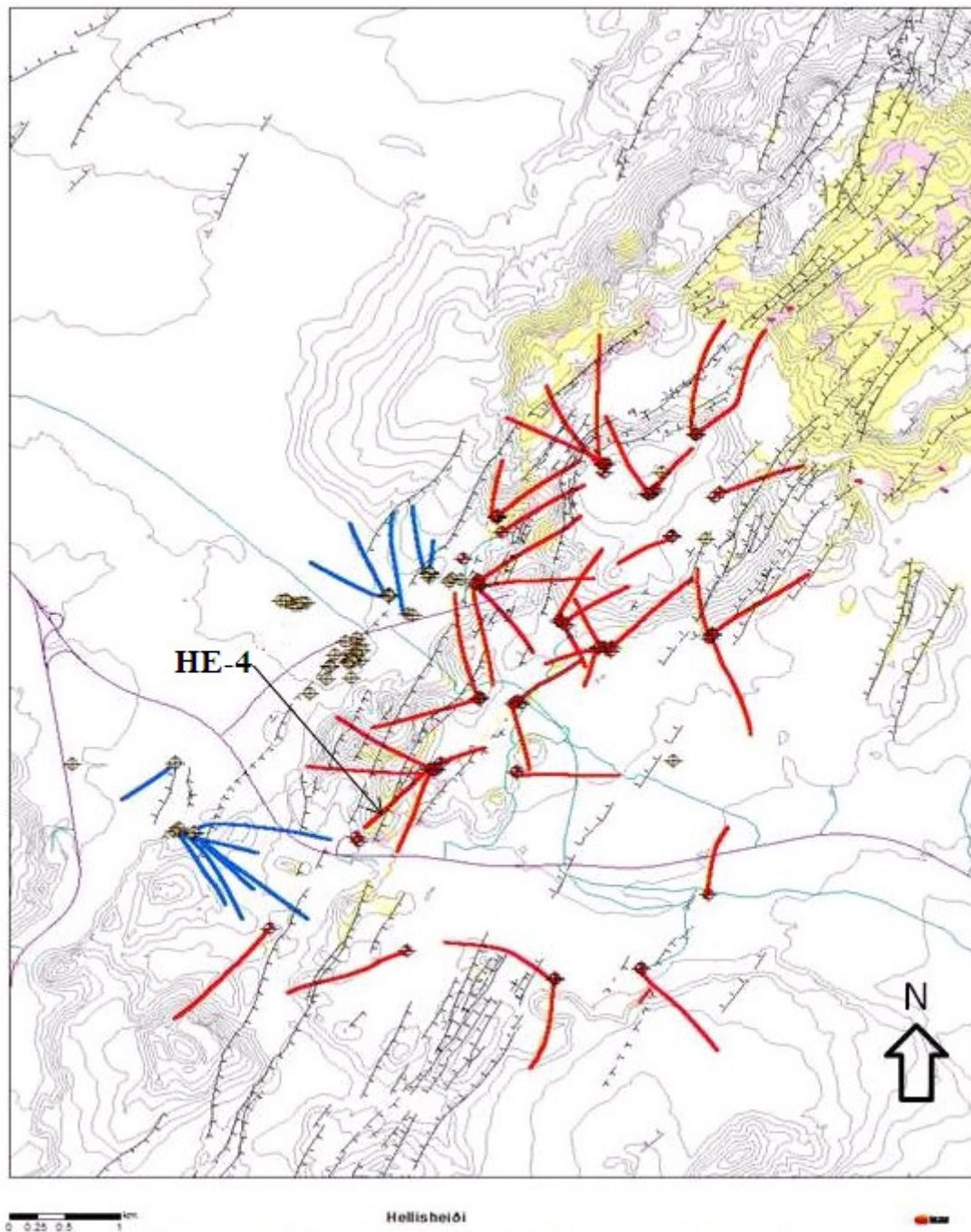


FIGURE 2: Hellisheidi geothermal field with exploration/production wells (red), reinjection wells (blue) and the location of well HE-4 (modified from Gudmundsson et al., 2001a)

1.2 Regional geology of Iceland

Iceland lies on the rift between the Eurasian plate and the North American plate which has a relative motion of 1 cm per year in each direction. The divergence of these major plates favours volcanic eruptions and earthquakes and forms the Mid-Atlantic Ridge on which Iceland rests. Furthermore, Iceland resides on a mantle plume (hot spot) which has induced frequent volcanic eruptions from time to time. The rift system cuts across the country from southwest to northeast (Figure 3). The existence of the hot spot results in Iceland having been more volcanically active than the oceanic rift throughout its

existence (Saemundsson, 1979). Iceland is geologically very young with its rocks formed within the last 25 million years. The stratigraphic succession of Iceland extends across two geological periods: the Tertiary and the Quaternary, where the oldest rocks exposed at the surface are only 14–16 million years old. Geological formations are grouped into three as Tertiary (16–3.3 million years), Plio-Pleistocene (3.3–0.7 million years) and upper Pleistocene formations which are <0.7 million years. The surface geology is almost entirely composed of igneous rocks of which about 80–85% is basaltic (mafic) in composition; acidic (felsic) and intermediate rocks amount to about 10% (Figure 3). The amount of sediments of volcanic origin is 5–10% in a typical Tertiary lava pile, but may locally be higher in Quaternary rocks (Saemundsson, 1979).

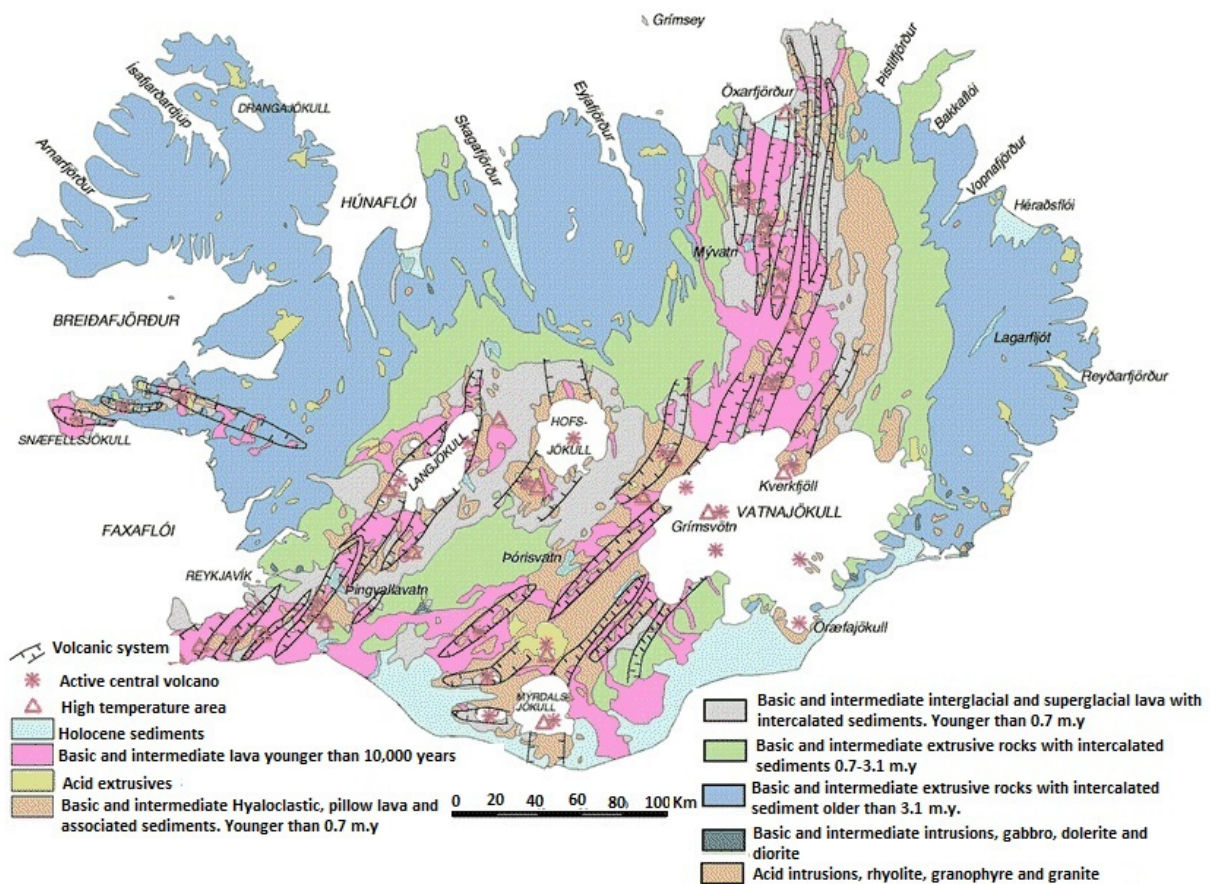


FIGURE 3: Geological map of Iceland showing oldest Tertiary rocks, Plio-Pliostocene eruptives, Holocene rocks and other young formations; volcanic systems follow the oceanic ridge (Jóhannesson and Saemundsson, 1999)

Volcanic rocks in Iceland are classified into three series: tholeiitic, alkalic and transitional. The tholeiitic rock series are confined to volcanic systems in the rift zones which delineate the crest of the Mid-Atlantic Ridge. The alkali and transitional series are confined to volcanic systems in the flank zones (Jakobsson et al., 2008). A volcanic system is the principle geological structure in Iceland; it consists of a fissure swarm, a central volcano and intrusives which often provide a potential for geothermal systems. Geothermal areas in Iceland are distinguished by its temperature at a depth of 1 km where areas with temperature $\leq 150^{\circ}\text{C}$ are considered low temperature systems while areas with temperature $\geq 200^{\circ}\text{C}$ are high temperature systems. The low temperature systems are mostly outside of the volcanically active zone and are related to active fractures and fault zones, as their heat source is hot rock at depth (Arnórsson et al., 2008).

The high temperature areas are confined to the active volcanic zone of tectonic rifting and volcanism with central volcanoes, fissure swarms and sometimes calderas. They are thought to draw heat both from the regional heat flow and from local accumulations of igneous cooling (dykes and sheets) at a shallow level in the crust (Fridleifsson, 1979).

1.3 Geological and tectonic settings of the Hengill area

Hengill volcanic complex is a high temperature geothermal area located at a triple junction where the Western rift zone, the Reykjanes peninsula and the South Iceland fracture zone meet. The geothermal area is connected to an active NE-SW trending fissure swarm. The main component of the volcanic system is a 40 km long and 3-5 km wide fissure swarm where rifting is most active and volcanic accumulation is highest in the central part of the Hengill complex, as shown in Figure 4. Rock formations are mainly volcanic and the largest part is built up of hyaloclastite formations erupted during glacial periods, while interglacial lavas erupted in the highlands flowed to the surrounding lowlands. Intermediate and felsic rocks are found at the western edge of the volcano but have also been found as intrusives in drill holes throughout the geothermal field (Franzson et al., 2010).

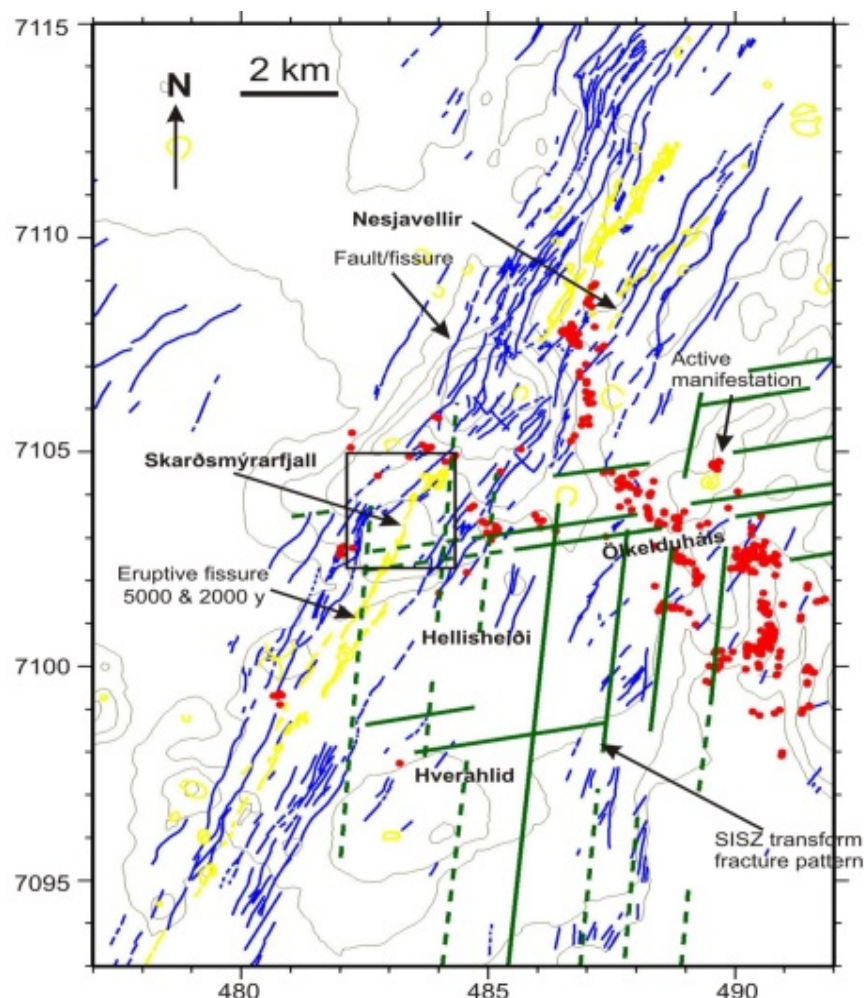


FIGURE 4: Map of the Hengill volcanic complex showing the topography, interpreted faults related to the transform fractures (green), faults related to the fissure swarm (blue) and postglacial eruptive fissures (yellow) cutting the central volcano (Franzson et al., 2010)

1.4 Previous geoscientific studies at Hellisheiði

Several scientific studies have been conducted in the Hengill area, including the Hellisheiði geothermal field, which show surface manifestations such as hot springs with temperatures ranging from 8°C to 99°C. Manifestations show both fossil and active thermal expressions such as steam vents, steaming grounds, warm soil and altered grounds (Saemundsson, 1995). The Hellisheiði surface area is characterized by two main features: hyaloclastite formations, which were formed sub-glacially, and postglacial lavas from volcanic fissures trending NE-SW. The age of the older is 5500 years and the

younger is about 2000 years (Saemundsson, 1995). The hyaloclastite and the lava series are generated from the Hengill central volcano. The hyaloclastite is categorised into three units based on glass contents: pillow basalt, breccia and tuff from low to high contents, respectively.

Various geophysical studies have been conducted in the Hengill area since the 1940s. Geophysical methods have been proven to be sensitive to alteration and the fluid content of the rocks and also reveal structures that influence the properties of the geothermal system. The most informative exploration method in defining the geothermal reservoir prior to drilling is, however, resistivity (Franzson et al., 2010). DC resistivity surveys using Schlumberger and dipole–dipole sounding, a Bouguer gravity survey, an aeromagnetic survey and a seismic refraction survey were conducted in the area in the late

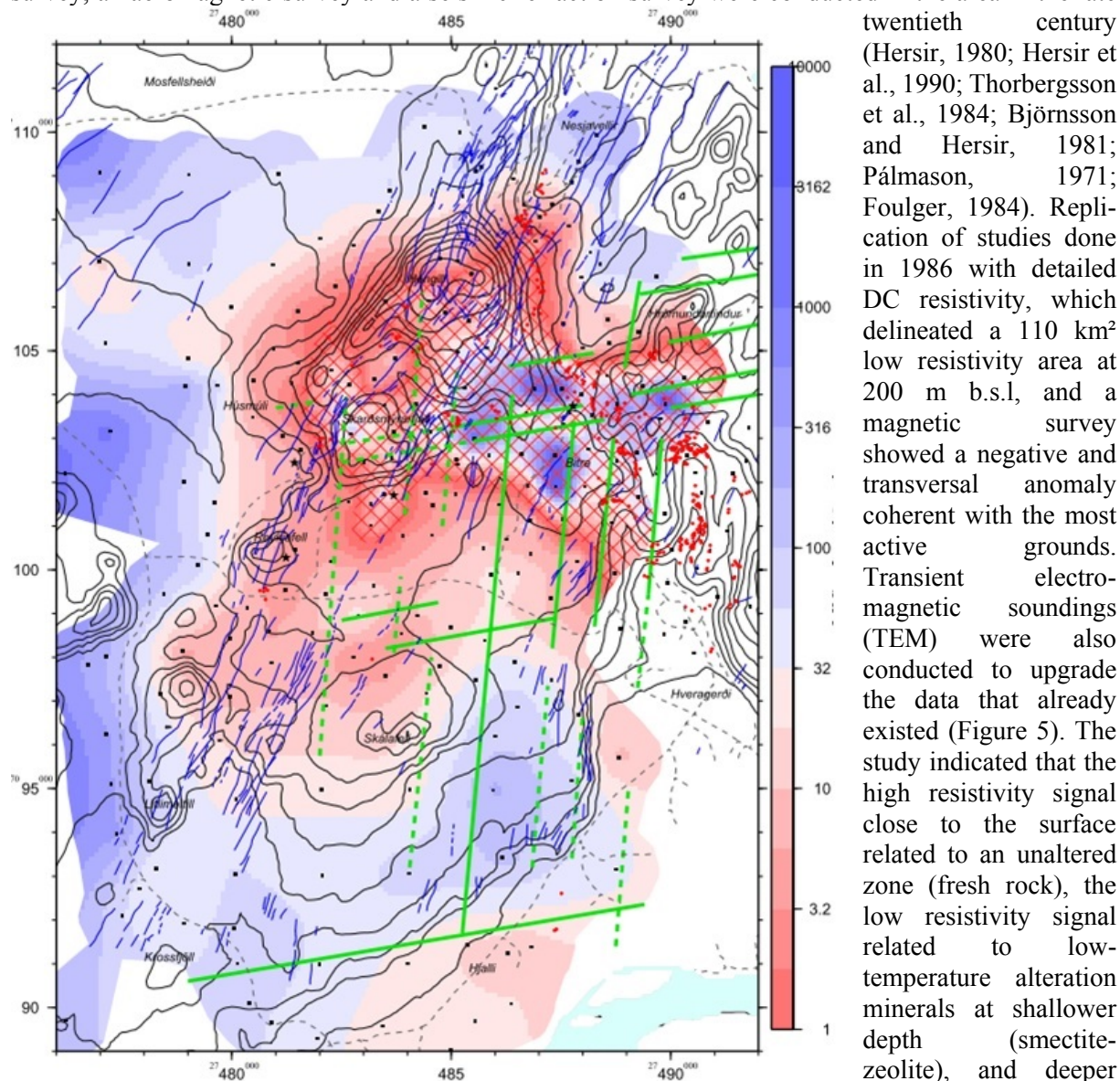


FIGURE 5: Hengill area, resistivity at 100 m b.s.l. according to a recent TEM survey, faults (blue/irregular lines) and interpreted earthquake fractures from recent seismic events (green/straight lines); Scale to the right shows resistivity in Ωm (Árnason and Magnússon, 2001)

twentieth century (Hersir, 1980; Hersir et al., 1990; Thorbergsson et al., 1984; Björnsson and Hersir, 1981; Pálmason, 1971; Foulger, 1984). Replication of studies done in 1986 with detailed DC resistivity, which delineated a 110 km² low resistivity area at 200 m b.s.l, and a magnetic survey showed a negative and transversal anomaly coherent with the most active grounds. Transient electro-magnetic soundings (TEM) were also conducted to upgrade the data that already existed (Figure 5). The study indicated that the high resistivity signal close to the surface related to an unaltered zone (fresh rock), the low resistivity signal related to low-temperature alteration minerals at shallower depth (smectite-zeolite), and deeper high resistivity to the formation of chlorite and less conductive alteration assemblages (Franzson et al., 2010).

2. BOREHOLE GEOLOGY

2.1 Brief history of drilling well HE-4

Well HE-4 is a directional exploration well, drilled east of Reykjafell mountain to a measured depth of 2008 m. The well has the following coordinates: X - 383,491.82, Y - 393,716.71 and Z - 404 m a. s. l. The well was designed to intersect the active fault and the volcanic fissure which lies southwest of Hengill, and the aim was to provide information about geothermal heat between Reykjafell mountain and the Hveradalir valley (Jónsson et al., 2001; Guðmundsson et al., 2001ab).

Drilling commenced on 31st August 2001 and involved three phases, as shown in Figure 6. The first phase was drilled with a 17 ½" drill bit, and a safety casing of 13 ⅜" to a depth of 300 m. The surface casing had already been set at 78 m. The well was planned to deviate from 300 m to a direction of 208° (towards southwest). The drilling rate was slow: 2.5 to 3.5 m/h to avoid the collapse of soft formations near the surface. The drilling of the first phase stopped at 305 m where temperature and caliper logs were conducted before the casing was set. A total of 24 m³ of concrete was used for cementing the casing. No circulation loss was encountered during this phase.

The second phase started on September 8th 2001. The phase was drilled with a 12 ¼" drill bit and cased with 9 ⅝" production casing; 50 l/s circulation loss was encountered at a depth of 496 m. Exercises to stop the leaking were not successful at first and various problems persisted, including eruptions due to high pressure in the hole. After repeated cementing and several temperature measurements, drilling started again after about a 4 day delay, still somewhat problematic. Drilling finally ended at 789 m where geophysical logging was conducted. After the casing had been set and cemented, gyro measurements were made, marking the end of phase 2.

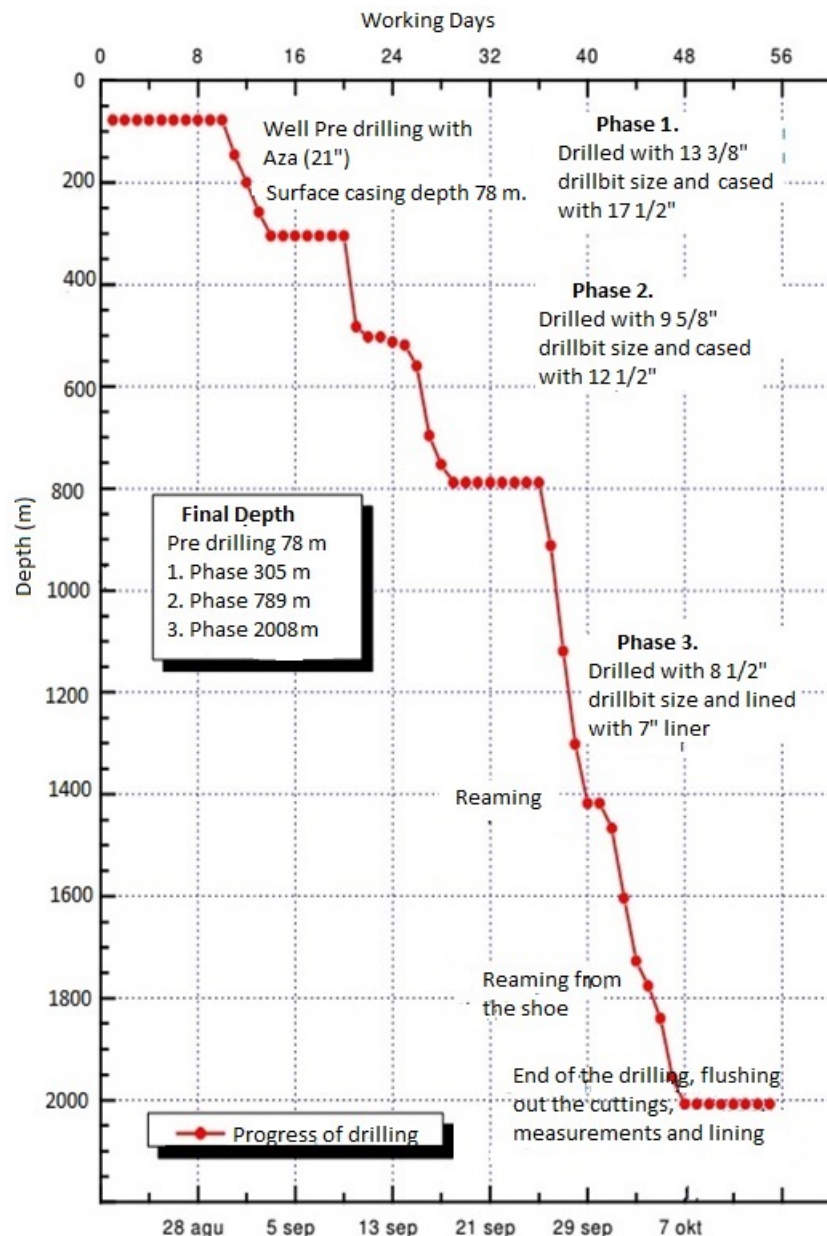


FIGURE 6: Drilling progress of well HE-4

The third section started on the 25th of September 2001 and was drilled from 789 m to 2008 m with an 8 ½" drill bit. At 1148 m, a fairly large feed point was crossed which caused a circulation loss of 37 l/s; hardly any circulation was retrieved from this depth until 1184 m. At 1270 m, circulation was lost again and, at around 1400 m, the drill bit got stuck for a while. As soon as the bit was free, reaming and washing started but the problem persisted for some time until enough reaming had been conducted. Drilling then continued down to 2008 m where torque was substantial. Temperature logs and gyro measurements were made, followed by geophysical logging. Close to the bottom the inclination measured around 45° and the azimuth around 198°. When all logging had been conducted, the 7" liner was set down on the 11th of October. Soon afterwards well testing was finished and phase 3 was completed on the 14th of October.

2.2 Analytical methods

Binocular microscope analysis; rock cuttings were sampled at an interval of 2 m during drilling. It is important to analyse wet samples to have clear visibility of any obscured features in the cuttings. The analysis of samples in the binocular microscope helps with analysing the rock type with its primary minerals, grain size, oxidation, alteration minerals and alteration intensity, fractures and vein fillings. About 600 samples were sampled from the upper 1200 m of well HE-4.

Petrographic microscope; the petrographic analysis is based on 34 thin sections from different depth intervals as representative samples from the upper 1200 m of well HE-4. The analysis is used to correlate and add valuable information on rock type, texture, primary minerals and their alteration and secondary minerals along with alteration sequence and porosity.

X-ray diffractometer analysis; the analysis is used to examine crystallized materials with emphasis on the clay minerals. The samples were selected from different depths from the upper 1200 m, emphasizing the areas with signs of different clay alteration, for identification of their types. The samples were placed in crucibles, then washed with distilled water to remove all dust or mud that might be stacked on them. The recommended sample size is not less than one full teaspoon topped up with water and placed in the shaker for about 3 hours to separate the clay from the rock matrix. When finished, the samples were mounted on glass, dried and were then ready for XRD-analysis. This method is very important for identifying clays and amphiboles which, in turn, provide information on the alteration temperatures. The XRD analyses of clay minerals in well HE-4 are found in Appendix I.

Fluid inclusion analysis; the analysis is conducted using microthermometry by gradually heating up the sample to the maximum temperature (homogenization temperature) of the fluid inclusions, so that the bubble within the fluid inclusions, trapped during crystallisation, disappears. Primary inclusions are those that form due to imperfections on the crystal surface during crystal growth. Generally, the mechanism for forming secondary inclusions involves the development of post crystallisation fractures initiated during mechanical or thermal stress. These cracks are then sealed by later fluids to form the characteristic trails of secondary inclusions which typically cross-cut earlier generations (Shepherd et al., 1985). The analysis provides direct information on the temperature during the formation of the hydrothermal minerals and was used in this study (along with the temperature of first appearance of alteration minerals and the formation temperature) for the interpretation of the thermal situation of the geothermal system.

The selection of samples in well HE-4 was based on the different intervals of the upper 1200 m aided by temperature logs and formation temperature, focusing on areas of temperature change and/or aquifers. Clear quartz crystal and platy calcite were selected, being some of the best representatives for analysing fluid inclusions.

2.3 Stratigraphy of well HE-4

The subsurface geology of this study covers several units of rock formations, mainly distinguished by crystallinity and volcanic glass contents. Figure 7 shows the lithology of the well HE-4. Hyaloclastite basalt formations are found to alternate within the HE-4 well column including basaltic tuff (distinguished by its high content of volcanic glass) basaltic breccia (partially crystalline basalt mixed with volcanic glass) and pillow lava (partially crystallised basalt) which comprises the smallest content of volcanic glass. Fine grained and fine to medium grained crystalline basalt were also encountered within the well, forming either sub-aerial lavas or intrusions. The formations are also described

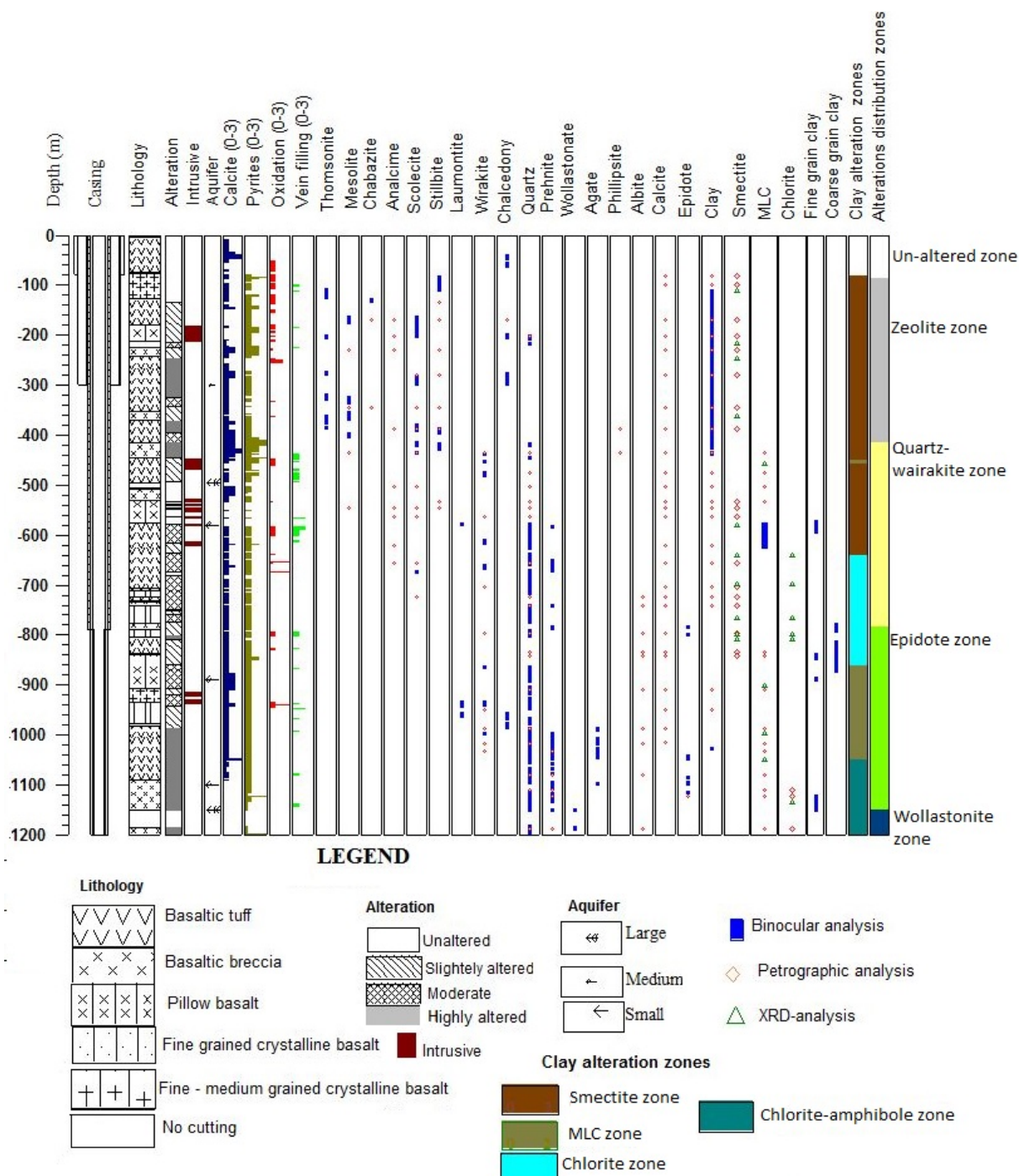


FIGURE 7: Lithology and distribution of alteration minerals in well HE-04 at 0-1200 m

according to their physical characteristics, mainly based on texture and the difference in alteration intensity from one unit to another. The description of the rocks is based on the binocular analysis with the aid of the petrographic analysis as explained below:

0–4 m. No sample

4–86 m. Basaltic tuff

Fine to medium grained tuff, with phenocrysts of olivine and plagioclase. Some of the tuff formation has been altered to palagonite. Some vesicles are seen in the upper part and some are filled by chalcedony while in the lower part the tuff is more consolidated with no vesicles. The colour ranges from dark – brown – grey and the rock shows slight alteration. Secondary oxidation minerals, such as limonite and siderite, appear more common between 52–72 m. Pyrite first appeared at 78 m. There are no cuttings from 74–76 m. It is very likely, however, that the tuff is continuous since it is homogeneous.

86–126 m. Crystalline basalt

Fine grained crystalline basalt, dark to grey in colour. Vesicles are filled with secondary minerals including stilbite and calcite. The rock is oxidized in the upper part where limonite and siderite are found. Pyrite also appears to be a common alteration mineral in this formation.

126–180 m. Basaltic tuff

Fine grained and dark grey in colour (consolidated tuff). In the lower section it is mixed with breccia basalt. The less oxidized formation has a high content of olivine. This formation is less vesicular than the one above and the vesicles are filled with calcite and amorphous silica. Clay alteration seems to appear in a disseminated way. Other secondary minerals are scolecite, mesolite and pyrite.

180–212 m. Basaltic breccia

Dark in colour, partially crystallised basalt cut through by fine grained basalt intrusives, with olivine and plagioclase phenocrysts. The formation is mixed with particles of transformed tuff. It is moderately oxidized showing some limonite alteration. Other secondary minerals are calcite, pyrite, thomsonite, chalcedony and clay in the lower part of the formation.

212–224 m. Basaltic tuff

The formation is dominated by light to green colours; it is fine grained and with olivine mottled phenocrysts. Clay alteration results in the green colours of the rock, and pyrite and calcite appear to be common.

224–242 m. Basaltic breccia

Fine grained and dark to brownish in colour, slightly fractured and filled with calcite and pyrite in the upper part. Olivine is altered to clay which is also deposited as vesicle fillings. Amorphous silica is also encountered.

242–352 m. Basaltic tuff

The formation is mixed with basaltic breccia in the upper part but dominated by fine grained basaltic tuff of brown to greenish colour. Fragments of crystalline basalt are encountered from 294 m to 312 m. The rock is slightly oxidized from 250–262 m, where the formation is also highly altered and more porous. Calcite, chalcedony and clay are common. Other alteration minerals are pyrite and zeolites (thomsonite and scolecite) in low amounts.

352–370 m. Basaltic breccia

Fine to medium grained basaltic breccia with brown to greyish colours. Fine grained basaltic tuff is encountered from 358 m to 360 m. Alteration minerals seem to be in low quantity but include clay, pyrite, calcite and zeolites (scolecite).

370–416 m. Basaltic tuff

Greenish to grey, fine to medium grained basaltic tuff. Some particles of fresh and fine crystallised basalt are encountered at 408 m which could be an indication of an intrusive. Pyrite appears in high quantity relative to calcite (platy calcite first appears at 392 m).

416–444 m. Basaltic breccia

Fine to medium grained basaltic breccia with colours ranging from light to grey to green. The rock is completely altered and more porous than before. Vesicles are filled with secondary minerals including platy calcite, clay, pyrite and zeolites (including thomsonite, stilbite and scolecite) are common. Quartz crystals first appear at 414 m, gradually increasing from there, and the high temperature zeolite wairakite appears a little bit further down (436 m according to the petrographic study).

444–530 m. Basaltic tuff

The formation is highly porous, very fine grained (ash like) more vesicular and altered, light to greyish in colour, fractured with vein fillings of calcite and silica minerals. An intrusive of fine grained crystalline basalt appears from 448 to 468 m. There is an interval of no cuttings between 494 and 504 m (loss of circulation) which indicates a permeable zone. Dominant secondary minerals are pyrite, clay and low amounts of calcite. Wairakite is first seen in the binocular analysis at 452 m whereas in the thin section it was seen at 436 m. Zeolite minerals are scolecite, stilbite and analcime; quartz seems to be common in this unit.

530–576 m. Pillow basalt

The formation varies from light to grey in colour. It is fine grained and interrupted by multiple losses of circulation from 534–538 m, 540–544 m, 548–562 m and 564–576 m. In the upper part of the formation there is fresh fine grained crystallised basalt with phenocrysts of olivine, considered an intrusive rock. Secondary minerals are quartz, calcite, clay and low amounts of pyrite.

576–706 m. Basaltic tuff

Altered basaltic tuff, fine to medium grained, green to brownish in colour. Primary minerals of pyroxene and plagioclase are seen. The rock is highly altered in the upper part down to 596 m and moderate alteration is seen from 598 m down to the bottom of the formation, fractured with micro veins filled by calcite. An intrusive of fine grained crystalline basalt is encountered from 618 m to 660 m. The representative alteration sequence is clay – calcites – clay – mixed layer clay – SiO₂- quartz and pyrite appear to be disseminated. Wairakite, scolecite (zeolite) and prehnite were also encountered. Between 678 m and 682 m there is a gap with no cuttings but the lithology remains homogeneous above and below.

*706–710 No cuttings**710–724 m. Fine grained crystalline basalt*

Brownish to grey crystalline basalt, plagioclase and olivine primary minerals appear as phenocrysts. The formation is moderately altered and mixed with low amounts of basaltic tuff. Secondary minerals are quartz, pyrite, prehnite, wairakite and a smaller amount of clay and amorphous silica.

724–732 m. Basaltic tuff

Fine grained, highly altered basaltic tuff, brownish to grey in colour with phenocrysts of plagioclase. Alteration minerals include very low amounts of pyrite, calcite and clay. Other alteration minerals are prehnite and quartz. At 732–734 m there were no cuttings.

734–740 m. Basaltic breccia

Fine grained, grey coloured basaltic breccia as the dominant formation mixed with particles of brownish basaltic tuff. Alteration minerals seem to be in low quantity and include pyrite, quartz and calcite.

740–776 m. Basaltic tuff

Consists of fine grained tuff, brownish to grey in colour with moderate alteration. The formation is highly vesicular and somewhat filled with amorphous silica and clay. Basaltic breccia appears at the interval of 752–758 m. Other secondary minerals are pyrite, quartz and calcite.

776–788 m. Basaltic breccia

The formation is a mixture of tuff and basaltic breccia with brown to grey colours, respectively. Coarse and fine grained clay, agate, calcite, quartz and pyrite are common and epidote (first appearance) is noted at 784 m.

788–804 m. Fine grained crystalline basalt

Dark grey, very fine grained basalt mixed with light brown basaltic tuff towards the bottom. Fractured and filled by calcite. Quartz, epidote, clay and pyrite are common alteration minerals.

804–838 m. Basaltic tuff

Highly altered fine grained, light brown tuff, mixed with basaltic breccia and greenish fine grained crystalline basalt. Multiple micro veins are seen, filled with calcite and amorphous silica.

836–906 m. Pillow basalt

Fine grained pillow basalt of yellowish to green colours. The yellowish green colour of epidote is seen in the formation but there are no well-developed crystals. Vesicles are filled with fine and coarse grained clay. An interval of dark to grey breccia basalt is seen from 870–874 m. Secondary minerals are quartz, pyrite and a high amount of calcite.

906–934 m. Fine – medium grained crystalline basalt

Green to dark, mixed with more fresh fragments of fine crystalline basalt at 910–914 m which presents an intrusive. The intrusive then reappears at 918–920 m, 928 m and 932 m, possibly representing traces of the intrusive from 910–914 m. In addition there is some amount of breccia and glassy basalt mixed in the lower section with brownish spots showing olivine that has been altered to clay. Other secondary minerals are quartz, pyrite, calcite, wairakite and laumontite.

934–978 m. Fine grained crystalline basalt

Green to dark, fine grained basalt, fractures filled with clay and chalcedony. Vesicles are filled with laumontite, clay and quartz. Pyrite is also seen.

*978–980 m. No sample**980–1090 m. Basaltic tuff*

Basaltic tuff is the dominant formation at this depth interval and is mixed with small amounts of breccia basalt. General texture is fine to medium grained and the colour ranges from light to grey to green. Coarse grained clay is seen and veins filled with calcite (platy calcite is also encountered). Other secondary minerals are quartz, pyrite, chalcedony, wairakite, agate; epidote is seen from 1040 m.

1090–1200 m. Basaltic breccia

The dominant lithology is basaltic breccia of greenish colour mixed with basaltic tuff all the way to the bottom. The lithology is interrupted by a gap of no cuttings from 1152–1184 m (circulation loss) but the lithology is believed to be homogenous down to 1200 m. Secondary minerals are epidote, quartz, pyrite and clay. Calcite is not seen in this unit. Wollastonite appears at 1150 m.

2.4 Intrusives

Intrusive rocks are identified by their compact nature, relatively low alteration, sometimes by oxidation found at their margins and they are normally younger than the host rock. Geophysical logs often show them to have relatively high $n-n$ and resistivity values (Franzson et al., 2005). Intrusive structures are important features of geothermal systems as they relate to permeability. Several intrusives were encountered at various depths in well HE-4 and all are fine crystallized basalt, indicating rather thin dykes or sills, found at 182–212 m, 528–580 m, 614–660 m, and 912–920 m (reappearing occasionally between 930–938 m). Minor amounts of intrusive grains were identified from fresh particles of fine crystalline basalt, indicating an intrusive nearby at 408 m. The intrusives identified from cuttings through binocular analysis are presented in Figures 7 and 8.

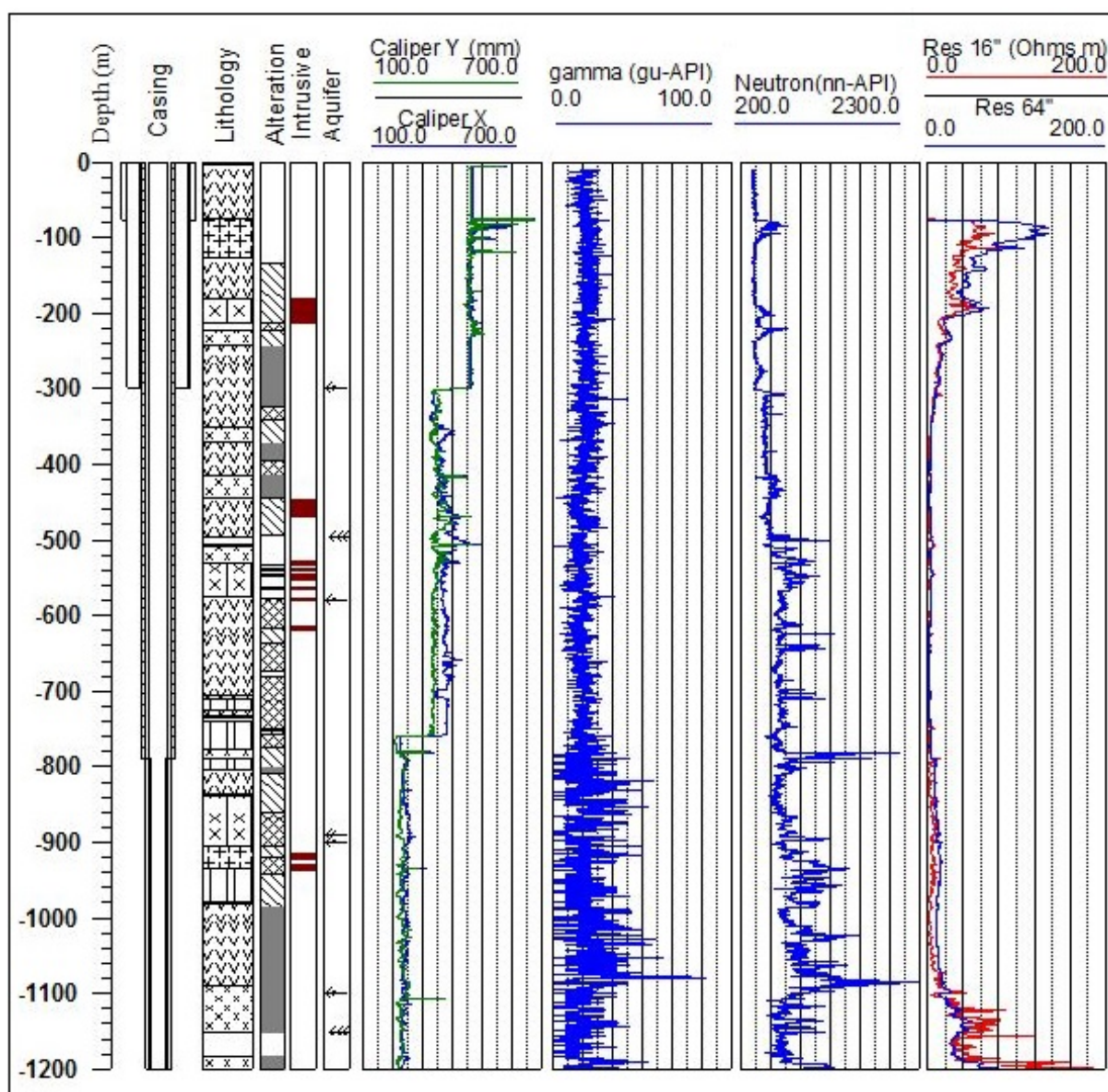


FIGURE 8: Feed points in relation to lithology, geophysical logs, intrusives and alteration intensity in well HE-4 (same legend as in Figure 7)

3. HYDROTHERMAL ALTERATION

Hydrothermal alteration occurs when fluids and reservoir rocks react to each other in hydrothermal systems. The reactions result in various changes by forming new rock properties including textures, changing porosity, permeability and chemical composition or generating new minerals commonly considered as secondary minerals. The factors that usually control alteration in geothermal systems are temperature, rock type, permeability, fluid composition and the duration of fluid-rock interactions (Browne, 1978; Elders et al., 1981).

Of all the different factors contributing to hydrothermal alteration, temperature plays a key role when studying and interpreting the changes of the original state of the reservoir rock by considering primary rock forming minerals and fluids within the reservoir. Temperature not only controls, to a degree, the composition of secondary mineral assemblages but also the rate of alteration processes (Reyes, 2000). The interpretation is based on the alteration minerals (secondary minerals) that have been studied according to their standard forming temperature. A comparison is made between the present information from surface to sub-surface geology through different methodologies including geochemical, geological and geophysical studies. Hydrothermal alteration helps with identifying and revealing present and past conditions in geothermal reservoirs.

3.1 Primary minerals

Primary minerals are rock forming minerals that form during rock crystallisation; these minerals are essential for the classification of the rock. The minerals form in a sequence or in sequential groups as detected by the chemistry and physical conditions under which the magma solidifies. Primary minerals tend to alter and form secondary minerals at conditions of high temperatures, high permeability and fluid activity in a hydrothermal environment (Gebrehiwot, 2010). Hyaloclastite and crystalline basaltic rock are the main rock types throughout well HE-4, and they are mainly composed of volcanic glass, olivine, plagioclase, pyroxene and opaques as the primary minerals. Their degree of susceptibility differs from one mineral to another as shown in Table 1 and Figure 9.

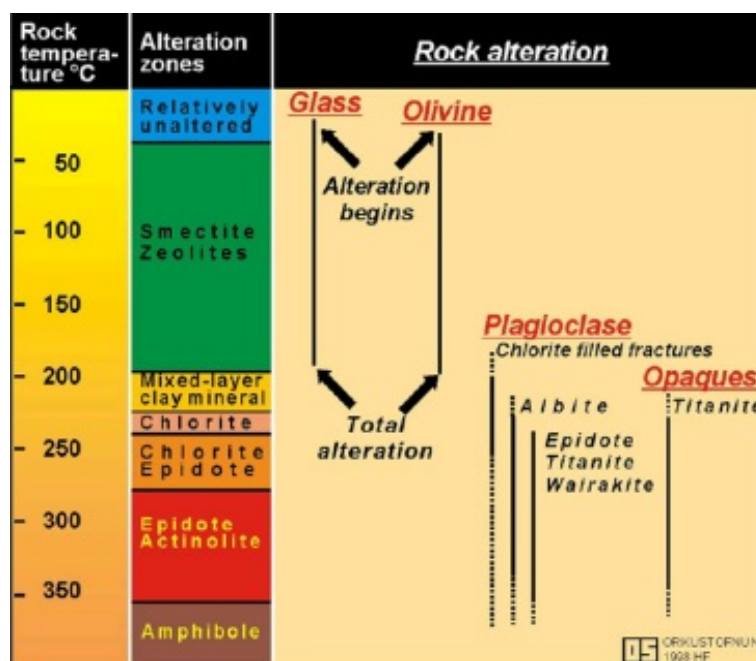


FIGURE 9: Mineral alteration temperature diagram (Franzson, 1998)

TABLE 1: Primary rock minerals and their alteration products in well HE-4

Susceptibility	Primary Mineral	Alteration Mineral Product
↓	Volcanic glass	Clay, zeolite, calcite, quartz
	Olivine	Clay, calcite, quartz
	Plagioclase	Clay, calcite, albite, wairakite, quartz, chlorite, epidote
	Pyroxene	Clay
	Opaques	

Volcanic glass is an amorphous (uncrystallised) product formed during the quenching of magma. Volcanic glass occurs in well HE-4 as a matrix material which shows highly vitreous lustre and has good conchoidal fracturing. Glass has low resistance to alteration compared to primary minerals. In well HE-4, clay, smectite and calcite are the common alteration minerals of glass which was completely altered from 656 m.

Olivine is one of the primary minerals formed in basaltic rocks (olivine tholeiite). It is the second most susceptible to alteration after glass. In thin section it is distinguished by its high birefringence, distinctive irregular fracture pattern, lack of cleavage, and its parallel extinction. Along its fractures the alteration products are usually clay, calcite and chlorite. Olivine can also alter to quartz although in well HE-4 there was no clear evidence of this. In binocular analysis, olivine mostly appeared as phenocrysts in the upper part of the well and seems to be completely altered from 724 m, according to the petrographic study.

Plagioclase is the most abundant primary mineral in igneous rocks. It is easily identified in thin section by its low relief, maximum interference colours are usually first-order grey or white, and twinning distinguishes plagioclase from most other minerals. Plagioclase is progressively altered to clay, calcite, albite, quartz, wairakite, chlorite and epidote as temperature increases. The first noticeable alteration of plagioclase in well HE-4 was to clay in cracks at 620 m which seems to increase the alteration at the lower depth of the well.

Pyroxene minerals are significant components of many intermediate and most mafic igneous rocks. Pyroxene is black or dark green in colour and forms prismatic crystals with vitreous lustre and perfect cleavage. Extinction at an inclined angle distinguishes it from olivine as well as its apparent cleavage and light brown colour in plain polarized light. Most pyroxenes seen in well HE-4 appeared in the groundmass and some as phenocrysts. Pyroxene started to alter to clay at 1032 m, showing more resistance than glass, olivine and plagioclase to high temperature.

Opaque minerals do not transmit light in transmitted light microscopes. They are usually magnetite (oxide mineral) in basalt. These minerals were hardly altered throughout the well although often there were signs of oxidation on their edges.

3.2 Distribution and description of hydrothermal alteration minerals

Hydrothermal minerals are derived from primary minerals or glass and form due to the physical and chemical composition in geothermal systems where temperature is the key factor (Reyes, 2000). In well HE-4, various hydrothermal minerals were observed including calcite, pyrite, clay, zeolites, quartz and epidote. These minerals are important in this study as the temperature at which they form is compared to the present formation temperature of the well and together they provide information about the situation of the current geothermal system surrounding the well. The distribution of alteration minerals encountered in well HE-4 is shown in Figure 7 and the standard temperature for the formation of some of the alteration minerals in Iceland can be seen in Table 2. A description of the alteration

TABLE 2: Some temperature dependent minerals in high-temperature areas in Iceland (Kristmannsdóttir, 1979; Franzson, 1998)

Minerals	Min. temp. (°C)	Max. temp. (°C)
Zeolites	40	120
*Laumontite	120	180
*Wairakite	200	
Smectite		<200
**MLC	200	230
Chlorite	230	>300
Calcite	50-100	280-300
Quartz	180	>300
Prehnite	240	>300
Epidote	230-250	>300
Wollastonite	270	>300
Actinolite	280	>300
*Belong to the zeolite group		
**Mixed-layer clay		

minerals along with their occurrence within the well is provided below:

Limonite forms by chemical weathering of iron rich minerals including olivine, pyroxene and magnetite, some of the main constituents of basaltic rock. Limonite mainly forms close to the surface where it is mostly associated with cold water with an abundance of oxygen. It is reddish brown in colour, and usually forms spherical precipitations within vesicles or fractures.

Siderite is a carbonate group mineral, spherical and brownish in colour and forms at shallow depths. It commonly appears together with limonite. These two minerals were encountered down to about 136 m in well HE-4.

Calcite is the most abundant alteration mineral in well HE-4, mainly filling pores and veins. The first appearance of calcite was at 20 m depth but was seen all the way to 1092 m. The temperature of calcite deposition is relatively difficult to determine, however, experience has shown that the mineral disappears at temperatures above 290°C (Franzson, 2000; Kristmannsdóttir, 1979). Different forms of calcite were encountered at different depths with platy calcite first appearing at 392 m and dog tooth calcite was clearly seen in a thin section at 280 m.

Pyrite belongs to the sulphides group and is most abundant in well HE-4 between 400-500 m, just above one of the large aquifers in the well (Figure 7). It is first noted at 80 m and seems to occur throughout the well with fluctuating intensity. Most of the pyrites are found to be deposited in disseminated forms and some as fillings in veins and vesicles. The existence of H₂S in geothermal systems results in the formation of pyrite and pyrite in abundance is often associated with permeability (Reyes, 2000).

Zeolites form a group of hydrous secondary minerals composed of sodium, calcium and aluminium silicates. Zeolites are generally white or colourless but they can show yellow or reddish colours due to impurities. As temperature indicators, zeolites form at relatively low temperature and they are dependent on the chemical composition of the solution. These minerals tend to precipitate in vugs and vesicles where they are classified into three different habits as fibrous/acicular, tabular/prismatic and granular (Saemundsson and Gunnlaugsson, 2014). In well HE-4, low temperature zeolites first appear at 84 m, only disappearing at 676 m. Remnants of them were identified in thin section at 834 m; below are the descriptions of the different types of zeolites encountered within well HE-4:

Analcime is clearly identified in the petrographic microscope through its trapezohedron crystal shape, by which it is also identified in the binocular microscope. It is colourless in plane polarized light (Figure 10) and almost isotropic in crossed polars. Analcime commonly has weak birefringence and may display lower first-order interference colours. These minerals commonly form at low temperatures at around 40°C and, in well HE-4, it started to appear at 170 m.

Thomsonite is an acicular radiating zeolite. These zeolites form dense masses of radiating clusters of prismatic crystals, filling vesicles or veins and are often associated with other zeolite minerals such as scolecite. Thomsonite tends

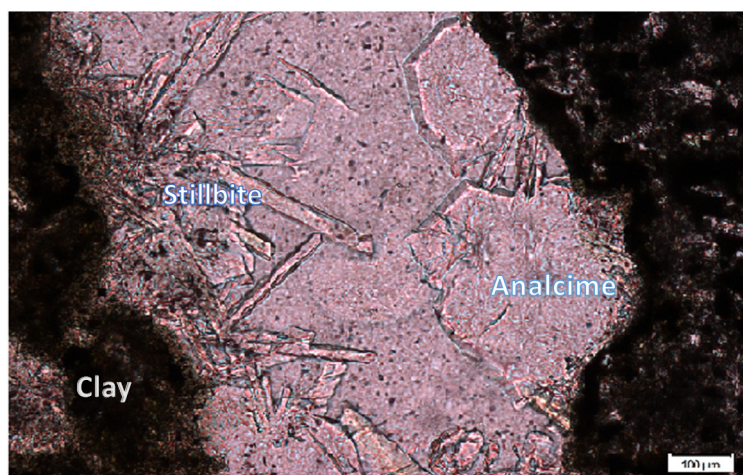


FIGURE 10: Photo from the petrographic microscope showing analcime, stilbite and clay at 280 m

to crystallize at a temperature of 30-40°C and was first noted at 106 m.

Scolecite/Mesolite: these are both fibrous zeolites with somewhat distinctive features where scolecite has thicker fibres while mesolite has thin fibres which are brittle and break easily. They are colourless or white with a vitreous lustre and often appear together in basaltic formations. They commonly form at around 70-80°C and, in well HE-4, they started to appear at 164 m.

Stilbite appears as rather thick, tabular crystals with pointed terminations. The crystals are white, transparent to translucent with a vitreous lustre, especially on the domed or oval ends of crystal bundles, while the broad face at the middle has a pearl lustre. Stilbite normally forms at temperatures around 90°C. In well HE-4 it was first seen at 84 m.

Chabazite forms at temperatures around 30°C. Chabazite was not identified in the binocular microscope and only seen in a thin section from 170 m in well HE-4. Chabazite occurs most commonly in voids and amygdales in basaltic rocks, the crystals are typically twinned and both contact twinning and penetration twinning may be observed.

Laumontite is a tabular zeolite that forms at somewhat higher temperatures than the low temperature zeolites. It is commonly white in colour and was first found at 934 m, indicating temperatures of 120°C. It is, however, not a reliable mineral for alteration temperature.

Wairakite is a high temperature zeolite forming at greater temperatures than 200°C. Wairakite was first seen at 452 m in the binocular analysis and in the petrographic microscope it was identified at 436 m by its conspicuous cross hatched twinning. It commonly occurs as an individual crystal or as glittering clusters (colourless crystals).

Quartz is colourless, milky to white or grey mineral with a conchoidal fracture. It forms hexagonal prismatic crystals which end in slanted faces meeting at a point. Quartz indicates temperature above 180°C and is considered a stable mineral. In well HE-4, quartz appeared between 202 m and 208 m, then disappeared and reappeared at 414 m. The shallow depth quartz seems to be a very local alteration brought on by an intrusive of fine grained crystalline basalt which probably caused localised raised temperatures. From the above scenario, quartz is considered to first appear at 414 m and is seen all the way to 1200 m in various basaltic formations within the well.

Albite is an alteration mineral derived from the alteration of the primary mineral plagioclase and sometimes occurs as precipitation filling vesicles. Albite is identified in thin sections by a cloudy appearance which makes the plagioclase twinning disappear. When well crystallised it has the appearance of the top of a roof. The albite alteration of plagioclase starts at a relatively high temperature, commonly forming at temperatures near 300°C (Kristmannsdóttir, 1979). It was first noted at 620 m in well HE-4. Albite is usually colourless or white and is, in some ways, similar to quartz but differs by its lower refractive index and its cloudy nature which is not seen in quartz. Albite was only seen as an alteration of plagioclase, not as a precipitation.

Chalcedony is the cryptocrystalline form of silica minerals; it has a waxy lustre, and may be semi-transparent or translucent. Most of the chalcedony seen in well HE-4 is white to grey or greyish blue in colour. Chalcedony forms at different depths, first seen at 112 m as a vesicle filling. The mineral appears and disappears all the way to 1032 m where it completely disappears.

Agate is a variant of chalcedony with bands of different colours generally following the contours of the cavity. Agate is commonly found with chalcedony and quartz and was seen at 784 m, disappearing again at 1098 m.

Prehnite appears as small spherical clusters of crystals, colourless to white in colour in the binocular microscope. In the petrographic microscope it is colourless in plane polarized light with a fairly high relief, while with crossed polars it shows strong interference colours and a bow-tie texture. In well HE-

4 it first appeared at 582 m in the binocular analysis and in thin sections it was found to be common from 988 m. This mineral indicates temperature above 240°C.

Wollastonite is commonly associated with high temperature minerals such as chlorite, epidote and actinolite. In well HE-4 it appeared together with chlorite radiating from the centre of the cavities, with a hairy like (fibrous) habit. It was found at 1150 m depth, indicating temperature of around 270°C.

Epidote is a high temperature alteration mineral and one of the most important ones for a geothermal production zone as it is usually easily identified by its yellowish green colour. The lower temperature stability of epidote is 240-250°C and it remains stable to well above 300°C (Browne, 1978). The mineral first appeared at a depth of 784 m and is found to be common from 1042 m, as seen in Figure 7.

Clay minerals are common alteration minerals associated with both weathering of rock and with hydrothermal alteration. Different types of clay form with respect to temperature variations from the surface to the bottom of the well, usually from low temperature to high temperature. Different methodologies have been used to distinguish the types of clay: binocular analysis and petrographic analysis are used to distinguish the presence of clay alteration minerals and their crystallinity with the help of XRD analysis of the cuttings. The following are the types of clay minerals found in well HE-4, arranged from low temperature to high temperature;

Smectite; this is the low temperature clay mineral commonly found near the surface at less than 200°C. Smectite is well identified in the petrographic microscope with its reddish to brown colours (with both plain polarized light and crossed polars). At around 82 m smectite was first found, confirmed by the XRD analysis at 94 m.

Mixed layer clay (MLC) is the complex of smectite and chlorite clay minerals. It forms at higher temperatures than smectite, in the range of 200-230°C, where smectite and zeolites are gradually replaced by chlorite as the dominant alteration mineral in the so-called mixed layered clay zone (Kristmannsdóttir, 1979). Mixed layer clay was suspected in the binocular microscope from its appearance of alternating bands of light green and dark green colours at 580 m and in thin section it seems to be common from 862 m. XRD analysis identified MLC first appearance at 450 m then disappearing and reappearing from 902 to 1050 m.

Chlorite is a high temperature clay mineral commonly associated with other high temperature minerals such as wollastonite, epidote and prehnite. Chlorite is commonly light green in colour and well identified in the petrographic microscope from its smooth or flat appearance. In the binocular microscope it was found at 1150 m filling the vesicle together with wollastonite and, in the petrographic microscope, clearly seen at 1188 m, whereas the XRD analysis indicates that chlorite appears together with smectite at 642-862 m then reappearing at around 1050 m (Figure 9).

Amphiboles are minerals of either igneous or metamorphic origin, the general group forms prism or needle like crystals and include tremolite, actinolite, tourmaline and hornblende. Colours can be green, black, colourless, white, yellow, blue, or brown. Actinolite forms as an alteration mineral in geothermal systems in Iceland but it was not identified in the binocular and petrographic analyses. Amphibole was, however, identified with XRD at 1050 m toward the bottom indicating temperature greater than 280°C.

3.3 Alteration mineral zonation

Alteration zones refer to the secondary minerals forming and dominating at a certain range of depth within the hydrothermal system, giving clues about the temperature. Alteration mineral zonation can differ from one geothermal system to another depending on the parent rock, the chemistry and temperature of the area. Icelandic geothermal systems are dominated with basaltic rock formations. From the group of alteration minerals identified in this study, and with respect to their temperature of

formation and sometimes the contradictory XRD clay analysis, the alteration zones in well HE-4 will be presented in two separate ways as follows;

1. Zonation depending on the distribution of alteration minerals

Based on the distribution and the first appearance of alteration minerals in well HE-4, which are stable at certain temperatures forming individual or groups of alteration minerals corresponding to Figure 9, six alteration zones were derived from low temperature to high temperature starting with an unaltered zone from the surface to a shallow depth, followed by the zeolite zone, quartz and wairakite zone, epidote zone and wollastonite zone.

2. Zonation depending on clay analysis

Five different zones of alteration were identified from the XRD analysis of clays, which was taken at different depths, combined with the petrographic analysis. The zones identified are as follows: from top surface to a shallow depth the zone is unaltered, followed by the smectite zone, chlorite zone, mixed layer clay zone and finally the chlorite-amphibole zone. On the basis of temperature and abundance of clay alteration within a certain depth interval, the following describe the clay zones with respect to depth:

- a. *Unaltered zone (0-82 m)*; from the two categorized zonations above, this zone is mainly comprised of surface alteration minerals forming from cold groundwater with temperature ranging from 0 to 40°C.
- b. *Smectite zone (82-642 m)*; defined by the first appearance and abundance of smectite clay where at a depth of 82 m it was identified through petrographic analysis in a slight amount (considered as first appearance), confirmed by the XRD analysis at 94 m. Temperature for the forming of smectite clay is less than 200°C.
- c. *Chlorite zone (642-862 m)*; the zone is comprised by the two independent clay minerals smectite and chlorite, where the existence of chlorite as a high temperature clay mineral indicates temperature above 230°C. Epidote first appears at 784 m, confirming that temperature.
- d. *Mixed layer clay zone (862-1050 m)*; is distinguished by a relatively high temperature above 200°C which is peculiar in well HE-4 because it forms below the chlorite zone. This could indicate fluctuations in the condition of the geothermal system.
- e. *Chlorite-amphibole zone (1050-1200 m)*; the zone is defined by the presence of abundant chlorite with amphibole alteration minerals first appearing at a depth of 1050 m. Both minerals are considered high temperature and, together, suggest temperatures more than 280°C.

3.4 Vein, vesicle fillings and mineral deposition sequences

Veins and vesicles act as hosts for the deposition of secondary minerals. Veins can appear as a single fracture or multiple veins within the rock, indicating active tectonic movements in the geothermal system. Rock porosity can be defined by the intensity of vesicles and veins throughout the formation. Hyaloclastite basaltic formations (glass rich rocks) seem to be more porous compared to lava formations (Kristmannsdóttir, 1979). Well HE-4 is predominantly comprised of hyaloclastite formations (basaltic tuff, basaltic breccia and pillow basalt).

In this study, the concentration of veins encountered along fractures that developed from intrusive events was quite common. This creates easy access for the deposition of secondary minerals. The deposition of alteration minerals infers a time sequence of deposition and temperature, this being one of the aids in determining whether the system is cooling or heating.

Concentrations of veins are found at different depth intervals within the well. Many of these relate to intrusions either nearby or fractures within intrusives. The intervals are: 142-148 m within basaltic tuff and near an intrusive, 446-492 m within basaltic tuff where veins tend to appear and disappear near an intrusive, 578-610 m within basaltic tuff near an intrusive, 789-796 m within fine grained crystalline basalt, 932-942 m within fine-medium grained crystalline basalt, and 1138-1144 m in basaltic breccia. The mineral sequence in well HE-4 is mainly comprised of clay and calcite as analysed in the petrographic analysis and its description in Table 3, showing the formation and deposition of secondary minerals with relation to time at different depths.

TABLE 3: Sequence of alteration minerals in well HE-4

Depth (m)	Lithology	Sequence from older to young
100	Fine crystalline Basalt	Clay→ calcite
134	Basaltic tuff	Clay → zeolite → calcite
170	Basaltic tuff	Zeolite → calcite → clay
202	Basaltic breccia	Smectite → calcite
230	Basaltic breccia	Smectite →calcite→zeolite
344	Basaltic tuff	Clay→ calcite
388	Basaltic tuff	Clay → calcite →zeolite
436	Breccia basalt	Sample 1: Zeolite → clay → calcite Sample 2: Calcite → zeolite
476	Basaltic tuff	Clay → zeolite → calcite
504	Basaltic tuff	Clay→ calcite
532	Pillow Basalt	Clay → calcite
546	Pillow Basalt	Fine grained clay →.calcite
562	Pillow Basalt	Low temp clay high temp clay→ calcite
620	Basaltic tuff	Clay → calcite → sio2 → quartz
656	Breccia basalt	Clay→ calcite → quartz
704	Breccia basalt	Clay → calcite → quartz
724	Fine crystalline basalt	Clay → calcite→ quartz
740	Basaltic breccia	Sample1: Clay →calcite → albite Sample 2: Clay → calcite → quartz
796	Fine crystalline basalt	Calcite → -clay smectite → mixed layer clay
834	Basaltic tuff	Clay → calcite
882	Pillow Basalt	Mixed layer clay → quartz
950	Fine crystalline basalt	Calcite → Wairakite
988	Basaltic tuff	Clay → calcite
1016	Basaltic tuff	Mixed layer clay → calcite
1080	Basaltic tuff	Mixed layer clay → quartz
1112	Basaltic breccia	Mixed layer clay → prehnite

Calcite as the major secondary mineral filling the veins (and vesicles) in well HE-4, first appeared at 84 m and remains all the way to 1092 m where it seems to disappear (indicating temperatures above 290°C). Other vein filling minerals in the well are chalcedony, pyrite, clay, amorphous silica and occasionally quartz. Other secondary minerals are mainly found in vesicles.

The deposition sequences (Table 3) show low temperature alteration minerals followed by high temperature alteration minerals, indicating heating up of the system. Clay and calcite dominate in a wide range within the well from the shallow depth to 834 m, whereas at lower depths from 882 m, mixed layer clay appears to be common with other high temperature alteration minerals, including quartz and prehnite. High temperature alteration minerals are also confirmed by the resistivity curve in Figure 8 where high peak readings are noted from 1050 m where chlorite, epidote and wollastonite are the dominant alteration minerals.

4. AQUIFERS/FEED ZONES

An aquifer is an important parameter in geothermal production as the main water-bearing permeable rock where steam and water phase originate. Location of the production casing and depth of the production part is dependent on aquifers within the well. Integrations of different data are used during interpretation. In this study, aquifers were identified mainly from the interpretation of temperature logs (Figures 8 and 11), caliper and neutron logs, circulation losses and the correlation of lithological units with intensity of alteration, presence of veins and lithological contacts. Based on neutron log interpretation, as explained by Steingrímsson, 2011, the slowing down process of fast neutrons in the rock formations is primarily controlled by the abundance of water in the surroundings, either water in pores and fractures in the rock formations or water bound in minerals, in other words: in geothermal alteration minerals.

Other considered parameters are penetration rate and pressure drops which can also support the deducing of aquifers within a geothermal system.

A total of seven aquifers were encountered in the upper 1200 m of well HE-4, classified as small or large. The aquifers in relation to various parameters used to identify them can be seen in Figure 8.

At 496 m a large aquifer is identified (total loss of circulation) and another large aquifer is at 1150 m (37 l/s loss of circulation). Aquifers at 300, 580, 890, 900 and 1100 m are all considered small.

Feed point 1: is a small feed point located at 300 m, identified by change in the inclination of the temperature log (Figure 11).

Feed point 2: this feed zone is found at 496 m within a basaltic tuff formation with high porosity. Circulation loss of 50 l/s was encountered during drilling and low readings of neutron and high peak of caliper are noted (indicating increased width of the well at that depth). The temperature logs show a slight change of temperature (inflow of water from the aquifer to the well) and the formation shows a number of vein fillings from 438 m to 496 m.

Feed point 3: is a small feed point at 580 m, identified by a slight change in temperature. The presence of a small intrusive is noted.

Feed points 4 and 5: these are small feed points located at 890 m and 900 m, respectively, both showing an increase in temperature. Lithologically it is within a pillow basalt unit. At this depth no loss of circulation was encountered, but low readings of neutron is seen.

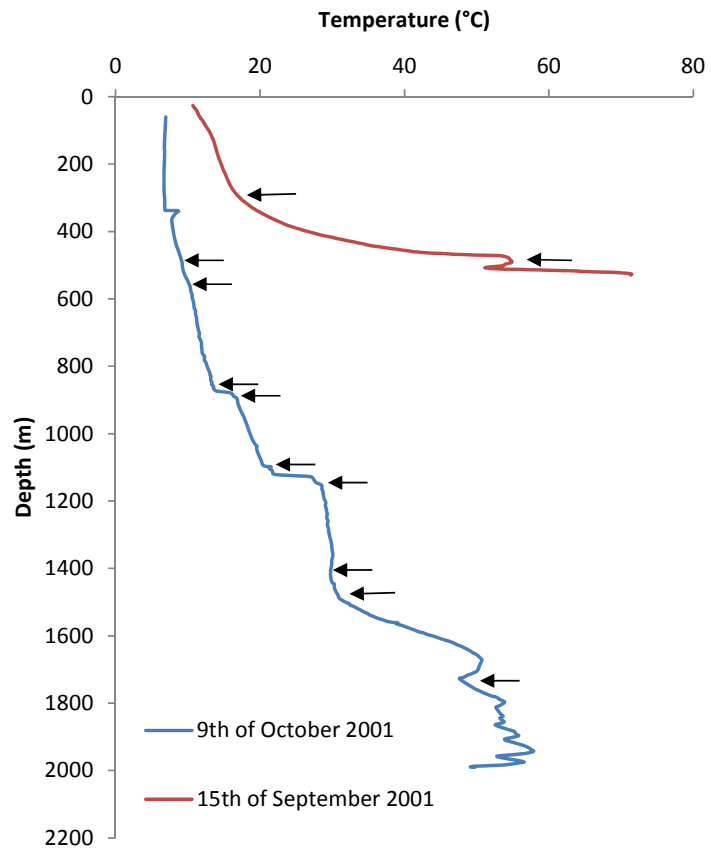


FIGURE 11: Temperature logs from the time of drilling showing aquifers with relation to temperature change in well HE-4

Feed point 6: at 1100 m it was identified by a sudden increase in temperature which correlates with an increase in caliper and a decrease in neutron readings. The formation is dominated by highly altered basaltic breccia.

Feed point 7: this large feed point is at 1150 m and caused a fluid loss of 37 l/ s. The lithology is dominated by basaltic breccia with high alteration and low neutron readings.

5. FLUID INCLUSIONS

The study of fluid inclusions reveals the temperature of fluid trapped during crystallisation of the minerals, which helps with determining the past conditions of the geothermal system. By comparing the temperatures of fluid inclusions to the present condition of the geothermal system, it is possible to determine whether the system is in equilibrium, cooling or heating.

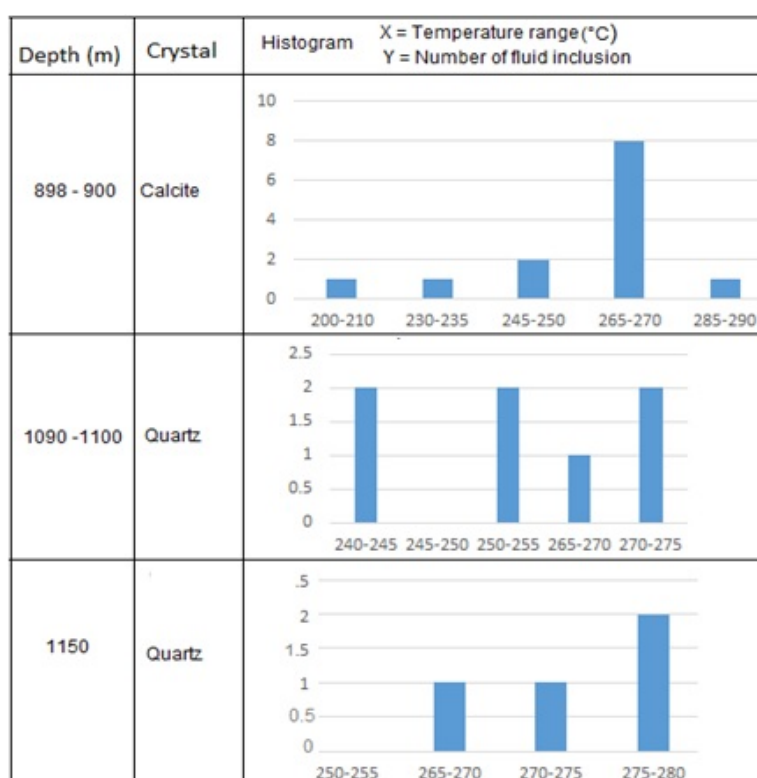


FIGURE 12: Histogram diagram showing the variations of homogenization temperatures with depth in well HE-4

The most common homogenization temperature for the calcite mineral is, however, close to the formation temperature. The quartz homogenization temperature is in a narrower range and is similar or slightly higher than the formation temperature.

6. DISCUSSION

The subsurface geology of well HE-4 is covered by two major formations which are hyaloclastite basalt formations and basaltic lava formations. Basaltic tuff, basaltic breccia and pillow lava seem to alternate and dominate in the well. Crystalline basalt appears in moderately thick layers of fine- and fine- to medium-grained crystalline basalt, representing interglacial lava flows and intrusive rocks.

Platy calcite and quartz crystals were studied through micro thermometry as representative samples from the system within the well at different depth intervals ranging from 898-900 m, 1090-1100 m and 1150 m, in close proximity with feed zones in the lower part of the studied well. A total of 24 fluid inclusion measurements were carried out which showed a range of homogenization temperatures (T_h) from 200°C as a minimum temperature and 290°C as a maximum temperature for calcite and 240-280°C for quartz, as described in Figure 12.

The homogenization temperatures show a wide range for the calcite, deviating quite a lot from the formation temperature and show temperatures all the way to the boiling point curve, but also down to 200°C, 60°C lower than the formation temperature of 260°C.

The distribution of alteration minerals in well HE-4 ranges from low temperature to high temperature starting with chalcedony, siderite and limonite found at a shallow depth in the well. Smectite, zeolite minerals appear at 82 and 86 m, respectively, followed by moderate temperature alteration minerals as zeolites are replaced by quartz, mixed layer clay, and wairakite from 414 m, 450 m and 452 m, respectively, in the middle zone of the well. High temperature alteration minerals like prehnite, epidote and wollastonite are common at the lower depth of the well from 1150 m.

Clay minerals show five zones of alteration starting with an unaltered zone from the surface, followed by the smectite zone at 82 m to 642 m, but interrupted with a mixed layer clay zone at 450-458 m. The chlorite zone is seen from 642-862 m, then the mixed layer clay zone at 862 to 1150 m, and the chlorite amphibole zone from 1050 m to 1200 m. From the sequence of the clay zones explained above, it can be deduced that it is different from the normal zonation of the area. Chlorite and mixed layer clay appear to alternate, and mixed layer clay is seen below chlorite suggesting lower temperatures at that depth. This is contradictory to other alteration data, such as the appearance of epidote at 784 m.

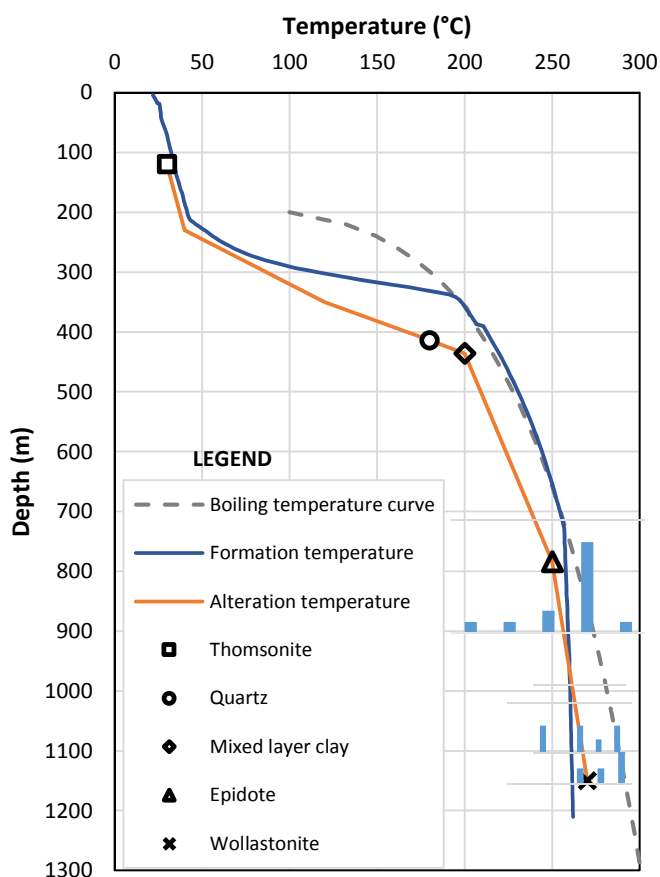


FIGURE 13: Formation temperature, alteration temperature, boiling temperature curves and homogenization temperature of well HE-4

The first appearance of five alteration minerals in different intervals within the well, depending on their standard temperature of formation in geothermal systems, derived a representative alteration curve and appears to be a little bit below the present formation temperature. Basing on the alteration curve in Figure 13 the system seems to be in equilibrium in the zeolite zone at the upper part to around 300 m. The onset of the crystallisation of quartz, mixed layer clay and epidote between 414 and 784 m seems to indicate lower temperatures than the current formation temperature, indicating heating up of the system.

The alteration mineral deposition sequence is, in general, dominated by clay and calcite from the shallow depth to near the bottom which shows the deposition sequence from low temperature alteration minerals to high temperature alteration minerals. Mixed layer clay seems to be more dominant in the alteration sequence from 842 m, followed by other moderate and high temperature minerals including quartz and prehnite, as identified from the petrographic analysis.

Fluid inclusion analysis of calcite shows the temperature range from 200°C to 290°C at 890-900 m. About 9 inclusions show higher temperature compared to the present formation temperature which does not exceeds 260°C, perhaps indicating cooling of the system. On the other hand, about five inclusions from the same crystal sample show a homogenization temperature lower than the formation temperature, perhaps indicating the heating of the system. This could represent fluctuations within the system at this depth.

At a depth of 1100 m, homogenization temperature of quartz crystal ranges from 240 to 275°C, showing the crystallisation to be in relative equilibrium with the formation temperature, while at the depth of

1150 m, the homogenization temperature for four inclusions shows relatively higher temperature than the formation temperature, indicating cooling of the system at the lower depth.

The occurrence of wollastonite at 1150 m makes the alteration temperature at the lower bottom of the well override the formation temperature, which correlates to the homogenization temperature of the quartz crystal at the same depth, as shown in Figure 13. The comparison of alteration temperature and homogenization temperature studied in well HE-4 with the formation temperature correlates well to the cross-section in Figure 14, showing the condition of the geothermal system in the area between wells HE-4, HE-7 and HE-6, indicating heating in the upper part and cooling in the lower part of the system.

A total of seven feed points were identified in the upper 1200 m. The small feed points at 580, 890 and 900 m are mainly related to pillow lava units. The larger feed points encountered at 496 and 1150 m are both associated with circulation losses with high peak of calliper at 496 m (indicating weakness in the rocks in that area) and a low reading of neutron. Furthermore, the alteration intensity towards the lower part can suggest increased permeability and may be related to the feed point at 1150 m. An intrusive is associated with the aquifer seen at 580 m.

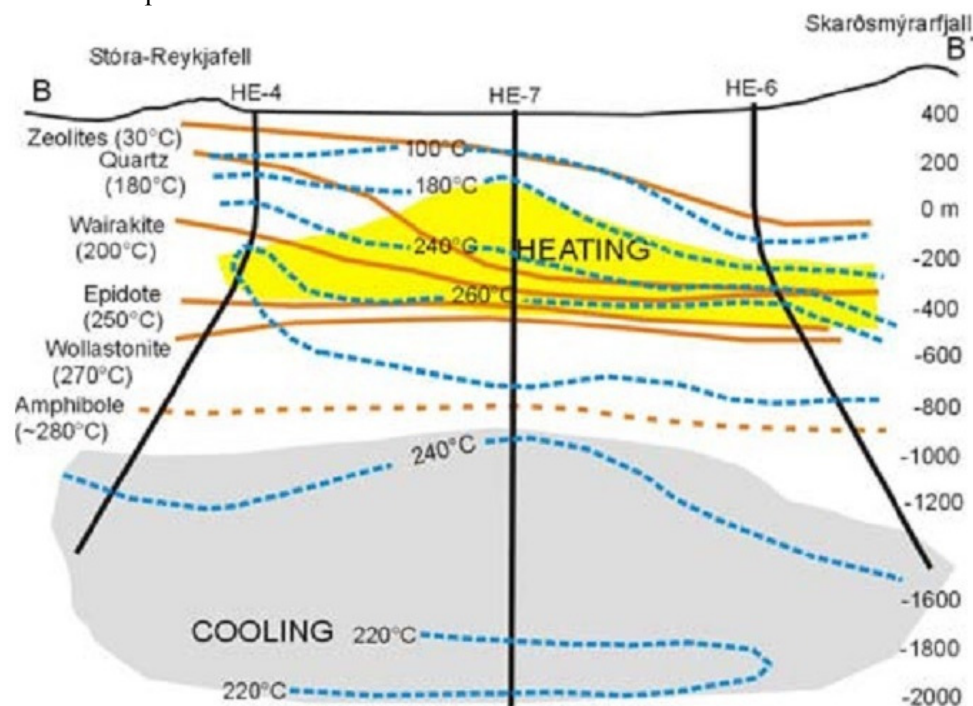


FIGURE 14: A cross-section showing a comparison of alteration and formation temperature between wells HE-4 and HE-6 in Hellisheidi, SW- Iceland (from Franzson et al., 2005)

7. CONCLUSIONS

From this study the following conclusions may be deduced:

- The stratigraphy of well HE-4 covers two major formations: a hyaloclastite basalt formation and a basaltic lava formation. Basaltic tuff, basaltic breccias and pillow lava (all part of the hyaloclastite formation) seem to alternate and dominate in a large part of the well. Crystallised basalt appears in moderately thick layers of fine- and fine- to medium-grained basalt, representing interglacial lava flows and intrusive rocks;
- Because of somewhat contradictory results between clay minerals and other temperature dependent minerals, it was decided to make two types of alteration zones: with respect to clay minerals on the one hand, and other alteration minerals on the other. Five alteration zones were

identified on the grounds of hydrothermal alteration mineral distribution from low temperature to high temperature, starting with an unaltered zone, followed by the zeolite zone, the quartz and wairakite zone, the epidote zone and the wollastonite zone. Clay alteration minerals also generated five zones starting with an unaltered zone, then the smectite zone which was interrupted by a thin layer of mixed layer clay, followed by the chlorite zone, the mixed layer clay zone and finally the chlorite amphibole zone;

- The feed points at 580 and 890 m are associated with the pillow lava units which can sometimes be more permeable than the surroundings, while the two large feed points at 496 and 1150 m are associated with circulation loss and high alteration intensity at 1150 m. Furthermore, an intrusive is clearly related to the feed point at 580 m; and
- Correlation of alteration temperature and homogenization temperature with formation temperature shows that the system is experiencing variable conditions. In the upper part of the well it seems to be in equilibrium, in the middle part from 414 to 784 m the system seems to be heating and in the lower part the system seems to be cooling.

ACKNOWLEDGEMENTS

I would like to express my gratitude to the UNU-GTP director, Mr. Lúdvík S. Georgsson and his deputy Mr. Ingimar G. Haraldsson for their appreciation and for providing me with the opportunity to attend this training programme, and also for their guidance and assistance throughout my time here. I am grateful to the UNU-GTP staff, Ms. Thórhildur Ísberg, Ms. Maria S. Guðjónsdóttir, Ms. Málfríður Ómarsdóttir and Mr. Markús A.G. Wilde, for their continuous help whenever required. I wish to give my thanks to all lecturers and staff members of ÍSOR and Orkustofnun for their comprehensive presentations and willingness to share their knowledge and experience, which broadened my knowledge in geothermal resources.

I am highly indebted to my supervisor, Ms. Helga M. Helgadóttir, for her excellent technical support, constant supervision and friendliness. My sincere credit goes to Dr. Hjalti Franzson, Dr. Björn S. Hardarson and Ms. Sveinborg H. Gunnarsdóttir for their excellent guidance and invaluable help during the preparation of the report. I extend my gratitude to Reykjavik Energy for providing and allowing access to the significant data of this study.

I would like to thank the Ministry of Energy and Minerals, as well as the Geological Survey of Tanzania, for granting me permission to attend this training.

Sincere gratitude goes to my lovely family and friends, my husband Obeid, my sons, Evan and Ean for their encouragement, motivation, prayers and patience during the entire period of training. I will run short of honour without expressing many thanks to Ms. Maria Mbeni, Mr. and Mrs. Stuart Heddi for their close attention to my sons during my absence - you all mean the world to me.

Thanks to all the 2014 UNU fellows for the ideas and good moments we shared during the entire six months period. Special acknowledgements go to the borehole geology classmates: Ms. Emily Kahiga, Ms. Moira Lunge-Bawasu and Mr. Djama Robleh, my housemates: Ms. Alice Uwase and Ms. Maria de Graça for good friendship and sharing their knowledge, skills and experiences during the course.

Finally, in Him I trust! I would like to thank God who made all things possible.

REFERENCES

- Arnórsson, S., Axelsson, G., and Saemundsson, K., 2008: Geothermal systems in Iceland. *Jökull*, 58, 269-302.
- Árnason, K., and Magnússon, I Th., 2001: *Geothermal activity in the Hengill area. Results from resistivity mapping*. Orkustofnun, Reykjavik, report, OS-2001/091 (in Icelandic with English abstract), 250 pp.
- Björnsson, A., and Hersir, G.P., 1981: Geophysical reconnaissance study of the Hengill high temperature area, SW-Iceland. *Geothermal Resources Council, Trans.* 5, 55-58.
- Browne, P.R.L., 1978: Hydrothermal alteration in active geothermal fields. *Annual Reviews of Earth and Planetary Science*, 6, 229-250.
- Elders, W.A., Hoagland, J.R. and Williams, A.E., 1981: Distribution of hydrothermal mineral zones in the Cerro Prieto geothermal field of Baja California, Mexico. *Geothermics* 10(3/4), 245-253.
- Foulger, G.R., 1984: *Seismological studies at the Hengill geothermal area, SW Iceland*. University of Durham, PhD thesis, 313 pp.
- Franzson, H., 1998: Reservoir geology of the Nesjavellir high-temperature field in SW-Iceland. *Proceedings of the 19th Annual PNOC-EDC Geothermal Conference, Manila*, 13-20.
- Franzson, H., 2000: Hydrothermal evolution of the Nesjavellir high-temperature system, Iceland. *Proceedings of the World Geothermal Congress 2000, Kyushu-Tohoku, Japan*, 2075-2080.
- Franzson, H., Gunnlaugsson, E., Árnason, K., Saemundsson, K., Steingrímsson, B., and Hardarson, B., 2010: The Hengill geothermal system, conceptual model and thermal evolution. *Proceedings of the World Geothermal Congress 2010, Bali, Indonesia*, 19 pp.
- Franzson, H., Kristjánsson, B.R., Gunnarsson, G., Björnsson, G., Hjartarson, A., Steingrímsson, B., Gunnlaugsson, E., and Gíslason, G., 2005: The Hengill Hellisheidi geothermal field. Development of a conceptual geothermal model. *Proceedings of the World Geothermal Congress 2005, Antalya, Turkey*, 6 pp.
- Fridleifsson, I.B., 1979: Geothermal activity in Iceland. *Jökull*, 29, 47- 53.
- Gebrehiwot Mesfin, K., 2010: *Subsurface geology, hydrothermal alteration and geothermal model of northern Skardsmýrarfjall, Hellisheidi geothermal field*. University of Iceland, MSc thesis, UNU-GTP, report 5, 65 pp.
- Guðmundsson, Á. Hjartarson, A., Guðmundsson, B., Friðleifsson Ó.G., Hermannsson, G., Ómar, G., Danielsen, E. P., Jónsson, S.S., 2001a: *Hellisheiði, well HE-4. 3. phase: Drilling of the production part from 789 m to 2008 m*. In Icelandic. Orkustofnun, OS-2001/081, 61 pp.
- Guðmundsson, B., Sveinn, S. J., Steingrímsson, B., Richter, B., Hermannsson, G., Danielsen, E. P., Thordarson, S., 2001b: *Hellisheidi, well HE-4. 2. phase: Drilling for 9½" production casing from 305 m to 789 m*. In Icelandic. Orkustofnun OS-2001/065, 62 pp.
- Hersir, G.P., 1980: *Electric and electromagnetic measurements across the Mid-Atlantic ridge in southwest Iceland, with special reference to the high temperature area of Hengill*. University of Aarhus, Mag. Scient. thesis, 165 pp.

Hersir, G.P., Björnsson, G., and Björnsson, A., 1990: *Volcanoes and geothermal systems in the Hengil area, geophysical exploration*. Orkustofnun, Reykjavik, report OS-90031/JHD-06 (in Icelandic), 92 pp.

Jakobsson, S.P., Jónasson, K., and Sigurdsson, I.A., 2008: *The three igneous rock series of Iceland*.

Jóhannesson H., and Saemundsson, K., 1999: Geological map 1:1.000.000. Icelandic Institute of Natural History. *Jökull*, 58 pp.

Jónsson, S.S., Steingrímsson, B., Guðmundsson, B., Richter, B., Hermannsson, G., Danielsen, P. and Thordarson, S., 2001: *Hellisheiði, well HE-4. 1. phase: Drilling for 13 3/8" safety casing to 305 m*. In Icelandic. Orkustofnun OS-2001/058, 25 pp.

Kristmannsdóttir, H., 1979: Alteration of basaltic rocks by hydrothermal activity at 100-300°C. In: Mortland, M.M., and Farmer, V.C. (editors), *International Clay Conference 1978*. Elsevier Scientific Publishing Co., Amsterdam, 359-367.

Pálmason, G., 1971: Crustal structure of Iceland from explosion seismology. *Soc. Sci. Islandica*, 40, Reykjavík, 187 pp.

Reyes, A.G., 2000: *Petrology and mineral alteration in hydrothermal systems: from diagenesis to volcanic catastrophes*. UNU-GTP, Iceland, report 18, 1998, 9 pp.

Saemundsson, K., 1979: Outline of the geology of Iceland. *Jökull*, 29, 7-28.

Saemundsson, K., 1995: *Geothermal and hydrothermal map of the Hengill area, 1:25,000*. Orkustofnun, Reykjavík.

Saemundsson, K., and Gunnlaugsson, E., 2014: *Icelandic rocks and minerals* (2nd ed.). Forlagið ehf. Reykjavík.

Shepherd, T.J., Rankin, A.H. and Alderton, D.H.A., 1985: *Practical guide to fluid inclusion studies*. Blackie and Sons, Glasgow, Great Britain.

Steingrímsson, B., 2011: Geothermal well logging cement bond and caliper logs. *Papers presented at Short Course on Geothermal Drilling, Resource Development and Power Plants, organized by UNUGTP and LaGeo, Santa Tecla, El Salvador*, 7 pp.

Thorbergsson, G., Magnússon, I. Th., Gunnarsson, Á, Johnsen, G.V., Björnsson, A., 1984: *Geodetic and gravity surveys in the Hengill area 1982 and 1983*. Orkustofnun, Reykjavík, report OS-84003/VOD-03 B (in Icelandic), 58 pp.

APPENDIX I: XRD clay mineral analysis results from well HE-4

TABLE 1: List of samples with XRD clay mineral analysis results from well HE-4

No.	Depth (m)	Untreated (Å)	Glycolated (Å)	Heated (Å)	Clay type
1	94	15.5	17.6	0	Smectite
2	112	16.68	16.68	10.44	Smectite
3	212	15.1	17	9.8	Smectite
4	218	15.64	15.64	10.44	Smectite
5	248	15.64	15.64	10.44	Smectite
6	286	15	17	9.8	Smectite
7	360	15	17	9.8	Smectite
8	362	13.05	13.05	10.17	Smectite
9	450	30/14.6/12.77	31/17.3/15	12-13/9.8	Smectite+MLC
10	458	14.55	14.55	7.19	MLC
11	472	30/14.4/12.9	31/17/15.5	12-13/9.8	Smectite+MLC
12	506	30/14.4/13	31/17/15	12.5/9.8	Smectite+MLC
13	522	No clay	No clay	No clay	No clay
14	530	15.2/12.77	17.02	9.8	Smectite
15	564	30/14.7/12.9	31/16.9/14.1	12/ 9.8	Smectite+MLC
16	580	14.59	14.59		Smectite
17	600	12.7	16.9	9.8	Smectite/ill
18	642	14.3/13.03	14.3/13.03	10.11/7.15	Smectite-Chlorite (illite)
19	644	14.88/12.75	16.98/15	9.8	Smectite-Chlorite (illite)
20	676	15.01/12.73	16.98/15	9.8	Smectite-Chlorite (illite)
21	698	14.01/13.03	14.01/13.03	10.11/7.15	Smectite-Chlorite (illite)
22	700	14.85/12.82	16.98/15	9.8	Smectite-Chlorite (illite)
23	734	14.94/12.89	16.86/14.35	9.9	Smectite-Chlorite (illite)
24	762	15.13/12.73	17.02/14.3	9.8	Smectite-Chlorite (illite)
25	766	14.95/13.83	14.95/13.83	10.11/7.26	Smectite-Chlorite (illite)
26	786	30/14.01/12.73	31/16.94/14.76	12/9.8	Smectite: ill. (MLC)
27	798	14.14/12.98	14.14/12.98	10.11/7.26	Smectite Chlorite.
28	802	15.01/12.88	16.9/15	9.8	Smectite-chlorite
29	810	14.16/13.08	14.16/13.08	9.93/7.26	Smectite
30	832	15.03/12.79	16.94/14	9.8	Smectite
31	862	30/14.4	31/15.4	12.1	Smectite/Chlorite.unst.
32	876	No clay	No clay		No clay
33	896	30/14.4	31/15.4	12.1	Smectite/Chlorite.unst.
34	902	31.07/14.59/12.64	31.07/14.59/12.64	7.26	MLC
35	930	30/14.69/13	31/16.94/15.58	10	Smectite+MLC
36	980	30/15.09/13.1	31/17.06/15.5	10	Smectite+MLC
37	996	31.61/14.59/12.64	31.61/14.59/12.64	7.26	MLC
38	998	30/15.09	31/17	14	Smectite/Chlorite.unst.
39	1036	30/15/12	31/17/15	12	MLC/Smectite/Chlorite
40	1050	30.45/14.30/12.34	30.45/14.30/12.34	7.26	MLC
41	1074	30/14	31/15	13	Smectite/Chlorite.unst.
42	1104	30/14	31/14.8	14.5	Chlorite. +MLC.
43	1136	14.3	8.6	7.2	Chlorite-Amphibole
44	1144	30/14	31/14.8	14.5	Chlorite-Amphibole.
45	1194	No clay	No clay	No clay	No clay
46	1230-1234	14.3	14.3	14.3	Chlorite. unst.
47	1236-1244	14.3	14.3	14.3	Chlorite. unst.

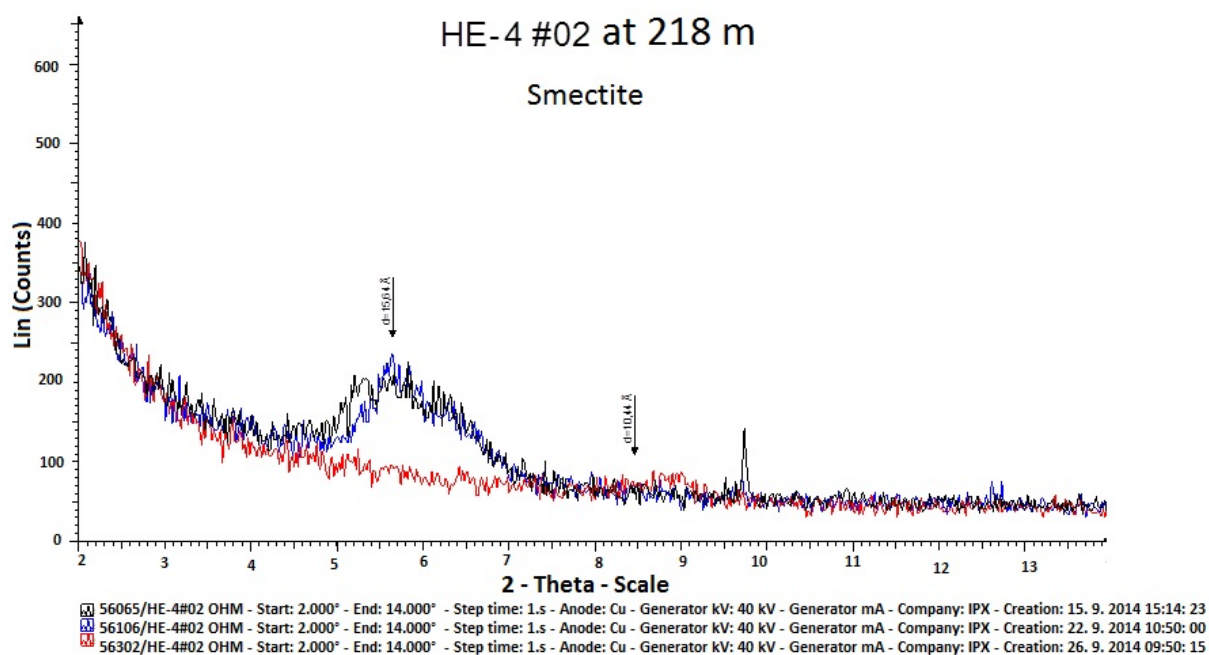


FIGURE 1: Well HE-4, XRD analysis showing the smectite clay minerals at 218 m

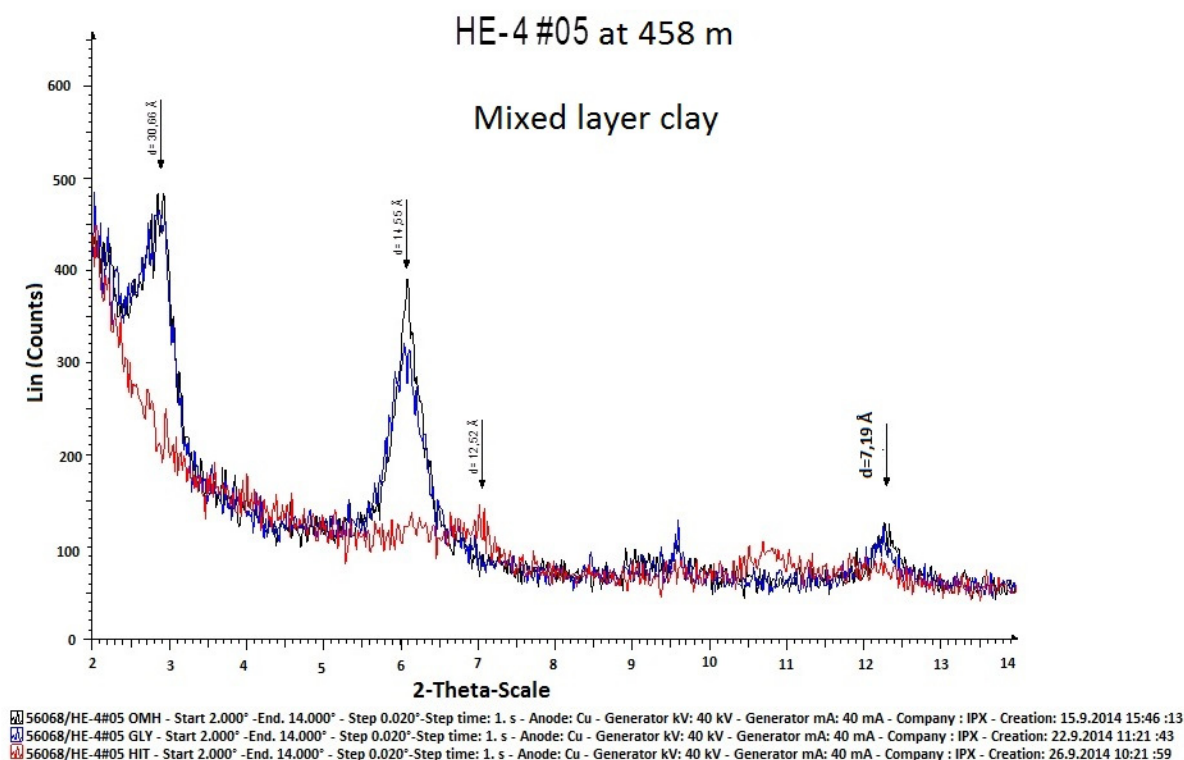


FIGURE 2: Well HE-4, XRD analysis showing the mixed layer clay at 458 m

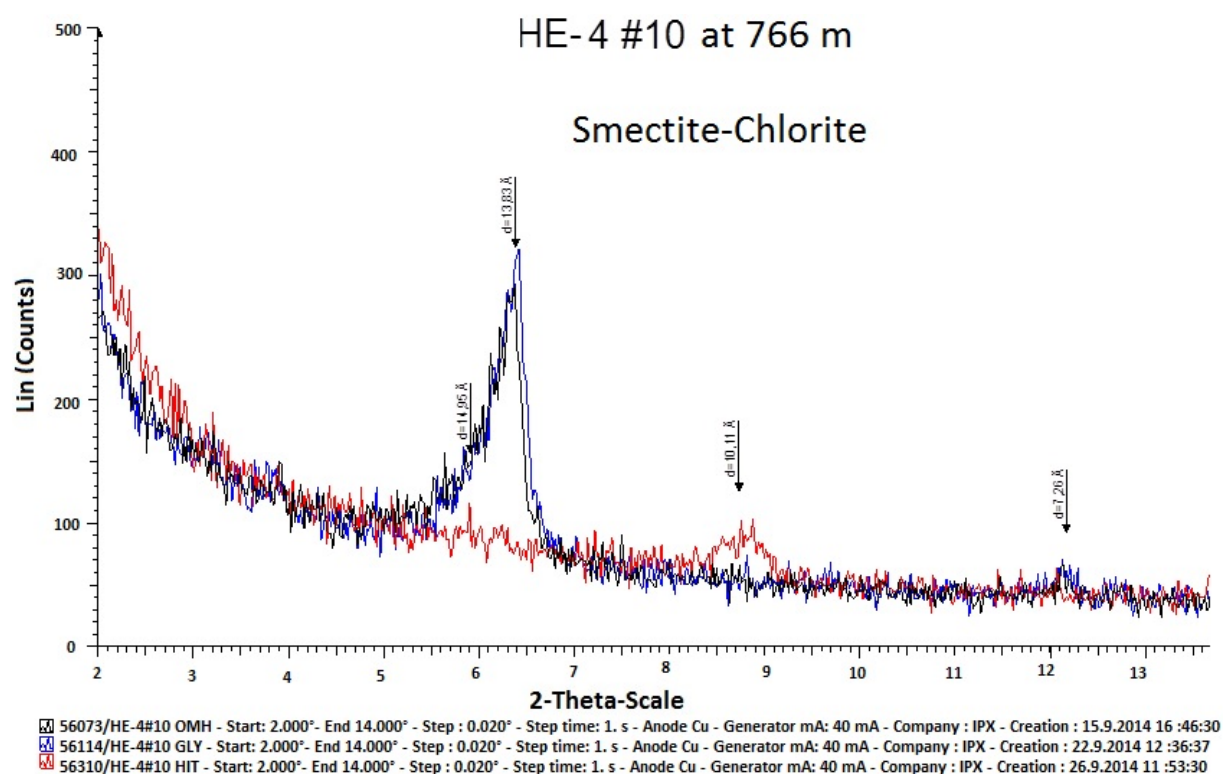


FIGURE 3: Well HE-4, XRD analysis showing the smectite-chlorite clay minerals at 766 m

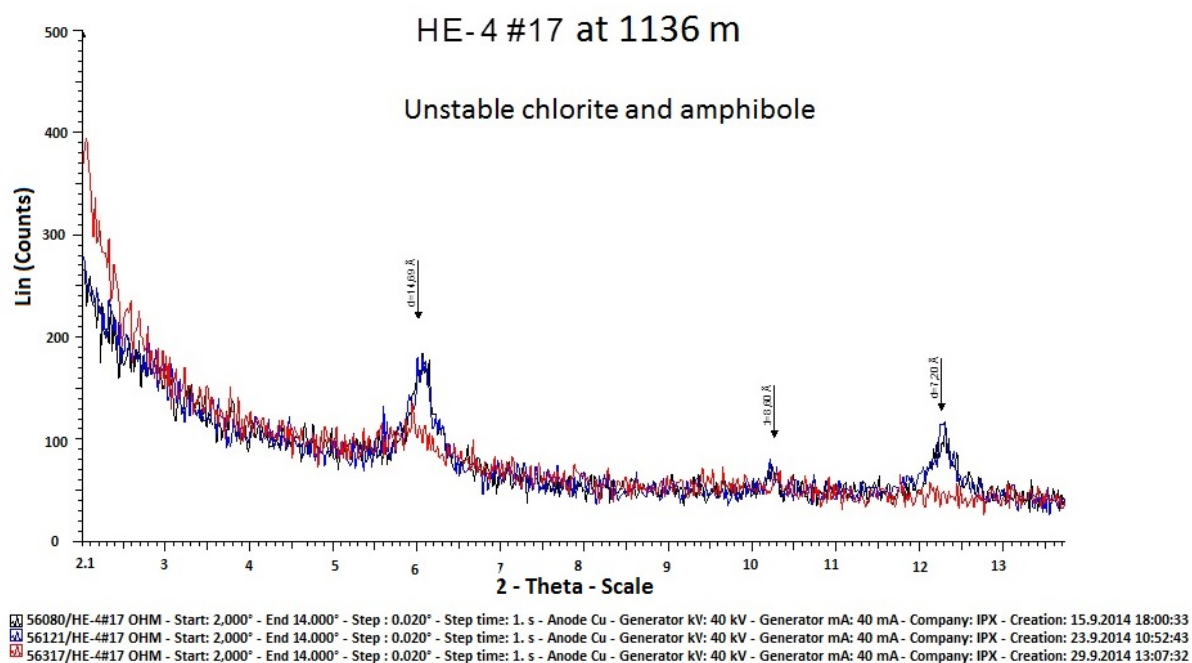


FIGURE 4: Well HE-4, XRD analysis showing the unstable chlorite and amphibole minerals at 458 m



UNITED NATIONS
UNIVERSITY

UNU-GTP

Geothermal Training Programme

Orkustofnun, Grensasvegur 9,
IS-108 Reykjavik, Iceland

Reports 2014
Number 21

PREDICTING OUTPUT CURVES FOR DEEP WELLS IN THE ASAL RIFT, DJIBOUTI

Miyir Mohamed Abdillahi

Ministry of Energy in Charge of Natural Resources

Immeuble Marabout;

P.O. Box 10010, Djibouti

REPUBLIC OF DJIBOUTI

miyirmed@gmail.com

ABSTRACT

Decade's long combined effort of various surface exploration campaigns and deep drilling has confirmed the existence of a high-temperature geothermal anomaly within the Asal Rift in Djibouti. Several km² of at least 1 km thick 240-350°C saline resource hosted in a basaltic extensional rift environment is seen. The high scaling potential of the very salty geothermal fluid encountered at depth is however a potential show stopper for long term operations. This is seen as rapid wellbore scaling deposition on the order of 3 cm/year. By doing a numerical wellbore model, calibrated with field data gathered earlier in well A-3 in the Asal Rift, a large 13^{3/8}" casing well design appears amongst the straightest forward scaling mitigation options. Coupled with a decision to operate future Asal Rift wells at wellhead pressures of 20 bars or more. The wellbore model infers a more beneficial wellhead output curve if a reservoir volume hotter than the current 260°C of well A-3 can be intersected. One interesting option in continuing the Asal Rift steam field development is therefore to drill a large diameter, ~2000 m deep directional well from A-3 towards the ~300°C temperature measured in well A-4. Thereby intersecting the presumable near-vertical fracture-dominated permeability of the rift zone, tapping the proven permeability in wells A-3 and A-6 right under the casing shoe and, ideally, finding more permeability at deeper and hotter levels in the bedrock near well A-4. As the reservoir near A-3 was suffering long term pressure drawdown due to the presumably tight outer reservoir boundaries, reinjection should be part of the steam field management strategy. Ideally, one or two successful wells drilled from A-3 towards A-4 can be used for early 5-10 MW production and then some of the older existing wells near A-3 for injection.

1. INTRODUCTION

Thanks to an exceptional geodynamic location, characterized by an emerged triple junction of the Red Sea, Gulf of Aden and East African Rifts, Djibouti hosts an undeveloped geothermal potential which has been explored since 1970. Unfortunately, the exploration has been interrupted many times by political, economic and technical reasons. Therefore, fossil fuel is currently used for power generation. A clean geothermal energy would constitute a key sector for economic and social development, assisting the country in alleviating poverty. Since 2011, a new campaign of exploration under international

financing and expertise has taken place. The new project aims to drill 4 wells in the Asal Region for an expected electrical production of 50 MW in the first phase. The technical issue of rapid downhole scaling depositions during discharge is, however, a main challenge of the project.

The objective of the current study is to predict wellhead output curves of new wells adapted to a high-salinity geothermal field like those found in Asal, Djibouti, and Reykjanes, Iceland. Eighteen scenarios of various well diameter, feedzone enthalpy and pressure are studied for well output from new and scale-free wells. The time impact of cumulative downhole scaling build-up on their output will also be studied. A wellbore simulator called Hola, calibrated with existing data collected during the long term production test of well Asal 3 was used to generate the possible output curves of a new enhanced well. Finally, a new well location will be proposed by incorporating all three characteristics, i.e. well diameter, the reservoir pressure and enthalpy.

2. GEOLOGICAL SETTING OF DJIBOUTI

The East African rift system (EARS) is a succession of rift valleys that extend over approximately 4000 km from the Afar Triangle in the north to Beira in Mozambique in the south. The EARS is a continental branch of the worldwide mid-ocean rift system. It includes the three major extensional structures: the Afar Depression, the Red Sea, and the Gulf of Aden, generally called the triple junction.

Djibouti is located in the eastern part of Africa at the junction of the plates (Figure 1). In Djibouti, areas of strong geothermal manifestations are located within the Asal and Hanle rifts in the Afar Depression. The surface manifestations appear to be fracture controlled and occur within the recent volcanic and sedimentary rocks or at the contact of recent and old formations (Jalludin, 2003).

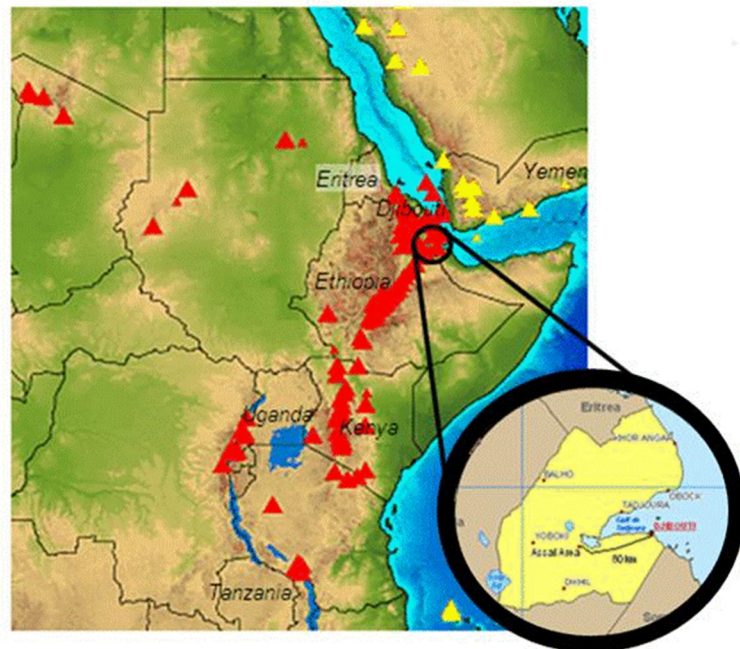


FIGURE 1 : East African Rift, with enlarged view of Djibouti (Smithsonian Institution, 2013); red triangles are active volcanoes

Figure 2 shows the geological settings of Djibouti in more detail (Elmi, 2005). Djibouti is characterized by largely Miocene to Holocene volcanic rocks and more recent alluvial deposits. Stratoid Series (1.5-3.5 My) cover the major part of the country, mainly in the central and western parts along a S-N axis. The northern part of Djibouti is characterized by volcanic formations of late Miocene age, with extensive and deeply faulted Mabila rhyolites (12-8 My) partly covered by Basalt of Dalha (7-4 My) gently dipping to the northwest. This geologic block is rather stable and appears to be a part of the Arabic Plate since oceanic spreading stopped along the Bab-El-Mandeb straight of the Red Sea and developed inside Afar for the last 3 to 4 My (Marinelli and Varet, 1973). Insignificant high-enthalpy geothermal potential is, therefore, expected there. On the western flank of this block, however, the Dalha Plateau sinks under the more recent basalts of the Stratoid series, itself deeply faulted. Near the triple state boundary with Ethiopia and Eritrea, an active axial range called Manda-Inakir was identified (Haga et al., 2012). Since then, the huge N-S fault zone linking Manda-Inakir and Asal Rift segments was interpreted as the surface

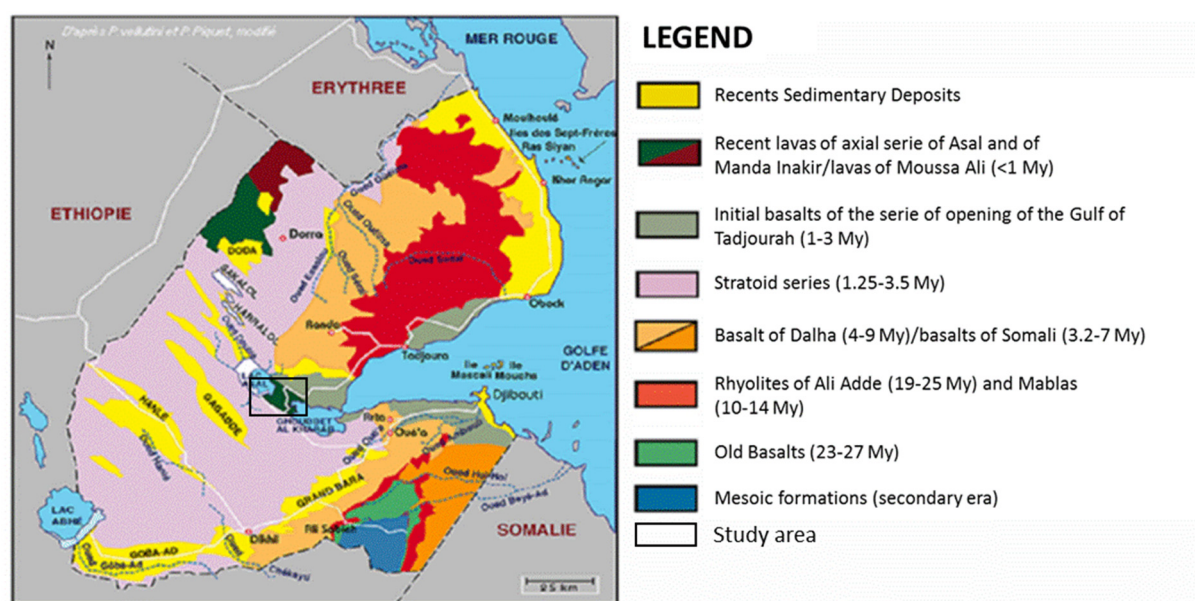


FIGURE 2 : Geological map of Djibouti (Elmi, 2005)

expression of a transform fault (Tapponier and Varet, 1974). Hence, an active plate boundary crosses through the westernmost part of this region, with a related geothermal heat source. The north is characterized by the recent basalt of Dalha (4-9 My), and rhyolite (19-25 My).

According to the Geothermal Energy Association (Omenda, 2008), the geothermal energy potential in Djibouti is estimated as 230-860 MWe based on prospects of the mains regions of the country such as Lake Abbe, Hanle, Gaggade – in the region of Tadjourah, Dorra – in the region of Obock, and Arta in the region of Arta.

The Asal geothermal area is located on an active rift zone that extends from the Ghoubbet Al-Kharab through Lake Asal, into the mountain range northwest of the lake and up through the Alol plains. The rift is also active on the northern shore of Ghoubbet Al-Kharab which represents the landward prolongation of the oceanic spreading axis of the Gulf of Aden and is bounded by two systems of opposite-facing faults (Battistelli et al., 1991). Figure 3 shows the field location and topographic features of the existing well field. This area has been explored for many years, mainly by French scientists, inspired by this very impressive northwest-southeast trending fault system. As Lake Asal is the lowest place in Africa, 153 m below sea level, there is a steady flow of seawater from the sea through the 10 km wide volcanic area between Ghoubbet Al-Kharab and Lake Asal. This flow goes mainly through the northern part of the area where tectonic movement is still active. The inflow has been estimated to be on the order of 20 m³ per second. In spite of this inflow, there are many fumaroles in the area and it is clear that the temperature below that is heating the lateral cold inflow toward Lake Asal must be very high.

3. DATA SOURCES

3.1 The Asal Rift drilling campaign

The Asal rift, initially explored in the 1960s, is an intensely faulted terrain that separates Lake Asal and Ghoubbet el Kharab. It is the northwest propagation of the Gulf of Aden Rift into the Afar Triple Junction. It can be viewed as an asymmetric rift within the rift structure with the internal rift being the most recent structural development of the region. The Asal geothermal field is hosted by this rift. The

outer rift extends southwest from the Loynoytali faults. The inner rift where the most recent tectonic and volcanic activity is concentrated extends between the Loynoytali faults in the southwest to the northeast Asal rift margin. Rift development took place on terrain made up of Afar stratoid series basalts (4-1 My) and is believed to have been initiated about 3.4 million years ago. The rift margins and floor are made up of rocks of the Asal series basalts that range in age between 0.7 My and present. They are basaltic in composition and were produced by three forms of eruption: sub-aqueous eruptions which produced large volumes of hyaloclastites commonly forming volcanic ring structures; the dominant fissure eruptions which produced the lava flows which cover the rift floor; and central eruptions that form the volcanic edifices such as the Fiale volcanic complex. The latest stage of magmatism continues to the present day as illustrated by the birth of a new volcano, Ardoukoba, in 1978. On account of this geological situation, the geothermal gradient is particularly high in the Asal Rift region. That is why this region was chosen for the implementation of geothermal energy projects. Very recent volcanic rocks dominate the Asal Rift region (MERN, 2004).

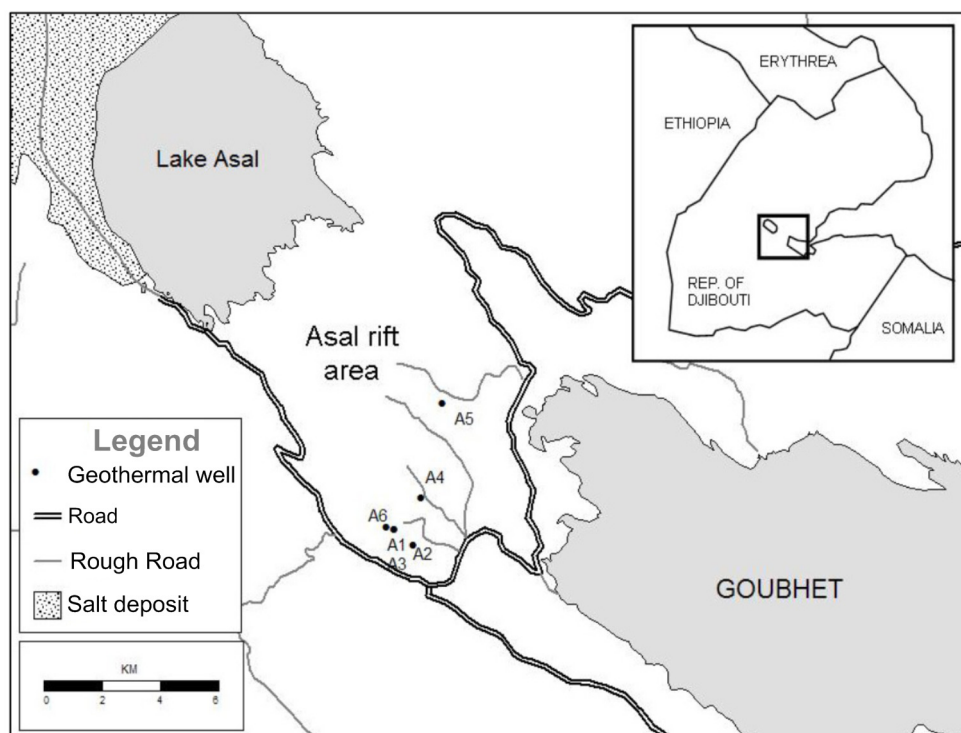


FIGURE 3 : Location of geothermal boreholes in the Asal Rift area (Elmi, 2005)

Three geothermal sectors have been suggested in the region of Tadjourah. These are named Gale le Goma, Fiale and South of the Lake Asal. The Asal area exploration began in 1975 with the drilling of two deep wells: A-1 and A-2 (BRGM, 1975; BRGM, 1980). Well A-1 had a final depth of 1154 m and well A-2 had a final depth of 1554 m. Well A-1 was able to produce 22 kg/s of high-salinity water. The measured maximum downhole temperature at 1040 m was 255°C before the flow tests, and 260°C during the flow test in 1981. Unfortunately, well A-2 is plugged inside the casing, possibly by drilling mud, and is not producing any steam. The water produced by well A-1 had a very high solids concentration of 128,000 mg/l. During its 1981 flow test, downhole scaling plugged the well in less than 3 months. New holes drilled in the area between Lake Asal and Ghoubbet Al-Kharab, about 10 km northeast of wells A-1 and A-2, were therefore suggested for continuation of the project, primarily because they might have better production characteristics than wells A-1 and A-2. Ideally, these would be similar to wells drilled in the Reykjanes field in Iceland: plain seawater inflow through an active basaltic rift zone (Jónsson, 1985).

In 1987/1988 six additional deep geothermal wells were drilled in Djibouti (Table 1). The first two wells, Hanle 1 and Hanle 2, were drilled in the plain of Hanle to 1623 and 2038 m depth, respectively. Unfortunately, they showed a maximum temperature of only 124°C at 2020 m. This site was consequently put on hold for further development. Instead, four additional wells were drilled in the Asal area (A-3, A-4, A-5 and A-6). Two of them, wells A-3 and A6, that are located close to the southwest margin of the rift, were productive (Figure 3). Their maximum temperatures recorded were 253°C and 265°C, respectively. Wells A-4 and A-5, drilled closer to the centre rift zone, were characterized by high temperatures, up to 350°C at 2100 m in well A-5. Unfortunately, these wells are not productive. Figure 4 shows the well temperatures.

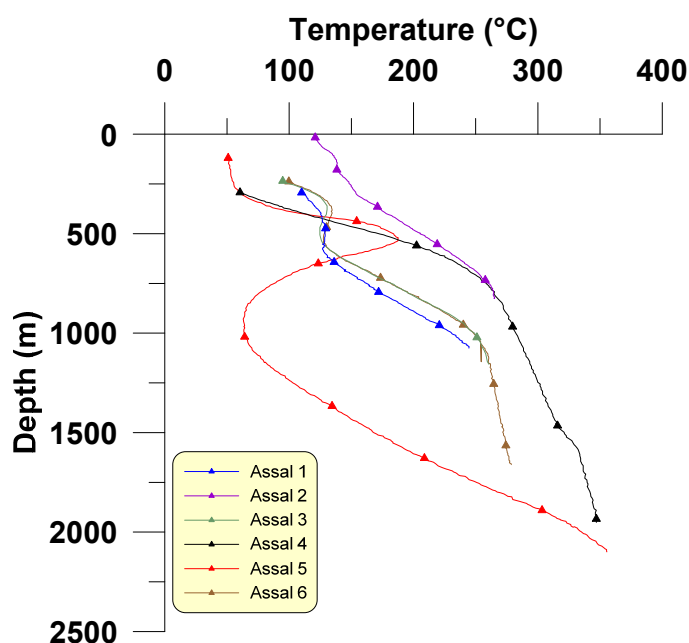


FIGURE 4 : Temperature profiles for all wells in the Asal Rift

The Asal Rift drilling operations was carried out under the technical supervision of Aquater (Aquater, 1988). On the basis of drilling wells A-4 and A-5 both hot but tight, a resistivity survey was done by Orkustofnun - the National Energy Authority of Iceland, delivered after the completion of well A-6 (Árnason and Flóvenz, 1995). This work was later revisited by Reykjavik Energy Invest and a new drilling phase was planned but was not realised due to the financial crisis that hit the world in late 2008 (Hjartarson et al., 2010).

TABLE 1: Status on drilled wells in Asal and Hanle Plain

Well	Total depth (m)	Max temperature (°C)	Status
A-1	1154	260	Productive, scale plug in well
A-2	1554	////	Plugged by drilling mud
A-3	1316	265	Productive
A-4	2011	344	Non-productive but hot
A-5	2105	359	Non-productive but hot
A-6	1761	281	Productive
Hanle 1	1623	72	Non-productive and cold
Hanle 2	2038	123	Non-productive and cold

Drilling of deep wells in the Asal Rift area revealed the existence of several aquifers at depths from 350 to 600 m, with salinity increasing with depth. Sphalerite and galena scaling were also observed in the wells, starting at the flash level at about 850 m depth (D'Amore et al., 1997).

3.2 Static temperature and pressure profiles in well A-3

Temperature and pressure data in well A-3 have been collected over the period of a long term production test. Figure 5 shows the static pressure and temperature profiles of the well, collected after thermal recovery but prior to the 3½ months of production testing. Theses profiles describe the static temperature and pressure profiles of the well below 300 m with a good approximation. Above that, the temperature

profiles were altered by boiling of the brine in the vicinity of the liquid level and by the presence of steam above that (Aquater, 1988). These data are used in a later section to calibrate a numerical model for the well.

3.3 Dynamic pressure and temperature profiles in well A-3

Dynamic downhole temperature and pressure field data, collected during a long-term production test of well A-3 at different dates, are presented below (Figures 6-8). Main results from the test were summarised as (Aquater, 1988):

- A decline on the reservoir pressure of 3.5-4 bar in the first period of increased production;
- An increase in the fluid temperature from 263 to 265°C at the wellbore and from 259 to 263°C at the flashing point;
- An increase of the MDP (Maximum Discharge Pressure) and a sizeable reduction in productivity at lower wellhead pressures (from 111 to 63 kg/s).

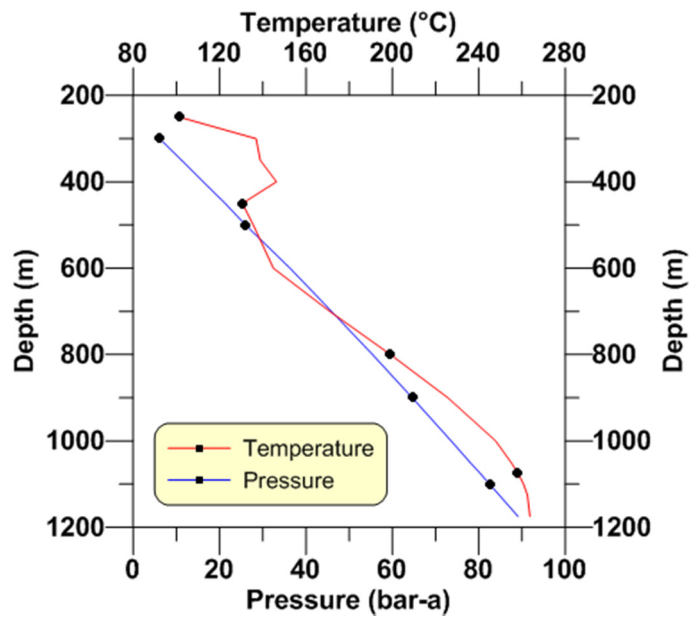


FIGURE 5: Static temperature and pressure profiles in well A-3

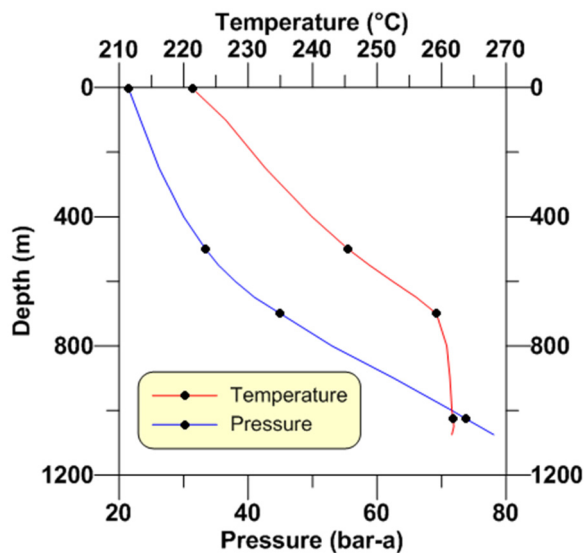


FIGURE 6: Well A-3 dynamic profiles at 26.3 kg/s (09/04/1987)

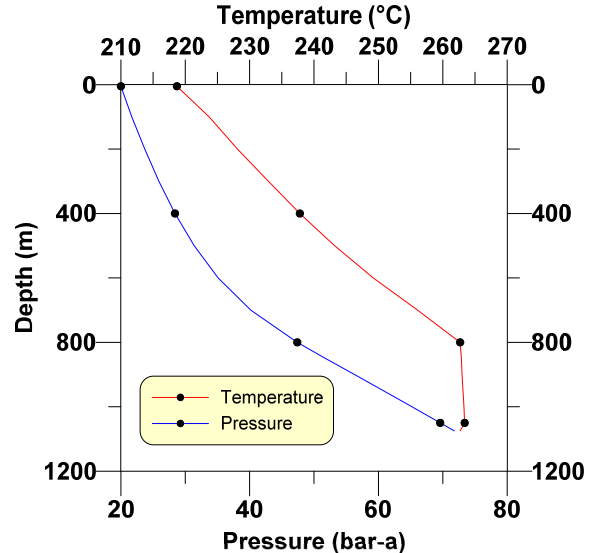


FIGURE 7: Well A-3 dynamic profiles at 49 kg/s (10/14/1987)

3.4 Caliper logs

Due to the high scaling potential of fluid coming to well A-3, a reduction of the wellbore diameter of 1.5 cm at the wellhead and 2 cm at the flashing point (Aquater, 1988) was observed by a caliper log (). The latter depth corresponds both to the deeper limit of scale deposits as detected by the caliper log, and to the approximate lower limit of flashing as seen in Figures 6-8. The caliper results are incorporated into the simulation discussed below, assuming that the scale volume has a linear function of cumulative production.

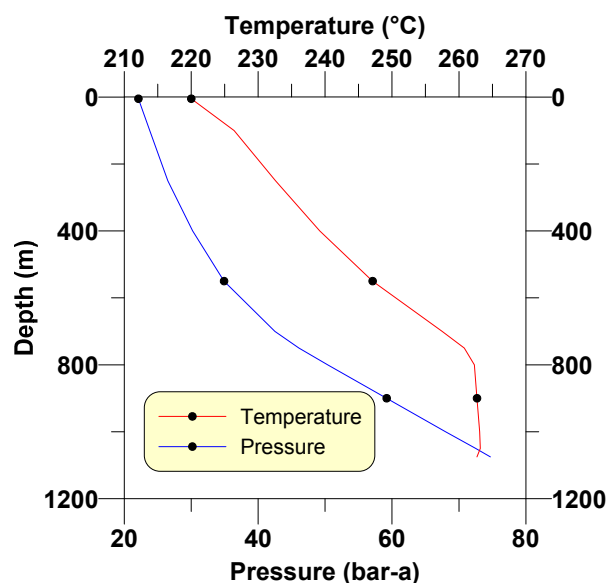


FIGURE 8: Well A-3 dynamic profiles at 42.5 kg/s (02/12/1987)

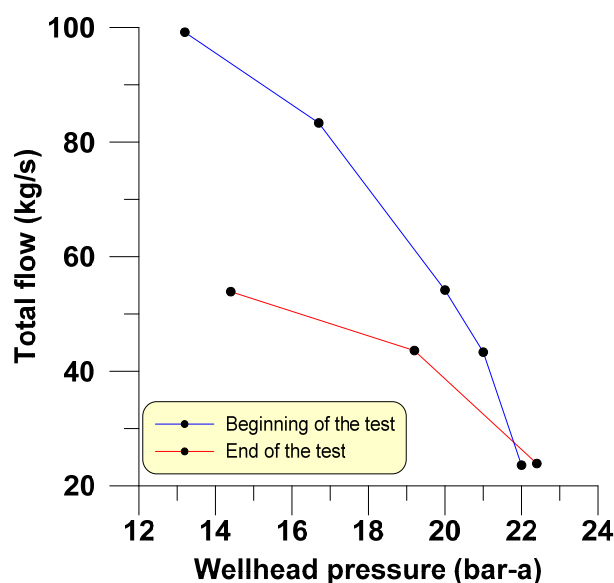


FIGURE 9: Wellhead output curves of well A-3 (Aquater, 1988)

Considering the results of the caliper log run at the end of the production period, a scale rate of about $1.0 \times 10^{-8} \text{ m}^3/\text{kg/s}$ was determined. The internal diameter at a given time was then calculated according to the cumulative production at that time, considering constant scale thickness from the surface down to 870 m (Battistelli et al., 1991).

3.5 Wellhead output curves with time

Wellhead output tests were performed at the beginning of well A-3 testing and near the end of the long term of production. Comparison of the two wellhead curves reveals that a sizeable negative change in well output occurred during that period (Figure 9).

There was a decline in the well output during the long-term production test and the Caliper log. (Figure 10) and it appears that scale build-up is to blame for the decline over about a 3 month period. For a given wellhead pressure (WHP), the corresponding observed total mass flow rate decreases drastically for the lower WHP.

3.6 Reservoir pressure drawdown

Pressure recovery tests were carried out early and later in the 3.5 month long production test. They show a fast recovery at the beginning of the

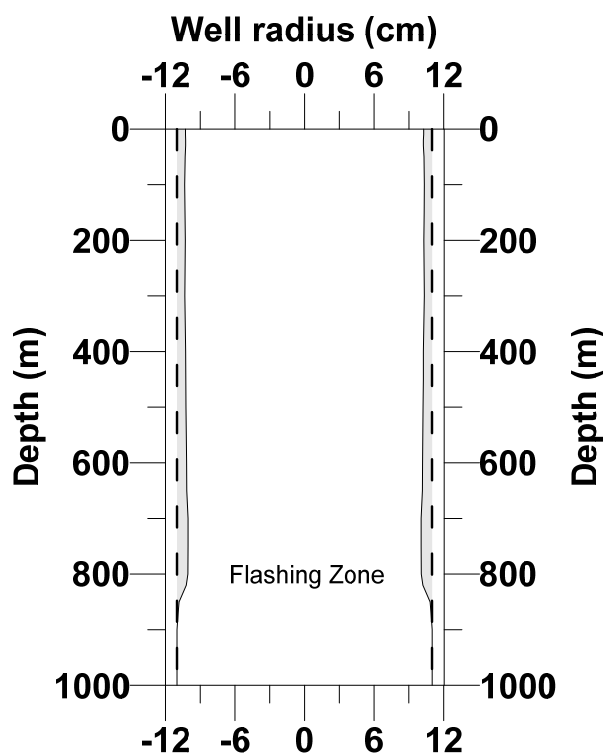


FIGURE 10: Caliper logs of well A-3

production test but slow at the end (Figure 11). This implies that a local, permanent reservoir drawdown of about 10 bars occurred between the two dates.

The reservoir pressure drawdown seen between September and December 1987 might be due to long term precipitation of salt water minerals, like anhydrite, making the reservoir's outer boundaries very tight with minimal natural recharge to the hot and permeable inner reservoir. Thus, it is likely that the Asal Rift reservoir pressure will decline rapidly at the beginning of production and only stabilise at high drawdown. Similar behaviour is seen in the Reykjanes field in Iceland (Sigurdsson, 2010). The Reykjanes behaviour, coupled with the observed reservoir pressure drawdown in well A-3, therefore suggests reinjection as a long term reservoir management strategy.

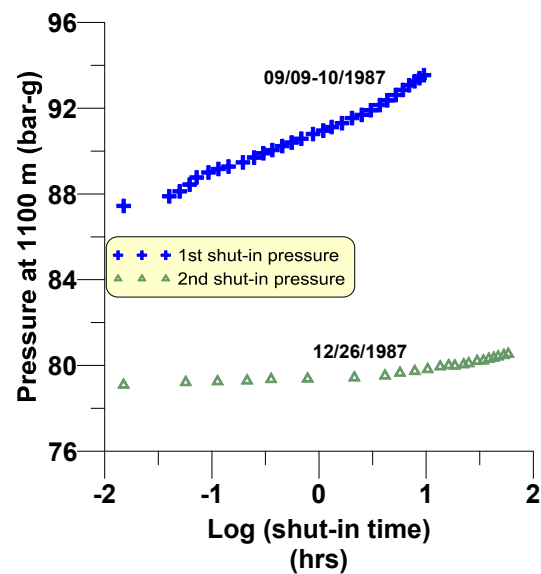


FIGURE 11: Pressure recovery curves at beginning (blue) and end (green) of 1988 flow tests (Aqater, 1988)

4. GEOCHEMISTRY AND SCALE DEPOSITION

The highly mineralised geothermal fluids encountered in a saline system like that in Asal, are subject to supersaturation. Successful operation of wells tapping such fluids is, therefore, strongly dependent on properly designing and implementing the right management strategy. One of the possibilities used for dealing with scales is to vary the depth of the flashing zone by adjusting the wellhead pressure to reduce the frequency of the mechanical scale removal of a well, and to insure that deposition is not occurring down in the open hole. Once it becomes known at what wellhead pressure the formation of scales is minimized, future wells should be developed with a perspective on the mitigation of the wellbore scale rate by having a production casing big enough to maximize the output of the well. This question is discussed in the following. Field case histories are from the Asal Rift and Reykjanes.

4.1 Generalities of silica deposition in geothermal fields

In hydrothermal areas silica deposition occurs at different depths in various forms. These include quartz, chalcedony, cristobalite, and amorphous silica. Quartz is the most stable form of silica, and has the lowest values of solubility. Deep geothermal water is usually in equilibrium with quartz at the prevailing reservoir temperature (Tassew, 2001). Deposition of quartz in wellbore and surface equipment is not a common problem, due to the slow rate of formation. Amorphous silica is, however, associated with changes in temperature of the geothermal water. This is when steam flashes out of the rising well and fluid cooling takes place. Deposition of amorphous silica from supersaturated water is, thus, an annoying scale when precipitated in surface equipment such as pipelines, separators, turbine nozzles, heat exchangers and re-injection wells. This is more troublesome in high-enthalpy geothermal fields as steam separation is taking place there and because of higher initial silica concentrations. In most fields, the steam separator is operated below the amorphous silica saturation line so as to avoid silica scaling in the pipelines and separator. Operation above the amorphous silica line will cause scaling but at very different rates, depending on the water composition, retention time and other factors (Tassew, 2001).

In high-enthalpy systems where scaling cannot be avoided, direct removal of solid deposits by reaming with a drilling rig from the zone of deposition is found effective if the deposition has not plugged the aquifers or the slotted liner portion of the well. Tests and experience also show that chemical inhibitors combined with pressure management methods can be applied to prevent the development of Galena (PbS) scales on wellbores in Asal (Virkir-Orkint, 1990).

4.2 Geochemistry of Asal wells

According to geochemical studies undertaken in the Asal Area (Correia et al., 1983), several groups of thermal springs have been identified: Manda Inakir and Korili springs, located in the eastern part of Asal; WadiKalou springs, located in the southern part of the Lake Asal; and Alifita and Eadkorar springs on the northern side of Asal.

Chemical analysis of the springs showed a relationship with sea water influx except for one, located in the southern part of Asal, in KalouWaddi. Other springs from the southern part and the northern part of the Lake showed mixing of the sea water and the lake water. The degree of mixing is more or less intense for each group of springs, according to the advancement of the reaction or to the interaction of varying proportions between water that has reacted intensely and sea water that has reacted poorly with basalt. It has been shown that the hyper-saline water of Lake Asal also contributes to the geothermal reservoir (Jalludin, 2011).

Table 2 shows the chemistry of several water samples collected from shallow aquifers in wells A-3 and A-6, and from Lake Asal. Mineralogical and isotopic studies in well A-2 have identified substantial water-rock interaction. Several estimations of the water/rock ratio have shown that zones of intense circulation exist. The upper part of the borehole is poorly altered in comparison to a rhyolite layer (at a depth interval of 300-600 m) and the lower parts of the borehole are indicative of substantial fluid circulation. Quartz, adularia, albite and epidote appear successively as a function of depth (Fouillac et al., 1989).

TABLE 2: Water composition in wells A-3 and A-6

Components	A3	A4	A5	A6	Lake Asal
pH	4,9	4,8	5,0	5,0	7,1
Na	37452	39839	13000	42000	101200
K	7273	6250	500	6000	5161
Ca	23928	20630	400	8532	2677
Mg	37	34	1500	700	12500
Cl	106000	103000	20000	52000	199155
SO4	32	12	2500	447	4320
SiO2	520	550	900		
HCO3	66	76	102	38	184
Li	31	17	33		6
F	7	4			
NH3	9,1	9,3			
Zn	3,1	5,6			
Pb	3,4	5,2			
Fe	6,7	4,4			

From the study (Virkir-Orkint, 1990) performed for comparison on collected samples from shallow aquifers in wells A-3 and A-6 and from Lake Asal, it appears that all aquifers encountered are mainly recharged by sea water.

4.3 Downhole scaling in well A-3

The production test performed on the productive wells A-3 and A-6 showed a high scale build up rate, both at the surface facilities as well as inside the wellbore, as shown by the caliper log (). The scale found in those wells mainly consisted of sulphides and silica. Sulphides start precipitating at temperatures close to those encountered at the downhole flashing zone, between 250 and 260°C, while silicas are present at a lower temperature of about 220°C. Decrease in well productivity with production

time was observed in well A-3. From the in-depth studies carried out, it was found that production decline was mainly due to frictional pressure losses within the wellbore caused by high relative roughness of a scale deposit (Aquater, 1988).

Conclusions from the drilling report on scaling problems encountered during the well test production performed in well A-3 and summarized in the final drilling report (Aquater, 1988) are:

- Calculated pH from the deep fluids indicates a rather acid condition, although compatible with the high content of Na and K.
- The measured amount of Fe was exceeded 4 to 6 times, for wells A-6 and A-3, respectively; the concentration was compatible with the equilibrium between the calculated H₂S and pyrite. This value is due to the aggressive action of brine which causes corrosion effects on the casing during its ascent.
- It was observed that, depending on the temperature at which sea water interacts with the surrounding rocks, as well as on the water-rock contact period, there is a difference in the ionic content of the fluids when compared with sea water.
- The water in Lake Asal is composed of very concentrated sea water, due to evaporation, and its CaSO₄ content is modified owing mainly to precipitation. Deep water seems to have no contact with Lake Asal waters and the Ca/Mg ratio is extremely different.
- Downhole fluids collected in well A-5 showed that the water at the centre of the rift has a much higher salinity than that on the borders.

Another study on scaling and corrosion in well A-3 was made by Virkir-Orkint (Virkir-Orkint, 1990) for the Djiboutian Electricity Company. The object of the study was the assessment of the scaling effect and corrosion on the wellbore and the determination of the optimum level of production for the well.

Table 3 shows the scale composition at the surface facilities of well A-3. A manifold was used for collecting samples at similar points of the facilities. A comparison of the analyses pointed out that the scale deposits were formed basically by the same elements. The only difference was the concentration of these elements due to the different Pb content. Laboratory chemical samples, taken at different points in the well, show a great difference between the scale compositions in the well.

TABLE 3: Chemical composition of scales from well Asal-3 (Ármannsson and Hardardóttir, 2010)

Constituent %	WH	OR	TP	SP	BP	SS	WB
P ₀ bar	20	17.7	17.7	17.7	17.7	0	0
SiO ₂	19.6	0	6.7	40.7	30.5	56.4	72.9
Al ₂ O ₃	3.7	0	1.0	4.3	3.4	8.6	2.7
Fe ₂ O ₃	22.5	0	6.7	31.8	25.8	14.8	2.7
MnO	2.3	0	0.9	5.8	3.7	0.7	0.2
MgO	1.6	0	0.1	0.7	1.1	0.2	0.2
CaO	0.6	0	0.6	1.6	1.4	8.4	12.8
Na ₂ O	4.4	0	0.3	1.4	1.7	8.1	0.8
K ₂ O	0.1	0	0	0.7	0.4	1.9	2.9
S	13.7	14.9	18.3	4.0	8.0	0.2	0.4
Cu	0.4	0	0	0.1	0	0.1	0.1
Pb	22.3	85.1	65.4	7.2	23.3	0.2	0.4
Zn	8.8	0	0	1.7	1.0	0.4	0.1

WH: Wellhead; OR: Separator line orifice pressure (90 mm); TP: Two phase pipe separator line; SP: Separator; BP: Brine pipe; SS: Single-drum silencer; WB: Weir box.

A special chemical and corrosion facility was used to determine the scaling rates with variable wellhead pressure. Results are shown in Figure 12. At lower flowing wellhead pressure (<17 bars) the scale rate is 9.2cm/year with a predominant component of iron silicates (FeSiO₃). At wellhead pressures above 18

bars, the scaling rate dropped 6-fold and the predominant precipitate component was that of Galena (Virkir-Orkint, 1990).

During the scales studies (Virkir-Orkint, 1990) in well A-3, two types of inhibitors developed by Nadar Chemical Company, based in Italy, were tested for sulphide inhibition, i.e. a sequestration agent for heavy metals (type Nadar 4093) and a sequestration and dispersing agent used against magnesium salts and silica (type Nadar 1008). Both inhibited metal sulphide formation. The former caused iron silicate formation and was deemed unsuitable; but the latter caused the formation of calcium chloride, which could be avoided by acidification, but corrosion problems still have to be resolved. Sodium formates have been used as reducing agents (Gallup, 1993) to control ferric silicate deposition, and it was found that the formate also mitigates against acid corrosion. As has been observed, the extent of iron silicate scaling in well A-3 is small above 16-18 bar-a; the recommendation is to keep the wellhead pressure above this value during discharge at flowing pressures (Ármansson and Hardardóttir, 2010).

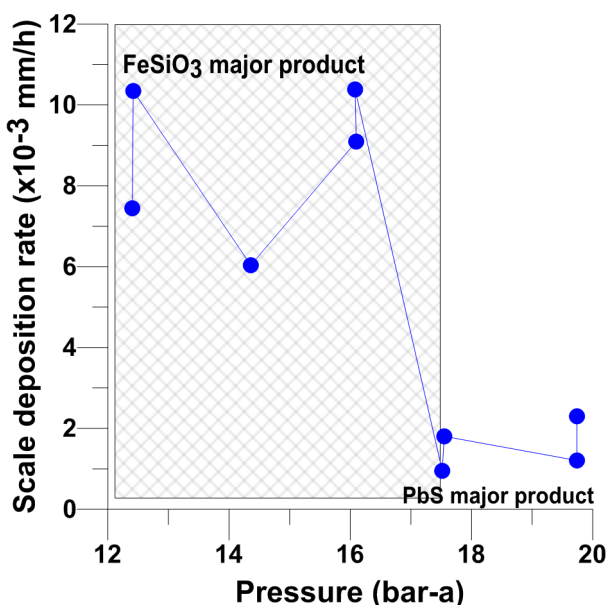


FIGURE 12: Scale deposition rates in well A-3 at different wellhead pressures (Virkir-Orkint, 1990)

4.4 Comparison between scaling rates in Reykjanes and Asal

The Icelandic geothermal field of Reykjanes is known to have similar behaviour as in Asal in terms of host rock and fluid. In order to better understand the scaling problems in Asal, comparison on scaling rates was made between these two fields. The scale deposit rates in the two fields were compared for wells RN-9, RN-10 and RN-11 in Reykjanes, and well A-3 in Djibouti.

Figure 13 shows the scaling rate in wells RN-9, RN-10 and RN-11 in Reykjanes. The scale deposit rate has increased as a function of decreasing sample pressure. However, although the scaling thickness measurements were not very accurate due to the rustiness of the iron coupons used for the collection of the scaling component, they will be used as a first approach in order to compare the scaling rates to what were obtained in Asal wells. From the Reykjanes wells, it can be said that at higher pressures the scale rate is around 5 mm/year, and at pressure below 15 bars, the scale rate is more or less double (Hardardóttir et al., 2005).

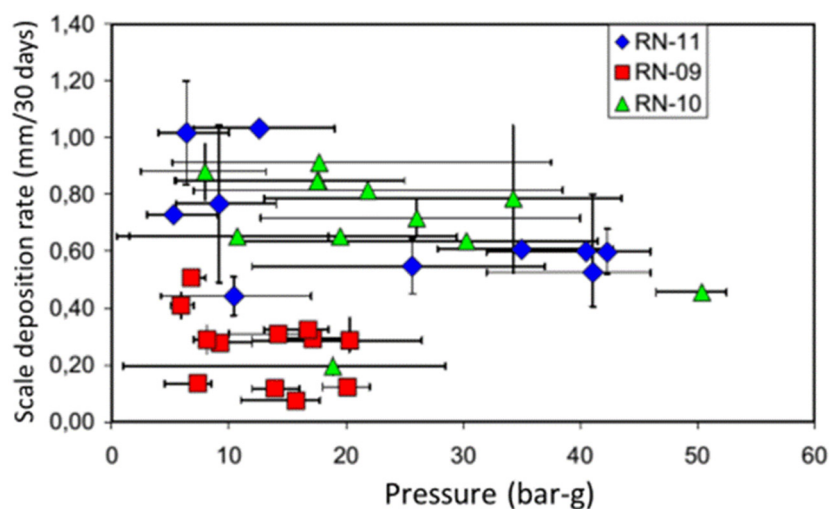


FIGURE 13: Rate of scaling in experiments in wells RN-9, RN-10, RN-11 (Hardardóttir et al., 2005)

Figure 14 summarizes the comparison on scale deposition rate between Asal and Reykjanes fields. It can be seen that for higher wellhead pressures the scale rate is at its minimum for both fields.

5. NUMERICAL WELLBORE MODELLING

The discussion above shows that the salty reservoir fluid encountered in the Asal Rift and elsewhere is far from easy to manage. Negative impact on the wellbore diameter and total flow can be particularly severe if care is not taken in operating these wells at the right wellhead pressure. The central part of the work done here is, therefore, to use the available downhole data on well A-3 to calibrate a well-reservoir model for a typical well in the Asal Rift. With such a model at hand, its three most sensitive parameters, i.e. wellbore diameter, feedzone pressure and feedzone enthalpy, can be studied for likely wellhead output curves. The goal is to identify which parameters can best help in ensuring future wellhead operating pressure being comfortable above the 18 bars threshold shown in Figure 12. Also, the study will look at the impact of having the slow but continuous ~3 cm/year cumulative scaling rate in new wells at a wellhead pressure above 18 bars and how that behaviour may impact well diameter design strategy and drilling targets. For clarity, the analysis is split into two sections. First, 18 scenarios of well output for new and scaling free wells is studied, while the latter section looks at the time impact of cumulative downhole scaling build-up, which unfortunately negatively impacts the total steam and brine coming from a well over time.

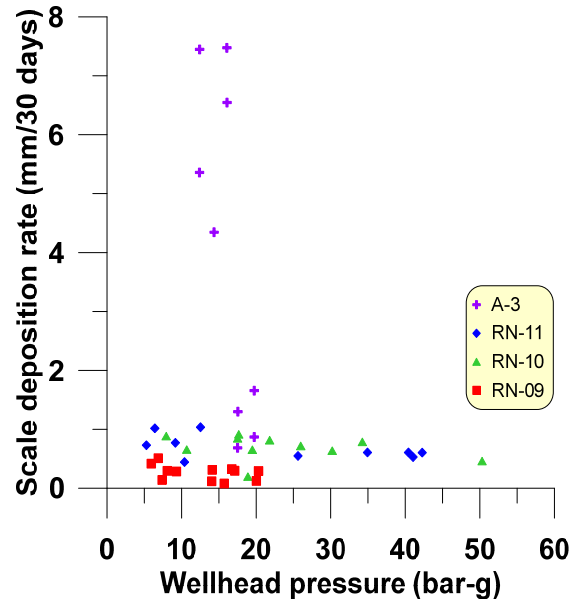


FIGURE 14: Comparison of thickness scale rate in Reykjanes wells and in Asal well A-3

5.1 The wellbore simulator Hola

The wellbore simulator Hola is used for generating output curves for well A-3 in the following steps. HOLA reproduces the measured pressure and temperature profiles in a flowing well and determines the thermodynamic properties of the water, and the relative flow rates at each feedzone for a given discharge condition at the wellhead (Björnsson and Böðvarsson, 1987). It has two approaches, summarized in Option 1 and Option 2 of the wellbore flow simulation. Option 1 needs known discharge conditions at the wellhead (pressure, flow and enthalpy), in addition to flow rates and enthalpies of all but the deepest feedzone. The simulator proceeds from wellhead to bottomhole to calculate the flowing temperature and pressure profile along the well. In Option 2, the user specifies the required flowing wellhead pressure and bottomhole pressure and for each feedzone, the productivity indices and properties of the reservoir fluid pressure and enthalpy. The simulator then proceeds from bottomhole to wellhead to calculate the expected wellhead output (wellhead enthalpy, flowrate, temperature, and phase composition) for the required wellhead pressure.

The flow of fluid in a geothermal well can be represented mathematically by two sets of equations. Between the feedzones, the flow is represented by: one-dimensional steady-state momentum, energy and mass flux balances, which are:

- Mass balance:

$$\frac{dm}{dz} = 0 \quad (1)$$

- Momentum balance: The total pressure gradient is the sum of the friction gradient, acceleration gradient and fluid elevation potential.

$$\frac{dp}{dz} - \left[\left(\frac{dp}{dz} \right)_{\text{fri}} + \left(\frac{dp}{dz} \right)_{\text{acc}} + \left(\frac{dp}{dz} \right)_{\text{pot}} \right] = 0 \quad (2)$$

- Energy balance:

$$\frac{dE_t}{dz} \pm Q = 0 \quad (3)$$

where \dot{m} is the total mass flow, P is pressure, E_t is the total energy flux in the well and z is the vertical depth coordinate. Q denotes the ambient heat loss over a unit distance. The plus and minus signs indicate downflow and upflow, respectively.

Between the well and the reservoir, the governing equation is:

$$\dot{m}_{\text{feed}} = PI \left[\frac{K_{rl}\rho_l}{\mu_l} + \frac{K_{rg}\rho_g}{\mu_g} \right] (P_r - P_w) \quad (4)$$

where \dot{m}_{feed} is the feedzone flowrate, PI is the productivity index of the feedzone, k_r is the relative permeability of the phases (subscripts l for liquid and g for steam), μ is the dynamic viscosity, ρ is density, P_r is the reservoir pressure and P_w is the pressure in the well.

The relative permeabilities are here calculated by linear relationships ($K_{rg} = S$ and $K_{rl} = 1 - S$, where S is the volumetric steam saturation of the reservoir) (Björnsson et al., 1993).

6. CALIBRATING A NUMERICAL WELLBORE MODEL FOR WELL A-3

6.1 Wellbore geometry

The present work uses flowing downhole data in well A-3 as a basis for a general complete reservoir-well model. The well was drilled in 1987 at the southwest border of the Asal Rift to 1316 m depth (Figure 3). The casing design of well A-3 consists of a 20" diameter surface casing to a depth of 192 m, 13 3/8" diameter for the anchor casing between 192-397 m, 9 5/8" diameter for the production casing from 1016 m up to the surface, and an open hole below that down to 1316 m (Figure 15). The well intersects its main feed zone at 1075 m depth, characterized by a temperature and pressure of around 258°C and 80 bars, respectively.

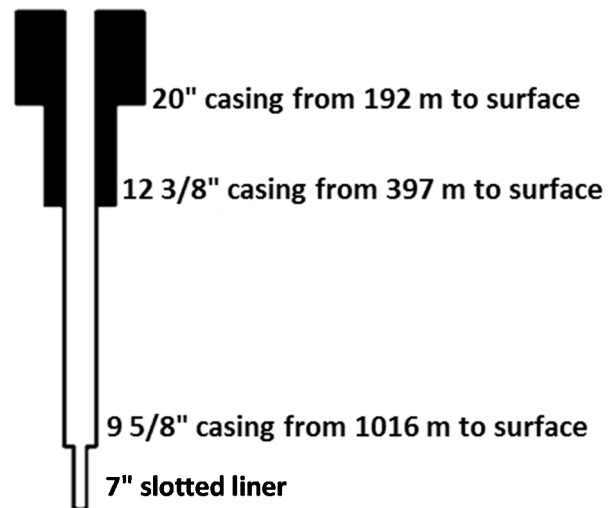


FIGURE 15: Casing design of well A-3

At the wellhead, the fluid has a high scaling nature with a weir box salinity of 180 g/l of NaCl and low gas content. The reservoir fluid is a single-phase liquid with high salinity content (115 g/l of NaCl) and a temperature range between 259 and 265°C (Aqater, 1988).

Analysis of pressure and flow variations, which occurred during the long term production test, indicate that the observed production decline is mostly due to the high rate of scaling in wellbore. The following

chapters of this report will focus on analysing the scaling in the wellbore, using the wellbore simulator "Hola", calibrated against existing field data for well A-3.

6.2 Estimating the well productivity index

The second mode of Hola is used to calibrate a numerical model for well A-3, in particular the productivity index (PI) described above. The default productivity index proposed by the software is first used as an initial guess for the reservoir and adjusted after iteration in order to fit the simulated output flow with the observed one. This was done for all the downhole data shown in Figures 6-8. This is summarized in Table 4.

TABLE 4: Estimated productivity indices for well A-3

Day	Date	Productivity index (m ³)	Flow (kg/s)	Wellhead pressure (bar-a)
1	09/04/1987	1.155×10^{-11}	26.3	21.5
2	10/14/1987	0.750×10^{-11}	49	20
3	12/02/1987	0.810×10^{-11}	42.5	19.4

The numerical models are calibrated against field data collected on three different dates (see Table 4). The first output date from Day 1 corresponds to the beginning of the production test, while Day 3 corresponds to the end.

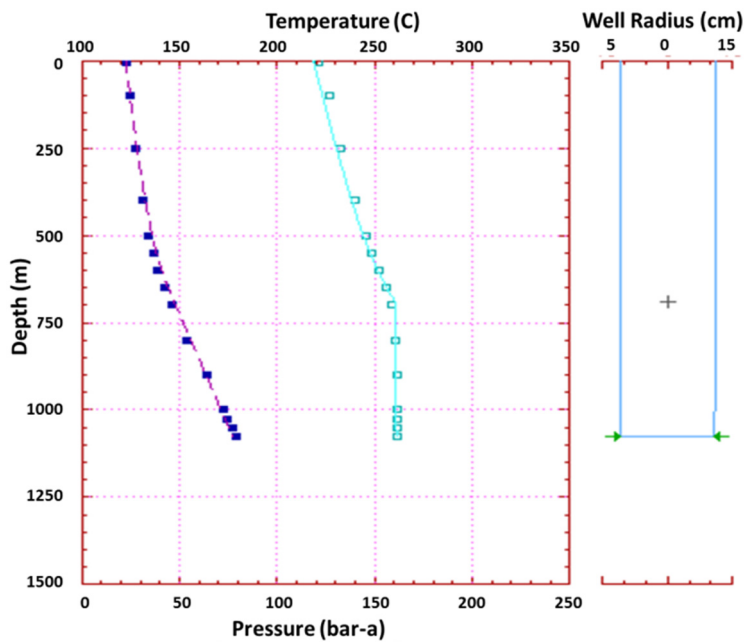


FIGURE 16: Model calibration from Day 1

the surface down to the bottom of the well. From Day 3, the observed bottomhole pressure and temperature used for the calibration were 78.1 bars and 261.2°C. The match was obtained by using a roughness value of 5×10^{-4} m from the surface down to the bottom.

The pressure and temperature profile matches were obtained for a reservoir productivity index of 1.55×10^{-11} m³ and 8.1×10^{-12} m³ for Day 1 and Day 3, respectively. The modelled productivity index of the reservoir decreased (Table 4) in the 3.5 month period between these two dates. The productivity index of the reservoir is, however, constant with the flow rate in most of the wells in the liquid phase.

Figures 16 and 17 show the match between the simulated temperature and pressure profiles from Hola wellbore simulator, with the measured ones recorded on the left based on output from the first day (Day 1) and the right side near the last day (Day 3) of the production test period. Field data from Day 1 demonstrate good matches for both the pressure and temperature profiles. These data have been used for estimating the productivity index (Table 4) which is the only model parameter required by the numerical modelling for the next steps of our studies. Measured data from Day 1 were 78.1 bars and 261.2°C for the pressure and temperature at 1075 m depth, respectively. The match was obtained by using a default steel pipe roughness value of 5×10^{-4} m from

The calibrated data from Day 1 to 3, as well as all the collected dynamic field data for well A-3, show a drop in pressure at the wellhead and at the feedzone of around 5 bars.

Figure 18 shows the calculated wellhead output curves of the well on the three dates. As stated in the previous section, the well has to be maintained at a high wellhead pressure of above 20 bar-a in order to minimize scaling inside the wellbore. The grey hashed part of Figure 18 is not considered for well A-3 because of the high scaling corresponding to the wellhead pressure values.

For a reference constant WHP of 20 bar-a, a decrease in the mass flow of 17 kg/s was observed from Figure 18 between the beginning and the end of the 3.5 month production test. The decrease can probably be interpreted as an indication of reduction in well diameter which occurred during that period due to scale deposition. Diameter reduction from the flashing point to the top of the well shown by the caliper log (Figure 9) could explain the decline in well output due to a reduction in well radius due to scale deposition.

7. PREDICTING CLEAN WELL OUTPUT CURVES

The use of wellbore simulator HOLA to assess the possible benefits of drilling larger, hotter and for higher pressure is discussed below. Well A-3 is already drilled with a 9 $\frac{5}{8}$ " production casing and 7" liner. The proposed large well design involves a 13 $\frac{3}{8}$ " production casing and a 9 $\frac{5}{8}$ " for the liner. The proposed study aims to characterize the effects of pressure and enthalpy variation in wellbore on the output curves of the well. Output prediction and analysis are performed with the simulator for two different production casings: a standard casing of 9 $\frac{5}{8}$ " and a large production casing of 13 $\frac{3}{8}$ ".

The study simulated a range of typical feed responses, summarized by Table 5, for both the standard well and the proposed new larger well design, in order to predict and compare the relative production that might occur in the wells in the future. The standard and large well designs have both been modelled as having a production casing shoe at 1075 m.

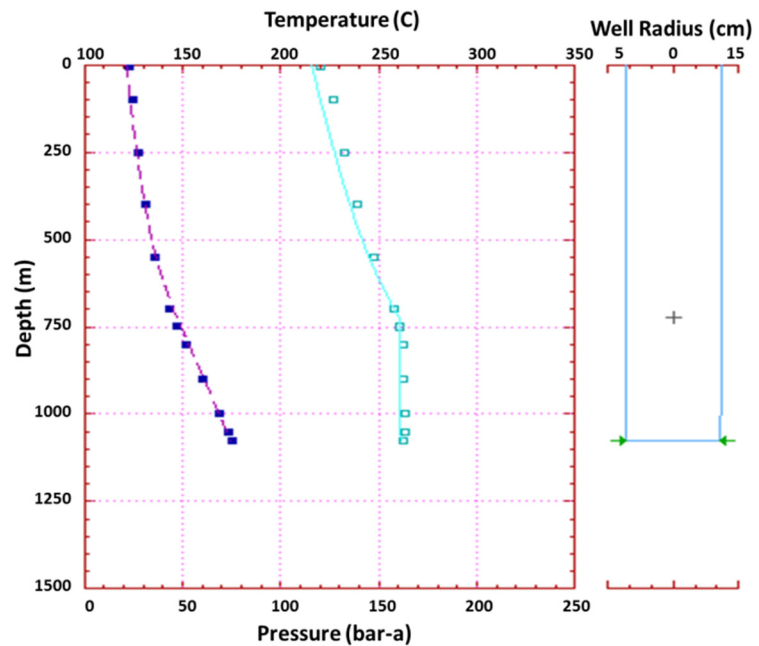


FIGURE 17: Model calibration from Day 3

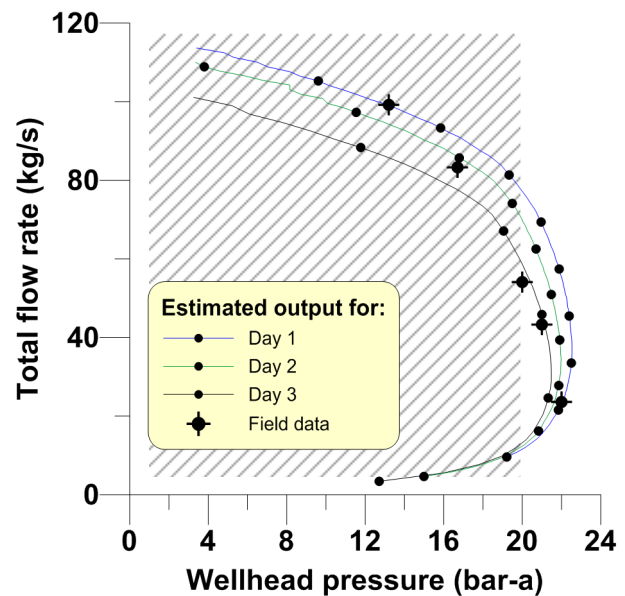


FIGURE 18: Predicted clean well output curves and measured output data for well A-3

TABLE 5: Scenarios used for predicting well output

	Pressure (bar-a)	Temperature (°C)	Enthalpy (kJ/kg)	Casing 1	Casing 2
				9 5/8"	13 3/8"
				Scenario	
Pressure 1	80.3	260	1126	A1	A2
		280	1227.4	A3	A4
		300	1335	A5	A6
Pressure 2	70.3	260	1126	B1	B2
		280	1227.4	B3	B4
		300	1335	B5	B6
Pressure 3	60.3	260	1126	C1	C2
		280	1227.4	C3	C4
		300	1335	C5	C6

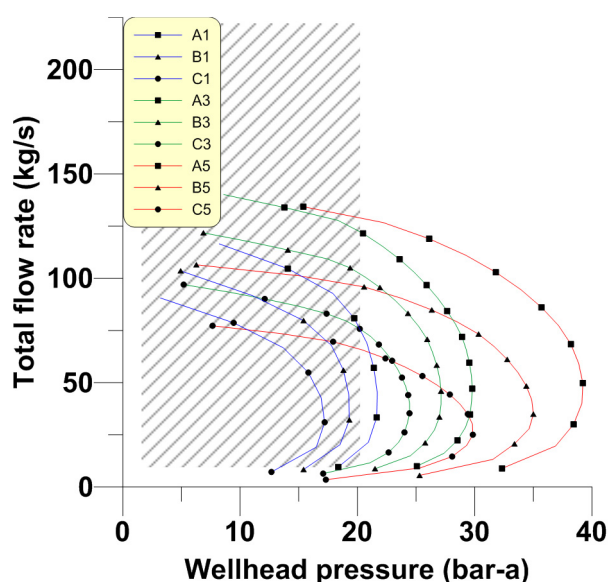


FIGURE 19: Clean well output curves for standard casing design

For each value of the feedzone pressure, three scenarios of enthalpy were simulated for the two casings which describe a combined effect on reservoir characteristics (fall in reservoir pressure and enthalpy variation in the reservoir).

Figure 19 shows the results of the standard casing to the simulation. The numerical model of the standard well was calibrated under a typical feed well enthalpy of 1126 kJ/kg (260°C) for a measured reservoir pressure of 80.3 bar-a, which corresponds to scenario A1 in Table 5. Predicted output curves in the required range of wellhead pressure (20 bar-a, or above) from the simulator indicates that a maximum flowrate of around 110 kg/s can be obtained according to those characteristics. The maximum output for this normal casing, assuming a required wellhead pressure of 20 bar-a, is obtained for a total flow rate of about 135 kg/s for a feedzone temperature at 300°C.

Figure 20 shows the results of the large well to the simulation. A representative large design well was modelled with the actual characteristics of the well, assuming a typical feedzone enthalpy of 1126 kJ/kg and a reservoir pressure of 80.3 bar-a, corresponding to scenario A2. Predicted output curves in the required range of wellhead pressure (20 bar-a, or above) from the simulator indicate that a maximum flowrate of around 220 kg/s can be obtained according to those characteristics. The maximum output scenarios for this casing, assuming a required wellhead pressure of 20 bar-a, is obtained in scenario A6.

Comparison made on well output between the standard and large casings is plotted in Figure 21. The results demonstrate a real increase in well output in the range of aimed wellhead pressure if the large diameter well is selected. At a particular given wellhead pressure, the results from the simulation infer that the well outputs are doubled by the large diameter well. The results also show the effect of the casing on the wellhead pressure, allowing a discharge at very high wellhead pressures, up to 39 bar-a. This indicates that using a 13 3/8" production casing will considerably improve the production of the well.

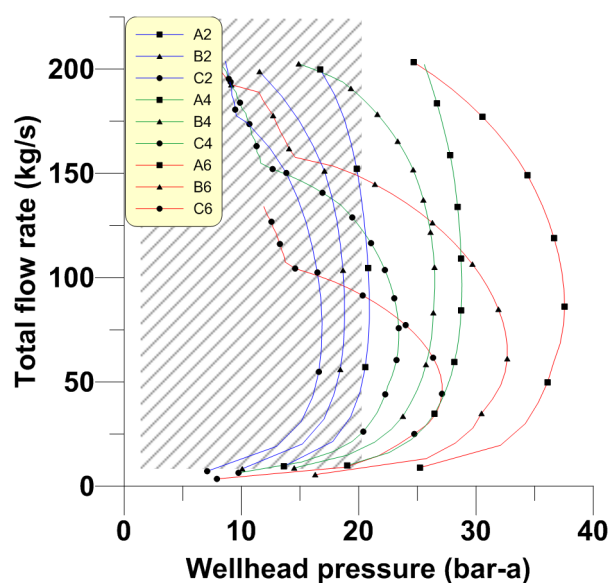


FIGURE 20: Clean well output curves for large casing design

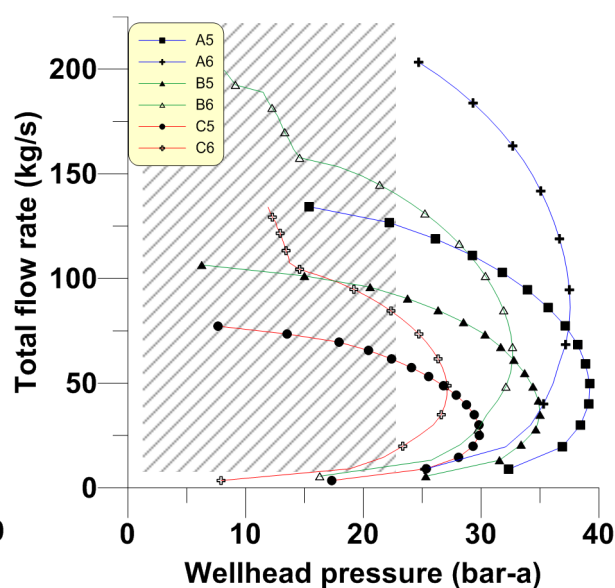


FIGURE 21: Comparison of wellhead output curves

8. MITIGATING IMPACTS OF LONG-TERM SCALING DEPOSITION

It is of interest to couple the gradual scale build-up in Asal wells at wellhead pressure above 20 bars to computed output curves. Table 6 shows how standard well diameter may change with time. Figure 22 shows and then describes computed wellhead output curves of the standard casing of well A-3. An observed reduction in wellbore diameter from 870 m up to the surface of the well of 3 cm/year (Aquater, 1988) is assumed. All the other characteristics of the well are considered as constant in order to emphasize the induced effect of scaling deposition on well output. Table 6 shows calculated well diameter, assuming the effect of scaling deposition on the wellbore for the actual casing of the proposed well.

TABLE 6: Wellbore diameter reduction due to scaling in the standard well

Time (year)	Casing 9 5/8"	
	Scale diam. (m)	Well diam. (m)
0	0	0.22
1	0.0325	0.1875
	0.0650	0.155
3	0.0975	0.1225
4	0.130	0.09
5	0.163	0.057

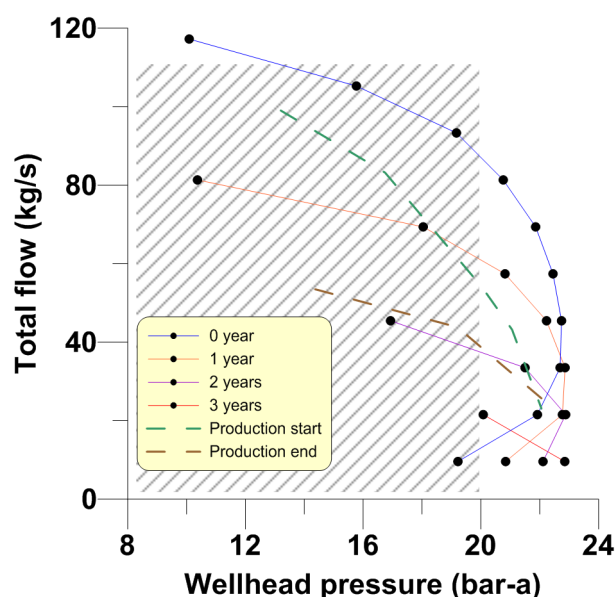


FIGURE 22: Measured and predicted output curves for standard casing in well A-3 and a 260°C feedzone

As previously stated, the scale deposition in the wellbore is pressure dependent. One way to deal with the scaling in the wellbore is to keep the well at a wellhead pressure above 20 bars. In the following studies, only the portion of the wellhead output curves above 20 bars is considered. Well output curves at high wellhead pressure for the standard casing (Figure 22) show that the well

output seems to be strongly impacted by scaling deposition in the wellbore. The plotted field data (red and green dashed lines in Figure 22), along with the simulated data, show that the well which has flowed before the production test seemed to have a scale deposit in the wellbore even before the production test.

Assuming a scale deposition in the wellbore, the well output curves of the new large diameter casing designed for well A-3 are described in Figure 23. An observed reduction on wellbore diameter from 870 mm up to the surface, equivalent to 3 cm/year (Aqater, 1988), is assumed. All the other characteristics of the well are assumed constant in order to emphasize the induced effect of scaling deposition on well output. Table 7 shows estimated well diameter while assuming the effect of scaling deposition in the wellbore for the proposed well.

TABLE 7: Wellbore diameter reduction due to scaling in the large well

Time (year)	Casing 13 $\frac{3}{8}$ "	
	Scale diam. (m)	Well diam. (m)
0	0	0.32
1	0.0325	0.2875
2	0.0650	0.255
3	0.0975	0.2225
4	0.130	0.190
5	0.163	0.157

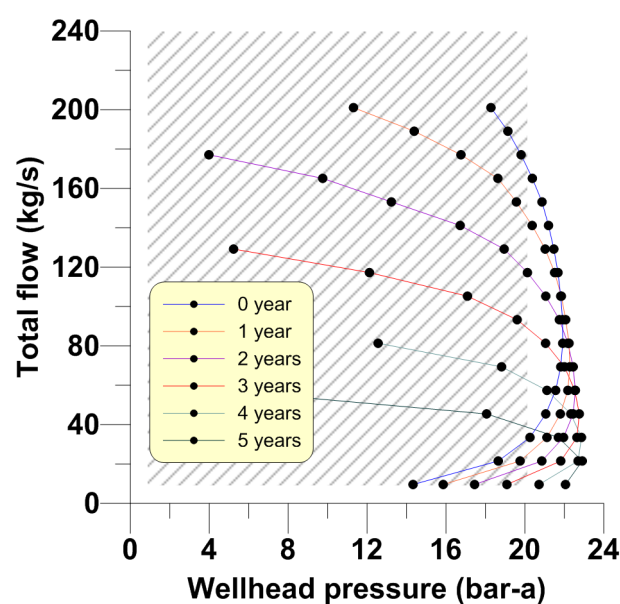


FIGURE 23: Scaling impact on a large casing well over time

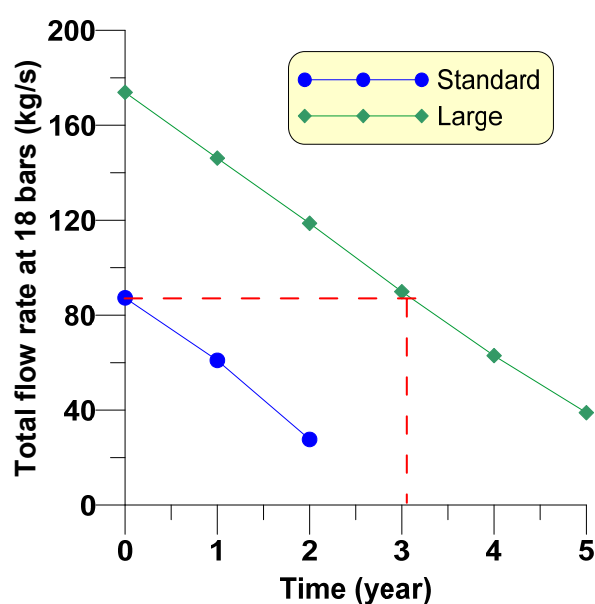


FIGURE 24: Effect of scale deposition with time on wellhead pressure at 18 bar-a

Figure 24 shows wellhead output curves at high wellhead pressure for the two casing designs. The figure shows that the well output is strongly impacted by scaling deposition in the wellbore. The plot of the well's output curves shows that the initial output flow predicted for the standard casing corresponds to the predicted output flow of the large casing well after 3 years of discharging at 18 bar-a. The initial output flow of the wells at high pressure (18 bars) is doubled by using a large casing (from 82 kg/s to 175 kg/s). One of the major benefits that can be obtained from a large design well, and emphasised clearly in Figure 24, is that after 3 years of 3 cm/year cumulative scaling, a standard well is nearly clogged while a large well is still flowing like a clean standard well. Despite the fact that the scaling cannot be completely eradicated from the well, an alternative management point of view could be developed from this casing; the frequency of mechanical cleaning operations or inhibitor operations might be reduced.

9. NEW WELL LOCATION AND DISCUSSION

The predicted wellhead output curves in Figures 19 and 20 show a very positive impact of raising the reservoir temperature being tapped by both well designs. It is, therefore, of interest to see if the existing temperature data collected in wells A-1 to A-6 can be used to propose an alternative new well location in the Asal Rift.

A proposed new large diameter well should be located between existing wells A-3 and A-4 (Figure 25). The new well will be drilled down to 2000 m via directional drilling in order to intersect both of the higher temperature areas next to well A-4 while also having the option of tapping the productive reservoir of well A-3. Such a decision is, however, a multidisciplinary operation and a sizeable pool of expertise is needed for a proper decision on the final well design and azimuth.

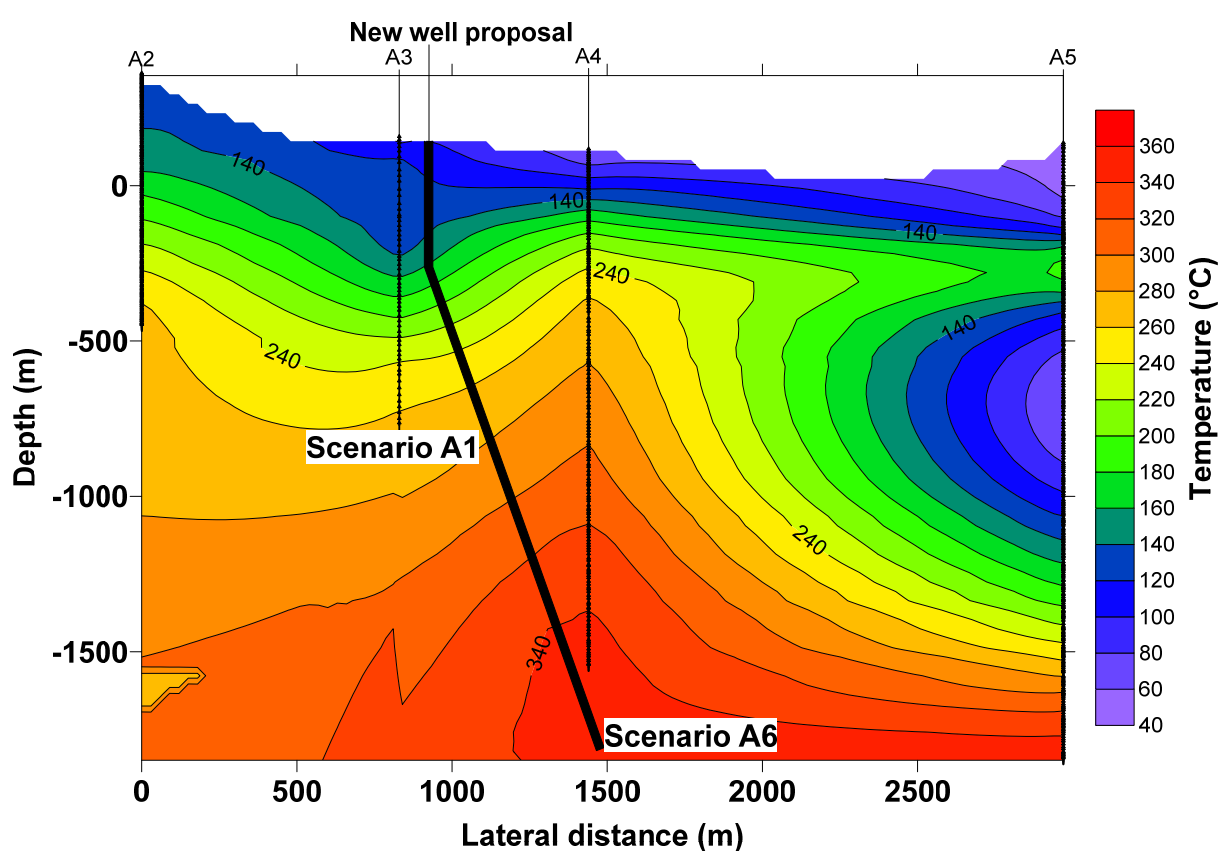


FIGURE 25: Temperature cross-section of Asal and proposed new well location

A nominal design of the new well might be:

- Total depth: 2000 m;
- Surface casing: 24";
- Anchor: 18⁵/₈";
- Production casing: 13³/₈";
- Slotted liner: 9⁵/₈".

10. CONCLUSIONS AND RECOMMENDATIONS

A long term production test conducted during the first and second Djibouti drilling campaigns in 1975 and 1987 constitute the background of this study. Numerical modelling and analysis of predicted output curves for Asal wells is based on a large quantity of available field data collected during that period.

Tests made on well A-3 show a pressure dependent scaling build-up of iron silicates (FeSiO_3), and galena (PbS) at lower and higher wellhead pressure, respectively. The results indicate a high scaling rate of 9.2 cm/year at the lower pressure which drops 6-fold at higher wellhead pressure (Virikir-Orkint, 1990). Reservoir pressure drawdown was observed from the collected data, probably due to salt precipitation, suggesting the need for reinjection.

Mode one and two of Hola Wellbore Simulator, calibrated with existing field data, was used for output predictions and show a good match for both temperature and pressure. A high productivity index, modelled for the reservoir, indicates the presence of a highly permeable feedzone in the vicinity of well Asal 3 at about 1075 m depth.

A new well was modelled to assess the possible benefits of drilling for a large diameter casing and liner, by using the simulator Hola, and then studied under 18 scenarios of various pressure and enthalpy for both standard and large casings. The study showed a reservoir dominated flow for well A-3 limited by wellbore diameter which indicates that using a large production casing in Asal would considerably improve the output at high wellhead pressure.

Modelled output flow of an Asal well at high wellhead pressure was doubled by using a large casing. After 3 years of 3 cm/year of cumulative scaling, the standard well was nearly clogged while the large well was still flowing like a new and clean standard well.

Directional drilling is proposed for a new well in Asal and it might be drilled between wells A-3 and A-4 down to 2000 m in order to intersect better enthalpy.

ACKNOWLEDGMENTS

The preparation and writing of this report faced many challenges. In particular, understanding in a short time what was done in 40 years of geothermal exploration in our main geothermal field in Djibouti. It has been possible with the unqualified help of my supervisor, Mr. Grímur Björnsson. I owe him my first and sincere appreciation for his helpful guidance and excellent advice during the preparation of this report.

I would like to address my thanks to Mr. Lúdvík S. Georgsson, the Director of the United Nation University, and to Dr. Ingvar Birgir Fridleifsson, the former Director as well as to our Director Managers, Mr. Abdourahman Haga, Mr. Bouh Moussa and Mr. Abdou Mohamed, for allowing me this opportunity to study here in Iceland and for their full support in my work.

I am very grateful to all the UNU staff, Mr. Ingimar G. Haraldsson, Ms. Thórhildur Iceberg, Ms. Frída Ómarsdóttir, Ms. María S. Gudjónsdóttir, and Mr. Markús A.G. Wilde, for providing all the necessary facilities which made my stay in Iceland comfortable and conducive to learning.

Special thanks go to Ms. Svanbjörg, Mr. Halldór Ármannsson and Ms. Vigdís Hardardóttir, who gave me important guidance through their research. Their ideas and concepts have had a remarkable influence on my work. Also, I want to thank all the ISOR staff for their assistance at all times.

Finally, I must express my gratitude to my colleagues, the UNU-GTP-2014 Fellows, for their amity. Special thanks and good luck to the reservoir engineers.

REFERENCES

Aquater, 1988: *Asal 3 final report*. Aquater, Djibouti, report (in French).

Ármannsson, H. and Hardardóttir, V., 2010: Geochemical patterns of scale deposition in saline high temperature geothermal systems. *Proceedings of the 13th International Symposium on Water-Rock Interaction, Guanajuato, Mexico*. Taylor and Francis Group, London, 133-136.

Árnason, K., and Flóvenz, Ó.G., 1995: Geothermal exploration by TEM-Soundings in the Central Asal Rift in Djibouti, East Africa. *Proceedings of the World Geothermal Congress 1995, Florence, Italy*, 933-938.

Battistelli, A., Rivera, J., and Ferragina, C., 1991: Reservoir engineering studies at the Asal field. Republic of Djibouti. *Geothermal Resources Council, Bulletin, Nov. 1991*, 280-289.

Björnsson, G., and Bödvarsson, G.S., 1987: A multi-feedzone wellbore simulator. *Geoth. Res. Council, Transactions, 11*, 503-507.

Björnsson, G., Arason, P., Bödvarsson, G.S., 1993: *The wellbore simulator HOLA. Version 3.1*. User's guide. Orkustofnun, Reykjavík, 36 pp.

BRGM, 1975: *French territory of Afars and Issas: Final report of survey*. BRGM, France, report (in French).

BRGM, 1980: *Testing of geothermal fluids. Lake Asal (Republic of Djibouti)*. BRGM, France, report (in French).

Correia, H., Demange, J., Fabriol, R., Gérard, A., Varet, J., 1983: *The Asal geothermal field, summary of data available on January 1, 1983*. BRGM, France, report BRGM/83-SGN-022-GTH (in French), 71 pp.

D'Amore, F., Guisti, D., and Abdallah, A., 1997: Geochemistry of the high-salinity geothermal field of Asal, Republic of Djibouti. *Geothermics, 27*, 197-210.

Elmi, D., 2005: Analysis of geothermal well test data from the Asal Rift area in the Republic of Djibouti, Iceland. Report 6 in: *Geothermal training in Iceland 2005*. UNU-GTP, Iceland, 39-59.

Fouillac, A.M., Fouillac, C., Cesbron, F., Pillard, F., Legendre, O., 1989: Water-rock interaction between basalt and high salinity fluids in the Asal Rift. *Chemical Geology, 76*, 271-275.

Gallup, D.L., 1993: The use of reducing agents for control of ferric silicate scale deposition. *Geothermics, 22-1*, 39-48.

Haga, A.O., Youssouf, S.K. and Varet, J., 2012: The Manda-Inakir geothermal prospect area, Djibouti. *Proceedings of the ARGeo-C4 Conference, Nairobi*, 9 pp.

Hardardóttir, V., Ármannsson, H. and Thórhallsson, S., 2005: *Characterization of sulfide-rich scales in brine at Reykjanes*. *Proceedings of the World Geothermal Congress 2005, Antalya, Turkey*, 8 pp.

Hjartarson, G., Gísladóttir, V., Gíslason, G. and Ólafsson, K., 2010: Geothermal development in the Asal Area, Djibouti. *Proceedings of the World Geothermal Congress 2010, Bali, Indonesia*, 8 pp.

Jalludin, M., 2003: An overview of the geothermal prospections in the Republic of Djibouti. Results and perspectives. *Proceedings of the 2nd Kenya Electricity Generating Company Geothermal Conference 2003, Nairobi- Kenya*.

Jalludin, M., 2011: State of knowledge of geothermal provinces in Asal. *Presented at Short Course VI on Exploration for Geothermal Resources, organized by UNU-GTP, KenGen and GDC, Naivasha*, 17 pp.

Jónsson, Í., 1985: Republic of Djibouti - country report. In: *Geothermal exploration project*. Institute Supérieur d'Etudes et des Recherches Scientifiques et Techniques, Djibouti, 175-178.

Marinelli, G., and Varet, J., 1973: *Structure and evolution of the Sud fo "Host Danakil"*. French Territories of Afar, Issas and Ethiopi, report, 1119-1122.

MERN, 2004: *Project-pipeline proposal for implementation under ARGeo*. Djibouti, report.

Omenda, P.A., 2008: Geothermal activity of the East African Rift. *Presented at Short Course III on Exploration for Geothermal Resources, organized by UNU-GTP and KenGen, Naivasha*, 12 pp.

Sigurdsson, Ó., 2010: The Reykjanes seawater geothermal system – its exploitation under regulatory constraints. *Proceedings of the World Geothermal Congress 2010, Bali, Indonesia*, 8 pp.

Smithsonian Institution, 2013: Global Volcanism Program, website: www.volcano.si.edu/gyp/

Tapponier, P. and Varet, J., 1974: *The Mak'arrasou area in Afar: Equivalence to oceanic transform faults*. Academy of Science, Paris, report (in French).

Tassew, M., 2001: Effect of solid deposition on geothermal utilization and methods of control. Report 13 in: *Geothermal training in Iceland 2005*. UNU-GTP, Iceland, 291-310.

Virkir-Orkint 1990: *Djibouti. Geothermal scaling and corrosion study*. Virkir-Orkint, Reykjavík, report, 109 pp.



UNITED NATIONS
UNIVERSITY

UNU-GTP

Geothermal Training Programme

Orkustofnun, Grensasvegur 9,
IS-108 Reykjavik, Iceland

Reports 2014
Number 22

FEASIBILITY STUDY OF USING A DOWNHOLE PUMPING SYSTEM IN MENENGAI WELL MW-17 FOR GEOTHERMAL UTILIZATION

Hilary Mwangeka Mwawasi

Geothermal Development Company - GDC

P.O. Box 17700-20100

Nakuru

KENYA

hmwawasi@gdc.co.ke, hngeka@yahoo.com

ABSTRACT

Utilization of low to moderate enthalpy fluids for electrical power generation is best carried out using a binary energy conversion system. Several technical variations of the binary cycle exist and include the Kalina cycle and the organic Rankine cycle (ORC). The generation of electrical power using pumped brine from well MW-17 is proposed in this report. The utilization scheme consists of an electrical submersible pump (ESP) of 45 kg/s production capacity and an ORC plant. Detailed calculations and optimization using Engineering Equation Solver (EES) software were carried out and show that an ESP of 700 kW tandem motor power is required. In the present study four working fluids (n-butane, isobutene, n-pentane and isopentane) were considered as possible working fluids in the thermodynamic cycle of the binary power plant created in EES and optimized to obtain optimum net power output. An optimum net power output of 832 kW (0.832 MWe) for a turbine inlet pressure of 7 bar using isopentane was indicated by the EES program runs.

1. INTRODUCTION

Menengai geothermal field development is one of several energy projects being implemented by the government of Kenya as part of its developmental blue print (Vision 2030) that aims at transforming the country into a middle income status economy. The project is being executed on behalf of the government's Ministry of Energy and Petroleum (MoE&P) by Geothermal Development Company Ltd. (GDC). The field is located approximately 180 km northwest of Nairobi and encompasses the Menengai volcano, the Ol' rongai volcanoes, Ol' banita plains and parts of the Solai graben to the northeast, an area measuring approximately 850 km² (Mibei and Lagat, 2011) bound by eastings 157000 and 185000 and northings 9966000 and the Equator (Figure 1).

Development of this geothermal resource is being carried out in phases with phase I (Menengai phase I) targeting the realization of enough steam to generate 400 MW (4 x 100) of power (Ngugi, 2012a). This involves drilling an estimated 120 geothermal wells, development of an associated infrastructure, construction of a steam and brine gathering system, environmental management, coordination of project related interface activities (construction of conventional & modular power plants and electricity transmission lines) and integrating direct use applications. GDC intends to avail realized steam (as fuel)

to independent power producers who will run the conventional and modular power generation plants (Ngugi, 2012b).

1.1 Drilling progress at Menengai

Drilling activities began in February 2011 using 2 land rigs (GDC drilling rigs 1 and 2), each with a 2000HP capacity. Three exploration wells, MW-1, MW-2 and MW-3, were drilled in the period from 12th February 2011 to 9th September 2011. Preliminary well test data of Menengai exploration wells, presented by Ofwona et al. (2011), indicated bottom hole temperatures above 300°C and a water rest level at 400 m in the wells. Discharge test results showed a total flow enthalpy of above 1200 kJ/kg for the case of well MW-1. In Suwai (2011), well measurement findings indicated a stabilized maximum total well discharge flow of around 45 kg/s from well MW-1. As of May 2014, production drilling was in progress with a total of 23 wells drilled. The number of land rigs deployed at the project was four (GDC drilling rigs 3 and 4 included) with approximately 80 drilling and support staff accommodated at the Menengai project camp. Well measurements and tests have indicated that hitherto the defined resource area is majorly characterized by high enthalpy dry and two phase steam.

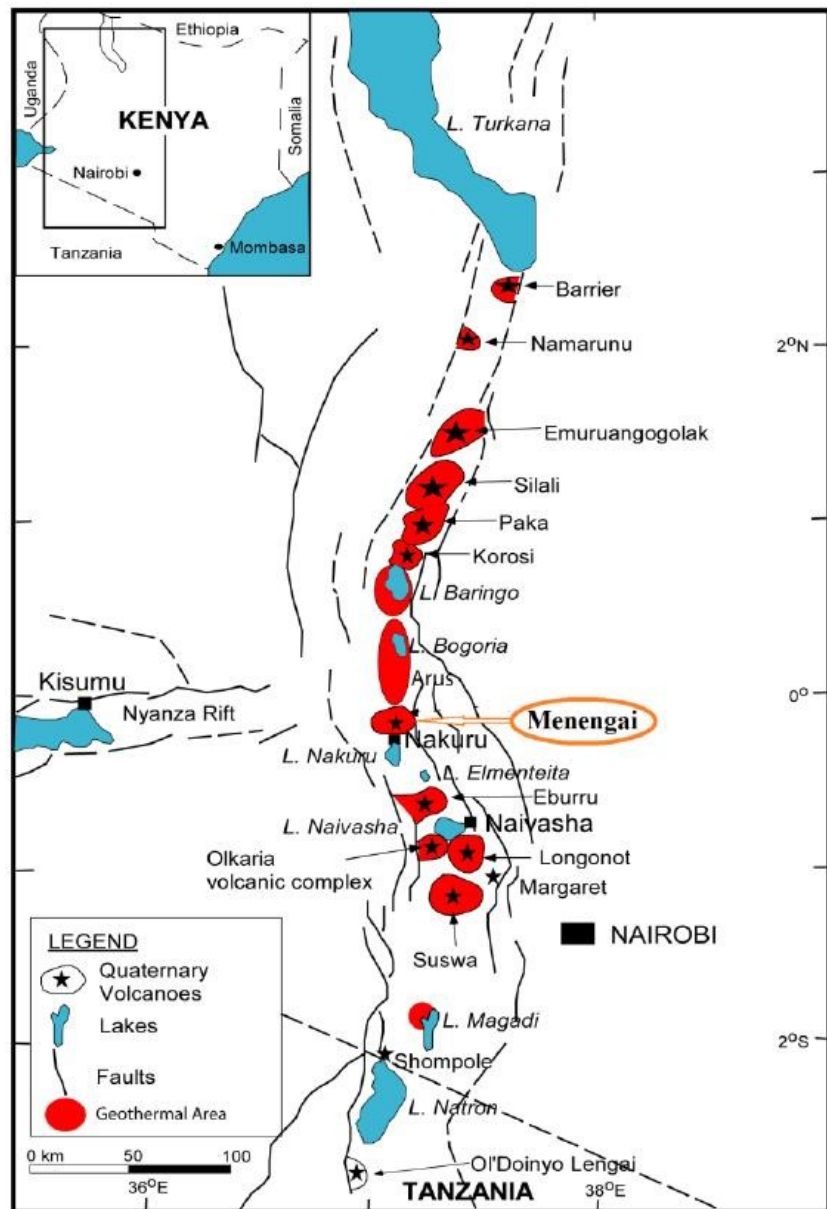


FIGURE 1: Map showing Menengai and other geothermal prospects along the Kenyan Rift Valley

1.2 Candidate well

Two wells were considered for geothermal utilization using a downhole pumping system. Wells MW-5A and MW-17 are located within the Menengai phase I project area.

1.2.1 Well MW-5A

Well MW-5A is located in the southern part of the Menengai caldera, almost immediately past the dome area, and is drilled to a depth of 2084 m. Downhole temperature and pressure profiles for well MW-

5A, attached in Appendix I, indicate the existence of permeable zones at 850, 1150, 1350, 1800 and 2000 m, respectively, and coincide with the occurrence of tuff intercalations and circulation loss zones. An isothermal section is evident in all profiles from the depth interval 1300 to 1800 m; from the hydrostatic pressure profiles, the water level is indicated to be at a depth of 400 m. The maximum bottom hole pressure is about 150 bars.

1.2.2 Well MW-17

This well was drilled in a southwest direction, also within the Menengai caldera. Downhole temperature and pressure profiles are also attached in Appendix I. From temperature profiles, permeable zones can be inferred at intervals 1000-1200 m, 1400-1600 m, 1800-1850 m and at the well bottom. In this well the isothermal section is conspicuous between 1100 and 1850 m, as seen in the heat-up period profiles. Post discharge attempt temperature profiles further indicate that the well has heated up, with the most recent profile indicating a maximum temperature of 175°C at a depth of 1000 m. Pressure profiles indicate a static water rest level that recedes between 445 and 470 m with a wellhead pressure (WHP) of about 130±10 psi (9 bar-g).

Well MW-17 presented a good candidate for generating electrical power using a downhole pump and a binary power plant unit and will be considered for the feasibility study in this report. Figure 2 shows well locations inside the Menengai geothermal field as of May 2014; wells MW-5A and MW-17 are enclosed in red squares.

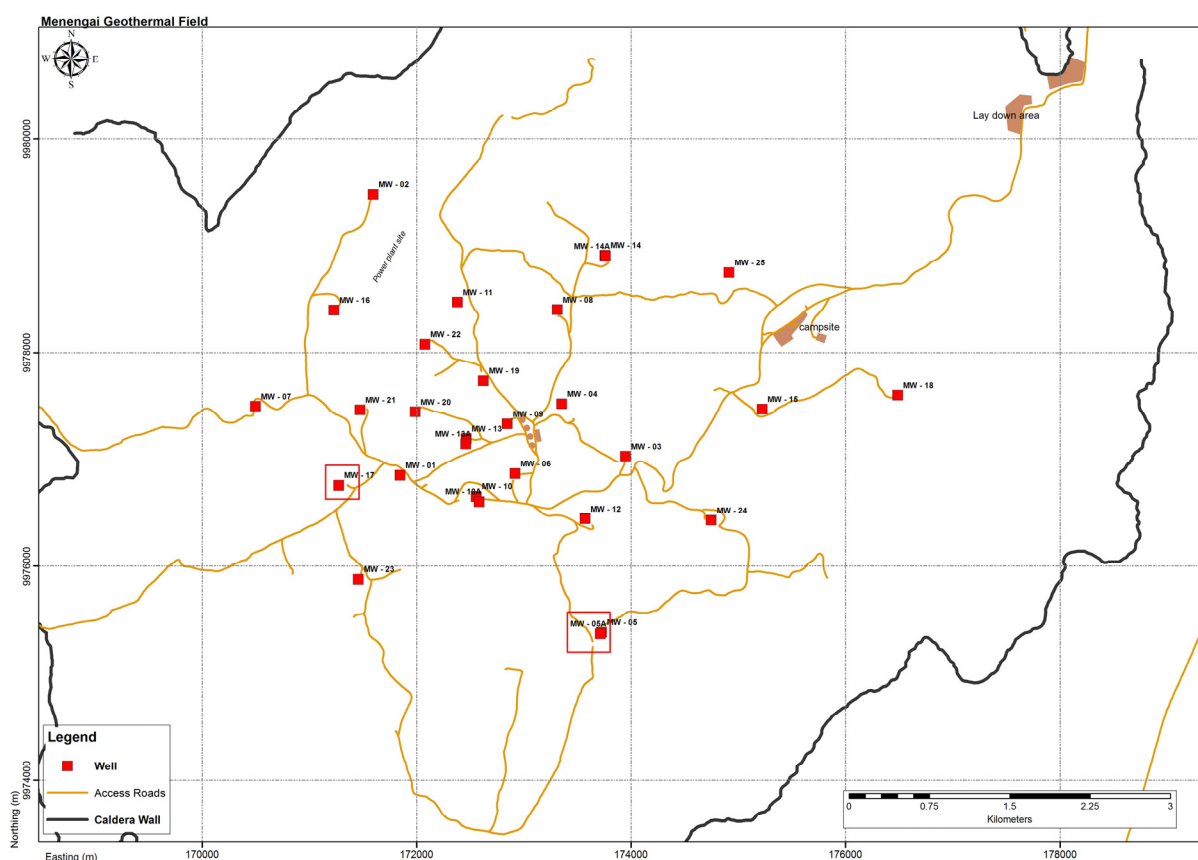


FIGURE 2: Map showing well locations in Menengai geothermal field

1.3 Project scope

This project aims to evaluate the viability of generating electrical power by using a downhole pump in Menengai well MW-17. Results of downhole temperature and pressure measurements for well MW-17 will be reviewed to enable design calculations and the selection of the proper pump system. A suitable combination of a downhole pumping system and a binary power cycle will be identified and the system analysed.

2. WELL FLOW MECHANISM

There are generally two types of well flow mechanisms, self-flowing or artificial lift. Geothermal wells with sufficient reservoir temperature above 190°C can self-flow. Below a temperature of 190°C, artificial lift is more often needed (Sanyal et al., 2007). Utilization of the pumped geothermal fluid for generation of electrical power involves combining the downhole pump system with a suitable power cycle. Technological innovations in the recent past have resulted in improvements in downhole pump resilience to hostile downhole environments, setting depths, gas handling capabilities, resistance to abrasion, performance and reliability.

2.1 Downhole pumps for geothermal wells

Downhole temperature conditions below 190°C are generally associated with medium to high enthalpy liquid phases. Though limited to the operating temperature of the pump, several benefits can be attributed to the use of downhole pumps in geothermal wells as outlined below:

- Greater generating capacity and no reduction in output due to well scaling;
- Increased production from each well, by lowering of water rest level;
- Higher wellhead temperature;
- No loss of steam to the atmosphere; better energy recovery; and
- Reduced calcite scale potential where geothermal fluids with high carbon dioxide content are kept under pressure.

Two types of downhole pumps are commonly used in geothermal wells, line shaft pumps (LSP) and electrical submersible pumps (ESP). The two types are distinguished from each other by the location of the driver. In LSP the driver, an electrical motor, is usually installed above the wellhead (on the surface) and drives the pump through a long shaft. The ESP has the electric motor located below the pump itself and together they are installed inside the wellbore at depth. Figures 3 and 4 give examples of typical LSP and ESP installation concepts.

2.2 Comparison of LSP and ESP

Culver and Rafferty (1998) gave a general comparison of line shaft and electrical submersible pumps as illustrated in Table 1.

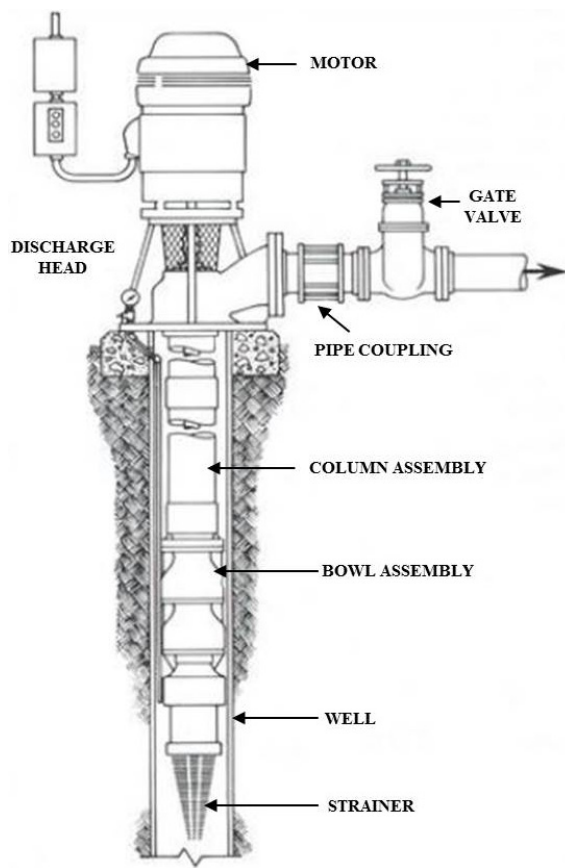


FIGURE 3: Line shaft pump LSP (Kaya and Mertoglu, 2005)

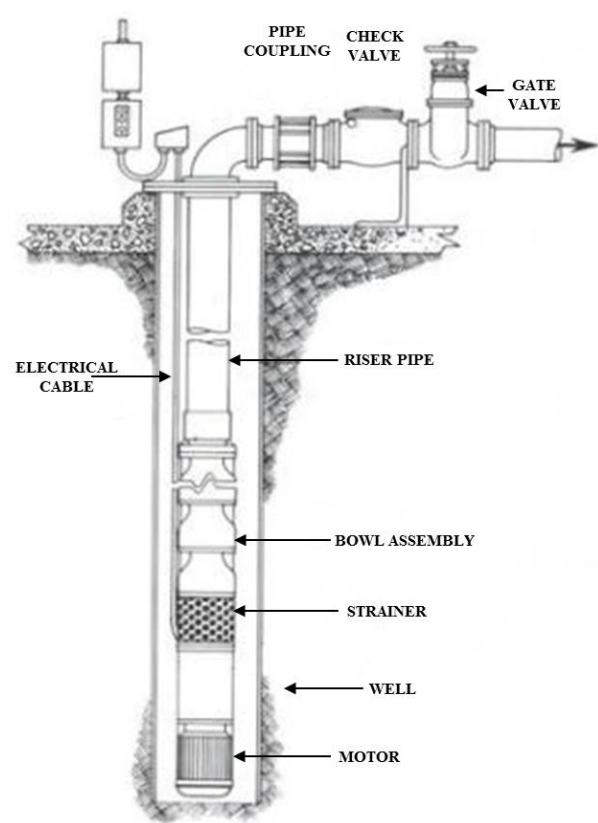


FIGURE 4: Electrical submersible pump ESP (Kaya and Mertoglu, 2005)

TABLE 1: Comparison of line shaft and electrical submersible pumps

Line shaft	Electrical submersible
Pump stage efficiencies in the range 68 – 78%. Lower head/stage and flow/unit diameter.	Pump stage efficiencies in the range 68 -78%. Have generally higher flow/unit diameter.
Higher motor efficiency, motor operates in air, little losses in power cable, and mechanical losses in shaft bearings.	Relatively lower motor efficiency, motor operates in oil at elevated temperatures, higher losses in power cable since partially submerged and attached to hot tubing.
Motor, thrust bearing and seal accessible at surface.	Motor, thrust bearings, seal and power cable in well, hence less accessible.
Usually lower speed (1750 rpm or less), lower wear rate.	Usually higher speeds (3600 rpm), higher wear rate.
Shallower setting, approximately 600 m maximum.	Deeper settings, up to approximately 3,650 m in oil wells.
Longer installation and pump pull time.	Less installation and pump pull time.
Well must be relatively straight or oversized to accommodate stiff pump and column.	Can be installed in crooked wells up to 4 degrees deviation per 100 ft. Up to 75 degrees off vertical.
Impeller position must be adjusted at initial start-up.	Impeller position set.
Generally lower purchase price at direct use temperatures and depth.	Generally higher purchase price at direct use temperatures and depth.

2.3 Downhole pump selection criteria

Selection of a downhole pump has for several installations been based on the following considerations:

- Setting depth;
- Well size;
- Well deviation;
- Well temperature;
- Wire-to-water efficiency;
- Power consumption costs;
- Lowest life cycle costs;
- Repair costs;
- Availability of spare parts; and
- Downtime costs.

These criteria were considered by carrying out a literature review on downhole pump installation experiences in several geothermal projects and published studies as presented in Kunaruk (1991), Ichikawa et al., (2000), Kaya and Mertoglu (2005), Genter et al., (2010), and Drader (2011). The pump setting depth was calculated for various possible flow rates from the well, taking into account the water rest level (L_V), minimum pump submergence (h_{min}) and drawdown in the well (L_N). Drawdown was assumed to be controlled by well losses. Current LSP technology is limited to a setting depth of 457 m (Sanyal et al., 2007); beyond this depth, the pump unit may be affected by vibration or loss of bowl unit efficiency due to the relative elongation between the outer system (column, impeller housings and shaft enclosing tube) and inners system (shaft and impellers). ESP technology has a considerably deeper setting depth and was, thus, determined as the ideal downhole pump for well MW-17.

2.4 ESP analysis and design theory

Similar principles are applicable in calculations for LSP and ESP (Frost, 2004). The design criteria vary depending on the production conditions and well fluid properties anticipated. A model was set up using Engineering Equation Solver (EES) software (F-Chart Software, 2014), based on the following downhole pump design criteria:

- Collection and analysis of available basic data for design, including: well data, production data, well fluid conditions, power sources and possible challenges (temperature, gas fraction, corrosion, deposition);
- Determination of production capacity and pump intake pressure;
- Calculation of the total dynamic head required, expressed in terms of pumped fluid column pressure;
- Selection of a suitable pump unit type based on manufacturer data available, done while ensuring the outer diameter (O.D.) of the pump unit fits inside the casing of the well;
- Calculation of required shaft output power and power consumption; the choice of motor should ensure the motor is large enough to withstand the maximum load without overloading it;
- Selection of the power cable type and size based on motor current, conductor temperature and space limitations; and
- Selection of accessories and optional equipment.

2.5 Basic design data

Well MW-17 was selected for this project. Available data included well casing data, temperature and pressure profiles, material properties and weather data.

2.6 Water rest level in well due to column heating

The static water column in the well gets heated up to pumping conditions. The temperature elevation leads to changes in water density and, consequently, the water rest level in the well. The water rest level in the well, due to heating (L_V), was estimated from the equation:

$$L_V = L_{\text{ref}} - L_C \quad (1)$$

where L_V = Water rest level in well due to column heating (m);
 L_{ref} = Reference major feed zone (m);
 L_C = Water column due to well heating (m).

The water column due to well heating (L_C), is estimated from the equation:

$$L_C = \frac{P_{\text{static}}}{(\rho_{\text{ref}} g)} \quad (2)$$

where P_{static} = Hydrostatic pressure at major feed zone (Pa);
 ρ_{ref} = Density of pumped medium at feed zone formation temperature (kg/m^3);
 g = acceleration due to gravity (m/s^2).

2.7 Production capacity and pump intake pressure

The production capacity was estimated to be in the range 15-60 kg/s. The pump intake pressure, commonly referred to as net positive suction head required (NPSH_R), is determined from pump curve performance curves supplied by manufacturers.

2.8 Total dynamic head required

The total dynamic head (P_D) required is calculated from equation:

$$P_D = P_S + P_H + P_f \quad (3)$$

where P_D = Total dynamic head (Pa);
 P_S = Discharge head pressure (Pa);
 P_H = Net water lift (Pa);
 P_f = Frictional loss in the discharge tubing (Pa).

The discharge head pressure (P_S) was determined based on the required pump delivery pressure.

Net water lift, (P_H), is calculated according to equation:

$$P_H = L_H \rho_t g \quad (4)$$

where L_H = Net water lift height (m);
 ρ_t = Density of pumped medium (kg/m^3);
 t = Temperature of pumped medium ($^{\circ}\text{C}$).

Net water lift height, (L_H), is calculated using equation:

$$L_H = L_V + L_N \quad (5)$$

where L_V = Water rest level in the well due to column heating (m);
 L_N = Draw down in well (m).

The draw down (L_N) in a well is calculated using Equation 4, however it is assumed that drawdown is predominantly controlled by well losses and, therefore, Equation 5 is used.

$$L_N = b_D m + c_D m^2 \quad (6)$$

$$L_N = c_D m^2 \quad (7)$$

where b_D = Laminar draw down co-efficient (m/(l/s));
 c_D = Turbulent draw down co-efficient (m/(l/s)²);
 m = Well total discharge (l/s or kg/s).

Friction head, (H_f), in the discharge tubing is calculated using the equation:

$$H_f = f V^2 \frac{L}{2gD_{in}} \quad (8)$$

where H_f = Friction head (m of fluid);
 f = Friction factor;
 V = Fluid velocity (m/s);
 L = Total length of discharge tubing (m);
 D_{in} = Discharge tubing pipe inner diameter (m).

The fluid velocity, (V), is calculated from the equation:

$$V = Q / \left(\frac{\pi D_{in}^2}{4} \right) \quad (9)$$

where Q = Volumetric flow rate (m³/s).

The frictional factor, (f), is calculated based on the Reynolds number (Re), using the Swamee – Jain equation (DiPippo, 2008) for turbulent flow:

$$Re > 5000, \quad f = \frac{0.25}{\left[\log_{10} \left(\frac{\varepsilon}{3.7D_{in}} + \frac{5.74}{Re^{0.9}} \right) \right]^2} \quad (10)$$

where ε = Absolute roughness.

The Reynolds number, (Re), is calculated by the equation:

$$Re = \frac{\rho_t D_{in} V}{\mu_t} \quad (11)$$

where μ_t = Dynamic viscosity of fluid.

Frictional loss in the discharge tubing, (P_f), is then calculated using the equation:

$$P_f = H_f \rho_t g \quad (12)$$

2.9 Pump setting depth

The pump setting depth, (L_S), is calculated from the equation:

$$L_S = L_H + h_{min} \quad (13)$$

where L_S = Pump setting depth (m);
 h_{min} = minimum pump submergence (m).

The minimum pump submergence, (h_{\min}), is calculated according to equation:

$$h_{\min} = \frac{P_j - P_u}{\rho_t g} 10^{5 + \text{NPSH}_R + h_{fb}} \quad (14)$$

where P_j = Boiling pressure of medium (bara);
 P_u = Barometric pressure (bara);
 NPSH_R = Net positive suction head required (m);
 h_{fb} = Pressure losses in bowl suction case (m).

2.10 Motor shaft power

The required motor shaft output power, (A_M), was calculated using equation:

$$A_M = A_D + A_F \quad (15)$$

where A_D = Power required by the pump unit (kW);
 A_F = Total mechanical losses (kW).

Power required by the pump unit, (A_D), is calculated using the equation:

$$A_D = \frac{P_D \rho_t m 10^{-6}}{\eta_{\text{pump}}} \quad (16)$$

where η_{pump} = Pump unit efficiency.

Total mechanical losses, (A_F), in an ESP are due to mechanical losses in the motor thrust bearing (A_L). The second term in Equation 15 is, thus, omitted. In the case of LSP, mechanical losses in the shaft bearing (A_O), would have to be included as calculated in equation:

$$A_F = A_L + A_O \quad (17)$$

The power consumption, (A_N), is calculated from the equation:

$$A_N = \frac{A_M}{\eta_{\text{motor}}} \quad (18)$$

2.11 Pump type

The pump type is selected by referring to manufacturer's pump performance curves. A pump type is chosen on the basis of expected production capacity and well casing size. The selected pump should operate within its operating capacity range and close to the pump's peak efficiency.

2.12 Optimum size of ESP components

This involves determining the sizes of the ESP system components that include pump, motor and accessories. This study takes a simplified approach to ESP system components sizing by considering pump unit stages and the break horse power required by the motor in sizing the pump and motor units.

Pump stages, (Z), are determined by rounding off calculated theoretical stages to the nearest integer using manufacturer pump stage performance curves and equation:

$$Z_{theoretical} = P_D / (P_I) \quad (19)$$

where

Z	= Pump stages;
$Z_{theoretical}$	= Calculated theoretical stages;
P_I	= Single stage head (from manufacturer pump performance curves).

The break horse power required by the pump, (BHP), is calculated from the equation:

$$BHP = Z(BHP_{stage})SG_{fluid} \quad (20)$$

where

BHP	= Brake horse power required by the pump;
BHP_{stage}	= Brake horse power per stage (from pump performance curves);
SG_{fluid}	= Specific gravity of pumped medium.

3. BINARY POWER SYSTEM

Binary type energy conversion systems are typically used to exploit low temperature geothermal resources (DiPippo, 2004). Several technical variations of the binary cycle exist and include the Kalina cycle and the organic Rankine cycle (ORC). These energy conversion systems employ a secondary working fluid of a lower critical temperature and pressure in comparison with water within a closed Rankine cycle.

3.1 System components

A binary power system has two closed loops in which the primary fluid (geothermal fluid) and secondary fluid (working fluid) circulate without coming into contact. The primary fluid is produced as a

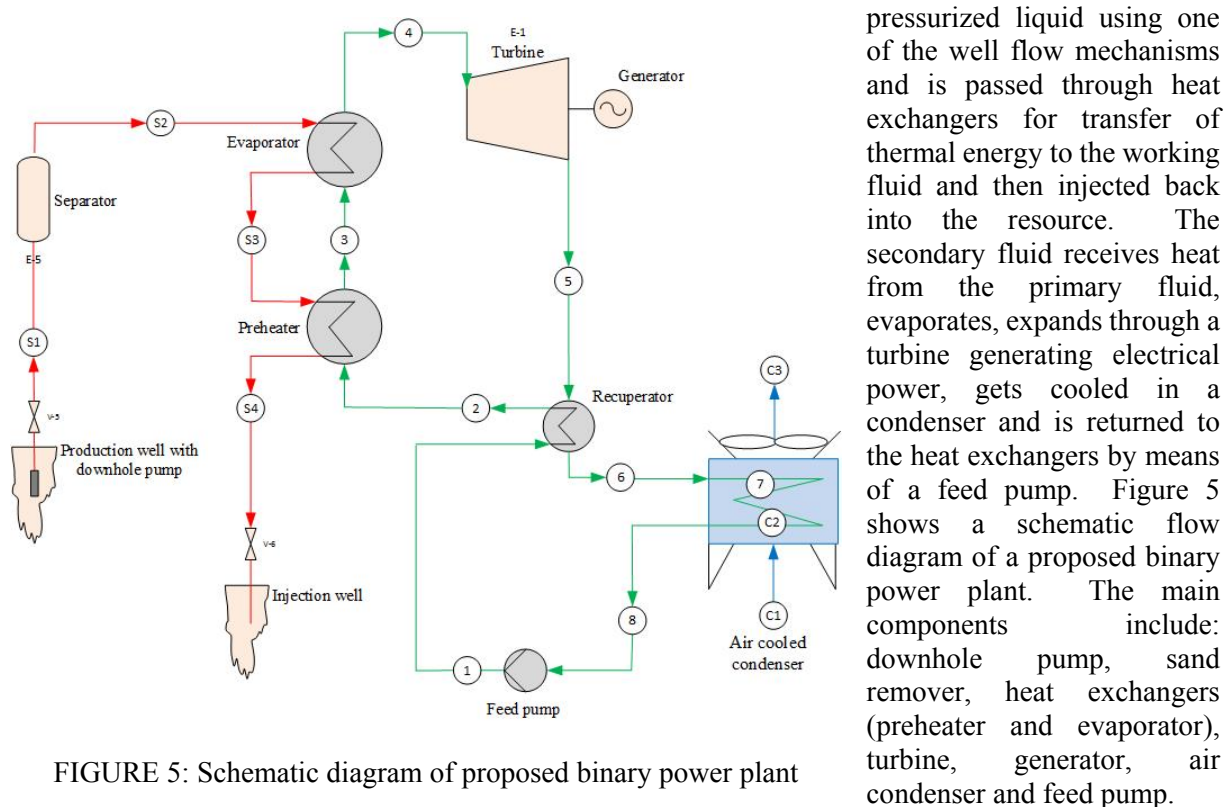


FIGURE 5: Schematic diagram of proposed binary power plant

3.2 Working fluid

Selection of the working fluid in binary power cycle is among the main considerations made. The choice has great implications on the performance of the power plant since irreversibilities associated with the heat transfer process have a negative impact on the overall efficiency of the cycle. The selection criteria for the fluid are thus based on fluid thermodynamic properties, stability of the fluid and compatibility with materials contacted, availability and cost, safety aspects and environmental impacts. Working fluids are generally classified as wet, dry or isentropic depending on the slope of the saturation vapour curve on a $T-S$ diagram. Negative slope characterises a wet fluid; positive slope signifies dry fluid and infinite slope characterises an isentropic fluid. Findings presented by Chen et al. (2010) summarize potential working fluids. Toxicity, ozone depletion potential (ODP), global warming potential (GWP) and atmospheric life time (ALT) continue to affect the use of chlorofluorocarbons with several already phased out and others being phased out in the near future. Hydrocarbons have continued to be used with appropriate safety measures due to their flammability.

3.3 Binary cycle analysis

A model was set up using Engineering Equation Solver (EES) software (F-Chart Software, 2014) based on a binary power cycle as shown in Figure 5. The model was run using several working fluids to determine maximum Net power output.

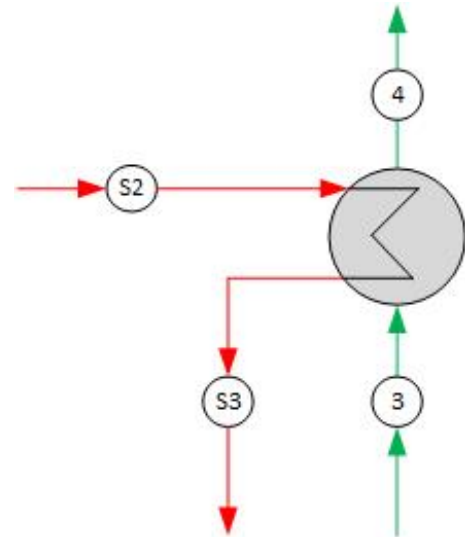


FIGURE 6: Evaporator

3.3.1 Evaporator

Figure 6 shows the evaporator. The geothermal fluid pumped from the well goes through the sand remover and enters the evaporator via station S_2 . This stream provides the heat of vaporization for the working fluid that comes as saturated liquid at evaporator pressure from the preheater and can be treated as isenthalpic, i.e. heat losses in the well and the discharge tubing are treated as negligible. Evaporation occurs from 3 to 4 along an isotherm of the working fluid. The vaporized working fluid is then fed into the turbine. The heat balance over the evaporator is given by equation:

$$Q_E = \dot{m}_{S2}(h_{S2} - h_{S3}) = \dot{m}_3(h_4 - h_3) \quad (21)$$

where

$$\begin{aligned} Q_E &= \text{Heat transfer in the evaporator;} \\ \dot{m}_{S2} &= \dot{m}_{S1} = \dot{m}_{S3} = \dot{m}_{\text{brine}} \\ &= \text{mass of geothermal fluid from the well;} \\ \dot{m}_3 &= \dot{m}_1 = \dot{m}_2 = \dot{m}_4 = \dot{m}_5 = \dot{m}_6 = \dot{m}_7 = \dot{m}_8 = \\ &= \dot{m}_{\text{fluid}} = \text{mass of working fluid.} \end{aligned}$$

3.3.2 Preheater

Figure 7 shows the preheater. The geothermal fluid enters via station S_3 after leaving the evaporator and leaves the evaporator at station S_4 . At this stage sensible heat is added to the working fluid coming from the recuperator through station 2 to bring it to its boiling point at station 3 as it leaves the preheater. The minimum difference in temperature between the entering geothermal fluid and the leaving working fluid is known as the “pinch-point”. Heat losses in the preheater are assumed to be negligible and the heat balance over the stage is given by equation:

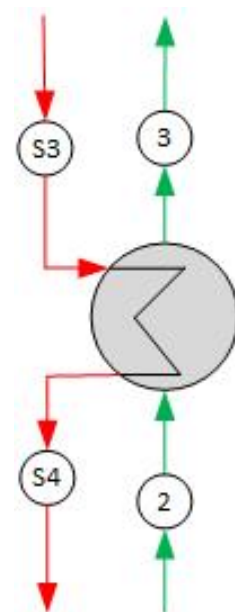


FIGURE 7: Preheater

$$Q_{ph} = \dot{m}_{S3}(h_{S3} - h_{S4}) = \dot{m}_6(h_6 - h_8) \quad (22)$$

where Q_{ph} = Heat transfer in the preheater.

For a constant heat capacity of the fluid, the enthalpy difference in the geothermal fluid may be replaced by the temperature difference:

$$Q_{ph} = \dot{m}_{S3}c_b(T_{S3} - T_{S4}) = \dot{m}_6(h_6 - h_8) \quad (23)$$

where c_b = Specific heat capacity of the geothermal fluid at constant pressure.

3.3.3 Turbine

The turbine converts thermal energy into mechanical shaft work used to generate electricity in the generator. Figure 8 shows the turbine. Vaporised fluid enters through station 4 and exits at station 5 as vapour. The expansion process over an ideal turbine is considered isentropic and has no irreversibilities that accompany real turbines. The entropy of vaporised fluid at station 4 equals that at station 5 and subsequently the reduction in enthalpy is the largest possible. The isentropic exit enthalpy is then the enthalpy at the same entropy as that of the inlet at exit pressure as given in Equation 20.

$$h_{S5} = h(s_4, p_5) \quad (24)$$

In real turbines, irreversibilities downgrade the performance of the equipment. Reduction in enthalpy is determined by the isentropic turbine efficiency, a parameter that expresses how efficiently a real turbine approximates an idealized one as specified by the turbine manufacturer. The real turbine exit enthalpy is found using the equation:

$$\eta_t = \frac{h_4 - h_5}{h_4 - h_{S5}} \quad (25)$$

where η_t = Isentropic turbine efficiency.

Turbine work output, (\dot{W}_t), is thus given by the equation:

$$\dot{W}_t = \dot{m}_4(h_4 - h_5) \quad (26)$$

3.3.4 Recuperator

Figure 9 shows the recuperator which is used for dry expansion type working fluid; turbine exit vapour containing extractable heat enters via station 5 and exits at station 6. The working fluid enters via station 1 and leaves through station 2. The recovery of heat helps in increasing the working fluid temperature before it enters the preheater, resulting in higher geothermal fluid exit temperature from the preheater. This leads to improved plant cycle efficiency. The heat balance over the turbine is given by the equation:

$$Q_R = \dot{m}_1(h_2 - h_1) = \dot{m}_5(h_5 - h_6) \quad (27)$$

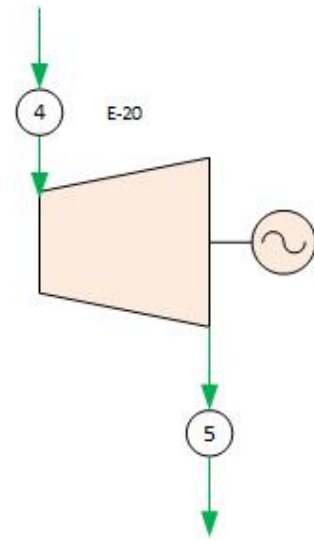


FIGURE 8: Turbine

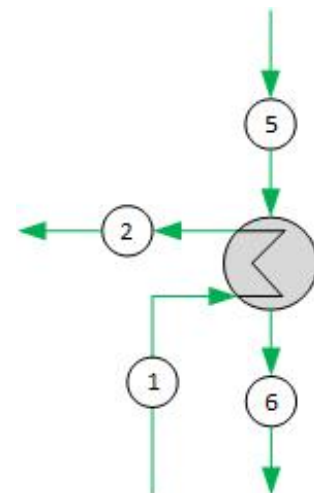


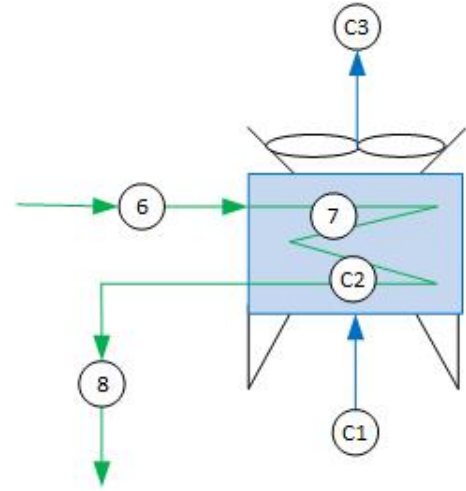
FIGURE 9:
Recuperator

3.3.5 Air cooled condenser

The condenser shown in Figure 10 is used to condense the hot working fluid from the recuperator. The working fluid enters the condenser at station 6 and leaves through station 8 as saturated liquid. Cooling air (ambient air) enters the condenser by means of suction pressure generated by fin-fans at station C₁ and leaves at station C₃. Heat rejected by the working fluid to the air is calculated by the equation:

$$Q_C = \dot{m}_a C_a \Delta T_{\text{cooling}} = \dot{m}_6 (h_6 - h_8) \quad (28)$$

where Q_C = Heat transfer through the condenser;
 \dot{m}_a = Mass of air;
 C_a = Specific heat capacity of air at constant pressure.



Heat transfer from the hot working fluid to the cool air is driven by the temperature difference. It follows that the highest temperature of the cooling air must not exceed the condensation temperature in the condenser. In general, a temperature value of 5°C is used as the temperature difference between the inlet working fluid and exit cooling air temperatures. The heat balance is thus calculated by:

FIGURE 10: Air cooled condenser

$$\dot{m}_a (h_{C3} - h_{C1}) = \dot{m}_{\text{fluid}} (h_6 - h_8) \quad (29)$$

The fan power, (W_{fan}), is calculated by:

$$W_{\text{fan}} = \frac{v_a \Delta P}{\eta_{\text{fan}}} \quad (30)$$

$$v_a = \frac{\dot{m}_a}{\rho_{a,\text{out}}} \quad (31)$$

where v_a = Volumetric flow rate of air (m³/s);
 ΔP = Pressure drop (Pa);
 η_{fan} = Efficiency of fan;
 $\rho_{a,\text{out}}$ = Density of air (kg/m³).

3.3.6 Feed pump

Figure 11 shows the pump; pump work is given by the equation:

$$W_{\text{fp}} = \dot{m}_{\text{fluid}} (h_6 - h_8) = \dot{m}_{\text{fluid}} (h_{6s} - h_8) / \eta_p \quad (32)$$

where W_{fp} = Work done by the feed pump;
 η_p = Isentropic pump efficiency.

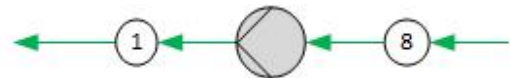


FIGURE 11: Feed pump

3.3.7 Heat exchanger area

The heat transfer equipment area is calculated using equation:

$$Q = UA(LMTD) \quad (33)$$

$$LMTD = \frac{(T_{hot,in} - T_{cold,out}) - (T_{hot,out} - T_{cold,in})}{\ln \left[\frac{T_{hot,in} - T_{cold,out}}{T_{hot,out} - T_{cold,in}} \right]} \quad (34)$$

where Q = Heat transfer through equipment (J or kJ);
 U = Overall heat transfer coefficient ($^{\circ}\text{C}/\text{m}^2$);
 A = Heat transfer area (m^2);
 $LMTD$ = Log mean temperature difference ($^{\circ}\text{C}$).

3.3.8 Assessment of binary cycle

Binary power plants are supplied with heat from a source of finite capacity. In most cases the initial brine temperature and consequent heat input are the same. Evaluation of a power plant therefore requires the use of an appropriate thermodynamic basis. The thermal efficiency, ($n_{th,I}$), of a binary power plant can be carried out according to the first law of thermodynamics, given as:

$$n_{th(I)} = \frac{W_{net}}{Q_{in}} \quad (35)$$

$$W_{net} = W_t - W_{parastic\ load} \quad (36)$$

$$W_{parastic\ load} = W_{feed\ pump} + W_{fan} + W_{downhole\ pump} \quad (37)$$

where W_{net} = Net power output;
 Q_{in} = Thermal heat energy supplied to the binary system;
 $W_{parastic\ load}$ = Power consumption by auxiliary binary plant equipment;
 $W_{feed\ pump}, W_{fan}, W_{downhole\ pump}$ = feed pump, fan and dowhole pump power.

The second law (or exergetic) efficiency relates to the maximum power (or work) output that can theoretically be obtained from a system, relative to its surrounding environment. Two approaches exist, namely “brute-force” and “functional” defined as follows:

- A brute-force exergy efficiency is the ratio of the sum of all output exergy terms to the sum of all input exergy terms.
- A functional exergy efficiency is the ratio of the exergy associated with the desired energy output to the exergy associated with the energy expended to achieve the desired output.

In DiPippo and Marcille (1984) the exergetic efficiency, ($n_{th,II}$), concept when applied to a power plant simplifies to the ratio of net power output to the exergy of the motive fluid serving as the energy source for the plant. The exergetic efficiency is given by:

$$n_{th(II)} = \frac{W_{net}}{E_{in}} \quad (38)$$

$$E_{in} = m_{geo\ fluid}(e_{geo\ fluid,in}) \quad (39)$$

$$e = h_r - h_o - T_o(S_r - S_o) \quad (40)$$

where E_{in} = Exergy of motive fluid inflow stream;
 $m_{geo\ fluid}$ = Mass flow rate of geothermal fluid inflow stream;
 $e_{geo\ fluid,in}$ = Specific exergy of motive fluid inflow stream;
 h = Specific enthalpy of fluid stream;
 S = Specific entropy of fluid stream;
 r = Set of reference motive source fluid conditions (temp. and pressure states);
 o = State of ambient (dead state) conditions (temperature and pressure).

4. WELL MW-17 UTILIZATION SCHEME CALCULATIONS

The utilization scheme calculations are divided into downhole pump performance and binary power plant model calculations. In this utilization scheme the wellhead discharge pressure is assumed to be 7 bar.

4.1 Downhole pump selection and performance calculations

4.1.1 Basic data

The main feed zone is assumed to be at the depth interval of 1000 – 1200 m. Density variations due to temperature elevation are limited to the determination of the water rest level in the well due to column heating calculations. Tables 2 and 3 give basic data used in the downhole pump system design.

TABLE 2: Well MW-17 casing data

Section	Setting depth (meters RT)	Open hole diameter (inches)	Casing outer diameter (inches)	Wall thickness (inches)	Nominal weight (Pound Per Foot - PPF)
Surface	68.37	26	20	0.438	94
Intermediate/Anchor	402.73	17 1/2	13 3/8	0.380	54.5
Production	1004.57	12 1/4	9 5/8	0.472	47
Liners landing	2212.00	8 1/2	7	0.362	26

TABLE 3: Material properties

Parameter	Value/Specification
Wellhead/Master valve	ANSI class 600
Discharge tubing internal diameter	3 inches
Commercial steel pipe internal roughness	0.045mm
Fluid density	1000 kg/m ³

4.1.2 General assumptions

Engineering Equation Solver (EES) software was used for the design model of the downhole pump. The following assumptions were made.

- The static water rest level in the well is taken to be at 450 m;
- Drawdown is dominated by well losses;
- Geothermal fluid properties are comparable to water thermodynamic properties;
- No challenges (abrasion, deposition, and corrosion, temp) due to fluid chemistry are anticipated;
- Pressure losses in bowl unit (h_{fb}) are negligible;
- The fluid is pumped at a temperature of 150°C;
- The pump is operated at full load; and
- SI units are used in all calculations.

4.1.3 Water rest level in well due to column heating

The water column due to well heating was calculated according to Equations 1 and 2 for two cases:

1. Partial heating of water column to pumping conditions from a depth of 1200 m upwards
2. Total heating of entire water column to pumping conditions.

Table 4 shows possible water column rise for the two cases.

TABLE 4: Initial water column rise

Effect	Static water rest level (m)	Water rest level in well due to well heating (m)	Column rise (m)
Partial heating of column	450	378	72
Total heating of column		352	98

The calculated column rise was found to be between 70 and 100 m. The rise corresponds to a water rest level in the well due to column heating in the range 350 -380 m at the onset of pumping before drawdown effects are felt. The ANSI class 600 wellhead is thus sufficient to hold the pump system discharge pressure at the onset of pumping.

4.1.4 Pump design results

The pump setting depth and total dynamic head were calculated based on a likely total well discharge mass flow in the range 15 – 60 kg/s. Table 5 shows results of the pump calculations.

The pump setting depths are in the range 436 – 529 m for the range of production capacity. Total dynamic head is calculated and varies from 46 to 61 bar while the motor power consumption is between 185 and 976 kW.

TABLE 5: Pump setting depth and total dynamic head calculations

Parameter		Values									
Mass flow	(kg/s)	15	20	25	30	35	40	45	50	55	60
Pump setting depth	(m)	436	441	447	455	464	474	486	499	513	529
Total dynamic head	(Bar)	46	47	49	50	51	53	55	57	59	61
Required motor shaft output power	(kW)	129	176	225	278	333	393	458	527	602	683
Motor power consumption	(kW)	185	251	322	397	476	562	654	753	860	976

4.1.5 Downhole pump sizing and accessories

ESP technology is currently limited to a maximum operating temperature of 204°C (400°F) and a maximum tandem motor power of 700 kW (974.5 HP) at 50 Hz or 872 kW (1170 HP) at 60 Hz. These ESP pump specifications allow production capacities from well MW-17 of up to 47 kg/s. Variable speed drives are commonly used to generate any frequency between 30 and 90 Hz (Bremner et al., 2006/07). This allows the ESP system to operate over a broader range of capacity, head and efficiency. The ESP system is thus proposed to include a variable speed drive as an accessory.

4.2 Binary power plant model calculations

4.2.1 Binary cycle conditions

The binary cycle specifications for the model are set as follows:

- Pumped brine mass flow rate = 45 kg/s
- Wellhead pressure = 7 bar
- Brine inlet temperature = 150°C
- Brine re-injection temperature = 80°C
- Assumed well enthalpy = 632.3 kJ/kg
- Isentropic efficiency of turbine (η_t) = 85%

- Efficiency of pump (η_p) = 75%
- Ambient temperature = 30 °C
- Pressure drops and heat losses in the system are neglected.

Overall heat transfer coefficients (U) of heat exchangers (Páll Valdimarsson, pers. comm.) are assumed as follows:

$U = 1600 \text{ W/m}^2\text{°C}$ for evaporator or vaporiser;

$U = 1000 \text{ W/m}^2\text{°C}$ for preheater;

$U = 400 \text{ W/m}^2\text{°C}$ for recuperator; and

$U = 800 \text{ W/m}^2\text{°C}$ for air called condenser.

Table 6 shows a summary of Menengai weather data used in the model calculations:

TABLE 6: Summary of weather data

Parameter	Maximum	Minimum	Average
Wind speed (m/s)	5.8	3.4	4.1
Relative humidity (%)	78	44	61
Dry bulb temperature (°C)	30	10	20
Barometric pressure (bar)			0.83

4.2.2 Model calculation results

A thermodynamic cycle model of the proposed binary power plant in Figure 5 was set up using Engineering Equation Solver (EES) software to enable detailed calculations. The EES code was then run using different working fluids to optimise net power output from the plant. Table 7 shows system parameters and results of isopentane, n-pentane, isobutane and n-butane.

TABLE 7: Summary of calculated power output

Working fluid	Turbine inlet pressure (bar-g)	Mass flow of working fluid (kg/s)	Gross output (kW)	Parasitic load (kW)	Net power output (kW)	ESP power (kW)	Total parasitic load (kW)	Thermal efficiency (%)
Isopentane	7	32.33	1546	713.6	831.9	654	713.6	6.2
n-pentane	6	28.74	1262	700.8	561.3	654	700.8	4.2
Isobutane	The pressure and temperature went above critical values							
n-butane	The pressure and temperature went above critical values							

Isobutane and n-butane went above their critical temperature and pressure. Results showed that isopentane gives the highest Net power output among the working fluid cycles studied. Maximum net output power of 831.9 kW was realised at a turbine inlet pressure of 7 bar and yielded a 6.2% thermal efficiency when considered on the basis of first law of thermodynamics. The parasitic load of the proposed plant is approximately 714 kW, majorly being load due to the ESP. Figures 12 and 13 show plots of Net power output against turbine inlet pressure for isopentane and n-pentane, while Figure 14 shows the proposed binary power plant cycle (isopentane) with EES values.

The proposed binary power plant undergoes the thermodynamic cycle, shown in Figures 15 and 16, in a temperature-entropy diagram and a pressure-enthalpy diagram, respectively.

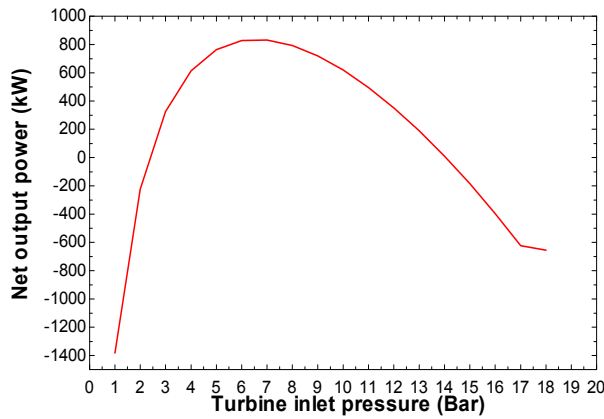


FIGURE 12: Net power output with isopentane as the working fluid

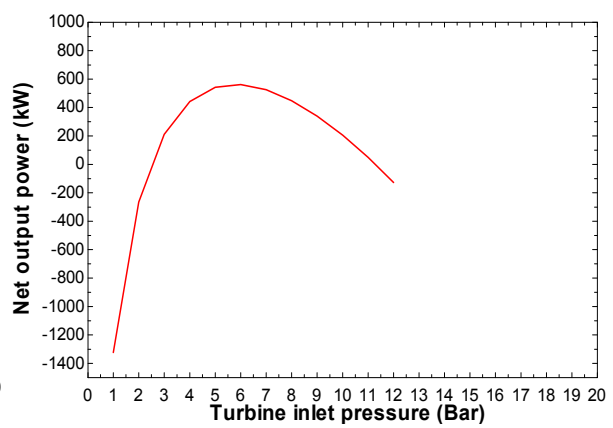


FIGURE 13: Net power output with n-Pentane as the working fluid

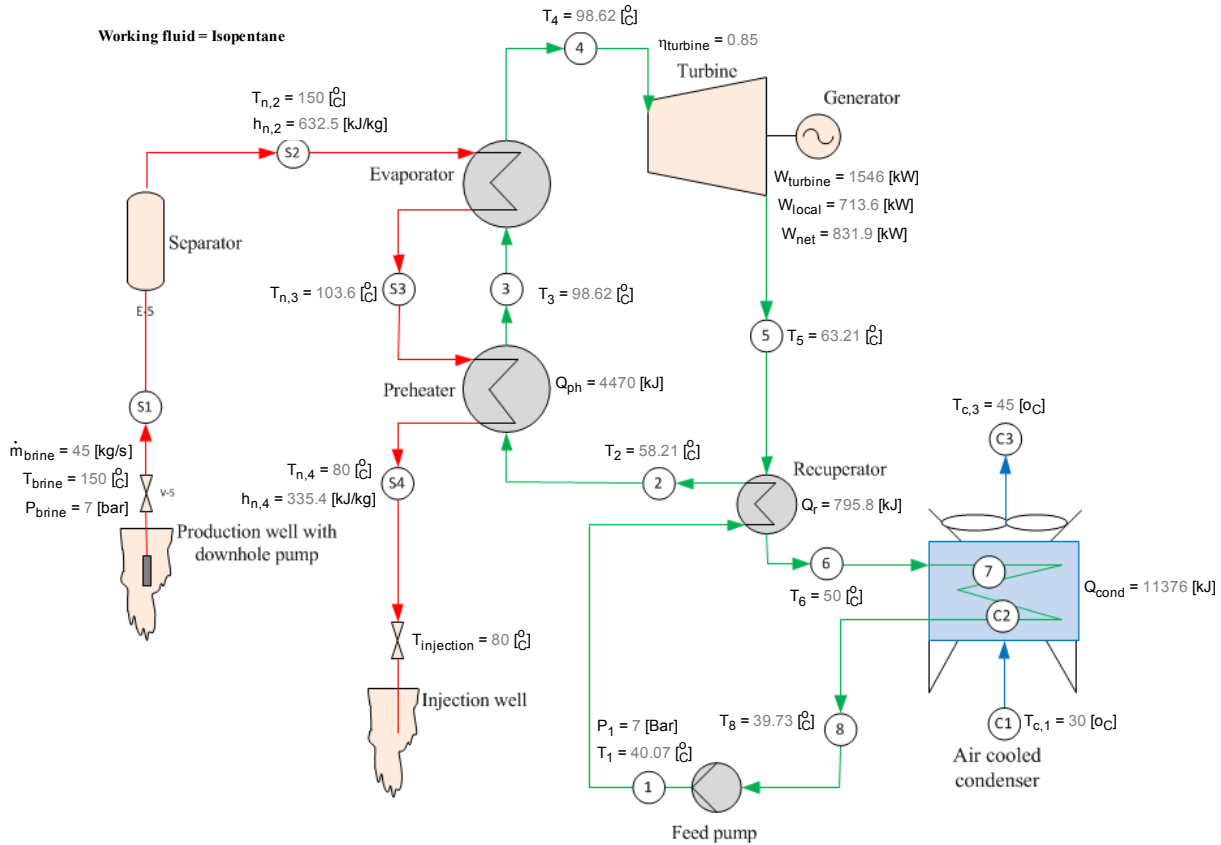


FIGURE 14: Proposed binary power plant cycle with EES values

4.3 Investment cost estimation of proposed utilization scheme

Geothermal projects are influenced by various costs which include initial investment costs, operation and maintenance costs, capital and financing costs, the costs due to economic factors and legal and regulatory costs. Calculation of initial investment can be used to give an indication of the cost of the geothermal power output. Ngugi (2012c) estimates the average installation costs in Kenya for geothermal projects is about 3.6 million US\$ (2.8 million €) per MWe. The cost of the utilization scheme

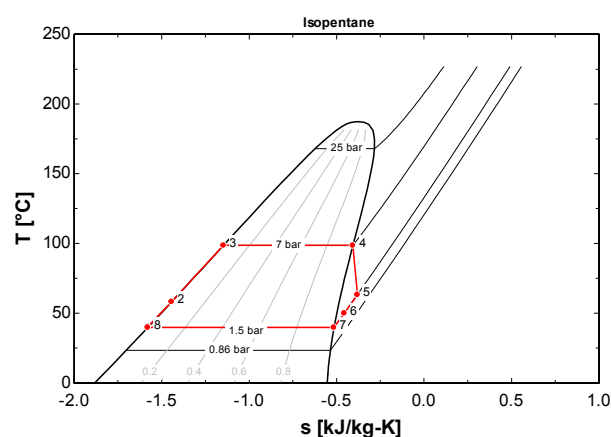


FIGURE 15: T-S diagram for proposed binary power cycle

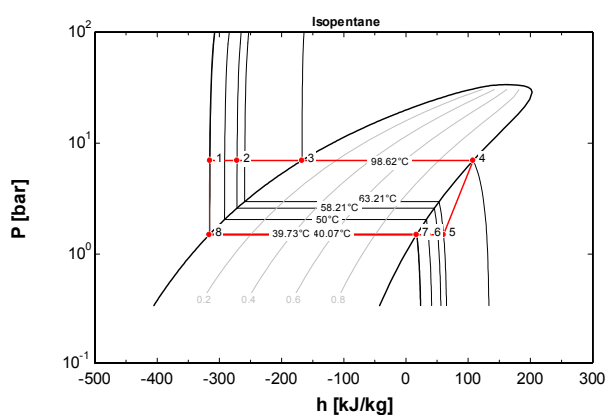


FIGURE 16: P-h diagram for proposed binary power cycle

was calculated using base costs of main plant equipment as estimated based on the experience of industry experts. In this study the costs assumed are thumb values. Table 8 shows proposed binary power plant costs based on isopentane as the working fluid.

TABLE 8: Proposed utilization scheme model based on assumed thumb values of equipment costs

S.no.	Equipment	Unit size	Basic cost / Unit size (€/m ² , kW)	Process heat value (kJ)	Equipment size (m ² , kW)	Cost of Equipment (€)
1	Preheater	m ²	300	4470	391.8	117,540.00
2	Recuperator	m ²	230	795.8	276.9	63,687.00
3	Air condenser	m ²	265	11376	2002	530,530.00
4	Evaporator	m ²	360	8896	279.3	100,548.00
5	Turbine	kW	340		1546	525,640.00
6	Feed pump	kW	500		39.54	19,770.00
Cost of mechanical equipment (35%)						1,357,715.00
Estimated binary plant cost						3,879,185.70
7	Downhole pump	kW	1000		655	655,000.00
Total estimated utilization scheme cost						4,534,185.70

The cost of mechanical equipment was assumed to represent 35% of the constructed binary plant costs (David Orn Benediktsson – Verkis Iceland, pers. comm.); this translates to a binary plant cost of 3.8 million € before considering the cost of a downhole pump. The total initial investment cost of the proposed utilization scheme is estimated at 4.5 million €.

5. CONCLUSION

Utilization of low to moderate enthalpy fluids for electrical power generation is best carried out using a binary system. This however requires careful considerations with regard to the energy conversion cycle options suitable for the project site being considered. The choice of the thermodynamic cycle working fluid ensures optimization of net power output from the plant. The proposed utilization scheme consists of a downhole electrical submersible pumping system and an organic Rankine cycle type binary power plant. The electrical submersible pump technology is currently limited to a pump capable of operating at a temperature of 204°C (400°F) and of 700 kW (974.5 HP) at 50 Hz, maximum tandem motor power.

In this study the performance of the binary power cycle was analysed with isobutene, n-butane, isopentane and n-pentane as possible working fluids. The main conclusion is that isopentane gives the

highest net power output. The utilization scheme is ideal for early generation and would contribute to an improved exergetic efficiency of Menengai geothermal field, considering the possibility of direct use application as presented by Kinyanjui (2013).

The total investment cost of the proposed utilization scheme is estimated at 4.5 million € and translates to 5.4 million € per MWe. The proposed utilization scheme cost shows a variance of 2.6 million compared to the average Kenya installation cost of geothermal projects. The variance may be attributed to an escalation in plant equipment prices and the additional cost of a downhole pumping system.

ACKNOWLEDGEMENTS

I am profoundly grateful to my employer, Geothermal Development Company, for according me the opportunity to attend this training programme. I am also grateful to Mr. Lúdvík S. Georgsson, Director of UNU-GTP, and Mr. Ingimar G. Haraldsson, Deputy Director, for the successful organization of the programme. My sincere gratitude goes to my supervisors, Mr. Thorleikur Jóhannesson and Mr. Davíð Örn Benediktsson for their guidance, knowledge sharing and positive criticism of my work. Many thanks go to Ms. Málfríður Ómarsdóttir, Ms. Thórhildur Ísberg and Mr. Markús A.G. Wilde for facilitating our stay and many field excursion travels. I am also thankful to the UNU Fellows for the time we shared together.

I am profoundly grateful to my family, my wife Catherine G. Wanjiru for her support and prayers, my son Nigel and daughter Hadassah for their braveness and endurance during my stay in Iceland. My heartfelt appreciation goes to my dear mother and brothers Samson and Timothy for their encouragement throughout the study period.

Thanks to Almighty God for giving me good health and wisdom.

REFERENCES

- Beck, S.B., and Collins, R., 2008: *Moody diagram*. University of Sheffield, available from webpage: en.wikipedia.org/wiki/File:Moody_diagram.jpg.
- Bremner, C., Harris, G., Kosmala, A., Nicholson, B., Ollre, A., Pearcy, M., Salmas, J.C., and Solanki, C.S., 2006/2007: Evolving technologies: Electrical submersible pumps. *Oilfield Review*, 18-4 (winter 2006/2007), 30-43.
- Chen, H., Goswami, D.Y., Stefanakos, E.K., 2010: A review of thermodynamic cycles and working fluids for the conversion of low-grade heat. *Renew. & Sustainable Energy Reviews*, 14-9, 3059-3067.
- Culver, G.G., and Rafferty, K.D., 1998: Well pumps. In: Lienau, P.J., and Lienau, B.C. (ed), *Geothermal direct use engineering and design guidebook (3rd ed.)*. Geo-Heat Centre, Oregon Institute of Technology, Klamath Falls, OR, 211-239.
- DiPippo, R., 2004: Second law assessment of binary plants generating power from low-temperature geothermal fluids. *Geothermics*, 33, 565-586.
- DiPippo, R., 2008: *Geothermal power plants. Principles, applications, case studies and environmental impact*. Elsevier Ltd., Kidlington, UK, 493 pp.

DiPippo, R., and Marcille, 1984: Exergy analysis of geothermal power plants. *Geothermal Res. Council, Trans.*, 8, 47-52.

Drader, D., 2011: *Improved power production efficiency of hydrothermal reservoirs using downhole pumps*. University of Iceland, MSc thesis, 60 pp.

F-Chart Software, 2014: EES, Engineering equation solver. F-Chart Software internet website, www.fchart.com/ees/ees.shtml.

Frost, J.A., 2004: Monitoring evaluating and optimizing down hole geothermal pump performance. *Presented at the "Down hole geothermal pump seminar", organized by Geothermal Resource Council, Indiana Wells, CA, Geothermal Resources Council, Transactions*, 28, 12 pp.

Genter, A., Georke, X., Graff, J., Cuenot, N., Krall, G., Schindler, M., and Ravier, G., 2010: Current status of the EGS Soultz geothermal project (France). *Proceedings of the World Geothermal Congress 2010, Bali, Indonesia*, 6 pp.

Ichikawa, S., Yasuga, H., Tosha, T., and Karasawa, H., 2000: Development of downhole pump for binary cycle power generation using geothermal water. *Proceedings of the World Geothermal Congress 2000, Kyushu - Tohoku, Japan*, 1283-1288.

Kaya, T., and Mertoglu, O., 2005: Engineering aspects of geothermal production well with down hole pumps. *Proceedings of the World Geothermal Congress 2005, Antalya, Turkey*, 8 pp.

Kinyanjui, S., 2013: Direct use of geothermal energy in Menengai, Kenya: Proposed geothermal spa and crop drying. Report 9 in: *Geothermal training in Iceland 2013*. UNU-GTP, Iceland, 109-141.

Kunaruk, U., 1991: Design and selection of deep well pumps for geothermal wells. Report 8 in: *Geothermal training in Iceland 1991*. UNU-GTP, Iceland, 51 pp.

Mibei, G., and Lagat, J., 2011: Structural controls in Menengai geothermal field. *Proceedings of Kenya Geothermal Conference*, Geothermal Association of Kenya, webpage: www.gak.co.ke/kgc2011, 5 pp.

Ngugi, P.K., 2012a: Kenya's plans for geothermal development – a giant step forward for geothermal. *Presented at the "Short Course on Geothermal Development and Geothermal Wells", organized by UNU-GTP and LaGeo, Santa Tecla, El Salvador*, 8 pp.

Ngugi, P.K., 2012b: Financing the Kenya geothermal vision. *Presented at "Short course on geothermal development and geothermal wells", organized by UNU-GTP and LaGeo, Santa Tecla, El Salvador*, 11 pp.

Ngugi, P.K., 2012c: What does geothermal cost? – The Kenya experience. *Presented at "Short course VII on exploration for geothermal resource", organized by UNU-GTP, GDC and KenGen, Naivasha, Kenya*, 13 pp.

Ofwona, C.O., Kipyego, E.K., and Suwai, J.J., 2011: Preliminary well test data of Menengai exploration wells. *Proceedings of the Kenya Geothermal Conference 2011, Nairobi*, Geothermal Association of Kenya, webpage: www.gak.co.ke/kgc2011, 4 pp.

Sanyal, S.K., Murrow, J.W., and Butler, S.J., 2007: Net power capacity of geothermal wells versus reservoir temperature – A practical perspective. *Proceedings of the 32nd Workshop on Geothermal Reservoir Engineering, Stanford University, Stanford, CA*, 7 pp.

Suwai, J.J., 2011: Preliminary reservoir analysis of Menengai geothermal field exploration wells. Report 32 in: *Geothermal Training in Iceland 2011*. UNU-GTP, Iceland, 799-826.

APPENDIX I: Wells MW-5A and MW-17 downhole profiles

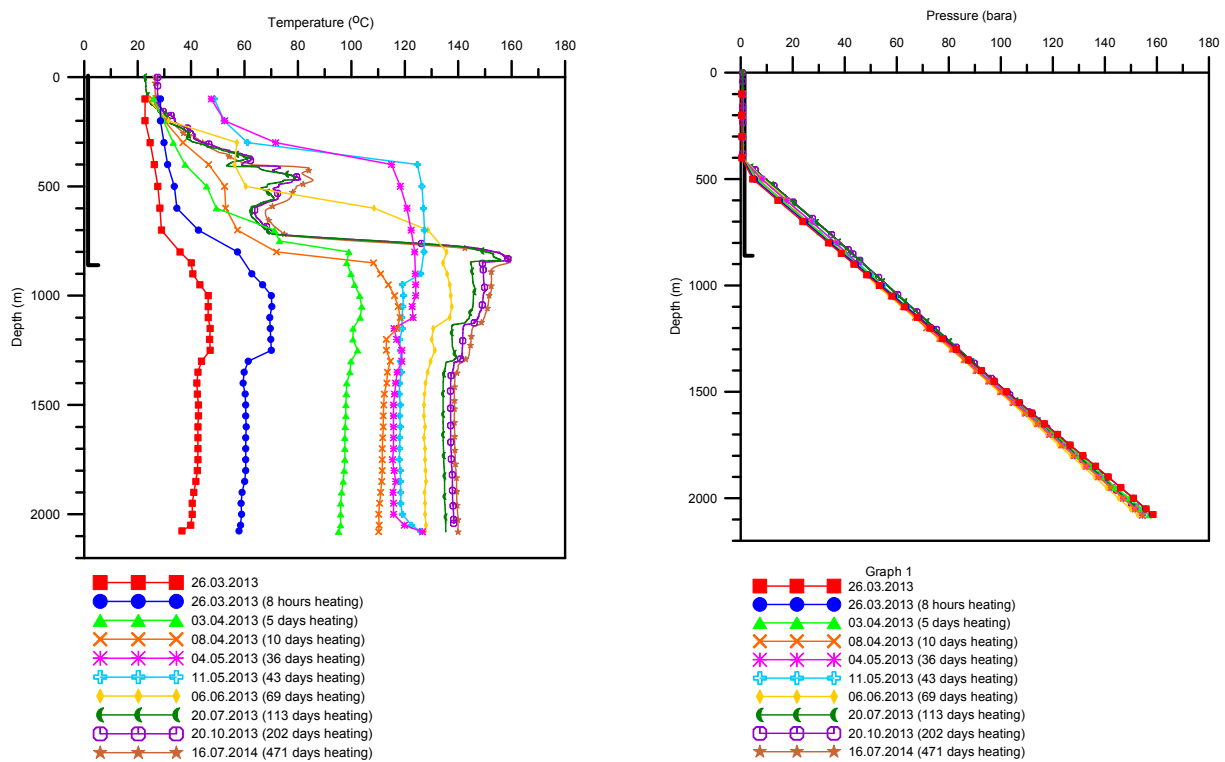


FIGURE 1: MW-5A measured temperature profiles on the left and pressure profiles on the right

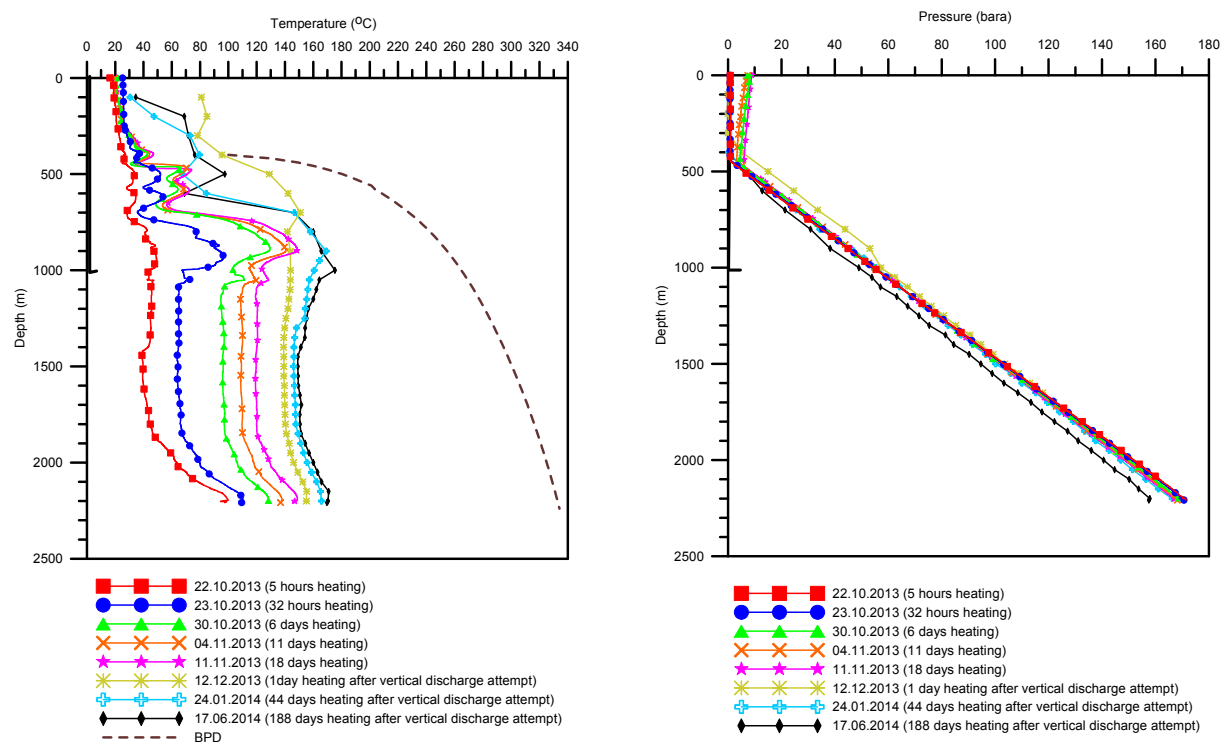
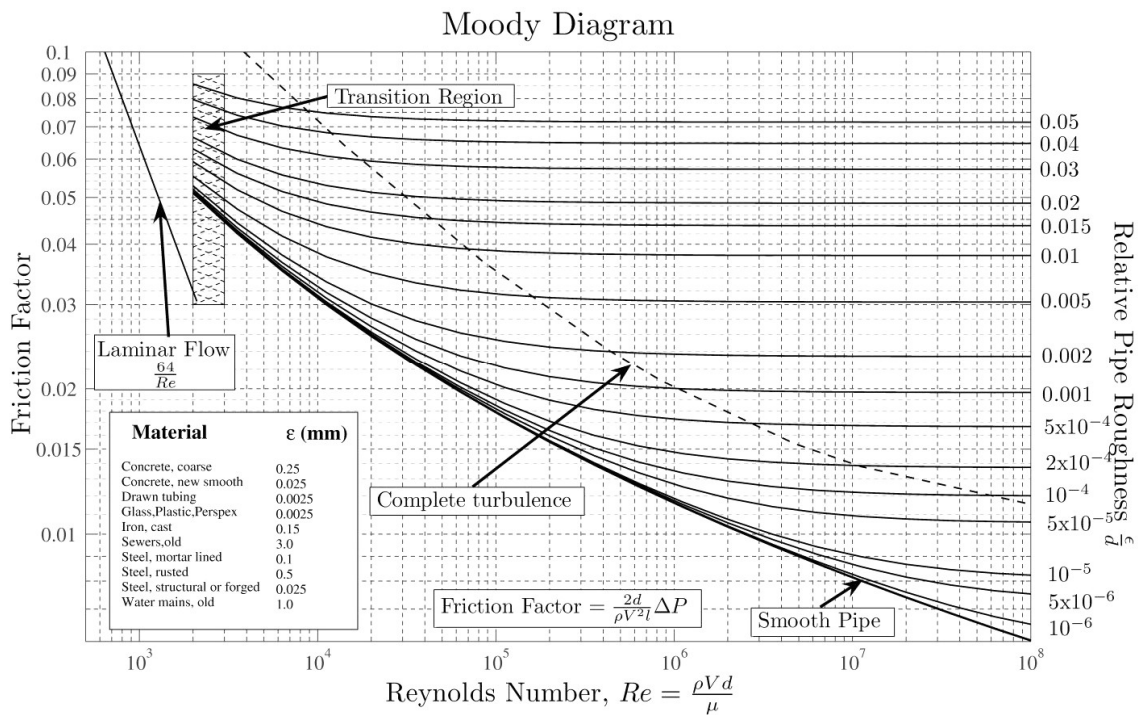


FIGURE 2: MW-17 measured temperature profiles on the left and pressure profiles on the right

APPENDIX II: Moody diagram (Beck and Collins, 2008)



APPENDIX III: An example of EES detailed calculations run

#####PROPOSED BINARY POWER CYCLE ANALYSIS#####Isopentane
run#####Hilary R. M. Mwawasi, UNU 2014#####Optimised run#####

"Cycle conditions"

eta_turbine=0.85
eta_pump=0.75
P_cond=1.5 "bar"
P_atmospheric=0.83 "bar"
T_ambient=30 "^o_C"
P_brine=7 "bar"
T_brine=150 "^o_C"
T_injection=80 "^o_C"
C_p_brine=Cp(Water,T=T_brine,P=P_brine)
"kJ/kg,degC"
m_dot_brine=45 "kg/s"

"Well conditions"

m_dot_well=m_dot_brine "kg/s"
P_well=P_brine "bar"
T_well=T_brine "^o_C"
h_well=Enthalpy(Steam_IAPWS,T=T_well,x=0)
"kJ/kg"
s_well=Entropy(Steam_IAPWS,T=T_well,x=0)
"kJ/kg"

"Station 1"

m_dot_n[1]=m_dot_well
P_n[1]=P_well
T_n[1]=T_well
h_n[1]=Enthalpy(Water,T=T_n[1],P=P_n[1])
s_n[1]=Entropy(Water,T=T_n[1],P=P_n[1])

"Station 2"

m_dot_n[2]=m_dot_n[1]
T_n[2]=T_n[1]
P_n[2]=P_n[1]
h_n[2]=h_n[1]
s_n[2]=s_n[1]

"Evaporator"

"Pinch-point = 5 degC"

Q_e=m_dot_[3]*(h[4]-h[3]) "kJ"
"m_dot_n[2]*(h_n[2]-h_n[3])=m_dot_[3]*(h[4]-h[3])"
m_dot_[3]=(m_dot_n[2]*(h_n[2]-h_n[3]))/(h[4]-h[3])
T[3]=Temperature(Isopentane,P=P[1],x=0)
P[3]=P[1]
h[3]=Enthalpy(Isopentane,P=P[1],x=0)

```

s[3]=Entropy(Isopentane,P=P[1],x=0)
T_n[3]=T[3]+5
P_n[3]=P_n[1]
h_n[3]=Enthalpy(Water,T=T_n[3],P=P_n[1])
P[4]=P[1]
T[4]=Temperature(Isopentane,P=P[4],x=1)
h[4]=Enthalpy(Isopentane,P=P[4],x=1)
s[4]=Entropy(Isopentane,P=P[4],x=1)

```

"Preheater"

```

Q_ph=m_dot_n[3]*(h_n[3]-h_n[4]) "kJ"
P[2]=P[1]
T[2]=T[5]-5
h[2]=Enthalpy(Isopentane,T=T[2],P=P[2])
s[2]=Entropy(Isopentane,T=T[2],P=P[2])
m_dot_[2]=m_dot_[3]
P_n[4]=P_n[1]
T_n[4]=T_injection
h_n[4]=Enthalpy(Water,T=T_n[4],P=P_n[4])
s_n[4]=Entropy(Water,T=T_n[4],P=P_n[4])
m_dot_n[3]=m_dot_n[2]

```

"Turbine"

```

W_turbine=m_dot_[4]*(h[4]-h[5]) "kW"
m_dot_[4]=m_dot_[3]
P[5]=P_cond
{s[5]=s[4]}
h_s[5]=Enthalpy(Isopentane,P=P[5],s=s[4])
h[5]=h[4]-(eta_turbine*(h[4]-h_s[5]))
T[5]=Temperature(Isopentane,P=P[5],h=h[5])
s[5]=Entropy(Isopentane,P=P[5],h=h[5])
m_dot_[5]=m_dot_[4]

```

"Recuperator"

```

"m_dot_1*(h_2-h_1)=m_dot_5*(h_5-h_6)"

```

```

Q_r=m_dot_[5]*(h[5]-h[6]) "kJ"
T[6]=50
P[6]=P_cond
h[6]=Enthalpy(Isopentane,T=T[6],P=P[6])
s[6]=Entropy(Isopentane,T=T[6],P=P[6])
m_dot_[6]=m_dot_[5]

```

"Air condensor"

```

"m_dot_a*(h_c3-h_c1)=m_dot_6*(h_6-h_8)"

```

```

Q_cond=m_dot_[6]*(h[6]-h[8]) "kJ"
m_dot_a=(m_dot_[6]*((h[6])-(h[8])))/((h_c[3])-(h_c[1])) "kg/s"
h_c[3]=Enthalpy(AirH2O,T=T_c[3],r=0.61,P=P_cond)
h_c[1]=Enthalpy(AirH2O,T=T_c[1],r=0.61,P=P_cond)
T_c[1]=T_ambient "°C"
T_c[3]=45 "°C"
P[8]=P_cond
T[8]=Temperature(Isopentane,P=P[8],x=0)

```

```

h[8]=Enthalpy(Isopentane,T=T[8],x=0)
s[8]=Entropy(Isopentane,T=T[8],x=0)
m_dot_[8]=m_dot_[6]
W_fan=(v_dot_a*dP_fan)/(eta_fan*1000) "kW"
v_dot_a=m_dot_a/rho_air "m^3/s"
dP_fan=52 "Pa"
rho_air=Density(AirH2O,T=45,r=0.61,P=P_atmospheric) "kg/m^3"
eta_fan=0.7
P[7]=P_cond
T[7]=T[8]
h[7]=Enthalpy(Isopentane,T=T[8],x=1)
s[7]=Entropy(Isopentane,T=T[8],x=1)

```

"Feed pump"

```

W_pump=m_dot_[1]*((h[1])-(h[8])) "kW"
s[1]=s[8]
h_s[1]=Enthalpy(Isopentane,P=P[1],s=s[1])
h[1]=h[8]+((h_s[1])-(h[8]))/eta_pump
P[1]=7
T[1]=Temperature(Isopentane,P=P[1],h=h[1])
m_dot_[1]=m_dot_[8]

```

"Evaporator heat transfer area (A_e)"

```

A_e=Q_e/(U_e*LMTD_e) "m^2"
U_e=1.600 "kW/m^2^o_C"
LMTD_e=((T_n[2]-T[4])-(T_n[3]-T[3]))/ln((T_n[2]-T[4])/(T_n[3]-T[3])) "°C"

```

"Preheater heat transfer area (A_ph)"

```

A_ph=Q_ph/(U_ph*LMTD_ph) "m^2"
U_ph=1.000 "kW/m^2^o_C"
LMTD_ph=((T_n[3]-T[3])-(T_n[4]-T[2]))/ln((T_n[3]-T[3])/(T_n[4]-T[2])) "°C"

```

"Recuperator heat transfer area (A_r)"

```

A_r=Q_r/(U_r*LMTD_r) "m^2"
U_r=0.400 "kW/m^2^o_C"
LMTD_r=((T[5]-T[2])-(T[6]-T[1]))/ln((T[5]-T[2])/(T[6]-T[1])) "°C"

```

"Air condenser heat transfer area (A_cond)"

```

A_cond=Q_cond/(U_cond*LMTD_cond) "m^2"
U_cond=0.800 "kW/m^2^o_C"
LMTD_cond=((T[6]-T_c[3])-(T[8]-T_c[1]))/ln((T[6]-T_c[3])/(T[8]-T_c[1])) "°C"

```

"Thermal efficiency (eta_th)"

```

eta_th=(W_net*100)/Q_in "%"
W_net=W_turbine-W_local "kW"
W_local=W_fan+W_pump+W_esp "kW"
W_esp=655 "kW"
Q_in=m_dot_n[1]*(h_n[1]-h_n[4]) "kJ/kg"

```



UNITED NATIONS
UNIVERSITY

UNU-GTP

Geothermal Training Programme

Orkustofnun, Grensasvegur 9,
IS-108 Reykjavik, Iceland

Reports 2014
Number 23

CEMENTING PROCESSES IN GEOTHERMAL WELL DRILLING: APPLICATION AND TECHNIQUES

Samuel Ikinya Ng'ang'a

Kenya Electricity Generating Company Ltd. - KenGen

P.O. Box 785-20117, Naivasha

KENYA

snganga@kengen.co.ke

ABSTRACT

During drilling of deep high temperature geothermal wells, zones of weak or fractured formations are encountered. These zones pose a challenge to the quality and effectiveness of the cementing process. Losses are encountered during cementing which require top jobs to complete and anchor the various casing strings back to surface with cement. The cement sheath should be able to withstand the cyclic thermal-induced loading through the operational life of a geothermal well. Cement is also used to plug zones of large circulation losses and to stabilize collapsing weak zones which slow down the drilling process. Well cementing is one of the operations which impacts the overall cost of well drilling process.

In deciding the type of cement slurry to be placed for each of the casing strings in the well's profile, adjustments are made on cement properties as per the strength of the open borehole walls (lithology). The open borehole wall's strength is dependent on geological conditions of the section to be cemented. Cement properties such as viscosity, thickening time and strength are of prime consideration when engineering for the highest probability of successful primary cementing operations (Lecourtier and Cartalos, 1993). The viscosity and thickening time must be optimized so that the slurry remains pumpable long enough to place the cement across the desired zones and achieve the top of cement (TOC). Additionally, cement should set as quickly as possible after pumping is stopped to minimize the wait on cement (WOC) time while achieving necessary structural integrity for retaining zonal isolation throughout the life of the well. The physical properties of cement need to be customized for the specific attributes of each well. Each well is unique in regard to pore pressure and the fracture gradient, bottom-hole temperature, bottom borehole pressure, physical properties of the formation, properties of the fluids already in the wellbore, wellbore deviation and annular space clearance. It is critical to perform cementing operations with cost and integrity of the operation in mind. With proper cementing procedures, drilling time and cost can be optimized (Halliburton, 2005).

Cement manufactured to API specification class A is usually utilized in Kenya, and additives are added to improve its properties and customize it to a particular well environment. This report gives an outline of different cement placement methods, both for plugging large circulation losses, and for casing cementing under certain conditions. The methods will be compared to the method applied in Olkaria, Kenya for primary casing cementing and remedial top cementing of casing at eight hour intervals. Quality assessment of the cementing process, through laboratory tests and post cementing assessment, through the use of cement bonding logs and temperature logs, is also discussed.

1. INTRODUCTION

One of the major challenges experienced during the drilling of geothermal wells in Olkaria, Kenya is cement losses during the cementing of casings, often requiring top jobs (backfills) to complete. Deep geothermal well drilling involves the installation of several casing strings of different sizes which are cemented fully back to the surface using different placement methods. A primary cementing job is planned with the objective of achieving the desired top of cement (back to surface) and reducing the number of cementing top jobs (backfills).

Other than cementing casings, cement is used to seal zones of large circulation losses and weak collapsing sections of the well, encountered during drilling of the casing sections, except for the production section of the well which is lined with slotted liners. Use of cement as a lost circulation material (LCM) is not only effective but it guarantees durable results and the best possible cementing of the casings. It also lowers the risk of stuck drill pipes and assists in circulation of drilling cuttings back to the surface (NZS, 1991).

Cementing operation processes mainly involve the components shown in Table 1 (Thórhallsson, 2014).

TABLE 1: Components of cementing process operation

No	Component	Function
1	Expertise	<ul style="list-style-type: none"> • Cementing engineer • Service company/Self cementing service • Suppliers
2	Modelling	<ul style="list-style-type: none"> • Drilling contractor • Calculation of slurry volumes, materials requirements, displacement volume, time
3	Placement methods	<ul style="list-style-type: none"> • Temperature and pressure during cementing • Open ended • Plug method • Inner string method • Reverse circulation method
4	Casing hardware	<ul style="list-style-type: none"> • Use of casing packer • Two stage cementing • Casing guide shoes • Cementing heads • Collars • Plugs • Centralizers
5	Cement and additives	<ul style="list-style-type: none"> • Dope and thread compound • Type of neat cement • Additives to be added- retarders, fluid loss, friction reducer and accelerator • Density control
6	Testing and quality control	<ul style="list-style-type: none"> • Cement laboratory test-rheology, thickening time, strength, water loss and density • Density measurement during mixing
7	Reporting	<ul style="list-style-type: none"> • Cement bond logs (CBL), temperature logs and pressure testing. • Cementing program • Casing tally • Cement report

The cementing method used in Olkaria, Kenya is the single stage plug method, which involves pumping a calculated volume of cement into the casing, placing a movable top plug on top of the cement, and then displacing the plug downward by pumping water on top of it. This forces the cement to flow out through the casing shoe at the bottom of the casing string and up the annulus between the casing and the wellbore. Top job (backfills) cementing through the annulus is required in most casing cementing to completely fill the cement to the surface. The cement is blended with retarder, anti-fluid loss, friction reducer, loss circulation materials and a light agent (Wyoming bentonite) to improve its properties and make it pumpable through the casing and up the annulus. Top job cementing is carried out through the annulus using neat (un-blended) cement in eight hour intervals till the casing is fully cemented. Cement samples collected during cementing are observed for hardening before drilling is continued. A summary in Tables 2 and 3 shows a typical cementing job analysis and casing data in Olkaria for well OW-43A.

TABLE 2: Cementing job summary of well OW-43A

Casing size	Casing weight (lb/ft.)	Setting depth (m)	Average specific weight (ASW) (kg/l)	Materials and data	Remarks
20"	94	58.73	1.68	Primary Cement used = 19.4 tons ASW = 1.682 kg/l Total Cement Used in 20" casing = 19.4 tons	Cement received on surface
13-3/8"	68.0 & 54.5	300.75	1.68 1.63 1.63 1.67 1.65	Primary Cement used = 36.8 tons ASW = 1.681kg/l Backfills 1 st backfill = 13.0 tons ASW = 1.68 kg/l 2 nd backfill = 19 tons ASW = 1.63 kg/l 3 rd backfill = 6.20 tons ASW = 1.67 kg/l 4 th backfill = 4.3 tons ASW = 1.65 kg/l Total cement used in 13-3/8" = 89.4 tons	No cement received on surface No cement received on surface No cement received on surface Cement received on surface but dropping Cement received on surface
9-5/8"	47	756.25	1.65 1.68 1.65 1.60	Primary Cement used = 28.7 tons ASW = 1.65 kg/l Backfills 1 st backfill = 12.40 tons ASW = 1.68 kg/l 2 nd backfill = 12.1 tons ASW = 1.65 kg/l 3 rd backfill = 6.9 tons ASW = 1.6 kg/l Totals cement used in 9-5/8" casing = 60.2 tons	No cement received on surface No cement received on surface. No cement received on surface. Cement returns received on surface.
Total cement used in OW-43A				168.9 tons	

TABLE 3: Casing data of well OW-43A in Olkaria

Casing Size	Weight (lb/ft.)	Grade	No. of joints	Length (m)	Casing shoe depth (m)
20"	94.59	K55	4	45.03	58.73
13-3/8"	54	K55	26	265.72	300.75
	68	K55	2	23.21	
9-5/8"	47	K55	66	730.41	741.79
7" Slotted liners	26	K55	205	2272.42	3001
7" blank liners	26	K55	2	22.18	

Assessment of the adequacy of casing cementing involves continual monitoring and recording of the returns and materials consumed with respect to time, during the course of every casing cementing operation. Correlation of such information with theoretical volumes of casing and annuli being filled provides information on the quality of the final casing cementation (e.g. premature return of a fluid may indicate inadequate mud removal or collapsed borehole; late returns may be caused by partial losses or an over-gauge hole). The correlation is necessary to optimize remedial cementing operations and to evaluate the integrity of the final cementation (NZS, 1991).

The geology of Olkaria area is generally characterized as follows:

0-100 m: Pyroclastic: This is a thick layer of unconsolidated clastic materials consisting of soils, volcanic ash and lithic rock fragments including pumice, tuff, obsidian, rhyolite and trachyte. This is a zone of soft and incompetent formation where caving-in is expected.

100-300 m: Rhyolite: This stratum consists of slightly altered rhyolitic lavas with minor intercalations of tuff. This formation is medium hard and is generally massive, though fractured. Minor losses during drilling are expected to occur.

300-650 m: Rhyolite and Trachyte: This zone is characterized by trachytic and rhyolitic lava flows. The formation is quite compact and massive and is expected to be medium hard. Alteration and oxidation intensities vary with depth and minor intercalations of tuff and rhyolite are expected. Minor losses are expected at fracture zones.

650-1400 m: Trachyte, tuff and basalt: This zone is generally massive but slightly fractured, characterized by trachyte, tuff, rhyolite and basalt intercalations. This zone is moderately altered and fractured and circulation losses are expected at fracture zones.

1400-2100 m: Trachyte with rhyolite and basalt: This zone is generally characterized by the trachytic and rhyolitic lava flows with minor basalt intercalations. The rock is expected to be moderately altered and fractured, but medium hard. Circulation losses are expected at fault or fracture zones.

2100-2500 m: Trachyte and rhyolite: Trachyte dominates this lower part of the well with occasional rhyolite. Thin intrusives are also expected to start appearing in this zone. The formation is medium hard to hard and is competent, therefore, not many problems are expected except minor losses or partial losses, especially at fracture or fault zones.

2500-3000 m: Trachyte with Syenitic and doleritic intrusions: This zone is composed of trachyte with occasional Syenitic and doleritic dyke intrusives. The formation here is compact and is expected to be hard and competent. Minor or partial losses are expected at fracture or fault zones.

The cemented casings are set as follows: Surface casing between 60 and 100 m, anchor casing between 300 and 400 m, and production casing between 750 and 1200 m, depending on the area being drilled. Figure 1 shows the well design and the depths of the casing strings.

2. WELL DESIGN AND CEMENTING

2.1 Geothermal well design

Well design is a detailed program of work to be undertaken during drilling of a well and it defines the desired final status. The design steps which are necessary to drill a deep well safely include (NZS, 1991):

- Geological and reservoir conditions of the area to be drilled;
- Determination of the casing depths and well completion;
- Selection of casing diameters, thicknesses, cementing material and programmes;
- Deciding the drilling fluids, drill string assemblies and wellheads; and
- Selection of the necessary equipment, tools, materials, support facilities and site requirements.

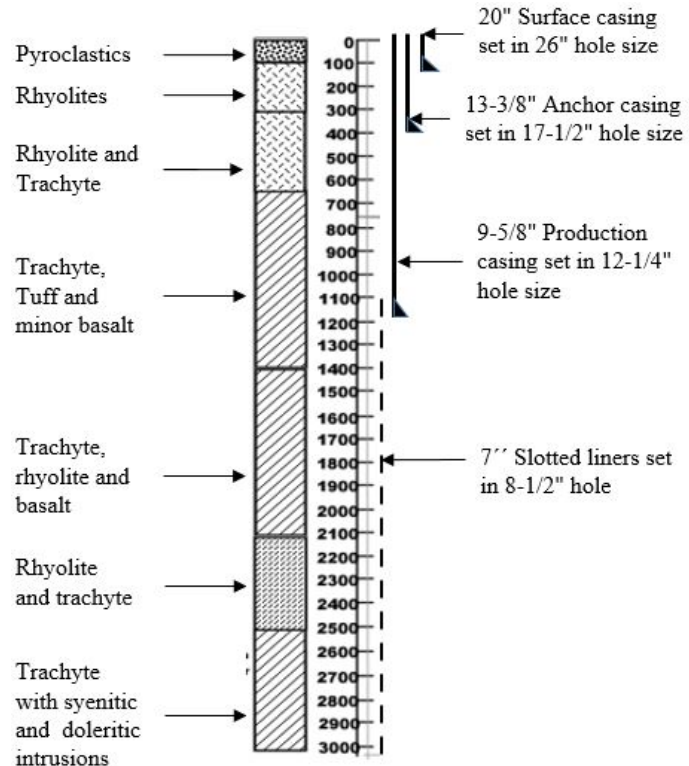


FIGURE 1: Well design in Olkaria Kenya (Kengen)

2.2 Functions of cementing

Cement plays a key role in the integrity of a geothermal well and is a critical component of the well designing process (Nelson, 2012). The wells act as a high pressure containment vessel at elevated temperature which should resist failure by deformation, fatigue, fracturing, and corrosion during its operating life (Agapiou and Charpiot, 2013). The two main functions of the casing cementing process are:

- To restrict fluid movement between the formations (zonal isolation); and
- To bond, anchor and support the casing together with associated wellhead equipment.

In addition cement assists in:

- Protecting the casing from corrosion;
- Preventing blowouts by quickly forming a seal; and
- Protecting the casing from shock loads in deeper drilling.

For open borehole condition and repairs, cement is used to:

- To seal off zones of high loss of circulation during drilling;
- Stabilize weak and collapsing wellbore sections;
- Plug (seal off) a well for abandonment;
- Plugging and side tracking/ directional drilling a hole around a non-retrievable fish or due to geological reasons; and
- To plug a well temporarily for re-casing (Hole, 2008a).

2.3 Casing equipment

Casings are connected together, either by screwing or welding, to form a casing string, which is then lowered into the drilled borehole. As the well deepens, the diameter of each casing string is usually smaller than the preceding one. The accessories fitted to a casing string to enable the cementing process to be carried out include (Hole, 2008a):

1. Guide shoe (float shoe) – fitted to the bottom of the first casing and is usually tapered in order to guide the casing toward the centre of the wellbore during installation, minimizing contact with the wellbore walls. It may contain a non-return valve to restrict fluid flow into the casing. Figure 2 shows two types of guide shoes commonly used;
2. Float collar-fitted between the first and the second casing or between the second and the third casing. It contains a non-return valve to prevent reverse flow of cement slurry. For the inner string cementing method, the float collar has a stab-in or latch receptacle to take in the drill pipe end fitted with a tag in adaptor. Figure 3 shows float collars commonly used;
3. Centralizers, fitted along the casing string at pre-determined intervals. They assist in preventing sticking of the casing while lowering them into the well and keeping the casing in the centre of the wellbore. Centralizing the casing ensures uniform placement of cement sheath in the annulus between the casing and the borehole wall. Figure 4 shows a bow centralizer;
4. Bottom plug - usually elastomer, used to separate cement and the drilling fluids in the well during the casing cementing method. It has a membrane which ruptures when it lands at the stop collar under the cement pressure in order to allow the flow of cement through;
5. Top plug - elastomer (rubber) separating cement slurry and the displacing fluid during the casing cementing method. Figure 5 shows top and bottom plugs;
6. Tag in adaptor and string centralizers - used when utilizing the inner string cementing method to adapt the drill pipe into the float collar receptacle. The centralizer (usually optional) aligns the drill pipe string to the centre of the casing for ease of stabbing or for latching the drill pipe cementing string to the float collar, depending on the type of inner string adaptation method used (Hole, 2008a).

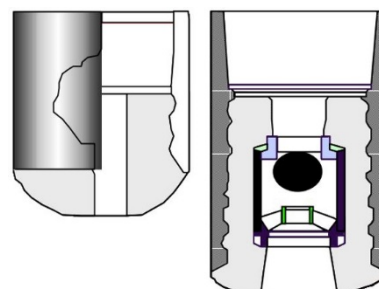


FIGURE 2: Guide shoes (Rabia, 2001)

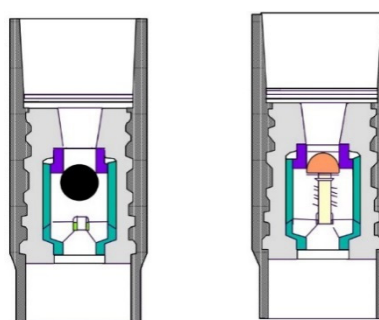


FIGURE 3: Float collars (Rabia, 2001)

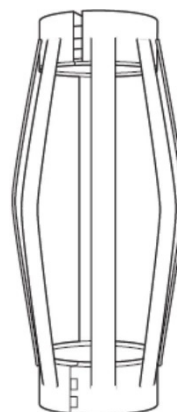


FIGURE 4: Bow centralizer (Bett, 2010)



FIGURE 5: Top plug-solid, and bottom plug-hollow (Rabia, 2001)

2.4 Cementing materials

Portland cement, used as the bonding compound between the casing and the formation, consists of mainly anhydrous calcium silicate and calcium aluminate compounds, which hydrate when added to water to provide strength and low permeability for zonal isolation. Other special grades/ formulations of cement are produced as per the API10 specification for well cementing, and are divided into classes A to H depending on the properties (Rabia, 2001). Cement additives are used to make different cement blends, depending on the wellbore conditions, and are classified according to the functions they perform (Nelson, 2012). They include:

1. Silica flour - this is fine-ground quartz which prevents strength retrogression and increases the porosity of cement in a high temperature environment (Guerra, 1998). According to the New Zealand code of practice for deep geothermal wells, silica flour of over 20% by weight of cement may result in the deterioration of the cement in the presence of carbonating ground waters (NZS, 1991);
2. Accelerators - they reduce the cement setting time and increase the rate of compressive strength development. Inorganic chloride salts are mainly used with calcium chloride being the most commonly used cement accelerator (Nelson, 1990);
3. Retarders - they are used to delay the setting time and extend the pumping time of cement slurry by slowing down the cement hydration process. They are added to counter the effects of high temperatures in the wellbore, especially in the anchor and production casing sections. Common retarders used include sugar and lignosulphonates (Rabia, 2001);
4. Extenders (light weight agent) - they reduce the amount of cement per unit volume (slurry density) and also increase the slurry yield. Water-based extenders, such as Wyoming bentonite, allow the addition of excess water to achieve slurry extension, while maintaining a homogeneous slurry, and prevent the development of excess free water (Nelson, 1990);
5. Fluid loss control agents - they control leakage (loss) of water from cement slurry into the formation, preserving the design properties of the cement slurry. Fluid loss agents decrease cement filtration by decreasing cement permeability or by increasing the viscosity of the aqueous phase of the cement. Finely divide particulate materials, such as bentonite, and water-based polymers, such as hydroxyethylcellulose (HEC), are the two main classes of anti-fluid loss agents (Nelson, 1990);
6. Lost circulation control agents - they limit the flow of cement slurry out of the well into the weak fractured formation and ensure that the cement slurry is able to fill the entire annular space. Medium coarse grade mica flakes are commonly used as loss of circulation agents (Nelson, 2012);
7. Dispersant (friction reducers) - they reduce slurry viscosity, which allows a lower pumping pressure during placement. Dispersants are negatively charged polymers which adsorb onto the positively charged particles, thereby reducing particle interaction and making them more mobile (Nelson, 1990); and
8. Antifoam agent - used to reduce air entrapment and foaming during mixing by altering the surface tension of the mixing water and the way cement solids disperse during mixing.

3. TYPES OF CEMENTING OPERATIONS

3.1 Casing cementing

There are three main casing cementing operations conducted during the drilling of a deep geothermal well, namely: surface casing, anchor casing and production casing. Cement has to support the casing uniformly to the surface as the thermal expansion stresses the steel beyond the yield point. It also has to block any fluid movement up the annulus, either from the formation or through a casing leak. When the casing to casing annulus has water entrapped by good cement, heating and expansion of the trapped water can lead to collapse of the inner casing (Thórhallsson, 2014).

Proper centralization of the casing, especially in a deviated well, and taking into account the hole's profile (kick off and build up) are essential for effective casing cementing. The other important factor is borehole cleaning of the drilling fluid prior to cementing, which should be continued even with all the casing downhole (last circulation). The last circulation improves borehole cleaning and, at the same time, cools the wellbore which is critical in geothermal well cementing. The casing string should be reciprocated periodically during circulation to avoid differential sticking, while also checking on the returns for cutting and circulation temperature (Lecourtier and Cartalos, 1993; NZS, 1991).

3.2 Cement plugging and loss of circulation control

3.2.1 Loss of circulation control

One of the major challenges in drilling a geothermal well is loss of circulation during drilling of highly fractured zones. Adequately cementing the casing through lost circulation zones is a major challenge and a major cost (Finger and Blankenship, 2010). If the loss of circulation cannot be regained through the use of loss circulation materials (LCM), the alternative is to use cement plugs for non-productive zones of the well that are to be cased off. Lost circulation plugs are used to isolate the fractured zones and create a seal between the zone and the wellbore. Open drill pipes positioned near the suspected loss zone are used to place the calculated quantity of cement slurry. A whole series of plugs is often required before a satisfactory result is obtained (Rickard et al., 2012).

In addition to the drilling time and material costs, loss of circulation plugging risks drilling pipes being filled with cement or, worse still, getting cemented in the well. To decrease the risks of difficulties, the tubular equipment that runs through the mixtures containing cement should be re-drillable (fibreglass or aluminium) (Lecourtier and Cartalos, 1993). Two main methods are normally used to seal loss circulation zones using cement plugging, namely the balanced plug method and the drift plug method.

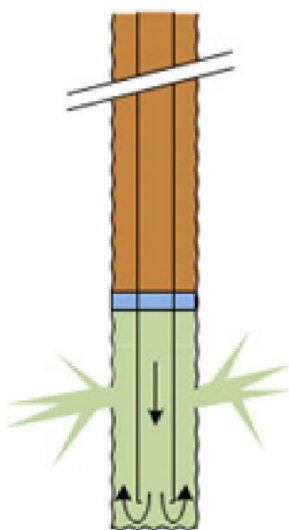


FIGURE 6: Balanced plug method (Rickard et al., 2012)

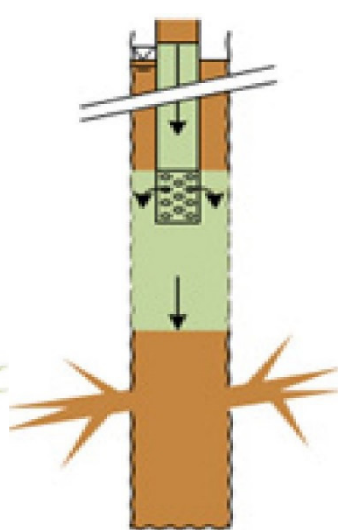


FIGURE 7: Drift plug method (Rickard et al., 2012)

The balanced plug method consists of pumping the desired quantity of cement slurry through the drill pipe or tubing until the level of cement outside is equal to that inside the string. Figure 6 shows the placement of the balanced plug method in a well. This process involves running the drill pipes past the loss zone and displacing cement as a balanced plug into and above the loss zone. Balanced plugs are effective when the loss rate is low enough that cement stops going into the formation long before it sets (Rickard et al., 2012).

Drift cement plug method involves placing the cement slurry above the loss zone and allowing it to flow (drift) downwards towards the loss zone as one single mass of cement. This method is effective for plugging severe loss of a circulation zone but is not suitable for partial loss of circulation. The method uses a diffuser to

divert the cement flow in a lateral direction, instead of vertical as in the balanced plug method. A cement diffuser is a piece of drill pipe plugged and bull-nosed on the bottom with several cut holes around the circumference. The lateral flow creates a piston-like plug in the borehole. The cement slurry is displaced to create a hydraulic head inside the drill pipe (Rickard et al., 2012). Figure 7 shows the placement of a drift plug in a well.

3.2.2 Cement plugging for repairs and abandonment

When side tracking a hole around a stuck bottom hole assembly, or changing the direction of drilling for geological reasons, a cement plug is placed at the required depth to change the wellbore direction or to help support a mechanical whipstock so that the bit can be guided in the desired direction. Cement plugging is used to seal off the well bore in a case of complete abandonment, due to drilling challenges or a producing well that has been damaged (Remedial Cementing, 2013).

4. CEMENTING PROCESS AND SLURRY DESIGN

4.1 Geothermal wellbore conditions

Effective cleaning of the wellbore prior to cementing through removal of the drilling fluid improves the quality of the bond between cement, casing and formation. One way of cleaning the wellbore is by the use of chemical washes which help remove the drilling mud through dilution, thinning (preventing mud flocculation and gelling) and dispersing it. Chemical washes are fluid with density and viscosity higher than the drilling fluid but lower than that of cement (containing dispersants and surfactants), which are pumped ahead before cementing to help remove the drilling mud through dilution, thinning and dispersing (Devereux, 1998).

Wellbore conditioning during the last bit run before tripping out helps in cleaning the wellbore before running the casings. After running the casings, circulation of water at least 110% of the casing internal volume is usually continued to further clean and condition the wellbore before cementing. This should be accompanied, where possible, with reciprocating the casing string up and down to scrape mud from the wall of the wellbore to ensure flow around all portions of the well (Bett, 2010).

4.2 Calliper logs

In preparing a well for cementing, it is important to measure the diameter of the borehole in order to estimate the volume of the cement slurry required. This is done by measuring the size and shape of the borehole (open hole) along its depth using a calliper logging tool. Multi-finger calliper tools utilize either mechanical or sonic means to measure the diameter of the well at numerous locations simultaneously, accommodating all the irregularities in the wellbore diameter. Other uses of calliper logs include detecting deformations, build up in case of scaling, and metal loss due to corrosion in casings. Even with a calliper log, it is advisable to have excess (allowance) volume (120%) to cover for losses and fill up the cavities in the wellbore (Schlumberger, 2014).

Figure 8 shows a calliper log and Figure 9 shows cement volume estimates from the logs for 9-5/8" casing of well HE-53 in Hellisheidi geothermal field in Iceland. The anchor casing of 13-3/8" was set at 300 m, while the production casing of 9-5/8" was set at 846 m. The total cement estimate was 34.89 m³.

4.3 Casing design

The main functions of the casing strings are:

1. Prevent borehole collapse in weak and fractured formations;
2. Allow safe drilling of the well; support and anchor the wellheads;
3. Fluid pressure control;
4. Protect and control contamination of subsurface aquifers;
5. Counter circulation losses during drilling;
6. Protect the integrity of the well against corrosion, erosion or fracturing; and
7. Define the production zone if the reservoir has more than one production zone (Rabia, 1987; Hole, 2008b).

Casings are characterized by three measurements, namely: diameter (nominal outside diameter), weight (weight per unit length-material thickness), and grade (materials tensile strength); their selection is guided by API (American Petroleum Institute) or equivalent ISO standards. Determination of casing depths depends on rock properties, formation fluid, surface casing setting, well control requirements and

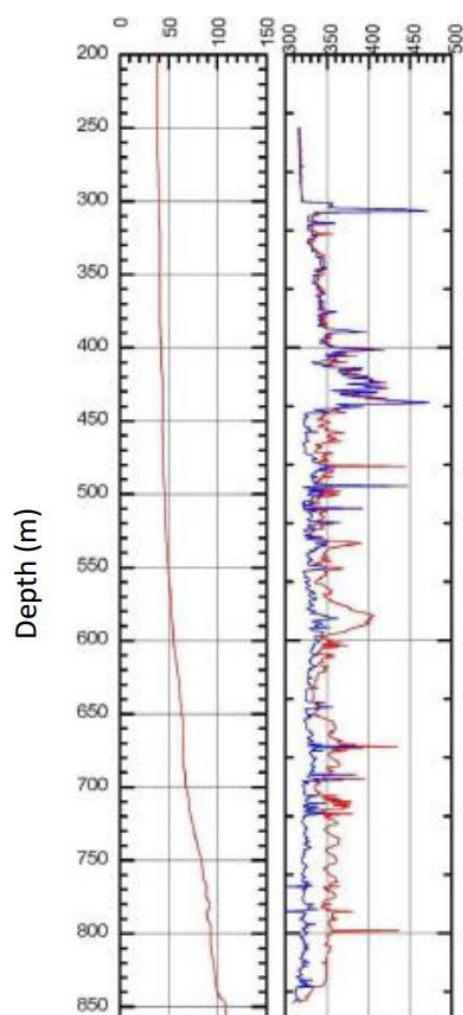


FIGURE 8: Calliper logs of well HE-53 in Hellisheidi, Iceland (Sveinbjornsson, 2014)

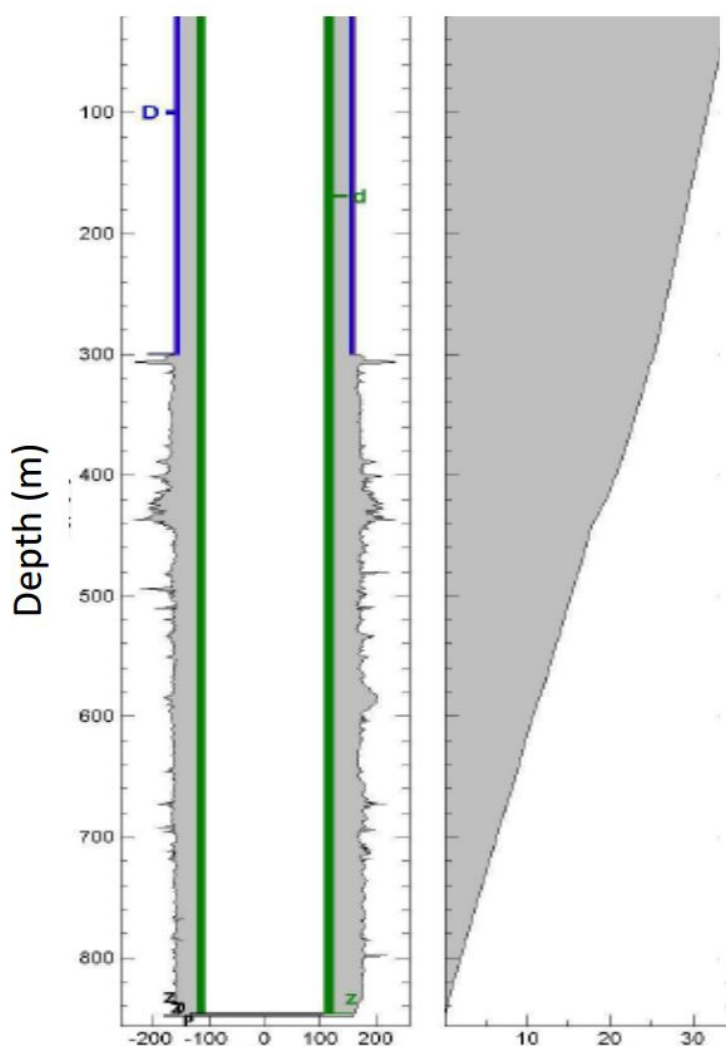


FIGURE 9: Cement estimate using calliper log of well HE-53 in Hellisheidi, Iceland (Sveinbjornsson, 2014)

regulatory requirements (Finger and Blankenship, 2010). Selection of casing depths is guided by the available drilling and well data but, in absence of the data, casing depths can be approximated using the boiling point depth curve (a column of water at boiling temperature throughout its depth) and the water table level (depth to be taken below the water table level). The pressure inside the well at the casing shoe for each casing string shall not exceed the overburden pressure (formation fracture pressure), assuming the well is filled with steam (NZS, 1991). Another criteria used in Iceland is to consider the pressure from a column of water or heavy mud inside the casing exceeding the pressure in the well at the casing shoe for two phase flow (Thórhallsson, 2014). Figure 10 shows casing selection using the New Zealand standard.

The following cemented casing strings are used in geothermal well drilling in Kenya:

1. Surface casing - this is run to prevent caving of weak near-surface formations, support initial drilling wellheads and to contain circulating drilling fluid. A typical size of this casing is 20" K55 94 lb/ft. in Kenya;
2. Anchor casing - protects the surface aquifers, prevents circulation losses during deeper drilling and supports the drilled wellhead and, later, the permanent wellhead after well completion. Typical casings utilized are 13-3/8" K55 54 lb/ft. and 68 lb/ft; and

3. Production casing - seals off low temperature aquifers, conveys geothermal fluids to the surface and supports drilling to the total depth of the well. Typical casings utilized are 9-5/8" K55 40 lb/ft. and 47 lb/ft. Casing strings and a liner commonly used in a geothermal well are shown in Figure 11.

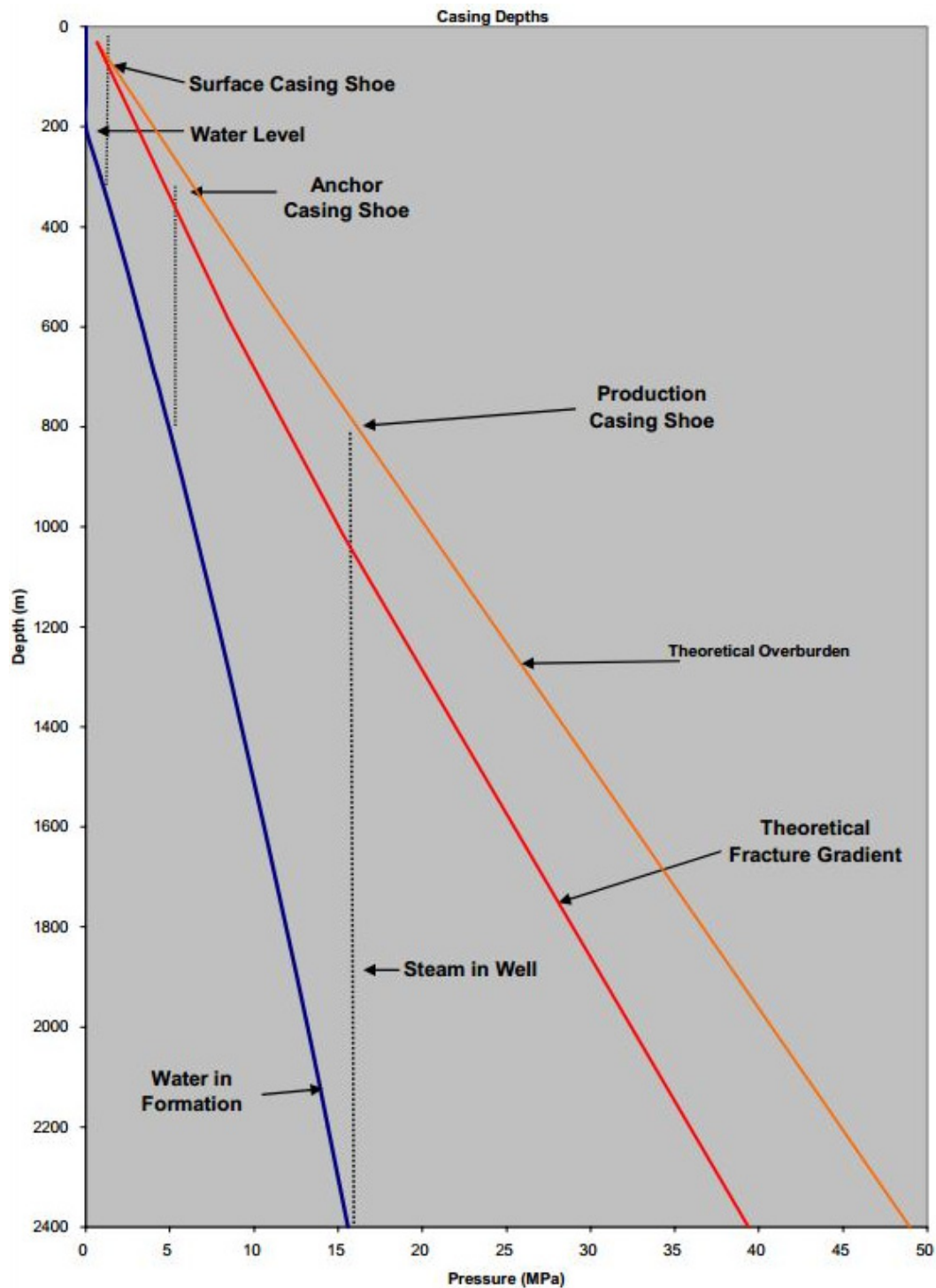


FIGURE 10: Theoretical casing selection (Hole, 2008b)

In well casing design, three types of loading are considered, namely: burst pressure, collapse pressure and axial loading, which are functions of the casing grade, wall thickness and tensile strength. The effects of pressure, temperature, and temperature changes which may occur during drilling and operation of a geothermal well should be considered. Casing string axial loading before cementing is a result of a casings' own weight less the buoyancy effect of the fluid in the well and the drag for deviated wells. However, after cementing the casing cannot expand freely and, therefore, compressive and tensile loading are induced due to temperature changes (Hole, 2008b). Internal fluid pressure can result in a casing bursting, especially before and during cementing, while external fluid pressure can result in casing collapse while displacing cement to the annulus and due to the column of cement after cementing. Safety margins are usually added while designing for the different casing loading situations.

4.4 Cement blending

Portland cement in Olkaria, Kenya is usually mixed with other additives to make a cement blend to be used for casing cementing. Neat (without additives) cement is mainly used for plugging a loss zone and is sometimes mixed with accelerators to shorten the setting time. Typical composition by weight of cement (BWOC) includes:

- Cement class A;
- Silica flour (proposed) - 15% to 20% (BWOC);
- Mica (LCM) - 3% BWOC;
- Wyoming Bentonite - 2% BWOC;
- Retarder - 0.3% BWOC;
- Fluid loss control - 0.3% BWOC; and
- Friction reducer (dispersant) - 0.3% BWOC.

Other additives added in new cement slurry designs are perlite, hollow microspheres and nitrogen gas for foamed cement slurry, all of which are aimed at lowering the cement density for improved geothermal casing cementing (Bett, 2010). Latex is also added to cement to improve on corrosion resistance, fluid loss control and high temperature solid-suspension properties. Slurries blended with latex have better wetting properties, low viscosities and increased resiliency resulting in increased bonding strength and a tighter annular seal. Advantages of foamed cement slurry include:

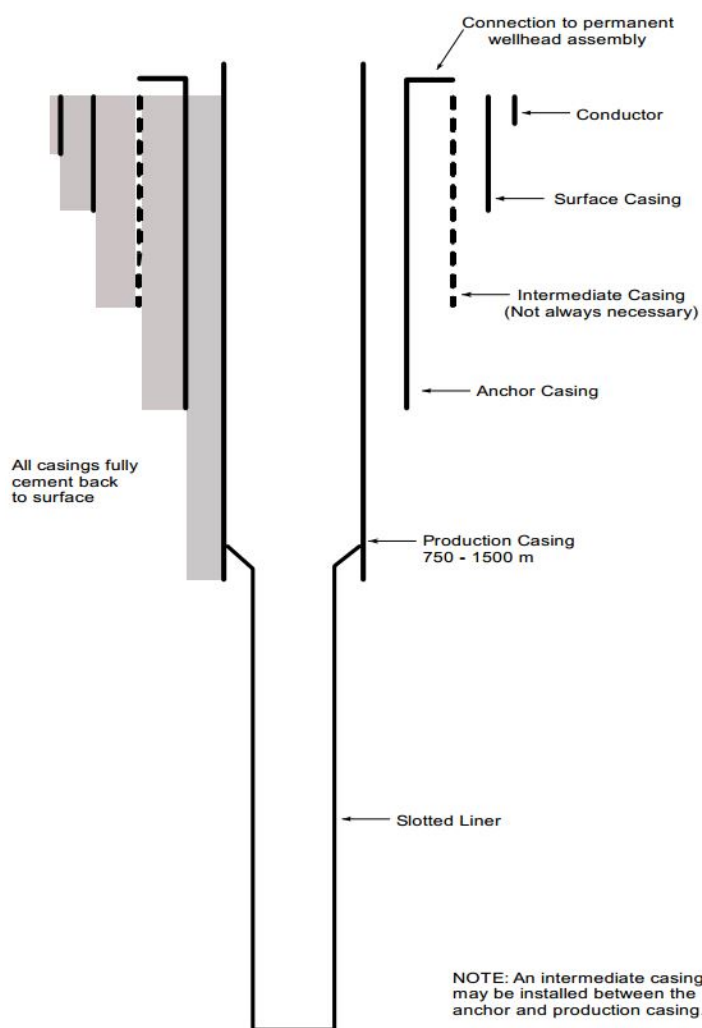


FIGURE 11: Casing strings and a liner for a typical geothermal well (Hole, 2008b)

- Low density which makes it easier to cement weak formations without exceeding the fracture pressure of the formation;
- Foamed cement develops very high compressive strength which enhances protection against gas invasion and reduces chances of casing corrosion; and
- Foamed cement is more ductile and can withstand thermal expansion and contraction without cracking and compromising the sealing effect (Hernández and Nguyen, 2009). Figure 12 shows schematic cement preparation.

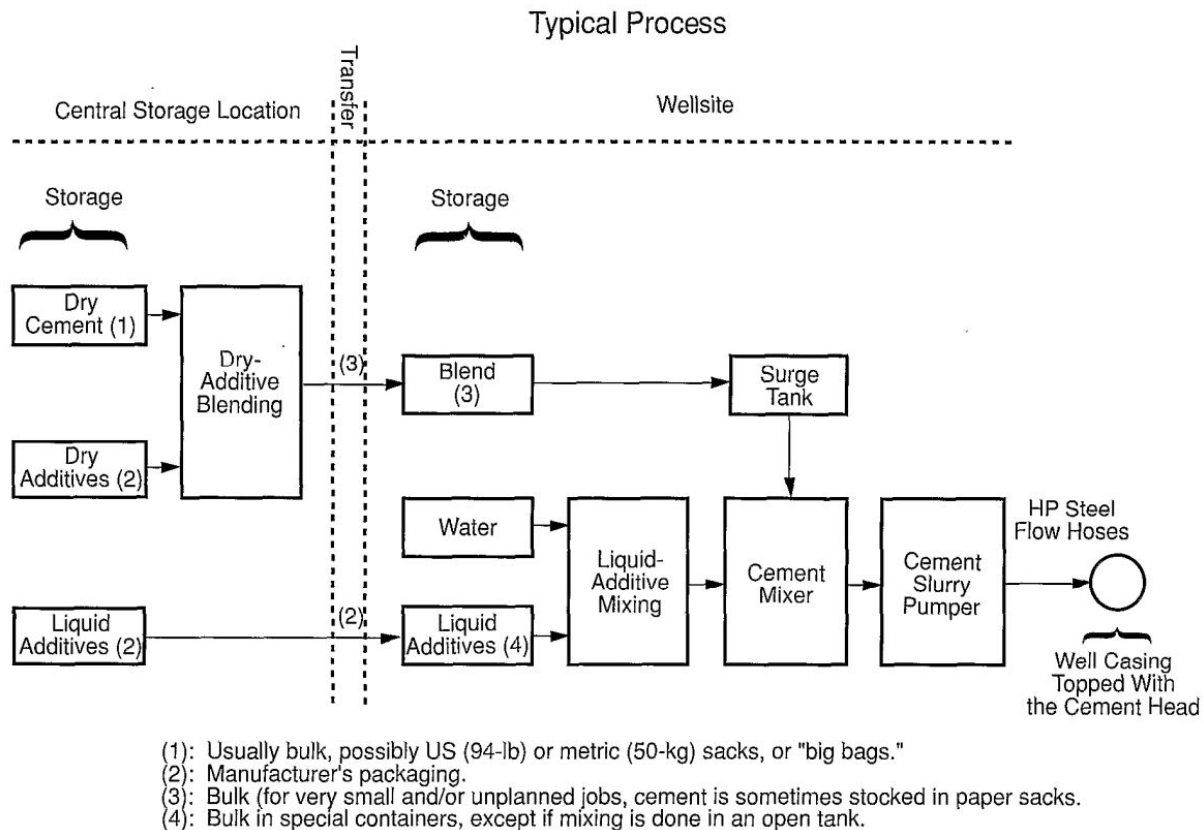


FIGURE 12: Cement mixing process (Nelson, 1990)

4.5 Cement mixing and pumping equipment

Cement and cement additives are usually handled in bulk for ease of blending and transportation to the rig site. Cement and dry additives are combined in a blending tank where they are weighed, depending on the blending recipe, and then are thoroughly mixed together to make the blended cement. The mixer is then blown, using compressed air, to the storage tanks. Blended and neat cement is stored in air tight steel silos (tanks) with capacities of up to 50 m³, aerated with compressed air during loading and offloading. Pneumatic transport tanks are used to transfer cement from the blending and storage site to the rig site in preparation for cementing.

During cementing, cement is mixed with water to form cement slurry, either by a jet mixer or a recirculation mixer. A jet mixer consists of a hopper, which controls dry cement flow, a mixing bowl where water is injected at high pressure to mix with dry cement, a discharge goose neck to control the slurry density, and a slurry tub contain the cement slurry for pumping. Slurry density is adjusted by controlling the rate of water and cement flow from the jets and hopper. A recirculation jet mixer recirculates some of the slurry through the mixing system, using a centrifugal pump feeding the displacement pump, thereby improving on the slurry homogeneity and viscosity. Density in the

recirculation jet mixer is controlled by opening or closing the sliding gate between the hopper and the mixer (Nelson, 1990).

Modern cementing units use recirculation mixer without jets; they are mainly composed of a high energy mixer (injector), a cement control valve which is either manual or computer controlled, an expanding tank to remove entrapped air and dust in the first mix, a mixing tank which acts as the measuring tank with stirrers to thoroughly mix the slurry, a circulation pump, a booster pump and a water pump. The centrifugal pump re-circulates the already mixed slurry and, at the same time, feeds the downhole displacement pumps. The booster pump boosts the suction pressure of the pumps, though it is not always used. The mixing process is computer controlled, with the computer using the water flow rate signal, the dry cement flow rate, the slurry pumping rate and the density signal to adjust the water-cement mixing ratio and, therefore, automatically adjust slurry density (Serva, 2011). Cementing units use a recirculation mixer with automatic density control for continuous mixing and pumping; they mainly come in three configurations: truck mounted, semitrailer mounted and skid mounted (Nelson, 1990). Figure 13 shows the schematic diagram of a recirculation mixer.

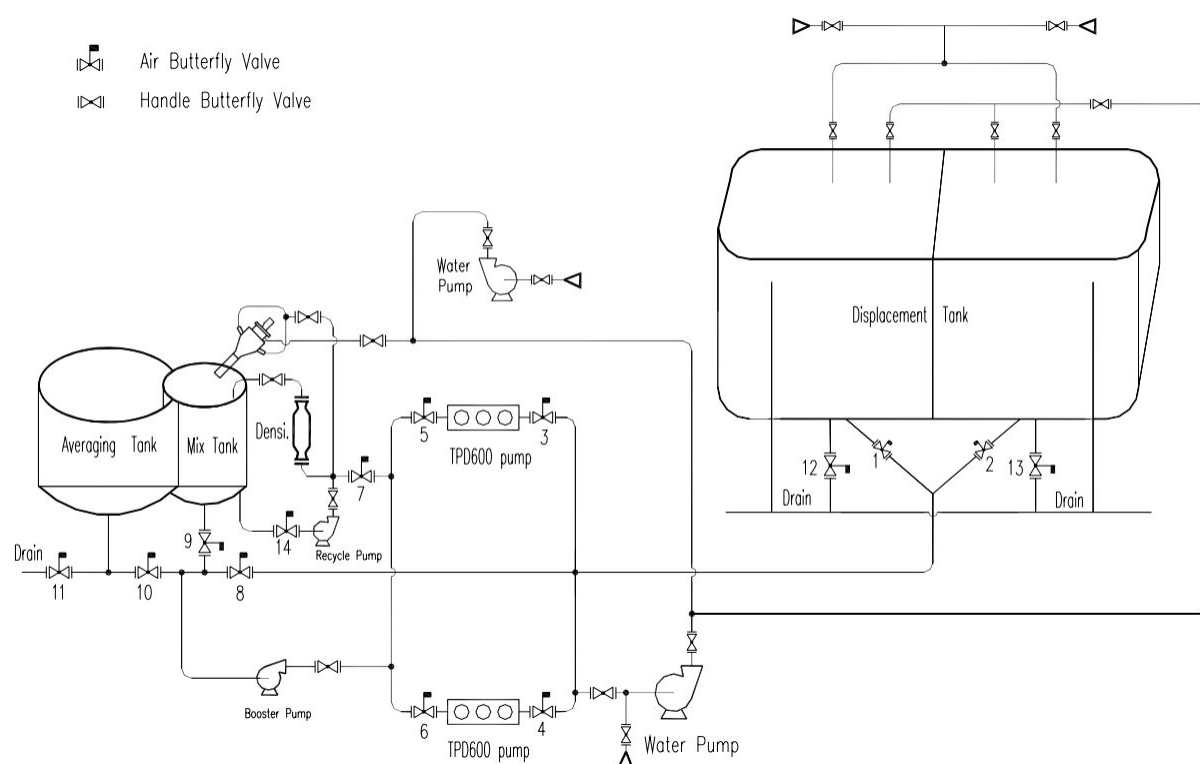


FIGURE 13: Recirculation mixing and pumping unit (Serva SJS, 2011)

5. CEMENTING TECHNIQUES

5.1 Inner string (stinger) cementing

This cement placement method involves pumping slurry through a drill pipe string attached to either the casing shoe or the float collar through a stab-in receptacle. The bottom end part of the drill pipe has a stab-in sub with seals to fit in the collar receptacle, and the lower part is fitted with centralizers, adapted to the size of the casing being cemented (Devereux, 1998). An inner string method is commonly used to cement large size casings run below 1000 m and has the following advantages:

- Reduces cement contamination;
- Eliminates the need for large cementing heads and plugs;
- Reduces the amount of cement to be drilled out;
- Decreases cement displacement time and pressure;
- Reduces slurry placement time;
- Reduces cement waste; and
- Cement is discharged outside the casing much faster (Halliburton, 2005).

The main disadvantage of an inner string method is the time taken to run in with the cementing string and the time taken to pull it out after cementing for long casing strings. Figure 14 shows stab in shoe, collar and stab in adaptor. Figure 15 shows different inner string methods (Halliburton, 2005).

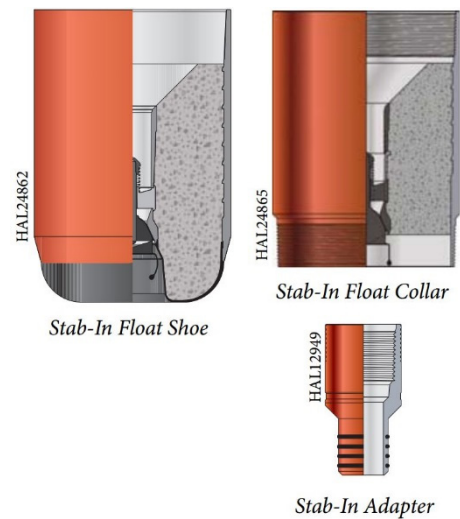


FIGURE 14: Stab-in shoe, collar and adaptor (Halliburton, 2005)

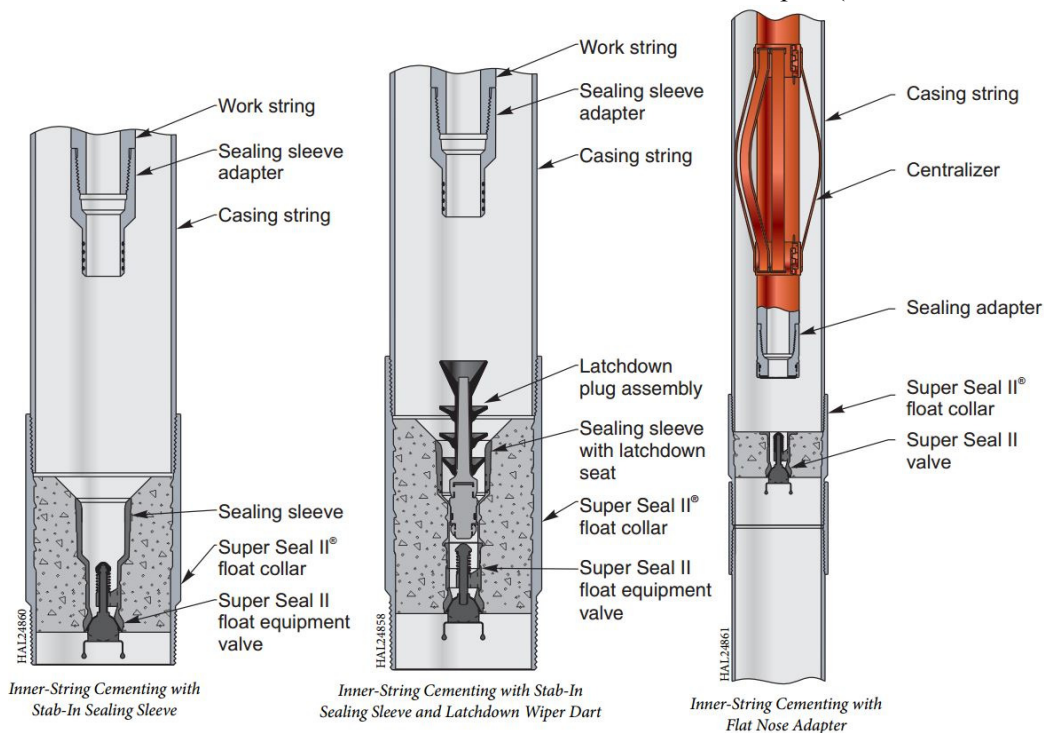


FIGURE 15: Inner string methods (Halliburton, 2005)

5.2 Single stage cementing

In this method, a calculated volume of cement slurry is pumped into the casing and is displaced out to the annulus through the casing shoe. The method uses two plugs, a bottom plug (optional) which displaces the drilling fluid and a top plug which displaces cement and separates it from the displacement fluid. The bottom plug has a membrane which ruptures, allowing cement slurry to flow through. But the top plug is solid in order to withstand high pressures, and it limits mixing of the displacement fluid with cement slurry. The top of the casing string is fitted with a cementing head which has compartments for holding the bottom and top plugs and allows cement to be pumped inside the casing. The bottom plug is optional, especially if the drilling fluid used is water, which is a common occurrence in geothermal well drilling. The major drawback of this placement method is that it is not flexible in adjusting the volume of cement to be pumped, even if there are no cement returns to the surface (Guerra, 1998). Figure 16 show the single stage casing cementing process.

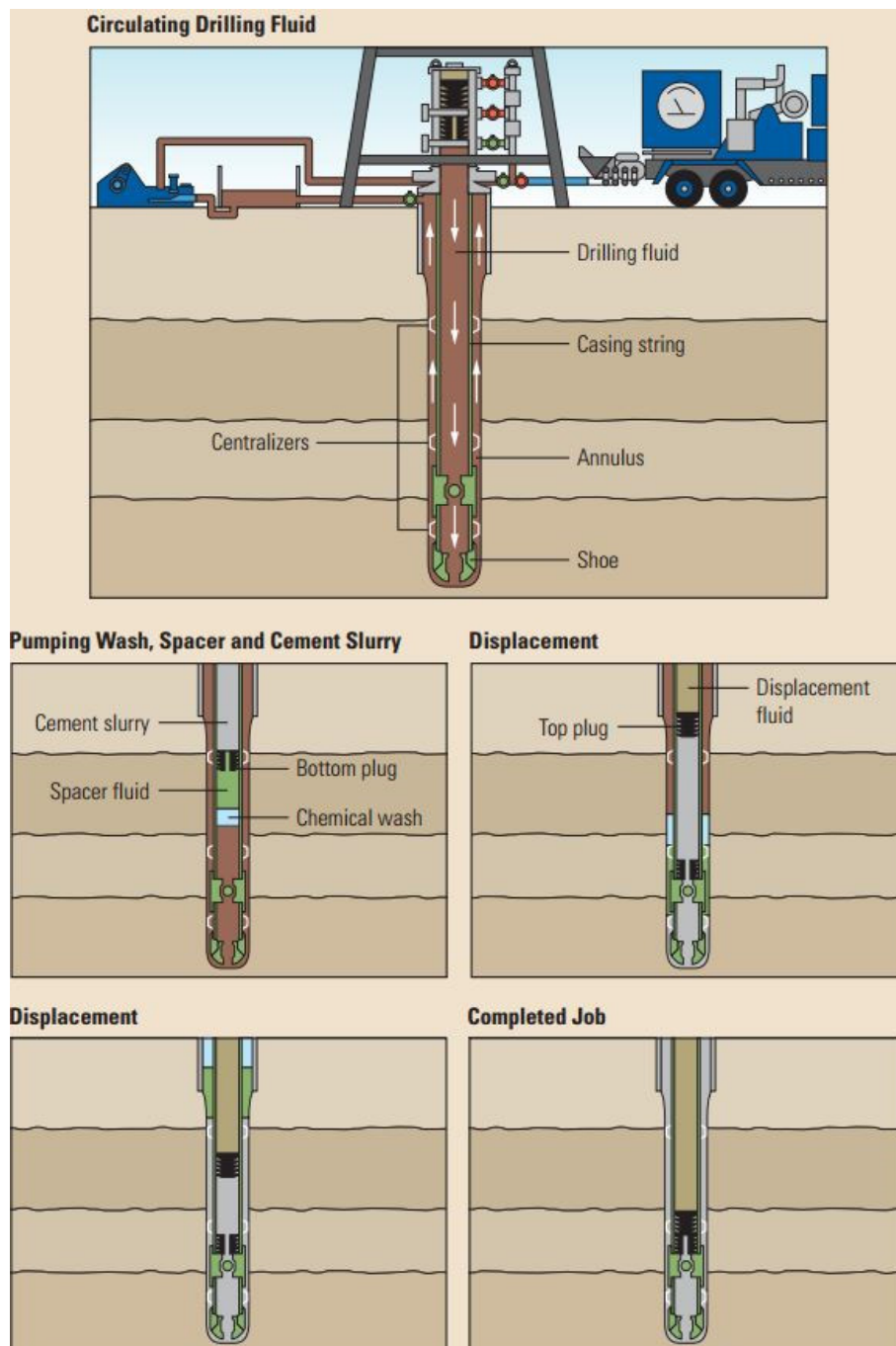


FIGURE 16: Single stage cementing process (Nelson, 2012)

5.3 Multiple stage cementing

The multiple stage cementing method is used to place cement slurry around the casing in stages at selected intervals. Two stage cementing is the most common of the multi stage cementing method and is used when (Halliburton, 2005):

- The hydraulic pressure head of cement is too high for the formation or casing;
- There is limited pumping time, especially in hot wells, to pump the desired quantity and quality of cement;

- Downhole conditions require different blends of cement slurry;
- Only certain portions of the wellbore require cementing; and
- In horizontal wells in oil drilling, where the bend radius of the well requires cementing.

The first stage is cemented using the conventional methods, while stage cementing collars (differential valves) designed to allow cement flow into the annulus when they are opened either by the use of a plug or hydraulic pressure, are used for stage cementing. After cementing, a closing or shut-off plug is deployed to block the casing side ports. Other stage cementing valves have a single sleeve which is opened by a special tool (sleeve positioner) run in after heavy packing. This method is used without limiting the number of stages and the plugs are not re-drilled. Also used together with a stage cementing valve is a multi-stage packer, located below the stage cementing valve which is inflated during the opening of the valve to minimize over-pressuring the zone below the stage valve (Lecourtier and Cartalos, 1993). Figure 17 shows a stage cementing collar.

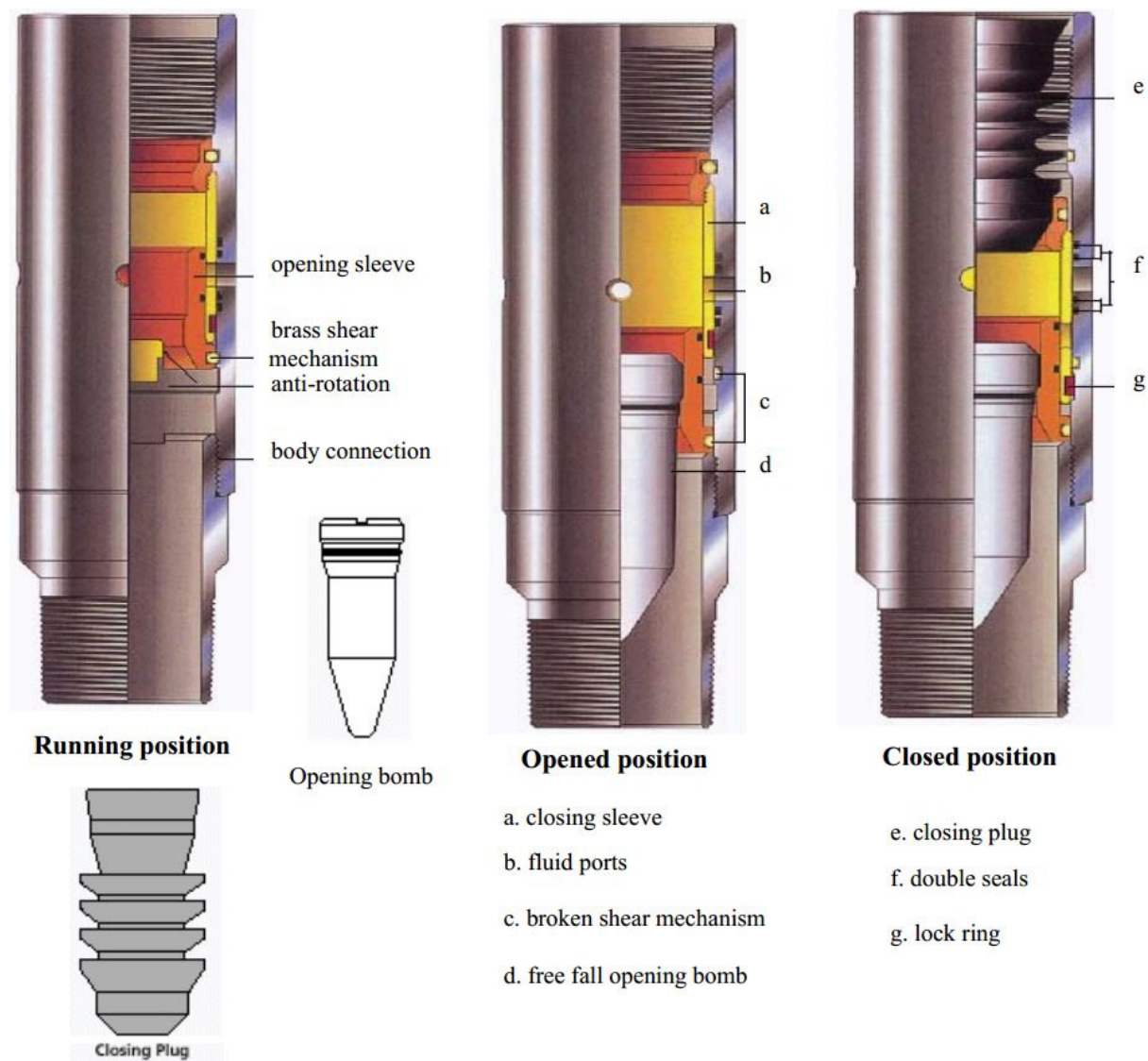


FIGURE 17: Stage cementing collars (Rabia, 2001)

5.3.1 External casing packers (ECP)

These are elastomeric elements (packers) used to isolate zones in the annulus when inflated with mud, cement or viscous fluid and can be incorporated when running casings. They are inflated through valves operated with shear pins, which break when the set pressure is reached, allowing fluid to enter; the closing valve shear pin breaks when the packer is fully inflated to the set pressure. The packers can be positioned above a loss zone to prevent cement slurry loss into the zone while the lower portion is cemented using other methods; they can also be used to cement sections of slotted liners which need to be isolated. The major disadvantage of packers is that they are the weak point areas and are susceptible to leakage, breaking the casing cement bond (Lecourtier and Cartalos, 1993). Figure 18 shows an external casing packer in running and inflating positions.

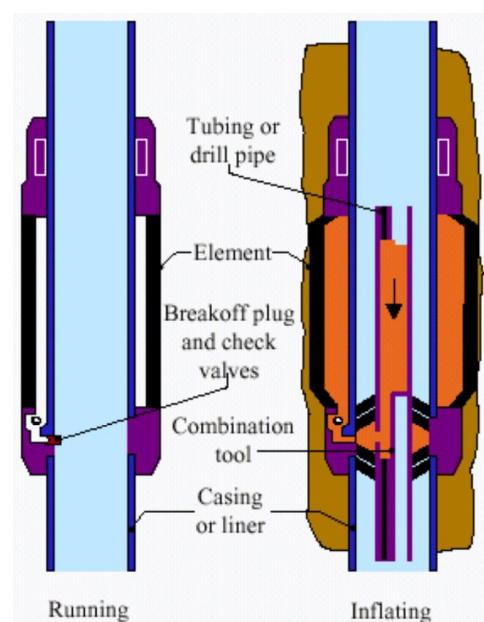


FIGURE 18: External casing packer during running and inflating (Rabia, 2001)

5.4 Reverse circulation cementing method

Reverse circulation cementing involves pumping cement slurry through the annulus, displacing the drilling fluid in the wellbore through the casing. The method is aimed at reducing the circulating bottom hole pressure (BHP), thus lowering the risk of cement slurry loss during cementing and eliminating the need for top jobs in order to complete cementing process. The major advantages of reverse cementing method are:

- It reduces the pressure applied to the formation during cementing since the fluid ahead of the cement has a lower density than the cement (lower effective circulating density);
- It minimizes the excess cement required for a cementing job since once the cement slurry reaches the bottom, mixing and pumping are stopped;
- It is possible to lower or stage manage retarder loading in cement slurry and, therefore, reducing the wait on cement time;
- The top cement in the annulus can be accelerated to reduce wait on cement time;
- Reduces cement pumping time since flow is by gravity and there is no displacement required; and
- Small top up job may be required to complete the cementing process in case the top of cement drops during setting.

The main challenge of reverse cementing is in knowing when competent cement has reached and circulated the bottom of the well. The main method used is the use of a tracer with a logging tool to indicate when cement enters the casing. Other methods include the use of stab in collars with a drill pipe for circulation of returns through the casing, if a marker (dye) is used, or to actuate a non-return valve when pulled out. Figures 19 and 20 show the reverse cementing process, using tracer and a drill pipe (Rickard et al., 2011; Spielman et al., 2006; Bour and Hernández, 2003; Hernandez, 2009).

5.5 Remedial casing cementing

The main objective of primary casing cementing is to fill up the annulus with cement back to the surface. However, in not all occasions are cement returns received on the surface due to loss of cement to the formation; then remedial cementing is required. The main method used to complete the cementing process is to fill cement through the annulus, sometimes with repeated top up jobs. This method poses

the danger of having water trapped between two top up jobs in the casing to casing annulus, if the remedial cementing is not well executed, leading to casing failure (Hole, 2008a).

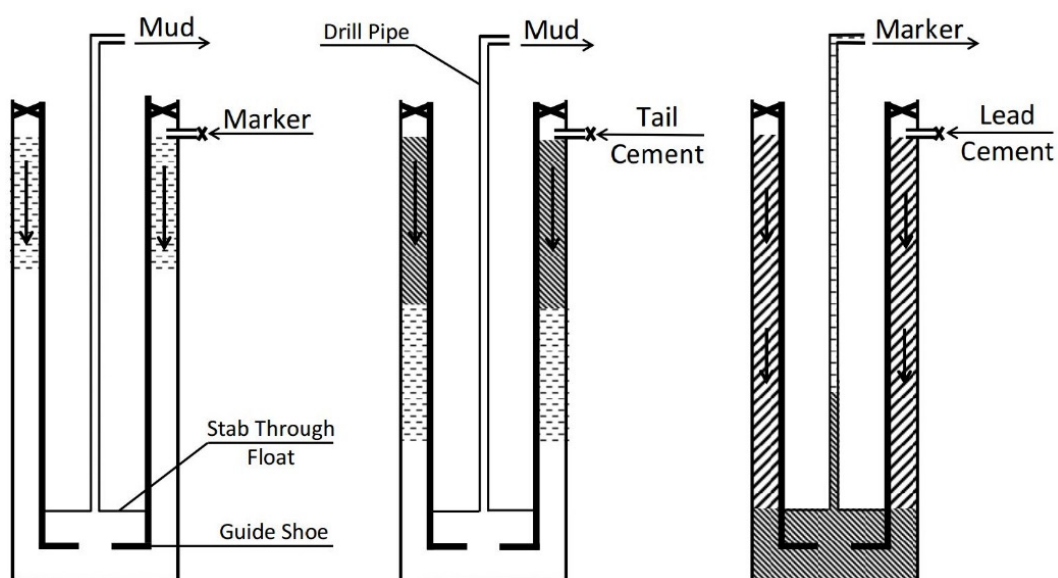


FIGURE 19: Reverse cementing process using drill pipe (Rickard et al., 2011)

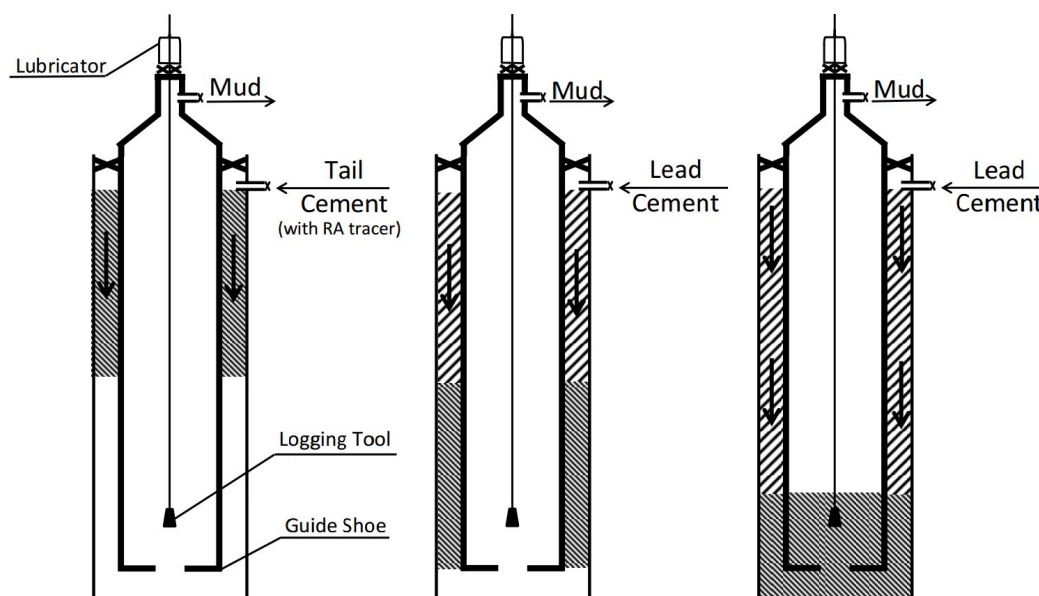


FIGURE 20: Reverse cementing process using tracer and logging tool (Rickard et al., 2011)

Other methods used include:

- a) *Squeeze cementing* where cement is forced into the annulus with the casing being perforated. This method is mainly used to repair poor primary cementing. Figure 21 shows squeeze cementing using an internal casing packer (Rabia, 2001);
- b) *Tie back cementing* which is mainly used for repairing production casing by cementing the liner back to the surface from the top liners;
- c) *Spaghetti cementing* which employs small diameter pipes to pump cement into the annulus. The pipes are run to the top of cement for shallow casing strings; and
- d) *Using gravel and sand* for shallow surface and conductor casing with large circulation losses: sand and gravel are placed first, then the cement slurry is pumped (Guerra, 1998).

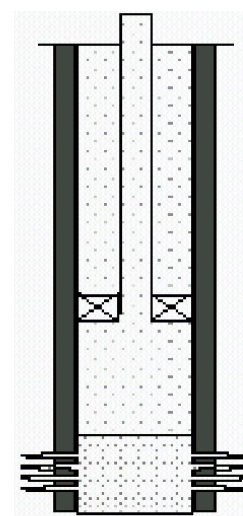


FIGURE 21:
Squeeze cementing
(Rabia, 2001)

6. QUALITY CONTROL AND POST CEMENTING LOGGING

6.1 Pre-cementing tests

Cement slurry formulations (design) are adjusted to suit wellbore conditions expected to be encountered during drilling. These conditions are simulated in a cement testing laboratory; cement blending recipes are adopted, based on the analysis results, to provide the best estimate for quantities of additives, slurry yield, mix water requirements, slurry gelling time and allowable pumping time. In geothermal, the main controlling factor in cement formulation is temperature, which affects the thickening time, setting time, rheology and compressive strength development.

Bottom hole circulation temperature (BHCT) represents the temperature at the bottom of the well after several hours of circulation; bottom hole static temperature (BHST), which is the undisturbed (natural) temperature (formation temperature) at the bottom of the well, is key in formulating cement slurry to be pumped downhole (Hole, 2008a). Parameters tested in cement slurry formulations include: thickening time, slurry density (specific gravity), fluid loss, free water, compressive strength, and rheology. These tests are conducted to determine the quantities of cement additives, such as retarders, accelerators, anti-friction materials, fluid loss control, lighting agents, free water control and silica flour, needed to prevent strength retrogression.

Thickening time test - is used to determine the time during which the cement slurry will remain in fluid state and be pumpable. Slurry thickening time should be enough to be pumped and displace cement back to surface. It is measured using a consistometer, in accordance to API 10B, which plots the viscosity (consistency) of cement slurry over time at the expected downhole temperature and pressure, and is expressed in Bearden units of consistency (BC) over a scale of 1 to 100 (Schlumberger, 2014). This test is used to determine the amount of retarder to be used to avoid over or under retardation of cement slurry. Figure 22 shows the output curve from a consistometer testing cement in Olkaria, mixed with 0.3% BWOC anti-fluid loss agent, 0.3% BWOC retarder and 0.3% BWOC dispersant.

Slurry density - is the measure of the mixing proportions of the dry cement blend and water to form the cement slurry. An increase in the cement slurry density favours displacement of drilling fluids during slurry placement but, at the same time, it increases the risk of circulation losses due to formation fracture. To modify slurry density, additives such as bentonite are added to soak extra water (extenders) for lighter slurry, or weighting agents such as barite are added to increase the density. Other methods include the use of hollow microspheres in the slurry or the use of foamed cement to lower the slurry density (Devereux, 1998).

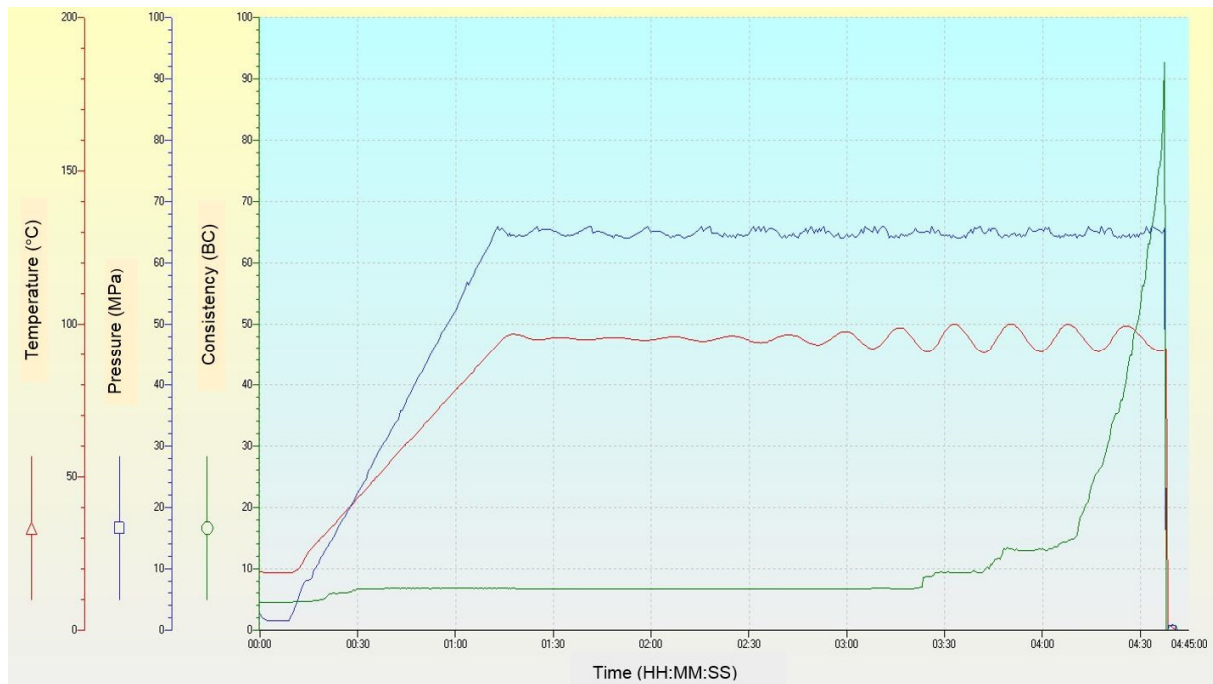


FIGURE 22: Thickening time output from a consistometer (Kengen, 2014)

Measurement of slurry density is done to determine the mix water required to yield the desired density during cementing. Cementing units have automatic density controls during mixing and pumping. Mud balance is used to confirm slurry density at the rig site during cementing (Guerra, 1998). Figure 23 shows a mud balance used to measure cement slurry density during cementing.

Free water - is a measure of the excess water in the cement slurry not required to fully mix the dry cement blend (Schlumberger, 2014). When cement is setting, free water separates from the slurry, settling at the top of the cement column or in small water pockets if the well is deviated. This water can create channels while moving at the top of cement, resulting in a poor cement bond or casing failure, if the water pockets are between the casing to casing annulus. Testing of free water involves mixing (homogenization) cement slurry in an atmospheric consistometer with a rotational speed of 150rpm at a temperature of 88°C. The mixer is then transferred to a settling 250 ml cylinder where it stays for two hours. The segregated free water settled on the top of the cement mixer after two hours is measured to determine the amount of free water. Cement additives (free water control agents) such as Wyoming bentonite are usually added to control free water in cement slurry. The maximum free water allowable for cementing slurry is 0.5% or less, especially for geothermal casing cementing (Bett, 2010; Guerra, 1998; Devereux, 1998).



FIGURE 23: Mud balance (Fann, 2012)

If cement is placed across a permeable formation, loss of filtrate will dehydrate the slurry, affecting its setting time, set strength and may lead to channelling. High fluid loss builds a thick filter cake that narrows the annulus, leading to increased annular pressure drop and possibly induced losses or fracturing (Devereux, 1998). The testing of fluid loss is done under simulated wellbore conditions in a stirring apparatus with a heating jacket to give the circulation temperature. The pressure differential between annular and formation pressure is simulated by pressurized nitrogen at 69 bars for 30 minutes. A screen and a filtration chamber simulate the permeable zone, and fluid loss is measured as filtrate volume per unit of time. The testing is done using API 10B guidelines which specify the size of the mesh to be used. It also recommends a maximum fluid loss of 100cc/30min for casing cementing, but lower values below

50cc/30min are recommended for permeable zones and directional wells (Devereux, 1998; Halliburton, 2005; Bett, 2010).

Compressive strength testing - is performed on cement slurry samples cured for 8, 12, 16 and 24 hours under simulated downhole temperature and pressure to determine the initial set time and the wait on cement time. Testing can be done by crushing the samples, using a hydraulic press, or using a sonic analyser to determine the compressive strength. Compressive strength failure pressure from the hydraulic press is used for comparison, since the testing is not done under downhole conditions, and the cement cube is unconfined in all directions, unlike in a well where cement is confined by formation and casings. Ultrasound compressive testing is non-destructive and the compressive strength development is monitored continuously during curing (Halliburton, 2005; Guerra, 1998, Devereux, 1998). Figure 24 show the output curve from a compressive strength test.

Rheology testing - is the measure of how cement slurry flows (viscosity) with respect to bottom hole circulation temperature, using a viscometer in order to properly predict pumping pressure during cementing. The slurry is first measured at ambient temperature and later conditioned to bottom borehole circulation temperature where viscosity readings at various rotational speeds are taken. A viscometer consists of a spring loaded shaft with a bob at the bottom in a rotating cylinder. The cylinder is rotated at variable speeds (200, 100, 60, 30, 6 and 3 rpm), creating a gap in which slurry flows deflect the bob due to increased drag. The drag in the shaft is transmitted to a precision spring where its deflection is measured and used to calculate the slurry viscosity (Halliburton, 2005).

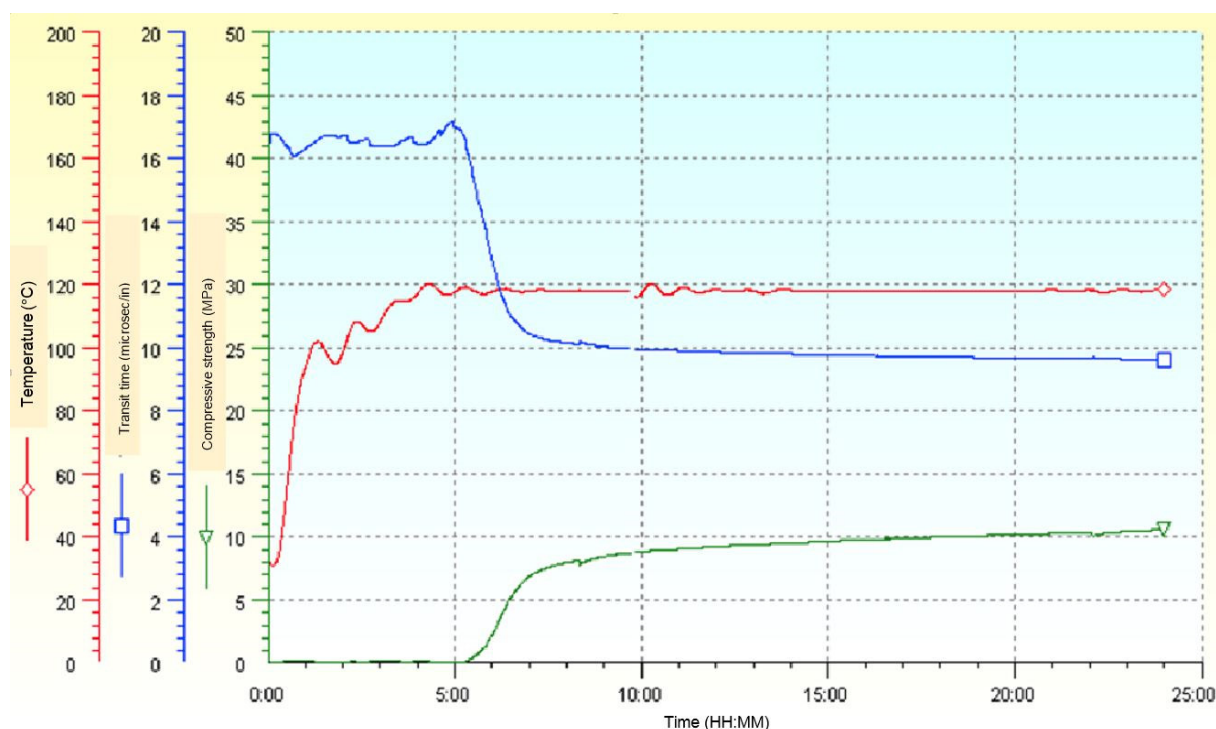


FIGURE 24: Compressive strength test (Kengen, 2014)

6.2 Post cementing evaluation

After casing cementing, there is need to establish the top of cement if there are no cement returns, confirm if the cement has cured before the next drilling operation, verify whether the whole casing string is uniformly covered with cement, and whether cement has bonded to the casing and formation. All

these can be established by running logging tools to assess the effectiveness of the cementing job. The most common methods are:

1. *Temperature logs for top of cement*: cement curing process is exothermic, thereby generating heat when it is setting. A temperature logging tool can be used to establish the top of cement if there are no cement returns to the surface. A sharp increase in temperature from the ambient will indicate the top of cement. Temperature logging needs to be done during the cement curing period (within 24 hours) as the reaction causing the temperature anomaly will fade with time. Figure 25 shows a temperature log indicating top of cement (Steingrímsson, 2011).
2. *Cement bond log (CBL)*: is used to evaluate the quality of the cement bond between casing to cement and cement to formation, and also indicate the top of cement. The travel time and amplitude of the continuous sound pulses generated by a transmitter are measured by the receiver, placed at a distance (usually 3ft) from the transmitter as a function of depth. The amplitude will be at maximum where there is no cement or poorly cemented sections, and at minimum where the casing is well cemented (Steingrímsson, 2011).
3. *Variable density log (VDL)*: this provides the full wave signal (graphical representation) of the sound pulses as they are received at the receiver as a function of depth. The wave form of the variable density log corresponds to the sound signal that has travelled through the casing, cement sheath and is reflected back from the formation to the receiver. If there is no cement or the section is poorly cemented, the waveform will be in the form of parallel black and white lines, indicating that the sound pulse did not reach the formation, while wavy grey lines indicate a good cement bond. This should correspond to the cement bond logs (Bridge7, 2014; Rabia, 2001).

In addition to locating the top of cement and the quality of the cement bond logs (CBL), variable density logs (VDL) can be used to monitor the rate at which the cement is setting and to locate water pockets in the cement column. Both the CBL and VDL are observed from the sonic or ultrasonic logging tools. Gamma-gamma and neutron-neutron logging tools can also be used to determine the quality of casing cementation (Steingrímsson, 2011). Different models of cement bond log interpretation are shown in Figures 26, 27, 28 and 29. Figure 30 shows a cement bond log for well OW-33 in Hellisheidi, Iceland.

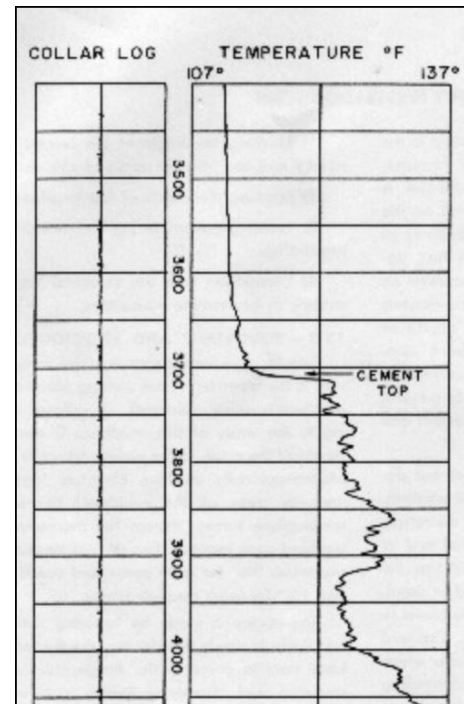


FIGURE 25: Temperature log showing top of cement (Crain, 2000)

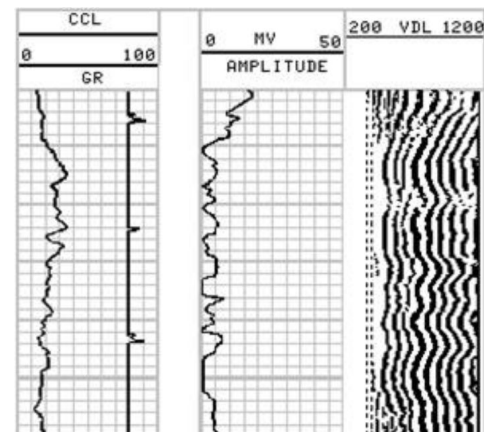


FIGURE 26: Cbl/vdl showing good cementation (Bridge7, 2014)

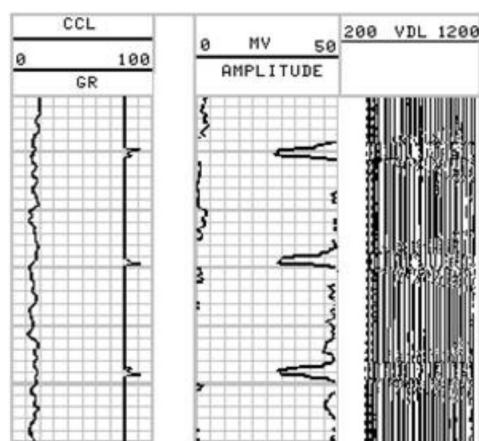


FIGURE 27: Cbl/ vdl showing no cement in the annulus (Bridge7, 2014)

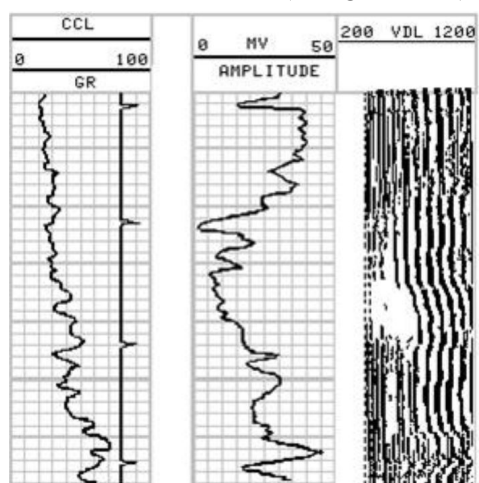


FIGURE 28: Cbl/ vdl showing partial cementation (Bridge7, 2014)

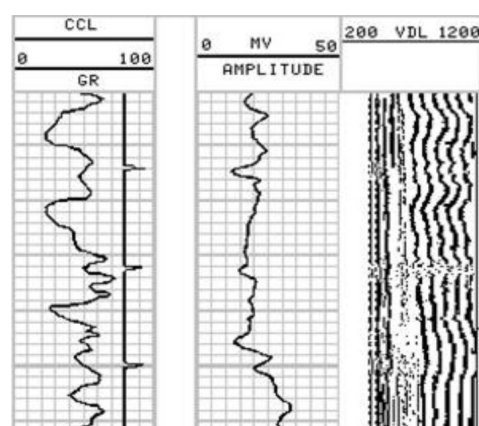


FIGURE 29: Cbl/vdl showing micro gap between casing and cement (Bridge7, 2014)

the casing shoe into the new formation. The wellbore is closed and incremental fluid pressure from 200 psi to 1000 psi is applied for ten minutes. If there is no pressure drop, drilling ahead continues. If there is pressure leakage noted, the leakage point is cemented (Bett, 2010, NZS, 1991; Schlumberger, 2014).

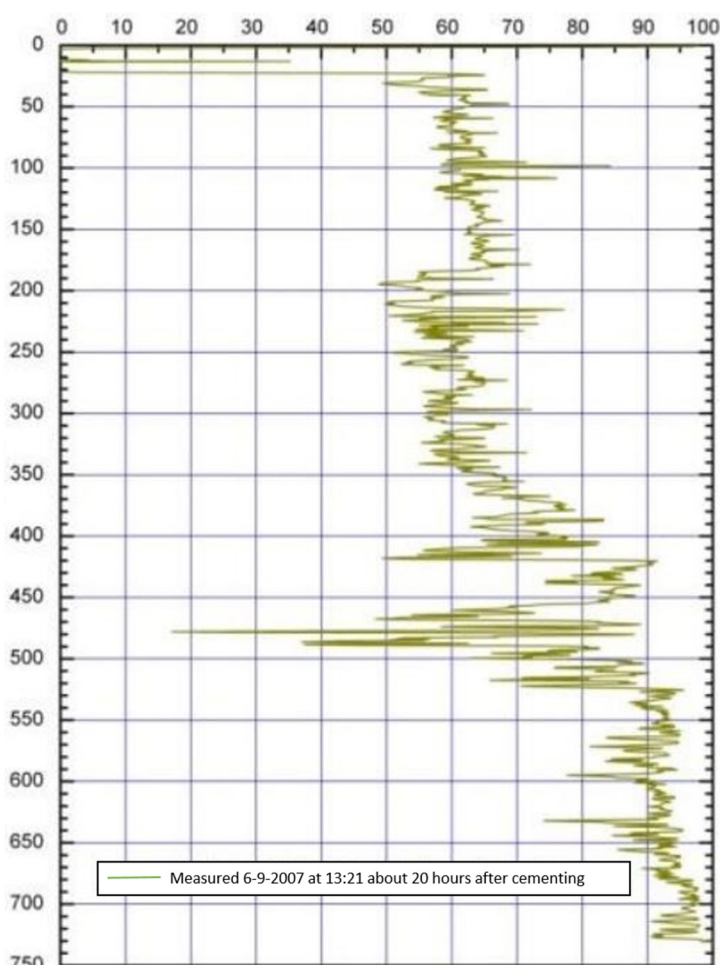


FIGURE 30: 20" Surface casing cementing

6.3 Shoe integrity pressure test (leak off test)

After the wait on cement time elapses, preparation for drilling the next section of the well starts with the installation of the blow out preventers. A pressure test is usually conducted to confirm the strength of the cement bond around the casing shoe and to ensure that there is no leakage to the formation above the casing shoe or to the previous annulus. It is also conducted after drilling a few metres (usually 3 m) into the new formation below the casing shoe to confirm the capability of the wellbore to withstand drilling fluid pressure for safe drilling of the next hole section. The casing cement bond is tested first by closing the blow out preventers and hydraulically pressurizing the cemented casing to 300 psi and observing any pressure drop for ten minutes. If the bond is holding, drilling out of cement then proceeds to three metres below

7. CASING AND PLUG CEMENTING ANALYSIS

7.1 Casing cementing of wells OW-43A, OW-40V and OW-731A

The cementing of surface, anchor and production casings of wells OW-43A, OW-40V and OW-731A in Olkaria, Kenya were analysed for the calculated cement volume required in the single stage cementing method. During casing cementing, the calculated cement volume is pumped into the casing and then displaced, using water into the annulus in the primary (first) cementing job. In cases where cement did not return to the surface in the primary cementing, backfills (top up) through the annulus were required to completely fill up the cement and complete the casing cementing. All the wells except well OW-43A's surface casing did not receive cement returns to the surface during primary cementing and required top up jobs to fully cement the casings. The cement volume used in the primary cementing was based on the casing size, drilled hole size and drilled depth. Extra (excess) volume was also added to cater for losses during cementing and cavities in the well bore.

Cement volume calculation for surface, anchor and production casing strings was compared with the actual cement used to complete the cementing jobs. Cement volume calculation was based on the Drilling Data Hand Book (DDH) casing and annular volume data, and by considering all the annular volumes which needed to be filled with cement during cementing (Gabolde and Nguyen, 2014). For annular calculation of the casing to the open borehole volume and the rat hole (open hole below the casing shoe), 100% excess cement was added to cater for losses into the formation. The calculations, together with the actual cement volumes used, are shown in Table 4 for 20" casing, Table 5 for 13-3/8" casing, and Table 6 for 9-5/8" casing. The well sections are shown in Figures 31, 32 and 33.

TABLE 4: Cement volume calculation for 20" surface casing

Casing size	20" Surface casing 94 lb/ft. K55		
Well number	43A	731A	40V
Rig floor height from the cellar H (m)	11.9	11.9	11.9
Drilled depth L (m)	59.2	56	56.8
Casing depth L_1 (m)	58.7	55.6	56.3
Casing shoe track length (length below the float collar) L_2 (m)	11.8	11.8	11.8
Rat Hole (open hole below the casing shoe) length $L_3=L-L_1$ (m)	0.5	0.4	0.5
26" drilled hole capacity in litres per metre (l/m)	342.5	342.5	342.5
Annular capacity between 20"casing and 26"drilled Hole in litres per metre (l/m)	139.8	139.8	139.8
20" casing internal Capacity in litres per metre (l/m)	185.3	185.3	185.3
Annulus Cement between 20"casing and 26" drilled hole V_1 (m^3)= (Length L_1 x Capacity)/1000	6.55	6.11	6.21
Shoe Track Cement Volume V_2 (m^3)= (Length L_2 x Casing capacity)/1000	2.19	2.19	2.19
Rat hole volume V_3 (m^3)= (length L_3 x 26" drilled hole capacity)/1000	0.17	0.14	0.17
Total Cement Volume= $V_1+V_2+V_3$ (m^3)	8.90	8.43	8.56
Total Cement Volume With Open Hole Excess 100% (V_1+V_3) (m^3)	15.62	14.68	14.94
Plug cementing during drilling m^3	0	0	6
Primary cementing m^3	11.54	14.5	7.38
Backfills m^3	0	1	22.2
Actual volume used m^3	11.54	15.5	35.6
Number of backfills	0	1	3
Number of plug jobs	0	0	1

TABLE 5: Cement volume calculation for 13-3/8" anchor casing

Description Well number	13-3/8" Anchor casing 54 lb/ft. K55		
	43A	731A	40V
Rig floor height from the cellar H (m)	11.9	11.9	11.9
Drilled depth L (m)	302.0	294.5	301.5
13-3/8" Casing Depth L_0 (m)	300.7	293.5	300.5
20" Surface casing depth L_1 (m)	58.7	55.6	56.3
17-1/2" Drilled hole depth (m)= $L-L_1$	243.3	238.8	245.2
Casing shoe track length (length below the float collar) L_3 (m)	11.8	11.8	11.8
Rat Hole (open hole below the casing shoe) length $L_4=L-L_0$ (m)	1.3	0.8	1.0
17-1/2" Open hole capacity in litres per metre (l/m)	155.2	155.2	155.2
13-3/8" Casing internal capacity in litres per metre (l/m)	80.64	80.64	80.64
Annular capacity between 13-3/8" casing and 17-1/2" open hole in litres per metre (l/m)	64.5	64.5	64.5
Annular capacity between 13-3/8" casing and 20" casing in litres per metre (l/m)	94.66	94.66	94.66
20" casing and 13-3/8" casing annular cement volume V_1 (m ³)= (Length L_1 x Annular capacity)/1000	4.43	4.14	4.20
Annular volume between 13-3/8" casing and 17-1/2" open Hole V_2 (m ³)= (Length L_2 x Annular capacity)/1000	14.84	14.59	14.98
Shoe Track Cement Volume V_3 (m ³)= (Length L_3 x 13-3/8" casing internal capacity)/1000	0.95	0.95	0.95
Rat hole volume V_4 (m ³)= (length L_4 x 17-1/2" drilled hole capacity)/1000	0.19	0.13	0.16
Total Cement Volume (m ³)= $V_1+V_2+V_3+V_4$	20.42	19.81	20.29
Total Cement Volume With Open Hole Excess(V_2+V_4) 100% (m ³)	35.46	34.52	35.43
Plug job during drilling	0	0	0
Primary cementing volume m ³	33.2	20.9	18.2
Backfills cement m ³	47.3	168.1	168.3
Actual volume used m ³	80.7	183.0	186.5
Number of backfills	4	15	12
Number of plug jobs	0	0	0

TABLE 6: Cement volume calculation for 9-5/8" production casing

Casing Well number	9-5/8" Production casing 47 lb/ft. K55		
	43A	731A	40V
Rig floor height from the Cellar H (m)	11.9	11.9	11.9
Drilled Depth L (m)	742.5	754.0	752.0
9-5/8" Casing Depth L_0 (m)	742.0	753.0	751.0
13-3/8" anchor casing depth L_1 (m)	300.7	293.5	300.5
12-1/4" Drilled Hole depth (m)= $L-L_1$	442.0	460.34	451.5
Casing shoe track length (length below the float collar) L_3 (m)	11.8	11.8	11.8
Rat Hole (open hole below the casing shoe) length $L_4=L-L_0$ (m)	0.71	1.1	1
12-1/4" drilled open hole capacity in litres per metre (l/m)	76.04	76.04	76.04
9-5/8" Casing internal capacity in litres per metre (l/m)	38.18	38.18	38.18
Annular capacity between 9-5/8" casing and 13-3/8" casing in litres per metre (l/m)	33.7	33.7	33.7

Casing	9-5/8" Production casing 47 lb/ft. K55		
Well number	43A	731A	40V
Annular capacity between 9-5/8" casing and 12-1/4" open hole in litres per metre (l/m)	29.1	29.1	29.1
13-3/8" casing and 9-5/8" casing annular cement volume V_1 (m^3)= (Length L_1 x Annular capacity)/1000	9.73	9.50	9.73
Annular volume between 9-5/8" casing and 12-1/4" open Hole V_2 (m^3)= (Length L_2 x Annular capacity)/1000	12.83	13.36	13.11
Shoe Track Cement Volume V_3 (m^3)= (Length L_3 x 9-5/8" casing internal capacity)/1000	0.45	0.45	0.45
Rat hole volume V_4 (m^3)= (length L_4 x 12-1/4" drilled hole capacity)/1000	0.05	0.08	0.08
Total cement volume (m^3)= $V_1+V_2+V_3+V_4$	23.07	23.39	23.36
Total cement volume with open hole excess(V_2+V_4) 100% (m^3)	35.96	36.84	36.55
Plug cementing during drilling m^3	0	316.7	0
Primary cementing m^3	25.85	16.70	17
Backfills m^3	28.3	31.40	21.00
Actual volume used m^3	54.15	364.80	38.00
Number of backfills m^3	3	2	4
Number of plug jobs	0	23	0

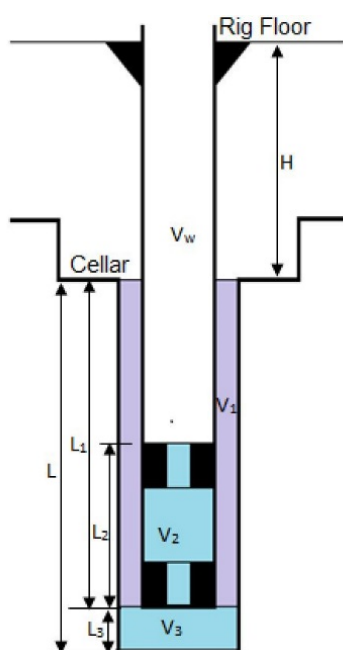


FIGURE 31: 20" Surface casing cementing

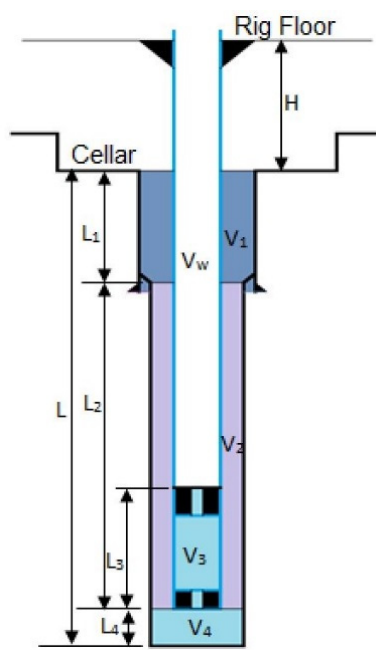


FIGURE 32: 13-3/8" Anchor casing cementing

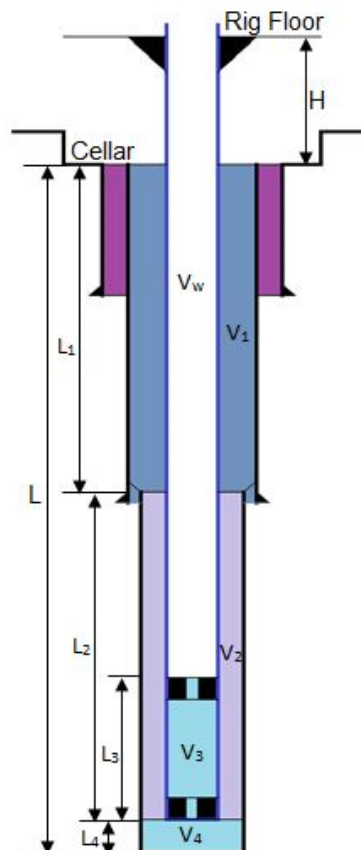


FIGURE 33: 9-5/8" production casing cementing

The calculated cement volume was compared to the actual cement used for the three casing strings in these three wells and is summarized in Table 7. The values were then compared, as shown in Figure 34.

TABLE 7: Comparison of calculated and actual cement used

Casing size	Calculated volume m ³	Actual volume used m ³	Extra volume used m ³
20" casing	45.3	62.6	17.3
13-3/8" casing	105.4	450.2	344.8
9-5/8" casing	109.4	140.3	30.9

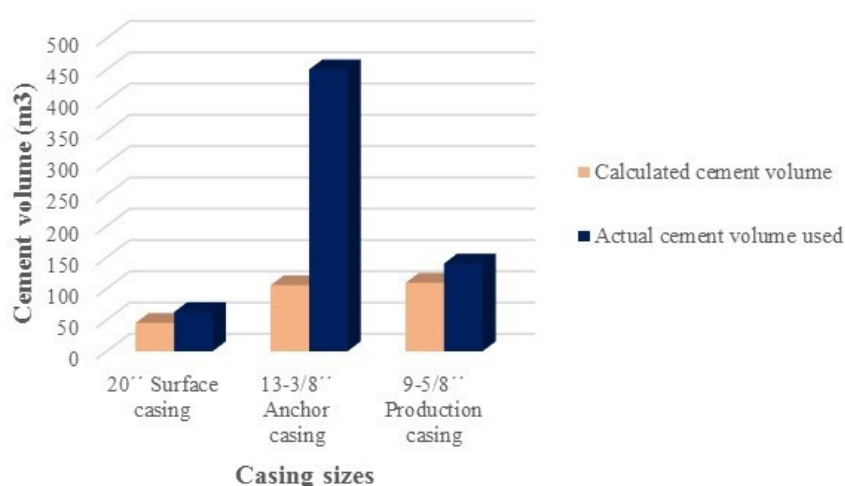


FIGURE 34: Comparison of calculated cement and actual cement used

and 3 in Appendix I. The total wait on cement time, both for casing cementing and a cement plug placed during drilling for the three wells is summarized in Table 8, then compared to the total drilling days in Figure 35.

TABLE 8: Wait on cement time in days and percentage of total drilling time

Well	Drilling days	Cementing days	Percentage %
OW-43A	154	5.3	3.5
OW-40V	61	9	14.8
OW-731A	96	33	34.4

7.2 Well OW-731A cement plugs

A total of twenty four plug jobs were conducted during drilling of the production casing section of well OW-731A. The volume of cement used, depth and wait on cement time after each plug are summarized in Table 9. The well was completed in 96 days but 24 days were used as wait on cement time, which is equivalent to 25% of the total drilling days.

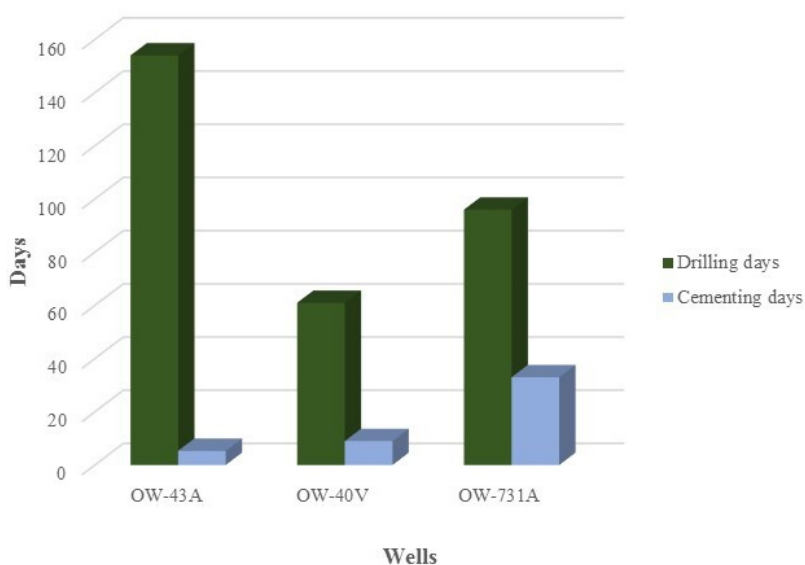


FIGURE 35: Comparison of total drilling days and wait on cement time

TABLE 9: Summary of plug cementing for well OW-731A

No.	Cement volume used (m ³)	Depth (m)	Wait on cement (hours)
1	14.20	204.00	24
2	15.00	204.00	24
3	15.00	200.00	24
4	15.00	235.00	24
5	14.00	233.00	24
6	20.00	233.00	24
7	15.00	203.00	24
8	10.16	203.00	24
9	15.60	201.00	24
10	20.50	199.00	24
11	16.00	371.00	24
12	10.25	371.00	24
13	12.09	371.00	24
14	10.27	309.00	24
15	15.02	302.00	24
16	6.02	293.00	24
17	9.02	293.00	24
18	15.07	365.00	24
19	15.05	391.00	24
20	15.21	377.00	24
21	6.60	383.00	24
22	15.43	383.00	24
23	10.00	383.00	24
24	6.20	396.00	24
Total	316.69		576 (24 Days)

7.3 Analysis of top up (backfill) cement volume used

Casing cementing using single stage cementing was analysed for sixty eight wells in Olkaria in order to compare the total cement volume placed through backfill cementing and the total cement volume used to fully cement the casing strings back to the surface. The summary of the backfill cement is shown in Table 10 and the results are compared in graph 3 (Figure 36). The complete cement volume analysis is shown in Table 11 in Appendix II

TABLE 10: Backfill cement volume comparison

Description	20" surface casing	13-3/8" anchor casing	9-5/8" production casing
Total backfill cement volume m ³	620.2	3167.8	1800.9
Total cement volume used m ³	1676.1	4638.5	3324.5
Percentage %	37.0	68.3	54.2

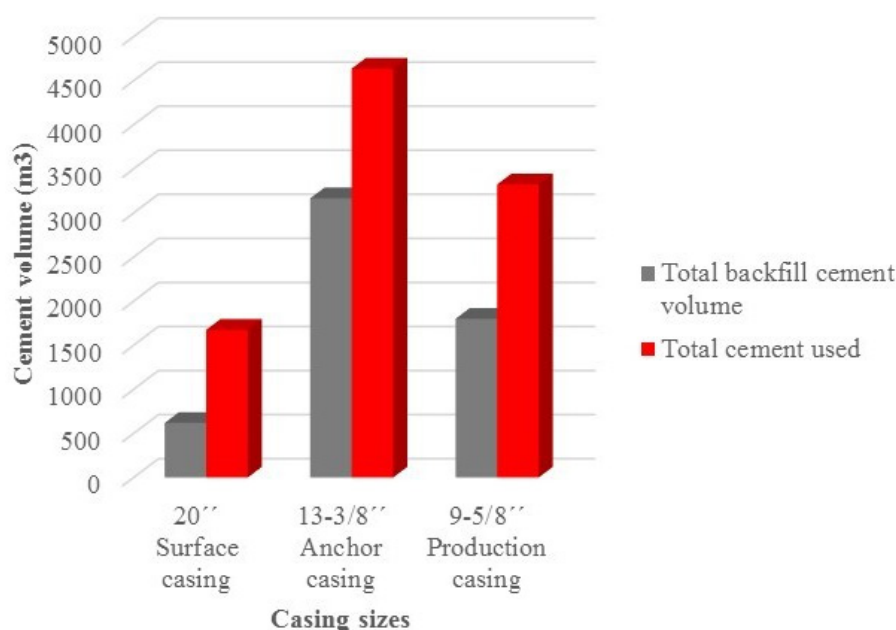


FIGURE 36: Comparison of backfill cement volume and total cement for casing cementing

8. CONCLUSIONS

The main conclusions drawn from this work are as follows:

- There is need to explore other viable cement placement techniques for both casing cementing and healing of lost circulation based on the challenges encountered during drilling.
- It is important to carry out calliper logging to assess wellbore conditions before running casing for casing cementing. Temperature/pressure logs can also assist in making the right decision on the wellbore conditions, the correct depth for cement plug placement during loss of circulation, and the expected challenges during running and cementing casings.
- Carrying out cement bond logging or temperature logging to locate the top of cement will help in the calculation of the cement volume to be placed during backfills and in reducing small backfill cementing and wait on cement time.
- There is need for immediate backfill cementing, especially for surface casing cementing since, in most cases, the cement volume involved is relatively small.
- Explore the use of inner string cementing or reverse circulation cementing, especially for anchor casing cementing which has the most backfill cementing jobs and large volume requirements.
- Review of the slurry design is necessary, aiming at lowering the cement slurry density to reduce pressure on the formation, and the best placement technique for the casing strings involved.
- Analysis of the viability of using light cement slurry, without compromising on the cement compressive strength and the additives to be used to lower the density, needs to be carried out, including the best placement techniques using the available cementing equipment.
- Introducing silica flour to a blend with Portland cement will improve on cement compressive strength retrogression at elevated temperatures, especially for production casing which is set in high temperature deeper sections of the geothermal wells. Another option is using other API classes of cement, e.g. class G cement, which is sulphate resistant in high temperature casing cementing.
- Analysis of the wait on cement time and the quantity of cement additives such as retarder, accelerators and anti-friction materials in the cement blend for casing cementing is important in adjusting the wait on cement time. Also, if temperature logging is used or there are good returns during drilling, the wait on cement (WOC) time can be adjusted according to formation temperatures. It is also critical to review the use of cement accelerators during placement of cement plugs.

ACKNOWLEDGEMENTS

I would like to sincerely thank the UNU-GTP director, Mr. Lúdvík S. Georgsson, and Deputy Director, Mr. Ingimar G. Haraldsson, for giving me this opportunity to take part in this six month geothermal training programme. I would like to extend my gratitude to the other UNU-GTP staff: Ms Thórhildur Ísberg - School Manager, Mrs. Frida Ómarsdóttir - Environmental scientist, and Mr. Markús A.G. Wilde - Service Manager, for their support and assistance during my stay in Iceland. Many thanks to the ISOR lecturers and instructors for their efforts, guidance and sharing of valuable knowledge during this training. I would like to sincerely thank my supervisor, Mr. Arnar B. Árnason, from Mannvit Engineering, for his good guidance and technical support during my project report writing. I am grateful to my employer, Kenya Electricity Generating Co. Ltd (KenGen), for giving me this opportunity to participate in this training.

Special thanks go to my family, especially my wife Joyce, daughter Caren and son Ryan, for their moral support and prayers, and to my colleagues in the 2014 UNU-GTP fellowship for your friendship and kindness. Above all, our almighty God - thank you for your care, protection, guidance and good health during my stay in Iceland.

NOMENCLATURE

ASW - Average cement slurry weight in kilograms per litre (Kg/l)
Lb/ft. - Casing weight in pounds per foot
Casing diameter - inches (")
BWOC - By weight of cement
 V_w - Volume of water in the casing cubic metres (m^3)
TOC - Top of cement
WOC - Wait on cement

REFERENCES

- Agapiou, K., and Charpiot, S., 2013: Cement and wellbore integrity. *Halliburton Cementing, International Cement Review*, August 2013.
- Bett, E.K., 2010: Geothermal well cementing, materials and placement techniques. Report 10 in: *Geothermal training in Iceland 2010*. UNU-GTP, Iceland, 99-130.
- Bour, D., and Hernandez, R., 2003: CO₂ resistance improved mechanical durability, and successful placement in a problematic lost-circulation interval achieved: reverse circulation of foamed calcium aluminate cement in a geothermal well. *Geothermal Resources Council, Transactions*, 27, 163-167.
- Bridge7, 2014: Cement bond interpretation. Bridge7, webpage: www.bridge7.com/grand/log/gen/casedhole/cbl.htm.
- Crain, E.R., 2014: Crain's petrophysical handbook - cement integrity logs part 1, webpage: spec2000.net/07-cementlog1.htm
- Devereux, S., 1998: *Practical well planning and drilling manual*. PennWell Corp., Tulsa, OK.
- Fann, 2014: *Mud balance model 140*. Fann Instrument Co., Houston, TX, website: www.fann.com.
- Finger, J., and Blankenship, D., 2010: *Handbook of best practice for geothermal drilling*. Sandia National Laboratories, CA, Sandia report, SAND2010-6048, 84 pp.

- Gabolde, G. and Nguyen, J.P., 2014: *Drilling data handbook* (9th edition). Editions Technip, Paris, 576 pp.
- Guerra, G., C.E., 1998: Cementing of geothermal wells. Report 6 in: *Geothermal training in Iceland 1998*. UNU-GTP, Iceland, 157-188.
- Halliburton, 2005: Foam cement delivers long term zonal isolation and decreases remedial costs. Halliburton newsletter, webpage: www.halliburton.com.
- Hernández, R., 2009: Reverse-circulation cementing and high performance geothermal cement. Halliburton webpage: www.halliburton.com.
- Hernández, R., and Nguyen, H., 2009: Foamed latex slurry and reverse circulation cementing enable drilling in lost circulation zone. *Geothermal Resources Council, Transactions*, 5 pp.
- Hole, H., 2008a: Geothermal well cementing. Petroleum Engineering Summer School, *Workshop 26, Dubrovnik, Croatia, June 2008*.
- Hole, H., 2008b: Geothermal well design - casing and wellhead. Petroleum Engineering Summer School, *Workshop 26, Dubrovnik, Croatia, June 2008*.
- KenGen, 2014: *Un-published well drilling programs and completion reports*. KenGen, Kenya.
- Lecourtier, M., and Cartalos, M.U., 1993: *Cementing technology and procedures*. Association for Research on Petroleum Drilling and Production Techniques (ARTEP), Editions Technip, Paris.
- Nelson, E.B., 1990: *Well cementing*. Schlumberger Educational Services, Texas.
- Nelson, E.B., 2012: Well cementing fundamentals. *Oilfield Review Newsletter*, Schlumberger Oilfield Glossary, webpages: www.glossary.oilfield.slb.com; www.sld.com/resources.
- NZS, 1991: *Code of practice for deep geothermal wells*. Standards Association of New Zealand, Wellington, NZ, New Zealand Standard 2403.
- Rabia, H., 1987: *Fundamentals of casing design*. Graham & Trotman, Ltd. Publishers, London.
- Rabia, H., 2001: *Well engineering and construction*. Entrac Consulting, 650 pp.
- Remedial Cementing, 2013: Remedial cementing. Petrowiki online resource center, webpage: [petrowiki.org/Remedial cementing](http://petrowiki.org/Remedial%20cementing).
- Rickard, B., Samuel, A.S., Alarcon, B., Bailey, A., and Howard, W., 2011: Reverse circulation cementing of geothermal wells: a comparison of methods. *Geothermal Resources Council, Transactions*, 35, 225-228.
- Rickard, W.M., Hernández, J., and Bailey, A., 2012: Drifting cement plugs for geothermal wells, *Geothermal Resources Council, Transactions*, 36, 317-320.
- Schlumberger, 2014: Schlumberger Ltd., website: www.glossary.oilfield.slb.com.
- Serva, 2011: PCT-621A twin pump cementing truck instruction manual. Serva SJS, webpage: www.SERVAgrou.com, China.
- Spielman, P., Hernández, R., and Nguyen, H., 2006: Reverse circulation of foamed cement in geothermal well. *Geothermal Resources Council, Transactions*, 30, 303-308.
- Steingrímsson, B., 2011: Geothermal well logging: cement bond and calliper logs. Presented at "Short Course on Geothermal Drilling, Resource Development and Power Plant", UNU-GTP and LaGeo, San Salvador, El Salvador, 9 pp.

Sveinbjornsson, B.M., 2014: *Case history: drilling well HE-53, Hellisheidi, Iceland*. UNU-GTP, Iceland, unpublished lecture notes.

Thórhallsson, S.: 2014: *Geothermal drilling technology*. UNU-GTP, Iceland, unpublished lecture notes.

APPENDIX I: Drilling progress diagrams for wells OW-43A, OW-731A and OW-40V

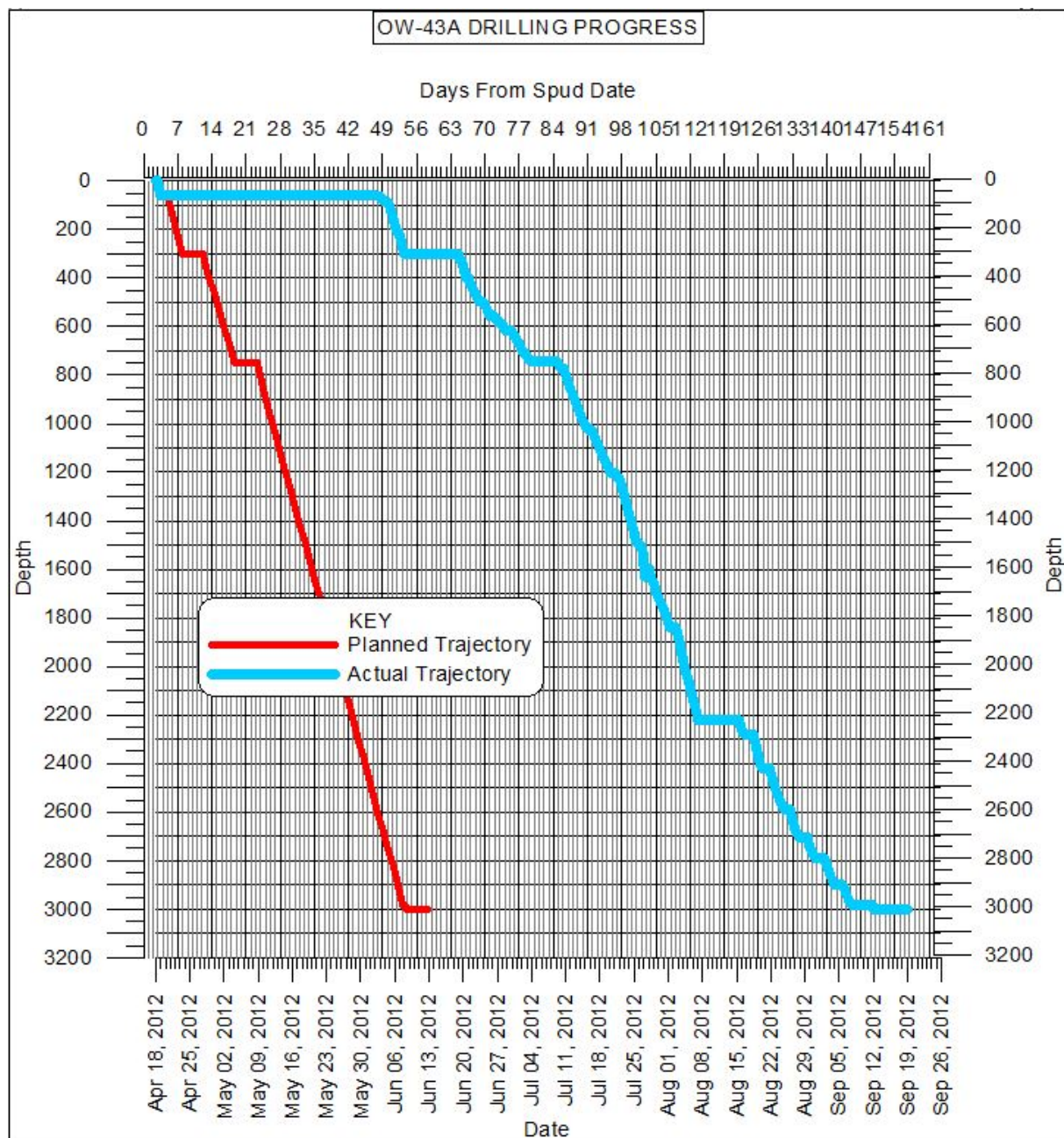


FIGURE 1: Drilling progress well OW-43A (Kengen, 2014)

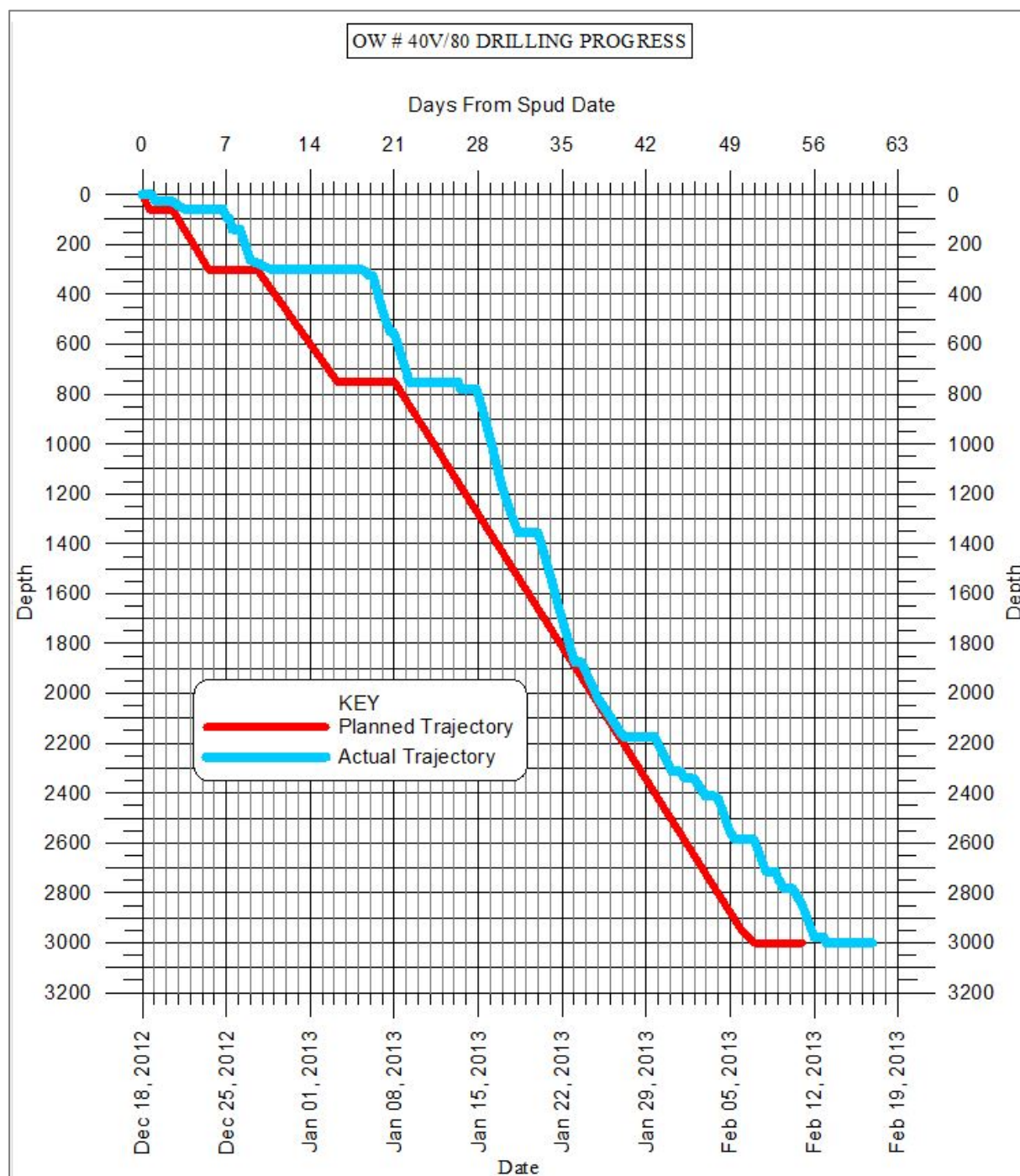


FIGURE 2: Drilling progress for well OW-40V (Kengen, 2014)

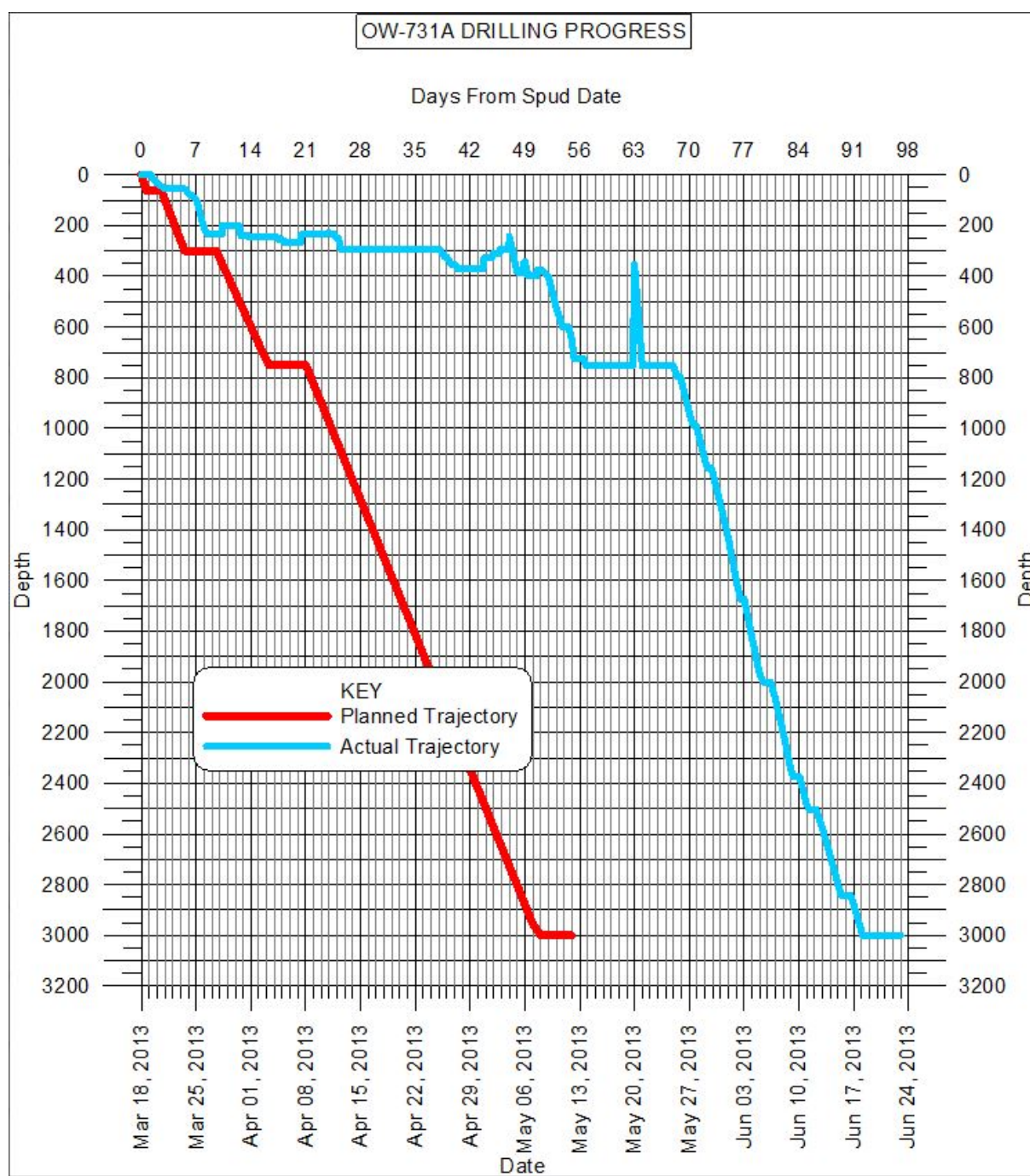


FIGURE 3: Drilling progress for well OW-731A (Kengen, 2014)

APPENDIX II: Summary of primary and backfill casing cementing

TABLE 1: Summary of the primary and backfill casing cementing in Olkaria, Kenya

No	20" surface casing		13-3/8" anchor casing		9-5/8" production casing	
	Total backfill cement volume (m ³)	Total cement volume used (m ³)	Total backfill cement volume (m ³)	Total cement volume used (m ³)	Total backfill cement volume (m ³)	Total cement volume used (m ³)
1	0.00	17.70	22.32	42.37	18.41	38.47
2	1.50	15.15	35.97	60.75	41.21	61.86
3	14.05	19.67	32.97	45.92	20.34	70.24
4	0.00	19.45	29.75	45.68	19.60	37.05
5	3.10	16.85	27.77	51.44	25.11	45.41
6	27.63	43.16	8.89	36.34	35.20	72.14
7	12.24	31.95	8.00	22.01	28.89	67.51
8	0.60	16.06	40.69	58.15	37.90	65.34
9	0.00	13.26	25.34	44.81	23.00	51.05
10	18.64	32.48	22.10	45.77	24.95	58.63
11	0.00	14.71	17.22	37.06	37.70	62.46
12	22.17	29.55	168.34	186.52	20.99	38.01
13	0.00	15.76	37.51	55.96	23.10	44.87
14	0.00	14.64	41.63	63.17	21.97	44.34
15	0.00	12.40	45.35	68.32	21.60	44.37
16	0.00	15.45	23.67	43.72	21.40	41.77
17	16.47	26.55	50.12	75.17	23.81	50.18
18	0.99	16.89	162.09	182.97	31.40	48.12
19	84.58	101.28	82.09	102.86	14.39	37.88
20	0.00	15.80	27.06	47.34	22.61	55.05
21	0.00	17.50	14.80	34.75	28.30	47.97
22	0.00	18.45	24.90	40.47	38.85	54.87
23	45.60	54.76	20.59	37.64	21.00	39.87
24	3.40	19.11	22.19	44.64	52.42	71.73
25	4.01	15.75	74.83	91.70	18.86	36.59
26	0.00	19.37	39.74	58.19	46.83	63.31
27	3.60	18.76	24.61	36.05	22.29	43.46
28	4.40	20.35	31.02	52.27	41.96	62.52
29	5.58	24.08	13.05	32.10	22.30	40.08
30	9.41	25.15	44.60	68.72	17.06	39.59
31	6.90	25.43	46.80	72.05	15.20	32.60
32	8.90	25.15	44.00	58.25	97.54	121.33
33	36.24	52.39	11.12	32.10	18.06	31.33
34	0.00	15.95	27.59	50.74	43.93	55.90
35	0.00	13.75	36.80	58.97	47.21	62.51
36	7.70	22.81	18.21	37.66	29.60	48.75
37	129.00	144.60	130.72	151.77	15.40	34.97
38	3.00	18.16	54.08	70.18	23.29	43.07
39	4.73	20.13	18.59	40.13	34.00	55.07
40	0.00	13.41	43.99	64.40	27.06	41.62
41	15.83	31.13	51.00	73.46	27.70	43.37
42	4.01	19.71	32.09	53.14	17.40	39.87
43	0.00	16.20	30.90	51.64	21.76	47.53

No	20" surface casing		13-3/8" anchor casing		9-5/8" production casing	
	Total backfill cement volume (m ³)	Total cement volume used (m ³)	Total backfill cement volume (m ³)	Total cement volume used (m ³)	Total backfill cement volume (m ³)	Total cement volume used (m ³)
44	27.35	43.41	86.96	113.21	22.25	43.14
45	6.57	22.57	33.23	65.30	15.60	43.85
46	0.00	18.04	32.09	52.54	14.30	33.92
47	0.00	17.30	22.01	42.79	26.20	89.97
48	20.01	36.25	80.51	102.87	17.30	49.35
49	2.96	21.50	70.39	100.06	25.71	52.17
50	2.96	17.06	9.00	33.44	10.00	31.44
51	7.17	20.48	167.00	195.15	11.97	41.82
52	0.18	17.27	98.14	128.09	36.65	61.54
53	0.00	17.24	44.63	66.64	69.98	84.22
54	14.30	26.71	52.90	72.05	41.52	66.89
55	0.00	17.45	47.27	80.42	28.30	54.14
56	0.00	14.50	27.14	54.28	23.22	45.50
57	3.47	20.26	6.50	37.70	17.66	44.33
58	0.00	16.85	40.65	58.84	28.31	59.52
59	0.45	16.50	35.99	55.59	72.05	100.90
60	8.19	25.74	122.66	156.68	1.08	17.58
61	5.40	25.55	29.75	39.20	6.74	19.67
62	1.00	16.69	19.71	41.27	30.06	60.00
63	0.00	13.64	15.40	39.97	27.00	46.94
64	4.73	23.37	160.81	185.06	2.30	16.70
65	2.60	19.04	12.90	33.99	6.61	23.06
66	0.90	15.75	25.30	42.60	24.50	45.24
67	11.57	31.02	23.71	53.77		
68	6.16	21.11	138.08	159.69		
Total	620.24	1676.14	3167.79	4638.52	1800.87	3324.54
Percent.	37%		68.29%		54.17%	



UNITED NATIONS
UNIVERSITY

UNU-GTP

Geothermal Training Programme

Orkustofnun, Grensasvegur 9,
IS-108 Reykjavik, Iceland

Reports 2014
Number 24

APPLICATION OF STABLE ISOTOPE GEOCHEMISTRY TO TRACING RECHARGE AND FLOW SYSTEMS OF FLUIDS IN THE OLKARIA GEOTHERMAL FIELD, KENYA

Melissa Nailantei Nkapani

Kenya Electricity Generating Company – KenGen

P.O. Box 785 – 20117, Naivasha

KENYA

mnkapani@kengen.co.ke

ABSTRACT

The long term success of any geothermal energy utilization depends on understanding groundwater movements and recharge areas. Water and steam condensates from subfields in the Olkaria geothermal field have been studied using the stable isotope ratios of hydrogen and oxygen to gain information on thermal fluid flow and to trace the origin of thermal waters.

Isotope fractionation factors and mass balance equations were used to characterize reservoir fluid composition of wells in the area, assuming single stage steam separation. Comparison of the two methods yields coherent results for the oxygen-18 isotope ratio, but the deuterium isotope ratio varies to some extent. The reservoir fluid isotope composition of the thermal waters suggests three recharge zones for the field: one from groundwater from the eastern Rift wall with δD about = -24‰; groundwater from the western Rift flank with δD about = -30‰; and the other from an evapo-concentrated source with δD about = 36‰. Qualitative interpretation of the available data suggests that the evapo-concentrated source largely contributes to the recharge of the East field, North East field and a part of the Domes field. Groundwater from the western rift wall recharges the West field of the area. The eastern Rift wall groundwater contributes to the southeast part of the Domes field.

The isotopic composition of some thermal waters in the Olkaria geothermal field indicates that there could be groundwater mixing between the waters from the flanks and the evapo-concentrated source. The chloride content of the recharge water cannot be used to determine the degree of mixing between these recharge zones because of the similar content of chloride in both types of water. Evolution of the water isotope composition of the well fluids over time indicates possible temporal variations related to the recharge zones. More data from boreholes and springs in the area must be collected to monitor the variations and evolution of water isotope composition in the field.

1. INTRODUCTION

The Olkaria geothermal field is a high temperature geothermal field located in the Kenya Rift valley about 120 km from Nairobi. The Kenya Rift valley is part of the East Africa Rift System (EARS) which

the Ololbutot fault zone have produced rhyolitic and obsidian flows, while eruptions in the Longonot and Suswa volcanoes have ejected pyroclastic ash which has blanketed much of the area (Lagat, 2004). Acidic lavas and their pyroclastic equivalent characterize the surface and near subsurface geology of the Olkaria geothermal field, which is inside a major volcanic complex that has been intersected by N-S trending normal faults. The main features of the structural geology of the volcanic complex, shown in Figure 2, include the ring structure which is characterized by numerous volcanic domes, interpreted as indicating the presence of a buried volcanic caldera. From the correlation of stratigraphy and alteration mineralogy zones in Olkaria, it can be deduced that the most prominent features are normal faults. The oldest faults follow the regional NW-SE trend and they define the shape of the stretched buried caldera: the

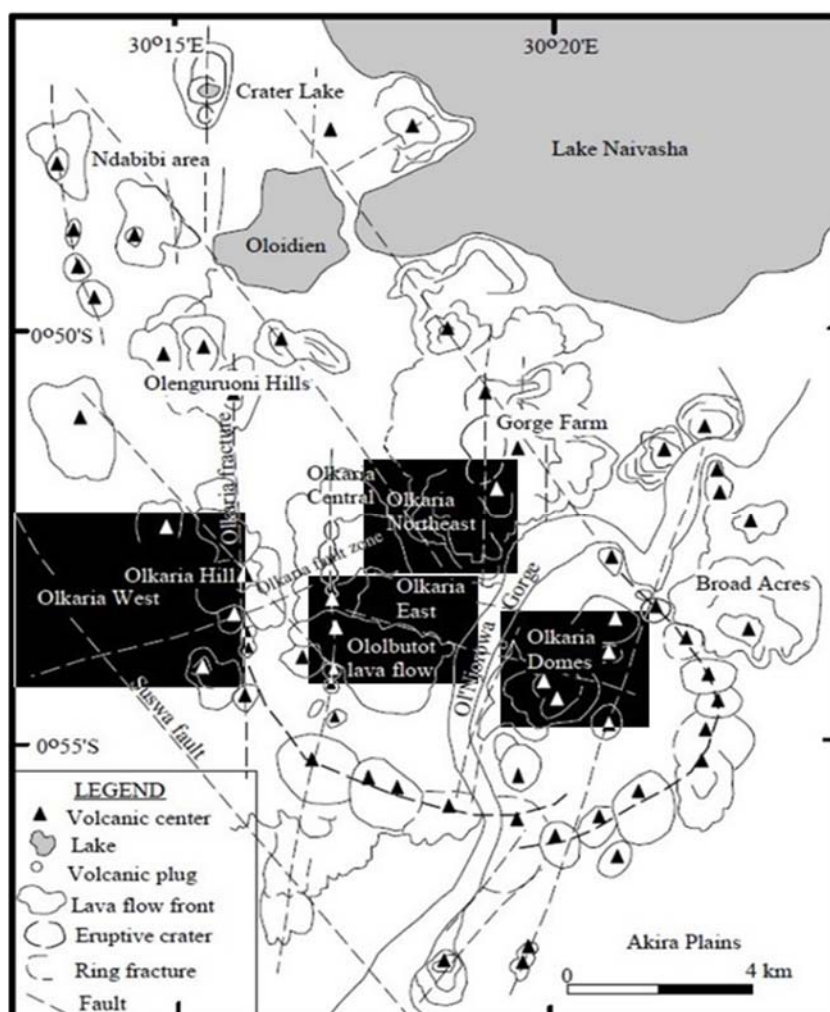


FIGURE 2: Structural geological map of the Olkaria geothermal field, from Clarke et al. (1990) also showing the study areas

the Gorge farm fault, Olkaria fracture and Suswa fault. Other younger faults include an ENE-WSW Olkaria fault and the Ololbutot fault, the Olkaria fracture and the Ol Njorowa Gorge trending in an N-S direction. The subsurface geology is characterized by tuffs, rhyolites, basalts and trachytes with minor intrusives. Structural features, including faults, dykes and intrusions, control the types and nature of fluid-rock interaction processes as well as fluid movement within the geothermal system (Mwania et al., 2014).

The first appearance of epidote (above 240°C) marks the upper limit to the Olkaria geothermal reservoir. The epidote zone is associated with the occurrence of high temperature clays like illite and chlorite. The zone occurs at a depth of about 500 m b.g.l. in the up-flow zones, and at around 800 m b.g.l. in the out-flow zones and sometimes deeper in the down-flow zones. Four (4) hydrothermal alteration assemblages defined by the first appearances of specific index minerals occur in the field including: a smectite-chlorite-illite zone (<300 m b.g.l.); a chlorite-illite zone (300-550 m b.g.l.); an epidote-chlorite-illite zone (550-1400 m b.g.l.); and an actinolite-epidote-chlorite-illite zone (1400-3000 m b.g.l.). The shallower occurrence of the high temperature mineral assemblages marks the upflow zone in the field. Three (3) major upflow zones, determined from the updoming of the alteration mineralogy and current measured temperatures in the Olkaria fields, were observed in the East/Northeast, Domes and Southeast fields (Mwania et al., 2014).

2. HYDROGEOLOGY OF THE RIFT VALLEY SYSTEM

The long term success of any geothermal energy utilization depends upon the understanding of groundwater movements and recharge areas. The hydrogeology of the Rift valley system has been extensively studied and reported by several authors. Allen et al. (1989), in their phase I report, collected physical hydrogeological data from over 600 boreholes drilled between the Tanzanian border in the south to Nakuru in the north. From the analysis of the data, they show that on a regional scale the Rift Valley system between Lakes Magadi and Lake Nakuru broadly exhibits the hydrogeological features observed for a valley - interfluvial system with prominent lateral groundwater flows from the Rift escarpment to the discharge areas on the Rift floor. In their phase II report, Allen and Darling (1992) studied the physical hydrogeology of the section of the Rift valley between Lake Baringo in the south and Lake Turkana in the north and also covered several quaternary volcanoes in the centre of the Rift, in particular Korosi, Paka, Silali and Emuruangogolak. From these, they obtained rainfall data from over 38 meteorological stations, surface water data and data from 70 boreholes, comparably lower than the number of boreholes used in the hydrogeological study of the area between Lake Magadi and Lake Nakuru. This is because this section of the Rift system is an arid and sparsely populated area where evaporation is evident and, therefore, called for the need to use indirect methods to assess groundwater conditions. Figure 3 shows a piezometric map designed by Allen and Darling (1992), based on lithological information, hydraulic data and construction details from boreholes drilled on Rift walls as well as from the Rift floor. The data they collected was used to construct a piezometric map of the southern part of the Kenya Rift. From this work they concluded that areas of groundwater recharge are on the east and west flanks of the Rift walls and discharge areas are on the Rift floor. Therefore, both Allen et al. (1989) and Allen and Darling (1992) concluded that the Rift floor obtains its groundwater recharge from the Rift escarpments, where substantial rainfall is present through grid faulting acting as channels for underground water; it has been suggested that these grid faults are quite active, implying that they are open.

Hydrogeologically, the structure of the Rift valley and, in particular, the major Rift faults and the system of grid faulting on the Rift floor, has a substantial effect on the groundwater flow systems of the area. Faults may facilitate flow by providing channels of fluid flow or they may be barriers to flow. Faulting in the Rift system along the axis of the Rift is mainly grid faulting. That is to say fluids flow along the axis of the Rift system and, therefore, cause groundwater flows from the flanks of the Rift towards the Rift floor to follow longer paths, reaching greater depths, and to align flows within the Rift along its axis. Therefore, groundwater flows from elevated recharge areas to low lying discharge areas, in this case to the Rift floor, where the Olkaria geothermal field is located.

2.1 Hydrogeology of Olkaria geothermal field and Lake Naivasha catchment

The Rift area around the Olkaria geothermal field is bounded by the Mau escarpment in the west, rising to an altitude of up to 3000 m, and the Nyandarua – Kikuyu Escarpment in the east, with an elevation of 3999 m. The area is further bounded by a relatively high lying fault, particularly the Kinangop plateau of 2100 m elevation in the Eastern rift. The floor of the Rift valley culminates near Lake Naivasha at 1884 m. Rivers Malewa and Gilgil, being perennial rivers, provide much of the recharge to the lake besides local precipitation. The Gilgil River has its headwaters high in the Bahati forests and drains parts of the eastern slopes of the Bahati escarpment. River Malewa is believed to derive its recharge from the western slopes of the high Nyandarua range (Allen et al., 1989). The lake has no surface outlet but still remains a fresh water lake in an area where evaporation rates are very high. This, therefore, indicates that this lake, which is located in the southern part of the Rift floor, has some subsurface drainage. Several researchers have tried to quantify subsurface discharge from the Lake Naivasha catchment area. McCann (1972) carried out a comprehensive hydrogeological study of the Rift valley catchment area and was able to quantify the groundwater flows of Lake Naivasha by defining evaporation rates, and the water inflow from direct precipitation and evapotranspiration values and, thus, arrived at a value of $34 \times 10^6 \text{ m}^3/\text{yr}$ as groundwater outflow from the lake. McCann (1974) and Sikes (1935) also used water

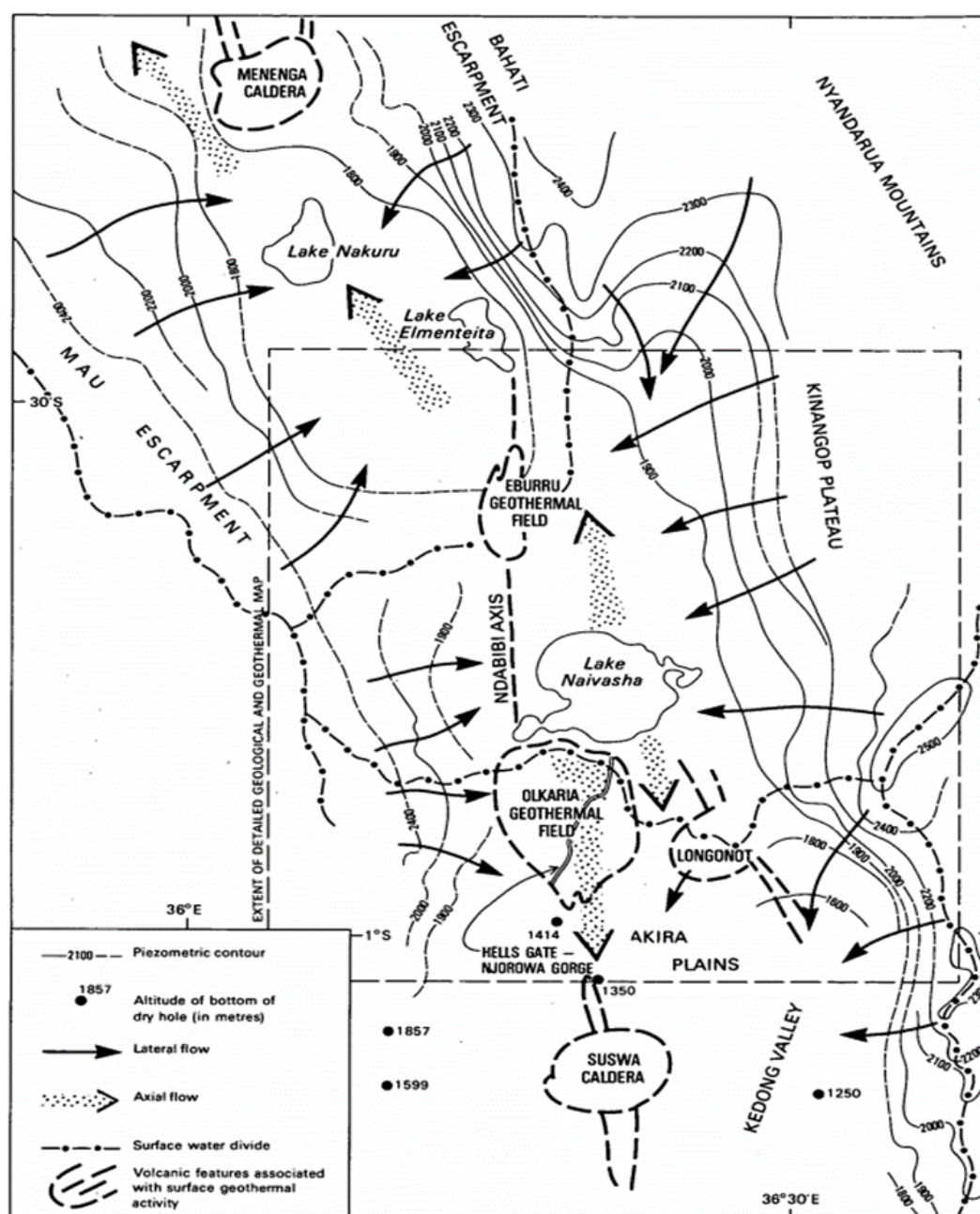


FIGURE 3: A piezometric map of the Kenya Rift Valley System, adapted from Allen et al. (1989)

balance studies, and estimated subsurface discharge from the lake as $43 \times 10^6 \text{ m}^3/\text{yr}$, which agrees reasonably well with McCann's values of $34 \times 10^6 \text{ m}^3/\text{yr}$. Panichi and Tongiorgi (1974) used an isotopic model and defined the isotope signatures of the influent waters and the lake water, as well as the evaporation from the lake, and arrived at a value of $254 \times 10^6 \text{ m}^3/\text{yr}$ as the groundwater recharge, much higher than the values reported by Sikes (1935) and McCann (1972). Allen et al. (1989) did stable isotope studies, recalculated the values obtained by Panichi and Tongiorgi (1974), and arrived at a value of $52 \times 10^6 \text{ m}^3/\text{yr}$ as the groundwater drainage from Lake Naivasha, close to what previous researchers obtained. So the subsurface drainage from Lake Naivasha can be estimated to be $50 \times 10^6 \text{ m}^3/\text{yr}$. The Naivasha catchment area is a more hydrogeologically complex environment, receiving water from direct precipitation and from the Rift flanks, either as stream flows or a subsurface flow, and discharging to the southern and northern sides as stated by various authors, particularly, McCann (1972) who used piezometric levels to suggest that the water from the lake was flowing in both northerly and southerly directions. Allen et al. (1989) used regional head gradients and permeability to try to quantify the

northern and southern flows and, according to their results, a north - south groundwater gradient of 0.05m/m exists over the Olkaria –Longonot area, and 0.1m/m in the Olkaria field, taking into account the estimated hydraulic conductivity of the area, and taking 5 km as flow depth. The southern flow at depth from Lake Naivasha was estimated to be $41 \times 10^6 \text{ m}^3/\text{yr}$.

The Olkaria geothermal field is located south of the lake; therefore, the recharge to this field could possibly be connected to groundwater on the Rift floor. Allen et al. (1989) used stable isotopes to trace Lake Naivasha's water. They found out that river waters discharging to the lake have a very depleted isotope composition, indicative of their origin at higher altitudes, more specifically the Nyandarua ranges. This is facilitated by major Rift faults, which act as conduits for lateral flow or barriers which lead to deeper flow paths, and by grid faulting, which tends to align flow paths within the Rift along its axis. However, the lake water is enriched in stable isotope ratios due to evaporation to which it is subject. They also indicated that the lake water appeared to be detected at least 30 km to the south of Suswa volcano, which is to the south of the Olkaria geothermal field. Arusei (1991) used halide ratios, a Cl/Br ratio diagram, to determine whether Lake Naivasha has an exposed groundwater table and also to determine the origin of recharge to wells in the Olkaria geothermal fields. He concluded that there exists a correlation between the escarpment Rift floor and geothermal waters and showed that the Olkaria geothermal reservoir gets recharge water from either the Rift groundwater or the escarpment waters, although he was not able to infer a single recharge from any of this. He was also able to conclude that Lake Naivasha is not an exposed groundwater table, since the concentrations of many of the constituents increase away from the lake. For this reason, he concluded that the flow in the lake is both in northern and southern directions.

Much cannot be done regarding hydrology if subsurface structures are not mentioned, because fractures control fluid movement to a great extent. The movement of water from the escarpment to the Rift floor is complicated by the geological structures present in this area. Understanding subsurface structures and hydrothermal alteration of the Olkaria geothermal area is essential in determining the characteristics of the reservoir and the behaviour of the geothermal fluid. The existence of faults and other structural features, like dykes and intrusions, is paramount in geothermal utilization, because they control the types and nature of the water rock interaction processes, as well as the fluid movement within the system. It is also necessary to determine the influence of the faults in the existing fault pattern and to map the fluid flow through available channels. Fault systems in the field include ENE-WSW, NW-SE, N-S, E-W structures and are associated with fluid movement. They are all defined as normal faults through the correlation of lithology and alteration mineralogy zones. These faults include the N-S faults (Ololbutot fault, Olkaria fracture and Olnjorowa Gorge), ENE-WSW (Olkaria fault) NW-SE (Gorge farm fault) and the Ring structure. These faults control fluid movements and also impact mixing fluid patterns.

3. FLUID CHEMISTRY

3.1 Characterization of fluid chemistry in Olkaria geothermal field

The East field is characterized by a shallow steam-dominated zone of >300 m thickness overlying a liquid reservoir. A deep liquid reservoir is present in the Domes field, which is evidenced by the chemistry of the fluids discharged, as well as from the temperature and pressure profiles reported for this field. Discharge data and production field monitoring data show a fairly high enthalpy in the Olkaria East and Northeast fields, with reported enthalpy values of >2100 kJ/kg. The West field enthalpy data show a fairly low enthalpy compared to the rest of the fields. In the Domes field, saturated liquid enthalpy is observed in the northwest part of the area, but high enthalpy in the southeast part. Various water types are discharged from these fields, evident from the reported chemistry of the fluids. Table 1 shows the chemical composition of well fluids used for isotope studies. The Olkaria East field discharges mostly fluids of the Na-Cl type with slightly elevated sulphate levels. This could be interpreted as showing the presence of an upflow zone. The Olkaria Northeast field also discharges fluids with Cl in

TABLE 1: Chemical composition of wells in Olkaria geothermal field

Well	Year	WHP (bar-g)	GSP (bar-g)	Enthalpy (kJ/kg)	pH@ 20°C	SiO ₂	B	Na	K	Ca	Mg	CO ₂	SO ₄	H ₂ S	Cl	F	CO ₂	H ₂ S	H ₂	CH ₄	N ₂
2	1988	4.5	4.2	2287	9	741	4.4	1067	190	0.7	0.1	126.7	47	0.14	813.5	0.072	110.7	3.64	6.94	1.07	2.91
4	1987	1.4	5.5	1533	8.7	635	2.9	362	65	0.3	0.1	88	15	0.9	500	68	104	6.42	4.07	0.28	4.52
6	1988	5	4.6	2378	8.88	541	8	398	51	2.68	0.14	76	24	0.23	759	45	160.1	2.28	9.18	1.46	0.66
10	1988	5.4	4.1	2457	8.48	482	13	769	106	0.24	0.13	62.5	99	0.9	882	123	131.1	7.53	9.5	0.72	0.11
11	1988	5.5	4.5	2222	8.85	601	7	479	75	0.88	0.5	102	40	0.27	677	83	105.8	1.95	6.23	0.77	0.15
13	1988	5	4.6	2400	9.65	857	4.2	415	59	1.39	0.2	251	24	4.45	351	83	96.7	1.81	13.31	0.46	1.43
14	1984	5.6	4.4	2600	5.75	638	1.52	584.5	102.3	0.6	0.39	116.1	89	0.34	582.4	52.85	174.8	5.8	15.55	0.33	0.68
15	1988	5	5	2600	8.8	447	4.1	920	151	2.19	0	133	100	17	1369	88	105.8	2.57	9.55	0.51	0.67
16	1988	5	4.8	2150	8.79	696	4.6	475	63	0.47	0	108.2	17.7	0.48	621	84	122.7	2.89	7.77	0.54	0.54
17	1987	4.8	4.2	2600	9.7	724	6.2	1092	168	3.7	0.08	246	77	1	1308	60	55.7	12.21	13.29	0.56	9.02
18	1988	7.5	4.5	2596	8.66	557	4.9	845	132	0.91	0.12	151	57	0.17	1273	125	81.6	2.45	0.43	0.29	10.69
19	1987	5	4.5	2500	9.15	689	10.3	666	124	0.7	0.03	57.2	61	2.7	796.2	104	275.3	25.2	10.62	0.73	0.49
20	1988	5	5	2300	8.85	676	8.1	566	90	1.24	0	141	43	0.54	894	95	78.1	2.44	8	0.17	0.42
21	1988	5	4.5	2390	9.5	643	4.6	436	72	0.96	0.08	290	137	6.39	401	63	168.1	3.65	11.69	0.37	1.95
22	1988	6	5	2610	9.63	488	3	492	70	1.22	0	290	34	6.8	298	61	198.7	3.65	10.85	0.27	0.82
23	1988	6	4.6	2400	9.44	643	4	350	43	0.99	0.15	226	20	1.6	259	161	81.5	3.16	10.13	0.16	0.77
24	1987	5	4.5	2460	9.09	732	8	659	126	0.7	0.4	114	78	0.2	800	124	143	4.65	10.01	0.59	0.67
25	1988	5	5	1920	9.03	726	4.2	583	130	0.65	0.5	141	32	1.2	658	69	81	183.8	3.26	8.62	0.27
26	1988	5.5	4.6	2025	9.37	599	3	408	70	0.1	0.06	102.1	38	1.6	282	52	223.3	11.86	12.99	0.39	0.62
701	1987	4.1	3.1	1255	9.4	605	3.4	476	92	0.81	0.05	128	90	4.76	685	50	228	8.79	6.14	0.73	2.7
703	1989	5.4	5.3	1820	9.5	509	3	719	144	0.43	0.06	180.4	37	0.61	946	81	129.3	1.86	5.08	0.68	1.04
709	1993	1.2	0.7	1047	10.17	682	4.7	290	102	0.3	0	191.1	71	2.72	703	48	122.2	0.62	0.01	0.09	2.45
714	1991	19.3	2.8	1125	9.64	649	5.5	594	123	0	0	211	42	10.2	684	57	174.1	9.9	2.42	0.54	4.31
719	1998	3.1	2.1	1038	9.3	700	5.6	690	90	0.2	0	345.3	26.2	23.18	604	83	498.4	22.68	5.7	1.06	11.32
301	2000	7.4	1.5	1180	8.67	855	6.8	1283	208	0.66	0.07		112	3.96	240	105	426.1	3.55	11.27	0.83	1.05
302	2000	5.7	1.8	1130	9.72	744	3.5	633	101	1.04	0.08	578	54	3.43	505	77	367.5	1.11	3.22	0.38	0.33
304	1999	3.9	2.6	875	8.13	364	3.3	959	74	3.48	1.73	1752	93	0.97	52	24	11462	2.66	7.37	1.72	0.94
306	1999	4	1.8	1019	9.15	551	6.3	850	96	1.2	0.08	1081	50	2.9	251	62	1136.8	2.89	7.83	0.94	0.56
901	1999	6.2	0.7	1600	9.36	636	5.7	453	73	0	0.1	361.6	47	16.5	290	77.7	339	23.7	10	1.5	6
902	1999	3.3	1	1338	9.61	800	2.6	509	37	0	0	482.8	109	2	205	52.3	361	1.9		2.2	
903	1999	3.8	1.4	1073	9.8	611	1.66	571	39	0	0	706	108	1.1	178	46.6	341	0.9	18.94	1.8	
914A	2010	2	3.2	2236	9.81	613.5	2.68	953.7	163.1	1.24	0	820.16	52.4	1.83	306		887.7	0.53		2.21	0.63
916A	2010	6	4	2500	9.46	570	3.46	525.1	184.2	1.32	0.56	301.18	67.9	1.63	323.4	235.2	225.9	0.43	14.87	1.22	21.31

excess of HCO_3 , except for a few wells. The West field water is predominantly of the bicarbonate type, which could be indicative of peripheral waters. In the Domes field, a mixture of fluids is produced, both Na-Cl and HCO_3 waters. It is clear from the water types discharged in these fields that subsurface geological structures control the movement of recharge fluids, as well as the fluid types observed in these areas.

Applications of the Na/K solute geothermometer, proposed by Fournier and Potter (1982), indicate temperatures between 250°C and 275°C for the East and Northeast fields, temperatures from 230 to 250°C for the West field, whereas the Domes field waters show temperatures $>270^\circ\text{C}$. The Cl distribution in the area delineates upflow zones and, from the interpretation of these chloride distribution maps, four distinct upflow zones are postulated in the East, Northeast, West and the Domes fields.

3.2 Application of stable isotope geochemistry

Water is by far the most abundant component of the geothermal fluid and also the major energy carrier in geothermal systems. The application of stable isotope geochemistry mainly involves natural isotopes that form water molecules being used to identify the source and track the movement of water, both on the surface and through underground channels. Table 2 shows the state and abundance of natural isotopes in water molecules. Isotope measurements have been used extensively in geothermal studies to provide information on the characteristics of the geothermal fields, particularly to provide information on mixing between water masses of different origins and temperature, define underground flow patterns and the degree of interaction with the reservoir rock, and also to provide information on the origin of various fluid components. Stable isotopes have proven to be ideal tracers because they are integral constituents of the water molecules.

TABLE 2: The water isotopes

Isotope	Average natural abundance	Half life
^1H	99.985	Stable
^2H	0.015	Stable
^3H	10^{-15}	12.43 years
^{16}O	99.76	Stable
^{18}O	0.20	Stable

Subsurface processes change the original isotopic characteristics of geothermal water. The exchange at high temperature, due to water-rock interactions, leads to an increase in the oxygen-18 content of the water, and a subsequent oxygen decrease in the country rock. This phenomenon can be identified on δD - $\delta^{18}\text{O}$ plots as the O^{18} of the water will plot towards less negative values (a positive oxygen shift). A negative oxygen isotope shift may also occur if the CO_2 content of the fluid is relatively high (Truesdell and Hulston, 1980). Generally, little or no corresponding shift is observed in the deuterium value because rocks contain relatively little hydrogen. Thus deuterium isotope ratio has been used as an excellent tracer in hydrological systems. In this report, the stable isotopes of deuterium and oxygen-18 are used to assess the source of recharge water in the Olkaria geothermal field, and to elucidate possible mixing patterns, and then to conceptualize a recharge model for the system.

According to Giggenbach and Stewart (1982), reservoir waters originating at temperatures above surface boiling, mostly cool as they ascend to the surface. This may be due to conduction, mixing with low temperature fluids or adiabatic boiling as a result of depressurization. Cooling by conduction will not alter the isotope composition of the reservoir fluid, but dilution and boiling have been known to cause characteristic changes to reservoir fluids. In high temperature geothermal systems, fluids boil during their rise to the surface as a result of depressurization, if the pressure is hydrostatic which is common for liquid-dominated reservoirs. Then the corresponding boiling temperatures follow a boiling point - depth curve. These secondary processes, affecting the isotope composition of geothermal fluids during

their rise to the surface, have to be corrected for when making appropriate interpretations of the isotope data. Steam separation due to adiabatic boiling has different effects, depending on the mode of phase separation. Truesdell et al. (1977) suggest two possible processes: a) one stage separation during which steam separates from the liquid continuously but stays with the ascending water, maintaining isotopic equilibrium, and then separates at one temperature, say at the wellhead temperature; and b) continuous steam separation where the steam separates from the parent water continuously as soon as it is formed. They later suggested that an intermediate process between these two processes exists in natural systems, with single step steam separation generally predominating. Generally, the fractionation of deuterium and oxygen-18, as a result of adiabatic boiling, leads to the enrichment of heavier isotopes in the water phase, and their depletion in the vapour phase, although deuterium is known to have a cross-over point at about 220°C, above which the normal fractionation is reversed and the heavy deuterium isotopes concentrate in the vapour phase as opposed to the liquid phase (Bottinga and Craig, 1968). The high rate at which isotopic equilibrium is attained in geothermal systems, between the liquid and vapour phases, defines the isotope distribution between the liquid phase and the vapour phase, assuming that equilibrium has been attained. This, therefore, implies that the distribution between the water phase and the vapour phase is governed by isotopic fractionation factors which are temperature dependent. These factors, denoted as α_D and $\alpha^{18}O$, were defined by Bottinga and Craig (1968) and are expressed in Equations 1 and 2. The relationship between the fractionation factors and the temperature is used later in this report to calculate reservoir fluid composition.

$$\alpha_{\text{effO}^{18}} = \frac{([H_2O^{18}]/H_2O^{16})_{\text{water}}}{([H_2O^{18}]/H_2O^{16})_{\text{vapour}}} \quad (1)$$

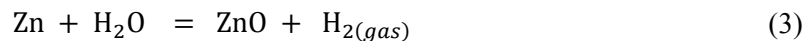
$$\alpha_{\text{eff(D)}} = \frac{([HDO]/H_2O)_{\text{water}}}{([HDO]/H_2O)_{\text{vapour}}} \quad (2)$$

Isotope data obtained from fumaroles, springs and lakes are interpreted with respect to the analytical results obtained. This is not the case for geothermal samples obtained from high temperature wells, for example from the Olkaria field. Isotope signatures of samples collected at the surface need to be recalculated to reservoir conditions in order to account for isotopic changes due to boiling and steam loss associated with the mode of phase separation.

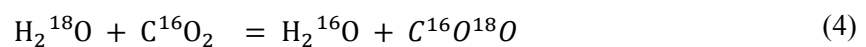
3.2.1 Stable isotope analysis and mass spectrometer calculation

Stable isotope analysis

At the Science Institute, University of Iceland, the stable isotope ratios of oxygen and hydrogen of water were analysed using a Finnigan MAT 251 Mass Spectrometer (prior to 2006) and a Thermo Delta Plus Mass Spectrometer thereafter. The deuterium content in the dataset from Sveinbjörnsdóttir (1988) was determined after reduction to molecular hydrogen (Coleman et al., 1982). Equation 3 shows the reaction involved in the analysis:



In the dataset from Karingithi (2000), the deuterium isotope ratio was determined by the method of Horita (1988), in which the water sample is equilibrated with H_2 gas using a Pt catalyst. The oxygen-18 ratio was determined after exchange with and determination on CO_2 , as shown in Equation 4 (Epstein and Mayeda, 1953).



In the datasets from ISOR in 2010 and 2012 (Sekento, 2012), the samples were measured on a Thermo Delta Plus Mass Spectrometer with continuous He flow, using the Gasbench device.

Mass spectrometer calculation

Absolute concentrations are difficult to determine; therefore, isotope analyses are always presented as relative abundances and, consequently, reported as ratios of proportion of light to heavy species in the

sample relative to those in the standard, for this case VSMOW (Vienna Standard Mean Ocean Water) (Geyh, 2000). Equations 5 and 6 show the methods of computation:

$$\delta_D\text{‰} = \left(\frac{(D/H)_{\text{Sample}} - (D/H)_{\text{VSMOW}}}{(D/H)_{\text{VSMOW}}} \right) 1000 \quad (5)$$

$$\delta_{O^{18}}\text{‰} = \left(\frac{(^{18}O/^{16}O)_{\text{Sample}} - (^{18}O/^{16}O)_{\text{VSMOW}}}{(^{18}O/^{16}O)_{\text{VSMOW}}} \right) 1000 \quad (6)$$

where D/H and $^{18}O/^{16}O$ represent isotope ratios in the sample and the standard.

3.2.2 Isotope composition of fluids

This report entails the interpretation of isotopic data from various subfields of the Olkaria geothermal field during utilization. Hence, several data sets, collected at different times, were used. Table 3 shows the isotopic composition of well fluids while in Table 4 there is mainly data from springs. Sveinbjörnsdóttir (1988) determined isotope ratios in liquid phase and steam condensate samples collected from 19 wells in the East field at 6 bar-a, and from wells OW-701 and OW-703 in the Northeast field. Data for two fumaroles and springs from the Hell's Gate area were also obtained from Sveinbjörnsdóttir's (1988) results. Karingithi (2000) collected liquid phase samples only from the Northeast, West and Domes fields. Results for the boreholes north of Lake Naivasha: Olsuswa and the Ndabibi borehole, were obtained from Sekento (2012). The isotope composition of groundwater from the Rift wall waters was obtained from Allen and Darling (1992). Ojiambo and Lyons (1993) reported isotope ratios for local and Kinangop precipitation.

Isotope analysis reported by Sveinbjörnsdóttir (1988), Karingithi (2000), and Sekento

TABLE 3: Isotope composition of wells fluid in the Olkaria geothermal field

Well	Location	Liquid phase		Steam phase	
		Oxygen ($\delta^{18}O\text{‰}$)	Hydrogen ($\delta D\text{‰}$)	Oxygen ($\delta^{18}O\text{‰}$)	Hydrogen ($\delta D\text{‰}$)
¹ 2	East	3.78	18	-0.45	1.3
¹ 4		5.35	32.6	-1.37	-4.2
¹ 16		4.02	17.4	-0.78	-1.5
¹ 10		5.04	27.8	-0.39	1.1
¹ 11		3.78	18.2	-0.39	2.3
¹ 13		4.47	25.3	-0.11	7.5
¹ 14		4.75	25	0.54	9.4
¹ 15		5.51	23.6	0.27	2.6
¹ 16		4.16	17.6	-0.25	-0.8
¹ 17		6.36	32	0.2	4.7
¹ 18		5.46	25.5	0.44	5.6
¹ 19		5.86	29	-0.18	-0.4
¹ 20		4.36	20.2	-0.5	-0.3
¹ 21		6.29	36.3	-0.36	5.1
¹ 22		4.85	26.7	-0.76	2.4
¹ 23		5.7	26	0.49	6.6
¹ 24		4.19	20.3	-0.3	3.2
¹ 25		3.76	17.8	-0.6	-0.5
¹ 26		4.38	24.2	-0.16	6.8
¹ 701	Northeast	3.45	24	-1.06	3.9
¹ 703		4.3	32.9	-1.03	3.7
² 709		4.18	23.7		
² 714		3.71	23.7		
² 719		3.43	22.3		
² 301		-0.16	-1.7		
² 302		0.87	7.6		
² 304		-2.21	-9.3		
² 306		-0.04	0.5		
² 307		-2.02	-5.8		
² 308	Domes	-4.55	2.5		
² 901		4.97	32.2		
² 902		3.22	21.8		
² 903		3.09	21.7		

¹ (Sveinbjörnsdóttir, 1988), ² (Karingithi, 2000)

(2012) was carried out at the Science Institute, University of Iceland, and the results are presented in the conventional delta notation in ‰ relative to the VSMOW standard (Vienna Standard Mean Ocean Water). The accuracy of the measurements for deuterium was 0.7 ‰, and for ^{18}O was 0.05 ‰.

TABLE 4: Stable isotope composition of precipitation, spring waters, fumarole steam, borehole fluids and Lake Naivasha water

Sample identity	Location	Sample description	Oxygen ($\delta^{18}\text{O}\text{‰}$)	Hydrogen ($\delta\text{D}\text{‰}$)
¹ Spring 1	Hell's gate	Warm	3.25	23.4
¹ Spring 2	Hell's gate	Warm	2.07	12.5
¹ Spring 3	Hell's gate	Warm	3.56	15.7
¹ Spring 4	Hell's gate	Warm	2.77	14.9
¹ Spring 5	Hell's gate	Warm	4.55	22.9
¹ Spring 6	Hell's gate	Warm	4.86	14.9
¹ Spring 7A	Hell's gate	Warm	3.69	16.2
¹ Spring 7B	Hell's gate	Warm	4.86	15.6
¹ Spring 8	Hell's gate	Warm	3.69	28.4
¹ Spring 10	Hell's gate	Warm	4.05	20.3
¹ Spring 11	Hell's gate	Warm	3.82	20.7
¹ Spring 12	Hell's gate	Warm	3.69	20
¹ Spring 13	Hell's gate		3.69	31.2
¹ Fumerole 1	Hell's gate		-0.5	9.1
¹ X-2 fumerole	Olkaria		-2.91	-6.2
⁴ Ndabibi borehole	North of L. Naiv.	cold	-2.9	-11.8
⁴ Olsuswa borehole	North of L. Naiv.	cold	3.1	20
³ Local sample		precipitation	-5.05	-32.75
³ Kinangop		Precipitation	-4.8	-28
¹ Mau Escarpment		precipitation	-0.33	-1.4
² 28	Eastern Rift wall	28°C	-4.8	-28
² 39	Eastern Rift wall	29°C	-4.5	-20
² 82	Eastern Rift wall	20°C	-4.1	-24
² 93	Eastern Rift wall	23°C	-3.5	-17
² 95	Western Rift wall	24°C	-3.5	-16
² 96	Eastern Rift wall	23°C	-4.7	-24
² 101	Western Rift wall	25°C	-5.3	-35
² 122	Western Rift wall	35°C	-4.8	-27
² Lake Naivasha			6.6	36

¹ (Sveinbjörnsdóttir, 1988); ² (Allen and Darling, 1992);

³ (Ojiambo and Lyons, 1993); and ⁴ (Sekento, 2012)

3.3 Characterization of reservoir fluid composition

Several physical processes may alter the isotopic characteristics of thermal waters during their ascent to the surface. These processes include: cooling by conduction; mixing of two different thermal waters; mixing of thermal waters with non-thermal waters; subsurface boiling and steam separation; as well as non-equilibrium surface evaporation. The recalculation of aquifer isotope composition is essential if the isotope composition of the thermal waters are to be used to trace their source. Cooling by conduction has not been known to cause characteristic changes in isotope composition of fluids. Shallow thermal aquifers are commonly prone to mixing with cooler waters, mainly originating from local precipitation, and mixing with thermal waters of meteoric origin that may originate in precipitation at higher elevation. The isotope signatures and the chemistry of these two water types are considerably distinct. The oxygen isotope ratio and the chloride content of the thermal waters help to distinguish between these water

types. Most of the wells drilled in the Olkaria geothermal field discharge fluids at high pressure. Therefore, the influence of cold water on shallow thermal reservoirs is considerably reduced. Isotopic fractionation, due to subsurface boiling and steam separation, is common in high temperature geothermal well fluids, such as those in the Olkaria field where aquifer temperatures are $>200^{\circ}\text{C}$. The fluid in these wells flows under pressure greater than the saturated vapour pressure and, therefore, a mixture of steam and water is discharged at the wellhead. Certain dissolved constituents in the liquid phase partition into the vapour phase, mainly the gases due to their low aqueous solubility. Most of the solutes initially dissolve in the liquid concentrate in the liquid phase and rarely partition into the vapour phase. Isotopes are also significantly fractionated during boiling. The light isotope oxygen 16 will concentrate in the vapour phase, while the corresponding oxygen-18 isotope is enriched in the liquid phase. Because of this fractionation, boiling in thermal waters will affect isotope composition, depending on the water-steam ratio and the mode of steam separation, i.e. single stage or continuous steam separation (Truesdell and Hulston, 1980). Liquid phase samples analysed by Sveinbjörnsdóttir (1988) were collected at atmospheric pressure at the weir box and, therefore, show enrichment in the heavier isotopes of deuterium and oxygen-18 as a result of boiling. The steam condensate was collected at 6 bar-a from most of the wells in the East field and in two wells from the Northeast field, wells OW-701 and OW-703. To calculate the deep fluid deuterium and oxygen-18 ratios for the water collected at 1 bar-a pressure, it is necessary to compute the water steam ratio at the point of sampling so as to recalculate the aquifer composition. The relative amount of water evaporating during adiabatic cooling in a well can be determined if the aquifer temperature is known. The well is assumed to receive the water in the liquid phase at a depth where the stationary pressure in the well is higher than the saturated vapour pressure of the water. When the water flows up the well, its temperature remains constant until the stationary pressure becomes equal to the saturated vapour pressure. At that point, the water begins to cool through adiabatic boiling; consequently, a mixture of steam and water is present in the well. As a result, the temperature of the water is lowered and the steam-to-water ratio increases as the mixture moves further upwards. This is expressed by the steam fraction denoted X in Equation 7:

$$X = \frac{H^{\text{dl}} - H^{\text{l}}}{H^{\text{v}} - H^{\text{l}}} \quad (7)$$

where H^{dl} is the enthalpy of saturated liquid at the reservoir temperature;
 H^{l} is the enthalpy of saturated liquid at the temperature of sampling;
 H^{v} is the enthalpy of saturated vapor at the temperature of sampling.

From the steam fraction calculated and the isotope fraction of the isotopes in the steam and water phases, the deep liquid composition can be computed from the conservation of mass equation expressed by Equation 8:

$$\delta_{\text{dl}} = \delta_{\text{l}}(1 - X) + \delta_{\text{v}}(X) \quad (8)$$

where δ_{dl} is the reservoir composition;
 δ_{l} and δ_{v} are the isotope ratios of the composition of the liquid and vapour, respectively.

The above methodology for evaluating the composition of the deep reservoir fluid was applied when samples of the two phases were collected. This was not the case for Karingithi's (2000) samples when only the water samples were available for measurements and interpretation. For this case, isotope fractionation factors were defined at specific temperatures by Bottinga and Craig (1968), taking into account the fractionation factors' dependence on temperature coming into play. Assuming that vaporization within geothermal reservoirs takes place at a phase equilibrium with the net removal of steam, changes in the isotope ratios maybe determined. The isotope composition of the deep reservoir fluid can be computed from water samples using Bottinga and Craig's (1968) Equation 9, where the effective isotope fractionation factor for the separation of the isotopes between the two phases is considered to be the ratio of the components in the water and vapour phases, respectively, and assuming that equilibrium conditions were met during isotope fractionation. Then the effective isotope fractionation factors can be replaced by the equilibrium constant:

$$1000 \ln \alpha = A + B(10^3/T) + C(10^6/T^6) + D(10^9/T^3) \quad (9)$$

where $\alpha_D = P_{H_2O}/P_{HDO}$ and $\alpha^{18}O = P_{H_2^{16}O}/P_{H_2^{18}O}$ and the numerical values for the constants are:

	HDO-H ₂ O	H ₂ ¹⁸ O-H ₂ ¹⁶ O
A	559.69	-7.174
B	-808.06	4.716
C	772.81	-0.058
D	-54.41	_____

From the formula of Bottinga and Craig (1968), it is found that the isotope fractionation factors at a temperature of 159°C, corresponding to a pressure of 6 bar-a, are given as $1000 \ln \alpha_D = 11.9$ and $1000 \ln \alpha^{18}O = 3.63$. Therefore, assuming a single stage steam separation, the vapour phase concentration can be computed using Equation 10:

$$1000 \ln \alpha_{A-B} = \delta_A - \delta_B \quad (10)$$

where δ_A and δ_B denote the respective ratios in the two phases.

Reservoir oxygen and deuterium isotope fluid composition for the Karingithi (2000) data was then computed using Equations 11 and 12, respectively:

$$(\delta D)_{dl} = (\delta D)_1 - X_{6\text{bar}} \times 1000 \ln \alpha(D) \quad (11)$$

$$(\delta^{18}O)_{dl} = (\delta^{18}O)_1 - X_{6\text{bar}} \times 1000 \ln \alpha(^{18}O) \quad (12)$$

3.3.1 Comparison between the two methods of reservoir fluid characterization

Table 5 shows the isotope ratio for reservoir fluid calculated using mass balance equations and isotope fractionation constants at the sampling temperatures. The Δ isotope ratio shows the difference between the two methods for evaluating the deep reservoir fluid, one using the conservation of mass equation where the two phases are available, and the other using isotope fractionation factors where only the liquid phase is available. From the computations, the calculated reservoir fluid oxygen-18 values agree quite well. The difference for the deuterium values of the deep reservoir fluid varies between $\delta D = -3.60\text{‰}$ and $\delta D = 0.23\text{‰}$. For some wells, the difference is much greater between the calculated deuterium isotope composition of the steam phase and the measured composition, but this difference is not seen in the computation of the reservoir fluid because the calculated steam fraction is relatively low.

4. RESULTS AND DISCUSSION

4.1 The $\delta D - \delta^{18}O$ relationships

Springs and boreholes

Figure 4 shows the water isotope composition of springs and boreholes within the Olkaria geothermal field. This is plotted along with a sample from Lake Naivasha and precipitation from the Naivasha area (local) and Kinangop. This is then plotted along with the Continental Africa rain line (CARL) and the Kenya Rift Valley evaporation line (KRVEL), defined by Ármannsson (1994) and Clarke et al. (1990), respectively. The Lake Naivasha sample shows enrichment in the isotope ratios with $\delta D = 36\text{‰}$ and $\delta^{18}O = 6.6\text{‰}$. This enrichment in the stable isotope ratios is explained by evaporation to which the lake water is subject. The precipitation samples show a depletion in the stable isotope ratios, i.e. $\delta D = -28\text{‰}$, and $\delta^{18}O = -4.8\text{‰}$ for the Kinangop sample, and slightly lower $\delta D = -32.7\text{‰}$ and $\delta^{18}O = -5.05\text{‰}$ for the local precipitation. The isotope composition of groundwater is represented by 13 warm springs sampled

TABLE 5: Aquifer composition calculated

Well	Location	H ₀ (kl/kg)	WB		Steam Oxygen ($\delta^{18}\text{O}\%$)	Steam Hydrogen ($\delta\text{D}\%$)	Calculated steam phase		Steam fraction(X) at 6 bar a	#Reservoir fluid Oxygen ($\delta^{18}\text{O}\%$)	#Reservoir fluid Hydrogen ($\delta\text{D}\%$)	#Reservoir Calculated Oxygen ($\delta^{18}\text{O}\%$)	#Reservoir Calculated Hydrogen ($\delta\text{D}\%$)	ΔOxygen ($\delta^{18}\text{O}\%$)	$\Delta\text{Hydrogen}$ ($\delta\text{D}\%$)
			Oxygen ($\delta^{18}\text{O}\%$)	Hydrogen ($\delta\text{D}\%$)			Oxygen ($\delta^{18}\text{O}\%$) – 6 bara	Hydrogen ($\delta\text{D}\%$) – 6 bara							
'2	East	2287	3.78	18	-0.45	1.3	-0.69	2.09	0.22	2.18	11.16	2.13	11.34	0.05	-0.18
'4		2350	5.35	32.6	-1.37	-4.2	0.68	14.38	0.19	3.21	20.38	3.61	23.98	-0.4	-3.6
'6		2378	4.02	17.4	-0.78	-1.5	-0.28	2.62	0.17	2.67	11.87	2.75	12.55	-0.08	-0.68
'10		2457	5.04	27.8	-0.39	1.1	0.67	11.83	0.15	3.62	20.42	3.77	21.99	-0.16	-1.57
'11		2222	3.78	18.2	-0.39	2.3	-0.54	2.95	0.18	2.45	12.55	2.42	12.67	0.03	-0.12
'13		2400	4.47	25.3	-0.11	7.5	-0.29	7.01	0.25	2.47	16.03	2.42	15.91	0.05	0.12
'14		2600	4.75	25	0.54	9.4	0.2	8.24	0.19	3.19	18.05	3.12	17.82	0.07	0.23
'15		2600	5.51	23.6	0.27	2.6	1.14	8.53	0.13	4.17	18.04	4.28	18.84	-0.12	-0.8
'16		2150	4.16	17.6	-0.25	-0.8	-0.35	1.99	0.21	2.54	10.79	2.52	11.38	0.02	-0.59
'17		2600	6.36	32	0.2	4.7	1.34	13.11	0.22	3.93	20.58	4.18	22.41	-0.25	-1.84
'18		2596	5.46	25.5	0.44	5.6	0.9	9.25	0.17	3.83	18.5	3.91	19.12	-0.08	-0.62
'19		2500	5.86	29	-0.18	-0.4	1.01	11.04	0.21	3.63	18.07	3.88	20.46	-0.25	-2.39
'20		2300	4.36	20.2	-0.5	-0.3	-0.17	4.15	0.21	2.65	12.7	2.72	13.61	-0.07	-0.91
'21		2390	6.29	36.3	-0.36	5.1	1.43	17.28	0.2	4	24.46	4.35	26.85	-0.35	-2.39
'22		2610	4.85	26.7	-0.76	2.4	0.5	10.84	0.15	3.41	19.72	3.59	20.98	-0.19	-1.25
'23		2400	5.7	26	0.49	6.6	0.95	9	0.2	3.78	18.1	3.87	18.57	-0.09	-0.47
'24		2460	4.19	20.3	-0.3	3.2	-0.36	3.92	0.22	2.48	13.04	2.47	13.2	0.01	-0.16
'25		1920	3.76	17.8	-0.6	-0.5	-0.69	2	0.22	2.16	10.75	2.14	11.3	0.02	-0.55
'26		2025	4.38	24.2	-0.16	6.8	-0.05	7.87	0.18	2.89	17.39	2.91	17.59	-0.02	-0.2
'701		1255	3.45	24	-1.06	3.9	-0.82	7.66	0.19	2.1	16.66	2.14	17.36	-0.04	-0.7
'703		1820	4.3	32.9	-1.03	3.7	-0.03	15.62	0.16	2.91	24.05	3	25.57	-0.16	-1.95
'2709	West	1047	4.18	23.7			-0.32	6.9	0.21			2.56	16.33		
'2714		1125	3.71	23.7			-0.65	7.11	0.2			2.26	16.66		
'2719		1037	3.43	22.3			-0.93	5.67	0.21			1.93	15.05		
'301		1180	-0.16	-1.7			-3.75	-13.18	0.24			-1.01	-4.19		
'302		1130	0.87	7.6			-2.95	-5.97	0.22			-0.12	3.31		
'304		874	-2.21	-9.3			-5.62	-20.29	0.1			-2.35	-9.55		
'306		1018	-0.04	0.5			-3.66	-11.48	0.17			-0.64	-1.57		
'307		852	-2.02	-5.8			-5.47	-17.19	0.09			-2.16	-6.33		
'308		780	-4.55	2.5			-7.94	-9.53	0.05			-4.5	1.74		
'2901		1600	4.97	32.2			0.38	14.05	0.19			3.3	23.64		
'2902	Domes	1338	3.22	21.8			-1.18	4.71	0.24			1.59	13.77		
'2903		1073	3.09	21.7			-1.12	5.75	0.19			1.83	15.42		
'3914A		2236	-	-			-	-				-0.54	8.2		
'3916A		2500	-	-			-	-				3.63	21.02		

¹ (Sveinbjörnsdóttir, 1988); ² (Karingthi, 2000); ³ (measurements by ISOR in 2010); # - calculated using mass balance equation

around the Hell's gate area, and two cold boreholes, Olsuswa and Ndabibi, located north of Lake Naivasha. The $\delta D - \delta^{18}O$ relationship shows that the spring data cluster close to the KRVEL, gives a mean of $\delta^{18}O = 3.7\text{‰}$, and a standard deviation of 0.9‰ . The mean $\delta D = 17.9\text{‰}$ with a standard deviation of 3.7‰ , excluding springs 8 and 13 which indicate a relatively high deuterium content of $\delta D = 28.4\text{‰}$ and $\delta D = 31.2\text{‰}$, respectively. The evapo-concentrated groundwater on the Rift floor has been suggested to be flowing in both northerly and southerly directions. Therefore, enrichment in the isotope ratios of the spring samples collected south of the lake indicates that their recharge is partly from an evaporated source. The Olsuswa and Ndabibi boreholes are located close to each other, but the water from these two boreholes shows different isotope ratios. The Ndabibi borehole water is depleted in oxygen-18 to about $\delta^{18}O = -2.9\text{‰}$ and deuterium to about $\delta D = -11.8\text{‰}$, while water from the Olsuswa borehole is enriched in oxygen-18 to about $\delta^{18}O = 3.1\text{‰}$ and deuterium to about $\delta D = 20\text{‰}$. This difference in the isotope ratio indicates that the Ndabibi borehole is getting its recharge mainly from precipitation, whereas the Olsuswa borehole is mainly recharged from the evapo-concentrated source. The difference in the isotope ratios between these two very close boreholes could, therefore, be explained with reference to underground channels that control fluid movements in the area. The deuterium ratio in all these samples, except that from the Olsuswa borehole, is significantly higher than the deuterium ratio of the local precipitation. Therefore, it is suggested that precipitation around the Naivasha area contributes insignificantly to groundwater in the area. However, more isotope data on precipitation in the area is needed to conclusively confirm this.

Samples from wells

Figure 5 shows the relationship between the vapour phase and the liquid phase isotope ratios of samples of thermal origin. The figure demonstrates that liquid samples are enriched in both oxygen-18 and deuterium, relative to their corresponding vapour phase samples. The isotope composition of fluids from Fumarole 1 and Fumarole X-2, located in the Hells Gate

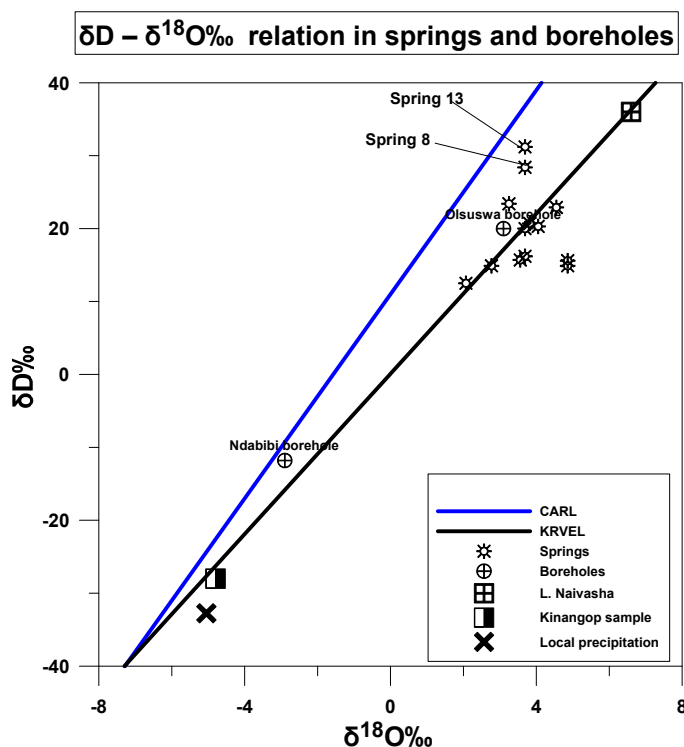


FIGURE 4: The $\delta D - \delta^{18}O$ relationships of springs and borehole water in the area around Olkaria geothermal field

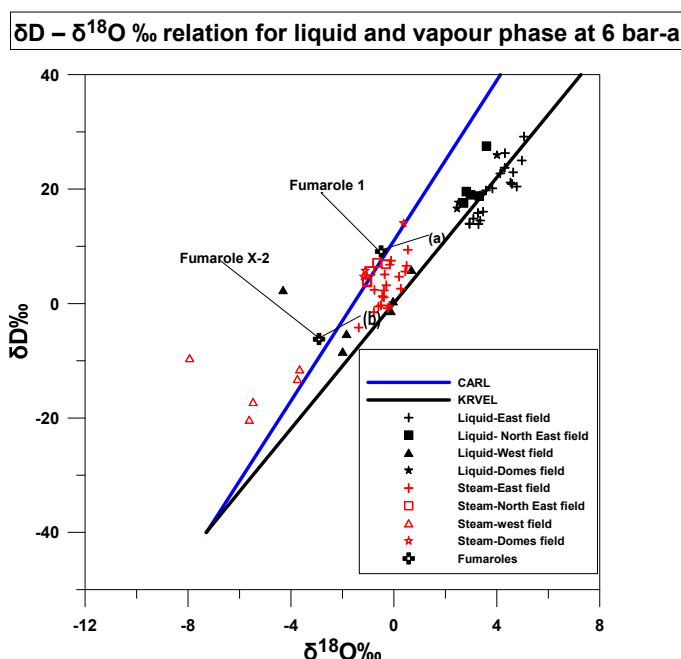


FIGURE 5: The $\delta D - \delta^{18}O$ relationship between liquid and vapour phase isotope ratios at 6 bar-a of Olkaria geothermal wells

area, are also shown in Figure 5. Fumarole 1 fluid shows depletion in the oxygen-18 ratio to about $\delta^{18}\text{O} = -0.5\text{‰}$, and enrichment in the deuterium isotope ratio to about $\delta\text{D} = 9.1\text{‰}$, whereas Fumarole X-2 fluid shows depletion in both the oxygen-18 and deuterium ratios to about $\delta^{18}\text{O} = -2.91\text{‰}$ and $\delta\text{D} = -6.2\text{‰}$, respectively. Assuming single stage steam separation, and that the samples from the two fumaroles tap fluids at reservoir temperatures close to the well temperatures in the area, then the liquid composition can be defined as shown in the plot as (a) and (b). From the figure, it can be seen that the isotope composition of Fumarole X-2 (b) is very close to that of the wells in the Olkaria West field, whereas Fumarole 1 (a) fluid is more related to that of the East field, although less influenced by the evapo-concentrated water source.

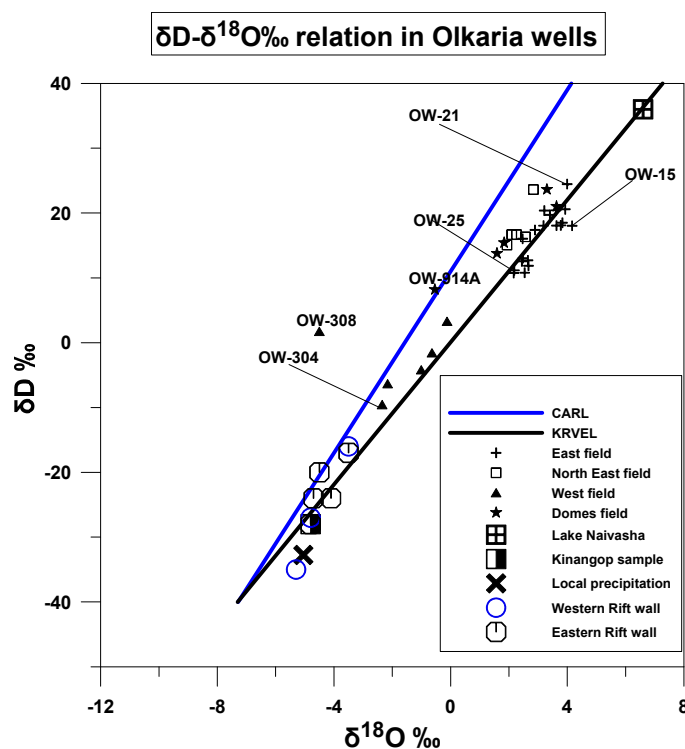


FIGURE 6: The $\delta\text{D}-\delta^{18}\text{O}$ relationship of aquifer fluids in Olkaria wells

than that from well OW-25, which shows the smallest oxygen shift ($\delta^{18}\text{O} = 2.16\text{‰}$) in the field. The larger oxygen isotope shift observed in the aquifer fluids of well OW-15 could be interpreted as deep circulation, and extensive water-rock interaction associated with the water. The mean δD value for the 19 well samples is 16.75‰ , with a standard deviation of 5.72‰ , with enrichment of deuterium observed in well OW-21: $\delta\text{D} = 24.46\text{‰}$. This enrichment in the deuterium isotope ratio in the well OW-21 sample could be explained with a larger component of the evapo-concentrated source. In Figure 6, the Northeast samples also plot close to the evaporation line. The mean $\delta^{18}\text{O} = 2.35\text{‰}$ is slightly lower than that from the East field. This could be a result of a high water-rock ratio, which could obscure oxygen isotope shifts in the fluids. The highest reported deuterium isotope ratio for the Northeast field samples is $\delta\text{D} = 24.05\text{‰}$, which is close to what was reported for the East field samples. Therefore, despite these two fields being located at some distance from each other, they still seem to get most of their recharge from the evapo-concentrated source, thus implying that these two subfields are hydro-geologically connected, and there possibly exist underground flow channels connecting these two fields to the same recharge. The Domes field samples, similar to the East field and the North East samples, plot close to the evaporation line, with the exception of the sample from well OW-914A which plots on the precipitation line. The well OW-914A sample exhibits isotope ratios of $\delta^{18}\text{O} = -0.54\text{‰}$ $\delta\text{D} = 8.20\text{‰}$; the well OW-916A sample, exhibiting $\delta^{18}\text{O} = 3.63\text{‰}$ and $\delta\text{D} = 21.02\text{‰}$ is located in the southeast part of the Domes field, Figure 7, shows distinct isotopic signatures despite the fact that these two wells are 800 m apart.

The $\delta\text{D} - \delta^{18}\text{O}$ relationship of the estimated aquifer fluid isotope composition within the Olkaria geothermal field is shown in Figure 6, along with that of groundwater from the eastern and western Rift walls, local and Kinangop precipitation, as well as Lake Naivasha water. In the figure, it can be seen that most of the groundwater from the Rift wall plots close to the intersection between the precipitation and the evaporation lines with isotope ratios of about $\delta^{18}\text{O} = -4.8\text{‰}$ and $\delta\text{D} = -28\text{‰}$, respectively, which is characteristic of high altitude precipitation. The Olkaria East field wells are mainly located on NW-SE and NE-SW trending faults, shown in Figures 7a and 7b. Isotope results are available for 19 wells in the East field, illustrated in Figure 6. These samples tend to cluster along the evaporation line. The mean oxygen-18 ratio is $\delta^{18}\text{O} = 3.12\text{‰}$ with a standard deviation of 0.66‰ . This shows that these samples have a relatively similar oxygen isotope ratio. The sample from well OW-15, located in the East field, shows a larger oxygen isotope shift ($\delta^{18}\text{O} = 4.17\text{‰}$)

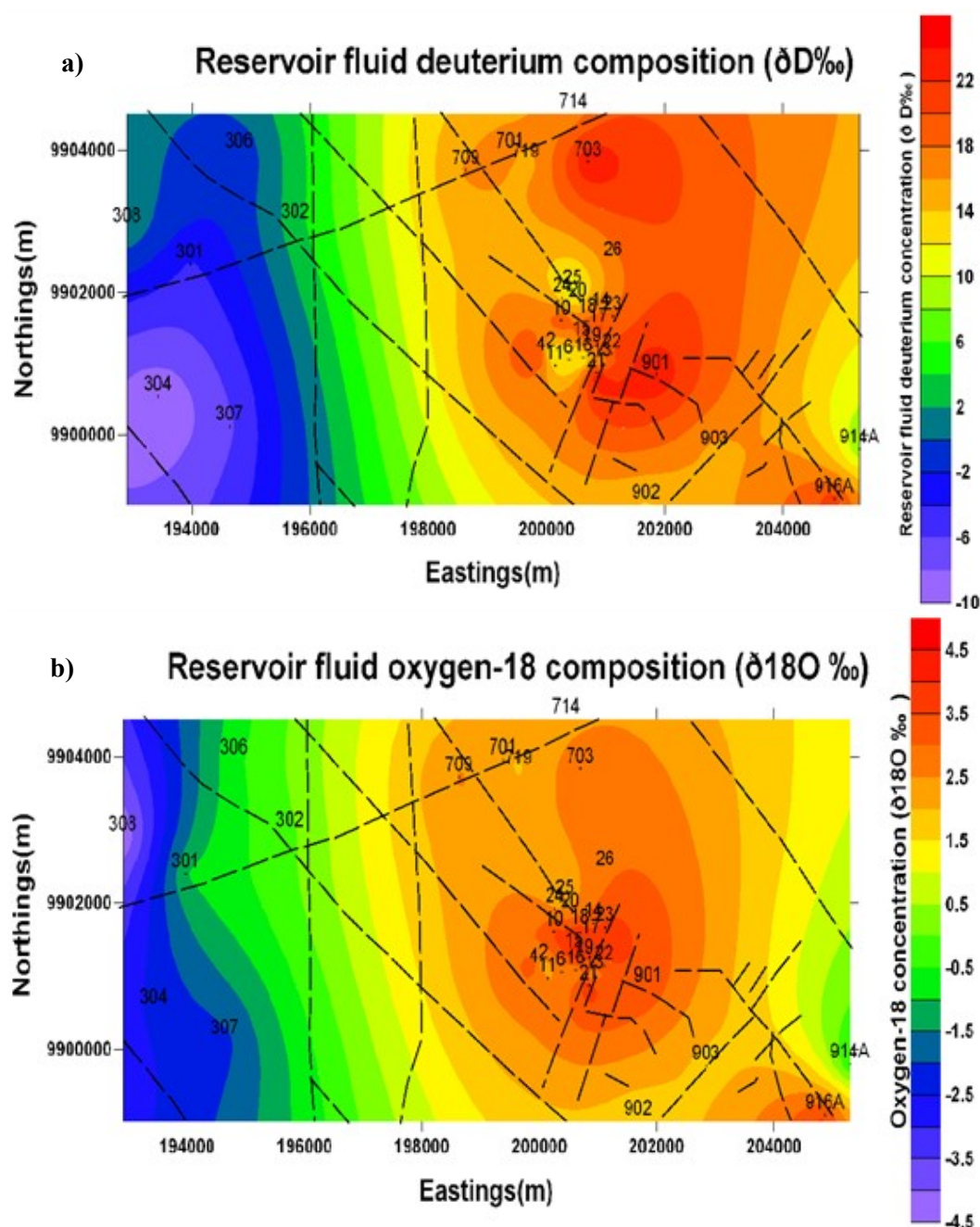


FIGURE 7: Shows the distribution of a) aquifer deuterium, and b) oxygen-18 isotope ratios associated with the structural geology of the Olkaria geothermal field

This could be explained by the effects of faults that control fluid movement in the area. The NW-SE trending fault cutting through well OW-916A, as shown in Figure 7, could possibly be acting as a barrier to escarpment water from the eastern flank which is possibly recharging well OW-914A. The possibility of the ring structure also controlling fluid movement cannot be ruled out, but that cannot be confirmed because of the scarcity of data from the area. The Olkaria West field exhibits a distinctly different recharge source compared to the rest of the fields. The samples from this field show a mean of $\delta^{18}\text{O} = -1.80\text{‰}$ and $\delta\text{D} = -2.77\text{‰}$ with well OW-304 fluid having a deuterium isotope ratio of $\delta\text{D} = -9.55\text{‰}$. It is suggested that these wells get their recharge from groundwater from the western Rift wall. The samples also indicate that there could be some mixing between water from an evapo-concentrated source and the rift wall groundwater along the evaporation line, with the waters of the rift wall providing a major contribution to the aquifers in this field. The negative oxygen isotope shift seen in the aquifer fluid of well OW-308 of the West field could be a result of CO_2 bubbling, caused by bicarbonate type

waters discharged in this field. The depleted deuterium content indicates lighter fluids, characteristic of fluids from high altitudes.

4.2 Evolution of reservoir fluid isotope composition of wells in Olkaria geothermal field

Table 6 shows the isotope composition variation with time for 6 wells in the Olkaria geothermal field. Data was obtained by Allen and Darling (1987), Sveinbjörnsdóttir (1988), and Karingithi (2000).

TABLE 6: Variations of reservoir Isotope ratios with time

Wells	1987		1988		2000	
	Oxygen ($\delta^{18}\text{O}\text{‰}$)	Hydrogen ($\delta\text{D}\text{‰}$)	Oxygen ($\delta^{18}\text{O}\text{‰}$)	Hydrogen ($\delta\text{D}\text{‰}$)	Oxygen ($\delta^{18}\text{O}\text{‰}$)	Hydrogen ($\delta\text{D}\text{‰}$)
OW-10	-1.71	-7.92	3.73	20.88	3.24	15.68
OW-16	2.48	4.42	2.54	9.02	2.18	6.52
OW-23	2.65	5.80	4.15	18.70	3.04	13.50
OW-15			4.26	16.99	3.12	13.09
OW-19			2.15	9.27	2.49	10.47
OW-25			4.20	20.21	3.37	18.61

Figure 8 shows characteristic changes of reservoir fluid deuterium composition in 6 wells in the East field, sampled between 1987 and 2000. Wells OW-15, OW-19 and OW-25 have available results only for the years 1988 and 2000, whereas results for wells OW-10, OW-16 and OW-23 are available for the years 1987, 1988 and 2000. The isotopic results show a drastic increase in the water isotope composition between the years 1987 and 1988. The much depleted value for well OW-10, compared to the other wells sampled at the same time, could be an analytical error. The figure also shows a decrease in the isotope ratio between the years 1988 and 2000 for almost all wells. This could be explained by temporal variations associated with recharge waters, particularly the amount of rainfall and the average relative humidity which affect the degree of evaporation in the area.

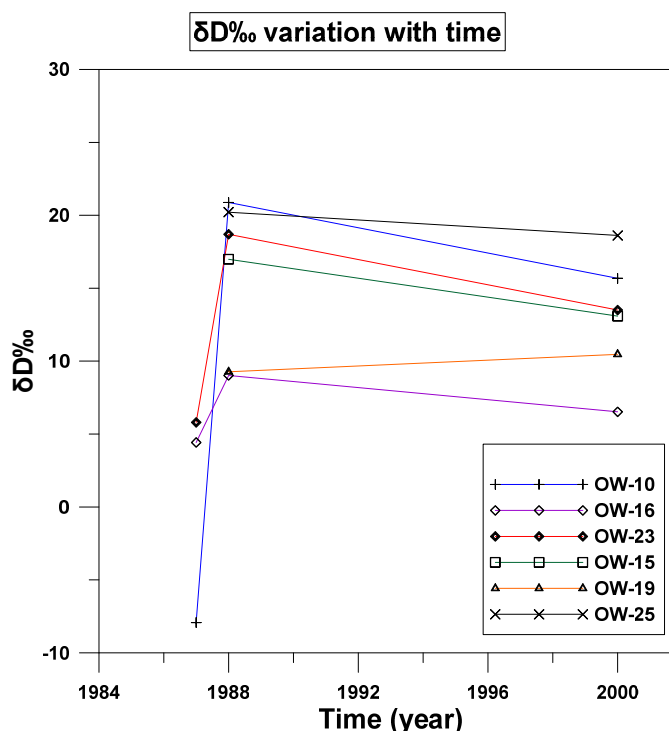


FIGURE 8: A plot showing deuterium isotope ratio variation with time in 6 wells sampled between years 1987 and 2000

4.3 Mixing of evapo-concentrated water with escarpment recharge water

A δD -Cl plot is presented in Figure 9. The figure shows that groundwater from the Rift wall and the evapo-concentrated water have a similar chloride concentration. This limits the use of chloride in indicating mixing patterns between these two recharge waters. It can be seen from the plot that the evapo-concentrated water contributes more to the recharge of most of the aquifer fluids than groundwater from the rift walls. The east, northeast and southeast parts of the Domes field show relatively similar deuterium isotope ratios, but the aquifer Cl concentrations of fluids in these fields

varies considerably between 300 mg/kg and about 1000 mg/kg in the East field, indicated in Figure 10, where the regional distribution of chloride is demonstrated. The Northeast field samples seem to lie between the two extreme cases. This high chloride could be explained as uptake of the chloride from the rocks or could possibly indicate upflow of deep geothermal fluid (Karingithi, 2000) which could be related to deep circulation of the recharge water in these fields. The West field fluid chloride concentration is relatively low or about 200 mg/kg.

4.4 The stable deuterium isotope as a natural tracer

The hydrogen isotope is the most widely used conservative isotope because it is inert and highly mobile (Arnórsson, 2000). It has been used extensively as a tracer to locate recharge zones to geothermal reservoirs because the water content of all common rocks is considered so low that isotopic exchange involving the hydrogen isotope is insignificant.

Therefore, the deuterium content of the waters will effectively not change during underground passage of water. However, its application as a natural tracer depends on the following assumptions: the groundwater is meteoric in origin; no changes in the isotope ratio take place underground; climatic conditions have not changed significantly in the area for at least 8000 years (Árnason, 1976). Reservoir fluid

deuterium has been used to trace the flow of recharge water in the Olkaria geothermal field, as indicated in Figure 11. The fluids recharging the East, Northeast and a part of the Domes field are waters showing enrichment in the hydrogen isotope; the waters recharging most of the aquifers in the West field and the southeast part of the Domes field indicate recharge from the escarpments.

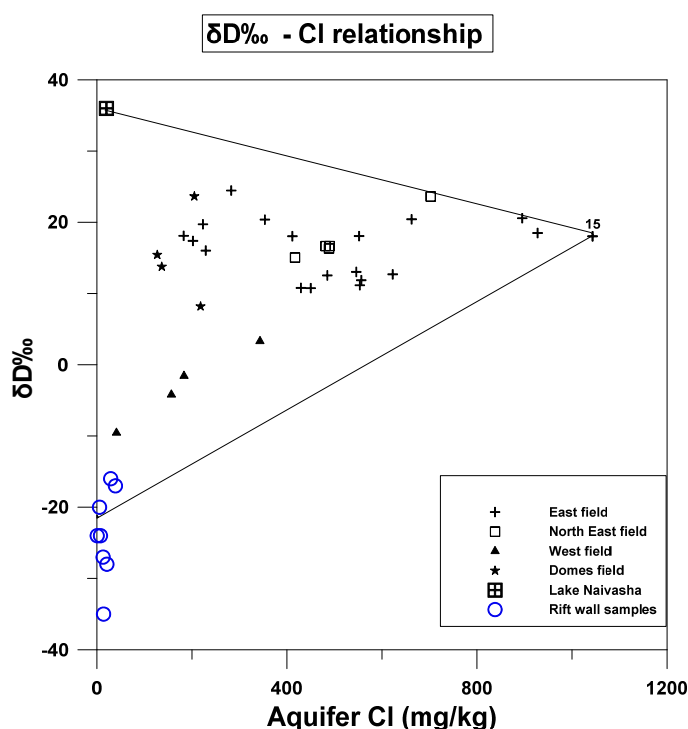


FIGURE 9: Aquifer δD -chloride relationship of wells in the area

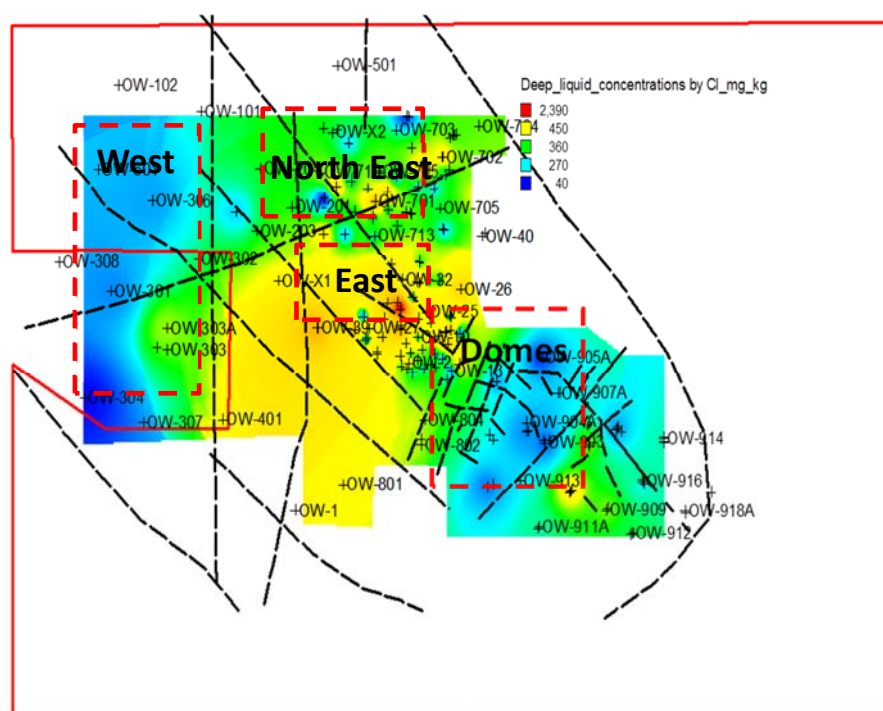


FIGURE 10: A contour map showing the Olkaria reservoir fluid chloride distribution map

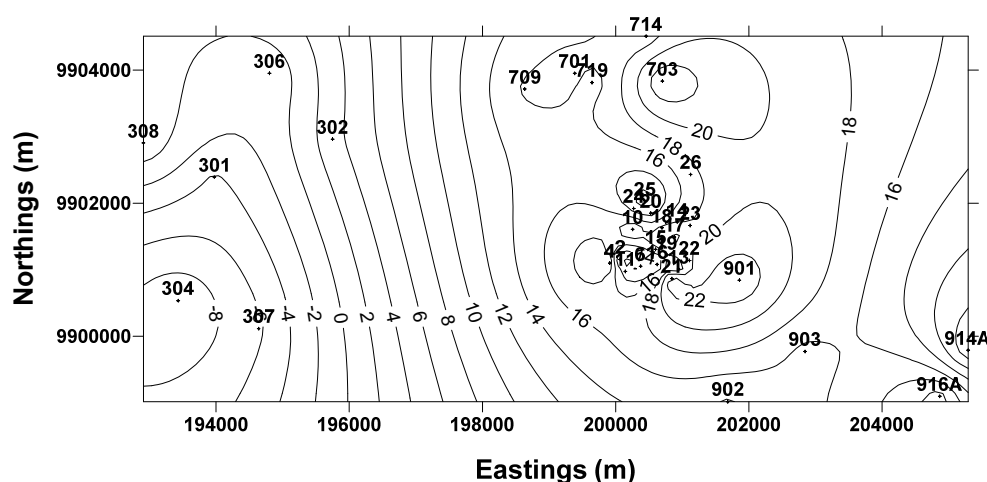


FIGURE 11: A contour map showing aquifer deuterium composition of wells in Olkaria field

4.5 A conceptual hydrological model of the Olkaria geothermal field

The thermal waters discharged in the Olkaria geothermal field are meteoric in origin. They are derived from high altitude precipitation through fault systems acting as underground channels; they reach greater depths where they acquire chloride from magmatic gases input or some amounts from host rocks and heat from volcanic intrusions in the area and, finally, through faults and fissures on the Rift floor. The Olkaria water isotope compositions suggest mixing of at least three components. These include groundwater from the eastern Rift wall, groundwater from the western Rift wall, and characteristic evapo-concentrated water. The deep thermal inflow into the Olkaria East and North East fields is enriched in the hydrogen isotope ratio, compared to local precipitation, as well as to precipitation from a high elevation, $\delta D = 24.46\text{‰}$; the oxygen isotope shift varies between $\delta^{18}O = 2.35$ and $\delta^{18}O = 3.12\text{‰}$. The most depleted waters in the field are reported in the West field with $\delta D = -9.55\text{‰}$ and an oxygen isotope shift of $\delta^{18}O = -2.77\text{‰}$. The fluids discharged in the Domes show a considerable range in the isotope ratio, suggesting mixing of the evapo-concentrated water with distant water to varying degrees.

The isotope composition of fumaroles and spring samples from the area indicates that the recharge is from Rift wall waters and evapo-concentrated water. The aquifer waters in Olkaria East, Northeast and some of the Domes wells get their recharge from the evapo-concentrated source, whereas the West field seems to be recharged by waters from the western Rift wall. Mixing of these water types is along the δD - $\delta^{18}O$ evaporation line with the evapo-concentrated water contributing largely to the recharge waters of the East and Northeast fields. The Domes field seems to be recharged by groundwater from the eastern Rift wall mixing with evaporated water, as indicated by results for some wells in the area. The contribution of the evaporated water to the West field is minimal, as reflected in the hydrogen isotope ratio of the aquifer fluids.

5. CONCLUSIONS

- The deuterium content of thermal waters within the Olkaria system has proven to be very useful in tracing the origin of the thermal water. Scarcity of isotope data, however, limits detailed interpretation of the groundwater hydrology.
- The Olkaria high temperature field receives a characteristic recharge from the Rift wall, and groundwater from an evapo-concentrated source recharges most of the wells in the area. Possible mixing of these waters is variable and dependent mostly on the influence of a fault system on the hydrology of the area.

- Olkaria West and the southeast part of the Domes area are least affected by recharge from the evaporated recharge water.
- The use of isotope fractionation factors and mass balance equations to characterize reservoir fluid composition yield coherent results for the oxygen-18 isotope ratios, but the deuterium isotope ratios vary to some extent.
- For six wells, more than one sample was available; the evolution of the water isotope ratios for these geothermal wells shows some changes in the isotope ratio of the water with time. This could be explained by temporal variations related to variations in the isotope composition of the recharge fluids.
- More work on isotope studies is ongoing and samples from recently drilled wells from the field have been collected together with new samples from older wells. The isotope composition of the samples will be determined at the Science Institute, University of Iceland. The results will be used to monitor variations in the hydrological regime of the area.

ACKNOWLEDGEMENTS

I would like to extend my appreciation to the Government of Kenya and Kenya electricity generating company - KenGen for granting me the opportunity to attend this training programme. I am also greatly indebted to Mr. Lúdvík S. Georgsson, director of the UNU Geothermal Training Programme, for his time and guidance during the six month period. Many thanks to Ms. Málfríður Ómarsdóttir, Mr. Markús A.G. Wilde, Mr. Ingimar G. Haraldsson and Ms. Thórhildur Ísberg for making the six months a great learning experience. Sincere gratitude goes to my supervisors, Halldór Ármannsson of ISOR and Dr. Árný Sveinbjörnsdóttir of the University of Iceland, for your time, patience and endless effort to make this work a success; your comments are highly appreciated. I would also wish extend my appreciation to the UNU-GTP 2014 fellows for sharing their knowledge and experience. Thanks to the chemistry group for the wonderful time and great company we have had together.

Special thanks to my family, my sister Josephine Milanoi, for your support, encouragement and prayers during my stay in Iceland. Finally, I am grateful to the Almighty God for guidance and blessings throughout the entire training period

REFERENCES

- Allen, D.J., and Darling, W.G., 1987: *Kenya Rift Valley geothermal project: Hydrogeology progress report*. British Geological Survey, report WD/OS/87/16, 65 pp.
- Allen, D.J., and Darling, W.G., 1992: *Geothermics and hydrology of the Kenya Rift Valley between Lake Baringo and Lake Turkana*. British Geological Survey, report SD/92/1, 39 pp.
- Allen D.J., Darling, W.G., and Burgess, W.G., 1989: *Geothermics and hydrogeology of the southern part of the Kenya Rift Valley with emphasis on the Magadi-Nakuru area*. British Geological Survey, report SD/89/1, 68 pp.
- Ármannsson, H., 1994: *Geothermal studies on three geothermal areas in West and Southwest Uganda*. UNDES, UNDP project UGA/92/002, report, 85 pp.
- Árnason, B., 1976: *Groundwater systems in Iceland traced by deuterium*. Soc. Sci. Islandica 42: 1-236.
- Arnórsson, S., 2000: Reactive and conservative components. In: Arnórsson, S. (ed.), *Isotopic and chemical techniques in geothermal exploration, development and use. Sampling methods, data handling, interpretation*. International Atomic Energy Agency, Vienna, 40-48.

- Arusei, M.K., 1991: *Hydrochemistry of the Olkaria and Eburru geothermal fields, Kenyan Rift valley*. UNU-GTP, Iceland, report 2, 39 pp.
- Bottinga, Y., and Craig, H., 1968: High temperature liquid-vapour fractionation factors for $\text{H}_2\text{O}-\text{H}_2\text{O}^{18}$. *Trans. Am. Geophys. Union*, 49, 356-357.
- Clarke, M.C.G., Woodhall, D.G., Allen, D., and Darling G., 1990: *Geological, volcanological and hydrogeological controls on the occurrence of geothermal activity in the area surrounding Lake Naivasha, Kenya, with coloured 1:100 000 geological maps*. Ministry of Energy, Nairobi, 138 pp.
- Coleman, M.L., Shepard, T.J., Durham, J.J., Rouse, J.E., and Moore, G.R., 1982: Reduction of water with zinc for hydrogen isotope determination. *Anal. Chem.*, 54, 993-995.
- Epstein, S., and Mayeda, T., 1953: Variations of ^{18}O content of waters from natural sources. *Geochim. Cosmochim. Acta*, 4, 213-224.
- Fournier, R.O., and Potter, R.W. II, 1982: A revised and expanded silica (quartz) geothermometer. *Geoth. Res. Council, Bull.*, 11-10, 3-12.
- Geyh, M., 2000: Volume IV: Groundwater – Saturated and unsaturated zone. In: Mook, W.G., (editor), *Environmental isotopes in the hydrological cycle – Principles and applications*. International Hydrological Programme, IHP-V, Technical Documents in Hydrology, IV (39), UNESCO, Paris.
- Giggenbach, W.F. and Stewart, M.K., 1982: Processes controlling the isotopic composition of water discharges from steam vents and steam-heated pools in geothermal areas. *Geothermics*, 11, 71-80.
- Horita, J., 1988: Hydrogen isotope analysis of natural waters using an H_2 -water equilibrium method: A special implication to brines. *Chem. Geol. (Isotope Geosc. Sec.)*, 72, 89-94.
- Karingithi, C.W., 2000: *Geochemical characteristics of the Greater Olkaria geothermal field, Kenya*. Report 9 in: *Geothermal training in Iceland in 2000*. UNU-GTP, Iceland, 165-188.
- Lagat, J.K., 2004: *Geology, hydrothermal alteration and fluid inclusion studies of the Olkaria Domes geothermal field, Kenya*. University of Iceland, MSc thesis, UNU-GTP, Iceland, report 2, 79 pp.
- McCann, D.L., 1972: *Preliminary hydrogeological evaluation of the long-term yield of catchment related to the geothermal prospect areas in the Rift Valley of Kenya*. UN report, 23 pp.
- McCann, D.L., 1974: *Hydrogeologic investigation of the Rift valley catchments*. Unpublished UN report, 47 pp.
- Mwania, M., Kandie, R., and Ronoh, I., 2014: *An update of geological conceptual model of the Greater Olkaria geothermal field*. KenGen, Kenya, internal report.
- Ojiambo, B.S., and Lyons, W.B., 1993: Stable isotope composition of Olkaria geothermal fluids, Kenya. *Geothermal Res. Council, Trans.*, 17, 149-153.
- Panichi, C., and Tongiorgi, E., 1974: *Isotope study of the hot water and steam samples of the Rift Valley*. UNDP report.
- Sekento, L. R., 2012: *Geochemical and isotopic study of the Menengai geothermal field, Kenya*. Report 31 in: *Geothermal training in Iceland in 2012*. UNU-GTP, Iceland, 769-792.
- Sikes, H.L., 1935: Notes on hydrology of Lake Naivasha. *J. East Africa & Uganda Nat. Hist. Soc.*, 14.
- Sveinbjörnsdóttir, Á.E., 1988: *Results of stable isotope measurements on samples from the Olkaria and Eburru geothermal fields, Kenya*. Kenya Power Company, Ltd., Science Institute, University of Iceland, report.
- Truesdell, A.H., and Hulston, J.R., 1980: Isotopic evidence on environments of geothermal systems. In: Fritz, P., and Fontes, C., *A handbook of environmental, isotope geochemistry*. vol. 1, ch. 5, 179-226.
- Truesdell, A.H., Nathenson, M., and Rye, R.O., 1977: The effects of subsurface boiling and dilution on the isotopic compositions of Yellowstone thermal waters. *J. Geophys. Res.* 82-26, 3694-3704.



UNITED NATIONS
UNIVERSITY

UNU-GTP

Geothermal Training Programme

Orkustofnun, Grensasvegur 9,
IS-108 Reykjavik, Iceland

Reports 2014
Number 25

WELL TEST ANALYSIS AND TEMPERATURE AND PRESSURE MONITORING OF KRAFLA AND NESJAVELLIR HIGH-TEMPERATURE GEOTHERMAL FIELDS, ICELAND

Leon Ntihakose

Rwanda Energy Group, Ltd.
Energy Development Corporation, Ltd.
P.O. Box 537, Kigali
RWANDA
ntihableon@gmail.com

ABSTRACT

The Krafla high-temperature geothermal field is located within the Krafla caldera lying within the active NE-SW striking rift zone of North-East Iceland, whereas the Nesjavellir geothermal field is a high-temperature geothermal system, part of the Hengill central volcano in SW-Iceland. Reservoir assessment and monitoring was conducted on wells NJ-15 and NJ-18, located in the Nesjavellir high-temperature geothermal field. For Krafla geothermal field, wells K-37 and K-38 were considered to assess the reservoir, and well K-18 was used for monitoring. Temperature and pressure logs, measured during the warm up of the wells, were analysed to estimate formation temperature and initial pressure. In order to understand the parameters that characterise the reservoir and the wells, injection tests were analysed and parameters such as the injectivity index, transmissivity, storativity, skin, wellbore storage, etc. were evaluated.

Transmissivity estimated for the wells selected in Nesjavellir were of the same order of magnitude as for the wells in Krafla, i.e. $10^{-8} \text{ m}^3/(\text{Pa}\cdot\text{s})$. Storativity for Krafla was higher than that of Nesjavellir, as can be expected in a two-phase reservoir. The wells in Nesjavellir are located at the outer boundaries of the geothermal reservoir and are liquid-dominated. This was further established by analysing the formation temperature and initial pressure. Temperature and pressure monitoring analyses at various depths were performed for Krafla on well K-18 from 1981 to 2013 and for well NJ-15 from 1985 to 2013; and for Nesjavellir well NJ-18 from 1988 to 2013. No significant change in temperature was observed in wells NJ-15 and NJ-18, but a linear constant pressure draw down of about 13 bar was observed in well NJ-15 from 1985 to 2013 and a rapid decline in pressure (20 bar) was observed in well NJ-18 from 2006 to 2013. In well KJ-18 in Krafla, a slow pressure decrease was observed.

1. INTRODUCTION

This report is a result of a reservoir analysis conducted in two geothermal areas, i.e. Nesjavellir geothermal field and Krafla geothermal field. Wells NJ-15 and NJ-18, located in Nesjavellir, were

selected while wells K-37 and K-38 were selected for Krafla. Formation temperature estimation, initial pressure and analysis of an injection test were performed on all wells. Moreover, pressure and temperature monitoring analyses were carried out on wells NJ-15, NJ-18 and K-38 as well as on well KJ-18 which is near well K-37. Formation temperature estimation at different borehole depths was obtained by using the ÍSOR software Berghiti (Arason et al., 2004). Formation temperature is important in decision making for selecting sites for new wells as well as for setting up a conceptual model. The ÍSOR software PREDYP (Arason et al., 2004) was applied to calculate the initial pressure. Injection test simulation was made by utilizing WellTester software (Júliússon et al., 2008) based on non-linear regression. For each well, the injectivity index was estimated. The injectivity index is a simple relationship, approximately reflecting the capacity of a well, which is useful for determining whether a well is sufficiently open to be a successful producer and for comparison with other wells (Axelsson and Steingrímsson, 2012).

In the next section the geothermal fields at Nesjavellir and Krafla will be introduced after which the theory of well testing will be presented. Injection tests from four wells will be analysed in Section 3. Temperature and pressure profiles during warm up will be analysed to deduce the formation temperature and initial pressure in each of the wells in Section 4 and, finally, temperature and pressure monitoring studies for both fields will be presented in Section 5, followed by conclusions in Section 6.

2. NESJAVELLIR AND KRAFLA GEOTHERMAL FIELDS

2.1 Nesjavellir geothermal field

The Nesjavellir geothermal field is a high-temperature geothermal system located in the Hengill central volcano in Southwest Iceland (Gíslason et al., 2005) (Figure 1). Several geological studies have been performed to understand the geothermal conditions of the Nesjavellir reservoir (Franzson, 1998; Franzson, 2000; Steingrímsson et al., 1990).

The geology of the area is characterised by hyaloclastite accumulation, lava accumulation and intrusive rocks. Hyaloclastite accumulation is dominant down to about 400 m b.s.l. below which lava accumulation dominates. The intrusive rocks, composed of basaltic dykes or sheets, characterise the section below 800 m depth and increase up to 80-100% intensity below 2000 m depth. Shallow-dipping dioritic sheet-like intrusions are also found at various depths and they contribute substantially to the permeability in the field, along with the basaltic intrusions.

Exploration drilling at Nesjavellir started with five wells in 1965. Additional 13 wells were drilled during the period of 1981-1985. A further 10 wells were drilled as step out and

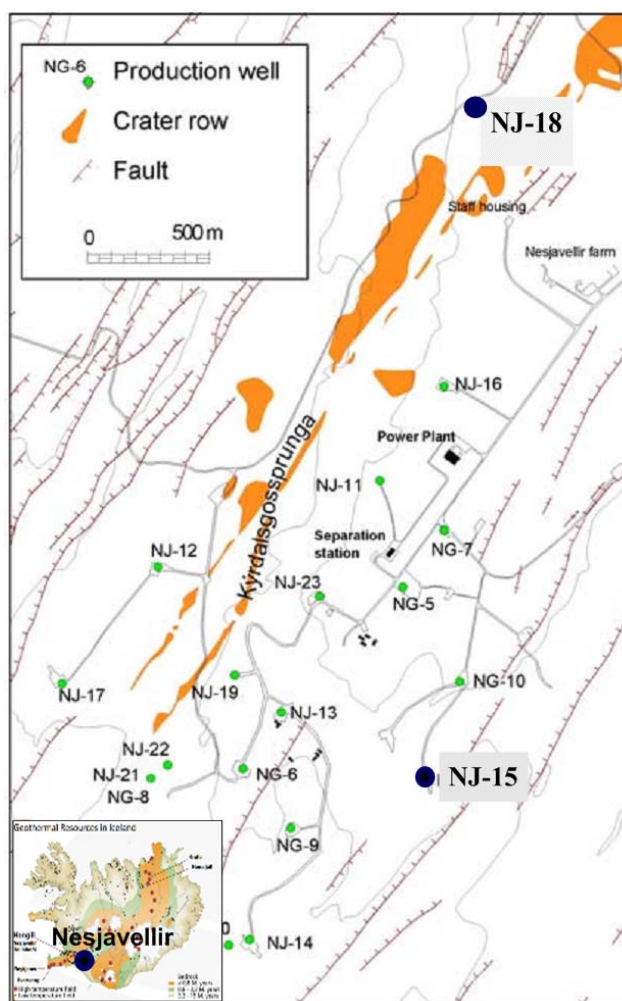


FIGURE 1: Locations of Wells NJ-15 and NJ-18 at Nesjavellir (modified from Gíslason et al., 2005)

make up wells, along with a few shallower reinjection wells.

Production of hot water from Nesjavellir for district heating in Reykjavík started in 1990 and power generation began in 1998. Reykjavik Energy (Orkuveita Reykjavíkur) is currently operating a 120 MW_e power plant and a 300 MW_{th} thermal unit in the Nesjavellir geothermal field.

Two wells, NJ-15 and NJ-18, in Nesjavellir (Figure 1) were selected for this study. Well NJ-15 is located at the outer border of the eastern part of the production area. It is a vertical well that was drilled in the autumn 1985 to a total depth of 1748 m. Well NJ-15 was connected to the steam supply system in October 1998 until July 1999. Since then, well NJ-15 has been closed and is currently used for temperature and pressure monitoring. Well NJ-18 is situated north of the production area. It is a vertical well, drilled in 1986 to a depth of 2136 m. It was not a productive well and was never connected to the steam supply system. It is currently used as a monitoring well.

2.2 Krafla geothermal field

The Krafla high-temperature geothermal system is located within the Krafla caldera (Figure 2) lying within an active N-S striking rift zone in Northeast Iceland (Ármannsson et al., 1987). The volcanic activity in this area is episodic, occurring every 250-1000 years, with each episode lasting 10-20 years. The most recent volcanic period started at the end of 1975 and ended in September 1984 with 9 eruptions and 21 tectonic events (Björnsson, 1985).

The Krafla geothermal field is subdivided into several sub-fields based on the chemical composition of the fluid from Krafla wells and geography (Ármannsson et al., 1987; Gíslason et al., 1978; Mortensen et al., 2009). These are Leirbotnar, Vítismór, Sudurhlíðar, and Hvíthólar (Figure 2). The Leirbotnar sub-field is divided into an upper and a lower reservoir zone. The upper reservoir to a depth of 1000-1400 m is liquid-dominated with a temperature of 190-220°C (Ármannsson, 2010). The zone below 1400 m depth has a temperature of about 300°C and boiling conditions occur below 2000 m where the temperature is 350°C. Well KS-01 has discharged in Sandabotnar, suggesting a two-phase fluid (boiling point curve) from a reservoir at about 260°C. Hvíthólar sub-field exhibits boiling characteristics down to 1000 m depth but is cooler and liquid-dominated below that depth (Ármannsson, 2010). In Sudurhlíðar (southern flanks of Mt. Krafla) and Vesturhlíðar (western flanks of Mt. Krafla) the boiling point curve is followed and a two-phase fluid of about 300°C is delivered. Similar characteristics were observed for the one well drilled in the Leirhnúkur area.

The geology of Krafla high-temperature geothermal system is dominated by basaltic lava, sub-glacially erupted hyaloclastites as well as intrusive bodies of basalt, dolerites and gabbro. Exploration drilling started in 1974 when a decision was made to build a 60 MWe power plant concurrent with drilling. Up to 2012, a total of 44 wells had been drilled in Krafla geothermal field. Re-injection is mainly done through well K-26 below 2000 m depth, but abandoned wells have also served temporarily for this purpose (Ágústsson et al., 2012).

Wells K-37 and K-38 (Figure 2) will be considered for this study for an injection test and formation temperature estimation as well as initial pressure; well K-18 will be used for the monitoring of pressure and temperature. Well K-38 is drilled in the western flanks (Vesturhlíðar) of mount Krafla which is a new site. Wells K-37 and KJ-18, on the other hand, are drilled into the southern flanks (Sudurhlíðar) of mount Krafla where there has been substantial production since 1980. A revised conceptual model developed by ISOR (Mortensen et al., 2009) showed that a pressure draw down of about 5 bar occurred in Leirbotnar sub-area after the expansion of the plant in the year 1999; on the southern flanks, where there has been substantial production since 1980, the pressure dropped significantly, probably about 20-30 bar.

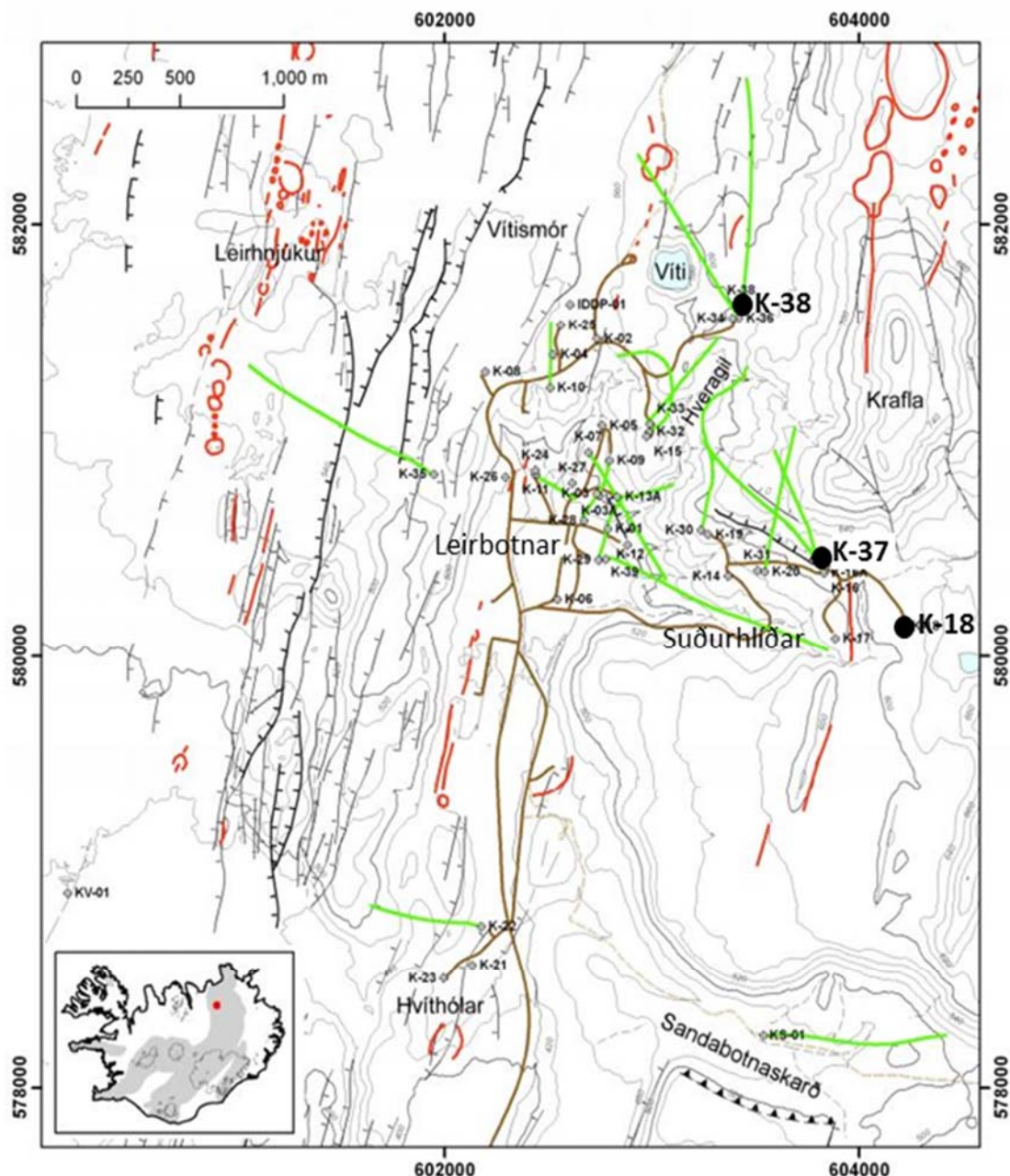


FIGURE 2: Map of Krafla geothermal field showing location of selected wells (modified from Mortensen et al., 2009)

3. INJECTION TEST

Injection tests in four wells were analysed by using ÍSOR WellTester software (Júlíusson et al., 2008) to estimate reservoir and well properties, two of them in the Nesjavellir geothermal field and two in the Krafla geothermal field. Injection tests are usually performed after drilling the production section of a well; the first parameter analysed is the injectivity index which gives an indication of how open the surroundings of the well are for flow, i.e. the change of pressure with change in the injection rate ((l/s)/bar).

In some cases the injection test is used for decision making and, in case of a too low injectivity index, drilling is continued in the hope of finding better feed zones at greater depth.

The following sections give a short theoretical background of injection well testing, followed by the summary of the well test results for wells NJ-15 and NJ-18 in Nesjavellir geothermal field, and wells K-37 and K-38, located in Krafla geothermal field.

3.1 Theoretical background

Well testing consists of producing from or injecting into a well at controlled rates and over periods of time and monitoring the response of the pressure in the same well and/or in adjacent observation wells. Well testing is performed in order to understand the conditions and flow capacity of a well and the parameters that characterise it and the reservoir. Parameters of interest include permeability, storativity, skin, wellbore storage, fracture properties, and the type of reservoir boundaries.

The pressure diffusion equation is used to calculate the pressure (p) in the reservoir after a given time (t) and at a certain distance (r) from an injection (or production) well receiving (or producing) fluid at a specific rate (Q). The following simplifying assumptions were made before the derivation of the equation:

- Horizontal radial flow;
- Darcy's Law applies;
- Homogeneous and isotropic reservoir and isothermal condition;
- Uniform thickness of reservoir (h);
- Single-phase flow and small pressure gradient;
- Constant permeability (k), porosity (ϕ), fluid viscosity (μ) and small and constant total compressibility (c); and
- The force of gravity is negligible.

The pressure diffusion equation is derived by combining the conservation of mass law, Darcy's law (conservation of momentum), and the equation of state of the fluid.

Law of conservation of mass

Consider the flow through a cylindrical shell of thickness, dr , situated at a distance, r , from the centre of the radial cylinder (Figure 3).

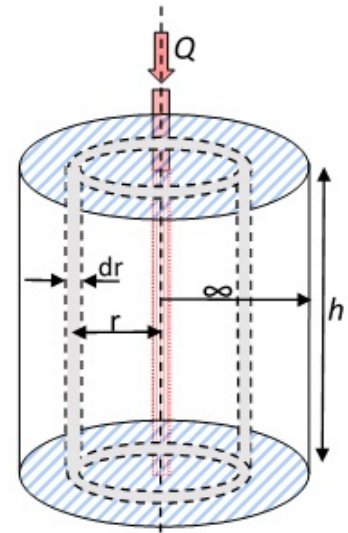


FIGURE 3: Radial flow through a cylindrical shell

Then applying the principle of conservation of mass, mass flow in – mass flow out = rate of change of mass within the control volume:

$$-\rho Q + (\rho Q + \frac{\partial(\rho Q)}{\partial r} dr) = 2\pi r \frac{\partial(\phi \rho h)}{\partial t} dr \quad (1)$$

or

$$\frac{\partial(\rho Q)}{\partial r} = 2\pi r \frac{\partial(\phi \rho h)}{\partial t} \quad (2)$$

- where, ρ = The density (kg/m^3);
 ϕ = The porosity (ratio $0 < \phi < 1$);
 Q = The volumetric flow rate (m^3/s);
 r = The radial distance (m) from the well;
 t = The time (s);
 h = The reservoir thickness (m).

Darcy's law or law of conservation of momentum

Darcy's law in radial form is

$$Q = 2\pi r h \frac{k}{\mu} \frac{\partial p}{\partial r} \quad (3)$$

where, p = The pressure (Pa);
 μ = The dynamic viscosity (Pa·s); and
 k = The formation permeability (m²).

Equation of state of the fluid (fluid compressibility at constant temperature)

$$c_w = \frac{1}{\rho} \left(\frac{\partial \rho}{\partial p} \right) \quad (4)$$

where c_w = Fluid compressibility;
 ρ = The fluid density (kg/m³);
 p = The pressure (Pa).

By combining Equations 2, 3 and 4, we obtain the pressure diffusion equation given by

$$\begin{aligned} \frac{1}{r} \frac{\partial}{\partial r} \left(\frac{r \partial p(r, t)}{\partial r} \right) &= \frac{\mu c_t}{k} \frac{\partial p(r, t)}{\partial t} = \frac{S}{T} \frac{\partial p(r, t)}{\partial t} \\ \frac{\partial^2 p}{\partial r^2} + \frac{1}{r} \left(\frac{\partial p(r, t)}{\partial r} \right) &= \frac{\mu c_t}{k} \frac{\partial p(r, t)}{\partial t} = \frac{S}{T} \frac{\partial p(r, t)}{\partial t} \end{aligned} \quad (5)$$

where $c_r = \frac{1}{1-\phi} \frac{\partial \phi}{\partial p}$ = The rock compressibility (Pa⁻¹);
 $c_t = \phi c_w + (1 - \phi) c_r$ = The total compressibility (Pa⁻¹);
 $S = c_t h$ = The storativity (m³/(Pa·m²) = m³/Pa = m³/N);
 $T = \frac{kh}{\mu}$ = The transmissivity (m³/(Pa·s)).

Equation 5 is the basic equation for well testing. Solutions for this equation can be obtained for different regimes depending on the initial and boundary conditions but that is beyond the scope of this project. The analysis of the injection test was done using WellTester software (Júlíusson et al., 2008) which was developed by the Iceland GeoSurvey (ISOR). The main parameters deduced from the WellTester simulation are explained in the manual for WellTester (Júlíusson et al., 2008) and follow below. Some of them are explained as well in the formulas above.

Transmissivity (T) describes the ability of the reservoir to transmit fluid, hence largely affecting the pressure gradient between the well and the reservoir. The higher the transmissivity, the easier it is for the fluid to flow through the rock matrix.

$$T = \frac{kh}{\mu} \quad \text{or} \quad T = \frac{kh\rho}{\nu} \quad (6)$$

where $\nu = \frac{\mu}{\rho}$ = The kinematic viscosity of the fluid (m²/s).

Storativity (S) is defined as the volume of fluid stored in the reservoir, per unit area, per unit increase in pressure (m³/(Pa·m²)). It depends on rock and fluid compressibility and phase change activity (Grant et al., 1982).

The injectivity index (II) is controlled by the injection flow rate and the change in stabilized reservoir pressure. It describes how the well is connected to the surrounding reservoir. Mathematically, the injectivity index (II) is represented as

$$II = \left| \frac{\Delta Q}{\Delta p} \right| \quad (7)$$

where ΔQ is the change in the injection flow and Δp is the change in the stabilized reservoir pressure ((l/s)/bar).

Wellbore storage coefficient (C) represents the volume of fluid that the wellbore itself will produce due to a unit drop of pressure (Grant and Bixley, 2011; Horne, 1995) (m^3/Pa). This mostly occurs due to fluid expansion or changing of the fluid level in the well. It is represented mathematically by:

$$C = \frac{\Delta V}{\Delta P} \quad (8)$$

where ΔV = The change in fluid volume in the well for the change in pressure ΔP .

Skin factor (s) is a dimensionless parameter (Van Everdingen and Hurst, 1953) and it characterizes the well condition: for a damaged well the permeability in the skin zone is less than reservoir permeability and $S > 0$, and for a stimulated one $S < 0$, meaning that the permeability of the skin zone is greater than the reservoir permeability.

Radius of investigation (r_e) is the approximate distance (m) at which the pressure response from the well becomes undetectable. Hence, this radius defines the area around the well being investigated, although the value of the parameter should be regarded more qualitatively. When boundary effects are seen in the data, the approximate distance from the centre of the well to the boundary will define the radius of investigation.

3.2 Testing of well NJ-15

An injection test of well NJ-15 was performed on 21/10/1995 where the pressure sensor was placed at 1590 m depth. Before the injection test started, injection was constant at 28.9 l/s of water. The injection test was conducted in four steps as shown in Table 1.

TABLE 1: Injection rate and pressure response

21/10/1995	Before starting	Step 1	Step 2	Step 3	Step 4
Time period	-	03:49-06:20	06:20-09:08	09:08-11:47	11:47-14:00
Duration (hr)	-	2:31	2:48	2:39	2:13
Injection (l/s)	28.9	18.9	29.3	40.6	0
Change in injection $ \Delta Q $		10	10.4	11.3	40.6
Pressure at the end of step (bar-g)	137.3	132.4	136.4	139.7	123.6
Change in pressure $ \Delta p $		5	4	3.3	16

Initial parameters that were used to describe the reservoir and well dimensions in this analysis are estimated reservoir temperature 280°C, wellbore radius 0.12 m, and estimated reservoir pressure of 135 bar which was deduced by WellTester software. Two types of models were considered for the reservoir, on one hand a homogeneous reservoir and on the other hand a dual porosity reservoir. The best fit between the model and the data was obtained for a homogenous reservoir, constant pressure boundary, constant skin and wellbore storage.

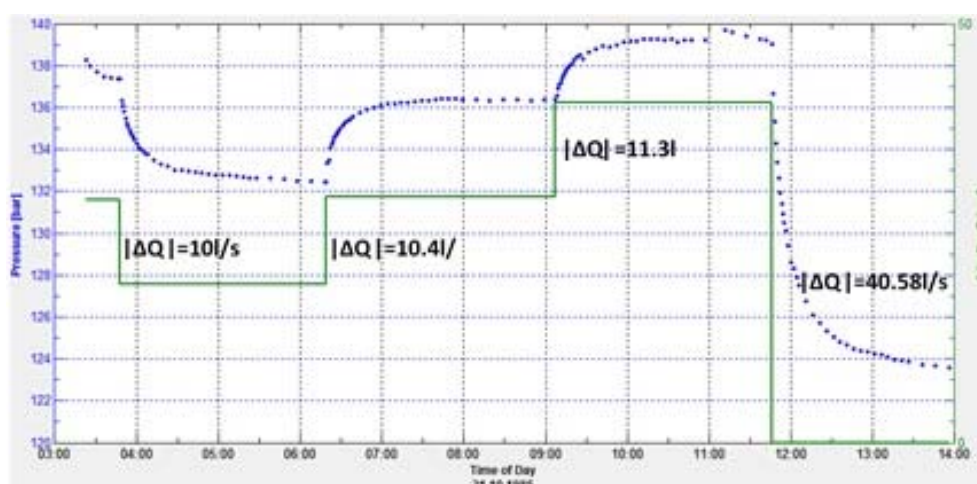


FIGURE 4: Step rate injection and pressure response for Well NJ-15

A non-linear regression analysis was performed to find the parameters of the model that best fit the data. The model fit with the data was best for step 1. Figure 4 shows the pressure response against time for various steps of injection as well as the change in injection for each step. In the following section the results from the interpretations of step one are shown in Figures 5, 6, and 7 and Table 2.

Figure 5 shows on a linear scale how the chosen model fits the data. Figure 6 shows the pressure measured for the step on a linear scale using a logarithmic timescale. Figure 7 shows the pressure change on a logarithmic scale, also using a logarithmic timescale, together with the derivative of the pressure response multiplied by the time passed since the beginning of the step. Table 2 shows the injectivity index and the reservoir parameters estimated by using the selected model. The skin factor is negative, as is usual in Iceland, which means that the well was enhanced and not damaged during drilling.

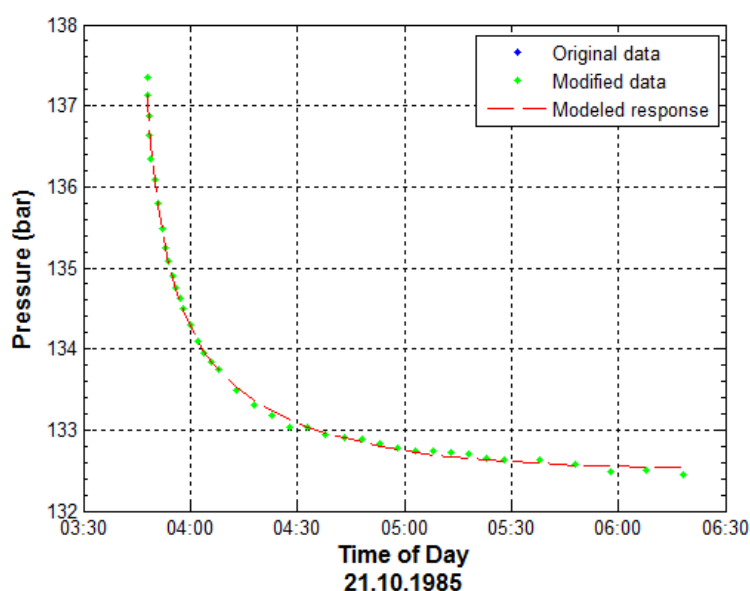


FIGURE 5: Pressure against time for model results and collected data for step 1

TABLE 2: Results from non-linear regression parameter estimate using injection data from well NJ-15

Reservoir parameters	1. step	2. step	3. step	4. step	Best estimate (Step 1)	Units
Transmissivity (T)	$1.3 \cdot 10^{-8}$	$1.4 \cdot 10^{-8}$	$2.5 \cdot 10^{-8}$	$1.2 \cdot 10^{-8}$	$1.3 \cdot 10^{-8}$	$\text{m}^3/(\text{Pa} \cdot \text{s})$
Storativity (S)	$6.4 \cdot 10^{-8}$	$2.3 \cdot 10^{-8}$	$2 \cdot 10^{-8}$	$2 \cdot 10^{-8}$	$6.4 \cdot 10^{-8}$	$\text{m}^3/(\text{Pa} \cdot \text{m}^2)$
Radius of investing. (r_e)	46	67	85	68	46	m
Skin factor (s)	-2.2	-3	-2.5	-3.5	-2.2	-
Wellbore storage (C)	$8.4 \cdot 10^{-6}$	$6.7 \cdot 10^{-6}$	$2.2 \cdot 10^{-5}$	$8 \cdot 10^{-6}$	$8.4 \cdot 10^{-6}$	$\text{m}^3/(\text{Pa})$
Permeability (k)	$4 \cdot 10^{-15}$	$1.3 \cdot 10^{-14}$	$2.7 \cdot 10^{-14}$	$1.3 \cdot 10^{-14}$	$4 \cdot 10^{-15}$	m^2
Reservoir thickness	296	106	92	91	296	m
Injectivity index (II)	2	2.6	3.4	2.6	2	(l/s)/bar

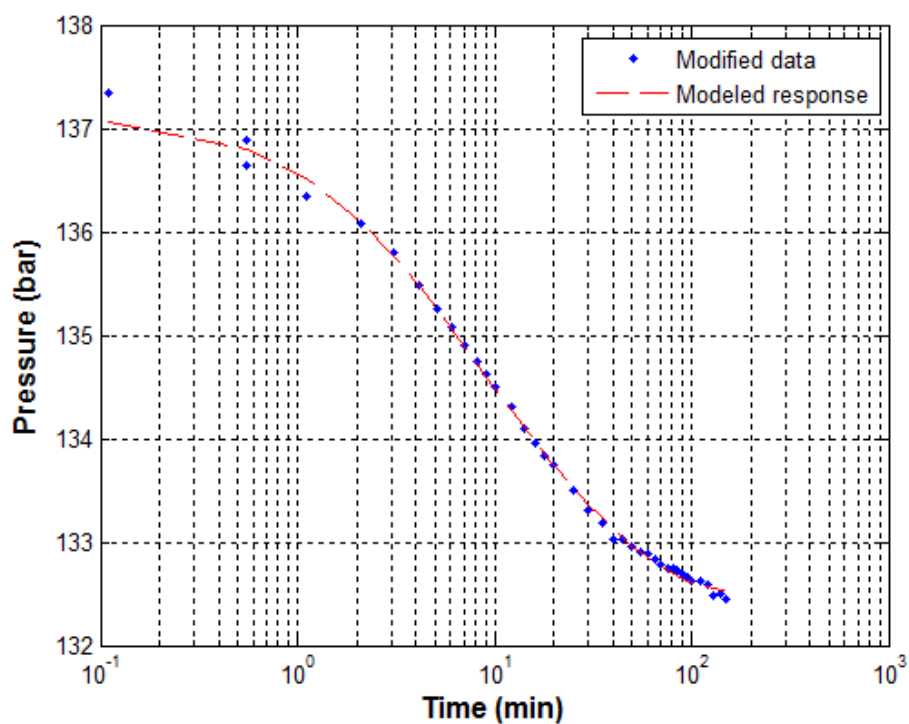


FIGURE 6: Pressure against time for model results and collected data for step 1 using logarithmic time scale

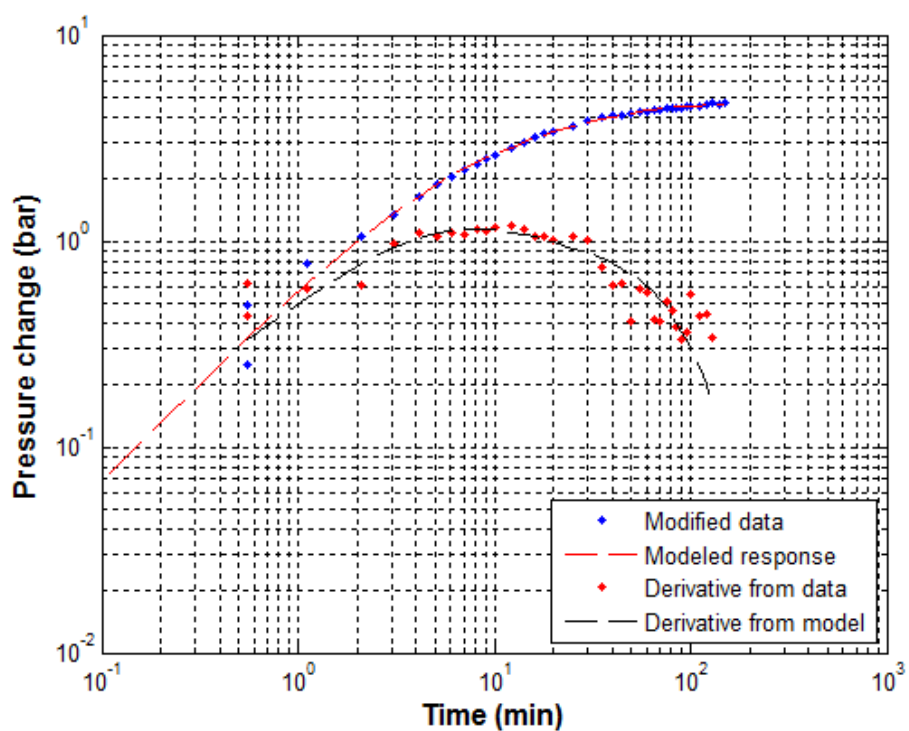


FIGURE 7: Pressure and its derivative against time for model results and collected data for step 1 on a log-log scale (see text)

3.3 Testing of well NJ-18

An injection test was performed in this well on 15/10/1986. The pressure sensor was stationed at 1710 m depth which was assumed to be the depth of the main feed zone. Before the injection test started, injection was constant at 24.2 l/s of water. The injection test was conducted in three steps as shown in Table 3.

TABLE 3: Injection rate and pressure response

15/10/1986	Before starting	Step 1	Step 2	Step 3
Time period	-	08:21-11:43	11:43-14:45	14:45-17:18
Duration (hr)	-	3:22	3:02	2:27
Injection (l/s)	24.2	36.7	24.2	0
Change in injection $ \Delta Q $		12.5	12.5	24.2
Pressure at the end of step (bar-g)	157.3	162.3	155.5	144
Change in pressure $ \Delta p $		5	6.8	11.6

To find the parameters of the model that best fit the data, a non-linear regression analysis was performed by using WellTester. The following initial parameters were taken to describe the reservoir: estimated reservoir temperature 280°C, wellbore radius 0.12 m and an estimated reservoir pressure of 135 bar, deduced from WellTester software. Homogenous reservoir, constant pressure boundary, constant skin and wellbore storage were selected for the reservoir model. Figure 8 illustrates the pressure response against time for various flow rates as well as the change in injection for each step. Figure 9 shows on a linear scale how the chosen model fits the data in step 3. Figure 10 shows the pressure measured for the step on a linear scale using a logarithmic timescale. Figure 11 shows the pressure change on a logarithmic scale, also using a logarithmic timescale, together with the derivative of the pressure response multiplied by the time passed since the beginning of the step. Table 4 shows the reservoir parameters estimated by using the selected model in WellTester. The results of the simulations for step 3 showed to be the best of the simulations.

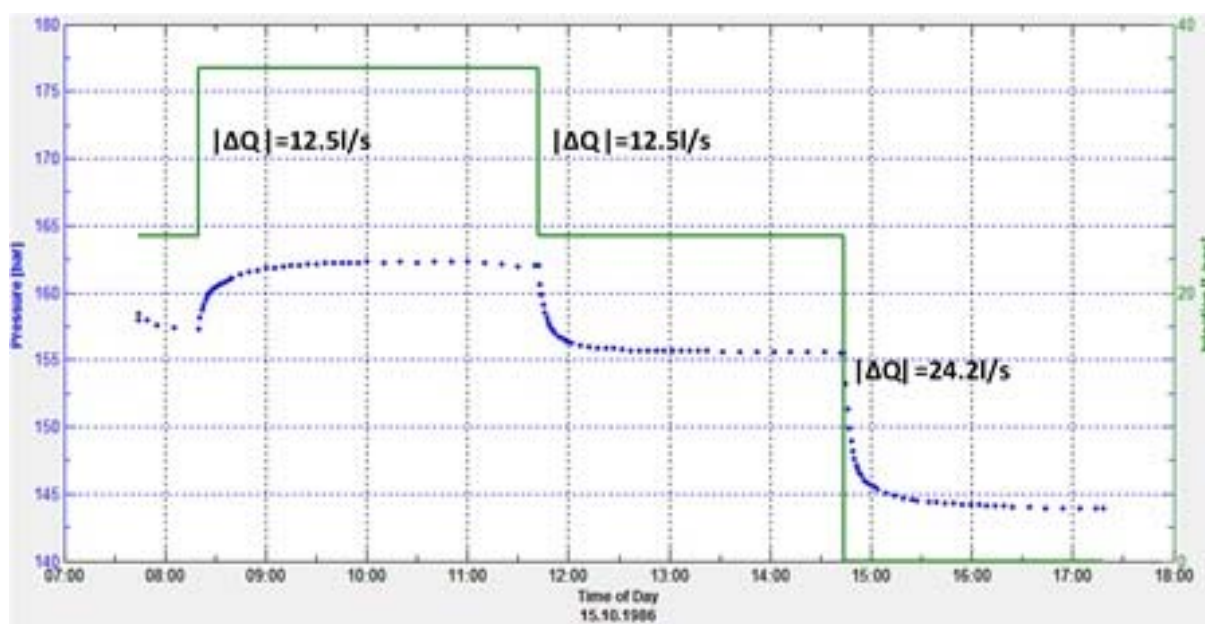


FIGURE 8: Step rate injection and pressure response for Well NJ-18

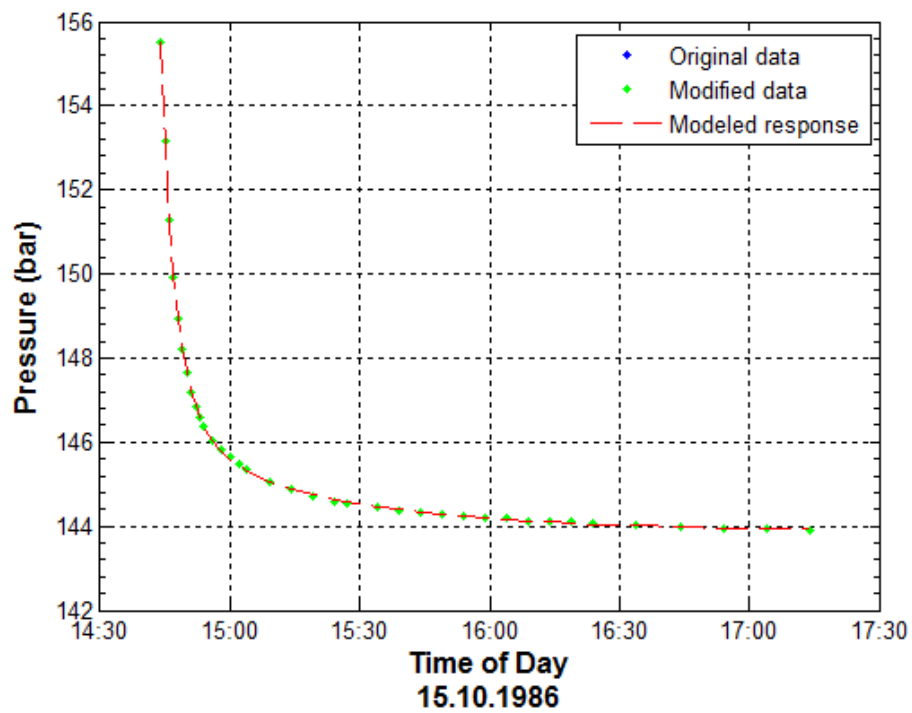


FIGURE 9: Pressure against time for model results and collected data for step 3

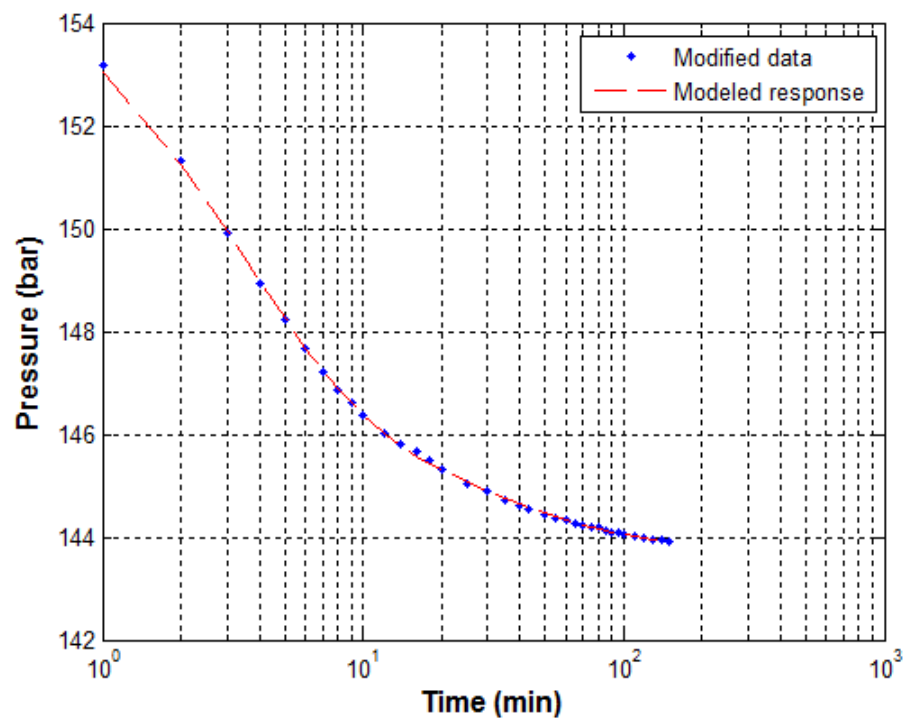


FIGURE 10: Pressure against time for model results and collected data for step 3, using a logarithmic time scale

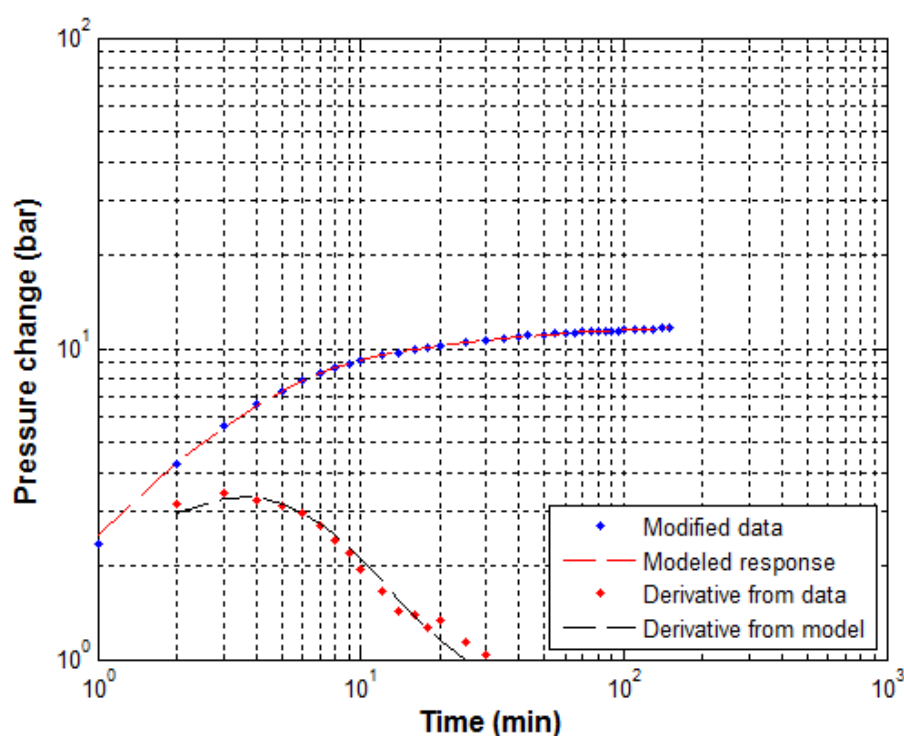


FIGURE 11: Pressure and its derivative against time for model results and collected data for step 3 on a log-log scale (see text)

TABLE 4: Results from non-linear regression parameter estimate using injection data from well NJ-18

Reservoir parameters	1. step	2. step	3. step	Best estimate (Step 3)	Unit
Transmissivity (T)	$1.1 \cdot 10^{-8}$	$1.7 \cdot 10^{-8}$	$2.8 \cdot 10^{-8}$	$2.8 \cdot 10^{-8}$	$\text{m}^3/(\text{Pa} \cdot \text{s})$
Storativity (S)	$7 \cdot 10^{-8}$	$4.6 \cdot 10^{-8}$	$1.3 \cdot 10^{-8}$	$1.3 \cdot 10^{-8}$	$\text{m}^3/(\text{Pa} \cdot \text{m}^2)$
Radius of investigation (r_e)	34	45	174	174	m
Skin factor (s)	-3.	-0.3	1.3	1.3	-
Wellbore storage (C)	$4.6 \cdot 10^{-6}$	$4.5 \cdot 10^{-6}$	$4.8 \cdot 10^{-6}$	$4.8 \cdot 10^{-6}$	$\text{m}^3/(\text{Pa})$
Permeability (k)	$3.1 \cdot 10^{-15}$	$7.6 \cdot 10^{-15}$	$4.6 \cdot 10^{-14}$	$4.6 \cdot 10^{-14}$	m^2
Reservoir thickness (h)	329	220	60	60	(m)
Injectivity index	2.5	2	2.1	2.1	(l/s)/bar

The values of transmissivity and storativity for NJ-18 are within the same range of magnitude as the value obtained from well NJ-15, and these values are within the range which is generally expected in Iceland.

3.4 Testing of well K-37

Well K-37 in Krafla is a directional well which was drilled from 04.10.2007 to 18.01.2008 to a total depth of 2187 m. An injection test of the well was performed at the end of drilling on 18.1.2008. The pressure sensor was positioned at 1420 m depth which was assumed to be the main feed zone. Before the injection test started, injection was constant at 20 l/s of water. The injection test was conducted in three steps as shown in Table 5.

TABLE 5: Injection rate and pressure response

18.01.2008	Before starting	Step 1	Step 2	Step 3
Time period	-	14:17 - 17:18	17:18 - 20:18	20:18 - 23:18
Duration (hr)	-	3:01	3:00	3:00
Injection (l/s)	20	35	50	20
Change in injection $ \Delta Q $	-	15	15	30
Pressure at the end of step (bar-g)	80	84	88	80.0
Change in pressure $ \Delta p $	-	4	4	8

Initial parameters that were used to describe the reservoir in this analysis are estimated reservoir temperature 320°C, wellbore radius 0.18 m, and an estimated reservoir pressure of 80 bar which was found by WellTester. Two types of models were considered for the reservoir: on one hand a homogeneous reservoir and, on the other hand, a dual porosity reservoir. A non-linear regression analysis was done to find the parameters of the model that best fits the data. The model best fitted the data in step 3, and the best results were obtained for a homogenous reservoir, constant pressure boundary, constant skin and wellbore storage.

Figure 12 shows the steps of the injection and the pressure response against time as well as the change in injection for each step during the test. Figure 13 illustrates on a linear scale how the chosen model fits the data for step 3. Figure 14 shows the pressure measured for the step on a linear scale using a logarithmic timescale. Figure 15 shows the pressure change on a logarithmic scale, also using a logarithmic timescale, together with the derivative of the pressure response multiplied by the time passed since the beginning of the step. Table 6 shows the reservoir parameters estimated by using the selected model.

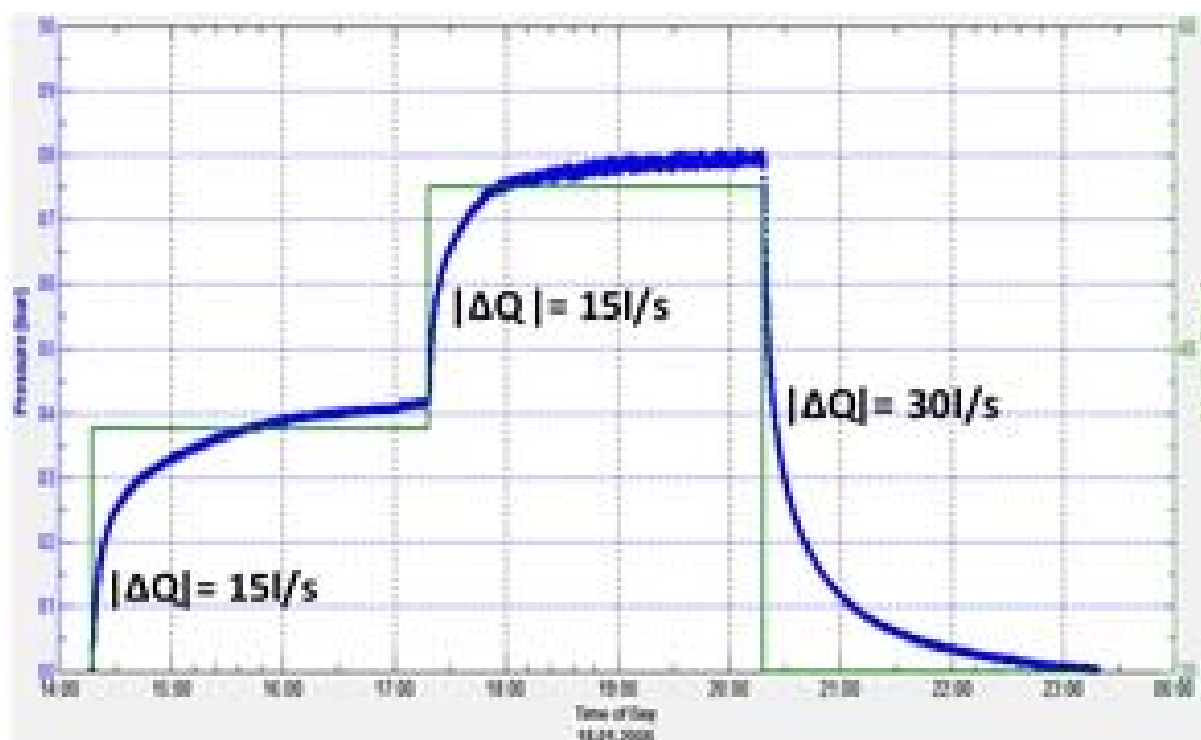


FIGURE 12: Step rate injection and pressure response for Well K-37

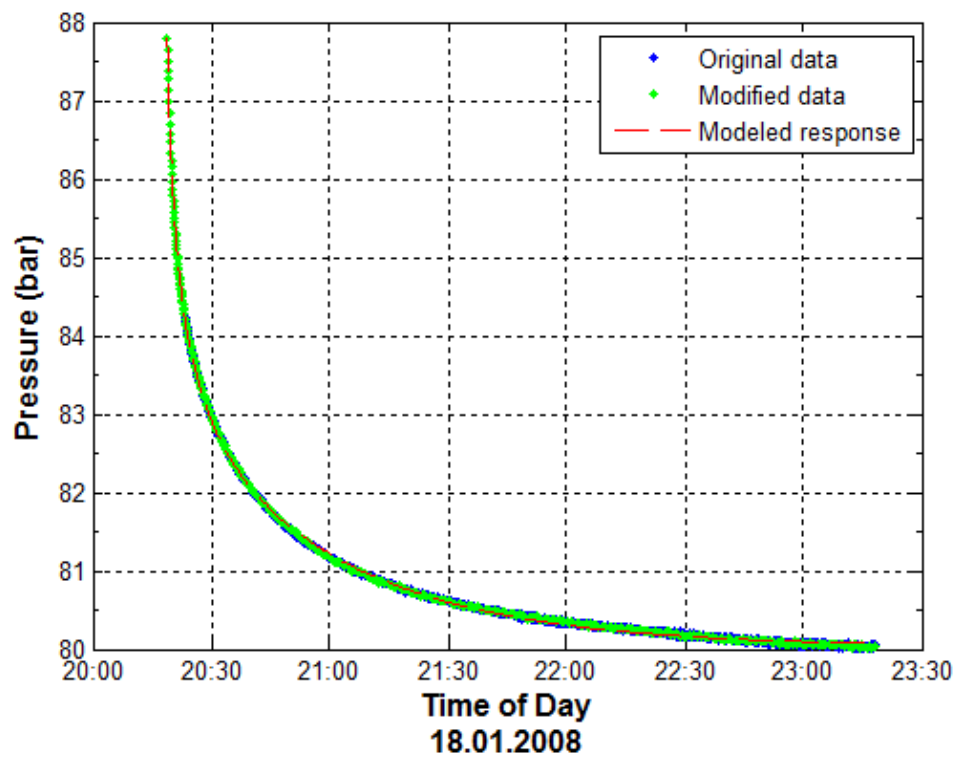


FIGURE 13: Pressure against time for model results and collected data for step 3

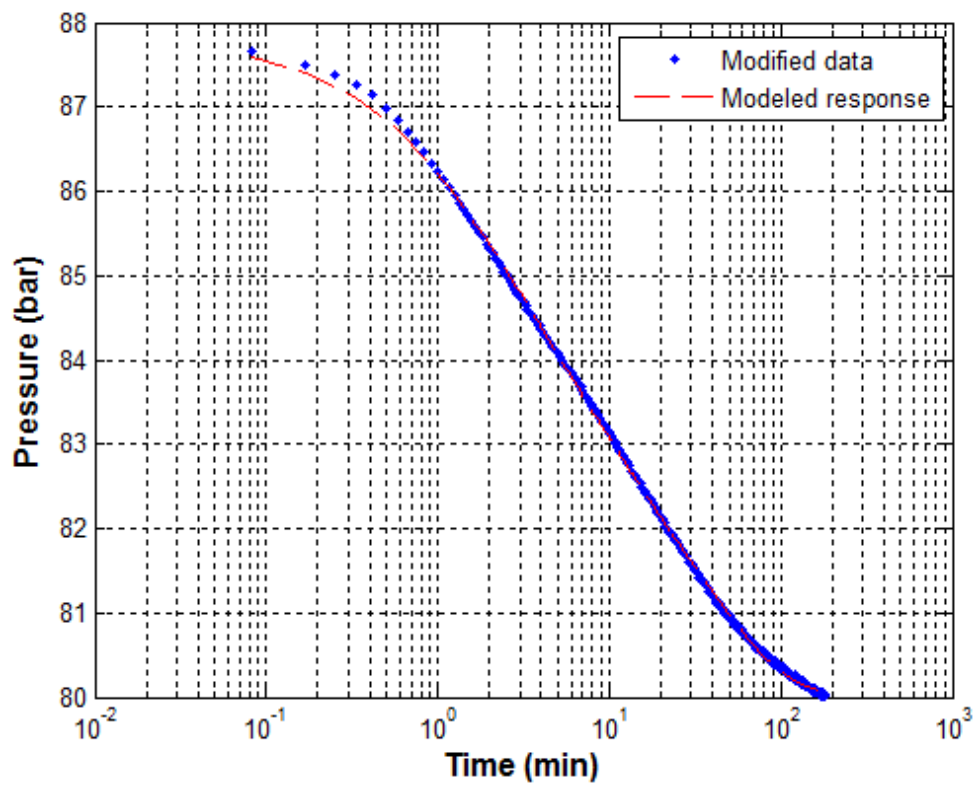


FIGURE 14: Pressure against time for model results and collected data for step 3, using a logarithmic time scale

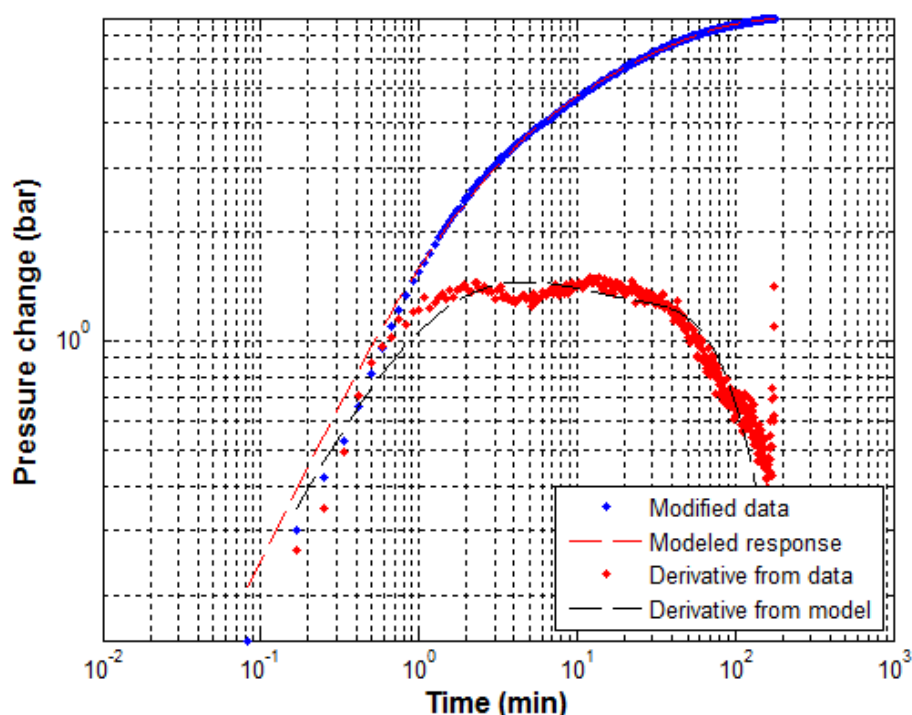


FIGURE 15: Pressure and its derivative against time for model results and collected data for step 3 on a log-log scale (see text)

TABLE 6: Results from non-linear regression parameter estimate using injection data from well K-37

Reservoir parameters	1. step	2. step	3. step	Best estimate (Step 3)	Units
Transmissivity (T)	$2.2 \cdot 10^{-8}$	$2.3 \cdot 10^{-8}$	$2.1 \cdot 10^{-8}$	$2.1 \cdot 10^{-8}$	$\text{m}^3/(\text{P} \cdot \text{s})$
Storativity (S)	$6.6 \cdot 10^{-8}$	$6.2 \cdot 10^{-8}$	$7.7 \cdot 10^{-8}$	$7.7 \cdot 10^{-8}$	$\text{m}^3/(\text{Pa} \cdot \text{m}^2)$
Radius of investigation (r_e)	287	60	61	61	m
Skin factor (s)	-2.4	-2.3	-2.5	-2.5	-
Wellbore storage (C)	$9.3 \cdot 10^{-6}$	$1.1 \cdot 10^{-5}$	$6 \cdot 10^{-6}$	$6 \cdot 10^{-6}$	$\text{m}^3/(\text{Pa})$
Permeability (k)	$1.36 \cdot 10^{-13}$	$1.3 \cdot 10^{-13}$	$1.3 \cdot 10^{-13}$	$1.3 \cdot 10^{-13}$	m^2
Injectivity index	3.6	4	3.9	3.9	(l/s)/bar

3.5 Testing of well K-38

Well K-38 is a directional well which was drilled from 26.04.2008 to 20.07.2008 to a total measured depth of 2693 m. An injection test was performed on 20/07/2008. The injection rate was constant, 45 l/s, before the injection test started. The injection was conducted in three steps, as illustrated in Table 7 and in Figure 16.

TABLE 7: Injection rate and pressure response

20/07/2008	Before starting	Step 1	Step 2	Step 3
Time period	-	02:59 - 05:58	05:58 - 10:30	10:30 - 13:35
Duration (hr)	-	3	4.5	3
Injection (l/s)	45	25	35	45
Change in injection $ \Delta Q $ (l/s)	-	20	10	10
Pressure at the end of step (bar-g)	117	109	113	116
Change in pressure $ \Delta p $ (bar-g)	-	8	4	3

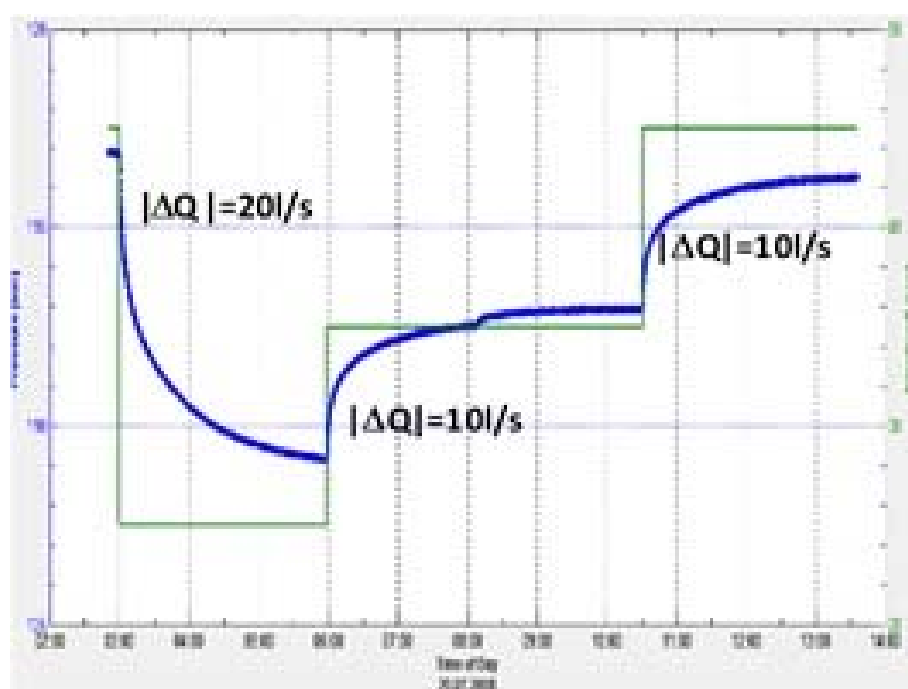


FIGURE 16: Step rate injection and pressure response for Well K-38

A non-linear regression analysis was done to find the parameters of the model that best fit the data. Initial parameters that were used to describe the reservoir in this analysis are estimated reservoir temperature 320°C, wellbore radius 0.18 m, and an estimated reservoir pressure 113 bar was found by WellTester. Two types of models were considered for the reservoir, on one hand a homogeneous reservoir and on the other hand a dual porosity reservoir. The best fit between the model and the data was obtained for a homogenous reservoir, constant pressure boundary, constant skin and wellbore storage.

Pressure change during step rate injection in K-38 as well as the change in injection for each step are illustrated in Figure 16. Figure 17 shows on a linear scale how the chosen model fits the data in step 3 and Figure 18 shows the pressure on a linear scale using a logarithmic timescale. Figure 19 shows the pressure change on a logarithmic scale, also using a logarithmic timescale, together with the derivative of the pressure response multiplied by the time passed since the beginning of the step.

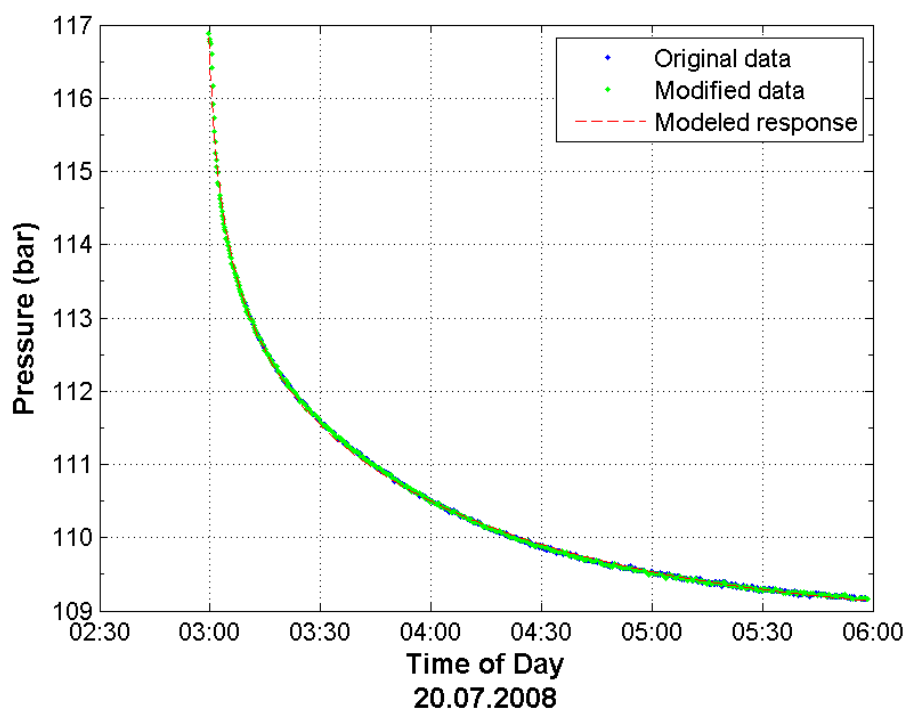


FIGURE 17: Pressure against time for model results and collected data for step 3

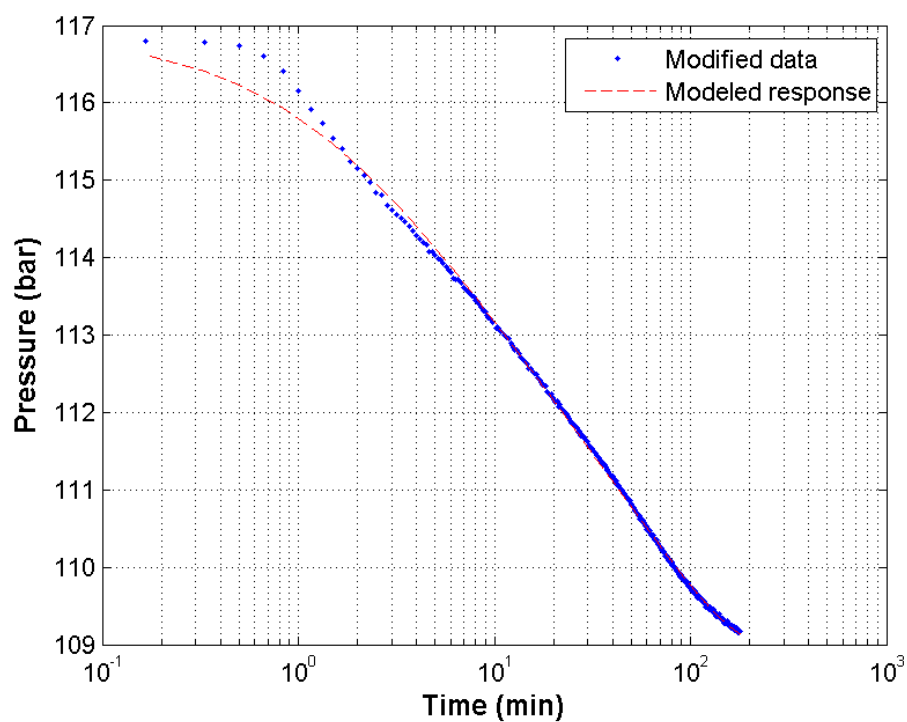


FIGURE 18: Pressure against time for model results and collected data for step 3, using a logarithmic time scale

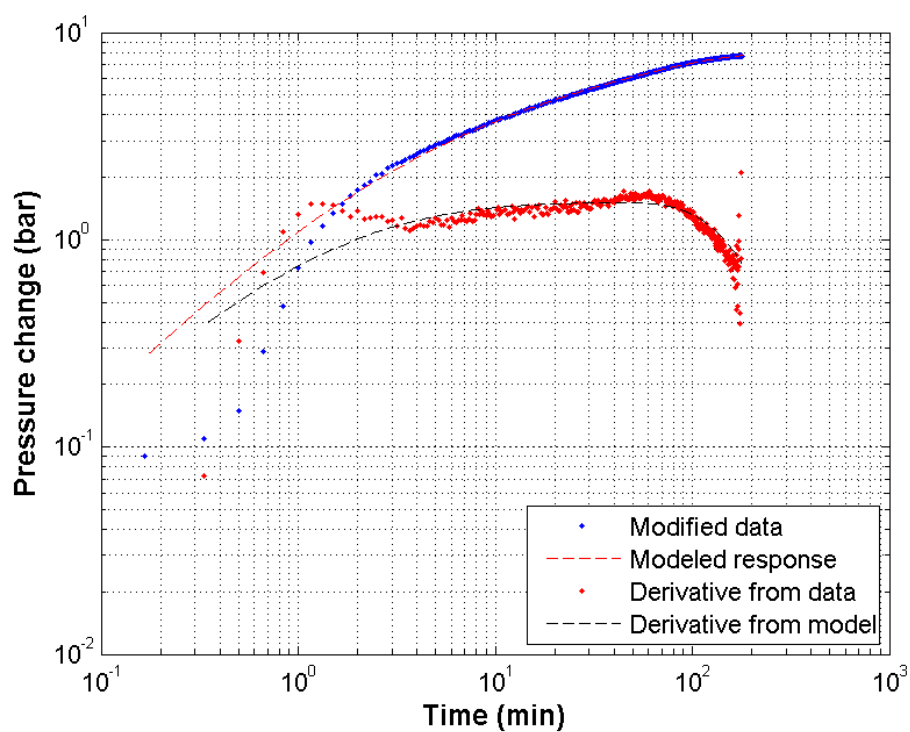


FIGURE 19: Pressure and its derivative against time for model results and collected data for step 3 on a log-log scale

Table 8 shows the reservoir parameters estimated by using the selected model.

TABLE 8: Results from non-linear regression parameter estimate using injection data from well K-38

Reservoir parameters	1. step	2. step	3. step	Best estimate	Units
Transmissivity (T)	$1.2 \cdot 10^{-8}$	$1.4 \cdot 10^{-8}$	$1.5 \cdot 10^{-8}$	$1.5 \cdot 10^{-8}$	$\text{m}^3/(\text{Pa}\cdot\text{s})$
Storativity (S)	$5.5 \cdot 10^{-7}$	$4.6 \cdot 10^{-7}$	$4.6 \cdot 10^{-7}$	$4.6 \cdot 10^{-7}$	$\text{m}^3/(\text{Pa}\cdot\text{m}^2)$
Radius of investigation (r_e)	71	83	26	26	M
Skin factor (s)	-1.9	-1.7	-1.8	-1.8	-
Wellbore storage (C)	$6.6 \cdot 10^{-6}$	$5 \cdot 10^{-6}$	$4.4 \cdot 10^{-6}$	$4.4 \cdot 10^{-6}$	$\text{m}^3/(\text{Pa})$
Permeability (k)	$1.1 \cdot 10^{-10}$	$1.4 \cdot 10^{-10}$	$1.6 \cdot 10^{-10}$	$1.6 \cdot 10^{-10}$	m^2
Injectivity index	2.6	2.7	3	3	$(\text{l/s})/\text{bar}$

The injectivity index for well K-38 is lower than for well K-37, showing a lower permeability in this part of the reservoir. This could mean that well K-37 intersects more permeable structures than well K-38. This could also be partly due to the higher negative values of skin factor for well K-37.

3.6 Summary of injection test results

Table 9 summarises the results obtained by well test analysis of injection tests in four wells, two at Nesjavellir and two at Krafla. Transmissivity estimated for selected wells in Nesjavellir is of the same order of magnitude as that of the wells in Krafla, i.e. $10^{-8} \text{ m}^3/(\text{Pa}\cdot\text{s})$, which is common in geothermal reservoirs in Iceland according to the report from WellTester with results and descriptions of the resulting parameters (Júliússon et al., 2008). The storativity for Krafla was higher than that of Nesjavellir for the selected wells which is also according to the report from WellTester, which says: “Common values for liquid-dominated geothermal reservoirs are around $10^{-8} [\text{m}^3/(\text{Pa}\cdot\text{m}^2)]$ while two-phase reservoirs might have values on the order of $10^{-5} [\text{m}^3/(\text{Pa}\cdot\text{m}^2)]$. Some of the wells in Krafla have a steam cap, including the two wells analysed, which shows a two-phase reservoir, but the selected wells in Nesjavellir are at the boundary of the reservoir and are liquid-dominated. Skin factor for the selected wells for both fields was negative as it usually is in Iceland. Permeability for wells in Krafla was higher than in the selected wells in Nesjavellir.

TABLE 9: Summary of the results of well test analysis for Krafla and Nesjavellir geothermal fields

Reservoir parameters	NJ-15	NJ-18	K-37	K-38	Unit
Transmissivity (T)	$1.3 \cdot 10^{-8}$	$2.8 \cdot 10^{-8}$	$2.1 \cdot 10^{-8}$	$1.5 \cdot 10^{-8}$	$\text{m}^3/(\text{Pa}\cdot\text{s})$
Storativity (S)	$6.4 \cdot 10^{-8}$	$1.3 \cdot 10^{-8}$	$7.7 \cdot 10^{-8}$	$4.6 \cdot 10^{-7}$	$\text{m}^3/(\text{Pa}\cdot\text{m}^2)$
Radius of investigation (r_e)	46	174	61.0	26	m
Skin factor (s)	-2.2	-1.3	-2.5	-1.8	-
Wellbore storage (C)	$8.4 \cdot 10^{-6}$	$4.8 \cdot 10^{-6}$	$6 \cdot 10^{-6}$	$4.4 \cdot 10^{-6}$	$\text{m}^3/(\text{Pa})$
Permeability (k)	$4 \cdot 10^{-15}$	$4.6 \cdot 10^{-14}$	$1.3 \cdot 10^{-13}$	$1.6 \cdot 10^{-10}$	m^2
Injectivity Index	2.7	2.2	3.8	2.8	$((\text{l/s})/\text{bar})$

4. TEMPERATURE AND PRESSURE PROFILES ANALYSIS

An analysis of temperature and pressure profiles was performed in four wells, two at Nesjavellir (NJ-15 and NJ-18) and two at Krafla (K-37 and K-38). The purpose of the analysis was to estimate the undisturbed conditions of the reservoir before drilling, i.e. formation temperature and initial pressure conditions. Berghiti and PREDYP programs included in the ISOR software package ICEBOX (Arason et al., 2004), were used to estimate the formation temperature and initial pressure, respectively. The software BOILCURV (Arason et al., 2004), also from the ICEBOX package, was used to estimate boiling conditions in the well. The following section outlines the theory related to the estimation of the

formation temperature, initial pressure and the boiling depth curve. After that, interpretation of the analysis of downhole temperature and pressure profiles for the selected wells is presented.

4.1 Formation temperature, initial pressure and boiling depth curve

4.1.1 Formation temperature

Knowledge of the formation temperature is important in the development and exploitation of geothermal reservoirs and especially in the estimation of reservoir potential. During drilling operations, the well and the close surroundings are cooled down by drilling fluid circulation and cold water injection. After drilling, the well is usually allowed to recover in temperature (warm up) from the cooling. The principal reservoir engineering research conducted during this period is repeated temperature and pressure logging. The temperature data thus collected is used to estimate the undisturbed system temperature, often called the formation temperature, as wells usually do not recover completely during the recovery period. Different methods can be used for this estimation, but the method most often applied is the so-called Horner method (Grant and Bixley, 2011).

The Horner method is a simple analytical technique for analysing recovery temperature to determine the formation temperature. In this method, the temperature recovery data is plotted against the logarithm of dimensionless Horner time, $\frac{(t_p + \Delta t)}{\Delta t}$, where t_p is the time at which circulation was stopped and Δt is the time passed since circulation stopped. A straight line is fitted to the data points, which is extrapolated to infinite Δt , i.e. when the Horner time becomes 1. The extrapolated temperature corresponding to this point is taken as the true reservoir temperature (Helgason, 1993). Figure 20 presents an example of a fit of the semi-log straight line relationship at 800 m for well NJ-15. The method is not applicable for all cases or at all depths in a well, for example not at depths where cross flow screens the actual temperature conditions.

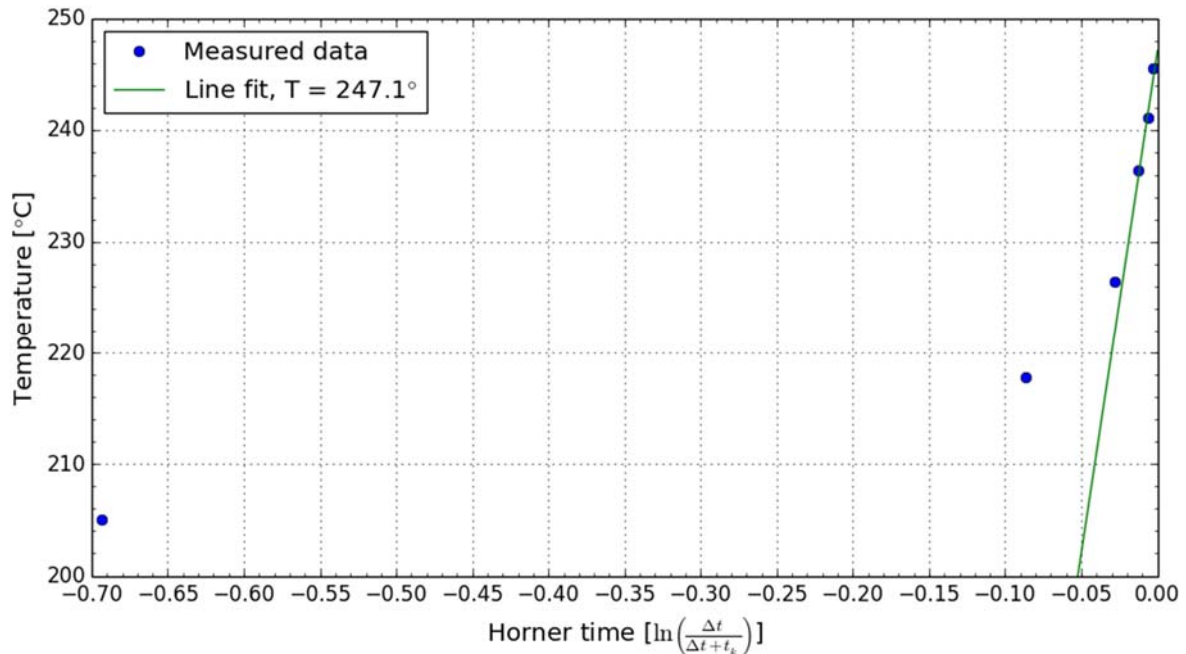


FIGURE 20: Formation temperature at 800 m in Well NJ-15

4.1.2 Boiling depth curve and initial pressure

Boiling curve with depth is described by the following integral (Arason et al., 2004):

$$p(z) = p_0 + g \int_{z_0}^z \rho_{sat}(p(z)) dz \quad (9)$$

where ρ_{sat} is a function of $p(z)$, which is the pressure at any depth z , p_0 is the pressure at some initial elevation z_0 , g is the acceleration of gravity and $\rho_{sat}(p(z))$ is the fluid density in a column of single-phase water at saturation pressure.

This formula is also used for PREDYP but in this case $\rho_{sat}(p(z))$ is replaced by $\rho(T(z))$, where $T(z)$ is the formation temperature with depth.

Equation 9 is non-linear and is solved numerically with the following formula:

$$p(z) = p_0 + g \sum_{i=1}^n \rho_{mean} \Delta z \quad (10)$$

where

$$\rho_{mean} = \frac{[\rho_{i-1}(p_{i-1}) + \rho_i(p_i)]}{2} \quad (11)$$

The total length z has been divided into n segments of length Δz and ρ_{mean} is the average density between the two depths z and Δz .

The problem is now to find the pressure and, hence, the saturation density $\rho_i(p_i)$ at our new depth $z+\Delta z$. This is done by using the Newton-Raphson iteration in the program BOILCURV. PREDYP program is used to calculate the initial pressure. The program calculates pressure in a static water column, if the temperature of the column is known (Arason and Björnsson, 1994). Both PREDYP and ICEBOX programs are found in the ICEBOX package.

4.2 Interpretation of temperature and pressure profiles for well NJ-15

Well NJ-15 is located in the eastern part of Nesjavellir geothermal field. It is a vertical well that was drilled in autumn 1985 to a total depth of 1748 m. Well NJ-15 was connected to the steam supply system from October 1998 until July 1999. Since then, well NJ-15 has been closed and is currently used for temperature and pressure monitoring. In the following section, temperature data which were collected during the warming up period were used to estimate formation temperature (Figure 21).

The temperature profiles in Figure 21 show a high gradient and linear profile, from 300 to 800 m, indicating a conductive zone. From 800 to 1300 m, there is a much lower gradient which could be due to a convective system and in this section the temperature is slightly less than a boiling condition but follows the boiling curve. Below 1300 m, there is an inversion in temperature down to 1500 m and an increase in temperature down to 1700 m. This inversion in temperature could be explained by a cold inflow at 1300 m.

The pressure profiles obtained during the warm up period and the initial pressure profile are shown in Figure 22. The pressure pivot point is located at around 1600 m and the pressure is 120 bar at that point.

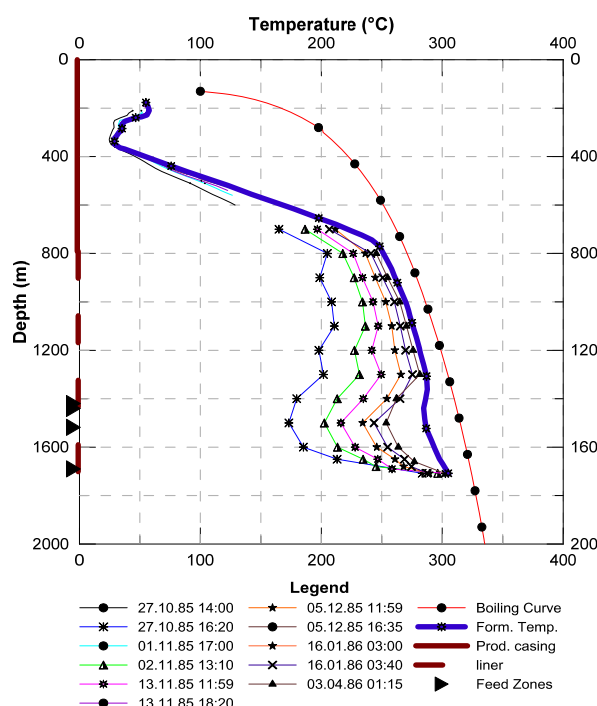


FIGURE 21: Temperature profiles for well NJ-15

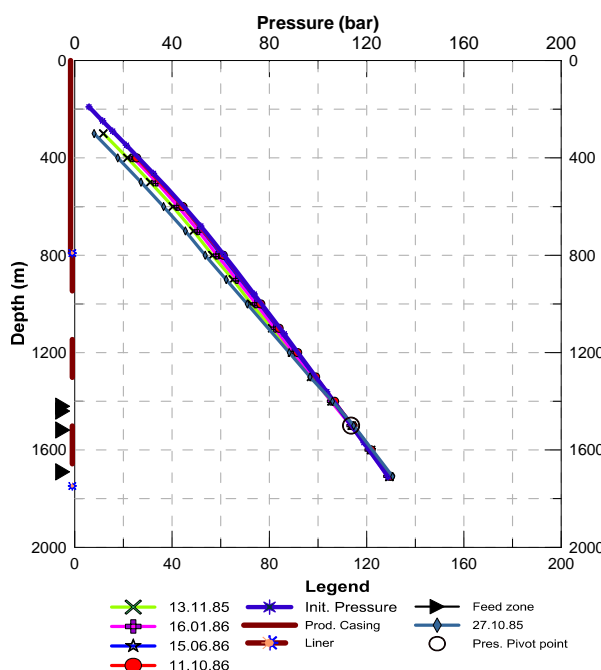


FIGURE 22: Pressure profiles for well NJ-15

To calculate the initial pressure, the estimated formation temperature profile from Figure 21 was substituted in the PREDYP program. The water level was adjusted in the calculations until the calculated profile matched the pivot point pressure. The pressure match was achieved with water levels at 203 m.

4.3 Interpretation of temperature and pressure profiles for well NJ-18

Well NJ-18 was drilled in 1986. It was not a productive well and was never connected to the steam supply system. It is currently used as a monitoring well. Temperature and pressure data were collected during the warm up period and were used to find the formation temperature and the initial pressure in a similar way as described for well NJ-15 in the previous section. Temperature profiles (Figure 23) show an increasing temperature with depth in the first 700 m. From 700 to 900 m, the temperature increases rapidly from 75 to 170 °C, and this suggests the possibility of a hot inflow within this range. Below 900 m there is a lower thermal gradient down to 1500 m and the zone can be interpreted as a convective zone but with poor permeability. Finally below 1700 m, the temperature gradient increases again down to the bottom of the well. Two feed zones are seen at 800 and 1700 m, respectively. The latest temperature profile is the same as the formation temperature profile between 800 and 1300 m.

Figure 24 shows the pressure profiles during warm up along with a pivot point that lies around 1700 m depth with a pressure of 150 bar.

To calculate the initial pressure, the estimated formation temperature profile from Figure 23 was inserted into the PREDYP software. The water level was adjusted in the calculations until the calculated profile matched the pressure pivot point.

4.4 Interpretation of temperature and pressure profiles for well K-38

Well K-38 in Krafla is a directional well located on the western flanks of Mt. Krafla which is a new

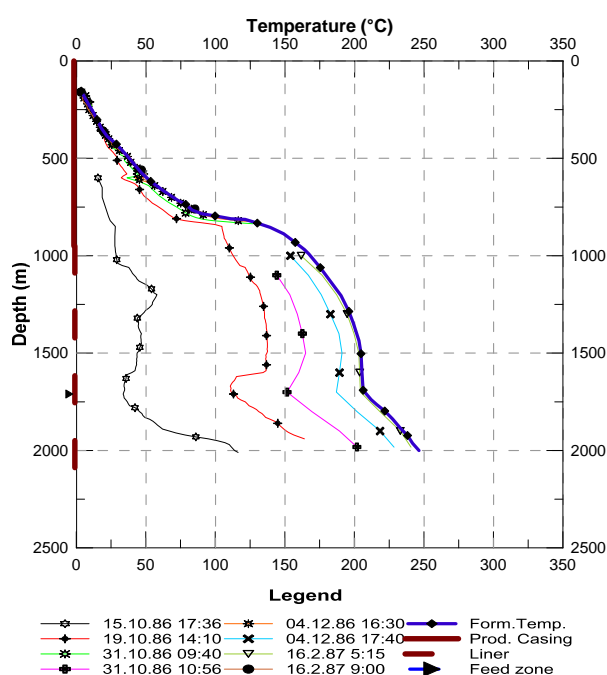


FIGURE 23: Temperature profiles for NJ-18

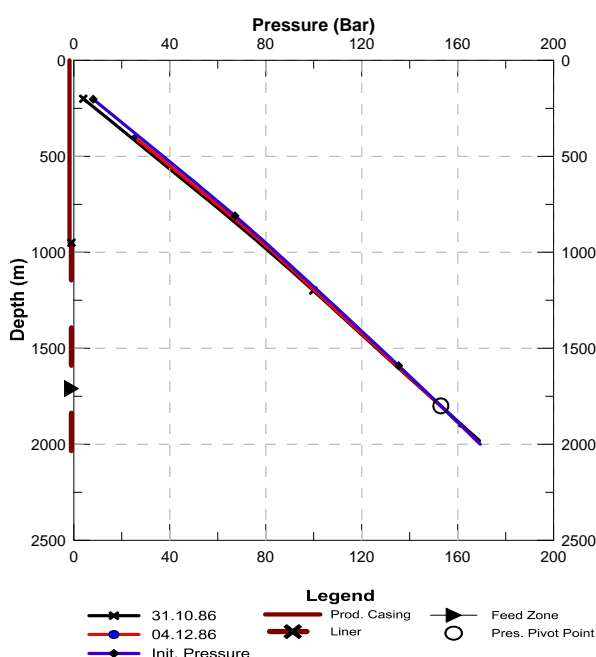


FIGURE 24: Pressure profiles for well NJ-18

well site in the field. It was drilled from 26.04.2008 to 21.07.2008 to a total depth of 2700 m with respect to the platform (2391.6 m TVD from the ground surface). Temperature profiles from July, August and September 2008 were used to estimate formation temperature (Figure 25). The formation temperature profile follows the boiling point curve in the top 1000 m. Two conductive layers were observed in the temperature profiles. The first layer (caprock) is located in the uppermost 300 m and the second layer (basement) between 1750 and 2000 m. There is a constant temperature zone between 300 and 1750 m depth. This zone can be interpreted as the reservoir (convective zone).

Figure 26 shows the pressure profiles during the warm up period. The pressure profiles show a pivot point at 2125 m where the pressure is about 130 bar (Figure 26). The pressure at the pivot point was

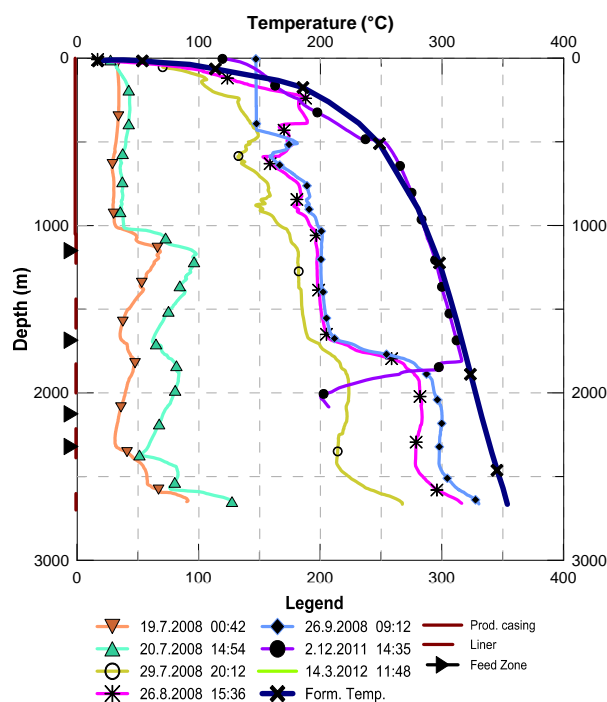


FIGURE 25: Temperature profiles for well K-38

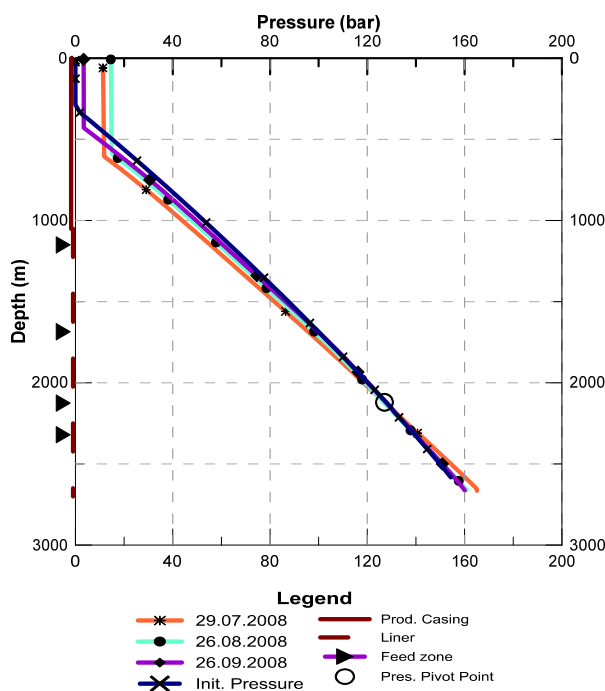


FIGURE 26: Pressure profiles for well K-38

used as a control point to estimate the initial pressure in a similar way as was described for wells NJ-15 and NJ-18 in the previous subsection.

4.5 Interpretation of temperature and pressure profiles for well K-37

Well K-37 in Krafla is a directional well drilled into the southern flanks of Mt. Krafla where there has been substantial production since 1980. It was drilled from 04.10.2007 to 18.01.2008 to a total depth of 2187 m. Downhole temperature and pressure data measured in January, March and April 2008 were used to estimate the formation temperature and initial pressure as shown in Figures 27 and 28.

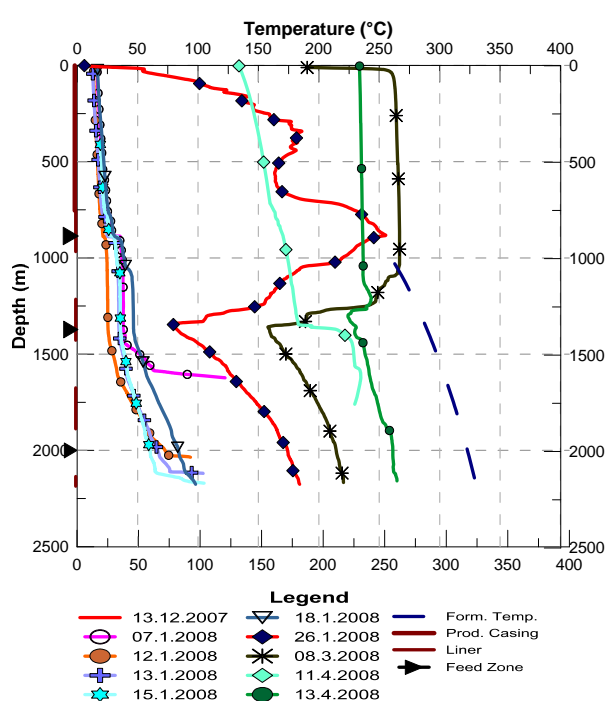


FIGURE 27: Temperature profiles for well K-37

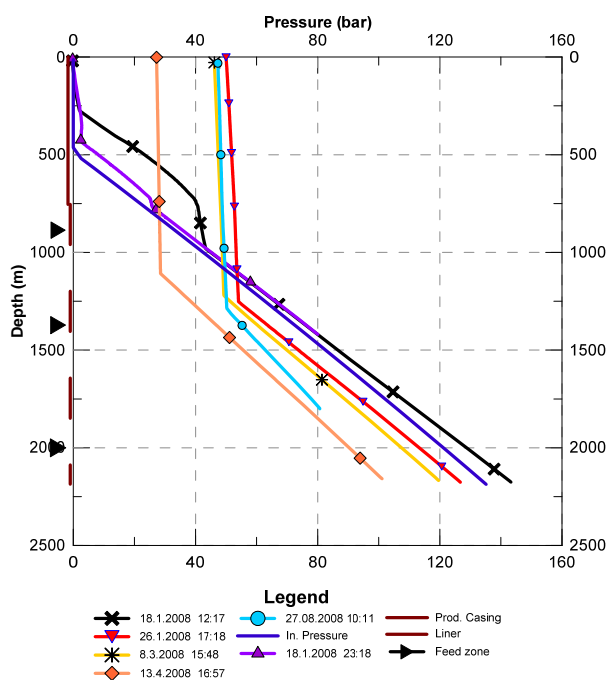


FIGURE 28: Pressure profiles for well K-37

Figure 27 shows the downhole temperature profiles and the formation temperature which follows the boiling point depth curve. However, the boiling point curve is shifted about 50 m due to drawdown in the system. Two major feed zones can be identified in the warm up temperature profiles: a hot inflow can be seen at 875 m depth and another feed zone can be observed at 1340 m. Between 0 and 300 m, the well shows conductive heating. Temperature profiles also indicate minor feed points at 590 and 1980 m.

Figure 28 illustrates the pressure profile during warm up. The pressure pivot point was not identified and the latest pressure profile (i.e. data measured on 27.08.2008) was used to determine the water level. Assuming this profile represents the actual reservoir conditions, the water level is at 450 m depth. Both formation temperature and initial pressure follow a boiling point curve as other wells on the southern flanks of the Krafla geothermal field (Mortensen et al., 2009).

5. PRESSURE AND TEMPERATURE MONITORING OF KRAFLA AND NESJAVELLIR GEOTHERMAL FIELDS

The purpose of careful monitoring of geothermal fields in utilization is to increase understanding of the geothermal fields, to prevent and to solve problems; the data is also necessary for simulation of

geothermal fields. The effect of “large-scale” mass-extraction on geothermal systems may induce pressure decline within the system which, in turn, causes flow from hot springs (and wells) to decline, discharge from steam-vents often to increase, increased recharge (often colder water) from outside, cooling of the reservoir, chemical changes (sometimes detrimental), surface subsidence as well as changes in micro-seismic activity (Axelsson and Halldórsdóttir, 2014). Three wells, two located in Nesjavellir geothermal field and one located in Krafla were considered for a monitoring analysis in this report.

5.1 Monitoring wells in Nesjavellir geothermal field

Through the existence of the Nesjavellir project, an extensive monitoring programme was carried out to monitor the response of the Nesjavellir geothermal system as well as to record the influence of utilization on the environment. A programme was set up to monitor the natural runoff from the field in the early 1980s, prior to the drilling and testing of production wells (Gíslason et al., 2005).

Since the start of drilling in the 1980s, downhole measurements, flow testing and chemical sampling have been included in the monitoring programme. Water levels or wellhead pressure are monitored when boreholes are not in production, depending on the characteristics of each borehole.

Since 1985, annual downhole temperature and pressure logs in idle wells have been measured and the data stored in the ÍSOR database (Gíslason et al., 2005). In the beginning several wells were available for the monitoring but, since production started, most production wells have been connected to the power plant, limiting the current monitoring programme to two wells: Well NJ-15 in the eastern part of the production area and well NJ-18, north of the production zone (Figure 1).

In this field, therefore, we will focus on the downhole pressure and temperature measurements performed on the two monitoring wells, i.e. wells NJ-15 and NJ-18, and continue the studies of these two wells. Data used for the analysis was collected from 1985 to 2013 and 1986 to 2013 for wells NJ-15 and NJ-18, respectively.

Figure 29 shows the formation temperature and initial pressure with the temperature and pressure history at 810 and 1590 m depths, considered to be the main feed zones for well NJ-15. Figure 30 illustrates formation temperature and initial pressure with temperature and pressure history at 1710 m, which is expected to be the main feed zone for well NJ-18. Formation temperature and initial pressure values at different depths were estimated from warm up data collected after drilling.

Measurement of temperatures at various depths for wells NJ-15 and NJ-18 shows no significant change in temperature with time, except in 2011 when a slight decrease in temperature was seen, and in 2012 a small increase in temperature was recorded for well NJ-15. This can be explained by the fact that, in May 2011, a flow test was carried out over a two week period; this could have allowed cold inflow from the eastern part of the hydrothermal system since well NJ-15 is located close to the eastern edge of the geothermal system. In March 2002, an injection test was conducted at well NJ-18 with 10 kg/s of 55°C of hot water injected into the well for three weeks. Temperature data measured during this period were not considered for this analysis. Since 2002 and up to 2013, there was a slow temperature recovery from 200 to 225°C.

Figure 29 shows a small decrease in pressure up to 1999, then a rapid decline from 1999 to 2013 at 810 and 1590 m. This rapid decrease in pressure may be due to the increase in production since 1999, observed in Figure 30. A linear constant pressure drawdown of about 7 bars was observed in well NJ-18 from 1985 to 2005 whereas from 2005 to 2013 the pressure decreased drastically to about 12 bars. Figure 31 shows the yearly production (kg/s) against time from 1984 to 2013.

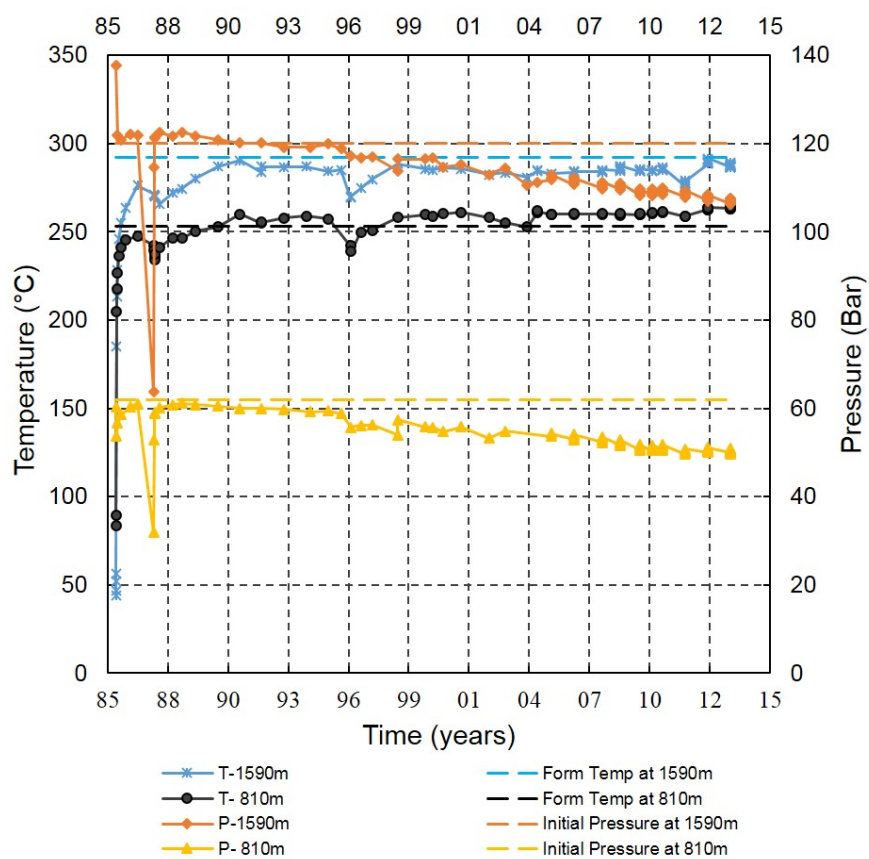


FIGURE 29: Temperature and pressure evolution from 1985 to 2013 for well NJ-15

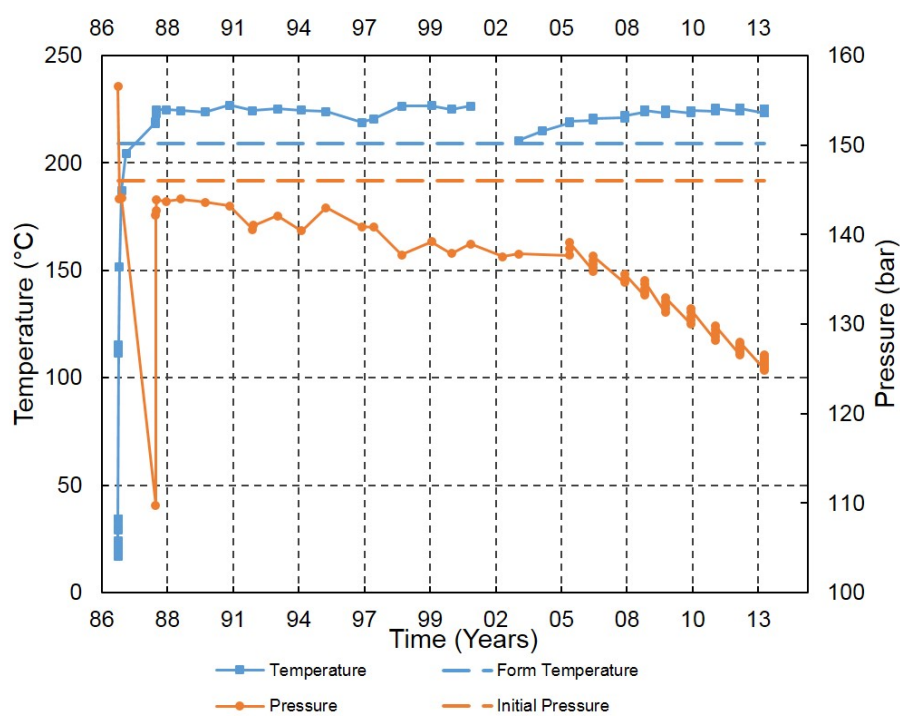


FIGURE 30: Temperature and pressure evolution at 1710 m from 1986 to 2013 for well NJ-18

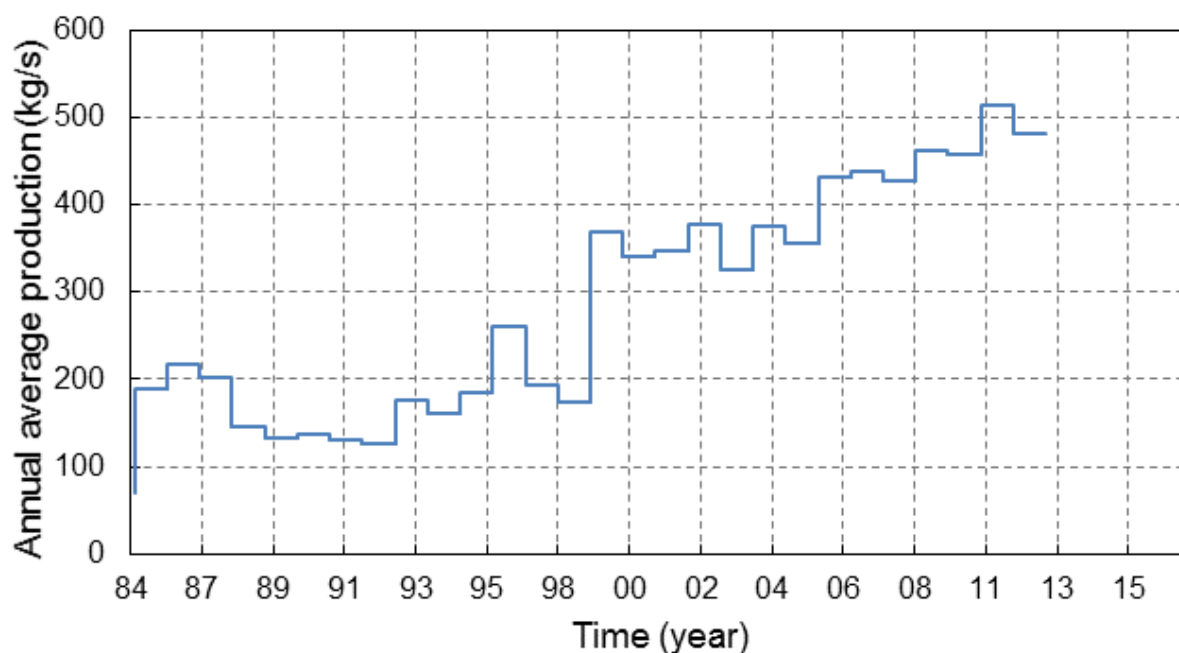


FIGURE 31: Average annual production in Nesjavellir from 1984 to 2013

5.2 Monitoring programme of Krafla geothermal field

Well KJ-18 was used for the monitoring programme of pressure and temperature evolution in Krafla geothermal system in this study. Well KJ-18 is located in the southeast part of Krafla geothermal field. It was drilled in 1981 to a total depth of 2215 m. During drilling, well KJ-18 was found to be very tight and it was decided not to put a slotted liner into it; production casing was set at 663m. During temperature recovery, it was found that the well was much colder than the wells to the west in the production area (Steingrímsson and Björnsson, 1996). Well KJ-18 was not a productive well and is currently used as one of the monitoring wells for Krafla geothermal system. Figure 32 shows the evolution of temperature at 1000, 1500 and 2000 m from 1981 to 2013 with the estimated formation temperature.

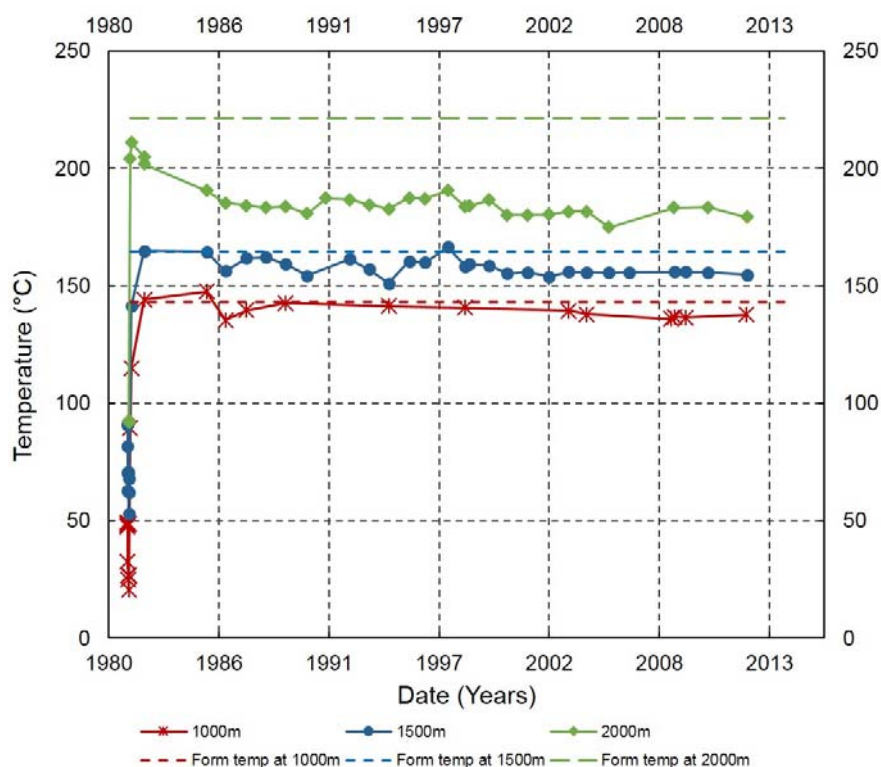


FIGURE 32: Pressure history for well K-18

As can be observed in Figure 32, there is a small change in temperature at 1000 m and 1500 m from 1981 to 2013. At 2000 m depth there is a rapid decrease from 1981 to 1988 and a small change in temperature since 1988 up to 2013. The rapid decrease in temperature at 2000 m was caused by a cold down flow from 1000 m feed point to the bottom of the well.

The pressure history is shown in Figure 33. From 1981 to 1991, the pressure had fallen by 6 bar once the production started in the area (Figure 34). The well showed little response to increased production in 1997. The well showed gradual linear pressure drawdown, about 15 bar since the beginning of production. Since the well is drilled at the eastern boundary of the geothermal field, the drawdown estimated from the monitoring data is probably an underestimate. Newly drilled wells on the southern flanks of Mt. Krafla show drawdown up to 30 bar (Mortensen et al., 2009). This was found by comparing the initial pressures of the wells. This corresponds roughly to 300 m change in water level and explains the depth to the water level in well K-37, as mentioned in the previous section.

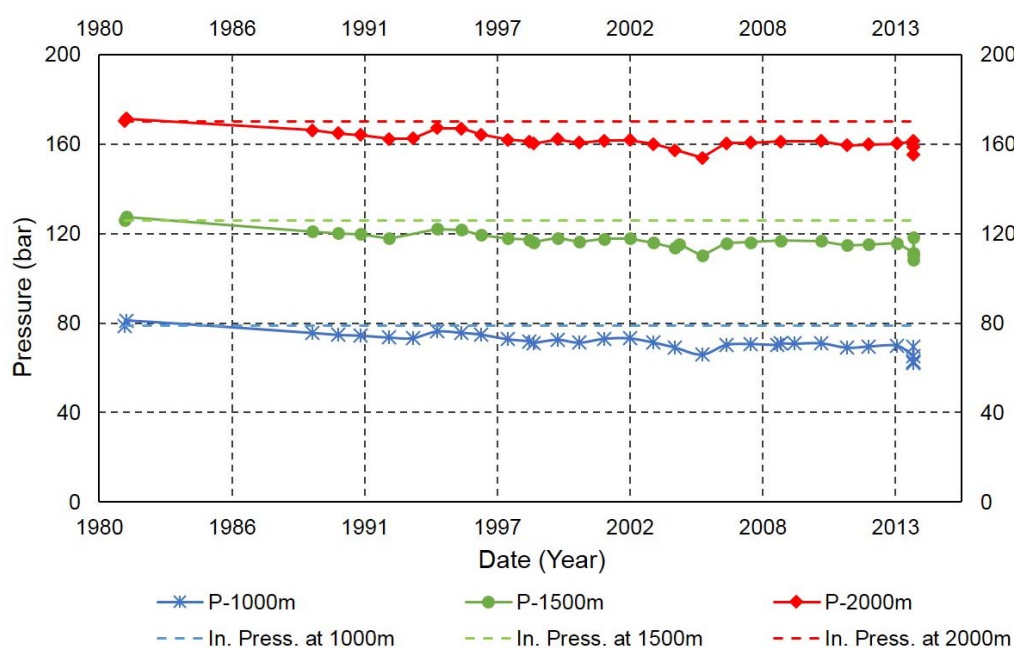


FIGURE 33: Pressure history for well K-38

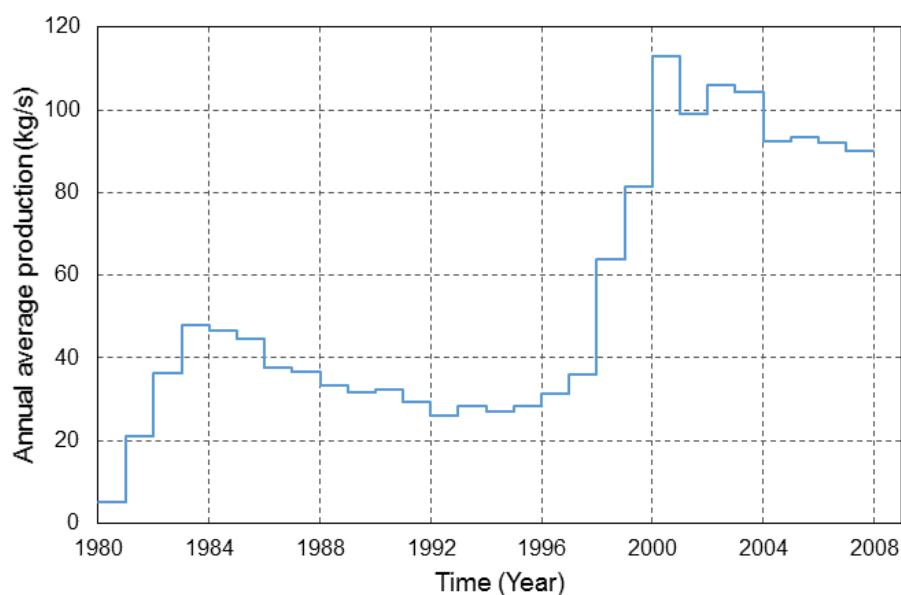


FIGURE 34: Average annual production from wells on the southern flanks of Krafla

6. CONCLUSION

Reservoir assessment and monitoring were conducted on selected wells in the Nesjavellir and Krafla high-temperature geothermal fields. Two wells, NJ-15 and NJ-18, were selected for reservoir assessment and monitoring for Nesjavellir and two other wells, K-37 and K-38, were selected for well test analysis for Krafla. Monitoring analysis was conducted only on well KJ-18 for Krafla.

In order to understand the parameters that characterise the reservoir and flow capacity of the selected wells, injection test analysis was performed and parameters such as injectivity index, transmissivity, storativity, skin, wellbore storage, etc. were evaluated. The WellTester program was used for the injection test analysis.

Transmissivity estimated for selected wells in Nesjavellir was of the same order of magnitude as for the wells in Krafla, i.e. $10^{-8} \text{ m}^3/(\text{Pa}\cdot\text{s})$, which is common in geothermal reservoirs in Iceland. The storativity for Krafla was higher than that of Nesjavellir for the selected wells. Some of the wells in Krafla have indeed, a steam cap, including the two wells analysed, which shows a two-phase reservoir, but the selected wells in Nesjavellir are at the boundary of the reservoir and are liquid-dominated. Skin factor for the selected wells for both fields was negative, as it usually is in Iceland. Permeability for the wells in Krafla was a little bit higher than in the selected wells in Nesjavellir. Wells NJ-15 and NJ-18 are probably not representative of the wells in Nesjavellir because they are located at the field boundaries. Perhaps these wells were drilled into a less permeable sector of the field.

Temperature and pressure profiles were analysed to estimate formation temperature and initial pressure. For wells NJ-18 and NJ-15, the highest formation temperatures were 250 and 300°C, respectively. Boiling was not observed for these wells, which indicates that these wells were drilled in a lower temperature part or at the boundary of the Nesjavellir field. Formation temperatures varied between 10 and 350°C and boiling was observed in the upper 1800 and 1000 m for wells K-38 and K-37, respectively. This indicates that these wells were drilled in a high-temperature reservoir.

Temperature and pressure monitoring at various depths were performed on well K-18 from 1981 to 2013 for Krafla, on well NJ-15 from 1985 to 2013, and on well NJ-18 from 1988 to 2013 for Nesjavellir. No significant change in temperature was observed in wells NJ-15 and NJ-18 but a linear constant pressure drawdown of about 13 bar was observed in well NJ-15 from 1985 to 2013 and a rapid decline in pressure (20 bar) was observed in well NJ-18 from 2006 to 2013. For Krafla geothermal system, slow pressure and temperature decreases were observed in well KJ-18 in general. The decrease in temperature is due to cold water down flow in the well, but the pressure decline is the effect of production in this part of the field. The well showed little response to increased production in 1997. The dynamic modelling methods such as lumped parameter models could be applied to calculate future predictions for future studies.

ACKNOWLEDGEMENTS

I wish to express my sincere gratitude to UNU-GTP Director, Lúdvík S. Georgsson, for the opportunity to complete this training. My thanks also go to my advisors, Dr. Svanbjörg Helga Haraldsdóttir and Ms. Saeunn Halldórsdóttir for their guidance and useful suggestions throughout the course of my work. I am also grateful to my home institutions, Rwanda Energy Group (REG) and National Capacity Building Secretariat (NCBS) for granting me study leave for this short course. Thanks are due to Landsvirkjun and Orkuveita Reykjavíkur for providing field data for my work. I would also like to thank the UNU-GTP staff: Ingimar Gudni Haraldsson, Thórhildur Ísberg, Markús A.G. Wilde, María S. Guðjónsdóttir, and Málfríður Ómarsdóttir for their kind assistance, and to all the 2014 UNU Fellows for their friendship. Finally, this paper is dedicated to my wife for her patience and continuous encouragement during my absence from home.

REFERENCES

- Ágústsson, K., Flóvenz, Ó.G., Gudmundsson, Á., and Árnadóttir, S., 2012: Induced seismicity in the Krafla high temperature field. *Geothermal Resources Council, Trans.*, 36, 975-980.
- Arason, Th., and Björnsson, G., 1994: *ICEBOX* (2nd edition). Orkustofnun, Reykjavík, 38 pp.
- Arason, Th., Björnsson, G., Axelsson, G., Bjarnason, J.Ö., and Helgason, P., 2004: *The geothermal reservoir engineering software package Icebox, user's manual*. ÍSOR – Iceland GeoSurvey, Reykjavík, report 2004/014, 53 pp.
- Ármannsson, H., 2010: The chemistry of the Krafla geothermal system in relation to the IDDP well. *Proceedings of the World Geothermal Congress 2010 Bali, Indonesia*, 5 pp.
- Ármannsson, H., Gudmundsson, Á., and Steingrímsson, B.S., 1987: Exploration and development of the Krafla geothermal area. *Jökull*, 37, 12-29.
- Axelsson, G. and Halldórsdóttir, S., 2014: *Management and monitoring of geothermal systems*. UNU-GTP, unpublished lecture notes.
- Axelsson, G. and Steingrímsson, B., 2012: Logging, testing and monitoring geothermal wells. *Presented at the short course on geothermal development and geothermal wells organized by UNU-GTP and LaGeo, in Santa Tecla, El Salvador*, 20 pp.
- Björnsson, A., 1985: Dynamics of crustal rifting in north-eastern Iceland. *J. Geophysical Research*, 90- B12, 10.151 – 10.162.
- Franzson, H., 1998: Reservoir geology of the Nesjavellir high-temperature field in SW-Iceland. *Proceedings of the 19th Annual PNOC-EDC Geothermal Conference, Manila, Philippines*, 13-20.
- Franzson, H., 2000: Hydrothermal evolution of the Nesjavellir high-temperature system, Iceland. *Proceedings of the World Geothermal Congress 2000, Kyushu-Tohoku, Japan*, 2075-2080.
- Gíslason, G., Ármannsson, H., and Hauksson, T., 1978: *Krafla, temperature conditions and gases in the geothermal reservoir*. Orkustofnun, Reykjavík, report OS-JHD-7846 (in Icelandic), 88 pp.
- Gíslason, G., Ívarsson, G., Gunnlaugsson, E., Hjartarson, A., Björnsson, G., and Steingrímsson, B., 2005: Production monitoring as a tool for field development; A case history from the Nesjavellir field, Iceland. *Proceedings of the World Geothermal Congress 2005, Antalya, Turkey*, 9 pp.
- Grant, M.A. and Bixley, P.F., 2011: *Geothermal reservoir engineering* (2nd ed.). Academic Press, NY, 359 pp.
- Grant, M.A., Donaldson, I.G., and Bixley, P.F., 1982: *Geothermal reservoir engineering*. Academic Press, NY, 369 pp.
- Helgason, P., 1993: *Step by step guide to Berghiti*. Orkustofnun, Reykjavík, Iceland.
- Horne, R.N., 1995: *Modern well test analysis, a computer aided approach* (2nd edition). Petroway Inc., USA, 257 pp.
- Júlíusson, E., Grétarsson, G.J., and Jónsson, P., 2008: *WellTester 1.0b, user's guide*. ÍSOR – Iceland GeoSurvey, Reykjavík, report ÍSOR-2008/063, 27 pp.

Mortensen, A.K., Gudmundsson, A., Steingrímsson, B., Sigmundsson, F., Axelsson, G., Ármannsson, H., Björnsson, H., Ágústsson, K., Saemundsson, K., Ólafsson, M., Karlsdóttir, R., Halldórsdóttir, S., and Hauksson, T., 2009: *Geothermal system in Krafla, summary of research on the geothermal system and revised conceptual model*. ISOR – Iceland GeoSurvey, Reykjavik, report ISOR-2009/057 (in Icelandic). 45 pp.

Steingrímsson, B., and Björnsson G., 1996: *Well tests in Krafla and Bjarnarflag in the year 1995*. Orkustofnun, report OS-96025/JHD-14 B (in Icelandic), 50 pp.

Steingrímsson, B., Gudmundsson, A., Franzson, H., and Gunnlaugsson, E., 1990: Evidence of a superficial fluid at depth in the Nesjavellir field. *Proceedings of the 15th Workshop on Geothermal Reservoir Engineering, Stanford University, California*, 81-88.

Van Everdingen, O.F., and Hurst, W., 1953: The application of the Laplace transformation to flow problems in reservoirs. *Trans. AIME*, 186, 305-324.

NOMENCLATURE

c_t	: Total compressibility (Pa^{-1});
c_w	: Fluid compressibility (Pa^{-1});
c_r	: Rock compressibility (Pa^{-1});
h	: Reservoir thickness (m);
II	: Injectivity index ($(\text{l/s})/\text{bar}$);
ϕ	: Porosity (%);
k	: Formation permeability (m^2);
p	: Pressure (Pa);
Q	: Volumetric flow rate (m^3/s);
ρ	: Fluid density (kg/m^3);
r	: Radial distance (m);
S	: Storativity ($\text{m}^3/(\text{Pa} \cdot \text{m}^2)$);
t	: Time (s);
T	: Transmissivity ($\text{m}^3/(\text{Pa} \cdot \text{s})$);
Δp	: Change in reservoir pressure (Pa);
ΔQ	: Change in the injection flow (m^3/s);
ν	: kinematic viscosity of the fluid;
C	: Wellbore storage coefficient (m^3/Pa);
ΔV	: Change in fluid volume (m^3);
s	: Skin factor;
r_e	: Radius of investigation (m);
t_p	: Circulation stop time (h);
hr	: Hour (h.);
T	: Temperature ($^{\circ}\text{C}$);
ρ_{sat}	: Saturation density (kg/m^3);
ρ_{mean}	: Average density (kg/m^3);
z	: Depth (m);
g	: Acceleration of gravity (m/s^2);
μ	: Dynamic viscosity ($\text{Pa} \cdot \text{s}$).



UNITED NATIONS
UNIVERSITY

UNU-GTP

Geothermal Training Programme

Orkustofnun, Grensasvegur 9,
IS-108 Reykjavik, Iceland

Reports 2014
Number 25

WELL TEST ANALYSIS AND TEMPERATURE AND PRESSURE MONITORING OF KRAFLA AND NESJAVELLIR HIGH-TEMPERATURE GEOTHERMAL FIELDS, ICELAND

Leon Ntihakose

Rwanda Energy Group, Ltd.
Energy Development Corporation, Ltd.
P.O. Box 537, Kigali
RWANDA
ntihableon@gmail.com

ABSTRACT

The Krafla high-temperature geothermal field is located within the Krafla caldera lying within the active NE-SW striking rift zone of North-East Iceland, whereas the Nesjavellir geothermal field is a high-temperature geothermal system, part of the Hengill central volcano in SW-Iceland. Reservoir assessment and monitoring was conducted on wells NJ-15 and NJ-18, located in the Nesjavellir high-temperature geothermal field. For Krafla geothermal field, wells K-37 and K-38 were considered to assess the reservoir, and well K-18 was used for monitoring. Temperature and pressure logs, measured during the warm up of the wells, were analysed to estimate formation temperature and initial pressure. In order to understand the parameters that characterise the reservoir and the wells, injection tests were analysed and parameters such as the injectivity index, transmissivity, storativity, skin, wellbore storage, etc. were evaluated.

Transmissivity estimated for the wells selected in Nesjavellir were of the same order of magnitude as for the wells in Krafla, i.e. $10^{-8} \text{ m}^3/(\text{Pa}\cdot\text{s})$. Storativity for Krafla was higher than that of Nesjavellir, as can be expected in a two-phase reservoir. The wells in Nesjavellir are located at the outer boundaries of the geothermal reservoir and are liquid-dominated. This was further established by analysing the formation temperature and initial pressure. Temperature and pressure monitoring analyses at various depths were performed for Krafla on well K-18 from 1981 to 2013 and for well NJ-15 from 1985 to 2013; and for Nesjavellir well NJ-18 from 1988 to 2013. No significant change in temperature was observed in wells NJ-15 and NJ-18, but a linear constant pressure draw down of about 13 bar was observed in well NJ-15 from 1985 to 2013 and a rapid decline in pressure (20 bar) was observed in well NJ-18 from 2006 to 2013. In well KJ-18 in Krafla, a slow pressure decrease was observed.

1. INTRODUCTION

This report is a result of a reservoir analysis conducted in two geothermal areas, i.e. Nesjavellir geothermal field and Krafla geothermal field. Wells NJ-15 and NJ-18, located in Nesjavellir, were selected while wells K-37 and K-38 were selected for Krafla. Formation temperature estimation, initial

pressure and analysis of an injection test were performed on all wells. Moreover, pressure and temperature monitoring analyses were carried out on wells NJ-15, NJ-18 and K-38 as well as on well KJ-18 which is near well K-37. Formation temperature estimation at different borehole depths was obtained by using the ÍSOR software Berghiti (Arason et al., 2004). Formation temperature is important in decision making for selecting sites for new wells as well as for setting up a conceptual model. The ÍSOR software PREDYP (Arason et al., 2004) was applied to calculate the initial pressure. Injection test simulation was made by utilizing WellTester software (Júliússon et al., 2008) based on non-linear regression. For each well, the injectivity index was estimated. The injectivity index is a simple relationship, approximately reflecting the capacity of a well, which is useful for determining whether a well is sufficiently open to be a successful producer and for comparison with other wells (Axelsson and Steingrímsson, 2012).

In the next section the geothermal fields at Nesjavellir and Krafla will be introduced after which the theory of well testing will be presented. Injection tests from four wells will be analysed in Section 3. Temperature and pressure profiles during warm up will be analysed to deduce the formation temperature and initial pressure in each of the wells in Section 4 and, finally, temperature and pressure monitoring studies for both fields will be presented in Section 5, followed by conclusions in Section 6.

2. NESJAVELLIR AND KRAFLA GEOTHERMAL FIELDS

2.1 Nesjavellir geothermal field

The Nesjavellir geothermal field is a high-temperature geothermal system located in the Hengill central volcano in Southwest Iceland (Gíslason et al., 2005) (Figure 1). Several geological studies have been performed to understand the geothermal conditions of the Nesjavellir reservoir (Franzson, 1998; Franzson, 2000; Steingrímsson et al., 1990).

The geology of the area is characterised by hyaloclastite accumulation, lava accumulation and intrusive rocks. Hyaloclastite accumulation is dominant down to about 400 m b.s.l. below which lava accumulation dominates. The intrusive rocks, composed of basaltic dykes or sheets, characterise the section below 800 m depth and increase up to 80-100% intensity below 2000 m depth. Shallow-dipping dioritic sheet-like intrusions are also found at various depths and they contribute substantially to the permeability in the field, along with the basaltic intrusions.

Exploration drilling at Nesjavellir started with five wells in 1965. Additional 13 wells were drilled during the period of 1981-1985. A further 10 wells were drilled as step out and make up wells, along with a few shallower reinjection wells.

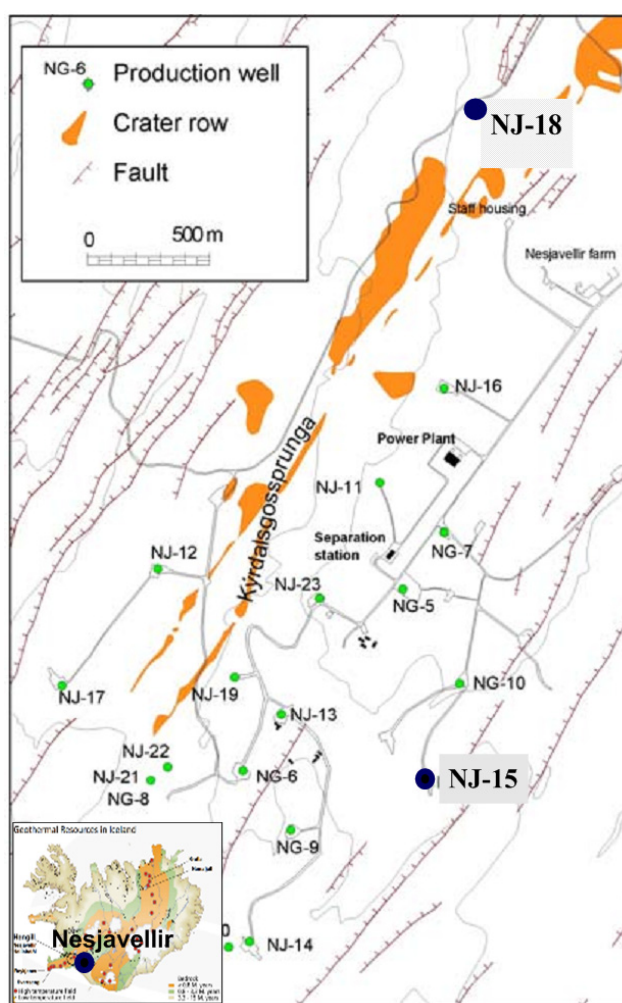


FIGURE 1: Locations of Wells NJ-15 and NJ-18 at Nesjavellir (modified from Gíslason et al., 2005)

Production of hot water from Nesjavellir for district heating in Reykjavík started in 1990 and power generation began in 1998. Reykjavik Energy (Orkuveita Reykjavíkur) is currently operating a 120 MW_e power plant and a 300 MW_{th} thermal unit in the Nesjavellir geothermal field.

Two wells, NJ-15 and NJ-18, in Nesjavellir (Figure 1) were selected for this study. Well NJ-15 is located at the outer border of the eastern part of the production area. It is a vertical well that was drilled in the autumn 1985 to a total depth of 1748 m. Well NJ-15 was connected to the steam supply system in October 1998 until July 1999. Since then, well NJ-15 has been closed and is currently used for temperature and pressure monitoring. Well NJ-18 is situated north of the production area. It is a vertical well, drilled in 1986 to a depth of 2136 m. It was not a productive well and was never connected to the steam supply system. It is currently used as a monitoring well.

2.2 Krafla geothermal field

The Krafla high-temperature geothermal system is located within the Krafla caldera (Figure 2) lying within an active N-S striking rift zone in Northeast Iceland (Ármannsson et al., 1987). The volcanic activity in this area is episodic, occurring every 250-1000 years, with each episode lasting 10-20 years. The most recent volcanic period started at the end of 1975 and ended in September 1984 with 9 eruptions and 21 tectonic events (Björnsson, 1985).

The Krafla geothermal field is subdivided into several sub-fields based on the chemical composition of the fluid from Krafla wells and geography (Ármannsson et al., 1987; Gíslason et al., 1978; Mortensen et al., 2009). These are Leirbotnar, Vítismór, Sudurhlíðar, and Hvíthólar (Figure 2). The Leirbotnar sub-field is divided into an upper and a lower reservoir zone. The upper reservoir to a depth of 1000-1400 m is liquid-dominated with a temperature of 190-220°C (Ármannsson, 2010). The zone below 1400 m depth has a temperature of about 300°C and boiling conditions occur below 2000 m where the temperature is 350°C. Well KS-01 has discharged in Sandabotnar, suggesting a two-phase fluid (boiling point curve) from a reservoir at about 260°C. Hvíthólar sub-field exhibits boiling characteristics down to 1000 m depth but is cooler and liquid-dominated below that depth (Ármannsson, 2010). In Sudurhlíðar (southern flanks of Mt. Krafla) and Vesturhlíðar (western flanks of Mt. Krafla) the boiling point curve is followed and a two-phase fluid of about 300°C is delivered. Similar characteristics were observed for the one well drilled in the Leirhnúkur area.

The geology of Krafla high-temperature geothermal system is dominated by basaltic lava, sub-glacially erupted hyaloclastites as well as intrusive bodies of basalt, dolerites and gabbro. Exploration drilling started in 1974 when a decision was made to build a 60 MWe power plant concurrent with drilling. Up to 2012, a total of 44 wells had been drilled in Krafla geothermal field. Re-injection is mainly done through well K-26 below 2000 m depth, but abandoned wells have also served temporarily for this purpose (Ágústsson et al., 2012).

Wells K-37 and K-38 (Figure 2) will be considered for this study for an injection test and formation temperature estimation as well as initial pressure; well K-18 will be used for the monitoring of pressure and temperature. Well K-38 is drilled in the western flanks (Vesturhlíðar) of mount Krafla which is a new site. Wells K-37 and KJ-18, on the other hand, are drilled into the southern flanks (Sudurhlíðar) of mount Krafla where there has been substantial production since 1980. A revised conceptual model developed by ISOR (Mortensen et al., 2009) showed that a pressure draw down of about 5 bar occurred in Leirbotnar sub-area after the expansion of the plant in the year 1999; on the southern flanks, where there has been substantial production since 1980, the pressure dropped significantly, probably about 20-30 bar.

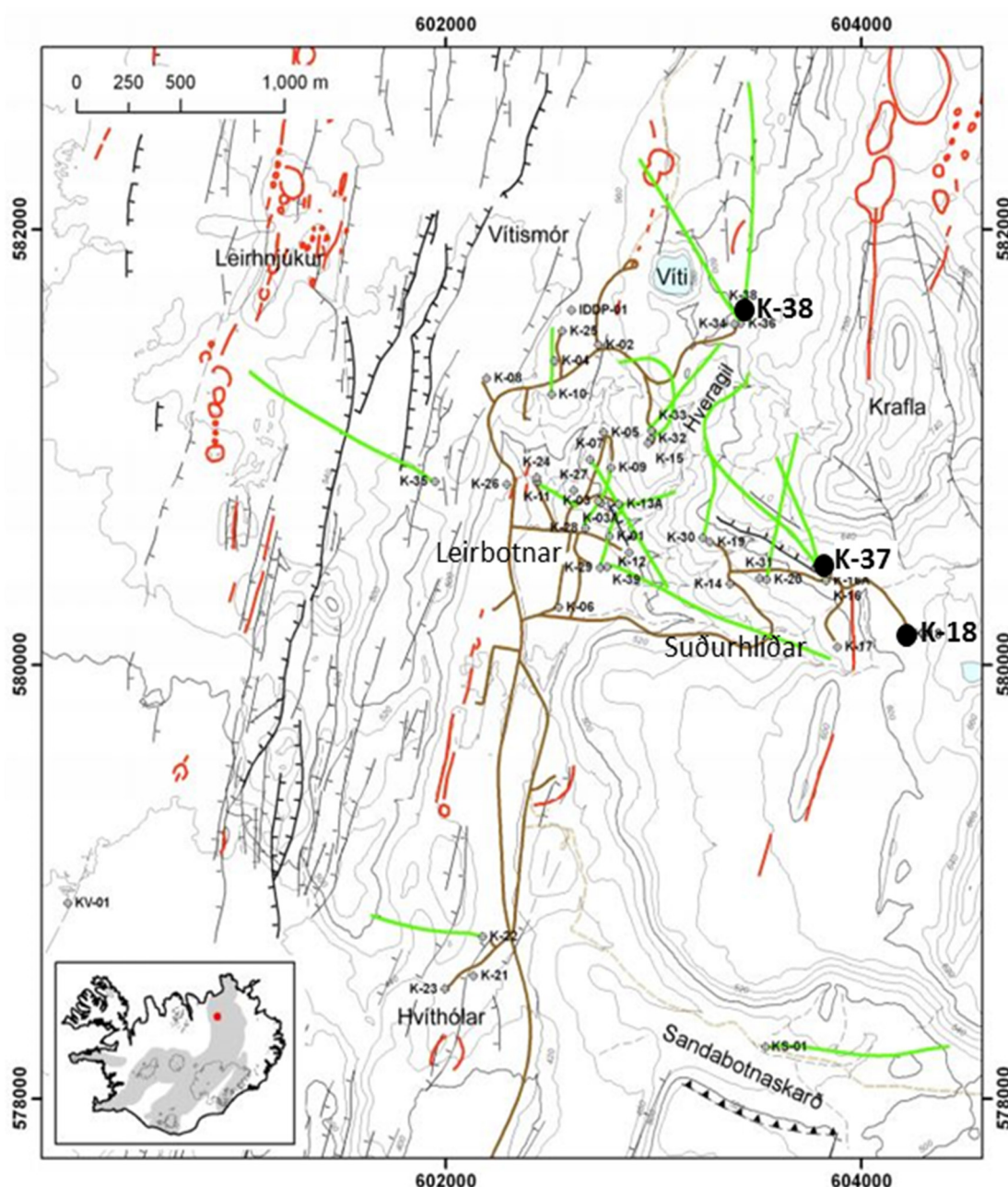


FIGURE 2: Map of Krafla geothermal field showing location of selected wells (modified from Mortensen et al., 2009)

3. INJECTION TEST

Injection tests in four wells were analysed by using ÍSOR WellTester software (Júlíusson et al., 2008) to estimate reservoir and well properties, two of them in the Nesjavellir geothermal field and two in the Krafla geothermal field. Injection tests are usually performed after drilling the production section of a well; the first parameter analysed is the injectivity index which gives an indication of how open the surroundings of the well are for flow, i.e. the change of pressure with change in the injection rate ($l/s/bar$).

In some cases the injection test is used for decision making and, in case of a too low injectivity index, drilling is continued in the hope of finding better feed zones at greater depth.

The following sections give a short theoretical background of injection well testing, followed by the summary of the well test results for wells NJ-15 and NJ-18 in Nesjavellir geothermal field, and wells K-37 and K-38, located in Krafla geothermal field.

3.1 Theoretical background

Well testing consists of producing from or injecting into a well at controlled rates and over periods of time and monitoring the response of the pressure in the same well and/or in adjacent observation wells. Well testing is performed in order to understand the conditions and flow capacity of a well and the parameters that characterise it and the reservoir. Parameters of interest include permeability, storativity, skin, wellbore storage, fracture properties, and the type of reservoir boundaries.

The pressure diffusion equation is used to calculate the pressure (p) in the reservoir after a given time (t) and at a certain distance (r) from an injection (or production) well receiving (or producing) fluid at a specific rate (Q). The following simplifying assumptions were made before the derivation of the equation:

- Horizontal radial flow;
- Darcy's Law applies;
- Homogeneous and isotropic reservoir and isothermal condition;
- Uniform thickness of reservoir (h);
- Single-phase flow and small pressure gradient;
- Constant permeability (k), porosity (ϕ), fluid viscosity (μ) and small and constant total compressibility (c); and
- The force of gravity is negligible.

The pressure diffusion equation is derived by combining the conservation of mass law, Darcy's law (conservation of momentum), and the equation of state of the fluid.

Law of conservation of mass

Consider the flow through a cylindrical shell of thickness, dr , situated at a distance, r , from the centre of the radial cylinder (Figure 3).

Then applying the principle of conservation of mass, mass flow in – mass flow out = rate of change of mass within the control volume:

$$-\rho Q + (\rho Q + \frac{\partial(\rho Q)}{\partial r} dr) = 2\pi r \frac{\partial(\phi \rho h)}{\partial t} dr \quad (1)$$

or

$$\frac{\partial(\rho Q)}{\partial r} = 2\pi r \frac{\partial(\phi \rho h)}{\partial t} \quad (2)$$

where, ρ = The density (kg/m^3);
 ϕ = The porosity (ratio $0 < \phi < 1$);
 Q = The volumetric flow rate (m^3/s);
 r = The radial distance (m) from the well;
 t = The time (s);
 h = The reservoir thickness (m).

Darcy's law or law of conservation of momentum

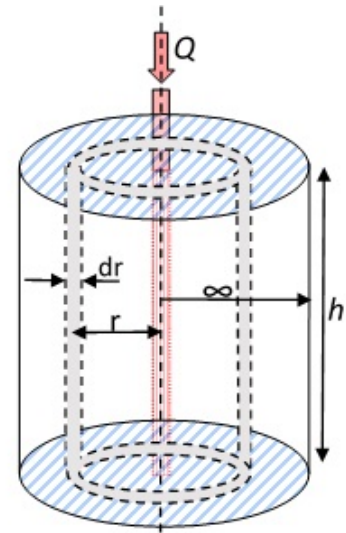


FIGURE 3: Radial flow through a cylindrical shell

Darcy's law in radial form is

$$Q = 2\pi r h \frac{k}{\mu} \frac{\partial p}{\partial r} \quad (3)$$

where, p = The pressure (Pa);
 μ = The dynamic viscosity (Pa·s); and
 k = The formation permeability (m²).

Equation of state of the fluid (fluid compressibility at constant temperature)

$$c_w = \frac{1}{\rho} \left(\frac{\partial \rho}{\partial p} \right) \quad (4)$$

where c_w = Fluid compressibility;
 ρ = The fluid density (kg/m³);
 p = The pressure (Pa).

By combining Equations 2, 3 and 4, we obtain the pressure diffusion equation given by

$$\begin{aligned} \frac{1}{r} \frac{\partial}{\partial r} \left(r \frac{\partial p(r, t)}{\partial r} \right) &= \frac{\mu c_t}{k} \frac{\partial p(r, t)}{\partial t} = \frac{S}{T} \frac{\partial p(r, t)}{\partial t} \\ \frac{\partial^2 p}{\partial r^2} + \frac{1}{r} \left(\frac{\partial p(r, t)}{\partial r} \right) &= \frac{\mu c_t}{k} \frac{\partial p(r, t)}{\partial t} = \frac{S}{T} \frac{\partial p(r, t)}{\partial t} \end{aligned} \quad (5)$$

where $c_r = \frac{1}{1-\phi} \frac{\partial \phi}{\partial p}$ = The rock compressibility (Pa⁻¹);
 $c_t = \phi c_w + (1-\phi) c_r$ = The total compressibility (Pa⁻¹);
 $S = c_t h$ = The storativity (m³/(Pa·m²) = m³/Pa = m³/N);
 $T = \frac{kh}{\mu}$ = The transmissivity (m³/(Pa·s)).

Equation 5 is the basic equation for well testing. Solutions for this equation can be obtained for different regimes depending on the initial and boundary conditions but that is beyond the scope of this project. The analysis of the injection test was done using WellTester software (Júlíusson et al., 2008) which was developed by the Iceland GeoSurvey (ISOR). The main parameters deduced from the WellTester simulation are explained in the manual for WellTester (Júlíusson et al., 2008) and follow below. Some of them are explained as well in the formulas above.

Transmissivity (T) describes the ability of the reservoir to transmit fluid, hence largely affecting the pressure gradient between the well and the reservoir. The higher the transmissivity, the easier it is for the fluid to flow through the rock matrix.

$$T = \frac{kh}{\mu} \quad \text{or} \quad T = \frac{kh\rho}{\nu} \quad (6)$$

where $\nu = \frac{\mu}{\rho}$ = The kinematic viscosity of the fluid (m²/s).

Storativity (S) is defined as the volume of fluid stored in the reservoir, per unit area, per unit increase in pressure (m³/(Pa·m²)). It depends on rock and fluid compressibility and phase change activity (Grant et al., 1982).

The injectivity index (II) is controlled by the injection flow rate and the change in stabilized reservoir pressure. It describes how the well is connected to the surrounding reservoir. Mathematically, the injectivity index (II) is represented as

$$II = \left| \frac{\Delta Q}{\Delta p} \right| \quad (7)$$

where ΔQ is the change in the injection flow and Δp is the change in the stabilized reservoir pressure ((l/s)/bar).

Wellbore storage coefficient (C) represents the volume of fluid that the wellbore itself will produce due to a unit drop of pressure (Grant and Bixley, 2011; Horne, 1995) (m^3/Pa). This mostly occurs due to fluid expansion or changing of the fluid level in the well. It is represented mathematically by:

$$C = \frac{\Delta V}{\Delta P} \quad (8)$$

where ΔV = The change in fluid volume in the well for the change in pressure ΔP .

Skin factor (s) is a dimensionless parameter (Van Everdingen and Hurst, 1953) and it characterizes the well condition: for a damaged well the permeability in the skin zone is less than reservoir permeability and $S > 0$, and for a stimulated one $S < 0$, meaning that the permeability of the skin zone is greater than the reservoir permeability.

Radius of investigation (r_e) is the approximate distance (m) at which the pressure response from the well becomes undetectable. Hence, this radius defines the area around the well being investigated, although the value of the parameter should be regarded more qualitatively. When boundary effects are seen in the data, the approximate distance from the centre of the well to the boundary will define the radius of investigation.

3.2 Testing of well NJ-15

An injection test of well NJ-15 was performed on 21/10/1995 where the pressure sensor was placed at 1590 m depth. Before the injection test started, injection was constant at 28.9 l/s of water. The injection test was conducted in four steps as shown in Table 1.

TABLE 1: Injection rate and pressure response

21/10/1995	Before starting	Step 1	Step 2	Step 3	Step 4
Time period	-	03:49-06:20	06:20-09:08	09:08-11:47	11:47-14:00
Duration (hr)	-	2:31	2:48	2:39	2:13
Injection (l/s)	28.9	18.9	29.3	40.6	0
Change in injection $ \Delta Q $		10	10.4	11.3	40.6
Pressure at the end of step (bar-g)	137.3	132.4	136.4	139.7	123.6
Change in pressure $ \Delta p $		5	4	3.3	16

Initial parameters that were used to describe the reservoir and well dimensions in this analysis are estimated reservoir temperature 280°C, wellbore radius 0.12 m, and estimated reservoir pressure of 135 bar which was deduced by WellTester software. Two types of models were considered for the reservoir, on one hand a homogeneous reservoir and on the other hand a dual porosity reservoir. The best fit between the model and the data was obtained for a homogenous reservoir, constant pressure boundary, constant skin and wellbore storage.

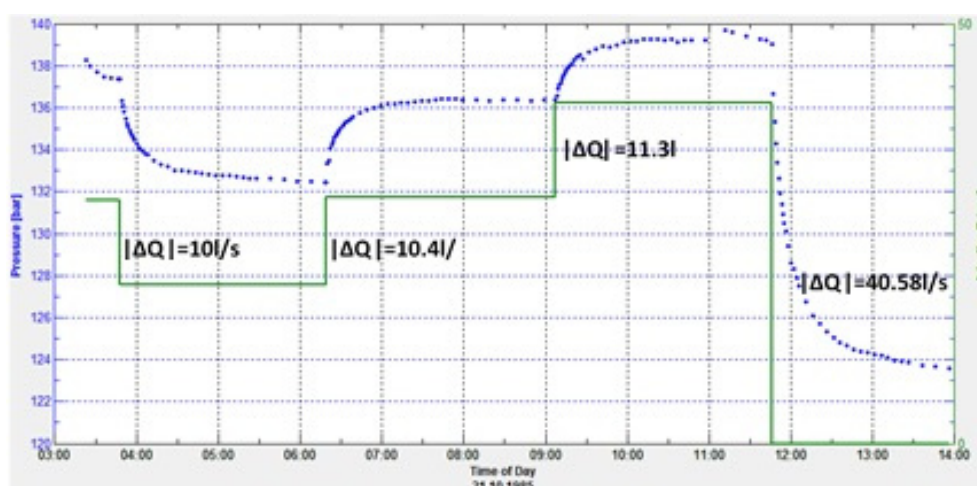


FIGURE 4: Step rate injection and pressure response for Well NJ-15

A non-linear regression analysis was performed to find the parameters of the model that best fit the data. The model fit with the data was best for step 1. Figure 4 shows the pressure response against time for various steps of injection as well as the change in injection for each step. In the following section the results from the interpretations of step one are shown in Figures 5, 6, and 7 and Table 2.

Figure 5 shows on a linear scale how the chosen model fits the data. Figure 6 shows the pressure measured for the step on a linear scale using a logarithmic timescale. Figure 7 shows the pressure change on a logarithmic scale, also using a logarithmic timescale, together with the derivative of the pressure response multiplied by the time passed since the beginning of the step. Table 2 shows the injectivity index and the reservoir parameters estimated by using the selected model. The skin factor is negative, as is usual in Iceland, which means that the well was enhanced and not damaged during drilling.

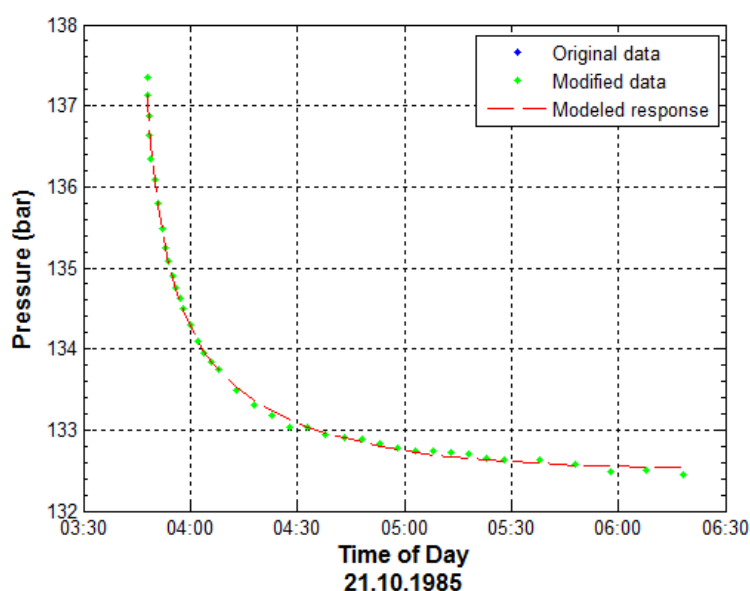


FIGURE 5: Pressure against time for model results and collected data for step 1

TABLE 2: Results from non-linear regression parameter estimate using injection data from well NJ-15

Reservoir parameters	1. step	2. step	3. step	4. step	Best estimate (Step 1)	Units
Transmissivity (T)	$1.3 \cdot 10^{-8}$	$1.4 \cdot 10^{-8}$	$2.5 \cdot 10^{-8}$	$1.2 \cdot 10^{-8}$	$1.3 \cdot 10^{-8}$	$\text{m}^3/(\text{Pa} \cdot \text{s})$
Storativity (S)	$6.4 \cdot 10^{-8}$	$2.3 \cdot 10^{-8}$	$2 \cdot 10^{-8}$	$2 \cdot 10^{-8}$	$6.4 \cdot 10^{-8}$	$\text{m}^3/(\text{Pa} \cdot \text{m}^2)$
Radius of investing. (r_e)	46	67	85	68	46	m
Skin factor (s)	-2.2	-3	-2.5	-3.5	-2.2	-
Wellbore storage (C)	$8.4 \cdot 10^{-6}$	$6.7 \cdot 10^{-6}$	$2.2 \cdot 10^{-5}$	$8 \cdot 10^{-6}$	$8.4 \cdot 10^{-6}$	$\text{m}^3/(\text{Pa})$
Permeability (k)	$4 \cdot 10^{-15}$	$1.3 \cdot 10^{-14}$	$2.7 \cdot 10^{-14}$	$1.3 \cdot 10^{-14}$	$4 \cdot 10^{-15}$	m^2
Reservoir thickness	296	106	92	91	296	m
Injectivity index (II)	2	2.6	3.4	2.6	2	(l/s)/bar

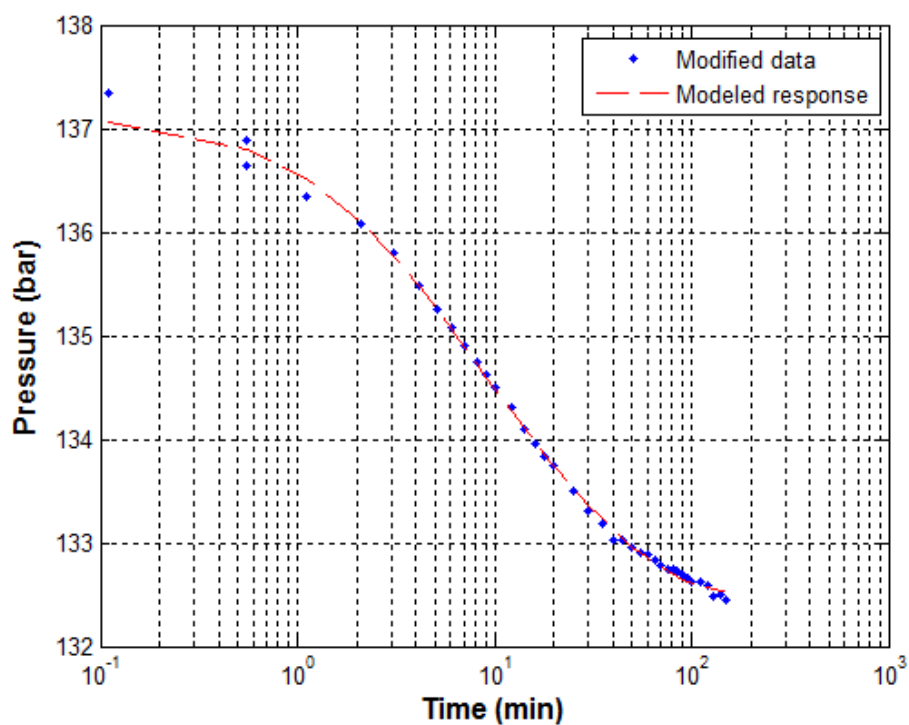


FIGURE 6: Pressure against time for model results and collected data for step 1 using logarithmic time scale

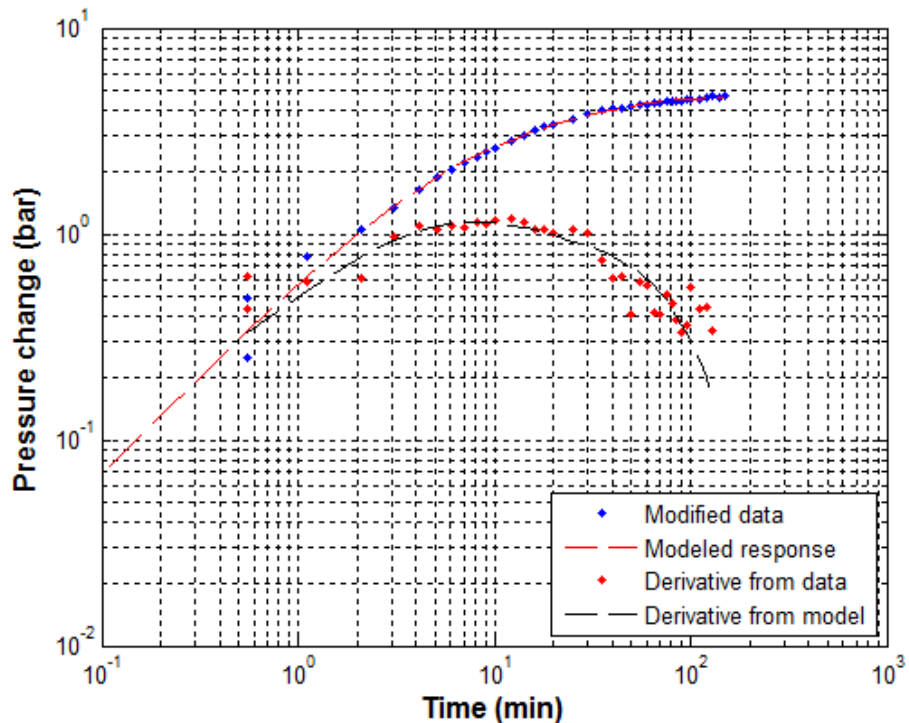


FIGURE 7: Pressure and its derivative against time for model results and collected data for step 1 on a log-log scale (see text)

3.3 Testing of well NJ-18

An injection test was performed in this well on 15/10/1986. The pressure sensor was stationed at 1710 m depth which was assumed to be the depth of the main feed zone. Before the injection test started, injection was constant at 24.2 l/s of water. The injection test was conducted in three steps as shown in Table 3.

TABLE 3: Injection rate and pressure response

15/10/1986	Before starting	Step 1	Step 2	Step 3
Time period	-	08:21-11:43	11:43-14:45	14:45-17:18
Duration (hr)	-	3:22	3:02	2:27
Injection (l/s)	24.2	36.7	24.2	0
Change in injection $ \Delta Q $		12.5	12.5	24.2
Pressure at the end of step (bar-g)	157.3	162.3	155.5	144
Change in pressure $ \Delta p $		5	6.8	11.6

To find the parameters of the model that best fit the data, a non-linear regression analysis was performed by using WellTester. The following initial parameters were taken to describe the reservoir: estimated reservoir temperature 280°C, wellbore radius 0.12 m and an estimated reservoir pressure of 135 bar, deduced from WellTester software. Homogenous reservoir, constant pressure boundary, constant skin and wellbore storage were selected for the reservoir model. Figure 8 illustrates the pressure response against time for various flow rates as well as the change in injection for each step. Figure 9 shows on a linear scale how the chosen model fits the data in step 3. Figure 10 shows the pressure measured for the step on a linear scale using a logarithmic timescale. Figure 11 shows the pressure change on a logarithmic scale, also using a logarithmic timescale, together with the derivative of the pressure response multiplied by the time passed since the beginning of the step. Table 4 shows the reservoir parameters estimated by using the selected model in WellTester. The results of the simulations for step 3 showed to be the best of the simulations.

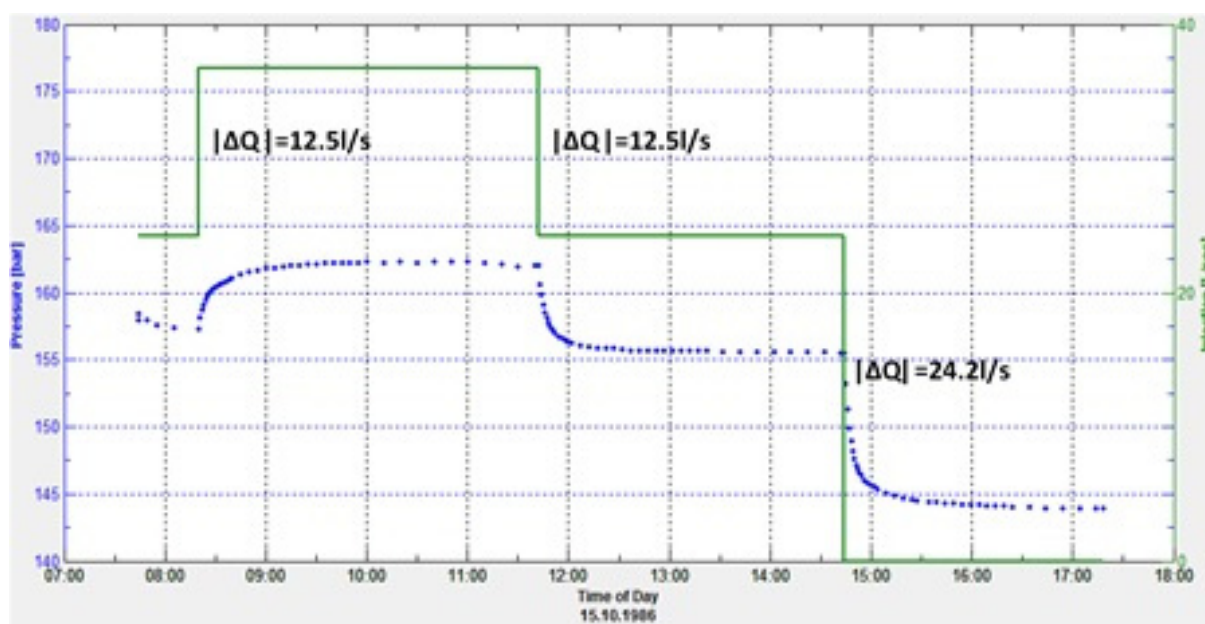


FIGURE 8: Step rate injection and pressure response for Well NJ-18

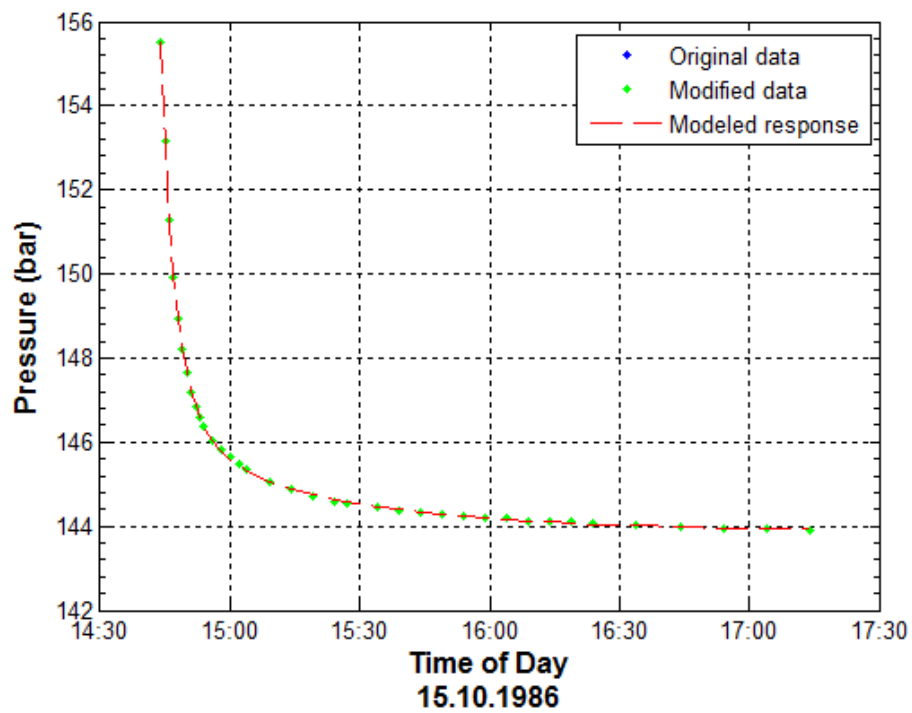


FIGURE 9: Pressure against time for model results and collected data for step 3

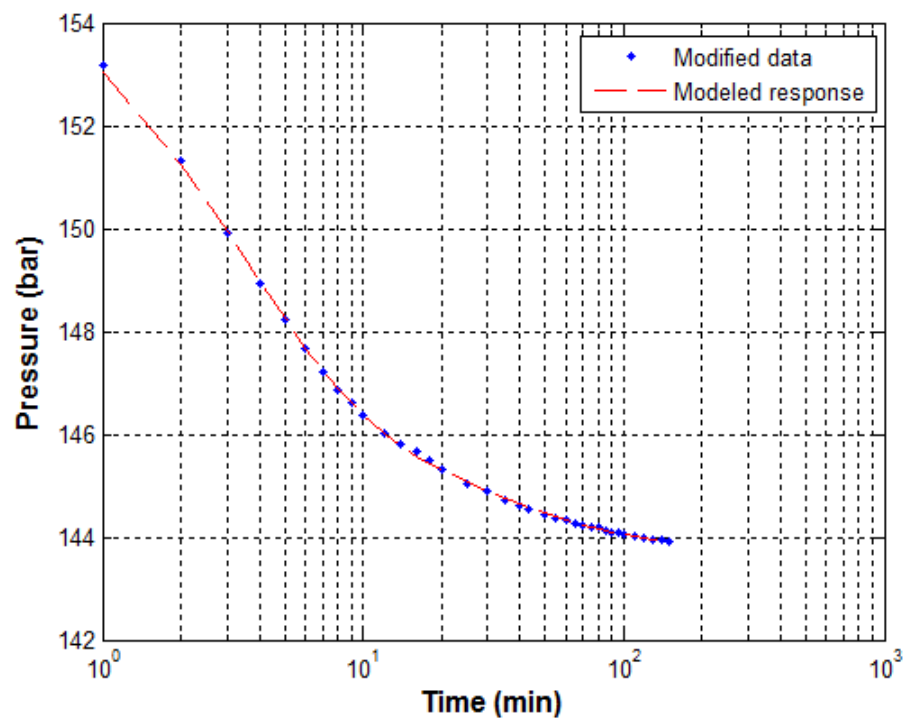


FIGURE 10: Pressure against time for model results and collected data for step 3, using a logarithmic time scale

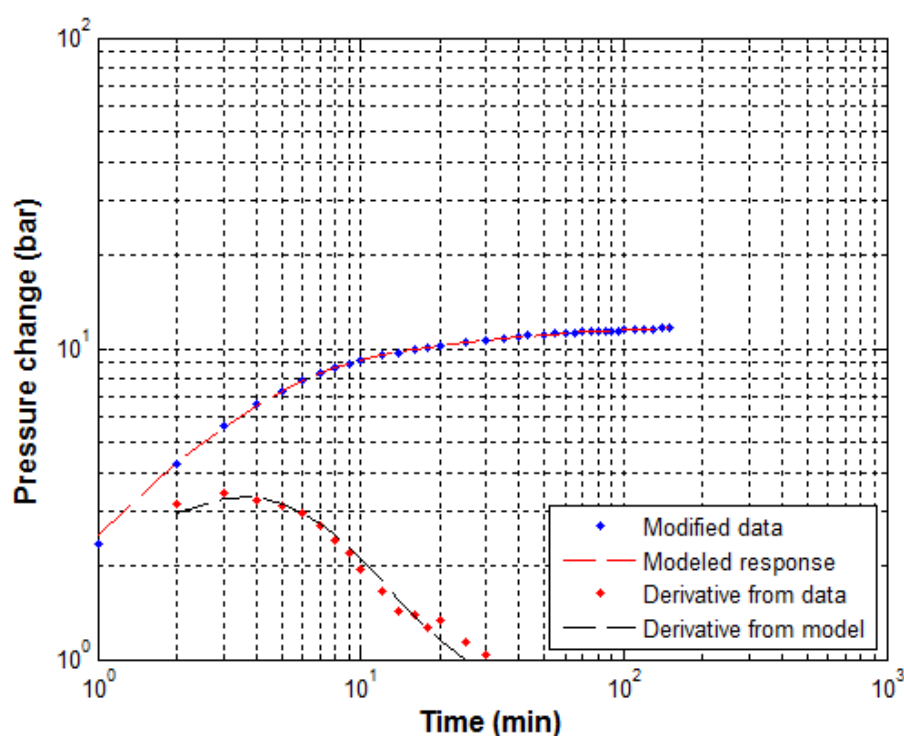


FIGURE 11: Pressure and its derivative against time for model results and collected data for step 3 on a log-log scale (see text)

TABLE 4: Results from non-linear regression parameter estimate using injection data from well NJ-18

Reservoir parameters	1. step	2. step	3. step	Best estimate (Step 3)	Unit
Transmissivity (T)	$1.1 \cdot 10^{-8}$	$1.7 \cdot 10^{-8}$	$2.8 \cdot 10^{-8}$	$2.8 \cdot 10^{-8}$	$\text{m}^3/(\text{Pa} \cdot \text{s})$
Storativity (S)	$7 \cdot 10^{-8}$	$4.6 \cdot 10^{-8}$	$1.3 \cdot 10^{-8}$	$1.3 \cdot 10^{-8}$	$\text{m}^3/(\text{Pa} \cdot \text{m}^2)$
Radius of investigation (r_e)	34	45	174	174	m
Skin factor (s)	-3.	-0.3	1.3	1.3	-
Wellbore storage (C)	$4.6 \cdot 10^{-6}$	$4.5 \cdot 10^{-6}$	$4.8 \cdot 10^{-6}$	$4.8 \cdot 10^{-6}$	$\text{m}^3/(\text{Pa})$
Permeability (k)	$3.1 \cdot 10^{-15}$	$7.6 \cdot 10^{-15}$	$4.6 \cdot 10^{-14}$	$4.6 \cdot 10^{-14}$	m^2
Reservoir thickness (h)	329	220	60	60	(m)
Injectivity index	2.5	2	2.1	2.1	(l/s)/bar

The values of transmissivity and storativity for NJ-18 are within the same range of magnitude as the value obtained from well NJ-15, and these values are within the range which is generally expected in Iceland.

3.4 Testing of well K-37

Well K-37 in Krafla is a directional well which was drilled from 04.10.2007 to 18.01.2008 to a total depth of 2187 m. An injection test of the well was performed at the end of drilling on 18.1.2008. The pressure sensor was positioned at 1420 m depth which was assumed to be the main feed zone. Before the injection test started, injection was constant at 20 l/s of water. The injection test was conducted in three steps as shown in Table 5.

TABLE 5: Injection rate and pressure response

18.01.2008	Before starting	Step 1	Step 2	Step 3
Time period	-	14:17 - 17:18	17:18 - 20:18	20:18 - 23:18
Duration (hr)	-	3:01	3:00	3:00
Injection (l/s)	20	35	50	20
Change in injection $ \Delta Q $	-	15	15	30
Pressure at the end of step (bar-g)	80	84	88	80.0
Change in pressure $ \Delta p $	-	4	4	8

Initial parameters that were used to describe the reservoir in this analysis are estimated reservoir temperature 320°C, wellbore radius 0.18 m, and an estimated reservoir pressure of 80 bar which was found by WellTester. Two types of models were considered for the reservoir: on one hand a homogeneous reservoir and, on the other hand, a dual porosity reservoir. A non-linear regression analysis was done to find the parameters of the model that best fits the data. The model best fitted the data in step 3, and the best results were obtained for a homogenous reservoir, constant pressure boundary, constant skin and wellbore storage.

Figure 12 shows the steps of the injection and the pressure response against time as well as the change in injection for each step during the test. Figure 13 illustrates on a linear scale how the chosen model fits the data for step 3. Figure 14 shows the pressure measured for the step on a linear scale using a logarithmic timescale. Figure 15 shows the pressure change on a logarithmic scale, also using a logarithmic timescale, together with the derivative of the pressure response multiplied by the time passed since the beginning of the step. Table 6 shows the reservoir parameters estimated by using the selected model.

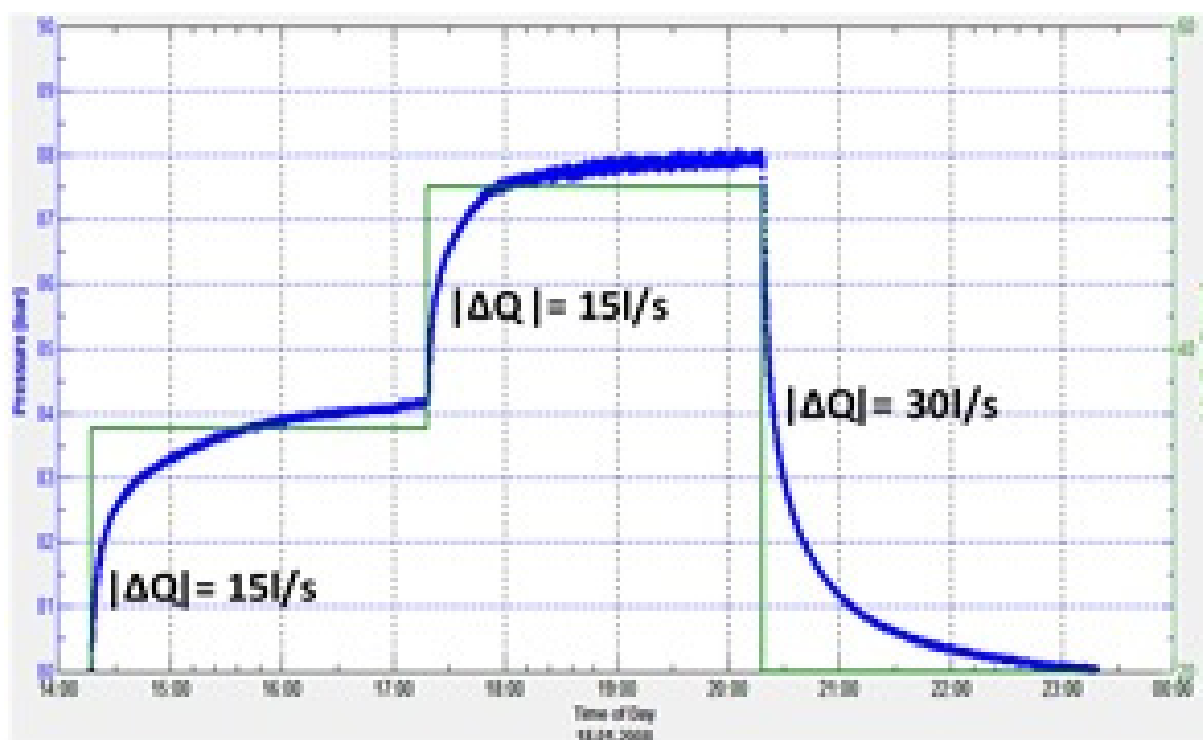


FIGURE 12: Step rate injection and pressure response for Well K-37

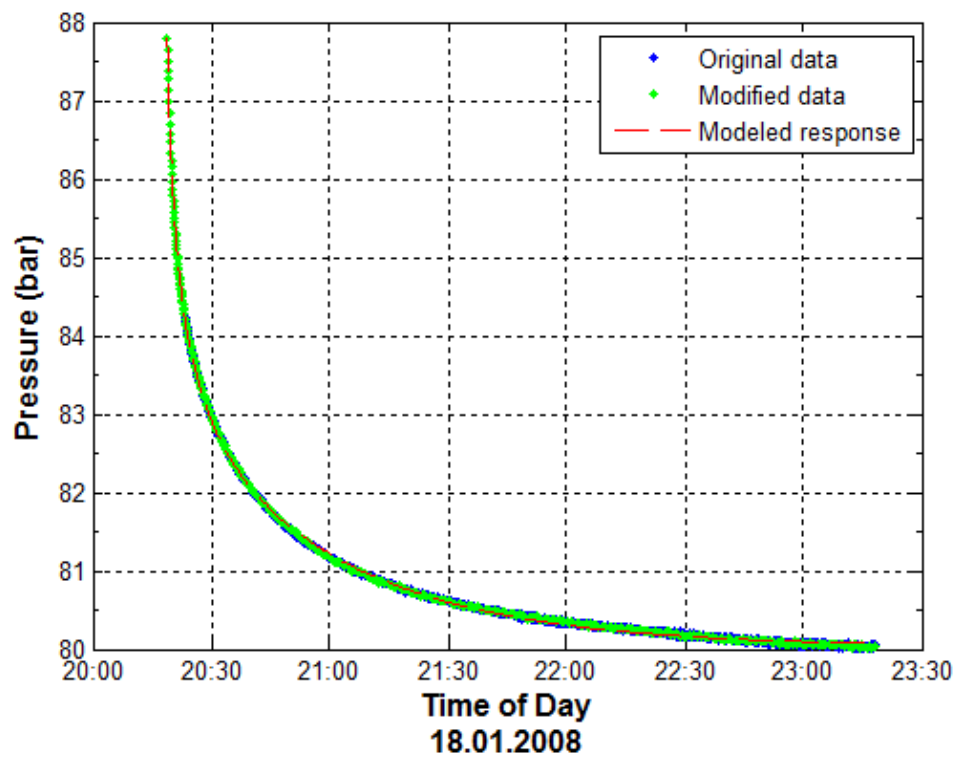


FIGURE 13: Pressure against time for model results and collected data for step 3

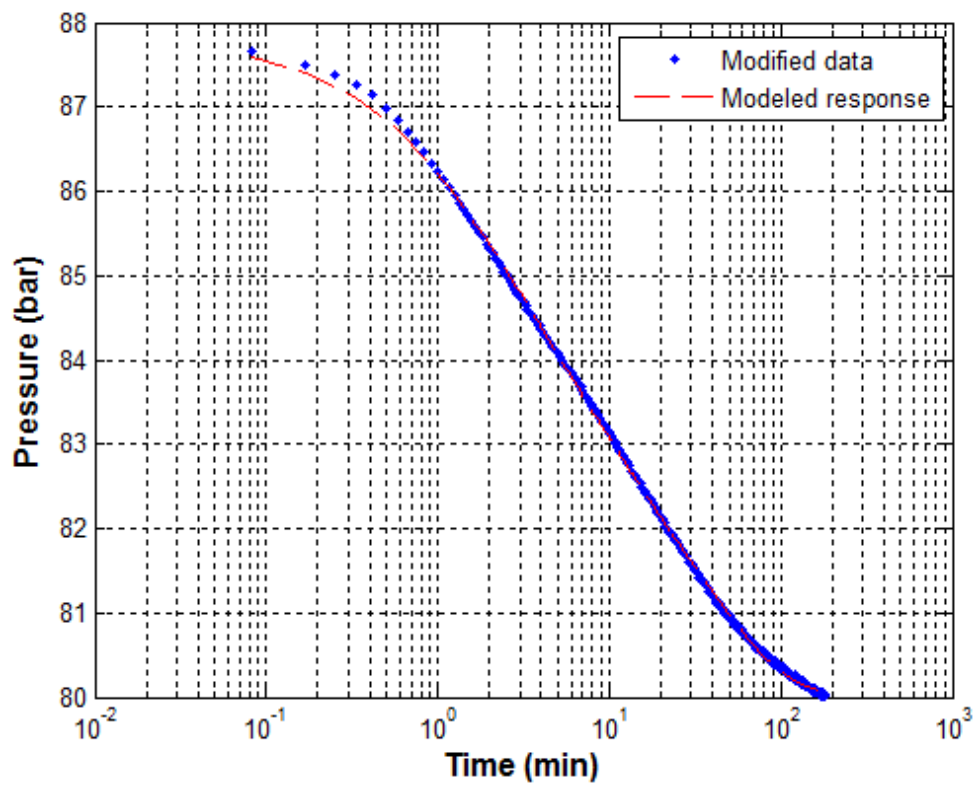


FIGURE 14: Pressure against time for model results and collected data for step 3, using a logarithmic time scale

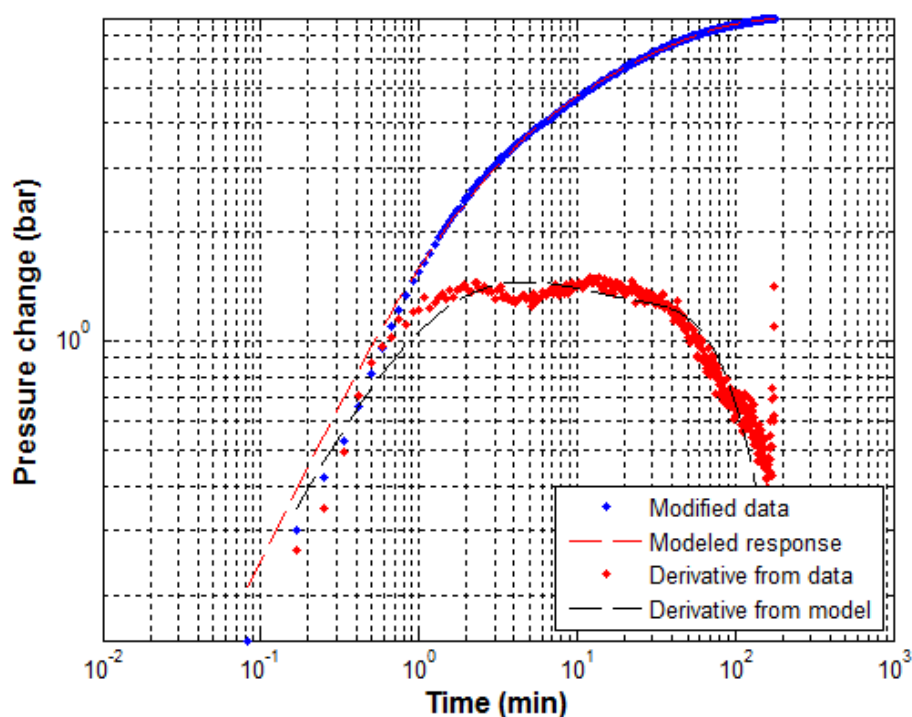


FIGURE 15: Pressure and its derivative against time for model results and collected data for step 3 on a log-log scale (see text)

TABLE 6: Results from non-linear regression parameter estimate using injection data from well K-37

Reservoir parameters	1. step	2. step	3. step	Best estimate (Step 3)	Units
Transmissivity (T)	$2.2 \cdot 10^{-8}$	$2.3 \cdot 10^{-8}$	$2.1 \cdot 10^{-8}$	$2.1 \cdot 10^{-8}$	$\text{m}^3/(\text{P} \cdot \text{s})$
Storativity (S)	$6.6 \cdot 10^{-8}$	$6.2 \cdot 10^{-8}$	$7.7 \cdot 10^{-8}$	$7.7 \cdot 10^{-8}$	$\text{m}^3/(\text{Pa} \cdot \text{m}^2)$
Radius of investigation (r_e)	287	60	61	61	m
Skin factor (s)	-2.4	-2.3	-2.5	-2.5	-
Wellbore storage (C)	$9.3 \cdot 10^{-6}$	$1.1 \cdot 10^{-5}$	$6 \cdot 10^{-6}$	$6 \cdot 10^{-6}$	$\text{m}^3/(\text{Pa})$
Permeability (k)	$1.36 \cdot 10^{-13}$	$1.3 \cdot 10^{-13}$	$1.3 \cdot 10^{-13}$	$1.3 \cdot 10^{-13}$	m^2
Injectivity index	3.6	4	3.9	3.9	(l/s)/bar

3.5 Testing of well K-38

Well K-38 is a directional well which was drilled from 26.04.2008 to 20.07.2008 to a total measured depth of 2693 m. An injection test was performed on 20/07/2008. The injection rate was constant, 45 l/s, before the injection test started. The injection was conducted in three steps, as illustrated in Table 7 and in Figure 16.

TABLE 7: Injection rate and pressure response

20/07/2008	Before starting	Step 1	Step 2	Step 3
Time period	-	02:59 - 05:58	05:58 - 10:30	10:30 - 13:35
Duration (hr)	-	3	4.5	3
Injection (l/s)	45	25	35	45
Change in injection $ \Delta Q $ (l/s)	-	20	10	10
Pressure at the end of step (bar-g)	117	109	113	116
Change in pressure $ \Delta p $ (bar-g)	-	8	4	3

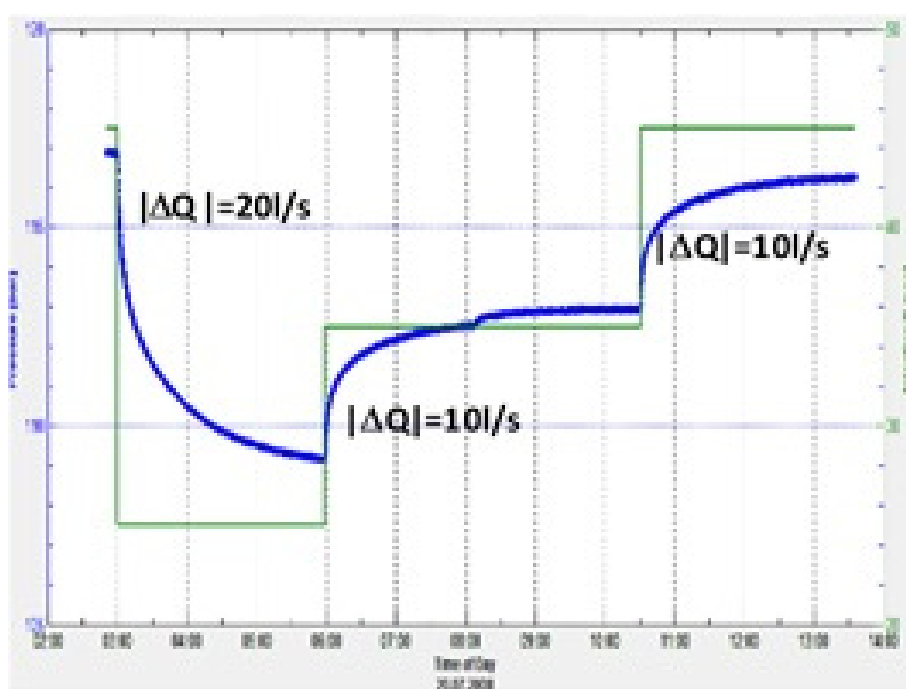


FIGURE 16: Step rate injection and pressure response for Well K-38

A non-linear regression analysis was done to find the parameters of the model that best fit the data. Initial parameters that were used to describe the reservoir in this analysis are estimated reservoir temperature 320°C, wellbore radius 0.18 m, and an estimated reservoir pressure 113 bar was found by WellTester. Two types of models were considered for the reservoir, on one hand a homogeneous reservoir and on the other hand a dual porosity reservoir. The best fit between the model and the data was obtained for a homogenous reservoir, constant pressure boundary, constant skin and wellbore storage.

Pressure change during step rate injection in K-38 as well as the change in injection for each step are illustrated in Figure 16. Figure 17 shows on a linear scale how the chosen model fits the data in step 3 and Figure 18 shows the pressure on a linear scale using a logarithmic timescale. Figure 19 shows the pressure change on a logarithmic scale, also using a logarithmic timescale, together with the derivative of the pressure response multiplied by the time passed since the beginning of the step.

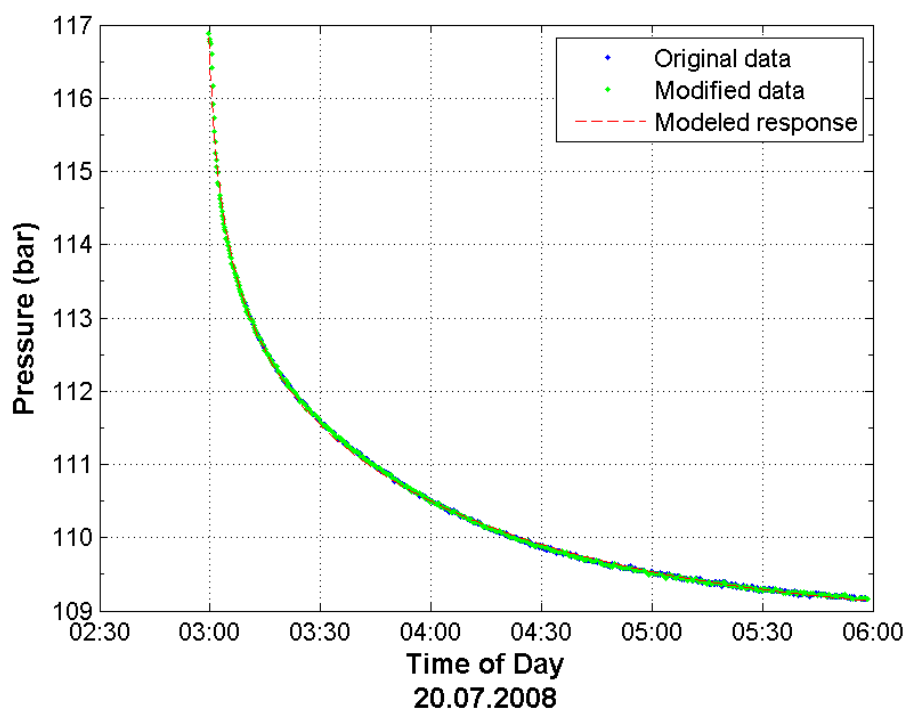


FIGURE 17: Pressure against time for model results and collected data for step 3

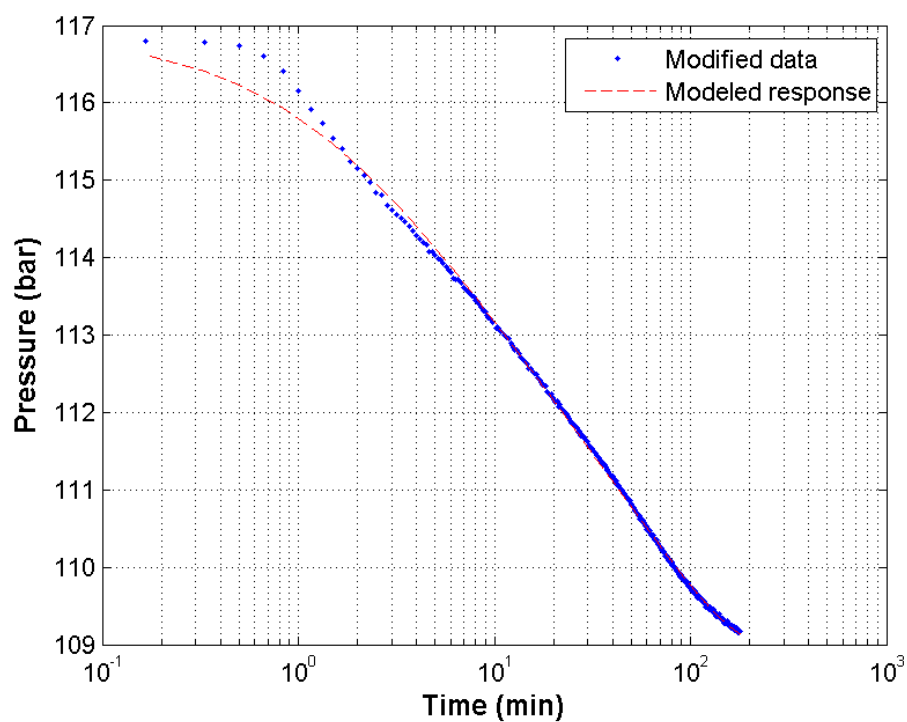


FIGURE 18: Pressure against time for model results and collected data for step 3, using a logarithmic time scale

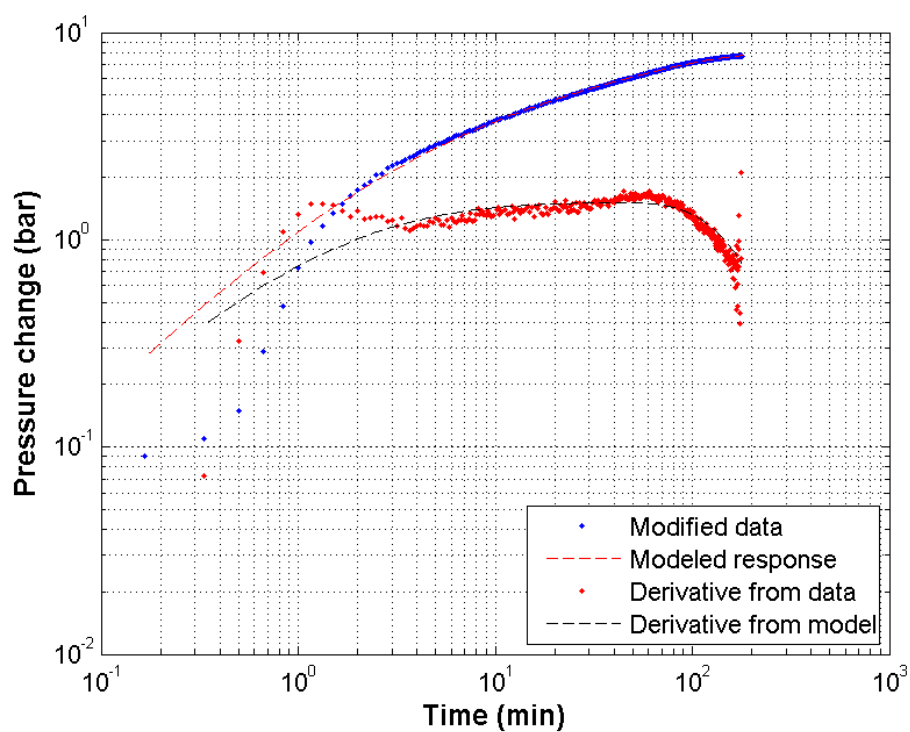


FIGURE 19: Pressure and its derivative against time for model results and collected data for step 3 on a log-log scale

Table 8 shows the reservoir parameters estimated by using the selected model.

TABLE 8: Results from non-linear regression parameter estimate using injection data from well K-38

Reservoir parameters	1. step	2. step	3. step	Best estimate	Units
Transmissivity (T)	$1.2 \cdot 10^{-8}$	$1.4 \cdot 10^{-8}$	$1.5 \cdot 10^{-8}$	$1.5 \cdot 10^{-8}$	$\text{m}^3/(\text{Pa} \cdot \text{s})$
Storativity (S)	$5.5 \cdot 10^{-7}$	$4.6 \cdot 10^{-7}$	$4.6 \cdot 10^{-7}$	$4.6 \cdot 10^{-7}$	$\text{m}^3/(\text{Pa} \cdot \text{m}^2)$
Radius of investigation (r_e)	71	83	26	26	M
Skin factor (s)	-1.9	-1.7	-1.8	-1.8	-
Wellbore storage (C)	$6.6 \cdot 10^{-6}$	$5 \cdot 10^{-6}$	$4.4 \cdot 10^{-6}$	$4.4 \cdot 10^{-6}$	$\text{m}^3/(\text{Pa})$
Permeability (k)	$1.1 \cdot 10^{-10}$	$1.4 \cdot 10^{-10}$	$1.6 \cdot 10^{-10}$	$1.6 \cdot 10^{-10}$	m^2
Injectivity index	2.6	2.7	3	3	$(\text{l/s})/\text{bar}$

The injectivity index for well K-38 is lower than for well K-37, showing a lower permeability in this part of the reservoir. This could mean that well K-37 intersects more permeable structures than well K-38. This could also be partly due to the higher negative values of skin factor for well K-37.

3.6 Summary of injection test results

Table 9 summarises the results obtained by well test analysis of injection tests in four wells, two at Nesjavellir and two at Krafla. Transmissivity estimated for selected wells in Nesjavellir is of the same order of magnitude as that of the wells in Krafla, i.e. $10^{-8} \text{ m}^3/(\text{Pa} \cdot \text{s})$, which is common in geothermal reservoirs in Iceland according to the report from WellTester with results and descriptions of the resulting parameters (Júlíusson et al., 2008). The storativity for Krafla was higher than that of Nesjavellir for the selected wells which is also according to the report from WellTester, which says: “Common values for liquid-dominated geothermal reservoirs are around $10^{-8} [\text{m}^3/(\text{Pa} \cdot \text{m}^2)]$ while two-phase reservoirs might have values on the order of $10^{-5} [\text{m}^3/(\text{Pa} \cdot \text{m}^2)]$. Some of the wells in Krafla have a steam cap, including the two wells analysed, which shows a two-phase reservoir, but the selected wells in Nesjavellir are at the boundary of the reservoir and are liquid-dominated. Skin factor for the selected wells for both fields was negative as it usually is in Iceland. Permeability for wells in Krafla was higher than in the selected wells in Nesjavellir.

TABLE 9: Summary of the results of well test analysis for Krafla and Nesjavellir geothermal fields

Reservoir parameters	NJ-15	NJ-18	K-37	K-38	Unit
Transmissivity (T)	$1.3 \cdot 10^{-8}$	$2.8 \cdot 10^{-8}$	$2.1 \cdot 10^{-8}$	$1.5 \cdot 10^{-8}$	$\text{m}^3/(\text{Pa} \cdot \text{s})$
Storativity (S)	$6.4 \cdot 10^{-8}$	$1.3 \cdot 10^{-8}$	$7.7 \cdot 10^{-8}$	$4.6 \cdot 10^{-7}$	$\text{m}^3/(\text{Pa} \cdot \text{m}^2)$
Radius of investigation (r_e)	46	174	61.0	26	m
Skin factor (s)	-2.2	-1.3	-2.5	-1.8	-
Wellbore storage (C)	$8.4 \cdot 10^{-6}$	$4.8 \cdot 10^{-6}$	$6 \cdot 10^{-6}$	$4.4 \cdot 10^{-6}$	$\text{m}^3/(\text{Pa})$
Permeability (k)	$4 \cdot 10^{-15}$	$4.6 \cdot 10^{-14}$	$1.3 \cdot 10^{-13}$	$1.6 \cdot 10^{-10}$	m^2
Injectivity Index	2.7	2.2	3.8	2.8	$((\text{l/s})/\text{bar})$

4. TEMPERATURE AND PRESSURE PROFILES ANALYSIS

An analysis of temperature and pressure profiles was performed in four wells, two at Nesjavellir (NJ-15 and NJ-18) and two at Krafla (K-37 and K-38). The purpose of the analysis was to estimate the undisturbed conditions of the reservoir before drilling, i.e. formation temperature and initial pressure conditions. Berghiti and PREDYP programs included in the ISOR software package ICEBOX (Arason et al., 2004), were used to estimate the formation temperature and initial pressure, respectively. The software BOILCURV (Arason et al., 2004), also from the ICEBOX package, was used to estimate boiling conditions in the well. The following section outlines the theory related to the estimation of the

formation temperature, initial pressure and the boiling depth curve. After that, interpretation of the analysis of downhole temperature and pressure profiles for the selected wells is presented.

4.1 Formation temperature, initial pressure and boiling depth curve

4.1.1 Formation temperature

Knowledge of the formation temperature is important in the development and exploitation of geothermal reservoirs and especially in the estimation of reservoir potential. During drilling operations, the well and the close surroundings are cooled down by drilling fluid circulation and cold water injection. After drilling, the well is usually allowed to recover in temperature (warm up) from the cooling. The principal reservoir engineering research conducted during this period is repeated temperature and pressure logging. The temperature data thus collected is used to estimate the undisturbed system temperature, often called the formation temperature, as wells usually do not recover completely during the recovery period. Different methods can be used for this estimation, but the method most often applied is the so-called Horner method (Grant and Bixley, 2011).

The Horner method is a simple analytical technique for analysing recovery temperature to determine the formation temperature. In this method, the temperature recovery data is plotted against the logarithm of dimensionless Horner time, $\frac{(t_p + \Delta t)}{\Delta t}$, where t_p is the time at which circulation was stopped and Δt is the time passed since circulation stopped. A straight line is fitted to the data points, which is extrapolated to infinite Δt , i.e. when the Horner time becomes 1. The extrapolated temperature corresponding to this point is taken as the true reservoir temperature (Helgason, 1993). Figure 20 presents an example of a fit of the semi-log straight line relationship at 800 m for well NJ-15. The method is not applicable for all cases or at all depths in a well, for example not at depths where cross flow screens the actual temperature conditions.

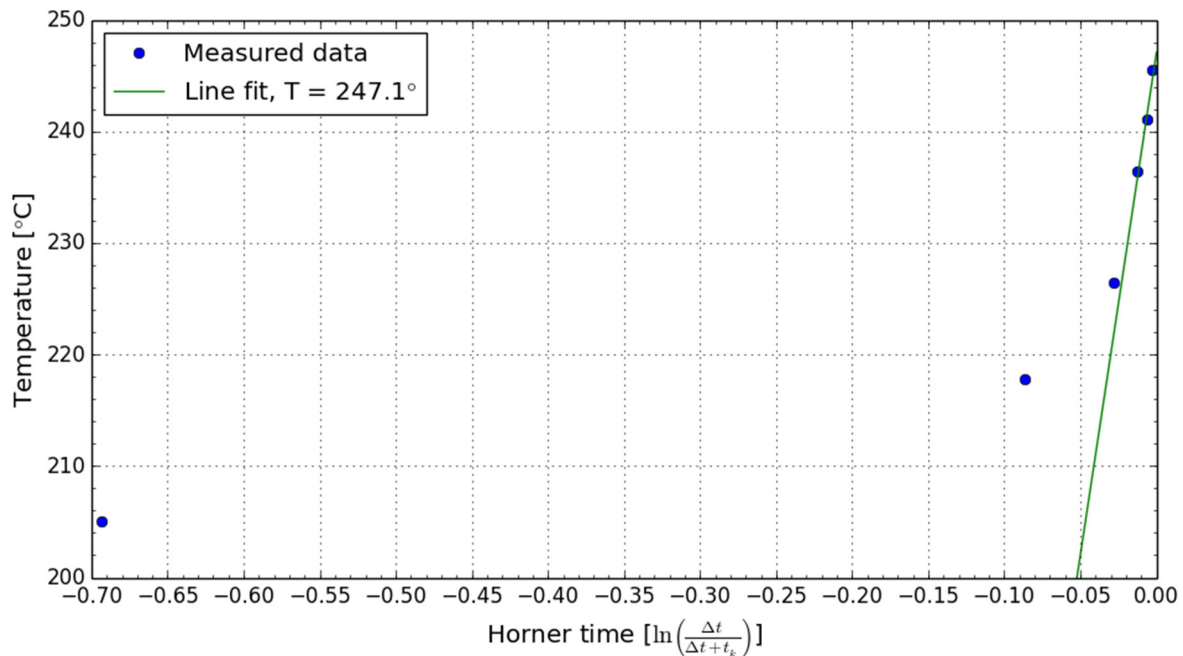


FIGURE 20: Formation temperature at 800 m in Well NJ-15

4.1.2 Boiling depth curve and initial pressure

Boiling curve with depth is described by the following integral (Arason et al., 2004):

$$p(z) = p_0 + g \int_{z_0}^z \rho_{sat}(p(z)) dz \quad (9)$$

where ρ_{sat} is a function of $p(z)$, which is the pressure at any depth z , p_0 is the pressure at some initial elevation z_0 , g is the acceleration of gravity and $\rho_{sat}(p(z))$ is the fluid density in a column of single-phase water at saturation pressure.

This formula is also used for PREDYP but in this case $\rho_{sat}(p(z))$ is replaced by $\rho(T(z))$, where $T(z)$ is the formation temperature with depth.

Equation 9 is non-linear and is solved numerically with the following formula:

$$p(z) = p_0 + g \sum_{i=1}^n \rho_{mean} \Delta z \quad (10)$$

where

$$\rho_{mean} = \frac{[\rho_{i-1}(p_{i-1}) + \rho_i(p_i)]}{2} \quad (11)$$

The total length z has been divided into n segments of length Δz and ρ_{mean} is the average density between the two depths z and Δz .

The problem is now to find the pressure and, hence, the saturation density $\rho_i(p_i)$ at our new depth $z + \Delta z$. This is done by using the Newton-Raphson iteration in the program BOILCURV. PREDYP program is used to calculate the initial pressure. The program calculates pressure in a static water column, if the temperature of the column is known (Arason and Björnsson, 1994). Both PREDYP and ICEBOX programs are found in the ICEBOX package.

4.2 Interpretation of temperature and pressure profiles for well NJ-15

Well NJ-15 is located in the eastern part of Nesjavellir geothermal field. It is a vertical well that was drilled in autumn 1985 to a total depth of 1748 m. Well NJ-15 was connected to the steam supply system from October 1998 until July 1999. Since then, well NJ-15 has been closed and is currently used for temperature and pressure monitoring. In the following section, temperature data which were collected during the warming up period were used to estimate formation temperature (Figure 21).

The temperature profiles in Figure 21 show a high gradient and linear profile, from 300 to 800 m, indicating a conductive zone. From 800 to 1300 m, there is a much lower gradient which could be due to a convective system and in this section the temperature is slightly less than a boiling condition but follows the boiling curve. Below 1300 m, there is an inversion in temperature down to 1500 m and an increase in temperature down to 1700 m. This inversion in temperature could be explained by a cold inflow at 1300 m.

The pressure profiles obtained during the warm up period and the initial pressure profile are shown in Figure 22. The pressure pivot point is located at around 1600 m and the pressure is 120 bar at that point.

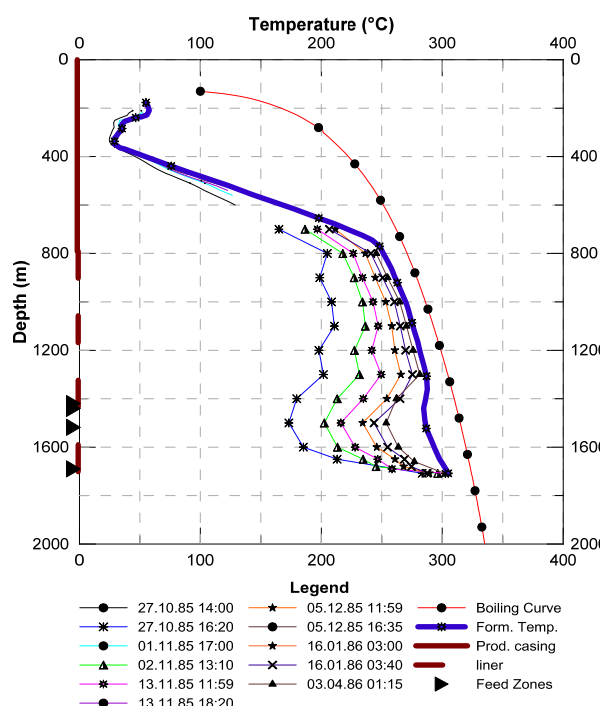


FIGURE 21: Temperature profiles for well NJ-15

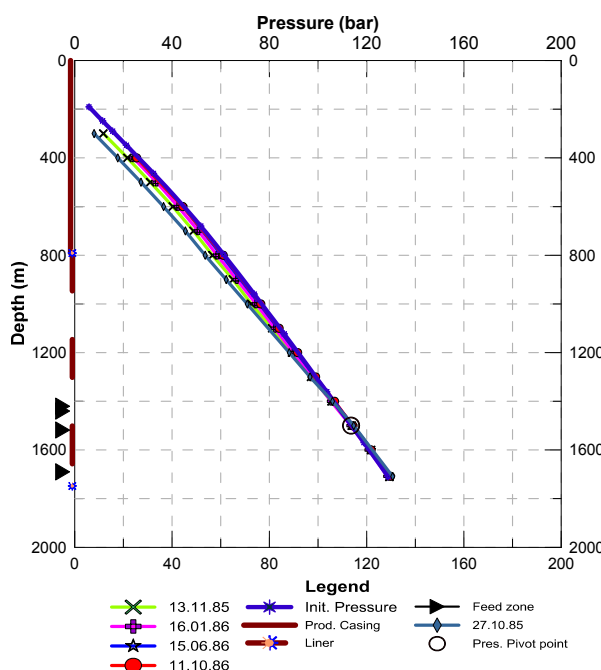


FIGURE 22: Pressure profiles for well NJ-15

To calculate the initial pressure, the estimated formation temperature profile from Figure 21 was substituted in the PREDYP program. The water level was adjusted in the calculations until the calculated profile matched the pivot point pressure. The pressure match was achieved with water levels at 203 m.

4.3 Interpretation of temperature and pressure profiles for well NJ-18

Well NJ-18 was drilled in 1986. It was not a productive well and was never connected to the steam supply system. It is currently used as a monitoring well. Temperature and pressure data were collected during the warm up period and were used to find the formation temperature and the initial pressure in a similar way as described for well NJ-15 in the previous section. Temperature profiles (Figure 23) show an increasing temperature with depth in the first 700 m. From 700 to 900 m, the temperature increases rapidly from 75 to 170 °C, and this suggests the possibility of a hot inflow within this range. Below 900 m there is a lower thermal gradient down to 1500 m and the zone can be interpreted as a convective zone but with poor permeability. Finally below 1700 m, the temperature gradient increases again down to the bottom of the well. Two feed zones are seen at 800 and 1700 m, respectively. The latest temperature profile is the same as the formation temperature profile between 800 and 1300 m.

Figure 24 shows the pressure profiles during warm up along with a pivot point that lies around 1700 m depth with a pressure of 150 bar.

To calculate the initial pressure, the estimated formation temperature profile from Figure 23 was inserted into the PREDYP software. The water level was adjusted in the calculations until the calculated profile matched the pressure pivot point.

4.4 Interpretation of temperature and pressure profiles for well K-38

Well K-38 in Krafla is a directional well located on the western flanks of Mt. Krafla which is a new

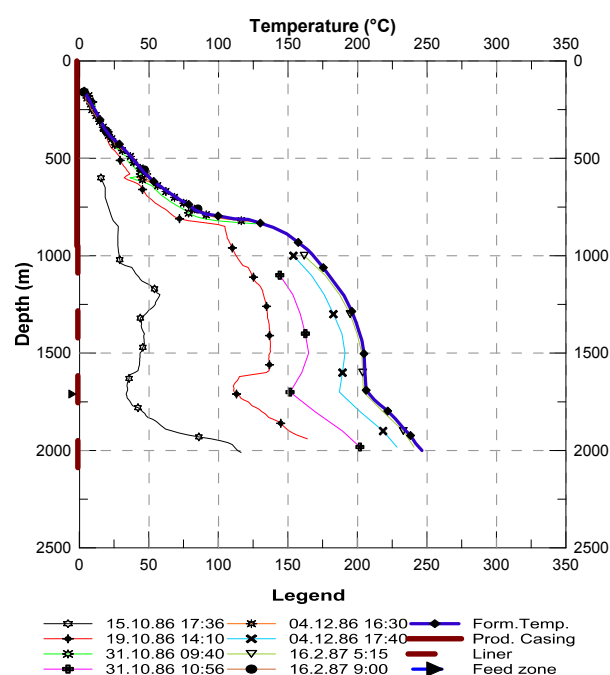


FIGURE 23: Temperature profiles for NJ-18

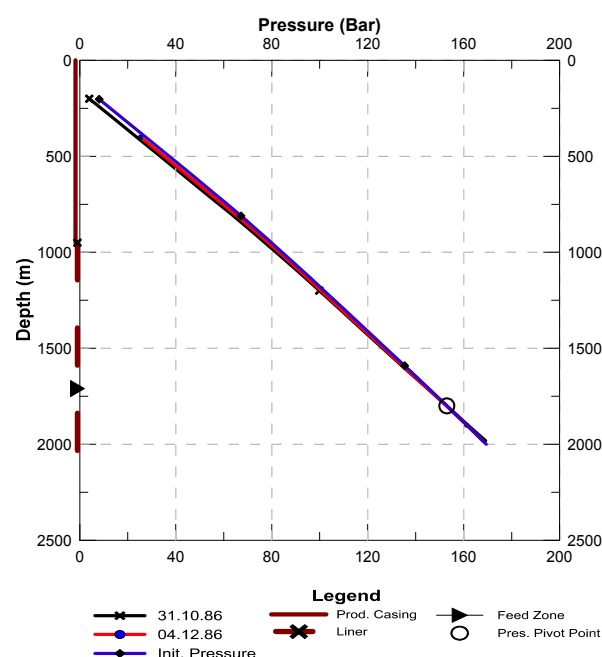


FIGURE 24: Pressure profiles for well NJ-18

well site in the field. It was drilled from 26.04.2008 to 21.07.2008 to a total depth of 2700 m with respect to the platform (2391.6 m TVD from the ground surface). Temperature profiles from July, August and September 2008 were used to estimate formation temperature (Figure 25). The formation temperature profile follows the boiling point curve in the top 1000 m. Two conductive layers were observed in the temperature profiles. The first layer (caprock) is located in the uppermost 300 m and the second layer (basement) between 1750 and 2000 m. There is a constant temperature zone between 300 and 1750 m depth. This zone can be interpreted as the reservoir (convective zone).

Figure 26 shows the pressure profiles during the warm up period. The pressure profiles show a pivot point at 2125 m where the pressure is about 130 bar (Figure 26). The pressure at the pivot point was

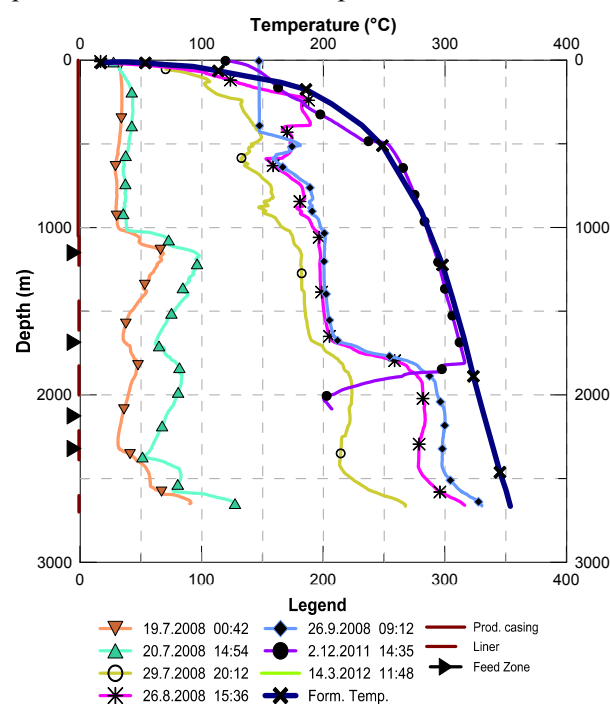


FIGURE 25: Temperature profiles for well K-38

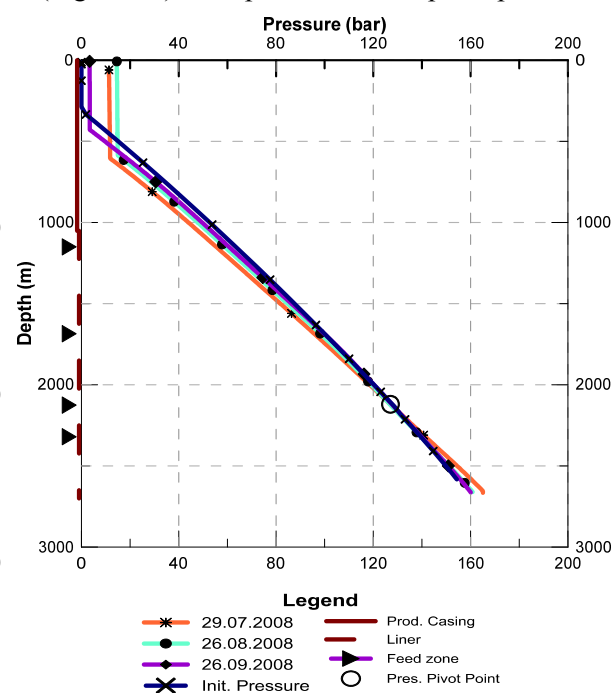


FIGURE 26: Pressure profiles for well K-38

used as a control point to estimate the initial pressure in a similar way as was described for wells NJ-15 and NJ-18 in the previous subsection.

4.5 Interpretation of temperature and pressure profiles for well K-37

Well K-37 in Krafla is a directional well drilled into the southern flanks of Mt. Krafla where there has been substantial production since 1980. It was drilled from 04.10.2007 to 18.01.2008 to a total depth of 2187 m. Downhole temperature and pressure data measured in January, March and April 2008 were used to estimate the formation temperature and initial pressure as shown in Figures 27 and 28.

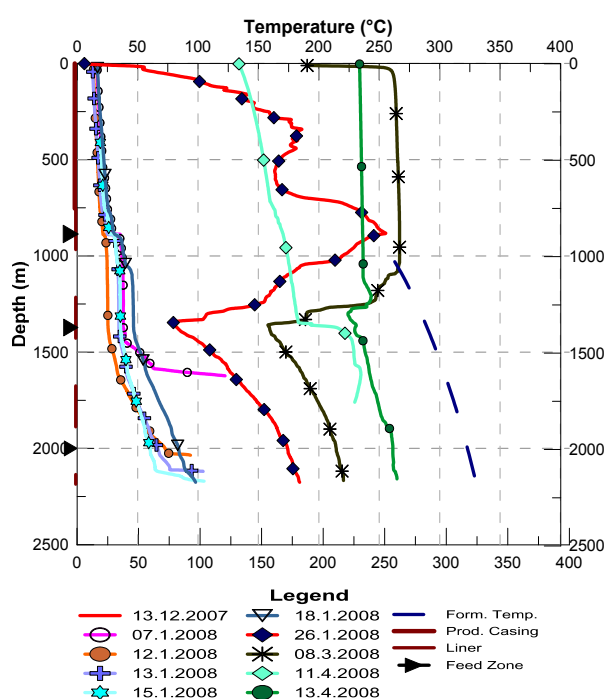


FIGURE 27: Temperature profiles for well K-37

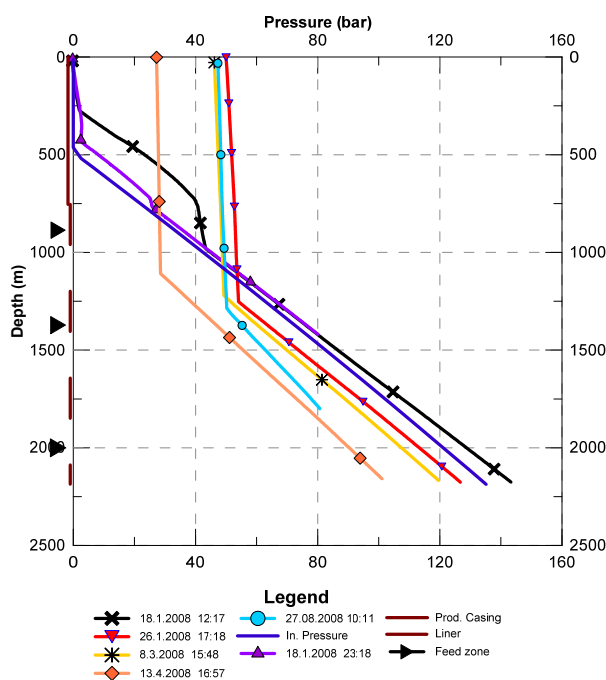


FIGURE 28: Pressure profiles for well K-37

Figure 27 shows the downhole temperature profiles and the formation temperature which follows the boiling point depth curve. However, the boiling point curve is shifted about 50 m due to drawdown in the system. Two major feed zones can be identified in the warm up temperature profiles: a hot inflow can be seen at 875 m depth and another feed zone can be observed at 1340 m. Between 0 and 300 m, the well shows conductive heating. Temperature profiles also indicate minor feed points at 590 and 1980 m.

Figure 28 illustrates the pressure profile during warm up. The pressure pivot point was not identified and the latest pressure profile (i.e. data measured on 27.08.2008) was used to determine the water level. Assuming this profile represents the actual reservoir conditions, the water level is at 450 m depth. Both formation temperature and initial pressure follow a boiling point curve as other wells on the southern flanks of the Krafla geothermal field (Mortensen et al., 2009).

5. PRESSURE AND TEMPERATURE MONITORING OF KRAFLA AND NESJAVELLIR GEOTHERMAL FIELDS

The purpose of careful monitoring of geothermal fields in utilization is to increase understanding of the geothermal fields, to prevent and to solve problems; the data is also necessary for simulation of

geothermal fields. The effect of “large-scale” mass-extraction on geothermal systems may induce pressure decline within the system which, in turn, causes flow from hot springs (and wells) to decline, discharge from steam-vents often to increase, increased recharge (often colder water) from outside, cooling of the reservoir, chemical changes (sometimes detrimental), surface subsidence as well as changes in micro-seismic activity (Axelsson and Halldórsdóttir, 2014). Three wells, two located in Nesjavellir geothermal field and one located in Krafla were considered for a monitoring analysis in this report.

5.1 Monitoring wells in Nesjavellir geothermal field

Through the existence of the Nesjavellir project, an extensive monitoring programme was carried out to monitor the response of the Nesjavellir geothermal system as well as to record the influence of utilization on the environment. A programme was set up to monitor the natural runoff from the field in the early 1980s, prior to the drilling and testing of production wells (Gíslason et al., 2005).

Since the start of drilling in the 1980s, downhole measurements, flow testing and chemical sampling have been included in the monitoring programme. Water levels or wellhead pressure are monitored when boreholes are not in production, depending on the characteristics of each borehole.

Since 1985, annual downhole temperature and pressure logs in idle wells have been measured and the data stored in the ÍSOR database (Gíslason et al., 2005). In the beginning several wells were available for the monitoring but, since production started, most production wells have been connected to the power plant, limiting the current monitoring programme to two wells: Well NJ-15 in the eastern part of the production area and well NJ-18, north of the production zone (Figure 1).

In this field, therefore, we will focus on the downhole pressure and temperature measurements performed on the two monitoring wells, i.e. wells NJ-15 and NJ-18, and continue the studies of these two wells. Data used for the analysis was collected from 1985 to 2013 and 1986 to 2013 for wells NJ-15 and NJ-18, respectively.

Figure 29 shows the formation temperature and initial pressure with the temperature and pressure history at 810 and 1590 m depths, considered to be the main feed zones for well NJ-15. Figure 30 illustrates formation temperature and initial pressure with temperature and pressure history at 1710 m, which is expected to be the main feed zone for well NJ-18. Formation temperature and initial pressure values at different depths were estimated from warm up data collected after drilling.

Measurement of temperatures at various depths for wells NJ-15 and NJ-18 shows no significant change in temperature with time, except in 2011 when a slight decrease in temperature was seen, and in 2012 a small increase in temperature was recorded for well NJ-15. This can be explained by the fact that, in May 2011, a flow test was carried out over a two week period; this could have allowed cold inflow from the eastern part of the hydrothermal system since well NJ-15 is located close to the eastern edge of the geothermal system. In March 2002, an injection test was conducted at well NJ-18 with 10 kg/s of 55°C of hot water injected into the well for three weeks. Temperature data measured during this period were not considered for this analysis. Since 2002 and up to 2013, there was a slow temperature recovery from 200 to 225°C.

Figure 29 shows a small decrease in pressure up to 1999, then a rapid decline from 1999 to 2013 at 810 and 1590 m. This rapid decrease in pressure may be due to the increase in production since 1999, observed in Figure 30. A linear constant pressure drawdown of about 7 bars was observed in well NJ-18 from 1985 to 2005 whereas from 2005 to 2013 the pressure decreased drastically to about 12 bars. Figure 31 shows the yearly production (kg/s) against time from 1984 to 2013.

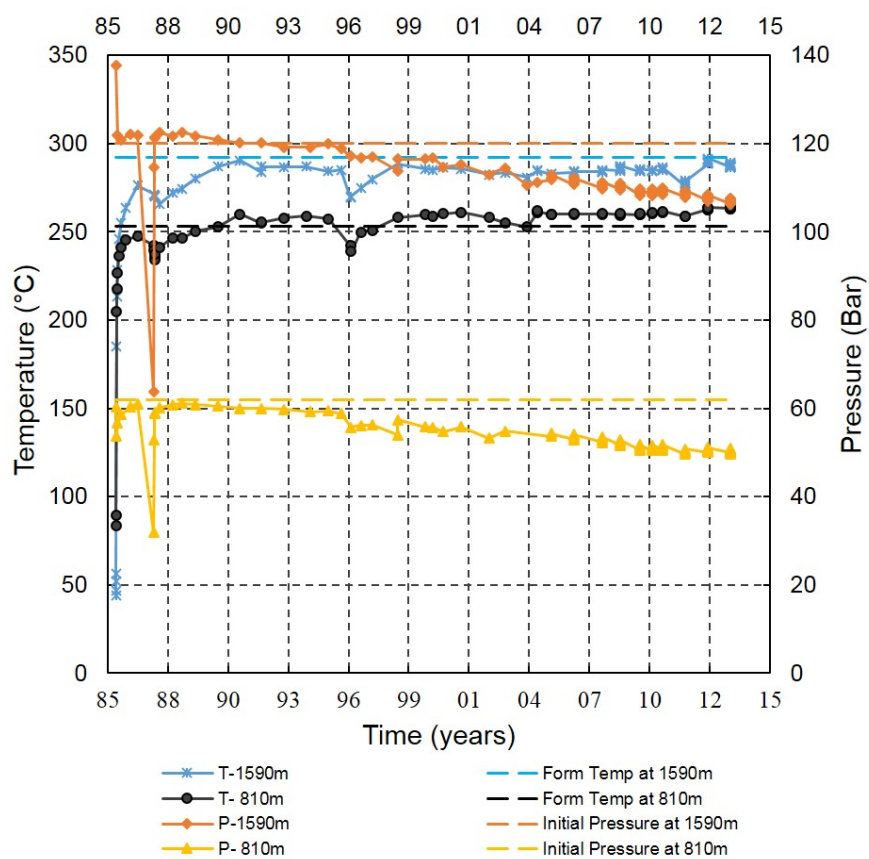


FIGURE 29: Temperature and pressure evolution from 1985 to 2013 for well NJ-15

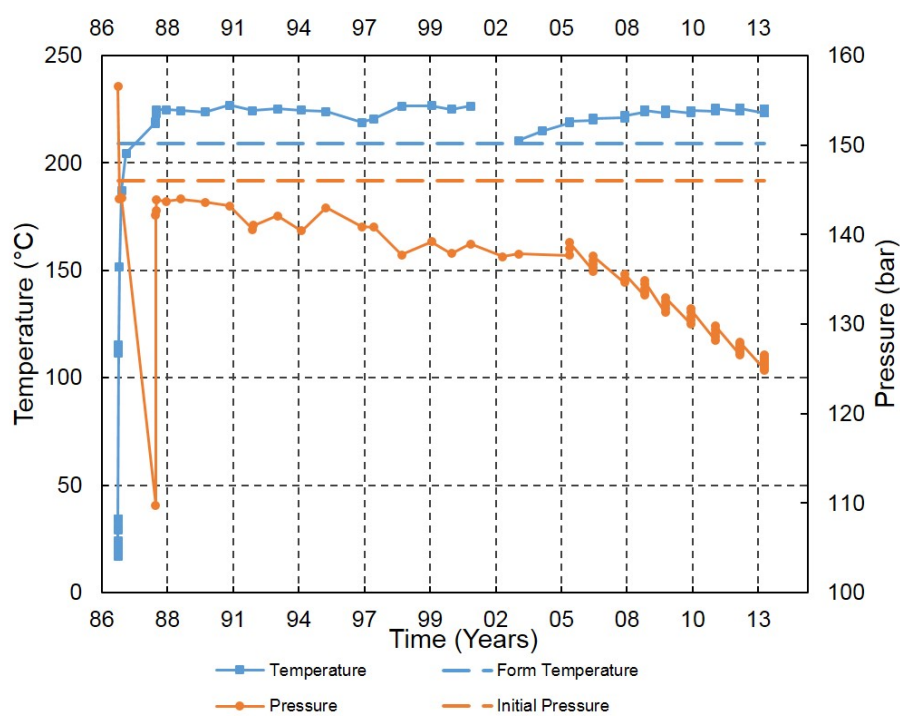


FIGURE 30: Temperature and pressure evolution at 1710 m from 1986 to 2013 for well NJ-18

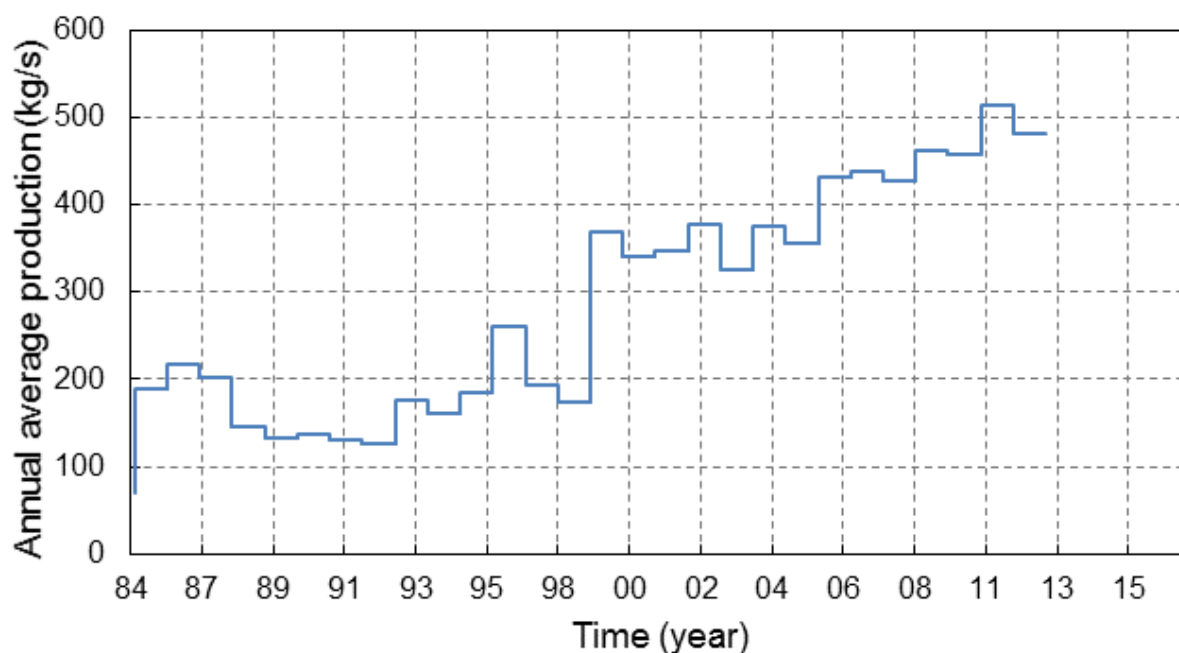


FIGURE 31: Average annual production in Nesjavellir from 1984 to 2013

5.2 Monitoring programme of Krafla geothermal field

Well KJ-18 was used for the monitoring programme of pressure and temperature evolution in Krafla geothermal system in this study. Well KJ-18 is located in the southeast part of Krafla geothermal field. It was drilled in 1981 to a total depth of 2215 m. During drilling, well KJ-18 was found to be very tight and it was decided not to put a slotted liner into it; production casing was set at 663m. During temperature recovery, it was found that the well was much colder than the wells to the west in the production area (Steingrímsson and Björnsson, 1996). Well KJ-18 was not a productive well and is currently used as one of the monitoring wells for Krafla geothermal system. Figure 32 shows the evolution of temperature at 1000, 1500 and 2000 m from 1981 to 2013 with the estimated formation temperature.

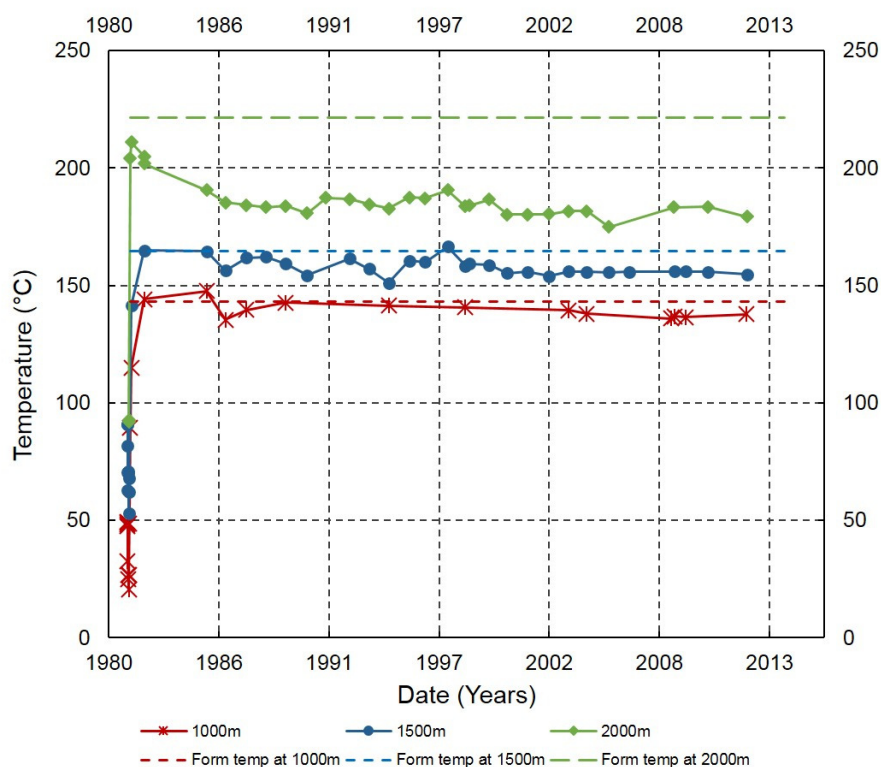


FIGURE 32: Pressure history for well K-18

As can be observed in Figure 32, there is a small change in temperature at 1000 m and 1500 m from 1981 to 2013. At 2000 m depth there is a rapid decrease from 1981 to 1988 and a small change in temperature since 1988 up to 2013. The rapid decrease in temperature at 2000 m was caused by a cold down flow from 1000 m feed point to the bottom of the well.

The pressure history is shown in Figure 33. From 1981 to 1991, the pressure had fallen by 6 bar once the production started in the area (Figure 34). The well showed little response to increased production in 1997. The well showed gradual linear pressure drawdown, about 15 bar since the beginning of production. Since the well is drilled at the eastern boundary of the geothermal field, the drawdown estimated from the monitoring data is probably an underestimate. Newly drilled wells on the southern flanks of Mt. Krafla show drawdown up to 30 bar (Mortensen et al., 2009). This was found by comparing the initial pressures of the wells. This corresponds roughly to 300 m change in water level and explains the depth to the water level in well K-37, as mentioned in the previous section.

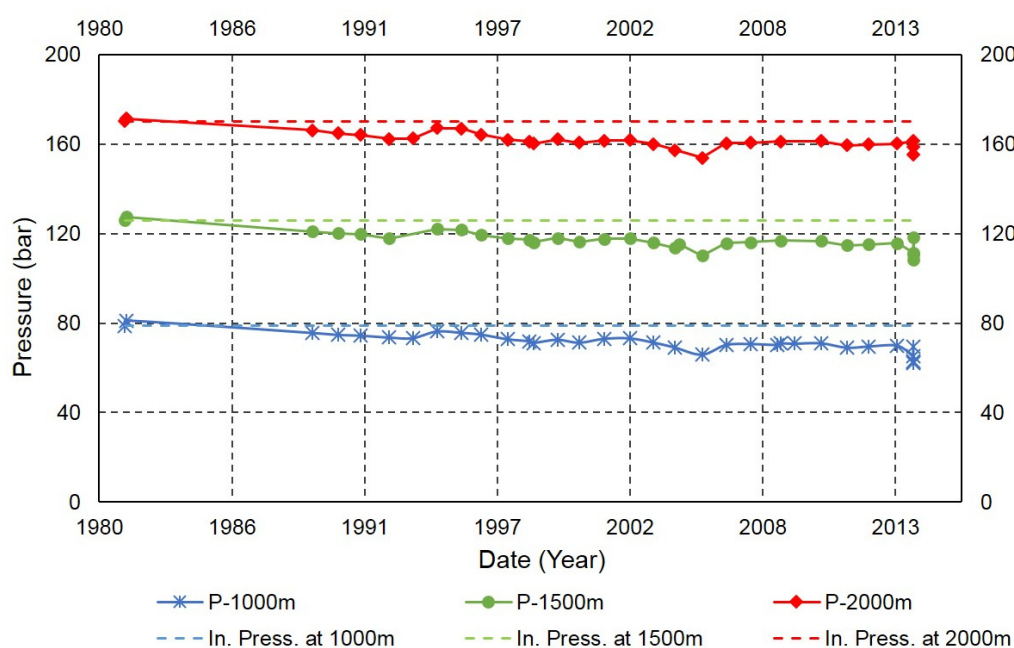


FIGURE 33: Pressure history for well K-38

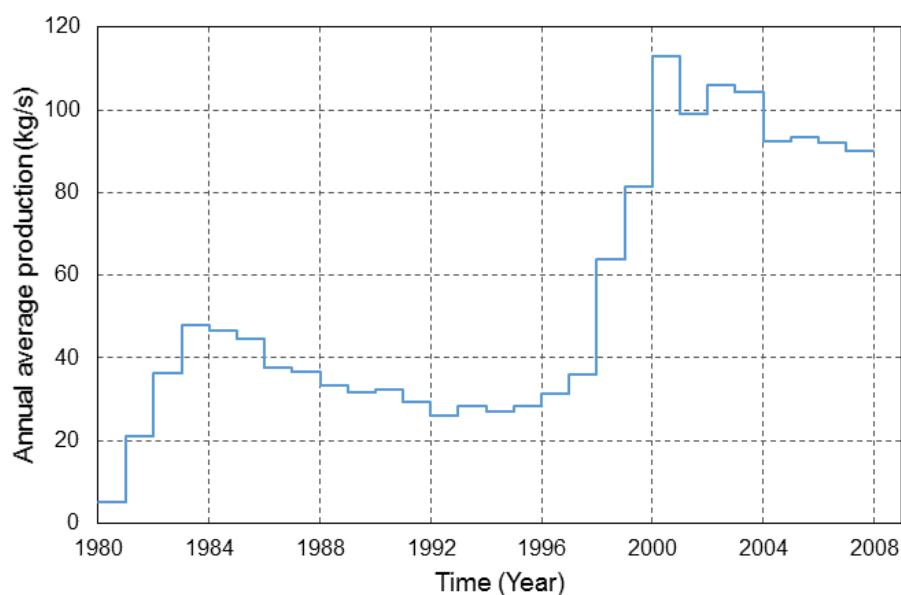


FIGURE 34: Average annual production from wells on the southern flanks of Krafla

6. CONCLUSION

Reservoir assessment and monitoring were conducted on selected wells in the Nesjavellir and Krafla high-temperature geothermal fields. Two wells, NJ-15 and NJ-18, were selected for reservoir assessment and monitoring for Nesjavellir and two other wells, K-37 and K-38, were selected for well test analysis for Krafla. Monitoring analysis was conducted only on well KJ-18 for Krafla.

In order to understand the parameters that characterise the reservoir and flow capacity of the selected wells, injection test analysis was performed and parameters such as injectivity index, transmissivity, storativity, skin, wellbore storage, etc. were evaluated. The WellTester program was used for the injection test analysis.

Transmissivity estimated for selected wells in Nesjavellir was of the same order of magnitude as for the wells in Krafla, i.e. $10^{-8} \text{ m}^3/(\text{Pa}\cdot\text{s})$, which is common in geothermal reservoirs in Iceland. The storativity for Krafla was higher than that of Nesjavellir for the selected wells. Some of the wells in Krafla have indeed, a steam cap, including the two wells analysed, which shows a two-phase reservoir, but the selected wells in Nesjavellir are at the boundary of the reservoir and are liquid-dominated. Skin factor for the selected wells for both fields was negative, as it usually is in Iceland. Permeability for the wells in Krafla was a little bit higher than in the selected wells in Nesjavellir. Wells NJ-15 and NJ-18 are probably not representative of the wells in Nesjavellir because they are located at the field boundaries. Perhaps these wells were drilled into a less permeable sector of the field.

Temperature and pressure profiles were analysed to estimate formation temperature and initial pressure. For wells NJ-18 and NJ-15, the highest formation temperatures were 250 and 300°C, respectively. Boiling was not observed for these wells, which indicates that these wells were drilled in a lower temperature part or at the boundary of the Nesjavellir field. Formation temperatures varied between 10 and 350°C and boiling was observed in the upper 1800 and 1000 m for wells K-38 and K-37, respectively. This indicates that these wells were drilled in a high-temperature reservoir.

Temperature and pressure monitoring at various depths were performed on well K-18 from 1981 to 2013 for Krafla, on well NJ-15 from 1985 to 2013, and on well NJ-18 from 1988 to 2013 for Nesjavellir. No significant change in temperature was observed in wells NJ-15 and NJ-18 but a linear constant pressure drawdown of about 13 bar was observed in well NJ-15 from 1985 to 2013 and a rapid decline in pressure (20 bar) was observed in well NJ-18 from 2006 to 2013. For Krafla geothermal system, slow pressure and temperature decreases were observed in well KJ-18 in general. The decrease in temperature is due to cold water down flow in the well, but the pressure decline is the effect of production in this part of the field. The well showed little response to increased production in 1997. The dynamic modelling methods such as lumped parameter models could be applied to calculate future predictions for future studies.

ACKNOWLEDGEMENTS

I wish to express my sincere gratitude to UNU-GTP Director, Lúdvík S. Georgsson, for the opportunity to complete this training. My thanks also go to my advisors, Dr. Svanbjörg Helga Haraldsdóttir and Ms. Saeunn Halldórsdóttir for their guidance and useful suggestions throughout the course of my work. I am also grateful to my home institutions, Rwanda Energy Group (REG) and National Capacity Building Secretariat (NCBS) for granting me study leave for this short course. Thanks are due to Landsvirkjun and Orkuveita Reykjavíkur for providing field data for my work. I would also like to thank the UNU-GTP staff: Ingimar Gudni Haraldsson, Thórhildur Ísberg, Markús A.G. Wilde, María S. Guðjónsdóttir, and Málfríður Ómarsdóttir for their kind assistance, and to all the 2014 UNU Fellows for their friendship. Finally, this paper is dedicated to my wife for her patience and continuous encouragement during my absence from home.

REFERENCES

- Ágústsson, K., Flóvenz, Ó.G., Gudmundsson, Á., and Árnadóttir, S., 2012: Induced seismicity in the Krafla high temperature field. *Geothermal Resources Council, Trans.*, 36, 975-980.
- Arason, Th., and Björnsson, G., 1994: *ICEBOX* (2nd edition). Orkustofnun, Reykjavík, 38 pp.
- Arason, Th., Björnsson, G., Axelsson, G., Bjarnason, J.Ö., and Helgason, P., 2004: *The geothermal reservoir engineering software package Icebox, user's manual*. ÍSOR – Iceland GeoSurvey, Reykjavík, report 2004/014, 53 pp.
- Ármannsson, H., 2010: The chemistry of the Krafla geothermal system in relation to the IDDP well. *Proceedings of the World Geothermal Congress 2010 Bali, Indonesia*, 5 pp.
- Ármannsson, H., Gudmundsson, Á., and Steingrímsson, B.S., 1987: Exploration and development of the Krafla geothermal area. *Jökull*, 37, 12-29.
- Axelsson, G. and Halldórsdóttir, S., 2014: *Management and monitoring of geothermal systems*. UNU-GTP, unpublished lecture notes.
- Axelsson, G. and Steingrímsson, B., 2012: Logging, testing and monitoring geothermal wells. *Presented at the short course on geothermal development and geothermal wells organized by UNU-GTP and LaGeo, in Santa Tecla, El Salvador*, 20 pp.
- Björnsson, A., 1985: Dynamics of crustal rifting in north-eastern Iceland. *J. Geophysical Research*, 90-B12, 10.151 – 10.162.
- Franzson, H., 1998: Reservoir geology of the Nesjavellir high-temperature field in SW-Iceland. *Proceedings of the 19th Annual PNOC-EDC Geothermal Conference, Manila, Philippines*, 13-20.
- Franzson, H., 2000: Hydrothermal evolution of the Nesjavellir high-temperature system, Iceland. *Proceedings of the World Geothermal Congress 2000, Kyushu-Tohoku, Japan*, 2075-2080.
- Gíslason, G., Ármannsson, H., and Hauksson, T., 1978: *Krafla, temperature conditions and gases in the geothermal reservoir*. Orkustofnun, Reykjavík, report OS-JHD-7846 (in Icelandic), 88 pp.
- Gíslason, G., Ívarsson, G., Gunnlaugsson, E., Hjartarson, A., Björnsson, G., and Steingrímsson, B., 2005: Production monitoring as a tool for field development; A case history from the Nesjavellir field, Iceland. *Proceedings of the World Geothermal Congress 2005, Antalya, Turkey*, 9 pp.
- Grant, M.A. and Bixley, P.F., 2011: *Geothermal reservoir engineering* (2nd ed.). Academic Press, NY, 359 pp.
- Grant, M.A., Donaldson, I.G., and Bixley, P.F., 1982: *Geothermal reservoir engineering*. Academic Press, NY, 369 pp.
- Helgason, P., 1993: *Step by step guide to Berghiti*. Orkustofnun, Reykjavík, Iceland.
- Horne, R.N., 1995: *Modern well test analysis, a computer aided approach* (2nd edition). Petroway Inc., USA, 257 pp.
- Júlíusson, E., Grétarsson, G.J., and Jónsson, P., 2008: *WellTester 1.0b, user's guide*. ÍSOR – Iceland GeoSurvey, Reykjavík, report ÍSOR-2008/063, 27 pp.

Mortensen, A.K., Gudmundsson, A., Steingrímsson, B., Sigmundsson, F., Axelsson, G., Ármannsson, H., Björnsson, H., Ágústsson, K., Saemundsson, K., Ólafsson, M., Karlsdóttir, R., Halldórsdóttir, S., and Hauksson, T., 2009: *Geothermal system in Krafla, summary of research on the geothermal system and revised conceptual model*. ISOR – Iceland GeoSurvey, Reykjavik, report ISOR-2009/057 (in Icelandic). 45 pp.

Steingrímsson, B., and Björnsson G., 1996: *Well tests in Krafla and Bjarnarflag in the year 1995*. Orkustofnun, report OS-96025/JHD-14 B (in Icelandic), 50 pp.

Steingrímsson, B., Gudmundsson, A., Franzson, H., and Gunnlaugsson, E., 1990: Evidence of a superficial fluid at depth in the Nesjavellir field. *Proceedings of the 15th Workshop on Geothermal Reservoir Engineering, Stanford University, California*, 81-88.

Van Everdingen, O.F., and Hurst, W., 1953: The application of the Laplace transformation to flow problems in reservoirs. *Trans. AIME*, 186, 305-324.

NOMENCLATURE

c_t	: Total compressibility (Pa^{-1});
c_w	: Fluid compressibility (Pa^{-1});
c_r	: Rock compressibility (Pa^{-1});
h	: Reservoir thickness (m);
II	: Injectivity index ($(\text{l/s})/\text{bar}$);
ϕ	: Porosity (%);
k	: Formation permeability (m^2);
p	: Pressure (Pa);
Q	: Volumetric flow rate (m^3/s);
ρ	: Fluid density (kg/m^3);
r	: Radial distance (m);
S	: Storativity ($\text{m}^3/(\text{Pa} \cdot \text{m}^2)$);
t	: Time (s);
T	: Transmissivity ($\text{m}^3/(\text{Pa} \cdot \text{s})$);
Δp	: Change in reservoir pressure (Pa);
ΔQ	: Change in the injection flow (m^3/s);
ν	: kinematic viscosity of the fluid;
C	: Wellbore storage coefficient (m^3/Pa);
ΔV	: Change in fluid volume (m^3);
s	: Skin factor;
r_e	: Radius of investigation (m);
t_p	: Circulation stop time (h);
hr	: Hour (h.);
T	: Temperature ($^{\circ}\text{C}$);
ρ_{sat}	: Saturation density (kg/m^3);
ρ_{mean}	: Average density (kg/m^3);
z	: Depth (m);
g	: Acceleration of gravity (m/s^2);
μ	: Dynamic viscosity ($\text{Pa} \cdot \text{s}$).



UNITED NATIONS
UNIVERSITY

UNU-GTP

Geothermal Training Programme

Orkustofnun, Grensasvegur 9,
IS-108 Reykjavik, Iceland

Reports 2014
Number 26

PRELIMINARY DESIGN OF A HOT WATER DISTRIBUTION SYSTEM FOR GREENHOUSE HEATING, OLKARIA, KENYA

Felix Kiio Nzioka

Kenya Electricity Generating Company – KenGen

P.O. Box 785 – 20117

Naivasha

KENYA

fjnioka@kengen.co.ke

ABSTRACT

Geothermal energy may be utilized directly or indirectly. Its main use in Kenya is the generation of electricity. Direct utilization of geothermal energy in Kenya is minimal. However, potential direct users are located a few kilometres from the already developed geothermal fields and there is usage potential for a hot water supply for greenhouse heating. Chemistry for re-injection brine has shown that a substantial amount of heat energy may be extracted from the brine without risk of silica scaling. Greenhouse farming requires temperature and humidity control for enhanced plant growth, especially during the night when temperatures are as low as 8°C. Heating domestic water with electricity is expensive in Kenya, therefore utilization of geothermal energy to heat it would be a much cheaper and greener option. Based on the saturation index of silica, the available heat energy of brine from Olkaria North East field is about 16.58 MWt using a mass flow rate of 238 ton/hr. at a supply temperature of 150°C and a return temperature of 90°C. In this study, an evaluation was made on direct use of geothermal energy for one greenhouse complex, one hotel and three residential estates. The study was aimed at coming up with a preliminary design for a hot water distribution system, mainly for greenhouse heating. The design model was generated using the Engineering Equation Solver (EES) software and the design was done as per ASME B31.3-2002 standards. The design considered has a closed loop circuit with heat exchangers at all ends. The total cost of the distribution network is €8,848,000 and the unit cost of heat production is €13.24 per MWh.

1. INTRODUCTION

Direct utilization of geothermal energy in the Olkaria geothermal field in Kenya has not been fully developed. The main focus has been geothermal electricity generation. The field is high-temperature field and liquid-dominated and produces two-phase fluids. Therefore, the mixture is separated before being utilized in power generation. Well site separator stations are located all over the production field and the separated brine is collected for re-injection. The separation occurs at a pressure of about 5 bar and a temperature of about 150°C. The brine has a significant amount of energy that could be extracted before re-injection. Potential applications could be binary electricity generation, greenhouse heating, balneology, industrial processes like drying, and hot water supply to residential areas and hotels. The

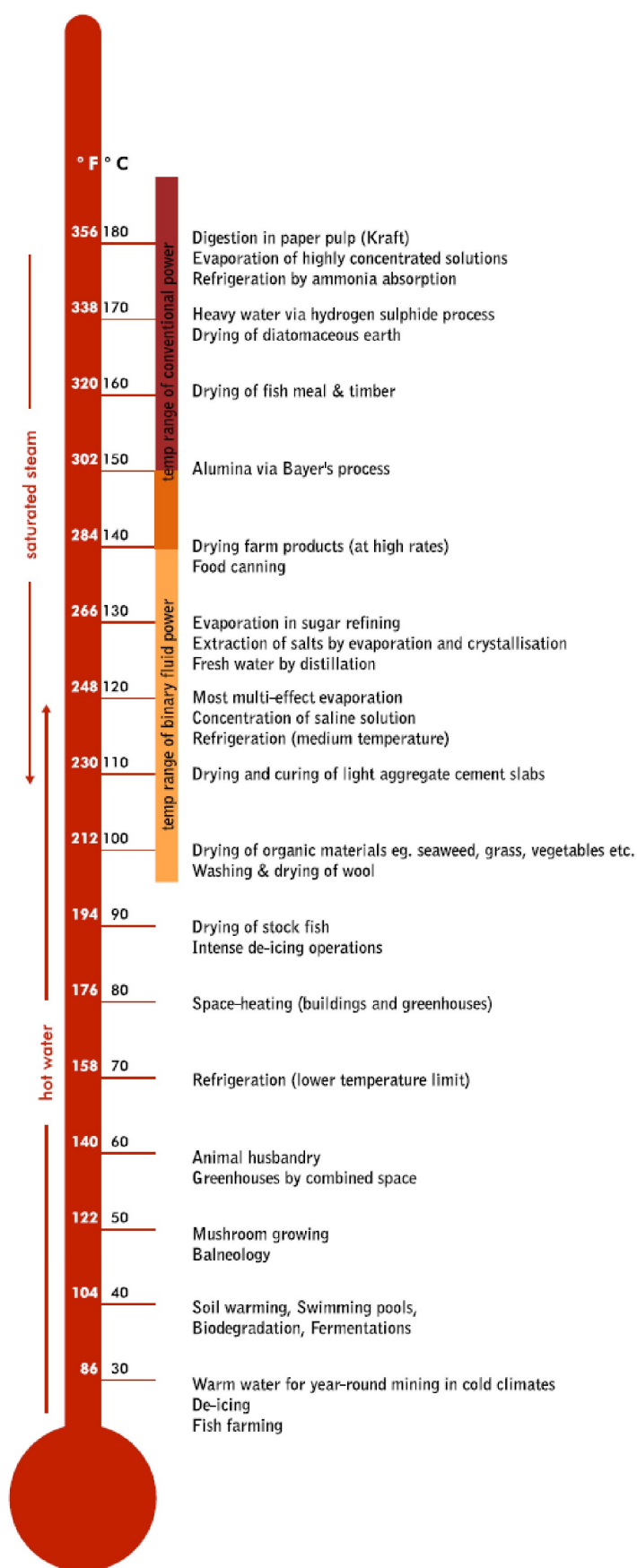


FIGURE 1: Lindal diagram (Líndal, 1973)

brine mass flow rate, for hot re-injection in the Olkaria North East field, is way above 500 t/hr. Electricity generation is the most important form of utilization of high-temperature geothermal resources, while low- to medium-temperature resources are better suited for non-electric applications (Figure 1) (Líndal, 1973). The Lake Naivasha region hosts many flower farming greenhouses, residential estates and hotels which are likely end users of the geothermal energy extracted from brine. The chemistry of the hot brine also determines the extent of the energy extraction. This study presents a preliminary design of a hot water distribution system for greenhouse heating and a hot water supply to residential areas and hotels within the Olkaria geothermal field. This was done by first doing a demand analysis, then transmission pipe design, pumps, heat exchangers and expansion tank sizing.

1.2 Direct utilization in Kenya

A number of direct uses of geothermal energy may be derived from the Lindal diagram (Figure 1). This will vary depending on the available resource. A cascade of direct use applications is possible at the various geothermal fields in the country. The current operational direct utilization of geothermal energy is in greenhouse heating at the Oserian Development Company Ltd (OCDL), Pyrethrum drying, water harvesting in Suswa and Eburru, a spa at Lake Bogoria and the new Olkaria Spa. OCDL has taken the lead in the utilization of geothermal energy for its greenhouses and is utilizing steam from a 1.28 MW well with a total mass flow of 51 t/hr, an enthalpy of 1475 kJ/kg, and an energy equivalent of 15.37 MWt (Lagat, 2010). Two-phase fluid from a well is being used in a heat exchanger to supply hot water to heat 50 hectares of the greenhouses at OCDL (Mburu,

2014). Heating greenhouses helps in temperature and humidity control (Figure 2), thus leading to a reduction in the growth of fungicides. The process of photosynthesis in plants requires carbon dioxide. It is for this reason that OCDL has incorporated a carbon dioxide extraction facility for enhanced plant growth. The carbon dioxide is extracted from the geothermal fluid. Brine sulphur and silica content have balneological effects on the human skin (Mangi, 2013). It is for this reason that the Direct Use and



FIGURE 2: Greenhouse heating at OCDL (Mangi, 2013)

Demonstration Centre (DUDC) in Olkaria was built. The other direct use applications to be demonstrated at the centre include a steam bath, a spa, a sauna, heating and cooling of buildings, hot water supply to residential areas and hotels, fish farming, drying of agricultural produce, greenhouse heating and irrigation (Mangi, 2013). Geothermal energy has also been used directly on a small scale in the drying of pyrethrum at Eburru. Farmers in this area have for decades utilized natural steam at a temperature of 98°C, emitted by fumaroles, to dry their pyrethrum flowers (Lagat, 2010).

1.3 Chemistry of Olkaria Northeast brine

The water and the gas chemistry in this field have been analysed in previous studies. Wambugu (1996) found that a hot NaCl type water reservoir exists with temperatures of 270-290°C at depth and major feed aquifers are located below 1300 m depth with a relatively saline fluid (Cl = 300-550 ppm). His study recommended re-injection of brine at temperatures above 170°C in order to avert the possibility of silica scaling. Olkaria Northeast field has a silica concentration of about 500-700 ppm and a pH of about 9 (Mburu, 2010). The wells in this field were connected to the power plant in 2003; brine from the wells is re-injected to four hot re-injection wells, namely wells OW R2, OW R3, OW 703 and OW 708. The mixed brine is monitored on a daily basis before re-injection. Recent predictions of amorphous silica precipitation out of solution, based on data from wells OW R2, OW 703 and OW 708 using the WATCH program, have shown that brine can be re-injected at a temperature of as low as 90°C, without the risk of silica scaling (Figure 3). The WATCH program helps to calculate the aqueous speciation of various components at several pre-determined temperature values for each mineral in order to obtain a log Q/K versus temperature relationship (Mburu, 2010). This study, therefore, considers the use of brine for wells OW 708 and OW R3 which have shown silica precipitation occurring at 90 and 135°C, respectively. Silica precipitation for well OW 703 was found to occur at around 145°C. Sampling data for well OW R2 was not available for the silica modelling. Silica polymerisation and precipitation do not occur at a significant rate until a reasonable degree of super saturation is achieved. Silica scaling problems are not experienced in practice until temperatures rather lower than the theoretical points are reached (Mburu, 2010). A case example from the Berlin geothermal power plant in El Salvador showed that pH adjustment using H₂SO₄ can enable brine to be cooled to lower temperatures without the risk of scaling. Brine pH modification has been shown to be effective and least expensive compared to other inhibitors (Guerra and Jacobo, 2012).

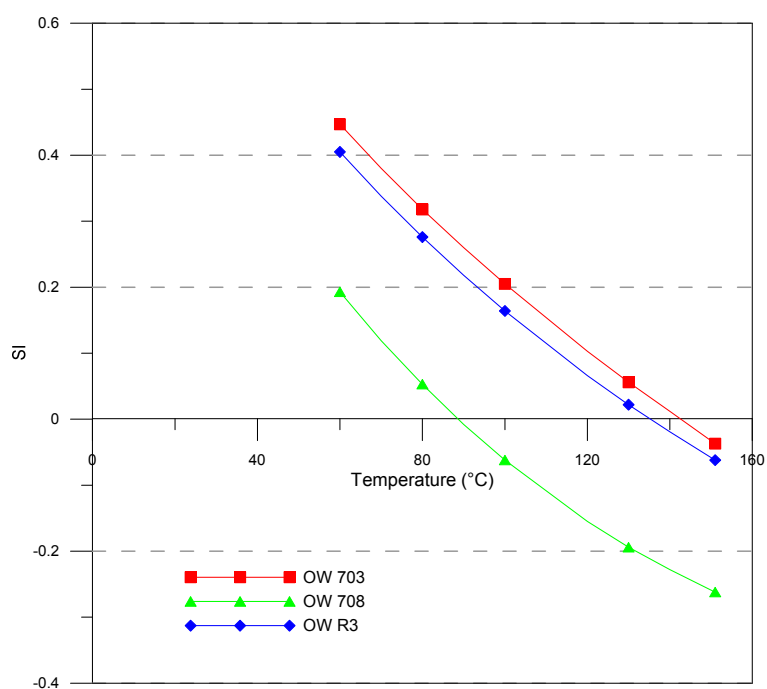


FIGURE 3: Silica Saturation Index (SI) for re-injection brine



FIGURE 4: Pipeline on the surface (modified from Onyango, 2012)

(Onyango, 2012). The Variable Topography Distance Transform method is used to find optimal paths across physical landscapes for pipelines carrying two-phase geothermal fluid, with the objective of minimizing the capital and operational cost of the pipeline. A distance transform finds the distance from each object point to pixel in an image, and maps the value of the distance to the closest object point (Kjaernested et al., 2013).

2.2 End use demand and flow analysis

Greenhouse farming is a major agricultural activity around Lake Naivasha. Many of the greenhouses major in cut flowers for export. If all greenhouses within a range of 30 km from Olkaria along Moi South Lake Road were heated with geothermal water, then the heat requirement would be enormous, or over 700 MWt (Table 1). The mass flow rate

2. PIPELINE DESIGN THEORY

Pipeline design involves several steps outlined in the following subsections.

2.1 Route selection

This is a process for identifying constraints, avoiding undesirable areas and maintaining the economic feasibility of the pipeline. Some of the factors that need to be considered are pipeline integrity, cost efficiency, environmental impacts, public safety and land use constraints.

This process involves the use of two methods, i.e. cost modelling comparison, and variable topography distance transforms. Pipelines can either be installed at the surface (Figure 4) or buried underground, where a is the horizontal distance between the two pipes and d is the depth (Figure 5). In most cases, the distribution of hot water is carried out using buried pre-insulated pipes. This study considers the use a mixture of both buried pipelines and surface pipelines. The method of route selection for this study is based on the total updated cost of the pipeline. Standard distance transform works with a binary digital image that consists of object points and non-object points

TABLE 1: Demand analysis

End use	Demand (MWt)
Residential houses	0.19
Hotels	0.05
Greenhouses	752.88
Total	753.12

considered in this study is 238 t/hr at a temperature of 150°C and a pressure of around 5 bar, and has an equivalent heat energy of about 17 MWt. This is the brine meant for re-injection into wells OW 708 and OW R3. Due to the prevailing conditions, only one greenhouse complex, Plantation Plants Kenya Limited, was evaluated for this study. The demand coverage for the greenhouse heating is around 78% of the total area under utilization. Other facilities looped into this distribution system are KenGen housing estates, OrPower housing estate and Fish Eagle inn. BS 6700 (BS, 2006) recommends that the hot water supply to dwellings should be 35-45 litres per person per day; these are the values which were used in the demand analysis for residential areas and hotels. Brine flow rates to re-injection wells in Olkaria North East field are shown in Figure 6. Assumptions made in the analysis include:

- a. Greenhouses: minimum temperature required inside greenhouse is 20°C; minimum outside temperature is 8°C; a single plastic sheet is used as the cover material; pipe installation is below the ceiling and on the ground between plots.
- b. Residential areas and hotels: Each family house has 6 members and each room has a full capacity of 2 people.

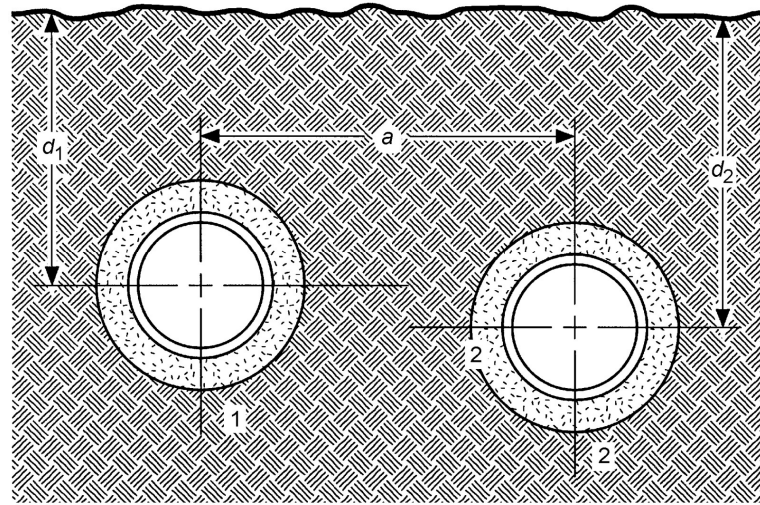


FIGURE 5: Schematic drawing of a pipeline buried underground (ASHRAE, 2008)

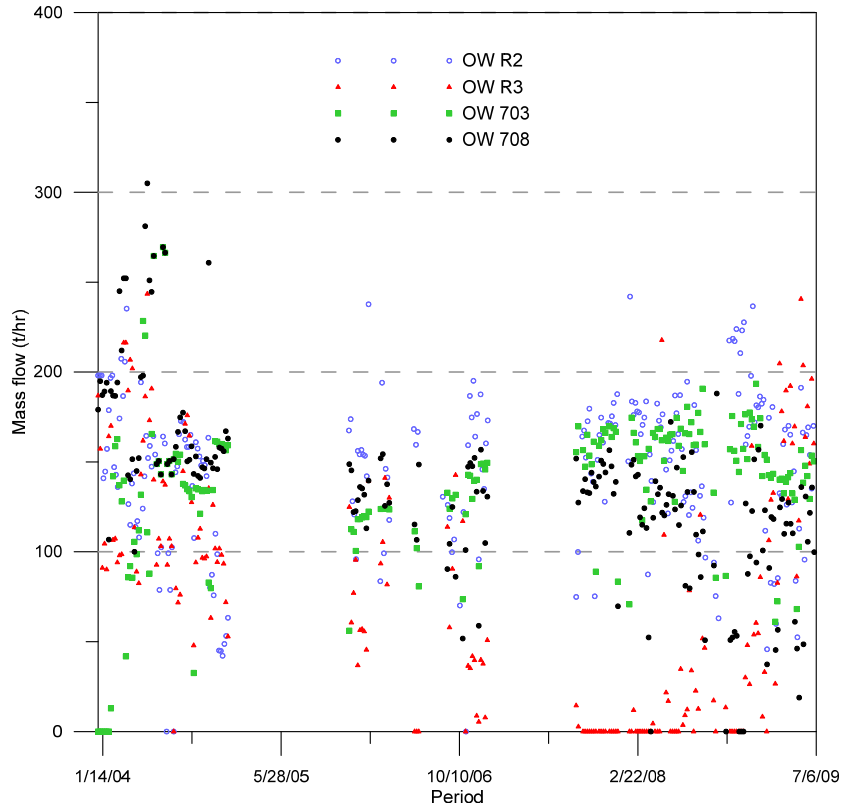


FIGURE 6: Brine mass flow rates to re-injection wells

Heating requirements of the green houses were calculated from the heat losses, Q , in the greenhouse (Equation 1). Heat losses in greenhouses are composed of two components (Panagiotou, 1996):

$$Q = Q_T + Q_I \quad (1)$$

where Q_T = Transmission losses through the roof and the walls (W);
 Q_I = Infiltration and ventilation losses due to the heating of cold outside air (W).

Surface areas of the cover materials of the greenhouses were estimated using Google Earth and then combined with the design temperature difference and a heat loss factor (Equation 3) which is the reverse of the overall thermal resistance:

$$Q_T = Q_{Tcover} + Q_{Trest} \quad (2)$$

where Q_{Tcover} = Transmission heat losses through the glazing-covering material (W);
 Q_{Trest} = Transmission heat losses through unglazed area (e.g. gutters, frames, masonry) (W).

and

$$Q_{Tcover} = \frac{A_{cover}}{R_{kcover}} (T_i - T_o) \quad (3)$$

where A_{cover} = Glazing area including frames (m²);
 T_i = Indoor temperature (°C);
 T_o = Design outside temperature (°C);
 R_{kcover} = Overall thermal resistance (m² °C/W).

The overall thermal resistance is given by Equation 4. Thermal resistance is dependent on the cover material, wind speed and heating system arrangement in the greenhouse (Appendix I):

$$R_{kcover} = R_{icover} + R_{\lambda cover} + R_{ocover} \quad (4)$$

where R_{icover} = Inside convection resistance (m² °C/W);
 $R_{\lambda cover}$ = Thermal conductivity resistance [m² °C/W];
 R_{ocover} = Outside convection resistance (m² °C/W).

Neglecting Q_{Trest} in Equation 2, Q_T is approximately equal to Q_{Tcover} , or:

$$Q_T \approx Q_{Tcover} \quad (5)$$

Infiltration losses are analysed by the air exchange method. The number of air exchanges is a function of wind speed, greenhouse construction, and inside and outside temperatures. Therefore Q_I is given by Equation 6:

$$Q_I = \frac{A_{cover}}{R_{vcover}} (T_i - T_o) \quad (6)$$

where R_{vcover} = Thermal resistance for infiltration caused by leaky joints (m² °C/W).

The heat energy available in hot water is calculated using Equation 7.

$$Q = mC_p\Delta T \quad (7)$$

where Q = Heat power (W);
 m = Mass flow rate (kg/s);
 C_p = Specific heat capacity (kJ/kg);
 ΔT = Temperature difference (°C).

2.3 Optimization of pipe diameter

The objective of pipe diameter optimization is to minimize the total updated cost based on the pipeline cost, pump station cost, and the annual operation and maintenance cost. According to Jónsson (2014), an increase in diameter increases the capital cost, while the total annual cost decreases and there is an optimum diameter with a minimum total updated cost (Figure 7). However, other factors like the maximum allowable velocity and pressure drop requirements also influence the size of the pipeline.

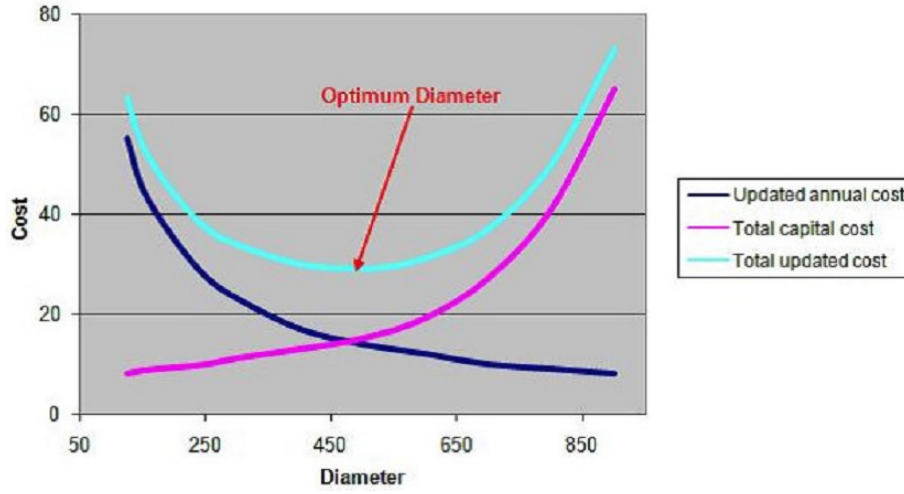


FIGURE 7: Optimum diameter selection based on total updated cost

Therefore, the pipeline should be sized by an economic pressure drop approach. The total updated cost is calculated by Equation 8:

$$C_T = C_c + C_a(1 - \frac{1}{(1+i)^N})/i \quad (8)$$

where C_T = Total updated cost;
 C_c = Capital cost;
 C_a = Annual operation and maintenance cost;
 i = Interest rate;
 N = Number of years of operation.

and

$$C_c = L_p c_p + n_b c_b + n_u c_u + n_v c_v + n_{pu} c_{pu} + L_p c_i \quad (9)$$

where L_p = Length of pipe (m);
 $c_p, c_b, c_u, c_v, c_{pu}, c_i$ = Cost of pipe, bends, connection units, pumps and pipe insulation, respectively;
 n_b, n_u, n_v, n_{pu} = Number of bends, connection units, valves and pumps, respectively.

The cost of other capital items like heat exchangers may be included in Equation 9. Maintenance costs for the distribution network should also be included in the annual cost (Equation 10).

$$C_a = C_{el} O_h P \quad (10)$$

where C_a = Annual operation cost;
 C_{el} = Cost of electricity per (kWh);
 O_h = Number of annual pump operation hours;
 P = Pump power (kW).

The frictional pump power, P , is given by Equation 11:

$$P = g \rho H_f Q / \eta \quad (11)$$

where g = Gravitational acceleration (m/s^2);
 ρ = Density of fluid, (kg/m^3);
 H_f = Frictional head loss (m);
 Q = Fluid flow rate, (m^3/s);
 η = Efficiency of motor and pump.

Frictional head, H_f (Equation 13), is determined by first calculating the fluid velocity, V , using Equation 12. In order to avoid corrosion, erosion and fluid water hammer in the pipeline, the velocity of the fluid should be kept below 3 m/s for water and 40 m/s for steam.

$$V = Q/A \quad (12)$$

$$H_f = fV^2 l_e / 2gD \quad (13)$$

where A = Cross-sectional area of pipe (m^2);
 f = Friction factor;
 l_e = Second equivalent length of pipeline (m);
 D = Inside diameter of pipe (m).

and

$$l_e = l_p + n_b h_b D_{in} + n_c h_c D_{in} + n_u h_u D_{in} + n_v h_v D_{in} \quad (14)$$

where l_p = Length of pipe (m);
 D_{in} = Inner diameter (m);
 h_b = 20 (Equivalent of bends);
 h_c = 20 (Equivalent length of connections, flow through);
 h_u = 20 (Equivalent length of expansion units);
 h_v = 13 (Equivalent length of gate valves fully open).

The pressure to pump (P_p) is given by Equation 20. The formula for determining the friction factor (f) used in Equation 13 depends on the value obtained for the Reynolds number, Re (Equation 15), such that:

$$Re = \rho V D / \mu \quad (15)$$

$$Re \leq 2100 \quad (16)$$

Then,

$$f = 64 / Re \quad (17)$$

And if,

$$Re \geq 2100 \quad (18)$$

then,

$$f = \frac{0.25}{\left(\log_{10} \left[\frac{\frac{\varepsilon}{D_{in}}}{3.7} + \frac{5.74}{Re^{0.9}} \right] \right)^2} \quad (19)$$

$$P_p = (\Delta Z + H_f) \rho g \quad (20)$$

where ε = Absolute roughness (m);
 μ = Viscosity (kg/ms);
 ΔZ = Elevation difference (m).

2.4 Thickness and pressure class

According to ASME B31.3-2002 (ASME, 2002), the nominal pipe thickness, t_n , should be larger or equal to the requisite pipe thickness, t_m , as shown in Equation 21. The temperature dependent coefficient for steel and other metals can be referenced from the standard for values of thickness lesser than a sixth

of the diameter. The same standard stipulates that the design pressure shall not be less than the pressure at the most severe condition expected during service.

$$t_n \geq t_m = \frac{PD}{(2(SE + Py)) + A} \quad (21)$$

where P = Design pressure (Pa);
 D = Outer diameter (m);
 S = Allowable stress (Pa);
 E = Welding factor;
 y = Temperature dependent coefficient;
 A = Additional thickness for milling and corrosion (m).

A pipe having a branch connection is weakened by the opening that must be made in it and, unless the wall thickness of the pipe is sufficiently in excess of that required to sustain the pressure, it is necessary to provide added reinforcements (Figure 8 and Appendix II).

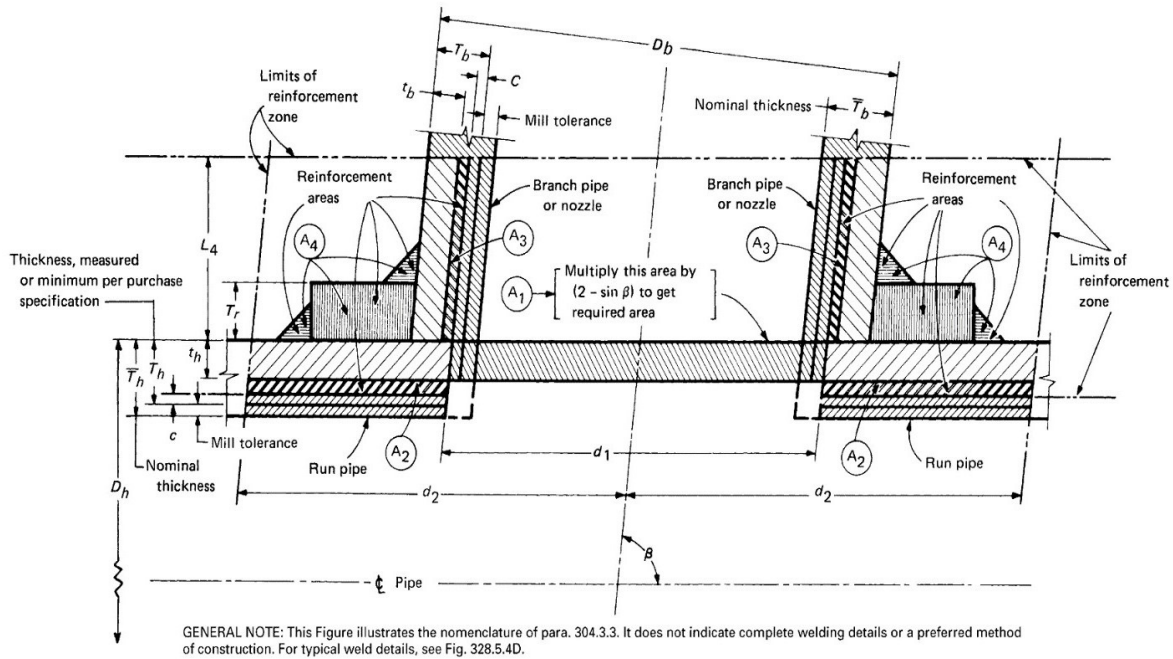


FIGURE 8: Branch connection reinforcement (ASME, 2002)

Reinforcement of branch connections is applicable for connections with a nominal diameter greater than $\frac{1}{4}$ of the nominal diameter of the run pipe.

$$d_1 = (d_b - 2(T_b - c))/\sin \beta \quad (22)$$

$$d_2 = d_1 \text{ or } (T_b - c) + (T_h - c) + d_1/2 \quad (23)$$

$$L_4 = 2.5 (T_h - c) \text{ or } (T_b - c) + T_r \quad (24)$$

$$A_1 = T_h d_1 (2 - \sin \beta) \quad (25)$$

$$A_2 + A_3 + A_4 \geq A_1 \quad (26)$$

where d_1 = Effective length removed from pipe at branch (m);
 d_2 = "Half width" of reinforcement zone (whichever is greater, but not greater than the diameter of run/header, D_h) (m);
 L_4 = Height of reinforcement zone outside of run pipe (m);

- T_b = Branch pipe thickness (measured or minimum per purchase specification) (m);
 T_r = Minimum thickness of reinforcing ring or saddle made from pipe (m);
 β = Smaller angle between axes of branch and run;
 A_1 = Required reinforcement area (m²);
 A_2 = Area resulting from excess thickness in the run pipe wall (m²);
 A_3 = Area resulting from excess thickness in the branch pipe wall (m²);
 A_3 = Area of other metal provided by welds and properly attached reinforcement (m²).

2.5 Mechanical stress analysis

A pipeline is subject to mechanical and thermal loads during its service life. This may be brought about by the effect of water moving inside the pipeline, thermal gradients and external effects of wind and seismic activities.

2.5.1 Allowable stress

The allowable stress (S) enables the calculation of the length between supports (L_s). The basis for the calculation of the allowable stress (Equation 27) is the yield limit ($R_{p/t}$) and the ultimate stress ($R_{m/T}$) at the calculated temperature. The values of the yield limit and ultimate stress differ from material to material.

$$S = \min \left(\frac{R_{m/T}}{3}, \frac{R_{m/h}}{3}, \frac{2R_{p/c}}{3}, \frac{2R_{p/h}}{3} \right) \quad (27)$$

$$S_h = \min \left(\frac{R_{m/h}}{3}, \frac{2R_{p/h}}{3} \right) \quad (28)$$

$$S_c = \min \left(\frac{R_{m/c}}{3}, \frac{2R_{p/c}}{3} \right) \quad (29)$$

- where S_h = Basic allowable stress during hot conditions (Pa);
 S_c = Basic allowable stress during cold conditions (Pa).

2.5.2 Sustained and occasional loads

According to the ASME B31.3 standards (2002), the design criteria for the distance between supports requires that the condition stated in Equation 30 be met for sustained loads:

$$\frac{PD_o}{(4t_m)} + (0.75i) \left(\frac{M_A}{Z} \right) \leq S_h \quad (30)$$

- where P = Design pressure (Pa);
 D_o = Outer diameter (m);
 t_m = Minimum thickness (m);
 i = Stress intensity factor, where $0.75i \geq 1.0$;
 M_A = Sustained bending moment (Nm);
 Z = Section modulus (m³).

Vertical sustained loads q_{sv} are a result of pipe weight, component weight and insulation weight and are calculated using Equations 31 to 33:

$$q_{sv} = q_p + q_e \quad (31)$$

$$q_p = \Pi g \rho_s \left(\frac{(D_o^2 - D_i^2)}{4} \right) \quad (32)$$

$$q_e = \Pi g \rho_e \left(\frac{(D_e^2 - D_o^2)}{4} \right) \quad (33)$$

where q_p = Pipe weight (N/m);
 q_e = Insulation weight (N/m);
 ρ_s = Density of steel (kg/m³);
 ρ_e = Density of insulation (kg/m³);
 D_e = Diameter of insulation (m).

The conditions in Equation 33 must be satisfied for occasional loads acting on a pipeline.

$$\frac{PD_o}{(4t_m)} + (0.75i) \left(\frac{M_A}{Z} \right) + (0.75i) \left(\frac{M_B}{Z} \right) \leq kS_h \quad (34)$$

where M_B = Dynamic bending moment (N/m);
 k = 1.20, if load is less than 1% of operational time;
= 1.15, if load is active for less than 10% of operational time and;
= 1.0 in other cases.

Vertical occasional loads (q_{ov} , Equation 35) are comprised of the weight of the medium (q_v , Equation 36) being transported, the snow weight (q_s , Equation 37, if applicable), and the seismic vertical load (q_{jv} , Equation 38):

$$q_{ov} = q_v + q_s + q_{jv} \quad (35)$$

$$q_v = \Pi g \rho_v \left(\frac{(D_i^2)}{4} \right) \quad (36)$$

$$q_s = 0.2SD_e \quad (37)$$

$$q_{jv} = 0.5eq_o \quad (38)$$

$$q_o = q_v + q_p + q_e \quad (39)$$

where S = Snow factor.

The horizontal occasional load (q_{oh} , Equation 40) acting on a pipeline is due to the wind load (q_w , Equation 41) and the horizontal seismic load (q_{jh} , Equation 42):

$$q_{oh} = \max(q_w + q_{jh}) \quad (40)$$

$$q_w = CpD_e \quad (41a)$$

and

$$p = \frac{v^2}{1.6} \quad (41b)$$

$$q_{jh} = eq_o \quad (42)$$

where C = Form factor;
 p = Wind pressure;
 v = Maximum wind speed (m/s);
 e = Seismic factor.

2.5.3 Length between supports

Pipe supports should be located at suitable points so as to support portions of the pipe weight and any other possible loads. The length between the supports should satisfy the conditions stated in Equation 43.

$$L_{sv}^2 \leq \left[kS_h - \frac{PD}{(4t_m)} \right] \frac{\left[\frac{\pi}{4} (D^4 - d^4) \right]}{\left[D(0.75i) \left\{ q_{sv} + (q_{ov}^2 + q_{oh}^2)^{1/2} \right\} \right]} \quad (43)$$

The horizontal length between supports depends upon the expansion arm. The conditions stated in Equation 44 should be met for both vertical constraint (L_{sv}) and horizontal constraint (L_{sh}):

$$\frac{PD}{(4t_m)} + (0.75i) \left\{ (q_{sv} L_{sv}^2) + ((q_{ov} L_{sv}^2)^2 + (q_{oh} L_{sh}^2)^2)^{1/2} \right\} / (8Z) \leq kS_h \quad (44)$$

2.6 Thermal stress analysis

Pipelines transporting hot water are subject to expansion, due to the temperature of the medium being conveyed. This expansion causes thermal stress along the pipeline. If this stress is not addressed and catered for during the design stage, it may lead to failure of the pipeline. It is also a good practise to design for flexibility since the pipe is constrained and its movement should be controlled. Jónsson (2014) suggested that the flexibility may be achieved by the use of expansion loops, expansion units and pre-stressed pipe. Thermal expansion along the pipe is calculated using Equation 45:

$$\Delta L = \alpha L \Delta T \quad (45)$$

and thermal strain (ϵ_x) is given by Equation 46:

$$\epsilon_x = \frac{\Delta L}{L} \quad (46)$$

where L = Pipe length (m);
 α = Coefficient of thermal expansion;
 ΔT = Temperature difference ($^{\circ}\text{C}$).

Thermal stress (σ_x) for a pipe with fixed ends is calculated using Equation 47:

$$\sigma_x = E \frac{\Delta L}{L} \quad (47)$$

Expansion loops may be symmetrical (Figure 9a) or asymmetrical (Figure 9b). Symmetrical expansion loops were considered in this study because leg H is used efficiently to absorb an equal amount of

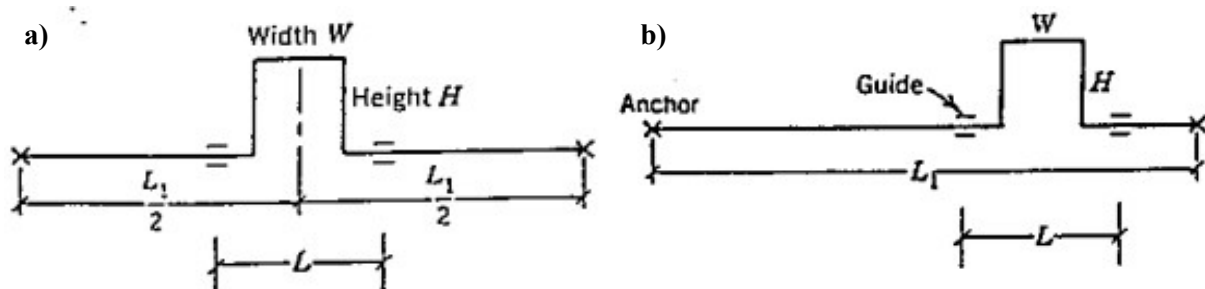


FIGURE 9: Expansion loops; a) Symmetrical; b) Asymmetrical

expansion from both directions (Kannappan, 1986). The total length (L_2) of the expansion loop may be determined from Figure 9a and is given by Equation 48:

$$L_2 = W + 2H \quad (48)$$

The M.W Kellogg chart (Appendix III) was used in the determination of stresses and loads on the expansion loop due to thermal expansion. Legs H and W are determined from Figure 10 and are given in Equations 49 to 50.

$$H = K_2 L \quad (49)$$

$$W = K_1 L \quad (50)$$

where K_1 and K_2 are constants which can be obtained from the ratios of leg W to the guide distance L , and leg H to the guide distance L , respectively. After using the M.W Kellogg chart to calculate the value of the Y-axis, given by Equation 51, the values of K_1 and K_2 are read from the chart:

$$Y - axis = \frac{L^2 S_A}{10^7 D \Delta} \quad (51)$$

where L = Length from A to B (Figure 10) (m);
 S_A = Code allowable stress range;
 D = Outside diameter of pipe (m);
 Δ = Expansion from A' to B' (Figure 10).

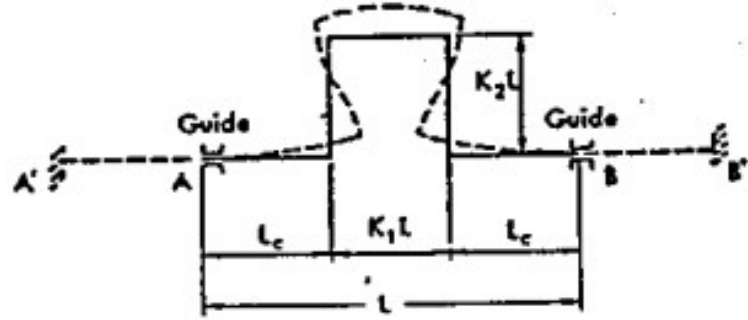


FIGURE 10: Stress and loads in a symmetrical expansion loop

2.7 Pump sizing

Pumps are sized depending on the flow rate required and the height of the lift. The capacity of the pump may be determined from pump curves which are developed by individual pump manufacturers. The curves basically show the performance characteristics based on varying flow rates and head. Pumps may be arranged in parallel or in series, depending on the flow and pressure requirements. The pump power required is also determined by the available static head and friction head, as shown in Figure 11. The frictional head (H_f) is calculated using Equation 13 and the static head is the elevation difference (ΔH)

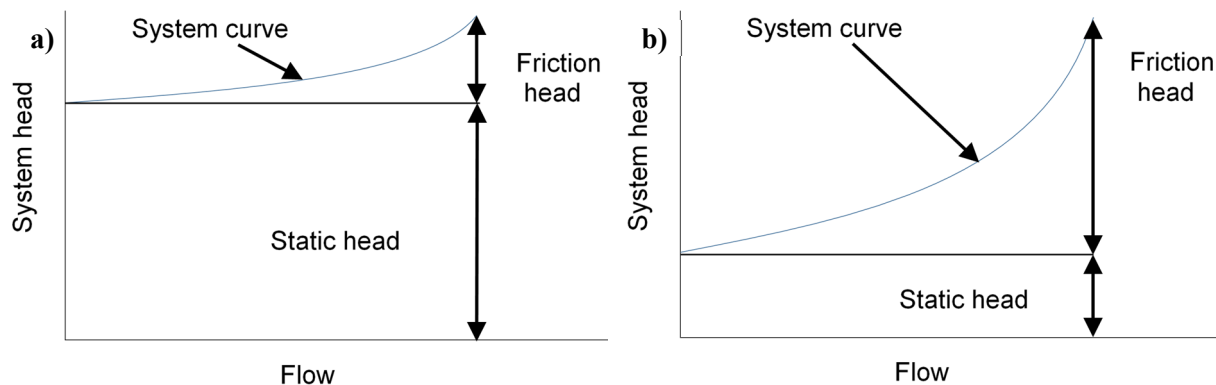


FIGURE 11: System characteristic with, a) Low friction head; and b) High friction head (modified from Jónsson, 2014)

from the lowest point to the highest point; therefore, the total system head (H_T) is given by Equation 52:

$$H_T = \Delta H + H_f \quad (52)$$

The total pump power (P_p) would then be given by Equation 53. Pumps are usually oversized to cater for possible future expansion of the system.

$$P_p = g\rho H_T Q / \eta \quad (53)$$

2.8 Heat exchanger sizing

Heat exchangers may either be of plate type or shell and tube type, and are used for heat exchange between a hot fluid and a cold fluid. Shell and tube heat exchangers are more pressure resistant than the plate type; it is for this reason that shell and tube heat exchangers were chosen for this study. Kakac et al. (2012) suggested a procedure for the design of shell and tube heat exchangers using Logarithmic Mean Temperature Difference (LMTD) method for heat exchanger analysis and includes the following steps:

- Establish the rate of heat transfer (Q) (Equation 7);
- Establish the Logarithmic Mean Temperature Difference (LMTD) (Equation 58) and obtain the correction factor (F) if necessary;
- Calculate the overall duty heat transfer coefficient (U) (Equation 56), assuming fouling to occur on one side;
- Determine area (A) from Equation 55.

$$Q = UA\Delta T_{lm} \quad (54)$$

$$Q = UAF\Delta T_{lm,cf} \quad (55)$$

$$\frac{1}{U} = \frac{1}{h_i} + R_{fi} + \frac{t}{k} + \frac{1}{h_o} \quad (56)$$

$$F = \phi(P, R, \text{Flow arrangement}) \quad (57)$$

$$LMTD = \frac{(T_{hot,in} - T_{cold,out}) - (T_{hot,out} - T_{cold,in})}{\ln \left(\frac{(T_{hot,in} - T_{cold,out})}{(T_{hot,out} - T_{cold,in})} \right)} \quad (58)$$

where ΔT_{lm} = LMTD ($^{\circ}\text{C}$);
 h_i = Inside heat transfer coefficient ($\text{W/m}^2 \text{ K}$);
 h_o = Outside heat transfer coefficient ($\text{W/m}^2 \text{ K}$);
 R_{fi} = Fouling factors;
 t = Wall thickness (m);
 k = Thermal conductivity (W/m K).

F is non-dimensional and depends upon temperature effectiveness, P , heat capacity ratio R , and the flow arrangement. Equation 54 can be used for multi-pass and cross-flow heat exchangers by multiplying ΔT_{lm} , which would be computed under the assumption of a counter-flow arrangement with a correction factor F as shown in Equation 55. LMTD correction factors for a shell and tube heat exchanger with two shell passes, or four or a multiple of four tube passes (Figure 12), may be obtained from charts in the Tubular Exchanger Manufacturers Association standards (TEMA, 1988).

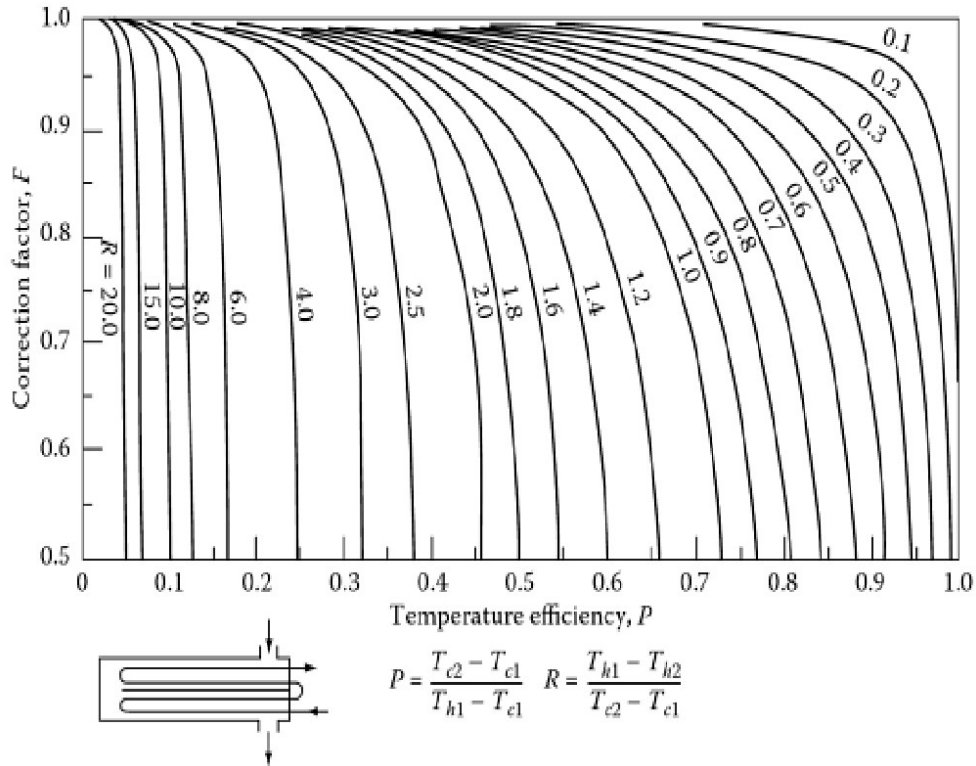


FIGURE 12: LMTD correction factors for a shell and tube heat exchanger with two shell passes, and four or a multiple of four tube passes

2.9 Expansion tank sizing

When cold water is heated up its volume increases; consequently, expansion tanks should be installed in hot water pressurized systems. Expansion tanks may either be pressurized or non-pressurized. The size of a closed expansion tank is determined by the volume of water in the system, system operating temperature, pressures in the system, and the location of the circulation pump. The expansion tank considered for this study is at atmospheric pressure, 30 m above the highest point on the pipeline. The volume of the expanded water (V_{exp}) is calculated using Equation 59; the size of the expansion tank ($V_{exptank}$) is given by Equation 60:

$$V_{exp} = V_p \frac{\rho_c}{\rho_h} \quad (59)$$

$$V_{exptank} = V_{exp} - V_p \quad (60)$$

where V_p = Volume in pipe (m^3);
 ρ_c = Density of cold water (kg/m^3);
 ρ_h = Density of hot water (kg/m^3).

3. PROPOSED DESIGN OF A HOT WATER DISTRIBUTION SYSTEM

The design consists of a closed loop circuit where water is heated up by the hot geothermal fluid in a shell and tube heat exchanger located at the first pumping station. The reason for this configuration was that the chemistry of the geothermal fluid from the field considered may not allow brine to be cooled below 90°C , without risk of silica scaling in the pipeline and in the re-injection wells. Brine is taken

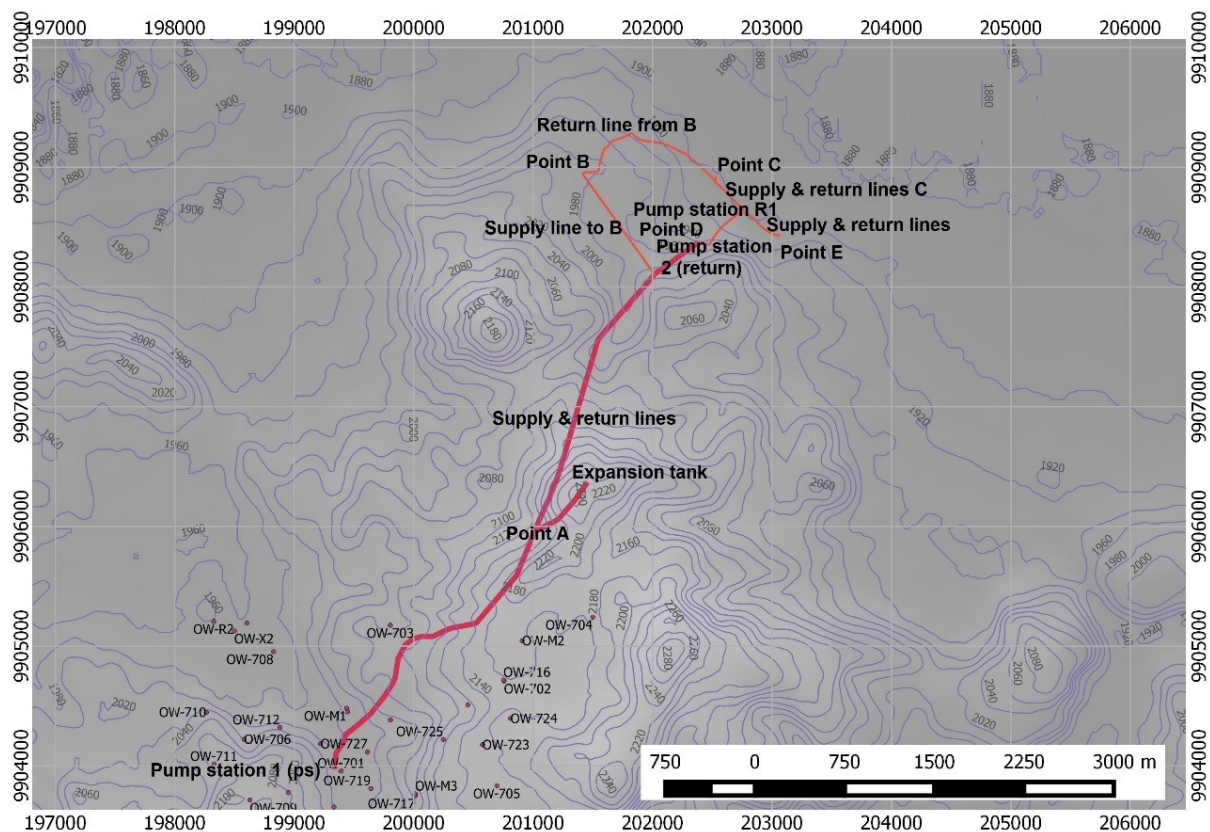


FIGURE 13: Site map showing the proposed flow path

directly from the re-injection line, then into the heat exchanger and back to the re-injection line. The system also has an expansion tank located along the pipeline at a distance of 30 m from the highest point on the pipeline. Make-up water for the main circuit should be topped up at pump station one. The pressure in line A-D is close to 30 bar. Shell and tube heat exchangers were considered at the end use points because they are more pressure resistant than plate type heat exchangers. In less steep areas, the pipeline may be buried underground. The return pipelines from points C, D and E follow the same path as the supply lines, except point B which would require a high-pressure pump capable of overcoming the pressure in the main return line, if the return line was to follow its supply line path. Therefore, the return flows to return line pumping station R1 (Figure 13). A schematic diagram of the proposed system is shown in Figure 14. An open loop circuit could have been considered as well, but this would have involved the setting up of a new water supply line and a water treatment plant, which could further increase the cost.

3.1 Design data

The pipeline is assumed to follow the already existing roads for ease of installation and maintenance. Figure 13 shows the site map with the proposed flow path. Pump station one is assumed to be located as near to the brine re-injection line as possible. Main supply and return lines are assumed to follow the same path, however, the return line from point B goes down the hill to connect with return lines from points C and E at return line pump station R1. The specifications for pipeline material, heat exchanger materials and expansion tank material used in this study are listed in Table 2. Polyurethane/Polyisocyanurate (PUR/PIR) insulation material may offer optimal insulation solution, compared to other insulation materials, due to their low thermal conductivity values and long term performance. Polyisocyanurate (PIR) has a higher hot surface performance temperature of 150°C while that of Polyurethane (PUR) is 110°C (Table 3). These insulation materials are CFC free and are suitable for large diameter pipelines, underground pipes and storage tanks (NGP Industries, 2014). Therefore, PIR pre-insulated insulated pipeline was selected for this study.

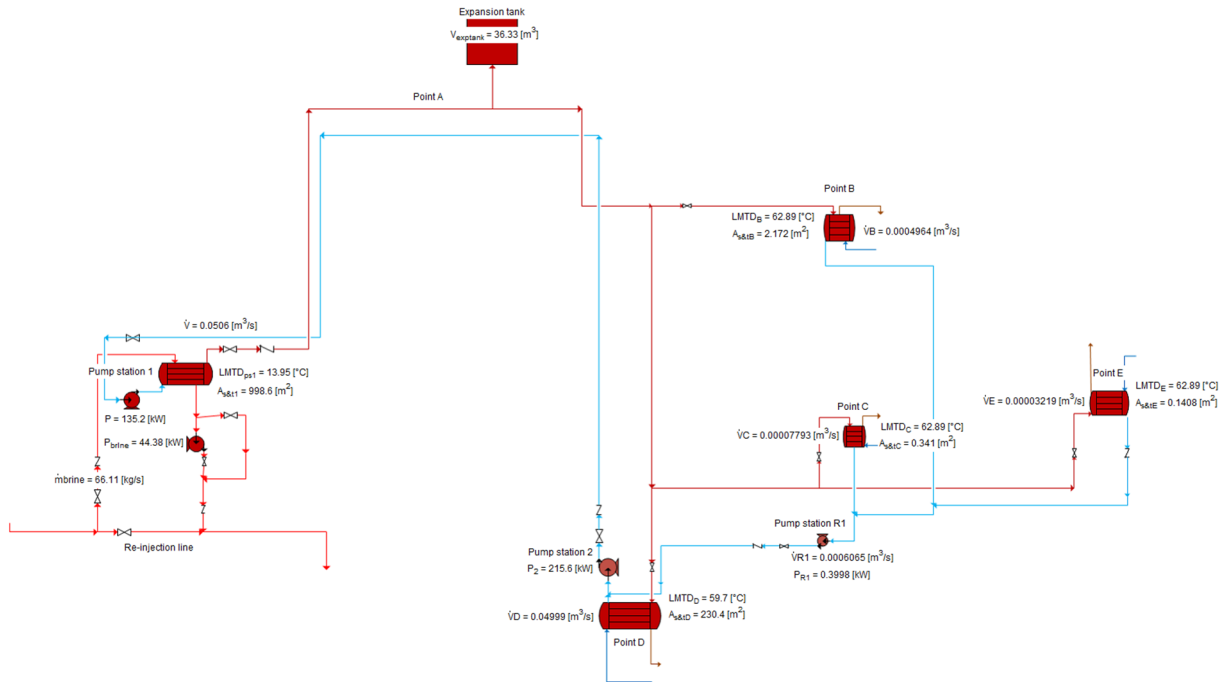


FIGURE 14: Schematic diagram of the distribution network

TABLE 2: Materials

Material	Type
Pipe material (pre-insulated)	S235
Heat exchanger tubes	SS316
Heat exchanger shell	S235
Insulation material	PIR

TABLE 3: Technical specifications for PUR/PIR insulation materials

Properties	Polyisocyanurate (PIR)	Polyurethane foam (PUR)
Density	$32 \pm 2 \text{ Kg/m}^3$	$36 \pm 2 \text{ Kg/m}^3$
Compression strength	172 KN/m^2	172 KN/m^2
Thermal conductivity	Max 0.021 W/mk	Max 0.021 W/mk
Temperature limit	$+ 150\text{-}200^\circ\text{C}$	$+ 110\text{-}180^\circ\text{C}$

Mean monthly values for weather data recorded from the Naivasha meteorological station (Mpusia, 2006) are shown in Figure 15. The mass flow rates for brine to the four hot re-injection wells in the Olkaria North East field are shown in Figure 6. Due to the limited available resource capacity, the entities shown in Table 4 were considered for this study. The maximum mean wind speed value from Figure 15 is 1.5 m/s . Typical values for overall duty heat transfer coefficient in shell and tube heat exchangers were referenced from Cheremisinoff and Cheremisinoff (1995). Branch connection pipes

TABLE 4: Sustainable demand

End use	Entity name	Point	Altitude (m)	Demand (MWt)
Residential houses	Kengen	B	1984	0.16
Residential houses	Orpower	C	1904	0.03
Hotels	Fish Eagle Inn	E	1906	0.01
Greenhouses	Plantation plants K, Ltd.	D	1946	16.37

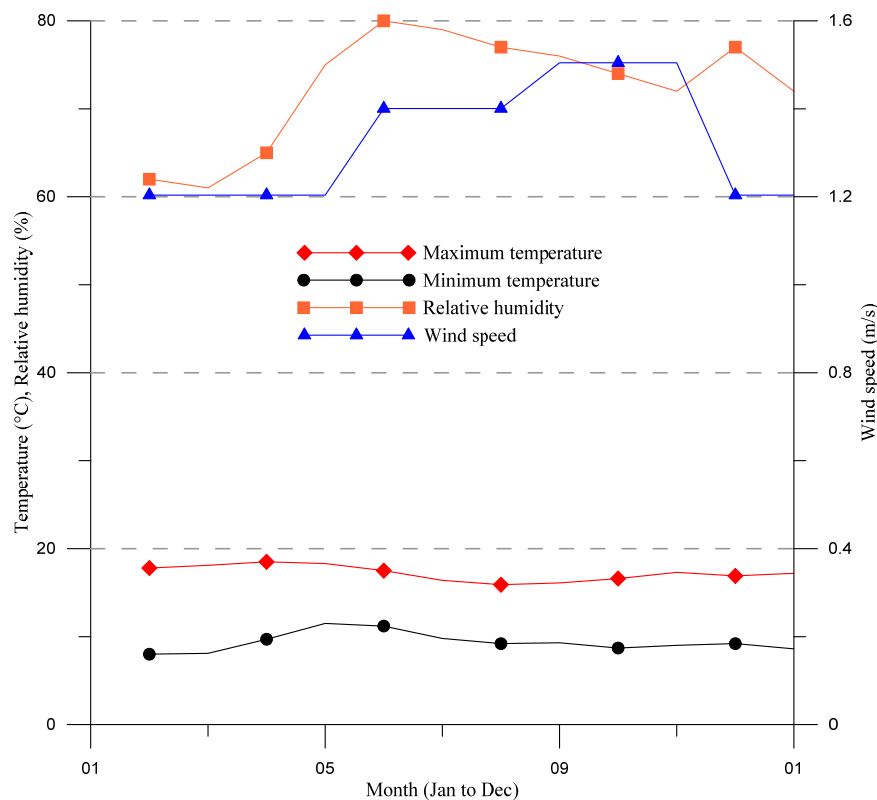


FIGURE 15: Mean monthly values for weather data in Naivasha

diameters were referenced from ASTM F681 – 82, (ASTM, 2008) (Standard practice for use of branch connections for fabricated joint, cut-in branch). The retail cost of electricity for industrial consumers of 0.072 USD/Kwh was picked from Kinyanjui et al. (2011). The altitude above sea level at pump station one is 2015 m, at pump station two it is 1946 m, at pump station R1 1901 m, and at point A 2211 m.

3.1.1 Assumptions

The assumptions made in the design are listed below:

- SI units were used in all calculations;
- Elevations of the various points were picked from Google Earth;
- Insulation thickness of 0.050 m;
- Additional thickness for milling and corrosion of 0.0015 m;
- Seismic factor of 0.24 for Olkaria;
- Pipe bend at every 60 m;
- Main circuit supply temperature of 145°C and a return temperature of 60°C;
- Combined motor and pump efficiency 77%;
- Cost of pipeline is in €/m and expansion tank is in €/m³ and are picked from cost of projects currently being handled by VERKIS Consulting Engineers, Iceland;
- Cost of pipe fittings, bends, pipe supports and civil works is included in the cost of pipeline;
- Cost of pump is in €/kW and includes cost of pump station house, piping and pump controls system;
- Cost of heat exchangers is in Euro/m² and is based on a study done by Reykjavik Energy;
- Cost of buried pipe to be equal to cost of above surface pipe;
- Cost uncertainty at this stage of design is estimated to be 20%;
- Cost of design and supervision 10%;
- Operation and maintenance cost: 4% for pumps and machinery with moving parts, 1% for pump stations civil structures and piping: 2% for heat exchangers: and 1% for rest of pipeline;
- Interest rate 6%;
- Distribution system life span of 30 years.

3.2 Results

The design model was generated from Engineering Equation Solver (EES) (see Appendix IV). From the model, two paths, A and B, were evaluated. The path with the lowest total updated cost was path A, as shown in Table 5; therefore, it was selected as the best path. The design of the system was done as per ASME B31.3 (2002). The design pressure for line ID Ps-A was 18 bar, while that of line ID A-D was 24 bar; therefore, pipes with pressure class PN 40 were selected. The allowable stress for hot conditions was 113 Mpa. The requested thickness obtained was 0.004 m and, comparing it with the nominal thickness of 0.005 m, satisfied the ASME B31.3 (ASME, 2002) condition for thickness and pressure class. The length between supports was 3.2 m; this condition was met. The results of the main circuit supply pipeline configuration are shown in Table 6, while those of the return pipeline are shown in Table 7. The results of the heat exchangers, expansion tank and pumping stations are shown in Table 8. An optimum pipe diameter for the main circuit supply and return lines was selected, after carrying out minimization of the total updated cost using different pipe diameters ranging from DN 100 to DN 500 with PN 40 as the pressure class. The pipe diameter which gave the lowest total updated cost is DN 200, as shown in Figure 16. From experience, it has been proven that the pressure drop in long pipelines should be around 10 mm/m; therefore, DN 200 was selected as the pipe diameter, satisfying all conditions by having a fluid velocity of 1.5 m/s, and a pressure drop of 13 mm/m.

TABLE 5: Route selection

Path	Description	Length supply pipe (m)	Length return pipe (m)	Diameter (mm)	Total up-dated cost (€)
A	Pump station across hill-point D	5610	5610	200	19,880,000
B	Pump station Olkaria road-point D	10200	10200	200	26,600,000

TABLE 6: Main circuit supply pipe line

Line ID	Length (m)	Diameter (mm)	Unit cost (€/m)	Cost (€)
Brine pipe	200	200	344	68,800
Ps - A	2400	200	344	825,600
A - D	3210	200	344	1,104,240
Expansion Tank connection pipe	457	200	344	157,208
Branch connection B	1260	100	180	226,800
Branch connection C	444	65	70	31,080
Branch connection E	474	65	70	33,180
Total				2,446,908

TABLE 7: Main circuit return pipe line

Line ID	Length (m)	Diameter (mm)	Unit cost (€/m)	Cost (€)
E-D	474	65	70	33,180
D-Ps	5610	200	344	1,929,840
Branch connection C, return	444	65	70	31,080
Branch connection B, return	1770	100	180	318,600
Return pipe R1	646	40	43	27,778
Total				2,340,478

TABLE 8: Heat exchangers, expansion tank and pumps

Item	Size	Unit	Unit cost (€/unit)	Cost (€)
Heat exchanger at ps1	998.6	m ²	500	499,300
Heat exchanger at B	2.172	m ²	500	1,086
Heat exchanger at C	0.341	m ²	500	170
Heat exchanger at D	230.4	m ²	500	115,200
Heat exchanger at E	0.1408	m ²	500	70.4
Expansion tank	36.33	m ³	500	18,165
Pump station 1, pump 1	135.2	kW	3500	473,200
Pump station 1, pump 2	44.38	kW	3500	155,330
Pump station R 1	0.3998	kW	3500	1,399
Pump station R 2	215.6	kW	3500	754,600
Total				2,018,521

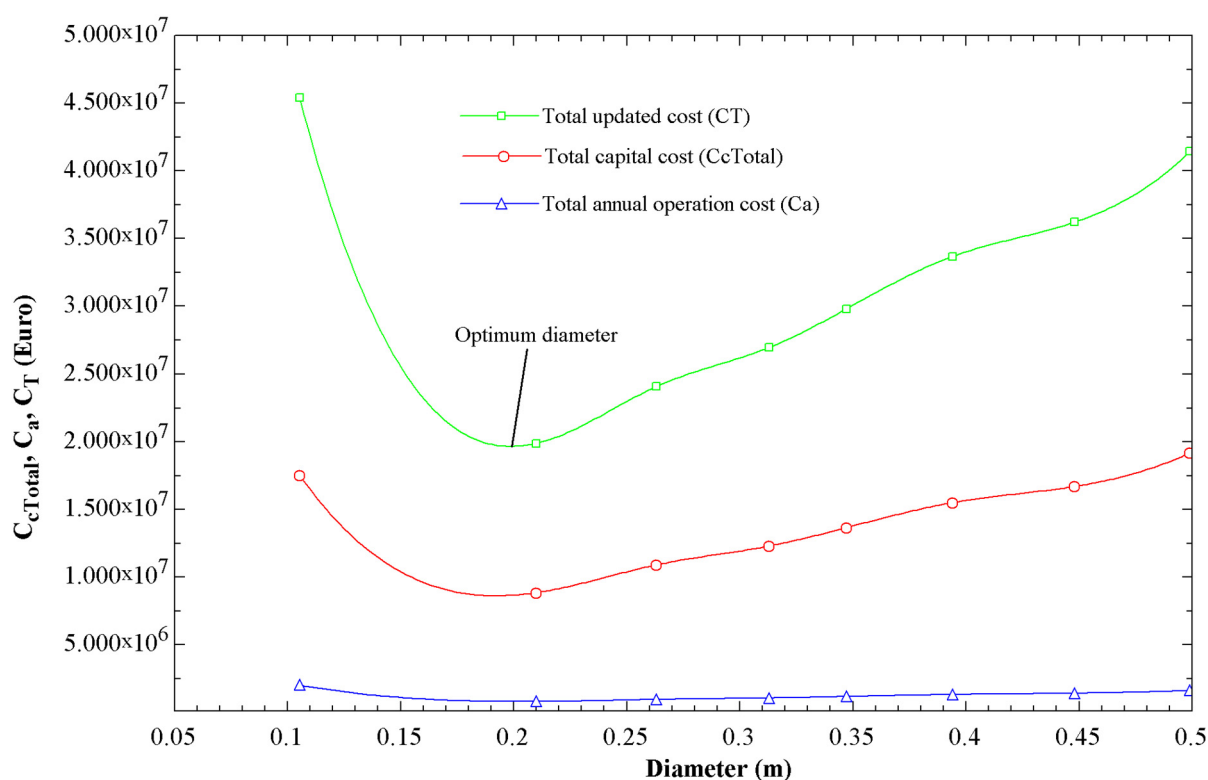


FIGURE 16: Optimum diameter selected based on minimum total updated cost

The total cost for the main circuit supply pipeline is €2,446,908 and for the return pipeline is €2,340,478. The total cost for the pumping stations is €1,384,529, for the heat exchangers is €615,827, and €18,165 for the expansion tank. The subtotal for the project is €6,805,907. Additional costs include € 680,591 for design and supervision, and € 1,361,181 for uncertainty (Figure 17). The grand total cost for the whole project is € 8,847,679.

3.3 Production cost analysis

The total project cost was further used to project the cost of heat per MWh. Annual operation and maintenance cost were calculated by the model developed in EES, as shown in Table 9. The maximum number of hours for full capacity operation was taken to be 10 hours per day, giving an annual

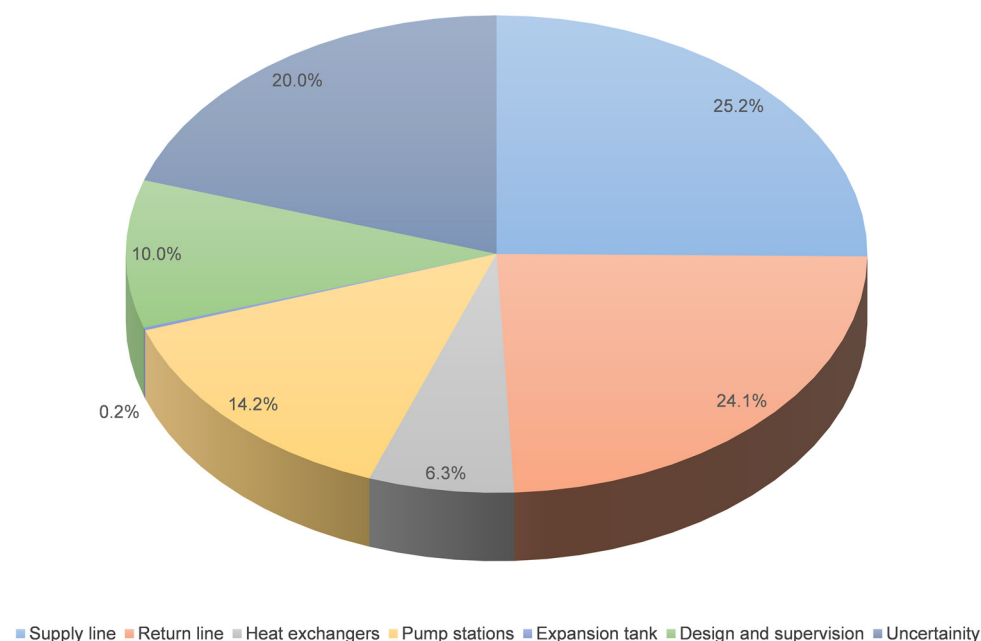


FIGURE 17: Percentage distribution of project cost

production of heat of 60,520 MWh/year. The heating capacity used is 16.58 MWt. The unit production cost of heat obtained is 13.24 €/MWh.

TABLE 9: Production cost

Item	Cost, €	Remarks
Capital cost		
Pipeline	4,787,386	Inclusive of pipe fittings, bends, insulation, valves, pipe supports and civil works
Heat exchangers	615,827	
Pump stations	1,384,529	Inclusive of pumps, controls, piping and civil structures
Expansion tank	18,165	Inclusive of construction materials and civil works
Design and supervision	680,591	
Uncertainty	1,361,181	
Total capital cost	8,847,679	
Annual operation and maintenance cost		
Pumps and moving parts	5,537	4% of pump and moving parts cost (about 10% of pump station cost)
Pump station pipi. & civil struct.	12,459	1% of pump station cost
Heat exchang. & expansion tank	12,317	2% of total hx cost
Main pipeline	48,056	1% of pipeline cost
Cost of capital, PMT	642,755	I is 6% and N is 30 years
Cost of electricity	80,035	10 h. daily operation, 0.072 USD/kWh which is equivalent to 0.0544 €/kWh at exchange rate of 1 USD=0.77 €
Total annual cost	801,158	
Capacity for heating, MWt	16.6	
Duration operation, oh, h./year	3650	10 hours of operation per day
Annual production of heat, MWh/year	60,520	
Unit production cost heat, kWh	1.354	€cents/kWh
Unit production cost of heat, MWh	13.24	€/MWh

4. CONCLUSIONS

The available energy extractable from geothermal brine from the North East field may not be adequate to satisfy heating requirements for all greenhouses within 30 km from Olkaria. The available resource may only satisfy 78% of the total heating requirements for the selected greenhouse complex. However, the resource may fully satisfy the hot water supply requirements for the three housing estates and one hotel considered in the study.

The results of the route selection showed that route A has the least total updated cost, compared to route B, and was therefore selected as the best route.

The results for diameter optimization showed that the suitable pipeline for the distribution network should have a diameter of DN 200 with a pressure class PN 40. The pressure drop obtained for the distribution network was 13 mm/m, and a fluid velocity of 1.5 m/s. The ASME B 31.3 (ASME, 2002) conditions for thickness and pressure class, length between supports and allowable stress were all satisfied.

A closed loop heating system is more suitable than an open loop system, due to the limitations of silica scaling. The shortest distance to the greenhouse complex considered in the study is around 5.6 km across the hill. The total capital cost for the distribution network is € 8,847,680, thus placing the unit production cost of heat at 13.24 €/MWh.

ACKNOWLEDGEMENTS

I thank the UNU-GTP management, especially the Director, Mr. Lúdvík S. Georgsson, for the opportunity to attend the 2014 fellowship programme. My acknowledgement also goes to my project supervisor, Mr. Óskar Pétur Einarsson of VERKÍS Consulting Engineers, for his continuous guidance and assistance in the project work. I also thank Mrs. María S. Guðjónsdóttir, Ms. Málfríður Ómarsdóttir, Mr. Ingimar G. Haraldsson, Mr. Markús A.G. Wilde and Ms. Thórhildur Ísberg, for their support throughout the entire training period. I also thank my fellow colleagues, who offered support in one way or another. My special thanks go to my employer, KenGen, for nominating me to attend the UNU-GTP programme.

I appreciate my family, Thecla and Ryan, for the moral support they gave me during the entire training period. My deepest thanks goes to the Almighty God for enabling me to successfully complete the training.

REFERENCES

- ASHRAE, 2008: *District heating and cooling*. American Society of Heating, Refrigerating and Air-Conditioning Engineers (ASHRAE) Inc., Atlanta, GA, 355 pp.
- ASME, 2002: *ASME code for pressure piping*. ASME B31.3–2002, revision of ASME B31.3-1999.
- ASTM, 2008: *Standard practice for use of branch connections*. ASTM F681 – 82.
- BS, 2006: *Design, installation, testing and maintenance of services supplying water for domestic use within buildings and their curtilages – Specification*. BS 6700:2006 (3rd edition).
- Cheremisinoff, P.N., and Cheremisinoff, N.P., 1995: *Process engineering data book*. Technomic Publishing Co., Inc., Lancaster, PE, 345 pp.

Guerra G., C.E., and Jacobo P.E., 2012: pH modifications for silica control in geothermal fluids. Presented at “Short Course on Geothermal Drilling, Resource Development and Power Plants”, UNU-GTP and LaGeo, San Salvador, El Salvador, 9 pp.

Jónsson, M.Th., 2014: *Pipe design*. UNU-GTP, Iceland, unpublished lecture notes.

Kakac, S., Liu, H., and Pramuanjaroenkij, A., 2012: *Heat exchangers selection, rating and thermal design*. Taylor and Francis Group, NY, USA, 150 pp.

Kannappan, P.E.S, 1986: *Introduction to pipe stress analysis*. John Wiley & Sons, Inc., NY, 255 pp.

Kinyanjui, B., Kibiru, G., Wasioya, B., Kiruja, E., Akuto, S., Simiyu, T., Nabaala, A., Mungai, K., Mabea, G., Mworira, B., Karembu, A., Kariuki, D., Kariuki, G., Cheboi, S., Kirui, S., Musyoka, B., Njeru, G., Njiraini, W., 2011: *Updated least cost power development plan, study period: 2011-2031*. Republic of Kenya, 203 pp.

Kjaernested, S.N., Jónsson, M.T., Pálsson, H., 2011: A methodology for optimal geothermal pipeline route selection with regards to visual effects using distance transform algorithms. *Proceedings of the 36th Workshop on Geothermal Reservoir Engineering, Stanford, CA*, 10 pp.

Lagat, J., 2010: Direct utilization of geothermal resources in Kenya. *Proceedings of the World Geothermal Congress 2010, Bali, Indonesia*, 7 pp.

Líndal, B., 1973: Industrial and other applications of geothermal energy. In: Lund et al. (2005), *World-wide direct uses of geothermal energy. Proceedings of the World Geothermal Congress 2005, Antalya, Turkey*, 20 pp.

Mangi P., 2013: Direct utilization in Kenya – A case of geothermal spa and demonstration centre at Olkaria, Kenya. Presented at “Short Course VIII on Exploration for Geothermal Resources”, UNU-GTP, KenGen and GDC, Naivasha, Kenya, 14 pp.

Mburu M., 2010: Feasibility study on direct utilization of energy from geothermal brine - a case study of Olkaria geothermal power plant, Kenya. *Proceedings of the World Geothermal Congress 2010, Bali, Indonesia*, 9 pp.

Mburu M., 2014: Geothermal energy utilization at Oserian flower farm Naivasha, Kenya. Presented at “Short Course VI on Utilization of Low- and Medium-Enthalpy Geothermal Resources and Financial Aspects of Utilization”, organized by UNU-GTP and LaGeo, Santa Tecla, El Salvador, 6 pp.

Mpusia, P.T., 2006: *Comparison of water consumption between greenhouse and outdoor cultivation*. International Institute for Geo-Information Science and Earth Observation, Enschede, Netherlands, MSc thesis, 86 pp.

NGP Industries, 2014: *Technical specifications for PUF/PIR pipe sections*. NGP Industries Ltd., webpage: www.ngpil.com/puf_products.php.

Onyango S.O., 2012: Preliminary design of the Menengai phase I steam gathering system. Report 26 in: *Geothermal training in Iceland 2012*. UNU-GTP, Iceland, 601-641.

Panagiotou, C., 1996: Geothermal greenhouse design. Report 11 in: *Geothermal training in Iceland 1996*. UNU-GTP, Iceland, 219-250.

TEMA, 1988: *Standards of the tubular exchanger manufacturers association*. TEMA.

Wambugu J.M., 1996: Assessment of Olkaria North-East geothermal reservoir, Kenya, based on well discharge chemistry. Report 20 in: *Geothermal training in Iceland 1996*. UNU-GTP, Iceland, 481-509.

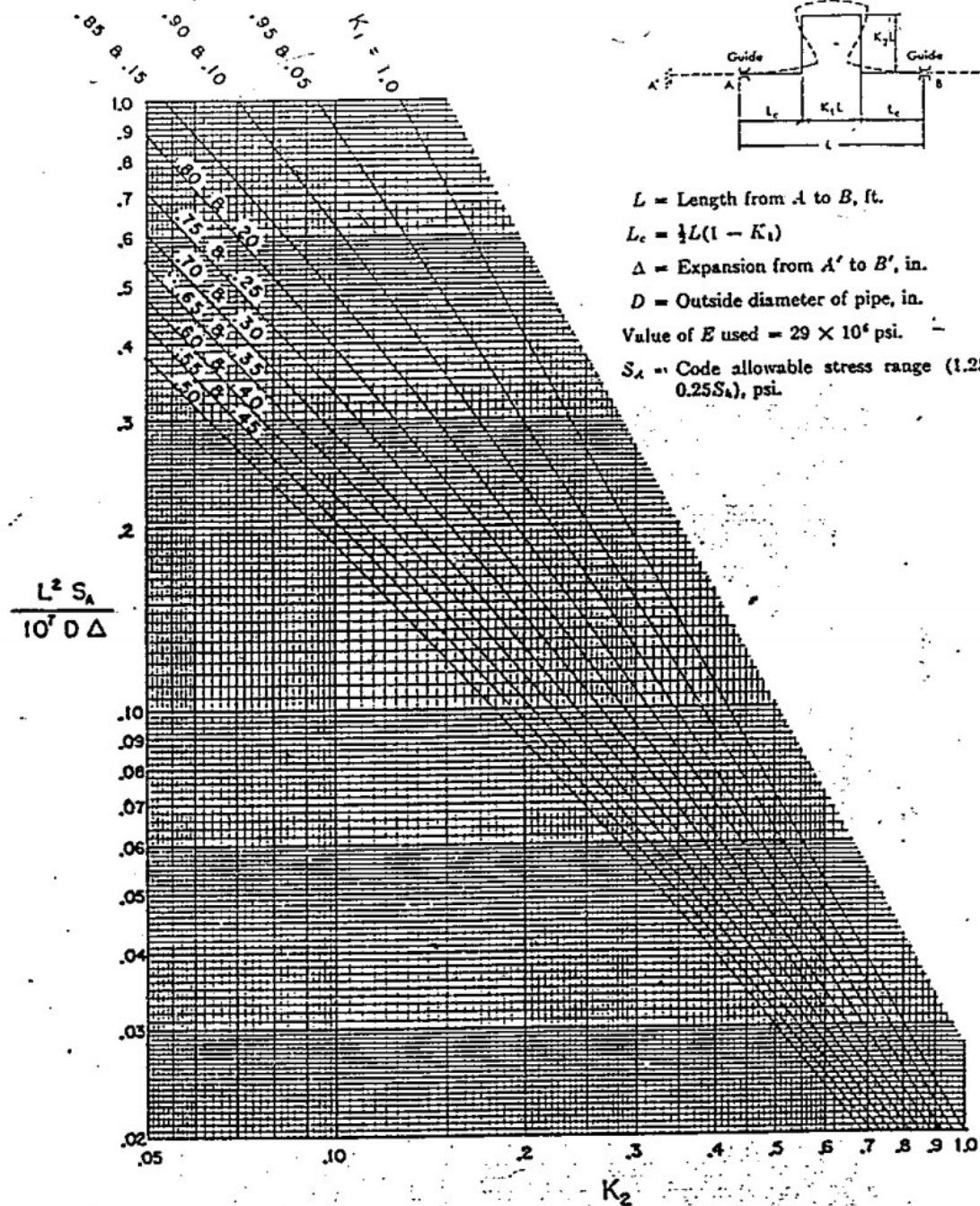
Appendix I: Greenhouse thermal resistance values (modified from Panagiotou, 1996)

Thermal resistance		m²°C/W
Greenhouse thermal resistance caused by air infiltration, R_{vcover} (DN 4701)	<i>Cover material</i>	
	Glass in putty	1.0
	Plastic film greenhouse	2.0
	Plastic tent (tunnel)	2.0
	Putty less glazing in metal frame with rubber gaskets	1.0
Greenhouse thermal resistance by conduction, $R_{\lambda cover}$ (DN 4701)	Single glass	0.01
	Plastic panel corrugated GFK 1 mm	0.01
	Double glass in steel frame	
	Space 15 mm	0.14
	Space 12 mm	0.11
	Space 6 mm	0.09
	Double poly frameless	
	Space 12 mm	0.15
	Space 5 mm	0.08
	Double plastic film, space 10 mm	0.10
Greenhouse thermal resistance by outside convection, R_{ocover} , as a function of wind speed (DN 4701)	Single plastic film (PVC, PE) thickness of 0.2 mm	0.01
	<i>Wind speed (m/s)</i>	
	1	0.102
	2	0.0725
	3	0.0562
	4	0.0459
	5	0.0388
	6	0.0307
	7	0.0346
	8	0.0277
Greenhouse thermal resistance by inside convection, R_{icover} (DN 4701)	9	0.0252
	10	0.0232
	<i>Heating system</i>	
	Pipes suspended from the ceiling	0.09
	Pipes on the walls	0.09
	Pipes under the raised tables	0.01
	Pipes on the floor between plots	0.12
	Fan coil units	0.09
	Unit heaters	0.01
	Finned pipes	0.09
	Combination of the above	0.1

BRANCH SIZE (NPS), in.

[illegible]

APPENDIX III: M.W. Kellogg chart



APPENDIX IV: EES model

```

{Demand analysis}
A_GSA=245000 {Greenhouse surface area}
T_ireqd=20 {Minimum required temperature inside greenhouse}
T_oreqd=8 {Minimum outside temperature}
Delta_Tgrhse=T_ireqd-T_oreqd
R_vcouver=2 {Thermal resistance by air infiltration, greenhouse with plastic cover}
R_ocouver=0.0873 {Thermal resistance by outside convection, at max air speed of 1.5 m/s}
R_lamdacover=0.01 {Thermal resistance by conduction, single plastic with 0.2 mm thickness}
R_icouver=0.10 {Thermal resistance by inside convection, pipe installation below ceiling and on floor between plots}
R_kcover=R_ocouver+R_lamdacover+R_icouver {Overall thermal resistance}
Q_t=A_GSA*Delta_Tgrhse/R_kcover {Transmission losses through roof and walls}
Q_i=A_GSA*Delta_Tgrhse/R_vcouver {Infiltration losses}
Q_TotalD=Q_t+Q_i {Total heat losses/heating requirement}
V_dotD=Q_TotalD/(Rho_TD*C_pw*(T_3-T_9)) {Volume flow rate required at point D}
n_hsB=293
n_oc=6 {Assuming 6 occupants per house}
V_dotperperson=0.0000005 {BS 6700 recommendation}
rho_T11=Density(Water,T=T_11,x=0)
Q_RqdB=n_hsB*n_oc*V_dotperperson*(T_11-T_10)*C_pw*Rho_T11
V_dotB=Q_RqdB/(Rho_TB*C_pw*(T_3-T_9))
n_hsC=46
rho_T13=Density(Water,T=T_13,x=0)
Q_RqDC=n_hsC*n_oc*V_dotperperson*(T_13-T_12)*C_pw*Rho_T13
V_dotC=Q_RqDC/(Rho_TC*C_pw*(T_3-T_9))
n_hsE=57
n_ocE=2
rho_T17=Density(Water,T=T_17,x=0)
Q_RqdE=n_hsE*n_ocE*V_dotperperson*(T_17-T_16)*C_pw*Rho_T17
V_dotE=Q_RqdE/(Rho_TE*C_pw*(T_3-T_9))
Q_Total=Q_TotalD+Q_RqdB+Q_RqDC+Q_RqdE
V_dot=V_dotD+V_dotB+V_dotC+V_dotE {Volume flow rate from PS to A}

{Pipeline portion one- PS to Point A}
H_ps=2015 "m" {pumping station altitude}
H_A=2211 "m" {altitude at point A}
Delta_H1=H_A-H_ps "m"
L_pstoA=2400 "m" {length of pipe segment from pumping station to point A}
T_fluid=150 "°C"
DN_1=0.210 {Taking DN 200}
DN_1=D_innxtstd
rho=Density(Water,T=T_fluid,x=0)
g=9.81 "m/s^2"
P_design1=rho*g*Delta_H1

{Pipe thickness and mechanical stress analysis}
V_fluid=V_dot/(pi*(DN_1)^2/4)
D_o=0.219 "m" {Taking next std nominal pipe dia of 250mm}
E=0.85 {welding factor for arc weld butt weld}
y=0.4 {Temperature dependent coefficient for steels for <480°C}
R_m@T=340 "MPa" {Ultimate stress of steel S235}
R_p@50=235 "MPa" {Yield stress of steel S235 with fluid at 50°C}
R_p@200=185 "MPa" {Yield stress of steel S235 with fluid at 200°C}
R_p@150=R_p@50+(R_p@200-R_p@50)/(200-50)*(150-50) "MPa" {Yield stress of steel S235 with fluid at 150°C}
S_basic1=min(R_m@T/3,R_p@50/1.5,R_p@150/1.5) "MPa" {Basic allowable stress}
S_h1=min(R_m@T/3,R_p@150/1.5) "MPa" {Allowable stress hot}
A_thickness=0.0015 "m" {Assumed additional thickness for milling and corrosion}
t_m1=P_design1*D_o/(2*(S_basic1*1000000*E+P_design1*y))+A_thickness "m" {requested thickness}

```

```

t_n=0.0045 "m" {thickness}
{Length between supports}
t_e=0.050 "m" {Assumed insulation thickness} {confirm}
D_ins1=D_o+2*t_e "m" {insulation diameter}
rho_steel=7850 "kg/m3" {Steel density}
rho_ins=830 "kg/m3" {Insulation density}
C=0.6 {Form factor for pipe}
v_w=1.5 "m/s" {Maximum wind speed Naivasha}
e_factor=0.24 {Seismic factor}
q_p=pi*g*rho_steel*((D_o)^2-(D_innxtstd)^2)/4 "N/m" {Pipe weight}
q_e=pi*g*rho_ins*((D_ins1)^2-(D_o)^2)/4 "N/m" {insulation
weight}
q_sv=q_p+q_e "N/m" {Vertical sustained load}
q_w=pi*g*rho*((D_innxtstd)^2)/4 "N/m" {Water weight}
q_jv=0.5*e_factor*(q_w+q_p+q_e) "N/m" {Seismic vertical load}
q_ov=q_w+q_jv "N/m" {Vertical occasional/dynamic load}
q_wind=C*((v_w)^2)/1.6*D_ins1 "N/m" {Wind load}
q_sh=e_factor*(q_w+q_p+q_e) "N/m" {Seismic horizontal load}
q_oh=q_wind+q_sh "N/m" {Horizontal occasional load}
(L_s1)^2=((S_h1*1000000-P_design1*D_o/(4*t_m1))*(pi/4*((D_o)^4-
(D_innxtstd)^4))/(D_o*(q_sv+((q_ov)^2+(q_oh)^2)^0.5)))^0.5 "m" {Length between supports, load factor k
taken as 1, stress intensity factor 0.75i=1 for straight pipe}
Z=pi/32*(D_o^4-D_innxtstd^4)/D_o
M_A1=q_sv*(L_s1)^2/8 {Sustained bending moment}
M_B1=(q_ov^2+q_oh^2)^(1/2)*(L_s1)^2/8 {Occasional bending moment}
W_sust=P_design1*D_o/(4*t_m1)+M_A1/Z {Condition for sustained loads, W_sust<=kS_h1}
W_occas=W_sust+M_B1/Z {Condition for occasional loads, W_occas<=kS_h1}

{Pressure drop due to friction along the pipe}
mu=Viscosity(Water,T=T_fluid,x=0) {absolute viscosity}
R_e=rho*V_fluid*D_innxtstd/mu
eps=0.0005 {roughness to cater for minor losses}
f=0.25/(log10((eps/D_innxtstd)/3.7+5.74/R_e^0.9))^2 {Friction factor}
n_b1=L_pstoA/60 {No. of bends}
n_v=2 {No. of valves}
n_u=0 {No. of T units}
n_c=0
h_b = 20*D_innxtstd {Equivalent length of bends}
h_c = 20*D_innxtstd
h_u = 20*D_innxtstd
h_v = 10*D_innxtstd
alpha=12.75*10^(-6) "1/°C" {Coefficient of thermal expansion for carbon steel at 150°C}
L_e=(L_pstoA+n_b1*h_b*D_innxtstd+n_c*h_c*D_innxtstd+n_u*h_u*D_innxtstd+n_v*h_v*D_innxtstd)
{Second equivalent length}
H_f=f*V_fluid^2*L_e/(2*g*D_innxtstd) {Head loss due to friction}
Delta_pdrop1=H_f*1000/L_pstoA {Pressure drop in mm/m}

{Pump power, pump station 1}
P_p=(Delta_H1+H_f)*rho*g "Pa" {Pump pressure}
eta_motor = lookup('Properties',2,'Column3')
eta_pump = lookup('Properties',1,'Column3')
eta=eta_motor*eta_pump
P=rho*g*(H_f+Delta_H1)*V_dot/eta/1000
P_ps1=P
L_brpipe=100 {Assumed}
p_inj=50 {Pressure in re-injection line is around 5 bar equivalent to 50m head}
rho_brine=Density(Water,T=T_2,x=0)
V_brine=(m_dotbrine/rho_brine)/(pi*(DN_1)^2/4) {velocity of return brine}
H_fbrpu=f*V_brine^2*L_brpipe/(2*g*D_innxtstd)
P_pbrnepu=H_fbrpu+p_inj {Brine pump pressure}
P_brpu=rho_brine*g*P_pbrnepu*(m_dotbrine/rho_brine)/eta/1000

```

```

P_brln=P_brpu
c_p=lookup('Price table (Euro)',2,'Unit cost')
c_b=lookup('Price table (Euro)',3,'Unit cost')
c_cn=0
c_u=0
n_pu1=1
c_v=0
c_pu=lookup('Price table (Euro)',8,'Unit cost')
c_pu1=P_ps1*c_pu
c_pubrln=P_brln*c_pu
c_ins=lookup('Price table (Euro)',11,'Unit cost')
c_exptk=lookup('Price table (Euro)',12,'Unit cost')
c_pipelnepsA=(L_pstoA+L_connpipe+L_brpipe*2)*c_p+n_b1*c_b+n_c*c_cn+n_u*c_u+
n_v*c_v+L_pstoA*c_ins+V_exptank*c_exptk
c_ps1=n_pu1*c_pu1+c_pubrln
c_hx1=A_s&t1*c_s&thx
C_c1=c_pipelnepsA+c_ps1+c_hx1

{Thermal expansion in pipes}
E_y=YoungsModulus(Carbon_steel, T=T_fluid) "Gpa"
T_cold=20
delta_T= T_fluid - T_cold
delta_L = alpha * L_pstoA* delta_T
epsilon_x = alpha/delta_T
Sigma_x = E_y*10^9 * epsilon_x
A_1 = pi*D_innxtstd*L_pstoA
F_a = A_1 * Sigma_x

{U_shape expansion loop}
Sc = min(R_m@T/3 , R_p@20/1.5 )
R_p@20=R_m@T+(R_p@50-R_m@T)/(50-0)*(20-0)
f_stress=0.3 {stress reduction factor for the maximum no. of displacement cycles ASME B31.3}
S_A=f_stress*(1.25*Sc + 0.25*S_h1)*1000000 {Allowable displacement stress range}
L_c=L_s1
K_1=0.5 {assumed}
L_c=1/2*L_x*(1-K_1)
Y_axis=(L_x)^2*S_A*0.000145038/10^7*D_o*delta_L {S_A converted to PSI for easy reference in the Kellogg
chart}
K_2=0.098 {As read from Kellogg chart}
W_loop=K_1*L_x
H_loop=K_2*L_x
L_loopbend=W_loop+2*H_loop {Total length of the U-expansion loop}

{Portion two- Point A to point D}
L_pstoD=5610 "m"
L_AtoD=L_pstoD-L_pstoA
L_bcB=1260
L_bcC=444
L_bcE=474
L_DtoR1=646
H_D=1946"masl" {altitude at point D}
Delta_H2=H_A-H_D
P_design2=rho*g*Delta_H2
n_b2=L_AtoD/60 {No. of bends}
n_u2=4 {No. of T units}
t_m2=P_design2*D_o/(2*(S_basic1*1000000*E+P_design2*y))+A_thickness "m" {requested thickness}
(L_s2)^2=((S_h1*1000000-P_design2*D_o/(4*t_m2))*(pi/4*((D_o)^4-
(D_innxtstd)^4))/(D_o*(q_sv+((q_ov)^2+(q_oh)^2)^0.5)))^0.5
L_e2=L_AtoD+n_b2*h_b*D_innxtstd+n_c*h_c*D_innxtstd+n_u2*h_u*D_innxtstd+n_v*h_v*D_innxtstd
H_f2=f*V_fluid^2*L_e2/(2*g*D_innxtstd)
Delta_pdrop2=H_f2*1000/L_AtoD {Pressure drop in mm/m}
c_bcp1=lookup('Price table (Euro)',6,'Unit cost')

```

```

c_bcp2=lookup('Price table (Euro)',7,'Unit cost')
c_s&thx=lookup('Price table (Euro)',10,'Unit cost')
c_pipelineAE=L_AtoD*c_p+L_bcB*c_bcp1+(L_bcC+L_bcE)*c_bcp2+n_b2*c_b+n_u2*c_u+n_v*c_v+
L_AtoD*c_ins
c_hx2=A_s&tB*c_s&thx+A_s&tC*c_s&thx+A_s&tD*c_s&thx+A_s&tE*c_s&thx
C_c2=c_pipelineAE+c_hx2

{Return pipeline}
DN_9=DN_1
T_9=60
Rho_T9=Density(Water,T=T_9,x=0)
Delta_HDtoA=H_A-H_D
n_b3=(L_DtoA+L_Atops)/60
n_u3=0
n_v3=2
L_e3=L_Totalrtnmain+n_b3*h_b*D_innxtstd+n_c*h_c*D_innxtstd+n_u2*h_u*D_innxtstd+n_v3*h_v*D_innxt
std
H_f3=f*V_fluid^2*L_e3/(2*g*D_innxtstd)
Delta_pdrop3=H_f3*1000/(L_Totalrtnmain) {Pressure drop in mm/m}
P_pretm=rho*g*(H_f3+Delta_HDtoA) {Pump pressure return line}
P_2=Rho_T9*g*(H_f3+Delta_HDtoA)*V_dot/eta/1000
P_ps2=P_2+P_R1
mu_R1=Viscosity(Water,T=T_9,x=0) {absolute viscosity}
DN_R1=0.0409 {DN 40}
V_R1=V_dotR1/((pi*DN_R1^2)/4) {Velocity of return pipe 1}
R_eR1=Rho_T9*V_R1*DN_R1/mu_R1
f_R1=0.25/(log10((eps/DN_R1)/3.7+5.74/R_eR1^0.9))^2 {Friction factor return pipe 1}
V_dotR1=V_dotB+V_dotC+V_dotE
H_R1=1901
Delta_HDR1=H_D-H_R1
n_bR1=L_R1toD/60
n_vR1=1
L_eR1=L_R1toD+n_bR1*h_b*DN_R1+n_vR1*h_v*DN_R1
H_fR1=f_R1*V_R1^2*L_eR1/(2*g*DN_R1)
Delta_pdropR1=H_fR1*1000/(L_R1toD) {Pressure drop in mm/m return line 1}
P_pretmR1=Rho_T9*g*(H_fR1+Delta_HDR1) {Pump pressure return line 1}
P_R1=Rho_T9*g*(H_fR1+Delta_HDR1)*V_dotR1/eta/1000 {Pump power for return line return line 1}
L_R1toD=L_DtoR1
L_bcEr=L_bcE
L_DtoA=L_AtoD
L_bcCr=L_bcC
L_bcBr=1770
L_Atops=L_pstoA
L_Totalrtnmain=L_DtoA+L_Atops
L_Totalrtnbrn1=L_bcBr {DN 100 pipe}
L_Totalrtnbrn2=L_bcCr+L_bcEr {DN 65 pipe}
c_R1p=lookup('Price table (Euro)',13,'Unit cost')
n_pu2=1
c_pu2=P_ps2*c_pu
c_pipelineR=L_Totalrtnmain*c_p+L_Totalrtnbrn1*c_bcp1+L_Totalrtnbrn2*c_bcp2+L_R1toD*c_R1p
c_ps2=n_pu2*c_pu2
C_c3=c_pipelineR+c_ps2

{Shell and tube heat exchanger, ps1}
LMTD_ps1=((T_fluid-T_3)-(T_2-T_9))/ln((T_fluid-T_3)/(T_2-T_9))
U_o=1190 "W/m2 oC" {Overall duty heat transfer coefficient from process engineering hand book}
C_pw=4180
T_2=90
Delta_Tbrine=T_fluid-T_2
m_dottonphr=238
m_dotbrine=m_dottonphr/3.6

```

```

Q_brine=(m_dotbrine*C_pw*Delta_Tbrine)/1000000 "Mw"
A_s&t1=Q_brine*1000000/(U_o*LMTD_ps1) {Outside area of metal surface through which heat is exchanged}
{Shell and tube heat exchanger, point B}
T_11=60
T_5=T_9
T_10=15
LMTD_B=((T_3-T_11)-(T_5-T_10))/ln((T_3-T_11)/(T_5-T_10))
Delta_TB=T_3-T_5
rho_TB=Density(Water,T=T_3,x=0)
m_dotB=V_dotB*rho_TB
A_s&tB=Q_RqdB/(U_o*LMTD_B)
{Shell and tube heat exchanger, point C}
T_13=T_11
T_6=T_9
T_12=T_10
LMTD_C=((T_3-T_13)-(T_6-T_12))/ln((T_3-T_13)/(T_6-T_12))
Delta_TC=Delta_TB
rho_TC=rho_TB
m_dotC=V_dotC*rho_TC
A_s&tC=Q_RqdC/(U_o*LMTD_C)
{Shell and tube heat exchanger, point D}
T_14=20
T_15=T_11
T_7=T_9
LMTD_D=((T_3-T_15)-(T_7-T_14))/ln((T_3-T_15)/(T_7-T_14))
Delta_TD=Delta_TB
rho_TD=rho_TB
m_dotD=V_dotD*rho_TD
A_s&tD=Q_TotalD/(U_o*LMTD_D)
{Shell and tube heat exchanger, point E}
T_8=T_9
T_17=T_11
T_16=T_10
LMTD_E=((T_3-T_17)-(T_8-T_16))/ln((T_3-T_17)/(T_8-T_16))
Delta_TE=Delta_TB
rho_TE=rho_TB
m_dotE=V_dotE*rho_TE
A_s&tE=Q_RqdE/(U_o*LMTD_E)
A_hxtotal=A_s&t1+A_s&tB+A_s&tC+A_s&tD+A_s&tE
{Branch connections}
DN_51=0.1053 {From ASTM F681 – 82 (2008) Standard Practice for Use of Branch Connections. Fabricated
joint (cut-in branch)}
DN_51o=0.114
DN_52=DN_51
DN_10=DN_52 {Assumed}
DN_11=DN_10
DN_61=0.064 {From ASTM F681 – 82 (2008) Standard Practice for Use of Branch Connections. Fabricated
joint (cut-in branch)}
DN_62=DN_61
DN_12=DN_62 {Assumed}
DN_13=DN_12
DN_71=DN_1
DN_72=DN_71
DN_14=DN_71
DN_15=DN_14
DN_81=DN_61
DN_82=DN_81
DN_16=DN_81

```

```

DN_17=DN_16
Beta=60
d_1bc=(DN_51-2*(t_n-A_thickness))/sin(Beta) {Effective length removed from pipe at branch}
d_2bc=(t_n-A_thickness)+(t_n-A_thickness)+d_1bc/2 {d_2bc=d_1bc because d_1bc > calculated d_2bc} {Half
width of reinforcement zone}
L_41=2.5*(t_n-A_thickness)
T_r=t_n
L_42=2.5*(t_n-A_thickness)+T_r
L_4=L_42 {Height of reinforcement zone outside of run pipe}
A_rf=t_m2*d_1bc*(2-sin(Beta)) {Required reinforcement area}

{Expansion tank, point A}
L_connpipe=457
T_3=145
rho_coldw=1000
r_pipe1=DN_1/2
r_pipe2=DN_51/2
r_pipe3=DN_61/2
h_pipe1=L_pstoA*2+L_AtoD*2
h_pipe2=L_bcB+L_bcBr+L_bcCr
h_pipe3=L_DtoR1+L_bcE+L_bcC+L_bcEr+L_R1toD
V_pipe1=pi*r_pipe1^2*h_pipe1
V_pipe2=pi*r_pipe2^2*h_pipe2
V_pipe3=pi*r_pipe3^2*h_pipe3
V_pipe=V_pipe1+V_pipe2+V_pipe3
rho_T3=Density(Water,T=T_3,x=0)
V_heatedh2o=V_pipe*rho_coldw/rho_T3
V_exptank=V_heatedh2o-V_pipe

{capital cost}
c_unc=lookup('Properties',8,'Column3') {cost of uncertainty}
c_d&sup=lookup('Properties',9,'Column3') {cost of design and supervision}
c_pipelineTotal=c_pipelnepsA+c_pipelineAE+c_pipelineR
c_psTotal=c_ps1+c_ps2
c_hxTotal=c_hx1+c_hx2
c_addtn=(C_c1+C_c2+C_c3)*(c_unc+c_d&sup)
C_cTotal=C_c1+C_c2+C_c3+c_addtn

{Annual cost}
c_elunit=lookup('Properties',4,'Column3') {USD/Kwh from LCPDP of Kenya}
o_h=lookup('Properties',7,'Column3')
P_Tpp=P_ps1+P_ps2+P_brne
PMT=C_cTotal/((1-1/(1+i)^N)/i)
c_pu&movingparts=0.10*c_psTotal
c_pscivil&piping=c_psTotal-c_pu&movingparts
c_o&mpu&movingparts=0.04*c_pu&movingparts
c_o&mpscivil&piping=0.01*c_pscivil&piping
c_o&mhx=0.02*c_hxTotal
c_o&mpipeline=0.01*c_pipelineTotal
c_o&maintTotal=c_o&mpu&movingparts+c_o&mpscivil&piping+c_o&mhx+c_o&mpipeline {O&M assumed
4% for pumps and moving parts, 1% for pump stations civil structures and piping, 2% for Hxs and 1% for rest of
pipeline}
C_elect=c_elunit*0.77*o_h*P_Tpp
C_a=PMT+c_o&maintTotal+C_elect

{Total updated cost, C_T}
i=lookup('Properties',6,'Column3')
N=lookup('Properties',5,'Column3')
C_T=C_cTotal+C_a/i*(1-1/(1+i)^N) {i& N assumed as 6% and 30 yrs}

{Unit production cost of heat}
P_heat=Q_brine*1000*o_h
c_heat=(C_a/P_heat)*1000 {Euro/MWh}

```




UNITED NATIONS
UNIVERSITY

UNU-GTP

Geothermal Training Programme

Orkustofnun, Grensasvegur 9,
IS-108 Reykjavik, Iceland

Reports 2014
Number 27

ANALYSIS OF STUCK PIPE INCIDENTS IN MENENGAI

Billy Awili Oketch

Geothermal Development Company - GDC

P.O. Box 17700-20100

Nakuru

KENYA

bawili@gdc.co.ke, billyawili@gmail.com

ABSTRACT

Stuck pipe, or sticking, and lost circulation are the two main events which cause non-productive time (NPT) in the drilling industry. A considerable amount of time and resources can be spent in efforts to free a stuck pipe. Sometimes, stuck pipe events result in breakage (either intentional or non-intentional) of the drill string, leading to a lot of money being spent on fishing. Unsuccessful fishing operations have resulted in costly alternatives including side-tracking or, worse still, well abandonment. Stuck pipe situations are very common around the world with most data gathered in the petroleum drilling industry. A stuck pipe situation has led to abandonment of a well in the Menengai drilling field, Kenya, as of the date of writing this paper. This paper explores the stuck pipe problem in geothermal well drilling. The paper presents causes of stuck pipe events, predicting their occurrence, and common methods used to free a stuck pipe. There is also a review of methods used to back off stuck string and fishing. Finally, an analysis is made of stuck pipe events in a few wells drilled in Menengai, Kenya, using the graphical analysis software *Easy View*. The results are then discussed to identify the causes of stuck pipe in Menengai.

1. INTRODUCTION

The Geothermal Development Company (GDC) is a Kenyan government-owned entity that plans to develop 5,000 Megawatts of geothermal energy by 2030 in various fields in Kenya. Currently, production drilling is ongoing in the Menengai high-temperature field located in Nakuru within the central Kenyan rift. Menengai comprises the Menengai caldera, The Ol’rongai in the northwest and parts of Solai graben to the northeast. Drilling in this field has been quite difficult due to formation challenges that have subsequently caused stuck pipe incidences, among other non-productive activities. A stuck pipe situation occurs in drilling when the drill string cannot be reciprocated along or rotated about its axis while in the well. An analysis of drilling data has shown that, on average, Menengai wells were stuck for six days (Okwiri, 2013) or 12% of total drilling time in Menengai (Makuk, 2013). The depth at around 2100 m (below Rotary Kelly Bushing) has been identified as particularly troublesome, leading to most of the stuck pipe incidences (Makuk, 2013). As of 1991, stuck pipe events were costing the drilling industry USD 200-500 million annually and occurred in 15% of the wells (Schlumberger, 1991). Sticking of the drill string is mostly viewed as an accident, although methods have been used to predict such events. It is usually a result of natural factors such as the presence of permeable formations (which can easily cave and slough) or abnormally high

pressured beds. Sticking can also be influenced by the degree of hole deflection and dogleg severity causing a keyhole. Drilling parameter changes can give hints to sticking problems that might occur later, e.g. during tripping out. Bailey et al. demonstrated in the Schlumberger article (Stuck Pipe - Causes, Detection and Prevention, Schlumberger, 1991) how a water loss (from drilling mud) event during drilling later caused differential sticking during tripping out. The high costs associated with sticking form the justification for a study of the causes of stuck pipe in Menengai, with a view to preventing them. Figure 1 shows the location of some of the wells drilled in Menengai.

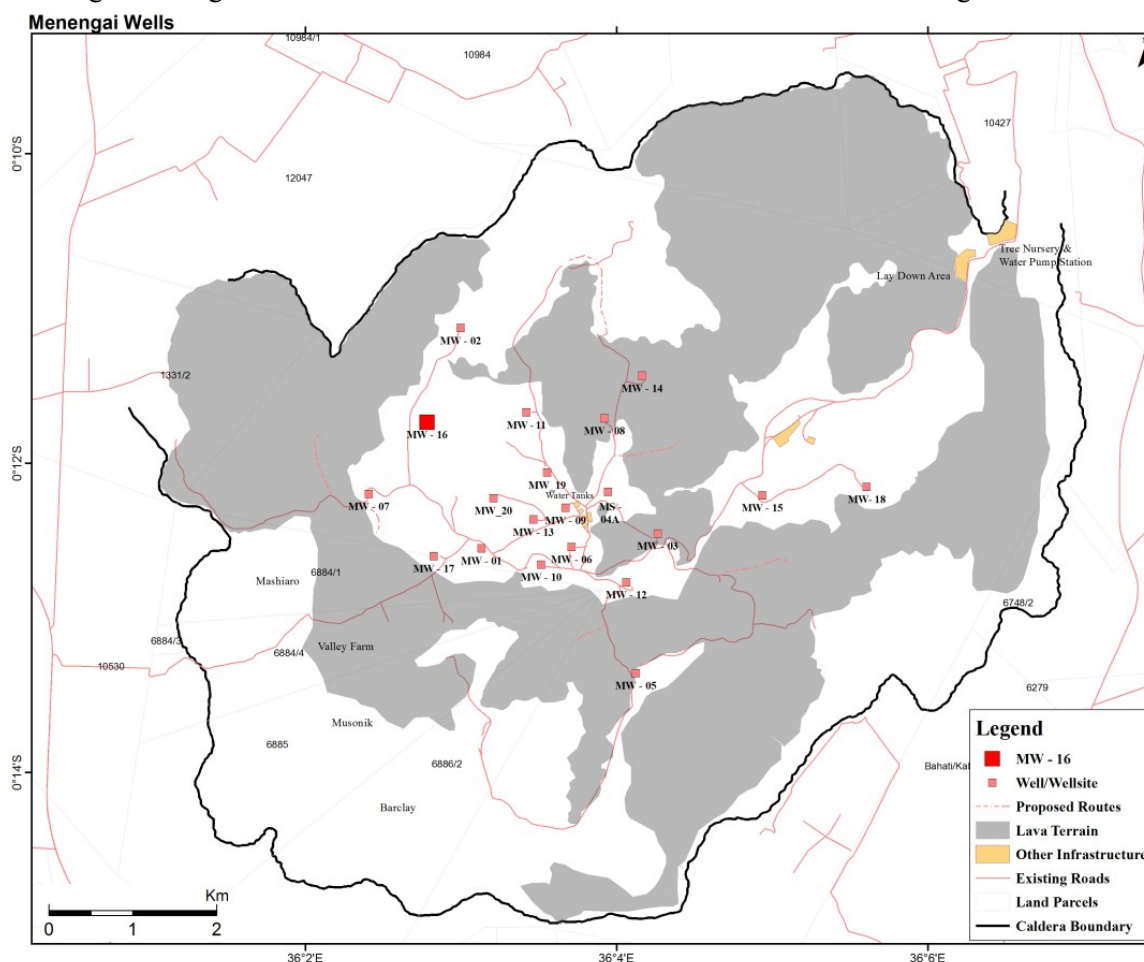


FIGURE 1: Menengai high-temperature field and location of wells (GDC, 2013)

2. CAUSES OF STUCK PIPE

There are basically 2 mechanisms for pipe sticking: differential sticking; and mechanical sticking. Their mechanism and causes are summarized in Table 1.

TABLE 1: Pipe sticking mechanism and causes (Rabia, 2001)

Mechanism	Differential Sticking	Mechanical Sticking	
Cause		Hole pack off	Formation & BHA (wellbore geometry)
	Differential Force	Settled cuttings Shale instability Fractured rocks Cement blocks	Key seating Mobile formations Under-gauge hole Micro doglegs and ledges
		Junk	Drilling into magma

2.1 Differential sticking

During drilling, the drilling fluid pressure is maintained at a higher value compared to the reservoir or formation pressure. When a permeable zone is reached, the difference in these pressures forces some of the fluid to seep into the permeable zone. As this happens, the solids in the drilling fluid are filtered out at the hole wall, forming a layer called a filter cake. If a substantial area of the string surface comes into contact with the cake formed, then only the outer wall surface exposed to the drilling fluid “sees” the higher drilling fluid pressure and the contact surface to the cake “sees” the lower formation pressure. This pressure difference pushes the pipe to stick to the hole wall and embed itself further into the filter cake with a great force (can reach more than a million pounds force). The string, thus, gets differentially stuck and the force required to pull it exceeds the yield point of the pipe. The signs of differential sticking are:

1. The pipe can neither be moved up or down nor rotated;
2. Circulation is unaffected.

The differential sticking force depends on the pressure differential and the area of contact with the porous formation zone, among other factors. To gain an understanding of factors that might influence the sticking force and the magnitudes, consider Figure 2.

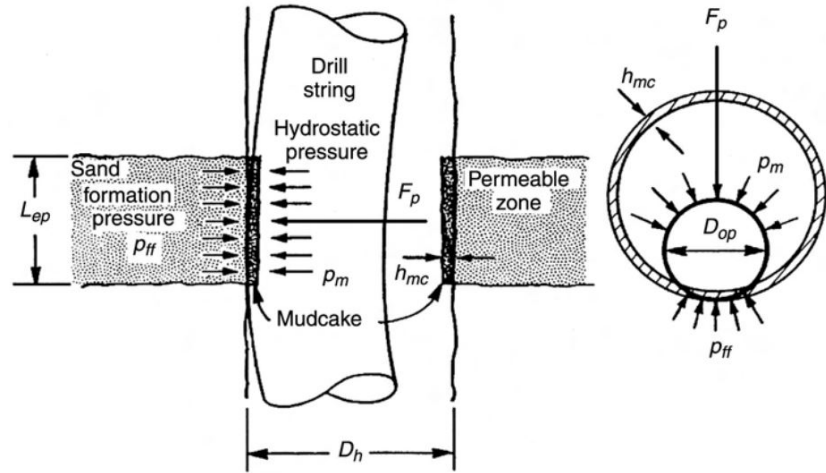


FIGURE 2: Differential pressure sticking (SPE, 2007)

$$\text{Differential force} = (\text{mud hydrostatic} - \text{formation pressure}) \times \text{area of contact}$$

From Figure 2:

$$\Delta p = P_m - P_{ff} \quad (1)$$

where P_m = Pressure acting outside pipe wall;
 P_{ff} = Formation fluid pressure; and
 Δp = The pressure differential.

The pull force, F_p , required to free the stuck pipe is a function of the differential pressure, Δp ; the coefficient of friction, f ; and the area of contact, A_c , between the pipe and mud cake surfaces:

$$F_p = f \Delta p A_c \quad (2)$$

where F_p = The pull force;
 f = Coefficient of friction; and
 A_c = Area of contact between the pipe wall and mud cake.

The area A_c can be simply said to be the length of pipe in contact with the mud cake multiplied by the length of the perimeter of the pipe in contact with the cake; this length can be estimated to be 20% of the perimeter. A more accurate estimate of the contact area may be given as:

$$A_c = 2L_{ep} \sqrt{\left\{ (D_h/2 - h_{mc})^2 - \left[\left(\frac{D_h}{2} - h_{mc} \right) (D_h - h_{mc}) / (D_h - D_{op}) \right]^2 \right\}} \quad (3)$$

$$\text{where } D_{op} \leq (D_h - h_{mc}) \quad (4)$$

Here, L_{ep} = Length of the permeable zone;
 D_{op} = Outside diameter of pipe;
 D_h = Diameter of hole; and
 h_{mc} = Mud cake thickness.

The dimensionless coefficient of friction f can vary from less than 0.04 for oil based mud to as much as 0.35 for weighted water-based mud with no added lubricants. Equations 2 and 3 show the controllable parameters that will cause a higher pipe sticking force. These are: a high differential pressure, thick mud cake (high continuous fluid loss to formation), low lubricity mud cake (high coefficient of friction) and excessive embedded pipe length in mud cake (delay of time in freeing operations).

Although hole and pipe diameters and hole angle play a role in the pipe sticking force, they are uncontrollable variables once they are selected to meet well design objectives. The shape of the collars can play a role in reducing sticking force, e.g. spiral or square drill collars will have lesser area in contact than cylindrical collars.

Differential sticking may be prevented by:

- Maintaining lowest continuous fluid loss;
- Keeping circulating mud free of drilled solids;
- Keeping a very low differential pressure with allowance for swab and surge;
- Using a mud system that yields smooth mud cake (low friction co-efficient);
- Maintaining drill string rotation at all times;
- Using grooved or spiral drill collars;
- Minimizing length of drill collars and Bottom Hole Assembly (BHA).

If differential sticking occurs, the following solutions are mostly used:

- Immediate working/jarring of the string downwards;
- Reducing drilling fluid hydrostatic pressure by gasifying with air or by diluting the fluid. Close attention must be paid to kick indicators while reducing hydrostatic pressure;
- Oil spotting around stuck portion of string;
- Washing over the stuck pipe.

2.2 Mechanical sticking

In mechanical sticking, the pipe is usually completely stuck with little or no circulation. This can be due to hole pack off (or bridging) or due to the formation and BHA (well geometry).

Hole pack off can be caused by any one or a combination of:

- Settled cuttings due to inadequate hole cleaning;
- Formation instability;
- Unconsolidated formations;
- Fractured and faulted formations;
- Cement blocks;
- Junk falling in well.

Formation and BHA (wellbore geometry) can also cause mechanical sticking through:

- Key seating;
- Under-gauge hole;

- Ledges and micro ledges;
- Mobile formations;
- Drilling into magma (special case; documented in Menengai and Krafla).

It is very important to understand the cause of a mechanical sticking problem because it is the key to knowing the correct action to take in freeing the stuck pipe.

2.3 Hole pack off causes

2.3.1 Settled cuttings

This is one of the major causes of a mechanical stuck pipe. It is where cuttings pack off or settle and build on the well bore and cause compaction around the BHA when the pipe is moved upwards. The compacted cuttings then prevent the string from coming up, especially during trip out. Figure 3 shows settled cuttings. The problem is more prone in highly deviated or horizontal wells since the cuttings tend to fall on the low side of the hole and are harder to clean out. These settled cuttings pile up and form beds and may compact against the BHA on trip outs. In vertical wells, good hole cleaning is achieved by the selection and maintenance of suitable mud parameters and by ensuring that the circulation rate chosen results in an annular velocity (around 100-120 feet/min) which is greater than the slip velocity of the cuttings. Besides causing stuck pipe, settled cuttings can also cause:

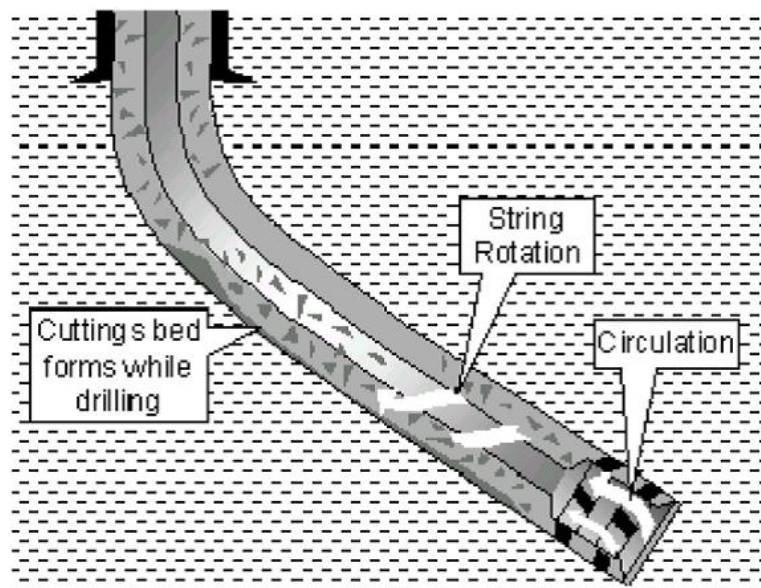


FIGURE 3: Settled cuttings due to poor hole cleaning (Rabia, 2001)

- Formation breakdown due to increased equivalent circulating density;
- Slow rate of penetration;
- Excessive overpull on trips;
- Increased torque.

Hole cleaning is one of the main solutions to prevent this stuck pipe problem and can be controlled by:

- Good mud rheology, especially yield point and gel strength;
- Controlling drill rate to ensure hole is clean;
- Checking volume of cuttings coming over to shale shaker;
- Controlling annular velocities;
- Recognizing increased over pull;
- Reciprocating and rotating pipe while circulating;
- Using viscous sweeps;
- Recognizing low side section of deviated holes;
- Regular wiper trips.

If sticking occurs, then:

- Attempt to establish circulation;
- Simultaneously apply downwards force gradually until circulation starts;
- Once circulation starts, rotate the string;
- In low angles holes, a weighted viscous pill should be used to 'float out' the cuttings;
- In high angle holes, a low viscous pill should be used to disturb the cuttings bed followed by weighted pills to carry cuttings out of hole.

2.3.2 Formation instability

This is as a result of tensile and compressive failure on the borehole wall. The borehole will fail in tension while drilling mud hydrostatic pressure induces stresses in the hole wall that exceeds the tensile strength of the rock. The borehole will fail in compression when the pressure of the drilling mud is insufficient to keep the shear stresses in the borehole wall below the shear strength of the formation (Rabia, 2001).

This problem can be solved by applying the rock mechanics principle to define working limits for mud weights to avoid tensile or compressive failure; here, the equations and methods applied in rock mechanics are quite complex and can be found in most geo-mechanics and rock mechanics literature. The result of formation instability is either borehole widening or contraction depending on the failure mode of the rock inside the well. Figure 4 shows the Inner Drucker-Prager criterion for predicting safe mud weights. Sticking to the fluids program can prevent the effects of formation instability.

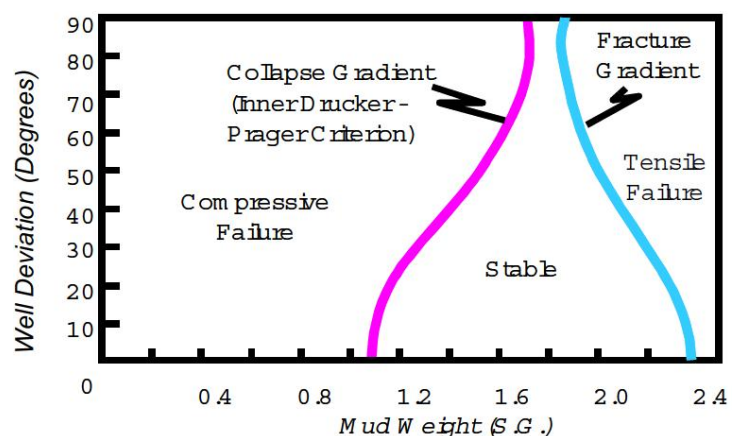


FIGURE 4: Safe mud weights envelope (Rabia, 2001)

Other solutions include making use of a well program that isolates a potential troublesome formation and speeding up the drilling process to cut down the time in drilling sensitive formations. Formation instability can be identified by the following:

- Large amounts of angular or splintery cuttings when circulating;
- Drag on trips;
- Large amounts of hole fill.

Formation instability will cause material to fall inside the hole, creating caves or contracting the wellbore and might cause sticking. Sloughing and caving are also due to formation instability. If these occur, then the solution is establishing circulation, then working the drill string, preferably downwards; when the string is freed, circulate all material out before changing the mud properties to continue drilling.

2.3.3 Unconsolidated formations

Unconsolidated formations are usually encountered near the surface and include loose sands, gravel and silts. These collapse due to low cohesive strength; they can collapse and jam the drill string. Signs of sticking due to unconsolidated formation include:

- Increased torque;
- Drag and pump pressure increase when drilling;
- Increased rate of penetration;
- Large fill on bottom.

This problem can be prevented by using a mud system with impermeable filter cake to reduce fluid invasion into rock. Reducing annular velocity by reducing the mud flow rate will also reduce erosion of the hole wall and also reduce removal of filter cake.

2.3.4 Fractured and faulted formation

Symptoms of fractured and faulted formation include:

- Large and irregular rock fragments at shale shakers;
- Increased torque, drag and rate of penetration;
- A small amount of lost circulation.

The fractured formation falls into the well due to stresses originally holding the formation together being relieved by drilling of the hole. Excessive vibration might also cause the drill string to whip down hole and dislodge the fractured rocks. The problem can be prevented by:

- Reducing drill string vibration;
- Minimizing surge pressures;
- Sufficient hole cleaning to reduce hole pack off.

If sticking occurs, jar the string. If this is not successful, an inhibited hydrochloric acid pill may be spotted around the stuck zone to break down the material surrounding the pipe.

2.3.5 Cement blocks

Cement blocks from the rat hole might fall into the well bore and cause sticking. This can be prevented by minimizing the rat hole to a maximum of 5 feet and ensuring good tail cement at the casing shoe. If sticking occurs due to cement blocks, jar the string or inject acid solution down hole to dissolve the cement.

Green cement is improperly set cement. Green cement can occur after setting a cement plug inside the casing or open hole. If the drill string is run too fast into the top of the cement and the cement is still green, then the cement can flash set around the pipe and cause permanent sticking. Flash setting is a phenomenon that is not very well understood but a possible explanation is that the energy release while circulating and rotating could be sufficient to cause it. A good practice to prevent this is starting circulation 2 or 3 stands above the expected top of the cement and also keeping a low weight on the bit.

2.3.6 Junk falling in the well

Junk in the well can happen and common junk includes pipe wrenches, spanners, broken metal, hard hats, tool dies etc. Junk can also fall from inside the well, e.g. broken packer elements, liner hanger slips and metal swarf from the milling operation. A preventative practice is to keep the hole covered when no tools are run into the hole or when fishing out junk before drilling continues. Tools should also be in good condition and should be regularly inspected before being run in the hole.

2.4 Formation and BHA (well geometry) causes

2.4.1 Key seating

Key seating is caused by the rotational drill string coming into contact with a soft formation. The rotational action causes the tool joint to erode a narrow groove in the formation, almost equal to the tool joint diameter. This groove diameter is smaller than regular BHA component diameters below the drill pipe. On pull out, the BHA might be pulled into the narrow key seat (groove), resulting in stuck BHA.

Key seats are often seen in doglegs and ledges since they allow the string to bend and provide points of contact between the tool joint and hole walls. Key seats may also occur in casing shoes in highly deviated wells.

Key seats can be identified by these signs:

- Circulation is free when the pipe is stuck;
- Hole is tight on tripping out only;
- Tight hole position can be correlate with positions of large outer diameter members of the BHA;
- Tight hole occurs at same depth on trips.

To get free from a string stuck in a key seat, jar downwards only until free movement and rotation happens (Figure 5). Once the string is free in a downwards direction, it should be slowly pulled past the key seat using minimum tension and slow rotation. A key seat wiper tool can be run on top of the collars to clear the key seat.

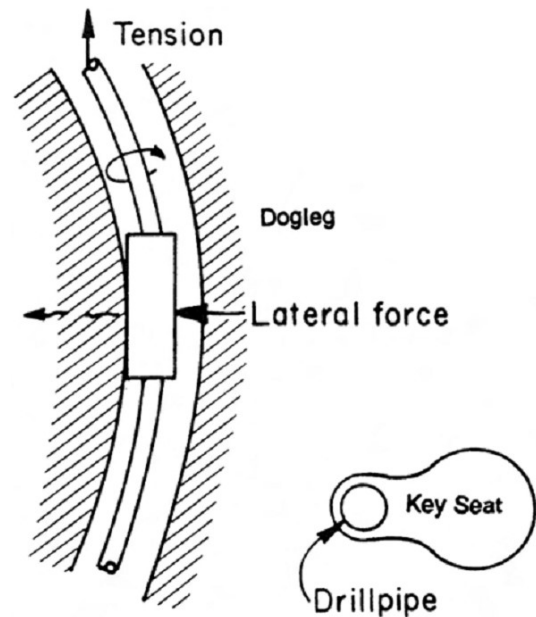


FIGURE 5: Pipe sticking caused by key seat (SPE, 2007)

2.4.2 Under-gauge hole

Drilling in an abrasive formation can result in bit and stabilizer gauge wear. The loss in gauge results in drilling an under-gauge hole. Not only is it costly to ream under-gauge sections, but a new full gauge bit and stabilizer being run in the hole can get stuck, too. This problem can be avoided by practicing caution when running in hole a new bit or stabilizer after pulling out an under-gauge bit.

2.4.3 Micro doglegs and ledges

These develop when drilling through layers of a formation of varying strength or dipping formations. A gauge hole is drilled in the harder zone and an oversized hole, caused by fluid erosion, is drilled in the softer zone. This oversized hole causes the bit and the BHA to be deflected to the low side of the hole causing a small dogleg when the next hard section is drilled (Rabia, 2001). When successive layers of hard and soft sections are drilled, then ledges and micro doglegs develop. This problem can be prevented by running slowly when tripping at alternating formation points; these areas should be noted and reamed through during trips. If sticking occurs, then jar up if stuck while running in or jar down if stuck while pulling out.

2.4.4 Drilling into magma

It has been shown that the 2011 m depth is particularly troublesome to drill through in Menengai field, Kenya (Makuk, 2013). It has also been observed that fresh glass was present in cuttings at 2082 m and 2174 m in wells MW04 and MW06, respectively (Mibei, 2012). It is believed that magma intrusions at these depths are rapidly chilled by the drilling fluid, producing glassy cuttings. Sticking problems were recorded at these depths and are believed to be related to the occurrence of glass (Mibei, 2012). The exact mechanism of sticking due to drilling into magma is not really known. The Iceland Deep Drilling Project well 1 was halted after having drilled into magma and gotten stuck, however the bit came up intact (Hólmgeirsson et al., 2010). It is reported that the magma pushed up on the drill string, lowering the hook load value. It is believed that explosive chilling of the magma (steam flashing) by drilling fluid downhole could, however, be related to this sticking problem.

A summary of signs of sticking and parameters to watch for stuck pipe problems can be well tabulated using the Baker Hughes INTEQ, 1995 workbook as shown in the Table 2, while common responses to stuck pipe problems are shown in Table 3. Figure 6 shows a flow chart that can assist in recognizing stuck pipe warning signs.

TABLE 2: Stuck pipe problems and indicators (Baker Hughes, INTEQ, 1995)

Problem \ Indicator	Torque	Pressure	Drill rate
Poor hole cleaning	Increase	Increase	Gradual increase
High overbalance	Gradual increase	No change	Gradual decrease
Mobile formations	Gradual increase	Increase	Gradual decrease
Fractured & faulted formations	Sudden erratic increase	May be unaffected	Sudden increase
Geo-pressured formations	Increase	Increase	Initial increase with a gradual decrease
Reactive formations	Gradual increase	Increase	Gradual decrease
Unconsolidated formations	Increase	Increase	Decrease
Junk	Sudden increase	No change	Sudden decrease
Cement blocks	Sudden increase	No change	Sudden decrease

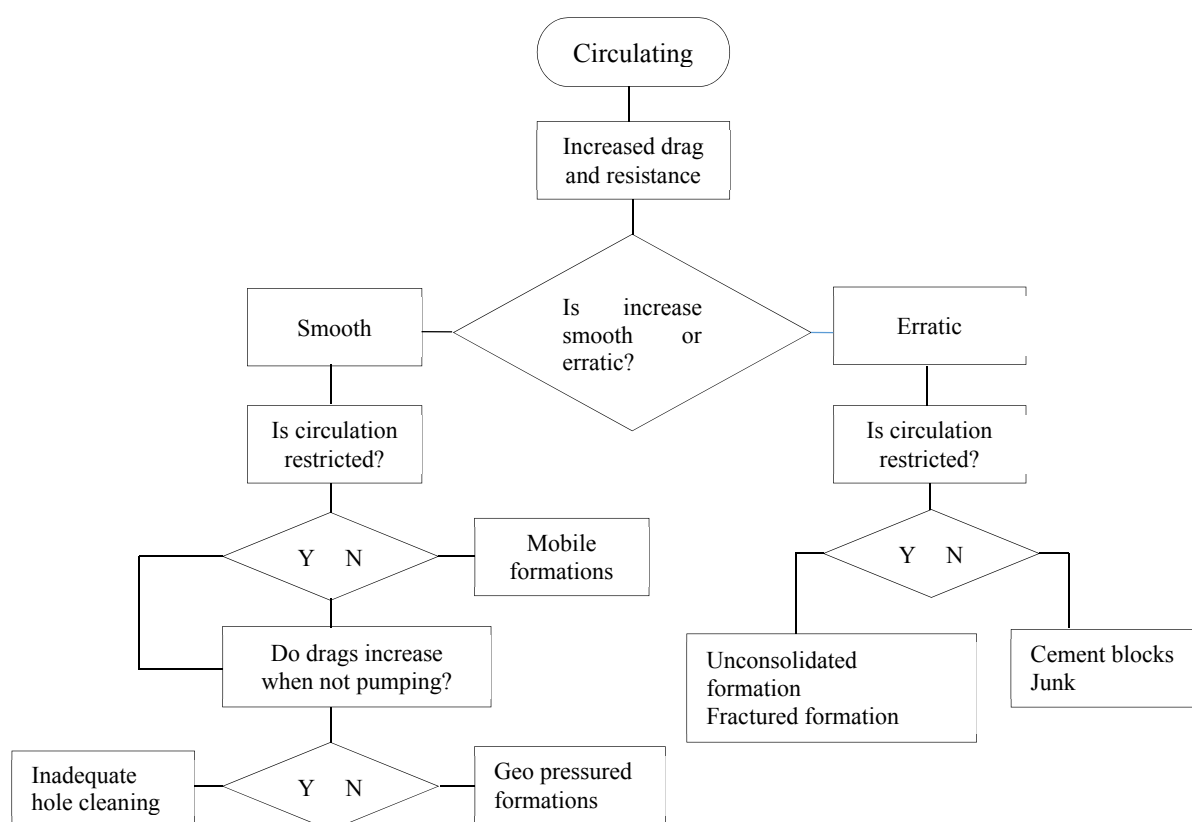


FIGURE 6: Flow chart showing stuck pipe warning signs when circulating (Kingdom Drilling, 2014)

TABLE 3: Response to analysis of borehole conditions (Baker Hughes INTEQ, 1995)

Drilling instrumentation	Borehole problem	Response of logging crew
Lithology identification and description	Formation related Differential sticking Cement related Under-gauge hole Poor hole cleaning	Identification of rock types and characteristics Identification of permeable sandstones Identification of cement in cuttings samples Identification of abrasive formations Amount of cuttings in samples
Depth and drill rate recorder	Formation related Wellbore geometry Poor hole cleaning	Identification of borehole problems from drill rate Reduced drill rate due to BHA hanging up on ledges Reduced drill rate due to poor transfer of WOB
Monitor calculations	All types of borehole problems	Monitor trends in hole conditions, and relating trends to lithology, hole deviation and BHA configuration
Pump stroke counters	Poor hole cleaning	Monitoring annular velocities to adequately clean borehole
Pore pressure evaluation	Geo-pressure differential sticking	Detecting abnormal or sub-normal pore pressure calculation of ECD and amount of overbalance
Lag time determination	Poor hole cleaning	Monitoring actual hole volume to determine actual versus theoretical lag time

3. FREE POINT DETERMINATION AND BACK-OFF OPERATIONS

At times, the driller is unable to free a stuck pipe, or the force required to pull the pipe free might be larger than the yield point of the weakest member in the driller string. At this point, the remedial measures normally applied involve spotting lubricating fluid around the troublesome area. The spotting procedure is facilitated by pinpointing the location of the stuck pipe, i.e. the depth of sticking, and is demonstrated by Figure 7.

1. An upward force F_1 is applied to the pipe. This must be greater than the total weight in air to ensure that the string is in tension;
2. A reference point is marked on the drill pipe at the surface, normally at the top of the rotary table;
3. A greater upwards force, F_2 is applied causing the free portion of the drill string to stretch by an amount, “e”. The stretch is measured above the reference point.

After these measurements are taken, we apply the equation below to get the stuck point:

$$SPL = 735 \times 10^3 \times \frac{(w)X(e)}{(F_2 - F_1)} \quad (5)$$

where SPL = Stuck pipe location;
 735×10^3 = Derivation of Young’s modulus for steel;
 w = Weight of drill pipe (lb/ft);
 e = Length of stretch (“);
 F_1 = Force applied when pipe is in tension (lb); and
 F_2 = Force applied to stretch the pipe to “e” pounds.

It should be noted that the stuck pipe location calculated using the above equation is a best guess due to the following reasons:

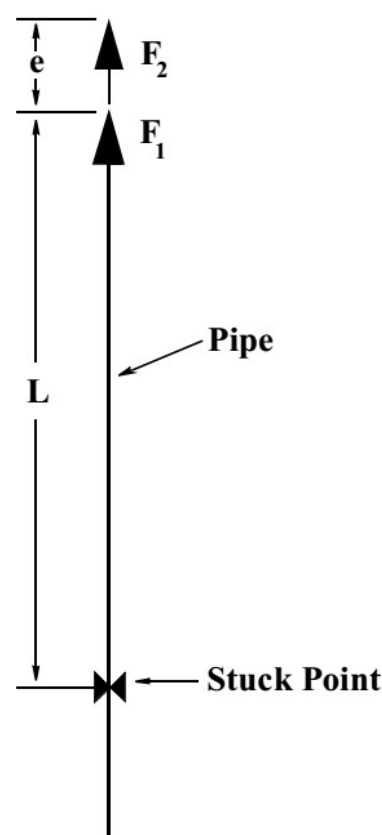


FIGURE 7: Determining stuck pipe variables (Baker Hughes INTEQ, 1995)

1. Hole friction can impede pipe stretch, especially in deviated wells;
2. The stretch measurement does not account for drill collars or heavy weight drill pipe response to pull.

For these two reasons, the equation should only be used as a starting point before a free point indicator tool is lowered through the string to determine the back off point. The accuracy range of this method is around ± 200 feet.

3.1 Free-point indicator tool

If spotting lubricating liquid around the stuck point does not work, then a free point indicator tool is lowered in the string to more accurately determine the stuck pipe location for backing off operations.

The free point indicator tool is displayed in Figure 8 and is designed to determine the location of sticking by measuring points in the drill string where tension and/or torque is zero. The tool has a series of axial strain gauges that measure tension/torque in the string. The string is tensioned and/or torqued and the gauge measures the strains in the string; a zero reading will indicate the stuck location. The degree of the stuck pipe will vary from totally stuck (0% free) to totally free (100% free) depending on the tool measurements downhole. We should note that torque and overpull measurements will be less accurate in deviated wells due to the friction between the drill string and the hole walls. The measurements are also not very accurate in wells with doglegs.

Usually, back off attempts are made where torque and tension readings are 80-90% of the free pipe. Practically, the back off point is chosen to be the next connection above the free connection which was broken on the last trip.

3.2 Backing off the string

Backing off refers to separating the free pipe from the stuck portion, usually at a threaded connection above the free point. It can be done mechanically by applying left hand torque or in combination with an explosive charge, the latter being the preferred. A string shot, which is an explosive charge, is placed across the connection to be separated. A Casing Collar Locator (CCL) is run in hole to locate the exact connection and where to place the charge; the CCL tool distinguishes between the thinner pipe body and thicker pipe connections. The back off procedure is outlined below:

- The explosive charge is run through the wire line to opposite the back off connection;
- Left hand torque is applied to the string with some over pull, the over pull/torque is maintained and the explosive charge run to the connection to be broken;
- When the charge is in position, the surface weight is slackened to the desired value and the charge is fired;

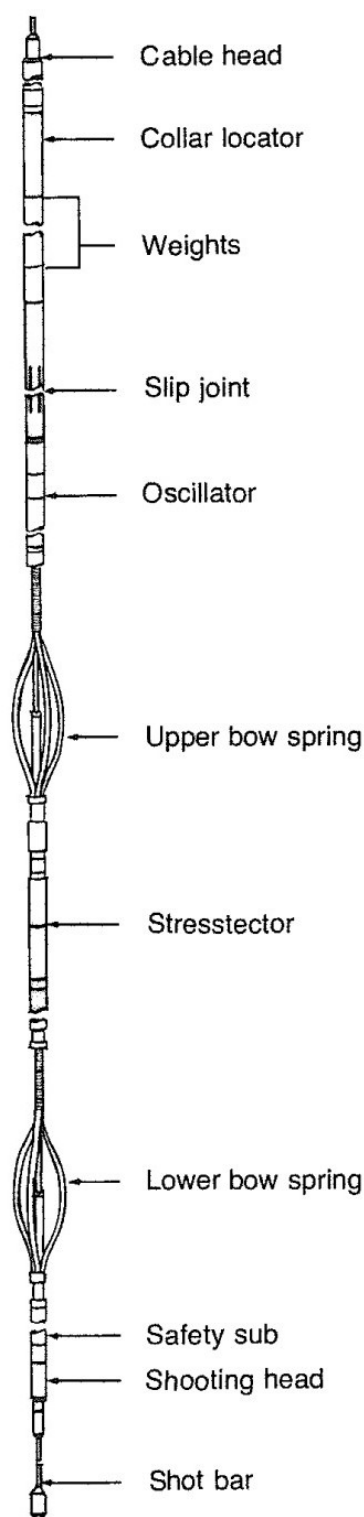


FIGURE 8: Free point tool
(Short, 1981 - Courtesy of
Dia-Log)

- After the charge is fired, the tool is pulled out to determine if the operation was a success; if it is, the weight indicator should show less weight on pick up;
- Sometimes, the connection doesn't get completely undone and so further left hand torque might be applied to completely undo the connection.

Sometimes, several other connections can become loosened and it is very important not to rotate the string while pulling out of the hole the stands that are above the back off point. Every joint must be torqued up when running in hole again. If the back off is at the wrong connection, it is sometimes possible to screw back in and attempt the back off again, but the chances of success are reduced.

Factors which may ensure success during back off include:

- Sufficient explosive charge that will also not damage the connection;
- Enough left hand torque;
- Backing off at a neutral point with just a small over pull.

It is often difficult to get explosives on site due to legal restrictions and, for this reason, mechanical back off is considered. Safety must be observed during back off operations because it is a dangerous operation that might lead to serious injury on the rig floor.

3.3 Twist off

This refers to breakage of the drill string while in hole. The risk of twisting off is usually greater when the drill string has many combinations of sizes of connections. This is because the heavier portions have greater momentum than the lighter, thinner tools in the same drill string. Stopping the pipe rotation quickly at the surface can cause twist off due to the momentum differences in the drill string, so large sized assemblies should be handled carefully. The slip area (usually 2-5 ft. below the tool joint) is also commonly a twist off prone area. Good drilling practices will make sure the slip area is not pre-damaged before drilling begins. Damaged pipes should be taken out of service and the string should also be regularly inspected for micro-ledges or thread damage. Washout is also a common cause of twist off. This is when the drilling assembly develops a hole due to erosion by particles in the high-pressure circulating mud. Wash outs can be detected by a process of elimination, i.e. surface equipment are checked for leakages first, then checks for down hole leakages related to the formation are also analysed; if both are ok, then further checks might lead to the discovery of a washed out portion of the string. Pump pressure and stroke recorders are very useful in analysing for washouts and should, therefore, be in good working condition.

Three cases of sudden snapping of the drill string were recorded in well MW16 in Menengai; the Easy View Screens at the time of snapping are shown in Figures 9, 10 and 11. In Figure 9, the string parted suddenly at 0740 hrs. At 0724 hrs, torque and WOB (weight on bit) suddenly dropped to 0. At 0740 hrs there was a drastic drop in the hook load from 33.23×10 kN to 11.81×10 kN, despite no rise in WOB and a constant hook height. At 0746 hrs, WOB was still 0 despite the string being lowered to 4.61 m. Subsequent picking up of the string only registered a maximum hookload of 27×10 kN, and slightly erratic rotary torque (mostly zero).

In Figure 10, at 0815 hrs, the torque suddenly dropped to almost zero; then very shortly afterward, the WOB also dropped from 4.22×10 kN to almost zero. WOB never changed between 0815 hrs to the end of this recording despite the hook height changing. The hook height went up from 7.49 m at 0815 hrs to 8.04 m at 0816 hrs but the hook load and WOB remained constant. The hook load dropped from about 47×10 kN to a constant value of 40×10 kN, indicating a snapped string. In Figure 11, it was observed how torque sharply descended from 14×10 kNm to almost zero at 0128 hrs. WOB then dropped sharply at 0129 hours despite a constant hook height of 2.16 m. It was also noted that the WOB was almost zero, yet the hook load was still around 59×10 kN (it should in fact be around 65×10

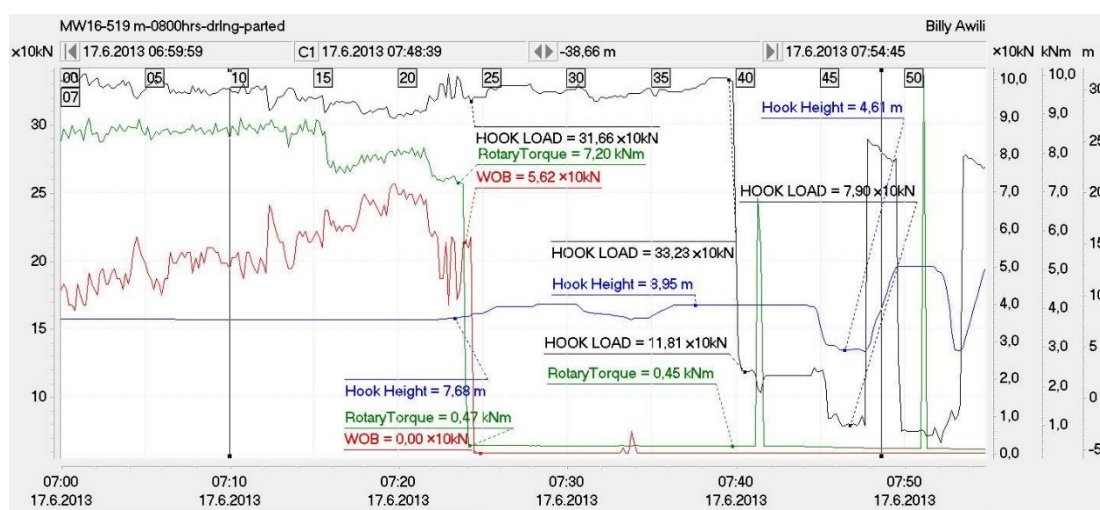


FIGURE 9: Parameters of snapping of drill string in well MW16 at 519 m

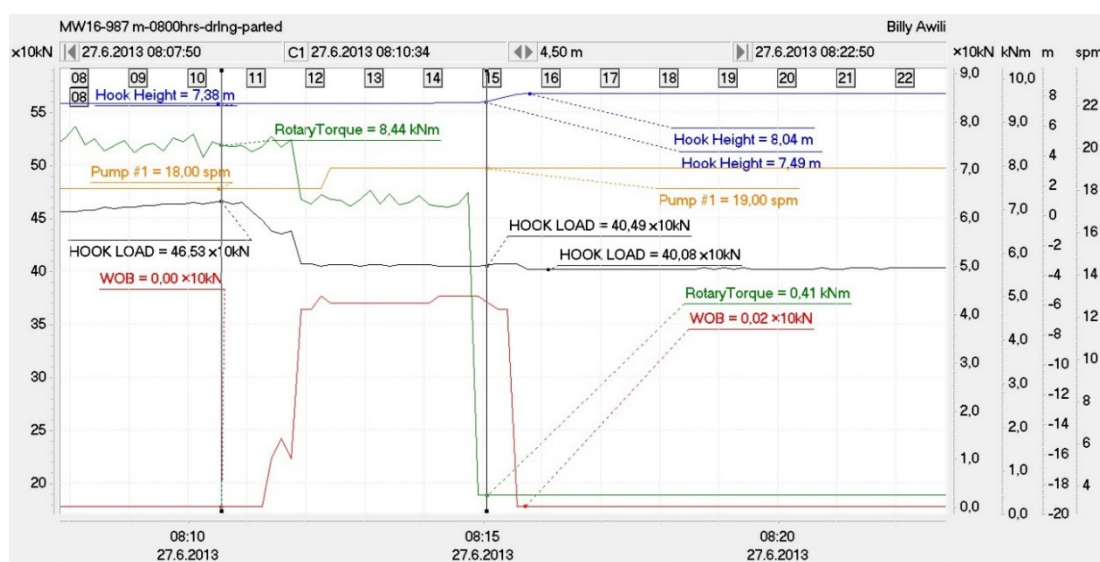


FIGURE 10: Parameters of snapping of drill string in well MW16 at 987 m

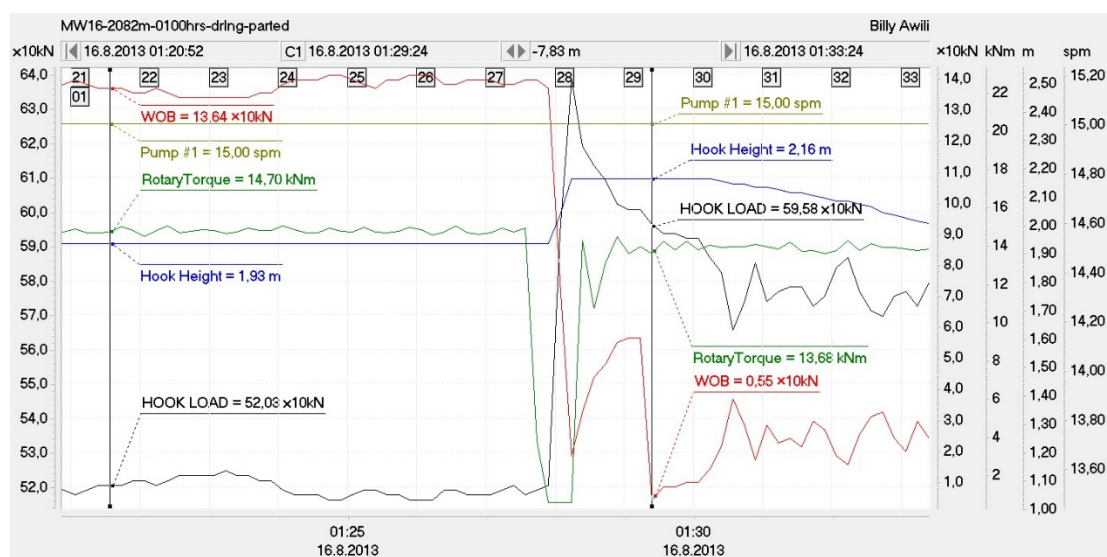


FIGURE 11: Parameters of snapping of drill string in well MW16 at 2082 m

kN when there is no WOB). The hook load also gradually dropped and while picking up the string it never got to the original hook load record of 65.6×10 kN, indicating a snapped string.

4. FISHING

Fishing is any operation or procedure to release, remove or recover tubular or other material in the well bore that adversely affects drilling, casing or completion operation (Short, 1981). Fishing operation success depends on being prepared, planning carefully, deciding correctly and knowing your fishing equipment. Fishing, generally means increased costs and all other options of economically getting out/releasing the string must be explored before fishing starts.

A review of previous fishing jobs in the area will give a good start in knowing about the formation characteristics, how sticking can occur, procedures used to fish, available tools and personnel or fishing service companies in the area. It is very important to keep accurate records of your tools, including the number of collars, drill collar size and clearance, types of jars and bumper subs, how safety joints are used etc.

After backing off, it is important to know the exact length, weight and other dimensions of the fish. Checking/inspecting the retrieved parts above the free point or backed off joint will give you an idea of what the top of fish looks like and will strongly influence the fishing assembly to be used.

A plan of action is also necessary after reviewing all the available data. It is also a good practice to try and get the fish in one piece. When fishing, select the tool that makes the strongest connection, usually a screw in connection (Short, 1981). An overshot is the second choice and a taper tap, a last resort. Milling should also be chosen as a last resort unless when dressing the fish top. Long milling jobs without properly circulating out the mills can cause them to pack around the fish and wedge it tighter. It sometimes occurs that the fishing assembly can also get stuck, leading to a second fish in hole. This problem can be avoided by careful study of the causes for the first stuck pipe and inspecting the parts backed off for indications of expected conditions down hole.

4.1 Fishing tools

The importance of selecting the best tool for the job cannot be over emphasized. The availability of fishing tools lessens with decreasing hole size (Short, 1981). It is also a fact that tools for smaller hole sizes have limited strength characteristics. Fishing tools can be run on tubular, wire line or both.

Most fishing jobs occur while using tubulars. A series of these tools have been designed to run on pipe and are operated with rotation, reciprocation or both. Some of the tools described may not be classified as fishing tools but they assist in the fishing job.

4.2 Mills

Mills do not have moving parts and they need torque to drill. Running mills on butt-shouldered tool joint type connections is better than on regular screw-type connection (tubing connection) since over-torqueing for long periods can lead to screw-type connection failures. Mills drill up junk and also dress off a fish top where it can be caught by a fishing tool. Figure 12 shows various mill types. Mills can also ream out collapsed casing, ream inside tubulars, e.g. scales and cut out sections of casing or window for side tracking. They have a cutting face specially designed with grooves to allow the passage of fluids and ground metal. The cutting face wears out after some use.

Junk mills can be flat, concave and ribbed and can ream almost any type of junk including bit cones. They expose the maximum cutting face to the junk. A concave mill is used when junk pieces are small and retains the small pieces in the hole before they are circulated out. Flat bottomed and ribbed mills are used to drill out larger junk pieces. Preferred clearance between hole size and casing and mills can be given by the manufacturer of the tool.

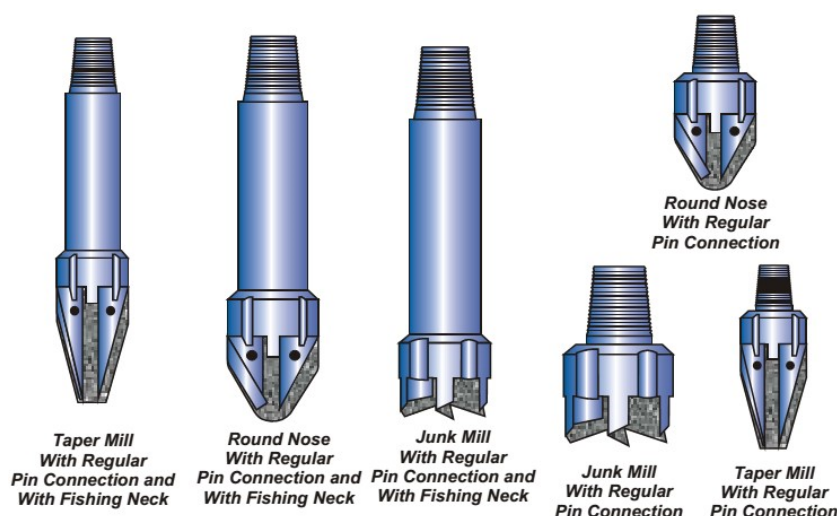


FIGURE 12: Assorted mills (Parveen, 2013)

Skirted mills have short sleeves connected to the lower outer edge of the mill which centres the mill over the fish.

Cement mills are similar to junk mills but the fuller-gauge provides an increased amount of cutting surface to mill cement. Roller cone bits are more efficient in drilling out cement but when the hole is small, the small bit used has weaker bearings that could result in lost cones, so the cement mill can be used in this case.

Pilot mills have a hard cutting surface bottom extension or can be connected to a pilot bit to mill drill collars, drill pipe, casing liners and rotary shoes. Sometimes they can be used to enlarge inside diameters so that fish can be caught with an inside catch tool.

Throated mill has a long heavily constructed body with cutting material on the mill bottom and some material deposited on the inside (throat) of the mill. It can be used to cut a fishing neck on the fish, and also to wash over the top of the fish, similar to a mill shoe.

4.3 Overshot

This is the most important and widely used tool in fishing. It consists of an upper sub, a bow or body, a lower sub that holds the grapples or slips and a guide shoe. Figure 13 shows an overshot and accessories. The tool can be run as a single unit to catch one size of fish or stacked to catch different sizes of fish. The overshot is usually connected at the bottom of a bumper sub-jar-collar assembly. The tool is lowered onto the fish, the top of the fish then passes through the shoe guide, through the slip

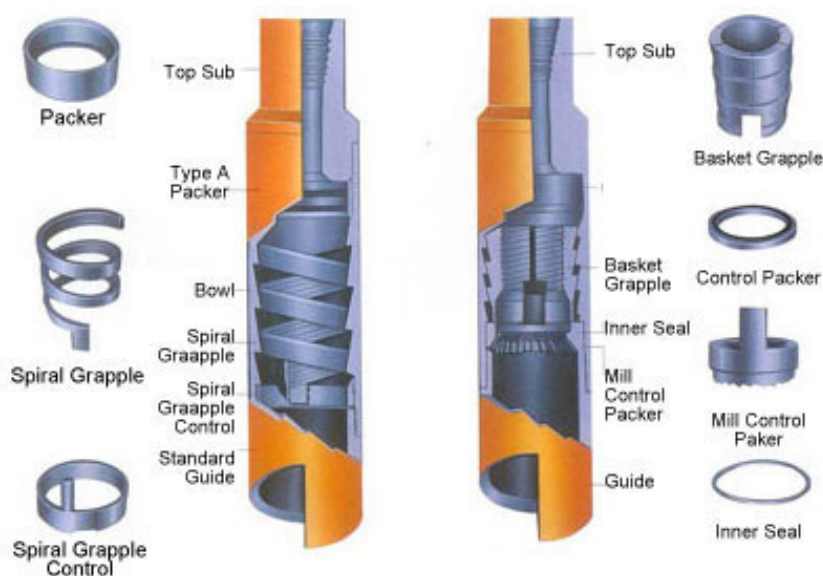


FIGURE 13: Bowen overshot and accessories (Parveen, 2013)

section and into the bowl of the overshot. When the fishing assembly is picked up, the slips (or grapples) firmly hold onto the fish. The fish is then worked until it is free and is pulled. String shots can be run down through the fish to back it off, or other operations can be conducted as needed. If the fish cannot be recovered or it becomes necessary to release the fish, the assembly is torqued to the right and bumped down to release the overshot slips. The fishing assembly can then be pulled out.

The overshot can be fitted with slips or grapples (basket or spiral). When basket grapples are used, the fish must have a clean top. Most overshots are fitted with a circulating pack off to enable cleaning/circulating out material on top of the fish before latching onto it, and through the fish after latching on. Some overshots have small mill shoes (guide, rotary and mule) at the bottom for dressing off the fish top before engagement. A bowl extension can also be fitted to the overshot to allow it to engage the fish at a lower depth than the fish top. A wall hook can be used to latch onto a fish that is laid over in a wash out. A knuckle joint can be used if the wall hook is unsuccessful.

4.4 Junk basket

Junk basket is similar in looks to an overshot, it has an upper body, a bowl (or basket), a sub to hold the retainer fingers and a shoe. Retaining fingers swivel upwards to let the junk pass up into the bowl and they return to their original horizontal position to retain the junk (bit cones, slip fragments, hand tools, etc.). Normally, some type of drag-tooth drilling shoe is used on the junk basket. Sometimes, the retaining fingers can break and release the fish. To solve this problem, the junk is drilled down until a core is cut and plugged to the bottom of the basket. The whole core plus the junk on top of core is then pulled out.

Reverse circulation junk basket has special channels and ports near the shoe that direct the fluid flow centrally from the periphery of the shoe into the centre of the basket. As the junk sweeps into the basket, the fluid moves through additional ports into the annulus. Figure 14 shows a picture of this tool. In operation, circulation is through the junk basket, around the shoe and up through the annulus. A ball is then dropped inside the tool to divert fluid flow and help sweep the junk into the basket.

4.5 Other fishing tools

Wash-over pipe. Specially sized tubes are connected to allow circulating out debris between its inner diameter and the fish outer diameter. The pipes are chosen to optimize circulation. The pipe is normally fitted with a wash over shoe at the bottom. The shoe has teeth to clear out the debris. The pipes can be connected at the bottom of an overshot assembly so that the fish is engaged once the debris is cleaned out.

The pipe spear or casing spear is used to catch the fish on its inside diameter. It has a cage fitted with a j-slot and is actuated by drag springs or friction blocks that contact the inner walls of the fish. It is run at the bottom of the fishing assembly and then positioned inside the fish. Left hand torque is then applied to release the slips; the whole assembly is then moved down a short distance and then picked

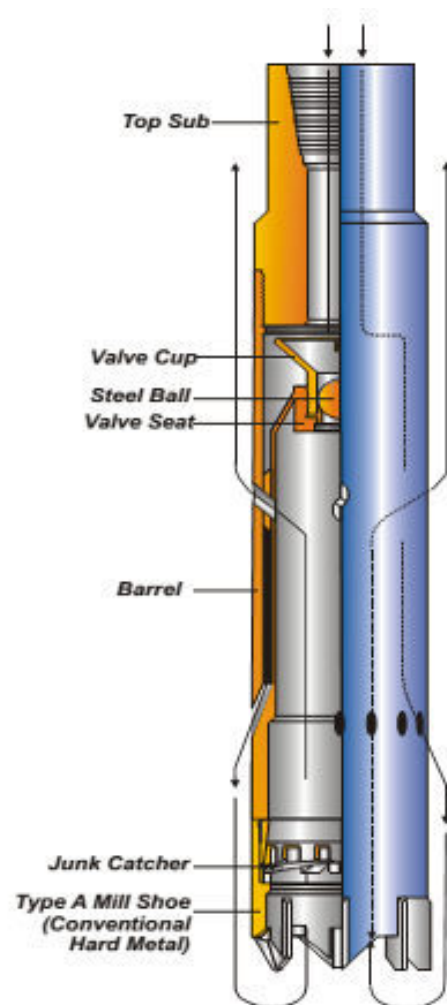


FIGURE 14: Reverse circulation junk basket (Parveen, 2013)

up slowly. The slips then move outwards and engage the inner wall of the fish. Torqueing right and bumping down will release the spear.

One demerit of the spear is that you cannot jar downwards while using them since this action releases the fish. The slips must also be released before the fishing tool can be pulled out since the slips are upside-down; so in case the spear assembly is stuck, it will be problematic to retrieve the spear alone.

Taper tap is an inside catch tool with an upper connection and a tapered body made of special steel. The tapered body has threads on its surface that are similar to those of a machine tap used to cut internal threads. It is connected to the bottom of the fishing assembly, run into the hole and screwed into the fish, which can then be pulled out after working, if necessary. It has several weaknesses: it is good in straight pulling but cannot withstand appreciable jarring or bumping. It works by cutting threads and so a longer tap would cut longer/stronger threads but then a longer tap also implies a tool that will break easily when bent. The threads cut are also weak so it's easy to jar the tool out of the fish. The tool has no releasing mechanism and if it were to be backed out of the fish, the top part of the fish would also become undone with the tap. The tool is usually released by jarring first but this can, at times, lead to breaking of the top, leaving a piece in hole. Jarring is usually done for a short time before the assembly is backed off above the tap and a more efficient fishing string run in hole. This tool is therefore used only in special occasions because of its many demerits.

Die collar is a tool that catches the external surface of a fish. Its upper part is connected to the bottom of a fishing assembly and the lower internal part is an elongated taper with threads. The tool cuts threads and then connects to the fish and then the fish is recovered. It cannot withstand long jarring periods and the thread connection to the fish is also weak.

Knuckle joint changes the direction of the line through the axis of the tools run below the knuckle joint from the line through the axis of the assembly above the knuckle joint. It is run at the bottom of the fishing assembly and is hydraulically actuated by mud pressure where the lower part is thrown out of alignment with the top part of the tool. This off-setting then is useful in catching fish in washed out sections of the hole. Bent subs and bent joints can perform the same function.

Wall hook is a hook shaped tool that is constructed as part of a washover shoe. It is used to guide the top of the fish towards the centre of the overshot in a washed out zone. It is positioned just off the top of the fish and the entire assembly is slowly rotated; the hook then guides the fish.

Jars deliver a sharp heavy upward impact on the equipment connected below them. The down hole assembly is first stretched and stores energy; then when the jars trip, the assembly above the jars travel upward rapidly for a distance equal to the stroke length of the jars. The travelling assembly is stopped suddenly at the end of the stroke and this imparts a force to the tools suspended from the jars. Collars are run immediately at the top of the jars to provide additional momentum/greater impact at the end of the stroke. Jars can be mechanical or hydraulic, the latter being more common. Jars are usually run above the fishing tool and below the collars.

Bumper sub complements the jars. It acts by driving the fish downwards. It consists of a free travelling mandrel that provides a stroke length. The string is picked up and lowered rapidly through the stroke length. At the end of the stroke, the fishing assembly imparts a sharp downward blow to the fish that is located below the bumper sub. Drill collars above the bumper sub increase the intensity of the downward blow. The bumper sub is located between the jars and the fishing tool.

Junk sub or *boot basket* catches large fragments in the fluid flow stream near the bit. The time needed to mill fragments/junk is, therefore, eliminated/reduced and consequently the life of the bit/mill is extended. It has tool joints at both ends and a bowl fixed on its body extending from near its bottom tool joint to about two thirds of the distance between the two tool joints. It is run immediately above a mill or bit. Milled metal pieces are carried over the annular space and into the bowl due to the reduced

fluid flow speed at the increased cross-sectional area at the bowl; Fluid flow at this area also causes eddy currents which make the debris drop into the bowl. The junk is retrieved on pull out.

Safety joints are run in the fishing assembly and release the assembly from the fish, if the fishing assembly must be pulled out for whatever reason, e.g. the jar in a fishing assembly might be malfunctioning and so the fishing assembly will need to be backed off to examine the jar. If there's no safety joint then it might be necessary to run a string shot to back off.

5. MENENGAI STUCK PIPE DATA ANALYSIS

Tables 4 and 5 show how stuck pipe events are distributed over the drilling activities in 10 Menengai wells. This table will assist in identifying operations during which stuck pipe mostly occurs.

TABLE 4: Drilling activities during stuck pipe in Menengai

Well	Depth of sticking (m)	Activity during sticking	No. of hours stuck	Freed	Hours spent fishing	Total drilling days (spud in to capping)	Total depth (m)
MW01	114	Drilling	1	Yes	0	79	2206
	125	Drilling	3	Yes	0		
	380	POOH	3	Yes	0		
	378	Casing-Stuck	-	Yes	0		
	2206	Casing	8	Yes	0		
MW02	109	POOH	72	Yes	0	125	3200
	133	RIH	<12	Yes	0		
	135	Ream	<12	Yes	0		
	165	POOH	1	Yes	0		
	207	Drilling	3	Yes	0		
MW03	213	Drilling	17	Yes	-	100	2112
	218	Drilling/Reaming	77	Yes	0		
	113	Drilling	0.75	Yes	0		
	167	Drilling	0.5	Yes	0		
	1187	Drilling	0.5	Yes	0		
MW04	2093	Drilling/Reaming	216	No back-off	648	83	2117
	2117	Drilling	216	No-parted string	0		
MW06	2202	Drilling	268	No-parted string	0	96	2202
MW07	59	Drilling	27	Yes	0	132	2136
	105	Drilling	<6	Yes	0		
	149	Drilling/Reaming	20	Yes	0		
	151	Drilling	5	Yes	0		
	1184	POOH	37	Yes	0		
MW08	2135	Drilling	9	No-parted string	0	126	2355
	58	Drilling	1	Yes	0		
MW09	1950	Drilling	1	Yes	0	107	2088
MW13	1648	RIH	2	Yes	0	161	2012
MW21	326	Drilling	4	Yes	0		2730

TABLE 5: Total hours stuck (10 wells)

Operation	Hours
Drilling	883.75
POOH	37
RIH	14
Total	934.75

Table 6 shows the history during selected stuck pipe events. The recommended pumping rates are calculated based on recommended good practices for geothermal drilling.

TABLE 6: Operational activities during sticking (from GDC well completion reports)

Well	Depth stuck (m) & date	Operational activities in a span of 24-48 hours	Pumping rates and returns
MW07	59 08-02-12	Drilled 26" well from 43.19 to 59.06 m with brine-returns OK. The drill string got stuck while making a connection. Worked the string and applied pull up to 200 klbf. Pumped hi vis mud at every 15 minutes while working stuck pipe up and down. No returns. Pumped L.C.M. in mud into the hole while working the string. Received returns to the surface. Pumped aerated water into the hole. Received returns on surface. The string was freed.	Approx. 1717 l/m full returns *Recommended pumping = 7295 l/m of water
MW07	149 20-02-12	Drilled 17-1/2" hole from 133 to 149.25 m with intermittent partial & full returns. Experienced drilling break from 134-138 m with cuttings fully flowing out. Circulated the hole at 149 m. While lifting the string off bottom, it got stuck with high torque and high Stand pipe pressure experienced. Worked the string up and down while pumping brine, then introduced air. Applied tension to 160 kN. Gained 1 foot. Thereafter, rotation and circulation was lost. Poured 2 drums drilling detergent into the active mud tank and pumped through the string. Not much progress observed. Pumped hi-vis mud into the hole. Very little gain observed. Worked the pipe up and down without gain. There was no pressure in the stand pipe pressure. All fluids pumped got lost into formation. Decided to cure loss zone by pumping hi-vis mud mixed with walnut shell and mica flakes. This was repeated several times. Worked the string and introduced air. Leakage on the stand pipe observed. Continued pumping brine at 200 strokes per minute while repairing the leakage. Introduced air and pressure indicated 800 psi. The string got free and full returns observed on the surface. POOH and prepared the string for plug job. Pumped 4 m ³ of cement slurry at 112 m. POOH to shoe and WOC to cure.	Approx. 2720 l/m full returns Recommended pumping = 3107 l/m of mud
MW07	1184 15-04-12	Drilled 12-1/4" hole from 1200 m to 1205 m with mud- Returns ok. Circulated the hole with 10,000 strokes of hi-vis mud to clean hole. POOH to shoe and did a wiper trip. Encountered a tight spot at 1070 m. Circulated the hole and spotted hi-vis mud at bottom. POOH from 1205 to 1184 m while back reaming. Pump went off while attempting to connect back the stand that had been removed. Saver sub damaged. Installed circulating head and circulated the hole - returns received on surface. On connecting the saver sub to string, it was noted that the string got stuck. Circulating with mud returns ok. Pumped high vis mud while working the string.	1717 l/m full returns Recommended pumping = 1413 l/m of mud
MW07	2135 25-05-12	Drilled 8-1/2" hole from 2134.09 to 2135.93 m with aerated water and foam - no returns. The string got stuck at 2135.93 m at 0200 hrs. Worked the string by applying torque. Circulated with aerated water and foam while working the string. Applied pull 310 klb and torque of 28 kNm. The string was freed at 1100 hrs and regained rotation. Circulated and POOH. POOH experiencing high drag from the bottom to 965 where there was no drag. Part of the BHA left in the hole. Two 6-1/2" drill collars, and 8-1/2" bit left in the hole. Waited for instructions from management. Decision made to RIH liners.	2040 l/m no returns Recommended pumping = 1100 l/m of water
MW09	1948 22-10-12	Drilling 8 1/2" hole with aerated water and foam. Partial returns. Drill string sticking from 2300 to 0000hrs.	2210 l/m partial returns. Recommended pumping = 1100 l/m of water

TABLE 6: Continued

MW21	326 28-12-13	Drilling 17-1/2" hole with water and mud sweeps till 326m. Got stuck at 0200 hours and lost circulation. Circulated hi-vis mud while working the string for 4 hours when string was freed. POOH after circulating to remove collapsed debris. POOH to 291 m and reaming the section between 291 and 326 m.	3060 l/m full returns *Recommended pumping = 6213 l/m of water
------	-----------------	--	--

*These water pumping rates are difficult to achieve practically and therefore the problem is mitigated by using high-viscosity mud sweeps at regular intervals to ensure sufficient hole cleaning. We also note that the upper sections of a well are usually drilled with slower ROP, and therefore the fluid annular velocity necessary for sufficient hole cleaning is lower. Cuttings also reach the surface faster since the well is still shallow.

5.1 Easy View diagrams and analysis

Drilling parameters during selected stuck pipe events were analysed using Easy View Software to easily recognise trends at the moment of sticking and before the stuck pipe event. The drilling data was recorded using data loggers at the rig site. This data was then downloaded in Excel files in 10 second intervals and has been the input into Easy View software. This analysis will assist in identifying the causes of the stuck pipe and possible solutions. The diagrams have been displayed and described in the subsequent pages. Other conditions not captured by the data loggers during the stuck pipe events have also been listed (these other conditions include pumping rates and amount of returns at shale shakers).

5.1.1 Well MW07 - Stuck at 2135 m at 0145 hrs during drilling

The trend in Figure 15 shows that the string got stuck at 0145 hrs. We see a sudden drop in WOB from 5.92 to 0 kN, the rpm also drops to 0 from 70. The pump rate, bit location and ROP remain constant. It can be observed that the driller then tries to pick up the string and it is stuck as it has to be pulled to over 84.35 tonnes. There were no circulation returns at the moment of sticking and the pumping rate was 2040 l/m of aerated foam and water.

The trends prior to sticking are displayed in Figure 16. From 0100 hrs to the sticking time at 0145 hrs, stand pipe pressure varies by 3 bar (between 5,27 MPa and 4.97 MPa). The other parameters appear to

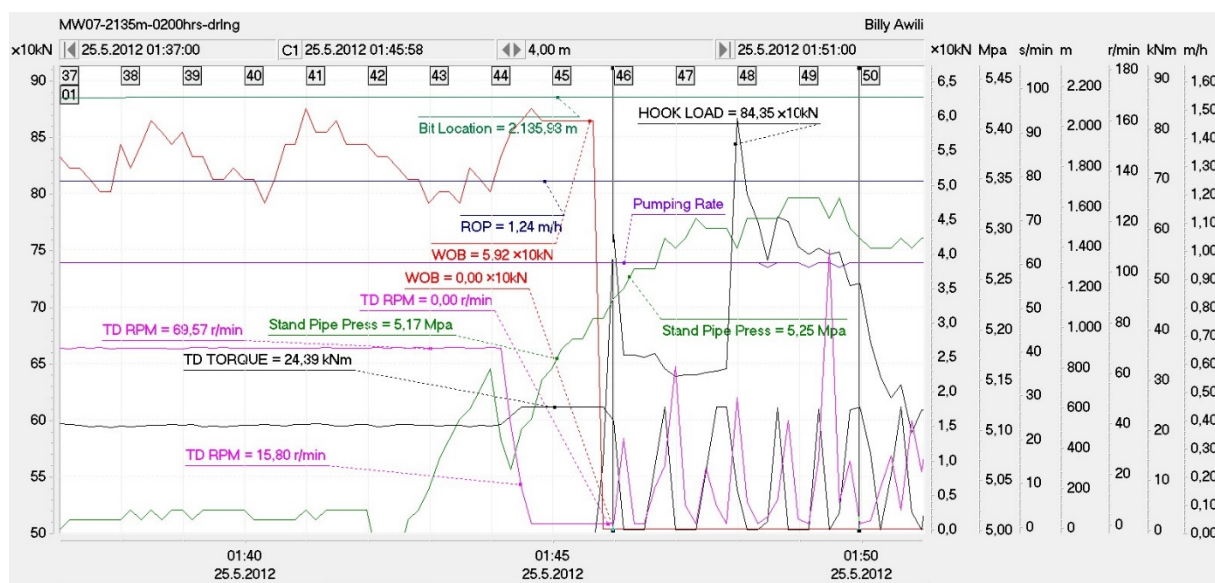


FIGURE 15: Parameters at sticking in well MW07 at 2135 m

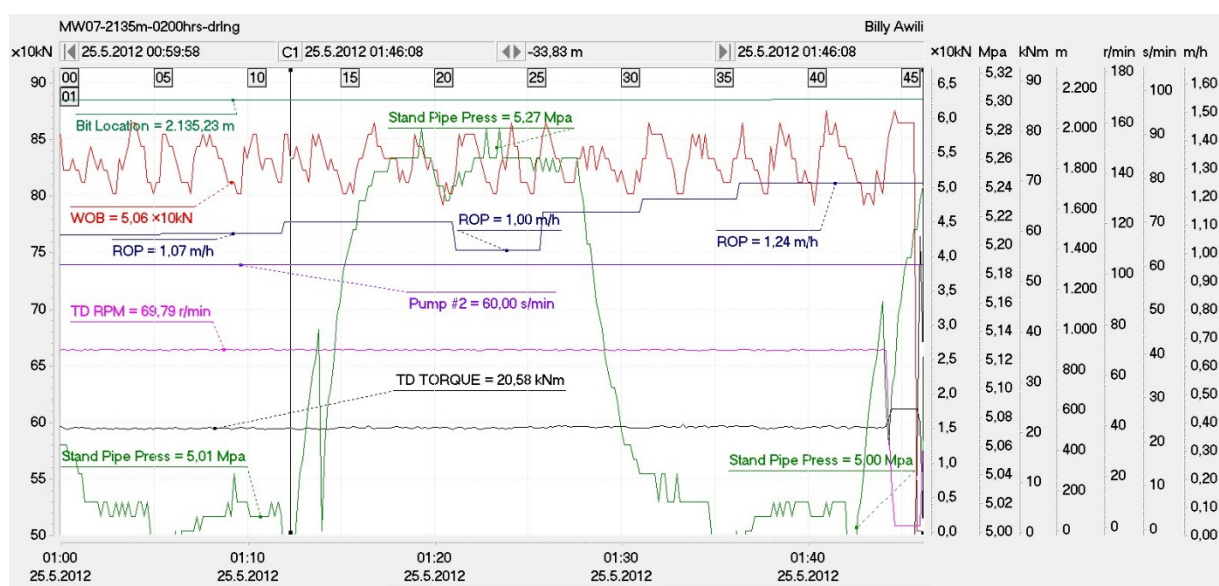


FIGURE 16: Parameters prior to sticking in well MW07 at 2135 m

be unchanging. Pumping rate was 2040 l/m of aerated foam & water and there were no returns prior to the sticking. Appendix I shows sample of data for production of Figure 16.

5.1.2 Well MW09 - Stuck at 1948 m at 2229 hrs during drilling

The trend in Figure 17 shows the parameters at the moment of sticking in well MW09 at 1948 m. The trends prior to sticking are shown in Figure 18. Appendix II shows sample of data for production of Figure 18.

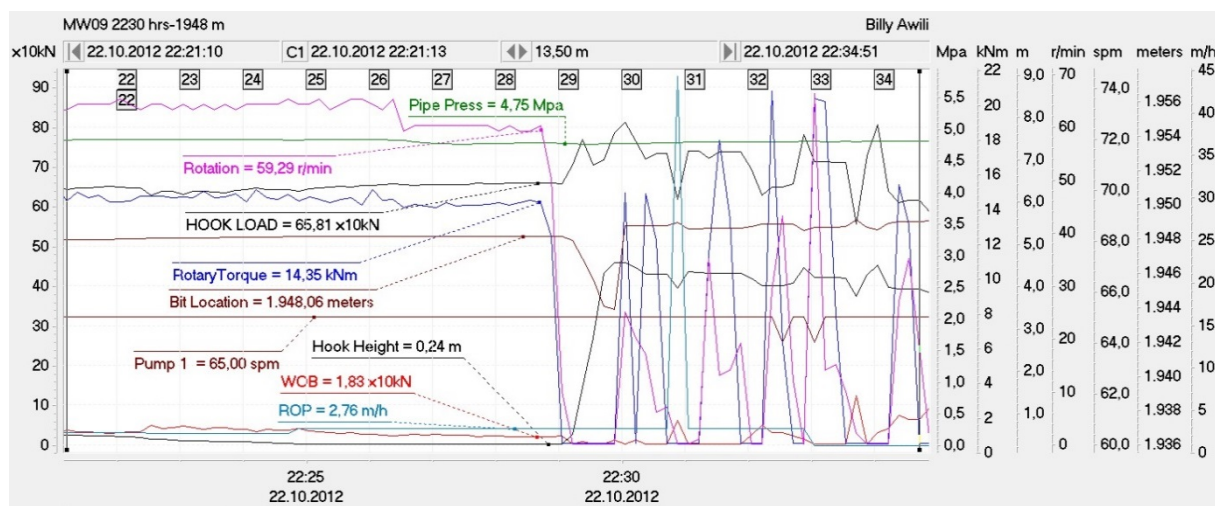


FIGURE 17: Parameters at sticking in well MW09 at 1948 m

We see that the string gets stuck at 2229 hrs when the rotation speed and rotary torque suddenly drop to zero. This occurs at the end of the drill pipe joint, evidenced by the value of hook height, i.e. the hook height is constant at about 0.41 m which implies it is the end of the current drill pipe joint. WOB is also observed to dip to zero. Pump rate and pressure do not change. There were partial returns during this stuck pipe event and the pumping rate was 2210 l/m of aerated water and foam. The trends, prior to sticking, show that the rotation speed, pipe pressure and torque are quite regular through the drilling of this joint of drill pipe, just until the sticking point.

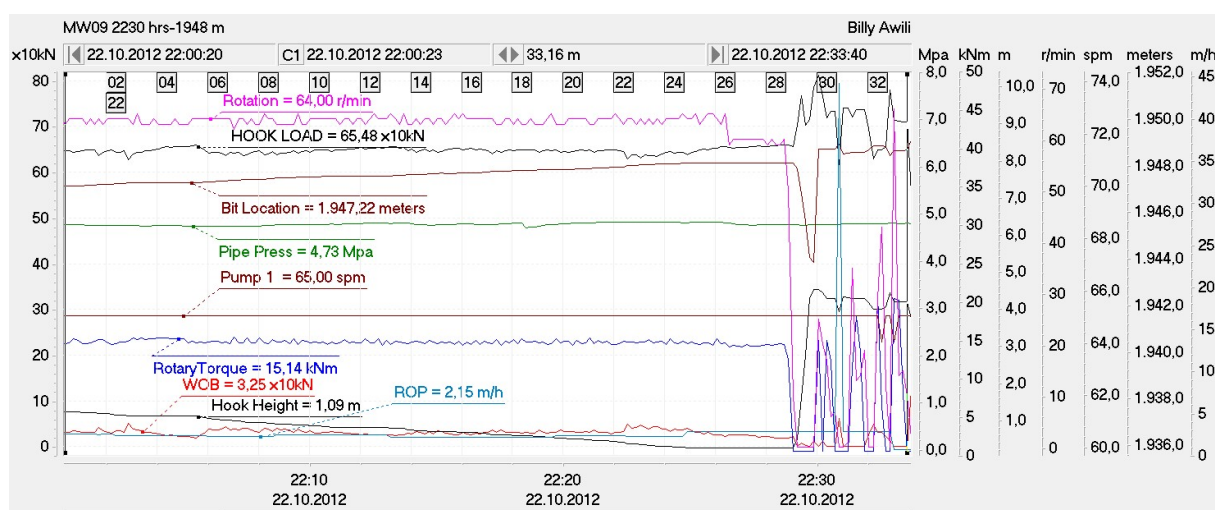


FIGURE 18: Parameters prior to sticking in well MW09 at 1948 m

The results seen in the above diagrams imply that the possible reasons and types of sticking are as shown in Table 7. Parameters not captured in Easy View have been obtained from Menengai well completion reports (see Table 6). Appendices 1 and 2 show samples of data sheets used in the Easy View analysis. The possible causes are inferred from notes on stuck pipe that were discussed earlier in this paper. The data necessary to carry out the Easy View analysis for most of the stuck pipe incidents, especially for the earlier wells, were unavailable.

TABLE 7: Possible causes of stuck pipe in Menengai wells

Well	Depth stuck (m)	Torque	WOB	ROP	Returns	Other	Possible cause
MW07	2135	Increase	Unchanged	Increase	No	Well inclined 24°	Pack-off caused by poor hole cleaning or a new lost circulation zone.
MW07	59	Freed by switching from drilling with brine to aerated fluid					Settled cuttings due to poor hole cleaning.
MW07	149	Sudden increase	-	Sudden increase	Full	Pipe pressure increase	Fractured & faulted formation.
MW07	1184	Freed by pumping water instead of mud					
MW09	1984	Sudden drop	Unchanged	Unchanged	Partial	Rotation speed suddenly 0.	Fractured & faulted formation. Cement block/junk
MW21	326	Unchanged	Unchanged	Sudden decrease	Partial	Circulated till free	Poor hole cleaning

6. DISCUSSION

The results show that the causes of stuck pipe are several in Menengai. Unconsolidated formation is problematic but has been mitigated through using cement plugs. As earlier mentioned, sticking due to fracture and faulted formation can be controlled by reducing drill string vibration, minimizing surge pressures and sufficient hole cleaning to reduce hole pack off. Sticking due to poor hole cleaning can be reduced by ensuring the hole is clean of cuttings. There are several ways to ensure good hole cleaning including ensuring good mud rheology, especially the yield point and gel strength, controlling the drill rate to ensure the hole is clean, checking the volume of cuttings coming over to the shale shaker and controlling annular velocities. Sticking caused by drilling through micro doglegs and ledges can be prevented by running slowly when tripping at alternating formation points; these areas should be noted and reamed through during trips.

6.1 Loss of returns while drilling with water and air

Drilling the production zone is quite a challenge, especially when there are no returns and cuttings cannot be carried to the surface. The drilling programme in Menengai usually recommends blind drilling in the production section when there are no returns. The choice of drilling fluid is restricted to water, aerated fluid and foam. Mud improves hole cleaning but cannot be used in the production zone since it will block the sensitive feeder zones. This problem can be solved by the use of liquid drilling fluid polymer. This compound increases water viscosity, thereby helping a lot with cutting carrying capacity; it does not affect formation permeability adversely. Polymer, however, does not improve gel strength and will, therefore, not suspend cuttings if pumping is stopped. Sweeping the hole with polymer can still be introduced in Menengai to assist in hole cleaning as it has been successfully used in Iceland.

6.2 Drill string snapping/ tubular washout

An incident of snapped string was encountered after one day of working a stuck pipe in well MW07 at 2135 m. The pull applied was 310,000 lb force and 28 kNm torque which still did not exceed the yield point (378,605 lb force tensile yield strength and 53 kNm torsional yield strength) of the 5" OD drill pipe (considered the weakest member of the drill string). The BHA snapped at a collar connection. Weakening of drill string members could be caused by drilling fluid wash out or corrosion by acidic water that is used as a drilling fluid. These two problems can be solved by using corrosion inhibitor compounds and by using caustic soda in the drilling fluid. Caustic soda is used to maintain alkalinity so that acidic fluids do not attack metal. Corrosion inhibitors work by various mechanisms to inhibit the oxygen present in drilling/production fluids from corroding pipes or equipment (Schlumberger Drilling, 2014). It has also been shown that aerated fluids erode drill pipes at a higher rate than non-aerated fluids (Budi Kesuma Adi Putra, 2008).

6.3 Deviation surveys

These can greatly assist in correcting trajectories and avoiding sticking related to hole geometry. The Totco survey tool and the electronic multi shot tool can be dropped in the drill string during trip outs to quickly measure the inclination. These tools are popular since they eliminate the non-productive time associated with setting up a conventional deviation survey.

ACKNOWLEDGEMENTS

I sincerely thank Mr. Lúðvík S Georgsson, Director of UNU-GTP, for his leadership in enabling us to enjoy our stay and studies in Iceland. A big appreciation goes to the government of Kenya (through GDC) & the government of Iceland for giving me the opportunity to study in Iceland. A big thank you goes to the able staff of UNU-GTP: Deputy Director Mr. Ingimar Guðni Haraldsson, School manager Ms. Þórhildur Ísberg, Environmental scientist Ms. Málfríður Ómarsdóttir, and the ever patient Services Manager Mr. Markús A.G. Wilde.

To my supervisor during this project, Mr. Thóroddur Sigurdsson, I give a big thank you. I would not have been able to really do any work on this project without his guidance. To Ms. Maureen Ambunya who greatly assisted me with the Easy View software, a big appreciation goes to her. Thanks to Isaac Makuk and Abraham Khaemba who assisted me in data collection.

I also sincerely thank Mr. Sverrir Thórhallsson who drew on his massive experience in sharing with me a lot of information concerning my project and geothermal drilling. We were particularly privileged to attend his lectures before he retired this year. Enjoy your retirement, Sir. Thank you to all the UNU lecturers.

To all my UNU-GTP colleagues of 2014 and my wife Caro, thank you. Be blessed.

Finally, thanks to Almighty Jehovah who protected me from illness and harm during my stay and studies.

NOMENCLATURE

BHA	= Bottom hole assembly;
ECD	= Equivalent circulating density;
ft	= Feet;
hi-vis	= High viscosity;
klbf	= Kilo pounds-force;
klbs	= Kilo pounds;
kN	= Kilo Newton;
kNm	= Kilo Newton-metre;
lb	= Pound;
l/m	= Litres per minute;
LCM	= Lost circulation material;
POOH	= Pull out of hole;
psi	= Pounds-force per square inch;
RIH	= Run in hole;
ROP	= Rate of penetration (m/h);
RPM	= Revolution per minute;
SPM	= Strokes per minute;
WOB	= Weight on bit (kN);
WOC	= Wait on cement;
"	= Inches.

REFERENCES

- Baker Hughes INTEQ, 1995: *Drilling engineering workbook*. Baker Hughes INTEQ, USA, 410 pp.
- Budi Kesuma Adi Putra, I.M., 2008: Drilling practice with aerated drilling fluid. Report 11 in: *Geothermal Training in Iceland 2008*. UNU-GTP, Iceland, 77-100.
- GDC, 2013: *Menengai well MW-16 geology report*. Geothermal Development Company – GDC, unpublished, internal report, 27 pp.
- Hólmgeirsson, S., Gudmundsson, Á., Pálsson, B., Bóasson, H., Ingason, K., and Thórhallsson S., 2010: Drilling operations of the first Iceland deep drilling well (IDDP). *Proceedings of the World Geothermal Congress 2010, Bali, Indonesia*, 10 pp.
- Kingdom Drilling, 2010: *Seven very useful stuck pipe flow chart examples*. Kingdom Drilling, webpage: www.kingdomdrilling.co.uk/de_stuck-pipe.aspx.
- Makuk, I.K., 2013: Reducing geothermal drilling problems to improve performance in Menengai. Report 16 in: *Geothermal training in Iceland 2013*. UNU-GTP, Iceland, 325-358.
- Mibei, G., 2012: Geology and hydrothermal alteration of Menengai geothermal field. Case study: wells MW-04 and MW-05. Report 21 in: *Geothermal training in Iceland 2012*. UNU-GTP, Iceland, 437-465.
- Okwiri, L.A., 2013: Geothermal drilling time analysis: A case study of Menengai and Hengill. Report 25 in: *Geothermal training in Iceland 2013*. UNU-GTP, Iceland, 577-598.
- Parveen, 2013: *Fishing and milling tools*. Parveen Industries PVT, Ltd., webpage, www.parveenoilfield.com/fishing-milling-tools.html.
- Rabia, H., 2001: *Well engineering and construction* (e-book). Entrac Consulting, UK, 779 pp.
- Schlumberger, 1991: *Schlumberger oilfield review 1991*. Schlumberger, report, October, 13-26.
- Schlumberger Drilling, 2014: *Corrosion inhibitor*. Schlumberger M-I SWACO, Ltd., webpage: www.slb.com/services/miswaco/services/completions/packer_fluids/corrosion_inhibitors.aspx.
- Short, J.A., 1981: *Fishing and casing repair*. PennWell Publishing Co., Tulsa, OK, 365 pp.
- SPE, 2007: *Petroleum engineering handbook II: Drilling engineering* (digital edition). SPE - Society of Petroleum Engineers, USA, 763 pp.

APPENDIX I: Sample data used to produce Figure 16

Date	Hook load	Wob	Stand pipe pressure	Rotary torque	Hook height	Pump #2	Pump #3	Drilling time	Bit location	Drilled depth	Td torque	Td rpm
yyyy.mm.dd hh:mm:ss	×10 kN	×10 kN	MPa	kNm	m	s/min	s/min	min/m	m	m	kNm	r/min
2012.05.25 01:39:59	48.98	5.06	5.02	0.57	17.13	60	60	48.23	2135.86	2135.86	20.75	69.38
2012.05.25 01:40:09	48.98	5.06	5.01	0.57	17.13	60	60	48.23	2135.86	2135.86	20.75	69.56
2012.05.25 01:40:19	49.33	4.72	5.01	0.56	17.13	60	60	48.23	2135.86	2135.86	20.97	69.38
2012.05.25 01:40:29	48.98	5.06	5.01	0.57	17.12	60	60	48.23	2135.86	2135.86	20.81	69.38
2012.05.25 01:40:39	48.47	5.57	5.01	0.57	17.1	60	60	48.23	2135.89	2135.89	20.59	69.38
2012.05.25 01:40:49	48.47	5.57	5.01	0.57	17.1	60	60	48.23	2135.89	2135.89	21	69.47
2012.05.25 01:40:59	47.95	6.09	5.02	0.57	17.08	60	60	48.23	2135.9	2135.9	20.91	69.56
2012.05.25 01:41:09	48.3	5.75	5.01	0.57	17.08	60	60	48.23	2135.9	2135.9	21.06	69.47
2012.05.25 01:41:19	48.3	5.75	5.02	0.57	17.08	60	60	48.23	2135.9	2135.9	20.94	69.84
2012.05.25 01:41:29	48.12	5.92	5.02	0.57	17.08	60	60	48.23	2135.9	2135.9	20.72	69.38
2012.05.25 01:41:39	48.47	5.57	5.02	0.57	17.08	60	60	48.23	2135.9	2135.9	20.69	69.56
2012.05.25 01:41:49	48.47	5.57	5.02	0.57	17.08	60	60	48.23	2135.9	2135.9	20.91	69.56
2012.05.25 01:41:59	48.47	5.57	5.02	0.56	17.08	60	60	48.23	2135.9	2135.9	20.91	69.56
2012.05.25 01:42:09	48.64	5.4	4.97	0.56	17.08	60	60	48.23	2135.9	2135.9	20.5	69.75
2012.05.25 01:42:19	48.64	5.4	4.97	0.57	17.08	60	60	48.23	2135.9	2135.9	20.62	69.47
2012.05.25 01:42:29	48.81	5.23	4.97	0.56	17.08	60	60	48.23	2135.9	2135.9	20.94	69.66
2012.05.25 01:42:39	48.98	5.06	5.01	0.57	17.08	60	60	48.23	2135.9	2135.9	20.94	69.56
2012.05.25 01:42:49	48.98	5.06	5.02	0.57	17.08	60	60	48.23	2135.9	2135.9	20.81	69.75
2012.05.25 01:42:59	49.33	4.72	5.04	0.56	17.08	60	60	48.23	2135.9	2135.9	20.81	69.56
2012.05.25 01:43:09	49.16	4.89	5.07	0.57	17.08	60	60	48.23	2135.9	2135.9	20.59	69.56
2012.05.25 01:43:19	49.16	4.89	5.09	0.57	17.08	60	60	48.23	2135.9	2135.9	20.78	69.66
2012.05.25 01:43:29	49.33	4.72	5.11	0.57	17.08	60	60	48.23	2135.9	2135.9	20.81	69.66
2012.05.25 01:43:39	48.81	5.23	5.12	0.57	17.08	60	60	48.23	2135.91	2135.91	20.53	69.56
2012.05.25 01:43:49	48.98	5.06	5.14	0.57	17.07	60	60	48.23	2135.91	2135.91	20.81	69.56
2012.05.25 01:43:59	49.16	4.89	5.16	0.57	17.06	60	60	48.23	2135.92	2135.92	20.72	69.84
2012.05.25 01:44:09	48.64	5.4	5.09	0.57	17.05	60	60	48.23	2135.93	2135.93	20.91	69.47
2012.05.25 01:44:19	48.3	5.75	5.06	0.57	17.05	60	60	48.23	2135.93	2135.93	22.66	39.09
2012.05.25 01:44:29	48.12	5.92	5.1	0.57	17.05	60	60	48.23	2135.93	2135.93	24.41	14.16
2012.05.25 01:44:39	47.95	6.09	5.11	0.98	17.05	60	60	48.23	2135.93	2135.93	24.38	0

Date	Hook load	Wob	Stand pipe pressure	Rotary torque	Hook height	Pump #2	Pump #3	Drilling time	Bit location	Drilled depth	Td torque	Td rpm
yyyy.mm.dd hh:mm:ss	×10 kN	×10 kN	MPa	kNm	m	s/min	s/min	min/m	m	m	kNm	r/min
2012.05.25 01:44:49	48.12	5.92	5.15	3.08	17.05	60	60	48.23	2135.93	2135.93	24.41	0
2012.05.25 01:44:59	48.12	5.92	5.16	3	17.05	60	60	48.23	2135.93	2135.93	24.38	0
2012.05.25 01:45:09	48.12	5.92	5.18	0.58	17.05	60	60	48.23	2135.93	2135.93	24.41	0
2012.05.25 01:45:19	48.12	5.92	5.19	0.6	17.05	60	60	48.23	2135.93	2135.93	24.41	0
2012.05.25 01:45:29	48.12	5.92	5.19	0.58	17.05	60	60	48.23	2135.93	2135.93	24.38	0
2012.05.25 01:45:39	48.12	5.92	5.21	0.58	17.05	60	60	48.23	2135.93	2135.93	24.41	0
2012.05.25 01:45:49	56.2	0	5.21	0.58	17.05	60	60	48.23	2135.93	2135.93	24.41	0
2012.05.25 01:45:59	76.31	0	5.23	0.58	17.05	60	60	48.23	2135.93	2135.93	21.78	0
2012.05.25 01:46:09	65.66	0	5.24	0.58	17.05	60	60	48.23	2135.93	2135.93	0	33.84
2012.05.25 01:46:19	65.66	0	5.26	0.58	17.05	60	60	48.23	2135.93	2135.93	0	0
2012.05.25 01:46:29	65.48	0	5.26	0.58	17.05	60	60	48.23	2135.93	2135.93	0	0
2012.05.25 01:46:39	65.83	0	5.26	0.58	17.05	60	60	48.23	2135.93	2135.93	12.53	14.16
2012.05.25 01:46:49	64.45	0	5.29	0.58	17.05	60	60	48.23	2135.93	2135.93	24.38	22.97
2012.05.25 01:46:59	63.77	0	5.28	0.58	17.05	60	60	48.23	2135.93	2135.93	0	62.25
2012.05.25 01:47:09	63.94	0	5.29	0.58	17.05	60	60	48.23	2135.93	2135.93	0	7.31
2012.05.25 01:47:19	63.94	0	5.31	0.58	17.05	60	60	48.23	2135.93	2135.93	0	0
2012.05.25 01:47:29	64.11	0	5.3	0.6	17.05	60	60	48.23	2135.93	2135.93	11.53	22.22
2012.05.25 01:47:39	64.28	0	5.3	0.58	17.05	60	60	48.23	2135.93	2135.93	24.44	7.12
2012.05.25 01:47:49	64.45	0	5.3	0.58	17.05	60	60	48.23	2135.93	2135.93	24.41	0
2012.05.25 01:47:59	86.62	0	5.28	0.58	17.05	60	60	48.23	2135.93	2135.93	8.03	49.88
2012.05.25 01:48:09	79.92	0	5.31	0.58	17.05	60	60	48.23	2135.93	2135.93	0	8.81
2012.05.25 01:48:19	77.52	0	5.31	0.57	17.05	60	60	48.23	2135.93	2135.93	0	0
2012.05.25 01:48:29	74.08	0	5.31	0.58	17.05	59	60	48.23	2135.93	2135.93	1.66	2.91
2012.05.25 01:48:39	77.86	0	5.31	0.58	17.05	60	60	48.23	2135.93	2135.93	24.28	9.38
2012.05.25 01:48:49	77.52	0	5.33	0.58	17.05	60	60	48.23	2135.93	2135.93	0	40.78
2012.05.25 01:48:59	75.28	0	5.33	0.58	17.05	60	60	48.23	2135.93	2135.93	0	1.78
2012.05.25 01:49:09	74.59	0	5.33	0.58	17.05	59	59	48.23	2135.93	2135.93	0	0
2012.05.25 01:49:19	75.11	0	5.33	0.58	17.05	60	60	48.23	2135.93	2135.93	23.94	25.88
2012.05.25 01:49:29	74.59	0	5.31	0.58	17.05	60	60	48.23	2135.93	2135.93	0	108.47
2012.05.25 01:49:39	74.77	0	5.33	0.57	17.05	59	59	48.23	2135.93	2135.93	3.28	8.44
2012.05.25 01:49:49	71.84	0	5.3	0.58	17.05	60	60	48.23	2135.93	2135.93	23.91	24.94

APPENDIX II: Sample data used to produce Figure 18

Date	Hook load	Wob	Pipe pressure	Rotary torque	Hook height	Rotation	Pump 1	Drilling time	Bit location
yyyy.mm.dd hh:mm:ss	×10kN	×10kN	MPa	kNm	m	r/min	spm	min/m	meters
2012.10.22 22:56:53	69.47	0	5.7	0.47	4.19	0	70	88.72	1948.62
2012.10.22 22:57:03	69.61	0	5.7	0.47	4.19	0	70	88.72	1948.62
2012.10.22 22:57:13	66.66	0.98	5.7	0.47	4.09	0	70	88.72	1948.72
2012.10.22 22:57:23	67.5	1.41	5.72	0.47	4.13	0	70	88.72	1948.69
2012.10.22 22:57:33	75.94	0	5.72	0.47	4.37	0	70	88.72	1948.46
2012.10.22 22:57:43	65.25	1.97	5.73	0.47	4.06	0	70	88.72	1948.75
2012.10.22 22:57:53	64.69	2.95	5.74	0.47	4.03	0	70	88.72	1948.79
2012.10.22 22:58:03	81	0	5.75	0.47	4.55	0	70	88.72	1948.28
2012.10.22 22:58:13	77.48	7.45	5.75	0.47	4.52	0	70	88.72	1948.28
2012.10.22 22:58:23	72.7	0.98	5.77	0.47	4.33	0	70	88.72	1948.48
2012.10.22 22:58:33	66.52	1.12	5.78	0.47	4.16	0	70	88.72	1948.66
2012.10.22 22:58:43	65.81	1.83	5.79	0.47	4.14	0	70	88.72	1948.69
2012.10.22 22:58:53	68.2	0.14	5.78	19.32	4.14	22	70	88.72	1948.69
2012.10.22 22:59:03	68.34	0	5.77	17.5	4.14	0	70	88.72	1948.69
2012.10.22 22:59:13	68.2	0	5.75	9.63	4.14	9	70	88.72	1948.69
2012.10.22 22:59:23	68.2	0	5.75	0.9	4.14	6	70	88.72	1948.69
2012.10.22 22:59:33	68.2	0	5.75	0.47	4.14	0	70	88.72	1948.69
2012.10.22 22:59:43	58.92	8.72	5.75	0.47	3.86	1	70	88.72	1948.97
2012.10.22 22:59:53	73.55	0	5.77	0.47	4.33	0	71	88.72	1948.47
2012.10.22 23:00:03	89.02	0	5.77	0.47	4.83	0	70	88.72	1947.98
2012.10.22 23:00:13	79.31	0	5.78	0.47	4.45	0	70	88.72	1948.32
2012.10.22 23:00:23	68.06	0	5.79	0.47	4.16	0	70	88.72	1948.65
2012.10.22 23:00:33	56.95	11.11	5.79	0.47	3.85	0	70	88.72	1948.96
2012.10.22 23:00:43	75.8	0	5.8	0.47	4.38	0	70	88.72	1948.45
2012.10.22 23:00:53	91.27	0	5.8	0.47	4.85	0	70	88.72	1947.97
2012.10.22 23:01:03	78.89	1.55	5.8	0.47	4.51	0	70	88.72	1948.3
2012.10.22 23:01:13	68.34	0.14	5.82	0.47	4.21	0	70	88.72	1948.6
2012.10.22 23:01:23	71.3	0	5.82	15.84	4.21	30	70	88.72	1948.59
2012.10.22 23:01:33	71.16	0	5.82	21.61	4.21	0	70	88.72	1948.59
2012.10.22 23:01:43	71.02	0	5.82	16.45	4.21	1	70	88.72	1948.59
2012.10.22 23:01:53	71.02	0	5.82	13.88	4.21	4	70	88.72	1948.59
2012.10.22 23:02:03	71.02	0	5.82	5.86	4.21	38	70	88.72	1948.59
2012.10.22 23:02:13	71.02	0	5.82	14.49	4.21	0	70	88.72	1948.59
2012.10.22 23:02:23	70.88	0	5.82	5.52	4.21	0	70	88.72	1948.59
2012.10.22 23:02:33	71.02	0	5.82	3.24	4.21	1	70	88.72	1948.59
2012.10.22 23:02:43	71.02	0	5.82	0.47	4.21	0	70	88.72	1948.59
2012.10.22 23:02:53	70.88	0	5.82	0.47	4.21	0	70	88.72	1948.59



UNITED NATIONS
UNIVERSITY

UNU-GTP

Geothermal Training Programme

Orkustofnun, Grensasvegur 9,
IS-108 Reykjavik, Iceland

Reports 2014
Number 28

INCREASED EXERGETIC EFFICIENCY BY USING A BACK PRESSURE TURBINE FOR HIGH WELLHEAD PRESSURES AT HELLISHEIDI GEOTHERMAL POWER PLANT

Abdelrahman Ali Osman

Ministry of Water Resources and Electricity
Renewable and Alternative Energy Directorate
Geothermal Energy Department
P.O. Box 787 Khartoum, Sudan
SUDAN

abdelrahman.aliosman@gmail.com, abdaiosm@hotmail.com

ABSTRACT

A study of utilizing geothermal wells with high wellhead pressures by using a back-pressure turbine as a topping unit, operating between 17.5 bar-a inlet pressure and 10 bar-a exhaust pressure, was applied for the existing Hellisheidi geothermal power plant. The study was carried out to determine the electrical power output that could be generated and the loss of exergy throughout the process. Using engineering equation solver (EES) and manual calculations, an output of 7.75 MW of electricity was calculated for the topping unit with 98% energy efficiency and 81.76% exergetic efficiency for a back-pressure turbine with an isentropic efficiency of 85%. The total exergy available in the steam is 89 MW while the exergy available in the steam exiting the turbine is 79 MW. Due to irreversibilities, 1.8 MW is destroyed in the turbine. In comparison, 6 MW of exergy is destroyed if a throttle valve is used instead of a back-pressure turbine to reduce the steam pressure from 17.5 bar-a down to 10 bar-a in order to be compatible with the inlet pressure at Hellisheidi geothermal power plant.

1. INTRODUCTION

1.1 General background

Renewable energy resources are a priority in today's global energy outlook due to the drastically increasing prices of fossil fuels and their high gaseous emissions. Geothermal energy, the thermal energy stored in the earth's crust, is considered to be an attractive renewable energy option.

Geothermal energy has been used since ancient times in many countries in the world, but was mainly used for bathing, cooking and washing. More recently, geothermal energy has been utilised for electricity production, district heating, green house farming, fish farming, drying, snow melting, and many other uses (Cordova, 2013).

Commercial electricity power generation from geothermal power plants started in 1914 when a 250 kW unit at Larderello in Italy provided electricity to the nearby cities of Volterra and Pomarance (DiPippo, 2007). Since then, many geothermal power plants have been installed around the world.

In the author's opinion, there can be many reasons for producing electricity from geothermal resources. At many locations, it is technically, economically and environmentally feasible, due to high availability, a high capacity factor, the ability to be used as a base load, low operational and maintenance cost and low CO₂ emissions.

Geothermal power plants can be divided into two main groups according to the enthalpy of the wells: steam cycles which are used at higher well enthalpies, and binary cycles for lower enthalpies.

In the steam cycles the geothermal fluid boils partly due to flashing in the wells; then the steam is separated from the brine and finally expanded in a turbine, producing positive work. Usually, the brine is rejected to the environment (e.g. re-injected into the reservoir or released at the surface), or it can be flashed again at a lower pressure before final disposal. The first type of cycle in which the fluid boils and the brine is separated at a high pressure is called the Single Flash cycle (SF), and the second one in which the brine is flashed again at a lower pressure is called a Double Flash cycle (DF) (Valdimarsson, 2011).

A binary cycle uses a secondary working fluid in a closed power generation cycle. A heat exchanger is used to transfer heat from the geothermal fluid to the working fluid, and the cooled brine is then rejected to the environment. The Organic Rankine Cycle (ORC) and Kalina cycle, used to exploit low to medium enthalpy geothermal resources, are both binary cycles with different types of secondary working fluids (Valdimarsson, 2011).

Geothermal resources have been classified as low, intermediate or high enthalpy resources according to their reservoir temperatures. The temperature ranges used for these classifications are arbitrary and they are not generally agreed upon (Lee, 1996). Temperature is used as the classification parameter because it is the easiest to measure and understand. In addition, temperature or enthalpy alone can be ambiguous in defining a geothermal resource because two independent thermodynamic properties are required to define the thermodynamic state of fluid. Geothermal energy is already in the form of heat, and from the thermodynamic point of view, work is more useful than heat because not all the heat can be converted to work. Therefore, geothermal resources should be classified by their exergy, a measure of their ability to do work. The basic concept of exergy is that it is the maximum work (or power) output that could theoretically be obtained from a substance at specified thermodynamic conditions relative to its surroundings (DiPippo, 2007). The exergy analysis is based on the Second Law of thermodynamics. Exergy analysis is applied for all components of a power plant in order to identify the exergy efficiencies, sometimes called Second Law efficiencies or utilization efficiencies.

1.2 Area of study

This study, to analyse the exergy balance of pressure reduction by the installation of a back pressure turbine as a topping unit in an existing power plant setup, was applied to the Hellisheidi geothermal power plant. The geothermal power plant, (Figure 1), is situated in the Hengill area, an active volcanic ridge in southwest Iceland. The plant's purpose is to meet an increasing demand for electricity and hot water for space heating in the industrial and domestic sectors. The maximum production capacity is 303 MW of electricity and currently 133 MW of thermal energy. Production of electricity began in 2006 when two 45 MW turbines were started, and then in 2007 an additional 30 MW low-pressure turbine was brought online. In 2008, two 45 MW turbines were added, using steam from boreholes in Skardsmýrarfjall among others. The thermal station producing hot water for space heating was introduced in 2010 and is currently producing 133 MW of hot water. In 2011, additional 2 x 45 MW units were installed in a separate power house (Kárason et al., 2012).

Geothermal activity in the Hengill area is connected with three volcanic systems. At least three volcanic eruptions have occurred in the Hengill area in the last 11,000 years, the most recent being 2,000 years ago. The Hengill area is part of the Hengill region, which covers 112 km² and is one of the most extensive geothermal areas in Iceland (Reykjavik Energy, 2014).



FIGURE 1: Hellisheidi geothermal power plant
(Power-Technology.com, 2014)

The idea is to install a back pressure turbine unit into the existing system instead of reducing pressure by using a throttling valve to utilize the geothermal energy of four new wells that operate at a high pressure and are located in Hverahlíð geothermal field, which is at a 5 km distance from Hellisheidi power plant. They are connected to the Hellisheidi plant to maintain the production of both electricity and hot water due to an annual 2.3% steam flow decline, due to pressure drawdown, from the primary reservoir utilized for the plant. Since the wells operate at a higher pressure than other wells connected to the plant, the pressure must be decreased by some process before the steam can be utilised in the existing turbines. It has become clear that the cost of connecting those four wells with high pressure to a back pressure turbine, and then to connect the exhausted steam to the existing power plant at Hellisheidi, is significantly less than the cost of drilling new wells to compensate for the pressure drop in the system. Another reason is to observe and study the behaviour of the Hverahlíð reservoir for a period of years in order to gain operational experience of the reservoir; thus, if the geothermal energy production from those wells is stable and steady, then the idea of implementing a new power plant in the Hverahlíð area would be an option.

1.3 Background review

The design inlet pressure for a condensing steam turbine is often below 8 bar-a in order to meet the estimated pressure drop until the geothermal reservoir reaches steady state. However, some of the geothermal well fields produce steam at much higher pressures than required for the condensing steam turbine, which could be considered unused energy. In this situation, the steam pressure must be reduced to the required inlet pressure of the turbine. Usually, the inlet pressure of the condensing steam turbines is restricted and cannot be increased; therefore, the idea of using a back-pressure turbine to extract this unused energy and to reduce the pressure becomes very attractive.

The technology of using a back-pressure turbine to extract energy from the excess steam pressure in condensing turbine geothermal power plants, which is sometimes called a topping unit, has been used in Leyte geothermal optimization project in the Philippines since 1997. It was done by ORMAT as an EPC turnkey contract. This project consists of four individual power plants, three of which have been using this technology of a topping unit, and the fourth using another technology called a bottoming unit. The total net power gained by using this technology is 49 MW which represents almost 10% of the total installed capacity of the four power plants of 502.5 MW. The net power gained is composed of 35.65 MW from topping units and 13.35 from the bottoming unit. The three power plants, which used topping units are: Tongonan power plant, Mahanagdong A and Mahanagdong B (Kaplan and Schochet, 2000).

Tongonan topping plant

The total installed capacity of the main Tongonan power plant was 112.5 MW. The inlet pressure of the plant is 6.83 bar-a, and the steam pressure from the well field is 11.14 bar-a. The ORMAT topping

units were added to generate maximum power while reducing the pressure from 11.14 bar-a to 6.83 bar-a. The topping unit consists of two 3.25 MW back-pressure turbines with high efficiency and reliability and simple construction. Each turbine is directly coupled to the opposite side of a common generator. The Tongonan topping plant consists of 3 topping units, generating 16.95 MW net power (Kaplan and Schochet, 2000).

Mahanagdong A topping plant

The total installed capacity of the main Mahanagdong A power plant is 120 MW. The inlet pressure of the plant is 6.83 bar-a while the resource pressure is 10.8 bar-a. The ORMAT topping units were added to generate maximum power while reducing the pressure from 10.8 bar-a to 6.8 bar-a. The Mahanagdong A topping plant consists of 2 topping units generating 12.45 MW net output (Kaplan and Schochet, 2000).

Mahanagdong B topping plant

The total installed capacity of the main Mahanagdong B power plant is 60 MW. The inlet pressure of the plant is 6.83 bar-a and the resource pressure is 10.8 bar-a. The ORMAT topping unit was added to generate maximum power while reducing the pressure from 10.8 bar-a to 6.8 bar-a. The Mahanagdong B topping plant consists of one topping unit generating 6.25 MW net (Kaplan and Schochet, 2000).

The total net power gained by the three topping plants is 35.65 MW in cost effective power (Kaplan and Schochet, 2000).

This technology has also been used in Wairakei power project, New Zealand since 1956 when it was redesigned by replacing the machines of the heavy water distillation plant with new turbines. Wairakei geothermal power plant has a total capacity of 47 MW. The redesign resulted in implementation of a new plant, called B station, beside the old plant, which is called A station, and the addition of new turbines in A station itself.

Wairakei A station

This plant consists of three pressure levels: high pressure, intermediate pressure and low pressure. The high pressure is 13.5 bar-a which enters 2 x 11.5 MW turbines and 2 x 6.5 MW turbines, and exits at 4.45 bar-a as intermediate pressure. This intermediate pressure from the high pressure turbines exhaust is accompanied by steam which comes from the intermediate pressure wells and goes to the intermediate pressure manifold. The steam from the intermediate pressure manifold goes through two branches to the intermediate pressure turbines and to B station. The 2 x 11.2 MW intermediate pressure turbines receive the steam at 4.45 bar-a, and exhaust steam at 1.0345 bar-a. The steam at 1.0345 bar-a enters 4 x 11.2 low pressure turbines which are condensing turbines, designed to exhaust steam under vacuum (Thain and Carey, 2009).

Wairakei B station

The Wairakei B station consists of 4 x 30 MW condensing turbines. These turbines work at an intermediate pressure of 4.45 bar-a inlet pressure and exhaust the steam under vacuum. The turbines also accept the pass-in steam from low pressure at 1.1 bar-a (Thain and Carey, 2009).

The total installed capacity of Wairakei geothermal power plant increased from 47 MW to 193.2 MW, 103.2 MW from A station and 90 MW from B station (Thain and Carey, 2009).

2. TECHNICAL DATA

2.1 Plant description

Hellisheidi power plant is the largest geothermal power plant in Iceland. The maximum capacity is 303 MWe of electricity and the production of hot water is currently 133 MWth.

Electricity generation was started in 2006 when 2 x 45 MW high-pressure turbine units were installed. In 2007, a 33 MW low-pressure turbine was installed and brought online. Additional 2 X 45 MW high-pressure turbine units were installed in 2008. In 2011, 2 x 45 MW high-pressure turbine units were installed in a separate power house. The production of hot water for space heating started in 2010. The high-pressure turbines are working at 8 bars gage pressure and the low pressure turbine works at 2.1 bars pressure (Kárason et al., 2012).

Hellisheidi geothermal power plant is owned and operated by ON Power (Orka Náttúrunnar), ON, which is a new subsidiary company of Reykjavik Energy (Orkuveita Reykjavíkur). ON is a power company that produces electricity, mainly by harnessing geothermal energy, to more than half of the population of Iceland. The company is one of the world leaders in the utilisation of geothermal energy for production of hot water and electricity.

Orkuveita Reykjavíkur has already purchased 2 x 45 MW condensing turbines planned to be commissioned in the Hverahlíd area. The project has been postponed, but 4 production wells have already been drilled and are able to provide steam for 45 MW of electricity production in a condensing unit. ON is connecting these wells to Hellisheidi power plant to gain operational experience with the reservoir. The connection is assumed to be in operation at the beginning of 2016.

After testing and an analysis of the geothermal fluid of the wells in Hverahlíd, it has become clear that the optimal separation pressure is higher than the initial design, indicating 17.5 bar-a instead of 10 bar-a. However, to connect the steam to the Hellisheidi power plant, the pressure has to be dropped to 10 bar-a. Therefore, it is of interest to investigate the feasibility of installing a back pressure turbine at Hverahlíd. The turbines have already been purchased for Hverahlíd Power Plant with 7.5 bar-a turbine inlet pressure; the back pressure turbine is expected to be a permanently installed unit and to be in operation for at least 30-50 years.

2.2 Project description

This study aims to analyse the energy and exergy of a back pressure turbine which could be added in the Hverahlíd area and to compare the benefits of adding this turbine to the benefits of using a throttling valve. The two options for connecting high enthalpy wells are shown in Figure 2.

For scenario one, the steam from high pressure wells goes to the separator through a throttling valve which adjusts the steam pressure to 17.5 bar-a. The separated steam enters the back pressure turbine at 17.5 bar-a of saturated steam and the separated water goes through a water phase pipeline to Hellisheidi power plant for further utilization before it ends in the re-injection system. The exhaust steam from the back pressure turbine at 10 bar-a goes to Hellisheidi Power Plant, reaching there at 9 bar-a due to pressure drop along the pipeline. For scenario two, the steam from the wells goes through a throttling valve, reducing its pressure from 17.5 bar-a to 10 bar-a, after which the steam is led directly to Hellisheidi geothermal power plant.

2.3 Back pressure turbine technical specifications

The technical specifications of the back pressure turbine, to be installed in the Hverahlíd area, should be compatible with the steam conditions from the four wells with high pressure in that area. The chemical composition of the steam is shown in Table 1, and the steam conditions for the back pressure turbine are shown in Table 2.

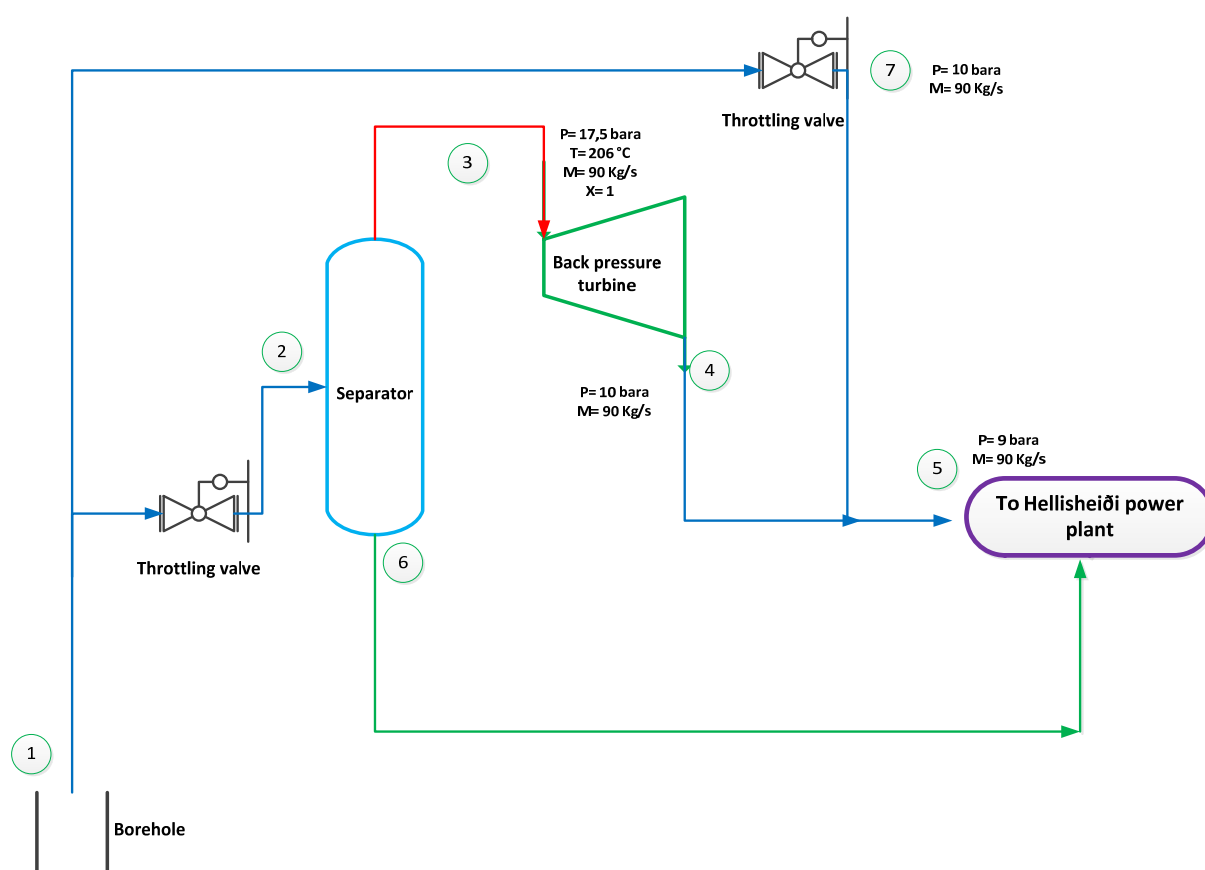


FIGURE 2: Flow diagram showing the two options of connecting the high enthalpy wells

TABLE 1: Chemical composition of the steam

Steam at 17.5 bar-a, 206°C	Range	Rated conditions
CO ₂	3000-10.000 ppm	8.000 ppm
H ₂ S	400 – 2.000 ppm	1.500 ppm
H ₂	4 – 200 ppm	100 ppm
CH ₄	0 – 5 ppm	2 ppm
N ₂	100 – 700 ppm	400 ppm

TABLE 2: The steam conditions

Conditions	Rated conditions	Unit
Rated steam consumption	90	kg/s
Main steam inlet pressure	17.5	bar-a
Main steam outlet pressure	10	bar-a
Main steam inlet temperature	206 (saturated steam)	°C
Frequency	50	Hz
Nominal voltage	11	kV
Generator power factor	0.80	-
Non condensable gas in steam	1.00	% by weight

Based on the above data, the specifications of the proposed back-pressure turbine and the generator are shown in Table 3. This study is applied for a specific turbine with an isentropic efficiency of 85%.

TABLE 3: Technical specifications for the back-pressure turbine-generator set

Parameter	Value	Unit
Throttle pressure	17.5	bar-a
Throttle temperature (Sat)	206	°C
Inlet enthalpy	2795	kJ/kg
Net throttle flow to turbine	90	kg/s
Included NCG flow	1.0	% by weight
Velocity through 2 x 400 mm DIN PN25 valves	44	m/s
Exhaust pressure	10.0	bar-a
Exhaust enthalpy	2704	kJ/kg
Exhaust temperature	180	°C
Exhaust moisture	3%	-
Turbine speed	5000	RPM
Generator speed	1500	RPM
Gross generator output	7.75	MWe
Theoretical steam rate (TSR)	33.470	Ton/MW-hr
Actual steam rate (ASR)	41.800	Ton/MW-hr
Auxiliary load	50	kW
Four-pole generator efficiency	98	%
Speed reduction gear box efficiency	98.5	%

3. THEORETICAL ANALYSIS

3.1 Exergy

Exergy is the theoretical maximum amount of work that can be acquired from a system at any state, pressure and temperature when operating with a reservoir at a constant pressure and temperature (Eastop and McConkey, 2009). The constant pressure and temperature are the surrounding environmental conditions state, called dead state. Dead state means that the working fluid at the exhaust exits in thermodynamic equilibrium with the surrounding conditions, thus the fluid has no more energy to deliver work and can be considered dead. Thermodynamic equilibrium requires that the system is in mechanical equilibrium (i.e. equal pressure), thermal equilibrium (i.e. equal temperature), and chemical equilibrium (i.e. equal reaction potential) with its surroundings. Chemical equilibrium does not take place in a practical sense in most geothermal power plants and can thus be disregarded; only mechanical and thermal equilibrium at dead state need be dealt with in calculating the exergy (DiPippo, 2007).

Exergy is based on the Second Law of thermodynamics which deals with the quality of the energy in addition to the quantity, while the first law of thermodynamics deals only with the quantity of energy and is only concerned with the amount of energy with no regard to its quality. Exergy can be divided into four different exergy components such as: physical exergy, kinetic exergy, potential exergy and chemical exergy, and can be expressed as follows (Bore, 2005):

$$\psi_{total} = \psi_{PH} + \psi_{KE} + \psi_{PE} + \psi_{CH} \quad (1)$$

where ψ_{total} = Total exergy;
 ψ_{PH} = Physical exergy;
 ψ_{KE} = Kinetic exergy;
 ψ_{PE} = Potential exergy; and
 ψ_{CH} = Chemical exergy.

A system may receive or discharge fluids from or to the surroundings, and exchange heat and work with the surroundings. The aim is to gain the maximum power output from the operation of the system. In order to achieve this ideal outcome, there are two thermodynamic conditions that must be met:

1. All processes taking place within the system must be perfectly reversible, which means that no losses occur because of friction, turbulence, or any other source of irreversibility; and
2. The state of all fluids being discharged from the system must be in thermodynamic equilibrium with the surroundings, which means that the leaving fluids have no more potential to do work relative to the surroundings (DiPippo, 2007).

According to the definition of the system, geothermal power plants can be considered an open system operating in steady state once they operate at their design operating conditions. An open system is one in which fluids are exchanged with the surrounding environment through its boundaries during the operation and, in steady operation, indicates that the values of all thermodynamic properties at any point in the system remain constant without changing with time.

In order to get an efficient and effective power plant, it is important to consider the quality and quantity of the energy used to reach a given objective. As mentioned before, the first law of thermodynamics deals only with the quantity of energy and affirms that energy cannot be created or destroyed, meanwhile the second law of thermodynamics deals with the quality of energy, i.e. it is concerned with the quality of energy to cause change, declination of energy during a process, entropy generation and lost opportunities to do work.

In other words, exergy is the expression for loss of available energy due to the generation of entropy in irreversible systems or processes. The exergy loss in a system or component is calculated by multiplying the absolute temperature of the surroundings by the entropy generated. The entropy is the ratio of the heat immersed by matter to the absolute temperature of the surrounding environment.

In open systems operating in steady flow, we deal with the balance of mass, energy, entropy and exergy according to the first and second laws of thermodynamics. Those four balances should be applied (Hepbasli, 2006).

For mass balance:

$$\sum_{i=1}^n m_i = 0 \quad (2)$$

where m_i = mass flow rate crossing each inlet or outlet;
 i = an index that accounts for all inlets and outlets of the system; and
 n = total number of inlets and outlets.

or:

$$m_i = m_{out} \quad (3)$$

where m_i = mass flow rate at inlet; and
 m_{out} = mass flow rate at outlet.

For energy balance:

$$\sum E_i = \sum E_{out} \quad (4)$$

where E_i = Total energy input
 E_{out} = Total energy output

or:

$$Q - W = - \sum_{i=1}^n m_i (h_i + 0.5 v_i^2 + g z_i) \quad (5)$$

where Q = Heat energy (thermal power) added to the system from the surroundings;
 W = Work output (mechanical power) developed by the system to the surroundings;
 h_i = Specific enthalpy of the fluid at each inlet or outlet;
 v_i = Velocity of the fluid at each inlet or outlet;
 g = Gravitational acceleration corresponding to the elevation; and
 z_i = Elevation of each inlet or outlet.

For entropy balance:

$$S_i - S_{out} + S_{gen} = 0 \quad (6)$$

where S_i = Entropy at inlet;
 S_{out} = Entropy at outlet; and
 S_{gen} = Entropy generated by the system due to irreversibility.

For exergy balance:

$$\sum Ex_{in} - \sum Ex_{out} = \sum Ex_{dest} \quad (7)$$

where Ex_{in} = Exergy input;
 Ex_{out} = Exergy output; and
 Ex_{dest} = Exergy destruction due to irreversibility.

In geothermal power plants we focus only on physical and chemical exergies because they are low-quality forms of exergy associated with matter and cannot easily be converted to work, while the kinetic and potential exergies are high-quality exergy forms associated with matter and can be fully converted to useful work (Bore, 2005). Commonly, in power plants we concentrate on physical exergy which exists in the fluid stream, heat transfer and work transfer. Therefore, the general exergy balance can be written as follows:

$$\sum Ex_{heat} - \sum Ex_{work} + \sum Ex_{mass,in} - \sum Ex_{mass,out} = \sum Ex_{dest} \quad (8)$$

where Ex_{heat} = Exergy associated with heat transfer through the system boundaries;
 Ex_{work} = Exergy associated with work transfer through the system boundaries;
 $Ex_{mass,in}$ = Exergy associated with the fluid streams at the inlet; and
 $Ex_{mass,out}$ = Exergy associated with the fluid streams at the outlet.

Exergy associated with heat transfer through the system boundaries can be determined as follows:

$$Ex_{heat} = \sum (1 - \frac{T_0}{T_k}) * Q_k \quad (9)$$

where Q_k = Heat transfer rate through the boundary at temperature T_k at location k ; and
 T_0 = dead state temperature.

Exergy associated with work transfer through the system boundaries can be written:

$$Ex_{work} = W \quad (10)$$

where W = Work.

Specific exergy associated with the fluid stream can be calculated by the following equation:

$$\psi = (h - h_0) - T_0(S - S_0) \quad (11)$$

where ψ = Specific exergy associated with the fluid stream;
 h = Specific enthalpy;
 S = Specific entropy;
 h_0 = Enthalpy at dead state conditions; and
 S_0 = Entropy at dead state conditions.

Therefore, the power output can be determined by:

$$W = m[(h_1 - h_2) - T_0(S_1 - S_2)] \quad (12)$$

And the maximum power output can be given by the equation:

$$W_{max} = m[(h_1 - h_0) - T_0(S_1 - S_0)] \quad (13)$$

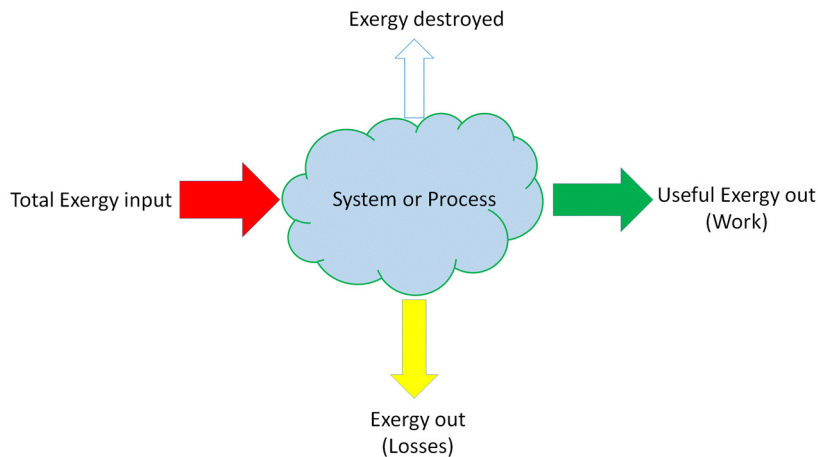
where h_1, h_2 = Enthalpy at the inlet and outlet, respectively; and
 S_1, S_2 = Entropy at the inlet and outlet, respectively.

3.2 Restricted dead state

Restricted dead state is the state in which a specific form of equilibrium is needed where only the mechanical and thermal equilibrium must be satisfied apart from the chemical equilibrium. This equilibrium is called thermo-mechanical equilibrium (Hepbasli, 2006).

3.3 Exergy balance (Exergy analysis)

An exergy analysis (or second law analysis) has been verified to be a powerful tool in the simulated thermodynamic analyses of energy systems. In other words, it has been commonly used in the design, simulation and performance evaluation of energy systems. The exergy analysis method is utilised to distinguish and to evaluate quantitatively the causes of the thermodynamic deficiency of the process under consideration. It can, therefore, indicate the possibilities of thermodynamic enhancement of the process under consideration, but only an economic analysis can decide the practicality of a possible enhancement.



Exergy analysis affords a mathematical method with which to evaluate the maximum work extractable from matter relative to a reference state (i.e. dead state) (Hepbasli, 2006). A simple diagram showing exergy balance is shown in Figure 3.

Exergy balance methods can indicate the quantity and quality of heat losses in the system or component and delineate the location of energy degradation (measure

FIGURE 3: A simple diagram showing exergy balance

and ascertain causes of energy degradation). Most of the thermodynamic limitations cannot be detected by an energy analysis. Some certain processes like throttling, heat transfers, expansion and friction contain no energy losses but they degrade the quality of energy and its ability to do work and, therefore, contain exergy losses (Bore, 2005). Exergy balance shows the exergy flow through a system or component, shown by the Sankey diagram in Figure 4.

3.4 Exergetic efficiency

In geothermal power plants it is better to calculate efficiency based on exergy, which is sometimes called the Second Law efficiency or utilization efficiency, rather than calculating the thermal efficiency (First Law efficiency). There are two different methods to determine the exergetic efficiency: “brute-force” and the “functional” method (Hepbasli, 2006). In the “brute-force” method, exergy efficiency for a system can be expressed as the ratio of the sum of all output exergy to the sum of all input exergy. In the “functional” method, exergy efficiency for a system can be expressed as the ratio of the exergy associated with the desired energy output to the exergy associated with the energy consumed to achieve the desired output. The brute-force method can be applied directly for each system regardless of the nature of the system, once all exergy flows have been determined.

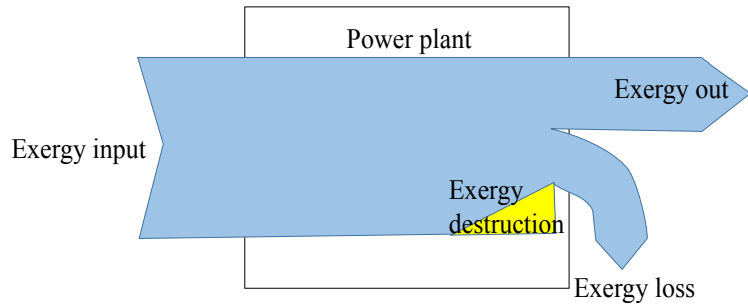


FIGURE 4: A Sankey diagram of exergy flow

The functional method cannot be applied until the purpose of the system is known and the working form of the efficiency equation can be formulated. Exergetic efficiency can be applied for a power plant or for each component separately.

3.4.1 Exergetic efficiency for turbine

With regard to the two different methods for calculating the exergetic efficiency, both methods can be applied for calculating the exergetic efficiency of the turbine. Assume that we have a turbine with steam entering through the inlet and leaving from the exhaust, as shown in Figure 5.

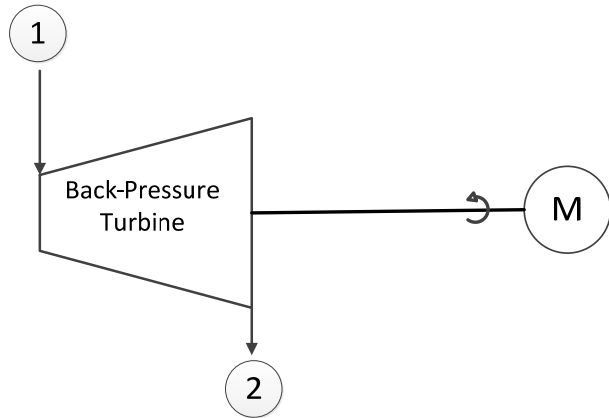


FIGURE 5: Simple turbine with inlet and outlet

The brute-force efficiency can be expressed as shown in Equation 14 and the functional efficiency can be expressed as in Equation 15.

$$\eta_{B.F}^{II} = \frac{W + Ex_2}{Ex_1} \quad (14)$$

$$\eta_{FUN}^{II} = \frac{W}{Ex_1 - Ex_2} \quad (15)$$

where $\eta_{B.F}^{II}$ = Brute-force efficiency;
 η_{FUN}^{II} = Functional efficiency;
 W = Work output; and
 Ex_1 and Ex_2 = Exergy at inlet and outlet, respectively.

4. RESULTS

A model was built using the software Engineering Equation Solver (EES) to calculate the energy and exergy flow of the back pressure turbine to be installed at Hverahlíd area for scenario one, shown in T-s diagram in Figure 6, and also to calculate the energy and exergy flow through the throttling valve for scenario two, shown in T-s diagram in Figure 7.

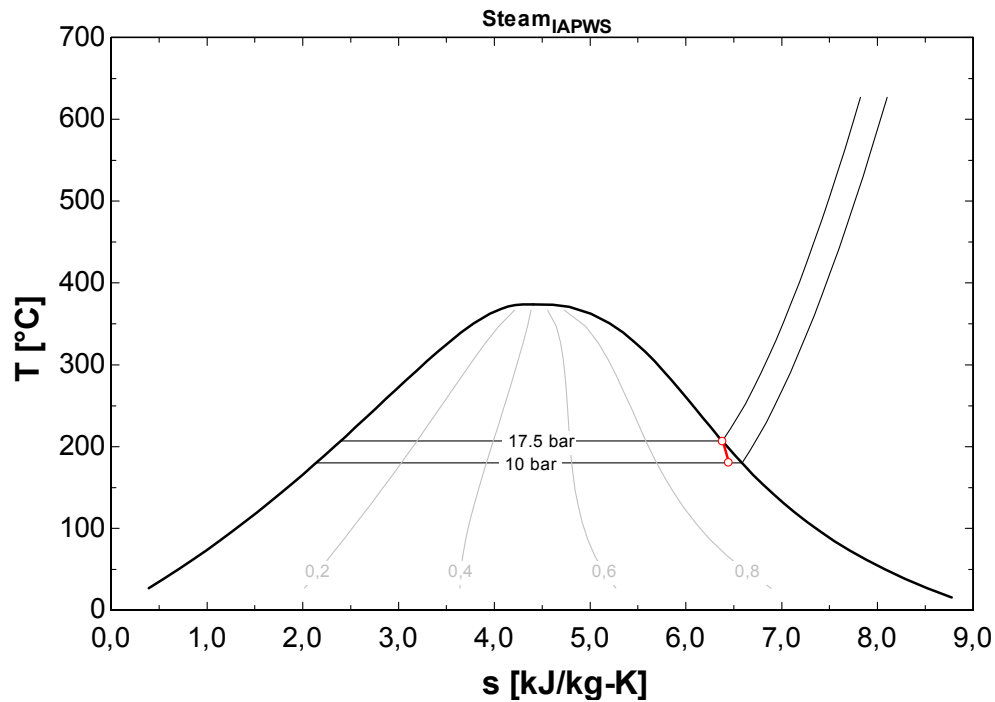


FIGURE 6: T-S diagram showing the process of expansion in the back-pressure turbine

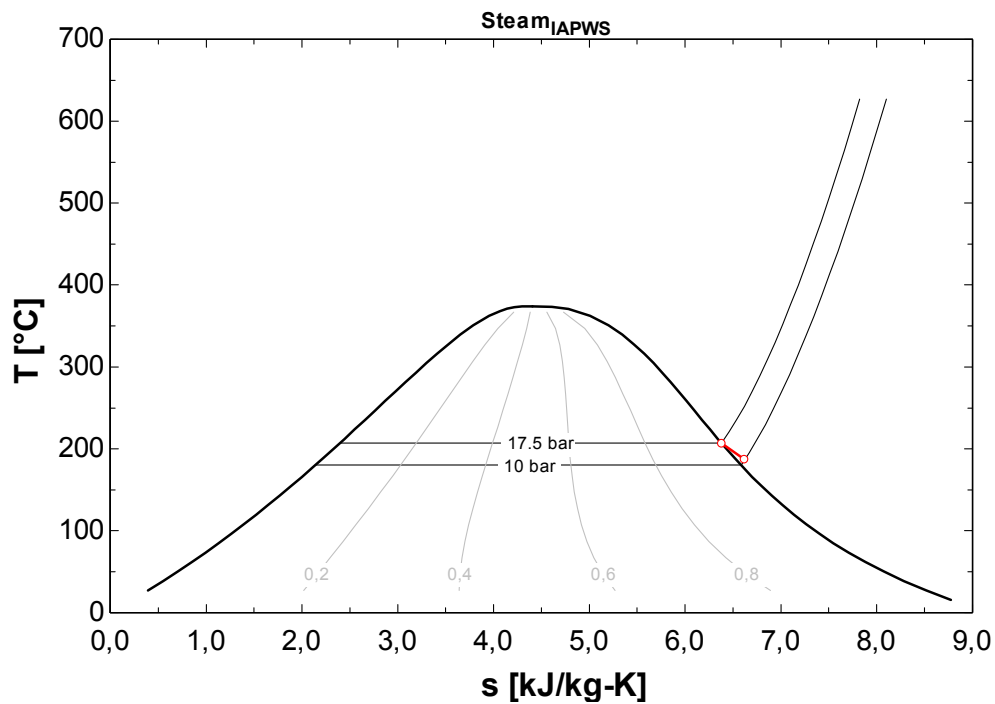


FIGURE 7: T-S diagram showing the processes of throttling due to the throttling valve

Many assumptions were made to simplify these calculations:

1. The flow of geothermal fluid is steady which means the mass flow in is equal to the mass flow out and there are no losses.
2. The turbine is thermally isolated which means there is no heat exchange between the turbine and the surrounding environment.
3. There is no heat exchange between the valve and the surroundings and no work is performed or produced during the process. Thus, the pressure drop across the valve is assumed to be isenthalpic.
4. Geothermal fluid has the same properties as pure water.
5. Kinetic exergy, potential exergy and chemical exergy are neglected.

4.1 Energy analysis

Energy can be defined as motion or the ability to cause motion. Commonly, energy is conserved in a process according to the First Law of Thermodynamics (Bore, 2005). In an energy analysis we calculate the energy input, the energy output, the isentropic work that can be done, the actual work and the energy efficiency.

4.1.1 Energy input

Energy input is the heat energy added into a turbine and is equal to the product of mass flow rate of the steam into a turbine and its enthalpy at entry.

$$E_i = m_i * h_i \quad (16)$$

where E_i = Energy input;
 m_i = Mass flow rate at the entry; and
 h_i = Enthalpy at the entry.

$$E_i = 90 \frac{kg}{s} * 2795 \frac{kJ}{kg} = 251,550 \frac{kJ}{s}$$

The energy input is thus 251,550 kW.

4.1.2 Energy output

Energy output is equal to the heat exhausted which is equal to the mass flow rate of the steam that exits the turbine multiplied by the enthalpy at the exit.

$$E_{out} = m_{out} * h_{out} \quad (17)$$

where E_{out} = Energy output;
 m_{out} = Mass flow rate at the exit; and
 h_{out} = Enthalpy at the exit.

$$E_{out} = 90 \frac{kg}{s} * 2704 \frac{kJ}{kg} = 243,360 \frac{kJ}{s}$$

The energy output is 243,360 kW.

4.1.3 Work done

Work done is the ideal or theoretical work that can be obtained in isentropic expansion in the turbine and is equal to the energy in the steam at the entrance into the turbine minus that at the exit.

$$W.D = E_i - E_{out} \quad (18)$$

where $W.D$ = Work done.

$$W.D = 251550 \frac{kJ}{s} - 243360 \frac{kJ}{s} = 8190 \text{ kW}$$

Work done is 8190 kW.

4.1.4 Actual power developed by turbine shaft

The Actual Power developed by the turbine shaft is the mechanical power produced by the turbine and is equal to the net power output from the generator divided by the gearbox efficiency and the generator efficiency.

$$P = \frac{\text{Generator Power}}{\eta_{Gearbox} * \eta_{Generator}} \quad (19)$$

where P = Actual power developed by turbine shaft;
 $\eta_{Gearbox}$ = Gear box efficiency; and
 $\eta_{Generator}$ = Generator efficiency.

$$P = \frac{[7750 \text{ kW}]}{0.98 * 0.985} = 8028.59 \text{ kW}$$

The actual power developed by turbine shaft is 8028.59 kW.

4.1.5 Energy efficiency (1st Law efficiency) of the turbine

Energy efficiency is the ratio of the energy output as mechanical power to the total energy in the system:

$$\eta_u = \frac{(\text{Actual power developed by turbine shaft})}{(E_i - E_{out})} \quad (20)$$

where η_u = Energy efficiency.

$$\eta_u = \frac{8028.59 \text{ kW}}{\left(251,550 \frac{kJ}{s} - 243,360 \frac{kJ}{s}\right)} = 98.03\%$$

The energy balance for the back pressure turbine is shown in the Sankey diagram in Figure 8.

All of the above calculations are for scenario one. For scenario two, it is known from the basics of thermodynamics that the enthalpy remains constant through throttling which means the energy before throttling is equal to that after throttling. Therefore, there is no energy loss due to throttling, although exergy is destroyed during the process.

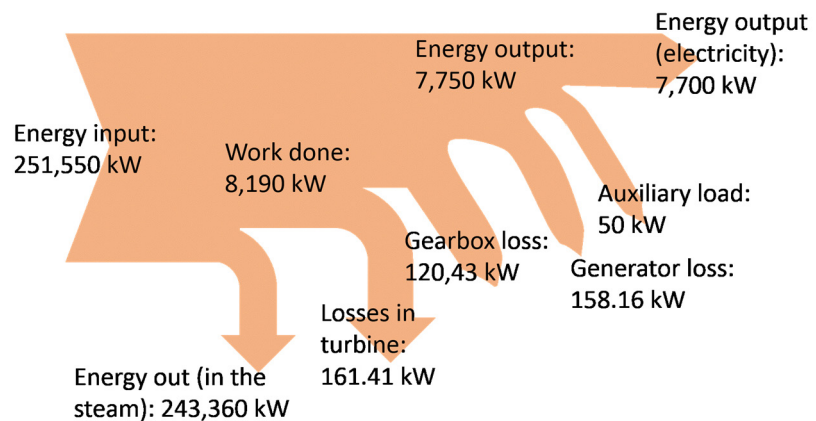


FIGURE 8: A Sankey diagram showing energy flow in the turbine

4.2 Exergy analysis

Exergy can be defined as work or the ability to cause work. Commonly, exergy is conserved in a reversible process, but is always consumed in an irreversible process according to the Second Law of Thermodynamics (Bore, 2005).

Exergy is always evaluated with respect to a reference environment (dead state). The reference environment is in stable equilibrium, acts as an infinite system and is a sink or source for heat and materials. It experiences only internal reversible processes, in which its intensive properties (i.e. temperature T_0 and pressure P_0) remain constant. In this analysis, the surrounding temperature and pressure are taken as $T_0 = 10^\circ\text{C}$ (283 K) and $P_0 = 1$ bar, based on weather and climate conditions at Hverahlid, Iceland. In exergy analysis we calculate the exergy input, the exergy out, exergy destruction and exergetic efficiency.

4.2.1 Exergy input

The total exergy associated with the fluid stream at the inlet of a turbine can be written as:

$$\psi_{in} = m_{in} * [h_{in} - h_0 - T_0 (S_{in} - S_0)] \quad (21)$$

where ψ_{in} = Exergy input;
 m_{in} = Mass flow rate input; and
 h_{in} and S_{in} = enthalpy and entropy at the inlet, respectively.

$$\begin{aligned} \psi_{in} &= 90 \frac{\text{kg}}{\text{s}} * \left[2795 \frac{\text{kJ}}{\text{kg}} - 42.12 \frac{\text{kJ}}{\text{kg}} - 283 \text{ K} * \left(6.388 \frac{\text{kJ}}{\text{kg}} \cdot \text{K} - 0.1511 \frac{\text{kJ}}{\text{kg}} \cdot \text{K} \right) \right] \\ &= 88905.36 \frac{\text{kJ}}{\text{s}} \end{aligned}$$

The exergy input is 88,905.36 kW.

4.2.2 Exergy out

The total exergy associated with the fluid stream at the exit of turbine can be written as:

$$\psi_{out} = m_{out} * [(h_{out} - h_0 - T_0(S_{out} - S_0))] \quad (22)$$

where ψ_{out} = Exergy out;
 m_{out} = Mass flow rate at the outlet; and
 h_{out} and S_{out} = Enthalpy and entropy at the outlet, respectively.

$$\begin{aligned} \psi_{out} &= 90 \frac{\text{kg}}{\text{s}} * \left[2704 \frac{\text{kJ}}{\text{kg}} - 42.12 \frac{\text{kJ}}{\text{kg}} \right. \\ &\quad \left. - 283 \text{ K} * \left(6.452 \frac{\text{kJ}}{\text{kg}} \cdot \text{K} - 0.1511 \frac{\text{kJ}}{\text{kg}} \cdot \text{K} \right) \right] = 79085.28 \frac{\text{kJ}}{\text{s}} \end{aligned}$$

The exergy out is 79,085.28 kW.

4.2.3 Exergy destruction in turbine

The total exergy destroyed in the turbine is due to irreversibility in the process or deficiencies of the turbine:

$$\psi_{des} = \psi_{in} - \psi_{out} - \psi_{power} \quad (23)$$

$$\psi_{des} = 889,015.36 \frac{kJ}{s} - 79,085.28 \frac{kJ}{s} - 80,28.59 kW = 1791.49 \frac{kJ}{s}$$

Exergy destruction in the turbine due to irreversibility is 1791.49 kW.

4.2.4 Exergy efficiency

For brute-force exergy efficiency, it is the ratio of the total exergies associated with the exergy out to the total exergies associated with the exergy input.

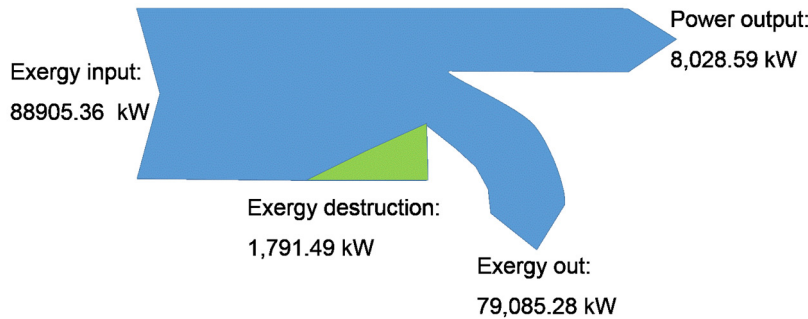
$$\eta_{B.F}^I = \frac{\psi_{power} + \psi_{out}}{\psi_{in}} \quad (24)$$

$$\eta_{B.F}^I = \frac{8028.59 + 79,085.28}{88,905.36} = 97.98\%$$

For functional exergy efficiency, it is the ratio of the exergy converted to useful work to the total exergy in the system:

$$\eta_{FUN}^I = \frac{\psi_{power}}{(\psi_{in} - \psi_{out})} \quad (25)$$

$$\eta_{FUN}^I = \frac{8028.59 kW}{88,905.36 \frac{kJ}{s} - 79,085.28 \frac{kJ}{s}} = 81.76\%$$



The exergy balance for the back pressure turbine is shown in the Sankey diagram in Figure 9.

The general layout of the back pressure turbine is shown in Figure 10.

For the second scenario, in which we connect these four wells with high wellhead pressure directly to Hellisheidi geothermal power

FIGURE 9: A Sankey diagram showing the exergy flow through the turbine

plant through a throttling valve, there will be some losses of exergy which can be determined as follows:

$$\text{Exergy loss (Destruction)} = Ex_{Upstream} - Ex_{Downstream} \quad (26)$$

The explanation is that the loss of exergy is equal to the exergy of the fluid before the throttling valve (Up-stream) less the exergy of the fluid after the throttling valve (Down-stream). As we know the enthalpy remains constant due to using throttling valve:

$$\begin{aligned} Ex_{Upstream} &= 90 \frac{kg}{s} * \left[2795 \frac{kJ}{kg} - 42.12 \frac{kJ}{kg} - 283 K * \left(6.388 \frac{kJ}{kg} \cdot K - 0.1511 \frac{kJ}{kg} \cdot K \right) \right] \\ &= 88,905.36 \frac{kJ}{s} \end{aligned}$$

The entropy at down-stream is the entropy at a pressure of 10 bar-a and enthalpy of 2795 kJ/kg.

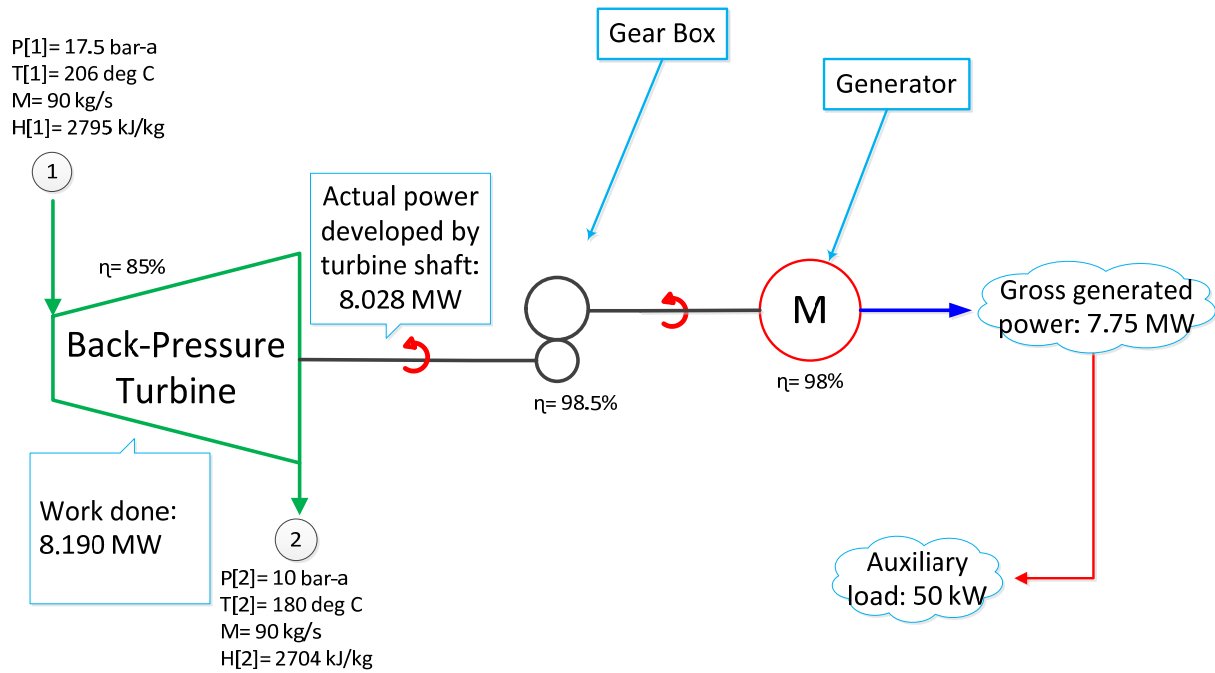


FIGURE 10: General layout of the back-pressure turbine

$$Ex_{Downstream} = 90 \frac{\text{kg}}{\text{s}} * \left[2795 \frac{\text{kJ}}{\text{kg}} - 42.12 \frac{\text{kJ}}{\text{kg}} - 283 \text{ K} * \left(6.625 \frac{\text{kJ}}{\text{kg}} \cdot \text{K} - 0.1511 \frac{\text{kJ}}{\text{kg}} \cdot \text{K} \right) \right]$$

$$= 82,868.97 \frac{\text{kJ}}{\text{s}}$$

$$Exergyloss(Destruction) = 88,905.36 - 82,868.97 = 6036.39 \text{ kJ/s}$$

The exergy destruction (loss) due to the throttling valve is: 6036.39 kW.

Exergy destruction in the throttling valve can be expressed in the Sankey diagram in Figure 11.

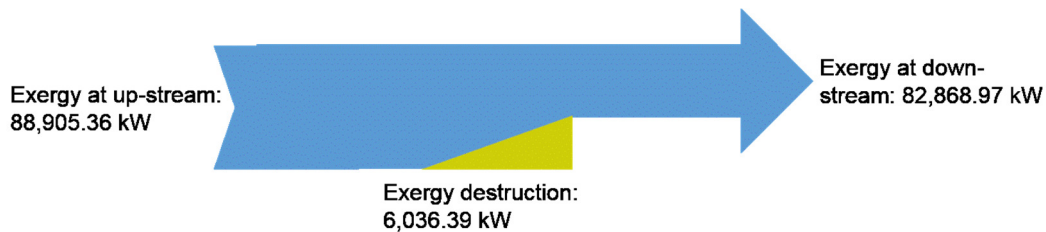


FIGURE 11: A Sankey diagram showing the exergy flow through a throttling valve

If a simple comparison is made between the two options (scenarios) of using a back-pressure turbine and reducing the pressure by using a throttling valve, we can clearly see that the steam leaving the back pressure turbine towards Hellisheidi geothermal power plant has an exergy of 79,085 kW while the steam from a throttling valve has an exergy of 82,869 kW. This results in higher potential for performing work in the steam if a throttle valve is chosen compared to the back pressure turbine. However, the difference in exergy of the exiting steam between the two scenarios is 3,783.69 kW, which is much less than the electricity produced by the back pressure turbine (7,750 kW). The back pressure turbine makes use of the exergy in the steam, and produces electricity, while the exergy drop within the steam led through a throttle valve is due to exergy destruction. Thus, a more reasonable way of reducing pressures of high-pressure geothermal wells, from a thermodynamic point of view, is by using a back pressure turbine instead of a throttle valve.

5. CONCLUSIONS AND RECOMMENDATIONS

From the study, the results can be summarized as:

1. The total exergy available in the steam is 89 MW.
2. A back-pressure turbine has an exergetic efficiency of 81.76% while its mechanical efficiency is 98%.
3. The exergetic efficiency gives a more accurate indication than the energy efficiency.
4. There is a possibility of producing electrical energy of about 7 to 8 MW by adding a backpressure turbine as a topping unit at Hverahlíd area with a drop of about 10 MW of exergy compared to an exergy drop of 6 MW when reducing the pressure from 17.5 bar-a down to 10 bar-a by using a throttling valve.
5. Some of the exergy is destroyed in the turbine (1.8 MW) and the throttling valve (6 MW) due to the irreversibility of the processes. Exergy destruction occurs in all components of a power plant due to irreversibilities.

A suggested recommendation is to conduct a study on the economic feasibility of installing a back pressure turbine, taking into account all the costs for installation and running and then comparing the costs with the revenue of selling the electricity generated from the back pressure turbine.

ACKNOWLEDGEMENTS

I would like to express my sincere gratitude to the Government of Iceland, the United Nations University Geothermal Training Programme (UNU-GTP) and my employer, Ministry of Water Resources and Electricity – Renewable and Alternative Energy Directorate for granting me this opportunity to attend this training programme. I owe my sincere appreciation to Mr. Lúðvík S. Georgsson, Director of UNU-GTP.

I would also like to thank my supervisors, Bjarni Már Júlíusson and Marta Rós Karlsdóttir from Orka Náttúrunnar for their assistance, support and advice during my project.

Many thanks go to Mr. Ingimar Haraldsson, Mrs. María S Guðjónsdóttir, Mr. Markús A.G. Wilde and Ms. Þórhildur Ísberg for their assistance during my stay in Iceland. Special thanks go to Mrs. Málfríður Ómarsdóttir.

I am grateful to Dr. Páll Valdimarsson and all the lecturers for giving us their time and their experience.

I give special thanks, special appreciation and my heartfelt gratitude to my family, my parents, all my brothers and sisters and my wife for their unwavering support and encouragement throughout the six months and especially for enduring my absence for six months, especially my wife, Taghreed, and my little son, Mohammed, for their love and emotional support, inspiring me to give my best in everything I do.

I would also like to thank all 2014 UNU-GTP Fellows for an unforgettable time during these six months, especially my group in geothermal utilization for all the discussions and the nice times we had together.

Finally, I wish to express my heartfelt gratitude to the almighty ALLAH for giving me the strength and for how far he has brought me.

REFERENCES

- Bore, K.C., 2005: Exergy analysis of Olkaria I power plant, Kenya. Report 5 in: *Geothermal training in Iceland 2005*. UNU-GTP, Iceland, 1-37.
- Cordova Geirdal, C.A., 2013: *Economic comparison between a wellhead geothermal power plant and a traditional geothermal power plant*. REYST - Reykjavik University, Reykjavík, MSc thesis, 117 pp.
- DiPippo, R., 2007: *Geothermal power plants. Principles, applications, case studies and environmental impact* (2nd Ed.). Butterworth Heineman, Elsevier, Kidlington, UK, 235 pp.
- Eastop, T., and McConkey, A., 2009: *Applied thermodynamics for engineering technologists* (5th ed.) Longman Scientific & Technical, Essex, 735 pp.
- Hepbasli A., 2006: A key review on exergetic analysis and assessment of renewable energy resources for a sustainable future. *Renewable & Sustainable Energy Reviews*, 12 (2008), 593–661. Webpage: www.elsevier/locate/rser, 630 pp.
- Kaplan, U., and Schochet, D.N., 2000: Improving geothermal power plant performance with topping and bottoming cycles, case histories in Iceland, New Zealand and the Philippine. *Proceedings of the World Geothermal Congress 2000, Kyushu-Tohoku, Japan*, 2111-2114 pp.
- Kárason, B., Cordova G., C.A., Atkins, D., Marino, M., and Bjarnason, V., 2012: *Utilization of high pressure steam for power generation, the case of Hellisheidi power plant*. Reykjavik University, Reykjavík, Interdisciplinary Project Course RM-6, 5 pp.
- Lee, K.C., 1996: Classification of geothermal resources – an engineering approach. *Proceedings of the 21st Workshop on Geothermal Reservoir Engineering, Stanford University, Stanford, CA*, 85-92 pp.
- Power-technology.com, 2014: *Power technology projects, Hellisheidi geothermal power plant, Iceland*, Kaplan, Power-technology.com, website: www.power-technology.com/projects/hellisheidi-geothermal-power-plant/hellisheidi-geothermal-power-plant1.html.
- Reykjavik Energy, 2014: *Information on the Hengill area*. Reykjavík Energy Co., Reykjavík, website, www.or.is/en/projects/hellisheidi-geothermal-plant.
- Thain, I.A., and Carey, B., 2009: *Fifty years of geothermal power generation at Wairakei*. *Geothermics* 38, 48–63.
- Valdimarsson, P., 2011: Geothermal power plant cycles and main components. *Presented at “Short Course on Geothermal Drilling, Resource Development and Power Plants”, organized by UNU-GTP and LaGeo, in Santa Tecla, El Salvador*, 24 pp.

APPENDIX I: EES calculation model

```

{Environment conditions}
P[0] = 1
T[0] = 10
h[0] = Enthalpy (Steam_IAPWS; P=P[0]; T=T[0])
s[0] = Entropy (Steam_IAPWS; P=P[0]; T=T[0])

"Steam inlet conditions"
m_dot[1] = 90 [kg/s] {Given in design documents}
P[1] = 17.5 [bar] {Given in design documents}
x[1] = 1 {Saturated steam at inlet}
T[1] = 206

{Calculated enthalpy and entropy according to inlet info}
h[1] = Enthalpy (Steam_IAPWS; P=P[1]; x=x[1])
s[1] = Entropy (Steam_IAPWS; P=P[1]; x=x[1])

"Steam outlet conditions"
P[2] = 10 [bar] {given in design documents}
T[2] = 180 {given in design documents}
m_dot[2] = m_dot[1]
x[2] = 0.97 {given in design documents 3% moisture content}

"Power production calculations"
W_out = 7750 [kW] {Given in design documents}
eta_gearbox = 0.985 {Value given in design documents}
eta_generator = 0.98 {Value given in design documents}

{Calculating turbine energy efficiency according to the power output given}
7750 =
eta_turbine * eta_generator * eta_gearbox * m_dot[1] * (h[1] - h[2])

{Ideal entropy at turbine outlet assuming an isentropic process}
s_i[2] = s[1]

{Ideal enthalpy at turbine outlet}
h_i[2] = Enthalpy (Steam_IAPWS; P=P[2]; s=s_i[2])

{Isentropic turbine power output}
W_is = m_dot[1] * (h[1] - h_i[2])

{Actual entropy at turbine outlet}
S[2] = Entropy (Steam_IAPWS; P=P[2]; x=x[2])

{Assuming the isentropic efficiency of the turbine is 85%}
eta_is = 0.85
{Calculating the enthalpy at the outlet according to the isentropic efficiency}
eta_is = (h[1] - h[2]) / (h[1] - h_i[2])

{Actual power output developed by turbine shaft}
W_act = m_dot[1] * (h[1] - h[2])

{Energy analysis}

{Energy input = m_dot * h_inlet}
E[1] = m_dot[1] * h[1]

{Energy output = m_dot * h_out}
E[2] = m_dot[2] * h[2]

{Work done = E_i - E_out}
W.D = E[1] - E[2]

{Energy efficiency (1st Law efficiency) of Turbine: eta_turbine = (Actual power developed by turbine shaft) / (E_i - E_out)}
energyefficiency = W_act / (E[1] - E[2])

{Exergy analysis}

{Exergy input}
Ex[1] = m_dot[1] * (h[1] - h[0] - (T[0] + 273) * (S[1] - S[0]))

{Exergy out}
Ex[2] = m_dot[2] * (h[2] - h[0] - (T[0] + 273) * (S[2] - S[0]))

{Exergy destruction}
Ex[3] = Ex[1] - Ex[2] - W_act

{Exergetic efficiency}
Exergetic Efficiency = W_act / (Ex[1] - Ex[2])

{For throttling valve}

{Exergy before throttling valve}
ExVlve[1] = m_dot[1] * (h[1] - h[0] - (T[0] + 273) * (S[1] - S[0]))

{Exergy after throttling valve}
h_th[2] = h[1] {Throttling}
ExVlve[2] = m_dot[2] * (h_th[2] - h[0] - (T[0] + 273) * (S_th[2] - S[0]))

{Entropy after throttling}
S_th[2] = Entropy (Steam_IAPWS; P=P[2]; h=h_th[2])

{Exergy destruction due to throttling valve}
ExVlve_dest = ExVlve[1] - ExVlve[2]

```




UNITED NATIONS
UNIVERSITY

UNU-GTP

Geothermal Training Programme

Orkustofnun, Grensasvegur 9,
IS-108 Reykjavik, Iceland

Reports 2014
Number 29

TEMPERATURE MODEL AND TRACER TEST ANALYSIS FOR THE RIBEIRA GRANDE GEOTHERMAL SYSTEM, SÃO MIGUEL ISLAND, AZORES

Maria da Graça Vaz de Medeiros Rangel

EDA RENOVÁVEIS, S.A.

Rua Francisco Pereira Ataíde, 1

9504-535 Ponta Delgada

PORTUGAL (AÇORES)

mrangel@eda.pt

ABSTRACT

On São Miguel Island (Azores - Portugal) EDA Renováveis, S.A., exploits the resources of the Ribeira Grande geothermal field, a 240°C liquid-dominated reservoir, and operates two binary ORC (organic Rankine cycle) geothermal power plants, Ribeira Grande and Pico Vermelho, with a combined capacity of 23 MW_e. At present, the production from the geothermal resource represents 43% of the total power production of the island and 22% of the archipelago of the Azores.

In 2008, a numerical model of the Ribeira Grande geothermal reservoir was recalibrated using up-to-date temperature, pressure, production and tracer test data. Forecasts of reservoir performance under several injection configurations were made, providing important information on how power production may be maximized, while minimizing the potential cooling impact caused by the return of injected water. Based on these forecasts, EDA Renováveis, S.A., decided to relocate the injection area in the Pico Vermelho sector, by drilling new injection wells farther from the production area.

The present work was developed under the scope of the final project for the Geothermal Training Programme of the United Nations University, in Iceland. An updated model of the temperature and pressure distribution in the Pico Vermelho sector of the Ribeira Grande geothermal field was developed based on warm-up temperature and pressure data from new wells PV9, PV10, PV11 and RG5, suggesting some continuity of the reservoir to the northeast, as previously indicated by AMT/MT surveys. A simulation and interpretation of the tracer test data conducted in the same sector of the field in 2007-2008, using the programs of the software package ICEBOX, is also part of this final project. The results show an overall strong hydraulic connection between the injection and production wells in this sector of the geothermal field.

1. INTRODUCTION

In Portugal, high-enthalpy geothermal resources can be found on the volcanic islands of Azores. The archipelago is situated in the North Atlantic Ocean, between latitudes 36°55'43"N and 39°43'23"N and

longitudes $24^{\circ}46'15''\text{W}$ and $31^{\circ}16'24''\text{W}$, and comprises nine inhabited islands spread over a distance of 600 km. The Ribeira Grande geothermal field is located on São Miguel, the largest island of the archipelago, with a total area of 745 km^2 (Figure 1).

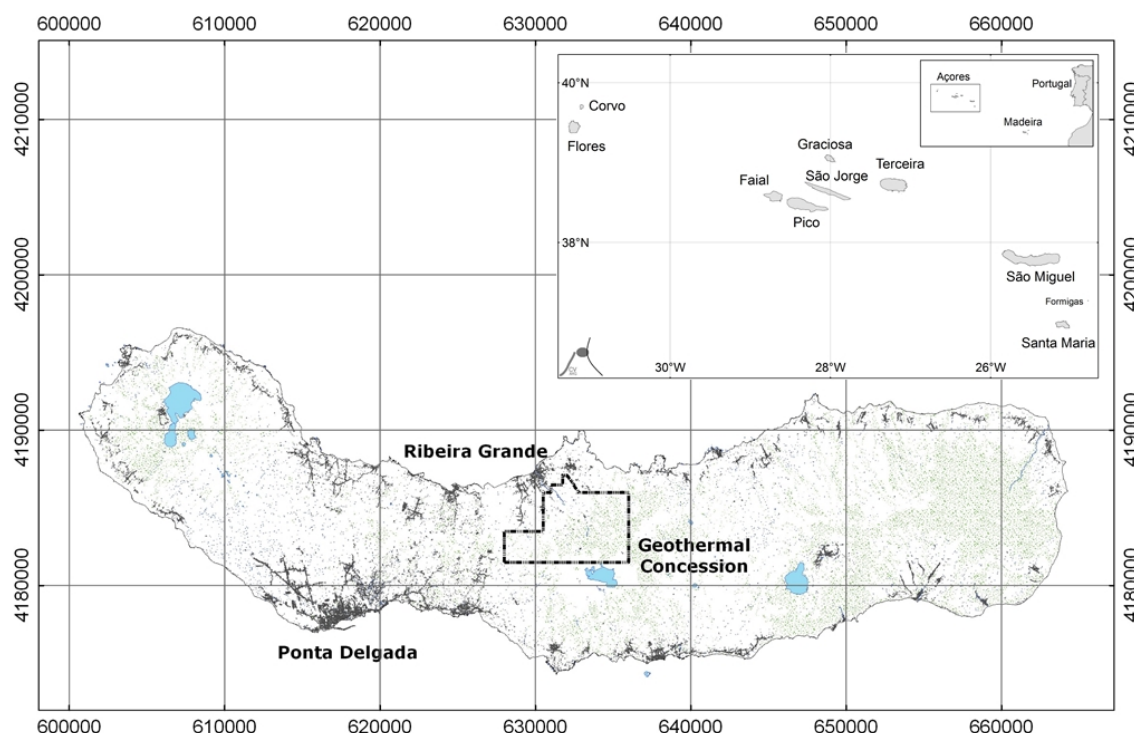


FIGURE 1: Geographic location of São Miguel Island (map provided by EDA Renováveis); map also shows the location of Ribeira Grande geothermal concession

The possible presence of high-enthalpy geothermal resources in the Azores became evident when, in 1973, geoscientists from Dalhousie University, while performing a deep drilling programme into the oceanic crust, decided to drill a research core-hole onshore, on São Miguel Island (north flank of Fogo volcano), intersecting formations with temperatures exceeding 200°C at 550 m depth, while steam erupted from the hole when the drill string was removed (Muecke *et al.*, 1974). Since then, and until the late 1980s, several geological, geochemical and geophysical surveys were conducted in the Ribeira Grande geothermal field, the results of which have been used to interpret the conditions of the reservoir during development of the field.

These geological exploration activities led to the present scenario of exploitation of geothermal resources on São Miguel Island, where EDA Renováveis, S.A. (owned by EDA – Electricidade dos Açores, S.A., the electric power utility of the region), following the work of previous regional government institutions in the development of geothermal projects, operates two binary Organic Rankine Cycle power plants: Ribeira Grande and Pico Vermelho. The power plants have a combined capacity of 23 MWe and are supplied by the geothermal fluid of deep wells drilled into the high-enthalpy, liquid-dominated Ribeira Grande geothermal reservoir. Figure 2 shows the location of the wells in the two sectors of the field: Cachaços-Lombadas and Pico Vermelho.

Nowadays, power production from geothermal resources represents about 43% of the electric consumption of the island of São Miguel and over 22% of the total demand of the archipelago. The need to meet the local government's policy of maximizing the use of clean, renewable and indigenous energy sources supports the expansion of geothermal projects in the Azores.

This paper was written under the scope of the final project of the six month geothermal training program of the United Nations University in Iceland and presents the results of the updated temperature and pressure distribution model of the Pico Vermelho sector of the Ribeira Grande geothermal field. A simulation and interpretation of tracer test data, collected in the same sector of the field in 2007-2008, is also part of this work.

2. RIBEIRA GRANDE GEOTHERMAL FIELD

2.1 General geological setting

The Azores islands stand astride the Mid-Atlantic Ridge following a NW-SE trend and emerge above the sea, in the North Atlantic Ocean, from a thick and irregular area of oceanic crust, roughly limited by the 2,000 m bathymetric curve (Azores Plateau). Some authors maintain that this structure is related to the presence of a deep mantle plume in the zone where the American, Eurasian and Nubian lithospheric plates meet at the “Azores Triple Junction” (Moore, 1990; Gaspar *et al.*, 2011).

Figure 3 shows the main tectonic features of the archipelago which are: in the west, the Mid-Atlantic Ridge (MAR); in the north, the North Azores Fracture Zone (NAFZ) and a complex alignment with a WNW-ESE direction, running from the MAR to the western limit of Gloria Fault (GF), designated as Terceira Rift (TR); in the South, the East Azores Fracture Zone (EAFZ). As a result of this complex geodynamic setting, seismic and volcanic activity is frequent in the region (Gaspar *et al.*, 2011).

The Ribeira Grande geothermal field is located on the north flank of the Fogo volcano, also known as Água de Pau Massif. Fogo volcano is located in the central part of the island of São Miguel, and is the largest of the three active central volcanoes of the island. The volcano rises to approximately 1,000 m and its summit caldera, with a lake occupying an area of 4.8 km², was formed as a result of numerous collapses and explosions, the most recent occurring during a sub-plinian eruption of 1563 followed by a basaltic flank eruption and the hydromagmatic explosive event of 1564 (Wallenstein *et al.*, 2007; Viveiros *et al.*, 2009; Moore, 1991).

The Fogo volcano is composed of a succession of trachytic to basaltic lava flows, trachytic domes, scoria cones, pyroclastic flows, lahars, pumice and ash deposits. Poorly exposed, the oldest deposits

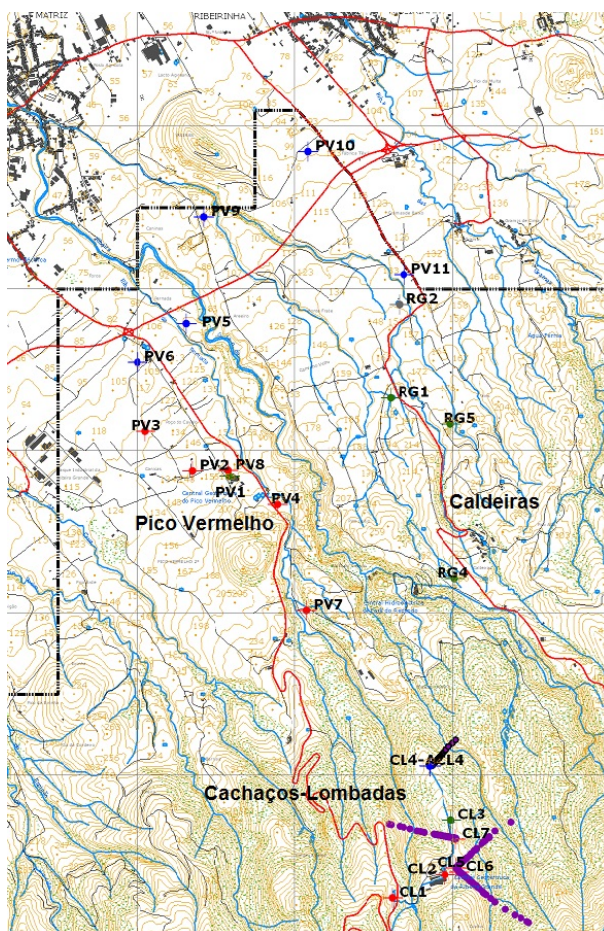


FIGURE 3: Surface map of the Ribeira Grande geothermal field showing location of wells (provided by EDA Renováveis)

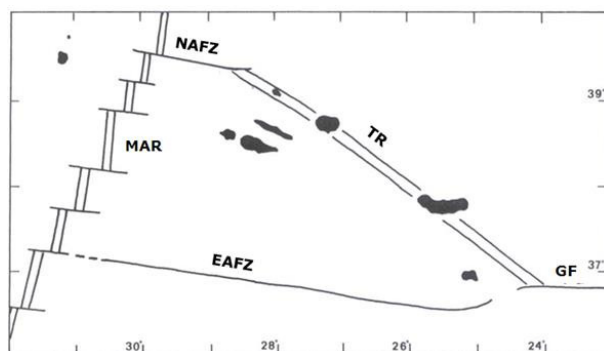


FIGURE 3: Main tectonic structures in Azores region (Gaspar, 1996)

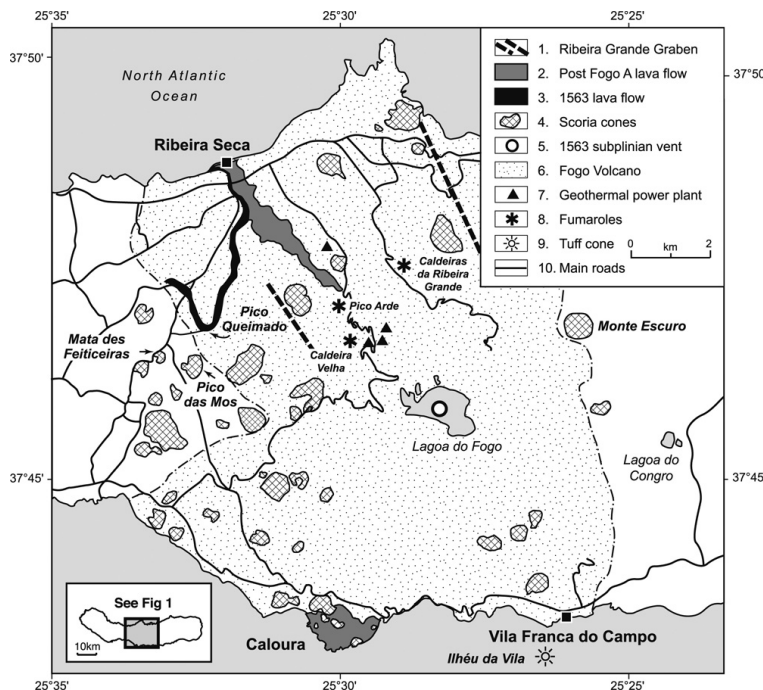


FIGURE 4: Morphostructural sketch of Fogo volcano (Wallenstein *et al.*, 2007)

date from more than 200,000 years ago (Figure 4) (Martini *et al.*, 2009; Wallenstein *et al.*, 2007). The northern flank of Fogo volcano is down-faulted by a NW-SE trending graben. It is also possible to observe NE-SW alignments and a circular system of faults, which might be responsible for the emplacement of trachytic domes on the upper part of the volcanic edifice (Silva *et al.*, 2012; Wallenstein *et al.*, 2007).

Several geothermal manifestations can be observed on this active central volcano, mainly on its northern flank, such as fumarolic fields, soil diffuse degassing areas, and thermal and CO₂ cold springs. Their locations are associated with the NW-SE fault system that defines the Ribeira Grande graben (Viveiros *et al.*, 2009).

2.2 Resume of the developmental history of the field

Ribeira Grande geothermal field was discovered through a research core-hole drilled in 1973 in Pico Vermelho area. Subsequent geological investigations conducted during 1975-1977 defined an extensive geothermal anomaly and, between 1978 and 1981, five exploratory wells were drilled in that area. In 1980, a 3 MW_e pilot plant based on a backpressure turbine from Mitsubishi was installed in Pico Vermelho sector, operating for 25 years.

In the southern sector of the field (Cachaços-Lombadas), a binary plant from Ormat (Ribeira Grande power plant) was installed in two phases: Phase A (5 MW_e) in 1994 and Phase B (8 MW_e) in 1998. Nowadays, the plant is supplied by the fluid from four geothermal wells and reinjection occurs through two injection wells. The total plant output is, on average, about 10 MW_e, less than the total capacity of the plant, due to insufficient fluid supply.

Meanwhile, in 2005, EDA Renováveis decided to proceed with further development of the Pico Vermelho sector, with the drilling of five new wells and replacement of the pilot plant with a new 10 MW_e binary plant. Due to the high productivity of the wells, Pico Vermelho power plant has a very flexible operation, needing only three of the five production wells available to provide the fluids needed for the plant.

2.3 Conceptual hydrogeological model

The Ribeira Grande geothermal field is an extensive, high-temperature geothermal system hosted by volcanic rocks (mainly a succession of trachytic to basaltic lavas and pyroclastic rocks) on the northern flank of the Fogo volcano. The geothermal reservoir is elongated in a northwest direction, and may have southwest and northwest boundaries that follow this trend, particularly at lower elevations. Up to the present, drilling has been insufficient to delineate the field's limits and the most

recent geoelectrical surveys indicate that it extends further to the northeast (GeothermEx, 2008; Ponte *et al.*, 2009; Pham *et al.*, 2010; Ponte *et al.*, 2010).

According to the conceptual hydrological model of the field, geothermal water with a maximum temperature of at least 250°C enters the reservoir in an upflow zone that is probably located in the southeast part of the field. The heat source for the hot water is presumably a body of magma or young intrusive rocks associated with the activity of Fogo volcano. According to isotopic analysis, the origin of the water is meteoric (GeothermEx, 2008; Ponte *et al.*, 2009; Pham *et al.*, 2010; Ponte *et al.*, 2010).

The principal flow direction into and within the reservoir at deeper levels is upward and to the northwest, following the northwest trend of faulting created by the regional tectonic setting, though there is probably some lateral flow toward the margins of the reservoir as well. At shallower levels (around -400 m elevation), a lateral, northwest flow appears to predominate over the upward flow, forming an extensive, relatively shallow reservoir in the Pico Vermelho sector (GeothermEx, 2008; Ponte *et al.*, 2009; Pham *et al.*, 2010; Ponte *et al.*, 2010).

The permeability of the Ribeira Grande geothermal reservoir is associated with the fractures in the volcanic rocks of the Fogo volcano. Well data from the geothermal field indicate that a sequence of pyroclastic rocks altered to clay forms a relatively impermeable cap at the top of the reservoir. The lower limit of the reservoir (at least in the northwest, lower-elevation Pico Vermelho sector of the field) seems to be formed by impermeable clastic volcanic rocks at or near the transition zone between subaerial and submarine deposits (GeothermEx, 2008).

The chemical composition of the geothermal water is relatively homogeneous throughout the field, being mainly of a Na-Cl type with high HCO₃. Although the reservoir contains predominantly liquid water, boiling occurs and forms a steam or two-phase zone at the top of the reservoir in some sectors of the field. Progressive boiling of the reservoir water as it flows to the northwest reduces the content of non-condensable gases in the Pico Vermelho sector, compared with the Cachaços-Lombadas sector, although the difference is generally minor (GeothermEx, 2008).

2.4 Geophysical exploration

The first geophysical surveys in the Ribeira Grande geothermal field were conducted in the 1970s and 1980s, including DC resistivity and controlled-source audio-magnetotelluric surveys. They identified a well-defined geophysical anomaly that extends from the coastal area near the city of Ribeira Grande upward toward the summit of the volcano. In 2006, new audio-magnetotelluric and magnetotelluric surveys were conducted, identifying a large low-resistivity anomaly extending into the area northeast of the Pico Vermelho – Caldeiras, which is believed to be the result of hydrothermal alteration. In 2009-2010, this extension of the reservoir was partially confirmed by the drilling of new wells PV9, PV10, PV11, RG4 and RG5 (GeothermEx, 2008).

2.5 Numerical model predictions

In order to support the development of the northern area of the geothermal field, the conceptual model of the reservoir was updated and a numerical model was first developed in 2003. In 2008, the numerical model of the Ribeira Grande field was re-calibrated, using up-to-date temperature, pressure and production data from the geothermal wells, as well as tracer test data. The updated model was used to generate forecasts of reservoir performance under various possible injection configurations; this yielded important indications of how power production from the geothermal resource of the Ribeira Grande field may be maximized, while minimizing potential detrimental impacts caused by the return of injected water (GeothermEx, 2008).

According to the model calculations, continued injection into the existing injection wells of the Pico Vermelho sector could induce significant thermal breakthrough in all of the Pico Vermelho production wells, causing a reservoir temperature decline of about 50°C over the next 30 years of production (GeothermEx, 2008).

Based on these forecasts, EDA Renováveis, S.A., decided to relocate the injection area in the Pico Vermelho sector. In 2009 and 2010, three new injection wells were drilled in the Pico Vermelho sector (PV9, PV10 and PV11) farther from the production area. In order to assess the area located northeast of Pico Vermelho, which was indicated by the previous AMT/MT results, exploration wells RG4 and RG5 were also drilled during the same drilling campaign.

3. ANALYSIS OF TEMPERATURE AND PRESSURE DATA

3.1 General concepts

Following the completion and testing of a geothermal well, either through injection or production, which give us the first estimates of well and reservoir properties, a period of warm-up is expected to occur for the well to recover in temperature after cooling was induced by circulation during drilling and cold water injection.

During the warm-up period, several temperature and pressure surveys are normally run and data is used to estimate the undisturbed reservoir temperature (formation temperature) and pressure, being essential for reservoir assessments of the geothermal resource, playing an essential role in the calibration of various reservoir models (Axelsson and Steingrímsson, 2012).

Convective processes outweigh conduction in geothermal systems as a means of heat transfer. Therefore, it is expected that wells with poor permeability heat up slowly, sometimes taking many months to completely stabilize, as the heating process is controlled by conduction, while permeable wells heat up more rapidly. The heat-up process is also dependent on the time-length of cooling during drilling, which is very variable (Grant and Bixley, 2011; Axelsson and Steingrímsson, 2012).

Commonly, for a long set of data, the Horner plot method is used for estimating the formation temperature. This method is a simple analytical method for analysing maximum bottom-hole temperatures to determine the formation temperature. The basic criteria for the technique is the straight-line relationship between the maximum bottom-hole temperature and $\ln(\tau)$ with:

$$\tau = \frac{\Delta t}{\Delta t + t_0}, \quad (1)$$

where τ = Horner time,
 Δt = The time passed since circulation stopped,
 t_0 = The circulating time,

We see that:

$$\lim_{\Delta t \rightarrow \infty} \ln(\tau) = 0. \quad (2)$$

Considering the above and the fact that the system must have stabilized after infinite time, the maximum bottom-hole temperature is plotted as a function of $\ln(\tau)$. Then, a straight line is drawn through the data and extrapolated to $\ln(\tau)=0$ to determine the formation temperature (Arason *et al.*, 2004). This method can also be applied to estimate the maximum temperature at a certain depth that has not been disturbed by cross-flow in the well.

The initial reservoir pressure, at a certain depth, is estimated through the intersection of several warm-up pressure profiles, which define the pressure pivot or pressure control point. If we consider a well with a single feed zone, the pressure in the well at the depth of this feed zone will be controlled by and become equal to the reservoir pressure. As the temperature of the wellbore fluid changes during the heating period, the density of the fluid also changes, but pressure at the feed zone is fixed by the reservoir pressure. Therefore, if a single feed-zone dominates a well, the pivot point defines the reservoir pressure at the feed-zone depth. If two, or more, feed-zones exist in a well, the pivot point defines average conditions instead (Grant and Bixley, 2011; Axelsson and Steingrímsson, 2012).

The reservoir pressure profile can't be measured directly in high-temperature wells. However, it can be estimated by hydrostatic extrapolation from the pivot point depth pressure value, using the formation temperature curve for the well to determine the water density as a function of depth. Estimating the reservoir pressure profile for all wells in the same field is important for understanding the pressure distribution in the reservoir (Steingrímsson, 2013).

3.2 Data from newly drilled wells

After drilling four new geothermal wells (PV9, PV10, PV11 and RG5 – see Figure 2), it was important to assess and update the information regarding the formation temperature and the initial reservoir pressure in the Pico Vermelho sector of the Ribeira Grande geothermal field. To do so, the warm-up temperature and pressure profiles were plotted along with the boiling point depth curve, against depth and elevation for each of the 10 geothermal wells of the Pico Vermelho sector. Afterwards, the formation temperature was estimated for the bottom-hole, as well as for other depths that have not been disturbed by cross-flow in the well, by using the software BERGHITI from the software package ICEBOX (Arason *et al.*, 2004). The Horner plot method was selected to determine the formation temperature. Figure 5 shows an example of a Horner plot for 500 m depth in the geothermal well PV11. After obtaining the formation temperature for several depths (preferably including the main feed zones), the formation temperature curve was drawn and plotted with the warm-up temperature profiles.

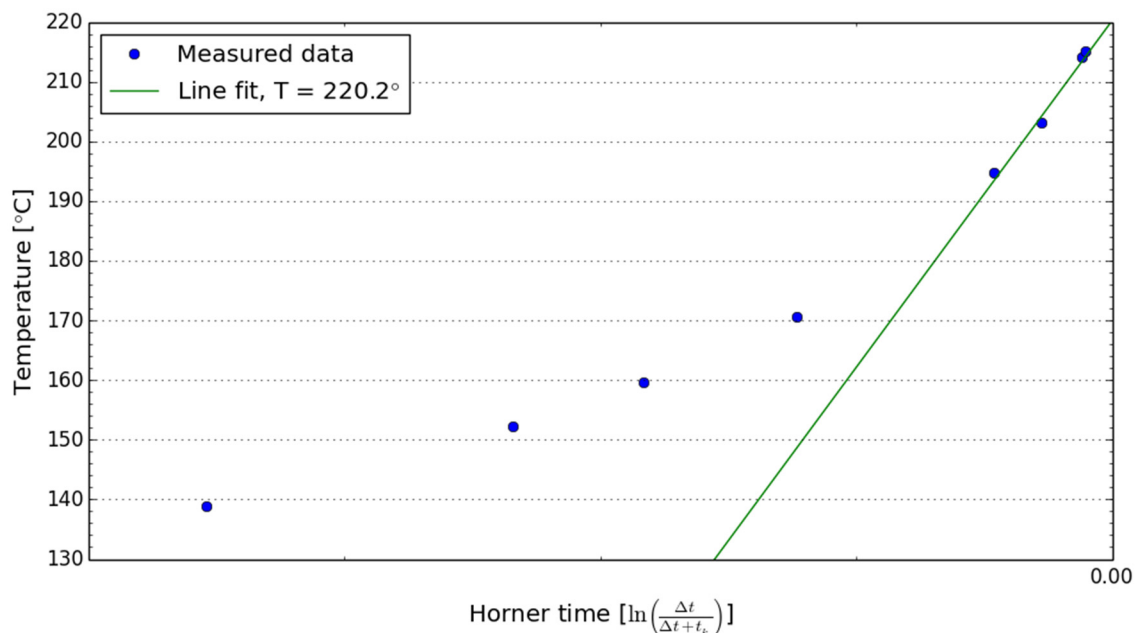


FIGURE 5: Horner plot for warm-up temperature data at 500 m depth in geothermal well PV11 (manual fitting)

For high-temperature wells, the boiling point depth curve (BPDC) is often plotted as a reference, as this curve defines the maximum possible formation temperature for the hydrothermal system, unless superheated conditions exist, which is an uncommon scenario (Steingrímsson, 2013).

To assess the initial reservoir pressure in that sector of the field, the software PREDYP from the software package ICEBOX (Arason *et al.*, 2004) was used. PREDYP computes pressure in a static water column for known temperatures and water levels (measured from wellhead) or wellhead pressure. The initial reservoir pressures were estimated for the same geothermal wells, considering the formation temperatures estimated previously. For each well, the reservoir pressure profile was adjusted to fit the most likely pressure pivot point of the well.

Figure 6 shows the warm-up temperature and pressure logs of the new geothermal wells PV9, PV10, PV11 and RG5, drilled in the northeast part of the Pico Vermelho sector along with the estimated formation temperature conditions and initial pressure. The temperature and pressure profiles, as well as the estimated formation temperature and initial pressure of the other Pico Vermelho geothermal wells, are presented in Appendix I.

Analysing Figure 6, we can verify that the water temperature is below the boiling point at all depths, with the exception of the last three logs of well RG5, indicating that, during the warm-up, some boiling might have taken place in the upper part of the well. Geothermal well PV9 seems to intersect the top of the reservoir between 300 and 400 m depth, and from that depth to around 600 m, the isothermal profile of the temperature logs indicates that convection is the dominant heat transfer process within the formation. At that depth, we can observe a temperature reversal, most likely associated with the total loss that occurred during drilling at 621 m depth (circulation was never regained while drilling the rest of the well). From that depth, which is probably the main feed zone of the well, to the well-bottom, well PV9 appears to have penetrated a permeable zone or multiple zones. The interval between 600 m and the bottom of the well took longer to warm-up, probably due to the fact that it stood in contact with the drilling fluid (cold fluid) for a longer time. The maximum formation temperature was estimated as 226.3°C at 600 m depth. The initial reservoir pressure is estimated to be 48.6 bar at the same depth.

Analysing the behaviour of the temperature profiles made during the warm-up period of well PV10, we verify that probably the survey made on November 30th should reflect the true formation temperature, as the well probably had reached thermal equilibrium. Therefore, formation temperatures increase rapidly with depth from the surface to about 350 m depth, probably while intersecting the caprock of the reservoir. Then, the top of reservoir seems to be intersected, as a gradual increase in temperature is observed, reaching a maximum of about 201°C at 500 m depth. A slight temperature reversal occurs, with temperatures declining to about 185°C at the bottom of the well. A pivot point is difficult to define in well PV10, however we can assume one at 500 m depth, where pressure is 39 bar. The behaviour of the temperature profiles in well PV10, with no indication of important feed zones, suggests that the well penetrates a peripheral zone of the Ribeira Grande reservoir in the Pico Vermelho sector of the field, probably near an outflow zone.

The geothermal well PV11 appears to have penetrated the reservoir near 400 m depth, with a possible inflow to the well at around 450 m. Formation temperatures reach 229.3°C at that depth. The initial reservoir pressure is estimated to be 39.3 bar at the same depth, where a pressure control point can be identified. The zone below the major loss zone (near 465 m) remained substantially cooled by drilling, when compared with the bottom of the well where permeability might be limited.

Well RG5 is located in the northeastern-most part of the field. From the analysis of temperature and pressure logs made during the warm-up period, it is reasonable to consider that the last temperature profile made on October 18th, 2010, reflects nearly stabilized conditions. The maximum formation temperature estimated is 229.4°C at 800 m depth. The initial reservoir pressure is estimated to be 52.3 bar at the same depth.

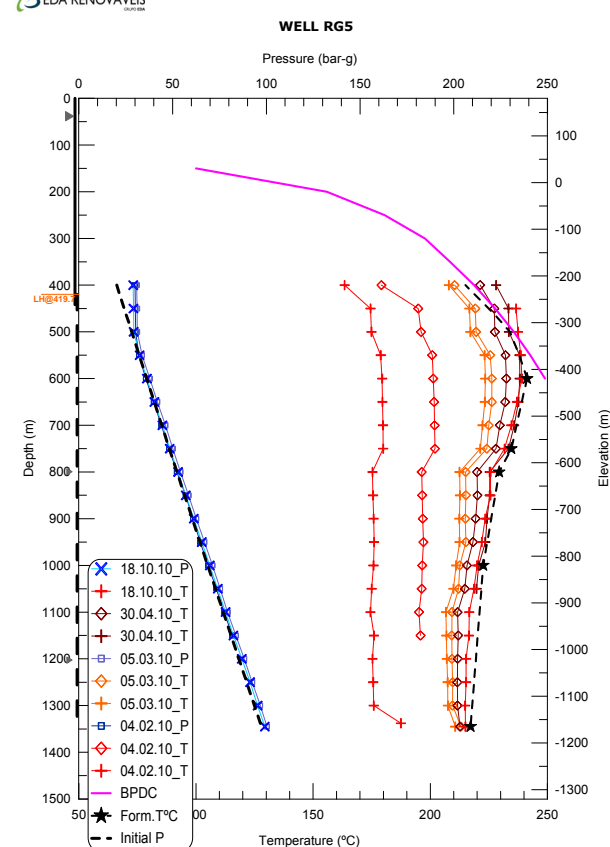
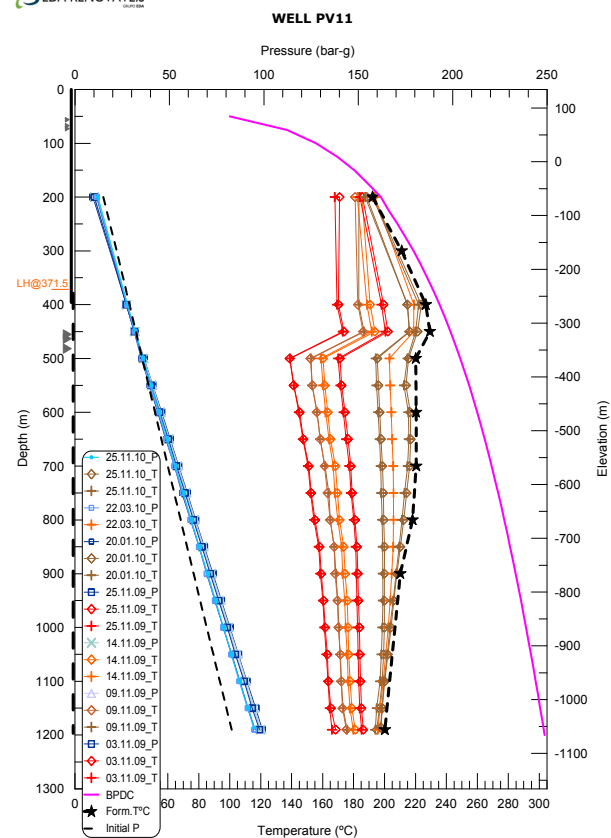
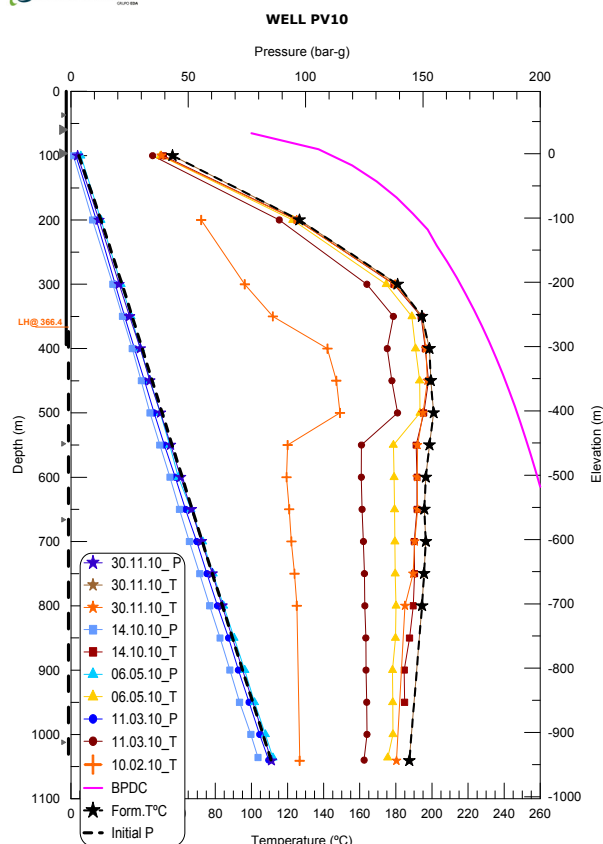
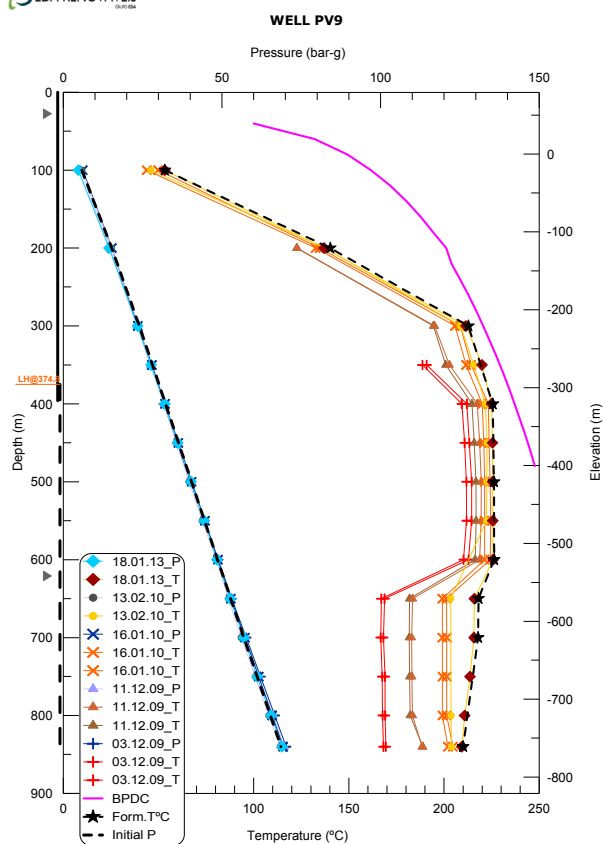


FIGURE 6: Warm-up temperature and pressure logs, as well as estimated formation temperature and initial reservoir pressure for geothermal wells PV9, PV10, PV11 and RG5

Formation temperature and initial reservoir pressure profiles were gathered and plotted as a function of elevation, both for new wells and for the other wells in Pico Vermelho (Figure 7). When comparing the formation temperatures estimated from the new wells drilled in Pico Vermelho (Figure 7A), we observe that well RG5 presents the highest temperatures (maximum temperature of about 241°C at 420 m b.s.l.) and well PV10 the lowest ones. This observation seems to be in accordance with the conceptual model of the Ribeira Grande geothermal field, where it is considered that the geothermal fluid, with a maximum temperature of at least 250°C, enters the reservoir through an upflow zone, probably located in the southeast part of the field (to the east of the wells in the Cachaços-Lombadas area) and flows laterally at shallower levels to the northwest, forming an extensive and relatively shallow reservoir in the Pico Vermelho sector. In Figure 7B, the formation temperature profiles estimated from wells PV2, PV4, PV7 and PV8 show that these wells are located in a permeable high-temperature reservoir zone (maximum temperature of about 245°C at 470 m b.s.l. in well PV4). Wells PV3 and PV5 present the lowest temperatures. Overall, in Pico Vermelho sector, the highest temperatures observed were between 200 m b.s.l. and 600 m b.s.l. Reservoir temperature and

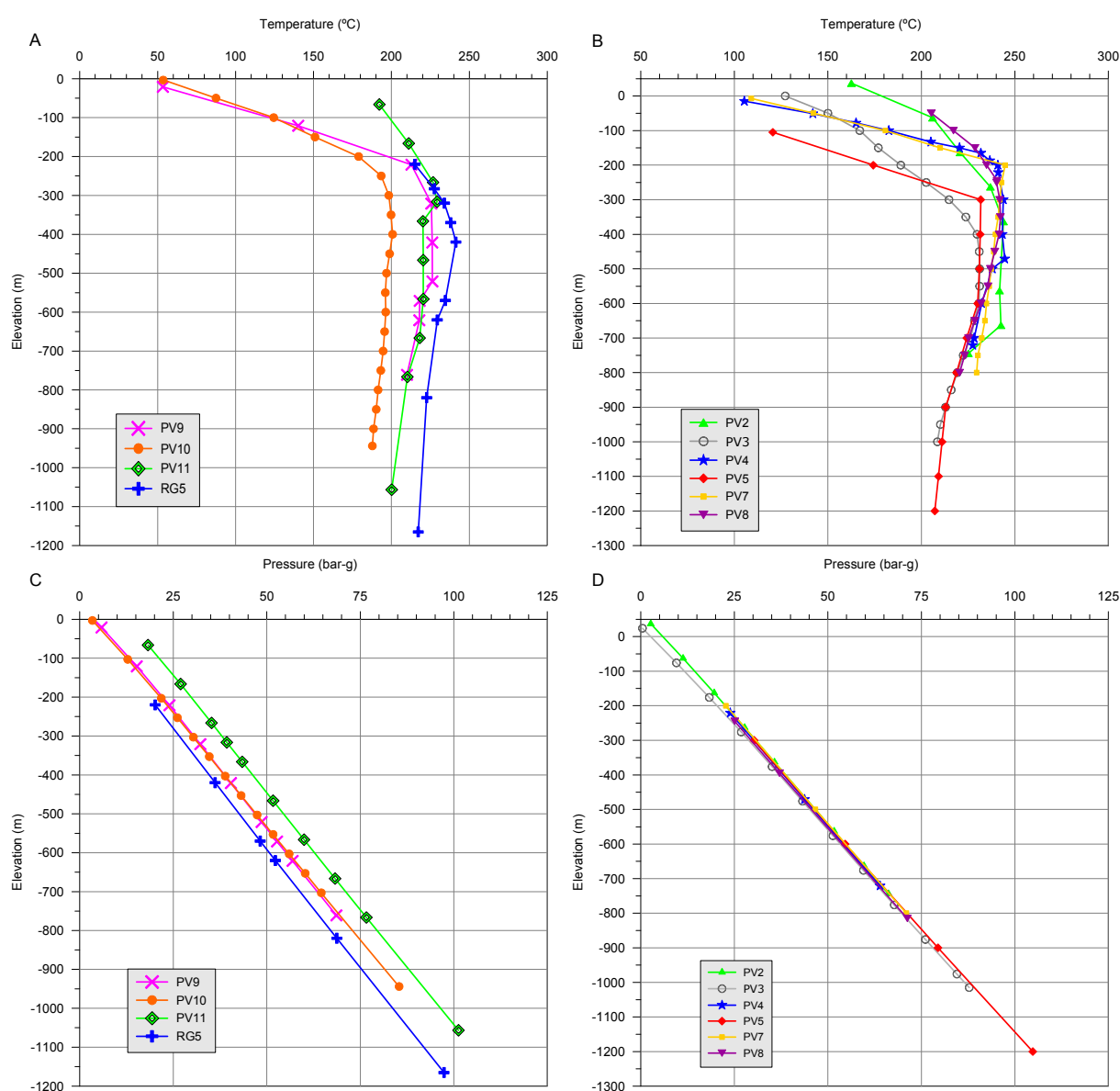


FIGURE 7: Formation temperatures profiles (A and B) and initial reservoir pressure profiles (C and D) estimated for the geothermal wells in the Pico Vermelho sector

permeability in the northwest part of the field, in the vicinity of wells PV3, PV5 and PV10, seem to be lower. Figure 7D shows a consistent initial reservoir pressure in the area of the older wells in Pico Vermelho (PV2 to PV8), while to the west the pressure seems to be lower around well RG5 and higher around well PV11 (Figure 7C). One possible interpretation of this variation can be related with the depth and permeability of the main feed-zones of the wells.

3.3 Temperature and pressure models

Based on the estimated formation temperature and initial pressure of the reservoir in the Pico Vermelho sector, temperature and pressure contour maps were drawn in order to show their distribution in this sector of the geothermal field. Figure 8 shows temperature contour maps, made at 200 m intervals, from 200 to 800 m b.s.l.

From the analysis of the temperature distribution in Figure 8, we note that at 200 m b.s.l., a zone of higher temperatures is present in the area of wells PV4, PV7 and PV8. At -400 m, temperatures are nearly isothermal over a significant distance in the SE-NW direction, slightly decreasing towards well PV10 (north-northeast). The 600 m b.s.l. map shows a temperature distribution with a similar pattern to the one at -400 m, but temperature has started to decrease. By 800 m b.s.l., the overall decrease in temperature of the Pico Vermelho sector indicates that the reservoir lies mainly above this level, where temperatures remain approximately isothermal. By incorporating the data from the new geothermal wells into the model, we verify that there is no sign of the existence of a boundary between them and the other wells, indicating a continuous reservoir in the overall Pico Vermelho sector. Furthermore, the newly drilled wells show no indication of a reservoir boundary in the eastern part of the geothermal field, which agrees with the results of the AMT/MT surveys.

Figure 9 shows the initial reservoir pressure contour maps at 200 m intervals, from 200 to 800 m b.s.l. Initial pressure conditions are often more difficult to estimate accurately than formation temperature, due to varying influential factors, and such contour maps are more difficult to interpret. From the analysis of the pressure distribution in Pico Vermelho sector, we observe that the pressure is higher in north and west part of the field, declining to the east, in the vicinity of well RG5. Thus, the pressure distribution pattern is somewhat the opposite of the temperature distribution, which can be explained by the fact that the pressure gradient is controlled by fluid density, which varies with temperature. Another condition to consider is the role of the main feed zones that are controlling the pressure distribution.

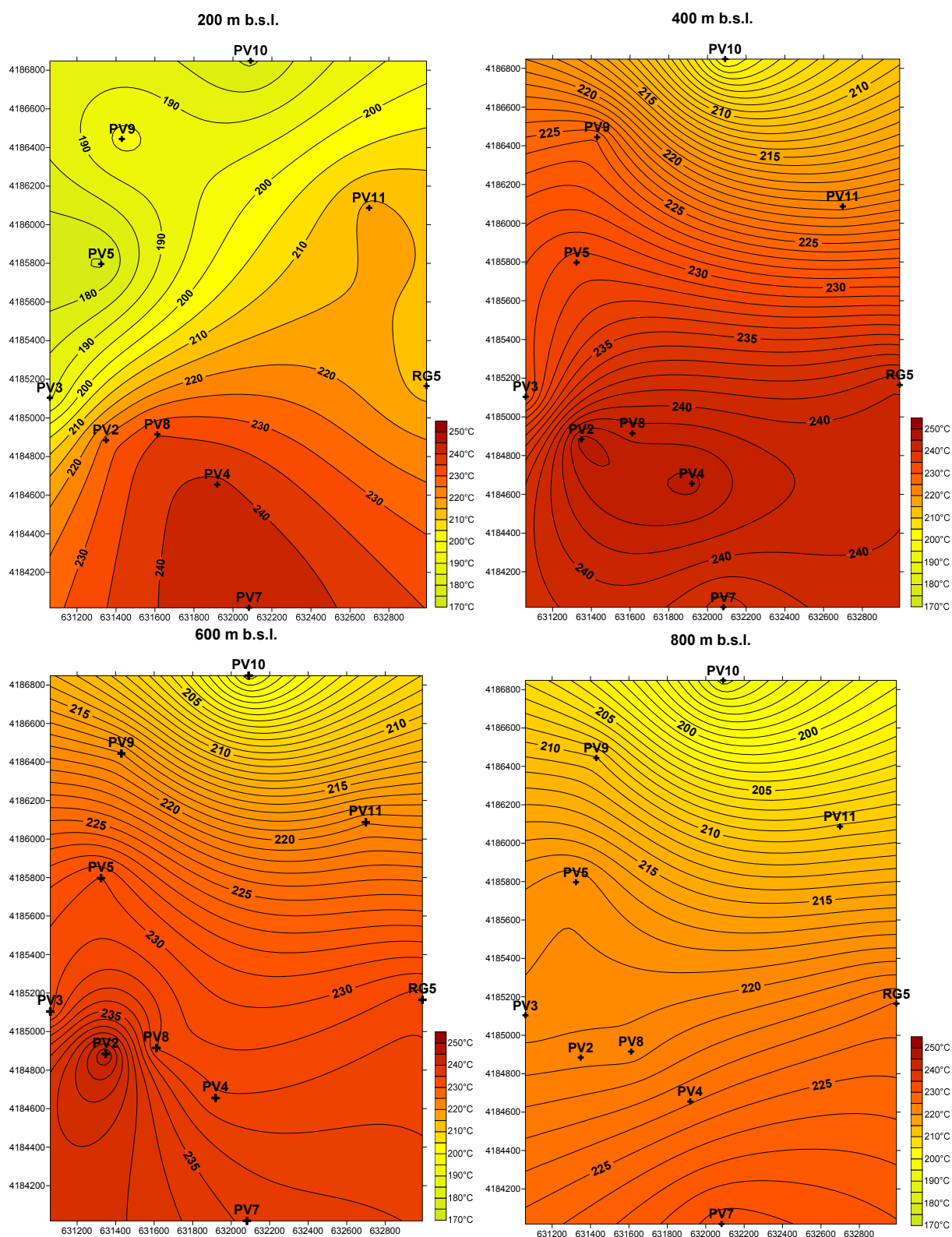


FIGURE 8: Contour maps of formation temperature at four different elevations (200, 400, 600 and 800 m b.s.l.)

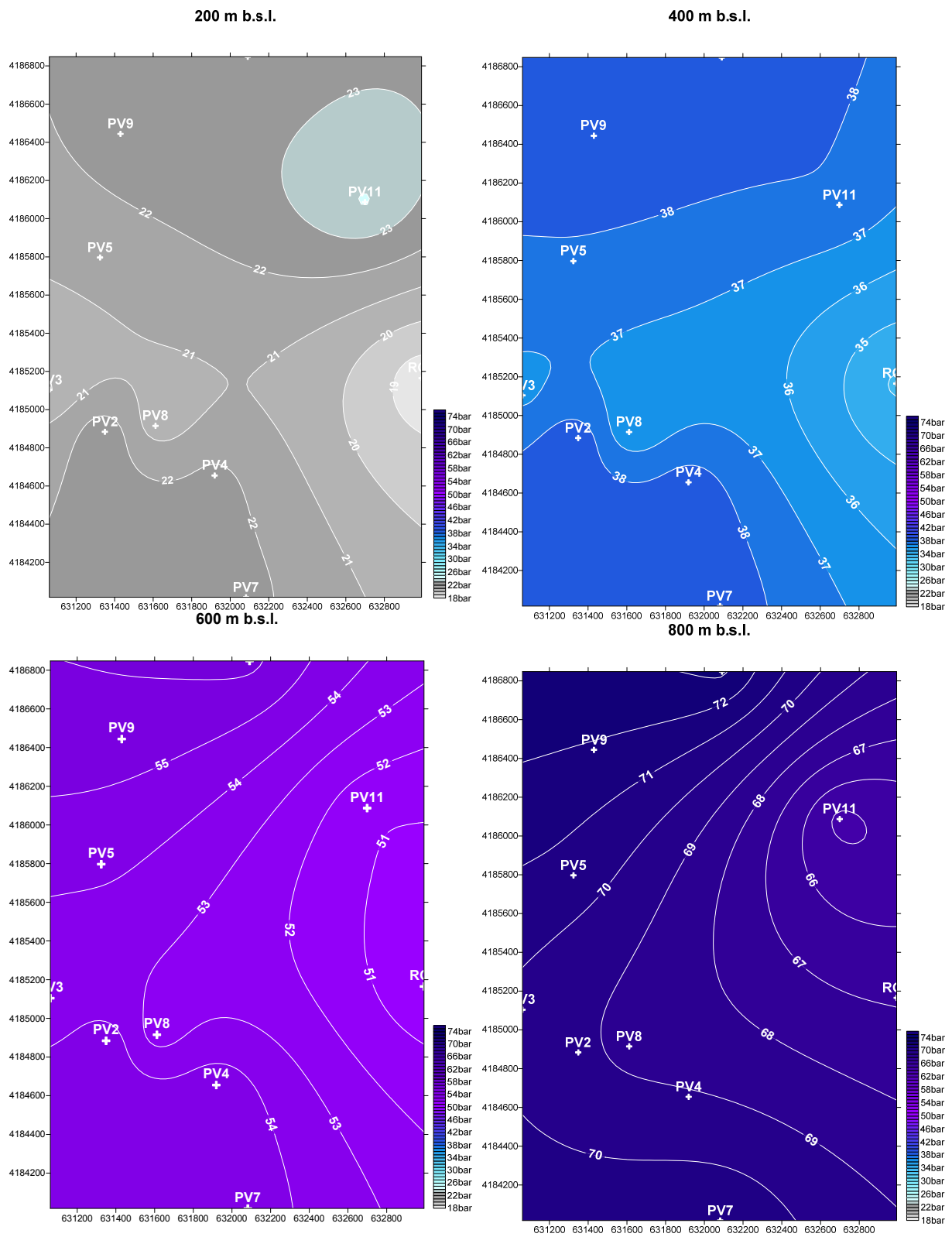


FIGURE 9: Contour maps of initial reservoir pressure at four different elevations (200, 400, 600 and 800 m b.s.l.)

4. ANALYSIS OF TRACER TEST DATA

4.1 Reinjection

One of the most important and challenging tasks of sustainable management of geothermal resources is related to the reinjection of the geothermal fluid after heat conversion into electricity at the power plants. Mass extraction during long-term production causes a pressure draw-down inside the geothermal reservoir. Through reinjection, additional recharge is provided to the reservoir and, as a result, the necessary pressure support is restored. Reinjection also enhances thermal extraction from reservoir rocks along flow-paths. The production potential of geothermal systems is mainly determined by pressure decline caused by mass extraction, but also by energy content. Pressure declines with time in closed systems or ones with limited recharge and, therefore, production potential is rather limited by lack of water than lack of energy (Axelsson *et al.*, 2005).

From the environmental point of view, reinjection is a proper option for the disposal of the geothermal fluid from power plants, contributing also to minimizing the surface subsidence caused by production induced pressure decline (Axelsson, 2012; Axelsson *et al.*, 2005). Nevertheless, there are some disadvantages associated with reinjection, namely the possible cooling of production wells, or cold-front breakthrough, often because of “short-circuiting” along direct flow-paths such as open fractures between the injection wells and the production area of the geothermal field. The proper equilibrium between providing the right pressure support to the reservoir and avoiding the cooling of the production wells is one of the most challenging tasks in the management of geothermal resources.

In order to evaluate the impact of reinjection on the decline of temperature in production wells, tracer tests are a powerful tool in geothermal management studies. According to Axelsson (2012), tracer tests provide information on the nature and properties of the flow-paths that connect injection and production wells and control the rate of cooling during long-term reinjection. The importance of tracer tests lies in the fact that the thermal breakthrough time (beginning of cooling) is usually several orders of magnitude greater (2 to 4) than the tracer breakthrough time, conferring tracer tests a predictive power.

The models used to interpret geothermal tracer test data are based on the theory of solute transport in porous and fractured hydrological systems, which includes transport by advection, mechanical dispersion and molecular diffusion (Axelsson *et al.*, 2005).

4.2 Tracer test in the Pico Vermelho sector

The exploitation scheme of geothermal resources in the Ribeira Grande geothermal field comprises the reinjection of all the geothermal fluid after heat conversion into electricity in the power plants.

In order to evaluate the overall hydraulic connection in the Ribeira Grande geothermal reservoir, a tracer test was conducted between October 2007 and May 2008. The test consisted of injecting three different types of naphthalene disulfonate tracers (1,6-NDS, 2,6-NDS and 2,7-NDS) into injection wells PV6, PV5, and CL4, respectively. Routine sampling for analysis of tracer returns was conducted from production wells CL1, CL2, CL5, PV2, PV3, and PV4 over a period of eight months. For the purpose of this work, we will only refer to the data from the Pico Vermelho sector (Pham *et al.*, 2010). The analysed tracer return data were used to further calibrate the numerical reservoir model. The results showed a rapid and relatively large magnitude return of the tracer injected into well PV6 in wells PV2, PV3 and PV4, indicating that well PV6 injection can have a detrimental effect on the fluid production temperature of these production wells. It could also be anticipated that well PV8 could also be negatively impacted by injection into well PV6, because this well is close to wells PV2 and PV4. Injection into well PV5 also indicated a negative impact on the temperature of the produced fluid of the Pico Vermelho wells, but to a lesser degree than well PV6. The tracer injected into well CL4, in

the southern part of the field (Cachaços-Lombadas sector), was not detected in the Pico Vermelho sector (Figure 10) (Pham *et al.*, 2010).

Under the current scheme of exploitation, the numerical model predicted that injection into wells PV5 and PV6 will cause significant cooling of the reservoir in the Pico Vermelho sector, at a rate of about 1.7°C per year (Pham *et al.*, 2010).

For the purpose of the present work, the data from the tracer test conducted in 2007-2008 in Pico Vermelho sector was analysed using the programs related to tracer test analysis and reinjection simulation, which are included in the software package ICEBOX (Arason *et al.*, 2004), taught at the Geothermal Training Programme of the United Nations University.

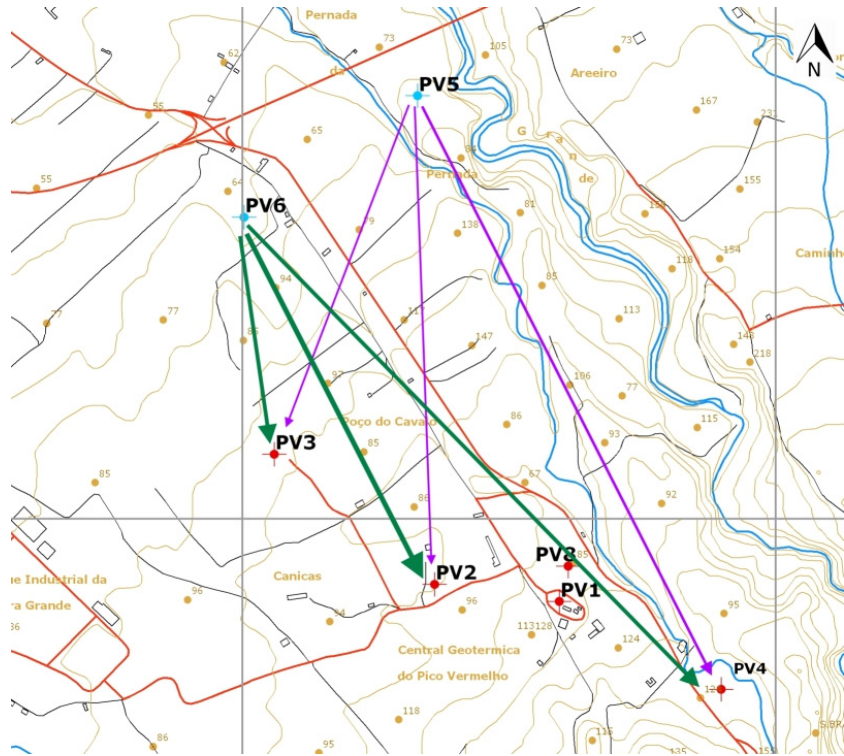


FIGURE 10: Tracer return pattern in Pico Vermelho sector (EDA Renováveis)

4.2.1 Tracer mass recovery

During tracer test analysis, the first step is to estimate the mass of tracer recovered during the test. Such an estimate is reached through the following equation:

$$m_i(t) = \int_0^t C_i(s)Q_i(s)ds \quad (3)$$

where $m_i(t)$ = Cumulative mass recovered in production well number i (kg), as a function of time;
 C_i = Tracer concentration (kg/L or kg/kg);
 Q_i = Production rate of well number i (L/s or kg/s).

The program TRMASS was used for this purpose. However, when the tracer sampling is carried out for a long period of time, considerably longer than the tracer breakthrough time, it is necessary to correct the tracer recovery for the amount of tracer which is recirculating in the system, due to the secondary return of tracer that was produced in the production wells and reinjected back into the reservoir. We can observe this effect through a relatively high concentration of tracer along the tail of the recovery curve, which causes the decrease of the slope of the tail of the curve. The program TRCORRC was used to correct that effect on the recovery curve. The results are presented in Figures 11–13.

Considering the average brine production rate of each of wells PV2, PV3 and PV4 during the tracer test and that 100 kg of each tracer were dissolved in 1 m³ of fresh water, the parameters related with the amount of tracer recovered for each pair of wells are summarized in Table 1.

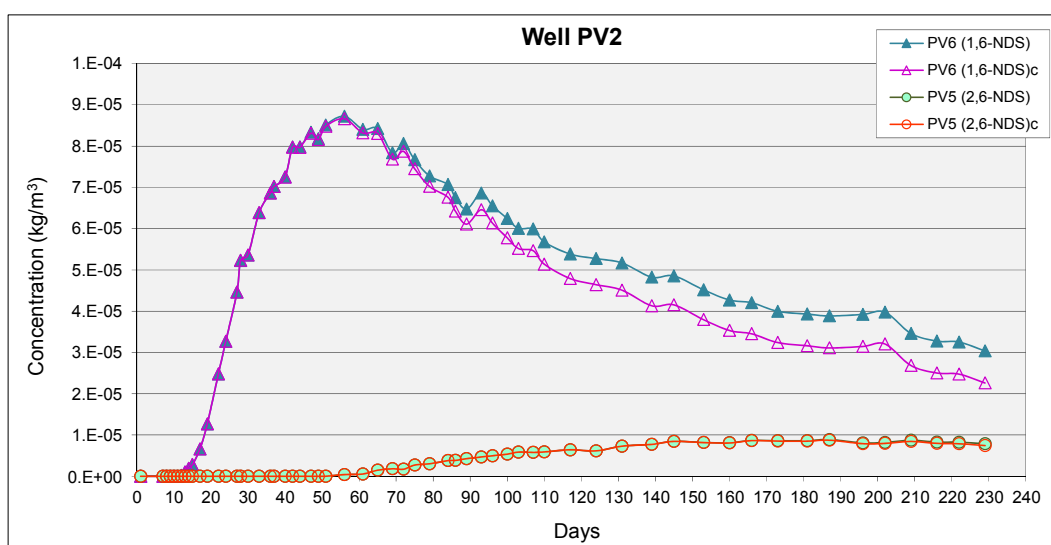


FIGURE 11: Adjusted (corrected for tracer recirculation) tracer recovery curves for well PV2

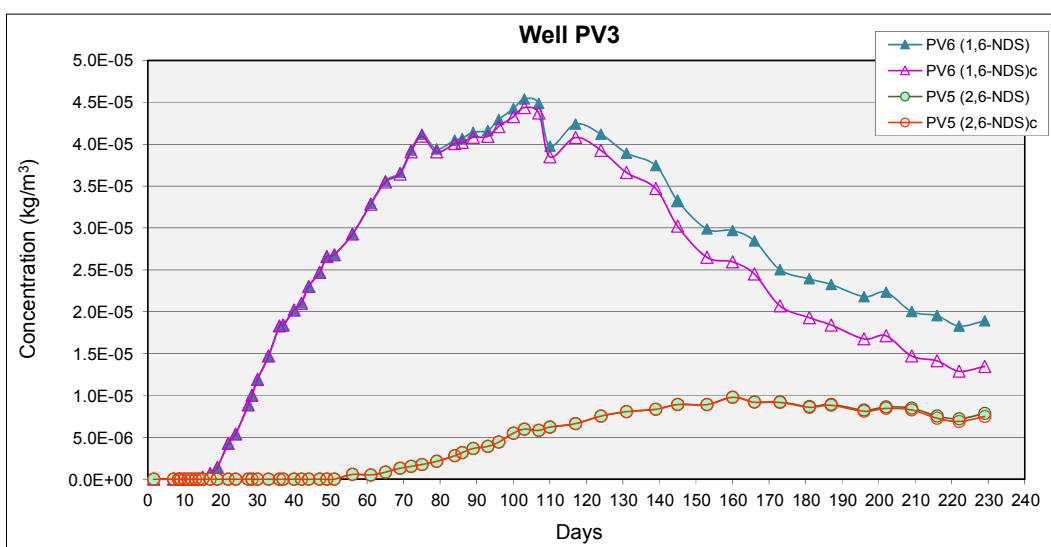


FIGURE 12: Adjusted (corrected for tracer recirculation) tracer recovery curves for well PV3

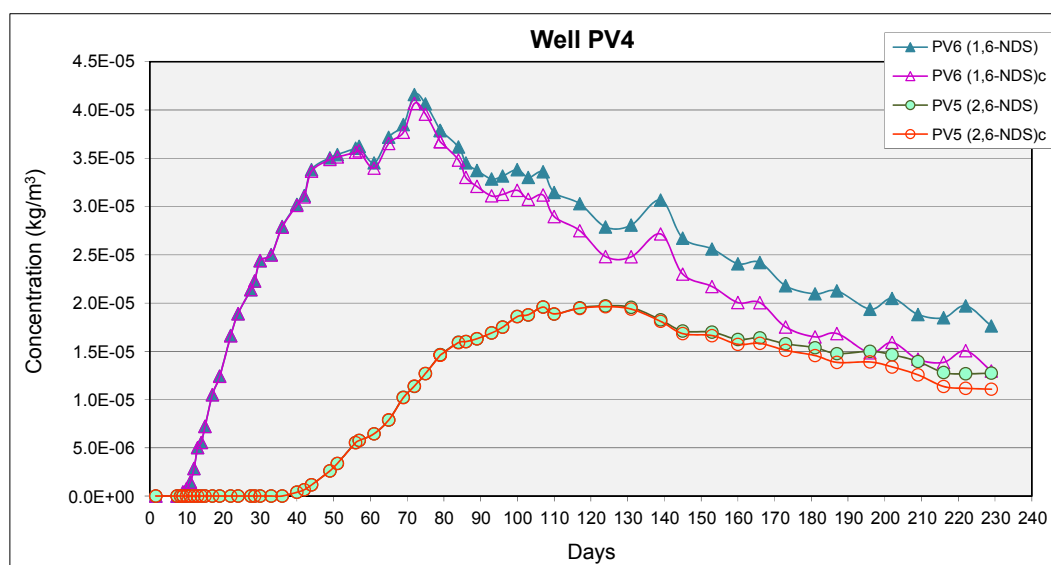


FIGURE 13: Adjusted (corrected for tracer recirculation) tracer recovery curves for well PV4

TABLE 1: Mass recovery results for geothermal production wells PV2, PV3 and PV4

Injection-production well pair	Maximum concentration (kg/m ³)	Tracer breakthrough time (days)	Mass recovery (%)
PV6-PV2	8.7x10 ⁻⁵	12	25.06
PV6-PV3	4.4x10 ⁻⁵	15	15.78
PV6-PV4	4.1x10 ⁻⁵	9	18.28
PV5-PV2	8.7x10 ⁻⁶	56	2.71
PV5-PV3	9.8x10 ⁻⁶	56	3.16
PV5-PV4	1.9x10 ⁻⁵	40	9.14

The results presented above suggest that injection well PV6 and production well PV2 have a strong hydraulic connection, since the 1,6-NDS tracer took only 12 days to first appear in the production well and the peak amount was about 8.7x10⁻⁵ kg/m³ (87 ppb). The connection between well PV6 and production wells PV3 and PV4 is also significant; however, the amount of tracer return is less than that observed in well PV2.

The returns of the 2,6-NDS tracer, injected into well PV5, show that this injection well has a weaker hydraulic connection with production wells PV2, PV3 and PV4, when compared with well PV6. This tracer had a significant return in well PV4 with a maximum concentration of 1.9x10⁻⁵ kg/m³, with a first arrival after 40 days.

4.2.2 Simulation and interpretation of data

During a first stage assessment, tracer test interpretation can be based on simple models, as presented by Axelsson *et al.* (2005). They describe a one-dimensional flow-channel model, where it is assumed that the flow between injection and production wells may be approximated by one-dimensional flow in flow-channels. According to the same authors, these channels may be parts of near-vertical fracture-zones or parts of horizontal interbeds or layers. The channels may be envisioned as being delineated by the boundaries of these structures, on one hand, and flow-field stream-lines, on the other. In other cases, these channels may have larger volumes involved in the flow between wells. In some cases more than one channel may be assumed to connect an injection well and a production well, for example connecting different feed-zones in the wells involved.

The mathematical equations that are the basis of the interpretation method for tracer tests are related to the differential equation for solute (chemical substance dissolved in fluid) transport, simplified for the case of one-dimensional flow (Equation 4):

$$D \frac{\partial^2 C}{\partial x^2} = u \frac{\partial C}{\partial x} + \frac{\partial C}{\partial t} \quad (4)$$

where D = Dispersion coefficient (m²/s), given by $D = \alpha_L u$;
 C = Tracer concentration in the flow-channel (kg/m³);
 x = Distance along the flow channel (m);
 u = Average fluid velocity in the channel (m/s), given by: $u = q/\rho A \phi$, with q the injection flow through the channel (kg/s); ρ the water density (kg/m³); A the average cross-sectional area of the flow channel (m²) and ϕ the flow channel porosity (%).

Because molecular diffusion is neglected in this simple model, and assuming an instantaneous injection of a mass of tracer at time zero, as well as conservation of the tracer according to $c \cdot Q = C \cdot q$, the solution to Equation 4 is given by:

$$c(t) = \frac{uM\rho}{Q} \frac{1}{2\sqrt{\pi Dt}} e^{-(x-ut)^2/4Dt} \quad (5)$$

where $c(t)$ = Tracer concentration in the production well fluid;
 Q = Production rate (kg/s);
 M = Mass of tracer injected at time $t=0$ (kg).

The results of the simulation give important information on the flow channel cross-sectional area ($A\emptyset$) and dispersivity (α_L), as well as the mass of tracer recovered through a given channel, which is equal to, or less than, the mass of tracer injected. In the case of two or more flow-channels, the analysis gives an estimate of these parameters for each channel. Through the estimates of a flow channel cross-sectional area, the flow channel pore space volume ($\chi A\emptyset$) can be estimated (Axelsson *et al.*, 2005).

The program TRINV simulates the tracer test data through inversion. A model with one or more flow-channels is defined by the user, and a first estimate of the model parameters is obtained. This DOS-mode program uses non-linear least-squares fitting to simulate the data and obtain the model properties, i.e. the flow channel volume, dispersivity (α_L) and tracer mass recovered (M_r). In addition to the distance between wells (along a flow channel) and volume of flow-paths, mechanical dispersion is the only mechanism assumed to control the tracer return curves in the method presented above. The model does not consider molecular diffusion, i.e., the delay of the tracers by diffusion from the flow-paths into the rock matrix, which causes the tracer to diffuse into the rock matrix when the tracer concentration in the flow path is high and vice-versa. Some authors claim that this effect can be negligible in fractured rock except when fracture apertures are small, flow velocities are low and rock porosity is high (Axelsson *et al.*, 2005).

It should be emphasised that many other models have been developed to simulate geothermal tracer tests. It is often possible to simulate a given dataset by more than one model; therefore, a specific model may not be uniquely validated (Axelsson *et al.*, 2005).

Considering the above, the tracer recovery curves were simulated for production wells PV2, PV3 and PV4 (Figures 14-16), and the principal results of the interpretation are presented in Table 2.

TABLE 2: Model parameters used to simulate tracer recovery for wells PV2, PV3 and PV4

Injection-production well-pair	Channel	Flow path distance χ (m)	Flow velocity u (m/s)	Cross-sectional area $A\emptyset$ (m ²)	Estimated volume $\chi A\emptyset$ (m ³)	Dispersivity (α_L) (m)	Mass recovery (%)
PV6-PV2	1	759	1.6×10^{-4}	32	24288	110	13.5
	2	1138.5	7.8×10^{-5}	101	114988	239	20.4
PV6-PV3	1	717	7.9×10^{-5}	82	58794	191	16.9
	2	1075.5	1.1×10^{-4}	8	8604	42	2.3
PV6-PV4	1	1331	1.6×10^{-4}	56	74536	555	24
PV5-PV2	1	904	5.1×10^{-5}	155	140120	144	5.7
PV5-PV3	1	770	4.9×10^{-5}	146	112420	79	5.1
PV5-PV4	1	1260	7.5×10^{-5}	202	254520	179	10.8
	2	1890	2.2×10^{-4}	23	43470	127	3.5

The flow path distance between each well pair was defined by calculating the distance between the most likely feed zones of the wells. For injection wells PV5 and PV6, the main feed zones were assumed to be located at -550 m and -950 m, respectively. For well pairs PV6-PV2, PV6-PV3 and PV5-PV4, two channels were required for the above simulation, assuming for the second flow channel a longer length (e.g. due to sinking of the colder, and denser, injection fluid to a greater depth before it ascends to the production feed-zone), corresponding to an addition of 50% of the length of the main flow channel. For every well pair, determinate coefficients of 99.5 to 99.7% were achieved, with the exception of well-pair PV6-PV4, with 98.6%, showing a very good match between the simulated curves and the measured tracer concentrations that were recovered in the production wells.

From the analysis of the model parameters, it is verified that the 1,6-NDS tracer that was injected into well PV6 was recovered at a higher percentage in the production wells than the 2,6-NDS tracer which was injected into well PV5, suggesting that the first injection well has a stronger connection with the production area of Pico Vermelho than injection well PV5. The greatest mass recovery percentage is observed for well pair PV6-PV2 (approx. 34%) and the lowest, about 5%, was observed for well pair PV5-PV3. If we consider the dispersivity, we verify that there is some heterogeneity in the results obtained. Great dispersivity is normally associated with heterogeneous flowpaths, which could be associated, for example, with a network of fractures controlling the flow, rather than just a single fracture. Results of Table 2 were used to calculate cooling predictions for the three production wells.

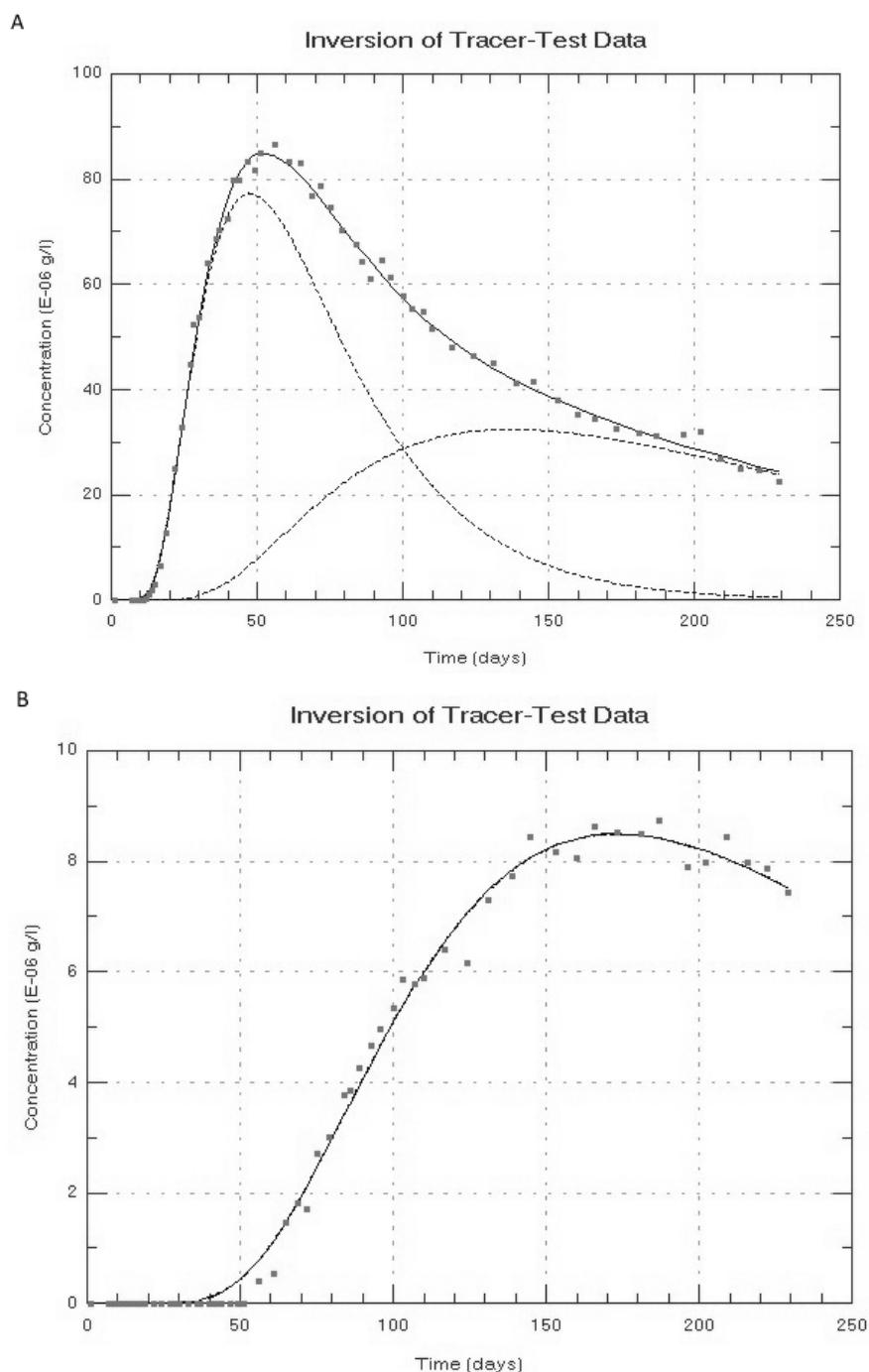


FIGURE 14: Observed (squares) and simulated tracer recovery curves for well PV2; A) Recovery of tracer 1,6-NDS (injected into well PV6); B) Recovery of tracer 2,6-NDS (injected into well PV5)

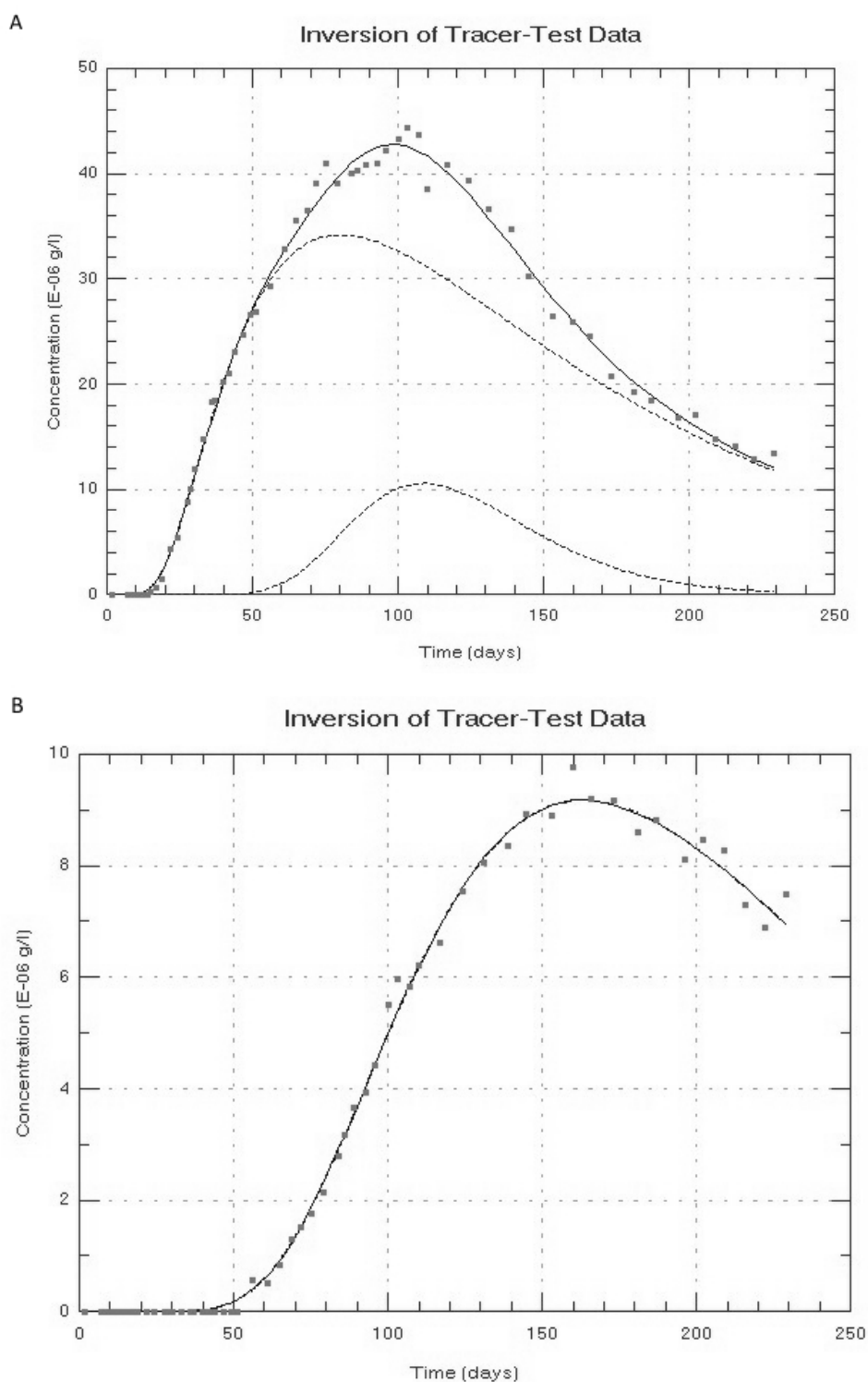


FIGURE 15: Observed (squares) and simulated tracer recovery curves for well PV3; A) Recovery of tracer 1,6-NDS (injected into well PV6); B) Recovery of tracer 2,6-NDS (injected into well PV5)

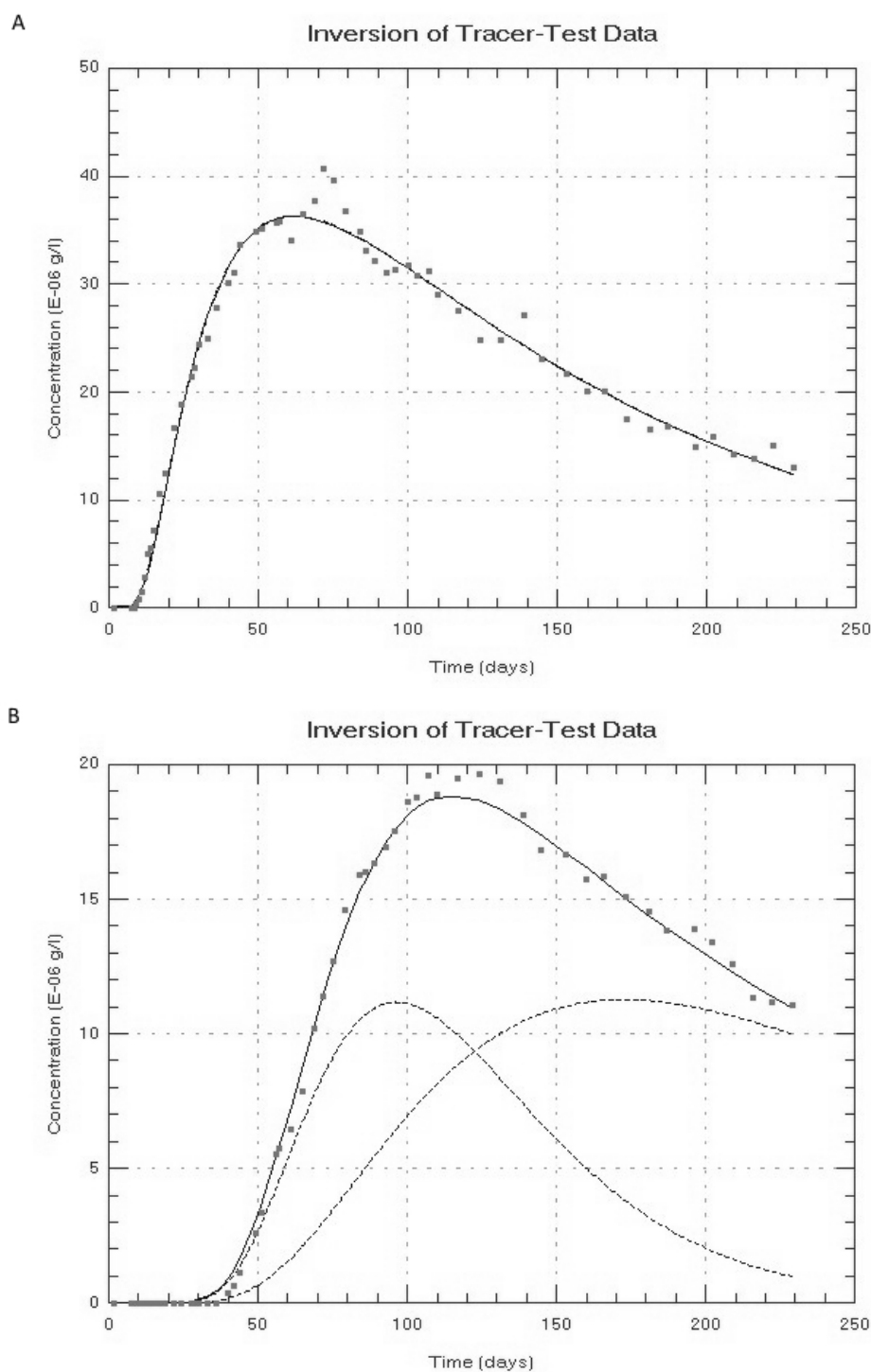


FIGURE 16: Observed (squares) and simulated tracer recovery curves for well PV4; A) Recovery of tracer 1,6-NDS (injected into well PV6); B) Recovery of tracer 2,6-NDS (injected into well PV5)

4.2.3 Prediction of temperature decline during long-term production

Temperature decline during long-term reinjection (thermal breakthrough) is not only determined by the volume of the flow-channel(s) involved, but also by the surface area and porosity of the flow-channel(s), as a large surface area flow channel leads to slow cooling and vice-versa. Therefore, it is important to have additional information on the flow-path properties/geometry or to make some

assumptions on those. Additional data, as temperature changes, or data on chemical variations should not be neglected as constraints for cooling predictions (Axelsson *et al.*, 2005).

The mathematical equations giving the response of the model for cooling predictions are:

$$T(t) = T_0 - \frac{q}{Q}(T_0 - T_i) \left[1 - \operatorname{erf} \left\{ \frac{kxh}{c_w q \sqrt{\kappa(t - x/\beta)}} \right\} \right] \quad (6)$$

$$\beta = \frac{qc_w}{(\rho c)_f hb} \quad \text{with} \quad (\rho c)_f = \rho_w c_w \phi + \rho_r c_r (1 - \phi) \quad (7)$$

where $T(t)$ = Production temperature (°C);
 T_0 = Initial reservoir temperature (°C);
 T_i = Injection temperature (°C);
 q = Injection flow-rate in each flow channel (kg/s);
 Q = Production rate (kg/s);
 x = Distance between injection and production wells (m);
 k = Thermal conductivity of reservoir rock;
 κ = Thermal diffusivity of rock (m²/s), given by $k/\rho c_p$, with k its thermal conductivity;
 ρ its density (kg/m³) and c_p its specific heat capacity (J/kg °C);
 ρ and c are density and heat capacity of water (w) and rock (r);
 h and b are height and width of a flow path (m);
 ϕ = flow path porosity (%).

Cooling predictions should be calculated considering two extremes regarding flow-channel dimensions: a small surface area, or pipe-like flow channel, which can be considered a pessimistic model with minimal heat transfer (rapid cooling); and a large surface area flow channel, such as a thin fracture-zone or thin horizontal layer, which can be considered an optimistic model with effective heat transfer (slow cooling).

Considering the scheme of reinjection for the Pico Vermelho power plant, at the time the tracer test was conducted (using wells PV5 and PV6 as injection wells with a total flow of around 145 kg/s of geothermal fluid), the program TRCOOL was used to calculate the theoretical temperature decline for production wells PV2, PV3 and PV4, for a period of 30 years, while considering both scenarios presented above.

The model parameters used for the cooling predictions for wells PV2, PV3 and PV4 can be found in Table 3. A pessimistic scenario was assumed, where the ratio between height (h) and width (b) of the flow channels was given by $h=5b$ and also an optimistic scenario, where that ratio was given by $h=100b$. For all cases, an average porosity of 15% was assumed for the predictions. The results of the cooling predictions are presented in Figure 17.

The cooling predictions indicate, for an optimistic scenario for well PV2, a temperature decline of about 22.5°C in 30 years and about 64°C for a pessimistic scenario. Regarding well PV3, we verify that the prediction for the same time period is less severe than for well PV2, with a drop in temperature of about 6°C, considering the optimistic scenario and around 38.6°C considering a more pessimistic scenario. Well PV4 is also strongly affected by cooling, with a temperature decline of about 20°C predicted for the optimistic scenario, and around 55°C considering the pessimistic scenario, for the same time period of 30 years.

When plotting the monitoring temperature data of wells PV2, PV3 and PV4 (represented as dots in Figure 17) together with the cooling predictions, between 2007 and 2014, we verify that: the pessimistic scenarios are unlikely, and that actually the observed data are close to being in-between the optimistic and pessimistic predictions. But if the injection into wells PV5 and PV6 is maintained for a

period of 30 years, it is not unlikely that the temperature in well PV2 will decline about 41°C ($\pm 21^{\circ}\text{C}$) and around 35°C ($\pm 15^{\circ}\text{C}$) in well PV4. Regarding production well PV3, the prediction of a significant decline in the temperature is more uncertain, as the well has been recovering its initial temperature. This increase of the measured temperature in well PV3 in the last couple of years is probably due to the fact that this well has not been producing on a continuous basis for the power plant and, therefore, has been to a large extent kept closed. In Pico Vermelho sector there is an excess of fluid production which allows a very flexible operation, requiring only three production wells to saturate the power plant (10 MW).

Although the model parameters used in 2007-2008 by GeothermEx (2008) to perform the cooling predictions are unknown, namely the geometry of the flow channel(s) and respective volume(s), we see that the results, obtained through the tracer test analysis presented here, are in general comparable with the ones predicted previously by GeothermEx, with a temperature decline of around 1.4°C per year for well PV2 and 1.2°C per year for well PV4. GeothermEx (2008) predicted an overall temperature decline of 50°C for the Pico Vermelho sector, which can also be compared with the predictions in Figure 17.

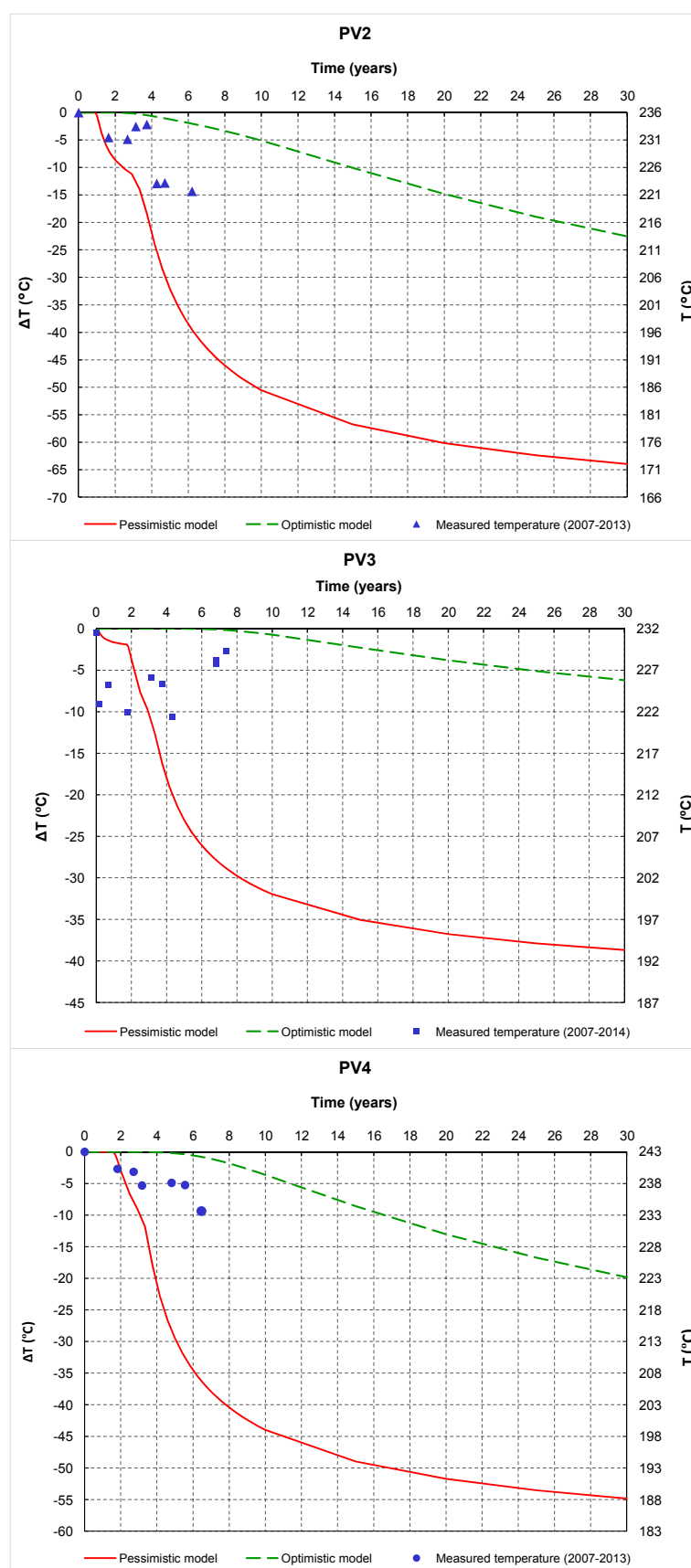


FIGURE 17: Cooling predictions for production wells PV2, PV3 and PV4, considering a period of 30 years

TABLE 3: Model parameters used for the cooling predictions for wells PV2, PV3 and PV4

Injection-production well-pair	Scenario	Channel	Flow channel distance x (m)	Flow channel width/thickness b (m)	Flow channel height/extent h (m)
PV6-PV2	Pessimistic	1	759	6.6	32.9
		2	1138.5	11.6	58
	Optimistic	1	759	1.5	150
		2	1138.5	2.6	260
PV5-PV2	Pessimistic	1	904	14.4	72
	Optimistic			3.2	320
PV6-PV3	Pessimistic	1	717	10.5	52.3
		2	1075.5	0.5	2.5
	Optimistic	1	717	2.3	234
		2	1075.5	0.1	110
PV5-PV3	Pessimistic	1	770	14	69.7
	Optimistic			3.1	311.6
PV6-PV4	Pessimistic	1	1331	8.6	43.2
	Optimistic			1.9	193
PV5-PV4	Pessimistic	1	1260	16.4	82
		2	1890	5.5	27.6
	Optimistic	1	1260	3.7	370
		2	1890	1.2	123.6

5. CONCLUSIONS

The Ribeira Grande geothermal field is a high-temperature, liquid-dominated system, hosted by volcanic rocks, mainly a succession of trachytic to basaltic lava flows and pyroclastic flows. The heat source of the reservoir is presumably a body of magma or young intrusive rock associated with the activity of the Fogo volcano and the origin of the water is meteoric. The system seems to be controlled by the NW faulting trend created by the regional tectonic setting. Well data indicate that a sequence of pyroclastic rocks, altered to clay, form a relatively impermeable cap at the top of the reservoir.

In order to estimate the formation temperature and initial reservoir pressure in the Pico Vermelho sector of the Ribeira Grande geothermal system, the warm-up temperature and pressure profiles of new wells PV9, PV10, PV11 and RG5 were analysed together with the warm-up temperature and pressure profiles of the other Pico Vermelho wells. Based on the estimated formation temperature and initial pressure of the reservoir, temperature and pressure contour maps were drawn in order to show their distribution in this sector of the field.

By incorporating the data from the new geothermal wells into the temperature model, we verify that the reservoir in Pico Vermelho lies mostly between the 200 and 800 m b.s.l. and there is no evidence of the existence of a boundary between the wells located to the west and the new ones located to the east, indicating a continuous reservoir in the overall Pico Vermelho sector.

In order to evaluate the overall hydraulic connection in the Ribeira Grande geothermal reservoir, a tracer test was conducted between October 2007 and May 2008. For the purpose of the present work, the data from the tracer test was analysed using the programs related to tracer test analysis and reinjection simulation which is included in the ICEBOX software package (TRCORRC, TRMASS, TRINV and TRCOOL). The results suggest a strong hydraulic connection between injection wells PV5 and PV6 and the production area in Pico Vermelho, as was previously predicted.

Cooling predictions based on the results of the tracer recovery modelling indicate, for an optimistic scenario in well PV2, a temperature decline of about 22.5°C in 30 years and about 64°C for a pessimistic scenario. Regarding well PV3, we verify that the prediction for the same time period is less severe than for well PV2, with a drop in temperature of about 6°C, considering the optimistic scenario and around 38.6°C considering the more pessimistic scenario. Well PV4 is also strongly affected by cooling, with a predicted temperature decline of about 20°C for an optimistic scenario and around 55°C considering a pessimistic scenario, for the same time period of 30 years. After comparing actual temperature monitoring for wells PV2, PV3 and PV4, we verify that the pessimistic scenarios are unlikely, but if injection into wells PV5 and PV6 is maintained for a period of 30 years, it is considered likely that the temperature in well PV2 will decline about 41°C ($\pm 21^\circ\text{C}$) and around 35°C ($\pm 15^\circ\text{C}$) in well PV4. The prediction for production well PV3 is uncertain, since the well has been recovering its initial temperature, possibly due to the fact that this well has been kept closed for the last couple of years.

ACKNOWLEDGEMENTS

I would like to address my acknowledgments to Mr. Lúdvík S. Georgsson, director of the Geothermal Training Programme of the United Nations University (UNU-GTP), as well as to all the technical staff of UNU-GTP, namely Mr. Ingimar G. Haraldsson, Ms. María Gudjónsdóttir, Ms. Málfríður Ómarsdóttir, Ms. Thórhildur Ísberg and Mr. Markús A.G. Wilde for the kind support provided during the training in Iceland. Sincere thanks to Dr. Gudni Axelsson and Ms. Saeunn Halldórsdóttir, from ÍSOR, for the supervision and guidance during the preparation of the present project.

A special word of appreciation is addressed to EDA Renováveis, S.A., for the support given during the training in Iceland and for allowing the use of the Ribeira Grande geothermal field data for the purpose of the present work.

REFERENCES

- Arason, T., Björnsson, G., Axelsson, G., Bjarnason, J., and Helgason, P., 2004: *ICEBOX – Geothermal reservoir engineering software for Windows, a user's manual*. ÍSOR, Reykjavík, report ISOR-2004/014, 80 pp.
- Axelsson, G., 2012: Role and management of geothermal reinjection. *Proceedings of the Short Course on Geothermal Development and Geothermal Wells, organized by UNU-GTP and LaGeo, Santa Tecla, El Salvador*, 22 pp.
- Axelsson, G. and Steingrímsson, B., 2012: Logging, testing and monitoring geothermal wells. *Proceedings of the Short Course on Geothermal Development and Geothermal Wells, organized by UNU-GTP and LaGeo, Santa Tecla, El Salvador*, 20 pp.
- Axelsson, G., Björnsson, G., and Montalvo, F., 2005: Quantitative interpretation of tracer test data. *Proceedings of the World Geothermal Congress 2005, Antalya, Turkey*, 12 pp.
- Gaspar, J.L., 1996: *Ilha Graciosa (Açores): Volcanological history and assessment of hazards*. University of the Açores, Azores, PhD thesis (in Portuguese), 256 pp.
- Gaspar, J.L., Queiroz, G., Ferreira, T., Amaral, P., Viveiros, F., Marques, R., Silva, C., and Wallenstein, N., 2011: *Geological hazards and monitoring at the Azores (Portugal)*. Articles, Disaster

Management Theme, Earth Observation (www.earthzine.org/2011/04/12/geological-hazards-and-monitoring-at-the-azores-portugal/).

GeothermEx, Inc., 2008: *Update of the conceptual and numerical model of the Ribeira Grande geothermal reservoir, São Miguel, Açores*. Report for SOGEO – Sociedade Geotérmica dos Açores, S.A.

Grant, M.A. and Bixley, P.F., 2011: *Geothermal reservoir engineering* (2nded.). Academic Press, NY, 359 pp.

Martini, F., Bean, C., Saccorotti, G., Viveiros, F., and Wallenstein, N., 2009: Seasonal cycles of seismic velocity variations detected using coda wave interferometry at Fogo volcano, São Miguel, Azores, during 2003-2004. *J. Volcanology & Geothermal Res.*, 181, 231-246.

Moore, R., 1990: Volcanic geology and eruption frequency S. Miguel, Azores. *Bull. Volcanol.* 52, 602–614.

Moore, R., 1991: Geology of three late Quaternary stratovolcanoes on São Miguel, Azores. *USGS Bull.* 1990, 1-26.

Muecke, G.K., Ade-Hall, J.M., Aumento, F., McDonald, A., Reynolds, P.H., Hyndman, R.D., Quintino, J., Opdyke, N., and Lowrie, W., 1974: Deep drilling in an active geothermal area in the Azores. *Nature* 252 (5481), 281–285.

Pham, M., Klein, C., Ponte, C., Cabeças, R., Martins, R., and Rangel, G., 2010: Production/injection optimization using numerical modeling at Ribeira Grande, São Miguel, Azores, Portugal. *Proceedings of the World Geothermal Congress 2010, Bali, Indonesia*, 6 pp.

Ponte, C., Cabeças, R., Martins, R., Rangel, G., Pham, M., and Klein, C., 2009: Numerical modeling for resource management at Ribeira Grande, São Miguel, Azores, Portugal. *Geothermal Resources Council, Trans.*, 33, 847-853.

Ponte, C., Cabeças, R., Rangel, G., Martins, R., Klein, C. and Pham, M., 2010: Conceptual modeling and tracer testing at Ribeira Grande, São Miguel, Azores, Portugal. *Proceedings of the World Geothermal Congress 2010, Bali, Indonesia*, 11 pp.

Silva, R., Havskov, J., Bean, C., and Wallenstein, N., 2012: Seismic swarms, fault plane solutions, and stress tensors for São Miguel Island central region (Azores). *J. Seismol.*, 9-1, 21 pp.

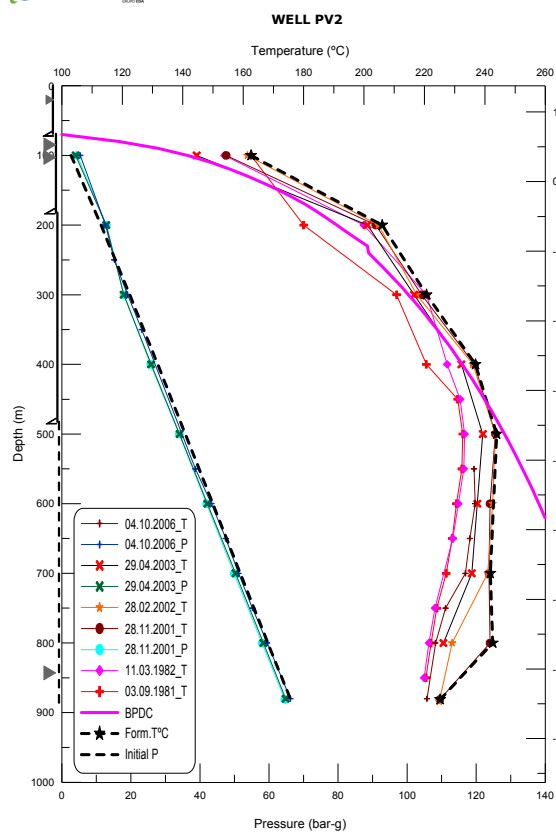
Steingrímsson, B., 2013: Geothermal well logging: temperature and pressure logs. Presented at “Short Course V on Conceptual Modelling of Geothermal Systems”, organized by UNU-GTP and LaGeo, Santa Tecla, El Salvador, 16 pp.

Viveiros, F., Ferreira, T., Silva, C., Óskarsson, N., and Hipólito, R. 2009: *Natural and anthropogenic influences on the gas geochemical monitoring at Fogo Volcano (São Miguel Island, Azores)*. VOLUME project, EU PF6 (No. 018471), 299-308.

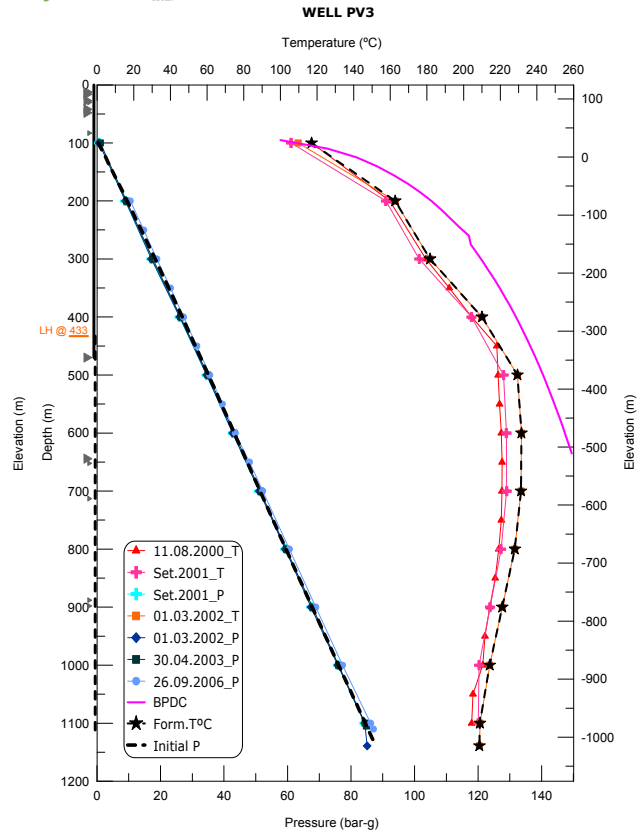
Wallenstein, N., Duncan, A.M., Chester, D.K., and Marques, R., 2007: Fogo Volcano (São Miguel, Azores): a hazardous edifice. *Géomorphologie: Relief, Processes, Environment*, 3, 259-270.

APPENDIX I: Warm-up temperature and pressure logs, as well as estimated formation temperature and initial reservoir pressure for geothermal wells PV2, PV3, PV4, PV5, PV7 and PV8

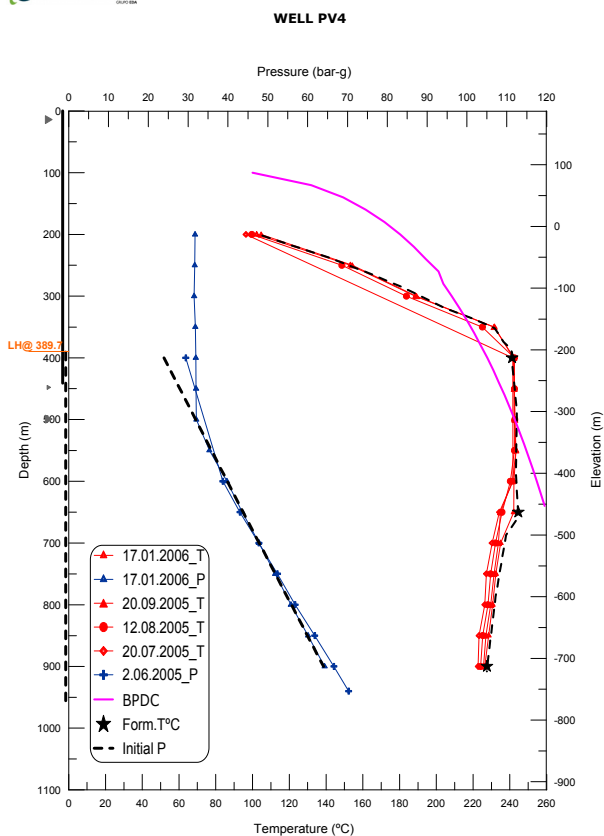
EDA RENOVÁVEIS



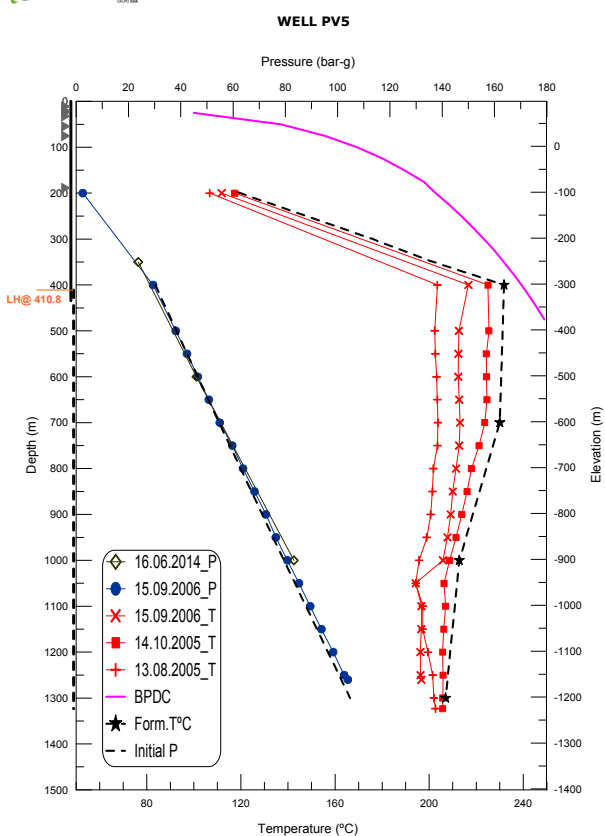
EDA RENOVÁVEIS

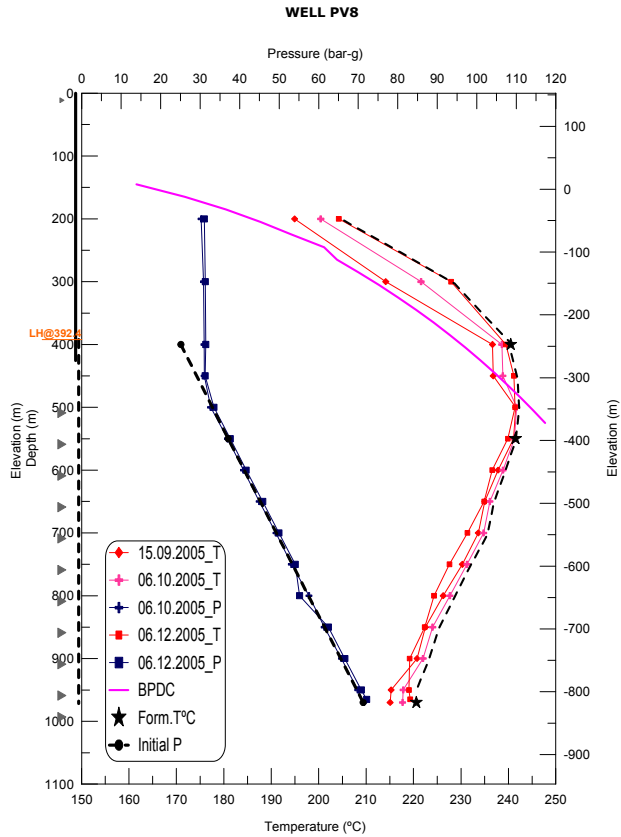
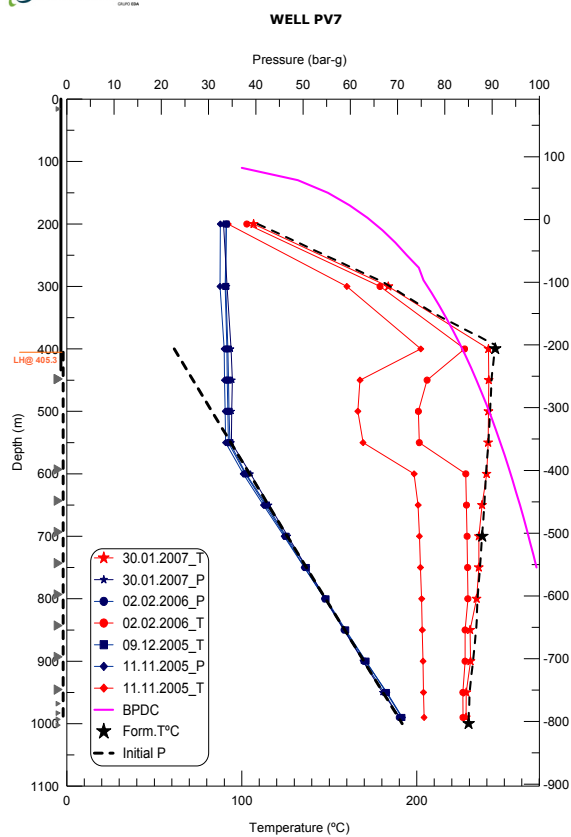


EDA RENOVÁVEIS



EDA RENOVÁVEIS







UNITED NATIONS
UNIVERSITY

UNU-GTP

Geothermal Training Programme

Orkustofnun, Grensasvegur 9,
IS-108 Reykjavik, Iceland

Reports 2014
Number 30

BOREHOLE GEOLOGY AND ALTERATION MINERALOGY OF WELL RN-12, REYKJANES GEOTHERMAL FIELD, SW-ICELAND

Djama Robleh Djama

Ministry of Energy in Charge of Natural Resources

P.O. Box 10010, Djibouti

REPUBLIC OF DJIBOUTI

jamajama3@hotmail.com

ABSTRACT

The current study focuses on high temperature geothermal well RN-12, which is located in the seawater-dominated geothermal system at Reykjanes field in SW Iceland. This is a vertical well, drilled in 2002 and reaching a total depth of 2506 m. The uppermost 1024 m are presented in this report. The well was kept offline until it was brought online for production in May, 2006 to feed the then-new 100 MW power plant. Drill cuttings were used to gather data from binocular and petrographic microscopes, and XRD and fluid inclusions analyses. Geophysical logs were used to corroborate conclusions derived from the cuttings. The lithology of well RN-12 contains hyaloclastite formations, such as tuff, breccia, tuff-rich sediments and pillow basalts in addition to basaltic lava flows and intrusions. The rock texture within these units range from fine-grained to medium-grained, even coarse-grained in some cases. Basalt intrusions were found at 360-396, 416-452, 460, 480-484, 500-510, 524-538, 542-576, 622-654, 708-752, 768-772 and 920-932 m. Two alteration groups were identified in the well, one based on the clay mineralogy zones, the other on the alteration mineral distribution zones. These sequences are: smectite-zeolite zone from 10 to 702 m; mixed-layer clay zone from 702 to 782 m; chlorite zone from 782 to 1024 m. The alteration mineral zones are: quartz zone from 70 to 260 m; prehnite zone from 260 to 610 m; epidote zone from 610 to 694 m; garnet zone from 694 to 762 m; and wollastonite zone from 762 to 1024 m. Thirteen small aquifers were identified in the well, all cased off, but three main feed zones were inferred at depths of 1000, 1300 and 2200 m. A fluid inclusion study from secondary quartz showed a homogenization temperature which ranges from 265 to 295°C. This temperature range correlates with the alteration and formation temperatures, which indicates that the well is in equilibrium with the geothermal system around well RN-12.

1. INTRODUCTION

This project report is a partial fulfilment of a six months training course at the United Nations University Geothermal Training Programme (UNU-GTP). The report focuses on the geological and geothermal aspects of well RN-12 which is one of the production/exploration wells in the Reykjanes geothermal field, SW-Iceland. Well RN-12 was drilled vertically down to 2506 m in the year 2002. Cuttings were sampled at 2 m interval for analysis and identification of subsurface formations and an

analysis of temperature dependent alteration minerals. The main analytical techniques used in this study were binocular and petrographic microscopic analyses, X-ray diffraction and a fluid inclusion analysis.

1.1 Purpose of the study

The main purpose of borehole geology is to analyse the various rock formations in order to understand the lithology, detect porosity and permeability, and estimate the alteration temperature by analysing alteration mineralogy, which gives indications on the conditions in the well and aids in deciding casing depths. This allows us to grasp the nature of the sub-surface and structural geology. The relationship between geology and permeability and knowing the hydrothermal alteration is a step towards predicting the shape of the geothermal system, its evolution and present state. These principles were applied to analyse well RN-12 in the Reykjanes geothermal system, in detail, by using drill cuttings and all available data collected during drilling, including geophysical logging.

2. OUTLINE OF GEOLOGY

2.1 Regional geology of Iceland

In a global view, Iceland is a unique geological system set on an active mid-oceanic spreading ridge. It is considered one of few places in the world where we can observe the evolution and mechanism of rifting above sea level. Iceland is located on the Mid-Atlantic Ridge, separating the plate boundary of the Eurasian- and North American plates which spread approximately 18 mm per year to the ESE and WSW (Saemundsson, 1979) (Figure 1), and situated on a top of a hotspot presumed to be fed by a deep mantle plume (e.g. Einarsson, 2008). Iceland's regional geology is the product of the relative movement of the Mid-Atlantic divergent plate boundary across the mantle plume (e.g. Hardarson et al., 1997). The exposed Iceland crust contains evidence of major ridge-jumps over the last 16 million years and this relocation of the magmatic focus has been a prominent process in the evolution of the

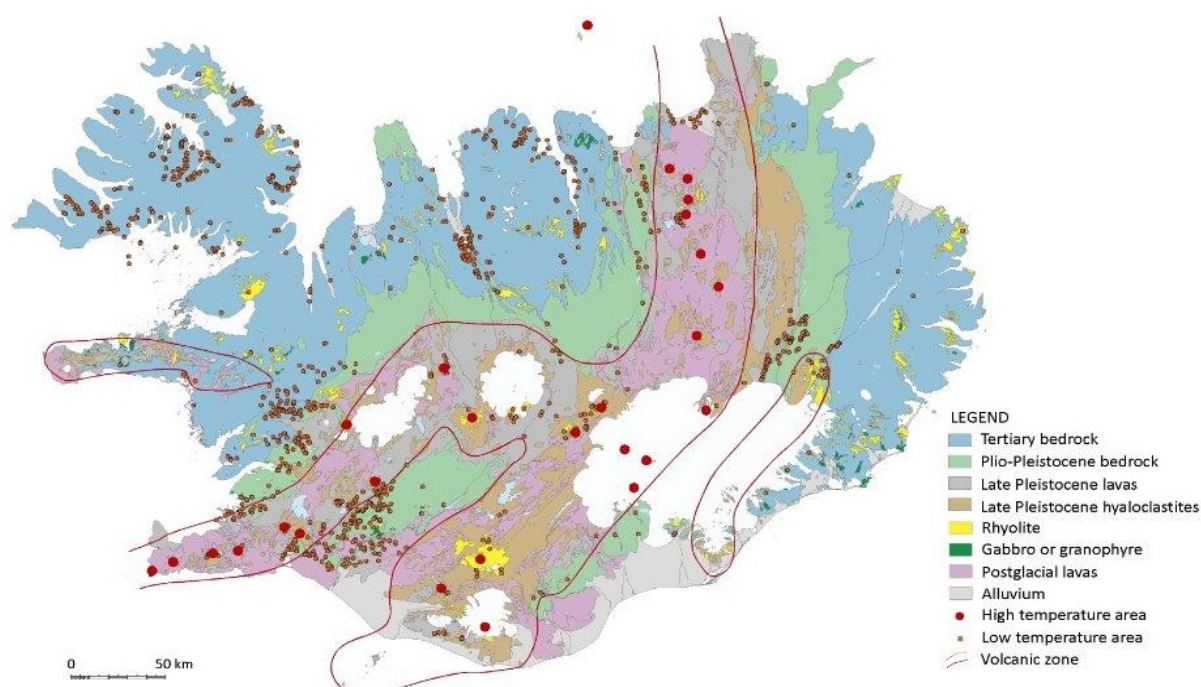


FIGURE 1: Geological map of Iceland (Jóhannesson and Saemundsson, 1999)

island (e.g. Saemundsson, 1979; Hardarson et al., 1997). On average, the spreading of the plates is 18 mm/year leading to a complex form of rift zones and transform fault zones (Figure 1). Iceland is almost entirely made up of volcanic rocks with basalts being 80-85% of the volcanic pile and evolved rocks constituting ~10%. Sediments of volcanic origin are 5-10% in a typical Tertiary lava pile but may be locally higher in Quaternary rocks. Quaternary formations are found along the margins of the rift zone while Tertiary basalts predominate to the east and west, away from the rift zone (Saemundsson, 1979).

2.2 Reykjanes high-temperature field

The Reykjanes peninsula is the south westernmost part of Iceland (Figure 2) and it is the landward extension of the sub-marine Reykjanes Ridge. Geologically, on the surface, the Reykjanes peninsula consists of hyaloclastites formed during the last glacial periods and of post-glacial basaltic lava flows. The volcanic activity in this area was intense during postglacial times; the number of eruptions is not known but estimated to be a few hundred (Höskuldsson et al., 2006). The peninsula hosts four volcanic centres and several geothermal fields: Reykjanes, Eldvörp and Svartsengi fields in the western part; the Krýsuvík field in the middle of the peninsula; and Brennisteinsfjöll and Hengill fields in the east (Figure 2).

The Reykjanes geothermal field is situated at the tip of the Reykjanes peninsula (Figures 1 and 2). Exploration of the Reykjanes geothermal field started in the early 1950s and a well was drilled there in 1956. Geological maps and surface exploration surveys were done in the 1960s (Lindal and Lúdvíksson, 1969). In the late 1960s, seven wells were drilled in the area to explore the extent of the field. In late 2002, the regional district heating company, Hitaveita Suðurnesja (HS Orka), decided to increase steam production in order to accommodate the demand for the power plant. A new drill site

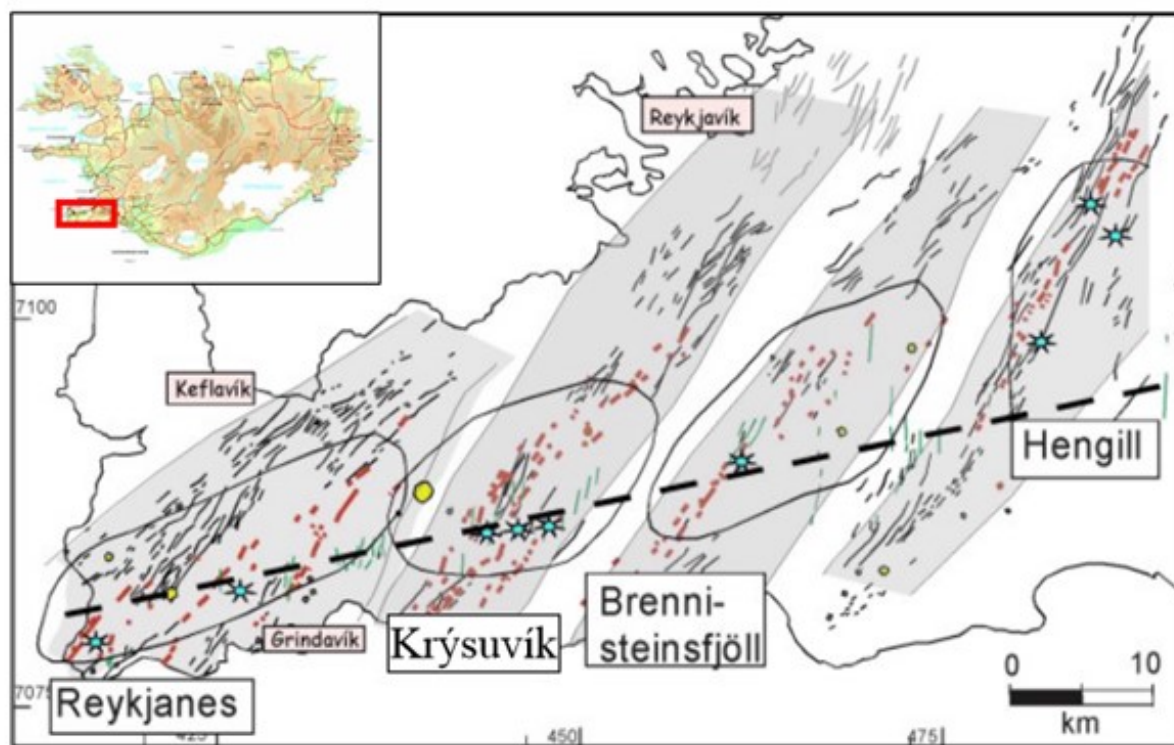


FIGURE 2: Map of the Reykjanes Peninsula showing fissure swarms as black lines, eruptive fissures as red lines, faults as green lines, geothermal fields as blue stars; four volcanic zones are circled, and the location of the plate boundary is shown as a dashed line (Jakobsson et al., 1978); Data from Árnason et al., 1986; Einarsson et al., 1991; Eyólfsson 1998; Hreinsdóttir et al., 2001; Sigurdsson, 1985; Saemundsson and Einarsson, 1980; Mawejje, 2007

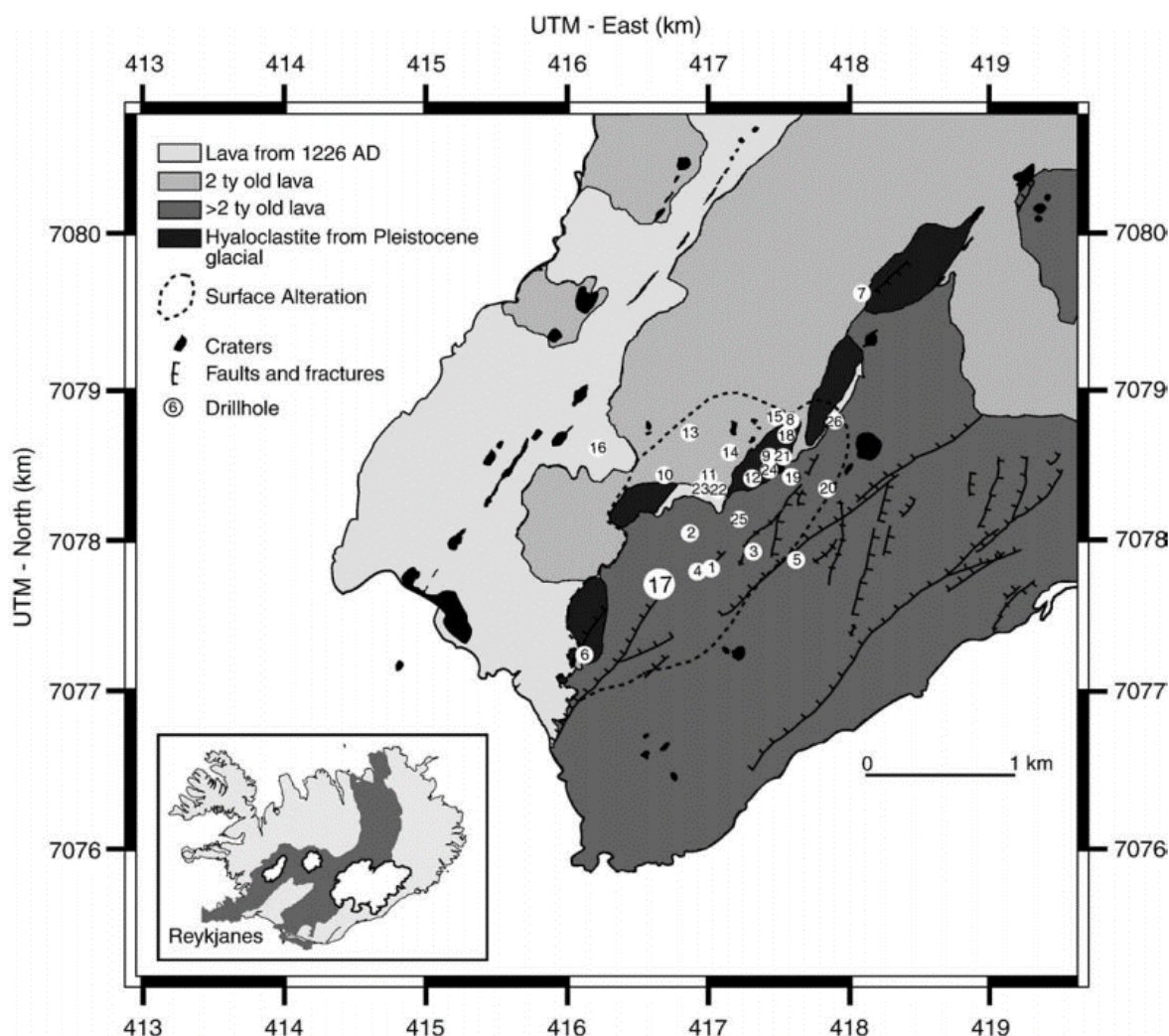
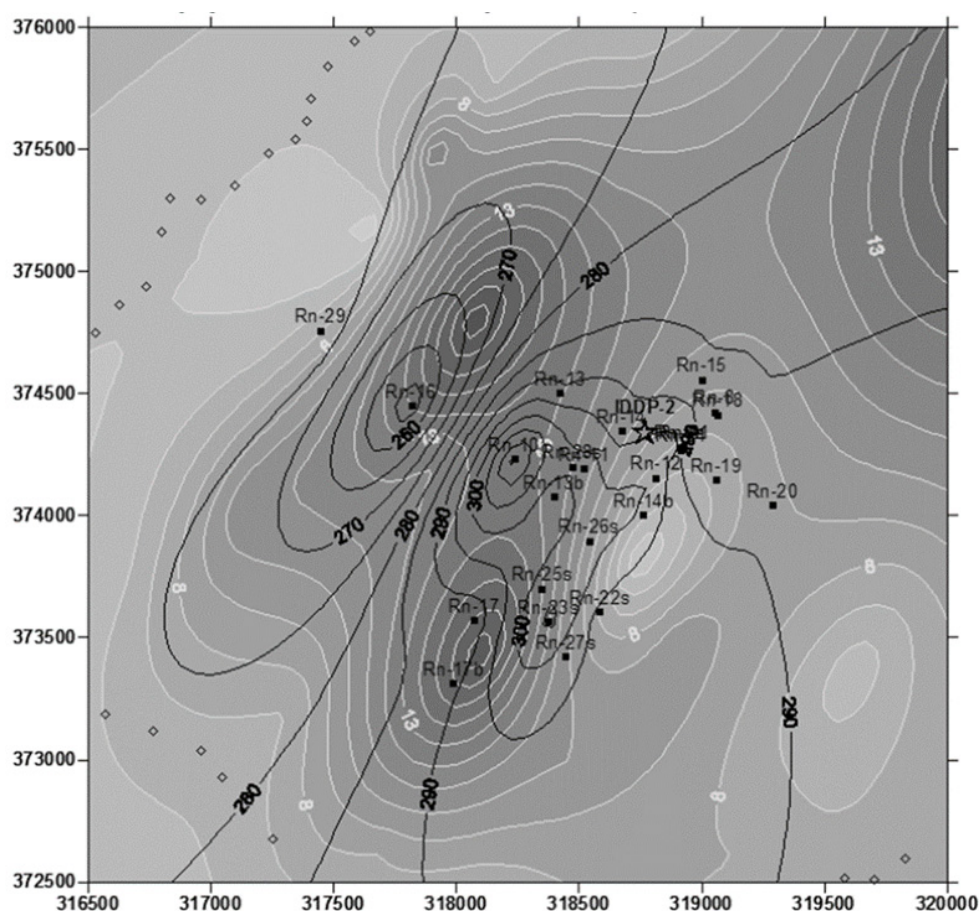


FIGURE 3: Map of the Reykjanes Peninsula showing major faults, fractures, lava flows, surface alteration and location of well RN-12 (map adapted from Saemundsson and Einarsson, 1980; Franzson et al., 2002; Fridleifsson et al., 2003; Marks et al., 2010)

for well RN-12 (Figure 3) was selected between wells RN-9 and RN-11 at Reykjanes at 63.82382°N, 22.68128°E and 18.13 m a.s.l. The number of the well is 18912 in the National Energy database. The drilling started on 22.10.2002 and ended on 17.12.2002 at 2506 m depth.

2.3 Geophysical studies in the Reykjanes area

Surface resistivity surveys in the Reykjanes area have been carried out since 1970 with continuous updating, including applying MT surveys. Early resistivity was measured by (DC) methods with a Schlumberger configuration, followed by TEM (transient electromagnetic) and subsequently MT surveys (Fridleifsson et al., 2011). Low resistivity was showing in the upper part of the field at 800 m depth with an extensional delimitation zone of around 10 km². The main up-flow zone was located by surface resistivity and concurred with the NE-SW eruptive fissure zone (Figure 4) with an intersection of a N-S trending up-flow zone in the central part of the field (Karlsdóttir, 2005). Recently, in 2010, MT surveys found that resistivity reached down to 20-30 km or more, revealing a low-resistivity body at 10 km depth under Reykjanes, consisting of a heat source seated below or a large magma body (gabbroic) that is cooling (Figure 4) (Fridleifsson et al., 2011).



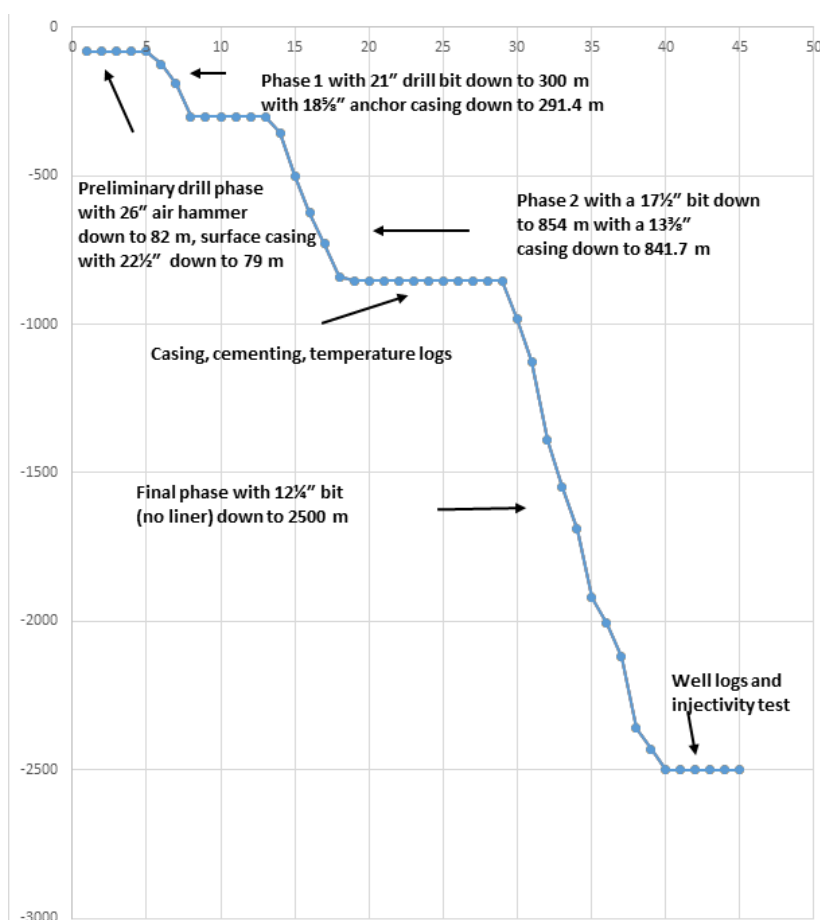


FIGURE 6: Drilling progress of well RN-12
(Jónsson et al., 2003; Richter et al., 2003)

Remark: all the depths mentioned and appearing on all figures in this paper are based on the distance from the rotary table. The rotary table is, in this case, 6.86 m from the top of the cellar.

3. SAMPLING AND ANALYTICAL METHODS

3.1 Analytical representation methods

Sampling and analytical methods

Drill cuttings from well RN-12 were sampled at 2 m intervals during the drilling operations. In this study, drill cuttings from well RN-12 are from 10 m down to 1024 m and were analysed at the ISOR geological laboratories, a total of 494 samples. Usually drill cuttings are analysed at the drill site by the use of a binocular microscope to enable the geologists to understand the sub-surface geological formations and conditions which help in applying the right drilling procedures. Representative samples of different rock units are then selected for further studies based on the formations and/or alteration.

3.2 Analytical methods

Binocular microscope: Drill cuttings from 2 m intervals were used. The samples were washed with clean water to remove impurities. Water was added to the sample box to enhance visibility. The binocular used was an Olympus ZX16. In the binocular microscope different rock formations were analysed, colours of the formations were noted as well as the rock type, grain size, mineralogy, alteration mineralogy and the intensity of the alteration.

Petrographic microscope: Representative samples from selected lithological units were selected and, in this study, 23 thin sections were analysed from 0 to 1240 m depth at: 30, 80, 96, 126, 268, 336, 394, 442, 482, 546, 600, 640, 694, 754, 812, 866, 940, 986, 1030, 1090, 1140, 1210 and 1240 m depth. Thin sections were mounted on a Leica petrographic microscope. The purpose of the petrographic analysis is to confirm the analysis and provide a more detailed study of different formations encountered in the well, study the mineralogical evolution in the well, and the alteration encountered in the well.

X-ray diffraction analysis: Samples were selected from representative lithological units and analysed for clays. Samples from: 24, 38, 68, 92, 104, 148, 158, 248, 280, 320, 356, 400, 456, 490, 542, 660, 672, 702, 782, 866, 924, 970, 998, and 1014 m depths were placed in a test tube, distilled water was added to dissolve the constituents, then the test tube was shaken and left in a rack so that the < 2 microns clay minerals were left in suspension. A few drops were placed on a marked glass slide and left to dry. That way the sample could be analysed using the XRD equipment. Ethylene glycol was added to the air dried sample and then the sample was heated to between 500 and 550°C. The samples were analysed in the XRD equipment after each treatment to identify the different types of clays based on the peak locations and their intensity in the XRD spectra. The results of the clay analyses samples for the well are listed in Appendix I.

Microthermometry and Leica microscope: Fluid inclusions are "bubbles" of fluid trapped within the host mineral during its deposition from its parent hydrothermal fluid. Fluid inclusions can be either primary or secondary. Primary fluid inclusions are trapped in the crystal lattice during growth while secondary fluid inclusions are trapped along healed cracks (Roedder, 1984). Fluid inclusions were identified in the prepared sample by use of a petrographic microscope. Double-polished thin sections (approximately 70 microns) of cuttings from well RN-12, which contained abundant quartz, were prepared for fluid inclusion analysis. The thin sections were mounted on a Linkam THS MG 94 heating stage for analysis. The inclusions were heated slowly until the fluid homogenization temperatures (i.e. the bubble disappears) were obtained. Homogenization temperatures of individual inclusions were measured at least twice and the results were recorded in 5°C intervals.

3.2.1 Use of geophysical logs

Neutron-neutron logs: The main purpose of neutron logs is to capture the quantity of hydrogen scattering and water trapped in the formation, as well as to estimate the formation porosity (Ásmundsson, 2011). Generally, the water content in the formation is a good indicator for porosity or alteration. Neutron logs are consequently used to locate porous formations.

Caliper logs: The main idea for using this tool is to measure the diameter of the well and precisely locate cavities and wash-outs in the well. That will allow predictions for the volume of cement necessary for casing operations. Caliper logs may also be used to locate feed-points or feed zones.

Temperature logs: The main purpose of using the temperature tools is to locate aquifers in a well. The logs also give an idea of the behaviour of the well and the formation temperature. This valuable information will determine and predict any blow-out risks as well of feed zones (Steingrímsson and Gudmundsson, 2005).

Resistivity logs: The contribution of the resistivity matrix and the formation fluid will reflect the rock porosity and hydrothermal alteration. Low alteration is shown as higher resistivity when compared to altered rocks.

Gamma ray logs: This logging tool is sensitive to radioactive isotopes within the rock (K, Th, U). It is used to determine the amount of clay and, therefore, alteration, in the rock formation and also to relate the quantity of SiO₂ in the rock. The logging, therefore, can identify if rocks are of evolved chemical composition (Stefánsson et al., 1982).

4. RESULTS

4.1 Stratigraphy of well RN-12 from surface down to 1024 m

The stratigraphy of well RN-12 consists of two main divisions: hyaloclastite and crystalized basalt. These two main formations are divided into series of rock units that alternate in sequences of hyaloclastites (pillow basalt, breccias and tuff), and crystalline rocks (lava flows, intrusions).

Hyaloclastite: Such formations are hydrated tuffs or breccias, rich in volcanic glass. They are formed during volcanic eruptions under water or ice. Sometimes traces of sideromelane and tachylite, with smaller amounts of minerals are seen. This formation contains some amounts of crystalline and partially crystalline rock fragments and, if unaltered, are characterised as highly porous, promoting circulation for cold water and geothermal fluid. However, when altered, they become less permeable and may form cap rocks (Franzson et al., 2011).

Basalt: This rock formation is a common extrusive igneous volcanic rock that is formed by cooling of magma as basaltic lava. The basalts are usually grey to black in colour, but with oxidation they tend to be brown or rusted. They occur as lava flows or pillow lavas. Generally lavas are formed after an eruption, characterised by the solidification and cooling of the rock. However, pillow lavas are formed during cooling of magma erupted in subglacial or submarine volcanic events.

Intrusives: Intrusive rocks found in this well are characterized by fine- to medium-grained basalt and are mostly unaltered compared to the surrounding rock formations. Most of the intrusive bodies are located at 360 to 396 m; 416 to 452 m; 460 m; 480 to 484 m; 500 to 510 m; 524 to 538 m; 542 to 576 m; 622 to 654 m; 708 to 752 m; 768 to 772 m and 920 to 932 m.

These analyses were carried out using the binocular microscope, with additional information from petrographic analysis in thin sections. Figure 7 shows the simplified lithology of the well along with the geophysical logs.

No cuttings 0-10 m

Basaltic tuff - 10-24 m:

Cuttings at this level are brownish to reddish, fine grained basaltic tuff, with vesicles filled with calcite and partially with clay through the pores. The presence of pyrite and thomsonite was observed in binocular and petrographic microscope.

Basalt - 24-76 m:

This formation can be divided into three layers. The upper part, from 24-40 m, consists of tuffaceous basalt, mostly crystallized, olivine and plagioclase, fine to medium grained, porous and mixed with greenish clay. Some oxidation occurred. Mixed-layer clay and fine to medium grained basalt appear between 40-50 m; this middle section is totally oxidized and crystalline, mostly plagioclase and olivine. The lowest part, from 50-76 m, contains basalt lava comprised mostly of aphyric fine crystalline grains, with a greyish light texture, that are slightly oxidized. Binocular and petrographic analyses show, beside the clay, the occurrence of pyrite, thomsonite, and quartz at 70 m. Also, there is some manifestation of calcite in all samples.

Basaltic tuff - 76-108 m:

This thin layer was trapped between two basaltic lava formations and consisted mostly of fine grained and glassy basalt tuff and clay. The texture is slightly less apparent compared to the formation above, but is commonly reddish with vesicles filled with calcite and pyrite; oxidation is observed. A petrographic microscope analysis shows the presence of anhydrite (90 m), smectite, chalcedony and chabazite.

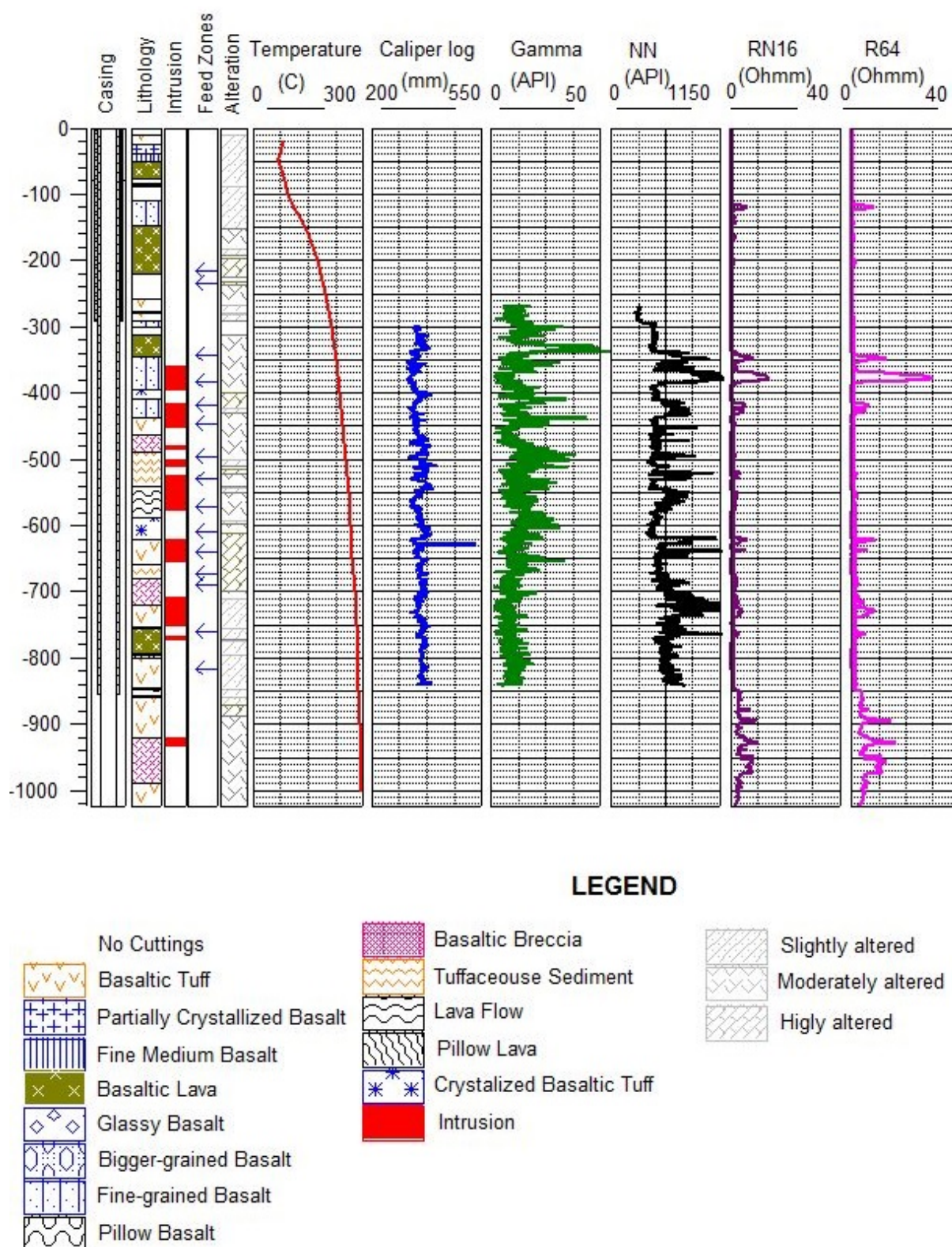


FIGURE 7: Simplified lithology and geophysical logs of well RN-12. Feed zones shown as arrows

Basalt (porphyritic basaltic lava) - 108-148 m:

This section shows two main layers. The top part is mainly of plagioclase porphyritic, sometimes glassy porous basalt, mixed with tuff. Noteworthy is the abundance of oxidation. The presence of clay calcite and pyrite is apparent. The bottom layer has fine grains of basalt lavas that are oxidized, and

calcite fills the pores of the vesicular grain from 110-148 m. Dark clay was also observed. Both petrographic and binocular analysis showed some alteration from glass to clay and also the formation of anhydrite.

Basalt (aphyric basaltic pillow basalt and lava flow) - 148-258 m:

This thick formation is divided into two layers. The upper part is a fine, granular basalt mixture of lava with tuff, and contains plagioclase and olivine crystals of light greyish texture. Pores are filled with clay. This zone has less pyrite and calcite than above and no oxidation. The bottom layer consists mainly of a combination of pillow lava and lava flows and is, fine- to medium-grained, plagioclase and olivine basalt. This zone has more pyrite, and calcite is at times platy; oxidation is abundant in the lower part. The most common alteration minerals are phillipsite, amorphous silica and quartz in the pores and some anhydrite.

Basaltic tuff - 258-346 m:

This section is structured into two layers of basaltic tuff. The upper part is dominated by an amalgam of basalt, clay and tuff. The succession is medium- to coarse-grained and the colour increases from light brown to dark brownish. The formation has abundant fractures and is largely porous and filled by ample calcite, dark clay and sulphites at around 260-290 m. The lower part of the tuff is more altered as the texture changes to dark brown in the bigger grains. There is a significant amount of calcite, sulphite silica and pyrite. The vesicles are totally filled with clay; petrographic analyses of the alteration minerals showed some albitizations of plagioclase, and the pyroxene is starting to alter into clay.

Basalt (porphyritic basaltic) intrusion - 346-396 m:

This formation is underlined by thin mixed sediment and tuff. The main part consists of a fine-grained, compact basalt intrusion mixed with tuff and sediment, changing in colour from greyish to dark. The tuff is partially crystallized. The deposition minerals are calcite, pyrite, and smectite. The lower part consists of a mixture of medium- to coarse-grained dark tuff and a crystalline intrusion. The pores are mostly larger than above and vesicles are filled by clay and calcite at the lower end along with pyrite. The petrographic analysis revealed some clay alteration, and the presence of anhydrite, feldspar, prehnite and quartz.

Basaltic tuff - 396-464 m:

This section is divided into three tuffs intersected by fine basalt. The top part is basaltic tuff, light grey to brownish and coarse-grained, containing some crystalline material. No oxidation is apparent in this part, however, the veins are filled by calcite, clay and prehnite. The middle part is mainly a mixture of tuff and fine-grained basaltic intrusion. The bottom part is partially basalt tuff, and vesicles in this section are filled by mixed-layer clay, calcite, possibly scolecite, anhydrite and quartz.

Porphyritic basaltic breccia - 464-542 m:

In this part of the well we can see the appearance of breccia with a mixture of tuff sediment and this zone is divided into two layers. The upper part is composed of brownish tuff down to 490 m, with some crystalline fragments and the texture is largely coarse-grained and vesicles filled with an abundance of calcite and clay. The lower part is a mixture of breccia and some fine sediment. Their texture is fine- to coarse-grained and largely brownish. The vesicles and fractures are filled with scolecite, quartz, anhydrite, calcite and pyrite. This zone is mixed with basaltic intrusive grains similar to the intrusive above.

Basalt (aphyric basaltic lava flow)-542-588 m:

This formation is mostly a lava flow and breccia, fine- to medium-grained. The grains are all partially glassy and plagioclase crystalline with small vesicles filled with clay, pyrite and calcite. Petrographic analyses revealed some depositions of quartz and clay. In general, there are few occasions where oxidation occurred.

Porphyritic basaltic breccia - 588-760 m:

This section is mainly composed of a mixture of glassy tuff, breccia and crystalline lava, dark to brownish on top. In the middle part, a thin layer of sediment and tuff mixture is found. The pores in this top part are mainly empty. However, the bottom layer that follows consists of a basalt breccia where the colour ranges from brownish to light brown; the breccia is abundantly fractured. The vesicles are filled with clay, pyrite, calcite, chalcopyrite, quartz, and epidote. Several intrusions are seen in this zone, and we observe a rapid increase in hydrothermal alteration with well-formed quartz and the appearance of epidote that followed from 690 m.

Aphyric basaltic pillow basalt - 760-854 m:

This zone is divided into two separate formations. The upper part is an intrusion of fine-grained basalt lava, mixed with tuff and some breccia which are greyish and glassy. The vesicles are filled with calcite, silica, actinolite, chlorite and epidote. From 790 m to the bottom of this zone we observe some pillow basalt mixed with tuff, fine-grained and slightly turning into a darkish colour. This zone ranges from glassy to partially crystalline and the vesicles are filled with mixed-layer clay and calcite. This zone shows slight oxidation.

Basaltic tuff - 854-920 m:

This zone consists of a breccia mixture of pillow basalt, pillow breccia and tuff. It is likely that the basalt fragments in this section are from intrusions. The appearance is light greyish to dark grey in colour with a dispersion of fine- to medium-grained fragments containing few vesicles. No oxidation appears in this zone, but the pores are filled with quartz, pyrite, and epidote. Some mixed-layer clay is apparent from 898-920 m.

Aphyric basaltic breccia - 920-1024 m:

This zone consists of a mixture of breccia and tuff, and is divided into two zones: The upper part is mainly formed of breccia that is light greyish in colour, and partially crystallized to fully crystallized basalt fragments. The most common alteration minerals are actinolite and epidote with fine-grained clay and calcite. The bottom part, from 990 m, contains more tuff, with some medium-to coarse-grained crystalline fragments. The vesicles in this zone are abundant, mostly filled with dark clay; epidote, chlorite and quartz. This zone shows significant alteration down to 1024 m.

4.2 Intrusions

An intrusion can be described as a body of magma that solidifies under Earth's surface. Intrusions usually appear fresh, sometimes with a coarse-grained texture in comparison to the host rock since the concealed subterranean magma cools slowly in concordance to the surrounding rock, giving time for the crystals to grow. However, small intrusions, like dykes, may be fine grained. Intrusive contacts are often associated with permeability as the surrounding host may become fractured as it is intruded into. Therefore, the surrounding boundaries are frequently oxidized as a result of water and heating (Gebrehiwot, 2010). Several intrusions have been identified in well RN-12 at: 360-396 m, 416-452 m, 460 m; 480-484 m; 500-510 m; 524 m- 538 m; 542-576 m; 622-654 m; 708- 752 m; 768-772 m; 920-932 m (Figure 6).

Intrusive unit I (360-396 m):

The section consists of fine- to medium-grained basalt that is greyish to dark in colour. The alteration starts at this level with the deposition of clay, anhydrite and quartz.

Intrusive unit II (416-452 m and 460 m):

This section contains fine- to medium-grained fragments and they are marginally light to dark in colour, plagioclase-phyric with some scolecite deposition.

460 m: This is a small intrusion, formed of basalt, fine- to medium-grained, light brownish and plagioclase porphyritic.

Intrusive unit III (480-484 m):

This thin intrusion is mixed with breccia which is largely brownish fine-medium grained, fractured, and the vesicles are filled by well-formed quartz.

Intrusive unit IV (500-510 m):

This thin layer is also relatively fresh, fine-grained basalt mixed with a breccia mixture and some grains of sediment. The presence of quartz is apparent at this level.

Intrusive unit V (524 m-538 m):

This is 14 m thick medium-grained basalt, with a light brownish colour, partially crystalline with plagioclase phenocrysts.

Intrusive unit VI (542-576 m):

This layer is basalt mixed with breccia, light brown to dark in colour. Veins are filled with quartz and significant oxidation is observed.

Intrusive unit VII (622-654 m):

Crystalline basalt mixed with glassy, brownish tuff comprise this layer. Pores in this range are empty.

Intrusive unit VIII (708-752 m):

This layer is a basalt intrusion, brownish to light brown, fine-medium grained. Epidote appears in the fillings. Some oxidation occurs in this zone.

Intrusive unit IX (768-772 m):

This layer is comprised of fine-medium grained basalt, glassy in places. Some micro-crystals of quartz and epidote are observed.

Intrusive unit X (920-932 m):

This final unit is a relatively fresh, medium-grained plagioclase-phyric basalt.

5. HYDROTHERMAL ALTERATION

When studying hydrothermal mineralogy, the meaning of alteration reflects the rock formations interacting with hot hydrothermal fluids. The science behind hydrothermal alteration interprets the conversion that occurs as a result of changes in the conditions to which the rocks are subject to causing primary minerals to be replaced by secondary minerals. The rocks change their composition either by removing, adding or redistributing their prime elemental components. This transformation can be determined in a chemical way or principally by the natural law of interaction between temperature, pressure and depth. In hydrothermal mineralogy, the alteration of the minerals caused by high temperatures has a predisposition that could define where the primary and secondary minerals will be found in the stratigraphy. This defined disposition also reveals the standard degree of formation of the minerals (Table 1). Temperature plays a key role in mineral alteration. As such, alteration minerals can give important information regarding temperatures to be expected in a well during drilling and is important when deciding casing depths. They are also very important when comparing mineral alteration curves to formation temperatures. A simplified and calibrated scale of hydrothermal alteration minerals is shown in Table 1.

TABLE 1: Index minerals reflected with temperature in high-temperature areas in Iceland (Kristmannsdóttir, 1979, Franzson, 1998)

Minerals	Min. Temperature (°C)	Max. Temperature (°C)
Zeolites	40	120
*Laumontite	120	180
*Wairakite	200	
Smectite		<200
**MLC	200	230
Chlorite	230	>300
Calcite	50-100	280-300
Quartz	180	>300
Prehnite	240	>300
Epidote	230-250	>300
Wollastonite	270	>300
Actinolite	280	>300

Notice: * Appropriate to zeolite, ** Mix Layer Clay

5.1 Distribution of hydrothermal alteration minerals

Hydrothermal alteration minerals form as the result of the alteration of primary minerals. During this evolution many stimuli come into effect like: temperature, permeability, fluid chemistry, rock formation and pressure (Brown, 1978; Kristmannsdóttir, 1979). In the case of well RN-12, the hydrothermal minerals found in the rocks vary from low temperature to high temperature minerals like, pyrite, analcime, calcite, mixed-layer clay, chlorite, prehnite, quartz, epidote and wollastonite. However, they all occur at shallow depths compared to other wells in the area (Figure 8).

The distribution of alteration minerals with depth in well RN-12 is shown in Figure 9, and all the different minerals are described below:

Calcite: This mineral is the most abundant alteration mineral in well RN-12. It is apparent that the deposition of calcite occurred mostly in several distinct zones and at least 8 of them have been clearly identified. These zones are at: 10-40, 90-100, 122-340, 372-398, 406-618, 664-698, 840-888 and 902-946 m. Most of these zones were identified in basalt tuff, breccia, pillow lava and lava flow. However, a lesser amount of calcite deposition was observed in intrusions and at the lower part of the well, between 950 and 1024 m.

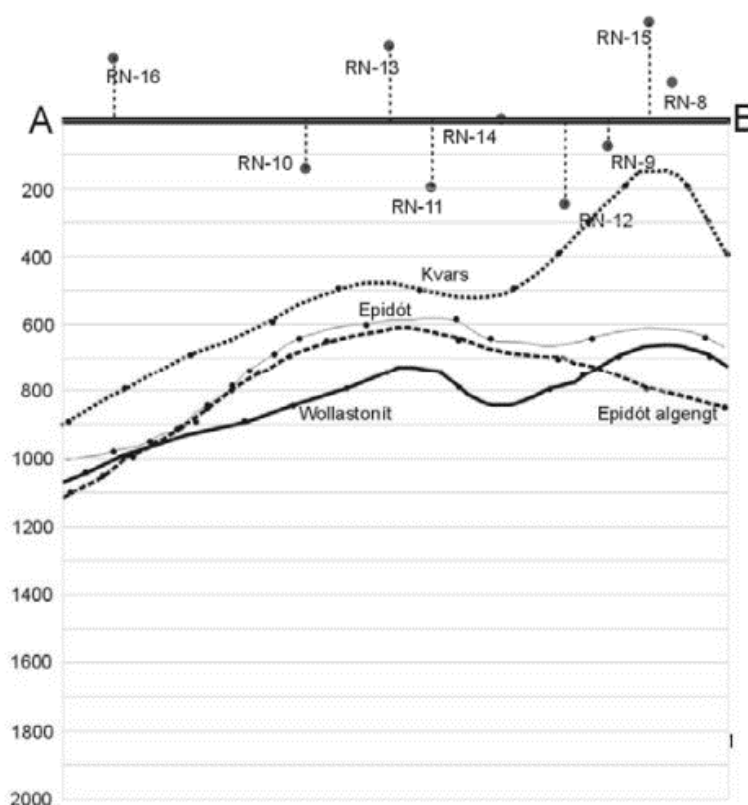


FIGURE 8: Depth to the first appearance of quartz, epidote and wollastonite in the area of well RN-12 (Franzson, 2004)

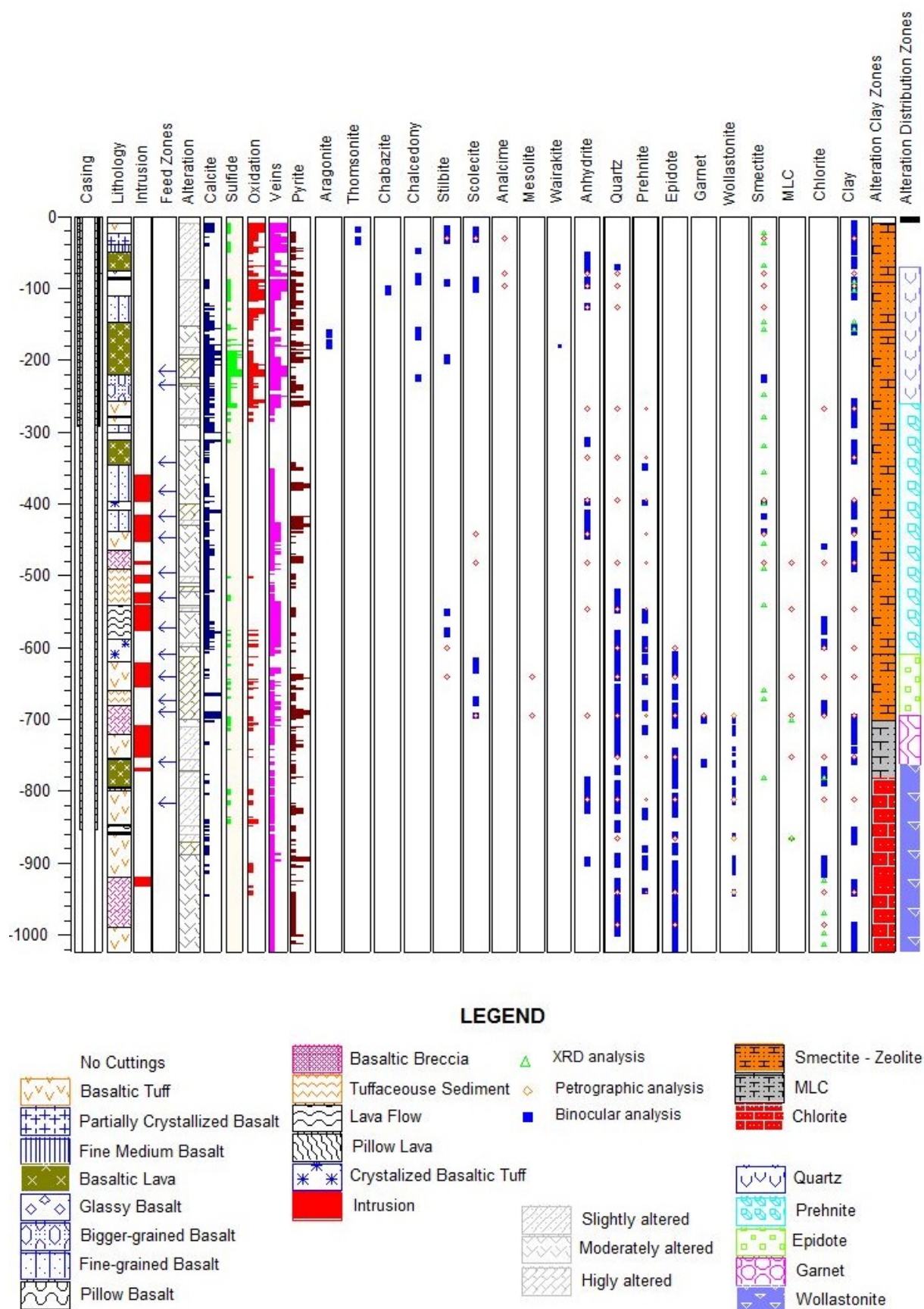


FIGURE 9: Distribution of hydrothermal alteration minerals, location of aquifers and alteration zones of well RN-12

Anhydrite: Due to salinity, this white, sometimes greyish, mineral was found in well RN-12, but seawater has access to the geothermal system (e.g. Tómasson and Kristmannsdóttir, 1972). The deposition of anhydrite commonly occurs as a vein filling and is most abundant at 60-90, 115-126, 310-320, 402-450 and 792-900 m. These depositions are all associated with hyaloclastite formations.

Pyrite: This mineral is common in most Icelandic wells and it is most abundant in eroded, highly altered rocks of extinct central volcanoes, where it forms shiny coatings on the surface of fissures, or clusters of glittering golden granules in the rocks (Saemundsson and Gunnlaugsson, 2014). In well RN-12, pyrite is most common at: 22-120, 128-202, 222-262, 418-446, 474-512, 544-594, 628-642, 658-798, 824-884, 912-924, and 930-1012 m. It appears that pyrite is more abundant in the upper part of the well and appears as bigger grains, then gradually becomes medium to fine crystal cubes until they get bigger again and more abundant from 658 to 900 m, and finally medium in size all the way to 1012 m. As a result, it appears that pyrite reflects permeability in the well as most of the depositions were concurrent with the feed zones.

Prehnite: Prehnite forms small spherical clusters of crystals with vitreous lustre, often pale green in colour, but sometimes white or greyish. When it is broken up, the crystal clusters appear to be radiating. Prehnite occurs mostly with epidote and other high-temperature minerals in basaltic rocks around and above 250°C. For well RN-12, it first appeared at: 260 and 350 m; and then at 550-720, 840, 880-940, 1090, 1190 and 1210 m.

Garnet: This is a group of minerals of varying composition. In Iceland, garnet is mainly andradite (iron-rich), grossular (calcium-rich) and hydro-grossular, the only form that contains water. It has been found in eroded extinct geothermal areas in the roots of central volcanoes, often with epidote (Saemundsson and Gunnlaugsson, 2014). In well RN-12, it was found in fissures close to and in an intrusion zone at 700-762 m. This mineral forms at 300°C and above.

Zeolites: Zeolites, like mesolite, chabazite, thomsonite and analcime, are generally low-temperature alteration minerals and are usually restricted to the upper parts of basaltic formations in hydrothermal system depositions. They are composed of sodium, calcium and aluminium silicates and tend to precipitate in vesicles. As thermometers, zeolites form at relatively low temperatures and are dependent on the composition of the hydrothermal fluids. For well RN-12, the sequence of deposition is at: 14-180, 442-600, and 810-870 m. Different zeolites are described below:

- A. *Mesolite:* Mesolite is white, translucent or greyish, but may be tinted by impurities, usually pink or red. It forms as small-scale fibrous radiating clusters or tuff. It was found between 616 and 694 m.
- B. *Chabazite:* Chabazite appears white or clear, rarely yellowish brown or slightly reddish. They are near-cubic crystals that are twinned, penetrating each other with corners projecting from their crystal faces. In this well they appeared along with chalcedony between 100 and 106 m.
- C. *Thomsonite:* It is a radiating zeolite, where the crystals are elongated, slightly flattened, rather thin fibres with slanted ends. Mostly they form dense masses of radiating clusters, with mammillary structures whose surface is finely bristled (Saemundsson and Gunnlaugsson, 2014). In well RN-12, thomsonite was relatively rare, appearing at 18, 32 and 36 m.
- D. *Analcime:* Analcime mainly forms colourless, or white, many-sided crystals with a vitreous lustre. It occurs either as individual crystals or as clusters which glitter, as in the case of the colourless crystals. This crystal was found in the well between 88 and 96 m.
- E. *Scolecite:* Scolecite is a typical fibrous zeolite, four-sided, often rather densely packed, flattened crystals which form groups or aggregates. It is colourless, or white, with vitreous or slightly silky lustre. In well RN-12, it appeared in the presence of other minerals like mesolite, analcime, thomsonite and chabazite at: 14-32, 36, 88-96, 100-106 and 616-694 m.
- F. *Stilbite:* This mineral appears in many forms but most commonly as thick, tabular crystals with pointed terminations. It is generally milky-white, but clear and translucent variants exist, and also coloured types, usually reddish-brown but sometimes greenish. Stilbite is mostly found in

basalt in the analcime zone and below. It is most abundant in tholeiite, low down in the lava pile. In well RN-12, stilbite was observed in thin sections and cuttings at around: 14-32, 88-96, 198-204 and 550-600 m.

G. Wairakite: This mineral is a calcium-rich variant of analcime (or a closely related mineral), but forms at higher temperatures than other zeolites, or at more than 200°C. It is well known in Iceland, but small in scale, and has mainly been found in boreholes in high-temperature geothermal areas (Saemundsson and Gunnlaugsson, 2014). In well RN-12, it was found at 180 m and 1090 m (Figure 10).

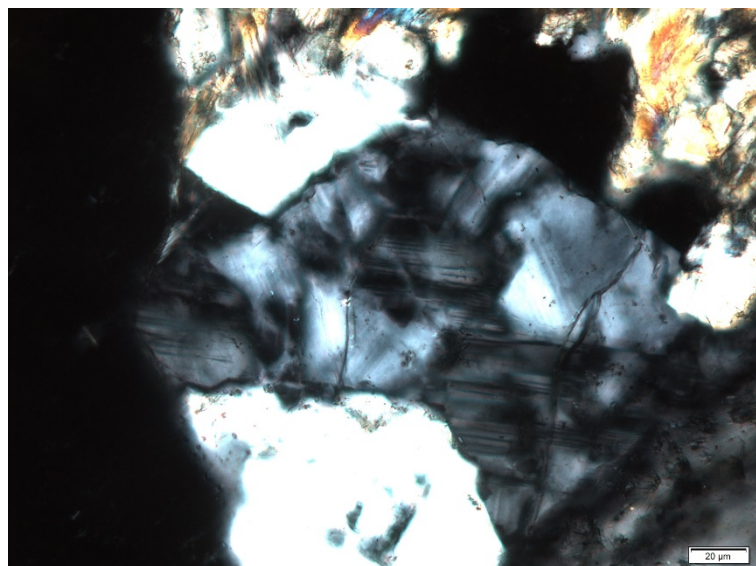


FIGURE 10: Wairakite found at 1090 m in well RN-12

H. Chalcedony: Chalcedony is a silica mineral often regarded as amorphous but, in fact, it forms tiny thread-like crystals which are just distinguishable under a microscope. It is commonly whitish, or greyish, while other colours have been found, such as pale blue, dark-brown to black, yellowish and greenish. It is commonly found as an amygdale in tholeiitic basalt and rhyolite. It was found in well RN-12 in cuttings and thin sections at: 158-162 and 222-226 m

Quartz: This mineral is generally white, milky-white or grey, and translucent or opaque. It forms hexagonal prismatic crystals which end in slanted faces meeting at a point, six-sided pyramid. In evolved igneous rock, it occurs as a primary mineral. In well RN-12, it appeared first at 70 m in an intrusion, and was observed in thin section from 480 m; however, they appeared well formed from 634 to 1024 m in cuttings and down to 1240 m in thin sections.

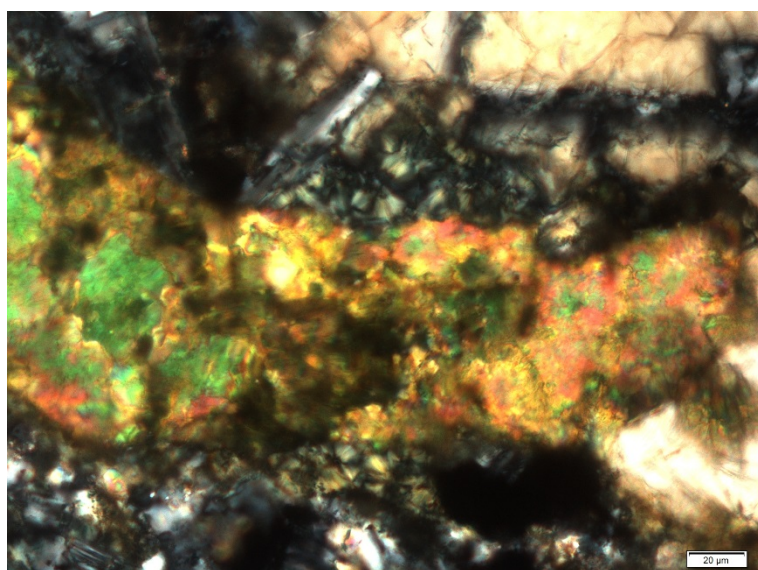


FIGURE 11: Epidote found in vein fillings at 754 m in well RN-12

Epidote: This mineral is generally micro-crystalline, forming a green or yellowish-green coating on the walls of cavities and veins. Its streak is white or slightly grey. Epidote forms in both basaltic and acidic rocks at temperatures around 230°C, and above. In well RN-12, the first appearance of epidote was in cuttings at: 610-638, 654-698, 750-832, 860-936 and 990-1024 m. In thin section, epidote was found fully grown at 754-1240 m (Figure 11).

Wollastonite: This white and fibrous mineral appears at temperatures above 270°C and is stable beyond 300°C. The rock becomes characteristically green, known as propylite. The colour is

mainly due to chlorite and epidote, typical for alteration at 200-300°C. Generally, wollastonite occurs with garnet and epidote in high temperature systems (Saemundsson and Gunnlaugsson, 2014). In Iceland, it is mainly found only in borehole cuttings. In well RN-12, the first appearance of this mineral was at: 698-720, 740-748, 760-764, 782-788, 798-816, 858-864, 892- 896, 900-912 and 938-944 m.

Clay minerals: These minerals are formed by the dissolution of the primary minerals in the basaltic rock formations or as depositions. Several factors govern the degree of alteration such as permeability in concordance with gas, temperature, formation activity, pressure and hydrothermal fluid composition (Marosvölgyi, 2009; Kristmannsdóttir, 1975; Browne, 1978; Reyes, 2000; Franzson, 2006; Franzson, 2008). They are common and abundant in hydrothermal systems. Clays are common alteration products of nearly all rock forming minerals. They are formed in both low and high temperature fields. In general, primary minerals such as plagioclase, pyroxene and olivine are altered into sub-class types of clays:

- A. *Smectite*: This mineral is a low-temperature clay (<200°C), fine-grained, often brownish or greenish, although black varieties occur, with low birefringence. It is found as a coating in altered rocks and distinct crystallisation could be seen under the microscope. Generally, smectite deposition could be found in the upper part of the geothermal field. In well RN-12, this clay was recognized at: 24-126, 148-356, 400-542 and 660-782 m, and under thin section from 30 to 180 m.
- B. *Mixed-layer clays*: This mineral is formed as a derivation from the degradation or aggradation of pre-existing clay minerals; it is a very useful mineral geothermometer (Harvey and Brown, 2000). The mixed-layer clays are, thus, the product of reactions involving clay mineral end members where different kinds of clay layers alternate with each other. In well RN-12, mixed-layer clay was found at: 482, 546, 640, 694, 760-854 and 898-1024 m.
- C. *Chlorite* can be recognized in cuttings by its green, radiating structure. However, it can be difficult to distinguish from smectite except by XRD. It has a greenish to brown colour, and its streak is green with coatings and lumps, often flaky with wavy flakes. It mostly forms at some depth in geothermal areas where temperature has exceeded 200°C (Reyes, 2000). As a result, chlorite is commonly formed with relatively high temperature alteration minerals. In well RN-12, the first appearance of chlorite occurred along with smectite at: 268, 460, 482, 560-580, 590-600, 680-694, 760-790, 893-918 and 940-1014 m.

5.2 Interpretative alteration of primary minerals

The main primary minerals in Icelandic basalt are glass, olivine, plagioclase, pyroxene and opaque minerals, mainly magnetite and ilmenite. Those minerals play a key role when they encounter hot hydrothermal fluids (Gebrehiwot, 2010; Franzson, 1998). In Figure 12, the alteration zones in Iceland are shown along with the alteration of primary minerals with increasing temperature. Table 2 shows the primary minerals in well RN-12 and their alteration products.

Glass: Placed here even though it is homogenous and without any crystal structure. The alteration of glass begins in

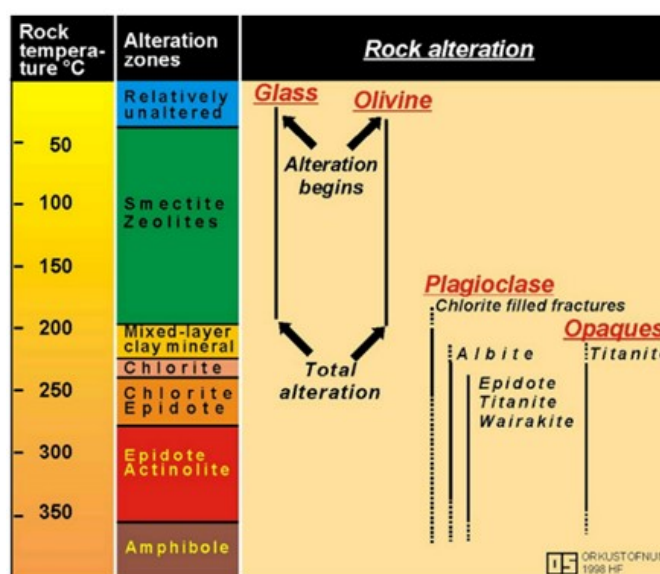


FIGURE 12: Alteration zones in Iceland with temperature and alteration of primary basalt rock (Franzson, 1998)

TABLE 2: Primary alteration minerals in well RN-12

Altered/unaltered	Alteration results
Glass	Clay \Rightarrow calcite \Rightarrow zeolite \Rightarrow quartz
Olivine	Clay \Rightarrow calcite \Rightarrow p. calcite \Rightarrow analcime \Rightarrow quartz
Plagioclase	Clay \Rightarrow calcite \Rightarrow quartz \Rightarrow wairakite \Rightarrow chlorite
Pyroxene	Clay \Rightarrow smectite \Rightarrow calcite \Rightarrow actinolite
Opaque	Clay \Rightarrow limonite \Rightarrow pyrite \Rightarrow mixed-layer clay

the upper part of well RN-12 and is radically turned into brownish clay with reddish oxidation down to 300 m, where it turns into mixed-layer clay and calcite. Later on through the depth it gets replaced by quartz from 336 m.

Olivine: Olivine forms a compositional series of minerals, based on the proportion of magnesium to iron. It forms yellowish-green to dark green small granules and is distinguished by its fracturing with indistinct cleavage (Saemundsson and Gunnlaugsson, 2014). In this well, olivine is fresh on top, then becomes oxidized (24 m) and gradually turns into clay. Through the well, olivine has a tendency to transform into calcite at around 200 m and phillipsite at around 280 m, then into platy-calcite at 268 m. At around 650 m, olivine was altered into analcime, followed by quartz.

Plagioclase: Plagioclase is part of the feldspar family and falls into the subdivision that contains the albite-anorthite compositional series. Textures are seen as flat crystals or columnar and granular, with parallel cleavage. Twinning is common and the colour is normally white or greyish-white, while some types are pale yellow or pink (Saemundsson and Gunnlaugsson, 2014). For well RN-12, the plagioclase starts to be transformed into albite from 120 m depth. At around 324 m to 352 m, we observed a transformation into silica. From 700 m to 912 m, plagioclase is altered into albite, chlorite and epidote.

Pyroxene: Commonly, pyroxene is referred to as a compositional series of minerals. It is black or dark green in colour, and forms prismatic crystals, either transparent or with a vitreous lustre, sometimes its streak is grey or green with uneven fractures. It is one of the principal rock-forming minerals in basalt and gabbro (Saemundsson and Gunnlaugsson, 2014). In well RN-12, it appears to be fresh at the beginning, however, it gets oxidized and, at around 90 m to 390 m, it tends to be glassy followed by clay alteration. After 900 m, it becomes altered into actinolite.

Opaque: In well RN-12, the alteration of opaques began with oxidation but, from 92 m, they tended to alter into clay and mixed-layer clay down to 620 m. At around 800 m, it was fresh, then turned into clay.

5.3 Sequence of alteration minerals

In general, the deposition of alteration minerals in geothermal systems occurs mainly in vesicles and fractures. The alteration mineral assemblages usually change from low-temperature to high-temperature with increasing depth, e.g. from quartz and wairakite to epidote, prehnite, wollastonite and actinolite (Koestono, 2007).

The sequence of alteration minerals in well RN-12 was analysed both with binocular and petrographic microscopes and can be seen in Table 3. The deposition of fine-grained clay was found in both vesicles and veins, sometimes seen as coarse-grained. Calcite is seen both before and after clay deposition and, towards the lower part, it is also seen coming after the high temperature mineral, quartz. Otherwise, the overall sequence shows that alteration minerals indicating higher temperature follow minerals indicating lower temperatures.

TABLE 3: Mineral deposition sequence of well RN-12

Depth (m)	Deposition sequence	Degree of alteration
30	Calcite \Rightarrow zeolite	Small
80	Clay \Rightarrow quartz	Moderate
96	Calcite \Rightarrow smectite	High
268	Clay \Rightarrow calcite	High
336	Prehnite \Rightarrow anhydrite	No alteration
394	Calcite \Rightarrow prehnite	Small
442	Zeolite \Rightarrow calcite	High
480	Clay \Rightarrow quartz	Moderate
482	Zeolite \Rightarrow quartz	High
546	Clay \Rightarrow quartz	High
600	Clay \Rightarrow quartz	High
640	Clay \Rightarrow quartz	High
694	Quartz \Rightarrow prehnite	Small
754	Quartz \Rightarrow epidote	High
812	Epidote \Rightarrow wollastonite	Moderate
866	Clay \Rightarrow quartz \Rightarrow wollastonite	Moderate
940	Quartz \Rightarrow epidote	High
986	Clay \Rightarrow quartz \Rightarrow epidote	Moderate
1030	Quartz \Rightarrow epidote	High
1090	Quartz \Rightarrow epidote \Rightarrow wairakite	High
1140	Clay \Rightarrow quartz \Rightarrow calcite	Moderate
1210	Clay \Rightarrow epidote \Rightarrow wollastonite	High
1240	Clay \Rightarrow epidote	High

5.4 Alteration zones

Geothermal systems are usually defined as either high or low temperature fields according to temperature at 1 km depth. Fields with temperature $<150^{\circ}\text{C}$ at 1 km depth are classified as low temperature while fields with temperature $>200^{\circ}\text{C}$ at 1 km depth are high temperature. This gives an idea of the alteration mineralogy at different depths within the systems (Kristmannsdóttir and Tómasson, 1978) although careful analysing is always necessary since variations in temperature are common. It must be noted that it is possible that alteration minerals in certain areas represent fossil conditions, therefore giving past formation temperatures. In Iceland, the alteration zones have been studied and, in general, agreed upon. It has been recognized that zeolites form below 100°C , quartz above 180°C , mixed-layer clays above 200°C , chlorite above 230°C , prehnite above 240°C , epidote above $230\text{--}250^{\circ}\text{C}$ and actinolite above 280°C (Kristmannsdóttir, 1979; Franzson, 1998; Saemundsson and Gunnlaugsson, 2014).

The alteration zones are based on petrographic, binocular and XRD analyses, and are mainly focused on clays to determine the alteration zones. In well RN-12, it was decided to divide the alteration zones into two parts (since some of the alteration minerals were in contradiction to the dominating clay in specific areas), giving clay alteration zones on one hand and alteration mineral distribution zones on the other because the alteration minerals (other than clays) show much higher temperatures in the well than the clays. It is possible that, due to the geothermal system in Reykjanes, the unconsolidated clay mineral deposition dominates the alteration, given the same results as well RN-17 (Hardardóttir, 2011, Marks et al., 2010). The clay alteration zones are:

Smectite-zeolite zone (10-702 m): This zone is characterized by an abundance of zeolites showing the low temperature of the upper part of the well. The presence of prehnite at 260 m may, however, indicate temperature > 240°C.

Mixed-layer clay zone (702-782 m): This thin zone was identified by XRD analysis and shows mixed-layer clay at this depth.

Chlorite zone (782-1024 m): A zone of chlorite mixed with minor epidote is seen at this depth. That demonstrates temperatures between 230-250°C (Brown, 1978; Franzson, 1987). At the same depth, alteration minerals such as wollastonite are seen, indicating higher temperatures.

Alteration mineral distribution zones are:

Quartz zone (70-260 m): Quartz appears at around 70 m (indicating >180°C) and is seen in thin sections down to around 150 m but then disappears until at 280 m. Zeolites still prevail at this depth and quartz may be showing locally raised temperatures.

Prehnite zone (260-610 m): The presence of prehnite it is noted at about 260 m and becomes abundant at around 600 m, indicating temperature higher than 240°C. The abundance of prehnite at around 600 m coincides with the first appearance of epidote.

Epidote zone (610-694 m): This zone is characterized with the disappearance of zeolites and the appearance of epidote in both fine crystals and as full grown. Epidote is abundant in this part of the well, indicating temperatures around 250°C.

Garnet (694-762 m) and wollastonite zone (762-1024): Garnet appeared in an intrusive zone, indicating localised raised temperatures caused by the intrusions, and is not seen below 762 m. Wollastonite was first seen at 698 m. These minerals indicate temperatures higher than 270-280°C.

To recap the interpretation of the history of alteration in this well, one must consider the alteration mineral assemblages in relation to their relative time of deposition (Table 3). The deposition of alteration minerals is quite complex in this well as there are contradictions between the clays and other alteration minerals. Some minerals may be close to the current formation temperature but some may be recording fossil circumstances.

When the results in Table 3 are compared with the alteration zones, the following depositional sequence may be plausible:

Calcite \Rightarrow Smectite \Rightarrow Quartz \Rightarrow Prehnite \Rightarrow Epidote \Rightarrow Wollastonite.

6. FLUID INCLUSIONS

Fluid inclusions are tiny bubbles, known as microscopic vacuoles, which are found in minerals such as quartz and calcite, trapped inside these crystals during crystallisation (primary inclusion) or recrystallization (secondary inclusion). Secondary inclusions are confined, or trapped, along restored cracks in the secondary crystals and provide crucial information about the history and condition of the geothermal system in terms of determining the thermal condition and history of the system, in particular, records of compositional and temperature conditions from the time the inclusions were formed (Roedder, 1984).

6.1 Interpretation of fluid inclusions analysis

Two quartz crystals were collected at different depth intervals, at 690 m and 844 m, from well RN-12; it was not necessary to polish the crystals as they were well formed and clear. In those two quartz crystals, nine fluid inclusions were studied at different temperature sequences (Figure 13 and Table 4). According to the results and the homogenization temperatures from those two depths, the fluid inclusions showed two high temperature groups. The first quartz crystal, from 690 m, had 5 inclusions and was showing temperatures varying between 265 and 280°C. The second quartz crystal, from 844 m, had 4 inclusions with temperatures varying between 270 and 295°C (Table 4). It is noted that the fluid inclusions from both quartz crystals enumerated the normal condition of the well as they were respectively concurrent with the temperature profile shown when the quartz fracture veins healed after crystallization. The precise implication of those fluid inclusions with the temperature in relation to the formation and alteration temperature is discussed in the next chapter.

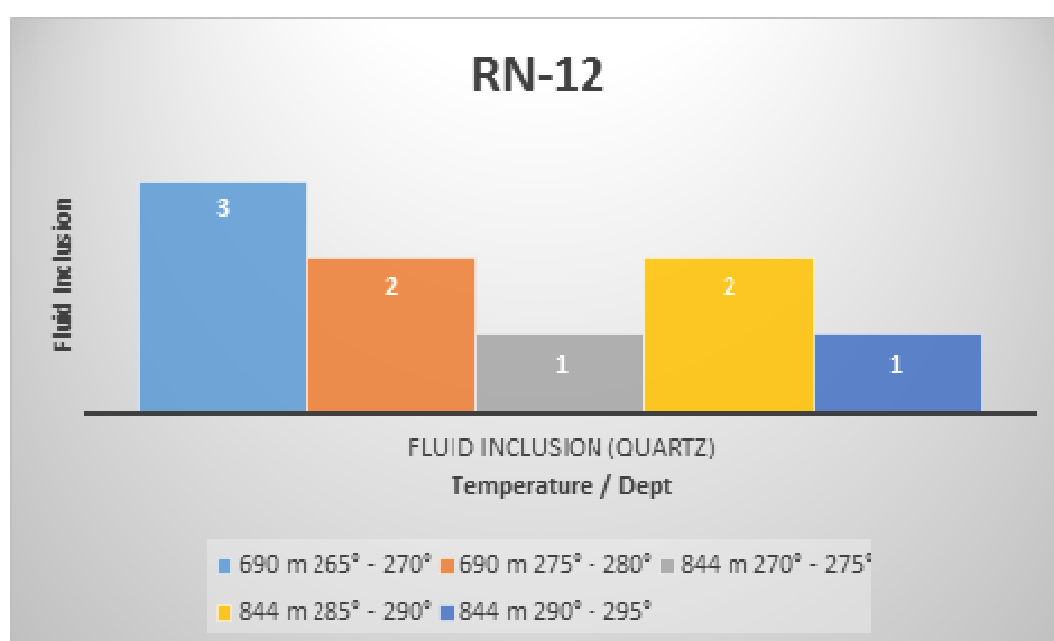


FIGURE 13: Fluid inclusions in quartz crystals at 690-844 m, well RN-12

TABLE 4: Fluid inclusion homogenization temperatures in well RN-12

Depth	Homogenization temp. (Th) ranges (°C)	No of fluid inclusions	Type of crystals
690	265 - 270	3	Quartz
	275 - 280	2	Quartz
844	270 -275	1	Quartz
	285 - 290	2	Quartz
	290 - 295	1	Quartz

6.2 Temperature and alteration temperature profile of well RN-12

The temperature profile of the well, taken after it had recovered after well completion, shows the formation temperature around the well (Figure 14). From the drill cutting analysis, the alteration temperature can be extracted, as seen in Figure 14. There is consistency between the formation and alteration temperatures, indicating equilibrium in the geothermal system, i.e. it is neither cooling nor

heating up; it is mainly in equilibrium. The homogenization temperatures, derived from the fluid inclusions, further support this conclusion, as they plot in line with both the formation and alteration temperatures (Figure 14).

7. AQUIFERS

Aquifers are typically in underground water-saturated permeable rocks. A geothermal aquifer is a permeable underground formation, or unconsolidated material, such as gravel or sand, which can carry hot fluids, and/or gases, which are subsequently mined, or extracted, for geothermal utilization.

In the case of Reykjanes, which is dominated by basalt and hyaloclastite, the fluid circulation is promoted in both cold groundwater and geothermal fluid but, with an increase in alteration, permeability tends to decrease (Franzson et al., 2011). However, frequently faults and fractures enable the fluids to pass through in higher permeability. The same applies to intrusive contacts, as the host rock is often fractured due to the intrusion. Permeability also occurs at lithological boundaries. Geophysical logs are often used to locate aquifers, in particular temperature logs. Drilling parameters, such as penetration rates and pumping pressure, may also be indicative of feed-zones. Circulation losses can also point to aquifers. A sudden abundance of alteration minerals in drill cuttings may show that an aquifer has been penetrated.

7.1 Study of aquifers in well RN-12

The upper part of the well RN-12 was drilled with mud for safety measures. Even though there were several feed zones identified and blocked by the casing off down to 841 m, it was difficult to identify the feed zones from the circulation losses, as the boundary between the circulation losses and the aquifers was masked by the amount of mud used for drilling. However, several aquifers were identified using temperature logs, circulation losses and abundant mineralization in the cuttings, such as quartz, epidote, pyrite and anhydrite. The aquifers of this well are described below and are shown in Figure 15.

Aquifers 1 and 2: These aquifers are located at the lower part of the anchor casing, at 215 and 235 m, respectively. They were indicated by loss of circulation in the basaltic lava formation.

Aquifers 3 and 4: Were located at 342 and 382 m, respectively. Aquifer 3 is in a basaltic lava formation while the other is in fine-grained basalt. However, both were related to intrusions that were

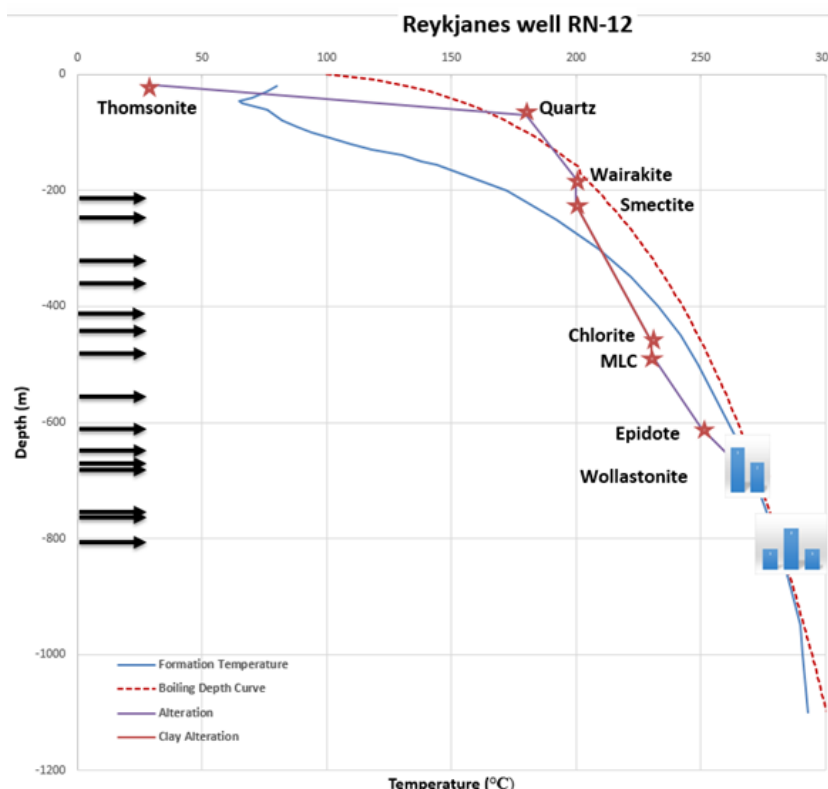


FIGURE 14: Well RN-12, formation temperature (blue line), alteration distribution (purple line, and clay zone (brown line), boiling curve (red broken line) temperature with fluid inclusion temperatures as columns

identified by temperature logs, in the cuttings and by high peaks in the resistivity log, a low peak in neutron- neutron and a higher peak on gamma.

Aquifers 5, 6 and 7: The first two were located in crystalized tuff at 418 and 447 m, respectively, while the last one is located in tuffaceous sediment at 496 m. The first two were identified by temperature logs and by higher resistivity, neutron-neutron and low caliper and gamma, but both are in an intrusion zone that is moderately altered. The last one was identified by low resistivity and higher peaks in gamma, neutron-neutron.

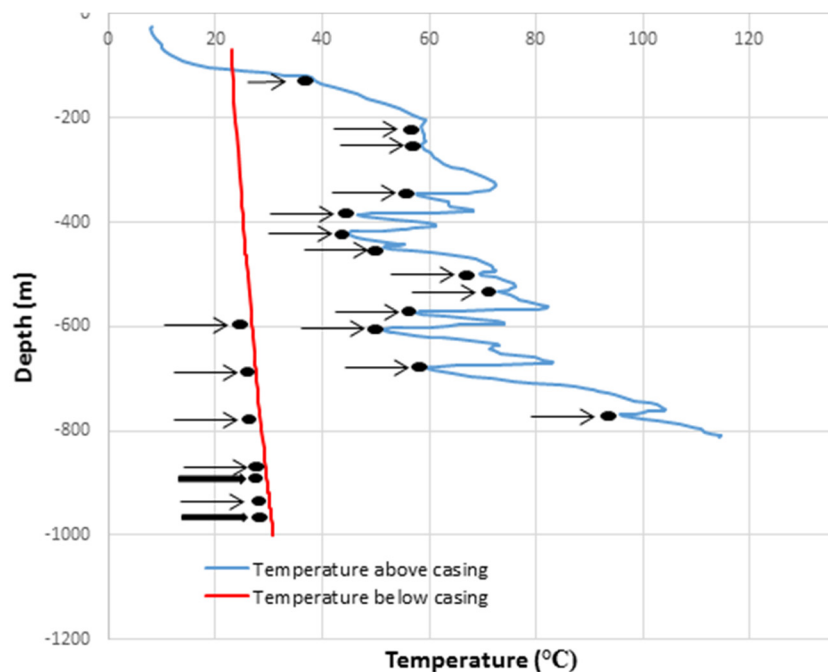


FIGURE 15: Small aquifers identified from temperature log in upper part and below production casing in well RN-12

Aquifers 8 and 9: They are located at 530 and 572 m, respectively. They are in tuffaceous sediment and a lava flow, respectively. Both were apparent from temperature logs and showed signs of high peaks in gamma and neutron-neutron, but low in resistivity; however, they were both in an intrusion zone.

Aquifers 10, 11, 12 and 13: They are located at 610, 640, and 673 and 690 m, respectively. All of them are located in basaltic breccia, basaltic tuff and tuffaceous sediment. They can be seen on temperature logs and have low peaks in neutron-neutron, low in resistivity and in gamma.

Aquifers 14, 15 and 16: They appeared at 760, 770 and 816 m, respectively. The first two are found in basaltic lavas and the third in basaltic tuff. They were apparent in temperature logs and the first two showed higher peaks in all the geophysical logs except in the caliper log, while the last one showed a higher peak in gamma and neutron-neutron and a lower peak in resistivity and the caliper.

All of the above aquifers were cased off.

Aquifers 17 and 18: Located at 900 and 968 m, respectively. The first one is in basaltic tuff and the second one is in basaltic breccia. They were both identified by temperature logs and high peak resistivity.

8. DISCUSSION

The main formations observed in well RN-12 were hyaloclastites such as basaltic tuff, breccia and pillow basalt, underlain by partially crystallized basalt and tuffaceous sediment. Crystalline formations include basaltic lavas and intrusions.

The deposition of hydrothermal minerals occurred in veins and vesicles and appears early in the well and is in abundance in the lower part of the section analysed for this well. They replaced gradually the primary minerals with increasing depth. It is noteworthy that most of the alteration minerals appeared at shallower depths than that observed in nearby wells like RN-11, RN-13 and RN-14. It appears that the hydrothermal alteration increased progressively from 200 m down to the bottom. The maximum increase was between 600-700 m, where the last of low temperature alteration minerals disappeared and high temperature minerals kicked in (Figure 9). Two classes of alteration zones were identified, one based on the clay analysis, the other on the alteration mineral distribution. The first one consists of a smectite-zeolite zone, a mixed-layer clay zone, and finally a chlorite zone. The second includes a quartz zone, a prehnite zone, an epidote zone, a garnet zone, and finally a wollastonite zone (Figure 9).

It seems as if the geothermal system on the Reykjanes Peninsula is in equilibrium in the immediate area around well RN-12. This can be deduced from, for example, Figure 14 which shows that alteration- homogenization and formation temperatures plot more or less together.

Most of the aquifers encountered in this section of the well are generally shallow and above the bottom of the production casing, which means that they were all cased off. Only two of them are below the production casing, at 900 and 968 m. It seems as though the aquifers correlate with intrusions and lithology. The feed-zones were identified by temperature logs, loss of circulation and geophysical logs, and an increased abundance of alteration minerals was observed in those zones.

9. CONCLUSIONS

The following conclusions can be deduced:

- The stratigraphy of well RN-12 is mainly comprised of hyaloclastite (basaltic tuff, basaltic breccia, and pillow basalt) in addition to basaltic lavas and intrusions;
- Alteration minerals show that most the high temperature minerals appear at relatively shallow levels with a rapid appearance of the minerals starting with quartz followed by prehnite, epidote and wollastonite at around 800 m. The alteration is shallower than that seen in nearby wells;
- Two types of alteration zones were identified, one based on the clay minerals and the other on the alteration mineral assemblages. The first one includes: a smectite-zeolite zone (10 - 702 m), a mixed-layer clay zone (702 – 782 m) and finally a chlorite zone (782 – 1024 m);
- The second type, based on the alteration minerals, includes: a quartz zone (70 – 260 m), a prehnite zone from 260 to 610 m, an epidote zone from 610 to 694 m, a garnet zone from 694 to 762 m and a wollastonite zone from 762 to 1024 m;
- Most of the aquifers encountered in this well were in the upper part of the well, above the lower limit of the production casing. Two feed zones were observed at around 900 and 968 m. Generally, most of the aquifers were related to intrusions, but some with fractures and lithological boundaries. Beyond that, major feed zones were inferred at depths of 1000, 1300 and 2200 m (Jónsson et al., 2003);
- Fluid inclusions show temperatures reaching 300°C. This correlates with the formation temperature and alteration temperature. This indicates that the geothermal system around well RN-12 is in equilibrium, showing no signs of cooling or heating up.

ACKNOWLEDGEMENTS

It has been and always will be a great honour and privilege to undergo this training. First I would like to sincerely acknowledge my gratitude to UNU-GTP Director, Mr. Lúdvík S Georgsson, and his deputy Mr. Ingimar G. Haraldsson, for giving me the opportunity to be part of the 6 month geothermal training programme in Iceland. I am pleased and thankful to the United Nation University Geothermal Training Programme Staff, Mr. Markús A.G. Wilde, Ms. Málfríður Ómarsdóttir, Ms. Thórhildur Ísberg, and Ms. Maria S. Gudjónsdóttir for making our lives easier and providing all necessary requirements to achieve my project. I also give warm thanks to all the lecturers from ISOR, Orkustofnun and others from overseas to give me the opportunity to comprehend all the presentations given by them, as well for HS Orka for allowing access to and use of data from well RN-12.

Great thanks go to Dr. Guðmundur Ómar Fridleifsson, Dr. Hjalti Franzson and Dr. Björn S. Harðarson for their guidance and preparation throughout the entire 6 month training. High thanks go to my supervisor, Mr. Steinhór Níelsson, for his expertise and guidance throughout my report, and my indebted gratitude goes to Ms. Helga M. Helgadóttir for her efforts in helping us acquire this new knowledge.

My notable appreciation and thanks go to Mr. Abdourahman Omar Haga, Director of Natural Resources at the Ministry of Energy and Natural Resources, for allowing me to attend this training.

My special gratitude goes to my close relatives, especially my mom, for giving me the effort to follow my dream of study.

Finally, I would like to thank all the 2014 fellows for their shared experience and for making the study program much more relevant and easier to attend during the 6 month training.

REFERENCES

- Árnason, K., Haraldsson, G.I., Johnsen, G.V., Thorbergsson, G., Hersir, G.P., Saemundsson, K., Georgsson, L.S., and Snorrason, S.P., 1986: *Nesjavellir, geological and geophysical exploration in 1985*. Orkustofnun, Reykjavík, report OS-86014/JHD-02 (in Icelandic), 125 pp.
- Ásmundsson, R.K., 2011: *Borehole investigations in geothermal systems*. UNU-GTP, Iceland, unpublished lecture notes.
- Browne, P.R.L., 1978: Hydrothermal alteration in active geothermal fields. *Annual Reviews of Earth and Planetary Science*, 6, 229-250.
- Einarsson, P., 2008: Plate boundaries, rifts and transforms in Iceland. *Jökull*, 58, 35-58.
- Einarsson, S., Jóhannesson, H., and Sveinbjörnsdóttir, Á.E., 1991: Krýsuvík Fires II. Kapelluhraun lava and the riddle of the age of Hellnahraun lava (in Icelandic, with English summary). *Jökull*, 41, 61-80.
- Eyjólfsson, V., 1998: *Mapping of fractures and Holocene volcanic vents in Fagradalsfjall, western Reykjanes Peninsula*. University of Iceland, Reykjavík, BSc thesis (in Icelandic), 70 pp.
- Franzson, H., 1987: The Eldvörp high temperature area, SW-Iceland: Geothermal geology of first exploration well. *Proceedings of the 9th NZ Geothermal Workshop, Auckland, NZ*, 179-185.
- Franzson, H., 1998: Reservoir geology of the Nesjavellir high-temperature field in SW-Iceland. *Proceedings of the 19th Annual PNOC-EDC Geothermal Conference, Manila*, 13-20.
- Franzson, H., 2004: *Reykjanes high-temperature field. Conceptual geological model*. ÍSOR –Iceland GeoSurvey, report ISOR-2004/01 (in Icelandic), 68 pp.

Franzson, H., 2008: Chemical transport in geothermal systems in Iceland, evidence from hydrothermal alteration. *J. Volc. Geoth. Res.*, 173, 217-229.

Franzson, H., Gudfinnsson, G.H., Frolova, J., Helgadóttir, H.M., Pauly, B., Mortensen, A.K., Jakobsson, S.P., 2011: *Icelandic hyaloclastite tuffs, petrophysical properties, alteration and geochemical mobility*. ÍSOR – Iceland GeoSurvey, Reykjavík, report ÍSOR 2011/064, 105 pp.

Franzson, H., Thordarson, S., Björnsson, G., Gudlaugsson, S.Th., Richter, B., Fridleifsson, G.Ó., and Thórhallsson, S., 2002: Reykjanes high temperature field, SW-Iceland, geology and hydrothermal alteration of well RN-10. *Proceedings of the 27th Workshop on Geothermal Reservoir Engineering, Stanford University, Stanford, Ca*, 233-240.

Fridleifsson, G.Ó., Albertsson, A., Elders, W.A., Sigurdsson, Ó., Karlsdóttir, R., and Pálsson, B., 2011: The Iceland Deep Drilling Project (IDDP): Planning for the second deep well at Reykjanes. *Geothermal Resources Council, Transactions*, 35, 347-354.

Fridleifsson, G.Ó., Ármannsson, H., Árnason, K., Bjarnason, I. Th., and Gislason, G., 2003. “Part I: Geosciences and Site Selection”. In: Fridleifsson, G.Ó. (ed.), *Iceland Deep Drilling Project, feasibility report*. Orkustofnun, Reykjavík, report, OS-2003-007, 104 pp.

Gebrehiwot Mesfin, K., 2010: *Subsurface geology, hydrothermal alteration and geothermal model of northern Skardsmýrarfjall, Hellisheidi geothermal field*. University of Iceland, MSc thesis, UNU-GTP, report 5, 65 pp.

Hardardóttir, V., 2011: *Metal-rich scales in the Reykjanes geothermal system, SW Iceland: Sulfide minerals in a seawater-dominated hydrothermal environment*. University of Ottawa, Department of Earth Sciences, PhD thesis, 311 pp.

Hardarson B.S., Fitton J.G., Ellam R.M and Pringle M.S., 1997. Rift relocation-A geochemical and geochronological investigation of a palaeo-rift in northwest Iceland, *Earth Planet.Sci.Lett.*, 153, 181-196.

Harvey, C., and Browne, P., 2000: Mixed-layer clays in geothermal systems and their effectiveness as mineral geothermometers. *Proceedings of the World Geothermal Congress 2000, Kyushu-Tohoku, Japan*, 1201-1205.

Höskuldsson, Á, Hey, R., Kjartansson, E., and Gudmundsson, G.B., 2006: The Reykjanes Ridge between 63°10'N and Iceland. *J. Geodynamics*, 43, 73-86.

Hreinsdóttir, S., Einarsson, P., and Sigmundsson, F., 2001: Crustal deformation at the oblique spreading Reykjanes Peninsula, SW-Iceland: GPS measurements from 1993 to 1998. *J. Geophys. Res.*, 106, 13,803-13,816.

Jakobsson, S.P., Jónsson, J., and Shido, F., 1978: Petrology of the western Reykjanes Peninsula, Iceland. *J. Petrology*, 19-4, 669-705.

Jóhannesson H., and Saemundsson, K., 1999: *Geological map 1:1.000.000*. Icelandic Institute of Natural History.

Jónsson, S.S., Kristjánsson, B.R., Gudmundsson, Á., Björnsson, G., Gunnarsson, G., Danielsson, P.E., and Thórhallsson, S., 2003: *Reykjanes – well RN-12. 3rd Phase, drilling of production part from 854 down to 2506 m depth*. Orkustofnun, Reykjavík, report OS-2003/010 (in Icelandic), 60 pp.

Karlsdóttir, R., 2005. *TEM-survey at Reykjanes 2004*. ÍSOR – Iceland GeoSurvey, Reykjavík, report ÍSOR-2005/002 (in Icelandic), 23 pp.

Koestono, H., 2007: Borehole geology and hydrothermal alteration of well HE-24, Hellisheidi geothermal field SW-Iceland. Report 10 in: *Geothermal training in Iceland 2007*. UNU-GTP, Iceland, 199-224.

Kristmannsdóttir, H., 1975: Hydrothermal alteration of basaltic rocks in Icelandic geothermal areas. *Proceedings of the 2nd U.N. Symposium on the Development and Use of Geothermal Resources, San Francisco*, 441-445.

Kristmannsdóttir, H., 1979: Alteration of basaltic rocks by hydrothermal activity at 100-300°C. In: Mortland, M.M., and Farmer, V.C. (editors), *International Clay Conference 1978*. Elsevier Scientific Publishing Co., Amsterdam, 359-367.

Kristmannsdóttir, H., and Tómasson, J., 1978: Zeolite zones in geothermal areas in Iceland. In: Sand, L.B., and Mumpton (editors), *Natural zeolites, occurrence, properties, use*. Pergamon Press Ltd., Oxford, 277-284.

Líndal, B., and Lúdvíksson, V., 1969: *A feasibility study of 250,000 ton salt plant at Reykjanes*. Report to the National Research Council (in Icelandic), Reykjavík.

Marks, N., Schiffman, P., Zierenberg, R., Elders, W.A., Fridleifsson, G.Ó., and Franzson H., 2010: Isotopic evidence of hydrothermal exchange and seawater ingress from anhydrite in the Reykjanes geothermal system: results from IDDP well RN-17. *Proceedings of the World Geothermal Congress 2010, Bali, Indonesia*, 4 pp.

Marosvölgyi, K., 2009: *Retrograde alteration of basaltic rocks in the Theistareykir high-temperature geothermal field, North-Iceland*. University of Iceland, Reykjavík, MSc thesis, 65 pp.

Mawejje, P., 2007: Geothermal exploration and geological mapping at Seltún in Krýsuvík geothermal field. Report 12 in: *Geothermal training in Iceland 2007*. UNU-GTP, Iceland, 257-276.

Reyes, A.G., 2000: *Petrology and mineral alteration in hydrothermal systems: from diagenesis to volcanic catastrophes*. UNU-GTP, Iceland, 1998, report 18, 77 pp.

Richter, B., Franzson, H., Kristjánsson, B.R., Jónsson, S.S., Gudmundsson, Á., Gunnarsson, G., Sigurdsson, Ó., Skarphéðinsson, K., 2003: *Reykjanes – well RN-12. 1st Phase, drilling for 18” surface casing from 119 to 300 m depth. 2nd phase, drilling for 13” production casing from 300 to 854 m*. Orkustofnun, Reykjavík, report OS-2003-008 (in Icelandic), 50 pp.

Roedder, E., 1984: *Fluid inclusions*. Mineralogical Society of America, Washington, DC, Reviews in Mineralogy, 12, 646 pp.

Saemundsson, K., 1979: Outline of the geology of Iceland. *Jökull*, 29, 7-28.

Saemundsson, K. and Einarsson, S., 1980: *Geological map of Iceland, sheet 3, SW-Iceland* (2nd ed.). Museum of Natural History and the Iceland Geodetic Survey, Reykjavík.

Saemundsson, K., and Gunnlaugsson, E., 2014: *Icelandic rocks and minerals*. 2nd edition, Published in Reykjavík, Forlagid ehf., Iceland, 232 pp.

Sigurdsson, F., 1985: *Groundwater and hydrogeology of the outer Reykjanes Peninsula*. Orkustofnun, Reykjavík, report OS-85075/VOD-06 (in Icelandic), 194 pp.

Stefánsson, V., Gudmundsson, Á., and Emmerman, R., 1982: Gamma ray activity in Icelandic rocks. *The Log Analyst*, XXIII-6, 11-16.

Steingrímsson, B., and Gudmundsson, Á., 2005: Geothermal borehole investigations during and after drilling. Presented at “*Workshop for Decision Makers on Geothermal Projects and Management*,” organized by UNU-GTP and KenGen, Naivasha, Kenya, 10 pp.

Tómasson, J., and Kristmannsdóttir, H., 1972: High-temperature alteration minerals and thermal brines, Reykjanes, Iceland. *Contr. Mineral. and Petrol.* 36, 123-134.

APPENDIX I: XRD clay analysis results from well RN-12

TABLE 1: Fluid inclusion homogenization temperatures in well RN-12

Sample no.	Depth (m)	D(001) untreated sample	D(001) glycolated sample	D(001) heated sample	D(002)	Minerals
1	24	15.18	0	10.39	0	Smectite
2	38	14.68	0	10.39	0	Smectite
3	68	0	14.24	10.39	0	Smectite
4	92	15.36	0	0	0	Smectite
5	104	13.85	14.45	10.15	7.77	Smectite
6	148	12.81	13.05	10.03	15.07	Smectite
7	158	15.25	13.39	10.03	0	Smectite
8	248	14.97	13.20	10.20	0	Smectite
9	280	15.59	15.09	10.20	0	Smectite
10	320	13.17	13.71	9.99	0	Smectite
11	356	13.71	13.16	9.99	7.24	Smectite
12	400	15.31	17.17	10.05	0	Smectite
13	456	15.65	17.47	10.05	0	Smectite
14	490	15.65	13.56	10.05	0	Smectite
15	542	15.65	0	10.05	0	Smectite
16	660	15.65	13.26	10.05	0	Smectite
17	672	15.38	14.15	10.05	0	Smectite
18	702	30.75	14.47	11.85	0	MLC
19	782	0	14.06	10.21	7.22	Smectite
20	866	15.00	31.50	11.68	7.33	MLC
21	924	0	14.70	0	7.23	Chlorite
22	970	15.09	0	0	0	Chlorite
23	998	14.77	7.74	7.22	0	Chlorite
24	1014	14.84	0	7.78	7.22	Chlorite

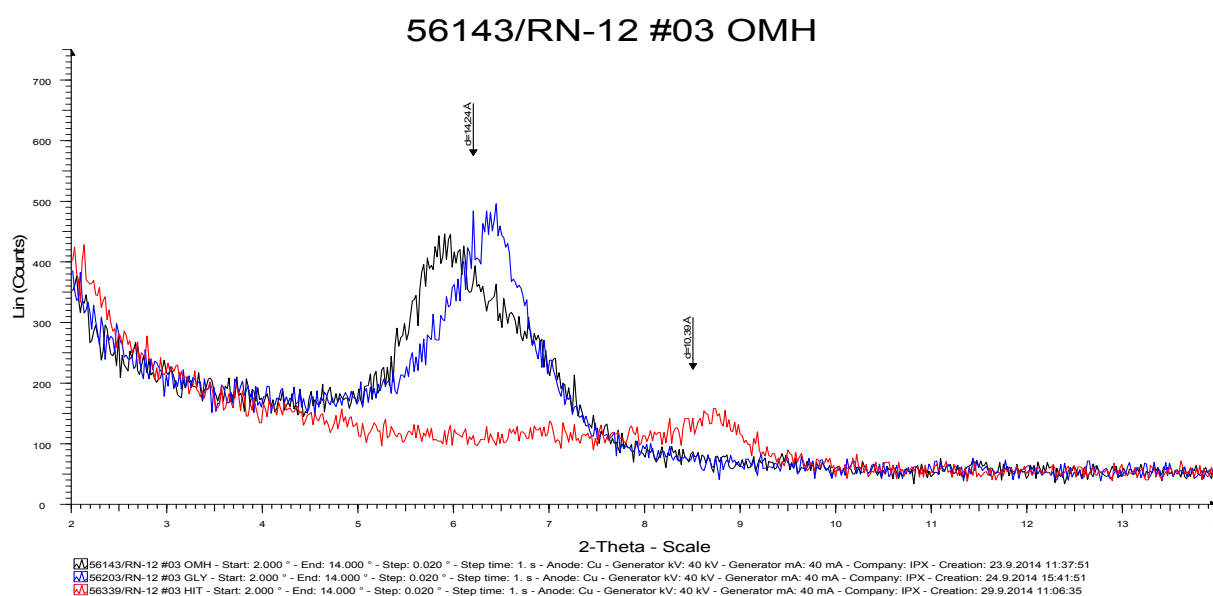


FIGURE 1: Well RN-12, XRD analysis of a sample 3 from 68 m

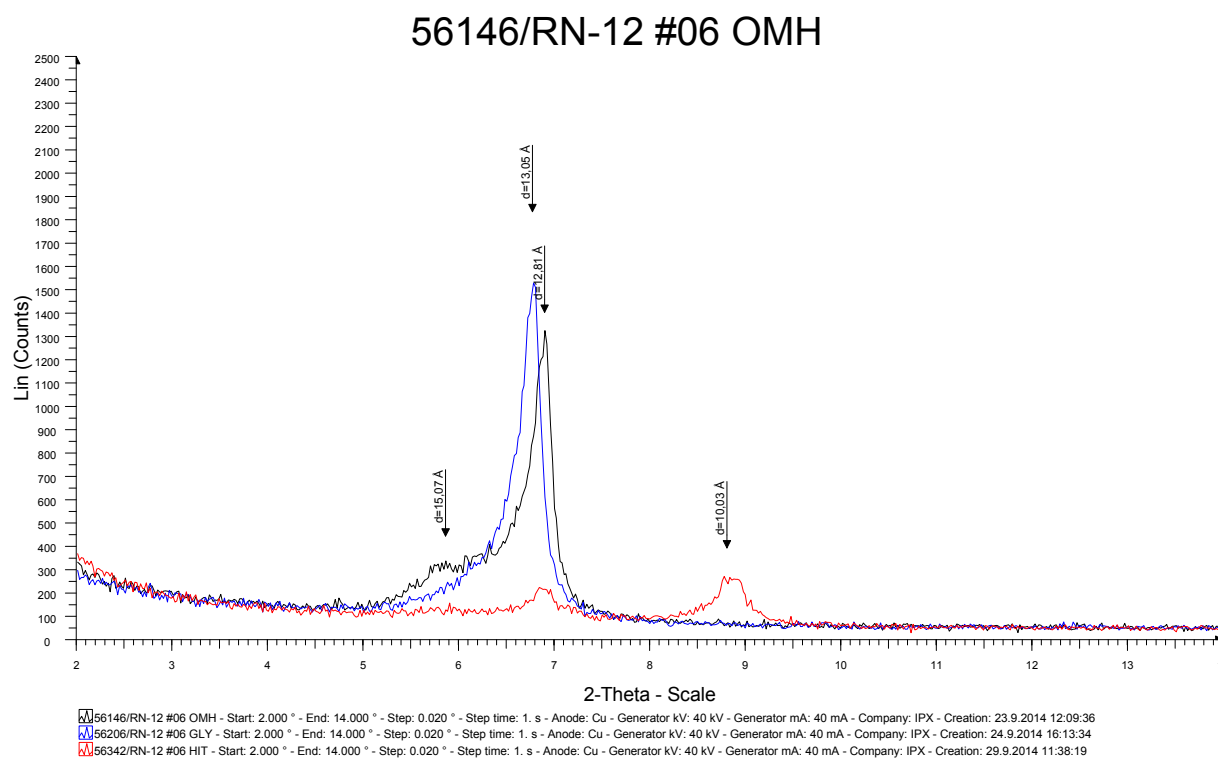


FIGURE 2: Well RN-12, XRD analysis of a sample 6 from 148 m

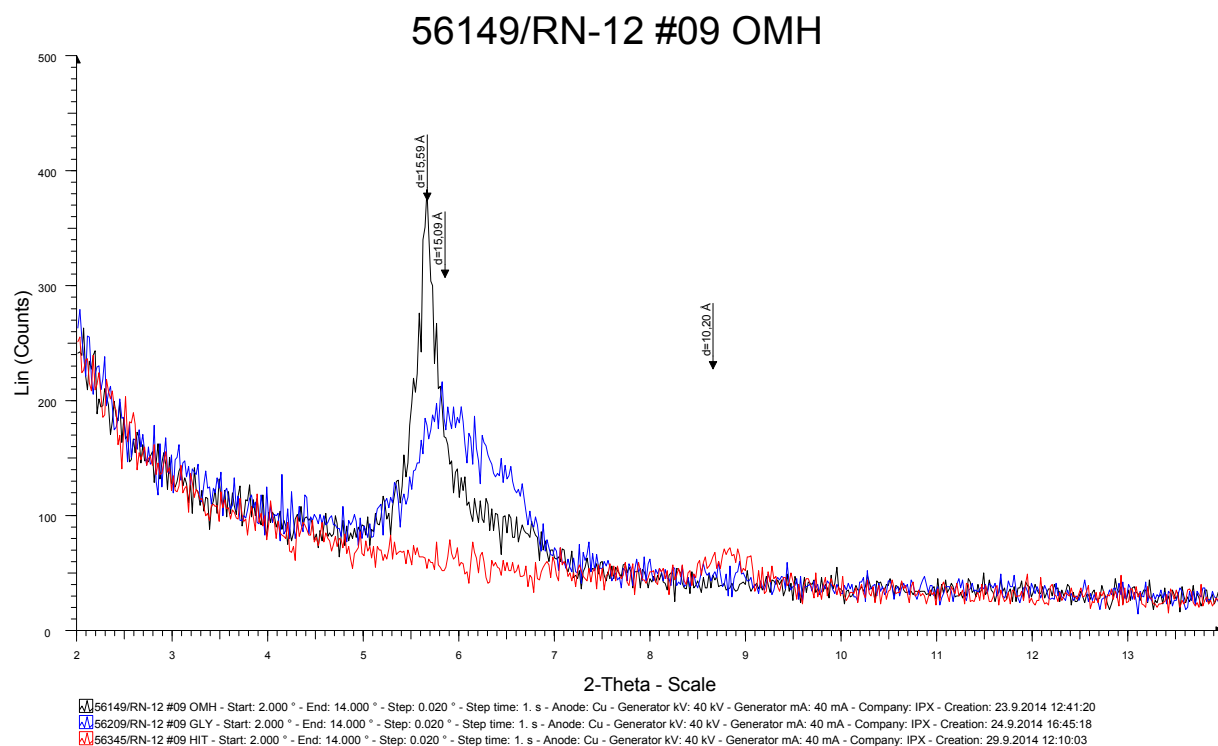


FIGURE 3: Well RN-12, XRD analysis of a sample 9 from 280 m

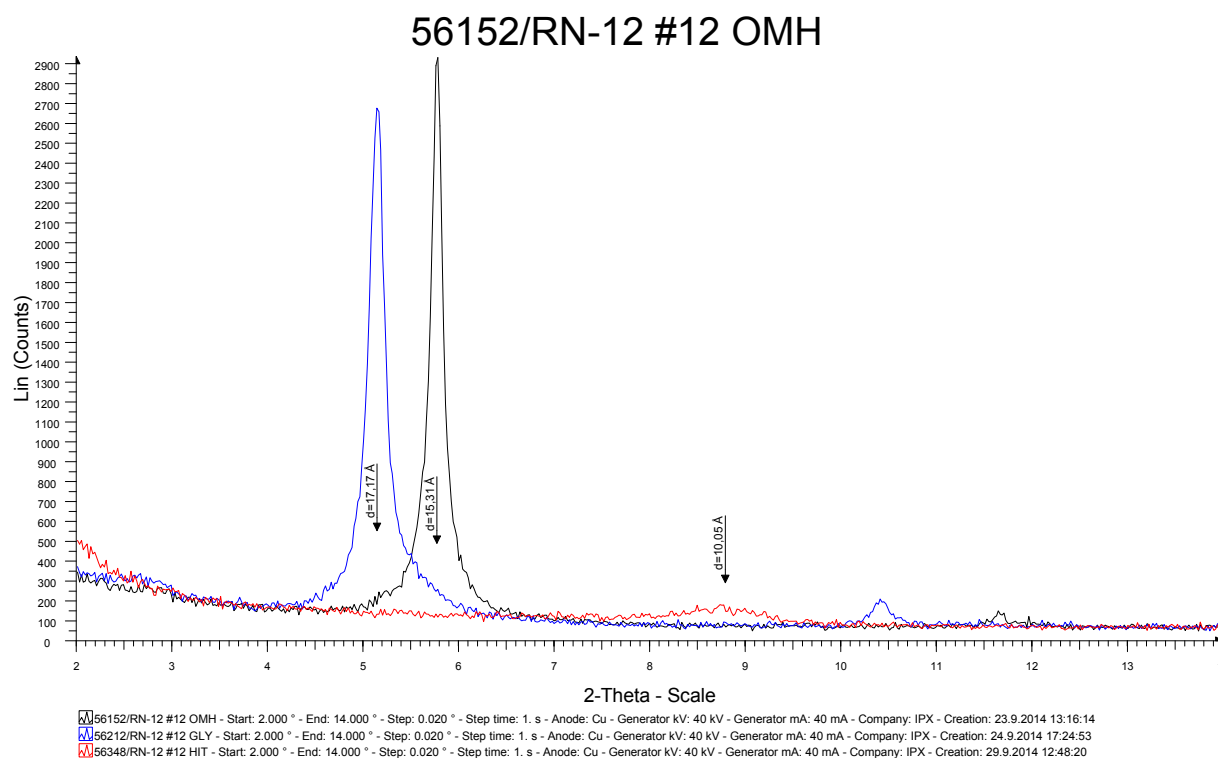


FIGURE 4: Well RN-12, XRD analysis of a sample 12 from 400 m

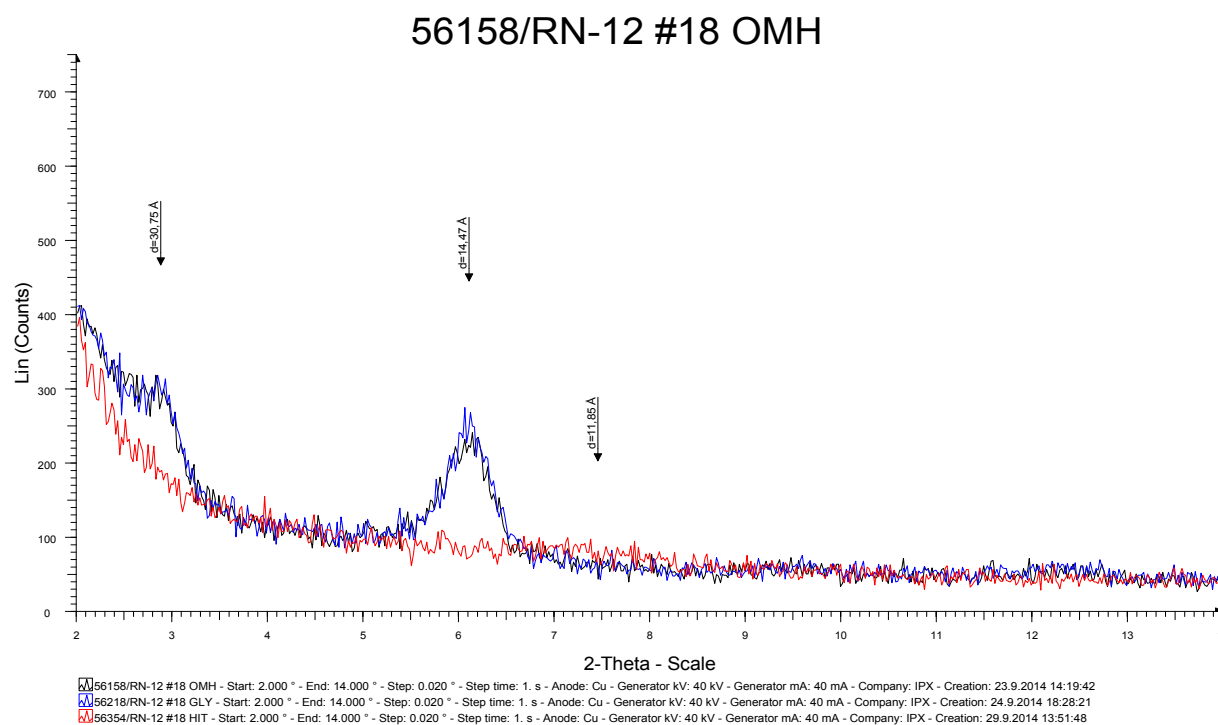


FIGURE 5: Well RN-12, XRD analysis of a sample 18 from 702 m

56160/RN-12 #20 OMH

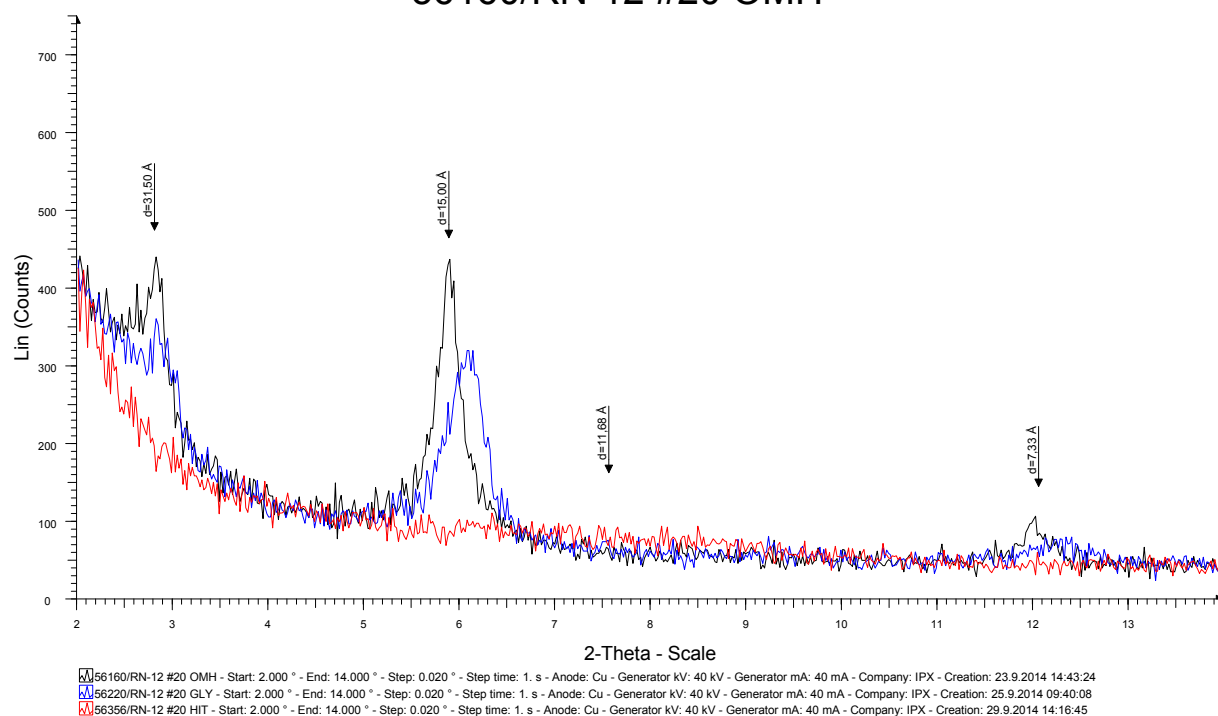


FIGURE 6: Well RN-12, XRD analysis of a sample 20 from 866 m

56161/RN-12 #21 OMH

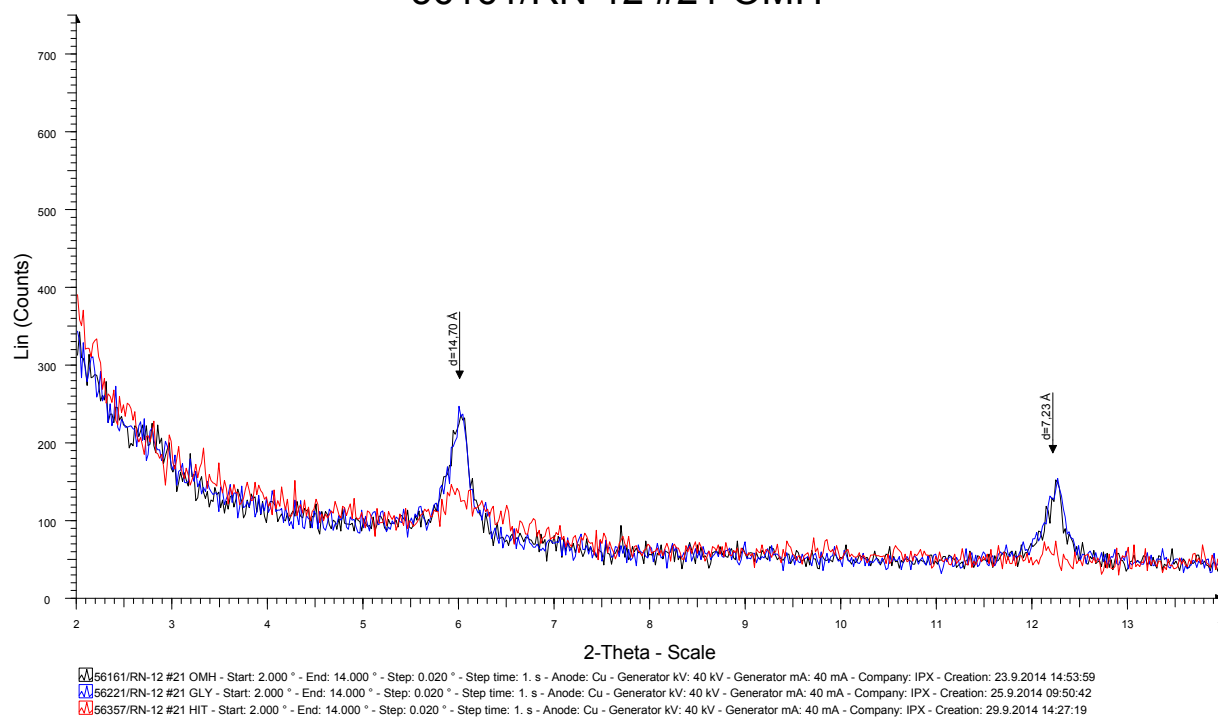


FIGURE 7: Well RN-12, XRD analysis of a sample 21 from 924 m

56163/RN-12 #23 OMH

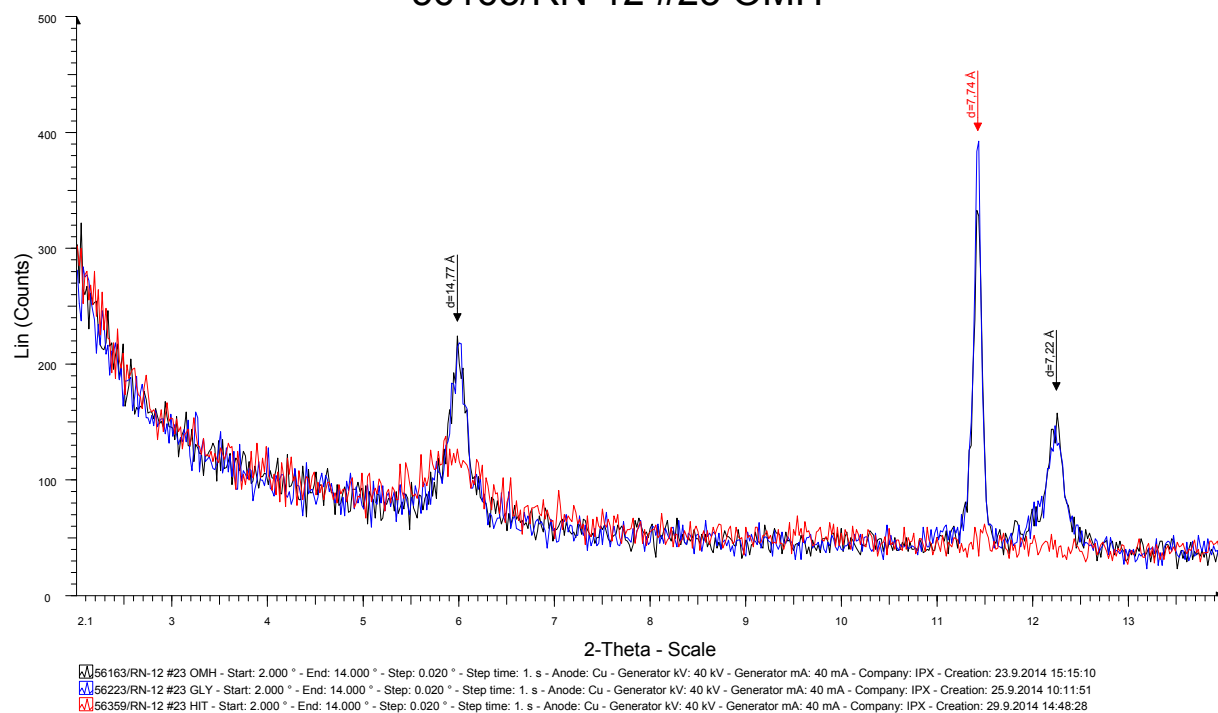


FIGURE 8: Well RN-12, XRD analysis of a sample 23 from 998 m

56164/RN-12 #24 OMH

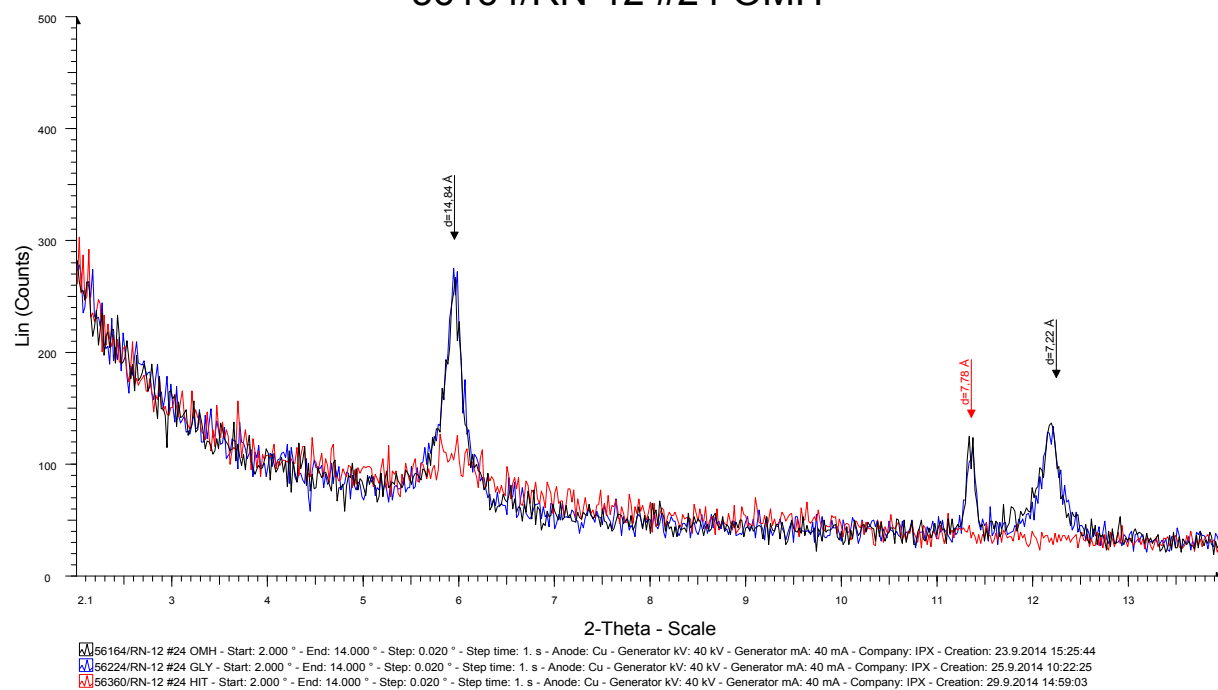


FIGURE 9: Well RN-12, XRD analysis of a sample 24 from 1014 m



UNITED NATIONS
UNIVERSITY

UNU-GTP

Geothermal Training Programme

Orkustofnun, Grensasvegur 9,
IS-108 Reykjavik, Iceland

Reports 2014
Number 31

PRELIMINARY TERMS OF REFERENCE (TOR) AND ENVIRONMENTAL IMPACT ASSESSMENT (EIA) OF GEOTHERMAL EXPLORATION DRILLING IN BUGARAMA, RWANDA

Alice Uwase

Ministry of Infrastructure

Rwanda Energy Group/Energy Development Company

Geothermal Development Division

PO Box 537

Kigali

RWANDA

uwasealice@gmail.com

ABSTRACT

Surface exploration studies for the Bugarama area were launched in 2014. Drilling is required to prove the existence of a geothermal resource. This report is based on experience accumulated during exploration drilling in Karisimbi in 2013, and on ESIA studies carried out for geothermal drilling projects in Rwanda. The first goal is to draw up the main procedures that must be followed during preparations for geothermal drilling, in order to ensure compliance with national and international regulations. Next is to present the preliminary terms of reference (TOR) for the ESIA that will be conducted during preparations for exploration drilling in Bugarama. Finally, a preliminary EIA of the three main environmental factors that the project is expected to impact i.e. noise, land acquisition and waste generation, is introduced. Mitigating measures are proposed for the mentioned impacts. The aim of this report is to provide a basis for future EIA work for geothermal exploration drilling in Rwanda. The main outcomes for a full EIA study are discussed.

1. INTRODUCTION

Rwanda is a landlocked country in East Africa, located along the Western Branch of the East African Rift system, with a surface area of 26,338 km², and a population estimate of 10.5 million inhabitants (NISR, 2012).

The Government of Rwanda has put emphasis on all developmental sectors to ensure a green economy in Rwanda. In fact, the protection of the environment and sustainable natural resource management are the cross-cutting areas of Rwanda Vision 2020, and the Economic Development and Poverty Reduction Strategy (EDPRS) Phase II, which was launched September 2013, with the following goals (MINECOFIN, 2000 and 2012):

“Sustain rapid economic growth and facilitate the process of economic transformation by increasing the internal and external connectivity of the Rwandan economy.”

This will be achieved through improved infrastructure, exports, and more integrated supply chains, while meeting demand in the energy sector, planting the seeds of a green economy, and better managing the process of urbanisation."

The main imperatives of the Energy sector are efficient use of energy, rationalizing energy pricing and subsidies, institutional development of the sector, and capacity building (AfDB, 2013), consequently financially supporting and focussing on renewable and environmentally friendly sources of energy such as hydropower, solar, and geothermal energy.

Geothermal research in Rwanda started in the 1980s and indicated the presence of a geothermal resource; two exploration areas have been identified, shown in Figure 1. The first area (Gisenyi, Karisimbi, and Kinigi) in the northwest region is associated with volcanoes; the second area (Bugarama) in the southwest region is associated with faults in the East African Rift, shown in Figure 2. Exploration for geothermal energy in the Karisimbi area culminated with drilling in July 2013, to prove the existence of a resource on the slope of the Karisimbi volcano. Even though the drilling was not successful, the research for geothermal energy in Rwanda carried on in the southwest region in the Bugarama area. In fact, reconnaissance surveys and surface exploration started in 1982 with the French Bureau of Geology and Mines (BRGM), but detailed surface studies were not launched until 2014. The geothermal areas to be investigated are located near the joint border between Burundi, RDC and Rwanda in the Bugarama area, and will be confirmed by exploration drilling.

A lot has been learned about the main environmental concerns of drilling activities, and from studies on the environmental and social impacts of geothermal drilling activities at Karisimbi and Kinigi. The purpose of this report is to best prepare for an environmental impact assessment (EIA) of the proposed exploration drilling in the geothermal area in Bugarama by preparing a preliminary TOR, along with a draft of an EIA on three of the main environmental factors that drilling would affect. EIA is a procedure used to examine the environmental consequences or impacts, both beneficial and adverse, of a proposed developmental project and to ensure that these effects are taken into account in project design. The EIA is, therefore, based on predictions. These impacts can include all relevant aspects of the natural, social, economic and human environment (Ogola, 2007).

This report is structured as follows. The main environmental laws and regulations required to gain consent for exploration drilling in a geothermal area are listed. Then the preliminary TOR is prepared and presented, following the EIA law in Rwanda and the World Bank guidelines. This section captures the main environmental factors/issues in Bugarama that need to be studied and dealt with in an EIA. In the last chapter, a draft of the EIA is presented with a particular focus on three key environmental factors that geothermal exploration activities in Bugarama can, and probably will, impact, including necessary mitigating activities.

2. ENVIRONMENTAL LAWS AND REGULATIONS IN RWANDA

2.1 Environmental laws and regulations

Here, the environmental laws and regulations in Rwanda are presented, along with decrees, statutory instruments and ministerial orders which deal with environmental protection. It also includes other laws and regulations that require consent for exploration drilling.

These are presented here in an attempt to inform developers at an early stage about the legal system in Rwanda and how they must prepare if they are planning extensive use of geothermal power.



FIGURE 1: Geothermal areas in northwest and southwest Rwanda (modified from JICA, 2013)

The first policy on environment protection and management was formulated in the Rwanda Constitution in 2003, followed by Organic Law n° 04/2005, establishing the Modalities of Protection, Conservation and Promotion of the Environment (Articles 67, 68, 69, and 70). Rwanda Environment Management Authority (REMA) is based on this law as is the definition of the responsibilities of involved stakeholders.

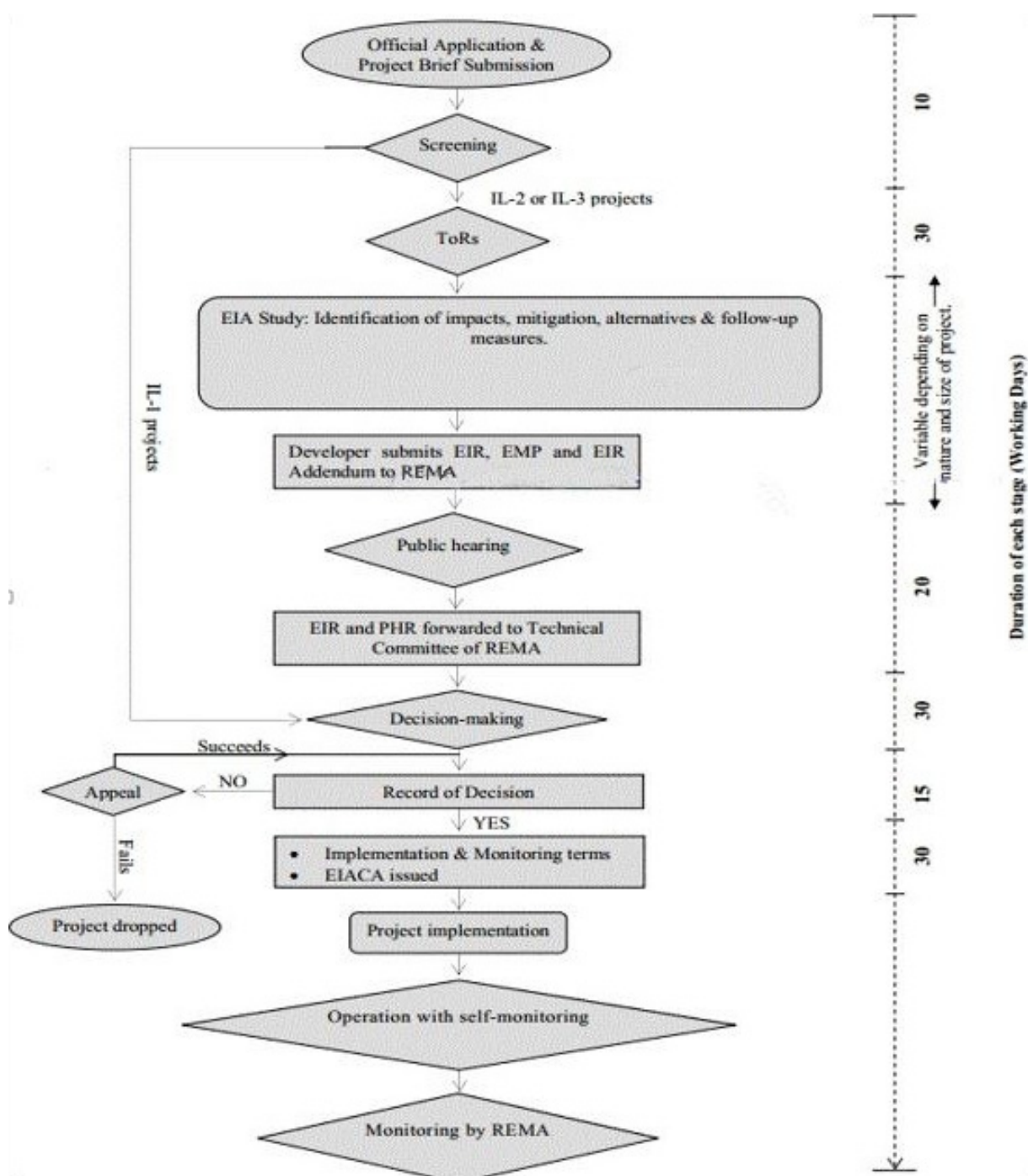


FIGURE 2: EIA procedure flowchart (from REMA, 2006)

National strategies and programs have been made to support the development of the country and take into account sustainable environmental and natural resource management, such as Rwanda Vision 2020, and The Economic Development and Poverty Reduction Strategy (EDPRS), which aims to reduce poverty through a pro-poor national growth agenda. Therefore, multiple laws and ministerial orders on social protection, land use, waste and environment management must be adhered to.

Laws and regulations are listed in Tables 1-4; their relevance to geothermal exploration activities must be noted in order to ensure that projects are in compliance with national regulations. In addition, Table 5 gives a list of the permits that geothermal drilling project require.

TABLE 1: National strategies

- Rwanda Vision 2020, 2000
- Rwanda constitution, 2003
- National Poverty Reduction Strategy, 2008
- Economic Development and Poverty Reduction Strategy (EDPRS) phase II, 2013
- The five year strategic plan for the environment and natural resources 2009-2013, 2008

TABLE 2: National policies

- Rwanda Environmental Policy, 2003
- The Mines and Geology Policy, 2004
- The National Land Policy, 2004
- The Water and Sanitation Policy, 2004
- Rwanda Land Policy, 2004
- Rwanda Health Sector Policy, 2005
- Rwanda Agricultural Policy, 2008
- Rwanda Water and Sanitation Policy, 2010
- National Forestry Policy, May 2010
- National Water Resources Management Policy, 2011

TABLE 3: Organic laws

- The Law on Forestry No 47/1988 of 5 December 1988
- The Land Act, 2004
- The Organic law determining the modalities of Protection, Conservation and Promotion of Environment in Rwanda No 04/2005
- The Organic law determining the Use and Management of land in Rwanda No 08/2005
- Presidential Order determining the structure, the responsibilities, the functioning, and the composition of Land Commissions No. 54/01
- The Land Valuation Law, promulgated in 2007
- The Land Expropriation Law promulgated No. 18/2007
- The Water Law No 62/2008

TABLE 4: Ministerial orders

Environment

- Ministerial Order relating to the requirements and procedure for environmental impact assessment No 003/2008
- Ministerial Order establishing the list of works, activities and projects that have to be undertaken in an environment impact assessment No 004/2008
- Ministerial Order establishing modalities of inspecting companies or activities that pollute the environment No 005/2008
- Ministerial Order regulating the importation and exportation of ozone layer depleting substances, products, and equipment containing such substances No 006/2008
- Ministerial Order establishing the list of protected animal and plant species No 007/2008

Land Use

- Ministerial Order determining the structure of Land Registers, the responsibilities and the functioning of the District Land Bureau No 001/2006
- Ministerial order determining the Land Title and Registration Law No 002/2008

Social

- Ministerial Order determining modalities of establishing and functioning of occupational health and safety committees No 01/20012

TABLE 5: Rwandan National Permit requirements (MML, 2013)

General construction permits required	Issuing authority	Comments
Approval on the terms of reference	RDB	Required under EIA general guidelines, 2006
EIA Implementation Order	RDB	Required under EIA general guidelines, 2006
EIA Certificate of Authorisation	RDB	Environmental organic law, 2005 and EIA general guidelines, 2006
Liquid wastes disposal and treatment	Rwanda Utilities Regulatory Agency (RURA)	Required under law No 39/2001 establishing RURA and the Directive on minimum requirements for liquid wastes disposal and treatment, 2009
Management of waste disposal site	RURA	Standards On The Management Of Waste Disposal Site, 2009
Construction Permit	District level approval	Law governing urban planning and building in Rwanda, 2012
Water permit	Ministry of Natural Resources (MINIRENA)/Rwanda Natural Resources Authority (RNRA)	Law for the use, conservation, protection and management of water resources, 2008

2.2 International agreements and requirements

When preparing a major geothermal exploration project, the authorities of the country involved must take into account several international agreements. In most countries, laws on EIA exist and are founded partly on Multilateral Environmental Agreements (MEAs), such as:

- The Espoo (EIA) Convention sets out the obligations of Parties to assess the environmental impact of certain activities at an early stage of planning. It also lays down the general obligation of States to notify and consult each other on all major projects under consideration that are likely to have a significant adverse environmental impact across boundaries. The Convention was adopted in 1991 and entered into force on 10 September 1997 (UNECE, 1991).
- The Rio Declaration (1992) was adopted to be a tool in the national decision making process during assessment of the environmental impacts of a project. The goal was to establish a new and equitable global partnership through the creation of new levels of co-operation among States, key sectors of societies and the public. In Europe, the laws and regulations on EIA and SIA are based on European Union (EU) directives and, in the USA, the Environment Protection Agency (EPA) has developed (EIA) Technical Review Guidelines for different sectors like energy (EPA, 2014).

Both EU directives and EPA guidelines are widely used as models for EIA laws and regulations around the world. In addition, it is well known that projects must comply with requirements from international banks if a project is to be funded by them. Investment banks like African Development Bank (AfDB), European Investment Bank (EIB), Japanese Bank for International Cooperation (JBIC) and, last but not least, the World Bank (WB) have environmental safeguards to ensure that financing of projects is not only based on the precautionary principle and preventative actions rather than mitigations, but also on sustainable development.

For instance, World Bank Operational Policy 4.01 on Environmental Assessment classifies projects into specific categories. Environmental screening projects are classified into four categories depending on

the type, location, sensitivity and scale of the project and the nature and magnitude of its potential environmental impacts:

- **Category A:** A proposed project is classified as Category A if it is likely to have significant adverse environmental impacts that are sensitive, diverse, or unprecedented. These impacts may affect an area broader than the sites or facilities subject to physical works. EA for a Category A project examines the project's potential negative and positive environmental impacts, compares them with those of feasible alternatives (including the 'without project' situation), and recommends any measures needed to prevent, minimize, mitigate, or compensate for adverse impacts and improve environmental performance. The borrower is responsible for preparing a report, normally an Environmental Impact Assessment (EIA) (or a suitably comprehensive regional or sectoral EA) that includes, as necessary, elements of the other instruments referred to in Paragraph 7 of Operational Policy 4.01.
- **Category B:** A proposed project is classified as Category B if its potential adverse environmental impacts on human populations or environmentally important areas, including wetlands, forests, grasslands, and other natural habitats, are less adverse than those of Category A projects. These impacts are site-specific; few if any of them are irreversible; in most cases, mitigating measures can be designed more readily than for Category A projects. The scope of EA for a Category B project may vary from project to project, but it is narrower than that of a Category A EA. Like a Category A EA, it examines the project's potential negative and positive environmental impacts and recommends any measures needed to prevent, minimize, mitigate, or compensate for adverse impacts and improve environmental performance. The findings and results of a Category B EA are described in the project documentation (Project Appraisal Document and Project Information Document).
- **Category C:** A proposed project is classified as Category C if it is likely to have minimal or no adverse environmental impacts. Beyond screening, no further EA action is required for a Category C project.
- **Category FI:** A proposed project is classified as Category FI if it involves investment of bank funds, through a financial intermediary, in subprojects that may result in adverse environmental impacts (WB, 1999).

The World Bank published guidelines regarding resettlement, which are widely used as a baseline in many countries. Note World Bank Operational Policy 4.04-Natural Habitat and the policy on Involuntary Resettlement/Relocation and Compensation of People, World Bank WB OP/BP 4.12.

2.3 EIA framework in Rwanda

The policy and the legal framework for an EIA were first found in the constitution of the Republic of Rwanda in 2003. Organic law No 04/2005, in determining the modalities of protection, conservation and promotion of the Rwandan environment, made Environmental Impact Assessment (EIA) mandatory for approval of many development projects, before implementation.

The objectives of the EIA in Rwanda are to identify adverse environmental consequences at an early stage, propose a way of avoiding negative impacts and, if that is not possible, propose mitigating measures and facilitate the decision making at the planning and design phase of the project. The findings of the EIA are a useful tool for project authorization and monitoring during construction, operation and demolition. Therefore, the general guidelines and procedures for an EIA were published in November 2006 to serve as a protocol for various stakeholders involved in the EIA process.

The governmental institution in charge of the environmental and social impact assessment (ESIA) process is the Rwanda Environment Management Authority (REMA), established by Organic law No. 04/2005. It shall coordinate and oversee all aspects of environmental management for sustainable development.

Some of the responsibilities are shared with the Rwanda Development Board (RDB). All applications for the EIA authorization certificate take place at RDB as it is the one stop place for investors (RDB, 2014). REMA is in charge of coordination, monitoring and supervision of all activities related to environmental protection.

According to the EIA Guidelines in Rwanda and Ministerial order N° 003/2008, the EIA process in Rwanda can be presented in the following steps:

a. Application and registration

In the first step of the EIA process, the developer submits an application for an EIA of a proposed project to REMA in the form of a brief introduction of the project, according to EIA Regulations. This introductory paper goes through a screening process.

b. Screening

Screening is carried out by REMA to determine the impact level of a proposed project which, in turn, determines the extent of the EIA study. Based on information in the Project Brief, REMA determines whether or not an EIA is required and the developer is accordingly notified. Screening enables early identification of environmental issues of major concern and the incorporation of appropriate mitigating measures. Screening also enables categorisation of projects according to their Impact Level (IL), as follows: IL 1: Projects not requiring further environmental analysis; IL 2: Projects not requiring a full EIA but necessitating a further level of assessment; IL 3 Projects require a full EIA.

c. Scoping and Terms of Reference

Scoping is the initial step of the Environmental Impact Study phase and involves input from relevant Lead Agencies, stakeholders and the developer in order to obtain their comments on what should be included in the study, and what alternatives should be considered. Scoping is a necessary step in the formulation of a detailed TOR for the impact assessment that will be done by the developer. The TOR sets objectives, defines the scope, and establishes the applicable strategy and methodology that shall be used to describe and assess the environmental impacts of the planned exploration drilling. TOR ensures that important issues are not overlooked by the EIA Experts and developers during EIA studies. The scoping report is submitted to REMA for review.

Within thirty (30) calendar days after receipt of the project brief and its analysis, the Authority shall submit the Terms of Reference to the developer for the Environmental impact study.

d. Environmental Impact Study, Assessment and Report

The Environmental Impact Study phase is the investigative stage of the EIA process; for this, a developer hires EIA experts. This phase begins when a developer selects expert(s) from a list of EIA experts provided by REMA. Within a period of five (5) working days after reception of the proposed experts, REMA will notify the developer of its acceptance or refusal of the proposal. The developer and EIA experts shall work together throughout the EIS phase to gather the necessary information on the environment and society, assess the project's impacts and develop adequate measures to mitigate negative impacts and enhance positive ones. An Environmental Impact Report (EIR) shall also include An Environmental Management Plan for the project.

e. Report review, and decision-making

After reserving the EIA report (or EIS) from the developer and his expert, REMA (the Authority) shall, within twenty (20) working days, accept the report or request additional information from the developer. Review of an EIA report submitted to REMA, enables subsequent decision-making on either approval or disapproval of a project. Depending on the nature of the project, the time limits mentioned above may be extended.

f. Project decommissioning/demolition or relocation

Upon project completion or when seeking relocation, a developer should prepare a decommissioning plan and submit it to REMA for approval. The decommissioning plan should include, but not be limited

to: assessment, existing environmental conditions, all proposed engineering works, mitigation activities associated with the removal of project facilities, and proposed restoration measures in the project area.

All the above mentioned steps are detailed in the General Guidelines and procedures for an Environmental Impact Assessment, published by REMA (the Rwanda Environment Management Authority) in November 2006.

3. PRELIMINARY TERMS OF REFERENCE (TOR) FOR THE EIA STUDY OF GEOTHERMAL EXPLORATION DRILLING IN BUGARAMA

The EIA process is a prerequisite to successful implementation of the project. The TOR outlines the EIA process that a developer must go through before consent for the exploration drilling can be given. Specifically, the TOR sets objectives, defines the scope, and establishes the applicable strategy and methodology that shall be used to describe and assess the environmental impacts of the planned exploration drilling. The TOR is a description of what must be included in the EIA report, how information shall be gathered and how the results shall be described in the report.

The EIA shall be prepared according to environmental procedures, laws and regulations of the Government of Rwanda and be consistent with the World Bank standards on EIA.

3.1 Background information

One of the energy sector's mandates in Rwanda is to establish environmentally sound and sustainable systems of energy production, procurement, transportation, distribution and end-use (AfDB, 2013). The Government of Rwanda (GoR) envisages increasing access to electricity and diversifying energy sources and is, thus, putting huge efforts into the diversification of energy sources in line with this diverse development of the country.

In fact, like in many other energy projects, geothermal exploration studies, from surface studies to drilling, were first fully funded by the GoR. The purpose of geothermal exploration is to prove the existence of a viable and renewable source of energy that can be economically utilised for electricity generation and/or direct use, thus contributing to the development of the country.

The geothermal exploration and development are managed by the geothermal development unit in the Rwanda Energy Group, which is in the Energy Development Company (Previously called Energy Water and Sanitation Authority) under the Ministry of the Infrastructure.

Environmental and Social Impacts Assessment Studies have been done for geothermal exploration drilling projects in Karisimbi and Kinigi areas in North Rwanda. According to the EIA guidelines in Rwanda, the projects were classified as category IL 3, requiring a full EIA as they were considered to have adverse environmental impacts where sufficient mitigations could not be prescribed (REMA, 2006). The ESIA studies resulted in both areas being put in category A (referring to World Bank guidelines), meaning that geothermal exploration drilling activities would negatively affect an area broader than the communities benefiting from the projects/infrastructure.

Surface studies are ongoing in the Bugarama area. The next step in the research of the area is to drill an experimental well in order to verify that there is usable energy.

More background information can be obtained from previous EIA study reports, as well as geoscientific surveys carried out for geothermal exploration in Rwanda.

3.2 Bugarama geothermal area

Exploration of geothermal resources in Rwanda began in the western (Gisenyi, Kibuye and Kinigi) and southern (Bugarama) regions of Rwanda in 1982, with the French Bureau of Geology and Mines (BRGM), and identified Gisenyi and Bugarama as potential sites for geothermal energy with estimated reservoir temperatures of over 100°C. No other geothermal survey has been conducted to confirm this.

In 2013, tendering procedures for a reconnaissance and geoscientific survey for the Bugarama area were completed. They were financed by the European Union in collaboration with the Icelandic International Development Agency (ICEIDA). The study was conducted in the Rusizi region which is shared by the Democratic Republic of Congo, Burundi and Rwanda. The scope of the work is to define the potential resource temperature, the geologic structures controlling the geothermal activity and the extent of the geothermal resources. The exploration study will conclude with a proposed drilling site for a deep (1400 to 1800 m) exploration well (Rusizi, 2013).

Bugarama geothermal area is located approximately 13 km southeast of the town of Cyangugu in the Rusizi district in the Western Province. It is located in a region of moderate altitude (900 m-1500 m). The Rwanda Meteorology Services reported that the highest temperatures in the country are found in Bugarama Valley (annual mean 23 - 24°C).

The region is mainly known for agriculture, based on rice and maize, and commerce activities with the neighbouring Democratic Republic of Congo.

The Bugarama geothermal area is well known from manifestations in the form of hot and warm springs and travertine deposits (Figures 3 and 4), which are mined and used as raw materials for a nearby cement factory.

The Mashyuza hot spring is a tourist attraction, where local communities and tourists come for bathing as the geothermal water is considered to be healthy or to have therapeutic effects.

The temperature of the water was measured by the geochemistry team from the geothermal development unit (GDU) in 2012 and was found to be 57°C.



FIGURE 3: Travertine deposits at Mashyuza hot springs (From GDU, 2012)



FIGURE 4: Mashyuza hot spring (Source, GDU)

3.3 Area of influence

The goal of the EIA is to identify the environmental factors that the project will impact, the extent of the impacts, their importance and the need to change the project to minimize negative impacts or find mitigations. The size of the area that will be affected by the project may not be clear in the beginning

and may vary, depending on the different affected environmental factors, for instance, the nuisance of noise that will come from construction, drilling and testing, plus the impact on the biodiversity, such as migrating animals, will extend the area of influence. There is currently no master plan in the district; however, the following map (Figure 5) does show the main land use in the area, such as the agricultural area, forests roads and villages. The rice farms are located along the rivers in the marshlands in the Bugarama Valley. A few geological structures, Mashyuza hot springs, and Bize are also marked.

Additional information about the area, such as maps of geological features or geophysical maps, have not been published, and the proposed location options for drilling sites have not been defined yet. In the final TOR, this information must be available on maps, at a scale of 1:5,000-1:20,000, as a basis for studies on different environmental factors, along with the master plan of the region and photographs.

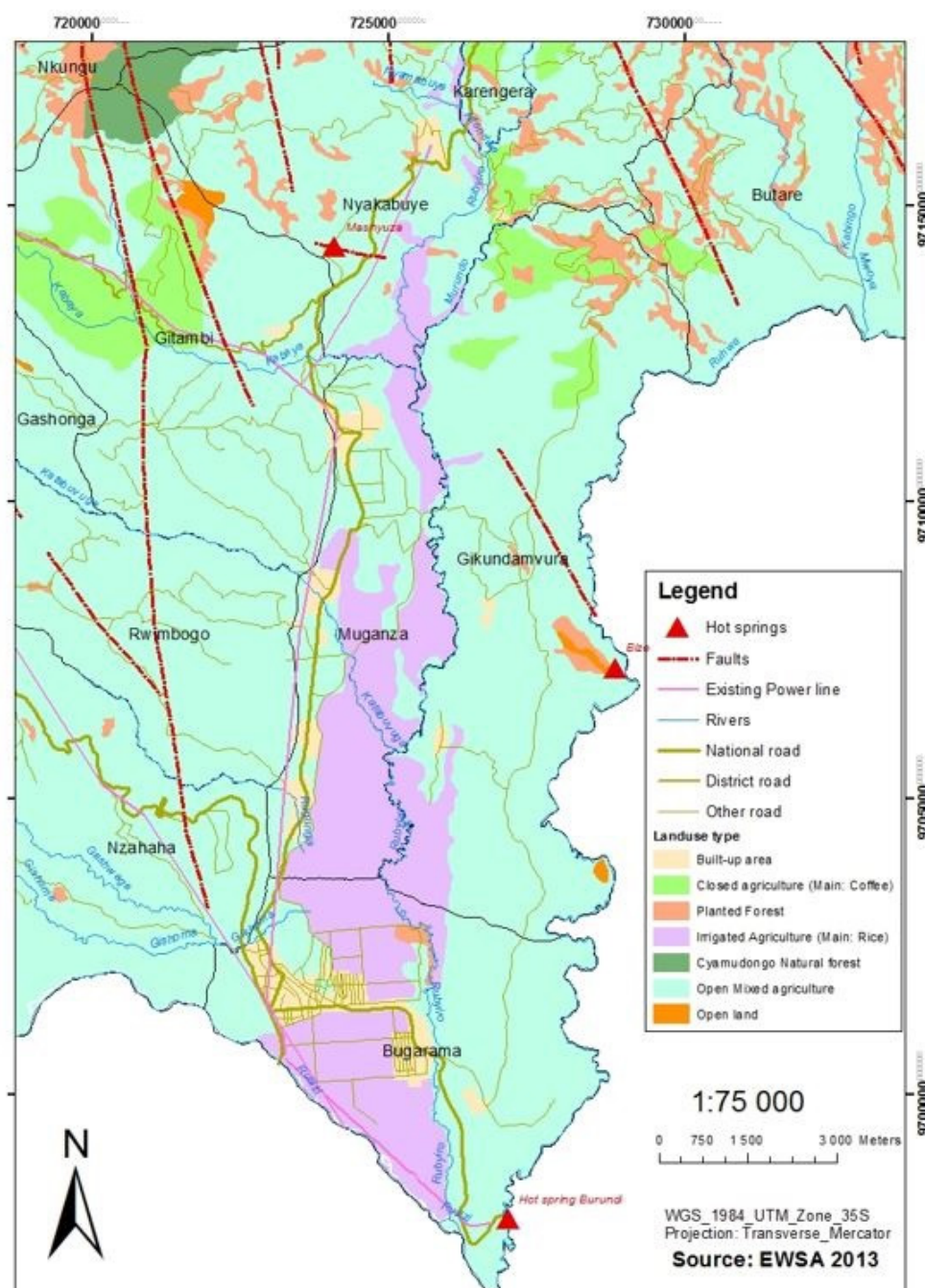


FIGURE 5: Land use map of Bugarama area

3.4 Description of the geothermal drilling exploration project

The scope of the planned exploration drilling is to define the potential resource temperature, the geologic structures controlling the geothermal activity, and the extent of the geothermal resource (Figure 6).



FIGURE 6: Karisimbi geothermal exploration drilling project, July 2013

The main components of the project in each construction area are:

- New roads and/or reconstruction of existing roads for the transport of machinery, and materials for the drilling activities;
- Drilling platform, from the standards used for Karisimbi geothermal drilling, the platform includes a settling pond for water disposal and space for the heavy machinery and offices, minimum size 3-6.000 m²;
- Water supply system comprised of water tanks, water supply pipelines and pumping houses; and
- Workers' accommodations and material storage yard.

In Table 6, the main project components and expected duration of the work in months are described

TABLE 6: Exploration drilling components and duration of construction/activities

Project component	Size (m×m)	Duration
Reconstruction and construction of access road	6 m width, length unknown	6 months
Construction of water pipeline, tanks and pump houses	Not known	6 months
Construction of campsite storage yard	100×35	4 months
Construction of storage yard	100×65	4 months
Site clearance of 3 drilling pads	150×85	5 months
Rig mobilization	-	1 month
Drilling activities of 3 wells	-	6 months

*Size and duration of activities is based on estimates/experience from the Karisimbi geothermal project and could be different for the Bugarama project. Most of the components in Table 6 are done simultaneously which considerably reduces the time of the whole project.

3.5 Objectives and requirements of the EIA study

The main objectives of the EIA are to:

- Ensure that the project is in accordance with laws and regulations in Rwanda;
- Compile the ecological and socioeconomic baseline conditions of the project area in Bugarama and the local communities that might be affected by the exploration drilling;
- Identify impacts of the project on the local community and how to make them as positive for the community as possible;
- Assess in detail the environmental, social, and health impacts that would result from the project;
- Inform and obtain input from stakeholders, (e.g. governmental authorities, the public, and local communities) and take into consideration their comments and concerns; and
- Develop an Environmental and Social Management Plan (ESMP) with mitigating measures resulting from the EIA.

The EIA study must: meet the requirements or recommendations of the applicable national and international regulations and standards; be guided by the policies, guidelines, and procedures of the relevant international treaties and agreements relevant to geothermal developmental activities.

The EIA should also follow the environmental assessment regulations of any other financing organizations involved in the project, and relevant international environmental agreements/conventions to which the country is part of, such as the World Bank Operational Policies (ArGeo EIA Framework, 2009).

The environmental factors that will be included in the EIA are chosen because of the impacts that the project is expected to have on the environment. The construction of roads and platforms, campsites and gravel mining will result in changes on the surface and include traffic. This can affect geological formations, soil and vegetation, landscape and visual values, historical monuments, housing and tourism. Also, the drilling operations will create noise and traffic that will be a nuisance to the people living in the area and to tourists.

With regard to this, the EIA will consider the project's impacts on the following environmental factors: Land use and conservation, water resources, noise, air quality, biodiversity, social aspects, solid wastes, natural hazards, tourism, geology, landscape and visual impacts. The EIA will deal with the impacts during construction, operation and demolition.

3.6 Scope of work of the EIA study

Basically, the EIA process consists of a baseline study describing the environment before the project starts. It assembles and evaluates the baseline data on the physical environment (geology, topography, soils, etc.), biological environment (flora, fauna, natural sites, etc.) and, finally, the socio-cultural environment in the area (population, land use and planned activities in the area). Based on the baseline information, the EIA must predict the magnitude, the extent and the duration (short or long term) of the potential impacts, whether the impacts are irreversible or reversible, and the size of the impact area. Then mitigating measures that the developer has decided to use are introduced and the applicable cost is evaluated.

The team for the EIA should include, but not be limited to, experienced specialists in the following areas:

- Meteorologist/Air Pollution Specialist;
- Geologist/Soil Engineer;
- Chemist/Water Pollution Specialist;
- Forester/Ecologist; and
- Social Scientist (Geographer).

3.6.1 Land use and conservation

For exploration drilling, the land that is disturbed by road construction, drilling platforms, preparation and storage, and campsite can be quite big and the surface morphology will be changed. With this in mind, the EIA study must identify and assess the impacts related to soil removal and land acquisition and, if needed, introduce mitigations.

Data shall be collected on the ownership of the land, plus the main land use in the area must be identified by mapping agriculture and forestry zones. Land acquisition processes must be learned and then a method for conducting those processes as smoothly as possible must be proposed. Geological formations will be mapped and described. If the project has impacts on protected natural sites, areas of natural interest and/or tourist areas, the EIA identifies the main stakeholders and involves them in the EIA process. A list of required permits that the developer must obtain is included in the project's consent. This information must be clarified in the EAR in text, on maps and with pictures.

3.6.2 Water resource

The developer must identify water bodies and water resources in the area such as lakes, rivers, springs and swamps; critical water points for local communities, like water protection areas, according to the local master plan, must be noted. They must also be shown on a map. The amount of water needed must be listed, both for consumption and for drilling. The site from where water will be taken must be clear, as well as where water pipes will be placed. The amount of waste water must be determined and how it will be treated and disposed of, including both sewage water from camps and drill water with cuttings. If it is necessary to protect the soil in the area from being contaminated by effluents from the project, a detailed description on protection measures is needed.

Depending on the selected water source for the drilling activities, the EIA study must assess the impact of the water abstraction on both surface water and groundwater in the area. This is done by reviewing existing information on the water bodies in the Bugarama area. In addition, a prediction model of the water abstraction, through all seasons and worse case scenarios, must be provided, along with the corresponding mitigations.

3.6.3 Noise

During geothermal drilling, due to the use of heavy machinery and drilling activities, noise is the main impact of the project on the surrounding environment. Various international standards on acceptable noise levels exist, e.g. in the World Bank guidelines, and from the World Health Organization. They must be used as background information to predict the impacts of the drilling work on the local communities. The developer must describe what type of silencers will be used during well testing and inform on expected noise levels.

Simulation models of the noise in the area from different activities such as drilling, testing and bleeding must be prepared. The results must be presented on a map, showing the noise level in various scenarios. The developer must do a background noise level survey in the area and predict the level of noise impacts from different phases of the project on the local community, and how long each phase will last.

3.6.4 Air quality

Information on meteorology and air quality is gathered and used to predict the potential impacts that a project can have on the air quality around the planned drilling sites.

Measurements of the concentrations of the main geothermal gas H₂S from surface manifestations, such as fumaroles and hot springs in the area, can help to predict the steam composition from the well. Information on wind speed and direction, and other meteorological information, needs to be used in a

model of the H₂S dispersion in the area during well testing, both for the worst case and with mitigations. If the necessary data is not available, it must be gathered, e.g. by putting up a mast with necessary instruments to obtain the minimum information.

3.6.5 (Biodiversity) Flora and fauna

The data collection on the existing fauna and flora shall be carried out with an ecological checklist. The results will be shown on maps, showing the distribution of the dominant and rare species of fauna and flora in the area, and the identification of unique habitats of animals. Potential impacts on flora and fauna must be assessed and, if necessary, relevant mitigations introduced.

3.6.6 Social aspects

The impacts on the local communities that the project may have must be mapped: positive impacts e.g. creating work for the local people; and negative, e.g. the need to buy land that will be destroyed by the project or the relocation of people for safety reasons, etc. The EIA study shall collect information on the demographic data in the Bugarama area, and identify administrative boundaries, demography and the main developmental sectors. The study must predict the magnitude and extent of the impact of the project on the local community.

3.6.7 Solid waste

In the EIA process, the solid waste must be clarified and, in the final EIA report, a list will be provided with the different types of waste, amounts, where it comes from, etc. The waste management program will be introduced along with how the developer plans to manage it.

3.6.8 Additional environmental issues

The EIA study should also deal with other aspects of the drilling activities such as natural hazards, tourism, geology, landscape and visual impacts.

The size of this report is limited and so is the time for preparing it; that does not allow as extensive a work as is needed for a good TOR.

The ESIA study is not limited to the above mentioned tasks; more will be added during the tender process for the study and during the selection of the consultants who undertake the work.

3.7 Expected outcome of the EIA study

The EIA study must include possible alternatives in terms of technology, site selection, design and construction techniques, etc. All the alternatives must be compared, taking into account the impacts on nature and society and costs. The EIA must include a no-project alternative and a comparison of all alternatives (including the Zero alternative).

If the accuracy and precision of the EIA report is good, the World Bank guidelines are followed, and the project is well prepared, then the geothermal exploration drilling project should be classified as category B: *If the projects potential adverse environmental impacts on human populations or environmentally important areas are less adverse than those of Category A projects. These impacts are site-specific; few if any of them are irreversible; and in most cases mitigation measures can be designed more readily than for Category A projects.*

In fact, Category B is normally more acceptable than Category A to external sponsors who might be interested in financing further studies in the area.

The main parts of an EIA report are a non-technical summary, the description of the project and the institutional framework in place. But mostly, the report must contain a baseline information and the analysis of the impacts of the project on the environment and the strategies to minimise or avoid the impacts through an ESMP and a Resettlement Action Plan. The proposed time for this EIA study is 60 calendar days.

The environmental impact assessment study of the above mentioned project should constitute, but not be limited to, all the above mentioned methodologies, the scope of work and all reported obligations.

4. PRELIMINARY ENVIRONMENT ASSESSMENT AND MITIGATIONS

4.1 Land use

When geoscientific surveys have been completed and drilling exploration wells is the next step to get further information on the geothermal system, the scientist must choose the sites for the exploration wells. It is normal that, in the beginning, 2-4 sites are introduced in the EIA process. In some cases, the location of the drilling sites is within a densely populated area and it would be necessary to buy the land and move the people. This can be a complicated process as it is necessary to find new land for the people.

Land acquisition is delicate and should, therefore, be carefully planned at an early stage of the EIA process to fulfil national and international regulations considering the main issue in the area, which is land shortage.

The World Bank's policy on involuntary resettlement (OP 4.12) applies to all land acquisition, impact on assets, negative impact on livelihood and/or any changes in access to resources due to a subproject, irrespective of whether or not affected persons must move to another location. This includes the restricted use of resources in a park or protected areas by people living inside or outside the areas which affect their daily lives (ArGeo, 2009).

The land acquisition process should start by complying with the national laws and WB guidelines. In fact, the World Bank's resettlement policy emphasizes some features that may differ from national policies, mainly on compensation costs. Where domestic law does not meet the WB standard of compensation, it is supplemented by additional measures necessary to meet the WB standard (ArGeo, 2009). This can be fulfilled by job opportunities to the people who are directly vulnerable to the project.

4.1.1 Current land use

Among the policies adopted to develop the Bugarama area is the crop intensification policy which facilitates access to national markets and, thus, improves the lives of local communities; this implies that the main land use in the area is agriculture. The main negative impact of a geothermal drilling project on the local community is the loss of farmland.

The drilling locations have not yet been decided but in the final EIA report all the main infrastructure for the geothermal project, and various options for them, if possible, will be shown on detailed maps (1:1000-1:5000) where different land use is shown and the environmental and social impacts are compared in the text. However, in this preliminary assessment, the lack of maps and various data on land use does not allow a detailed assessment of the expected impacts of the project on the land use and people in the area.

4.1.2 Impact on land use

Considering that the Bugarama area is one of the highest populated sectors in the country (1266 p/sq.km), the main impact of the project is the land loss by the local community. Measures to avoid and minimize the negative impacts from that must be explained and discussed in more detail in the final ESIA report.

The project will directly affect the local people as it will destroy agricultural land and private houses. Any kind of activity that affects the local population in this way is considered to be causing involuntary resettlement. The local authorities and the developer have to come to an agreement on how that will be arranged. A program to prepare the process of land acquisition must be made in the beginning of the EIA process and should be made in cooperation with the local authorities, from the district level to the cell level. The program would include meetings where the exploration drilling project is introduced and necessary supporting documents are handed out. The documents would include detailed information on the project. In this phase, how the drilling project fits into the master plan of the area would also be discussed with the local authorities. At a later stage, when more information has been collected and the impacts of the drilling project in the area are clearer, more meetings and a public hearing should take place. All the comments collected from the local authorities and the public shall be used in the EIA process and also at the later planning and project design level of the project.

A Resettlement Action plan (RAP) must, therefore, be presented in the final EIA report, containing specific and legally binding requirements to be abided by, to resettle or compensate before the project is given a consent and its implementation begun.

At the national level, existing land laws define the regulations and requirements to be complied with in case of land acquisition. In fact, the Organic Law N° 08/2005 of 14/07/2005 determines the use and management of land in Rwanda. It states that any land without the boundaries of towns and municipalities established by law, or presidential order, is rural land.

The expropriation law on public interest: N°18/2007 of 19/04/2007 (Republic of Rwanda, 2007), presents the rules to be followed during land acquisition on projects for public interests on behalf of the Government. Research for geothermal energy can be classified as part of the valuable minerals and other natural resources in the public domain (Article 5). In addition, ministerial order N °002/16.01 of 26/04/2010 determines the reference land price outside Kigali city (Republic of Rwanda, 2010).

Another severe impact of the project could be on tourism in this area, which is known for its hot springs, attracting hundreds/thousands of tourists every year. Changes in the hot springs, or access to them, could have negative impacts on work in the tourism sector, but also positive impacts. In the final EIA report, tourism in the area and its value for the community must be described and discussed in detail. That discussion must include different options on how possible negative impacts could be minimised and, if necessary, include relevant mitigations that the developer is ready to provide.

4.1.3 Conclusions

The developer's main goal and the result from the EIA process must be to:

- Avoid any displacements of households;
- Minimize space needed for the infrastructure such as drilling platforms and new roads;
- Choose the areas which are least suitable for agriculture;
- Use existing road tracks;
- Avoid disturbing sensitive geothermal manifestations; and
- Avoid areas which are tourist attractions.

It is most likely that some residents must be moved. However, from experience during Karisimbi exploration drilling, positive impacts also come with the project. Some of them are:

- Temporary employment that contributes to poverty reduction, especially if vulnerable local people such as farmers with limited land are employed;
- Improved infrastructure with rebuilt roads. In fact, Rusizi is a rural area so there are few public infrastructures, especially roads. Inadequate roads raise transport costs, which forces poor people to sell and purchase at local markets and increases unemployment;
- The geothermal exploration project created opportunities for businesses, both directly and indirectly related to the project, and contributed to a local increase in commerce activities; and
- Improved roads might improve tourism in the area for those coming to visit the hot springs of Bugarama.

4.2 Solid waste generation and management

Sources of wastes at the drilling site can be divided in two main parts: household waste from the campsites, paper and plastic containers and, secondly, cuttings from drilling and scrap metals.

In the EIA process, the solid waste must be delineated and, in the final EIA report, there will be a list with the different types of waste, amounts and origins, etc.

A waste management program will be introduced, including how the developer plans to manage the waste. That will include:

- Localizing adequate landfills for the disposal of wastes, mainly from households, by checking the master plan of the region and getting the approval of the local authority (district level);
- Control waste from the construction sites (platforms), equipment & workers camp through a Construction Waste Management Plan;
- Put in place a grade & sort waste management system to manage garbage and other forms of waste generated;
- Environmental education for the workers and people living in the worker's camp, as well as the people operating food kiosks, on proper waste management practices. The main idea of the program is to show people the importance of good management of hazardous materials and also the importance of separating different types of waste. Tidiness on the platform can also be a part of reducing the risk of accidents. Immediately, SWMP to be developed by / communicated to contractors;
- Consider possibilities of waste reduction, reuse and recycling, especially paper and plastic containers that can be recycled by the local community;
- Carry out periodic environmental audits that also cover waste management;
- Inspection of drill site and campsites; and
- Identify measures for minimisation of waste generation and safe disposal of construction, operation and decommissioning wastes. This will include all hazardous substances used and produced during the Project, controlled by a Material Safety Data Sheet (MSDS). The chemical composition of the drill cuttings needs to be analysed and, if there are no chemicals (like arsenic) that can pollute the environment, the cuttings will be buried on the site of the drilling platform. Otherwise, the cuttings must be taken to an adequate landfill.

In the last section, some mitigating measures to be adopted will be introduced.

4.3 Noise

4.3.1 Sources of noise during geothermal exploration activities

Most likely the drilling will take place in forests and rural areas so the noise during drilling activity will mainly affect people living in proximity to the drilling.

The main sources of noise can be divided into two groups. The first one is noise from construction work, during site clearance for the platform, the layout of pipelines, building the campsite, and road reconstruction. All these need the presence of heavy machinery which cause noise, affecting the closest receptors and maybe at some distance. In addition, traffic on the road is expected to increase during construction and drilling.

The second and the one that can have the most negative impacts, is the noise from the drilling activity. That is temporary, 6-8 weeks, and rarely exceeds 90 dB (A). The noise from discharging boreholes may exceed 120 dB (A) (Kristmanndóttir and Ármannsson, 2003). Table 7 shows the main source of noise and the noise levels of different operations at the rig site when drilling.

TABLE 7: Noise from some drilling activities (Hunt, 2001)

Activity	Noise level (dBA)
Air drilling	120 (85 with suitable muffling)
Discharging wells after drilling	Up to 120
Well testing	70-110 (if silencers used)
Heavy machinery	Up to 90
Well bleeding	Up to 85 (65 if rock muffler is used)
Mud drilling	Up to 80
Diesel engine to operate compressors and electricity	45-55 (if suitable muffling is used)

Drilling a well may take 6-8 weeks, depending on the depth of the well, difficulties during the drilling, and pumping at the end. How long the effect will last is dependent on the number of wells to be drilled and later tested, and whether they will be tested one after another or many at the same time.

During well testing, liquid and vapour flow directly into the silencer which reduces noise. The silencer can be of different types and will be described in the final EIAS. Estimates indicate that noise from the hole in well testing is in the range of 70-110 dB (A) at the platform. Commonly, 200 m away from the borehole during testing, the noise level goes down to 60 dB (A) and at 500 m down to 50 dB (A). It can be expected that the limits of 40 dB (A) noise levels are achieved within 1,500 m (VSÓ, 2013). This can take 1-2 months, but bleeding can last for years.

Since the area is highly populated, the disturbance from the noise will mainly affect people working and/or living within 500 m radius. However, this impact is temporary as explained before. In the final EIAS, the noise dispersion model will be shown and that will take into account the vegetation and landscape barriers in the area around individual wells.

There are no known standards, guidance or legislation applicable to environmental noise in Rwanda. However, international regulations can be applied such as WBG EHS General Guidelines on Noise Management. Environmental, Health, and Safety Guidelines for Geothermal Power Generation can be used as guidelines. Table 8 presents the World Bank and World Health Organization noise exposure standards.

TABLE 8: World Bank and WHO noise exposure standards, (WB, 1999; WHO, 1999)

Receptor	Maximum allowed Leq (hourly) in Db(A)			
	World Bank		World Health Organization	
	Day time (07:00-22:00)	Night time (07:00-22:00)	Day time (07:00-22:00)	Night time (07:00-22:00)
Residential institutional and educational	55	45	50	45
Industrial and commercial	70	70	85	85

*Leq is the equivalent continuous sound pressure level

4.3.2 Mitigating measures

To meet requirements on noise levels, mitigating measures must be taken in order to avoid noise impacts both day and night in residential areas (nearest households). These could be:

- When siting and designing the project, take advantage of the natural topography and vegetation as a noise buffer;
- During drilling and well testing, reduce noise by using silencers, and rock mufflers;
- Conduct regular noise monitoring every month at the same locations: in the closest sensitive location such as households, school, health centres, during drilling and critical operations such as air drilling; and
- Conduct regular meetings with the local community to record complaints about noise from the drilling activities.

5. CONCLUSIONS

In this report, the main factors of geothermal drilling for both exploration and production purposes were described. It involves civil work that consist of roads construction, water supply installation, worker's camp, storage yard, preparation of drilling pads and the drilling itself. If the exploration wells are not used as production wells or the platforms used for further drilling, they will be demolished and that must be part of the EIA. The above mentioned works affect the environment and the public's land use, water resources, air quality and noise. The effects can also affect the biodiversity and local people in the project area. The TOR is prepared to serve as a guideline for a future EIA, addressing the environmental and social issues that might arise from drilling activities specifically in the Bugarama area.

The preliminary TOR was prepared to give an example so that future EIA studies in the Bugarama area are conducted in accordance with national laws and international requirements. Surface studies in Bugarama were launched in 2014 and will be finalize by drilling 1400 to 1800 m wells to assess the available resource. Based on experience gained during drilling in Karisimbi, the TOR presents the main issues that need to be included in the ESIA study. It also gives an idea of the assessment methodology, and how the results must be presented. The TOR is not definitive, due to the lack of information on the results of the surface studies and information on where the exploration wells are planned to be located. Therefore, the area of influence is not known and the preliminary TOR must be looked at as a tool to be used for the final TOR for the ESIA study.

The laws, EIA framework and procedures in Rwanda provide the main tasks that need to be undertaken in order to fulfil the requirements to obtain the certificate of authorization for geothermal exploration

drilling. On the other hand, international requirements, such as the World Bank policies, provide complementary guidelines on the assessment of environmental issues of the drilling activities that are not addressed in the national law, such as noise, but also include the major requirements for projects to be funded by the WB.

However, the preliminary EIA of the project showed that the project will have the most impact on three environmental factors. Those are land use, noise and the generation and disposal of solid waste. It showed that land acquisition for the project is a delicate procedure. The Bugarama area has a high population density so there is a scarcity of land available for agriculture. The most important mitigations are to avoid displacements of households and minimize the space needed for the infrastructure, such as the platform and new roads. It is also important to choose areas which are least suitable for agriculture, use existing road tracks and avoid disturbing sensitive geothermal manifestations and tourist attractions. As there are no national guidelines on noise, the World Bank and WHO policies must be followed during drilling activities, and monitoring must ensure that the level of noise is acceptable, both for the workers and neighbouring communities.

A more comprehensive EIA must be done for geothermal exploration drilling in the Bugarama area.

ACKNOWLEDGEMENTS

My thanks go to the Government of Iceland, and the United Nations University for offering me this Fellowship, and to the Ministry of the Infrastructure of Rwanda for granting me the study leave, and for supporting my application. I am grateful for the opportunity to attend the UNU-GTP fellowship; it has allowed me to expand my knowledge and meet fellows from all over the world.

I thank the UNU GTP staff for the continuous assistance throughout the six months: the Director of UNU-GTP, Lúdvík S. Georgsson; Deputy Director: Ingimar G. Haraldsson. Thanks go to María S. Guðjónsdóttir, Thórhildur Ísberg, Mr. Markús A.G. Wilde and Málfríður Ómarsdóttir.

My warm thanks go to my supervisor, Thóroddur F. Thóroddsson, for his constant guidance and knowledge sharing and to Brynhildur Davídsdóttir for the follow up and advice during my project research.

Thanks to my family and friends for their support and prayers.

REFERENCES

AfDB, 2013: *Rwanda energy sector review and action plan*. African Development Bank Group, report, 108 pp.

ARGeo, 2009: *Environmental and Social management framework*. Africa Rift Valley Geothermal, Development Program, 68 pp.

EPA, 2014: Technical review guidelines for Environmental Impact Assessments in the tourism, energy and mining sectors. US Environmental Protection Agency, webpage: www2.epa.gov/international-cooperation/technical-review-guidelines-environmental-impact-assessments-tourism.

GDU, 2012: *Field report on Bugarama prospect*. Geothermal Development Unit, internal report, 9 pp.

Hunt, T.M., 2001: *Five lectures on environmental effects of geothermal utilization*. UNU-GTP, Iceland, report 1, 109 pp.

JICA, 2013: *Data collection for geothermal development in Rwanda*. Japan International Cooperation Agency, internal report.

Kristmannsdóttir, H., and Ármannsson, H., 2003: Environmental aspects of geothermal energy utilization. *Geothermics*, 32, 451-461.

MINECOFIN, 2000: *Rwanda vision 2020*. Ministry of Finance and Economic Planning, Kigali, Rwanda, 29 pp.

MINECOFIN, 2012: *Economic development & poverty reduction strategy (EDPRS) 2013 – 2018*. Ministry of Finance and Economic Planning, Kigali, Rwanda, 34 pp.

MML, 2013: *Karisimbi final ESIA report, vol. II*. Mott MacDonald Ltd., Karisimbi Geothermal Exploration Drilling Project 3, 11 pp.

NISR, 2012: *2012 population and housing census*. National Institute of Statistics, Rwanda, 166 pp.

Ogola, P.F. A., 2007: Environmental impact assessment general procedures. *Presented at Short Course II on Surface Exploration for Geothermal Resources, organized by the UNU-GTP and KenGen, Naivasha*, 7 pp.

RDB, 2014: Environmental Impact Assessment. Rwanda Development Board, webpage: www.rdb.rw/one-stop-centre/environment-impact-assessment.html

REMA, 2006: *General guidelines and procedures for environmental impact assessment*. Rwanda Environmental Management Authority, Kigali, Rwanda, 52 pp.

Republic of Rwanda, 2007: *The expropriation law in public interest N°18/2007 of 19/04/2007*. Official Gazette of the Republic of Rwanda.

Republic of Rwanda, 2010: *Ministerial order N °002/16.01 of 26/04/2010 determines the reference land price outside Kigali city*. Official Gazette of the Republic of Rwanda.

Rusizi, 2013: *District potentialities assessment for the integrated and self-centred local economic development*. Rusizi district, report, 243 pp.

UNECE, 1991: Introduction to Espoo Convention 1991. United Nations Economic Commission for Europe, environmental policy, webpage: www.unece.org/env/eia/eia.html.

VSÓ, 2013: *EIA proposal. Eldvörp, Grindavík. Access road, drilling pads and exploration*. VSÓ engineering, Reykjavík, 29 pp.

WB, 1999: *Environmental assessment*. World Bank, Operation policies, OP 4.01, 34 pp.

WHO, 1999: *Guidelines for community noise*. World Health Organization, report.



UNITED NATIONS
UNIVERSITY

UNU-GTP

Geothermal Training Programme

Orkustofnun, Grensasvegur 9,
IS-108 Reykjavik, Iceland

Reports 2014
Number 32

GEOCHEMICAL STUDIES OF GEOTHERMAL FLUID AND EVALUATION OF WELL TEST RESULTS FROM WELLS SM-01, SM-02 AND SM-03, SOL DE MAÑANA FIELD, GEOTHERMAL PROJECT, LAGUNA COLORADA, BOLIVIA

Daniel Gustavo Villarroel Camacho

Empresa Nacional de Electricidad (ENDE)

Av. Ballivián N°503, Cochabamba

BOLIVIA

daniel.villarroel@ende.bo, danielg.villarroel@gmail.com

ABSTRACT

ENDE (National Electricity Company of Bolivia) carried out well testing of wells SM-01, SM-02 and SM-03 in the geothermal field Sol de Mañana in 2013, twenty six years after they were drilled. Temperature, pressure and spinner logging were carried out under static (non-flow) and discharging conditions. The flow rates and enthalpies were measured using the Russell James and TFT methods and the results obtained showed a good correspondence between the two methods. According to the steam flow obtained by TFT, wells SM-01, SM-02 and SM-03 may generate 7, 7.8 and 8.2 MWe, respectively. Samples of brine and steam were collected during discharge through each of the four orifice plates used during the tests. Samples for silica analysis were not properly preserved. Calculations based on silica concentrations, such as reservoir concentrations, and temperatures, based on geothermometers, were not reliable due to silica polymerization. A Na/K geothermometer was in agreement with temperatures obtained from logs. Ternary diagrams of cations and anions showed a reservoir temperature of 280°C and classifies the fluid as mature water. Amorphous silica is expected to form at 150°C and 4.8 bar-a. The calcite solubility curve showed an uncommon behaviour, perhaps due to unreliable pH values. A mineral called Teschemacherite (NH_4HCO_3) was observed in well SM-02. Teschemacherite is a possible cause of the clogging of well SM-05. A special approach was performed in order to determine the scaling potential of Teschemacherite but, unfortunately, the necessary thermodynamic information was not available.

1. INTRODUCTION

1.1 Location and description

Bolivia is located in the centre of South America between the meridians 57°26' - 69°38' western longitude and 9°38' - 22°53' southern latitude. The South American tectonic plate is bordered by the Nazca and Antarctic plates to the west. These three plates meet at the Chile triple junction, and Bolivia is located above the subduction of the Nazca Plate. Bolivia is divided into the Andes to the west and

Amazon land to the east. The Bolivian Andes are comprised of three main ranges: Cordillera Occidental to the west (on the border with Chile), Cordillera Central, and Oriental to the east.

In addition to these mountain ranges, the Altiplano plateau extends over a large area between the Cordillera Occidental and the Cordillera Central. The plateau is around 700 km long and has a maximum width of approximately 200 km. The average elevation is close to 3.750 m a.s.l.

1.2 Geology

The geothermal field of Sol de Mañana is located in the Cordillera Occidental in the southwest part of Bolivia, close to the triple border of Bolivia-Chile-Argentina. The rocks exposed at the surface were formed principally during the Tertiary and Quaternary periods (SERGEOTECMIN, 1996), as shown in Figure 1.

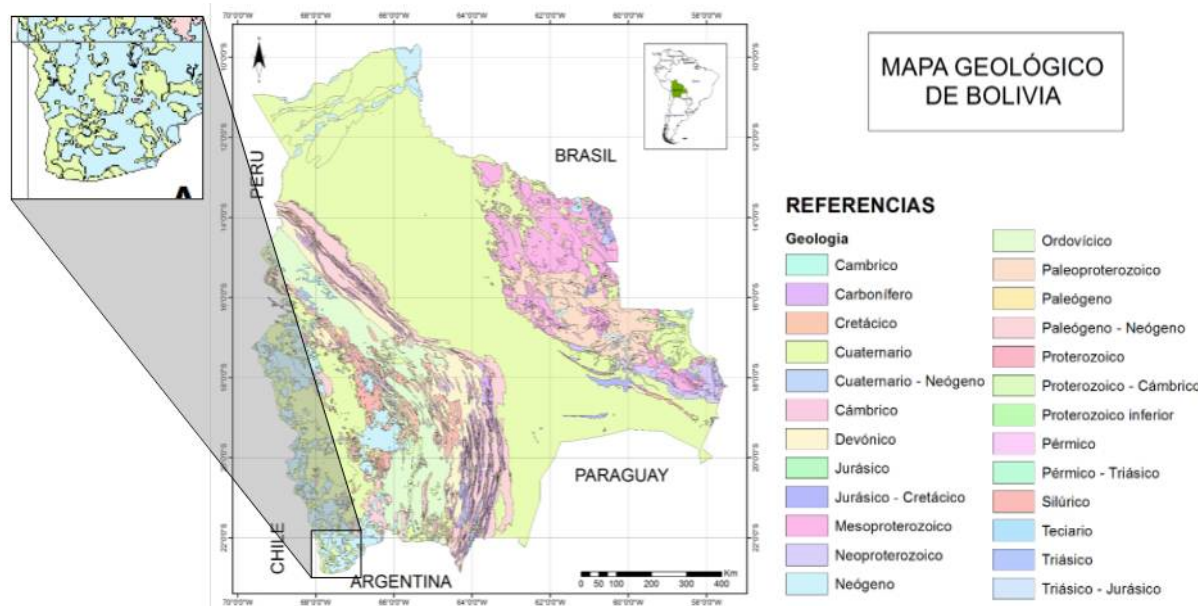


FIGURE 1: Geological map of Bolivia, with emphasis on the area of geothermal field Sol de Mañana (SERGEOTECMIN, 1996)

2. BACKGROUND

ENDE (National Electricity Company) and GEOBOL (Bolivian Geological Survey) started geothermal development in Bolivia in the 1970s with a reconnaissance study in Cordillera Occidental of the Western Andes Mountains which constitute the border with Chile. Forty two major geothermal manifestations have been studied and it was concluded that there are significant geothermal potential in the southwest region (GEOBOL, 1976).

In 1976, ENDE and the Ministries of Energy and Hydrocarbons, with funds from the United Nations Development Programme – UNDP, began evaluating Bolivian geothermal potential, based on the study by GEOBOL. Seven prospective geothermal areas were identified: Volcán Sajama, Empexa, Salar de la Laguna, Volcán Ollague-Cachi, Laguna Colorada, Laguna Verde and Quetena. Three of the seven fields were considered the most promising: Laguna Colorada, Sajama, and Valle de Río Empexa. They are located along the Occidental Cordillera of the Andes.

From 1978 to 1980, ENDE carried out a prefeasibility study for geothermal power plant construction in Laguna Colorada¹. In 1989, a technical-economic evaluation was done, considering the installation of a 30 MW_e plant (ENDE, 1989).

In 1988, the government of Italy, through ENEL, and with technical cooperation of YPFB (Bolivian Oil Company), drilled the first geothermal well in Bolivia: Apacheta – 1. Wells SM-01, SM-02, SM-03 and SM-04 were drilled from 1988 to 1989. All of these wells produced steam except for well SM-04. However, well SM-04 has good permeability and could be used as an injection well. Well production varies between 350 and 370 t/h of geothermal fluid (steam and brine). Temperature and pressure logs indicated a reservoir temperature of 250-260°C and 30-48 bar, respectively (Villarroel, 2014).

From 1991 to 1992, ENDE deepened the reinjection well SM-04 from 1474 to 1726 m, and drilled production well SM-05. Unfortunately, due to a change in the political situation, the project was suspended in 1993.

From 1996 to 1997, ENDE contracted the Engineering Services of CFE of México to define the potential of the geothermal resources. CFE's study confirmed that the minimum potential of the field is 100 MWe. CFE concluded that the potential of the field is 120 MWe for 25 years, with the development of 20 production wells and 7 reinjection wells, for approximately 4400t/h of brine (CFE, 1997).

In 2010, Japan International Cooperation Agency – JICA, and the government of Bolivia started discussions on the finances of the construction of a 50 MWe geothermal power plant in Sol de Mañana, based on feasibility studies of 100 MWe done in 2008 and 2010 by West – JEC. This study contains a conceptual model of the field (Figure 2) (West JEC, 2010).

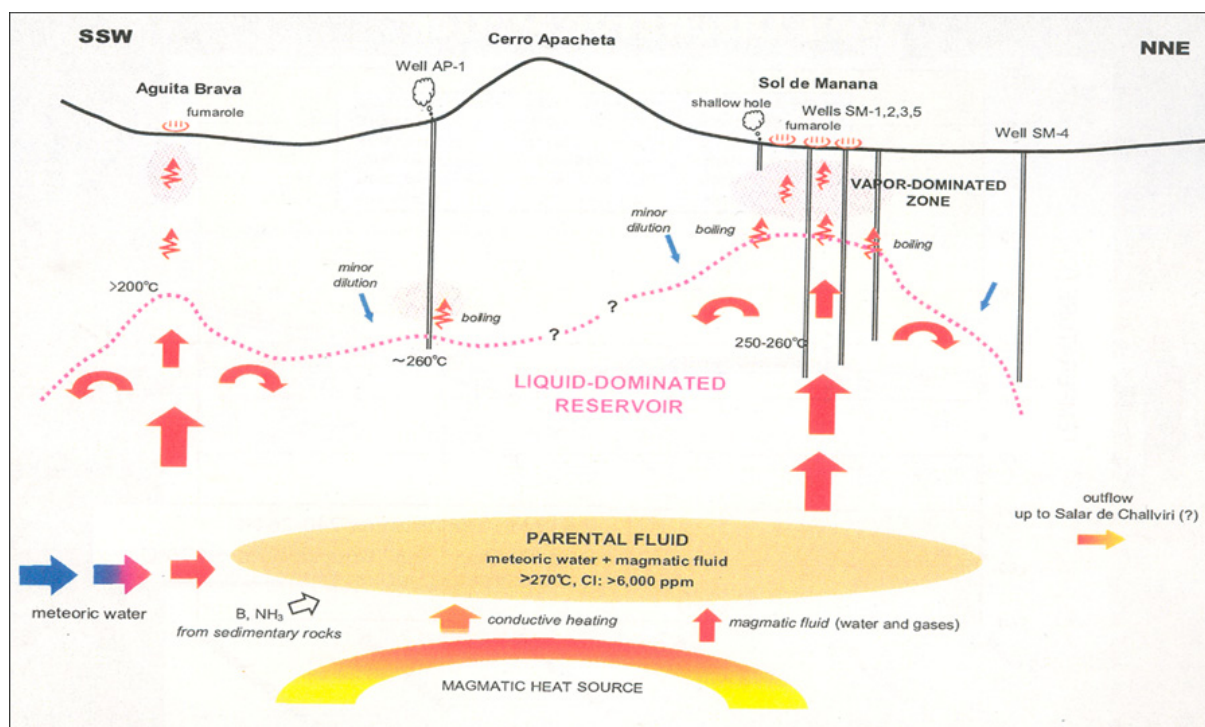


FIGURE 2: Conceptual model of geothermal field Sol de Mañana (West JEC, 2010)

¹ Laguna Colorada is not the geothermal field name, but just the representative name of the area where ENDE has its field camp. Sol de Mañana is the geothermal field's name.

In May 2011, the project's preparatory phase (phase zero) started. Wells SM-01, SM-02, SM-03 were tested, and reinjection into well SM-04 was carried out from Nov. 2012 - May 2013. Due to an obstacle in well SM-05, it was not possible to log and test the well (Villarroel, 2014). An MT survey was carried out in early 2014 by Teranov and CGG. A resistivity profile from SSW to NNE is shown in Figure 3.

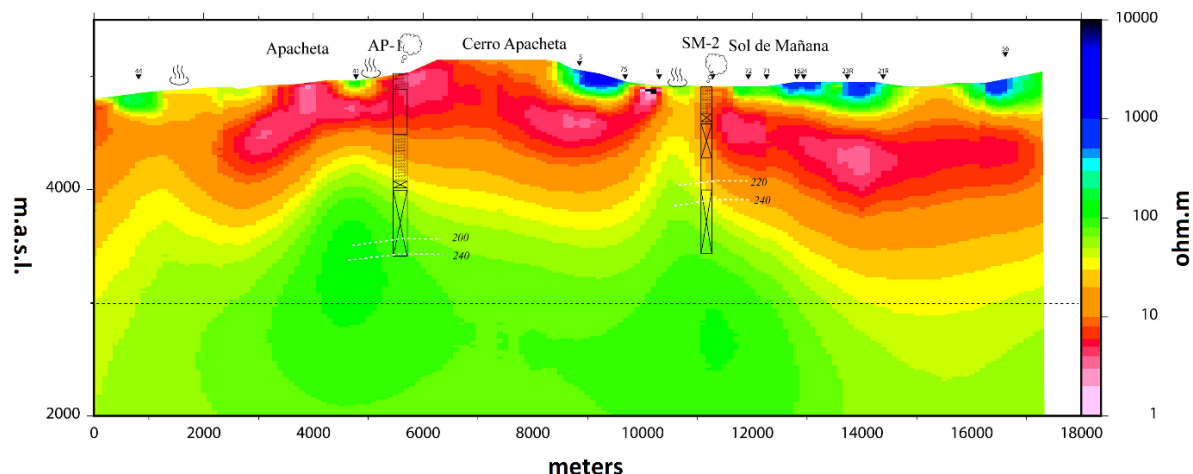


FIGURE 3: Resistivities in a SSW-NNE cross-section through the geothermal system Sol de Mañana (Teranov and CGG, 2014)

The data collected in phase zero is described and summarized in this report: well logs (temperature, pressure and spinner) in static and discharging conditions, different methods to measure the enthalpy and flow rate, evaluation and interpretation of the geochemical data, and estimation of possible scaling with emphasis on Tschermacherite (NH_4HCO_3) which was found in well SM-02, calcite and amorphous silica. Water from hot springs within the geothermal field has been monitored since 2011 in order to identify baseline conditions. The monitoring points LCN-1, LCN-2, LCN-3 and LCN-4 are located north of the project site, close to Laguna Colorada and the points Challviri, Polques I and II are situated at the east part of the field (Figure 4).

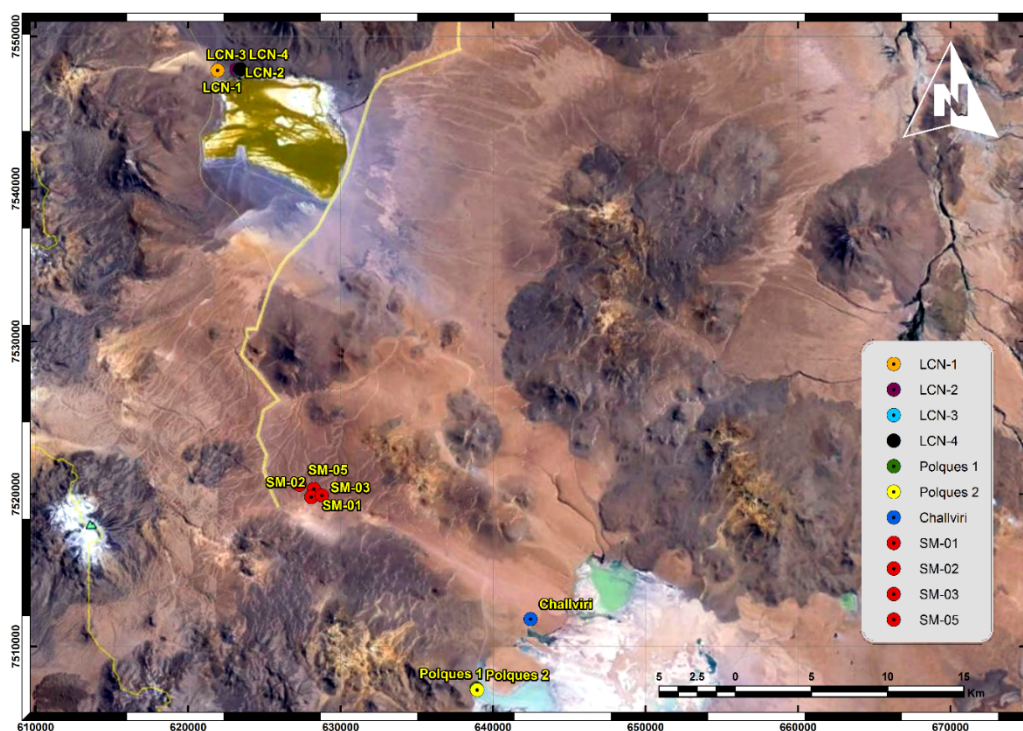


FIGURE 4: Location of monitoring points and Wells SM-01-SM-05

3. CHEMICAL CHARACTERISTICS OF DISCHARGE FROM WELLS SM-01, SM-02 AND SM-03

3.1 Status of the wells

3.1.1 Drilling history of well SM-01

The production well SM-01 was drilled in 1988 to a depth of 1180 m. The geological formations which the well passed through are considered to be of one main lithotype that is an ignimbrite of dacite composition with variable colours. The ignimbrite consists of quartz, plagioclase, biotite and hornblende, immersed in a vitreous matrix with a chaotic texture. Study of drill cuttings revealed three distinct hydrothermal alteration zones:

- Heulandite zone: 0 - 400 m;
- Quartz – chlorite zone: 400 - 780 m; and
- Epidote zone: 780 – 1180 m.

Quartz is stable at temperatures above 180°C (Franzson et al., 2003) and epidote appears at temperatures above 250°C (Franzson et al., 2008).

In general, the logged temperature corresponds to the hydrothermal mineralogical associations. The continuous increase in temperature downwards to the top of the reservoir (230 – 240°C) and the absence of significant losses of circulation suggests conductive conditions in the upper part of the well. An isothermal profile at the end of the well suggests a convective reservoir with an appreciable permeability.

The temperature logs clearly showed a temperature gradient of 20-35°C/100 m and a variation temperature of 230 – 240°C from 977 m to the bottom of the well. The pressure at 1000 m depth was 43 bar. An injection test, carried out when the well had reached a depth of 1180 m, showed values of $2.8 \text{ m}^3 \cdot \text{h}^{-1} \cdot \text{bar}^{-1}$ (ENEL, 1989a).

3.1.2 Drilling history of well SM -02

The drilling of production well SM-02 started in 1988 and was completed in 1989 at 1486.5 m depth. The strata in the upper part are characterized by dacitic ignimbrites, followed by dacitic lavas. Dacitic ignimbrites are found in the deeper part of the well. The study of secondary minerals shows four hydrothermal alteration zones:

- Clay minerals zone: 0 – 400 m;
- Wairakite zone: 525 – 800 m;
- Wairakite-epidote zone: 800 – 900 m; and
- Epidote- adularia zone: 950 – 1486.5 m.

Wairakite appears at temperatures close to 200°C (Steingrímsson et al., 1986) and epidote appears at temperatures above 250°C (Franzson et al., 2008).

The well crossed some low-absorption capacity formations between 810 and 1200 m, partial losses at 920 m and total loss of circulation at 1486.5 m, where an injectivity test revealed an index of $67 \text{ m}^3 \cdot \text{h}^{-1} \cdot \text{bar}^{-1}$ (ENEL, 1989b).

3.1.3 Drilling history of well SM-03

The production well SM-03 was drilled in 1989 down to 1406 m depth. The strata are characterized by formations of dacitic ignimbrites from the top to 970 m depth. No cuttings were returned from greater

depth due to total loss of circulation. It was possible to distinguish three zones of hydrothermal alterations:

- Clay minerals zone: 0 – 500 m;
- Quartz - chlorite zone: 500 – 705 m; and
- Epidote zone: 705-977 m.

Quartz is stable at temperatures above 180°C (Franzson et al., 2003) and epidote appears at temperatures above 250°C (Franzson et al., 2008).

The injectivity reaches $26.9 \text{ m}^3 \cdot \text{h}^{-1} \cdot \text{bar}^{-1}$ at the bottom. The temperature logs showed a thermal gradient of 20-25°C/100 m with variations of 98.2 – 186.61°C between 315-734 m depth (ENEL, 1990).

3.2 Logs of wells SM-01, SM-02 and SM-03

Temperature and pressure logging are normally carried out in order to locate feed zones, to study flow between feed zones, estimate the magnitude (permeability) of individual feed points and estimate formation temperatures. The temperature distribution in geothermal systems is determined by heat and fluid flow (water and steam) through the system.

The estimation of the formation temperature is the first step to understand how the system works and to setting up a conceptual model (Steingrímsson, 2013). The temperature profile also permits a simple definition of reservoir properties: 1) when rock is impermeable, heat is transported by conduction; the profile showed a gradient in function on the thermal conductivity of the rock; 2) when rock is permeable, heat transported is by convection; the profile shows an isothermal curve (Grant and Bixley, 2011).

Pressure is an essential parameter in geothermal reservoir studies. This property controls fluid flow in the reservoir. Logging is carried out in order to: study well conditions (fluid flow, boiling, etc.); map reservoir pressures; study transient pressure variations due to fluid injection or production; monitor long term pressure changes due to exploitation. Global pressure variations in the reservoir are the driving force for fluid flow; time variations of the pressure reflect changes in the flow pattern and the fluid reserve of the reservoir (Steingrímsson, 2013).

Temperature and pressure logs were carried out in static and discharging conditions, using electronic geothermal tool K-10. Spinner logs were also collected for discharging conditions. Due to an obstacle inside well SM-05, it was not possible to conduct logs in that well.

3.2.1 Well logs in static conditions

The temperature and pressure logs in static conditions in wells SM-01, SM-02 and SM-03 were collected on December 5th, 4th and 3th 2012, respectively. The logs are shown in Figure 5; a comparison of the pressures and temperatures at 900 m depth is shown in Table 1:

TABLE 1: Measurements of pressure and temperature at 900 m depth for wells SM-01, SM-02 and SM-03 at static conditions

Well	Pressure [bara]	Temperature [°C]
SM-01	32.9	238.7
SM-02	26.9	230.4
SM-03	31.7	235.4

According to Figure 5, the water levels in static (no-flow) conditions are located at 850, 700 and 530 m depth for wells SM-01, SM-02 and SM-03, respectively. At these points, the pressure (constant from initial level) shows a gradient in function of the water density.

Well SM-01 shows an increase in temperature from 20 to 180°C in the first 550 m; at this depth, the temperature increases suddenly to 230-235°C which is interesting as the water table is not reached until at ~900 m depth. From 600 to 1000 m, the temperature remains almost constant at this value. From surface down to 500 m, the temperature gradually increases from 25 to 185°C, possibly due to the presence of gases in this part of the well.

Well SM-02 shows a rapid increase in temperature until it reaches 185°C in the uppermost 50 m and remains constant down to the water table at 700 m depth. The low temperature in the uppermost 50 m is possibly due to the presence of gases. At 700 m, the temperature increases with a gradient of 20°C/100 m until it reaches approximately 235°C. Finally, an isothermal gradient was registered from 970 to 1150 m (235°C).

Well SM-03 shows a constant temperature between 0-530 m depth where a positive change in the gradient occurs, as does the pressure log at the same depth. Temperature remains constant at 250°C when it reaches 1200-1400 depth.

3.2.2 Well logs in discharging conditions

Production testing of well SM-01 was performed in December 2012. In order to evaluate the production well in different operating conditions, four orifice plates (2, 4, 6 and 10 inches) were used during the test. Unfortunately, the logs for the 10 inch orifice plate are not available for this well. The temperature, pressure and spinner logs are shown in Figure 6a.

The logging tool reached 1000 m depth in well SM-01. The temperature profile (Figure 6a) did not show drastic changes during the log and presented the same profile for each orifice plate. The temperature at 1000 m was 249°C. The same behaviour was observed in the pressure profiles. Pressure reached 40 bar at the same depth. The spinner graph showed the same behaviour for 4 and 6 inch orifice plates but registered lower values for the 2 inch orifice plate.

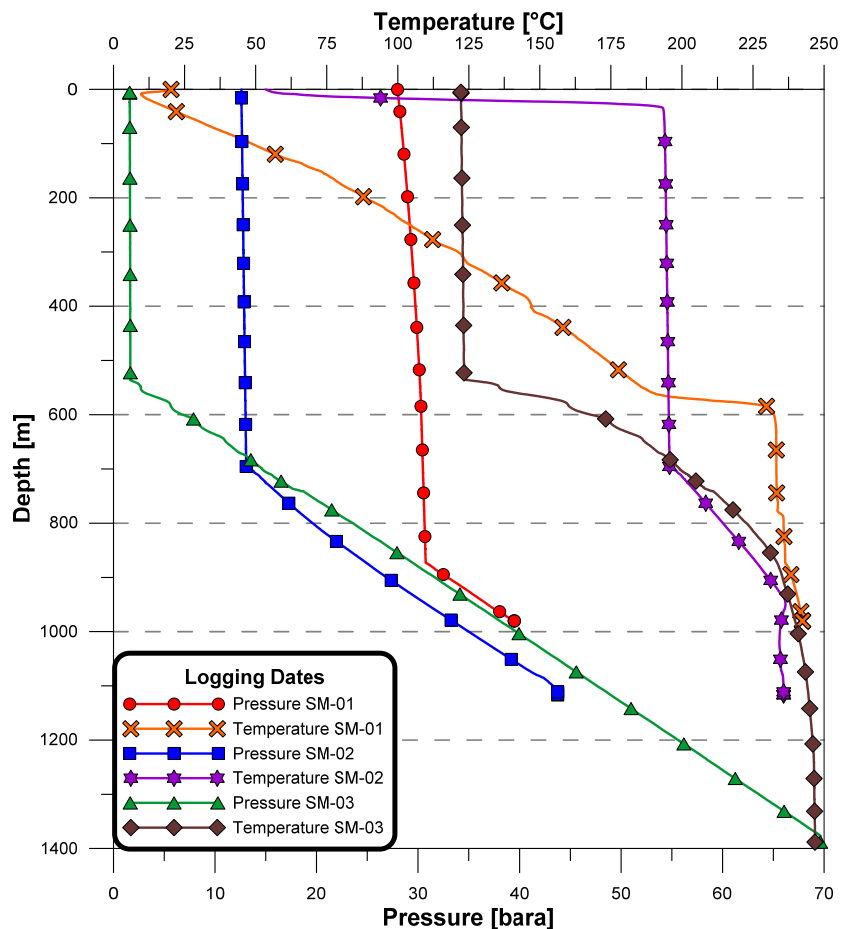


FIGURE 5: Temperature and pressure logs in static conditions for wells SM- 01, SM-02 and SM-03

The testing of well SM-02 was carried out in April 2013. Orifices plates of 2, 4, 6 and 10 (completely open) inches in diameter were used during the test. Unfortunately, logs during discharge through the 10 inch orifice plate are not available.

The logging tool reached 1250 m depth in well SM-02. The temperature profile (Figure 6b) did not show drastic changes until at 1050 m where an isothermal behaviour was observed for each orifice plate. The temperature measured at 1250 m was 250°C. The same behaviour was observed in the pressure profile. The spinner graph showed the same behaviour for 4 and 6 inch orifice plates but registered low values for the 2 inch orifice plate.

Finally, testing of well SM-03 was performed in February 2013, using the same sized four orifices plates mentioned above (Figure 6c). The temperature profile remained constant from 950 to 1300 m with a measured temperature of 247°C. The spinner logs indicated inflow in the region below 1250 m depth.

3.3 Description and comparison of two methods used to determine flow and enthalpy

3.3.1 Russell James method

The lip-pressure method is a relatively economical and convenient method for measuring two phase flows, such as in geothermal wells, due to its advantages of simplicity in both hardware and instrumentation, and its ability to accommodate relatively large flows with less expensive test equipment. The technique is based on an empirical formula developed by James (1966) and is also based upon measurements made in wells with a low content of non-condensable gas or dissolved solids (Kruger and Ramey, 1978).

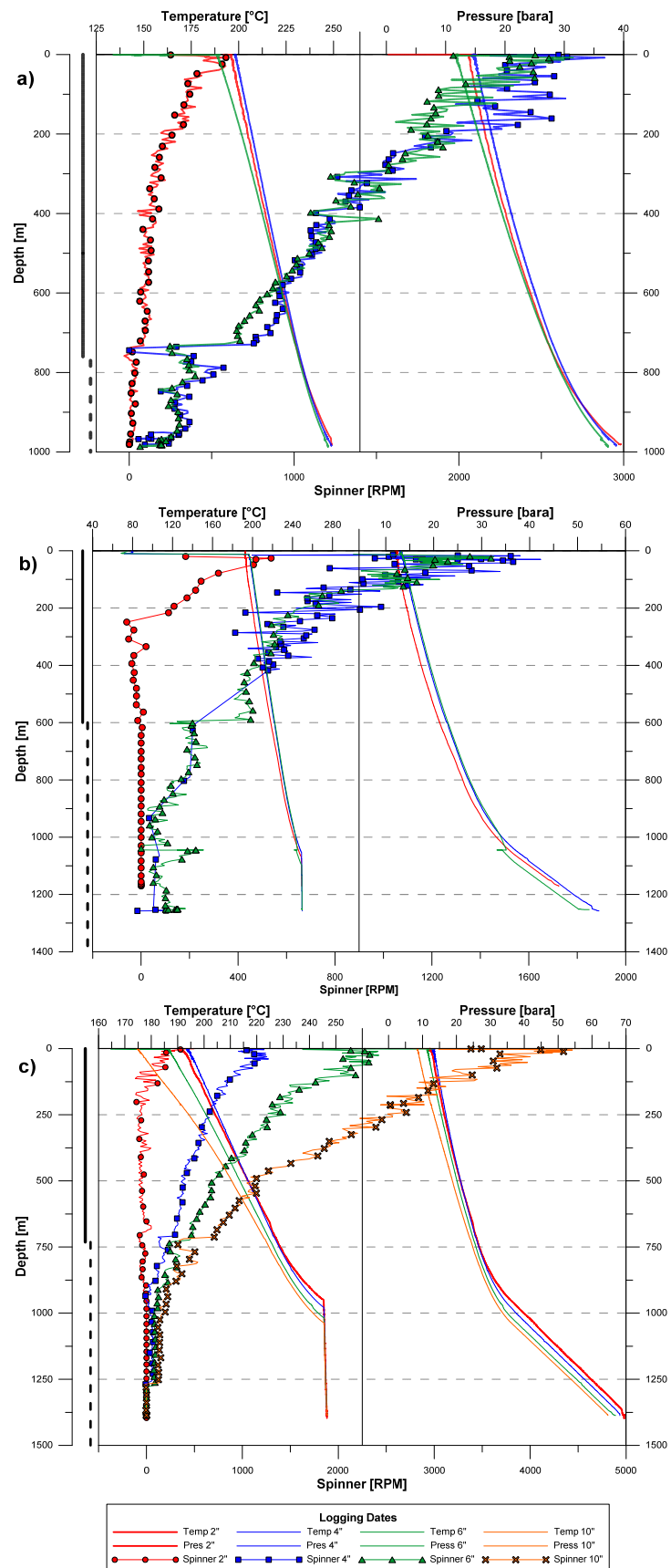


FIGURE 6: Temperature, pressure and spinner logs for wells (a) SM-01, (b) SM-02 and (c) SM-03 in discharging conditions

When the geothermal fluid is discharged to the atmosphere, it reaches sonic velocity on its way into an atmospheric pressure separator (or silencer). The lip pressure is measured at the expansion chamber, installed between the discharge pipeline and the silencer. Equation 1 relates mass flow, enthalpy and lip pressure as follows (Grant and Bixley, 2011):

$$\frac{G \times H^{1.102}}{P^{0.96}} = 663 \quad (1)$$

where G = W/A ;
 W = Mass flow [$T \cdot h^{-1}$];
 A = Cross-sectional area of the pipe [cm^2];
 H = Enthalpy of the mixture [$kJ \cdot kg^{-1}$];
 P = Lip pressure [bara].

The separated water flow is readily measured in a weir box or manifold installed behind the silencer. The equation to relate the total flow and the enthalpy is given by Equation 2:

$$W = W_{wa} \frac{h_{sa} - h_{wa}}{h_{sa} - H} \quad (2)$$

where W = Total flow [$T \cdot h^{-1}$];
 W_{wa} = Flow of liquid measured in the manifold [$T \cdot h^{-1}$];
 h_{sa} = Enthalpy of steam at atmospheric pressure [$kJ \cdot kg^{-1}$];
 h_{wa} = Enthalpy of liquid at atmospheric pressure [$kJ \cdot kg^{-1}$];
 H = Enthalpy of the mixture [$kJ \cdot kg^{-1}$].

The average atmospheric pressure in Sol de Mañana is 567 mbar.

Then, in order to solve Equations 1 and 2 simultaneously, the iteration starts with an arbitrary value of total enthalpy and calculates the total flow in both cases; the iteration finishes when the values of total flow are highly similar to a specific enthalpy value.

3.3.2 Tracer flow test method

Tracer flow testing (TFT) procedures are increasingly becoming the standard method for flow testing wells at operating geothermal power plants. The method allows for on-line testing of the wells, avoiding disruptions to power station operations and the need for dedicated well test facilities (Grant and Bixley, 2011).

The TFT procedure involves the quantitative injection, at precise rates, of relatively small amounts of chemical tracers (for steam and brine) into the discharge line of the production wells. The dilution of tracers depend on the flow rate, i.e. the higher the flow, the lower the concentration. At some distance downstream, steam and brine are sampled and analysed for the tracers. Sampling points must be far enough downstream from the injection point in order that the tracer becomes fully mixed with the two phase flow (Lovelock, 2006).

Equations 3 and 4 are used to calculate liquid and vapour phase flow rates (Grant and Bixley, 2011):

$$W_w = \frac{W_T}{C_{TW} - C_{BW}} \quad (3)$$

$$W_v = \frac{W_T}{C_{TV} - C_{BV}} \quad (4)$$

where W_W = Mass flow rate of liquid phase;
 W_T = Tracer injection mass flow rate;
 W_V = Mass flow rate of vapour phase;
 C_{TW} = Concentration of tracer in liquid phase by weight;
 C_{BW} = Background concentration of tracer in liquid phase;
 C_{BV} = Background concentration of tracer in vapour phase.

The TFT method also permits the calculation of the enthalpy, when the flow rates of liquid and steam and the conditions of sampling are known.

3.3.3 Results of flow measurements

Well testing was carried out between December 2012 and April 2013. Testing of wells SM-01, SM-02 and SM-03 was performed in December, April and March, respectively, and every well was monitored for one month (approximately one week per orifice plate); the results of the measurements of the flow rate and enthalpy are listed in Table 2.

In order to measure the sonic velocity of the fluid, an expansion chamber was installed at the end of the pipeline ahead of the silencer. A pressure gauge was installed into the expansion chamber to measure the lip pressure. Additionally, a weir box was installed behind the silencer in order to determine the flow rate of the separated brine.

The TFT method was carried out using a fluorescent and SF6 as liquid and steam tracers, respectively. The samples of brine and steam were collected in Webre separators installed 15-20 m past the injection point. In order to determine the concentration of the tracers in the brine and steam samples, a fluorimeter and electron capture detector (ECD) equipment were used, respectively.

TABLE 2: Results of flow rate measurements and enthalpy calculations, using the Russell James method and TFT method

Well	OP [inch]	WHP [barg]	Russell James method			TFT method				MWe ^b
			Total Flow [T/h]	Enthalpy [kJ/kg]	Steam Flow [T/h] ^a	Pres. Sep. [bara]	Total Flow [T/h]	Enthalpy [kJ/kg]	Steam Flow [T/h]	
SM – 01	2	14.3	43.2	1160.1	15.2	2.2	48.0	1075.2	12.3	1.7
	4	15.0	159.4	1076.2	50.1	6.8	166.7	1130.8	35.3	4.9
	6	12.2	251.5	1120.0	83.9	7.3	243	1064.9	42.4	5.9
	10	10.7	289.0	1112.6	95.5	8.7	285.7	1099.8	51	7
SM – 02	2	13.2	41.1	1102.9	13.4	1.9	38.8	1067.9	10.2	1.4
	4	14.4	145.7	1088.0	46.6	7.3	148.8	1166.8	33.4	4.6
	6	11.4	237.7	1091.8	76.4	5.6	234.6	1069.2	46	6.4
	10	9.6	283.7	1092.8	91.3	6.0	288.1	1075.9	56.2	7.8
SM – 03	2	12.7	38.1	1186.6	13.8	1.9	-	-	-	-
	4	13.5	146.7	1071.3	45.8	7.0	-	-	-	-
	6	11.7	208.7	1058.5	64.0	8.7	-	-	-	-
	10	8.9	270.0	1068.6	84.0	4.6	274.1	1083.7	59.1	8.2

^a Calculations take into account the flow of brine measured in a weir box.

^b Calculations from the steam flow obtained with TFT method and the assumption: It takes about 2 kg/s of high pressure steam (7 bar-a) to generate 1 MW of electric power in high-efficiency turbines (Steingrímsson, 2014).

The results of the enthalpy and flow rate are similar, with variations of less than 7% and 5%, respectively.

3.4 Chemical composition of brine and steam

Brine and steam samples were collected during the discharge tests. The samples were collected using a webre separator, connected to the two phase pipeline, 15 m from the wellhead. Two phase samples were collected during discharge through each of the four orifice plates for each of the three wells. Samples for isotopic analysis of steam and brine and chemical analysis of condensate were collected, only while discharging through the 10 inch orifice plate. The analytical results for the 10 inch samples are shown in Table 3.

TABLE 3: Results of chemical analysis of brine and steam from wells SM-01, SM-02, SM-03

Chemical analysis of water separated				Chemical analysis of steam condensate			
Sample well	SM-01	SM-02	SM-03	Sample well	SM-01	SM-02	SM-03
Orifice Plate	10"	10"	10"	Orifice Plate	10"	10"	10"
Date	1.01.13	25.04.13	23.02.13	Date	1.01.13	25.04.13	23.02.13
WHP [bara]	10.8	9.5	8.9	WHP [bara]	10.8	9.5	8.9
P.Sep. [barg]	8.1	5.4	4	P.Sep. [barg]	7.7	5.0	3.6
Na [mg/kg]	4060	4080	4310	B [mg/kg]	1.78	1.96	1.36
K [mg/kg]	704	697	720	SiO ₂ [mg/kg]	0.257	1.55	1.79
Ca [mg/kg]	206	192	219	Cl [mg/kg]	0.681	17.6	4.67
Mg [mg/kg]	0.042	0.027	0.100	Cond. [umhos/cm]	89.2	136	116
Li [mg/kg]	42.6	41.4	44.5	Lab pH	7.25	6.71	6.55
Sr [mg/kg]	3.92	3.64	3.94	δ ² H (‰), H ₂ O	-9.41	-10.15	-6.51
Ba [mg/kg]	0.392	0.372	0.251	δ ¹⁸ O (‰), H ₂ O	-88.6	-91.8	-82.1
Fe [mg/kg]	<0.05	<0.05	0.224	Chemical analysis of NCG ^a			
B [mg/kg]	162	161	157	Sample well	SM-01	SM-02	SM-03
SiO ₂ [mg/kg]	784	1330	619	Orifice plate	10"	10"	10"
Al [mg/kg]	0.284	0.032	0.104	Litres Gas/Kg	0.39	0.41	0.36
Sb [mg/kg]	0.681	0.681	0.445	condensate			
As [mg/kg]	27.4	27.9	33.1	Sample Gas/Steam	656	701	565
Mn [mg/kg]	0.094	0.092	0.093	Ratio [mg _{gas} /kg _{steam}]			
Cl [mg/kg]	7160	7100	7500	CO ₂ [% v/v]	85.2	88.3	78.0
F [mg/kg]	3.8	4.07	4.03	H ₂ S [%v/v]	8.13	6.06	7.6
Br [mg/kg]	6	5.94	6.14	NH ₃ [%v/v]	4.1	3.6	3.86
SO ₄ ²⁻ [mg/kg]	27.4	28.9	30.5	Ar [%v/v]	0.011	0.00859	0.0127
HCO ₃ ⁻ [mg/kg]	22.9	30.7	<2	N ₂ [%v/v]	2.26	1.75	1.55
CO ₃ ²⁻ [mg/kg]	<2	<2	<2	CH ₄ [%v/v]	0.338	0.282	0.173
NH ₄ ⁺ [mg/kg]	2.1	1.97	2.27	H ₂ [%v/v]	<6.4	<2.18	8.8
CO ₂ [mg/l]	16.5	22.1	<2	CBE%			
Iodide	<5	<5	<5		1.08	1.82	2.16
Cond. [umhos/cm]	22400	21900	22700				
TDS (Calculated)	13200	13700	13600				
Lab pH	6.98	7.12	4.32				
δ ² H (‰)	-82.7	-82.4	-91.7				
δ ¹⁸ O (‰)	-6.77	-6.63	-9.76				

^a Gas concentrations in volume percent of dry gas.

Samples for silica analysis were not properly preserved when collected. The silica analyses were carried out in two ways: The samples were acidified to pH 2 with nitric acid and analysed; this way was called "as received". However, due to silica polymerisation, a considerable amount of silica precipitated. Sodium hydroxide was added to the remaining sample fractions until pH 12 was reached before it was heated to 100°C for about 40 minutes; this way was called "digested". Table 3 shows only values for silica "digested". For these reasons, the calculations which used silica concentrations, e.g. geothermometers, were not reliable.

A significant variation was observed between the pH measured during the sampling and the pH issued by the laboratory, 7.31 at 8.6°C and 4.32 at lab temperature (20-25°C), respectively, for well SM-03. These pH and silica variations could be related as silica polymerization may change the pH of water

samples in two ways: by formation of oligomers that tend to decrease pH, and by removal of monomeric silica (weak acid) that tends to increase pH (Karingithi et al., 2010). Unfortunately, there are no pH field values for other wells to confirm that theory, and it was not possible to compare with the pH analysed in the laboratory. As the pH values are important in chemical modelling, this may have caused inaccuracies in the models/calculations discussed in this report.

While sampling the water phase, it is a common procedure to try to avoid possible degassing effects from the bottles, especially for the analysis of pH. Degassing is associated with loss of CO₂, and the concentration of CO₂ in the samples is highly related to the carbonate species (H₂CO₃, HCO₃⁻, CO₃⁻²). In this regard, if a sample is degassed, the pH tends to decrease. In order to avoid these issues, it is always recommended to measure the pH as soon as possible. The liquid samples from wells SM-01, SM-02 and SM-03 were not properly preserved and the pH measurements were carried out many days after the samples were collected. Thus, it is possible that degassing may have affected the pH measurements.

All the results issued by the laboratory are shown in Table 3, as well as the sampling conditions and wellhead pressure. The chemical speciation program WATCH (Bjarnason, 2010) was used to calculate the composition of the reservoir liquid and scaling potential. The WATCH program considered an atmospheric pressure of 1013 mbar. The input data were corrected, as the average atmospheric pressure in the field is 567 mbar (5000 m a.s.l.).

Table 4 shows the concentrations of the components in the reservoir, as calculated by the WATCH program at reservoir temperatures of 249, 250 and 247°C for wells SM-01, SM-02 and SM-03, respectively. The ion activity and solubility product constants, Q and K, for some minerals were obtained from the WATCH program. Scaling potential will be discussed in Chapter 3.7. However, it is necessary to mention that the calculations indicated a calcite oversaturation in the reservoir. The most likely explanation is the lack of accurate pH values. The saturation state was corrected and re-calculated in order to obtain corrections for the pH value. The calculated pH was 6.33 and 6.01 for wells SM-01 and SM-02, respectively; it was not necessary to make a correction in the pH for well SM-03.

TABLE 4: Calculated composition of the reservoir liquid from wells SM-01, SM-02 and SM-03, assuming reservoir temperatures of 249, 250 and 247°C, respectively

	SM-01	SM-02	SM-03
B [mg/kg]	134.54	128.90	124.00
SiO ₂ [mg/kg]	651.09	1064.79	488.88
Na [mg/kg]	3371.7	3266.4	3404.0
K [mg/kg]	584.65	558.02	568.65
Mg [mg/kg]	0.035	0.022	0.079
Ca [mg/kg]	171.08	153.71	172.96
F [mg/kg]	3.156	3.258	3.183
Cl [mg/kg]	5946.2	5684.2	5923.4
SO ₄ [mg/kg]	22.75	23.14	24.09
Al [mg/kg]	0.236	0.026	0.082
Fe [mg/kg]	0.000	0.000	0.177
TDS [mg/kg]	10962.2	10968.2	10741.1
CO ₂ [mg/kg]	116.1	148.9	107.3
H ₂ S [mg/kg]	7.56	6.97	8.09
NH ₃ [mg/kg]	3.65	3.65	3.85
H ₂ [mg/kg]	0.00	0.00	0.56
O ₂ [mg/kg]	0.00	0.00	0.00
CH ₄ [mg/kg]	0.15	0.15	0.09
N ₂ [mg/kg]	1.73	1.65	1.36
pH	5.08	5.76	5.27

All the calculations were performed using these pH corrected values. Dramatic changes in the concentrations of the components and/or species, e.g. the values of the Charge Balance Error (CBE), were not observed.

The CBE was calculated using Equation 5:

$$CBE(\%) = \frac{\sum z_{cat} m_{cat} - \sum z_{an} m_{an}}{2[\sum z_{cat} m_{cat} + \sum z_{an} m_{an}]} \cdot 100\% \quad (5)$$

where z_i = Charge of cation or anion i ;
 m_i = Molal concentration of i [mol/kg].

When the value of CBE is less than 10%, the analysis of samples can be considered complete; the most representative compounds have been taken into account for the analysis.

Table 4 shows the concentration of the components at reservoir conditions, while the temperature was obtained from the logs (Section 3.2). The concentrations are similar between the wells with some exceptions, such as silica (discussed above), aluminium and iron. However, it is necessary to continue sampling and chemical analysis in order to confirm the values.

3.5 Classification of thermal waters

The most common type of fluid found at depth in high-temperature geothermal systems is with near-neutral pH, with high chloride concentrations compared to the anions. However, other types of water can be derived from geothermal fields, owing to chemical or physical processes. (Nicholson, 1993).

In this sense, the representation of the concentrations of the principal anions and cations are useful in order to classify the types of waters. In this report, the diagrams Cl-HCO₃-SO₄ and Na-K-Mg were used in order to classify the waters.

3.5.1 Cl-SO₄-HCO₃ Ternary diagram

The Cl-SO₄-HCO₃ ternary diagram is commonly used to classify geothermal fluids on the basis of the major anion concentrations. The plot aids in identifying the various water types, and assists in recognizing waters which are most suitable for geothermometry. The construction of the triangular graph result is relatively easy; the relationships between the anions are given by Equation 6 (Nicholson, 1993):

$$\sum Anion = C_{Cl} + C_{SO_4} + C_{HCO_3} \quad (6)$$

$$\%Cl = \frac{C_{Cl}}{\sum Anion} 100 \quad ; \quad \%SO_4 = \frac{C_{SO_4}}{\sum Anion} 100 \quad ; \quad \%HCO_3 = \frac{C_{HCO_3}}{\sum Anion}$$

where C_x = Concentration of the species [mg·kg⁻¹].

Bicarbonate represents the total concentration of all carbonate species in the water. According to the location of the points on the graph, the fluid can be classified into the following categories:

- **Mature waters:** These kinds of water contain high concentrations of chloride and are known as “alkali-chloride” or “neutral-chloride”; they are typical of the deep geothermal fluid found in most high-temperature systems where the pH is usually neutral. Chloride is used as a tracer in geothermal investigations because it is a conservative ion in geothermal fluids, as it does not take part in reactions with rocks after it has dissolved (Dolgorjav, 2009).
- **Peripheral waters:** Contains high concentrations of bicarbonates, possibly due to mixing with cold groundwater or can indicate the presence of carbonate rocks (Wei, 2006).

- **Steam heated waters:** The dominant cation is sulphate; these waters can originate from the condensation of geothermal gases into the liquid near the surface, but sometimes their origin can be related to equilibria deep down in the geothermal systems, and that may even be useful for interpretation. Although usually found near the surface at <100 m depth, sulphate waters can penetrate to depth through faults in the geothermal system. Since the concentration of silica and most cations is only the product of near-surface leaching, such steam-heated waters cannot be employed in geothermometry, as the concentrations of the dissolved constituents bear no relation to the mineral-fluid equilibria in the reservoir (Nicholson, 1993).

The Cl-SO₄-HCO₃ diagram for the geothermal fluid and the hot springs of Sol de Mañana field is presented in Figure 7.

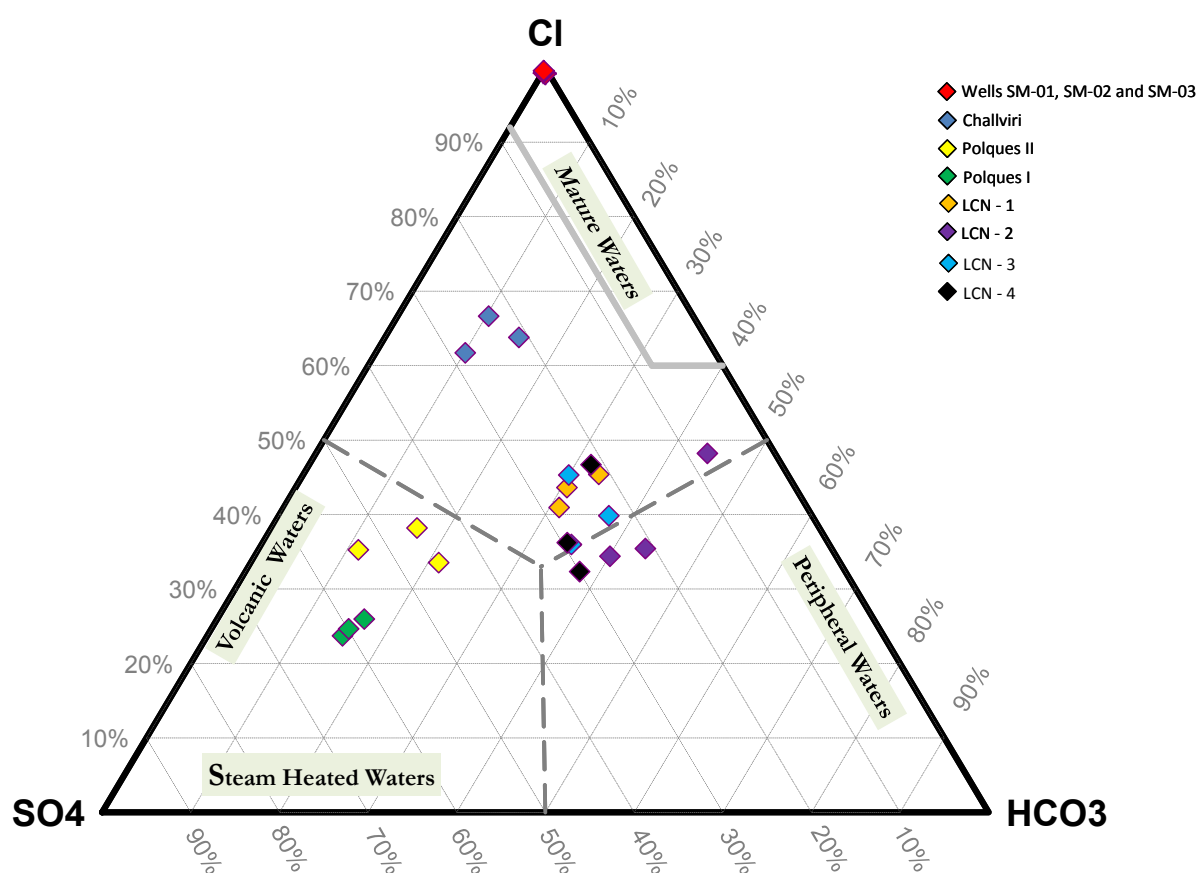


FIGURE 7: Cl-HCO₃-SO₄ ternary diagram for wells SM-01, SM-02, SM-03 and the hot springs of Sol de Mañana field

The points identifying the fluid from the wells are located in the chloride corner. It is common to observe this behaviour in high temperature systems with neutral pH. However, the issues with pH from these wells were explained in the previous section.

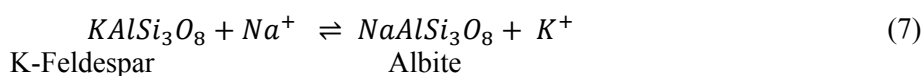
The points identifying the hot waters collected from surface manifestations (i.e. LCN-1, LCN-2, LCN-3 and LCN-4) show a similar concentration of the three species. These monitoring points are located around 30 km north of the geothermal field (Figure 4) and are not thought to be related to these waters. The hot water of LCN-1, LCN-2, LCN-3 and LCN-4 may postulate the presence of another heat source in Laguna Colorada.

Challviri shows a similar relationship of sulphate, comparative to the points of LCN, but different in chloride and carbonates. Polques I and II are the points with the highest relative content of sulphate. These manifestations may be influenced by the condensation of geothermal gases.

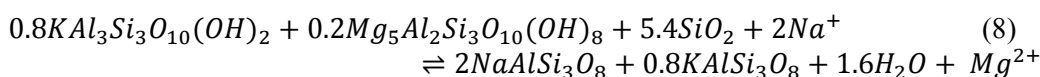
3.5.2 Ternary diagram Na-K-Mg

The Na-K-Ca ternary diagram is used to classify waters into fully equilibrated, partially equilibrated and immature waters, based on the relationships between these three cations, and can also determine reservoir temperature (geothermometer). In general, geothermometers can provide very good approximations when the water is fully equilibrated. The relationships between these cations are based on the following three reactions (Saudi, 1999):

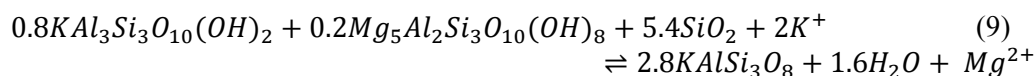
The relationship between potassium and sodium is given by Equation 7 (Giggenbach, 1998):



The relationship between sodium and magnesium is given by: muscovite, clinochlore, silica and ion sodium with albite, k-feldspar, water and ion magnesium (Equation 8) (Giggenbach, 1998):



And finally, the relationship between potassium and magnesium: muscovite, clinochlore, silica and ion potassium with k-feldspar, water and ion magnesium (Equation 9) (Giggenbach, 1998):



This ternary diagram is constructed, based on these ion relationships. Points representing the liquid from the wells and hot springs are plotted in Figure 8.

According to Figure 8, the points representing the wells are plotted in the zone of full equilibration with a temperature of 280°C in the reservoir. The points representing liquid from LCN-1, LCN-2, LCN-3, LCN-4, Challviri, Polques I and II are plotted in opposite corners with a relatively high concentration of magnesium. Higher concentrations of magnesium can indicate near-surface reactions leaching Mg from the local rock, or dilution by groundwater (Nicholson, 1993).

3.6 Geothermometers

Geothermometers are a valuable tool in the evaluation and monitoring of geothermal reservoirs. It is based on mineral solubility, e.g. silica, exchange reactions Na-K, Na-K-Ca, etc. (see Chapter 3.5.2) and in gas mineral equilibria, such as CO₂, H₂, CO₂-H₂ and others (Arnórsson, 2000).

For a successful use of geothermometers, it is important to apply the following assumptions: the concentration of the elements or species is controlled only by a temperature-dependent mineral-fluid reaction; the reactions reach equilibrium in the reservoir; there is no mixing or dilution of the deep fluid; no near-surface reactions; and there is an abundance of the minerals and/or dissolved species in the rock-fluid system for the reaction to occur readily (Nicholson, 1993).

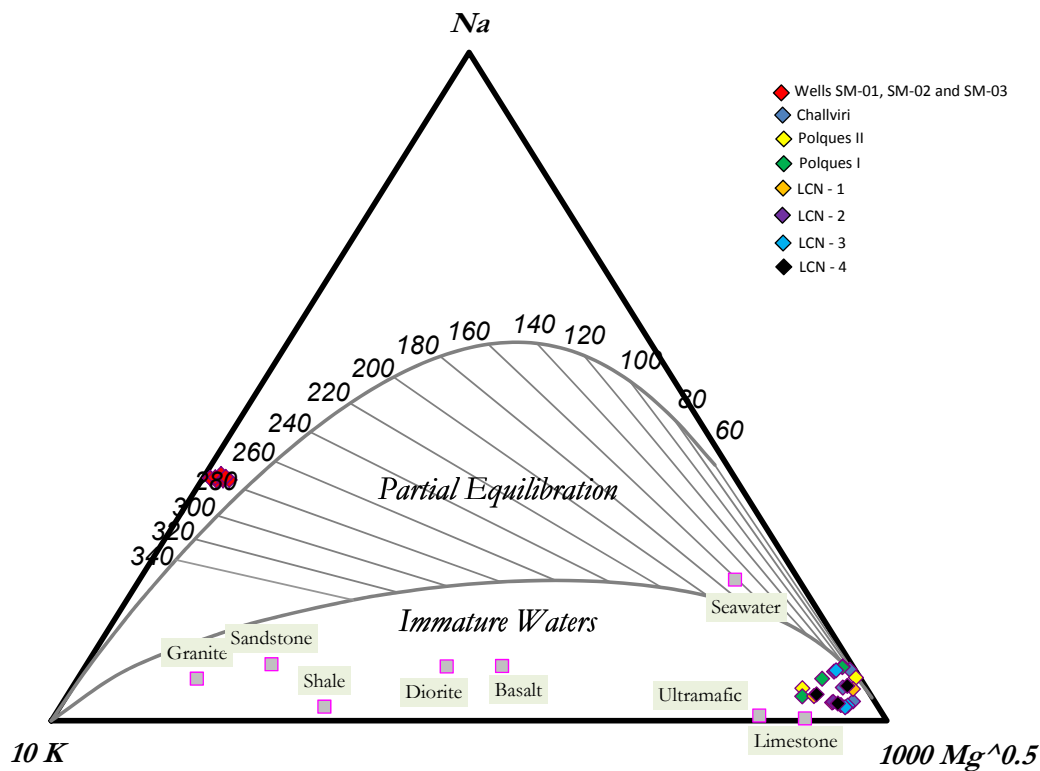


FIGURE 8: Na-K-Mg ternary diagram for wells SM-01, SM-02, SM-03 and the hot springs of Sol de Mañana field

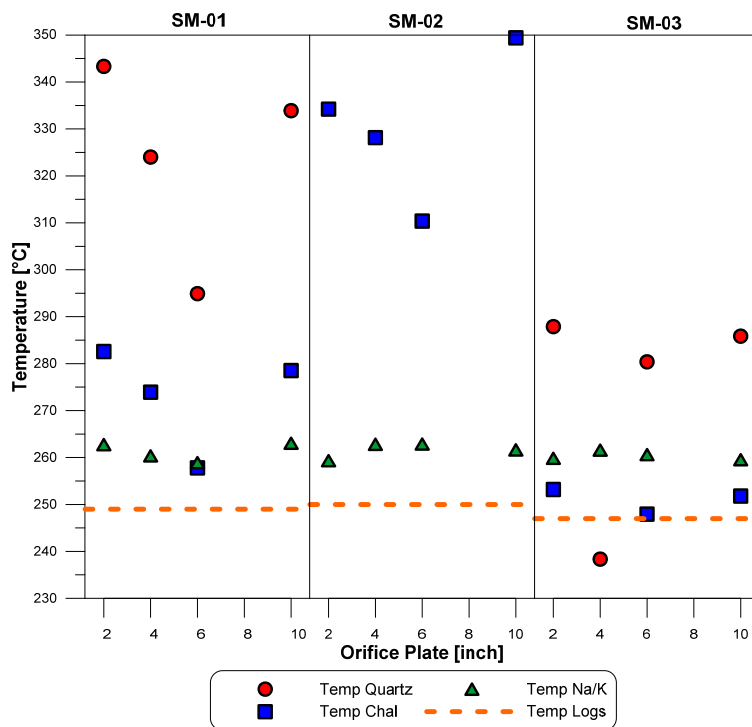


FIGURE 9: Comparison between calculated temperature based on quartz, chalcedony and Na/K geothermometers and logs for wells SM-01, SM-02 and SM-03; Quartz temperature was not plotted for well SM-02 due to shown values of more than 370°C

3.6.1 Water geothermometers

Theoretically, any cation ratio and any uncharged aqueous species concentration can be used as a geothermometer, as long as equilibrium prevails. In this way, many geothermometers have been studied and applied since the last century. Currently, silica (quartz and chalcedony), Na-K and Na-K-Ca are the most important geothermometers. Figure 9 shows a comparison between the measured reservoir temperature in wells SM-01, SM-02 and SM-03 and calculated temperatures based on quartz, chalcedony and Na/K geothermometers. The equations used for the calculation of the geothermometers are given in Table 5.

Temperatures based on quartz and chalcedony (silica) are not in agreement with the temperature measured, due to silica polymerisation, but a considerable

amount of silica precipitated during the transport of the samples to the laboratory, as was explained in Section 3.4. The digestion was performed in the remaining sample, after the first analysis (called “as received”) (Section 3.4). Probably this explains the relatively high silica concentration and the high values of calculated temperature based on these geothermometers. According to Table 5, the relationship between silica and the temperature is direct.

TABLE 5: Geothermometer equations for liquid phase

Geothermometer	Equation (T°C)	Source
$T_{qtz,FP} (SiO_2)^a$	$-42.2 + 0.28831S - 3.6686 \times 10^{-4}S^2 + 3.1665 \times 10^{-7}S^3$ $+ 77.034 \log S$	(1)
$T_{chal,AR} (SiO_2)^a$	$\frac{1112}{4.91 - \log S} - 273.15$	(2)
$T_{Na/K,AR} (Na/K)^b$	$\frac{1319}{1.699 + \log Na/K} - 273.15$	(3)

(1) Fournier and Potter (1982); (2),(3) Arnórsson et al. (1983)

^a S is SiO₂ in [mg·kg⁻¹]. ^b Na/K in [mg·kg⁻¹]

However, the Na/K geothermometer shows a very stable relationship for all the wells in all the operating scenarios. The average temperature of 260°C is a very good representation of the temperature obtained in the logs.

3.6.2 Gas geothermometers

Gas geothermometers have been developed since the 1980s and, currently, their use is common around the world, especially when geological exploration is carried out and the ratios of steam/water, gas/steam and others are unknown (Arnórsson, 2000).

Figure 10 shows the temperature of gas geothermometers applied to the wells and the fumaroles located around the wells. The temperature, based on H₂S, has a good relationship with the temperature measured in the wells. However, for the fumaroles, the values were relatively high. The same happens with the temperature of CO₂; the values for wells SM-01 and SM-03 were not plotted, due to the very low values.

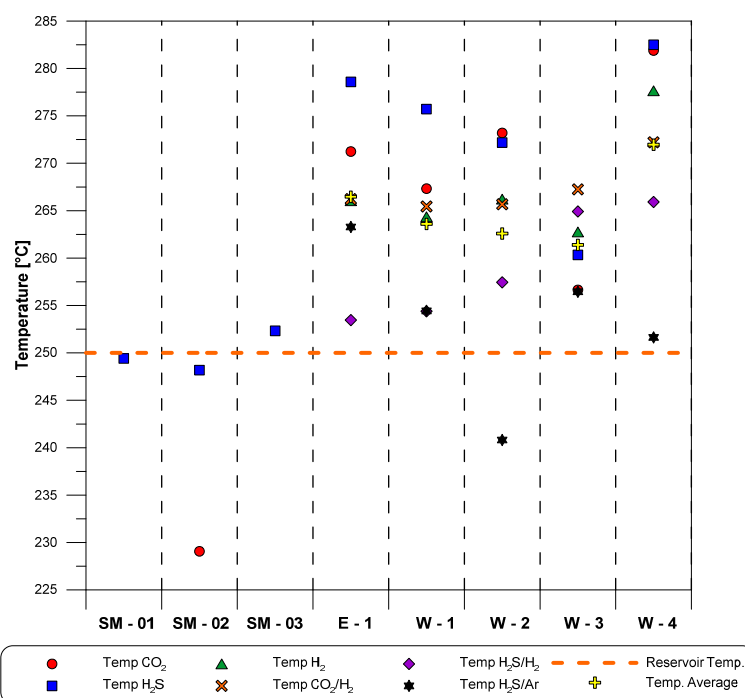


FIGURE 10: Comparison between reservoir and gas geothermometer gases for wells SM-01, SM-02, SM-03 and fumaroles points E-1, W-1-4, located on the geothermal field

In the case of fumaroles, the sensitivity of CO₂ and H₂S can be affected by condensation, boiling and dilution in the upflow below the manifestation. The use of geothermometers based on gas ratios removes such problems. The Argon concentration from an atmospheric source in the deep geothermal fluid is equal to that of air-saturated water (Arnórsson, 2000). The H₂S/Ar geothermometer gave a temperature close to the temperature of the reservoir. However, the average of all the geothermometers used in this

case present a value between 265 and 270°C. The Equations with which the geothermometers were calculated are shown in Table 6.

TABLE 6: Geothermometer equations of gases

Geothermometer	Equation (T°C)	Source
$T_{CO_2} (CO_{2,g})^a$	$-44.1 + 269.25Q - 76.88Q^2 + 9.52Q^3$	(1)
$T_{H_2S} (H_2S_g)^b$	$246.7 + 44.8Q$	(1)
$T_{H_2} (H_{2,g})^b$	$277.2 + 20.99Q$	(1)
$T_{CO_2/H_2} (CO_{2,g}/H_{2,g})^b$	$341.7 - 28.57Q$	(1)
$T_{H_2S/H_2} (H_2S_g/H_{2,g})^b$	$304.1 - 39.48Q$	(1)
$T_{H_2S/Ar} (H_2S_g/Ar_g)^c$	$4.108Q^2 + 42.265Q + 137.6$	(2)

Q denotes the logarithm of the respective gas concentration or gas ratio $\log (\text{mol} \cdot \text{kg}^{-1})$

(1) Arnórsson and Gunnlaugsson (1985); (2) Arnórsson et al. (1998)

^a For all waters; ^b All waters above 300°C and waters in the range 200-300°C for $Cl > 500$ ppm. ^c Ar concentrations in geothermal reservoirs waters are equal to those in air-saturated water at 5°C

3.7 Speciation calculations and mineral saturation

As mentioned in Chapter 3.4, the WATCH program is a powerful tool used to describe the aqueous speciation distribution in the aquifer. WATCH has a thermodynamic database of some minerals (anhydrite, calcite, prehnite, wairakite, etc.). In order to determine possible scaling, the program allows the user to take into account different boiling steps for evaluation of the equilibrium state. The saturation state is evaluated by comparing the reaction quotient Q and the equilibrium constant of solubility K. Therefore, at equilibrium $K=Q$; for an under-saturated solution, $Q < K$, and for a super-saturated solution, $Q > K$ (Arnórsson, 2000).

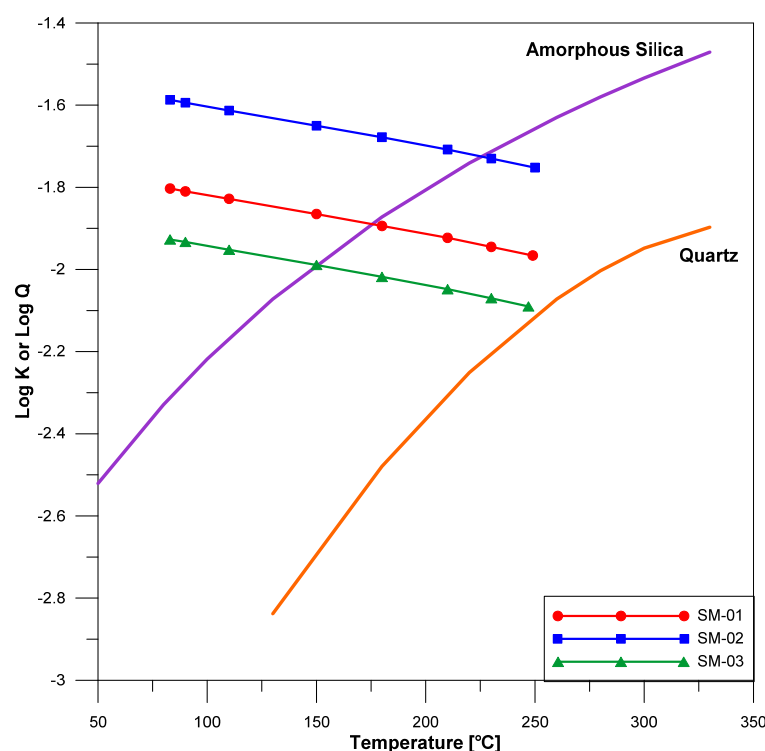


FIGURE 11: Reaction quotient Q for wells SM-01, SM-02 and SM-03 as a function of temperature; lines representing equilibrium of quartz and amorphous silica are shown with red and blue lines respectively.

The saturation index ($SI = \log Q / \log K$) was calculated for quartz-amorphous silica and calcite. A special approach was made for the solubility characteristic of Teschemacherite (NH_4HCO_3), a mineral which was found in well SM-02 and which is possibly the cause for the clogging of well SM-05.

Figure 11 shows the saturation index of silica, as a function of temperature assuming seven boiling steps from 230 to 83°C, this last one corresponding to the boiling temperature at the atmospheric pressure of the field. The boiling process assumed conservation of mass and enthalpy and the temperature at reservoir was taken from Section 3.2.2.

The aim of this graph is to evaluate the transition between the crystalline state of silica at

reservoir temperature and the temperature at which amorphous silica is expected to form and cause scaling inconveniences.

As was explained in Chapter 3.4, there were problems in the analysis of silica, presumably due to the effects of precipitation. Therefore, the reaction quotient Q will be not considered for wells SM-01 and SM-02 in the analysis of Figure 11, as the measured silica concentration does not correspond with the “real” reservoir conditions. Taking into account the value of Q for well SM-03, it is possible to predict silica scaling problems at 150°C and 4.8 bar-a. However, it is necessary to confirm this statement.

In the same way, the analysis of calcite solubility was performed assuming seven adiabatic boiling steps, as was mentioned for evaluating silica. Figure 12 shows the saturation index as a function of temperature.

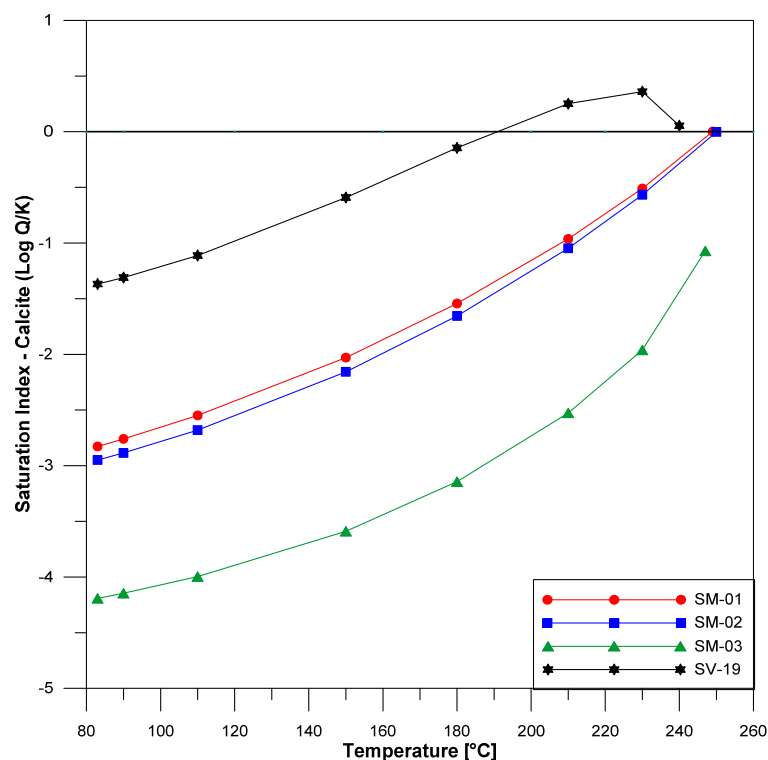


FIGURE 12: Saturation index of calcite for the wells of Sol de Mañana field and for well SV-19 of the Svartsengi geothermal field

When the calculation of calcite solubility was performed, an unusual behaviour was noted. When the boiling starts, an increase of the log Q/K ratio of calcite is commonly observed before it decreases as the boiling continues. An example of such behaviour, based on a sample from well SV-19 in Svartsengi (Iceland) was also plotted. The analytical results from well SV-19 are shown in Appendix I. For calculation of the calcite saturation index from the wells of Sol de Mañana field, the pH assumptions are described in Section 3.4.

The pH is highly associated with concentrations of carbonate ions in the water (See Section 3.4.) and with the concentration of calcite. The concentrations of carbonates in a solution are directly proportional to pH; when the pH decreases, the concentration of calcite also decreases. This statement was confirmed when making variations in the pH values in WATCH program for wells SM-01 and SM-02.

3.7.1 Teschemacherite

Teschemacherite (bicarbonate of ammonia - NH_4HCO_3) is a mineral which was found during phase zero in well SM-02; it is presumably clogging well SM-05. Frederick Edward Teschemacher (1791-1863) was the first who described the mineral; its distribution in the world was found in Argentina, South Africa and on the Chincha and Gunaípes Islands off the coast of Peru (Anthony et al., 2003).

The occurrence of Teschemacherite, inside the wellhead of the Broadlands geothermal drillhole BR 9 (New Zealand), is the only reference known describing this mineral (at the moment), in geothermal settings, encountered to date (Browne, 1972).

In order to define the curve of solubility (Saturation Index) for this mineral, Equations 10-12 of the reaction and the quotient Q are defined as follows:



$$\log Q = \log a_{NH_4^+} + \log a_{HCO_3^-} \quad (11)$$

$$\log Q = \log(\gamma_{NH_4^+} \cdot []_{NH_4^+}) + \log(\gamma_{HCO_3^-} \cdot []_{HCO_3^-}) \quad (12)$$

where a = Activity;
 γ = Activity coefficient;
 $[]$ = molar concentration.

The values of the concentration and coefficient of activity were obtained from WATCH, assuming the same seven adiabatic boiling steps mentioned in the sections above. The results are shown in Table 5.

TABLE 5: Values for quotient Q for wells SM-01, SM-02 and SM-03 at seven steps boiling

Temperature [°C]	SM-01 log Q	SM-02 log Q	SM-03 log Q
Temp. d.l. ^a	-9.106	-9.027	-10.21
230	-9.699	-9.624	-9.926
210	-9.780	-9.704	-10.09
180	-9.748	-9.678	-10.16
150	-9.674	-9.612	-10.15
110	-9.603	-9.557	-10.13
90	-9.596	-9.553	-10.14
83	-9.600	-9.557	-10.14

a: Temperature of deep liquid: 249, 250 and 247°C, respectively

The thermodynamic properties used for the calculation of the solubility constant of the equilibrium K, are shown in Table 6. Unfortunately, as it was not possible to obtain values of molar heat capacity at constant temperature, Cp, for the mineral, the calculation of SI could not be performed in this study.

TABLE 6: Thermodynamic properties for the ammonium cation, bicarbonate and teschemacherite (Wagman et al., 1982)

	$\Delta_f H^\circ$ [kJ·mol ⁻¹]	$\Delta_f G^\circ$ [kJ·mol ⁻¹]	S° [J·mol ⁻¹ ·K ⁻¹]	Cp [J·mol ⁻¹ ·K ⁻¹]
NH ₄ ⁺	-132.51	-79.31	113.4	79.9
HCO ₃ ⁻	-691.99	-586.77	91.2	
NH ₄ HCO ₃	-849.4	-665.9	120.9	

4. CONCLUSIONS

The temperature and pressure logs and the chemical composition of the discharge from wells SM-01, SM-02 and SM-03 postulate the same reservoir temperature, the similar chemical composition and that they are hydrogeologically connected. These three wells presented an isothermal profile that indicates a convective system.

According to a Cl-SO₄-HCO₃ ternary diagram, the geothermal fluid could be classified as mature water of neutral pH with relatively high concentrations of chloride. A Na-K-Mg ternary diagram indicated a fully equilibrated reservoir liquid with a reservoir temperature of 280°C, whereas liquid from the hot springs in the area showed signs of mixing with cold groundwater.

Considering the diagram of silica scaling potential, amorphous silica is expected to precipitate at 150°C and 4.8 bar-a.

The temperature obtained from Na/K, H₂S, H₂S/Ar and H₂S/H₂ geothermometers is in agreement with the measured reservoir temperature. Geothermometers based on the silica concentration gave unreliable results, due to incomplete sampling procedures. For that reason, it is recommended to improve the sampling procedures and treatment, e.g. measure the pH in the field and carry out the analysis of H₂S, carbonates and others as soon as possible (preferably on the same day of sampling) and to dilute sample fractions used for silica analysis. Gas geothermometers based on the ratios of two components represent the temperature better than geothermometers based on one compound, suggesting a condensation or dilution in the fumaroles.

In order to determine future scaling problems, it is necessary to determine a value for the equilibrium constant (K) for tescmacherite.

ACKNOWLEDGEMENTS

I would like to thank the Government of Iceland and especially the United Nations University – Geothermal Training Programme for giving me a scholarship to take part in the six months course. Special gratitude goes to Mr. Lúdvík S. Georgsson and Mr. Ingimar G. Haraldsson for giving me the opportunity to participate in this course and for their support in completing this training.

Many thanks go to Ms. María Gudjónsdóttir, Ms. Thórhildur Ísberg and Mr. Markús Wilde for their assistance and training facilitation through the 6 months. Special thanks to Málfríður Ómarsdóttir for her friendship, constant support and for being the best swimming teacher in the world.

I extend my gratefulness to my supervisors: Mr. Dadi Thorbjörnsson, for his guidance, patience, compromise and for sharing his vast knowledge and experience, and Mr. Thráinn Fridriksson, who is an excellent professor and friend; good luck in your new adventure, Thráinn! Special thanks go to Mr. Manabu Sugioka for believing in me.

Finally, thanks go to my parents and my brother for their huge love and comprehension and to God for showing me the correct way.

REFERENCES

Anthony, J.W., Bideaux, R.A., Bladh, K.W., and Nichols, M.C., 2003: Tescmacherite. In: Anthony, J.W., Bideaux, R.A., Bladh, K.W., and Nichols, M.C., *Handbook of mineralogy. V. Borates, carbonates, sulfates*. Mineralogical Society of America, Chantilly, VA, 791 pp, website: www.handbookofmineralogy.org/pdfs/teschemacherite.pdf

Arnórsson, S., 2000: *Isotopic and chemical techniques in geothermal exploration, development and use. Sampling methods, data handling, interpretation*. International Atomic Energy Agency, Vienna, 351 pp.

Arnórsson, S., and Gunnlaugsson, E., 1985: New gas geothermometers for geothermal exploration – calibration and application. *Geochim. Cosmochim. Acta*, 49, 1307-1325.

Arnórsson, S., Gunnlaugsson, E., and Svavarsson, H., 1983: The chemistry of geothermal waters in Iceland. II. Mineral equilibria and independent variables controlling water compositions. *Geochimica et Cosmochimica Acta*, 47, 547-566.

- Arnórsson, S., Andrésdóttir, A., Gunnarsson, I., and Stefánsson, A., 1998: New calibration for the quartz and Na/K geothermometers – valid in the range 0-350°C (in Icelandic). *Proceedings of the Geoscience Society of Iceland Annual Meeting*, April, 42-43.
- Bjarnason, J.Ö., 2010. *The speciation program WATCH* (vers. 2.4). ISOR – Iceland GeoSurvey, Reykjavík.
- Browne, P.R.L., 1972: Occurrence of Teschemacherite in a geothermal well at Broadlands, New Zealand. *American Mineralogist*, 57, 1304-1305.
- CFE, 1997: *Certification of potential of Sol de Mañana field, Bolivia*. CFE, internal report (in Spanish), submitted to ENDE, Bolivia.
- Dolgorjav, O., 2009: Geochemical characterization of the thermal fluids from the Khangay area, central Mongolia. Report 10 in: *Geothermal Training in Iceland 2009*. UNU-GTP, Iceland, 125-150.
- ENDE, 1989: *Geothermal power plant for Central Sol de Mañana, feasibility study for 30 MW*. ENDE, report (in Spanish).
- ENEL, 1989a: *Geothermal feasibility study in the área of Laguna Colorada. Report of the well SM-01, BOL/84/007*. Empresa Nacional de Electricidad- ENDE, internal report (in Spanish), 111 pp.
- ENEL, 1989b: *Geothermal feasibility study in the área of Laguna Colorada. Report of the well SM-02, BOL/84/007*. Empresa Nacional de Electricidad - ENDE, internal report (in Spanish), 179 pp.
- ENEL, 1990: *Geothermal feasibility study in the area of Laguna Colorada. Report of the well SM-03*. Empresa Nacional de Electricidad - ENDE, internal report (in Spanish), 163 pp.
- Fournier, R.O., and Potter, R.W. II, 1982: A revised and expanded silica (quartz) geothermometer. *Geoth. Res. Council Bull.*, 11-10, 3-12.
- Franzson, H., Zierenberg, R., and Sciffman, P., 2008: Chemical transport in geothermal systems in Iceland Evidence from hydrothermal alteration, *J. Volc. Geoth. Res.*, 173, 217-229.
- Franzson, H., Gunnarsson, G., Danielsen, P., Sigurðsson, O., Hermannsson, G. and Skarphéðinsson, K., 2003: *Reykjanes - Well RN-13: Drilling report*. Orkustofnun, Reykjavik, report, OS-2003/030 (in Icelandic), 64 pp.
- GEOBOL, 1976: *Geothermal resource evaluation for Bolivia*. Cochabamba, Bolivia, report (in Spanish).
- Giggenbach, W.F. 1998: Geothermal solute equilibria. Derivation of Na-K-Ca geoindicators. *Geochim. Cosmochim. Acta*, 52, 2749-2765.
- Grant, M.A., and Bixley, P.F., 2011: *Geothermal reservoir engineering* (2nded.). Elsevier, USA, 359 pp.
- James, R., 1966: Measurements of steam-water mixtures discharging at the speed of sound to the atmosphere. *New Zealand Engineering*, 21-10, 437.
- Karingithi, C.W., Arnórsson, S., and Grönvold, K., 2010: Processes controlling aquifer fluid compositions in the Olkaria geothermal system, Kenya. *J. Volcanol. & Geotherm. Res.*, 196-3/4, 57-76.
- Kruger, P., and Ramey, H. 1978: An evaluation of James' empirical formulae for the determination of two-phase flow characteristics in geothermal wells. *Proceedings of the 4th Workshop on Geothermal Reservoir Engineering*. Stanford University, Stanford, CA, 7 pp.

Lovelock, B. 2006: Flow testing in Indonesia using alcohol tracers. *Presented at 31st Workshop on Geothermal Reservoir Engineering, Stanford University, Stanford, CA*, 5 pp.

Nicholson, K., 1993: *Geothermal fluids: chemistry and exploration techniques*. Springer-Verlag, Berlin, 268 pp.

Saudi, A.S.A.S., 1999: The Geothermal of thermal fluid in the geothermal field near Alia airport in Jordan and Selfoss geothermal field, S-Iceland. Report 13 in: *Geothermal training in Iceland 1999*. UNU-GTP, Iceland, 333-356 pp.

SERGEOTECMIN, 1996: *Geological map of Bolivia*. Servicio Nacional de Geología y Técnico de Minas, La Paz, Bolivia.

Steingrímsson, B., 2013: Geothermal well logging: temperature and pressure logs. *Presented at "Short Course on Conceptual Modelling of Geothermal Systems", organized by UNU-GTP and LaGeo, Santa Tecla, El Salvador*, 16 pp.

Steingrímsson, B., 2014: *Discharge measurement and injection tests*. UNU-GTP, Iceland, unpublished lecture notes, 64 pp.

Steingrímsson, B., Fridleifsson, G.Ó., Sverrisdóttir, G., Tulinius, H., Sigurdsson, Ó and Gunnlaugsson, E., 1986: *Nesjavellir, well NJ-15, drilling, investigations and production characteristics*. Orkustofnun, Reykjavik, report OS-86028/JHD-08 (in Icelandic), 119 pp.

Teranov and CGG (Compagnie Générale de Géophysique), 2014: *Geothermal project Laguna Colorada magnetotelluric survey Sol de Mañana.*, CGG, internal report submitted to ENDE, Bolivia.

Villarroel, D., 2014: Geothermal development in Bolivia. *Presented at "Short Course on Utilization of Low- and Medium-Enthalpy Geothermal Resources and Financial Aspects of Utilization", organized by UNU-GTP and LaGeo, Santa Tecla, El Salvador*. 6 pp.

Wagman, D., Evans, W., Parker, V., Schumm, R., Halow, I., Bailey, S., Churney, K., Nuttall, R., 1982: *The NBS tables of chemical thermodynamic properties. Selected values for inorganic and C1 and C2 organics substances in SI units*. J. Physical & Chemical Reference Data, USA, 407 pp.

Wei, W., 2006: Geochemical study of the Xianyang low-temperature geothermal field, Shaanxi Province, China. Report 22 in: *Geothermal training in Iceland 2006*. UNU-GTP, Iceland, 501-522.

West JEC, 2010: *Preparatory study for the geothermal development of Sol de Mañana, Bolivia*. West JEC, internal report (in Spanish), submitted to ENDE, Bolivia.

APPENDIX I: Laboratory analysis from well SV-19, Svartstengi – Iceland

Water sample (conc.:ppm)		Steam sample (conc.:%)	
pH/°C	7.92/25	Ar	1.5
B	7.8	CH ₄	0.17
Ca	1130	H ₂	3.02
Cl	14540	N ₂	72.26
CO ₂	8.9	O ₂	23.06
F	0.21	CO ₂ [mg/kg]	1600
K	1080	H ₂ S [mg/kg]	32
Mg	0.34		
Na	7320	<i>Physical and other data:</i>	
NH ₃	0.71	Sample No.	20140186
SiO ₂	479	Gas/steam [Lgas/kg condensate]	0.08
SO ₄	26.7	Data sampling	8.5.2014
		Sampling pressure [bar-g]	12.8
		Sampling temperature [°C]	194.4



UNITED NATIONS
UNIVERSITY

UNU-GTP

Geothermal Training Programme

Orkustofnun, Grensasvegur 9,
IS-108 Reykjavik, Iceland

Reports 2014
Number 33

CALCIUM CARBONATE SCALING CONTROL IN GEOTHERMAL WELL PV8 IN SAO MIGUEL, AZORES, COMBINING CHEMICAL INHIBITION AND MECHANICAL REAMING

Valdemar de Viveiros Pereira

EDA Renovaveis S.A.
Rua Francisco Pereira Ataíde, 1
9504-535 Ponta Delgada
Azores
PORTUGAL
vpereira@eda.pt

ABSTRACT

The formation of calcium carbonate (calcite) is a major scaling problem that occurs in geothermal fields around the world, leading to a quick decline in well output and impacts on power plant production. There are several methods that can be used for the prevention of calcite scaling and the rehabilitation of affected production wells.

In Ribeira Grande geothermal field, in addition to prevention by injection of chemicals to inhibit scaling, reaming is used in well PV8. Currently at Ribeira Grande field, the main method used in reaming involves quenching and cooling the well prior to the operation and this affects well performance. This study pursues the development of a method that involves reaming the calcite without cooling the well by allowing it to flow. The main focus of this report is the design of equipment (kind of a Stripper) and work procedures to enable mechanical cleaning of calcium carbonate deposits inside a well, discharging the deposits to a silencer.

1. INTRODUCTION

Ribeira Grande geothermal field, located on the Azorean island of Sao Miguel, is the only exploited high enthalpy Portuguese geothermal field, with a total installed capacity of 23 MWe in two plants. In progress is a study for the construction of a new 3 MWe power plant at Terceira, another island of the Azores Archipelago.

The formation of calcite scaling inside wellbores has occurred in Ribeira Grande geothermal field since the start of exploitation. According to the temperature data taken inside the wellbores, upon boiling at a flash point temperature ($\sim 240^{\circ}\text{C}$), the fluid become super saturated in relation to calcite (Calcite Saturation Index, $\text{SI} > 0$), increasing the potential for deposition and the obstruction of wells. As a result, a chemical calcite inhibitor was injected through the installation by way of a mechanical system in each well for down-hole injection; this system includes a chemical metering pump, lubricator, valves, stainless steel capillary tubing, tanks and facilities to mix a diluted inhibitor product.

The application of the calcite inhibitor is a successful method adopted to prevent the formation of scaling in the wells. It has demonstrated very good results, with regard to the maintenance of the internal wellbore and, therefore, power production. Despite the success of this method in well PV8, which supplies the Pico Vermelho power plant, a small rate of calcite scale deposition was nevertheless observed. The calcite deposits in well PV8 are usually mechanically cleaned using one small drill rig, Ingersoll Rand RD-20, by reaming out the deposit with a tricone bit (with tungsten carbide teeth for soft formations), while always keeping the well quenched with the injection of fresh water. This report will describe the development of a wellhead assemblage and procedure designed to ream the calcite deposits without cooling the well. Instead, the well is kept hot and flowing to a separator pipe line, where the calcite cuttings can be gathered.

2. RIBEIRA GRANDE GEOTHERMAL FIELD

2.1 Characterization of the field and well PV8

Ribeira Grande Geothermal field, located on the island of Sao Miguel, one of the nine islands that comprises the Portuguese Archipelago of Azores, has been explored since 1990 by the local public company EDA RENOVAVEIS S.A., owned by EDA, S.A., the Power Utility of the region. Two binary power plants were installed in this field, developed with ORMAT technology. The Ribeira Grande Power Plant is located in the southern upper side of the field, and the Pico Vermelho Power Plant is located on the northern side of the field near Ribeira Grande city, the second biggest city on the island (Figure 1). The combined installed capacity of this field is 23 MWe, 13 MWe in the Ribeira Grande power plant, and 10 MWe in the Pico Vermelho power plant. All the electricity produced by these power plants is for the island grid. In 2013, the total generation was over 174 GWh, corresponding to 43% of the total electric energy consumption in Sao Miguel and 23% for the Azores region.

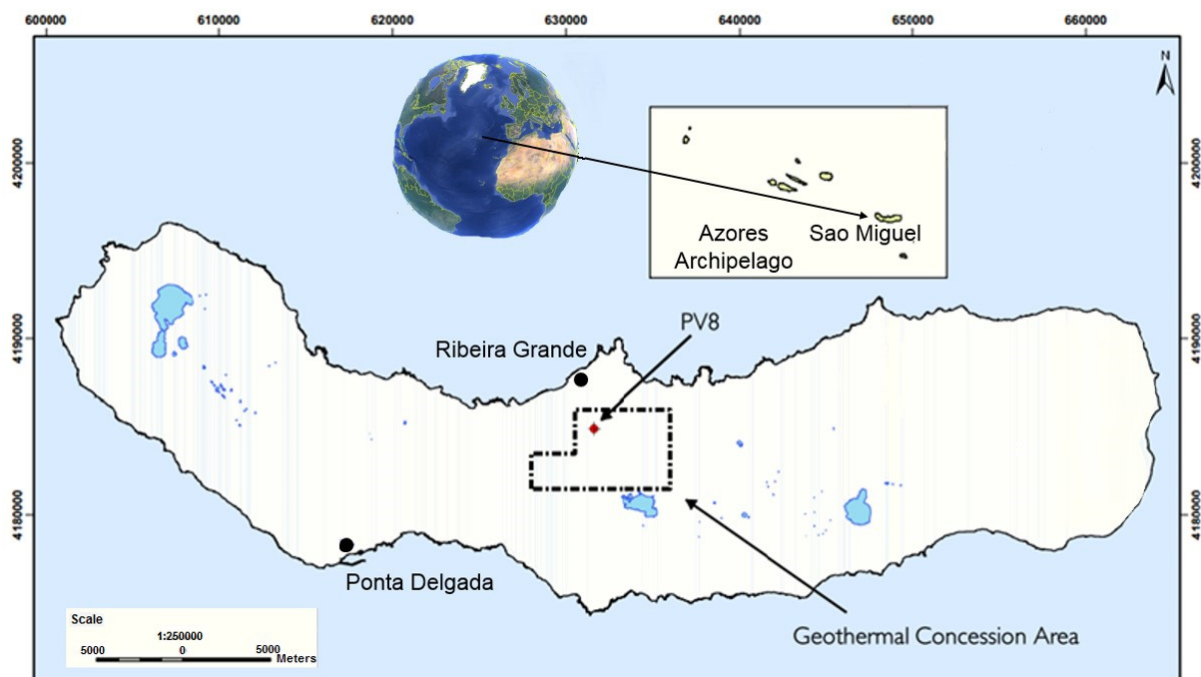


FIGURE 1: Location map of the Ribeira Grande geothermal field on Sao Miguel Island, Azores (adapted from GeothermEx. Inc., 2006)

All the production wells in the Ribeira Grande geothermal field have a tendency towards deposition of calcium carbonate CaCO_3 (calcite) scaling. For that reason, each well requires a chemical scale inhibition system that blocks the formation and progress of this kind of scaling in the wells. The chemical inhibitor concentration is adjusted according to the chemical properties of the geothermal fluid produced by each respective well.

Well PV8 is a vertical well with a large diameter production casing that is supplying the Pico Vermelho power plant. It is one of the three most powerful wells in the field, delivering a normal flow rate of 26 kg/s, which represents about 3.5 MWe in the production of this power plant. Well PV8 has a similar profile to recent wells drilled after 2005 in the geothermal field, completed according to the large diameter well profile: a 13-3/8" production casing, API K55, 68 lb/ft and a 9-5/8" slotted liner, API K55, 40 lb/ft, with shoe located at a total depth of 971.6 m. The wellhead has a 12" ANSI 900 master valve connected to a casing head, which is welded to the top of the 13-3/8" production casing. The casing head has two side outlets connected to 3" ANSI 900 gate valves, one of which is linked to the wellhead gauge and the other to the choke line but, when needed, as a kill line for the injection of cold water during well interventions. The 12" spool with two side outlets is connected to the top of the master valve and to the bottom side of the Tee that supports the 12" ANSI 900 lateral valve which is connected to the power plant pipe line. Above the Tee, on top of the wellhead is assembled a 3" ANSI 900 gate valve, which allows the installation of the lubricator used in the calcite inhibition system. Figure 2 presents the technical profile of the well, including casings and wellhead components.

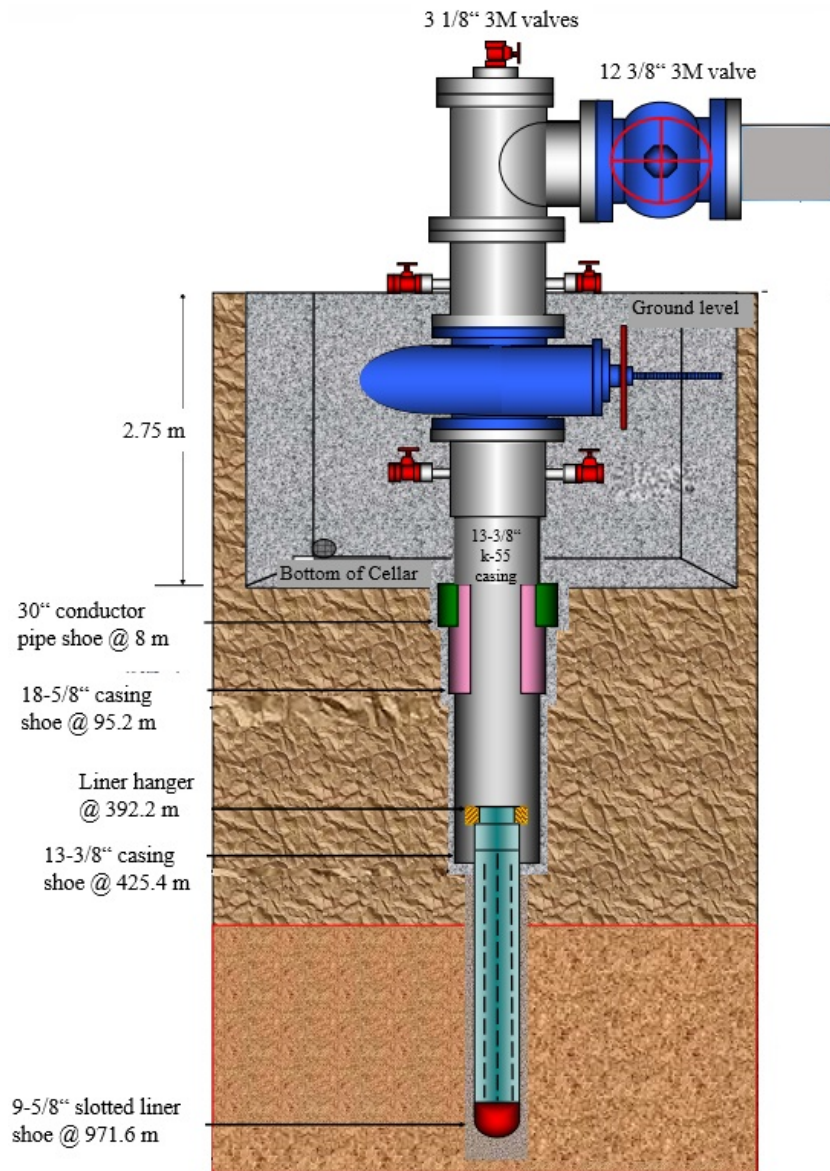


FIGURE 2: Profile of well PV8 (adapted from GeothermEx. Inc, 2006)

After the completion of well PV8, as is common in all wells of this field, extensive well tests were conducted that include an injectivity test (in the completion phase), flow testing (after the drill rig leaves the site), and several pressure/temperature surveys, which are very important in the evaluation of the formation pressure and temperature.

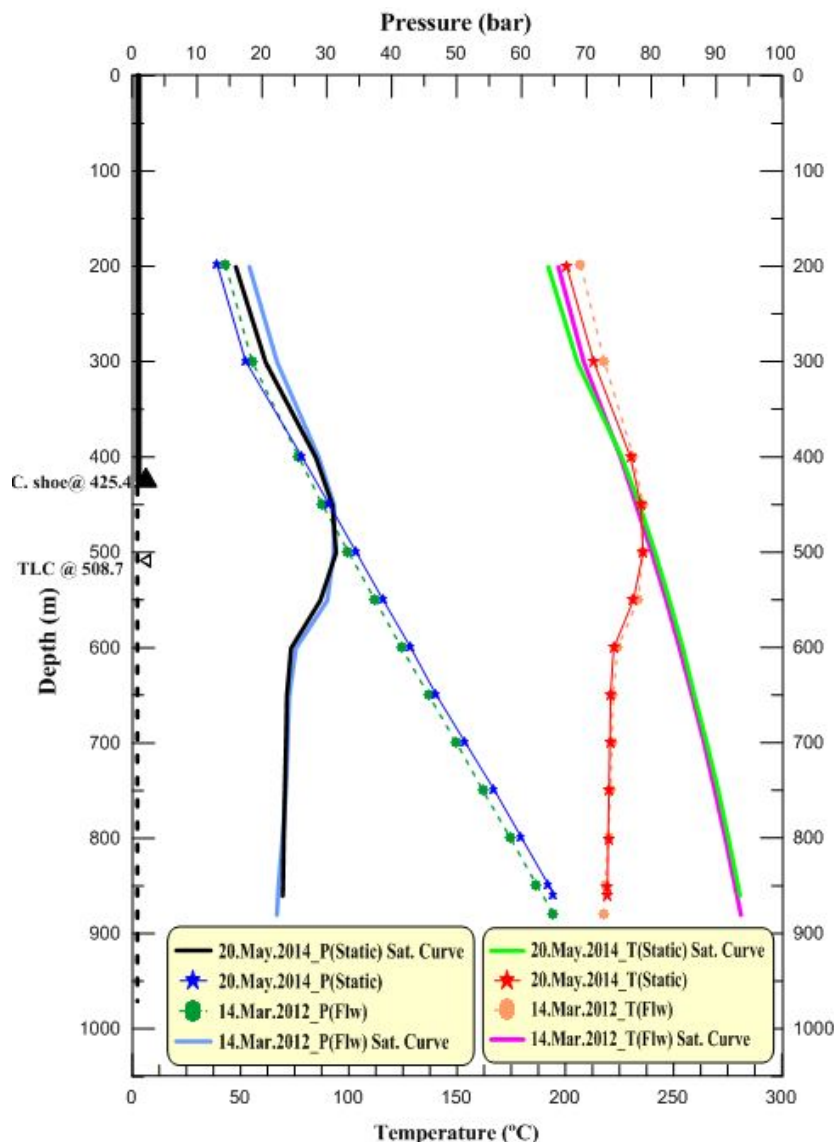


FIGURE 3: Temperature, pressure and saturated curves for well PV8, measured in static and flowing surveys

Figure 3 shows the temperature and pressure downhole logs made in static and dynamic (flowing) surveys inside well PV8, using Kuster KTG/KTP mechanical tools. Based on the temperature and pressure curves, represented by the lines with symbols in Figure 3, the respective saturation temperature and pressure curves according to steam tables are shown by solid lines. In the dynamic survey, the control valve of the well was 10% open, to reduce the flow rate from the well to the power plant.

This was done to maintain the integrity of the tools, allowing for running in and out inside the well against the flow. The dynamic survey was performed from the bottom of the well up to a depth of 300 m. From 300 m to the surface, the logging was made in static conditions, with the control valve totally closed. Observing the flow curve for pressure, one can see the change in the gradient above 300 m after stopping the flow. If electronic tools were used to do the surveys (i.e. a Kuster

K10G memory tool) instead of mechanical tools, the real pressure variation above 300 m could be seen, in this case, probably a curve instead of a straight line between the two measurement points. As described in the legends for Figure 3, the left side plots are related with pressures and the right side plots with temperatures. One can see on the depth axis a schematic drawing of the well casing program, with the 13-3/8" casing shoe located at 425.4 m. Total loss in circulation during drilling occurred at 508.7 m, and the total depth of the well with the slotted liner shoe is 971.6 m.

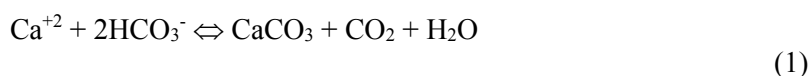
Observing the static plot using the pressure gradient from the bottom to the depth of 300 m, one can infer the water level inside well PV8, probably at a depth of 100 m. Analysing the plots, the main thing to be observed is the maximum temperatures located at 450-550 m depth, followed by a small decrease (temperature reversal) below this depth to the bottom of the well. In fact, this depth matches the main circulation loss found during the drilling of the well and corresponds to the hot permeable zone, with temperatures of 231-237°C (static temperature log). Regarding the temperature profiles, below a depth of 600 m, additional permeable zones could exist, but with reduced permeability when compared to the upper zone. The intersection of the saturation curves with the measured temperature and pressure logs indicates that the boiling point is located inside the slotted liner at around 460 m.

2.2 Calcite scaling in well PV8

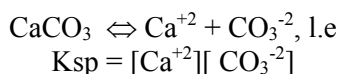
2.2.1 Calcite scaling formation

Calcite scaling is one of the three known naturally occurring polymorphs of calcium carbonate (CaCO_3) minerals, besides aragonite and vaterite, and is one of the most common carbonate deposits that occur in geothermal wells. Calcite scale is white coloured and can easily be distinguished from silica (another type of common scale in geothermal sites) by putting a drop of hydrochloric acid on a piece of scaling; if gas bubbles are formed, it is calcite (Thorhallsson, 2006). Usually calcite is extensively spread in the altered rocks of geothermal systems, often in the amount of 1% by volume, but it can be much more abundant at some levels in specific parts of the sites. Normally, the high abundance of calcite deposits results from large amounts of boiling water rising to upper levels (Arnórsson 1989). According to several studies made in geothermal sites, calcite scaling is quite common in wells drilled in reservoirs with temperatures in the range of 140-280°C. The Ribeira Grande geothermal field falls into this category, with an estimated formation temperature in the range of 235-245°C. In this type of reservoir, geothermal fluids are usually calcite-saturated and become calcite supersaturated inside the wells, after boiling and flashing to lower temperatures reduces the CO_2 in the water phase due to its transfer to the steam phase. Therefore, the release of CO_2 by degassing increases the pH of the water phase, and increases the concentration of carbonate. It is mostly this increase in concentrations that produces the change from saturated water to super saturated water with respect to calcite, resulting in precipitation (Arnórsson, 1989).

The following chemical reaction shows how the carbonates contribute to calcite scales:



Solubility product based on:



The calcite deposits are mainly found inside wells just above the flashing zone. The flashing depth can be moved up and down if changes in the flow rate are made (by changing wellhead pressure). In reservoirs with temperatures above 260°C, calcite scaling is not as problematic because the dissolved calcite in geothermal waters decreases with increasing temperature.

2.2.2 Calcite scaling potential of well PV8

The Saturation Index (SI) is used as a measure of mineral deposition in geothermal waters, defined as:

$$SI = \log \frac{Q}{K} \quad (2)$$

where Q is the reaction quotient or activity product of the mineral which is being analysed in the dissolution reaction in a non-equilibrium state, and K is the equilibrium constant or solubility product. When in the mineral solution $Q = K$, the system is in equilibrium and $SI = 0$, meaning that the studied mineral is saturated in the solution; if $Q > K$, the mineral solution is super saturated and the $SI > 0$; if $Q < K$, the mineral solution is under saturated and $SI < 0$.

In order to identify the state of the fluid in well PV8, with regard to calcite scaling potential, the WATCH program was used to calculate $\log Q$ and $\log K$, needed for the SI equation. This program is very helpful in analysing calcite scaling potential. The WATCH program calculates the final types of concentrations, solubility products and activity products, using the initial fluid concentrations as input (steam and water sampled at the surface), taking into consideration that the fluid boils adiabatically, starting at the reference temperature (240°C for well PV8) (Bjarnason, 2010).

Table 1 shows the liquid fluid samples, gas data analysis, and the general data taken from well PV8 on 19.11.2013, all of which was then used as input to feed the Watch program. The general data came directly from the main installed sensor readings in the pipeline and power plant (pressure, temperature, flow rate. For WATCH calculations, the enthalpy must be known and is determined by well testing or measuring the flow of both phases. The liquid and gas concentrations are obtained from chemical analyses from two laboratories. The total CO₂ value related to the liquid sample was calculated using the values of the available concentrations of HCO₃ and CO₃ from the laboratory analyses.

TABLE 1: General data and deep fluid concentrations at separator pressures (mg/kg) in well PV8

General data to input into the WATCH program												
Date	Separator pressure	Meas. temp	Enthalpy	Flow rate	Real formation temp	Hypothetical formation temp						
19.11.13	4.5 bar.a	148°C	1144 kJ/kg	31 kg/s	240°C	300°C						
Liquid sample												
pH/Temp	CO ₂	B	SiO ₂	Na	K	Mg	Ca	F	Cl	SO ₄	Fe	TDS
9.6/18°C	167.86	4.7	555	1334	246	0.025	1.93	22	1900	205	0.08	5140
Gas sample												
			CO ₂	H ₂ S	NH ₃	N ₂	CH ₄	H ₂				
			4820	24.2	47.1	39.2	0.121	0.109				

Based on the data in Table 1, the WATCH program computed several results for different product concentrations. For the present study, the calcite concentrations were computed for the given range of temperatures (300°C, 280°C, 260°C, 240°C, 220°C, 200°C, 180°C, 160°C, 140°C), considering 2 (two) reference temperatures, 240°C (real or most approximate value for the formation temperature on the site) and 300°C (the hypothetical formation temperature). The same initial sample concentrations were used; these results could be important for observing changes in the calcite scaling index, when using a higher formation temperature. The minimum temperature chosen was 140°C, which is less than that actually observed in the well.

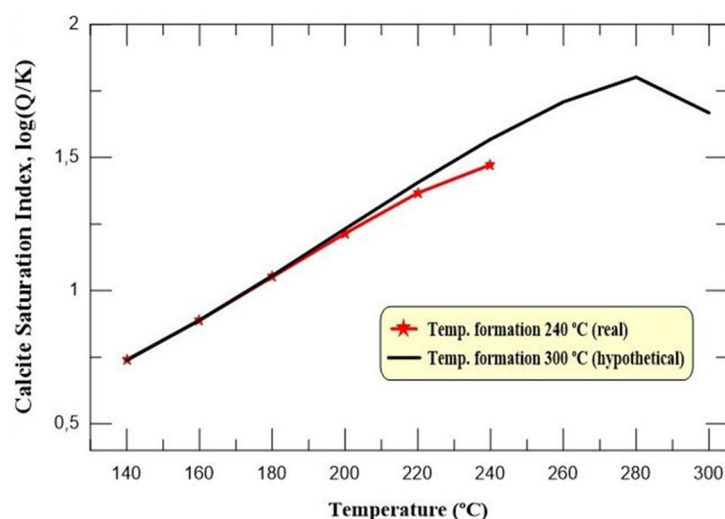


FIGURE 4: Calcite saturation index of fluid samples from well PV8

In analysing the plot in Figure 4, it is clear that the $SI > 0$ ($SI > 0.7$ for all temperatures), meaning that the fluid in well PV8 is super saturated for all the temperatures selected. Even if the reservoir had the same mineral concentrations in the water at a higher formation temperature, for example 300°C, the calcite *Saturation Index* would be higher than zero and the water would be super saturated (black curve in the graph). Figure 4 shows a decrease in the SI value with a decrease in temperature; consequently, there is a minor probability of scaling.

In order to maintain good control of well PV8's performance, a monitoring plan was developed, taking into consideration frequent go-devil surveys; results will be utilized to quantify the progress of scaling deposits with time and evaluate the continuous condition of the borehole.

2.2.3 Historic occurrences in well PV8

Well PV8 started to produce for the Pico Vermelho power plant in December of 2006. After less than one year in operation, the first problem related to calcite scaling deposits in the borehole occurred, forcing closing of the well and resulting in the need for a workover operation to release the stuck 1/4" diameter capillary tubing for the calcite inhibitor, and to clean deposits from the well. The first symptom of this problem was verified by the power plant operators as a gradual decrease in the flow rate (about 80 ton/h) for the same opening of the control valve (22%) and a wellhead pressure which declined from 16.2 bar to 12 bar. During the extraction operation of the inhibitor downhole equipment for inspection, it was realised that the capillary tubing was stuck in the hole due to calcite scaling and it was not possible to finish the work. About 5 months later, it was possible to release the tubing and recover the downhole equipment by injecting aqueous HCl into the well in order to dissolve the calcite and then lift the tubing out of the well using a crane. The well was quenched during this operation.

After this occurrence, a study was made to try and understand the probable causes for the problem, keeping in mind that the water on this side of the geothermal field was very similar to the rest of the field and the scale inhibitor product always worked well for wells located in the upper part of the field which supply the first power plant.

EDA Renovaveis analysed and then modified the following items in well PV8, and consequently in some other wells in the field:

- Injection of a new type of product for the inhibition of calcite, selected according to the water chemistry of the well;
- Adjusted the inhibitor concentration according to each well specifications;
- Adjusted the depth of injection of the inhibitor product in each well to below the onset of boiling; and
- Adjusted the maintenance plan for the inhibitor system, reducing the time interval for replacement of the life-limited parts, concerning pumps, tubing and downhole equipment, based on experience.

Table 2 shows the well intervention history of well PV8, significant occurrences due to calcite scaling and actions taken to recover the output. All the interventions executed inside the well, reported in the following table, were made with the well quenched.

Table 2 shows that during the first 6 years that well PV8 was able to produce, on average, about 37 % of the time it was out of service because of occurrences related to calcite scaling. The total power production was, however, not affected due to management of the other wells connected to the Pico Vermelho power plant. Since November, 2012, the date of the last workover, up to the present date, the well has been producing normally to the power plant, despite evidence of partial calcite deposition in the wellbore, according to go-devil surveys that are made every 1.5 months to monitor the diameter open to flow.

Figure 5 shows a photo taken during a fishing operation of the capillary tubing made in well PV8, where the top of the master valve can be seen after removing the annular BOP. The BOP had to be removed in order to allow the passage of the tangled inhibitor tubing out of the well. This part of the work must always be executed in as short a time as possible while continuously pumping cold water at a high rate; there is no well control device mounted above the master valve. In Figure 5, it is possible to observe the large block of calcite deposited on the outside of the tubing, indicating that for some reason the chemical inhibitor was not totally effective in the prevention of scaling.

TABLE 2: Main historic occurrences in well PV8, since the start of production of the power plant

Date	Historic Occurrences
December, 2006	Pico Vermelho power plant and well PV8 start operating.
September, 2007	Decreasing flow rate and wellhead pressure in well. Inhibitor tubing got stuck during the extraction operation.
February, 2008	Operation to release the inhibitor equipment from the wellbore. Injection of aqueous HCl from surface and lifting out with a crane.
December, 2008	Attempt to clean calcite scaling in wellbore using a Coiled Tubing unit, without success.
July, 2009	Reaming of the wellbore using the Ingersoll Rand RD-20 rig with 12-1/4" and 8-1/2" tungsten tricone bits. The reaming was successful.
December, 2010	Rupture in the inhibitor tubing during extraction to inspect, losing large amount of the capillary tubing.
January, 2012	Fishing operation to recovery the capillary tubing.
October, 2012	Rupture in the inhibitor tubing during extraction for inspection, losing about 180 m of the capillary tubing.
November, 2012	Fishing operation to recovery the capillary tubing.

Figure 6 shows a diagram of the calcite deposition in the wellbore of well PV8, according to the reaming operation executed in 2009. After fishing, the calcite reaming operation was executed from 270 m to about 540 m depth. This depth is in accordance with the analysis of the plots in Figure 3, where the flash point was estimated to be around 460 m depth. Usually the reaming operations done in the well PV8 were conducted down to about 700 m, without rotating the bit below 550 m, to optimize the operation. As the well was already killed, the remaining part of the well could be checked after the fishing and reaming operation with a go-devil.



FIGURE 5: Recovery of inhibitor tubing during the workover operation conducted in Well PV8 in December, 2014

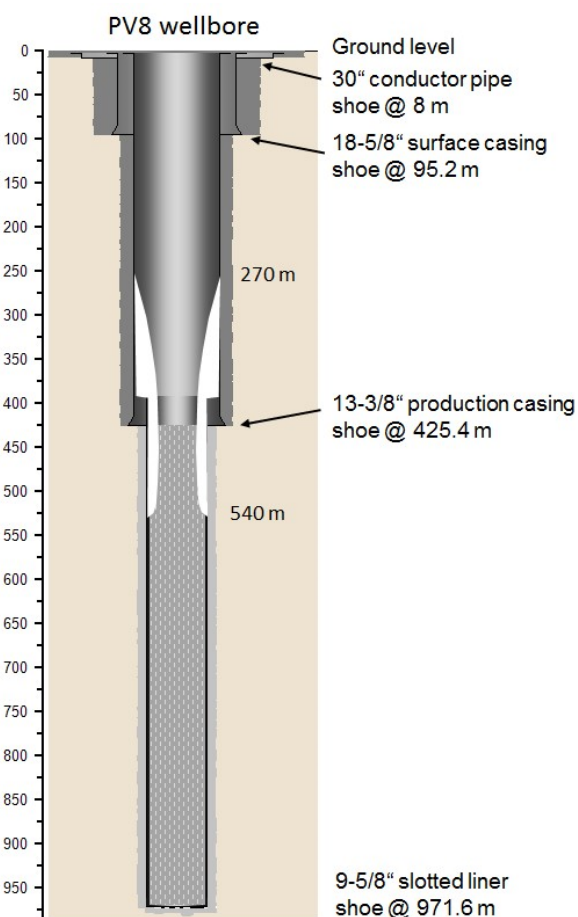


FIGURE 6: Representation of calcite deposits in Well PV8 wellbore in 2009

3. METHODS TO CONTROL CALCITE SCALING IN RIBEIRA GRANDE GEOTHERMAL FIELD

3.1 Inhibition by chemical injection in the wells

According to the chemical composition of the geothermal fluid, it has a large tendency to form calcite deposits in the boreholes. Chemical inhibition was adopted as the best choice, in order to avoid expensive workover operations related with reaming or chemical cleaning of the wells and taking them out of service. Every production well of both power plants in Ribeira Grande field has installed an inhibitor system that allows the injection of a chemical calcite inhibitor inside the wells at a calculated depth, according to the estimated flash point depth, as shown in the case of well PV8 (Figure 3).

The main inhibitor system used for the chemical injection in the wells is shown in Figure 7, and consists of the following equipment:

- Metering pump for continuous injection of a small dose of chemical inhibitor at pressures up to 59 bar;
- Lubricator set, consisting of a 5 m long 3" steel pipe with a stuffing box mounted on the top and a ram BOP (valve) connected on the bottom. The lubricator allows the installation of downhole equipment in the well under pressure;
- Downhole equipment consists of the inhibitor chamber (high pressure valve) and a sinker bar;
- Nickel-Iron-Chromium INCOLLOY Alloy 825 capillary tubing (1/4" OD), used to transport the inhibitor from the surface to the downhole equipment.

In Figure 7, the assemblage of the inhibitor system equipment in the well is shown. The pre-diluted inhibitor is transported from the automatic dilution station at the plant (Figure 8) and discharged in the inhibitor tank, which supplies the chemical inhibitor to the well. With an electrical metering pump, the flow rate can be adjusted to the quantity of calcite inhibitor desired, according to the calculated inhibitor concentration to be maintained. This injection is made continuously when the well is producing, only stopping for periodic extraction of the downhole tools for inspection, according to the preventive maintenance plan.

Considering the lower efficiency of the old chemical inhibitor, based on a carboxylic acid aqueous solution, it was decided to replace it. When the new wells started to produce, the decision was made to use the calcite chemical inhibitor *NALCO pHREEdom(R) 5200M*, a formulation of liquid polymeric dispersants and a patented inhibitor, specially designed to prevent the deposition of calcium carbonate.

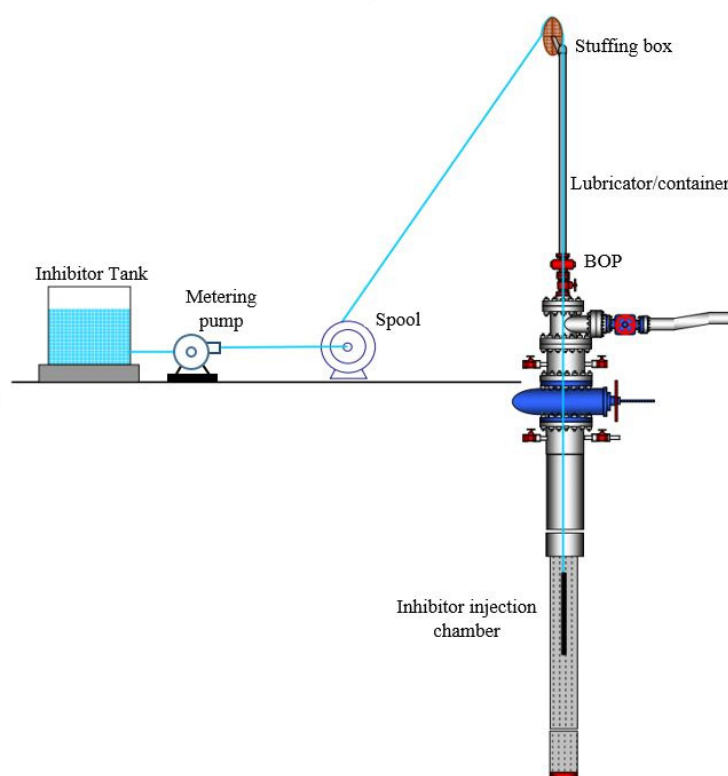


FIGURE 7: Inhibitor system installed in production wells



FIGURE 8: Station for water decalcification and inhibitor dilution

This product is very effective in extreme conditions of temperature and pressure and in a wide range of pH environments (NALCO, 2006). Until now, the use of this new calcite inhibitor was recognized as a good solution for the prevention of calcite scaling.

In the mixing station shown in Figure 8, the calcite inhibitor is diluted with fresh water after decalcification in the proportions calculated for each well. Mostly the wells in the field receive a calcite inhibitor dosage of 3 ppm in the well fluid but, according to the particularity of well PV8, the final dosage is about 9 ppm.

3.2 Detection and control of calcite progress using calipers in the wells

The deposition of calcite scaling in the boreholes and wells can be detected with time if data from the wells is frequently gathered; normally it is possible to observe a decrease in the flow rate and wellhead pressure. When that occurs, the amount of calcite scaling inside the casing is probably already significant. Even when inhibition by chemical injection is being used, the presence of calcite scaling on the capillary tubing can be seen during its periodic extraction for inspection and for running Pressure/Temperature surveys.

Go-devils and calipers are probably the best tools for detecting the location and for monitoring the amount of calcite scaling, through variations in the diameter open to flow.

Figure 9 shows different types of tools used in down-hole surveys for detecting calcite scaling; they are described below:

- A. Go-devils of different diameters, constructed and used by EDA RENOVAVEIS for detection of calcite inside the casings by running in the well on a wireline until it stops;
- B. Go-devil on a sinker-bar with interchangeable baskets of different diameters, used in Iceland;
- C. Electrical caliper logging tool, with 2, 3, 4 arms or multi-fingers, used all over the world in geothermal, gas and oil industry. Such tools and cables have temperature limitations and are used when the wells are quenched;
- D. Kinley Microscopic multi-finger caliper tool; this is used for sophisticated work above the pressure and temperature of the electronic caliper tools (maximum of 315°C).

EDA Renovaveis developed and uses Go-devils, as shown in Figure 9A, in a full range of diameters, from 3" - 12". This go-devil has a basket made of copper wire soldered with silver and has a copper pin in the connection between the basket and the sinker bar to work as a safety pin. The go-devil is normally run in the wellbore, starting at the maximum to the minimum diameter allowable and is lowered until it stops at the scale obstruction at their respective depths. In case the go-devil basket gets stuck inside the well, the pullback strength in the wireline should be enough to break the safety pin, permitting the recovery of the sinker bar and wireline. The copper material is favoured for ease of later fishing or milling operations. The go-devil shown in Figure 9B is also constructed from copper wires and easy to drill-out materials. Both go-devils are suspended by wireline and can be used in very high temperature wells without losing performance.

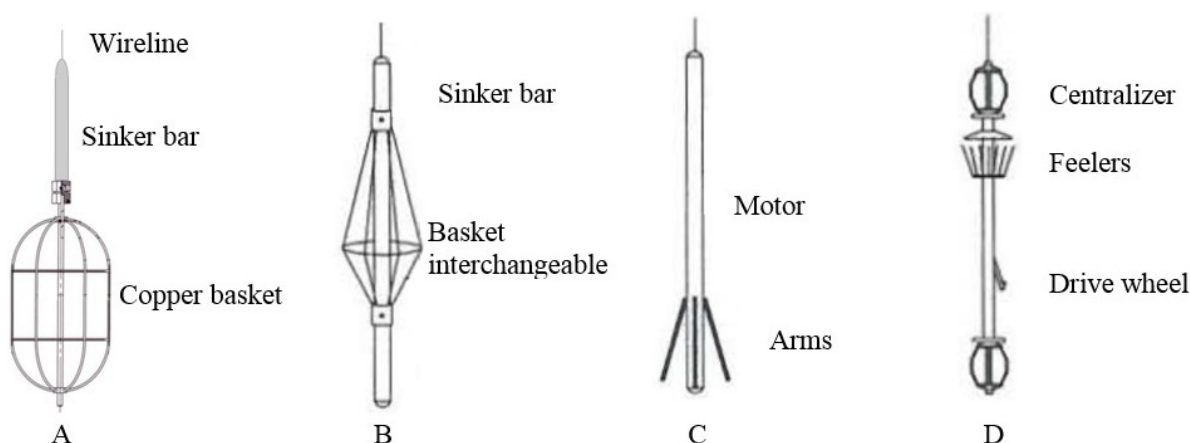


FIGURE 9: Go-devils (A and B) and caliper logging tools (C and D) used in calcite scaling surveys (modified from Molina, 1995)

The caliper logging tools shown in Figure 9C can be mechanical or electronic. These tools are equipped with mechanical arms (from 3 to 60 units) and are opened down hole with a small electric motor installed in the logging probe. The recovery data from caliper logging tools are collected continuously when connected to the surface read-out unit through an electrical cable and inspected in real time, or the data can be saved in a memory slot inside the tool and analysed after pulling out. In the surveys, the tools are run in the wells through a lubricator and begin measuring the diameter of the wellbore from the bottom to the surface, after opening up the arms. Because of the electrical parts and the cable, the maximum service temperature for these tools is about 150 - 180°C.

The Kinley Microscopic caliper shown in Figure 9D can operate in wells outside the temperature and pressure ranges of the electronic calipers, up to a maximum of 315°C. Generally, the well is logged in a single pass from the bottom to the surface, using the caliper feelers independently to record its movements in the chart inside the tool.

EDA RENOVAVEIS frequently uses go-devils, as shown in Figure 9A, for calcite scaling monitoring and fishing operations in the wells. Less frequently, accurate caliper logs related with corrosion, isolated pits or integrity of casing are made.

3.3 Wellhead pressure control to change the localization of the calcite

The depth of calcite deposition can be changed from about 50 m up or down in the borehole by varying the flash point location. The pressure at a certain depth is related to the pressure in the wellhead and is controlled by opening the control valve. If the well has available pressure and flow rate, it is possible to adjust the scaling deposition depth. Usually, the main idea is to allow the calcite to scale inside the production casing, where it is possible to ream it without damaging the slotted liner.

In the case of well PV8, it is not possible to use the wellhead pressure to move the position of calcite scaling up about 60 m to a level inside the production casing, because usually it is producing at around 16 bar WHP in order to have the flow rate required for the power plant. It is thus not practical to manage the production by increasing the WHP in order to avoid scaling inside the slotted liner.

3.4 Mechanical reaming of calcite with the well quenched using a small rig

Reaming calcite scaling consists of cleaning the scaling deposit from inside the well by using a tricone bit or a taper milling tool, running it in the well after quenching and maintaining a constant injection of cold water. Mechanical reaming is a common operation executed in well PV8 when fishing for the inhibitor tubing trapped in the wellbore by calcite scaling. The company owns a small truck-mounted drill rig, Ingersoll Rand RD-20, with a top-drive, 50 ton of hook load capacity and has a qualified crew. The rig is very well suited for this kind of workover operation.

The reaming operation is normally executed in 2 days, but the fishing can vary from 1 to 2 weeks, depending on the amount of tubing lost and the round trips required until catching the inhibitor chamber and weight bar. In this case, it is always necessary to make a final round to the bottom to make sure that the well is open. The injection of cold water throughout the fishing and cleaning operations is prejudicial to well production considering the following aspects:

- Scale sediments fall to the bottom and cross to the formation through the slotted liner, which will make the well shallower, and decrease permeability (by blocking formation fractures);
- Cooling the formation near the wellbore;
- Cooling and retracting the production casing;
- Negative effect of repeated thermal cycling of the cemented casings as it can cause it to break;
- Time of the total workover operation, including the fishing prior to reaming, in some cases; and
- Recovery time after the operation in order to regain the initial conditions of the well (mainly temperature with negative effect in the production).

Figure 10 shows the rig setup used for fishing and reaming operations in the wells in the Ribeira Grande geothermal field, where the drill rig is supported by a steel substructure and the crew work at an upper level platform at about 2 m above ground.

The preparatory work done before the workover operation includes: disassembling the wellhead components above the master valve and disconnecting from the power plant pipe line. After this the substructure is installed where the drill rig will be settled on the well pad. Then the drill rig, pumps, water tanks and water pipes and hoses are rigged up.

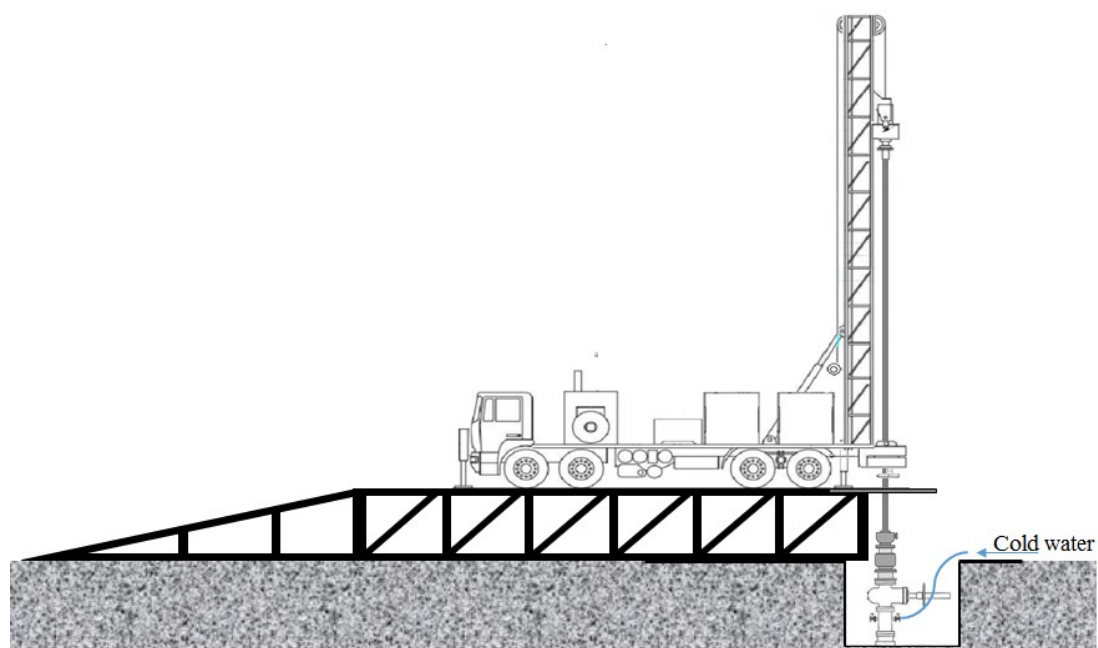


FIGURE 10: Reaming of calcite with the well quenched using a small drill rig (no scale)

On the day of the operation, the well control equipment, composed of a 9API 3000 annular blowout preventer (BOP) and a Ø7 1/16 rotating head, is connected to the master valve. The first tricone tungsten teeth bit used is Ø8 1/2 and it runs easily through the annular BOP. The well is killed by a triplex pump injecting cold water at 20 l/s (usually starting at 40 bar) through the Ø3 1/8 kill line valve, located on the casing head and monitored by a pressure gauge connected to the other Ø3 1/8 valve of the casing head. Once the well has been quenched and is in suction, with a wellhead pressure less than zero (WHP < 0 bar), the pumping of cold water is changed over to a centrifugal pump, which keeps the flow rate at around 20-30 l/s, with less consumption of fuel than the triplex pump and can supply a high flow rate.

The Ingersoll Rand RD-20 rig used for this operation has standard Ø4 1/2 Atlas Copco type drill pipes, in 30' lengths, and the bottom hole assembly (BHA) is simply the tricone bit + float valve + cross-over to the drill pipes. There is no need to use additional drill collars in the drill string as the well is always quenched and the scale deposits in the wellbore are soft to ream. The tricone bit is also cooled by the injection of cold water inside the drill pipes during reaming. After reaming in the slotted liner section, the Ø8 1/2 bit is pulled out of the well and changed over to a Ø12 1/4 bit to repeat the same operation inside the production casing. With the conclusion of the calcite cleaning, the equipment is moved off the well pad and the wellhead components are reconnected to the master valve and power plant pipe line and the chemical inhibitor system is installed again. The well recovers rapidly and can start to produce again two days after the workover operation.

3.5 Methods to overcome calcite scaling damage inside the formation

Methods for overcoming calcite scaling damage inside the formation are related to acid cleaning, described in the next chapter, or deepening or sidetracking from an existing well or modifying the casing program design for new wells:

- *Deepening the well*, is an option when knowing the existence of a new favourable productive layer (through the geology of wells near this location). For drilling inside the well, taking out the existing slotted liner can be considered, followed by drilling with the same bit size. The alternative is to drill with a small bit size inside the slotted liner and installing a new slotted liner below the old one;
- *Deviation of the well by side-tracking*, can be done if there are problems with calcite scaling blocking the slotted liner or indications of mechanical problems in the casing when it is not possible to remove the liner. One option is to initiate side tracking inside the casing, using what is called a casing exit system. It consists of a whipstock (special tool which is settled in the casing) to open a “window” in the casing form, while another hole is drilled as a sidetrack. The sidetrack can then have a new liner installed;
- *New well design*, can be considered if the flash point and loss of circulation depths are known and are consistent for wells drilled in the same area, with calcite scaling deposits inside the slotted liner. In this case the design of new wells with a deeper production casing is feasible to locate the flash point inside this casing. Future reaming operations would then be inside the production casing and the liner would not be affected by scaling that occurred out in the host rock; and
- *New well design, considering shallow wells open-hole*, which can produce from the steam cap of a reservoir, avoiding the formation of calcite in the wellbore (same principle as done at Svartsengi geothermal field, in Iceland) (Björnsson, 1999).

3.6 Acid cleaning of calcite scaling

Acid cleaning is also a method that can be used to remove calcite deposits from the wellbore or the formation. This method consists of injecting a solution of HCl and water into the well through the wellhead or inner string. The HCl is very effective in removing deposits by dissolving the carbonates and even other scale products, especially when HF is added as a booster. This is considered an expensive method and should not be done often (Morales, 2012).

4. MECHANICAL CLEANING OF SCALE DEPOSITS IN WELL PV8 WHILE DISCHARGING

4.1 Main wellhead configurations for workover

The adoption of methods to ream calcite scaling in wells while discharging has a long history in Iceland and in some other countries where this problem has a great impact on production. In Iceland, this method for reaming scales has been used for over half a century in a field where the calcite deposition is controlled to occur inside the production casing and no chemical injection of a scale inhibitor is implemented. The annual workover operations are relatively inexpensive and the wells recover their original output even after 30 years in operation.

The following section presents types of wellhead configurations used in reaming operations in high temperature wells.

4.1.1 Mechanical reaming of calcite scaling using a stripper and a gland

This method of using a gland and a special stripper was developed and implemented in Iceland in the early 1980s with the intension of reaming calcite scaling with wells discharging to a silencer pipe line to eliminate the thermal cycles in the well and formation and to extract the scaling cuttings. Figure 11 shows the general configuration and the main components used for this method.

The dimensions of the components are small and easy to connect and very useful in wells with a shallow cellar. A small rig can easily stand on the ground or on a steel substructure. It is not represented in the drawing, but a high pressure piston pump should always be connected to the kill line valve, in case of any occurrence with the need to kill the well (has occurred once). The configuration shown is recommended to be used in wells with wellhead pressures up to 20 bar; when flowing, the pressure on the stripper and gland components is greatly reduced because of metal seals in the wellhead and a condensing chamber for steam that bypasses the seals.

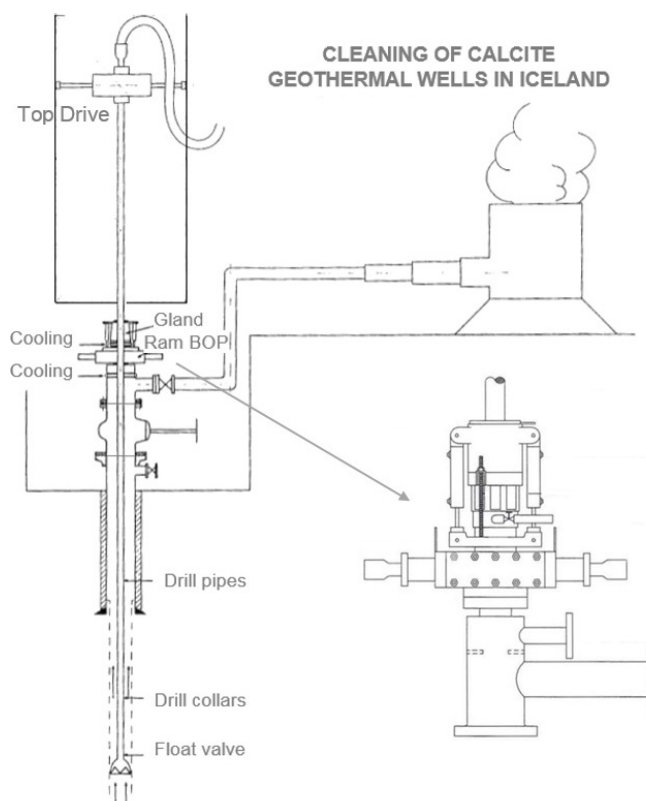


FIGURE 11: Mechanical reaming of calcite scaling in Iceland in the 80s and 90s (adapted from Molina, 1995)

The operation starts after all the components in Figure 11 are mounted and the tricone bit is inserted inside the diverter from below. After that, the lateral valve connecting the diverter to the pipe line silencer is opened and cold water is injected through the upper lateral outlet on the diverter. The flow of cold water running in the gland and diverter must be adjusted during the operation to quench the steam and cool the condensing chamber. After opening the master valve, the drill string is run in the hole until reaching the top of the scaling plug to start drilling out the scale deposits.

Figure 12 shows a wellhead configuration that was used in Iceland for scale reaming operations of wellbores at Svartsengi geothermal field. The wellhead has two main components, A - the stripper and B - the gland. The stripper is a type of diverter with two lateral outputs, separated internally by a flange with a metal seal to allow drill pipes to pass through it. In this diverter the well pressure is controlled when the fluid is flowing to the silencer pipe line. The gland is included in the top section of the wellhead and it works like a stuffing box or stripper, with an internal seal against the drill pipes when compressed vertically by the effect of the hydraulic cylinders. This gland and the internal ram rubbers of the BOP are continuously cooled by water during the reaming operation and the grip of the hydraulic cylinders is adjusted with the presence of leakage between the gland and the drill pipes. The drill pipes operated with this method have to be outside flush in order to enable sealing by the stripper and ensure long service life of the metal seal.

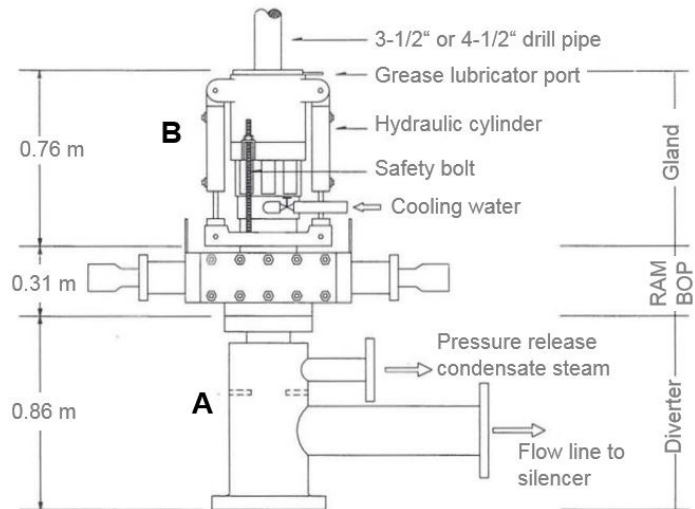


FIGURE 12: Wellhead configuration prototype used in Iceland (adapted from Molina, 1995)

4.1.2 Mechanical reaming of calcite scaling using a stripper and a rotating head

The main principle of using this method for reaming scales is similar to the one explained in the last section, but in this case the operation can be done in deeper wells, with a high range of pressure and temperature, as compared to the configuration considered before. This wellhead configuration provides a higher level of security of the operation, since the total length is greater for the seal and a complete BOP stack is installed as for normal drilling. For this operation, a large rig is required with a higher substructure to provide room for the wellhead equipment.

The wellhead configuration of Figure 13 is currently in use in Iceland at Reykjanes and the stripper mechanism included in it has been continuously developed, increasing the reliability of the reaming operation. Here, full wellhead pressure is maintained by water inside the spool marked A.

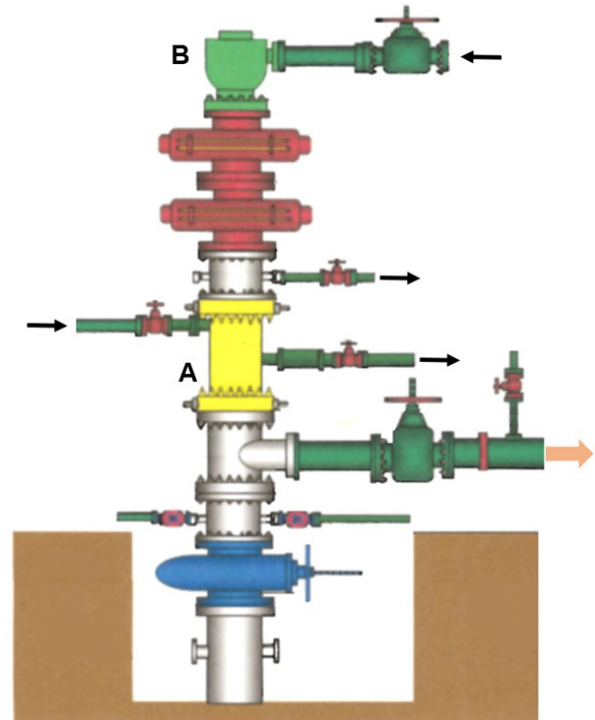


FIGURE 13: Wellhead configuration used nowadays in Iceland (Jardboranir, pers. comm.)

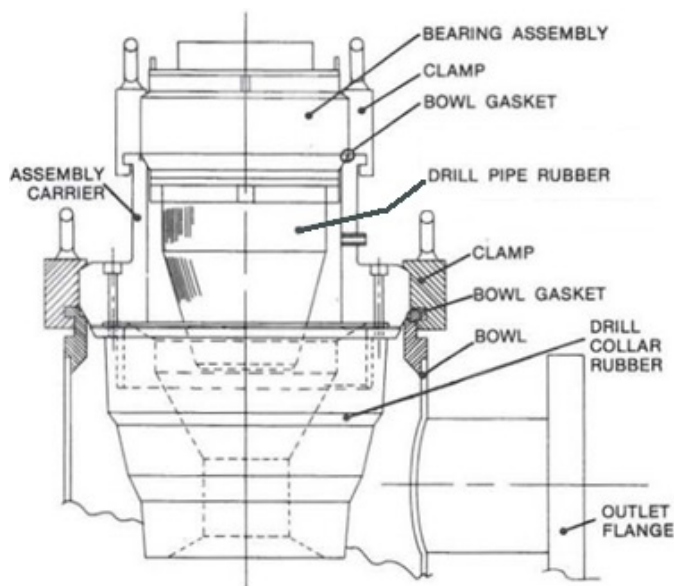


FIGURE 14: Standard rotating head model for geothermal wells (Molina, 1995)

drill pipes and drill collars are outside flush, because they have to pass through the internal plates of the stripper of the same diameter. The rotating head shown (Williams Tools Co., Inc) is constructed to hold 34.5 bar when rotating and about 140 bar when in static utilization (Molina, 1995).

The main component of the wellhead shown in Figure 13 is the stripper (labelled A). Inside it are two steel plates with aligned holes, with almost the same size of the drill pipes' outside diameter; the stripper is used to build up the pressure of the geothermal fluid in the Tee below. Cold water is injected in port 1 to condense the steam which crosses the bottom steel plate in the stripper and leaves the stripper via output 2, at a higher temperature (Figure 15). The flow of cold water in the stripper is increased or decreased by means of gate valves in order to maintain a low temperature inside the equipment and to balance pressure inside the stripper to match the pressure of geothermal fluid in the wellhead Tee.

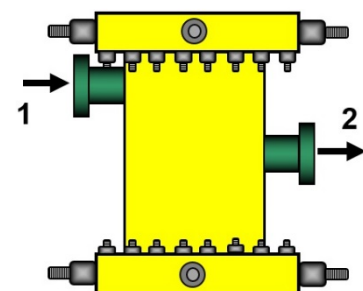


FIGURE 15: Stripper developed for reaming in geothermal wells in Iceland

4.2 Design of stripper mechanism for use in well PV8 while discharging

In this section the author proposes a design for a wellhead and stripper device. Most of the other equipment selected is from commercial pressure control equipment known in the drilling industry and used for workover operations. The design of the stripper mechanism to be used in well PV8 considers the following aspects:

- Specifications of the available drill rig;
- Optimization of the existent steel substructure where the rig will be settled;
- Dimensions of the cellar of the well PV8;
- Total height available for the wellhead configuration, including stripper, ram BOP and rotating head;
- Operating conditions of well PV8 during discharge (wellhead pressure and temperature);
- Acquisition of drill components, drill pipes, drill collars, cross-overs subs; and
- Adaptations on the rig table and pipe handler.

Reaming with this process requires an accurate management of pressure and temperature inside the wellhead components. In the upper part of the wellhead is the most important component, the rotating head (label B in Figure 13). The rotating head is normally responsible for diverting the flow during drilling, but in this assemblage its function is to hold the cold water pressure during cooling of the internal parts of the BOP equipment (rotating head, ram pipe BOP and ram block BOP).

Figure 14 shows a cutaway of a standard rotating head preventer which uses two internal rubbers (for pipes and collars); the position of the rubbers, the bearing assembly and the outlet flange that is used for the injection of the cold water can be seen. In this particular configuration, the

The specifications of the equipment are selected to meet the dimensions of well PV8's cellar and the pressure and temperature to enable the reaming operation.

4.2.1 Well PV8's cellar

The cellar of well PV8 has the following dimensions:

Height is 2.75 m;
Width is 2.5 m;
Length is 3 m;
Height from top of master valve to ground level is 0.51 m.

4.2.2 Steel rig substructure

The existing steel substructure to settle the rig has the following dimensions:

Substructure height= 1.61 m, concrete pads = 0.20 m, combined substructure height = 1.81 m;
Width of the substructure is about 2.7 m;
Total length of the 5 drilling rig modules, including the ramp, is 19.5 m.

4.2.3 Stripper mechanism

The stripper mechanism will be constructed of a heavy wall pipe reducer **12**-ANSI 900 x 7 1/16-3M with a holed steel plate welded inside the bottom flange and with a 3" flanged pipe on the lateral output, as shown in Figure 16.

The top flange 7 1/16-3M connects to the single ram double studded BOP and the bottom flange is **12** ANSI 900 to connect to the Tee.

The steel material grade to use in the stripper tools is AISI 4130 Annealed or equivalent, which is similar to the master valve flanges. In the centre of the steel plate there is a threaded steel sleeve which can be replaced when the internal clearance to the pipes exceeds the acceptable due to wear.

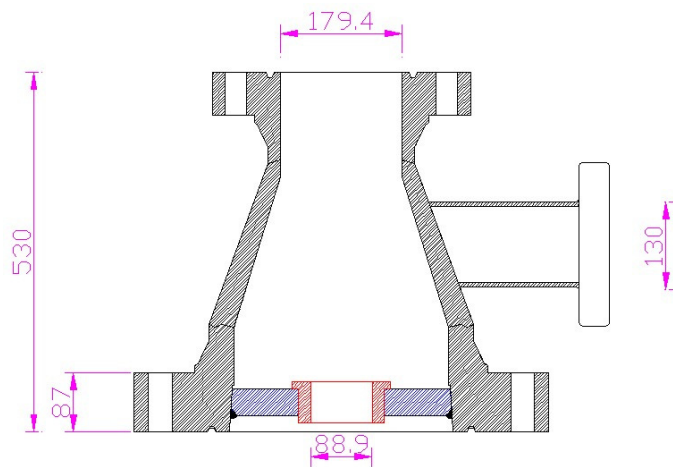


FIGURE 16: Design of the stripper for reaming calcite operation in well PV8, considering the presented dimensions in mm

The main function of the welded steel plate is to reduce the pressure and let the drill string pass through. Above the plate, the flowing cold water condenses the steam that bypasses the steel sleeve and allows the operation of the ram BOP and rotating head rubbers at low temperature and pressure.

4.2.4 Single Ram pipe BOP

To allow the installation in the available space under the rig table and the master valve, the selected BOP for use in the workover wellhead is a Single Ram Pipe BOP, prepared for work with pipes with 3 1/2 OD. Figure 17 shows the specifications of the chosen Ram BOP from the constructor *Shaffer* (Varco, 2002), which has a total height of 285.5 mm, one of the smallest in the market.


Single Ram Blowout Preventer Shaffer Model Chasovoy Hydraulic Cylinder		
Nominal flange	7 $\frac{1}{16}$ " - 3000	
Type of connection	Stud x Stud	
Overall height (mm)	285.5	
Overall length, bonnets closed (mm)	1,638.3	
Overall length, bonnets open (mm)	2,051	
Overall width (mm)	523.7	
Working pressure PSI (bar)	3,000 (207)	
Test Pressure PSI (bar)	10,000 (690)	
Ring Gasket	R-45	
Maximum operating pressure to close and open PSI (bar)	3,000 (207)	
Ratio	8.47:1	
Volume of hydraulic fluid (l)	2.27	
Piston stroke	103.2	

FIGURE 17: Specifications of the single ram double studded BOP selected for reaming calcite operation in Well PV8; the BOP shown in the picture is not the selected one

4.2.5 Rotating Head

The rotating head selected to mount on the wellhead is a *Washington Series 1400* (shorty), which has a maximum service pressure of 300 PSI (20.69 bar), as shown in Figure 18. This equipment will be used to keep the pressure of the cold water in the upper part of the wellhead. The maximum pressure rating is high enough to also hold the pressure of the well while discharging (about 15 bar), in case something happens to the steel plate seal welded in the stripper.


Nominal Flange	A	B	C	Sleeve Bore D	Body Bore E	F	G	Ring Gasket	Outlet Flange
7 $\frac{1}{16}$ " - 3000	34 $\frac{3}{4}$ "	28 $\frac{1}{4}$ "	17"	24 $\frac{1}{8}$ "	7 $\frac{1}{16}$ "	12 $\frac{9}{16}$ "	12"	R-45	7"
									
Dynamic Test Pressure (Rotating)				300 PSI					
Static Test Pressure				500 PSI					
Maximum rpm (intermittent)				150 rpm					
Stripper rubber mounting				Bolt-on					
Top drive				Yes					
Oil system				Self-contained pressurized					

FIGURE 18: Rotating head selected for reaming calcite in well PV8 (Washington Rotating Control Heads, Inc., 2012)

4.2.6 Drill rig Ingersoll Rand RD-20

The rig available for workover operations is an Ingersoll Rand RD-20, manufactured in 1986 and purchased by *EDA Renováveis* in 2005. The rig has been used by EDA for maintenance operations in geothermal wells and for drilling shallow water wells.

The main specifications of the rig are listed below:

- Manufactured in 1986, with complete overhaul in 2003;
- Hydraulic top-drive unit, with pullback capacity of 50 tons and pull-down capacity of 13.6 tons;
- Maximum depth rating of 1200-1500 m, depending on the drill sting;
- Rotary torque of 1000 kg. m;
- Mounted on a 4 axle Pettibone truck; and
- Rig Handler converted to work with 4 1/2OD Atlas Copco drill pipes, with 30' length.

In Figure 19, the drill rig that will be used in the reaming operations of well PV8 is shown. Modifications on the handler and rig table will be performed to allow handling of the outside flush drill pipes with a new diameter. This also requires the acquisition of rotary slips and safety clamps to support the 3 1/2 OD pipes and collars during the operation. For the initial part of running into the hole, the pressure inside the well will push the drill string up due to a piston effect.



FIGURE 19: Drill rig Ingersoll Rand RD-20

4.2.7 Drill Collars and Pipes

In order to optimize the total height and weight of the wellhead equipment, the selection of the drill pipes and drill collars is for outside flush drill pipes with 3 1/2 OD. According to the specifications of the rig, the length of the collars and pipes should be 30' in length.

According to the main specifications for drill collars and drill pipes shown in Table 3, the total weight of each drill pipe is 166.53 kg and drill collar is 362 kg. Usually when discharging, the WHP in well PV8 is around 16 bar, so we can consider utilization of drill collars to overcome a wellhead pressure of 20 bar. In this case it will need 4 drill collars (corresponding to 36 m DC length) to equalize the piston effect with the weight of the drill string to use the drill pipes.

TABLE 3: Specifications of drill pipes and drill collars for reaming operation
(Thomson International, Inc, 2012)

	Flush drill pipes	Flush drill collars
Outside diameter (inch)	3-1/2"	3-1/2"
Inside diameter (inch)	1-3/4	1-1/2"
Length (m)	9.1	9.1
Weight (kg/m)	18.3	39.73
Thread type	2-3/8 IF	2-3/8 IF

To reach a depth of 600 m will require 4 drill collars and 62 drill pipes.

4.3 Cleaning procedure using the Ingersoll Rand RD-20 rig

The pull-down required in a reaming operation was calculated, considering the diameter and weight of the drill string, as reported in Section 4.2, when referring to the specifications of drill pipes and drill collars. Figure 20 shows the pull-down force required to overcome the pressure inside the well, considering 4 (four) different wellhead pressures. In the drill string to be utilized, the use of 4 (four) drill collars was considered followed by the drill pipes. Observing the Figure, for the usual WHP = 15 bar, the use of 3 drill collars (27.3 m) would be enough to overcome the pressure in the wellbore. After 27 m, the operation could proceed normally, without any pull-down or arrangements in the rig table to hold the drill string from being pushed up when adding a new drill pipe.

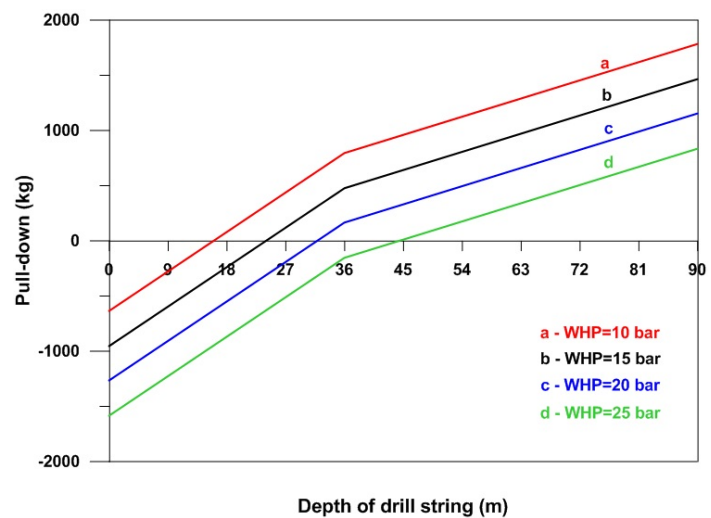


FIGURE 20: Pull-down required to overcome pressure inside well using 3 ½ OD drill rods and pipes

4.3.1 Cleaning procedure

The cleaning operation will take place after running the go-devil logging tool to confirm the calcite scaling depth for each internal diameter. Figure 21 shows a scheme with the main equipment (wellhead equipment, drill rig, rig substructure and silencer pipe line) mounted at the well pad to perform the reaming operation.

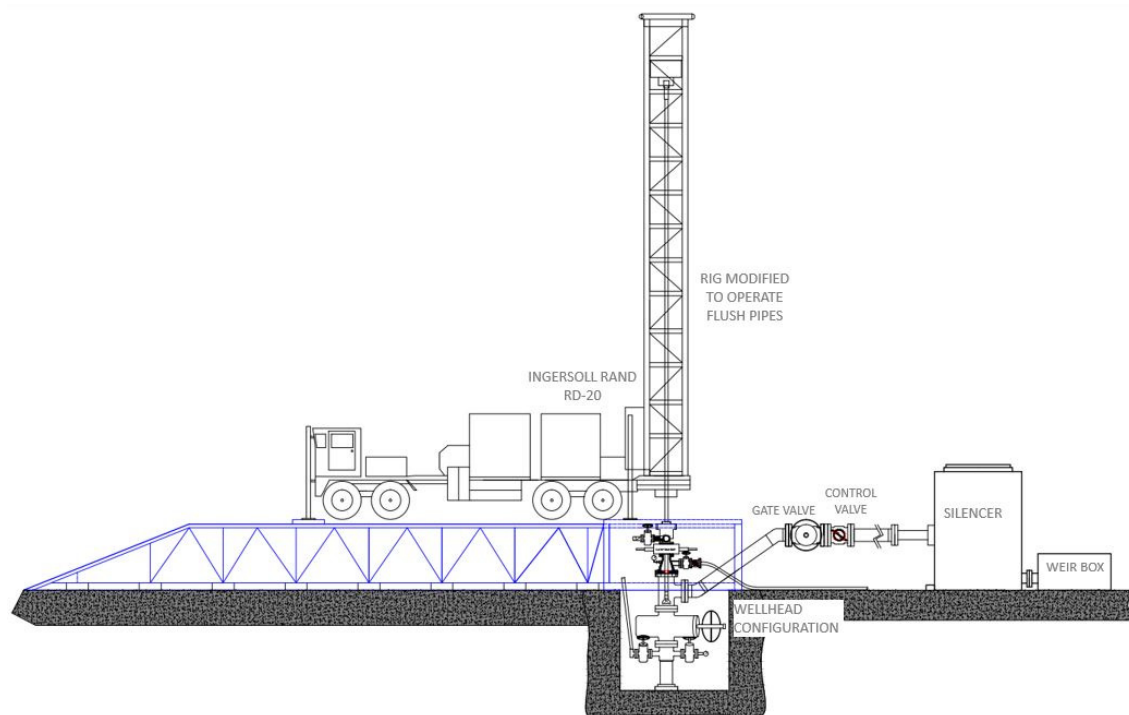


FIGURE 21: Drill rig settled to reaming calcite operation while discharging to the silencer pipe line

According to the dimensions presented in Point 4.2, the total length of the wellhead configuration (Tee, Stripper, Ram BOP and Rotating head) is about 2.25 m, but above ground level it is just 1.88 m, because half of the Tee height is inside the cellar. Considering that the total elevation of the rig (steel substructure, concrete pads and wooden supports) is 1.93 m, the wellhead can fit the available space, with enough free space under the rig table to lift the top of the rotating head, in case rubbers need to be replaced.

The proposed procedure for reaming calcite scaling in well PV8 consists of the following:

4.3.2 Assemblage of equipment and materials on the well pad of the well

1. Close the master valve and disassemble the wellhead equipment above it, including the lateral valve that connects the wellhead to the power plant separator pipe line.
2. Mount the rig steel substructure on the well pad. Install the 12" Tee above the master valve.
3. Mount the silencer pipe line connected to the lateral output of the 12" Tee, locating the control valve (butterfly valve) near the Tee, as shown in Figure 21.
4. Position of the drill pipe trailer is aligned with the drill rig, triplex pump parallel to the drill rig, and the centrifugal pump that will be used to pump cold water inside the stripper near the cellar.
5. The stripper, ram pipe BOP and rotating head are bolted in place. First the BHA (bottom hole assembly) composed of 8-1/2" bit, float valve sub and a 2 m length drill collar (3 1/2 OD) is passed inside the bolted assembly prior to it being mounted on the wellhead Tee, as the bits are too large to pass through the wellhead assembly above.
6. After installing the equipment with the BHA to the Tee, the 4" valve is connected to the rotating head (label 1 in Figure 22) and a 3" valve connected to the stripper output (label 2 in Figure 22) to conduct the cold water with the condensate to the waste pit. Temperature and pressure gauges should be connected to the stripper output before the 3" valve.
7. High pressure hoses and pipes are connected from the centrifugal water pump to the rotating head valve (non-returning valve at the end of the hose, before 4" valve, (label 1 in Figure 22), from stripper output valve (label 2 in Figure 22) to the waste pit pipe line and from the triplex pump to the 3" valve in the casing head (kill line label 4 in Figure 22). Check the supply of cold water to the pumps.

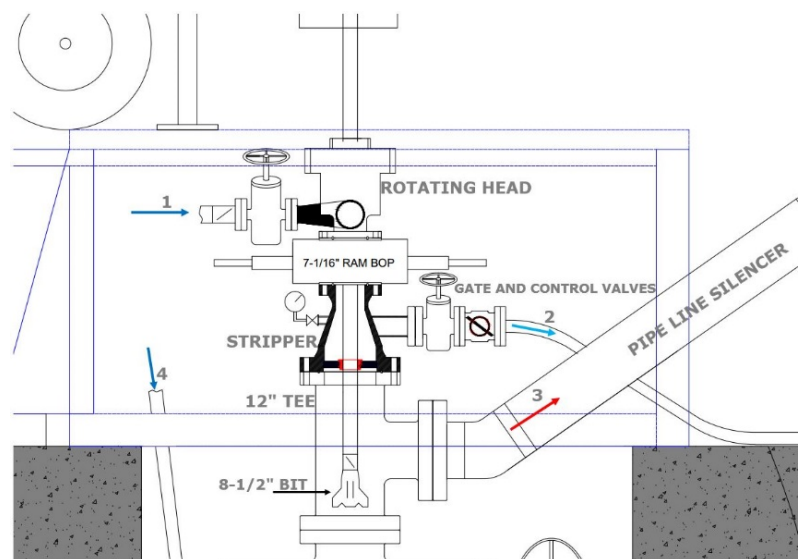


FIGURE 22: Wellhead configuration during reaming calcite operation (zoom of the wellhead); the connected pipes are rotated 90° in the Figure for better illustration

4.3.3 Operation procedure

1. Settle drill rig at the top of the steel substructure as shown in Figure 21, level the rig table, connect the first rod to the BHA and torque it.
2. Open the 4" and 3" valves on the rotating head input and stripper output and start pumping in cold water. Slowly close the valve on the stripper until the pressure reaches about 3 - 4 bar.
3. Check that the butterfly control valve is ~10% open and then open gradually the 12" master valve to fully open.
4. Control the flow rate of the geothermal fluid (steam and water) to the silencer pipe line and the pressures in the well and in the stripper.
5. Pull-down the first drill collar until the top of it gets to the rig table and hold the collar with slips. Below the table hold the collar with slips and steel cables to keep the collar in that position during the time the top drive picks up the second collar.
6. Continue with the same procedure until the third collar, which should be enough to overcome the well pressure; after that just start holding the pipes in the rig table with slips.
7. Run in the drill pipes to the depth of the bit tag on top of the calcite scaling (according also with the logging tools' measured depth) and start the reaming operation, adjusting the control valve opening to the minimum flow required to bring out the calcite cuttings to the silencer.
8. The calcite reaming operation continues until all the scaling is reamed and the cuttings are out of the well, which will be at about 600 m depth.
9. Pull out the BHA, paying attention to the need to hold the BHA with pull-down, when the drill collars reach the rig table.
10. Close the master valve, stop pumping cold water and disconnect the pipes and hoses from the 4" and 3" valves. Disassemble the connection between the stripper and the 12" Tee. Lift up the bolted assembly (stripper, ram pipe BOP and rotating head) to change over to the 12-1/4" bit.
11. Connect all the equipment again and repeat the same procedure (from steps 2 to 9) to do the reaming operation inside the production casing in the upper part of the well until 392.2 m depth (top of liner hanger).
12. After finishing the cleaning operation and extracting the BHA, the master valve is closed and the centrifugal pump stopped. The Tee and bolted assembly (stripper, ram pipe BOP and rotating head) are removed from the wellhead above the master valve.
13. The go-devil logging operation is conducted to check if the well is OK to resume production to the power plant. If it is OK, all the equipment, including drill rig, rig substructure, pumps and pipe line silencer are carried off of the well pad.
14. Mount the permanent wellhead equipment and lateral 12" valve on the well and start production to the power plant.

4.4 Benefits of cleaning wells while discharging

Reaming calcite while discharging, compared to reaming with the well quenched, has the following benefits:

- Calcite cuttings are removed from the well during the operation and do not deposit in the bottom or inside the formation (clogging the inner spaces) as it occurs when it is quenched;
- Temperature in the wellbore and formation do not change, as the well does not have to be quenched with cold water;
- Casing keeps the same properties and cement bond remains good, because there is no thermal cycling due to changes of temperature; and
- Total time for the well out of service is reduced.

The selection of this new method for reaming the scale deposits, combined with a monitoring program, improves production, maintenance of equipment, and material performance.

5. CONCLUSIONS

The accurate use of the methods referred to in this report guarantees improvement of the productive life of wells and, consequently, the maintenance of geothermal fields. For the case analysed, the adoption of the procedure for reaming calcite scaling in well PV8 while discharging (without quench), will achieve immediate results, preserving the good conditions of the cemented casing and reservoir and, at the same time, the calcite cuttings are carried out from the well avoiding letting them fall to the bottom of the slotted liner. The utilization of both methods – *chemical inhibition* and *reaming*, for controlling calcite deposition in well PV8 will prevent non desirable fishing and cleaning operations and, therefore, reduce unexpected time breaks in well production. To minimize the non-productive time of the well, preventive measures for controlling calcite deposition and scheduling cleaning operation should be carried out.

In order to deal effectively with problems related with calcite scaling in the wells, the following steps should be considered:

1. Identification of the type of scaling and the main reason for its deposition in the well.
2. Install down-hole equipment for treating the water with a scale inhibitor. If already installed, improve inhibitor selection and dosage.
3. Removal of any scale that forms in spite of chemical inhibition by mechanical reaming or chemical cleaning with acid.
4. Deepening or side tracking of wells are methods for recovering output lost to damaged casings or scaling out in the formation.

The main conclusions of the study are presented below:

- The tendency for the formation and deposition of calcite in the boreholes of the Ribeira Grande geothermal field imposed the application of methods for prevention of this occurrence and rehabilitation of the wells in case it occurs;
- The injection of the calcite scaling chemical inhibitor NALCO pHREEdom (R) 5200M, since November 2012, has proven to be a good solution in the prevention of calcite deposits in the wells of Ribeira Grande geothermal field. However, in well PV8, the inhibitor only delays the formation of calcite, making it necessary from time to time to ream the well to remove the deposited calcite or fish for broken capillary tubing; and
- Calcite reaming in a well when it is discharging to a separator pipe line allows large benefits: reduction of the time the well is out of service; the temperature in the formation near the well is maintained (because no cold water is used to quenched the well); no thermal cycling in the casing and, therefore, no effect on the properties of the cement or casing steel.

ACKNOWLEDGEMENTS

I want to sincerely thank Mr. Lúdvík S. Georgsson, the director of United Nations University Geothermal Training Programme, and all the UNU staff of Orkustofnun. I also want to thank Mr. Carlos Ponte, the executive member of the board of *EDA Renovaveis S.A.* for giving me the opportunity to come to study here in Iceland and for allowing me to use the data from the company. I thank United Nations University and the government of Iceland for providing funds for my study. My sincere appreciation goes to my supervisor, Mr. Sverrir Thórhallsson, for his support and guidance in my project. I thank all the UNU lecturers who taught me, and the UNU fellows for their good company and support. Finally, I want to thank my wife Ana, my mother Maria, and my family for their moral support during the six months of the UNU course.

REFERENCES

- Arnórsson, S., 1989: Deposition of calcium carbonate minerals from geothermal waters-theoretical considerations. *Geothermics*, 18, 33-39.
- Bjarnason, J.Ö., 2010: *The speciation program WATCH* (vers. 2.4). ÍSOR – Iceland GeoSurvey, Reykjavík.
- Björnsson, G., 1999: Predicting future performance of a shallow steam-zone in the Svartsengi geothermal field, Iceland. *Proceedings of the 24th Workshop on Geothermal Reservoir Engineering, Stanford University, Stanford, CA*, 7 pp.
- GeothermEx, Inc., 2006: *Completion report of well PV8 Pico Vermelho geothermal project*, São Miguel, Açores. GeothermEx, Inc., report 40, 44 pp.
- Morales A., M., 2012: *Acid stimulation of geothermal wells in Mexico, El Salvador and the Philippines*. UNU-GTP, report 20, 419-436.
- Molina A., G.G., 1995: Rehabilitation of geothermal wells with scaling problems. Report 9 in: *Geothermal Training in Iceland 1995*. UNU-GTP, Iceland, 207-240.
- NALCO, 2006: *Product Bulletin: 5200M*. Nalco Europe B.V., the Netherlands, 3 pp.
- Thompson International, Inc., 2012: *The total package - complete drill string from “Top to Bottom”*. Thompson International, Inc., website: www.thompsoninternational.com/Thompson%20Intl%20Catalog.pdf.
- Thórhallsson, S., 2006: Common problems faced in geothermal generation and how to deal with them. *Workshop for Decision Makers on Geothermal Projects in Central America 2006, San Salvador, UNU-GTP and LaGeo*, 8 pp.
- Varco, 2002: *Pressure control – Shaffer ram BOPs*. Varco, LP, website: <http://wenku.baidu.com/view/99afcb697e21af45b307a8ef.html>, 24-25.
- Washington Rotating Control Heads, Inc, 2012: *Series 1400 rotating control heads*, Washington Rotating, website: www.washingtonrotating.com/1400-rotating-control-heads-shorty-24.aspx.



UNITED NATIONS
UNIVERSITY

UNU-GTP

Geothermal Training Programme

Orkustofnun, Grensasvegur 9,
IS-108 Reykjavik, Iceland

Reports 2014
Number 34

FLUID-ROCK INTERACTION AND INITIAL AQUIFER GEOCHEMISTRY IN THE OLKARIA GEOTHERMAL SYSTEM

Edwin Wafula Wanyonyi

Kenya Electricity Generating Company Ltd. - KenGen

P.O. Box 785-20117, Naivasha

KENYA

ewwafula@kengen.co.ke

ABSTRACT

The Olkaria geothermal field is one of the quaternary volcanic centres in the Kenyan Rift valley. Geochemical methods have been applied in studying the elemental origin and reactions at depth. Fluid-rock interaction is one of the key reactions of interest in geothermal systems. Two models have been postulated in the evaluation of aquifer fluid composition. The first model assumes a single-phase liquid aquifer, while in the second model one assumes a two-phase fluid aquifer: vapour and liquid. The concentration of non-volatile components is unaffected by the choice of model except for fluid discharges approaching dry vapour. However, the concentration of volatiles is greatly influenced by the selection of a model for calculating aquifer fluid composition. As a consequence, solute geothermometers like quartz and Na/K have similar temperatures for the two models, whereas gas geothermometers like H₂S show distinctively lower values when assuming two-phase aquifers. Many common minerals observed within the Olkaria geothermal system are observed to be saturated, including calcite, fluorite, epidote-clinzoisite, prehnite, feldspars and pyrite. Based on this, the mineral-fluid equilibrium is considered to control the fluid chemical composition. Mineral buffer reactions are considered to control the H₂S and H₂ volatile concentrations, whereas the concentration of CO₂ may either or both be controlled by mineral equilibria in the geothermal system or by an external source.

1. INTRODUCTION

Geochemistry is one of the major disciplines that have been applied in the exploration and development of geothermal systems. The primary goal of geochemical study of geothermal fluids is to trace their elemental origin and reactions. The latter makes the basis for estimating subsurface temperatures based on the chemical composition of samples collected at the surface. Among the key reactions of interest in geothermal systems is fluid-rock interaction. Previous studies have demonstrated a close approach to equilibrium between common geothermal minerals and the fluids within the reservoir, hence controlling the composition of most major elements in the fluid (Giggenbach, 1981; Arnórsson et al., 1983). However, the assessment of fluid-rock equilibria from the fluid composition of surface well discharges largely relies on the assumptions made when calculating the subsurface aquifer fluid composition. In the case of two-phase well discharges that have measured enthalpies closely corresponding to liquid-only aquifers and the aquifer temperatures, the assumption of adiabatic boiling upon ascent is considered valid. On the other hand, many well discharges have excess enthalpy

characteristics, i.e. a high vapour-to-liquid water ratio relative to a liquid-only aquifer and the aquifer temperatures. In this case, the cause of the excess enthalpy has to be taken into consideration when assessing the aquifer fluid composition. The reasons for such an excess enthalpy character may be many, including vapour formation in the aquifer due to heat induced boiling and the formation of aquifer vapour. Alternatively, depressurization boiling may lead to separation of vapour and liquid water, either fully or partially, the latter referred to as phase segregation. In recent years, phase segregation has been concluded to be the cause of excess enthalpy in many cases, whereas heat induced boiling is less well documented (Arnórsson et al., 2007; Karingithi et al., 2010; Scott et al., 2014). This project aims to assess the aquifer conditions and fluid-rock interaction based on two different models. Model 1 is based on a calculated enthalpy and considers a single-phase liquid only reservoir, while model 2 considers a two-phase liquid and vapour reservoir. Model 2 is based on a measured enthalpy and considers the presence of excess enthalpy in the system. In the evaluation of the initial aquifer composition, both models are postulated and the results are compared. The component concentrations for volatile and non-volatile species are considered in characterising the initial aquifer conditions from the two models. Geothermometer temperatures are also determined considering these aquifer concentrations and a comparison is done with the measured reservoir temperatures. Then it will be possible to determine what the contributing process to the excess enthalpy in the wells could be. The mineral saturation state is dependent on the aquifer composition of the fluid. Thus, the mineral saturation state for selected minerals: andradite, grossular, calcite, clinozoisite, epidote, fluorite, magnetite, prehnite, pyrite, pyrrhotite and wollastonite, are modelled.

2. OLKARIA GEOTHERMAL SYSTEM

2.1 Study area

The Olkaria geothermal project is located approximately 120 km northwest of Nairobi, on the floor of the southern segment of Kenya's Rift Valley. The Olkaria concession covers an area of 204 km². About 14 prospects have been identified in the Kenyan Rift Valley as having a potential for geothermal development. Of these, geothermal exploration has been done in almost all these areas, but currently development is limited to Olkaria, Eburru and Menengai Geothermal fields. Currently, 217 wells have been drilled in Olkaria, both vertical and directional wells, including reinjection, monitoring and production wells. The Olkaria geothermal field is divided into seven sectors: Olkaria E, Olkaria NE, Olkaria C, Olkaria SW, Olkaria NW and Olkaria SE (Figure 1). Production from geothermal resources started in 1981 with the construction of the Olkaria I power plant that currently has a production capacity of 45 MW. An additional 140 MW power plant is under construction in this part of the field. In the Olkaria NE, the Olkaria II power plant exists with a production capacity of 105 MW. An additional power plant is under construction that will add a further 140 MW to the grid in the Olkaria domes area.

2.2 Geology

According to Strecker et al. (1990), the Olkaria volcanic complex is part of the volcanic centres in the Central Kenya Rift, associated with quaternary silicic volcanism. These include the Suswa, Longonot, Eburru and Menengai volcanic centres. The Olkaria geology has been divided into five broad litho-stratigraphic groups based on the age of the stratigraphy and lithology. These include the Mau tuffs, Plateau trachytes, Olkaria basalts and upper Olkaria volcanics (I only count 4, not 5.). The rocks occurring on the surface in the Olkaria geothermal area include rhyolite flows and pyroclastic deposits. Lacustrine deposits crop out in isolated occurrences within Olkaria but are abundant closer to Lake Naivasha. The distal deposits have been associated with previous high stands of Lake Naivasha (Naylor, 1972). The latest ash-fall deposits that blanket most lava flows in Olkaria originated mainly from Longonot volcano and, to a smaller extent, from Suswa volcano (Odongo, 1984). The youngest volcanic activity at Olkaria occurred about 250 years ago and produced the Ololbutot lava flow, which is an



FIGURE 1: Map of the Greater Olkaria volcanic complex showing major structures (from Clarke et al., 1990)

important landmark in the area (Clarke et al., 1990). The Mau formation is the geothermal reservoir rock for the western sector. In the eastern Olkaria geothermal field, there occurs a basaltic formation at between 1000-1500 m above sea level. The formation is considered a cap-rock (aquitard) to the geothermal system and temperatures rise sharply below it. The formation is absent in the west field. Overlying the basalt formation is the upper rhyolite unit that extends from the east to the western fields.

The fault system in Olkaria is dominated by a N-S pattern. Other common trends are NW and ENE. A ring structure defined by lava domes occurs in the eastern Olkaria area and marks the eastern and southern boundary of the Domes field. Sheets of recent and quaternary lavas, pyroclastics and lacustrine sediments blanket most of the faults in the area. The N-S faults are active and open since the dominant tectonic regime within the central rift is extensional with a minimum stress field oriented in a general WNW-ESE direction (Strecker et al., 1990).

Hydrothermal mineral characterisation is one of the important parameters in the classification of geothermal systems. Kandie et al. (2014) described the hydrothermal minerals of the Olkaria system as analysed from well cuttings. The alteration minerals have been defined by the occurrence of certain specific index minerals and clay minerals. These are: smectite-zeolite zone (0-300), mixed Layer Clay (smectite-chlorite-illite zone), chlorite-illite zone (300-550 m), epidote-chlorite-illite zone (550-1400 m) and actinolite-epidote chlorite-illite zone (1400-3000 m). Lagat (2004) classified the hydrothermal mineralogy of the Olkaria geothermal system. The main minerals identified are: albite, actinolite, biotite, calcite, chlorite, chalcedony, epidote, fluorite, garnet, illite, adularia, pyrite and quartz.

2.3 Geochemistry

The Olkaria geothermal field has varied chemistry in the different sectors within it. The water discharged from wells in the Olkaria field is low in dissolved solids, compared to water from most other drilled high-temperature geothermal fields in the world, with chloride concentrations in the water at the weir box ranging between 50 and 1100 ppm. The water from wells in Olkaria East and Northeast are the highest in chloride. The high chloride could be a result of up-flow of deep high-temperature geothermal fluid, although progressive boiling by heat flow from the rock may also be a contributing factor, as in the Olkaria East field. A study by Wambugu (1995) established that in Olkaria West field the chloride concentrations are quite low, except in well OW-305, which discharges water similar to that discharged from the wells in the Olkaria East and Olkaria Northeast fields. Well OW-305 is thought to be tapping the up-flow fluid in the Olkaria West field. The well discharges in Olkaria West are distinctly highest in carbon dioxide. The CO₂ source is considered to be predominantly from the magma heat source of the geothermal system, although carbon present in the rock may contribute as much. The chloride, sulphate and bicarbonate ternary plots show that wells in the Olkaria East production field and in Olkaria Northeast discharge sodium-chloride type water, while the Olkaria West has a bicarbonate water type. Wells in the Olkaria Central and Domes fields discharge a mixture of chloride and bicarbonate water. Temperature and pressure distributions across the entire field have been studied and indicate that fluid movement in the Olkaria geothermal area is associated with tectonic structures. The Olkaria East reservoir is two-phase, at least to the depth penetrated by the deepest wells. High temperatures are observed in Olkaria West, Olkaria Northeast and Olkaria Domes, while lower ones are observed in Olkaria Central. The ENE-WSW trending Olkaria fault zone is the most important permeable structure in the entire Olkaria geothermal area. The geothermal reservoir in the north (including Olkaria Domes) is liquid-dominated and has no steam cap, whereas south of the fault the reservoir is a liquid-dominated two-phase system overlain by a steam-dominated zone (Ambusso and Ouma, 1991). The Olkaria reservoir has a shallow two-phase steam-dominated zone at 240-250°C, and a deeper zone that is liquid-phase at up to 340°C. Mixing of this liquid in lower shallower zones results in high total enthalpy conditions in some wells, causing excess enthalpy in the well discharge by excess boiling. Enthalpy-chloride diagrams from the well indicate a deep upwelling of a fluid at 320°C to 340°C, cooling to 280°C before the onset of boiling and mixing in the NE production field and E production field sectors. Enthalpy-chloride models for the domes area suggest that deeper temperatures are closer to 330°C and that reservoir boiling seems to start at this temperature without prior cooling. Na/K ratios have been used to locate major up-flow zones in geothermal fields (Arnórsson and D'Amore, 2000) with the lowest ratios being closest to up-flow zones. The Na/K geothermometer is based on this ratio with high temperatures obtained at lower ratios. Na/K temperatures for the Olkaria field sectors show good agreement with measured temperatures at 0 m above sea level. The temperatures, together with the chloride distribution in the field, delineate zones of up-flow in the geothermal area. The Na/K temperature shows distinct up-flow zones in each of the three sectors of the Olkaria field, but delineates a subtle one for Olkaria west around wells OW-301 and OW-308.

3. DATA BASE AND DATA HANDLING

The principle method used in the acquisition of geochemical data is sampling and analysis of well discharges. The data used in this study is from 24 wells in the Olkaria geothermal system, with 15 of these wells representing wells that are currently under production. The data is referred to from the analysis by Karingithi, et al. (2010)

3.1 Sampling and analysis

Sampling and collection of fluids for chemical analysis were based on the procedures described by Arnórsson et al. (2007) for high temperature wells. These wells discharge a two-phase fluid and

sampling and collection of samples was done on the two-phase line. The liquid and steam samples were collected using a webre separator. Fluid was allowed to flow into the separator by opening the vents. The valves in the separator were adjusted so that the pressure in the webre separator was close to that in the well head. The sampling pressure and temperature were recorded. For the liquid sample, the needle valve and the ball valve of the webre separator were completely opened to release steam and to ensure that only liquid was sampled from the water port (no bubbles), collected into different bottles. A micrometre filter paper was used in the filtration of the liquid samples to remove the colloidal particles. A 250 ml filtered sample acidified with 1 ml nitric acid was collected for analysis of major cations. A 10 ml sample, diluted with 90 ml deionized water, for silica analysis was collected to slow down the polymerisation of the monomeric silica in solution. A 100 ml filtered sample was precipitated with 2 ml zinc acetate for sulphate analysis. A 250 ml filtered sample was collected for analysis of boron, chloride and total solids. A 500 ml untreated sample for analysis of pH, Carbonate and conductivity was collected in a tightly corked glass bottle to avoid contamination with air. Hydrogen sulphide was titrated on site. The steam sample was collected by fully opening the water valves completely and adjusting the needle and ball valves of the separator until a dry steam was obtained. The steam was collected to an evacuated double port bottle containing 50 ml of 40% NaOH, using tubings from the separator port. The CO₂ and H₂S dissolve in the caustic solution; the other gases collect in the free space in the bulb.

The analysis was done according to standard methods for geothermal fluid analysis, as described by Ármansson and Ólafsson (2000). Analysis for H₂S in the liquid sample was done in the field by titration, using 0.001 M HgAc₂ with a dithizone indicator. 5 ml of NaOH was put in a 50 ml volumetric flask and filled with the sample. 0.1-5 ml was put in an Erlenmeyer flask and 5 ml acetone was added and the volume was brought up to 10 ml with distilled, deionized water. Silica analysis samples were diluted to slow the polymerization of silica. The method used for silica analysis is spectrophotometric, using the absorbance of the yellow β-molybdosilicic acid complex at a wavelength of 410 nm. The fluoride concentrations were determined with an ion selective electrode with standards prepared from NaF. The working standards were prepared from a 1000 ppm stock solution with working ranges of 5-500ppm and 0.5-50 ppm. The chloride analysis was done by argentometric titration with Silver Nitrate, using potassium chromate as an indicator. The sample was titrated with 0.1 AgNO₃, where the end point is the appearance of the first permanent orange colour.

3.2 Charge balance

Geochemical interpretation is based on data sampled and analysed from well discharges. This data, however, needs to meet certain criteria before credible information on the well chemistry is certain. Ways have, therefore, been devised to ensure that good data is used in the geochemical interpretation.

The first of these is the ionic balance check. Normally, it is expected that the geothermal fluids are close to neutral solutions and, hence, the negative charge and the positive should be close to null. A mathematical expression called the charge balance error has been devised to set limits within which to consider a chemical analysis as acceptable. The charge balance error can be determined based on Equation 1, although the program WATCH version 2.4 (Bjarnason, 2010) was run to accurately determine the ionic balance, given that it considers the speciation of the compounds. From the program, a balance of +/- 15 percent is considerable and the data can be used.

$$CBE \% = \left(\frac{\sum Z_{cat} M_{cat} - \sum Z_{an} M_{an}}{\sum Z_{cat} M_{cat} + \sum Z_{an} M_{an}} \right) \cdot 100\% \quad (1)$$

where Z_{cat} is the charge of a given cation, M_{cat} is the molal concentration of the respective cation, Z_{an} is a charge of a given anion and M_{an} is the molal concentration of the respective anion.

The pH of a fluid is an important parameter, in that the mineral solubility depends on it. The pH, on the other hand, varies with the temperature of the fluid. The practise is to measure the pH at the sample site and record the temperature. On some instances, however, the pH is taken in a laboratory away from the sampling site. In such a case, the recorded pH may not represent the accurate pH of the fluid. This is because in high temperature systems, the sample would already have polymerised silica. The removal of monomeric silica in the solution increases the pH of the solution (Karingithi et al., 2010). If such is the case, then a pH correction has to be calculated on the WATCH program, especially for fluids with pH above 9.

3.3 Aquifer fluid composition

Geochemical interpretations are based on samples that are collected from well discharges at the surface. To understand the fluid-rock interactions at depth, however, the chemical composition of the fluid at aquifer conditions has to be calculated. The approach chosen here is to calculate the aquifer fluid composition involved either by assuming liquid only in the reservoir and no excess enthalpy, or alternatively assuming two-phase vapour and a liquid reservoir (Table 1).

For the models, conservation of mass and energy is assumed, i.e.

$$m_i^t = m_i^v X + m_i^{lq} (1 - X) \quad (2)$$

where m_i^t is the total concentration of the i-th component, and m_i^v and m_i^{lq} are the concentration in the vapour and liquid phase of the same component, respectively.

For the enthalpy of the system, we have:

$$h^t = h^v X + h^{lq} (1 - X) \quad (3)$$

where h^t is the total enthalpy of the system, h^v and h^{lq} are the enthalpies of the vapour and liquid phases, respectively, and X is the steam fraction given by:

$$X = \frac{h^t - h^{lq}}{h^v - h^{lq}} \quad (4)$$

The WATCH program version 2.4 (Bjarnason, 2010) was used to calculate the aquifer fluid composition from the data on the well discharge composition. In the case of a liquid-only reservoir, the reservoir enthalpy of the system was calculated assuming liquid-only water to be present at reservoir temperatures. In the case of a two-phase vapour and liquid water reservoir, the measured discharge enthalpy was included to solve the formulas of mass and enthalpy. The former approach is termed Model 1 here, and the second approach is Model 2.

3.4 Geothermometry

Chemical geothermometers have been applied in the estimation of reservoir temperatures. These include both the solute geothermometer and gas geothermometer. The three geothermometers included here were silica, Na/K and H₂S.

The silica geothermometer is based on quartz solubility at >180°C, according to the chemical reaction:



The quartz solubility constant, as well as the silica geothermometer temperatures, are based on Gunnarsson and Arnórsson (2000) to give:

$$t_{qtz} = -54.8 + 0.3729.X - 5.602 \times 10^{-4}.X^2 + 5.719.10^{-7}.X^3 + 73.917.\log X \quad (6)$$

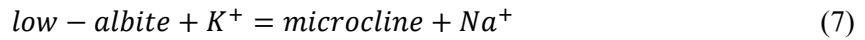
where X is the SiO₂ concentration in ppm.

TABLE 1: Chemical analysis of water and steam wells in Olkaria; component concentration for water samples are in mg/kg, and mmole/kg for steam

Well	GSP	WHP	Enth. (Kj/Kg)	Aquifer T	pH	B	SO ₄	Cl	CO ₂	F	H ₂ S	SiO ₂	Ca	Li	Na	K	Mg	Fe	Al	CO ₂	H ₂ S	CH ₄	H ₂	N ₂
Water sample																								
2	4.8	5.8	1839	251	9.07	6.8	28	764	74	69	1.02	643	0.73	0.5	557	92	0.010	0.020	0.660	101.1	5.61	0.722	2.94	1.94
5	4.8	5.5	2599	240	8.75	8.7	70	933	73	71	1.19	624	1.08	1.3	668	102	0.010	0.030	1.110	101	5.61	0.111	2.33	2.28
10	4.8	6	2531	261	8.57	12.9	61	1190	78	76	0.17	773	2.46	1.2	805	144	0.050	0.050	0.830	70.5	4.33	1.433	1	5
11	5	5.1	1894	246	8.94	5.7	21	696	69	64	0.34	597	0.58	1.1	497	81	0.000	0.020	0.700	53.3	9.27	0.611	2.61	1.72
15	4.5	5	2140	242	9.43	5.9	54	658	92	57	9.86	576	0.56	1.1	526	83	0.010	0.020	0.790	55	5.44	0.444	3.55	2.83
16	4.8	5	1534	228	9.37	4.9	44	586	97	64	7.14	502	0.35	1.2	503	67	0.030	0.010	0.490	68.3	4.83	0.278	4.27	6.16
19	5.2	5.5	1871	229	9.51	4.6	57	392	126	70	22.1	548	0.49	1.073	425	54	0.040	0.020	0.910	58.8	5.77	0.389	3.72	5.44
20	5.4	5.5	2541	255	8.98	14.3	22	822	110	95	1.19	778	0.92	1.789	610	97	0.050	0.380	0.430	101	9.33	0.333	4	1.28
23	5	6.1	2191	242	9.44	4	42	221	132	75	7.88	653	0.9	0.813	370	52	0.050	0.040	0.710	81	7.27	0.167	5.27	2.5
26	7.2	7.5	1881	247	9.39	2.2	24	309	104	68	13.6	657	0.24	1	336	51	0.040	0.250	0.930	129.3	9.21	0.222	4.22	3.33
28	2.1	8.1	2446	234	9.27	6.2	104	478	72	50	4.59	625	1.33	1.2	441	61	0.010	0.120	0.860	41.6	4.88	0.056	2.33	2
29	2.1	8.5	2158	241	8.87	10.1	30	509	82	84	3.91	609	0.75	1.2	417	63	0.030	0.060	0.670	45	6.66	0.056	3.77	3.33
30	2.1	8	2196	256	8.6	3.9	50	527	48	52	1.03	768	0.27	1.234	406	71	0.030	0.910	1.600	55	6.61	0	0.39	2.55
202	1.5	5.2	1104	225	9.3	2.5	75	354	1246	53	2.38	320	0.79	0.98	743	128	0.040	0.020	0.860	155.4	0.56	0.278	0	0.89
301	1.5	7.4	1653	262	8.67	6.8	112	240	2465	105	3.96	855	0.66	0.887	1283	208	0.070	0.020	0.670	4260.1	3.55	0.833	1.05	11.27
302	1.8	5.7	1234	256	9.72	3.5	54	505	578	77	3.43	744	1.04	1.5	633	101	0.080	0.020	0.780	367.5	1.11	0.389	0.33	3.22
304	2.6	3.9	1672	190	8.13	3.3	93	52	1752	24	0.97	364	3.48	1.331	959	74	1.730	0.140	0.520	11462	2.66	1.721	0.94	17.37
306	1.8	4	1037	224	9.15	6.3	50	251	1081	62	2.9	551	1.2	1.2	850	96	0.080	0.090	1.380	1136.8	2.89	0.944	0.56	7.83
709	1.9	7.1	1921	276	9.93	5.1	73	770	318	28	6.54	649	1.41	1.8	846	218	0.040	0.020	0.890	56.1	1.44	0.278	1.89	3.05
714	2.8	14.9	1303	267	9.54	3.6	35	682	135	66	8.44	739	0.88	1.4	557	108	0.060	0.010	1.050	81	4.38	0.333	1.22	3.39
719	2.9	8	1259	241	9.38	4.8	83	544	162	46	4.46	588	1.09	1.15	536	81	0.040	0.020	1.510	155.4	5.33	0.444	1.05	4.11
901	1.6	4.3	1854	220	9.8	2.4	124	280	566	80	18.3	529	0.72	2.6	506	57	0.030	0.030	0.680	186.5	4.94	0.333	2.44	5.16
902	1	3.2	1108	209	9.55	1.5	100	212	434	52	2	477	1.31	1.3	448	41	0.050	0.080	2.120	178.7	0.5	0.777	0.06	13.54
903	1.3	4	953	206	9.43	1.1	103	178	634	46	3.51	443	0.71	1.8	493	47	0.040	0.020	1.220	278.1	1.05	0.722	0.22	18.98

GSP = sampling pressure (bar g); WHP = well head pressure (bar g); Enth = enthalpy (kJ/kg); T = temperature (°C)

The Na/K geothermometer is based on the equilibrium between low-albite and microcline, according to the chemical reaction:

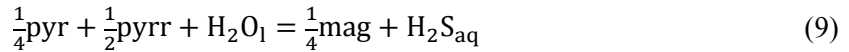


The temperature function based on the solubility of low-albite and microcline is given by Arnórsson and Stefansson (1999):

$$t_{Na/K} = 733.6 - 770.551.Y + 378.189.Y^2 - 95.753Y^3 + 9.544.Y^4 \quad (8)$$

where Y is the logarithm of the Na^+/K^+ activity ratio.

The H_2S geothermometer temperatures were calculated based on the chemical reaction:



using the proposed equation given by Karingithi et al. (2010):

$$t_{H_2S} = 252.7 + 65.573.Z + 5.063.Z^2 + 0.1641.Z^3 \quad (10)$$

where Z is the concentration of H_2S in the aquifer water in mmol/kg.

3.5 Mineral saturation

The mineral saturation state is calculated, based on:

$$SI = \log(Q/K) \quad (11)$$

where K is the equilibrium solubility constant and Q is the activity product (Q) given by:

$$Q = \prod_i a_i^{v_i} \quad (12)$$

and a_i is the respective aqueous specie's activities raised to the power of its stoichiometric coefficient, v_i , which is negative for reactants and positive for products. Here, the aqueous speciation was calculated using the WATCH 2.4 program (Arnórsson et al., 1982; Bjarnason, 2010). The solubility constants for the pure minerals and mineral buffer reactions were taken from Karingithi et al. (2010). All minerals were taken to be pure, i.e. their activities were assumed to be unified. The minerals considered in this study, together with their equilibrium constant temperature functions, are given in Tables 2 and 3.

4. AQUIFER FLUID COMPOSITION

The aquifer fluid composition was assessed with the aid of the WATCH program (Arnórsson et al., 1982; Bjarnason, 2010) version 2.4. The program uses the chemical composition of vapour and water collected at the surface from well discharges. Two approaches were used to calculate the aquifer fluid composition; Model 1 assumes a liquid-only aquifer, and Model 2 assumes a two-phase aquifer of vapour and water. The results and the aquifer fluid composition of the two models are shown in Tables 4 and 5.

The concentrations of non-volatile elements for the two models are similar, except for the discharge fluids that approach that of pure steam. Yet, the concentrations of non-volatiles in the liquid phase of two-phase reservoirs are somewhat lower in most cases. Non-volatile elements include, for example, SiO_2 , Na, K, Ca, Mg, Cl, F, SO_4 , Al and Fe. With respect to volatiles like CO_2 , H_2S , H_2 , and CH_4 , a marked difference was observed between the two models. The reason for this is the volatiles partitioning into the vapour phase, some completely upon initial boiling like H_2 and CH_4 , whereas others are distributed between the two phases, like CO_2 and H_2S . As a result, the aqueous concentration of the

non-volatiles is low when assuming two-phase reservoirs, compared to single-phase liquid reservoirs. Also, as the CO_2 and H_2S are among the major acids buffering the aquifer water pH, the assumption of liquid-only reservoirs results in lower pH values, the difference being ~ 0.5 on the pH scale.

TABLE 2: Temperature equations for equilibrium constants and corresponding mineral dissolution reactions; they are valid in the range 0-350°C at P_{sat}

Reaction	LogK(T)
1 $\text{and} + 8\text{H}_2\text{O} = 3\text{Ca}^{+2} + 2\text{Fe}(\text{OH})_2^- + 3\text{H}_4\text{SiO}_4^0$	+940.225-154193.3/T+0.58092.T-0.0002971.T ² - 421.737logT
2 $\text{cal} + 2\text{H}^+ = \text{Ca}^{+2} + \text{H}_2\text{O} + \text{CO}_{2\text{aq}}$	-68.271+4385.24/T-0.007525.T+25.856.logT
3 $\text{czo} + 12\text{H}_2\text{O}_1 = 2\text{Ca}^{+2} + 3\text{Al}(\text{OH})_4^- + 3\text{H}_4\text{SiO}_4^0 + \text{OH}^-$	+36.052-6854.78/T+0.13236.T-0.00013749.T ² -33.508.logT
4 $\text{epi} + 12\text{H}_2\text{O}_1 = 2\text{Ca}^{+2} + \text{Fe}(\text{OH})_4^- + 3\text{Al}(\text{OH})_4^- + 3\text{H}_4\text{SiO}_4^0 + \text{OH}^-$	+893.547-27077.4/T+0.54124.T-0.0003022.T ² -398.380.logT
5 $\text{flu} = \text{Ca}^{+2} + 2\text{F}^-$	+66.54-4318.T-25.47.logT
6 $\text{gro} + 4\text{H}^+ + 8\text{H}_2\text{O}_1 = 3\text{Ca}^{+2} + 2\text{Al}(\text{OH})_4^- + 3\text{H}_4\text{SiO}_4^0$	-517.662+17623.7/T-0.14343.T+203.808.logT
7 $\text{mag} + 4\text{H}_2\text{O}_1 = 2\text{Fe}(\text{OH})_4^- + \text{Fe}^{+2}$	+949.951-24258.2/T+0.51474.T-0.0002402.T ² -417.136.logT
8 $\text{pre} + 10\text{H}_2\text{O}_1 = 2\text{Ca}^{+2} + 2\text{Al}(\text{OH})_4^- + 3\text{H}_4\text{SiO}_4^0 + 2\text{OH}^-$	+833.950-25642.8/T+0.5035.T-0.0002941.T ² -369.297.logT
9 $\text{pyrr} + 2\text{H}^+ + \text{H}_{2\text{aq}} = 2\text{H}_2\text{S}_{\text{aq}} + \text{Fe}^{+2}$	-3.043-1579.06/T-0.001987.T-0.120.logT
10 $\text{pyrr} + 2\text{H}^+ = \text{H}_2\text{S}_{\text{aq}} + \text{Fe}^{+2}$	-3.043-1579.06/T-0.001987.T-0.120.logT
11 $\text{qtz} + 2\text{H}_2\text{O}_1 = \text{H}_4\text{SiO}_4^0$	-34.188+197.47/T-5.851.10 ⁻⁶ .T ² +12.245.logT
12 $\text{wol} + 2\text{H}^+ + \text{H}_2\text{O}_1 = \text{Ca}^{+2} + \text{H}_4\text{SiO}_4^0$	-127.096+8151.38/T-0.02981.T-49.282.logT

The source for the thermodynamic data used to derive these equations is given in chapter 3 of the text. Also referred to from Karingithi et al., (2010). Unit activity has been taken for minerals and water. The minerals considered are: and: andradite, cal: calcite, czo: clinzoisite, epi: epidote, flu: fluorite, gro: grossular, mag: magnetite, pre: prehnite, pyrr: pyrite, qtz: quartz, wol: wollastonite.

TABLE 3: Temperature equations for the equilibrium constants for mineral pairs that control gas concentrations in solution; the equations are valid in the range 0-350°C at P_{sat}

Species	Reaction	LogK(T)
CO_2	$\text{czo} + \text{cal} + \frac{3}{2}\text{qtz} + \text{H}_2\text{O} = \frac{3}{2}\text{pre} + \text{CO}_{2\text{aq}}$	-0.890+7251/T ² -1710.6/T+0.004188T+0.000002683.T ² -0.064logT
CO_2	$\frac{2}{5}\text{czo} + \text{cal} + \frac{3}{5}\text{qtz} = \frac{3}{5}\text{gro} + \frac{1}{5}\text{H}_2\text{O}_1 + \text{CO}_{2\text{aq}}$	-1.449-40536/T ² -2135.9/T+0.0065639T+0.000002725.T ² -0.193logT
H_2S	$\frac{1}{3}\text{pyrr} + \frac{1}{3}\text{pyrr} + \frac{2}{3}\text{pre} + \frac{2}{3}\text{H}_2\text{O}_1 = \frac{2}{3}\text{epi} + \text{H}_2\text{S}_{\text{aq}}$	13.608+592324/T ² -9346.7/T-0.043552T+0.000029164T ² +5.139logT
H_2S	$\frac{2}{3}\text{gro} + \frac{1}{3}\text{pyrr} + \frac{1}{3}\text{pyrr} + \frac{2}{3}\text{qtz} + \frac{4}{3}\text{H}_2\text{O}_1 = \frac{2}{3}\text{epi} + \frac{2}{3}\text{wol} + \frac{2}{3}\text{H}_2\text{S}_{\text{aq}}$	13.659+555082/T ² -9256.6/T-0.043608T+0.000028613T ² +5.148logT
H_2S	$2\text{gro} + \frac{1}{2}\text{pyrr} + \frac{1}{2}\text{mag} + 2\text{qtz} + 2\text{H}_2\text{O} = 2\text{epi} + 2\text{wol} + \text{H}_2\text{S}_{\text{aq}}$	-0.836-216659/T ² -2847.3/T+0.008524T-0.000002366T ² +0.152logT
H_2S	$\frac{1}{4}\text{pyrr} + \frac{2}{2}\text{pyrr} + \text{H}_2\text{O}_1 = \frac{1}{4}\text{mag} + \text{H}_2\text{S}_{\text{aq}}$	13.589+590215/T ² -9024.5/T-0.044882T+0.000029780T ² +5.068logT
H_2	$\frac{2}{3}\text{pyrr} + \frac{2}{3}\text{pre} + \frac{2}{3}\text{H}_2\text{O}_1 = \frac{2}{3}\text{epi} + \frac{2}{3}\text{pyrr} + \text{H}_{2\text{aq}}$	-1.640-124524/T ² -777.19/T-0.0005501T+0.000007756.T ² -0.565logT
H_2	$\frac{2}{3}\text{gro} + \frac{4}{3}\text{pyrr} + \frac{2}{3}\text{qtz} + \frac{4}{3}\text{H}_2\text{O}_1 = \frac{2}{3}\text{epi} + \frac{2}{3}\text{wol} + \frac{2}{3}\text{pyrr} + \text{H}_{2\text{aq}}$	-1.544-151109/T ² -752.389/T-0.0005868T+0.000007080T ² -0.532logT
H_2	$6\text{gro} + 2\text{mag} + 6\text{qtz} + 4\text{H}_2\text{O}_1 = 6\text{epi} + 6\text{wol} + \text{H}_{2\text{aq}}$	1.444-273812/T ² -3962.1/T+0.002401T+0.000001304T ² -0.979logT
H_2	$\frac{2}{3}\text{pyrr} + \text{H}_2\text{O}_1 = \frac{3}{4}\text{pyrr} + \frac{1}{4}\text{mag} + \text{H}_{2\text{aq}}$	-1.654-95456.8/T ² -621.84/T-0.001257T+0.000007569T ² -0.600logT

The source of the thermodynamic data is as described in Table 2.

TABLE 4: Aquifer fluid composition based on a two-phase liquid and vapour reservoir (Model 2); concentrations are in mg/kg Output from the program WATCH (Bjarnason, 2010)

Well	pH	B	SO ₄	Cl	CO ₂	F	H ₂ S	SiO ₂	Ca	Na	K	Mg	Fe	Al	CO ₂	H ₂ S	CH ₄	H ₂	N ₂
Water phase															Vapour phase				
2	7.52	5.3	22	595	83	54	17.64	501	0.57	434	72	0.008	0.016	0.514	5679.7	224.01	14.830	7.61	69.64
5	7.42	5.6	45	602	55	46	12.84	402	0.7	431	66	0.006	0.019	0.716	4649.6	198.47	1.860	4.92	66.81
10	7.51	8.6	41	795	54	51	12.42	516	1.64	537	96	0.033	0.033	0.554	3298.7	154.6	24.430	2.15	148.86
11	7.50	4.5	17	550	39	51	26.73	472	0.46	393	64	0	0.016	0.553	39.1	26.73	0.020	0.01	0.07
15	7.83	4.6	42	509	54	44	27.21	446	0.43	407	64	0.008	0.016	0.611	2762.4	199	8.090	8.15	90.07
16	7.78	4.1	37	492	71	54	22.99	421	0.29	422	56	0.025	0.008	0.411	4139.0	186.6	6.090	11.79	235.92
19	7.97	3.8	47	326	73	58	37.91	455	0.41	353	45	0.033	0.017	0.756	3081.7	211.22	7.340	8.84	179.35
20	7.61	9.8	15	564	78	65	30.49	533	0.63	418	67	0.034	0.261	0.295	4696.3	330.68	5.640	8.53	37.87
23	7.85	3.1	33	172	79	58	35.94	508	0.7	288	40	0.039	0.031	0.552	4000.6	261.42	2.990	11.9	78.3
26	7.67	1.8	20	252	110	56	34.61	537	0.2	274	42	0.033	0.204	0.760	6846.0	352.74	4.290	10.28	112.54
28	7.68	4.1	68	312	30	33	17.48	408	0.87	288	40	0.007	0.078	0.562	1992.4	177.04	0.980	5.11	60.82
29	7.63	7.3	22	366	34	60	22.84	438	0.54	300	45	0.022	0.043	0.482	2316.2	252.33	1.040	8.84	108.35
30	7.29	2.7	34	362	36	36	13.97	527	0.19	279	49	0.021	0.625	1.098	2842.0	257.38	0.000	0.92	83.84
202	8.31	2.0	60	283	1101	42	6.07	256	0.63	594	102	0.032	0.016	0.687	22522.0	14.94	15.370	0	86.24
301	7.50	4.8	80	171	5078	75	14.5	609	0.47	913	148	0.05	0.014	0.477	301545.0	173.29	21.900	3.48	518.13
302	7.69	2.6	40	373	1148	57	9.01	549	0.8	467	75	0.059	0.015	0.576	62522.0	83.13	27.030	2.89	393.53
304	7.08	3.0	84	47	2763	22	2.63	330	3.15	869	67	1.566	0.127	0.471	564270.0	99.46	30.950	2.13	545.57
306	7.26	5.1	40	203	2102	50	13.3	446	0.97	688	78	0.065	0.073	1.117	246029.0	282.82	81.590	6.1	1189.75
709	8.42	3.4	49	518	196	19	20.65	437	0.95	569	147	0.027	0.014	0.599	3479.0	48.85	6.220	5.33	119.26
714	7.66	2.6	26	498	248	48	31.46	539	0.64	406	79	0.044	0.007	0.766	12686.0	317.62	20.840	9.62	373.28
719	7.58	3.8	66	429	231	36	25.52	464	0.86	423	64	0.032	0.016	1.192	16379.7	297.82	17.650	5.26	286.11
901	8.29	1.9	97	218	464	62	59.89	412	0.56	394	44	0.023	0.023	0.530	10067.8	159.57	6.560	6.05	177.59
902	7.98	1.2	82	174	437	43	4.02	391	1.07	367	34	0.041	0.066	1.736	18428.5	22.61	30.080	0.29	916.84
903	7.69	0.9	86	149	769	38	7.18	370	0.59	412	39	0.033	0.017	1.020	56475.0	76.18	58.360	2.24	2691.69

TABLE 5: Aquifer fluid composition based on a single-phase liquid-only reservoir (Model 1); concentrations are in mg/kg; output from program WATCH (Bjarnason, 2010)

Well	pH	B	SO ₄	Cl	CO ₂	F	H ₂ S	SiO ₂	Ca	Na	K	Mg	Fe	Al	CO ₂	H ₂ S	CH ₄	H ₂	N ₂
Water phase															Steam phase				
2	6.60	5.4	22	608	965	55	39.76	512	0.58	444	73	0.008	0.016	0.526	0	0	0	0	0
5	6.47	7.1	58	767	853	58	35.07	513	0.89	549	84	0.008	0.025	0.912	0	0	0	0	0
10	6.72	10.0	47	920	766	59	33.67	597	1.9	622	111	0.039	0.039	0.641	0	0	0	0	0
11	6.67	4.6	17	564	501	52	60.22	484	0.47	403	66	0	0.016	0.567	0	0	0	0	0
15	6.94	4.8	44	535	526	46	42.61	469	0.46	428	68	0.008	0.016	0.643	0	0	0	0	0
16	6.82	4.2	37	497	537	54	30.95	426	0.3	426	57	0.025	0.009	0.416	0	0	0	0	0
19	7.04	3.9	49	334	492	60	48.04	467	0.42	362	46	0.034	0.017	0.775	0	0	0	0	0
20	6.74	11.3	17	652	1004	75	66.55	617	0.73	484	77	0.04	0.302	0.341	0	0	0	0	0
23	6.91	3.3	34	181	752	61	51.19	535	0.74	303	43	0.041	0.033	0.582	0	0	0	0	0
26	6.72	1.8	20	257	1049	56	64.39	546	0.2	279	42	0.033	0.208	0.773	0	0	0	0	0
28	6.78	4.9	83	380	432	40	37.71	497	1.06	351	49	0.008	0.095	0.684	0	0	0	0	0
29	6.72	7.9	23	397	500	66	53.03	475	0.58	325	49	0.023	0.047	0.523	0	0	0	0	0
30	6.46	2.9	37	393	650	39	57.96	573	0.2	303	53	0.022	0.679	1.194	0	0	0	0	0
202	7.32	2.0	60	284	2351	43	5.68	257	0.63	596	103	0.032	0.016	0.690	0	0	0	0	0
301	6.33	4.9	81	174	53017	76	35.93	621	0.48	932	151	0.051	0.015	0.487	0	0	0	0	0
302	6.90	2.6	40	374	4625	57	12.36	551	0.8	469	75	0.059	0.015	0.578	0	0	0	0	0
304	5.56	3.0	85	48	42321	22	8.21	335	3.2	882	68	1.59	0.129	0.478	0	0	0	0	0
306	6.36	5.1	41	204	10334	50	20.97	447	0.97	689	78	0.065	0.073	1.119	0	0	0	0	0
709	6.36	5.1	41	204	10334	50	20.97	447	0.97	689	78	0.065	0.073	1.119	0	0	0	0	0
714	7.71	3.5	51	536	972	19	19.48	452	0.98	589	152	0.028	0.014	0.619	0	0	0	0	0
719	7.04	2.6	26	499	1054	48	46.16	541	0.64	408	79	0.044	0.007	0.769	0	0	0	0	0
901	6.64	3.8	66	432	1541	36	41.06	467	0.86	425	64	0.032	0.016	1.198	0	0	0	0	0
902	6.99	2.0	101	228	1978	65	46.02	431	0.59	413	46	0.024	0.025	0.554	0	0	0	0	0
903	6.69	0.9	86	149	2517	39	8.75	371	0.59	413	39	0.034	0.017	1.022	0	0	0	0	0

The causes for aquifer vapour leading to excess enthalpy of the well discharge at the surface may be two. Heat may be added to the fluid, for example from a hot rock or molten magma, leading to induced boiling at the reservoir temperature. Alternatively, depressurization boiling in the producing aquifer leads to the formation of vapour and water. The vapour phase has a much lower density compared to the liquid water phase and may, therefore, separate depending on the geohydrological conditions of the system. The liquid is assumed to be adsorbed onto mineral grain surfaces, hence being retained in the aquifer. As a result, vapour flows, in excess of water, into the well bore, increasing the vapour-to-water ratio and, hence, the discharge enthalpy. Karingithi et al. (2010) concluded that the cause of excess enthalpy and reservoir vapour was likely caused by phase segregation in the producing aquifer rather than heat addition. This was concluded based on the relationship between the non-volatile concentrations in the discharge fluids. For example, the concentration of Cl in the liquid phase of the well discharge was observed to be relatively constant as a function of discharge enthalpy, whereas the Cl concentration in the total discharge was observed to decrease with increasing enthalpy. Such a trend suggests that phase segregation is the principle process of excess vapour and enthalpy formation (Arnórsson et al., 2007; Scott et al., 2014). The calculated aquifer vapour fraction ranges from an almost liquid-only aquifer ($X^{\text{vapour}} = \sim 0$) to almost pure vapour ($X^{\text{vapour}} = \sim 1$), resulting in a discharge enthalpy ranging from ~ 900 kJ/kg to >2500 kJ/kg.

5. GEOTHERMOMETRY

The aquifer temperatures were calculated based on the reservoir fluid composition for three geothermometers, quartz (t_{qtz}), Na/K ($t_{\text{Na/K}}$) and H_2S ($t_{\text{H}_2\text{S}}$), and those were compared to the measured down-hole temperatures of the producing aquifers. The geothermometer temperatures were both calculated assuming a liquid-only reservoir (Model 1) and two-phase reservoirs (Model 2). The geothermometer temperature functions are listed in Section 2. The results are given in Table 6. In Figure 2 (A & B) and Figure 3, the results are compared to the reservoir temperatures.

The calculated $t_{\text{Na/K}}$ for the two models yields the same results. This is to be expected given the temperature is based on the ion ratio of two non-volatiles that are not partitioning between the liquid and vapour phases. Moreover, the measured and calculated Na/K temperatures are in very close agreement, generally within $\pm 10^\circ\text{C}$.

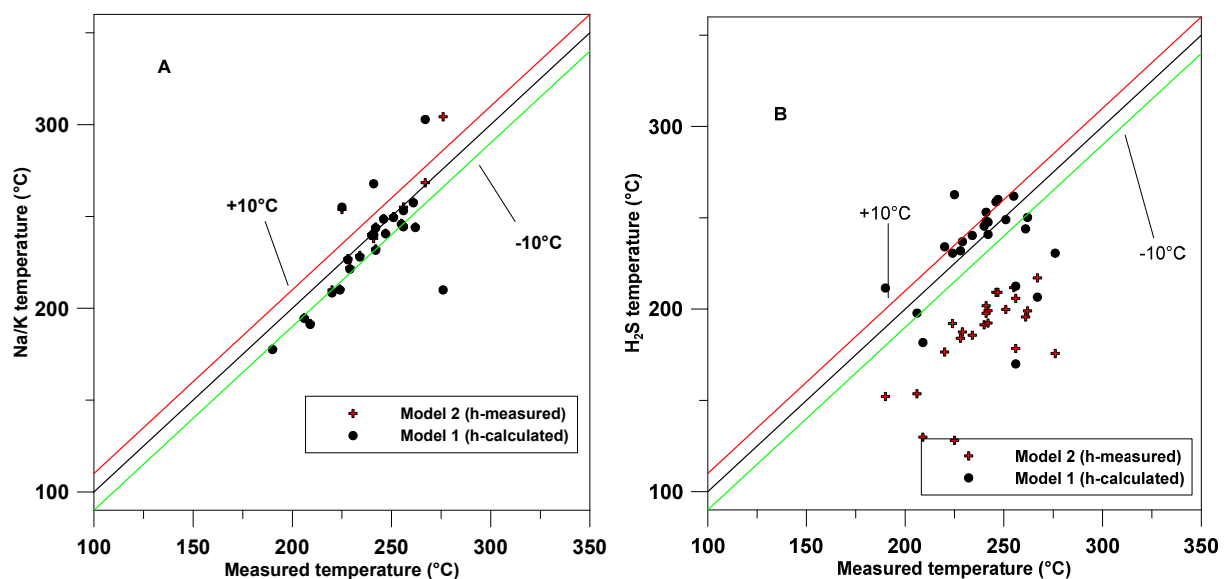
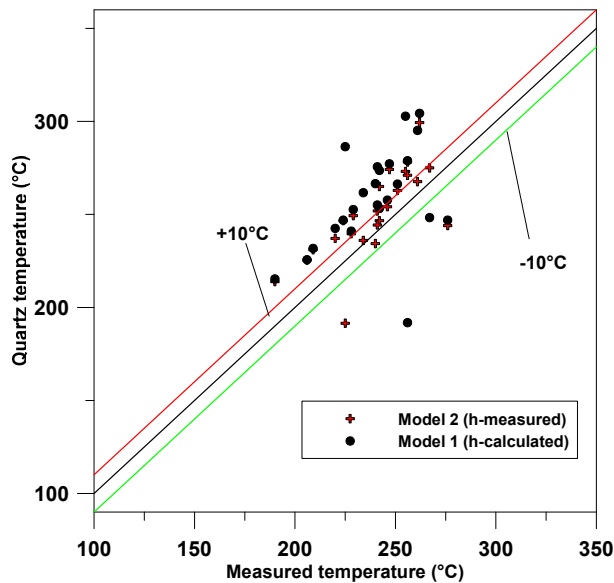


FIGURE 2: (A) $T_{\text{Na/K}}$ and (B) $T_{\text{H}_2\text{S}}$ comparison with reservoir temperature

TABLE 6: Geothermometer temperatures (°C) for Olkaria wells

Well	Enthalpy kJ/kg	Aquifer T	$t_{NaK}(1)$	$t_{NaK}(2)$	$t_{Qtz}(1)$	$t_{Qtz}(2)$	$t_{H_2S}(1)$	$t_{H_2S}(2)$
2	1839	251	249	250	266	263	249	200
5	2599	240	240	240	267	234	245	191
10	2531	261	257	258	295	268	244	196
11	1894	246	249	249	258	254	259	209
15	2140	242	244	244	253	247	241	192
16	1534	228	226	227	241	240	232	184
19	1871	229	221	222	253	249	237	187
20	2541	255	246	246	303	273	262	212
23	2191	242	232	232	274	265	248	199
26	1881	247	241	241	277	274	260	209
28	2446	234	228	229	262	236	240	186
29	2158	241	240	240	255	244	253	198
30	2196	225	255	255	286	271	263	206
202	1104	256	253	254	192	191	170	128
301	1653	262	244	244	304	299	250	199
302	1234	256	244	245	279	278	213	178
304	1672	190	178	178	215	214	212	152
306	1037	224	210	210	247	247	231	192
709	1921	276	210	304	247	244	231	176
714	1303	267	303	268	248	275	207	217
719	1259	241	268	238	276	252	248	202
901	1854	220	208	210	242	237	234	177
902	1108	209	191	192	232	231	182	130
903	953	206	194	195	226	225	198	154

Enthalpy = measured enthalpy (kJ/kg); t_{NaK} = sodium potassium geothermometer;
 t_{Qtz} = quartz geothermometer; t_{H_2S} = hydrogen sulphide geothermometer;
 1 = model based on single-phase liquid aquifer.

FIGURE 3: T_{Qtz} comparison with reservoir temperature

The H_2S temperature for the two models varies considerably. The model based on measured enthalpy has lower H_2S temperature compared to the liquid enthalpy model. This is because in Model 1, a single-phase liquid aquifer was assumed, resulting in higher H_2S concentration in the aquifer fluids and higher temperatures compared to Model 2 which assumed two-phase aquifer fluids. Compared to the measured temperatures, the results of Model 1 are much closer, usually within 10-15°C, whereas the results when assuming two-phase reservoirs were systematically lower than the measured temperatures of >40°C. Karingithi et al. (2010) concluded that the cause of excess enthalpy of the well discharge was caused by phase segregation. This means that the aquifer fluid is close to being a single-phase liquid and then, upon depressurization boiling in the producing aquifer, phase separation occurs. As a result, Model 1,

assuming a single-phase liquid reservoir, may be closer to the initial reservoir aquifer conditions; this coincides with the observation of close t_{H_2S} and measured temperatures.

The quartz temperatures calculated for the two models show systematically higher values than the measured aquifer temperatures, whereas the results of the two models applied for estimating the aquifer composition are reasonably close. The reason for these discrepancies may be twofold. Firstly, the function used for the calculation of the quartz temperature was based on quartz solubility and may not be entirely correct at $>250^{\circ}\text{C}$. Alternatively, the reason could be related to too high calculated SiO_2 concentrations in the reservoir, caused by phase segregation that was not taken into account in the aquifer model calculations.

6. FLUID-ROCK INTERACTION

The process of fluid-rock interaction results in the dissolution of the rock and its primary minerals and the formation of alteration minerals. In consideration of fluid-rock interaction, we assume that there is a localised equilibrium between the minerals and the solution. Therefore, temperature and pressure are bound to affect the state of saturation of the different minerals in the system. The Olkaria geothermal system has a liquid-dominated reservoir. Therefore, the enthalpy in the aquifer liquid is usually taken to be that of steam-saturated water at the aquifer temperature. However, some wells have been noted to have excess enthalpy. In the determination of the equilibrium conditions, an important part is the aquifer composition; how it is modelled will determine what state of equilibrium there is. In this analysis, we modelled the impact of the two models on the saturation state of the minerals. Lagat (2004) discussed the hydrothermal minerals that are found within the Olkaria geothermal system. Adularia, albite, biotite, calcite, chlorite, pyrite, epidote, Fe-oxides, fluorite, garnet and illite are the major minerals that have been analysed from drill cuttings. Pyrrhotite, magnetite and wollastonite have not been comprehensively sited but, nevertheless, we discuss their equilibrium with solution in the system. In this study, we discuss the saturation state of andradite, grossular, calcite, clinozoisite, epidote, fluorite, magnetite, prehnite, pyrite, pyrrhotite and wollastonite.

6.1 Calcite, fluorite and wollastonite

The calcite saturation in the aquifer fluid of the selected Olkaria wells is shown in Figure 4A and is based on mineral solubility equations in Tables 2 and 3. The values for the calcite activity product generally plot around the equilibrium constant or closely approach the equilibrium constant line for the majority of the samples. However, there are some parts that indicate a deviation from the equilibrium constant at both under-saturation and over-saturation. The saturation index based on the calculated enthalpy model, i.e. assuming the aquifer enthalpy to be that of steam-saturated water at aquifer temperature, has most of the values indicating under-saturation of calcite in the aquifer. Most of the wells plot below the equilibrium curve with around -2 SI units, while wells 202 and 302 from the Olkaria Central and West sectors are over-saturated. The wells in this part of the field have very high dissolved CO_2 to the order of > 1000 ppm, considered high for the Olkaria system, and pH in the range of 9. The second model based on the measured enthalpy, i.e. the measured enthalpy of the discharge being higher than that in the aquifer, indicates equilibrium although some samples were super-saturated with respect to calcite. Some samples were under-saturated but this seems to be a systematic error. In this model, the wells in the East part of the field are in equilibrium or approaching equilibrium. This equilibrium will shift depending on the boiling process and the precipitation of calcite, as seen from the two models and the CO_2 and pH values applied in the modelling of the equilibrium.

The fluorite saturation state is shown in Figure 4B. The system is under-saturated with respect to fluorite for most of the field. This under-saturation is consistent for both models and is up to as high as 2.5 SI units. Some wells in the East sector of the field indicate an approach to equilibrium or slight super-saturation. The depicted super-saturation is consistent for both models although it is minor to magnitudes of 0.5 SI units. This super-saturation is centred in wells 20, 29, 23 and 20 which are in a zone of heating

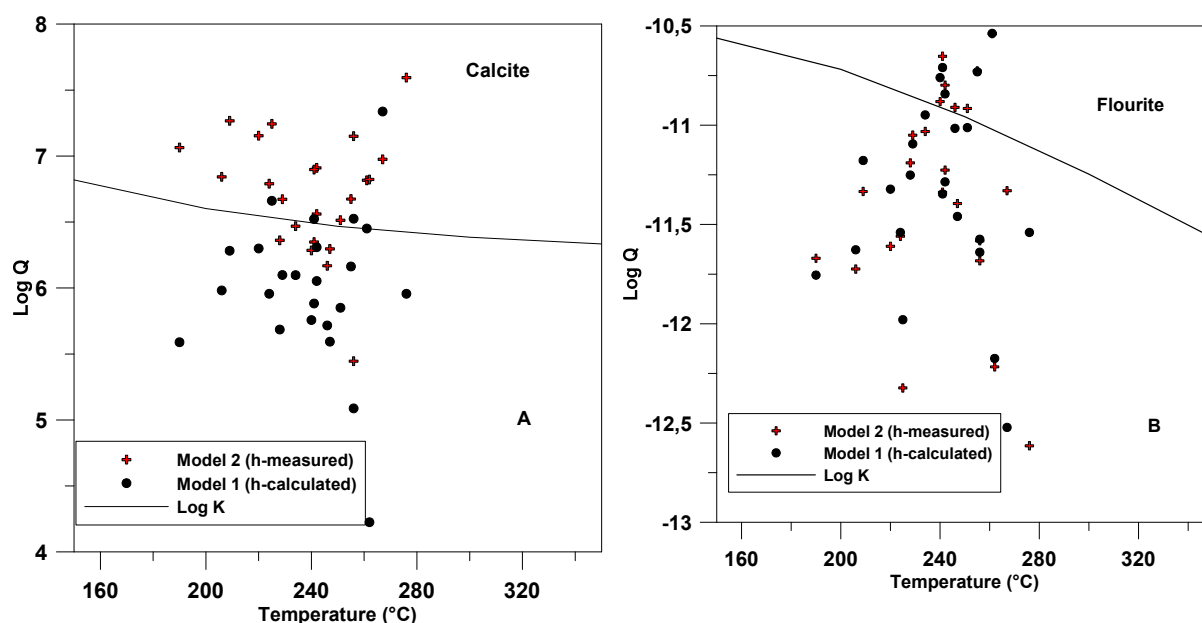


FIGURE 4: Saturation state of aquifer water with respect to (A) calcite and (B) fluorite

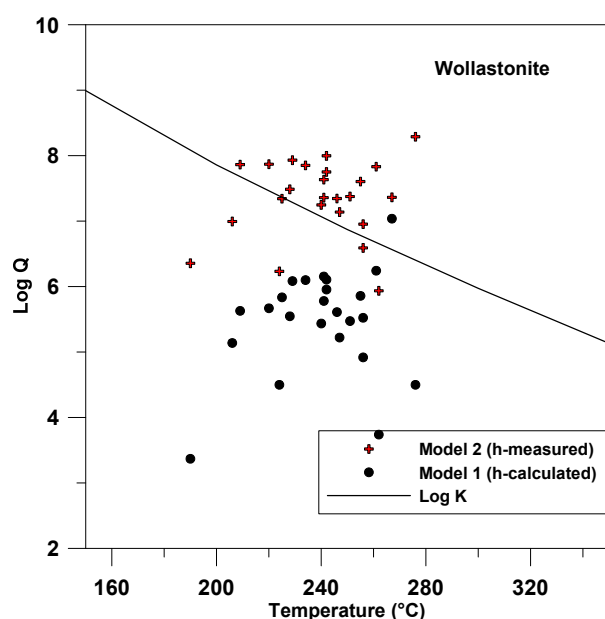


FIGURE 5: Saturation state of aquifer water with respect to wollastonite

up-flow in the Olkaria system. Fluorite generally shows retrograde solubility and will be affected by depletion of Ca^{+2} in the solution.

The saturation state of wollastonite is presented in Figure 5. It is seen that a clear pattern emerges where the two models give distinctively different saturation states for wollastonite. The activity product of the mineral, based on the measured enthalpy model, shows a definite super-saturation of wollastonite, although there are some scattered samples it is close to equilibrium. These are probably a systematic error. The activity products obtained from the model, based on calculated enthalpy, indicate an overall under-saturation of wollastonite in the system. The saturation state of wollastonite is based on the activity of Ca^{+2} . Thus, the values for the activity of Ca^{+2} in the two models differ, hence the difference in the observed saturation state for wollastonite in the Olkaria system.

6.2 Magnetite, pyrite and pyrrhotite

The saturation state of pyrite, pyrrhotite and magnetite is shown in Figures 6 and 7, respectively. Magnetite was observed to be super-saturated in almost all cases, independent of the assumptions made for calculating the aquifer fluid composition. There is a scatter of the SI values, ranging from -27 to -22 SI units. On the other hand, the waters were observed to be under-saturated with respect to both pyrite and pyrrhotite, by up to 2 and 4 SI units, respectively.

Pyrite has been observed as an alteration mineral in the Olkaria system, whereas magnetite and pyrrhotite are not (Lagat, 2004). Magnetite super-saturation implies that it may, however, form, whereas

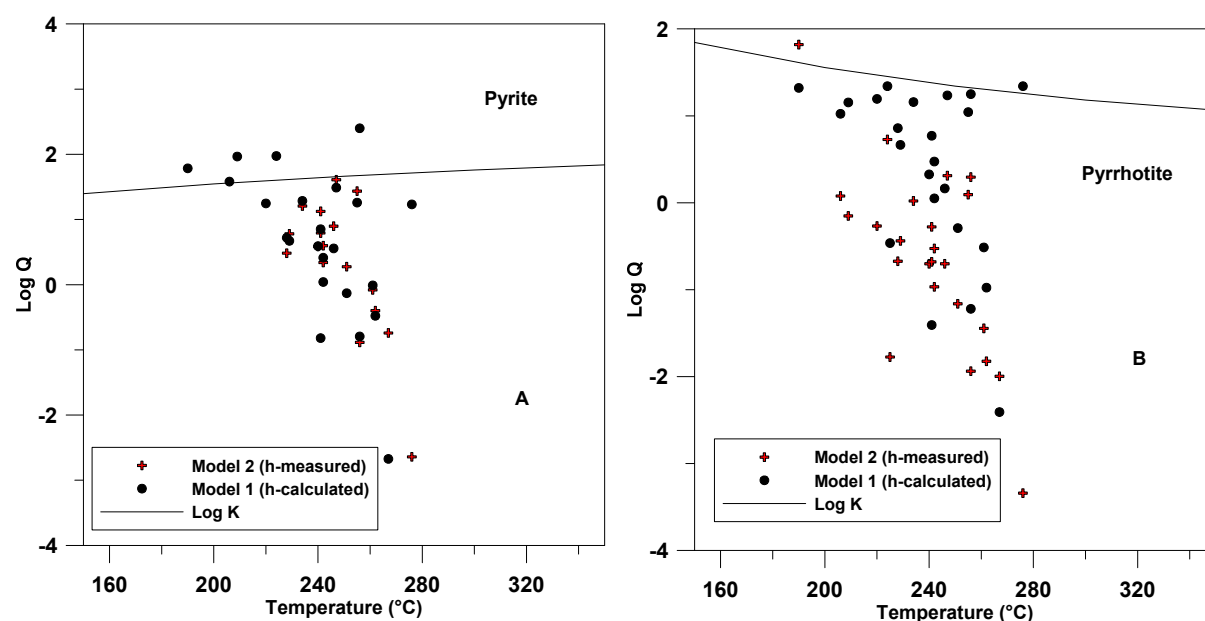


FIGURE 6: Saturation state of aquifer water with respect to (A) pyrite and (B) pyrrhotite

pyrite and pyrrhotite under-saturation suggests that these minerals are unstable and not forming; this is somewhat conflicting with the observed mineralogy at Olkaria. The discrepancies may be related to difficulties in computing the activities of iron containing aqueous species. Firstly, iron is found in two oxidation states, Fe^{II} and Fe^{III} ; magnetite contains both, whereas pyrite and pyrrhotite only containing Fe^{II} . In geothermal fluids, both oxidations may exist, depending on temperature and pH (Gunnlaugsson and Arnórsson, 1982). In order to calculate the equilibrium of Fe aqueous speciation, a redox couple needs to be selected, this being the $\text{H}_2\text{S}/\text{SO}_4$ couple in WATCH. As pointed out by Stefánsson and Arnórsson (2002), overall redox equilibrium may not exist, making the estimation of the ration of $\text{Fe}^{\text{II}}/\text{Fe}^{\text{III}}$ from the $\text{H}_2\text{S}/\text{SO}_4$ ratio questionable. Also, as pointed out by Arnórsson et al. (2002), the thermodynamic equilibrium constants for Fe^{II} and Fe^{III} under hydrothermal conditions are somewhat uncertain, resulting in large uncertainties in the calculated $\text{Fe}^{\text{II}}/\text{Fe}^{\text{III}}$ ratio and the Fe^{II} and Fe^{III} aqueous speciation.

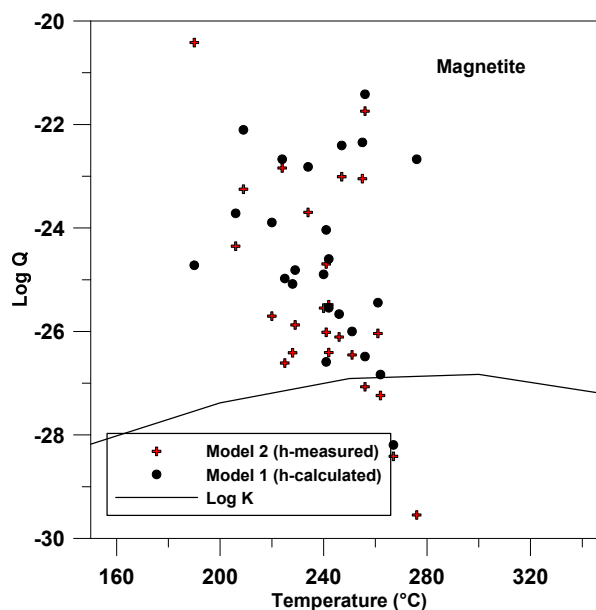


FIGURE 7: Saturation state of aquifer water with respect to magnetite

6.3 Andradite-grossular, clinozoisite-epidote and prehnite

Andradite and grossular are end members of the garnet solid solution. Grossular has the formula $\text{Ca}_2\text{Al}_2\text{Si}_4\text{O}_3$ where the Al can be replaced by Ferric ion, while the Ca is partially replaced by ferrous ion. The andradite end member is represented by $\text{Ca}_2\text{Fe}_2\text{Si}_3\text{O}_{12}$. The activity product of andradite from Figure 8A indicates a general super-saturation of andradite in the Olkaria system, as analysed for both models. Four samples show equilibrium, but this are suspected to be a result of a systematic error. The saturation state of andradite, based on the second model however, has a smaller deviation from equilibrium of about 2.0 SI units.

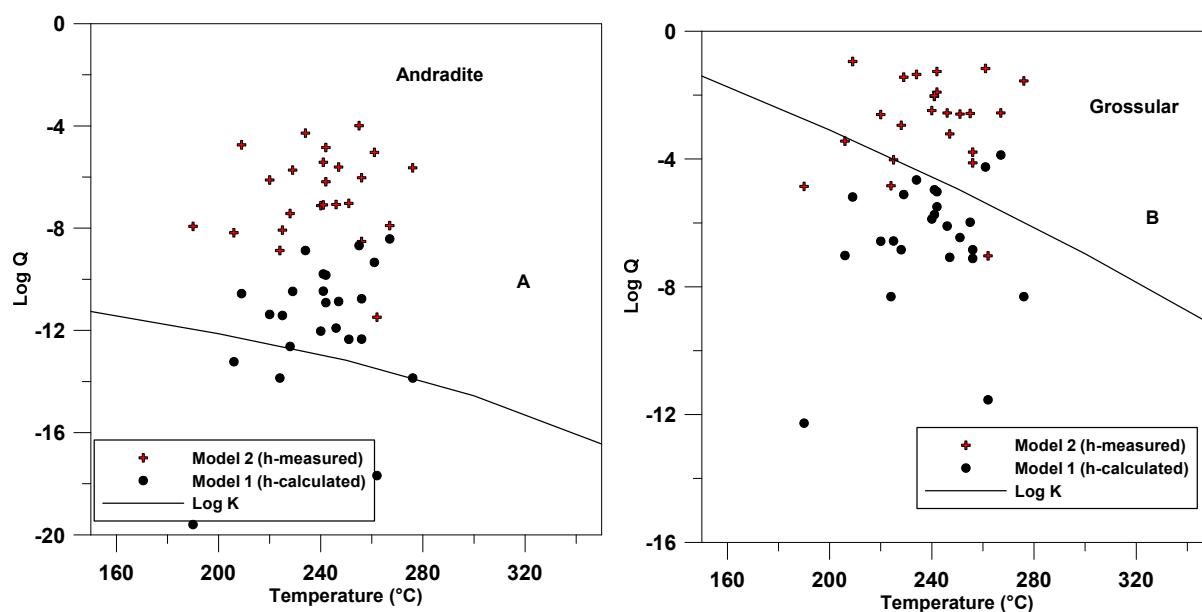


FIGURE 8: Saturation state of aquifer water with respect to (A) andradite and (B) grossular

Figure 8B indicates the activity product of the mineral grossular. The two models used indicate different saturation states for grossular. The model based on measured enthalpy indicates super-saturation of grossular in solution for the whole Olkaria system. The model based on calculated enthalpy indicates under-saturation of grossular for the Olkaria system.

Epidote is a common mineral in the Olkaria system and is used as an indicator mineral for high temperature zones within the Olkaria reservoir. The epidote in Olkaria has the composition $\text{Ca}_2\text{FeAl}_2\text{Si}_3\text{O}_{12}(\text{OH})$. The activity product of epidote from Figure 9B indicates that, overall, the aquifer water in the Olkaria system is epidote super-saturated, based on both the models. Clinzoisite forms a continuous solid solution series with epidote and is obtained by substitution of Fe^{+3} in the Al site. The model based on the calculated enthalpy shows that the aquifer water in Olkaria closely approaches equilibrium, as the activity products are scattered around the equilibrium constant curve. However, the wells, located in Olkaria West and Olkaria Central, show a slight under-saturation with respect to clinzoisite, based on this model. The second model, based on measured enthalpy, indicates super-

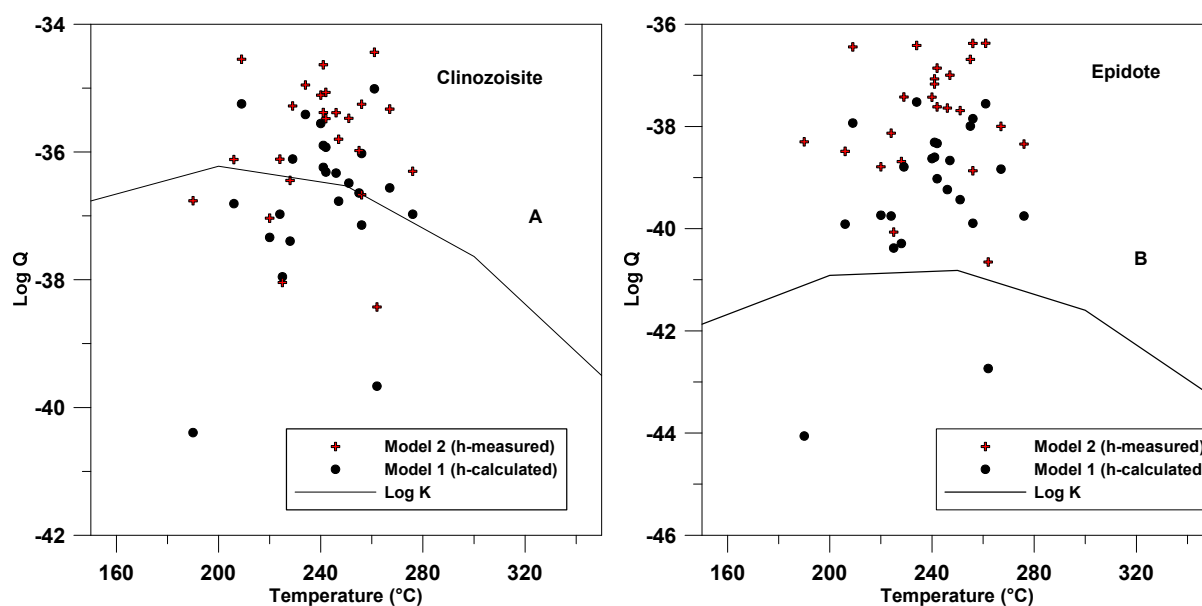


FIGURE 9: Saturation state of aquifer water with respect to (A) clinzoisite and (B) epidote

saturation of clinozoisite in the aquifer water. The wells in Olkaria West and Olkaria Central closely approach equilibrium for this model. Some samples, however, show under-saturation, possibly the result of a systematic error. The composition of epidote in the Olkaria system lies between the clinozoisite and epidote end-member composition, possibly resulting from the observed saturation with respect to the end-member mineral composition (Karingithi et al., 2010). Moreover, the aqueous speciation of iron is somewhat uncertain and $\text{Fe}(\text{OH})_4^-$ aqueous activity may be possibly over-estimated, resulting in super-saturation of Fe^{III} -bearing minerals like epidote and magnetite.

Prehnite is expressed by the chemical formula $\text{Ca}_2\text{Al}(\text{AlSi}_3\text{O}_{10})(\text{OH})_2$ where Fe^{3+} could substitute for Al in the structure. Prehnite has a variable saturation state, based on the two models. The model based on calculated enthalpy shows that the activity product of prehnite scatters around the equilibrium constant curve (Figure 10). Super-saturation is very minimal around the Olkaria system, based on this model. The activity product based on the measured enthalpy model shows a systematic super-saturation with respect to prehnite for the aquifer water in Olkaria. Three samples deviate from this, but could possibly be errors.

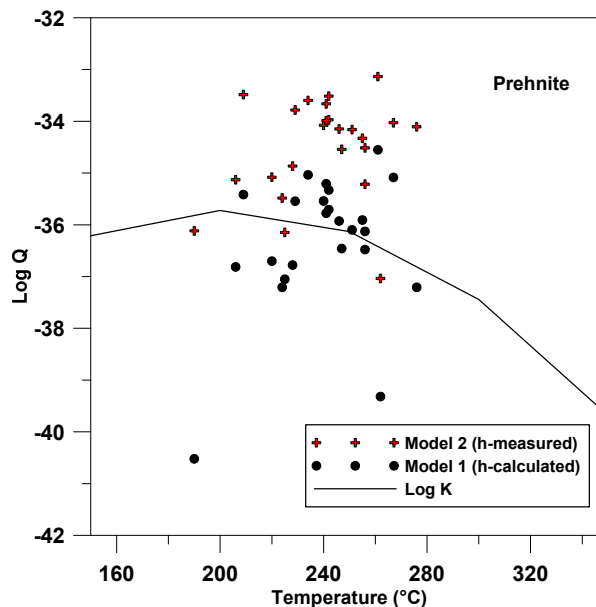


FIGURE 10: Saturation state of aquifer water with respect to prehnite

6.4 Gas equilibria

Concentrations of reactive gases can be controlled by equilibrium with respect to specific mineral assemblages. Various mineral assemblages have been expressed that can control this reaction, as seen in Table 3. Figure 11A shows the state of equilibrium between H_2 and four mineral assemblages, based on the two models. The model based on measured enthalpy shows a complete departure from

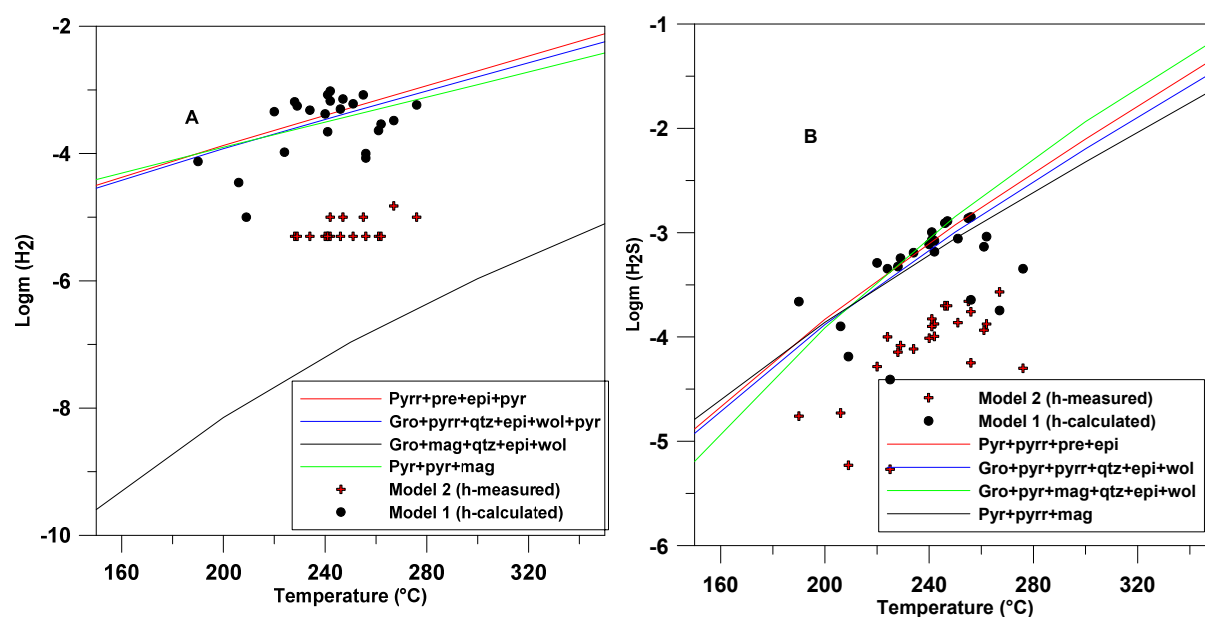


FIGURE 11: State of equilibrium between (A) dissolved H_2 ; and (B) H_2S in the aquifer water and mineral buffers

equilibrium with all the mineral assemblages. On the other hand, the model assuming a liquid-only aquifer shows close to equilibrium with respect to H_2 . What controlling mineral buffer reactions are involved is hard to assess as many show very close equilibrium H_2 concentrations.

Figure 11B shows the state of equilibrium between H_2S and four different mineral assemblages. The H_2S concentrations, based on the measured enthalpy, show a considerable departure from equilibrium with all the four mineral assemblages, whereas those calculated assuming a liquid-only aquifer are very close to equilibrium with respect to several mineral buffer reactions. As with H_2 , it is very difficult to assess exactly which minerals are involved.

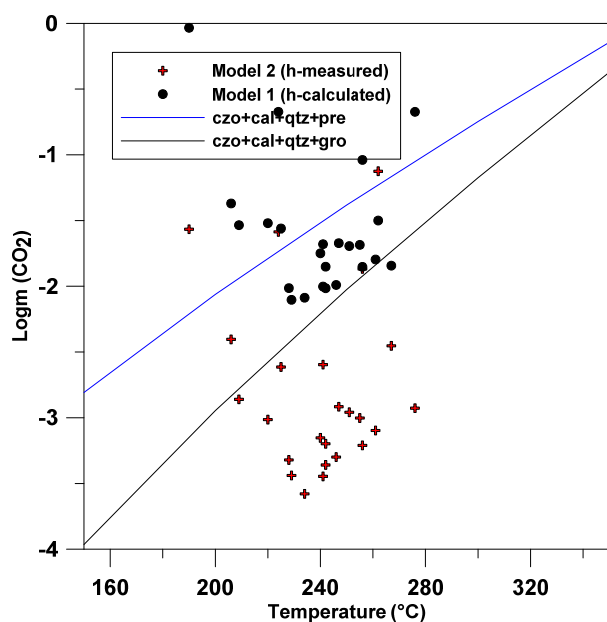


FIGURE 12: State of equilibrium between dissolved CO_2 in the aquifer water and mineral buffers

Figure 12 illustrates the state of equilibrium of CO_2 concentrations in Olkaria aquifer waters with two mineral assemblages. The concentrations based on the measured enthalpy are below equilibrium with the mineral assemblage. On the other hand, for Model 1 assuming a liquid-only reservoir, closer to equilibrium conditions are observed between the proposed mineral buffer reactions and the calculated aquifer CO_2 concentrations. The fluids in the Olkaria East and Northeast closely approach equilibrium with the mineral assemblage clinozoisite-calcite-quartz-grossular, whereas the fluids in the Dome sector have concentrations that closely approach equilibrium with the mineral assemblage clinozoisite-calcite-quartz-prehnite. However, bearing in mind all the uncertainties associated with the calculation of the aquifer fluid composition and its relationship with the exact equilibrium CO_2 concentration with respect to the mineral buffer reactions, it is very difficult to assess with confidence which minerals are truly involved in buffering the concentration of CO_2 in the aquifers of the Olkaria geothermal system.

7. SUMMARY AND CONCLUSIONS

The fluid composition and mineral-fluid interaction in the Olkaria geothermal system were studied. Fluid-rock interaction is one of the key reactions of interest in geothermal systems. There is a close approach to equilibrium between common geothermal minerals and the fluids within the reservoir, controlling the composition of most major elements in the fluid. The assessment of fluid-rock equilibria from the fluid composition of surface well discharges largely relies on the assumptions made when calculating the subsurface aquifer fluid composition. Two models were applied in the evaluation of aquifer fluid composition. Model 1 is based on a calculated enthalpy and considers a single-phase liquid-only reservoir. Model 2 considers a two-phase liquid and vapour reservoir and uses the measured enthalpy. The concentrations of non-volatile elements for the two models are similar, except for the discharge fluids that approach that of pure steam. Yet, the concentrations of non-volatiles in the liquid phase of two-phase reservoirs are somewhat lower in most cases. There is a marked difference between the two models in the case of the volatiles. The reason for this is the volatiles partitioning into the vapour phase, some completely upon initial boiling like H_2 and CH_4 , whereas others are distributed between the two phases like CO_2 and H_2S . As a result, the aqueous concentrations of the non-volatiles are low when assuming two-phase reservoirs, compared to single-phase liquid reservoirs. The model based on measured enthalpy has lower H_2S temperature compared to the liquid enthalpy model. This is because,

in Model 1, a single-phase liquid aquifer was assumed, resulting in higher H₂S concentrations in the aquifer fluids and higher temperatures compared to Model 2, which assumed two-phase aquifer fluids. The initial aquifer was taken to be a single-phase liquid that was undergoing phase separation. As a result, Model 1 which assumes a single-phase liquid reservoir may be closer to the initial reservoir aquifer conditions, as it coincides with the measured temperatures. The Ca-Al minerals show varying equilibrium, based on the model used. The measured enthalpy evaluations show a general super-saturation of the minerals grossular, andradite, clinozoisite, epidote and prehnite in the Olkaria aquifer water. The aquifer water, based on this system, is degassed relative to equilibrium and, thus, there is lower non-volatile concentration in the water. The liquid enthalpy values show that the Ca-Al minerals closely approach equilibrium with the aquifer water. A simultaneous equilibrium between clinozoisite, prehnite, quartz and the solution then fixes the activity of the Ca⁺². The Fe^{II} minerals pyrite and pyrrhotite are under-saturated in the Olkaria aquifer water, based on the two models, while magnetite is super-saturated. This is a discrepancy, given that pyrite is found in the Olkaria system. The thermodynamic equilibrium constants for Fe^{II} and Fe^{III} under hydrothermal conditions are somewhat uncertain, resulting in large uncertainties in the calculated Fe^{II}/Fe^{III} ratio and the Fe^{II} and Fe^{III} aqueous speciation. Moreover, the aqueous speciation of iron is somewhat uncertain, and Fe(OH)₄⁻ aqueous activity may possibly be over-estimated, resulting in super-saturation of Fe^{III}-bearing minerals like epidote and magnetite. The H₂ and H₂S concentrations in the aquifer water of the single-phase liquid reservoir are closely controlled by equilibrium with specific mineral assemblages. Which controlling mineral buffer reactions are involved is hard to assess, as many show very close equilibrium to these concentrations. With uncertainties associated with the calculation of the aquifer fluid composition and the relationship to the exact equilibrium CO₂ concentration with respect to the mineral buffer reactions, it is very difficult to assess with confidence which minerals are truly involved in buffering the concentration of CO₂ in the aquifer Olkaria geothermal system.

ACKNOWLEDGEMENTS

I would like to express my sincere appreciation to Mr. Lúdvík S. Georgsson, Director of UNU-GTP, for the opportunity to participate in the Geothermal Training Programme in 2014. I would also like to thank the UNU staff: Mr. Ingimar G. Haraldsson, Ms María S. Guðjónsdóttir, Ms Málfríður Ómarsdóttir, Ms Þórhildur Ísberg and Mr. Markús A.G. Wilde, for their assistance and support during my stay in Iceland. I would also like to thank my supervisor, Prof. Andri Stefánsson, for his guidance, support and sharing of valuable knowledge in the course of my project. I would also wish to thank Mr. Þráinn Fridriksson for his support and advice. My appreciation also goes to the Kenya Electricity Generating Company for granting me leave to attend this training. Finally, my gratitude goes to my family, friends and UNU-GTP 2014 fellows for their support.

REFERENCES

- Ambusso, W.J., and Ouma, P.A., 1991: Thermodynamic and permeability structure of Olkaria North-east geothermal field: Olkaria fault. *Geothermal Resources Council, Transactions*, 15, 237-242.
- Ármannsson, H., and Ólafsson, M., 2000: *Collection of geothermal fluids for chemical analysis*. ÍSOR – Iceland GeoSurvey, Reykjavík, report ISOR-2006/101, 17 pp.
- Arnórsson, S., and D'Amore, F., 2000: Monitoring of reservoir response to production. In: Arnórsson, S. (ed.), *Isotopic and chemical techniques in geothermal exploration, development and use. Sampling methods, data handling, and interpretation*. International Atomic Energy Agency, Vienna, 306-341.
- Arnórsson, S., and Stefánsson, A., 1999: Assessment of feldspar solubility constants in water in the range 0-350°C at P_{sat}. *Am. J. Sci.*, 299, 173-209.

- Arnórsson, S., Gunnlaugsson, E., and Svavarsson, H., 1983: The chemistry of geothermal waters in Iceland. II. Mineral equilibria and independent variables controlling water compositions. *Geochim. Cosmochim. Acta*, 47, 547-566.
- Arnórsson, S., Sigurdsson, S. and Svavarsson, H., 1982: The chemistry of geothermal waters in Iceland I. Calculation of aqueous speciation from 0°C to 370°C. *Geochim. Cosmochim. Acta*, 46, 1513-1532.
- Arnórsson, S., Stefánsson, A., and Bjarnason, J.Ö., 2007: Fluid-fluid interaction in geothermal systems. *Reviews in Mineralogy & Geochemistry*, 65, 229-312.
- Arnórsson, S., Bjarnason, J.Ö., Giroud, N., Gunnarsson, I., and Stefánsson, A., 2006: Sampling and analysis of geothermal fluids, *Geofluids*, 6, 203-216.
- Arnórsson, S., Gunnarsson, I., Stefánsson, A., Andrésdóttir, A., and Sveinbjörnsdóttir, A.E., 2002: Major element chemistry of surface- and ground waters in basaltic terrain, N-Iceland. I. Primary mineral saturation. *Geochim. Cosmochim. Acta*, 66, 4015-4046.
- Bjarnason, J.Ö., 2010. *The speciation program WATCH* (vers. 2.4). ISOR – Iceland GeoSurvey, Reykjavík.
- Clarke, M.C.G., Woodhall, D.G., Allen, D., and Darling G., 1990: *Geological, volcanological and hydrogeological controls on the occurrence of geothermal activity in the area surrounding Lake Naivasha, Kenya, with coloured 1:100 000 geological maps*. Ministry of Energy, Nairobi, 138 pp.
- Giggenbach, W.F., 1981: Geothermal mineral equilibria. *Geochim. Cosmochim. Acta*, 45, 393-410.
- Gunnarsson, I. and Arnórsson S., 2000: Amorphous silica solubility and the thermodynamic properties of $\text{H}_4\text{SiO}_4^\circ$ in the range of 0° to 350°C at P_{sat} . *Geochim. Cosmochim. Acta*, 64, 2295-2307.
- Gunnlaugsson, E., and Arnórsson, S., 1982: The chemistry of iron in geothermal systems in Iceland. *J. Volcanol. & Geotherm. Res.* 14, 281-299.
- Kandie, R., Mwanja, M. and Rono, I., 2014: *An update of the geological conceptual model of the greater Olkaria Geothermal field*. KenGen - Kenya Electricity Generating Company Ltd., internal report.
- Karingithi, C.W., Arnórsson, S., and Grönvold, K., 2010: Processes controlling aquifer fluid compositions in the Olkaria geothermal system, Kenya. *J. Volcanol. & Geotherm. Res.*, 196-3/4, 57-76.
- Lagat, J.K., 2004: *Geology, hydrothermal alteration and fluid inclusion studies of the Olkaria Domes geothermal field, Kenya*. University of Iceland, MSc thesis, UNU-GTP, Iceland, report 2, 71 pp.
- Naylor, W.I., 1972: *Geology of the Eburru and Olkaria prospects*. U.N. Geothermal Exploration Project, report.
- Odongo, M.E.O., 1984: *Geology of the Olkaria volcanic complex*. KPC, Kenya, internal report GL/OW/20.
- Scott, S., Gunnarsson, I., Arnórsson, S. and Stefánsson, A., 2014: Gas chemistry, boiling and phase segregation in a geothermal system, Hellisheidi, Iceland. *Geochimica et Cosmochimica Acta*, 124, 170-189.
- Stefánsson, A., and Arnórsson, S., 2002: Gas pressures and redox reactions in geothermal fluids in Iceland. *Chemical Geology*, 190, 251-271.
- Strecker, M.R., Blisniuk, P.M., and Eisbacher, G.H., 1990: *Rotation of extension direction in the Central Kenya Rift*. *Geology*, 18, 299-302.
- Wambugu, J.M., 1995: *Geochemical update of Olkaria West geothermal field*. Kenya Power Company, Ltd., internal report, 40 pp.



UNITED NATIONS
UNIVERSITY

UNU-GTP

Geothermal Training Programme

Orkustofnun, Grensasvegur 9,
IS-108 Reykjavik, Iceland

Reports 2014
Number 35

ANALYSIS OF VARIATIONS IN THE CHARACTERISTICS OF THE GEOTHERMAL FLUID PRODUCED FROM THE SUDUREYRI LOW-TEMPERATURE GEOTHERMAL SYSTEM IN NW-ICELAND

Yid-Lai Zelada Quán

Ministerio de Medio Ambiente y Recursos Naturales (MARN)

Km 5 ½ Carretera a Santa Tecla, Calle y col. Las Mercedes

San Salvador, San Salvador

EL SALVADOR

yzelada@marn.gob.sv, yidlai.quan@gmail.com

ABSTRACT

Problems associated with calcite scaling and drastic changes in fluid composition have limited the utilization of geothermal resources at Sudureyri in Ségundafjörður, NW-Iceland. Despite a relatively high production rate recorded during the first years of operation of the Sudureyri District Heating Service, the system showed a recovery during a later decrease in production rates. The geochemical and temperature record for this geothermal system extends from 1975 until 2014. The geochemical record suggests an intrusion of a more saline component in the producing reservoir. Comparing the characteristics of the saline fluid by a simple mixing process, it was evident that it was formed by seawater-basalt interaction. The fluid composition shows enrichment in calcium and silica, and loss of magnesium and sodium, compared with seawater. As a potential alteration product, the formation of smectite has been considered.

Knowing the system's behaviour at high production rates, a simple lumped model was used to simulate production temperature and chloride concentration, in order to predict cooling and the chemical composition of the geothermal fluid, in terms of the concentrations of some of the major species in the system; this included calcium, for different production scenarios. From the fluid characteristic predictions, it is possible to identify production scenarios that might endanger system operation. From the results of the assessment, it is believed that the system can sustain production equivalent to that recorded for 2013 (8.4 kg/s) for the next ten years. However, in those ten years the fluid is expected to reach chloride concentrations on the order of 220 ppm, and calcium concentrations of 45 ppm. At this rate of production, no significant drop is expected in the fluid temperature. For the simulation, the volume of the reservoir, porosity, the hot recharge rate and the temperature of colder inflow (saline fluid) were used as variables.

1. INTRODUCTION

The main use of geothermal energy in Iceland is for space heating; in 2010, this resource covered about 89% of the space heating requirement, through numerous district heating systems (Axelsson et al.,

2010). For small communities the geothermal resource has become an accessible and affordable energy alternative to meet the heating demand, which however requires effective and reliable management to ensure energy security.

Hitaveita Sudureyrar (Sudureyri District Heating Service) utilizes the geothermal resource at Sudureyri (Laugar), located in the northwest part of Iceland, by using two production wells. One of them is well LA-2, drilled to 684 m depth in 1975, and the other is well LA-5, drilled to 1141 m depth in 1984-1985. The long term management and monitoring of Sudureyri's geothermal resource provides elements for the characterization of reservoir properties, and application of models in order to predict system responses at different rates and periods of exploitation. Relatively high rates of production during the early years of utilization of the resource showed evidence of over-exploitation, suggesting the influence of seawater intrusion, which is not unexpected as the geothermal system is partly under the ocean-fjord, Súgandafjörður.

The purpose of the project described in this report is to predict changes in the composition of the geothermal fluid to define operating limits for different utilization scenarios, based on the particular utilization experience for the field. For this purpose, the changes in the characteristics of the fluid over time were evaluated, identifying both background and natural state conditions, as well as abnormal conditions caused by the utilization. The interaction of the seawater system with reservoir fluid was first addressed through a simple mixing model and, consequently, the role of fluid-rock interaction was evaluated. Finally, a simple lumped model was used to simulate changes in production temperature and chloride concentrations and, thus, identify principal properties of the reservoir. The model was, consequently, used to calculate predictions for different future utilization scenarios. Results and conclusions are presented at the end.

2. GEOLOGICAL BACKGROUND

The Sudureyri geothermal system in Súgandafjörður is located in the West Fjords, NW-Iceland, which is the largest peninsula in Iceland. The geology of the West Fjords is mainly characterized by basic and intermediate extrusive rocks with intercalated sediments, older than 3.1 m.y. (Figure 1). Geological studies indicate that the bedrock is composed of basalts.

The lava pile is cut by dykes and faults with a dominant NW-SE orientation, parallel to the strike direction. Benjamínsson (1981) showed that hydrothermal manifestations are widespread in the area and that the location of the hot springs is controlled by dykes and faults. The surface hydrothermal activity in this part of Iceland is classified as low-temperature activity, from just above ambient temperature up to 100°C. Flow rates are also variable but natural flows extend up to ~5 L/s.

The regional thermal gradient varies from 50°C km⁻¹ in the west to about 70°C km⁻¹ in the east. There is, however, a temperature anomaly with gradients over 100°C km⁻¹ to the south of the peninsula (Pálmason and Saemundsson, 1979).

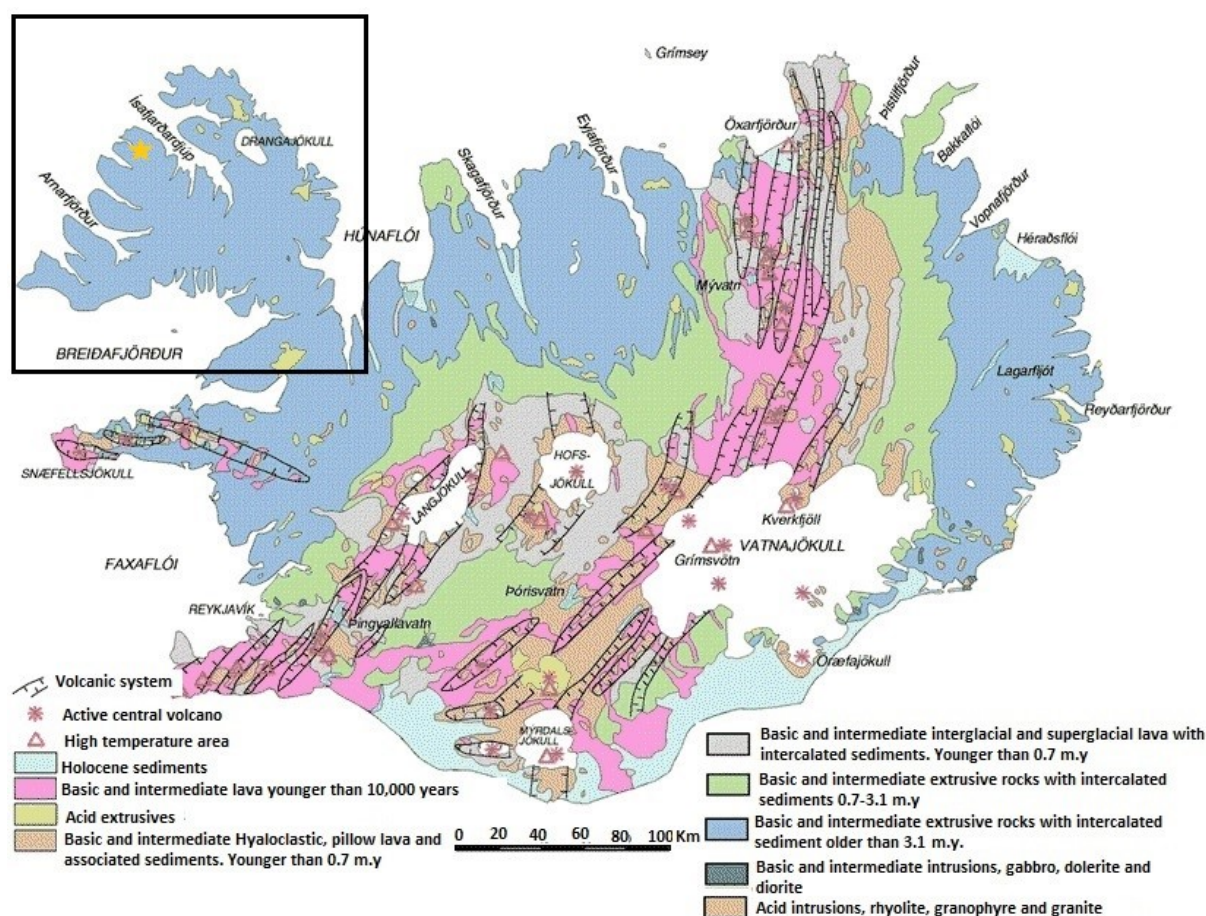


FIGURE 1: Geological map of Iceland (Jóhannesson and Saemundsson, 1999); the box marks the location of the West Fjords, the yellow star marks the location of Sudureyri

3. GEOTHERMAL EXPLORATION AND DEVELOPMENT IN SÚGANDAFJÖRDUR

The utilization of the geothermal resource at Sudureyri started by supplying hot water to a bathing pool located in the region. Studies that preceded the drilling of deep wells, including geochemical exploration and geophysical studies, aimed at increasing the flow of hot water to the pool. The temperature, calculated using a silica geothermometer for samples collected in 1960, indicated a reservoir temperature of 85°C and the chloride concentration was measured at 56 ppm. Samples collected in 1974 indicated a reservoir temperature of 69°C. In 1974, three elongated magnetic anomalies were identified, which were interpreted as dykes (Stefánsson et al., 1975).

Five wells have been drilled in the geothermal area of Sudureyri in Súcandafjörður. After successfully drilling well LA-02, Hitaveita Sudureyrar (Sudureyri District Heating Service) was founded in 1977 and put into service the following year. In the early days of the district heating system in Sudureyri, the composition of the fluid changed drastically; the chloride concentrations and calcium deposition increased, destroying the downhole pump of well LA-02 in 1978, and repeated cleaning operations were required in the well.

The successful drilling of well LA-05 in 1985 allowed for the temporary replacement of well LA-02 for the supply of hot water, from 1986 to 1998. Until 1998, the wells never operated simultaneously

(Ólafsson, 1999). Before drilling well LA-05, wells LA-03 and LA-04 were drilled in the geothermal area but neither has been used as a production well.

Basic information on the wells is presented in Table 1, and their location is shown in Figure 2. Currently, the system has two production wells: LA-02 and LA-05.

TABLE 1: Drilling operations in the Sudureyri field (Ólafsson, 1999)

Well	Year	Depth (m)	Latitude	Longitude	Description
LA-01	1967	15.5	66.111300	-23.459482	Temperature gradient
LA-02	1975	549	66.111300	-23.459482	Production well
LA-02	1976	684			Dredging production well
LA-02	1980	684			Cleaning production well
LA-02	1984	684			Cleaning production well
LA-02	1987	684			Cleaning production well
LA-03	1981	521	66.112850	-23.465134	Borehole
LA-04	1982	405	66.110384	-23.458017	Borehole
LA-05	1984-1985	1141	66.110267	-23.457883	Production well

Figure 2 shows the major faults and dikes which have been observed. It was considered likely that the main up-flow channel is connected close to well LA-02 on the east side (Gudmundsson and Flóvenz, 1981).

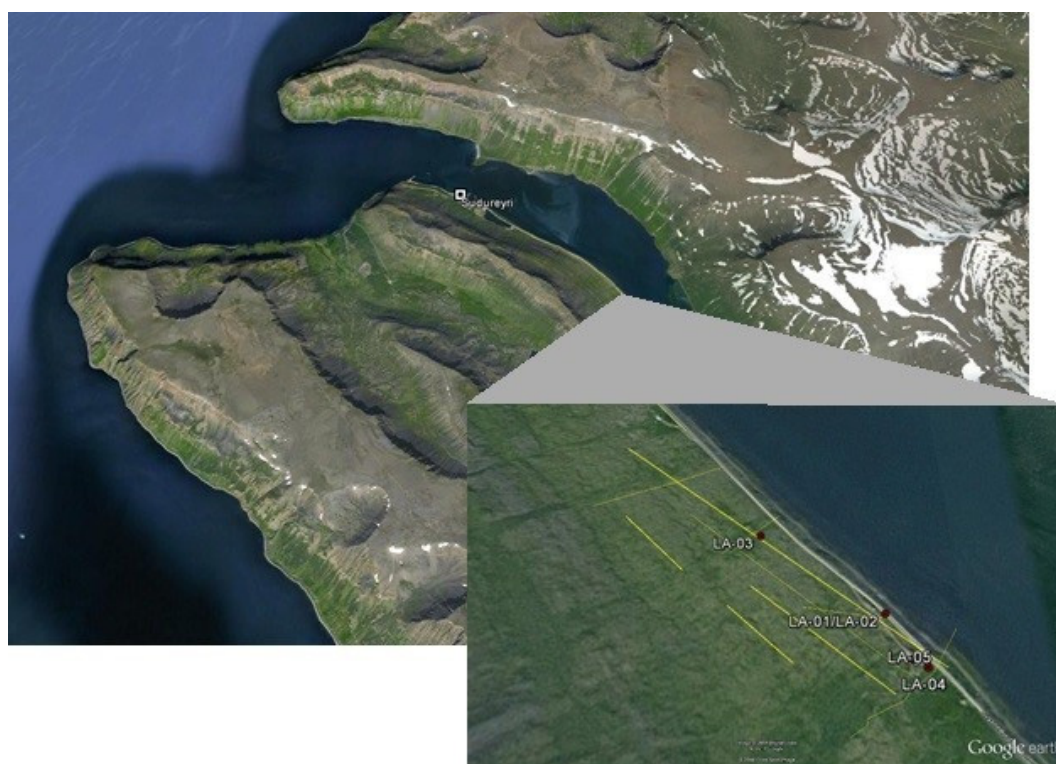


FIGURE 2: Well location and major faults and dikes in the Sudureyri fields (modified from Bai Liping, 1991)

The production data used are available in the database of Iceland GeoSurvey (ISOR). At the same time, production records indicated in geochemical monitoring reports were considered, detailed below.

The maximum production of the field was reached during the first years of operation (Flóvenz et al., 1982). From 1990 to 1991, there was an overall reduction in field production, associated with the start-up of a boiler (Sverrisdóttir and Kristmannsdóttir, 1994); however, since 1998, with the reconnection of well LA-02, the production has been slowly increasing. The total production from the field and from well LA-02 are illustrated in Figure 3.

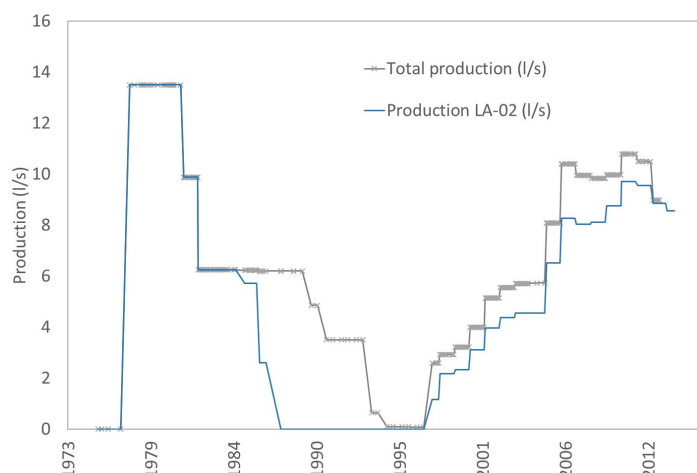


FIGURE 3: Production history

4. CHEMICAL CHARACTERISTICS OF THERMAL FLUIDS

The geochemical dataset for the Sudureyri geothermal system consists of 390 samples collected in the period from 1975 to 2014 from the field's production wells; of these, 272 were collected from well LA-02 and the remaining 118 from well LA-05. The samples were collected by personnel from Hitaveita Sudureyrar or by Iceland GeoSurvey (ÍSOR). Since 1995, the geochemical record included 6-12 samples per year for each well that is in production. Most of these samples are partial samples, for the determination of conductivity, chloride and sulphate only; this prohibits the rigorous fluid characterization of all the samples. However, for well LA-02, a number of complete samples exist, one sample per year in 1975, 1979, 1980, 1982, 1998, 2001, 2003, 2005 and 2011, and two samples per year for 1976 and 1998. The complete samples include measurements of pH, temperature, major cations (Na, K, Ca and Mg), boron, silica, chlorides, total carbonate carbon, sulphates, and other complementary parameters. For well LA-05, the complete samples are limited to those collected in 1987, 1992, 1994, 1998 and 2011. The composition of complete samples is given in Table 2.

TABLE 2: Measured chemical composition of the fluid from wells LA-02 and LA-05

Date	Well LA	Sample number	Sample temp. ^a (°C)	Liquid phase (mg/kg)																	Cond (μS/cm)	Cond/T (°C)	TDS
				pH ^b	pH/T (°C)	SiO ₂	B	Na	K	Mg	Ca	Al	Fe	F	Cl	SO ₄	CO ₂ ^c	H ₂ S					
17/02/2011	02	20110041	63	9.46	22.2	57.5	0.13	109.0	1.04	0.14	20.50	0.04	0.01	0.28	120	78.8	7.9	0.013	709	25.0	414.0		
03/06/2005	02	20050152	64	9.63	23.2	57.1	0.08	100.0	1.09	0.04	14.10	0.04	0.02	0.30	98	78.9	9.9		584.	25.0	367.0		
21/07/2003	02	20030557	64	9.57	23.8	57.0	0.09	93.2	0.79	0.02	10.30	0.04	0.04	0.31	84	77.0	9.3		252.0				
12/07/2001	02	20010206	64	9.71	19.8	57.1	0.09	94.1	1.25	0.00	9.97	0.04	0.01	0.31	78	74.3	10.1	0.040	519	25.0	340.0		
31/03/1998	02	19980248	64	9.74	23.4	60.9	0.06	90.6	0.88	0.01	8.70	0.05	0.01	0.41	57	78.1	9.1	0.090	496	25.0	390.0		
01/05/1982	02	19820058	63	9.43	21.0	51.9		145.3	1.71	1.72	60.46			0.29	260	95.3	9.2		1075	21.7	659.9		
13/11/1980	02	19800161	62	9.50	20.0	54.0		137.7	1.75	0.04	44.10			0.33	209	91.5	9.2		901	22.5	553.1		
06/11/1979	02	19790134	63	9.59	20.0	56.0		126.4	2.00	0.37	33.90			0.30	169	84.7	7.0	0.090	599	14.0	484.0		
14/12/1978	02	19780089	64	9.30	20.0	58.0		105.6	1.10	0.15	21.40			0.28	128	76.5	3.1		599	22.0	423.0		
03/05/1978	02	19780018	60	9.66	18.0	55.0		121.0	1.20	0.26	27.80			0.39	168	75.4	5.7		671		488.0		
03/08/1976	02	19760111	64	9.80	17.0	59.0		87.6	0.99	0.02	6.10			0.30	63	71.2	9.5	0.090	420		295.8		
28/02/1976	02	19760024	63	9.63	19.0	60.0		83.3	1.20	0.04	6.70			0.36	72	68.6	8.3		444		327.0		
03/12/1975	02	19750186	62	8.81	21.0	53.0		117.7	1.90	0.32	11.60			0.33	131	72.1	7.0		599		413.0		
17/02/2011	05	20110038	53	8.88	21.2	45.0	0.15	170.0	1.41	3.06	67.70	0.01	0.00	0.21	309	86.4	9.5		1287	25.0	724.0		
01/04/1998	05	19980250	57	9.56	23.6	53.6	0.04	89.7	0.77	0.07	9.22	0.02	0.01	0.36	70	71.1	14.4		500		301.0		
11/07/1994	05	19940147	58	9.45	22.4	53.0	0.12	97.7	0.86	0.28	13.20			0.29	109	77.3	9.2				362.0		
11/03/1992	05	19920050	58	9.51	19.0	53.0	0.10	126.0	1.16	1.56	28.10		0.01	0.30	169	85.0	11.0		763	25.0	398.8		
28/07/1987	05	19870085	58	9.13	23.0	50.1		190.1	1.92	6.32	80.57		0.03	0.32	340	106.1	11.0		1346	23.1	807.0		

a: Measured temperature; b: pH at measured temperature reported in the column to the right;

c: Total carbonate carbon as CO₂; d: Conductivity at measured temperature reported in the column to the right

The geochemical record for well LA-02 covers the following periods: 1975 and 1976, prior to the operation of Hitaveita Sudureyrar; 1978 to 1986, which marks the beginning of production from the well; and from 1998 to 2014. As mentioned above, in the period between 1987 and 1997, the production from the field was confined to well LA-05, so no geochemical records are available for well LA-02 for this period.

Well LA-05 has a continuous geochemical record from 1986 to 1989, and from 2005 to 2012. For the period between 1990 and 2005, only isolated records are available.

In addition to the monitoring record, geochemical monitoring reports published by ÍSOR exist for the periods 2012-2013 (Ólafsson, 2014), 2010-2011, (Óskarsson, 2012), 2007-2010 (Ólafsson, 2010), 2006 (Ólafsson, 2006), 2002-2003 (Ólafsson, 2003), 2000-2001 (Hardardóttir, 2002), 1999-2000 (Hauksdóttir and Ólafsson, 2000), 1998 (Ólafsson, 1999), 1997 (Ólafsson, 1998), 1995-1996 (Ólafsson, 1997) and 1994 (Sverrisdóttir and Kristmannsdóttir, 1994).

4.1 Evolution of the geochemical characteristics of the field

The high production rates recorded during the first years of operation of well LA-02, estimated to be between 13 and 14 L/s, involved a significant increase in the concentration of chloride. Inspection of Figures 4a and 4c shows that the salinity increased steadily with each year that the well was producing in the period between 1977 and 1986.

Initial Cl concentration in well LA-02 in 1976 was around 63 ppm, but in 1978 the Cl concentration had increased to 127 ppm, and in 1986 the concentration reached 290 ppm. The well's period of inactivity allowed the chloride concentration to recover to the initial value, and the production temperature of the well increased. Upon commissioning of well LA-05 as the main producer in the field (1986-1998), the chloride concentration for that well was higher than those recorded in well LA-02 (Figure 4c). The high chloride concentration initially observed decreased following the reduction of production from the field.

Geochemical monitoring reports for the field, published by Orkustofnun and later ÍSOR, attributed the high concentrations of chlorides in well LA-05, relative to the concentrations in well LA-02, to a drain in well LA-04 toward the ocean (Ólafsson, 1999), or an inflow of ocean-water into a shallow feed-zone in the latter well that consequently flowed down the well and exited through a deeper feed-zone and finally passed to well LA-02.

There are significant differences in the geothermal fluid from wells LA-02 and LA-05, including the concentration of chloride, total dissolved solids and temperature. The average temperature in well LA-02 is 65.1°C, while the average temperature in well LA-05 is 7°C lower (57.9°C). Additionally, the fluid in well LA-05 is more saline, with an average TDS (total dissolved solids) of 850 ppm. The average TDS in well LA-02 is 650 ppm. According to Arnórsson (1975), the increased chloride content in some low-temperature areas near the coast is, with little doubt, due to the percolation of sea water into the rock mixing with water of meteoric origin; nevertheless, the magnitude of the marine component in the thermal water will depend on porosity and flow rates of each geothermal system.

The variations in the chloride content were accompanied by changes in the concentrations of other major components, including calcium and sodium. Using the 1976 sample from well LA-02 as a baseline value, with a calcium concentration of 6.1 ppm, the Ca concentration increased to ten times the initial value (60.5 ppm) by 1982. Again, when well LA-05 went into operation, the Ca concentrations were even higher than those recorded in well LA-02, up to 106.2 ppm.

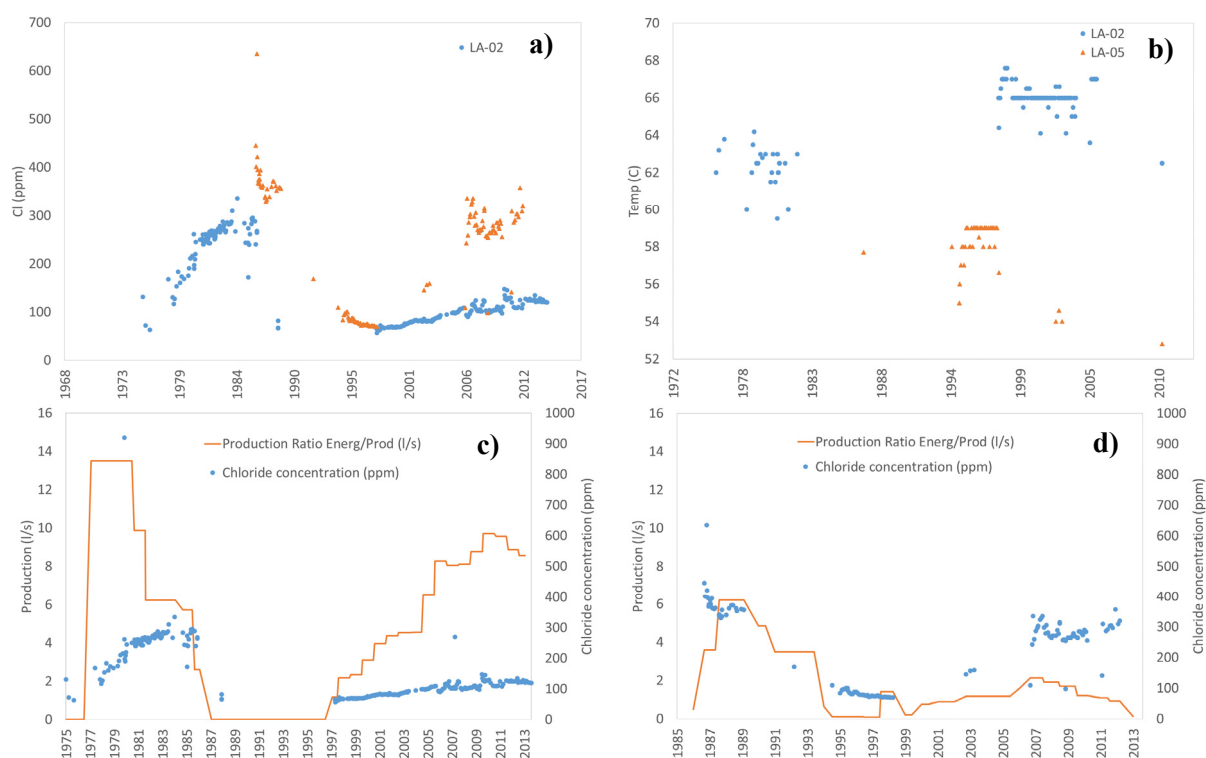


FIGURE 4: Development of: a) Chloride concentration in wells LA-02 and LA-05; b) Calcium concentration in wells LA-02 and LA-05; c) Chloride in well LA-02 along with production values; d) Chloride in well LA-05 along with production values

The fluid shows systematic changes in chemical composition with time. Therefore, it is difficult to establish a mechanism to describe the different populations. With the purpose of illustrating the behaviour of fluid composition, Table 3 gives the concentrations of the main components at different moments in the development of the field, and at different production rates. Also, in Figure 4, the historical behaviour of chloride and temperature is shown.

TABLE 3: Chemical composition of geothermal waters from wells LA-02 and LA-05 in Sudureyri

	Well LA-02	Well LA-02	Well LA-05	Well LA-05
Production (L/s)	0	9.9	6.2	1.4
Date	03/08/1976	01/05/1982	27/07/1987	01/04/1998
Temperature (°C)	63.8	63.0	57.7	56.6
pH/°C	9.80 / 17	9.43 / 21	9.13 / 23	9.56 / 24
CO ₂ (t) (ppm)	9.5	9.2	11.0	14.4
SiO ₂ (ppm)	59.0	51.9	50.1	53.6
Na (ppm)	87.6	145.3	190.1	89.7
K (ppm)	0.99	1.71	1.92	0.77
Mg (ppm)	0.02	1.72	6.32	0.067
Ca (ppm)	6.10	60.46	80.57	9.22
F (ppm)	0.30	0.28	0.32	0.36
Cl (ppm)	63.4	260.0	339.5	69.7
SO ₄ (ppm)	71.2	95.3	106.1	71.1
TDS (ppm)	295.8	659.9	807.0	301

A continuous, but not significant, decline has been identified in the pH value for the period between 1976 and 1982, with coefficients of variation for the evaluation period being 2.7% for well LA-02, and

2.8% for well LA-05. The average pH values recorded were 9.53 and 9.29 for wells LA-02 and LA-05, respectively.

In temperature, the most significant changes are an increase of 3.7°C in the average temperature recorded for the period 1998-2013 (66.0°C), relative to the average temperature between 1975 and 1986 (62.3°C), for well LA-02. The increase in temperature was noted after a period of less production from the well.

4.2 Classification of geothermal waters

A classification of the waters was carried out on the basis of the relative content of the three major anions $\text{Cl-SO}_4\text{-HCO}_3$ and a diagram based on the relative Na+K, Ca and Mg concentrations. Figure 5

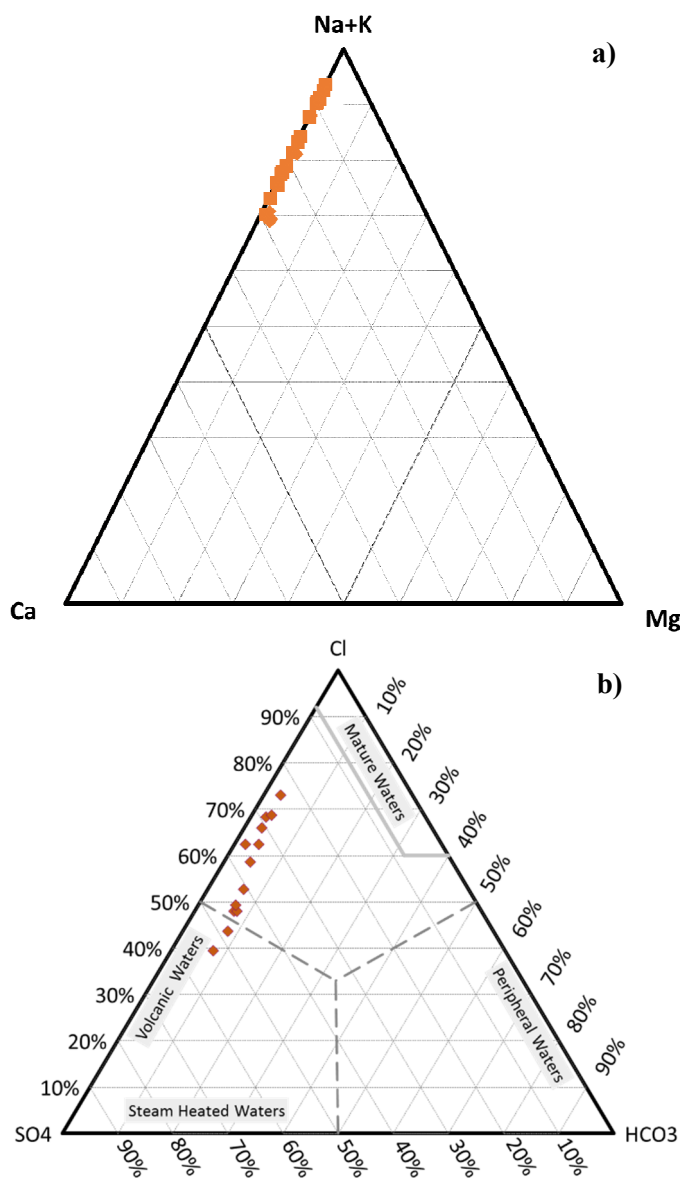


FIGURE 5: Classification for complete samples from wells LA-02 and LA-05: a) (Na+K)-Ca-Mg ternary plot; b) Cl-SO₄-HCO₃ ternary plot (Giggenbach, 1991)

depicts ternary diagrams showing these cation and anion concentration ratios for the Sudureyri geothermal waters. Additionally, Figure 5b illustrates the composition of different types of thermal waters: mature waters, steam-heated waters, volcanic waters and peripheral waters.

Chloride-rich waters are generally found near the up-flow zones of geothermal systems. High SO₄ steam-heated waters are often encountered over the more elevated parts of a field. This diagram can also be used to assess possible mixing of groundwater and geothermal fluid, as the degree of separation from the Cl corner towards the HCO₃ corner is the result of interaction of the CO₂ charged fluids at lower temperatures (Arnórsson, 2000).

Figure 5a shows that sodium and potassium are the dominant cations in the system, but mixing with a more calcium-rich component is evident. Figure 5b shows that chloride is the predominant anion in most samples, but there are a few samples where sulphate is the predominant anion and, again, the pattern indicates mixing with a more SO₄-rich component.

This behaviour in the distribution of the anions is commonly associated with volcanic systems, however, in the Sudureyri geothermal waters, it is more likely due to the contribution and mixing of seawater into the system, given the abundance of these ions in the waters. The mixing trend seen for the cations supports this interpretation.

Giggenbach's Na-K-Mg triangular diagram allows a clear distinction to be made between waters suitable for the application of ionic solute geothermometers and, at the same time, allows deeper equilibration temperatures and the effects of a variety of processes such as re-equilibration and mixing of waters of different origins (Giggenbach, 1988). The temperature dependant equations adopted for the construction of the ternary diagram are (Giggenbach, 1988):

$$\log \left(\frac{c_{K^+}^2}{c_{Na^+}} \right) = 1.75 - (1390/T) \quad (1)$$

$$\log \left(\frac{c_{K^+}^2}{c_{Mg^{2+}}} \right) = 14.0 - (4410/T) \quad (2)$$

where T is the absolute temperature in K.

The intersection of the isotherms corresponding to the K-Na and K-Mg subsystems corresponds to the composition of water in equilibrium with the two mineral systems and is labelled as “full equilibrium curve” (Figure 6).

Most of the samples show that the water composition shifts to lower temperatures and falls below the full equilibrium line (partial equilibration zone), reflecting the addition of magnesium in different amounts. These waters have probably been mixed with colder water. This behaviour is consistent with the potential intrusion of seawater into the system. A few samples are located in the “immature waters” area and are, therefore, considered unsuitable for the evaluation of K/Na-feldspar equilibrium temperatures. It should, however, be noted that the ternary diagram reflects temperatures between 60 and 100°C, consistent with the measured temperatures for the wells.

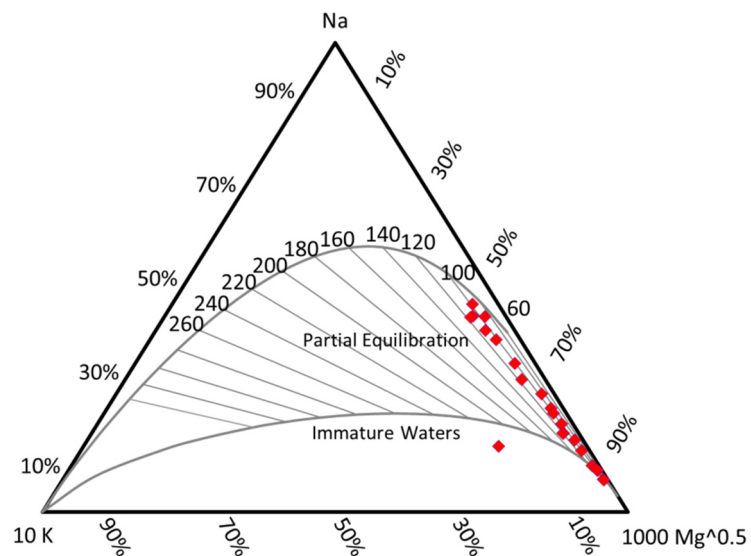


FIGURE 6: Na-K-Mg equilibrium diagram (Giggenbach, 1988) with data from the Sudureyri geothermal system (red diamonds)

4.3 Seawater-basalt interaction and the mixing process

When sea water and groundwater mix, the concentration of components such as sodium, potassium, calcium, chloride, magnesium and sulphate in the water increases, relative to the groundwater concentration, but concentrations of other components such as silica and fluoride could decrease.

Chloride is considered to be a conservative species in the system, i.e. it does not take part in the formation of secondary minerals and, therefore, can be used for characterizing potential mixing processes in the reservoir. If the variation in the concentration of chloride is due to the mixing of cold and hot water in the upflow, a linear correlation between the chloride concentration and the concentration of other components is expected, also dominated by the mixing process.

The relationship between the concentrations of chloride on one hand, and individual components on the other, was studied, using the available samples from both wells, in order to identify relative changes. Pearson's correlation coefficient was used as a measure of the strength of the correlation between the concentrations. The results are given in Table 4.

TABLE 4: Pearson's correlation coefficient indicating the relationship between the concentrations of different species with respect to chloride concentration, for the period between 1978 and 2014 in wells LA-02 and LA-05

	CO ₂	SiO ₂	Na	K	Mg	Ca	F	Br	SO ₄
R	0.0681	-0.7759	0.9889	0.7252	0.8321	0.9884	-0.6018	0.9976	0.8825

A linear relationship between two components in mixing geothermal waters, where one component is certainly conservative, suggests the other component is also conservative. Bromide shows this behaviour, in accordance with it being considered conservative, in advance. Nevertheless, sodium and calcium also show a strong correlation with the chloride concentration in the system. For low-temperature systems, which involve fluid-rock interaction, some of the major components (Ca, Mg, Na, K, HCO₃, SO₄, SiO₂) are expected to be reactive. The reactive nature of all of these components is due to their tendency to precipitate from solution, forming secondary minerals (Arnórsson, 2000).

It should be noted that silica and fluoride show negative coefficients. This indicates that if the concentration of chloride in the system increases, then the concentration of these components will decrease. On other hand, total carbonate and fluoride have low correlation coefficients, to some extent the behaviour of the reactive components.

The high correlation shown by sodium and calcium concentrations, with that of chloride, allows the development of empirical equations for the mixing (Table 5). Regarding the content of sulphate, Figure 7 shows that wells LA-02 and LA-05 exhibit behaviour slightly offset relative to each other, so that empirical equations for the system, and both wells, are proposed.

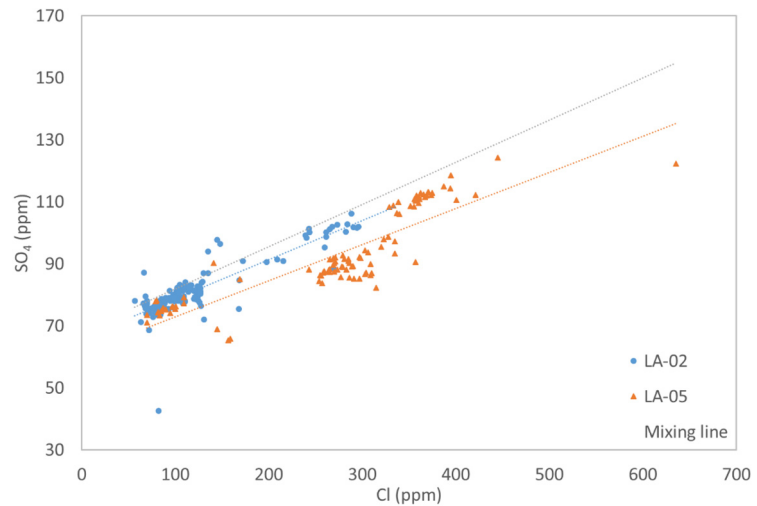


FIGURE 7: Relationship between sulphate and chloride concentrations in wells LA-02 and LA-05, along with the proposed mixing line for geothermal water and seawater

TABLE 5: Empirical relationship between concentrations of different constituents, with respect to chloride

Equations	R ²	Equat. no.
$[Na] = 0.3536 * [Cl] + 64.474$	0.9779	(3)
$[Ca] = 0.2639 * [Cl] - 11.262$	0.9769	(4)
$[SO_4] = 0.0994 * [Cl] + 68.018$	0.7788	(5)
$[SO_4] = 0.1263 * [Cl] + 66.074$	0.7558 ^a	(6)
$[SO_4] = 0.1166 * [Cl] + 61.184$	0.7624 ^b	(7)

a) Well LA-02; b) Well LA-05

A mixing process was simulated in terms of concentrations in the dilute geothermal fluid at baseline (undisturbed state), and seawater composition. As a reference value, the values for the geothermal fluid concentration measured in 1998 for well LA-02 (after a period of less use for 12 years) were considered, which defines the minimum chloride content for the period. The seawater concentration published by Arnórsson (1978) was assumed.

TABLE 6: Expected geothermal and seawater composition in Sudureyri

	Geothermal water	Seawater
Na	90.61	10556
K	0.88	380
Mg	0.011	1272
Ca	8.7	400
SiO ₂	60.9	3
SO ₄	76.07	2649
F	0.41	1.3
CO ₂	9.06	114
Cl	56.68	18980

The equation for the mixing line is given by the following expression:

$$[C_i] = \frac{[C_{seawater}] - [C_{geothermalw}]}{[Cl_{seawater}] - [Cl_{geothermalw}]} ([Cl_i] - [Cl_{geothermalw}]) + [C_{geothermalw}] \quad (8)$$

where C_i represents the concentration of the species of interest, under the assumption of a perfect mixing process, and Cl_i represents the respective concentration of chloride.

The results are shown in Figure 8. Note, that the sulphate distribution trends towards the mixing line (Figure 7), whereas the sodium, potassium, magnesium and calcium concentrations show a deviation from the geothermal-seawater mixing line. The content of sulphates in fresh cold groundwater in Iceland is generally less than 5 ppm (Arnórsson, 1975). It is also estimated that the sulphate content in water, where the temperature is less than 100°C, is governed by the leaching of the rock (Arnórsson, 1975).

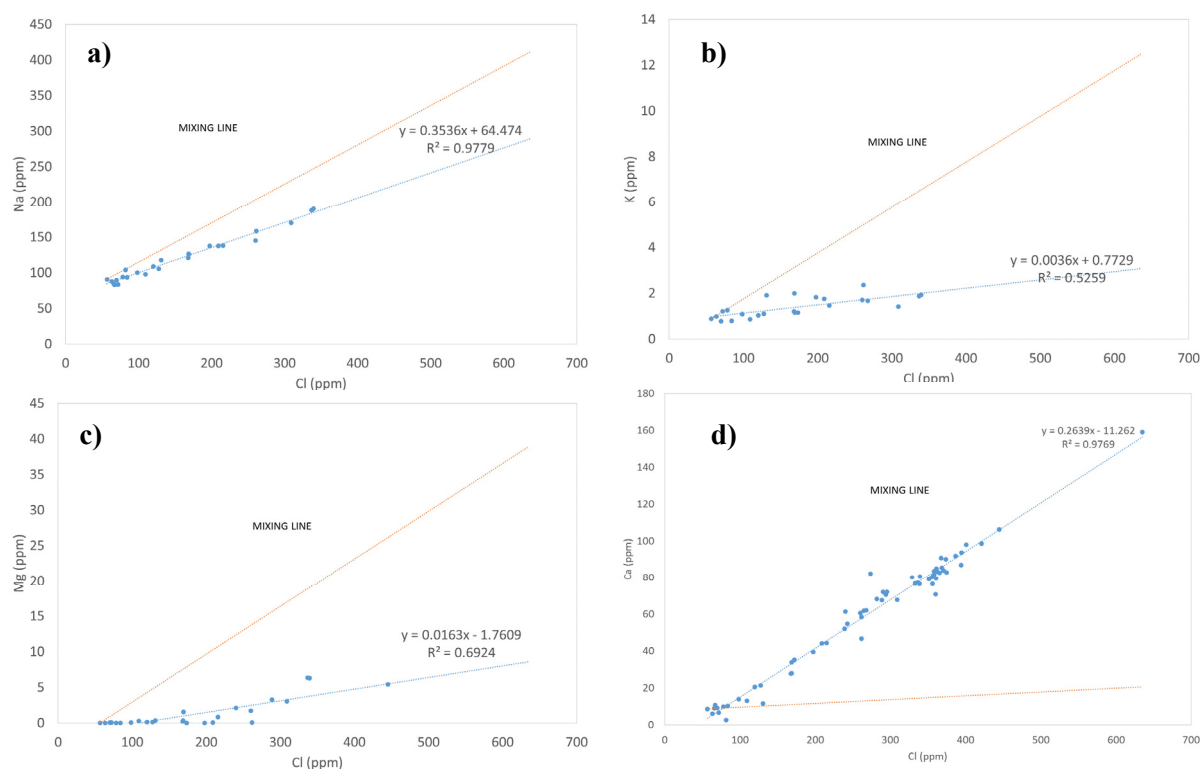


FIGURE 8: Concentrations of Na, K, Mg and Ca, as a function of Cl concentration in wells LA-02 and LA-05 (a, b, c and d, respectively), along with the proposed mixing line for geothermal water and seawater

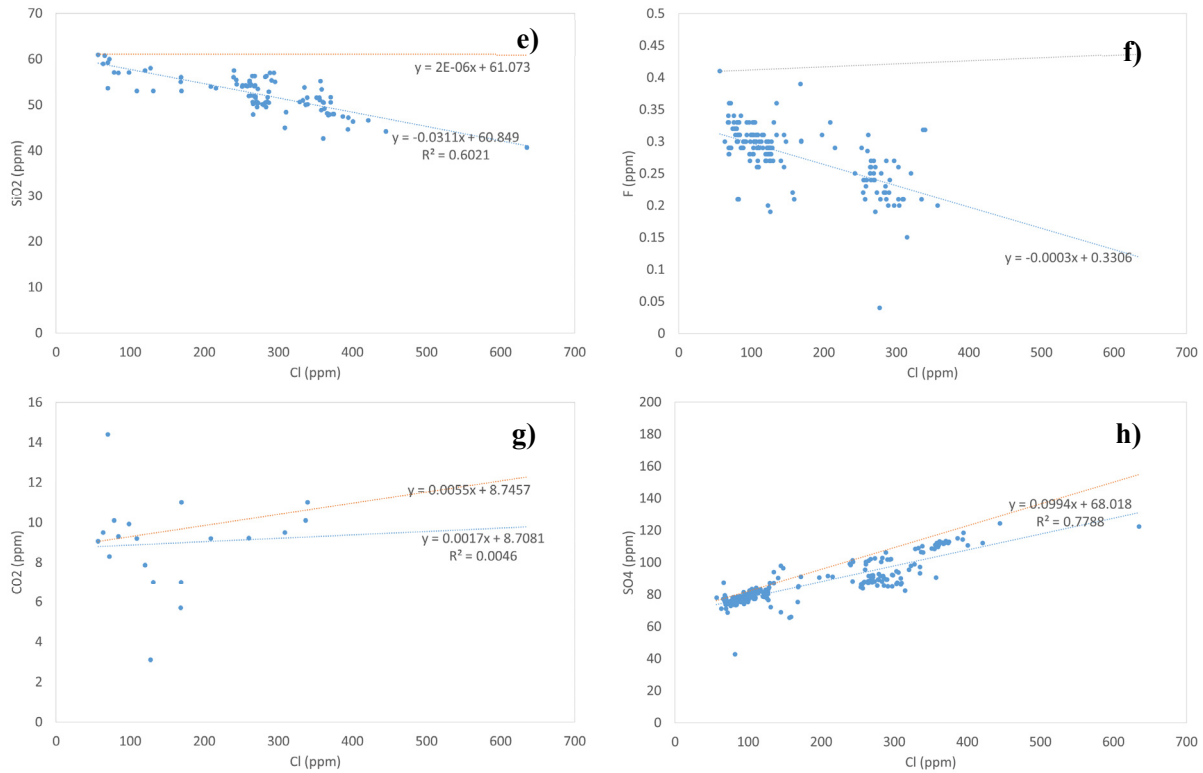
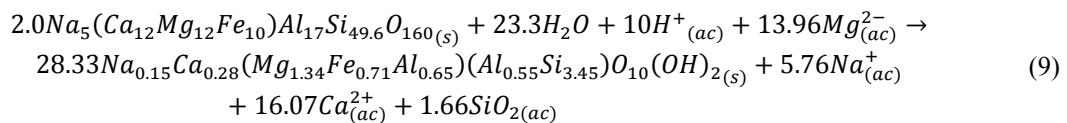


FIGURE 8 cont.: Concentrations of SiO₂, F, CO₂ and SO₄, as a function of Cl concentration in wells LA-02 and LA-05 (e, f, g and h, respectively), along with the proposed mixing line for geothermal water and seawater

The Sudureyri system has quartz temperatures between 90 and 101°C, and sulphate concentrations ranging between 10.6 and 92.7 ppm. The enrichment of sulphate is clearly associated with a mixing process.

The measured concentration of calcium is above the geothermal-seawater mixing line, possibly associated with higher values of calcium in the cold fluid fed into the system than the seawater values. Moreover, the concentrations of sodium, magnesium, potassium, fluoride and silica are lower than estimated by the mixing process. When a fluid, such as seawater, is being modified through chemical reactions with the rock, the conservative components such as chloride remain constant, so when some cations decrease in concentration, others increase.

The mixing trends shown in Figure 8 suggest that the saline component has been modified through reactions with the rock at geothermal temperatures. The saline component has gained calcium and lost magnesium, sodium, and potassium relative to seawater. The consistency of the mixing trends furthermore indicates that there is a substantial amount of saline fluid with a fairly constant chemical composition. These chemical changes suggest the probable formation of a magnesium-rich alteration phase, possibly smectite. The reaction, considering the interaction of seawater with basalt glass, could be described according to the following equation (Seyfried and Bischoff, 1979):



To further explore the effects of smectite formation, the difference between the concentrations of magnesium, resulting from direct mixing of geothermal water with seawater, and the measured magnesium concentrations was assumed to correspond to the amount of magnesium consumed in the reaction process. For a direct mixing process in which chloride concentrations of 200 ppm are reached, magnesium concentrations levels should be around 9.6 ppm. Measured concentrations, corresponding

to the same chloride concentrations, are on the order of 5 ppm, indicating that about 4.6 ppm of magnesium was removed from the liquid phase.

On the other hand, the measured concentration of calcium is higher than what corresponds to the mixing process between geothermal water and seawater. For a chloride concentration of 200 ppm, a calcium concentration of 12 ppm would be expected. The product of the smectite reaction with calcium is estimated to add 8 ppm (considering Mg as the limiting reactant), giving a total of 20 ppm. Even though the reaction process shows considerable enrichment of calcium in the aqueous phase, the measured calcium concentrations in samples with chloride concentrations of 200 ppm are even higher, in the range of 64 ppm (Figure 9).

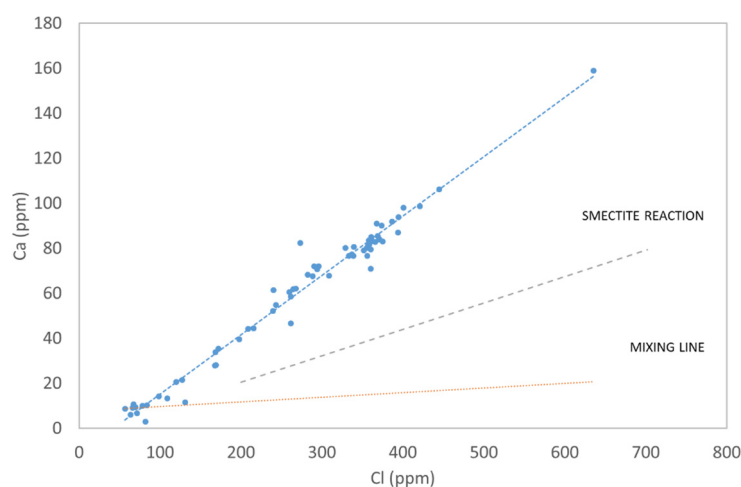


FIGURE 9: Relationship between calcium and chloride concentrations in wells LA-02 and LA-05, along with the proposed mixing line for geothermal water and seawater without (red) and with (green) the smectite formation reaction

The formation of smectite in the system explains the magnesium consumption, compared to that originally available in the fluid. At the same time, the calcium enrichment in the fluid is only partially explained. However, the stoichiometric generation of smectite, based on the magnesium available, is not sufficient to explain the measured values. This suggests the potential formation of other species rich in magnesium, ion exchange reactions, or an additional contribution associated with the dissolution of anhydrite by the inflow of cold seawater to the system.

The reaction of smectite suggests a small, but not negligible, sodium gain. Also, a gain of silica is observed. The enrichment of these components is inconsistent with the behaviour of the fluid shown in historical records. For these species, it is necessary to consider the temperature dependence of the solubility of these components, in particular with respect to chalcedony and alkali feldspars.

One of the phenomena noted, as a result of the interaction of basalt with seawater in low-temperature systems, is a drop in pH associated with the removal of magnesium, and the corresponding formation of hydrogen ions (Seyfried and Bischoff, 1979). This has also been seen here where, associated with the mixing process, there has been a slight decrease of pH values. The lowest pH measured was 8.8 and the highest was 9.8.

5. ANALYSIS OF MINERAL EQUILIBRIA

The saturation index (SI) for a given mineral dissolution reaction is defined as:

$$SI = \log(Q/K) \quad (10)$$

where Q is the quotient of ionic activities and K is the solubility product for the mineral under consideration (function of temperature).

If $SI = 0$, the system is in equilibrium, but if SI is positive, the solution is super-saturated and the mineral may precipitate.

Q is given by:

$$Q = \frac{a_C^c \cdot a_D^d}{a_A^a \cdot a_B^b} \quad (11)$$

for the reaction:



where the reactants are the species A and B and the products the species C and D. The lower case letters designate the stoichiometric coefficients of the respective chemical species.

The relationship between concentration and activity is given by:

$$a_i = m_i \gamma_i \quad (13)$$

where a_i is activity, m_i the molal concentration, and γ_i the activity coefficient.

The individual activity coefficients for charged aqueous species were calculated from the extended Debye-Hückel equation:

$$-\log \gamma_i^* = \frac{AZ_i^2 \sqrt{I}}{1 + aB\sqrt{I}} + B^*I \quad (14)$$

where I is the ionic strength, a is the effective diameter of aqueous ions, and A , B and B^* are temperature dependent parameters.

The saturation index of calcite and other minerals was evaluated for the Sudureyri data, using the WATCH speciation program (Arnórsson and Bjarnason, 1993) for the complete water samples from Well LA-02. The results are illustrated in Figure 10.

Calculations show that the system is slightly super-saturated for low albite and microcline (stable K-feldspar at low temperatures). This coincides with indications in the literature for low temperature systems, up to 150°C (Arnórsson et al., 1983).

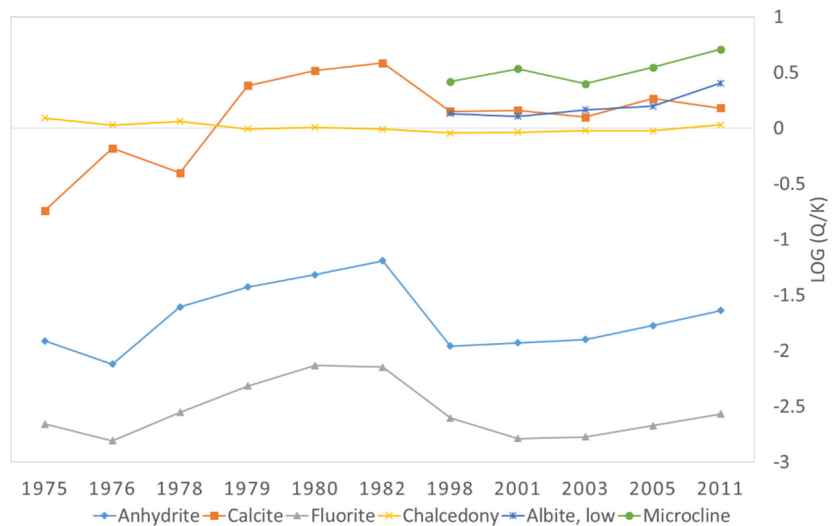


FIGURE 10: Mineral equilibrium calculated for well LA-02

Chalcedony is very close to saturation for all samples. In young basalt hosted geothermal systems at temperatures below ~180°C, it is expected that silica be controlled by the solubility of chalcedony (Fridriksson and Ármannsson, 2007). However, mixing of cold groundwater with thermal water may lead to silica super-saturation in the mixture if the original thermal water was in equilibrium with chalcedony. This is because the solubility of chalcedony increases more rapidly than the temperature (Arnórsson, 1975).

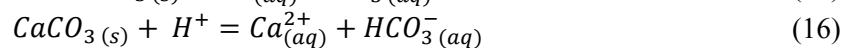
The historical record does not give any evidence of super-saturation with chalcedony, which might result from a mixing process with cold water. However, because of the limited temperature decay in the system, one should not expect drastic changes in the solubility and the mineral equilibrium after the mixing process.

5.1 Calcium saturation state

Calcite is super-saturated for the period between 1978 and 2011 (Figure 10). Experience in Iceland of utilization of low-temperature reservoirs has shown that geothermal waters are, in general, slightly super-saturated with respect to calcite but, in most cases, scaling problems are not encountered as long as the water has a saturation index ($\log(Q/K)$) below about 0.4 (Bai Liping, 1991). The calcite saturation index exceeded this critical level for the samples collected between 1978 and 1982.

It is noteworthy that other factors have been identified that promote the deposition process, such as salinity. It is expected that if the total concentration of dissolved solids in the water is high, then precipitation will occur faster than in more diluted water (Sverrisdóttir and Kristmannsdóttir, 1994).

The solubility of calcite can be described by the following reactions:



The average pH value for well LA-02 was 9.53, and 9.29 for well LA-05. At these pH levels, inorganic carbon is mainly present as bicarbonate (HCO_3^-) and carbonate (CO_3^{2-}).

By observing in detail the behaviour of fluorite, calcite and anhydrite, depending on the concentrations of calcium and ionic species of carbonate, it is observed that the concentration of the bicarbonate ion describes the general trend of the saturation indices of these minerals (Figures 11 and 12). The concentration of Ca^{2+} shows an increasing trend from 1976 to 1982, however the rise in the saturation index is not of the same magnitude.

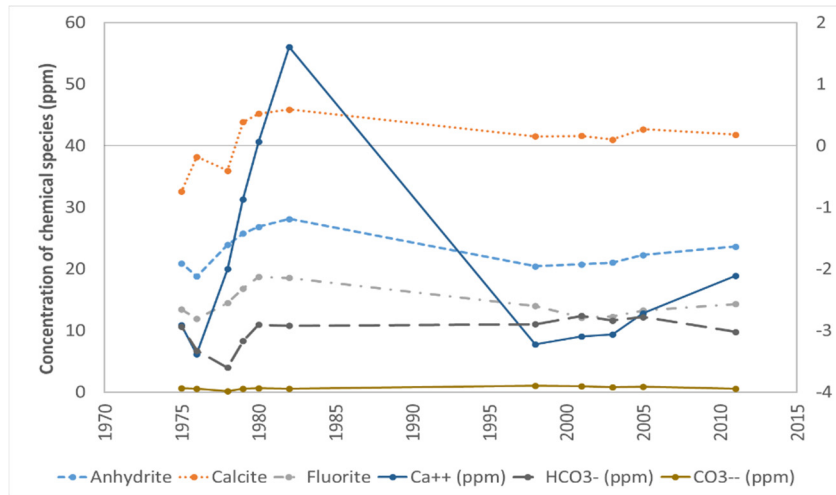


FIGURE 11: Saturation indices of anhydrite, calcite and fluorite along with concentrations of calcium and carbonate species in well LA-02

When evaluating a function of the activities of the calcium carbonate and bicarbonate species, a minimum was observed in 1982. While the concentrations and activities of the species are directly proportional (Equation 13), in this case there is an increase in the concentration of calcium and most of the other main components, thus increasing the ionic strength of the system and reducing the associated activity coefficient, as shown in Figure 13.

Calcite (CaCO_3) formation prevails over the formation of other calcium minerals. The reduced availability of calcium ions, limits the concentrations of other calcium minerals such as fluorite (CaF_2) and anhydrite (CaSO_4) and, consequently, the saturation index of these species. Fluorite (CaF_2) and anhydrite (CaSO_4) are under-saturated for all samples considered. Anhydrite saturation is generally linked to high-temperature systems (Arnórsson, 1975).

By modelling, the conductive cooling process (Figure 14) shows that with the decline in temperature, the solubility of anhydrite increases, while the solubility of the feldspars decreases. Note that low albite and microcline described the same trend, suggesting that the mineral balance of these species is not independent.

6. GEOTHERMOMETER TEMPERATURE

Geothermometers were applied in order to identify those that best described the behaviour of the Sudureyri system, and because there are systematic variations between the estimated temperatures. The quartz-, chalcedony- and Na/K-geothermometers were considered. The expressions are given below:

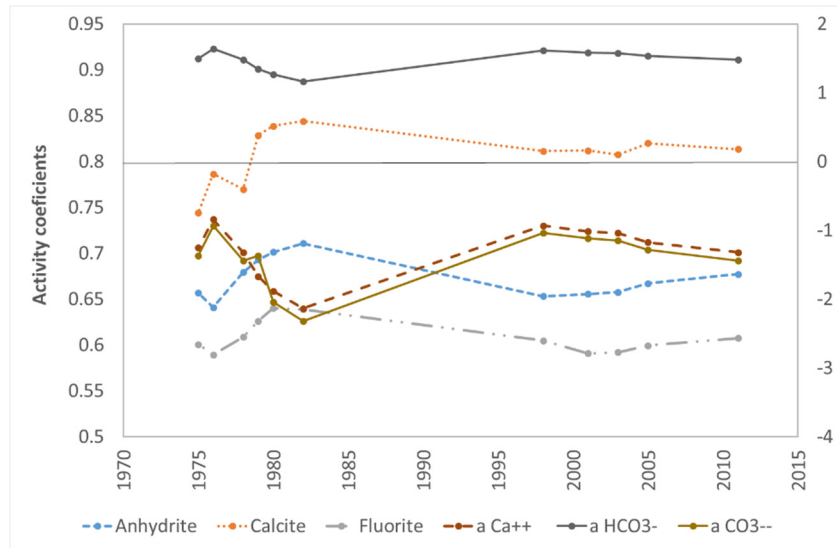


FIGURE 12: Saturation indices of anhydrite, calcite and fluorite along with activity coefficients of calcium and carbonate species in well LA-02

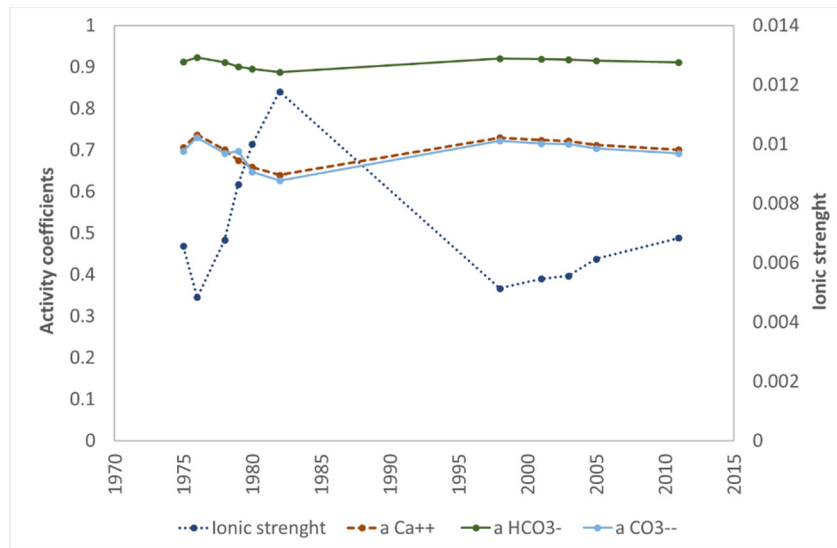


FIGURE 13: Ionic strength along with the activity coefficients of calcium and carbonate species in well LA-02

$$T_{\text{Na/K}}(^{\circ}\text{C}) = \frac{1319}{1.666 + \log \frac{\text{Na}}{\text{K}}} - 273.15 \quad (17)$$

$$T_{\text{chalcedony}}(^{\circ}\text{C}) = \frac{1112}{4.91 + \log \text{SiO}_2} - 273.15 \quad (18)$$

$$T_{\text{quartz}}(^{\circ}\text{C}) = -42.2 + 0.28831 \text{SiO}_2 - 3.6686 \times 10^{-4} \text{SiO}_2^2 + 3.1665 \times 10^{-7} \text{SiO}_2^3 + 77.034 \log(\text{SiO}_2) \quad (19)$$

The Na/K and chalcedony geothermometers were retrieved from Arnórsson et al. (1998), and the quartz geothermometer from Fournier and Potter (1982).

The average temperature recorded for well LA-02 is 65.1°C. As the geothermal water is not boiling at these conditions, the measured temperature at the wellhead is expected to correspond to the temperature of the reservoir. Analyses of spring waters by independent methods have suggested that at temperatures below 190°C, the reservoir temperature should be estimated using the chalcedony geothermometer (Henley et al., 1984).

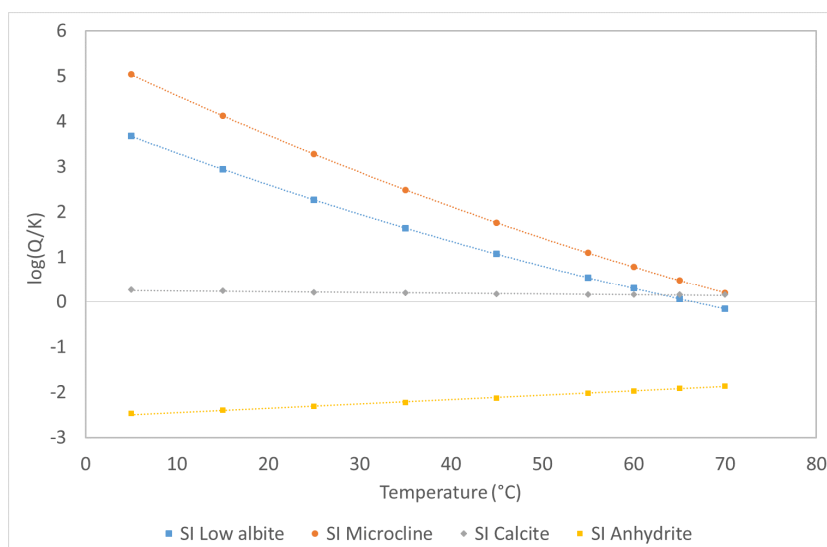


FIGURE 14: Saturation indices of low albite, microcline, calcite and anhydrite against temperature

By comparing the results with the measured temperature, it is observed that the estimated chalcedony geothermometer temperature has the smallest deviation from the temperature in the reservoir (Figure 15). This is consistent with the results of mineral balance. It can therefore be concluded that the chalcedony geothermometer is not significantly affected by the effects of mixing in the reservoir, i.e. that dissolved SiO_2 readily reaches equilibrium with chalcedony after mixing.

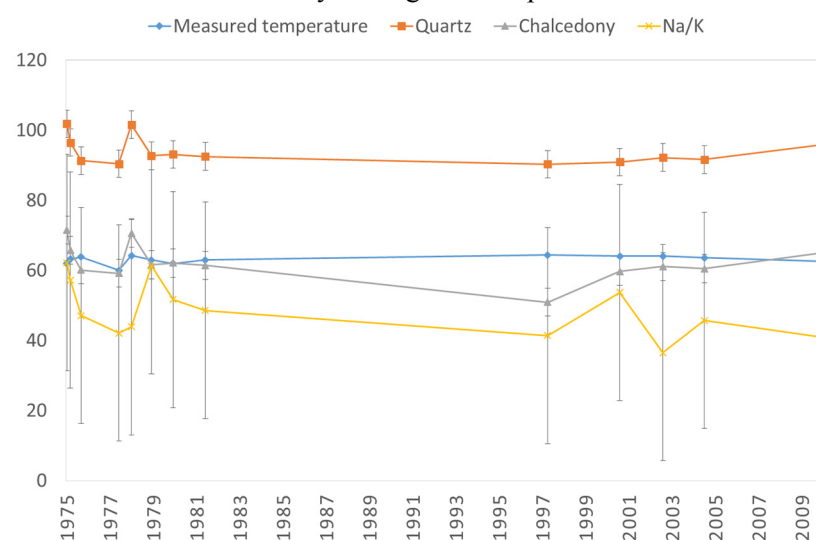


FIGURE 15: Comparison between geothermometer temperatures and observed temperature for well LA-02

Also, the minimum and maximum temperatures given by the quartz, chalcedony and Na/K geothermometers were evaluated, using the concentrations of silica, sodium and potassium corresponding to the average value and one standard deviation ($\mu \pm \sigma$). Figure 15 shows the quartz, chalcedony and Na/K temperatures, along with the measured temperature.

The error bars in Figure 15 show the evaluated minimum and maximum temperature calculated by the quartz, chalcedony and Na/K geothermometers, using the concentrations of silica, sodium and potassium corresponding to $\mu \pm \sigma$.

The Na/K geothermometer, while yielding lower temperatures than those measured, magnifies variations in fluid temperature. This is a rather unusual behaviour, but is probably due to the considerable changes in concentrations of these ions when mixing with seawater and the slow kinetics of Na-K exchange between feldspars and aqueous alkali solutions below 300°C (Marini, 2000).

7. SIMULATION OF TEMPERATURE AND CHEMICAL COMPOSITIONAL CHANGES BY A COLDER INFLOW MODEL

7.1 Description of the model

A simple lumped parameter model was used to simulate the observed changes in temperature and chloride concentration at Sudureyri, which is part of the effect of inflow of saline fluid into the geothermal system (seawater modified through reactions with the basalt), observed during production.

A graphical representation of the system, illustrated in Figure 16, shows an infinite groundwater system (sea water in this case), with water temperature T' , and solute concentration C' . The Sudureyri system constitutes a sea-water reservoir. The production part of the geothermal system has a volume V , variable temperature $T(t)$ and solute concentration $C(t)$. The initial temperature and concentration are denoted by T_0 and C_0 , respectively. In addition, there is a constant inflow of R kg/s from the outer and deeper parts of the geothermal system, with temperature T_R and concentration C_R (Björnsson et al., 1994).

The expressions used for modelling the behaviour of the conservative species concentrations and temperatures were presented by Björnsson et al. (1994) and are listed below.

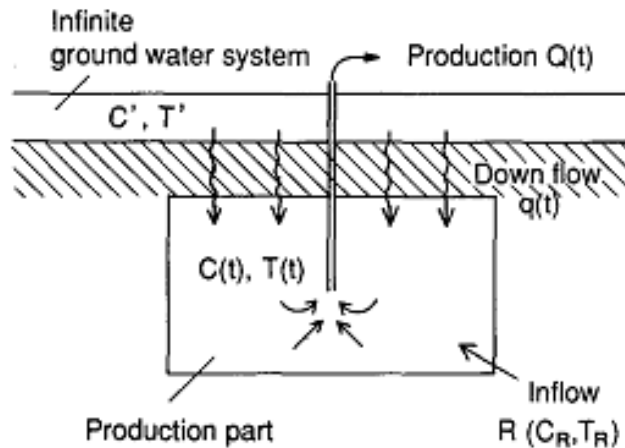


FIGURE 16: Simple model used for simulating inflow of saline fluid (Björnsson et al., 1994). A variable production of Q kg/s starts at time $t = 0$. The down-flow of groundwater (in this case seawater) is q kg/s, which is also variable. In the natural state, before $t = 0$, the production is assumed to be zero.

7.2 Chemical changes

The conservation of a chemical substance that does not react with the reservoir rock, is given by:

$$V \frac{d(\rho_w \phi C)}{dt} + QC = qC' + RC_R \quad (20)$$

where ρ_w = Density of the geothermal fluid (water);
 ϕ = Porosity of the rocks in the production part of the system.

Rewritten, the equation becomes:

$$\frac{dC}{dt} + \alpha(q + R)C(t) = \alpha q C' + \alpha R C_R \quad (21)$$

with

$$\alpha = \frac{1}{V \phi \rho_w} \quad (22)$$

Considering $q = Q - R$, and solving for a constant production, we obtain:

$$C(t) = C_0 e^{-\alpha t} + \left[\frac{(Q - R)C' + RC_R}{Q} \right] (1 - e^{-\alpha t}) \quad (23)$$

In the case of variable production, the time-series can be discretised in time, resulting in:

$$C_i(t) = C_{i-1} e^{-\alpha Q_i \Delta t_i} + \left[\frac{(Q_i - R)C' + RC_0}{Q_i} \right] (1 - e^{-Q_i \Delta t_i}) \quad (24)$$

7.3 Energy balance and temperature

According to Wang Guiling (1991), the conservation of energy, or heat, in this lumped model can be expressed by:

$$V < \rho c > \frac{dT}{dt} = C_v (qT' - QT + RT_R) \quad (25)$$

where $< \rho c >$ is the volumetric heat capacity of the reservoir, and C_v is the heat capacity of water.

Approximating the value of q as above results in the following:

$$T(t) = T_0 e^{-\beta t} + \left[\frac{(Q - R)T' + RT_R}{Q} \right] (1 - e^{-\beta t}) \quad (26)$$

where

$$\beta = \frac{Q}{V < \rho c >} \quad (27)$$

At the same time, $< \rho c >$ is given by the following expression:

$$< \rho c > = (1 - \varphi) \rho_r C_r + \varphi \rho_w C_w \quad (28)$$

Discretizing by intervals for a variable production results in:

$$T(t) = T_{i-1} e^{-\beta Q_i \Delta t_i} + \left[\frac{(Q_i - R)T' + RT_0}{Q_i} \right] (1 - e^{-\beta Q_i \Delta t_i}) \quad (29)$$

7.4 Methodology

The measured chloride concentrations were adjusted to reflect a single annual value. For the years in which multiple samples are available, the first measured value during the second half of each year is selected for this purpose.

The equations suggested by the model (Equations 20-29), were developed in an Excel spreadsheet. Model fitting was performed by varying the relevant parameters to minimize the sum of the squared deviations between measured values and simulated concentrations, for chloride and temperature simultaneously, according to the following equation:

$$\sum A(T_{sim} - T_{measured})^2 + A([Cl]_{sim} - [Cl]_{measured})^2 \quad (30)$$

The optimization method uses the GRG Nonlinear Solving method and Evolutionary algorithms, both in the Solver Package of Microsoft Excel.

The optimization variables considered were: producing reservoir volume, porosity, hot recharge of the system and temperature of the colder inflow. According to the developers (Frontline Systems, 2014), the GRG method is capable of finding a *locally optimal* solution. Therefore, there should be no other set of values, for the decision variables, close to the current values that yields a better value for the objective function. Thus, conditions for local optimality have been satisfied (to within a certain predefined tolerance). In order to evaluate different local solutions, the order of magnitude of the pivot value of reservoir volume was changed.

How the variables were constrained is listed in Table 7. The limits for the recharge rate are fixed; they were established by considering the historical field production.

TABLE 7: Constraints of the inflow model

	Variable	Unit	Lower limit	Upper limit
V	Volume of production part of geothermal reservoir, or the mixing volume	m ³	1000	
R	Recharge	kg/s	2.00/0.10	100.00/6
ϕ	Porosity of reservoir	-	0.05	0.15

8. SALINE INFLOW SIMULATION RESULTS

8.1 Chloride concentrations, measured and simulated

Assessing the behaviour described by Equations 24 and 29, it is seen that for zero production, the functions are undefined. Also, a very low production value is simply a break-point approach.

For well LA-02, in which the period of analysis incorporates a long period of inactivity (1986-1998) and the subsequent recovery period, the model does not converge to a reliable fit ($r^2=0.6019$). The measured and modelled concentrations are presented in Figure 17. For this reason, the time series for well LA-02 is split into two periods, 1975-1986 and 1998-2013. The production values in 1975 and 1997 correspond to the initial production (t_0) for both periods. Results of the modelling are presented in Table 8 and Figure 18.

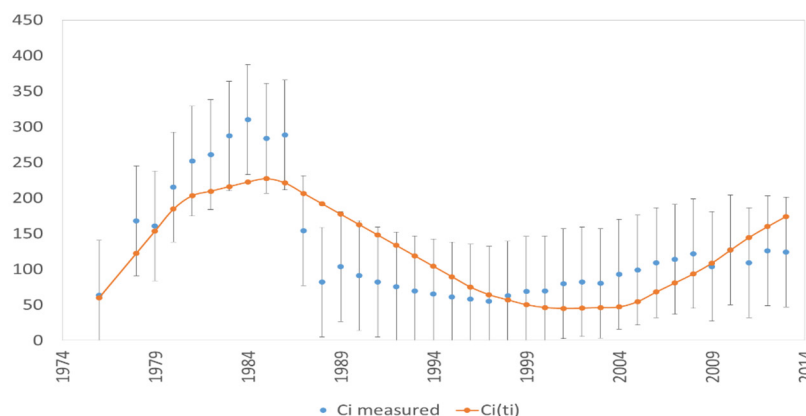


FIGURE 17: Chloride concentrations for well LA-02, measured and simulated, for the period 1975-2013

TABLE 8: Results of the iterative simulation process for well LA-02

	Variable	Unit	1975-1986	1997-2013
V	Volume of production part of geothermal reservoir, or the mixing volume	m ³	1.23×10^9	9.10×10^9
R	Recharge	kg/s	2.89	2.00
ϕ	Porosity of reservoir	-	0.127	0.050

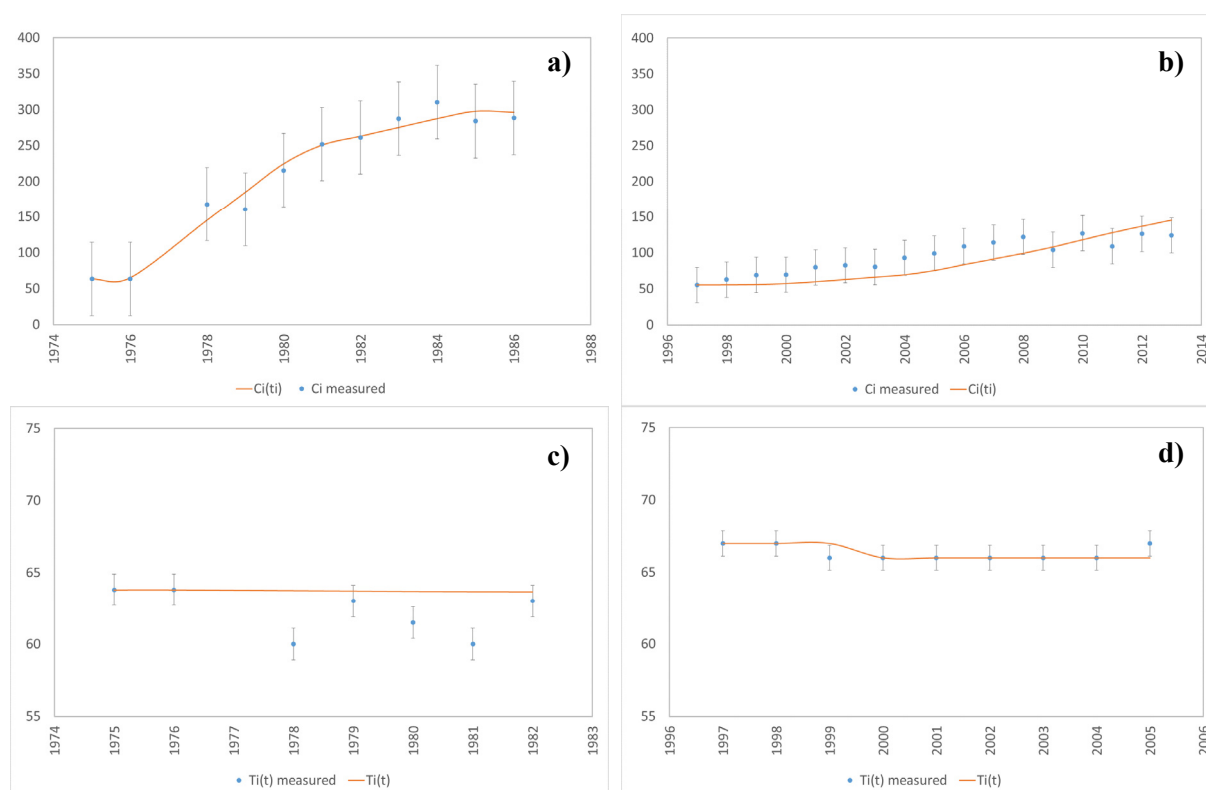


FIGURE 18: Results of the modelling of well LA-02: a) Chloride concentrations (ppm) 1975-1986; b) Chloride concentrations (ppm) 1997-2013; c) Temperature (°C) 1975-1986; d) Temperature (°C) 1997-2013; error bars show the standard deviation of concentrations and temperatures for the respective period

The average production for the period 1976-1986 is 7.91 kg/s, and 5.90 kg/s for the period 1998-2013. Recharge rates correspond to 37% and 34% of the average yield for each period, respectively.

It is of note that the model for the more recent period suggests a greater reservoir volume, as well as a reduction in the estimated porosity and hot system recharge. Reduction in porosity, if it were real, could be associated with depositional processes associated with the super-saturation of species through the intrusion of seawater. The coefficients of determination and correlation to the concentration of chlorides for each of the periods are shown in Table 9.

TABLE 9: Correlation and determination coefficients for measured and simulated chloride concentrations in well LA-02

		1975-1986	1997-2013
Pearson's correlation coefficient	r	0.9865	0.8767
Determination coefficient	r^2	0.9732	0.7686

In well LA-05, for which there are no long periods of disuse, the fluctuations in production levels (0.12-6.20 L/s) prevent a good fit of the model (Figure 19). The production record, concentration and temperature records are, therefore, segmented into two periods, the first 1985-1998, and the second 2001-2013. The results of the simulation for well LA-05 are presented in Table 10 and Figure 19.

TABLE 10: Results of iterative simulation process for well LA-05

Variable		Unit	1985-1998	2002-2013
V	Volume of production part of geothermal reservoir, or the mixing volume	m ³	4.46×10^8	1.15×10^8
R	Recharge	kg/s	6.00	0.7653
φ	Porosity of reservoir	-	0.1173	0.1500

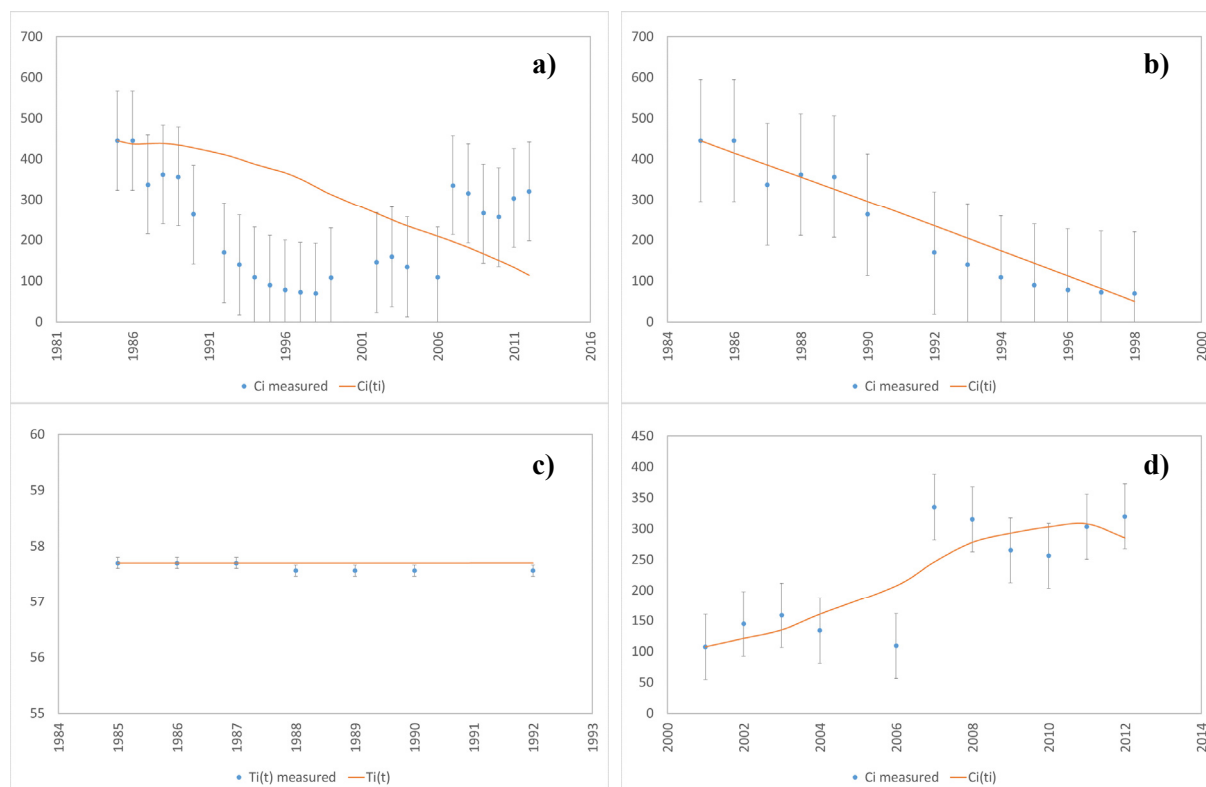


FIGURE 19: Results of the modelling of well LA-05; a) Chloride concentrations (ppm) 1985-2013; b) Chloride concentrations (ppm) 1985-1998; c) Temperature (°C) 1985-1998; d) Chloride concentrations (ppm) 2002-2013; error bars show the standard deviation of concentrations and temperatures for the respective period

The simulation of well LA-05 (Table 11) yields a smaller volume of the producing reservoir, or mixing volume, relative to that estimated for well LA-02. The constant reduction in the chloride content of the fluid in the period between 1986 and 1998 masks the recharge values, and suggests a greater contribution from the hot recharge to the system. However, it must be considered that for the period in question, there was an overall reduction in field production, mainly through well LA-02, which could affect well LA-05 if an interconnection exists between the wells.

TABLE 11: Correlation and determination coefficients for measured and simulated chloride concentrations in well LA-05

		1985-1998	2002-2013
Pearson's correlation coefficient	r	0.9051	0.8258
Determination coefficient	r^2	0.8191	0.6820

The average production from well LA-05, for the period 1986-1998 is 3.4 kg/s, and 1.2 kg/s for the period 2001-2013. Recharge rates correspond to 179% and 65% of the average yield for each period, respectively.

8.2 Predicted temperature and chemical composition changes for well LA-02

The main objective of modelling a geothermal system is to assess its production potential, which can be seriously restricted by changes in temperature and chemical composition. For this purpose, the simulation model parameters: reservoir volume, porosity, recharge and temperature of colder inflow were used to predict future changes in the characteristics of the fluid produced at Sudureyri. The model developed for well LA-02 for the period 1978-1986 reflects closely the concentration and temperature measured; nevertheless, it does not describe the behaviour for the period 1998-2013 as well.

To define future variations in production, the period 1997-2013 was considered for well LA-02. The prediction modelling was performed by assuming constant production for 5, 10 and 15 years. The constant production rates considered corresponded to the average production reported for the period 2012-2013 (8.38 kg/s), a production of 10 kg/s, corresponding to a previously planned expansion in production and a production of 13.21 kg/s, corresponding to the maximum historical production. Also, scenarios of reduced production were evaluated, assuming half the production reported for the period 2012-2013, 4.19 kg/s, (under this scenario, the contribution of the hot recharge would be equivalent to 48% of the production) and the production equivalent to the calculated recharge (2.0 kg/s). The estimated chloride concentration and the predicted behaviour of the fluid are presented in Table 12 and Figure 20.

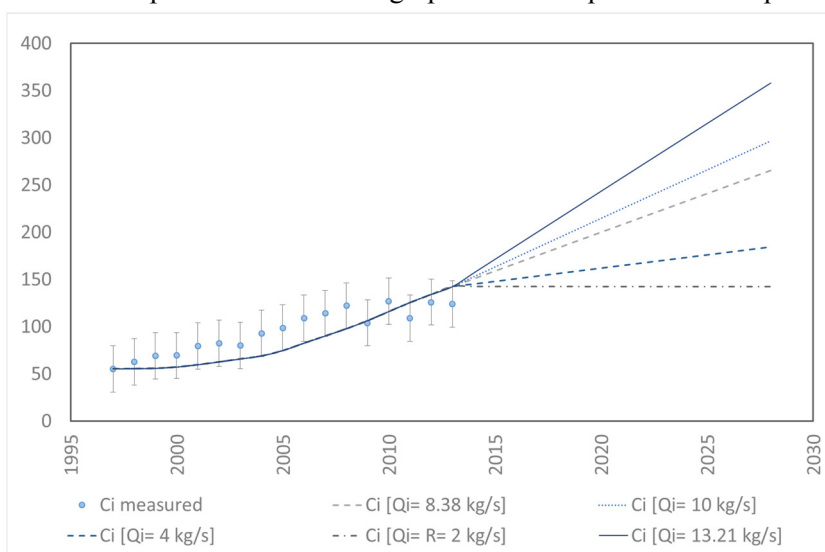


FIGURE 20: Predicted chloride concentrations for well LA-02 for different future scenarios described in the text; error bars show standard deviation in the chloride concentrations for the period 1998- 2013

TABLE 12: Predicted chloride concentrations in well LA-02

Scenarios	$Q_i=13.21$ kg/s	$Q_i=10.00$ kg/s	$Q_i=8.38$ kg/s	$Q_i=4.19$ kg/s	$Q_i=2.00$ kg/s
5 years	215	194	183	156	142
10 years	286	245	224	171	142
15 years	358	296	265	185	142

At a production rate equal to the estimated recharge, no effects are expected, according to the simulated values. For a production equivalent to the production in the period 2012-2013, an increase of 48% in chloride concentrations in the system (to 183 ppm) is expected within five years. Similar values are projected after fifteen years with production of 4.19 kg/s.

It is expected that the maximum values in chloride concentrations, measured during the period 1980-1986 in well LA-02 (approximately 260 ppm, with peak values up to 335 ppm), will be encountered within fourteen years at a production of 8.38 kg/s, within twelve years at a production of 10 kg/s, and within eight years at a production rate of 13.21 kg/s. Such chloride concentrations did precede the discontinuation of well operations in the 1980s. At lower production rates for the modelled scenarios, these chloride concentrations are not encountered, according to the predictions.

Using the correlation between the calcium, sodium and sulphate concentrations and chloride concentration (Equations 3-7, Section 4.3), the predicted concentrations of these species for different scenarios were calculated. The results are presented in Tables 13-15:

TABLE 13: Predicted sodium concentration in well LA-02

Scenarios	$Q_i=13.21$ kg/s	$Q_i=10.00$ kg/s	$Q_i=8.38$ kg/s	$Q_i=4.19$ kg/s	$Q_i=2.00$ kg/s
5 years	140	133	129	120	115
10 years	166	151	144	125	115
15 years	191	169	158	130	115

TABLE 14: Predicted calcium concentration in well LA-02

Scenarios	$Q_i=13.21$ kg/s	$Q_i=10.00$ kg/s	$Q_i=8.38$ kg/s	$Q_i=4.19$ kg/s	$Q_i=2.00$ kg/s
5 years	43	38	35	28	25
10 years	61	51	46	32	25
15 years	80	64	56	36	25

TABLE 15: Predicted sulphate concentration in well LA-02

Scenarios	$Q_i=13.21$ kg/s	$Q_i=10.00$ kg/s	$Q_i=8.38$ kg/s	$Q_i=4.19$ kg/s	$Q_i=2.00$ kg/s
5 years	93.2	90.6	89.2	85.8	84.0
10 years	102.3	97.0	94.4	87.6	84.0
15 years	111.3	103.5	99.6	89.4	84.0

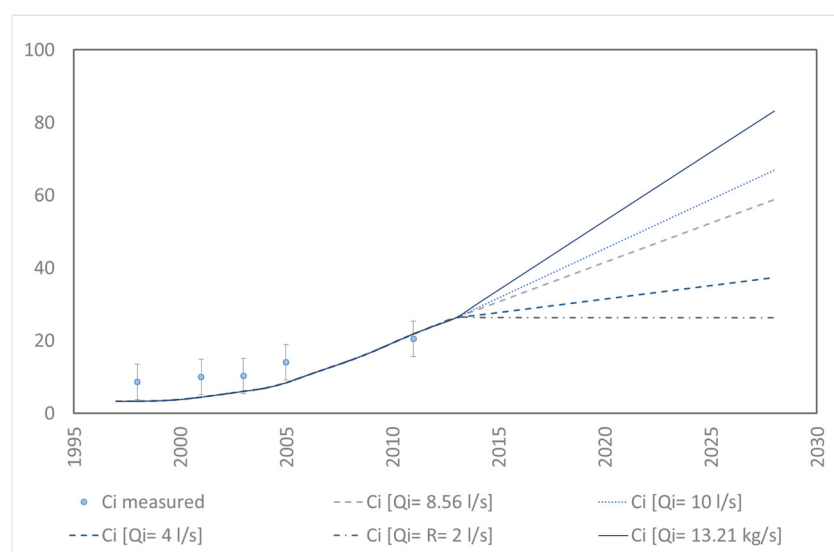


FIGURE 21: Predicted calcium concentration in well LA-02 for different future prediction scenarios

Figure 21 presents the calcium concentration predicted by the simulation model for different future production scenarios. Error bars show the standard deviation in the measured concentration of calcium for the period 1998-2013.

The calculation of the saturation index of calcite requires the activity of the carbonate ion in the system, but this could not be determined, as no correlation has been identified between the concentrations of chloride and the inorganic carbon species. On the other hand, for the determination of the

activities of species, it is necessary to consider all components to properly include the effects of ionic strength.

9. DISCUSSION AND CONCLUSIONS

Systematic changes in the chemical composition of geothermal fluid, during the operation of Hitaveita Sudureyrar, have been associated with an additional recharge of fluid with a high content of sodium, calcium, chloride and sulphate, which are the components that have the most dramatic changes. Given the proximity of producing wells to the coastline, historically the recharge fluid has been considered to be heated seawater. The variations in the properties of the geothermal fluid have posed operational constraints for resource exploitation in Sudureyri, which has led to decreased production and the requirement for backup heating systems.

Production wells, LA-02 and LA-05, operated alternately from 1977 to 1998. The evaluation of the historical behaviour of the fluid during the transition intervals between wells shows similar values in the chemical compositions of the geothermal fluid, and suggests interconnection between the two wells. The historical averages reveal significant differences in the characteristics of the fluids from these wells, associated with temperature and salinity, indicating that well LA-05 has a higher relative contribution of seawater recharge.

Mixing models reveal that seawater recharge to the system interacts with the basaltic bedrock at geothermal temperatures, based on the enrichment of calcium, and loss of magnesium and sodium. Smectite is considered a potential alteration product.

The formation of smectite in the system may explain the magnesium consumption and the partial enrichment of calcium in the fluid. However, the stoichiometric generation of smectite, based on the available magnesium, is not sufficient to explain the measured values. This suggests the potential precipitation of other minerals rich in magnesium, such as magnesium silicates, ion exchange reactions or an additional contribution associated with the dissolution of anhydrite, by the inflow of cold seawater to the system. Mineralogical evaluation, enabling the identification of alteration products formed during the interaction of basalt and seawater, is therefore required.

Simple models were set up to evaluate the properties of the reservoir, on the basis of variations in production, the concentration of chloride and the temperature, for the periods 1975-1986 and 1997-2013 for well LA-02, and the periods of 1985-1998 and 2002-2013 for well LA-05. The models, based on the most recent records, suggest a production volume of the geothermal reservoir for well LA-05 to be 0.1 km³, and for well LA-02 to be 9 km³. The recharge rate for the most recent periods suggests a hot recharge of 0.76 kg/s for well LA-05 and 2 kg/s for well LA-02. These properties, coupled with higher temperature measured in the well, suggest that well LA-02 is located closer to the recharge zone.

By comparing simulation scenarios, the estimated properties of the reservoir for the periods 1976-1986 and 1998-2013, indicate a possible reduction in porosity. This could be a consequence of the reduction in production rates, as a consequence of deposition of minerals such as calcite in the interstitial spaces of the reservoir rock.

Operational limits were assumed for systematic variations in fluid composition, mainly the chloride concentration, based on maximum values measured during the period 1980-1986 in well LA-02 (approximately 260 ppm) which preceded the temporary replacement of the well. These values are predicted to be reached again within 14 years at a production of 8.4 kg/s, 12 years at a production of 10 kg/s, or 8 years at a production of 13.2 kg/s. For lower production rates for the modelled scenarios, these values are not reached. The lumped inflow simulation does not suggest changes in the temperature of the fluid entering the system, despite changes in the composition of the fluid.

The gaps in the existing production records limit the development of a more accurate model, so implementing a more comprehensive and continuous monitoring programme, with the development of resource management tools for greater accuracy, is required.

ACKNOWLEDGEMENTS

My first sincere gratitude is expressed to the United Nations University Geothermal Training Programme (UNU-GTP) and the Government of Iceland for granting me this opportunity. Special thanks go to Mr. Lúdvík S. Georgsson, Director, for his invaluable support during my application process, and to Mr. Ingimar G. Haraldsson, Ms. Málfríður Ómarsdóttir, Ms. Thórhildur Ísberg, Mr. Markús A.G. Wilde, and Ms. María Gudjónsdóttir, for their coordinated assistance during this training.

I extend my gratefulness to my supervisors, Dr. Gudni Axelsson, Mr. Finnbogi Óskarsson and Dr. Thráinn Fridriksson, for guiding me throughout this project and sharing with me their knowledge and experience.

Thanks to my employer, the Ministry of Environment of Natural Resources of El Salvador, for granting me permission to attend this six months course. Special thanks to all the UNU Fellows for the time and shared experiences; it was enjoyable to be with you.

My sincere appreciation goes to Frida and Fernando, for making me feel at home, and to my family and friends, whose names are in the middle of these lines, for their patience and support. And lastly, but most of all, to God, who made everything possible.

REFERENCES

- Arnórsson, S., 1975: Application of the silica geothermometer in low-temperature hydrothermal areas in Iceland. *Am. J. Sci.*, 275, 763-783.
- Arnórsson, S., 1978: Major element geochemistry of the geothermal seawater at Reykjanes and Svartsengi. *Mineral Mag.*, 42, 209-220.
- Arnórsson, S., 2000: *Isotopic and chemical techniques in geothermal exploration, development and use. Sampling methods, data handling, interpretation*. International Atomic Energy Agency, Vienna, 351 pp.
- Arnórsson, S., Andrésdóttir, A., Gunnarsson, I., and Stefánsson, A., 1998: New calibration for the quartz and Na/K geothermometers – valid in the range 0-350°C (in Icelandic). *Proceedings of the Geoscience Society of Iceland Annual Meeting, April*, 42-43.
- Arnórsson, S., and Bjarnason, J.Ö., 1993: *Icelandic Water Chemistry Group presents the chemical speciation programme WATCH*. Science Institute, University of Iceland, Orkustofnun, Reykjavík, 7 pp.
- Arnórsson, S., Gunnlaugsson, E., and Svavarsson, H., 1983: The chemistry of geothermal waters in Iceland II. Mineral equilibria and independent variables controlling water compositions. *Geochim. Cosmochim. Acta*, 47, 547-566.
- Axelsson, G., Jónasson, Th., Ólafsson, M., Egilson, Th., and Ragnarsson, Á., 2010: Successful utilization of low-temperature geothermal resources in Iceland for district heating for 80 years. *Proceedings of the World Geothermal Congress 2010, Bali, Indonesia*, 9 pp.
- Bai Liping, 1991: *Chemical modelling programs for predicting calcite scaling, applied to low temperature geothermal waters in Iceland*. UNU-GTP, Iceland, report 3, 1991.
- Benjaminsson, J., 1981: *Chemical composition of geothermal waters in Vestfirðir*. Orkustofnun, Reykjavík, report OS81010/JHD04 (in Icelandic), 121 pp.

Björnsson, G., Axelsson, G., and Flóvenz, Ó.G., 1994: Feasibility study for the Thelamörk, low-temperature system in N-Iceland. *Proceedings of the 19th Workshop on Geothermal Reservoir Engineering, Stanford University, California*, 5-13.

Flóvenz, Ó.G., Sigurdsson, Ó., and Thórhallsson, S., 1982: *Hitaveita Sudureyrar. Results of exploration*. Orkustofnun, Reykjavík, report OS82123/JHD36B (in Icelandic), 11 pp.

Fournier, R.O., and Potter, R.W., 1982: An equation correlating the solubility of quartz in water from 25° to 900°C at pressures up to 10,000 bars. *Geochim. Cosmochim. Acta*, 46, 1969-1973.

Fridriksson, T., and Ármannsson H., 2007: Application of geochemistry in geothermal assessments. Presented at “Short Course on Geothermal Development in Central America – Resource Assessment and Environmental Management”, organized by UNU-GTP and LaGeo, Santa Tecla, El Salvador, 8 pp.

Frontline Systems, 2014: *Basic solver - GRG nonlinear solving method stopping conditions*. Frontline Systems, website: www.solver.com/content/basic-solver-grg-nonlinear-solving-method-stopping-conditions.

Giggenbach, W.F., 1988: Geothermal solute equilibria. Derivation of Na-K-Mg-Ca geosensors. *Geochim. Cosmochim. Acta*, 52, 2749-2765.

Giggenbach, W.F., 1991: Chemical techniques in geothermal exploration. In: D’Amore, F. (coordinator), *Application of geochemistry in geothermal reservoir development*. UNITAR/UNDP publication, Rome, 119-144.

Gudmundsson, J., and Flóvenz, Ó.G., 1981: Exploration drilling at Laugar in Ségundafjörður 1981. Orkustofnun, Reykjavík, report JSG-ÓGF-81/07 (in Icelandic), 10 pp.

Hardardóttir, V., 2002: *Hitaveita Sudureyrar: Chemical monitoring in 2002 until mid-2003*. Orkustofnun, Reykjavík, report OS-2002/028 (in Icelandic), 5 pp.

Hauksdóttir, S., and Ólafsson, M., 2000: *Hitaveita Sudureyrar: Chemical composition of water from the production well 1999-2000*. Orkustofnun, Reykjavík, report OS-2000/075 (in Icelandic), 10 pp.

Henley, R.W., Truesdell, A., and Barton, P.B. Jr. H., 1984: *Fluid-mineral equilibrium in hydrothermal systems*. Society of Economic Geologists, Reviews in Economic Geology, 1, 267 pp.

Jóhannesson H., and Saemundsson, K., 1999: *Geological map 1:1.000.000*. Icelandic Institute of Natural History.

Marini, L., 2000: *Geochemical techniques for the exploration and exploitation of geothermal energy*. Dipartimento per lo Studio del Territorio e delle sue Risorse, Università degli Studi di Genova.

Ólafsson, M., 1997: *Hitaveita Sudureyrar: Chloride in water from hole LA-05*. Orkustofnun, Reykjavík, report MÓ-97-01 (in Icelandic), 2 pp.

Ólafsson, M., 1998: *Hitaveita Sudureyrar: Chemical monitoring 1997*. Orkustofnun, Reykjavík, report MÓ-98-05 (in Icelandic), 2 pp.

Ólafsson, M., 1999: *Hitaveita Sudureyrar: Chemical composition of water from the production well 1998*. Orkustofnun, Reykjavík, report OS-99011 (in Icelandic), 12 pp.

Ólafsson, M., 2003: *Hitaveita Sudureyrar: Chemical monitoring in 2002 until mid-2003*. Orkustofnun, Reykjavík, report MÓ-2003-07 (in Icelandic), 5 pp.

Ólafsson, M., 2006: *Hitaveita Sudureyrar: Conductivity and chloride concentrations in water from wells 2 and 5 until November 2006*. ÍSOR - Iceland GeoSurvey, Reykjavík, report ÍSOR-06208 (in Icelandic) 5 pp.

Ólafsson, M., 2010: *Hitaveita Sudureyrar: Monitoring of chemical composition of water from production well of district heating 2007 - 2010*. ÍSOR – Iceland GeoSurvey, Reykjavík, report ÍSOR-2010/061 (in Icelandic), 15 pp.

Ólafsson, M., 2014: *Hitaveita Sudureyrar: Monitoring of chemical composition of water from production well of district heating 2012 and 2013*. ÍSOR - Iceland GeoSurvey, Reykjavík, report ÍSOR-2014/005 (in Icelandic), 12 pp.

Óskarsson, F., 2012: *Hitaveita Sudureyrar: Monitoring of chemical composition of water from production well of district heating 2010 and 2011*. ÍSOR - Iceland GeoSurvey, Reykjavík, report ÍSOR-2012/012 (in Icelandic), 15 pp.

Pálmason, G., and Saemundsson, K., 1979: Summary of conductive heat flow in Iceland. In: Cermak, V., and Rybach, L. (eds.), *Terrestrial heat flow in Europe*. Springer-Verlag, Berlin, 218-220.

Seyfried, W., and Bischoff, J.L., 1979: Low temperature basalt alteration by seawater: an experimental study at 70°C and 150°C. *Geochim. Cosmochim. Acta*, 43. 1937-1947.

Stefánsson, V., Sæmundsson, K., and Arnórsson, S., 1975: *Geothermal observations in Súgandaffjörður 1974*. Orkustofnun, Reykjavík, report OS-JHD-7503 (in Icelandic), 7 pp.

Sverrisdóttir, G., and Kristmannsdóttir, H., 1994: *Hitaveita Sudureyrar: Chemical composition of geothermal water*. Orkustofnun, Reykjavík, report OS-94047/JHD-27-B (in Icelandic), 7 pp.

Wang Guiling, 1991: *Modelling of the Urridavatn low-temperature geothermal system in E-Iceland*. UNU-GTP, Iceland, report 12, 40 pp.